Wiley Series in Corrosion

R. Winston Revie, Series Editor

CÉSAR A. C. SEQUEIRA

HIGH TEMPERATURE CORROSION

FUNDAMENTALS AND ENGINEERING



WILEY

High Temperature Corrosion

WILEY SERIES IN CORROSION

R. Winston Revie, Series Editor

Corrosion Inspection and Monitoring · Pierre R. Roberge
Microbiologically Influenced Corrosion · Brenda J. Little and Jason S. Lee
Corrosion Resistance of Aluminum and Magnesium Alloys: Understanding, Performance, and Testing · Edward Ghali
Metallurgy and Corrosion Control in Oil and Gas Production · Robert Heidersbach
Green Corrosion Inhibitors: Theory and Practice · V. S. Sastri
Heterogeneous Electrode Processes and Localized Corrosion · Yongjun Tan
Stress Corrosion Cracking of Pipelines · Y. Frank Cheng
Corrosion Failures: Theory, Case Studies, and Solutions · K. Elayaperumal and V. S. Raja
Challenges in Corrosion: Costs, Causes, Consequences and Control · V. S. Sastri
Metallurgy and Corrosion Control in Oil and Gas Production, Second Edition · Robert Heidersbach
High Temperature Corrosion: Fundamentals and Engineering · César A. C. Sequeira

High Temperature Corrosion

Fundamentals and Engineering

César A. C. Sequeira
Instituto Superior Técnico, Universidade de Lisboa, Lisboa, Portugal

WILEY

This edition first published 2019
© 2019 John Wiley & Sons

All rights reserved. No part of this publication may be reproduced, stored in a retrieval system, or transmitted, in any form or by any means, electronic, mechanical, photocopying, recording or otherwise, except as permitted by law. Advice on how to obtain permission to reuse material from this title is available at http://www.wiley.com/go/permissions.

The right of César A. C. Sequeira to be identified as the author of this work has been asserted in accordance with law.

Registered Office
John Wiley & Sons, Inc., 111 River Street, Hoboken, NJ 07030, USA

Editorial Office
111 River Street, Hoboken, NJ 07030, USA

For details of our global editorial offices, customer services, and more information about Wiley products visit us at www.wiley.com.

Wiley also publishes its books in a variety of electronic formats and by print-on-demand. Some content that appears in standard print versions of this book may not be available in other formats.

Limit of Liability/Disclaimer of Warranty
In view of ongoing research, equipment modifications, changes in governmental regulations, and the constant flow of information relating to the use of experimental reagents, equipment, and devices, the reader is urged to review and evaluate the information provided in the package insert or instructions for each chemical, piece of equipment, reagent, or device for, among other things, any changes in the instructions or indication of usage and for added warnings and precautions. While the publisher and authors have used their best efforts in preparing this work, they make no representations or warranties with respect to the accuracy or completeness of the contents of this work and specifically disclaim all warranties, including without limitation any implied warranties of merchantability or fitness for a particular purpose. No warranty may be created or extended by sales representatives, written sales materials or promotional statements for this work. The fact that an organization, website, or product is referred to in this work as a citation and/or potential source of further information does not mean that the publisher and authors endorse the information or services the organization, website, or product may provide or recommendations it may make. This work is sold with the understanding that the publisher is not engaged in rendering professional services. The advice and strategies contained herein may not be suitable for your situation. You should consult with a specialist where appropriate. Further, readers should be aware that websites listed in this work may have changed or disappeared between when this work was written and when it is read. Neither the publisher nor authors shall be liable for any loss of profit or any other commercial damages, including but not limited to special, incidental, consequential, or other damages.

Library of Congress Cataloging-in-Publication Data

Names: Sequeira, C. A. C., author.
Title: High temperature corrosion : fundamentals and engineering / César A. C. Sequeira.
Description: First edition. | Hoboken, NJ : Wiley, 2018. | Series: Wiley series in corrosion | Includes bibliographical references and indexes. |
Identifiers: LCCN 2018048729 (print) | LCCN 2018049203 (ebook) | ISBN 9781119474425 (Adobe PDF) | ISBN 9781119474449 (ePub) | ISBN 9780470119884 (hardcover)
Subjects: LCSH: Corrosion and anti-corrosives. | Metallurgy. | Electrochemistry.
Classification: LCC TA462 (ebook) | LCC TA462 .S3948 2018 (print) | DDC 620.1/1223–dc23
LC record available at https://lccn.loc.gov/2018048729

Cover design by Wiley
Cover image: Courtesy of César A. C. Sequeira

Set in 10.25/12pt TimesLTStd by SPi Global, Chennai, India

Printed in the United States of America

10 9 8 7 6 5 4 3 2 1

Dedicated to
Maria Elisa,
my eternal wife

Contents

Preface xi

Acknowledgments xvii

1 Introduction 1

1.1 Definition of High Temperature Corrosion 1
1.2 Historical Development 1
1.3 High Temperature Corrosion Phenomena 3
1.4 High Temperature Materials 3
1.5 Corrosive Environments 27
1.6 Films and Scales 31
1.7 Academic Impact of High Temperature Corrosion 33
1.8 Industrial Impact of High Temperature Corrosion 38
1.9 Questions 46
References 46
Further Reading 47

2 Metallurgical Structure and Metals 48

2.1 Imperfections in an Essentially Perfect Structure 48
2.2 Solidification 56
2.3 Alloys 62
2.4 Iron and Steel 72
2.5 Deformation and Recrystallization 79
2.6 Fracture and Fatigue 91
2.7 Questions and Problems 97
References 98
Further Reading 99

3 High Temperature Equilibria 100

3.1 Introduction 100
3.2 Thermochemical Analysis 100
3.3 Electrochemical Analysis 119
References 128
Further Reading 129

4 Lattice Defects in Metal Compounds 130

4.1 Introduction 130
4.2 Defect Reactions 133
4.3 Defect Equilibria 135
4.4 Equilibrium Constants 141
4.5 Questions 144
References 144
Further Reading 145

5 Diffusion in Solid-State Systems 146

5.1 Introduction 146
5.2 General Theory of Diffusion 146
5.3 Diffusion Coefficients 150
5.4 Matano–Boltzmann Analysis 153
5.5 Kirkendall Effect 154
5.6 Darken Analysis 155
5.7 Factors Influencing Diffusion 156
5.8 Impurity Diffusion in Metals 158
5.9 Grain Boundary Diffusion in Metals 158
5.10 Diffusion in Solid Oxides 160
5.11 Morphology of Reaction Products 163
5.12 Measurement of Diffusion Parameters 164
5.13 Questions and Problems 168
References 168
Further Reading 169

6 High Temperature Electrochemistry 171

6.1 Introduction 171
6.2 Electrochemical Nature of Molten Salt Corrosion 171
6.3 The Single Potential of an Electrode 172

6.4 Equilibrium Diagrams 173
6.5 The Tafel Relationship 173
6.6 Corrosion Potential–pO^{2-} Relationship 175
6.7 Electrochemical Polarization and Monitoring 177
6.8 Electrochemical Nature of Metal Oxidation 179
6.9 Usefulness of Electrochemical Cells 181
6.10 Current–Potential Measurements on Solid Electrodes 182
6.11 Simple Concepts of Oxide Semiconductors 183
6.12 Conduction Processes in Ionic Oxides 186
6.13 Common Solid-State Electrochemical Situations 190
References 194
Further Reading 195

7 Oxidation 196

7.1 Introduction 196
7.2 Thermodynamic Considerations 197
7.3 Kinetic Considerations 199
7.4 Defect Structures 201
7.5 Compact Scale Growth 208
7.6 Multilayered Scale Growth 212
7.7 Oxidation Resistance 214
7.8 Oxidation of Engineering Materials 224
7.9 Conclusions 228
7.10 Questions 229
References 229
Further Reading 231

8 Sulfidation 233

8.1 Introduction 233
8.2 The Process of Sulfidation 233
8.3 Sulfidation Kinetics 235
8.4 Sulfidation of Selected Materials 236
8.5 Defect Structures of Metal Sulfides 240
8.6 Questions 243
References 243
Further Reading 244

9 Carburization and Metal Dusting 245

9.1 Introduction 245
9.2 Carburization 245
9.3 Alloy Resistance to Carburization 251
9.4 Metal Dusting Problem 255
9.5 Metal Dusting Mechanisms 256
9.6 Alloy Resistance to Metal Dusting 260
References 262
Further Reading 263

10 Nitridation 264

10.1 Introduction 264
10.2 Nitridation Mechanisms 264
10.3 Nitridation in Industrial Media 265
10.4 Questions and Problems 273
References 274
Further Reading 275

11 Halogenation 276

11.1 Introduction 276
11.2 Metal–Halogen Reactions 277
11.3 Alloy–Halogen Reactions 279
11.4 Laboratory Studies 280
11.5 Conclusions 282
11.6 Questions 282
References 282
Further Reading 283

12 Corrosion by Hydrogen and Water Vapor 284

12.1 Introduction 284
12.2 Corrosion by Hydrogen 284
12.3 Corrosion by Water Vapor 290
12.4 Conclusions 293
References 294
Further Reading 295

13 Corrosion in Molten Salts 296

13.1 Introduction 296
13.2 Corrosion Process 296
13.3 Thermodynamic Diagrams 298
13.4 Corrosion Rate Measurements 299
13.5 Test Methods 299
13.6 Fluorides 303
13.7 Chlorides 304
13.8 Nitrates/nitrites 305
13.9 Hydroxides 309
13.10 Carbonates 309
13.11 Vanadates 312
13.12 Sulfates 314
13.13 Prevention of Molten Salt Corrosion 321
13.14 Summary 321
References 322
Further Reading 324

14 Corrosion in Molten Metals 325

14.1 Introduction 325
14.2 Corrosive Processes 326
14.3 Industrial Liquid Metals 332
14.4 Conclusions 338
References 339
Further Reading 339

15 Hot Corrosion 340

15.1 Introduction 340
15.2 Engine Description and Materials 340
15.3 Early Studies 341
15.4 Mechanisms of Hot Corrosion 349
15.5 Hot Corrosion of Gas Turbine Alloys 351
15.6 Methods of Evaluating Hot Corrosion 354
15.7 Prevention of Corrosion 356
15.8 Conclusions 358
15.9 Questions 358
References 359
Further Reading 360

16 Fireside Corrosion 361

16.1 Introduction 361
16.2 Coal-Fired Boilers 362
16.3 Coal-ash Corrosion 371
16.4 Oil-Fired Boilers 373
16.5 Corrosion in Waste Incinerators 379
16.6 Plant Experience with Fireside Corrosion 380
16.7 Conclusions 388
References 389
Further Reading 389

17 Testing and Evaluation 391

17.1 Introduction 391
17.2 Testing Equipment and Monitoring 392
17.3 Optical Microscopy 394
17.4 Thermogravimetry 395
17.5 Spectroscopy 398
17.6 Diffraction Techniques 402
17.7 Electron Microscopy 409
17.8 Electron Spectroscopy and Ion Scattering 416
17.9 Surface Microscopy 424
17.10 Optical Spectroscopy 428
17.11 Nondestructive Inspection Techniques 439
17.12 Traditional Electrochemical Methods 445
17.13 Nontraditional Electrochemical Methods 453
17.14 Combined Electrochemical Methods 459
References 472
Further Reading 475

18 Protective Coatings 477

18.1 Introduction 477
18.2 Coating Systems 477
18.3 Coating Processes 480
18.4 Coating Degradation 496
18.5 Summary and Future Trends 499
18.6 Questions 500
References 500
Further Reading 501

19 Examples of Engineering Importance 502

19.1 Introduction 502
19.2 Molten Carbonate Fuel Cells 504
19.3 Solid Oxide Fuel Cells 516
19.4 Direct Carbon Fuel Cells 524
19.5 Nuclear Power Plants 531
References 546
Further Reading 549

20 Case Studies 551

20.1 Making Stainless Steels 551
20.2 Corrosion Protection of Turbine Blades 551
20.3 Oxidation of Silicides for VLSI Applications 556
20.4 Naphthenic Acid Corrosion in Petrochemical Plants 560
20.5 Oxidation of Ceramic Matrix Composites 562
20.6 Shell Corrosion of Rotary Cement Kilns 563
20.7 Corrosion of Steels in a Linear α Olefin Plant 564
References 565
Further Reading 565

Appendix A 566

List of Acronyms 591

Glossary of Selected Terms Used in High Temperature Corrosion 596

Author Index 615

Subject Index 629

Preface

The science and engineering of gas–solid, liquid–solid, and solid–solid processes, which can involve high temperature reactions with oxygen, sulfur, nitrogen, carbon dioxide, water vapor, molten sulfates, chlorides, carbonates, vanadates, fluorides, etc., has evolved greatly over the past 50–60 years. Numerous symposia and colloquia have been held on the subject and have been widely attended by researchers from all over the world. One of the many factors enabling advancement of our understanding of the field is the creation and evolution of new, sophisticated instruments and techniques that allow a better analysis of scale compositions and structures.

The numerous details of high temperature corrosion (HTC) have led to thousands of publications over the years and to the writing of only relatively few books on the subject. Moreover, the early books suffered from lack of extensive data on various metals and alloys, the nonexistence of good experimental equipment, and an emphasis on materials that were important in the era in which the books were written. Many universities now have courses on oxidation and other forms of HTC, but the availability of texts continues to be limited. The following books have been very useful:

- N. Birks, G.H. Meier, and F.S. Pettit, Introduction to the High-Temperature Oxidation of Metals, Cambridge University Press, Cambridge, UK (2006).
- E. Fromm, Kinetics of Metal-Gas Interactions at Low Temperature – Hydriding, Oxidation, Poisoning, Springer-Verlag, Berlin, Germany (1998).
- A.S. Khanna, High Temperature Oxidation and Corrosion, ASM International, Materials Park, Ohio, USA (2002).
- P. Kofstad, High Temperature Oxidation of Metals, John Wiley, New York, USA (1966).
- P. Kofstad, High Temperature Corrosion, Elsevier, London, UK (1988).
- G.Y. Lai, High-Temperature Corrosion and Materials Applications, ASM International, Materials Park, Ohio, USA (2007).
- S. Mrowec, Defect and Diffusion in Solids, Elsevier Science Publications, London, UK (1980).
- M. Schütze, Protective Oxide Scales and Their Breakdown, The Institute of Corrosion, John Wiley, Chichester, UK (1997).
- M. Schütze and H.J. Grabke, eds., Metal Dusting, Carburization and Nitridation, EFC 41, Woodhead Publishing Ltd., Cambridge, UK (2006).

The main differences between the present book and the competitive books listed above are:

- None of them cover most of the HTC types (e.g. oxidation, sulfidation, nitridation, molten salts, fuel-ash corrosion, H_2S/H_2 corrosion, molten fluoride/HF corrosion, carburization).
- Many books on HTC concern fundamental studies of material-gas processes. In other words, aspects related to diffusion in HTC oxidation are well treated, but the books provide little engineering data to help engineers make informed material selection decisions.
- The present book covers fundamental science and engineering of HTC, in a balanced way, so that an academic researcher or PhD student or an engineer in industry will find it of interest.
- The present book includes up-to-date information accompanied by more than 1500 references, 80% of which cover the last 25 years.
- The present book includes details on systems of particular engineering importance at this time, namely, on the corrosion of high temperature fuel cells, and nuclear power plants.

- The present book includes an up-to-date summary of experimental methods, many of which have not been covered in earlier books.

The current book has 20 chapters, whose contents are briefly described hereafter.

The first chapter begins to examine historical aspects of the development of HTC. Then, the three key components of the corrosion phenomena frequently encountered in high temperature industrial processes are summarized. In the following sections, materials and their design for use at high temperatures, common and not so common hostile environments at high temperature, and the barriers (films, scales) that separate the material and environment and that, in many situations, are necessary to develop the desired corrosion resistance are presented. HTC occurs behind walls as high temperature processes are usually shielded from their environment. However, it can be lifetime and performance determining in a number of everyday examples, its minimization requiring a proper understanding of the underlying principles of corrosion, which involve plant engineering, metallurgy, chemistry, materials science, system design, or failure analysis. So, the academic and industrial impacts of HTC form the themes of the following sections. In this context, corrosion economics, safety, environment damage, and corrosion management are aspects of particular concern.

Basic high temperature phenomena that require attention are changes in dimensions, microstructures, mechanical properties, and other topics under the heading of physical metallurgy. It is no longer possible to neglect the metallurgical aspects of the corrosion problem. Imperfections in an essentially perfect structure, solidification, alloys, iron and steel, deformation and recrystallization, and fracture and fatigue are described in Chapter 2. It is expected to provide an introduction to physical metallurgy primarily intended for undergraduate students at universities and polytechnics, but, additionally, industrial technicians or engineers will be aided in identifying their in-plant corrosion problems. Seventy-three figures fully support the text, illustrating the fundamental points.

An important tool analysis of HTC problems is equilibrium thermochemistry, which, although not predictive of kinetics, allows to ascertain which reaction products are possible, whether or not significant evaporation or condensation of a given species is possible, the conditions under which a given reaction product can react with a condensed deposit, etc. This standard method of thermochemical analysis is commonly used in metallurgical equilibria involving reactions between a gas and a solid as a function of temperature, and the complexity of the ambivalent oxidation usually dictates that the thermochemical analysis be represented in graphical form. Chapter 3 deals with six types of thermochemical diagrams: Ellingham diagrams, integral free energy–concentration diagrams, vapor species diagrams, stability diagrams for one metal/two nonmetals, 2D stability diagrams for two metals/one nonmetal, and phase stability diagrams for two or more metals. The subject of thermodynamics (or phase equilibria) of metal-fused salt systems in high temperature corrosive environments has been treated in a manner exactly analogous to aqueous solutions by the formation of Pourbaix, i.e. plots of electrode potential (oxidizing potential) versus basicity, being treated in this chapter by constructing and properly detailing an oxidizing potential basicity diagram for iron in molten sodium sulfate.

The lattice of an actual crystal always contains imperfections or defects. Important properties of the crystal, such as diffusion of ions, result from the existence of defects, and, as a consequence, mass transport in the scale formed by oxidation can be explained on the basis of its defect chemistry and crystal structure. An understanding of reaction mechanisms in HTC requires a precise knowledge of defect structures in solids. The growth of a compact or a porous scale, as well as its structure, is largely determined by the presence of the lattice defects. This is analyzed in Chapter 4 on lattice defects in metal compounds. The considered topics include point defects and defect structures, defect reactions and relevant examples, defect equilibrium constants and their significance for defect reaction including electronic imperfections.

Besides its scientific interest, diffusion is of enormous practical relevance for industry and life, ranging from steelmaking, growth of oxide scales, sintering, and high temperature creep of metals to oxide/carbon dioxide exchange in the human lung. Chapter 5 is confined to diffusion in condensed matter, namely, in metals, binary alloys, and oxides. Emphasis is on very basic fundamental aspects, the contents being roughly characterized by the headings general theory of diffusion, diffusion coefficients, Matano–Boltzmann analysis, Kirkendall effect, Darken analysis, factors influencing diffusion, impurity diffusion in metals, grain boundary diffusion in metals, diffusion in solid oxides, morphology of reaction products, and measurement of diffusion parameters. The chapter includes many references for readers at the forefront of the subject; it is primarily intended for graduate students and corrosion scientists.

Many studies from both theoretical and experimental viewpoints and fundamental approaches made along the last 70 years suggested, with sufficient credibility, electrochemical mechanistic models for the observed corrosion at high temperature. Thus, the chemical reactions established at solid–solid, solid–liquid, and solid–gas interfaces during the growth of corrosion products can be visualized as oxidation–reduction electrode processes; in other words, it is acceptable that high temperature oxidation, sulfidation, halogenation, nitridation, carburization, and molten salt

corrosion are processes of electrochemical nature. In Chapter 6, basic aspects of traditional electrochemistry, solid-state electrochemistry, and molten salt electrochemistry are described to show how HTC can be further understood and mitigated. Headings include electrochemical nature of molten salt corrosion, the single potential of an electrode, equilibrium diagrams, the Tafel relationship, corrosion potential–pO^{2-} relationship, electrochemical polarization and monitoring, electrochemical nature of metal oxidation, usefulness of electrochemical cells, current–potential measurements on solid electrodes, simple concepts of oxide semiconductors, conduction processes in ionic solids, and common solid-state electrochemical situations. The chapter is primarily intended for graduate students and corrosion scientists.

Oxidation is an important HTC phenomenon. Metals or alloys are oxidized when heated to elevated temperatures in air or in highly oxidizing environments, such as combustion atmospheres with excess air or oxygen. Many metallic components are subject to oxidation in engineering applications. Starting in 1933, a number of very significant contributions to the theory of oxidation of metals in alloys were published by Wagner, which still form the most comprehensive theoretical basis even in today's discussion of the mechanisms of HTC. There have been quite a number of other pioneering papers in the field that can, however, not be quoted here due to space limitations. Chapter 7 summarizes the main factors for determining the nature and extent of gas–metal reactions that are of paramount importance to understand the subject. In this context, the following topics are analyzed: thermodynamic considerations, kinetic considerations, defect structures, compact scale growth, multilayered scale growth, oxidation resistance, and oxidation of engineering materials. Recent hot topics such as metallurgical factors affecting alloy oxidation, early stages of oxidation and the nature of metal–oxide interface, secondary effects during oxidation in dry environments, and accelerated degradation in the presence of molten oxidants are also underlined in this chapter. The information is primarily intended for students and industrial scientists and engineers.

Hot combustion atmospheres derived from fuels containing sulfur, as in superheaters, heat exchangers, gas turbines, etc., are a source of concern due to the interaction between metals and alloys and hydrogen sulfide, sulfur dioxide, sulfur trioxide, or elemental sulfur itself. Interaction with sulfur dioxide (and/or trioxide) may produce scales consisting of the oxides alone, or oxide plus sulfide, or even sulfate, but, in Chapter 8, the reactions that led to the formation of sulfide scales on metals and alloys only will be considered. The chapter is mainly confined to a brief theoretical consideration of the sulfidation behavior of metals and alloys, discussing the basic phenomena involved in the process. Accordingly, first, an overall picture of the sulfidation process is given, which is more amplified in three further sections concerning the kinetics of sulfidation of metals, the sulfidation behavior of alloys, and the defect structure of metal sulfides.

Chapter 9 deals with carburization and metal dusting. Carburization involves the formation of internal carbide precipitates, occurring in the cracking tubes used in ethylene and other olefin plants, in the heat treatment of components associated with carburizing furnaces, and for reformer tubes used in the steam reforming of natural gas. Metal dusting is a catastrophic carburization that occurs at temperatures of 430–900 °C when a process gas stream consists primarily of H_2/CO and CO_2 along with some hydrocarbons with high carbon potentials. This chapter describes the mechanisms of carburization and metal dusting and poses practical problems, discussing solutions, on the alloy resistance to carburization and metal dusting. It is a valuable informational resource for industrial scientists and engineers.

Chapter 10 gives a brief review on nitridation, a process that results in the formation of nitrides in a material. It results from exposure to reducing high temperature environments with high nitrogen activity. Since nitrides are inherently hard, brittle phases, nitridation can produce local or widespread loss of material strength and possible metal wastage. In the present review, information on nitridation mechanisms and nitridation in industrial media will be found.

Halogens and many halogen compounds are very corrosive. Hence, materials for containing and handling halogens and corrosive halogen compounds must be selected with particular care. In Chapter 11, oxidation and corrosion theories are applied to the problems of destructive metal and alloy halogenation. Metal–halogen and alloy–halogen reactions and many laboratory studies are reviewed.

The effect of water vapor on the oxidation behavior of metals and alloys at high temperature has been summarized in many recent reviews. Hydrogen is also a gas that causes serious industrial problems, particularly in refinery vessels and other high temperature equipment, many times associated with water and/or water vapor. Steels, carbon, and Cr–Mo steels, low-alloy steels, and other materials can suffer hydrogen attack or hydrogen damage at high temperature, which results in rupture failures of steel components and/or microfissures in boiler tubes and other industries. The purpose of Chapter 12 is to provide a brief discussion of the corrosion reactions involving H_2 and/or H_2O, which are a really important subject of HTC. At first, particular attention is given to the concept, mechanism, detection, and prevention of corrosion by hydrogen; hydrogen damage in coal-fired boilers and petroleum refining is shown to be a serious issue when the water chemistry is not properly controlled under normal operating conditions. In the

subsequent section, the corrosion by water vapor is considered. The kinetics and mechanisms of oxidation are analyzed by using concepts of solid-state chemistry focused on the themes of proton incorporation, volatility of metal hydroxides, and plasticity of oxide scales. The chapter is primarily intended to graduate students and industrial scientists and engineers.

Interest in the use of molten or fused salts in industrial processes is being accelerated by the increasing demand for the production of refractory metals, actinides, lanthanides, and transition and light metals by processes involving fused salts, by the use of molten salts in high temperature batteries and fuel cells, and also by the novel chemical engineering techniques that have been developed in the nuclear energy industry. Chapter 13 focuses on key aspects of molten salt corrosion processes and on corrosion data useful in selecting high temperature materials. Corrosion processes, thermodynamic diagrams, corrosion rate measurements, test methods, electrochemical studies on fluorides, chlorides, nitrates/nitrites, hydroxides, carbonates, vanadates, and sulfates, as well as prevention of molten salt corrosion, are the considered topics.

The corrosion behavior of metals, alloys, and ceramics in liquid metals is a complex problem involving simple dissolution (chemical corrosion), electron transfer processes (electrochemical corrosion), physical erosion (when there is a swift flow of melt relative to the surface of the solid), fouling, embrittlement, and stress corrosion, and these phenomena have a real impact on many industrial applications. Chapter 14 discusses several types of corrosive attack of materials by liquid metals, namely, simple dissolution, alloying between liquid metal and solid metal, intergranular penetration, impurity reactions, temperature-gradient mass transfer, and concentration-gradient mass transfer. Then, interactions of important engineering materials with molten aluminum, zinc, lead, lithium, sodium, magnesium, mercury, and other metals are reported.

Many very important engineering systems operating at high temperatures (650–1100 °C) involve contact of metallic or ceramic materials with combustion product gases or other oxidizing gases containing inorganic impurities, namely, gas turbines, steam generators, incinerators, and numerous petrochemical process vessels. As the gases are cooled, corrosive fused salt films may condense on the hardware to generate an accelerated degradation known as hot corrosion. A wealth of literature exists on the kinetics of hot corrosion and on the resulting microstructures. The solubilities of oxides and their dependencies on melt basicity and oxygen activity constitute important information to interpret hot corrosion mechanisms. Chemistry, electrochemistry, phenomenology, and experimental work all aid in the interpretation of hot corrosion of metals. In Chapter 15, the hot corrosion of gas turbines is particularly studied. The gas turbine engine is described, and its main materials and corrosiveness are noted. Early studies of the phenomenon and the alloy–Na_2SO_4 reactions are reviewed. The mechanisms of hot corrosion, with particular reference to acidic and basic fluxing, are analyzed. Hot corrosion of gas turbine alloys, methods of evaluating hot corrosion, and its prevention are subjects also discussed.

High temperature fireside corrosion is best outlined by admitting the presence of molten or semi-molten deposits. Obviously, corrosion is affected by transport processes across deposits and by reactions occurring at gas-deposit interfaces and deposit-metal surfaces. The presence of a molten phase is a sufficient prerequisite to stimulate both transport processes and heterogeneous reactions, providing a more intimate contact between metal and corrodents. An additional factor is the presence of SO_3, which, besides stabilizing the physical state of deposits, enhances corrosion by increasing the metal oxide solubility in the molten phase and, acting as oxygen carrier, by increasing the oxidizing power of deposits. It is the aim of Chapter 16 to briefly delineate mechanisms, remedies, materials problems, and other current views related with this field of coal-ash corrosion, oil-ash corrosion, and vanadic corrosion, which is encountered in coal-fired boilers, oil-fired boilers, and waste incinerators. The chapter also includes a brief summary of industrial experience on fireside corrosion in Denmark, Germany, Holland, the United Kingdom, and Japan.

Chapter 17 covers a large number of surface analytical and electrochemical techniques used for HTC science and engineering. The surface analytical techniques provide the necessary information on the surface chemical composition, structure, topography, defects, and mechanical and electronic properties, in close relationship with the kinetic data on corrosion that are obtained by electrochemical techniques. Topics are focused on testing equipment and monitoring, optical microscopy, thermogravimetry, spectroscopy, diffraction techniques, electron microscopy, electron spectroscopy and ion scattering, surface microscopy, optical spectroscopy, nondestructive inspection techniques, traditional electrochemical methods, nontraditional electrochemical methods, and combined electrochemical methods. Well-established techniques such as AES, TEM, and EIS and many newer techniques such as GDOES, FTIR, solid-state voltammetry, ellipsometry, electrochemical quartz crystal microbalance, and electrochemical noise analysis are discussed. Extensive references and 80 figures aid the study of this essential subject. The chapter is of primary interest to university students and researchers, industrial scientists, and engineers.

There are many measures to protect the materials against their degradation at elevated temperatures, but the great stringent requirement of high temperature strength and corrosion resistance is a composite system in which

mechanical strength is achieved by alloy development and corrosion resistance by surface coating or surface modification. Corrosion and oxidation protective coatings work by forming a thin oxide barrier on the surface, which is extremely thin, able to reform the oxide coat should some of it become damaged due to cracking, spallation, etc. Chapter 18 briefly deals with diffusion, overlay and thermal barrier coatings, and processes for their application, which are available for protection. These include chemical vapor deposition, pack cementation, out-of-pack cementation, physical vapor deposition, plasma spraying, high velocity oxygen/fuel, and other coating processes. Brief considerations on coating degradation and present and future applications are also described.

Among the various industries in which HTC is a widespread problem, the energy arena involving (i) the study of processing and properties of high temperature materials and (ii) the experimental observations to predicting behavior, from scientific principles to engineering design and from atomic scale models to performance while in use, constitute the aim of Chapter 19 as described for two types of energy technologies: advanced energy conversion sources, and more precisely, high temperature fuel cells, and nuclear power plants. The first section presents the operating principles of a molten carbonate fuel cell (MCFC) and then analyzes corrosion issues in the anode materials, cathode materials, electrolyte and matrix, wet seal, bipolar current collectors, and hardware materials. Future directions of MCFCs are also included. The second section deals with the solid oxide fuel cell, describing the cell and concentrating on the interconnect-related corrosion issues, and protective coatings for metallic interconnects. The third section describes direct carbon fuel cells (DCFCs), giving particular attention to the various types of DCFCs, and their corrosion issues. The last section moves to the theme of nuclear power plants. The nuclear renaissance is highlighted, as well as recent nuclear reactor types. Advanced materials for nuclear reactors, and corrosion in nuclear applications, are also discussed.

Chapter 20, the last chapter, is a collection of case histories or practical solutions adapted from recent literature on practical and fundamental problems that have been analyzed and subsequently solved using relatively innovative approaches. The following seven cases are examined: making stainless steels, corrosion protection of turbine blades, oxidation of silicides for VLSI application, naphthenic acid corrosion in petrochemical plants, oxidation of ceramic matrix composites, shell corrosion of rotary cement kilns, and corrosion in a linear alpha olefin plant. These solutions span a wide range of industrial problems frequently encountered in a variety of high temperature environments.

It is the experience of the author that the material in this book can serve as a basic textbook for a two-semester MSc course. It provides enough information for the students to understand the underlying principles of HTC and to carry out some laboratory work when the instructor is posing more practical problems, then discusses solutions, refers some of the extensive references contained in the book, and teaches basic techniques as described in Chapter 17. Any industrial scientist or engineer whose work involves material selection, system design, process operations, or failure analysis will find this book to be a valuable educational and information resource.

The author has received his education in universities in Europe and North America and has a combined experience as teacher and researcher in the fields of corrosion and electrochemistry of over 40 years. The present book is a product of this experience.

Lisbon, August 2017 CÉSAR A. C. SEQUEIRA

Acknowledgments

I cannot adequately express my gratitude to my wife, Maria Elisa, whose crucial efforts and encouragement played the greatest role in sustaining me through the challenge of writing this book. Even during her prolonged sickness she was a permanent light driving my way. Our children, Jorge Augusto, César José, Rita Alexandra, and Catarina also deserve my appreciation for their help and understanding.

I am particularly grateful to Winston Revie that invited me to consider writing a book in the Wiley Series of Corrosion, for which he is the Series Editor. From the moment I prepared a detailed outline of this book, he gave me his full support, including numerous and helpful suggestions and comments, and timely critiques helping me to enhance and preserve the quality of the chapters. Grateful appreciation is also expressed to Bob Esposito and his staff at John Wiley & Sons, Inc. in Hoboken, NJ, for their patience and permanent support. Finally, I would like to acknowledge Maria da Glória Dias. Along this great enterprise, not so she processed the book with excellence, but she also assisted me in many ways to bring the enterprise to a successful conclusion.

Lisbon, August 2017 CÉSAR A. C. SEQUEIRA

Chapter 1

Introduction

1.1 Definition of High Temperature Corrosion

The term *corrosion* has its origin in Latin. The Latin term rodere means "gnawing" and corrodere means "gnawing to pieces." The term *high temperature* means always temperatures high enough that water, when present in the corrosive environment, will be present as the vapor rather than the liquid. In contrast to room temperature corrosion, high temperature corrosion (HTC) is characterized by high rates of the formation of corrosion products and strong material degradation.

The subject of HTC is capable of extensive investigation and theoretical treatment. It is normally found to be a very satisfactory subject to study. The fundamental treatment covers a wide range of materials science, chemical, and physical principles and can be approached by people of a wide range of disciplines who, therefore, complement each other's efforts. The subject of HTC is also of considerable engineering interest, because there are many traditional and engineering industries that face HTC problems.

It is rather interesting to start this introduction by examining the main historical aspects of the developments of HTC.

1.2 Historical Development

The attainment of high temperatures has been important in the development of civilization for many centuries. Fired ceramics, extraction of metals from their ores, and the development of casting, forging, and the optimization of metal properties by heat treatment are all high temperature processes of considerable antiquity. However, the high temperatures were contained by refractories, and in use most metals saw only modest temperatures. This began to change with the industrial revolution. The first heat engines introduced at the end of the eighteenth century were large steam pumps to remove water from deep mines, and these operated at fairly low temperatures. However, the desire for improved efficiency pushed boiler temperatures progressively higher, first to develop engines for power production in factories and then for locomotives. Today, the main steam temperatures in advanced utility boilers are about 650 °C, with the outer surface of the heat exchangers in contact with the combustion gases perhaps 50 °C higher. In Europe, Japan, and the United States, plans are now afoot to raise the main steam temperature to perhaps as high as 800 °C.

The introduction of the internal combustion engine in the late nineteenth century introduced the need for materials capable of operating for long times exposed to high temperature combustion gases without noticeable surface damage, in particular the exhaust valves, which are difficult to protect by cooling. Again, as part of the drive for higher efficiencies and higher specific power outputs, the idea of supercharging was introduced, and the most common method was the turbocharger. The conditions to which the small turbocharger rotor was exposed resulted in the development of a class of castable high temperature alloys, of which Co–10% Ni–35% Cr–7, 5% W–0.5% C is an example. The introduction of electricity as a major energy source at the beginning of the twentieth century led to the development of electric heating for industrial systems, and the problems of producing a wire capable of forming a radiant heater with a surface temperature of the order of 850 °C became a major challenge, which was solved by the development of Ni 20% Cr alloys, which can be drawn into wires, but which have adequate creep strength and good oxidation resistance at the desired use temperature.

The next major challenge was the introduction of the aviation gas turbine in 1940 in Germany and the United Kingdom, and this continues to be the pacing technology for the development of high temperature alloys to this day. For this application, it becomes difficult to reconcile alloy design demands for adequate high temperature mechanical properties and those for adequate corrosion resistance, and this has led to a separation of these functions. An alloy with good mechanical properties and perhaps marginal

High Temperature Corrosion: Fundamentals and Engineering, First Edition. César A. C. Sequeira.
© 2019 John Wiley & Sons, Inc. Published 2019 by John Wiley & Sons, Inc.

corrosion resistance is protected by the application of a coating that has excellent corrosion resistance but marginal mechanical properties. A further complication is that the turbine inlet temperatures have now risen to over 1350 °C, while the intrinsic strength capability of the best alloys currently available hardly exceeds 1000 °C. This is handled by cooling the hot components, but the formation of the cooling passages places further demands on the castability of the high temperature alloys.

All of these high temperature applications of metals and alloys demand materials that have a variety of properties such as strength, toughness, fatigue resistance, creep resistance, formability, and not least resistance to degradation by reaction with the environment. Essentially all potential metallic materials are unstable in these high temperature environments, and the various oxidation processes are highly exothermic. The only reason it is possible to have materials that can be used at all is that the reaction product – the oxide – forms a "protective layer" on the component surface, and it is the ways in which this is possible that form the basis of the science of high temperature oxidation and corrosion resistance. Here, the term oxidation is associated with corrosion because in most aggressive high temperature environments, oxidation often participates in the HTC reactions, regardless of the predominant mode of corrosion. In fact, alloys often rely upon the oxidation reaction to develop a protective scale to resist corrosion by other forms of high temperature attack, and so it can be said that oxidation is the most important HTC reaction but, strictly speaking, high temperature oxidation is only one type of HTC.

The first paper that expressly addressed high temperature oxidation was that by Gustav Tammann in 1920. He enumerated the "parabolic law," i.e. the rate of oxidation of metal decreases as oxide layer thickness increases. In 1922 he established the logarithmic law of oxidation of metals. However, the first paper that lays out the basics of the problem as we know it was that by N.B. Pilling and R.E. Bedworth in 1923. They defined "high temperature" as that at which the transport of the reactive components through the protective layer was the principal determinant of the reaction rate (as opposed to the situation in aqueous corrosion processes at close to ambient temperatures). They showed that under these circumstances it could be expected that the rate of reaction would diminish as the protective scale thickened, leading to a "parabolic rate law." They also highlighted the problems associated with forming an adherent crack-free protective oxide layer on the oxidizing surface because of the volume changes associated with the oxidation process. The discussion to this seminal paper shows that others were thinking along similar lines at the time. Six years later, Leonard B. Pfeil introduced the concept of movement of metal outward rather than oxygen inward into the oxide layer, and in 1934 Portevin, Prétet, and Jolivet carried out extensive studies on the oxidation of iron and its alloys. At the same time, the discovery that oxides contained lattice defects and that the transport processes within them are determined by the motion of these defects allowed a more quantitative approach. This was recognized by Carl Wagner, who produced an important body of work over the course of the next twenty years largely defining how we now look at the basic theory of the bulk transport processes in oxides. Of significance was the derivation of Wagner's equation by Hoar and Price in 1938. In recent years, however, the recognition that in many cases the transport processes involve short-circuit paths, such as grain boundaries, has introduced further complications into this elegant picture.

The problem of the integrity of the protective oxide was not part of Wagner's contribution, and its practical solution for the high temperature alloys that were developed for the applications mentioned above was discovered essentially by accident in the early 1940s. It was found that very small amounts of what are now called "reactive elements" added to the alloys introduced a remarkable improvement in the apparent integrity of the protective oxide, particularly in its resistance to thermal cycling. The reasons for this effect are still a matter of considerable debate.

Other important contributions in the 1939–1948 period were those of Cabrera and Mott, postulating that oxide film growth is controlled by ions jumping from site to site over intervening energy barriers. Mott's theory was then highly criticized by Karl Hauffe that performed significant work on the oxidation of alloys. During the 1920–1940 period, other relevant studies on oxidation at high temperature deserve reference: these are the interference method of obtaining thickness of oxide films (Tammann 1920–1926), the spectroscopic method to obtain thickness of oxide film (Constable 1927), and the X-ray and electron diffraction methods to study oxide films (Finch Quarrell 1933).

The earliest treatments of oxidation problems considered simple systems, with a single oxidant (usually oxygen) and a pure metal, although in practice high temperature-resistant materials were always alloys. More recently, approaches such as in multicomponent diffusion theory have been applied, and the growth of oxides on polyphase materials has been analyzed. These approaches have been greatly assisted by the development of modern characterization techniques.

In recent years, the problem of HTC in relatively complex environments, such as mixed gases with low oxygen activities but significant carbon or sulfur activities, or environments in which molten alkali salts may be deposited on the alloy surface, has become of much greater importance. Theoretical models for some aspects of these situations have been developed, but they are still not fully understood. Many challenges still exist!

In view of the practical importance of this area, and the intellectual problems it presents, it is not surprising that an enormous amount of published literature on fundamentals and engineering of HTC has been produced. Research activities, case histories, practical solutions, etc. have been published over the last 50 years by well-known scientists and engineers, whose names can be listed below:

C.B. Alcock	B.K. Gupta	J.R. Nichols	J. Stringer
A. Atkinson	M.G. Hocking	E.J. Opila	J.B. Wagner, Jr.
J. Bénard	B.E. Hopkins	F.S. Pettit	D.P. Whittle
N. Birks	A.S. Khanna	B.A. Pint	G.C. Wood
N.S. Bornstein	P. Kofstad	J.W. Quadakkers	
M.A. Decrescente	O. Kubaschewski	A. Rahmel	
F. Gesmundo	G.Y. Lai	R.A. Rapp	
B. Gleeson	E. Lang	M. Schütze	
J.A. Goebel	G.H. Meier	J.L. Smialek	
G.W. Goward	S. Mrowec	K.E. Stern	
H.J. Grabke	K. Natesan	K.N. Strafford	

Clearly, the list is by no means exhaustive, and there are an extensive number of other international authorities from leading academic and nonacademic organizations that have provided novel and relevant aspects on HTC. All this experience has been extremely rich to the current state of knowledge on HTC.

1.3 High Temperature Corrosion Phenomena

Failure of construction elements in high temperature applications can be due to interaction of the environment with the material, resulting in loss of protection and subsequent accelerated degradation, or to accidental overheating due to poor process control. Both oxidizing and reducing environments can exist at high temperature, and both can lead to HTC. Depending on the oxygen activity of the environment, one or other mode of HTC may predominate. Apart from oxidation, which is the most predominant HTC reaction, sulfidation, carburization, hydrogen attack, halide attack, and molten salt and molten metal attack are also important modes of HTC. More peculiar phenomena such as metal dusting, hot corrosion, green rot, *black plague*, pesting, phase changes, etc. can occur during high temperature service, which can be responsible for component failures.

During exposure of high temperature-resistant materials, in many cases a *scale* is produced from corrosion products that protects the underlying metal against further attack. If the integrity of the film is impaired by blistering, shear cracking, or flaking of the scale or if the scale is dissolved or volatilized, the corrosive atmosphere has free access to the metal surface and corrosion will continue in some cases with very high rates of corrosion.

It is clear from the preceding considerations and those from Section 1.2 that the HTC system is mainly composed of a material at high temperature, an aggressive or hostile environment, and a film or scale that is the corrosion product of the material–environment interaction. It is necessary to understand both the characteristics of each key component of the HTC system and the interactions between the components. This is really the main objective of this book. In the next sections, beginning considerations are described about materials and their design for use at high temperatures, common and not so common hostile environments at high temperature, and the barriers (films, scales) that separate the material and environment and that in many situations are necessary to develop the desired corrosion resistance. These three key components of the HTC system, which are more frequently encountered in various industrial processes, are summarized schematically in Figure 1.1.

1.4 High Temperature Materials

The operation of materials in high temperature application involves unusual constraints not seen in other application.

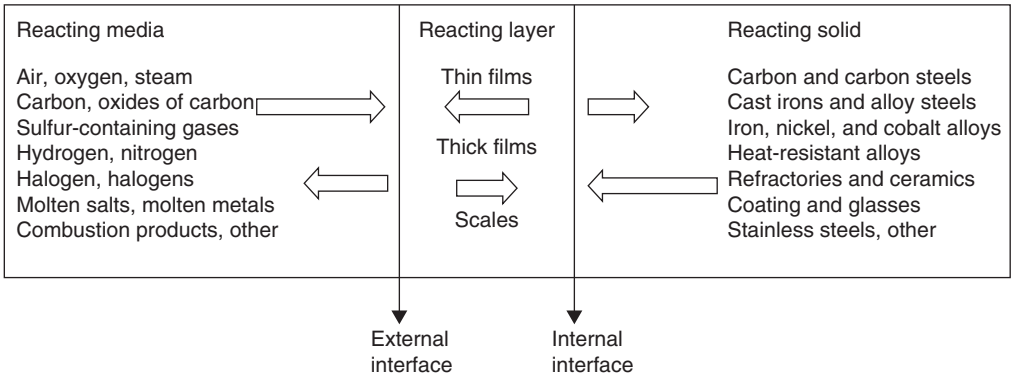


Figure 1.1 Key components of the HTC system.

High melting point, high Young's modulus, good creep resistance and high temperature strength, and microstructure stability at high temperature are requirements of the mechanical properties of the material that need to be met. Additional criterion for material selection at high temperatures is to meet the requirements of the chemical properties of the material. These include materials with very low rates of corrosion at the temperature of interest, or that form thin, slow-growing scales that are impervious to the environment, or that form protective scales strongly resistant to the aggressive environment. In many situations, the material cannot be tailored to meet simultaneously the structural capability requirement to carry load and the requirement for corrosion resistance. The overall protection requires the use of coatings that provide barriers between the alloys and the outer environment.

A rough hierarchy of common engineering alloys for high temperature service would include the following:

- Low-alloy steels, which form M_3O_4 (M = Fe, Cr) surface layers, are used to temperatures of about 500 °C.
- Titanium-based alloys, which form TiO_2, are used to about 600 °C.
- Ferritic stainless steels, which form Cr_2O_3 surface layers, are used to about 650 °C. This temperature limit is based on creep properties rather than oxidation rate.
- Austenitic Fe–Ni–Cr alloys, which form Cr_2O_3 surface layers and have higher creep strength than ferritic alloys, are used to about 850 °C.
- Austenitic Ni–Cr alloys, which form Cr_2O_3 surface layers, are used to about 950 °C, which is the upper limit for oxidation protection by chromia formation.
- Austenitic Ni–Cr–Al alloys, aluminide, and MCrAlY (M = Ni, Co, or Fe) coatings, which form Al_2O_3 surface layers, are used to about 1100 °C.
- Applications above 1100 °C require the use of ceramics-, nickel-, and cobalt-based superalloys or refractory metals. The latter alloys oxidize catastrophically and must be coated with a more oxidation-resistant material, which usually forms SiO_2.

Although most engineering alloys are known by their popular names that were derived from their trade names, all alloys have very specific names or numbers. One of the most important designations is the unified numbering system (UNS) number. Other designations such as ASTM, SAE, ASME, AWS, etc. are also widely used to designate wrought products, castings, and weld filler metals. Cross-references between the different specifications of the American, British (BSI), Japanese (JIS), and German (DIN) systems are published (Bringas 1993).

In many respects, the behavior of a material reflects its chemical nature, particularly the dominant type of chemical bonding that holds its atoms and molecules together. Chemical bonds fall into two categories, primary and secondary.

The primary bonds involve some type of transfer of electrons, from one atom to another. Due to this transfer, some atoms become positively charged, and some become negatively charged. The atoms with opposite charge are then attracted to each other, producing primary bonds that are very strong. There are three different *primary bonds*: *metallic*, *ionic*, and *covalent*. Metallic bonding is nondirectional, and so it allows ready movement of dislocations, producing the ductile behavior that is characteristic of metals. Covalent bonding is highly directional, leading to the brittle behavior that is characteristic of many ceramics.

The *secondary bonds* cause attractions even when there is no overall charge. Neutral atoms or molecules may have a dipole, a distribution in charge within the atom or molecule. These dipoles provide for bonding between neutral atoms or molecules when a positive dipole on one molecule is attracted to the negative dipole on an adjacent molecule, producing a secondary bond. Water molecules have permanent dipoles, and the resulting bonds are called *hydrogen bonds*. Even molecules without permanent dipoles may develop temporary distributions in charge, which produce *van der Waals bonds*. Both types of secondary bonds are much weaker than the primary bonds, and the van der Waals bonds are weaker than the hydrogen bonds. These bonds are especially important in organic polymers, including wood.

A material whose chemistry is dominated by primary bonds is strong and stiff, while a material dominated by secondary bonds is weak. Thus, it is important to consider the chemical composition and bonding in engineering materials in order to gain a general understanding of the mechanical properties, strength, and stiffness. Deterioration of materials often involves specific chemical reactions with constituents in the environment, so the chemical composition is also important in order to understand the durability of these materials.

There is one other aspect of a material that influences its behavior: this is the *microstructure*. Microstructure refers to the way that individual constituents are arranged inside the material. A material may be porous or dense. A constituent may be small or may be large and easily recognized without the assistance of a microscope. Likewise, a constituent may be well dispersed throughout a material or may be clustered. The microstructure of a material often depends on how the material was processed, whether cooled from a molten state or formed by some chemical reaction between a solid and a liquid. The microstructure itself often depends on the chemical composition. Some compounds occur with characteristic shapes reflecting the arrangement of atoms into crystalline patterns, while others have no regular atomic arrangement.

To understand the properties of engineering materials for high temperature application, it is important to consider their chemical composition and their microstructure.

Chapter 2 provides an introduction to physical metallurgy that begins with a discussion of the structure and metals followed by a discussion of mechanical properties including strengthening mechanisms. The remainder of this section begins with a classification of high temperature materials and then discusses some of the materials more relevant to our interest, including their chemical properties and briefly reviewing the specifications and operational requirements imposed on them for high temperature service. High temperature coatings are discussed in Chapter 18.

1.4.1 Classification of Materials

The technically relevant materials can be classified into two groups – metallic materials and nonmetallic materials. As a further useful classification, metallic materials can be subdivided into ferrous metals and nonferrous metals. The ferrous metals can be classified into steel and cast iron. Iron–carbon alloys with a carbon content lower than 2% are defined as steels, and iron–carbon alloys with more than 2% carbon are known as cast iron. According to DIN EN 10027 (1992), steel alloys can be subdivided on the basis of application or chemical composition or quality groups, i.e.:

- Structural steels (normal and high strength).
- Steels for heat treatment and surface hardening.
- Stainless steels.
- Free cutting steels.
- Tool steels.

An example of a typical classification based on different applications is presented in Table 1.1. While plain carbon steels and steels with a total alloying content of up to 12% are not generally selected for resistance to HTC (the material choice is largely dictated by cost, ease of fabrication, and mechanical properties), they are often required to operate in high temperature aggressive environments. For instance, the power generation, refuse incineration, and chemical process industries use many miles of low-alloy steel heat exchanger tubes. Hence, the high temperature oxidation properties of low-alloy steels are often important in determining component life.

Nonferrous metals include nickel, cobalt, titanium, zirconium, refractory metals (tungsten, molybdenum, tantalum, and niobium), etc. Refractory metals can withstand temperatures for extended periods of time in excess of 1000 °C, but they cannot be used above 1200 °C without oxidation protection, because their oxides melt and even vaporize much below the metals' melting temperatures. Nickel and cobalt are the major elements of superalloys, materials widely used in critical regions of jet engines and gas turbines, because they contain elements for solution hardening and dispersion hardening that increase their load-carrying abilities at high temperature.

Temperature-resistant nonmetallic materials are called refractories and/or technical ceramics. Some properties of typical manufactured nonmetallic high temperature materials are given in Table 1.2.

Table 1.1 Classification of steel grades DIN EN 10027 (1992)

Steel grade	Characteristics, example	Quality grade
Structural steels for the building trade, bridge construction, vehicle and mechanical engineering		
Structural steels (DIN EN 10025)	Unalloyed and low-alloy C steels, yield strength 180–360 MPa, S235JR, S355JR (A516 Gr. 65/70)	Basic steels
High-strength structural steels (DIN EN 10113–2/3)	Micro-alloyed steels (Ti, Nb, V, B, Zr), yield strength 460–960 MPa. S460 N or S460 M (ASTM A63.3, Gr. E). S690 V (ASTM A517 Gr. F)	Quality steels
Steels for heat treatment		
QT steels (DIN EN 10083–1/3)	Mn/CrMo/V-alloyed steels with 0.2–0.6% C, high strength, C45E (ASTM A576 Gr. 1045) 42CrMo4 (ASTM A434 Class BB)	Quality steels
Steels with special properties		
Low temperature steels (DIN EN 10028–4)	Ni-alloyed steels with excellent toughness between −60 and 195 °C, 10Ni14, X8Ni9	Alloyed high grade steels
Stainless steels (DIN EN 10088–1/3)	12% Cr steel, austenitic stainless steel, duplex stainless steel X3CrNiMo13–4 (A182 Gr. F 6 NM) X20Cr13 (A276 Type 420) X2CrNi19–11 (A182 Gr. F 304L) X2CrNiMoN22–5 (A182 Gr. F 51)	Alloyed high grade steels
Heat-resisting steels (DIN EN 10095 draft)	Cr/Ni/Al/Si-alloyed steels, high temperature application 800–1100 °C, X10CrAlSi7, X10CrAlSi25, X10CrNiTi18–10, X15CrNiSi25–21	Alloyed high grade steels

Table 1.2 Some properties of typical manufactured nonmetallic high temperature materials

Material	Specific heat at 1000 °C (cal/g/°C)	Coefficient of thermal expansion at average RT–1000 °C(°C × 10^6)	Thermal conductivity at 800 °C (cal/cm^2/cm/°C/s)	Total emissivity at 800 °C (%)	Electrical resistivity at 600 °C(Ω cm)
Silica glass	0.30	0.5	0.006	70	10^6–10^7
Alumina (dense)	0.30	8.5	0.016	45–60	10^9–10^{11}
Silicon carbide (dense)	0.30	4.5	0.09–0.17	86	Semiconductor very dependent on impurities
Graphite	0.45	2–5	0.1–0.25	86–90	$6–20 \times 10^{-4}$

1.4.2 Cast Irons

When *cast iron* is exposed to high temperature under oxidizing conditions, oxidation of the metal results, with the formation of a surface scale. In addition, the dimensions of the component become distorted. Although such dimensional changes can occur also in inert atmospheres or in vacuum, the evidence available suggests that this "growth" is frequently associated with oxidation, and accordingly it is appropriate to consider it as an aspect of the corrosion of the iron.

Components designed for high temperature duty may either remain at a steady high temperature for their entire life or, as more commonly happens, may undergo cyclic variation between a minimum temperature, often room temperature, and a maximum temperature. The maximum temperature involved may be either above or below the critical temperature range of the iron. This is the range within which the transformation between ferrite or pearlite and austenite occurs, and for the majority of unalloyed irons, it may be regarded as being 700–850 °C.

Conditions of cyclic reheating are more severe than conditions of steady high temperature, and cyclic reheating through the critical range is particularly liable to cause excessive growth of the iron.

Generally, the studies that have been carried out suggest that growth of up to 40% by volume can occur within the first 40 hours of cyclic reheating to 900 °C with a frequency of 1–4 hours/cycle, while subsequent cycling produces growth at a rate rarely exceeding 20% increase in volume in 100 hours. The rate of growth that develops increases with increase in temperature and possibly also with increase in frequency of cycling. Although the fact that a 60% increase in volume may occur after only 140 hours of cyclic reheating suggests that unalloyed iron is totally unsuited for such applications, iron is in fact extensively used under such conditions, e.g. furnace doors and fire bars. This may be partly because these applications involve cycling frequencies lower than those that cause the very high rates of growth mentioned, but undoubtedly a major fact determining the use of unalloyed cast iron for such duties is its cheapness, which outweighs the superior growth resistance of more highly alloyed and more expensive irons.

At temperatures below the critical range, much less growth occurs, rarely exceeding 3% for 100 hours of cycling reheating. Here too the rate of growth depends on the temperature and the frequency of cycling. At temperatures below 400 °C, growth becomes negligible for most irons, while below 350 °C it is negligible for all irons. This threshold is probably related to the marked decrease in strength that occurs when irons are heated above 400 °C, which results in the component being more easily distorted by the development of the internal volume changes. Clearly, unalloyed irons have a very considerable usefulness up to about 700 °C, and even in a steam plant, where dimensional stability is important, there is a case for the use of unalloyed iron at temperatures up to 400 °C.

At temperatures below the critical range, an important cause of growth is *graphitization*, i.e. the decomposition of the carbide constituent of pearlite to give ferrite and graphite. Unalloyed irons usually contain up to 0.8% combined carbon, and complete graphitization of this can theoretically result in a volume increase of 1.6%. This value has been confirmed by Gilbert and White (1963) who have shown that ferritizing a fully pearlitic iron gives a linear growth of up to 0.7% (i.e. about 2.1% volume increase). Clearly, the rate of growth due to this mechanism will be controlled by the stability of the carbide in the pearlite, and this will vary with the composition of the iron. The presence of certain elements, notably silicon, decreases the stability of the carbide, while it is stabilized by the presence of other elements, namely, chromium. An iron with a low silicon content and containing some chromium may thus be expected to have good resistance, but since excessive carbide stability can lead to a hard, brittle alloy, there is a limit to the benefit that can be derived from such stability. It should be emphasized that unless large amounts of carbide-stabilizing elements are present in the iron, all that will be achieved is a slower rate of growth; there will not be a decrease in the total growth possible.

Phosphorus appears to have a beneficial effect on the growth rate. At subcritical temperatures, it helps to

stabilize the carbide, while at temperatures up to about 900 °C, the presence of the hard phosphide eutectic network restricts the deformation to which the much more ductile matrix would otherwise be subject. Since the phosphide eutectic melts at about 950 °C, irons containing appreciable amounts of this constituent should clearly not be exposed to this temperature.

Another cause of growth that is of equal importance with graphitization is the penetration of oxides into the metal along the graphite flakes. This presumably takes place because oxidizing gases can be adsorbed on the graphite and so allowed access to the metal/graphite interface. Since the oxides are more bulky than the metal from which they are derived, internal stresses are set up and growth results. As might be expected, the amount of growth due to internal oxidation increases as the graphite content increases and also as the section size increases, since this leads to a coarsening of the graphite. On the other hand, a white iron that contains no graphite is very growth resistant since it does not readily graphitize, nor is it easily penetrated by oxidation. For similar reasons, nodular graphite irons are resistant to growth.

At temperatures above the critical range, the maximum amount of growth due to graphitization may account for less than 10% of the total growth observed. Undoubtedly a large contribution to the total growth is made by the oxidation of the iron, since the stresses set up in the oxide layers by the differences between the expansion of the oxides and the iron during the alternate heating and cooling cycles generate cracks in the scale, which prevent the reaction from ever becoming self-stifling.

All the remarks so far made have been concerned with conditions of cyclic reheating. When an alloy is held at a steady temperature above the critical range, some growth will arise from graphitization, partly offset by the contraction involved in the ferrite–austenite transformation, but most of the growth will be due to oxide penetration.

Work carried out by Gilbert (1959) on irons maintained at 500 °C for 64 weeks has shown that in ordinary unalloyed flake irons, graphitization and oxidation cause roughly equal amounts of growth and that as the carbon content increases, the effect of oxidation becomes more important and the overall rate of growth increases. Nodular graphite irons grow very slowly under these conditions.

Irons designed specifically for good oxidation and growth resistance have highly oxidation-resistant matrices, containing either no carbides at all or very stable carbides, and have critical temperatures either below room temperature or above the maximum temperature anticipated. The alloys most commonly used are Silal, Niresist, Nicrosilal, and Fe–30Cr. Details of these irons and their properties are given in Table 1.3. The extremely fine graphite structure present in Silal probably makes a major contribution to its good heat resistance. However, when Silal is produced with nodular graphite, its heat resistance is further enhanced.

Two other alloys that have been used for their good oxidation and growth resistance are Cralfer (Fe–7Al–0.75Cr) and Fe–14.5Si. The production of the former, however, entails considerable difficulties, while the latter has poor mechanical properties and poor resistance to thermal shock, with the result that neither is extensively used for this purpose today.

1.4.3 Unalloyed and Low-Alloy Steels

On a tonnage basis, carbon and *low-alloy steels* are the most widely used engineering materials. An acceptable corrosion rate for a low-cost material such as plain carbon steel is approximately 0.2 mm a year or lower. Otherwise, unalloyed and low-alloy steels must be protected by appropriate methods. The most important alloying element of iron is carbon. The phase diagram of iron–carbon is discussed in Chapter 2.

The mechanical properties of unalloyed and low-alloy steels are determined by their chemical composition, microstructure, and heat treatment. The strength of structural steels, in particular, has been improved continuously in recent decades (Figure 1.2). On the basis of structural steels St37 and St52, new fine-grained structural steels with a yield strength up to 960 MPa (StE 690, StE 960) were developed. In a first step, the alloy content of normal structural steels was increased to furnish greater strength. But this concept was restricted by the requirement of weldability. A higher alloy content commonly reduces weldability, which is expressed by the carbon equivalent (CEV) for structural steel. For arc welding, the CEV must be in the range of 0.35–0.70. With increasing CEV preheating becomes necessary to avoid cold cracking:

$$\mathrm{CEV} = \%\mathrm{C} + (\%\mathrm{Mn}/6) + ([(\%\mathrm{Cr} + \%\mathrm{Mo} + \%\mathrm{V}])/5) + ([(\%\mathrm{Ni} + \%\mathrm{Cu}])/15) \quad (1.1)$$

Higher strength and improved toughness was achieved by combined thermomechanical treatment and/or tempering from the hot-forming temperature. Modern high-strength structural steels are micro-alloyed steels containing Ti, Nb, Zr, and B to impart a fine-grained structure. The main applications of high-strength structural steels are pressure vessels, pipelines, and construction of apparatus.

The toughness of steel was also increased by improved ladle and process metallurgy. Most accompanying elements – sulfur and oxygen – can be removed by vacuum ladle treatment (vacuum oxygen decarburization, VOD/argon oxygen decarburization, AOD) and calcium injection into the liquid melting bath, and so the number of nonmetallic inclusions, e.g. sulfides and oxides, in the alloy is considerably reduced. Today, a sulfur content

Table 1.3 Heat-resisting irons

Name	Composition					Structure	Mechanical properties			Critical temperature (°C)	Growth characteristics
	Total carbon	Si	Ni	Cr	Cu		Ultimate tensile strength (MN m^{-2})	Elongation (%)	Hardness (H_B)		
Silal	2.5	6.0	–		–	Fine graphite in silico-ferrite matrix	154	Nil	280	>920	Nil after 80 × 1 ½ h at 870 °C
Nicrosilal[a]	2.0	5.0	20.0	2.0	–	Fine graphite in austenitic matrix with some complex carbides	216	2	140	<20	<1% by length after 240 h at 950 °C
Niresist[a]	3.0	2.0	20.0	2.0	—	Fine graphite in austenitic matrix with some complex carbides	232	2	150	<20	<1% by length after 240 h at 950 °C
	3.0	2.0	14.0	2.0	7.0						
High chromium iron	1.5	1.0	–	30	–	Complex carbides in chromium-ferrite matrix	463	Nil	320	>1100	<1% by length after 240 h at 950 °C

[a]These irons may sometimes contain up to 5% Cr, which slightly improves the heat resistance and makes the alloy stronger and harder.

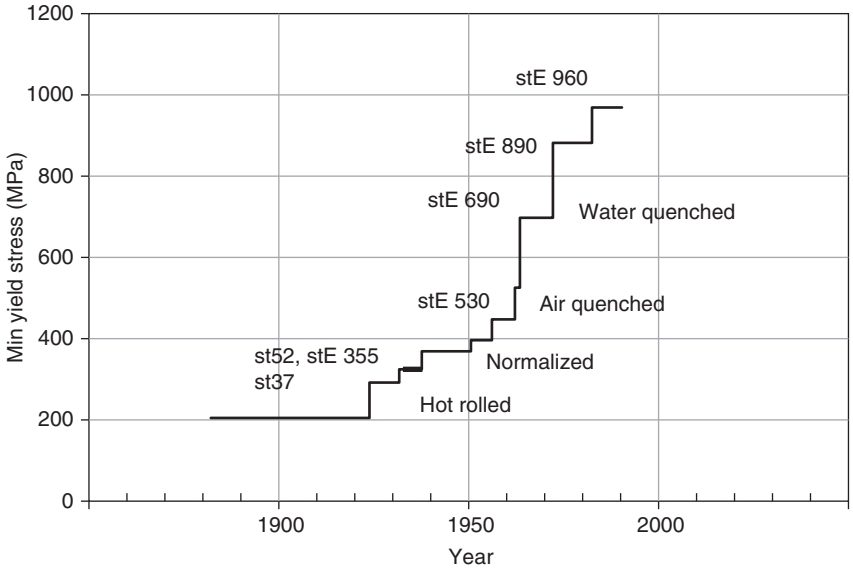


Figure 1.2 Development of high-strength weldable structural steels.

below 20 ppm and an oxygen content below 30 ppm can be reached.

The formation of calcium–sulfur compounds, in particular, influences the properties of the material. Calcium–sulfur compounds have an increased deformation resistance during hot rolling and remain nearly spherical. In the absence of calcium, injection of manganese sulfides with a very low deformation resistance will normally be obtained. During hot rolling, long banded manganese sulfide inclusions are formed, and this reduces the toughness (lamellar tearing). Spherical nonmetallic inclusions reduce the directionality of notch impact toughness and reduce susceptibility to *hydrogen-induced cracking* (HIC).

Additional alloying elements can influence the stability range of a crystal structure. Austenite is stabilized by the alloying elements Mn, Co, Ni, N, and C; ferrite is stabilized by Cr, Mo, Si, Al, Ti, and Nb. The opening up or shrinking of the γ phase field enables the development of austenitic and ferritic steels. For austenitic stainless steels, Cr, Ni, and Mo are the major alloying elements. It is clear that many of the reported element additions increase the HTC resistance, strength, toughness, microstructural stability, and creep resistance of the substrate alloy.

1.4.4 Stainless Steels

Stainless steels are a versatile group of engineering materials. They have good corrosion resistance and good fracture toughness in a wide range of working conditions, such as chemically aggressive environments, cryogenic temperatures, and high temperatures. The strength–toughness ratio of some of the stainless steel grades is unique when compared with other engineering materials. Therefore, the worldwide use of stainless steel is growing about 5% a year within the traditional and new applications.

Stainless steels are iron (Fe)-based alloys, which contain 11–30 wt% chromium (Cr), low carbon (C), and nitrogen (N) content. The presence of chromium in those amounts creates an oxide "passive layer" (spinel) on the surface of the steel, thus protecting the metal against corrosion. Stainless steels can also contain other elements, such as Ni, Mo, Si, Mn, Ti, Nb, and N, which are added for different purposes.

Table 1.4 shows some of the major advancements in the history of the industrial use of stainless steels.

Stainless steels can be divided into four main groups according to their microstructure, namely, martensitic, ferritic, austenitic, and austenitic–ferritic steels. Typical compositions for each group are shown in Table 1.5.

Martensitic and ferritic stainless steels have a ferritic microstructure when delivered to customers. The *ferrite* phase that has a body-centered cubic (BCC) crystal structure and the *austenite* phase that exhibits a face-centered cubic (FCC) crystal structure differ significantly from each other with respect to their mechanical properties. The combination of these two phases, present in the austenitic–ferritic (duplex) grades, produces unique mechanical properties such as very high yield strength and excellent corrosion resistance.

The most common austenitic stainless steel is the 18Cr–9Ni (EN 1.430I, AISI 304). In this material, the austenite phase is metastable, which means that it can transform to the martensitic phase by the application of an external driving force, such as strain, or by bringing the material to low temperatures. Another interesting phenomenon exhibited by this steel is that after solidification (casting, welding), the microstructure can contain some percent (0–15%) of delta ferrite, which is the high temperature phase of iron. The reason for this is due to

Table 1.4 Development of industrial use of stainless steel

Decade	Industrial use in larger scale
1930	War industry (martensitic steels)
1940	Fertilizer industry
1950	Petrochemical/wood processing/clothing industry and housekeeping
1960	Nuclear power stations (hot water), food industry, hospitals, varied range of consumer goods
1970	Environmental control (fuel gas desulfurization, closed circulations, waste water treatment, exhaust tubes), building industry (panels, decoration, roofs, elevators, etc.)
1980	Offshore technology, new energy technology, cryogenics, architecture, coal gasifying, transportation industry (trains and bus coach, liquid transportation containers)
1990	Load-bearing structural components (in building industry)
2000+	Automotive structural parts (crash zone), lightweight structures (welded sandwich panels, cold-deformed sheets)

Table 1.5 Composition of stainless steels according to EN 10088-I and corresponding ASTM/AISI grade

		ASTM	Composition, wt% according to EN 10088-I				
Steel group	EN	AISI	C, max.	Cr	Ni	Mo	Others
Martensitic	1.4006	410	0.08–0.15	11.5–13.5	–	–	–
	1.4028	420	0.26–0.35	12.0–14.0	–	–	–
Ferritic	1.4003	—	0.03	10.5–12.5	0.3–1.0		
	1.4512	409	0.03	10.5–12.5	–	–	Ti:6x(C + N) … 0.65
	1.4016	430	0.08	16.0–18.0	–	–	
	1.4521	"444"	0.025	17.0–20.0	–	1.8–2.5	Ti:4x(C + N) + 0.15 … 0.80
Austenitic–ferritic	1.4362	S32304	0.03	22.0–24.0	3.5–5.5	0.10–0.60	N: 0.05–0.20
	1.4462	S32205	0.03	21.0–23.0	4.5–6.5	2.5–3.5	N: 0.10–0.22
Austenitic	1.4318	301LN	0.03	16.5–18.5	6.0–8.0	–	N: 0.10–0.20
	1.4301	304	0.05	17.0–19.5	8.0–10.5	–	N < 0.11
	1.4306	304L	0.03	18.0–20.0	10.0–12.0	–	N < 0.11 N: 0.12–0.22
	1.4311	304LN	0.03	17.0–19.5	8.5–11.5	–	Mn: 6.0–8.0, N: 0.15–0.20
	1.4371	–	0.03	16.0–17.0	3.5–5.5	–	N < 0.11
	1.4436	316	0.05	16.5–18.5	10.5–13.0	2.5–3.0	N < 0.11
	1.4404	316L	0.03	16.5–18.5	10.0–13.0	2.0–2.5	N: 0.12–0.22
	1.4406	316LN	0.03	16.5–18.5	10.0–12.0	2.0–2.5	Cu: 1.2–2.0
	1.4539	NO8904	0.02	19.0–21.0	24.0–26.0	4.0–2.5	Cu: 0.5–1.5, N: 0.15–0.25
	1.4547	S31254	0.02	19.0–21.0	24.0–26.0	6.0–7.0	Cu: 0.5, N: 0.4, Mn: 2.0
	1.4652	S32654	0.01	24	22	7.3	

the fact that the composition of this steel is very close to the composition required to produce the formation of the ferrite phase. By increasing the Ni content in this steel, to approximately 12–14%, the stability of austenite increases, and thus neither *martensite* transformation takes place during deformation nor ferrite precipitation during solidification (Brooks and Thompson 1991).

Figure 1.3 shows the equilibrium diagram for Fe–Cr alloys. In this diagram, it is evident that for chromium contents higher than about 12%, only the ferrite phase is stable up to approximately 810 °C. Another phase present in the *phase diagram* is the sigma phase (45% Cr–55% Fe), which is stable for chromium contents in the range of 10–85% and in the temperature interval of 500–810 °C. In the chromium range of 0–12%, an austenite loop region appears in the phase diagram between temperatures of 850 and 1400 °C. The size of this austenite loop is strongly influenced by the carbon and nitrogen contents. Figure 1.4, which shows the influence of carbon and nitrogen on the austenite loop, can be used for the evaluation of the microstructure of ferritic stainless steels that are not alloyed with titanium or niobium.

As discussed before, the addition of nickel to stainless steels stabilizes the austenite phase. Figure 1.5 shows the phase diagram for the Fe–Cr–Ni system with contents of 70% and 60%. Iron contents of approximately 70% correspond to grade 18Cr–9Ni, which are the most used stainless steels. In the diagram it is clear that the

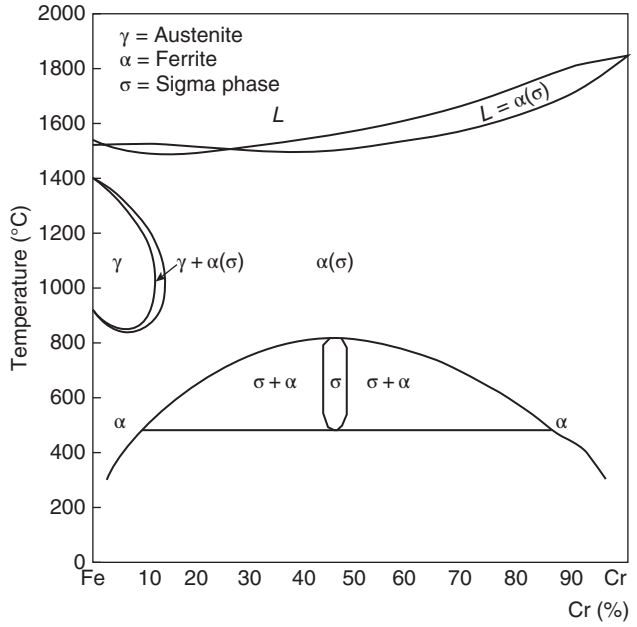


Figure 1.3 Fe–Cr phase diagram (Kubaschewski 1982).

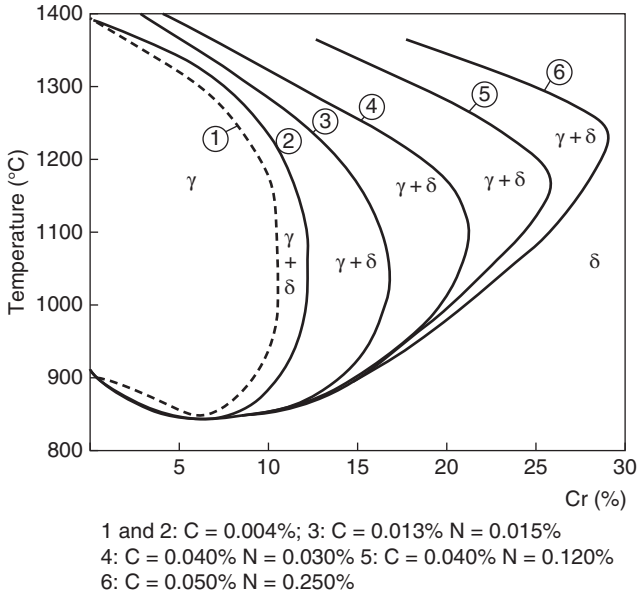


Figure 1.4 Thermal convection loop.

18Cr–9Ni stainless steel begins to solidify as delta ferrite. During cooling to room temperature already in the solid state, delta ferrite transforms gradually to austenite, and at room temperature the stainless steel exhibits a pure austenite phase. During casting or welding, the cooling rates involved are extremely fast, and thus diffusion of carbon and other alloy elements between the delta ferrite and the austenite phase is sluggish, which induces some delta ferrite to remain in the microstructure at room temperature.

The phase diagram at 70% Fe is also very useful to the evaluation of austenitic–ferritic (duplex) steels, in which the composition is typically 22Cr–5Ni–3Mo. For this composition, the microstructure is pure ferritic from the solidus line to about 100 °C. Below 1000 °C the ferritic microstructure partially changes to austenite, and at room temperature austenite/ferrite ratio is about one. The phase diagram at 60% Fe is important for the evaluation of high-alloyed austenitic stainless steels, such as alloys of the type 25Cr–15Ni.

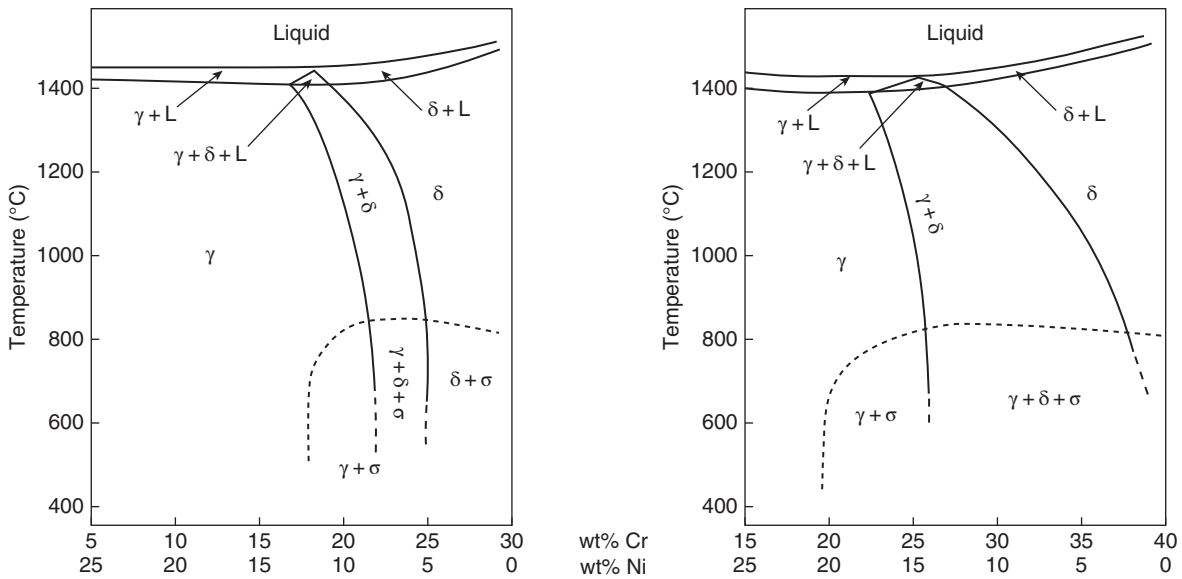


Figure 1.5 Stages in thermal gradient mass transfer.

Table 1.6 Mechanical and physical properties of stainless steel

		Tensile test values, EN 10088–2				Physical properties	
Steel group	EN	$R_{p0.2}$, N mm^{-2} min. 20 °C	N mm^{-2} 300 °C	R_m (N mm^{-2})	A_{80} % min.	Expansion coefficient, 20–100 °C (10^{-6} K^{-1})	Thermal conductivity, 20 °C (W mK^{-1})
Ferritic	1.4003	280	215	450–650	20	10.4	25
	1.4512	210	180	380–560	25	10.5	25
	1.4016	260	200	450–600	20	10.0	25
Austenitic–ferritic	1.4362	420	(255)	600–850	20	13.0	15
	1.4462	480	(290)	660–950	20	13.0	15
Austenitic	1.4301	230	110	540–750	45	16.0	15
	1.4318	350	170	650–850	35	16.0	15
	1.4371	300	165	650–850	45	16.0	15
	1.4436	240	127	550–700	40	16.0	15
	1.4529	300	170	650–850	40	16.0	15

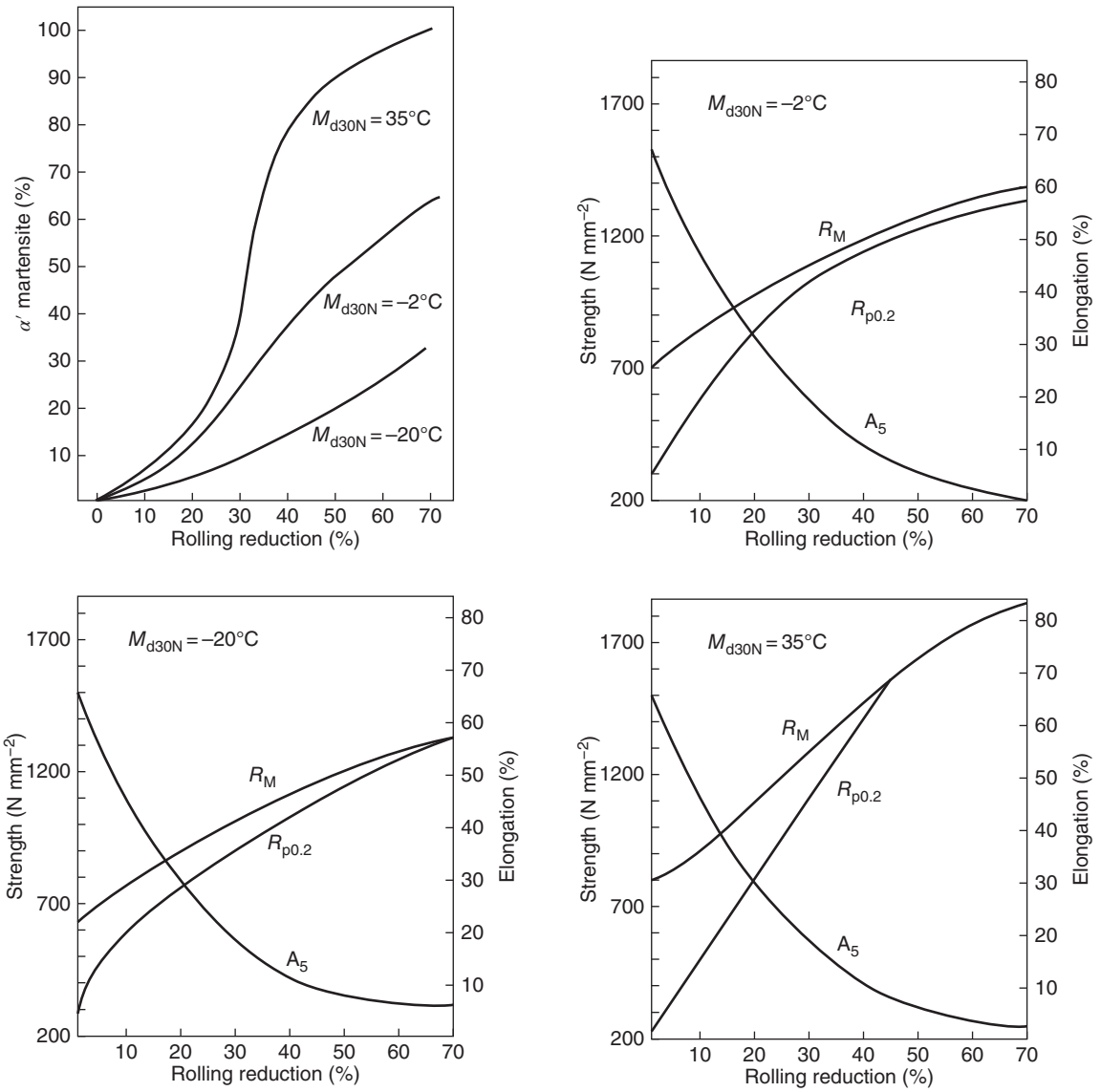


Figure 1.6 The effect of cold rolling reduction on the volume percentage of martensite and the corresponding strength and ductility of austenitic 18/8 stainless steels for different M_{d30N} values.

Table 1.6 shows some examples of mechanical and physical values for ferritic, austenitic–ferritic, and austenitic stainless steels. As discussed above, during cold deformation, an 18Cr–9Ni austenitic stainless steel transforms partly to martensite. The ability to form martensite during cold working can be expressed as a M_{d30N} value, which is the temperature at which 30% cold deformation causes 50% of martensitic structure. This can be expressed as Nohara et al. (1977)

$$\begin{aligned} M_{d30N}(^{\circ}C) = {} & 551 - 462 \times (\%C + \%N) - 9.2 \times \%Si \\ & - 8.1\% \times \%Mn - 13.7 \times \%Cr - 29 \\ & \times (\%Ni + \%Cu) - 68 \times \%Nb - 18.5\% Mo \\ & + 1.42 \times (\text{grain size ASTM} - 8) \end{aligned} \quad (1.2)$$

Figure 1.6 shows the effect of cold rolling reduction on martensite formation and the associated strength and ductility of austenitic stainless steels at different M_d values. Austenitic stainless steels show a unique combination of strength and ductility in the cold-rolled condition.

Austenitic stainless steels in the cold-rolled condition are also part of the Euro standard 10088-2 and ASTM designation A-666. The Euro standard specifies the strengths as R_m values, whereas the ASTM designation specifies the $R_{p0.2}$, R_m, and A_5 values (Table 1.7).

In the production of stainless steel products, good formability is often required. The most common forming types are bending, drawing, and lathe spinning/flow turning. In bending, the bending radius is a critical material parameter. Generally speaking, the following bending radii, shown in Table 1.8, can be used.

Table 1.7 Cold-worked austenitic stainless steels in the Euro standard EN 10088–2 and ENV 1993–1-4; Eurocode 3 and correspondence to ASTM A-666

Strength class	EN, yield strength, f_y min. (N mm^{-2})	ASTM, ultimate strength, f_u min. (N mm^{-2})	A-666 correspondence
C700	350	700	1/8 Hard
C850	530	850	1/4 Hard
C1000	750	1000	1/2 Hard
C1150	900	1150	3/4 Hard
C1300	–	1300	Full hard

Table 1.8 Minimum bending radius of austenitic and ferritic stainless steels, thickness up to 4.75 mm (Davis 1996)

Steel grade, AISI	Minimum bending radius, t = thickness
301, 302, 304, 316	$\frac{1}{2}\,t$
430, 410	t

In *drawing*, the strength of the material can be described in the form (true stress–true strain)

$$\sigma = k\varepsilon^n \quad (1.3)$$

where σ is the stress, ε is the strain, n is the strain hardening exponent, and k is a constant.

During the drawing operation of the sheet, three different strains can be defined, namely, ε_1 (drawing direction), ε_2 (transverse direction parallel to the surface), and ε_3 (transverse direction and perpendicular to the surface). These strains can be expressed as follows:

- $\varepsilon_1 = \ln(l/l_0)$, where l_0 is the initial length of the workpiece and l the final length.
- $\varepsilon_2 = \ln(wl/w_0)$, where w_0 is the initial width of the workpiece and w the final width.
- $\varepsilon_3 = \ln(t/t_0)$, where t_0 is the initial thickness of the workpiece and t the final thickness.

The strain ratio $r = \varepsilon_2/\varepsilon_3$ can be calculated from the drawing direction by using $\varepsilon\varepsilon_1$. The r value represents the tendency of the metal sheet for deformation along the width and thickness. Normally, the mechanical properties vary as a function of the direction, and thus drawing properties can be described by the anisotropy parameters r_n and Δr, where r values have been measured along the 45° and 90° direction relative to the rolling direction of the sheet:

$$\text{Normal strain ratio} : r_n = (r_0 + r_{90} + 2r_{45}) \quad (1.4)$$

$$\text{Planar strain ratio} : \Delta r = (r_0 + r_{90} - 2r_{45}) \quad (1.5)$$

The deep drawability of the material can also be studied with the "Swift cup test" in which the cup, shown in Figure 1.7, is deep-drawn with different initial blank diameters. The largest initial blank (diameter) drawn without cracking specifies the *limiting drawing ratio* (LDR). The planar anisotropy can also be measured with the "Swift cup test." This factor is called the *earing index* (%), shown in Figure 1.7.

The values for different formability tests are shown in Table 1.9 for the two common stainless steels EN 1.4301 and EN 1.4016. Austenitic stainless steels have higher values of n than ferritic stainless steels and therefore exhibit better properties during expansion (stretching) ($\varepsilon_1 > 0$ and $\varepsilon_2 > 0$), whereas ferritic steels perform better in deep drawing because of their high r_n values. In ferritic stainless steels, the r_n and Δr very much depend on the crystallographic texture, which is influenced by the rolling and heat treatment procedures.

The *forming* process can be described by forming limit diagrams (FLDs), which show the behavior of materials in two planar strain (ε_1, ε_2) conditions. Figure 1.8 shows the principal diagram for austenitic and ferritic steels, for which

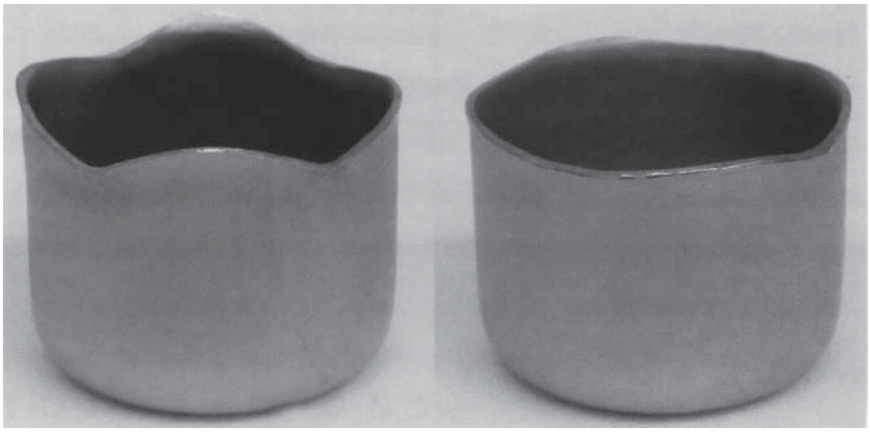


Figure 1.7 Swift cup test samples with different ear heights.

Table 1.9 Typical values of formability parameters for austenitic (EN 1.4301) and ferritic (EN 1.4016) stainless steels

Steel EN	n	r_n	Δ_r	Earing index (%)[a]	LDR
1.4301	0.50–0.70	1.0–1.3	0.45	5–7	2.00–2.05
1.4016	0.20–0.25	1.1–1.6	0.50	8–12	2.05–2.10

[a]Swift cup test.

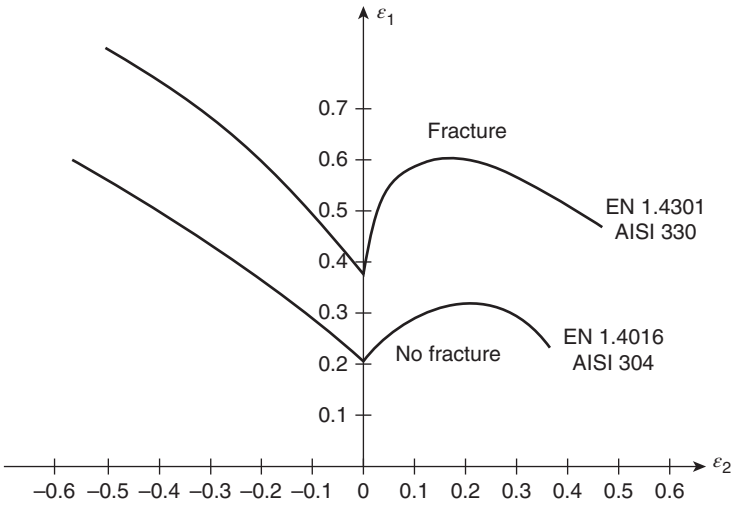


Figure 1.8 Forming limit diagram (to fracture) for austenitic and ferritic stainless steels.

the limits to cracking can be seen. The left side of the diagram is related to deep drawing ($\varepsilon_1 > 0$ and $\varepsilon_2 < 0$) and the right part related to expansion ($\varepsilon_1 > 0$ and $\varepsilon_2 > 0$).

Welding is the most common joining method for steels. Adhesive bonding, mechanical joining, brazing, and soldering can also be used to join thin stainless steel sheets. However, most large stainless steel structures, such as tubes, containers, and machines, are typically joined by welding. Arc, resistance, and laser welding are the most common welding methods for stainless steels.

The weldability for stainless steels can be studied with an original *Bystram diagram* (Figure 1.9), which is based on the well-known Schaeffler diagram (Schaeffler 1949), which shows the expected stable phases in the steel after arc welding. The diagram relates the steel composition to the problems encountered in welding. The most common austenitic stainless steels (1.4318, 1.4301, 1.4404, etc.) have been designed to be in the optimal point of the Bystram diagram.

On the basis of the Bystram diagram, stainless steels can be divided into different categories concerning weldability in arc welding. In martensitic stainless steels and in the ferritic 1.4016 steel, the reason for poor weldability is the formation of the brittle martensite phase in the weld and

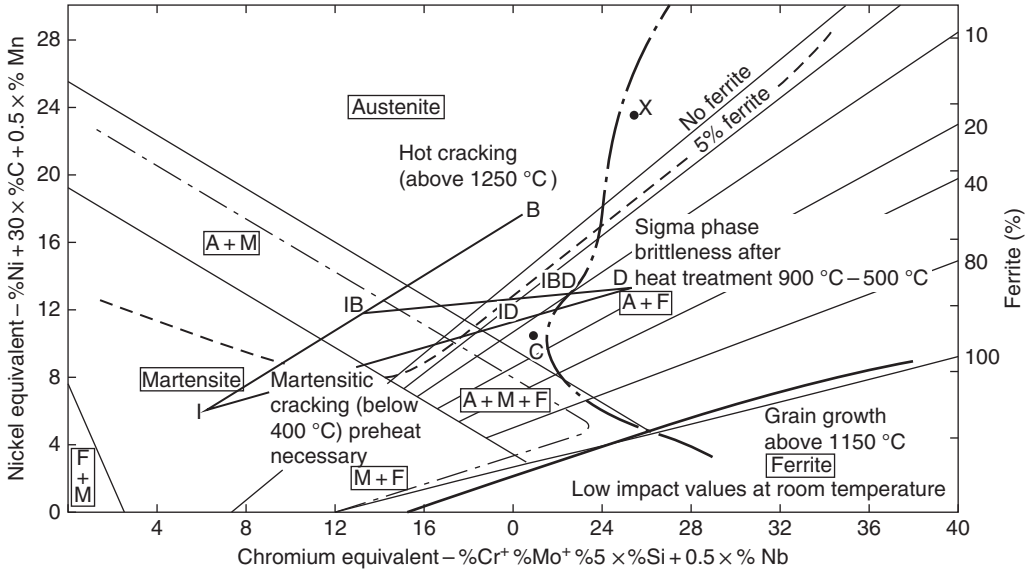


Figure 1.9 Bystram diagram for stainless steels in arc welding (Bystram 1956).

in the base metal heat-affected zone (HAZ). In addition, ferritic stainless steels (1.4512 and 1.4521) can have their ductility and impact toughness at low temperature degraded because of grain growth during welding. Good results have been obtained with the more modern low carbon ferritic steel 1.4003, which exhibits fine dispersed martensite in the microstructure after welding. By limiting the welding energy, low ductile-to-brittle transition temperatures (−40 °C) have been obtained in the HAZ. In the case of austenitic–ferritic steels, there is some susceptibility to ferrite grain growth and intermetallic phase formation during the welding thermal cycle. Therefore, limited welding energy is needed. On the other hand, austenitic stainless steels have very good general weldability characteristics. However, because of large coefficients of thermal expansion and low thermal conductivity, austenitic stainless steels have a tendency to hot cracking, which can become a problem for good weldability. Therefore, sulfur and phosphor contents, which increase hot cracking susceptibility, have been often restricted to a maximum of about 0.001% and 0.002%, respectively.

The basic importance of chromium in relation to *passivity* in the resistance of steels to aqueous corrosion is paralleled by its role as the most important alloying element in practice in securing the high temperature oxidation resistance of heat-resisting steels. It is not surprising, therefore, that these two aspects of corrosion resistance developed together, and early investigators of the chromium–iron alloys showed interest in the potential usefulness of these materials for high temperature oxidation resistance. Thus, Hatfield (1927), discussing early studies in France, has indicated that the scaling resistance of Fe–Ni–Cr alloys was appreciated at least as early as 1917.

It can therefore be said that it is the chromium content of the stainless steels that in the main establishes the steels susceptibility to general oxidation/corrosion. Stainless steels are also susceptible to local corrosion, called grain boundary corrosion, which is caused by the precipitation of $Cr_{23}C_6$ along grain boundaries, leading to Cr-depleted zones in the vicinity of grain boundaries. This type of corrosion has nearly been completely eliminated in the modern low carbon steels.

One other severe type of corrosion formed only in austenitic stainless steels is the stress corrosion cracking mechanism, in which fine cracks grow across the microstructure assisted by Cl-ions, stress, and temperatures above 60 °C. A typical case is the welded or cold-formed structure when used at high temperatures in water or steam. High nickel stainless steel grades (20% Ni) are not as susceptible as 8–10% Ni grades. Ferritic stainless steels are immune to stress corrosion cracking.

In the United Kingdom the rapidly growing interest in high-alloy steels after World War I coincided with expanding needs of industry for materials of improved strength and oxidation resistance at elevated temperatures. Aeroengine developments, rising steam temperatures and pressures in power production, and the increasing importance of high temperature, high pressure processes in oil-cracking and synthetic chemistry were all contributory factors in the development of heat-resisting steels from the 1920s. Nowadays, the heat-resisting steels are used for a wide range of general engineering and chemical engineering applications where the corrosion resistance, and in some instances strength, of the lower-alloy steels is inadequate. The martensitic steels, because of their lower oxidation resistance, are normally used for the less

onerous conditions, and certain limitations in ease of fabrication generally preclude their use for large structures and containment vessels. Their combination of moderate corrosion resistance plus strength at modest temperatures has led to widespread use as turbine disks and blades, bolts, and similar parts. They have also been used on steam plant for the less onerous conditions.

The ferritic steels are limited in scope because of lack of hot strength, but the cheaper types such as 430 are used in sheet form for the fabrication of parts such as heat exchangers. The higher chromium varieties are of importance in being much more resistant to sulfur attack than the nickel-bearing types and so are widely used as superheater supports or in sulfide-roasting furnaces, mainly as castings. Strength limitations and brittleness call for care in design.

The austenitic steels combine good oxidation resistance with ease of fabrication and thus are most widely used. In addition, while being quite weak at room temperature, they are among the strongest materials in the 550–750 °C range and are thus widely used for this purpose. Typical applications are furnace parts, heat exchangers, gas turbine parts, steam superheaters and piping, and chemical plant equipment for containing reactions and products at elevated temperatures.

1.4.5 Nickel-Based Alloys

Nickel and nickel alloys have useful resistance to a wide variety of corrosive environments typically encountered in various industrial processes. In many instances, the corrosive conditions are too severe to be handled by other commercially available materials, including stainless and super stainless steels. Nickel by itself is a very versatile corrosion-resistant metal, finding many useful applications in industry. More importantly, its metallurgical compatibility over a considerable composition range with a number of other metals as alloying elements has become the basis for many binary, ternary, and other complex nickel-based alloy systems, having very unique and specific corrosion-resistant and high temperature-resistant properties for handling the modern-day corrosive environments of chemical process, petrochemical, marine, pulp and paper, agrochemicals, oil and gas, heat treat, energy conversion, and many other industries. These alloys are more expensive than the standard 300 series stainless steels due to their higher alloy content and more involved thermomechanical processing and, hence, are used only when stainless steels are not suitable or when product purity and/or safety considerations are of critical importance. HTC depends on the chemical composition, the microstructural features of the alloy as developed during thermomechanical processing, the various reactions occurring at the alloy/environment interface, and the chemical nature of the environment itself.

The most common nickel-based alloys are generally known by their commercial names such as Hastelloy, Inconel, Monel, and Incoloy alloys even though they all have a unique UNS number. For example, when people refer to Inconel alloy, they are usually talking about the 600 series of alloys, i.e. Alloy 600 (UNS N06600) or Alloy 625 (UNS N06625).

The latter one-half of the twentieth century saw a phenomenal growth in the development of new nickel alloys, including Ni–Fe alloys (Invar, Pernifer, Magnifer, Hymn 80), the high performance Ni–Cr–Mo "C" family alloys (625, C-276, C-4, C-22, 686, C-2000, 59, Mat 21), and the following high temperature alloys: 602CA, 603GT, 2100GT, 45TM, 230, 625, X, 626Si, HR160, 718, 617, 214, Nimonic series, Udimet series, and others.

The effects of the various elements in alloys that are used for HTC are presented in Table 1.10.

In nickel-based alloys, the major elements for imparting specific properties or a combination of properties are chromium, silicon, aluminum, titanium, molybdenum, cobalt, tungsten, and carbon. Others, such as yttrium and rare earths, niobium, tantalum, and zirconium, play very specific roles in improving certain HTC characteristics. These alloying elements can also be classified as follows:

Protective scale formers	Cr as Cr_2O_3, Al as Al_2O_3 and Si and SiO_2
Solid solution strengtheners	Mo, W, Nb, Ti, Cr, Co
Age-hardening strengtheners	Al + Ti, Al, Nb, Ta
Carbide strengtheners	Cr, Mo, W, Ti, Zr, Ta, Nb
Improved scale adhesion (spallation resistance)	Rare earths (La, Ce) Y, Hf, Zr, Ta

Papers by Friend (1980), Heubner (1987), and Lai (1990) provide detailed information on high temperature alloy systems. The nickel–iron alloys are a class of alloys (Sims et al. 1987) containing 15–60% iron and 25–60% nickel with the FCC structure of γ austenite as a matrix and strengthened by precipitates with additional benefits from solid solution and grain boundary strengthening. These alloys are less expensive than Ni- and Co-based superalloys. Ni–Fe alloys may be classified into five groups:

Group 1: This group is relatively Fe rich with 25–35% Ni and less than 2% Ti. The strengthening phase is the coherent FCC γ' (called gamma prime) precipitates. The use temperature is limited to 650 °C (1200 °F). Commercial alloys in this group include Tinidur, V-57, and A-286.

Group 2: This group is rich in Ni (>40%) with increased contribution from a solid solution. Strengths of this

Table 1.10 Alloying elements and their major effects in high temperature alloys

Alloying elements	Main feature	Other features
Cr	Improves oxidation resistance. Detrimental to nitriding and fluorination resistance	Improves sulfidation resistance. Beneficial to carburization and metal dusting resistance
Si	Improves oxidation, nitriding, sulfidation, and carburization resistance. Detrimental to nonoxidizing chlorination resistance	Synergistically acts with chromium to improve high temperature degradation
Al	Independently and synergistically with Cr improves oxidation resistance. Detrimental to nitriding resistance	Helps improve sulfidation resistance. Improves age-hardening effects
Mo	Improves high temperature strength. Improves creep strength; detrimental to oxidation resistance at higher temperatures	Helps with reducing chlorination resistance
W	Behaves similarly to molybdenum	
Nb	Increases short-term creep strength; may be beneficial in carburizing; detrimental to nitriding resistance	
C	Improves strength; helps nitridation resistance; beneficial to carburization resistance; oxidation resistance adversely effected	
Ti	Improves hardening strengthening	Detrimental to nitriding resistance
Mn	Slight positive effect on high temperature strength and creep; detrimental to oxidation resistance; increases solubility of nitrogen	
Co	Reduces rate of sulfur diffusion; hence helps with sulfidation resistance; improves solid solution resistance; improves solid solution strength	
Ni	Improves carburization, nitriding, and chlorination resistance; detrimental to sulfidation resistance	
Y and RE	Improves adherence and spalling resistance of oxide layer and hence improves oxidation, sulfidation, and carburization resistance	

group of alloys exceed those of the iron-rich group. Commercial members of this group of alloys are Inco X-750 and Inco 901.

Group 3: This group is rich in Ni and owes its strength to coherent body-centered tetragonal (BCT) γ''(called gamma double prime) precipitates. Inco 706 and 718 are examples of this group, with the latter being one of the most used alloys of this class. The temperature capability of these alloys extends from cryogenic to 650 °C (1200 °F).

Group 4: This group is an Fe-rich Fe–Ni–Co alloy with low thermal expansion achieved through removal of Cr and Mo, which stabilize ferrite in the structure. The strength of this group of alloys is derived primarily from the coherent FCC γ' precipitates. Commercial members of this class are Inco 903 and 909 with temperature capability limited to 650 °C (1200 °F). Elimination of Cr makes the alloys more susceptible to oxidation and corrosion.

Group 5: The unique feature of this Ni-rich group is the absence of coherent precipitates. Some of the members of this group derive from precipitates of carbides, nitrides, and carbonitrides. Others (Hastelloy X and N-155) are solid solution strengthened. The application temperature of the latter for non-stressed application is limited to 1093 °C (2000 °F).

The C family of alloys has found widespread application in chemical and petrochemical industries producing various chlorinated, fluorinated, and other organic chemicals, agrochemicals and pharmaceutical industries producing various biocides, pollution control flue-gas desulfurization (FGD of coal-fired power plants, wastewater treatment, incinerator scrubbers) (Agarwal and Ford 1998), pulp and paper, oil and gas (sour gas production), marine, and many others.

Alloy C-22, due to its higher chromium content, is an improvement upon Alloy C-276 in highly oxidizing media. The introduction of Alloy 59 in 1990 and industry recognition of the benefits of Alloy C-276 over Alloy C-22 in highly reducing environments led to a resurgence in Alloy C-276 usage. Alloy C-22, an alloy of the 1980s, has been superseded by alloys of the 1990s, i.e. Alloy 59, Alloy 686, and Alloy C-2000. Alloy 59 has found a wide number of applications, and these continue to increase as its superior corrosion resistance, excellent production ability, weldability, and thermal stability are recognized (Agarwal et al. 2000). Alloy 686 and Alloy C-2000 are also finding specific applications in various industries.

1.4.6 Cobalt-Based Alloys

Most cobalt-based alloys in industrial use are derivatives of the experimental cobalt-based alloys produced by Elwood Haynes over a century ago (Uhlig and Revie 1985). The most important applications of cobalt-based alloys are under conditions of wear or erosion in the presence of a corrosive environment. Cobalt-based alloys have high yield strengths, high work hardening rates, and limited fatigue damage under cyclic stresses. One of the most important alloying elements in cobalt-based alloys is chromium, which provides resistance to corrosion. In cobalt-based hardfacing alloys, chromium also acts as the primary carbide former.

Nickel helps stabilize the FCC structure for service cases where improved ductility is needed. The main resistance to wear of the cobalt-based alloys is conferred by the cobalt itself. Cobalt has a low stacking-fault energy, which favors planar slip over cross slip of the dislocations. As a result of this deformation mechanism, the alloy work hardens rapidly. The stable crystalline structure of cobalt at room temperature is, moreover, *hexagonal close packed* (HCP); the high temperature FCC structure is, however, usually retained in the commercial wrought alloys. The excellent resistance of cobalt-based alloys to galling is attributed to their ability to absorb stress by allotropic transformation (from the FCC to HCP) and twinning. Galling resistance is also attributed to the planar slip mechanism, which circumscribes the damage to the outer surface, thus avoiding fracture paths deep into the material. The combination of these mechanisms results in the excellent resistance of cobalt-based alloys to *cavitation*, *erosion–corrosion*, and sliding wear.

The harder and less ductile cobalt-based alloys are often used as hardfacing materials under conditions when resistance to abrasive wear is needed. Some hardfacing alloys contain approximately 1–3% carbon, which is needed for carbide formation. Carbide-forming cobalt-based alloys have been in existence for almost one hundred years and are generally known by the commercial name of Stellite alloys. Other cobalt-based hardfacing alloys contain from 2% to 3% silicon (Si), which participates in the formation of intermetallic Laves phases in the form of $Mo(Co,Si)_2$ (Betteridge 1982). The cobalt-based intermetallic alloys are generally known as Tribaloy alloys. Besides hardfacing weld overlays, both Stellite and Tribaloy alloys can also be used as castings and powder metallurgy parts.

The first reported high temperature applications of the cobalt–chromium alloys were the hardfacing (weld overlay) of engine valves and hot trimming dies in the 1920s (Gray 1974). However, the event that led to the evolution of cobalt–chromium high temperature alloys was the use of Vitallium® alloy for the investment casting of aircraft turbocharger blades in the late 1930s. This cobalt–chromium–molybdenum alloy, which was actually designed for aqueous corrosion and wear resistance and was in use as a dental and orthopedic implant material, was found to have the required combination of high temperature strength, high temperature microstructural stability (when the carbon content was slightly reduced), oxidation resistance, and castability (Sullivan et al. 1970).

To increase the thermal stability of Vitallium alloy, 2.5 wt% nickel was added. The resulting composition was renamed Stellite 21 or modified Vitallium alloy. The use of nickel to stabilize the high temperature cobalt alloys was carried further with the development of cast X-40 (Stellite 31) and wrought HAYNES 25 alloy (L-605) in the 1940s and of cast MAR-M® 509 and wrought HAYNES 188 alloy in the 1960s. The X-40, HAYNES 25 alloy, and MAR-M 509 contain ~10 wt% nickel, whereas HAYNES 188 only contains 22 wt% nickel (Table 1.11).

It is also important that from the development of X-40 onward, tungsten was preferred over molybdenum as the primary solid solution strengthening element in the high temperature cobalt alloys, inferring that it is a more effective high temperature strengthener than molybdenum, on an atomic percentage basis, which is consistent with its atomic size. Molybdenum, on the other hand, remained the preferred element for aqueous corrosion resistance.

The microstructures of the high temperature cobalt alloys are discussed in detail in Sims and Hagel (1972) and ASM International (1985). In the solution-annealed and

Table 1.11 Nominal composition of high temperature cobalt alloys

	Co	Cr	W	Mo	C	Ni	Fe	Si	Others
X-40 (Stellite 31)	Balance	25.5	7.5		0.5	10.5	2		B–0.01
MAR-M 509	Balance	24	7		0.6	10			Ta–3.5 Ti–0.2 Zr–0.5
HAYNES 25 (L-605)	Balance	20	15	1 max	0.1	10	3 max	0.4 max	Mn–1.5
HAYNES 188	Balance	22	14		0.1	22	3 max	0.35	Mn–1.5 max B–0.015 max La–0.03

quenched condition, the wrought materials, HAYNES 25 alloy and HAYNES 188 alloy, exhibit simple microstructures consisting of a sparse dispersion of M_6C carbides in an FCC solid solution. In service, within certain high temperature ranges, they undergo microstructural changes, the most significant being the precipitation of $M_{23}C_6$ at grain boundaries and along stacking faults and, in the case of HAYNES 25 alloy, the precipitation of Laves intermetallic phase. The precipitation of carbides can provide useful increases in strength. The precipitation of Laves phase is undesirable, since it results in significant loss of ductility.

The cast materials exhibit complicated microstructures. The MAR-M 509, for example, contains both $M_{23}C_6$ and MC carbides in the as-cast condition, due to the deliberate addition of active carbide formers, such as tantalum. These carbides provide considerable strength, even prior to extended high temperature service during which additional fine carbide dispersions are created (Sims and Hagel 1972).

One of the main benefits of the high temperature cobalt alloys is their resistance to sulfidation (hot corrosion) in gas turbine engines. This phenomenon, which is believed to involve the dissolution of the normally protective oxide films by sodium sulfate (created by airborne salts and residual sulfur in gas turbine fuels), is a problem up to ~980 °C (1800 °F), above which sodium sulfate volatilizes and is relatively innocuous.

HAYNES 25 alloy exhibits good resistance to oxidation up to ~1000 °C. HAYNES 188 alloy possesses even higher oxidation resistance, by virtue of the lanthanum addition (0.03 wt%), which reduces the tendency of protective oxide films to spall away during thermal cycling. HAYNES 188 alloy can be used in high temperature oxidizing environments to ~1150 °C.

The cobalt alloys are attacked by some molten metals, notably aluminum and bismuth. However, they are very resistant to zinc and tin alloys and have been widely used in decasting and zinc galvanizing.

1.4.7 Superalloys

This is a unique class of complex alloys based on Ni and Co (and to some extent Fe) that not only exhibit extraordinarily high strength but also maintain strength across a wide elevated temperature range, hence the name *superalloys*. Some of these alloys are used in load-bearing application at ≥80% of their melting point. The two metals are attractive because of their high melting point and crystal structures amenable to extensive alloying. Whereas Ni exhibits FCC crystal structure, Co is HCP at room temperature. Alloying element additions are generally used to stabilize Co in the FCC form. A number of processes in which metals are strengthened are discussed in Section 2.5.

Strengthening mechanisms used to produce practical Ni and Co superalloys include the following (Donachie and Donachie 2002; Sims et al. 1987):

1. *Strengthening of the austenitic γ phase by solid solution*: The γ phase constitutes the matrix of the alloys. Several metallic elements dissolve in the γ matrix (Cr, Co, Fe, Mo, Ta, W, and Re in Ni-based alloys and Ni, Cr, Mo, W, Nb, and Ta in Co-based alloys), randomly replacing the matrix atom (Figure 1.10a). Because of their size difference relative to the matrix, the substituting solute atoms create stress fields that impede dislocation motion by interacting with the stress fields of dislocations. Slowing dislocation movement increases strength. This mechanism operates in both Ni- and Co-based superalloys.
2. *Precipitates of various carbides within the grains and at the grain boundaries*: Carbon, which is invariably present in the matrix, forms carbides with some of the alloying elements (MC-type carbide with Ti,

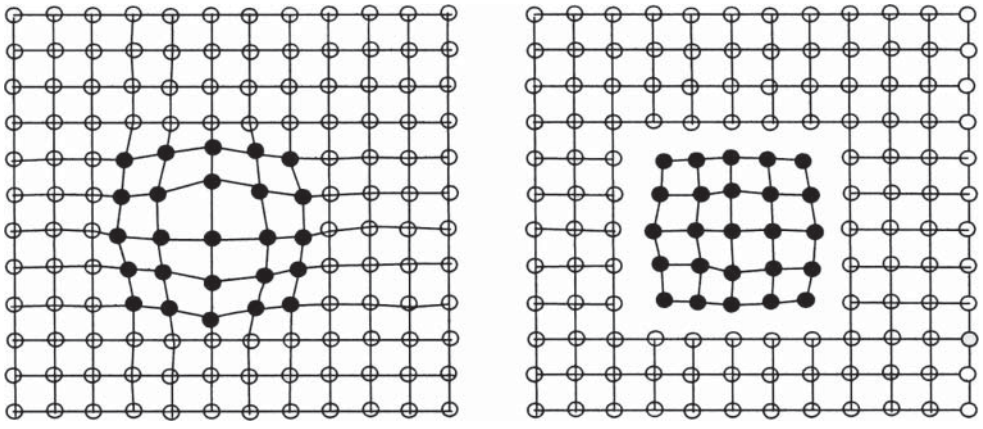


Figure 1.10 Schematic of (a) a coherent precipitate with large strain fields indicated by distortion of the lattice and (b) an incoherent precipitate.

Ta, W, Mo, Hf, and Nb and $M_{23}C_6$-type carbide with Cr, W, and Mo in Ni-based alloy; in Co-based alloys, MC-type carbide with Ti- and $M_{23}C_6$-type carbide with Cr) during processing and heat treatment. Carbides within grains impede dislocation motion, thereby increasing strength. Grain boundary carbides pin boundary movement, discouraging grain growth. They also impede grain boundary sliding. The carbides together with the solid solution provide the primary mechanism for strengthening of Co-based superalloys. For Ni-based superalloys, these mechanisms are secondary to γ' and γ'' precipitation strengthening.

3. *Coherent FCC γ' and BCT γ'' precipitates*: Precipitates of the ordered intermetallic compound of composition Ni_3Al, known as gamma prime, γ', provide the primary mechanism for strengthening Ni-based superalloys. Supplemental strengthening is achieved from solid solution and carbide precipitates. In the γ' crystal structure, the Ni sites may also contain Co, Cr, and Mo, while the Al sites may contain Ti and Nb. The unique characteristic of the γ' structure is that it is coherent with the γ matrix. Figure 1.10 compares schematically the matrix–precipitate interface for coherent and incoherent precipitates. Coherent interfaces have low energy. The precipitates have, therefore, little driving force for growth in size, and therein lies the clue to the strength retention of γ'-strengthened superalloys over a wide high temperature range. These fine and hard precipitates impede dislocation motion, resulting in a spectacular increase in strength.

The size and volume fraction of γ' are critical parameters affecting creep and fatigue strength of the alloys. The former is controlled by the Al + Ti content and ranges from 0.2 for wrought Fe–Ni superalloys to greater than 0.6 in Ni-based superalloys. The size ranges between 0.2 and 0.5 μm. Fine-size γ' precipitates have spherical morphology, whereas larger sizes tend to be cuboidal.

In some superalloys containing Fe such as Inco 718, the predominant strengthening phase is γ'', which has a BCT structure with composition Ni_3Nb. The γ''phase is coherent with the γ matrix and provides high strengths in the low to moderate temperature regime. However, above 650 °C (1200 °F), γ'' decomposes to either γ' or δ, resulting in a significant drop in strength.

For some creep-strength-critical applications, such as rotating turbine blades in modern gas turbine engines, Ni-based superalloys in polycrystalline form are not acceptable because they tend to fail at grain boundaries oriented transversely to the centrifugal force of rotation, which is along the blade axis. These blades are produced by the process of casting, which involves melting of appropriate alloys in a furnace and pouring the melt into a ceramic shell.

The creep properties of the alloys can be significantly improved by eliminating transverse grain boundaries and encouraging columnar grains oriented parallel to the blade axis. Such grain structures are achieved through "directional solidification" by modifying the casting process so that heat is removed from the melt by slowly pulling the ceramic shell from the furnace. Further increases in creep properties have been made possible by eliminating grain boundaries altogether in single-crystal superalloys. This is achieved by using a grain selector or appropriate seeds in the casting process.

1.4.8 Refractories

Temperature-resistant nonmetallic materials are called refractories. They are ceramics with melting temperatures in excess of 1400 °C. Apart from having a high melting point, they must be chemically inactive. Metallic oxides with large heats of formation are thus particularly suitable. Some melting points are given in Table 1.12.

The oxides are widely used (i) because there are many naturally occurring oxides; (ii) because oxides typically have very strong bonds to withstand high temperatures, for example, Al_2O_3, MgO, SiO_2, and ZrO_2; and (iii) because oxides are generally stable in air. Non-oxide refractories are also available, for example, SiC, AlN, Ce_2O_3, and graphite. These refractories are unaltered by temperatures well in excess of 1500 °C (>2700 °F) but require some oxygen protection if used directly in air.

Refractory oxides are classified as *acidic* or *basic*, depending on whether, if soluble, they give acidic or basic solutions in water. The acidic refractories (silica, quartz, ganister) are rich in SiO_2. The basic ones contain mainly lime (CaO), magnesia (MgO), and *calcined dolomite* (CaO·MgO). Alumina (Al_2O_3) is fairly neutral. Where

Table 1.12 Melting points of oxides

Oxides	Melting points (°C)
ThO_2	3500
ZrO_2	2800
MgO	2640
BeO	2520
CaO	2500
$ZrO_2 \cdot SiO_2$	2430
Cr_2O_3	2280
UO_2	2230
Al_2O_3	2020
$MgO \cdot Al_2O_3$	2000
TiO_2	1850
SiO_2	1713
Fe_3O_4	1600
Fe_2O_3	1460
FeO	1370

chemical reaction with the charge or furnace gases rules out both acidic and basic refractories, it may be necessary to use one of the more expensive *neutral refractories* (e.g. *chromite* $Cr_2O_3 \cdot FeO$, graphite, SiC, TiC, and metals such as Mo).

Besides melting point and chemical stability, the other important properties of refractories are as follows:

1. *Mechanical strength and dimensional stability at high temperatures*: Compressive loads usually of the order of 50 psi (pounds in.$^{-2}$) have to be supported.
2. *Thermal shock resistance (spalling resistance)*: Temperature gradients produce thermal strains that can break brittle materials. Good thermal conductivity (e.g. SiC, graphite, metals) or a small coefficient of thermal expansion (e.g. SiC, Si_3N_4, Pyrex glass) gives resistance to thermal shock. Magnesia is susceptible at low temperatures because it undergoes changes of crystal structure but good at high temperatures because it has a low expansion coefficient.
3. *Thermal conductivity*: For furnace linings, a low conductivity (e.g. porous brick) is required. For recuperators, crucibles, and muffles, the conductivity should be high. Refractories that withstand the highest temperatures (as used in steelmaking furnaces) are usually moderately good conductors. It is thus necessary to use a series of refractory linings, the most refractory ones on the inside and the most insulating ones on the outside.

The most important acidic refractories are silica bricks. These are cheap high temperature refractories that, when fairly pure (>96% SiO_2), remain strong up to about 1680 °C. They are widely used for the roofs of steelmaking furnaces. The *fireclays* (*china clay*; *kaolinite*, $Al_2O_3 \cdot 2SiO_2 \cdot 2H_2O$) are based on silica and alumina. Fireclay itself contains 20–45% Al_2O_3, is neutral, and when fairly pure can be used up to 1500 °C. Low-grade fireclays contain FeO and other impurities that lower the melting point and are usable only up to 1200 °C. *Sillimanite* (45–70% Al_2O_3) and *mullite* (70–100% Al_2O_3) are more expensive but can be used in the range of 1700–1800 °C and have good spalling resistance.

Lime is not much used, despite its refractoriness, because it hydrates. *Magnesite* (80–90% MgO) can withstand very high temperatures, but its high temperature strength is low because the $MgO/SiO_2/FeO$ glass needed to bond its crystal grains together softens at high temperatures. Magnesite has good thermal conductivity, but its spalling resistance is reduced by its high coefficient of thermal expansion. It has excellent chemical resistance to *basic slags*, as used in steelmaking. Dolomite is a cheaper alternative to magnesite but has a tendency to hydrate. *Chrome-magnesite* ($Cr_2O_3 \cdot MgO$) is used for the roofs of basic open-hearth steelmaking furnaces. It has better high temperature strength and spalling resistance than MgO, although it tends to swell by absorbing FeO if used near the earth.

The problem of refractory containers for molten reactive metals at high temperatures is difficult. The following refractory oxides, when pure, are generally favored:

1. *Thoria, ThO_2*: Stable in oxidizing atmospheres up to its melting point (≅3500 °C) and nonvolatile under vacuum up to 2000 °C.
2. *Magnesia, MgO*: Useful in oxidizing atmospheres but easily reduced in reducing atmospheres at temperatures well above the boiling point of magnesium (1100 °C).
3. *Zirconia, ZrO_2*: A chemically stable high temperature refractory but tends to change its crystal structure.
4. *Alumina, corundum, Al_2O_3*: Stable in oxidizing atmospheres up to 1800 °C, but slightly reactive in reducing atmospheres and volatile under vacuum.
5. *Urania, UO_2*: Stable in reducing atmospheres and under vacuum up to 2000 °C, but forms higher oxides in oxidizing atmospheres.

Several natural refractories are best examined in terms of the SiO_2–Al_2O_3 phase diagram (Figure 1.11).

Quartzite, which is predominantly SiO_2, is a widespread rock. It will withstand 1500 °C, even in the presence of fluxes such as CaO, FeO, and MgO. It is vulnerable to Al_2O_3, and therefore, the raw materials must be chosen accordingly. In contrast, fireclay refractories withstand higher temperatures if they are enriched in Al_2O_3. The best grade clays dissociate on heating as follows:

$$Al_2Si_2O_5(OH)_4 \rightarrow Al_2O_3 + 2SiO_2 + 2H_2O\uparrow \qquad (1.6)$$

This *calcination* leads to a 45 : 55 ratio of Al_2O_3–SiO_2. From Figure 1.11 we see that additional Al_2O_3 produces a progressively higher liquidus temperature. When the Al_2O_3–SiO_2 ratio exceeds ∼72–28, the solidus is also above 1800 °C (>3300 °F).

The predominant refractories for steel and copper production are the basic refractories. These come from calcination of carbonate rocks, for example,

$$CaCO_3 \rightarrow CaO + CO_2\uparrow \qquad (1.7)$$

and

$$MgCO_3 \rightarrow MgO + CO_2\uparrow \qquad (1.8)$$

The resulting oxides (which give basic characteristics to aqueous solutions) possess very high melting temperatures (MgO: 2800 °C; CaO: 2550 °C). Their usable temperatures, however, are appreciably below these high figures

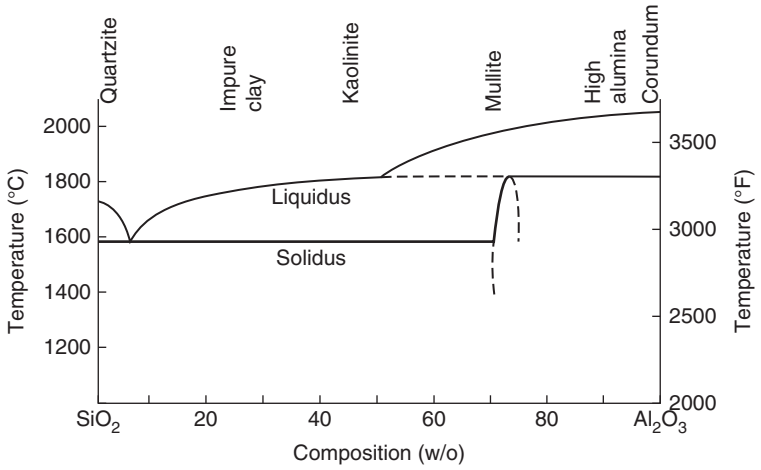


Figure 1.11 Aluminosilicate refractories. Silica refractories are readily obtainable from quartzite, but the Al_2O_3 must be held low. Clays and other aluminosilicates are more refractory when enriched in Al_2O_3.

because they react extensively with other oxides; the lowest eutectic of the $CaO–Al_2O_3$ system is ~1400 °C. The ceramist intentionally avoids such combinations, just as a metallurgist avoids the use of certain metals in oxidizing environments.

Typically, refractory materials are pressed into brick shapes and are laid in furnace walls – most generally without mortar. Monolithic walls both of rammed mixes and of "gunned" mixes receive increasingly wide usage. The latter may be compared to the spray gunning of concrete, except that they are applied to the red-hot interior walls of a furnace where they dry and sinter almost immediately. Such spraying applications have the advantage of repairing furnaces without using extended periods of time for cooling and reheating the massive structures. However, sprayed refractories are never as dense as pressed brick.

In addition to temperature resistance, refractories must resist *spalling*. This is thermal cracking, chiefly from the sharp temperature gradients in the wall of a furnace. Several factors go into the *spall resistance index* (SRI) of a refractory. Chief among them are thermal diffusivity, h; the strength, S; the coefficient of thermal expansion, α; and the elastic modulus, E:

$$\text{SRI} = hS/\alpha E \tag{1.9}$$

A low *coefficient of thermal expansion*, α, leads to smaller dimension changes, and a smaller elastic modulus, E, introduces less stress from the dimension changes that are restrained. Unfortunately, neither of these factors may be altered for a given material. A high thermal diffusivity, h, prevents a sharp temperature gradient but also leads to greater heat losses. This factor is partially controllable in a given refractory by the amount of porosity. The strength factor, S, may also be varied. Ideally, a strong material resists fracture and therefore spalling. In practice, however, high strengths may lead to fewer, but major, cracks with extensive material losses. If the refractory produces many small, less damaging cracks, it is possible for dimensional adjustments to occur without major spalling. Thus actual spalling does not correlate perfectly with Eq. (1.9).

Insulating refractories receive added attention with increased energy costs, particularly since all types of furnaces are major fuel consumers. One approach to reduce heat losses is to increase the wall thicknesses and lower the temperature gradient. This is not always possible, either because of material costs or design restrictions on space. A second approach is to introduce porosity within the refractory. This may involve a less dense pressing of the brick; it may also be achieved through the introduction of sawdust or similar combustible materials within the original mixture so that voids are introduced when the final product is fired; finally, lower thermal transfer is carried out in fibrous products with very low packing factors. The familiar glass wool is such a product that is amenable to moderate temperature exposures. Fibers of refractory materials are available for temperatures up to ~1700 °C to achieve significant fuel savings in industrial furnaces.

1.4.8.1 Selection of a Refractory Material

An example of selection of high temperature material is provided by crucibles used for melting nonferrous metals on an industrial scale.

The main requirements can be summarized as follows:

1. Good heat transfer, needing high thermal conductivity and emissivity.
2. Resistance to severe thermal shock.
3. Chemical resistance to both the liquid metal and the fluxes and slags that are used to develop during use.
4. Sufficient refractoriness (1200 °C) and mechanical properties to withstand the conditions and handling.
5. Reasonably cheap.

Table 1.13 Possible crucible materials

Material	Properties				
	1	2	3	4	5
	Heat transfer	Thermal shock	Chemical resistance	Refractoriness	Cost
Fused silica	Poor	Good	Poor	Poor	Fairly cheap
Sintered alumina	Fair	Poor	Fair	Good	Moderately expensive
Fireclay	Poor	Poor	Good	Fairly good	Cheap
Silicon carbide (pure)	Good	Fairly good	Good	Good	Expensive
Graphite	Good	Good	Good	Poor[a]	Fairly cheap
Stainless steel	Fairly good	Good	Poor[b]	Good	Expensive

[a]Oxidizes at about 300 °C.

[b]Tends to dissolve in liquid metal.

Of these properties, good *thermal shock* resistance is absolutely necessary, as any crack in a crucible through which metal can leak renders it valueless. Refractoriness is obviously also needed, while sufficient mechanical strength is also imperative.

Chemical resistance can be viewed in a different angle, as it governs life. Although sufficient resistance to withstand one melt is essential, after this, it is a matter of balancing cost and life, and the cheapest cost per melt will probably be preferred.

Heat transfer will also be tied to economics, and the cost of the crucible must then be viewed in the light of fuel costs, labor, and other time-dependent costs. It is easily seen that the final material selected will be a compromise (Table 1.13).

No material is really satisfactory and other pure refractory materials give the same results. This situation has been resolved by using a composite of fireclay and graphite, which combines the best features of both materials. A further improvement is often obtained by the addition of silicon carbide.

With present day's interest in composites, it could be assumed that this was a recent development, but, in fact, composite fireclay–graphite crucibles were first introduced in 1850.

It is of interest to speculate on the reasons for the improved thermal shock resistance of what is, in practice, a dispersion of flake graphite in a fireclay matrix. The thermal conductivity is higher than that of fireclay, and, by analogy with studies reported by Hasselman (1969) on carbide–graphite composites, so is the critical strain. Both of these factors will increase the thermal shock parameter:

$$R = \frac{KS}{\alpha E} \tag{1.10}$$

where K is the *thermal conductivity*. However, the author doubts if this entirely accounts for the improvement, particularly as it is known that the flake graphite particle size is important. It seems likely that crack propagation is important in this case and the "relative damage" approach to thermal shock resistance would be appropriate in this instance.

In summary, in the industrial applications of nonmetallic high temperature materials, the most important properties are those governing mechanical integrity since, if this is lost, the material has usually failed. The properties influencing mechanical integrity are thermal shock resistance, chemical stability, and chemical properties.

Other factors, such as rate of corrosion, will govern life and hence will usually be of next greatest importance.

Thus, properties such as thermal conductivity or thermal expansion that affect thermal shock resistance will be important where there is a likelihood of *thermal stresses*. When this is not the case, such properties will govern the convenience or efficiency of operation and will be important economically but will not be prime factors in material selection.

For these reasons, thermophysical properties are often of rather secondary interest in industry. Nevertheless, the usually rather painstaking determination of thermophysical properties could have important repercussions in the refinement of materials and processes or the progress of innovation.

1.4.9 Other Materials

The more relevant materials to our interest include those described in Sections 1.4.2–1.4.8. But there are other industrial corrosion-resistant materials that deserve interest, at least to some extent and for some specific applications. These materials are briefly discussed next.

1.4.9.1 Refractory Metals

The refractory metals, such as W, Mo, and Ta, melt above 2400 °C (>4000 °F). They are rigid (high elastic modulus), and they have a high density (Table 1.14). Unfortunately, they cannot be used above 1200 °C (2200 °F) without

Table 1.14 Refractory metals

Metal	Density ($g\,cm^{-3}$)	Melting temperature, °C (°F)	Youngs modulus, GPA (10^6 psi)
Tungsten	19.3	3410 (6170)	345 (50)
Tantalum	16.6	2996 (5420)	185 (27)
Molybdenum	10.2	2610 (4730)	325 (47)

oxidation protection, because their oxides melt and even vaporize much below the metal's melting temperatures. The most successful oxidation protections are coatings that contain silicon and similar elements. These form a glassy surface. Such a surface layer has low permeability for the gases encountered in service and retard further oxidation. A $MoSi_2$ coating (0.1 mm) will protect molybdenum for 30 hours at 1650 °C.

1.4.9.2 Titanium Alloys

Titanium and its alloys (Donachie 2000) have very attractive structural properties. The metal has a low density of $4.54\,g\,cm^{-3}$, about 60% of that of steel and nickel- and cobalt-based superalloys, a high melting point of 1668 °C (3035 °F), and excellent corrosion resistance. Titanium exhibits an HCP structure called α, which transforms into a BCC structure β on heating to above 883 °C (1621 °F). Titanium alloys are very strong and, on a density-corrected basis, form some of the strongest alloys available. Because of their high strength and low density, titanium alloys are extensively used in gas turbine engines as fan blades, compressor blades and vanes, disks, and cases. One of the limitations of titanium alloys is their susceptibility to interstitial formation during processing or application above 600 °C (1100 °F) stabilizing the α phase. This occurs by the spontaneous capturing of oxygen (as well as carbon and nitrogen). The α phase forms a brittle skin known as the "α case." The formation of the α case debits structural properties of the alloys. Prior to any processing, the α case, therefore, needs to be chemically or mechanically removed.

Titanium alloys fall in one of three families depending on the predominant phases: the α alloys, the α–β alloys, and the β alloys. In the α alloys, the α phase is stabilized by the addition of Al, which raises the β transus, the transus being the temperature boundary between the single-phase and two-phase regions (Figure 1.12a). The β alloy, on the other hand, contains elements such as V, Nb, Mo, Cr, W, Fe, Co, and Si, all of which stabilize the β phase by lowering the β transus (Figure 1.12b). In the α–β alloy, both phases exist. A few elements such as Zr, Sn, and Hf are neutral in that they do not stabilize either of the phases but contribute to property improvement. The α

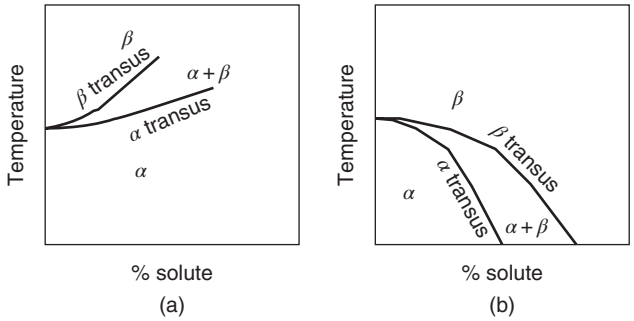


Figure 1.12 Schematic of (a) α and (b) β alloy stabilization.

alloy derives its strength from solid solution strengthening due to Al and Sn. Every 1% Al addition increases strength by about 8 ksi (55 MPa), while a 4 ksi (28 MPa) increase comes from every 1% addition of Sn. The α alloys are insensitive to heat treatment due primarily to the lack of second phases. The β alloys always contain small amounts of the α phase. The size and distribution of the α phase are controlled by a combination of thermal and mechanical treatments. The improved strength is derived from this second-phase precipitate. The most useful titanium alloys, however, consist of both α and β phases. These alloys are amenable to heat treatment, which is beneficially used to control both solid solution strengthening and precipitate hardening. A number of commercially available titanium alloys are shown in Table 1.15.

When exposed to an oxygen-containing atmosphere at elevated temperature, titanium alloys not only dissolve oxygen and form α phase but also oxidize. The product of oxidation is a TiO_2 (titania) scale. Oxygen easily diffuses through titania, and therefore, unlike alumina on many aluminum-containing alloys, titania is non-protective against continued oxidation.

To protect titanium alloys against oxidation at elevated temperatures, several coating systems such as platinum aluminides (Gurrappa and Gogia 2001), magnetron-sputtered Ti–Al (Leyens et al. 1996), and Ti–Al–Cr (Leyens et al. 1997) have been investigated. Some of these coating processes are covered in Chapter 18.

Table 1.15 Some commercially available titanium alloys

Alloy	Phase composition	Maximum use temperature [°C (°F)]
Ti–6Al–4V	$\alpha\beta$	315 (600)
Ti–6Al–2Sn–4Zr–2Mo	$\alpha\beta$	510 (950)
Ti–6Al–2Sn–4Zr–2Mo–Si	$\alpha\beta$	565 (1050)
Ti–5.5Al–4Sn–4Zr–0.3Mo–1Nb–0.55Si	Near α	593 (1100)

1.4.9.3 Intermetallics

An *intermetallic* can loosely be defined as a compound formed by the combination of two or more metal (or metalloid) elements, generally, but not always, falling at or near a fixed stoichiometric ratio and ordered on at least two or more sublattices (Welsch and Desai 1996).

High temperature intermetallics have been vigorously pursued since the early 1950s for the aerospace and power generation industries. They can potentially meet the needs for low density, higher operating temperatures, and reduced cooling requirements, in particular for aircraft applications, where weight savings can be converted into increased power and/or efficiency.

There are hundreds of binary intermetallics with melting points in excess of 1500 °C (Westbrook and Fleischer 1994). Some also have better specific properties (e.g. are less dense) than the Ni-based superalloys. In addition, the long-range-ordered superlattice structure of many intermetallics leads to reduced dislocation mobility and slower diffusion processes at elevated temperatures (Welsch and Desai 1996), often resulting in excellent high temperature strength and creep resistance. However, the same factors that lead to these excellent high temperature mechanical properties also contribute to the "Achilles heel" of most intermetallic compounds, severe brittleness, especially at ambient temperatures.

Overall, Ni aluminides, Fe aluminides, Ti aluminides, Nb aluminides, precious metal and exotic aluminides, Laves phases and *in situ* composites, silicides, and beryllide intermetallics, which contain at least one of the four metallic-based elements corresponding to the protective oxides Cr/Cr_2O_3, Be/BeO, Al/Al_2O_3, and Si/SiO_2, are being increasingly used, particularly in less demanding intermediates to high temperature applications (Gesmundo et al. 1993; Meier 1996; Nichols et al. 1997; Perkins and Meier 1990; Wojcik 1998).

1.4.9.4 Advanced Ceramics

HTC of metals and alloys has been more extensively studied than HTC of ceramics. Recently, however, structural ceramics are finding more and more applications in high temperature systems, and HTC of structural ceramics becomes an important field of study. Apart from the ceramics discussed in Section 1.4.8, there are now advanced ceramics with enhanced mechanical properties and improved thermal conductivity, electrical conductivity, and a better oxidation and corrosion resistance. They can be classified according to the type of protective oxides they form.

These include silica formers, alumina formers, boria formers, and transition metal oxide formers. Most of the literature covers silica formers since there are a number of near-term applications for these materials. Basic oxidation mechanisms, water vapor interactions, volatilization routes, and salt-induced corrosion were discussed for these materials. Less information is available on alumina-forming ceramics. However, the rapid oxidation rate in water vapor appears to be a major problem. Boria formers show rapid oxidation rates due to the formation of a liquid oxide film and are volatile in the presence of water vapor due to highly stable H_x-B_y-O_z(g) species formation. Transition metal carbides and nitrides also show rapid oxidation rates due to rapid transport in the oxide scale and cracking of that scale.

Multicomponent ceramics allow the optimization of various physical properties. These include ceramics that form multicomponent oxides as well as fiber-reinforced ceramic matrix composites. However, the oxidation behavior of these materials is complex when compared with pure materials. The leading fiber-reinforced composites are silicon-based and contain continuous SiC fibers with coatings of graphite carbon or hexagonal boron nitride (Bornstein 1996; Fox 1998; Jacobson 1989, 1993; Narushima et al. 1997; Rapp 1986).

1.4.9.5 Nuclear Reactor Materials

Radiation – by energetic neutrons, by ultraviolet light, by β rays, (accelerated electrons), or by other forms of particles and rays – introduces energy very locally within a material. A single electron, atom, or bond may receive the full impact, while neighbors experience only the aftereffects. An atom may be knocked out of the crystal lattice to introduce a vacancy and an interstitial; a bond may be broken to cut a molecule in two; an electron may be knocked away from an atom to produce an ion; or a proton may be knocked out of a nucleus to transmute an element. All of these modify the structures of the exposed materials and, hence, the properties.

We call these changes radiation damage, since the property losses are generally more critical to the exposed material than the property gains by recovery. The effects of radiation on various materials are particularly important in electric, magnetic, and nuclear applications.

Metals are particularly suitable for nuclear reactors because, in addition to their usual engineering and manufacturing properties, they have high thermal conductivities and are immune to radiation damage by ionization.

The mobility of point defects also enables many metals, particularly FCC metals, to be fairly insensitive to knock-on radiation damage.

Many severe difficulties remain, however. Often, the materials that, for nuclear reasons, are most essential to use have many difficult metallurgical and engineering features. They may be difficult to extract (e.g. Be), may contain undesirable and not easily removable impurities (e.g. Hf in Zr, H

in stainless steel), may have awkward crystal structures or undergo crystallographic transformations (e.g. U and Pu), may oxidize readily (e.g. U and graphite), may be brittle, particularly after irradiation (e.g. U, Be, and ferritic steel), and may be highly toxic (Pu and BeO).

The main fuel element material for the earlier types of gas-cooled reactors is *uranium*.

For more advanced reactors, working at higher temperatures, the crystallographic transformations that set in above 660 °C have largely ruled out the use of uranium in its metallic state, and most recent reactor designs are based on the use of *ceramic* fuels, particularly oxides and carbides of U, Pu, and Th. Uranium dioxide is now widely used in both water-cooled and advanced gas-cooled reactors because of its chemical stability and high melting point, although its low thermal conductivity is a disadvantage. Attempts have been made to develop liquid metal fuels (e.g. U in liquid Bi), but problems of liquid metal attack on their containers have proved difficult.

The main moderator materials in use are *graphite* and *heavy water*. Graphite suffers from effects of knock-on radiation damage (stored energy and radiation growth), although these become fairly unimportant at temperatures above about 250 °C, where much of the radiation damage anneals out. At higher temperatures, oxidation is a problem, but this has been overcome in advanced gas-cooled reactors by adding a trace of methane to the carbon dioxide coolant.

Materials for fuel cans have to satisfy several stringent requirements. The can must provide a complete and reliable envelope to prevent escape of radioactive fission products and to protect the fuel from chemical attack. It must itself be chemically compatible with the fuel and resistant to attack by the coolant. It must endure severe neutron and fission fragment irradiation. It must be made of a material with a low neutron absorption cross section. It must have a good thermal conductivity. The can wall must be thin, both to conserve neutrons and also to minimize the temperature drop from the fuel to the coolant, and yet it must also be strong if the fuel itself is mechanically weak or if it is required to withstand a pressure of fission gases created by the fuel.

For gas-cooled reactors, using uranium metal fuel, *magnesium* is the main canning material. The two main contenders for UO_2 fuel cans in advanced gas-cooled reactors have been *beryllium* and *austenitic stainless steel*. Despite its very low neutron cross section, beryllium has not so far been used, because of its cost and low ductility. Stainless steel cans are now used successfully. The main problem has been to produce very clean, inclusion-free steel to manufacture it into very thin tubes (0.015 in. wall thickness), this thinness being necessary to minimize neutron losses in this material of moderate neutron absorption cross section. A remaining problem is some embrittlement that appears after prolonged irradiation at high temperatures. This appears to be caused by the formation of small helium gas bubbles on grain boundaries, created by the neutron-induced decomposition of boron, present in trace amounts in the steel.

In fast reactors, the problem of neutron absorption in the fuel can is less severe, and metals such as *stainless steel* and *niobium* are used. Compatibility with the liquid sodium coolant is a problem. The oxygen content of the sodium has to be kept very low (<10 ppm) to avoid corrosion of the can.

In water- and steam-cooled reactors, corrosion in high temperature water (e.g. 280 °C at 1000 psi pressure) or steam at 500 °C presents special problems for canning materials. *Zirconium* (with hafnium removed) is the favored material, usually in the form of *zircaloy* (1.5% Sn, 0.15% Fe, 0.05% Ni in Zr) or other alloys (e.g. Zr–2.5% Nb, Zr–Cr–Fe). Additions of about 0.4% tellurium improve the resistance of zirconium to corrosion and absorption of hydrogen in water at high temperatures and pressures (Ahmad and Keys 1975; Cox and Donner 1973; MacEwen and Hastings 1975; Sabol and Dalgaard 1975).

Important issues on the properties and HTC behavior of materials for nuclear reactors are addressed in Section 19.1 (Baerlecken et al. 1961).

1.4.10 Producers of High Temperature Materials

A partial listing of companies producing and supplying high temperature materials is given below. Each company produces an extensive range of high temperature metallic and nonmetallic materials, and a more complete listing can be found at the web addresses provided:

Avesta Sheffield, www.avesta-sheffield.com

Carpenter Technology Corporation, Inc., www.cartech.org

Copper Development Association, Inc., www.copper.org

Corrosion Materials, www.corrmtls.com

Deloro Stellite, www.stellite.com

Hamilton Precision Metals, Inc., www.hpmetals.com

Haynes International, Inc., www.haynesintl.com

Inco Alloys International, www.incoalloys.com

Krupp VDM Technologies Corp., www.krupvdm.de

Nickel Development Institute, www.nidi.org

Rolled Alloys, www.rolledalloy.com

Sandvik Steel, www.sandvik.com

Special Metals Corporation, www.specialmetals.com

Titanium Metals Corporation, www.timet.com

Wah Chang-Oremet, www.wahchang.com

Trademarks	Company
Hastelloy, Haynes, Ultimet, C-22, C-2000, G-30, and B-3	Haynes International Inc.
Incoloy, Inconel, and Monel	Inco Alloys International
Stellite and Tribaloy	Deloro Stellite, Inc.
Elgiloy	Elgiloy Co.
Havar	Hamilton Precision Metals, Inc.
20Cb-3	Carpenter Technology Corporation
Nicrofer	Krupp VDM
MP35N	SPS Technologies

1.5 Corrosive Environments

1.5.1 Air and Oxygen

Although corrosion by oxidation in air is undoubtedly the type of attack of greatest practical importance, it is remarkable that relatively few cases are entirely free from the complications arising from contamination of the reacting atmosphere. Except in the case of heating by electrical means, contamination arises from the combustion products, in gaseous, liquid, or solid form, while with electrical heating the oxidation is often complicated by the presence of fumes or vapor arising from the materials being processed.

Perhaps the closest approach to pure oxidation in everyday conditions arises in domestic electric heating appliances where the elements are exposed to air. At some points the elements are necessarily in contact with supporting refractories, and if these are not of adequate purity, accelerated corrosion leading to early failure can occur. In a similar way, the sheathed radiant-type elements of electric cookers usually fail owing to the corrosive effects of contaminants such as animal fats or salts from spilled liquids.

Wires for these applications are commonly assessed by a standardized test such as that described in ASTM B76–81, which involves electrical heating for periods of 2 minutes. to a temperature of 1177 °C (or other temperature depending on the composition of the wire) until failure by burnout occurs.

In the case of alloys having one constituent considerably more reactive to oxygen than the others, conditions of temperature, pressure, and atmosphere may be selected in which the reactive element is preferentially oxidized. If conditions are selected so that the inward diffusion of oxygen is faster than outward diffusion of the reactive element, the oxide will be formed as small dispersed particles beneath the surface of the alloy. The phenomenon is known as *internal oxidation* and is of quite common occurrence, usually in association with a continuous surface layer of oxides of the major constituents of the alloy.

The corrosion rate can be influenced considerably by the presence of small proportions of contaminants, particularly if these are adsorbed onto the metal surface and thus influence the nature of the initially formed film of corrosion product. The presence of water vapor in air is, of course, of greatest practical importance, and marked effects from this cause on the scaling rate of steel have been reported; the direction of the observed effect has not been constant, and it is possible that the influence of hydrogen, formed by dissociation of the water, in decarburizing the steel is a factor of importance. Similarly, it has been reported that humidity influences the life of nickel–chromium wires for electrical heating elements subjected to the ASTM life test referred to earlier, a change from dry air to air saturated with water vapor at normal temperature reducing the life by approximately one-half. The nitrogen in air can sometimes play a significant role in corrosion, particularly in relation to steels containing chromium or aluminum, which have high affinities for nitrogen; even in cases in which the nitrogen does not enter into the chemical processes of corrosion, it may influence the rate of attack by oxidation, presumably by being adsorbed onto the metal surface. Thus different reaction rates may result from using on the one hand dry air and on the other pure oxygen at the equivalent partial pressure of the oxygen in the air.

1.5.2 Steam

Corrosion by essentially pure steam arises principally in connection with power generating plant. Temperatures up to about 600 °C in association with pressures up to about 15 MN m^{-2} are involved, although in the most advanced supercritical installations being planned for the future, temperatures of 700 °C and pressures of 50 MN m^{-2} are under consideration. The highest temperatures occur in the superheater tubes, but it is probable that the severest corrosion conditions on these components will arise from the presence of fuel ashes on the outside of the tubes rather than from the steam on the inside. Perhaps the most critical components in such installations will be the main steam pipes, which are more highly stressed than the superheater tubes. The corrosion resulting from the action of high temperature steam generally leads to the formation of oxides, although hydroxides may be formed. The reaction depends on the dissociation pressure of the oxide in relation to the partial pressure of the oxygen in the water vapor.

The importance of the dissociated hydrogen in contributing to the decarburization of carbon steels in water vapor has already been mentioned.

1.5.3 Carbon and Oxides of Carbon

The importance of these agents in leading to HTC has increased considerably in recent years as a result of the

development of graphite-moderated nuclear reactors using carbon dioxide as coolant. Reaction between carbon dioxide and graphite leads to the presence of a small content of carbon monoxide (which increases with increasing temperature) in the atmosphere. The formation of oxide films results from the presence of dissociated oxygen, but at the same time *carburization* may occur with steels or alloys having constituents that form stable carbides. Indeed, carbon monoxide, sometimes with additions of hydrocarbons, is a very effective gas-carburizing agent for steels, as the partial pressure of the oxygen is insufficient to lead to oxidation of iron. In the case of materials forming more stable oxides, e.g. chromium-containing steels or alloys, oxidation may proceed in parallel with carburization.

1.5.4 Sulfur-Containing Gases

Sulfur-containing atmospheres are of importance mainly in the effect that they exert when present in small proportions in combustion products, but studies have been made of the effects of pure sulfur vapor, hydrogen sulfide, and sulfur dioxide on various metals. The effect of pure sulfur is usually straightforward, leading to the formation of a sulfide film, which may be more or less protective according to its structure and properties. Some sulfides have low melting points, or form low-melting-point eutectics with the metal, and in these cases attack is rapid above the critical temperature, usually taking the form of *intergranular penetration*. For example, in the nickel–sulfur system, a eutectic forms at 645 °C, whereas in the iron–sulfur system the minimum melting point is 988 °C. Hence it is normally found that iron-based alloys are more satisfactory than nickel-based alloys in sulfurous atmospheres at temperatures within this range. Attack by hydrogen sulfide bears some similarity to that by sulfur, the hydrogen having a negligible effect in most cases. Sulfur dioxide, however, frequently behaves differently as the formation of oxide films apparently largely prevents the absorption of sulfur.

1.5.5 Hydrogen

Attack upon metals by hydrogen rarely results in the formation of surface films of compounds since the gas is usually readily soluble in the metal, with a high rate of diffusion, and hydrides, if formed, are generally rather unstable. The effect of hydrogen usually follows from its reducing action on certain constituents in the alloys; probably the most familiar examples of this are the *decarburization* of steels by the conversion of carbides to volatile hydrocarbons and the embrittlement of tough-pitch copper by the reduction of intergranular oxide. Hydrogen occurs as a major constituent of the atmosphere in furnaces used for bright annealing or for brazing, and in such cases the temperatures involved may rise to as high as 1200 °C. In the chemical engineering field, many processes of synthesis or hydrogenation are carried out with hydrogen-rich atmospheres at temperatures up to about 600 °C and at pressures arising to 1000 atm. Much of the understanding of the attack on steels by hydrogen has been obtained from work on problems arising in the chemical industry.

1.5.6 Nitrogen

Although nitrogen is the major constituent of air, it plays a minor role in the scaling of most metals on heating in air, its effect being completely overshadowed by that of oxygen. This follows from the fact that the dissociation pressures of the nitrides of the more common metals are greater than the partial pressure of nitrogen. Chromium, aluminum, and some of the less common metals such as titanium, molybdenum, and tungsten, however, form stable nitrides, which can result from heating materials containing these elements in air. Reaction between nitrogen and metals is of principal importance, however, in reducing atmospheres, particularly in cases in which absorption of nitrogen is deliberately sought, i.e. in the surface hardening of steels by nitridation. The atmosphere in such cases is anhydrous ammonia, dissociation of which occurs at the surface of the steel, although only a small proportion of the resulting nitrogen is absorbed. Materials resistant to nitrogen and not acting as dissociation catalysts for ammonia are required as containers for such treatments, and stainless steels of 18/8 or 25/20 types or Inconel (76Ni–15Cr–8Fe) have been widely used.

1.5.7 Halogens and Halogen

The halogens are particularly important in high temperature environments because many of the metallic halides have relatively high vapor pressures, and the corrosion products are therefore vaporized instead of forming protective surface layers. This is particularly true in the case of chromium and aluminum, both important constituents of heat-resisting alloys. However, the attack is mainly on the metals rather than on oxides, so that an initially formed oxide film confers appreciable protection and the action of halogens in a predominantly oxidizing atmosphere is much less than in a reducing atmosphere. Small traces of acid gases such as hydrochloric acid can, however, considerably accelerate oxidation rates in air, particularly of copper-based alloys.

1.5.8 Molten Salts

A wide variety of molten salt baths is used in industrial practice, and there exists a corresponding wide range of possible chemical reactions with metallic parts being heated in the baths or with the containers holding the baths.

Baths consist largely of mixtures of nitrates, carbonates, or halides of the alkaline or alkaline earth metals, and these generally have a ready solubility for oxides of other metals. Hence, although the salt baths may be sufficiently oxidizing to react with the alloys concerned to form oxide, this product is taken into solution in the bath and does not form a protective scale; attack therefore progresses steadily. In some cases, absorption of components of the salt mixture into the alloy may occur, with either deleterious or beneficial results. Thus, with baths containing borates, reduction of boric oxide may occur by the action of reactive constituents such as aluminum, resulting in the absorption of boron into the alloy; with nickel-based alloys a low-melting-point eutectic may then be formed with serious effects on the properties of the alloy. On the other hand, alkali-cyanide baths are used for the heat treatment of steel parts, absorption of carbon and nitrogen into the steel giving surface hardening.

Molten salt environments are fully treated in Chapter 13.

1.5.9 Molten Metals

If the major constituents of a solid alloy in contact with a liquid alloy are highly soluble in the latter without formation of compounds, progressive attack by solution is to be expected. If, on the other hand, a stable intermetallic compound is formed, having a melting point above the temperature of reaction, a layer of this compound will form at the interface and reduce the rate of attack to a level controlled by diffusion processes in the solid state. By far the most serious attack, however, occurs in the presence of stresses, since in this case the liquid alloy, or a product of its reaction with the solid alloy, may penetrate along the grain boundaries, with resulting embrittlement and serious loss of strength.

Molten metals as a corrosive environment are discussed more fully in Chapter 14.

1.5.10 Refractories, Ceramics, Glasses, Etc.

The possible attack on metals and alloys by materials of this type may be considered in a manner similar to attack by molten salts. If a molten phase exists in the material at the temperature under consideration, it is possible that solution of the oxides formed by the alloy will occur, thus preventing the formation of a protective film. Molten glasses act in this manner, and refractories with traces of impurities, perhaps in localized regions, can act very similarly. Minerals such as mica and asbestos frequently give rise to troubles due to impurities, which either lower the melting point or impair the electrical insulation at elevated temperatures. These materials, which are silicates of magnesium and calcium, often contain small quantities of iron oxides or sulfides and other impurities, which make them unsuitable for use at temperatures above 500 or 600 °C, particularly if electrical insulation characteristics are required.

A possibility that must be considered is that of reaction between a refractory and an alloy occurring in consequence of the reduction of a constituent of the refractory by a metal in the alloy. Thus alumina has a higher *free energy* of formation than silica, and therefore aluminum is capable of reducing silica. At a high enough temperature, if oxygen is not available in the atmosphere to combine with the aluminum, this reaction is likely to take place. In order to avoid reactions of this type, only pure and very stable refractories such as alumina, magnesia, zirconia, or beryllia should be used in contact with reactive metals at high temperature.

1.5.11 Combustion Products

The various gas mixtures arising from the *combustion* of fuels form the major group of atmospheres, leading to the hot corrosion of metals. Almost all natural and processed or synthetic fuels consist predominantly of hydrocarbons, carbohydrates, or more complex carbon compounds, so that the principal constituents of the combustion products are the oxides or carbon and water vapor, together with the residual nitrogen from the air. In conditions of incomplete combustion, the gases may contain hydrogen, hydrocarbons, and carbon monoxide in appreciable proportions, with only small proportions of oxygen, while when complete combustion is effected with excess air, these reducing gases will be absent, but there will be larger amounts of oxygen.

In most fuels, some sulfur-containing compounds are present, and the combustion gases then contain sulfur dioxide, sulfur trioxide, or sometimes hydrogen sulfide. It is thus evident that under ordinary working conditions, it is not uncommon for equipment to be subjected to atmospheres whose compositions vary from time to time, and this is one factor that can lead to abnormally accelerated corrosion rates. In particular, when the atmosphere can vary from oxidizing to reducing in character, the equilibrium constitution of the scale formed on an alloy may change, with resulting cracking or porosity in the layer. The protective action of a coherent scale is thus much reduced.

Combustion of coal may take place in conventional fixed beds using lump coal and in which temperatures up to 1300 °C may be reached; by entrained flow in which pulverized coal is injected into the combustion zone with the air, reaching temperatures up to 1500 °C; or in the more recently developed systems of fluidized-bed combustion, again using pulverized coal but with temperatures restricted to below about 900 °C. While most processes operate at near to normal pressure, some fluidized-bed processes are designed for pressures up to about 20 atm.

The environments involved are basically those referred to under "Combustion Products," but the corrosive attack on metallic components is to a major extent due to alkali metal sulfates formed from constituents in the coal and deposited in a molten condition on the metals. For components immersed in the bed of a fluidized-bed system, the lower temperatures lead to less volatilization of the alkali sulfates, but low partial pressures of oxygen may reduce the effect of oxide scales in minimizing sulfur attack.

A particular type of corrosion observed with nickel–chromium and nickel–iron–chromium alloys and involving both carburization and oxidation takes place at temperatures around 1000 °C in carbon-containing atmospheres. The attack, which is termed *green rot*, on account of the color of fractured surfaces of the attacked alloy, occurs particularly in atmospheres of the bright-annealing type when they are contaminated with carbon-containing gases or vapors but can also arise with incompletely burnt hydrocarbon fuels. This type of attack has been reported to be considerably accelerated by cyclic variations of the atmosphere from oxidizing to reducing.

Apart from the direct corrosive action of the gaseous products from burnt fuels and coal, an important effect frequently arises from the deposition of *ashes* on the metal surfaces involved. Ashes normally consist of complex mixtures of compounds of oxides, the compositions varying very widely and the precise state of combination being uncertain. Present-day composition of ashes ranges as follows (in wt%):

SiO_2	Al_2O_3	CaO	HgO	Na_2O	K_2O	Cl_2	P_2O
25–60	15–40	1–20	0–5	0.2–3	0.2–5	0–5	0–1

The corrosive attack by an ash is frequently critically dependent on the temperature, accelerating steeply when the melting point of a particular ash constituent is exceeded. This is particularly noticeable in the case of the vanadium-containing ashes from crude or residual mineral oils that seriously attack most heat-resisting alloys when the temperature is above about 650 °C, the melting point of vanadium pentoxide. The rapid attack follows fluxing of the normally protective oxide scale by the ash, and the attack on the underlying metal may be in the form of further oxidation or may include attack by sulfur compounds or other active constituents of the ash. Various investigators have compared the rates of attack on different alloys by selected real or synthetic ashes, and somewhat contradictory results have been reported. It is probable that the different conclusions arose from the difference in character of the attack, which follows initial penetration of the protective scale, on account of variations in composition of the selected ashes.

The deposits formed in internal combustion engines by high-octane petrols may be classed as ashes; they consist of mixtures of lead oxides, bromides, and sulfates derived from the antiknock additives and, of course, exert their main corrosive effect on the parts operating at the highest temperature: the exhaust valves and the sparking-plug electrodes.

The formation of an ash is not always deleterious since a layer of a less reactive material may serve to restrict access to the alloy of more reactive agents either in the ash itself or in the atmosphere. The erosive action of ash also has to be considered in addition to the purely corrosive action. With high-speed gas streams, as in gas turbines, *erosion* is frequently the more important effect.

1.5.12 Other Environments

Many other corrosive environments are found in high temperature processes embracing *gasification*, *liquefaction*, etc. Some of them are briefly described here.

Coal gasification processes also use fixed-bed, fluidized-bed, and entrained-flow methods but involve the supply of restricted amounts of air or oxygen to burn some of the coal to provide the heat source and steam to yield the required gaseous product. The latter may be mixtures of hydrogen and carbon monoxide as a substitute for natural gas or as industrial fuel gas, or methane for chemical feedstock. The various processes are all carried out at elevated pressures and at temperatures ranging from 500 °C to over 1800 °C. While the major metallic components of the plant, such as the reaction vessel, may be refractory lined to minimize the temperature reached and to protect them to some extent from the environment, other critical components such as heat exchanger tubes may be exposed. The atmosphere is highly reducing with low oxygen and high sulfur partial pressures and a high carbon activity.

Liquefaction of coal involves the extraction of carbon by solvents at high pressures and at temperatures up to about 500 °C, followed by separation of the extract, which is then hydrogenated in the presence of a catalyst to yield hydrocarbon oils. The corrosion conditions are not regarded as severe.

In most processes of coal conversion, the corrosive action of the gaseous environment may be aggravated to some degree by the erosive action of the entrained solids, the ashes, or partly burned fuel termed *char*.

The high temperatures and high gas velocities arising in gas turbine engines have led to much concern at the threat of corrosive attack on critical components. Turbine entry temperatures may range between 700 and 1300 °C, and while, for aeroengines, refined fuels with low sulfur content are used, oxidation may be a significant problem, and corrosion may be aggravated by contaminants such as sulfates and chlorides introduced either in minor amounts in the fuel or, more seriously, in the ingested atmosphere. Aircraft operating in marine environments such as from aircraft carriers, or helicopters involved in sea rescues or oil

rig servicing, are particularly vulnerable to hot corrosion of turbine components. For the higher gas temperatures, air-cooled turbine blades are used, restricting the metal temperature to below about 1150 °C, the maximum permissible with the most advanced materials on grounds of creep and fracture resistance. Even the protective coatings are widely used both to provide increased corrosion resistance and to give thermal insulation. Coatings of a number of different types have been developed, embracing intermetallic compounds, usually *aluminides*, formed by diffusion or overlay techniques, and oxide ceramic coatings, primarily based on zirconia, applied by spraying. Erosion of turbine components may also pose serious difficulties to aircraft operating in sandy locations, while imperfect combustion may lead to erosion by carbonaceous residues from the fuel.

Industrial gas turbines generally operate at lower temperatures than aircraft jet engines but may be more susceptible to hot corrosion because they may use less refined fuels, even crude or residual oils containing relatively high proportions of sulfur or vanadium. Coatings of the type referred to above are increasingly being used to provide protection.

A further environment in which interest has been shown in recent years arises in the use of helium as the primary coolant in high temperature nuclear reactors. The gas is circulated continuously around the reactor core and a secondary heat exchanger, and becomes contaminated, mainly with hydrogen and carbon monoxide from the graphite moderator. Tests in the temperature range of 650–800 °C have shown that surface and intergranular oxidation and carburization can occur, affecting the long-time creep-rupture properties of materials.

1.6 Films and Scales

1.6.1 Nature of Reaction Products

The study of corrosion is essentially the study of the nature of metal reaction products (corrosion products) and of their influence on the reaction rate. It is evident that the behavior of metals and alloys in most practical environments is highly dependent on the solubility, structure, thickness, adhesion, etc. of the solid metal compounds that form during a corrosion reaction. These may be formed naturally by reaction with their environment (during processing of the metal and/or during subsequent exposure) or as a result of some deliberate pretreatment process that is used to produce thicker films or to modify the nature of existing films. The importance of these solid reaction products is due to the fact that they frequently form a kinetic barrier that isolates the metal from its environment and thus controls the rate of the reaction; the protection afforded to the metal will, of course, depend on the physical and chemical properties outlined above.

In general, in high temperature system films, scales and complex corrosion products may be formed depending on the nature of the metallic material and of its environmental conditions. The distinction between a *film* and a *scale* is not well defined, but it is usual to use the former when referring to a thin continuous layer of reaction product (visible or invisible) while the latter is normally used for thick high temperature layer(s) (always visible).

This section describes in general terms the variation in the nature of very thin films originating in the initial reaction of a metal with its environment and their progression to the thicker overgrowths that control the kinetics. Recent developments in instrumental techniques have led to significant advances in the characterization of these film- and scale-forming systems, and some of the experimental approaches available are provided in Chapter 17. Here, we consider essentially the products of reaction formed by a gaseous oxidizing atmosphere (solid–gas systems). Surface reaction products formed in solid–liquid metal systems, solid-fused salt systems, and more complex systems will be considered in the chapters dealing directly with these systems.

1.6.2 Thin-Film Regime

The application of ultrahigh vacuum techniques to low-energy electron diffraction (LEED) studies of very clean metal surfaces in low pressure oxidizing and sulfidizing atmospheres over a range of temperatures above ambient has provided detailed information on the initial states of interaction. The following sequence of events is generally observed in the case of exposure to oxygen:

1. Rapid physical adsorption of molecular oxygen.
2. Chemisorption of atomic oxygen to form a partial or complete monolayer.
3. Further chemisorption of atomic oxygen into a second layer and/or further physical adsorption of O_2.

In stage 2 a distinct structural modification to an expanded lattice at submonolayer coverages has been observed on several metals, indicating that the oxygen ions become progressively incorporated into the metal lattices. These two-dimensional crystals then gradually transform into a three-dimensional metal oxide lattice as more oxygen becomes incorporated. Subsequent exposure to high temperature conditions (>1000 °C) has confirmed the extreme stability of the stage 2 state.

Similarly, under low temperature conditions (<25 °C), three stages have been recognized and defined as follows:

1. Physical adsorption of oxygen resulting in the formation of one or more monolayers of oxide and requiring no activation energy.

2. Electron tunneling through the stable oxide film to the adsorbed oxygen, which sets up a potential and causes ion drift, thus resulting in logarithmic oxide growth.
3. Film rearrangement resulting in the formation of oxide subgrain and grain boundaries; these paths of easy ion migration promote the formation of oxide "islands" and result in an increase in the growth rate of the oxide.

Oxide films formed at low temperatures are initially continuous and amorphous but may undergo local crystallization with the incorporation of the oxide "islands," a process that is facilitated by water, heat, high electric fields, and mechanical stress (Fehlner and Mott 1970).

Studies of thermally grown oxides in the thin-film region (<100 nm) have revealed on single-crystal substrates interesting details of epitaxy, stress generation, mosaic structure and film topography, and oxidation rate anisotropic behavior. Mismatch between the oxide lattice and the metal substrate gives rise to stresses that may find relief in the generation of mosaic structures consisting of small crystallites (5–100 nm diameter) whose lattices are slightly twisted or tilted with respect to one another. Their boundaries represent potential paths of easy diffusion through the oxide.

The uniformity of film thickness is dependent upon temperature and pressure. The nucleation rate rises with pressure, such that at pressures above atmospheric the high rate of nucleation can lead to comparatively uniform oxide films, while increase in temperature reduces the density of oxide nuclei and results in nonuniformity. Subsequently, lateral growth of nuclei over the surface is faster than the rate of thickening until uniform coverage is attained, when the consolidated film grows as a continuous layer.

Growth of oxide nuclei may also be accompanied by the appearance of whiskers and platelets under certain conditions (Grauer and Feitknecht 1966). It has been demonstrated that oxidation of iron in air at about 200 °C initially leads to nuclei of Fe_3O_4 developing to form a porous layer. Over this homogeneous oxide layer, nuclei of α-Fe_2O_3 appear and spread over the Fe_3O_4, but no γ-Fe_2O_3 is observed. After 30 days, whiskers of the α-Fe_2O_3 appear, ultimately reaching a length of 1 μm. At higher temperatures, too, whiskers of α-Fe_2O_3 appear and subsequently develop into crystallographic platelets. In general, products of this nature occur as fine features from otherwise protective films.

1.6.3 Scale-Forming Regime

In considering film growth at higher temperatures, a changeover to diffusion control, which is dependent on concentration gradients, tends to give rise to parabolic and paralinear kinetics as substantial scales form at a thickness of 1–100 μm or more. This is the area of vital concern in the development and application of engineering alloys for high temperature resistance and is in distinct contrast to the thin-film regime. Nevertheless, the initial state of the metal surface can still influence subsequent oxidation behavior. Thus, different oxidation patterns may be observed depending upon whether the surface is electropolished, hydrogen reduced, mechanically abraded, or cathodically pretreated. When metals of variable valency are subjected to the oxidizing potential gradient across the scale, a duplex or multiple series of layers forms. The classical case of iron oxidized above 600 °C has been well established (Grauer and Feitknecht 1966), and it has been shown that the system consists of Fe/FeO/Fe_3O_4/Fe_2O_3/O_2. In these situations film thickening occurs by transport of cations, anions, vacancies, and electrons across the various phase boundaries, which is possible owing to the nonstoichiometric composition of the various coexistent oxides (see sections on lattice defects in metal oxides, continuous oxide films, and the oxidation resistance of low-alloy steels).

A rather different situation arises when mild steel is exposed to dilute sodium hydroxide at 300–360 °C. Here a duplex Fe_3O_4 scale is formed, consisting of an inner adherent protective film in contact with an outer poorly adherent crystalline layer of magnesite (see section on discontinuous oxide films).

In alloy systems, the course of events is complicated by factors such as:

1. The affinity of the component metals for each other and for the nonmetal.
2. The diffusion rates of atoms in the alloy and or ions in the compounds.
3. The mutual solubilities of the products present in the oxidation layers.
4. The formation of ternary compounds, e.g. spinels (see Table 1.16).
5. The relative volumes of the various phases.

In practice, thermal cycling rather than isothermal conditions more frequently occurs, leading to a deviation from steady-state thermodynamic conditions and introducing kinetic modifications. Lattice expansion and contraction, the development of stresses, and the production of voids at

Table 1.16 Spinel phases encountered in alloy oxidation

n-Type	$MgFe_2O_4$	$ZnCo_2O_4$
	$NiFe_2O_4$	$MgAl_2O_4$
	$ZnFe_2O_4$	$ZnAl_2O_4$
p-Type	$MgCr_2O_4$	$ZnCr_2O_4$
	$FeCr_2O_4$	$CoAl_2O_4$
	$CoCr_2O_4$	$NiAl_2O_4$

the alloy–oxide interface, as well as temperature-induced compositional changes, can all give rise to further complications. The resulting loss of scale adhesion and spalling may lead to *breakaway oxidation* in which linear oxidation replaces parabolic oxidation (see section on discontinuous oxide films).

Examination of the structural consequences of these complex interacting factors is now being elucidated in considerable detail by systematic application of electron optical and X-ray analysis techniques, as well as by a range of other methods.

In certain systems the oxidation reactions may lead to a particularly protective single phase being formed at the surface, e.g. magnesite (Fe_3O_4) in the case of iron and steel and γ-Al_2O_3 in the case of aluminum. The "spinel" ($MgAl_2O_4$) lattice is important in relation to the protection it affords to alloys used at high temperatures, and such structures often occur with a continuously varying stoichiometry as a "double oxide" phase, which may provide an effective kinetic barrier to the oxidation process (e.g. $NiO \cdot Cr_2O_3$ spinel in Cr–Ni–Fe alloys). Some examples are given in Table 1.1.

The spinel structure is of special significance in the corrosion behavior of iron and alloy steels at high temperatures.

Its crystallographic unit cell can be represented as $8XY_2O_4$ (or $X_8Y_{16}O_{32}$) in which the valencies of the metal ions X and Y may be (a) X^{II}, Y^{III}; (b) X^{IV}, Y^{II} (giving rise to the so-called "2-3 spinels" or the "4-2 spinels"); and (c) X^{VI}, Y^{I}. The structure is based on a cell containing 32 oxygen atoms in a close-packed cubic arrangement. This provides for the incorporation of the X atoms in eight equivalent tetrahedral sites and the Y atoms in 6 equiv. octahedral sites. "Inverse" spinels follow a different arrangement, represented by $Y(XY)O_4$, in which half of the Y atoms are located tetrahedrally, while remaining Y atoms together with the X atoms are randomly arranged among the 16 octahedral positions. More generally, some spinels exist with a fraction λ of Y cations in tetrahedral sites where $0 < \lambda < ½$.

It should be noted that single metal oxides such as Fe_3O_4 and Co_3O_4 are inverse spinels, while Mn_3O_4 is a normal spinel. The spinel structure is prominent in the oxides on iron and aluminum. The oxides M_2O_3 (and also the hydroxides and oxyhydroxides $M(OH)_3$ and $MO \cdot OH$) exist in the α and γ forms. Corundum and hematite represent the isostructural α forms, while the γ forms have cubic spinel-like structures deficient in metal ions. For example, in γ-Fe_2O_3 there are only $21⅓$ Fe^{3+} ions per unit cell of 32 O^{2-} ions, and these are randomly distributed among the eight tetrahedral and 16 octahedral "available" sites. In magnesite, represented as Fe^{3+} $(Fe^{2+}Fe^{3+})O_4$, one-third of the cations are Fe^{2+}, and continuous interchange of electrons between Fe^{2+} and Fe^{3+} ions in the 16-fold positions accounts for its extremely high electronic conductivity. Careful oxidation of Fe_3O_4 yields γ-Fe_2O_3, which may be converted back into Fe_3O_4 by heating *in vacuo* at 250 °C. Because wüstite (FeO) ideally has the NaCl-type structure (FCC anion lattice), with four Fe^{2+} and four O^{2-} ions per unit cell, deviations from stoichiometry lead to not every octahedral site being filled in the metal-deficient lattice (e.g. at 570 °C $Fe_{0.93}O$ contains cation vacancies and compensating Fe^{3+} ions). At lower temperatures, disproportionation occurs:

$$4FeO \rightleftharpoons \alpha\text{-}Fe + Fe_3O_4 \qquad (1.11)$$

Therefore, the relationship between these interconvertible structures originates from a cubic anion lattice of 32 O^{2-} ions in the cell. With 32 Fe^{2+} ions in the octahedral holes, stoichiometric FeO is formed. Replacement of a number of Fe^{2+} ions with two-thirds of their number of Fe^{3+} ions maintains electrical neutrality but provides nonstoichiometric $Fe_{1-x}O$. Continual replacement in this way to leave 24 Fe atoms in the cubic cell produces Fe_3O_4, and further exchange to an average of $21⅓$ Fe^{3+} ions leads to γ-Fe_2O_3:

$$Fe_{1-x}O \rightarrow Fe_3O_4 \rightarrow \gamma\text{-}Fe_2O_3 \qquad (1.12)$$

In actual oxidation, the cubic anion lattice becomes extended by the addition of new layers of close-packed O^{2-} ions into which Fe atoms migrate to give rise to the appropriate stable structures.

The defect γ-structures may be stabilized by the presence of Li^+ or H^+ ions (e.g. $LiFe_5O_8$). Cation diffusion rates in these and other lattices developed on metal surfaces play an important role in governing corrosion behavior.

These considerations on the nature of films and scales involving ionic crystals, lattice defects, and nonstoichiometry are further analyzed in Chapters 4, 5, 7, and 8.

1.7 Academic Impact of High Temperature Corrosion

Sections 1.4 and 1.5 describe the key components and principal phenomena of HTC encountered in various industrial processes. To deal effectively with HTC and its associated problems, it is necessary to understand the mechanistic aspects of corrosion and its principal modes, apart from providing meaningful engineering data to help engineers make informed materials/process selection decisions.

It is convenient to classify HTC reactions under the following categories:

(i) *Solid → products*, as in decomposition reactions brought about by thermal means. Typical examples are the decompositions of WO_3, MoO_3, TiO_2, etc., yielding mixed-valence phases:

$$MO_n\,(s) \rightarrow MO_{n-x}\,(s) + \tfrac{1}{2}\,xO_2 \qquad (1.13)$$

where M = W, Mo, Ti, etc. In these reactions, the oxygen loss does not occur randomly from the parent lattice to create isolated oxygen vacancies; instead oxygen loss is accommodated by collapse of the structure in specific crystallographic directions, creating crystallographic shear (cs) planes. Decomposition of V_2O_5 to form V_6O_{13} involves the $(1\bar{3}0)$ cs plane, and the two oxides intergrow just as the Magneli phases W_nO_{3n-1} and W_nO_{3n-2}, based on (120) and (130) cs planes, intergrow in reduced WO_3.

(ii) *Solid + gas → products*, as in oxidation, sulfidation, carburization, etc. Perhaps the most widely studied solid–gas reaction is the tarnishing of metals by reactive gases such as oxygen and halogens (Hannay 1976). Tarnishing is essentially an oxidation reaction giving rise to solid products such as metal oxides and halides that form layers on the metal surface. The initial stages of oxidation, when gas chemisorption and nucleation phenomena dominate, have shown that different faces of a crystal exhibit different reactivities. The tendency of a metal to become tarnished in a particular atmosphere is governed by both thermodynamic and kinetic factors. The thermodynamics of high temperature solid–gas reactions forming fairly thin or thick product layers is examined in Chapter 3. The kinetics and mechanism of these reactions are examined in Chapters 7–12.

(iii) *Solid + solid → products*, as in the formation of complex oxides from simpler components. These reactions fall into two categories: *addition reactions* (e.g. $ZnO + Fe_2O_3 \rightarrow ZnFe_2O_4$) and *exchange reactions* (e.g. $ZnS + CdO \rightarrow CdS + ZnO$). The general mechanism of solid–solid reactions consists of initial formation of one or more solid products that spatially separate the reactants. Subsequent reaction requires mass transport through product layers. When at least one of the reactants is in the form of a single crystal and the other in a compressed pellet form, the kinetics of the reaction follows a parabolic law analogous to the tarnishing of metals.

Solid–solid reactions are, as a rule, exothermic, and the driving force of the reaction is the difference between the free energies of formation of the products and the reactants. A quantitative understanding of the mechanism of solid–solid reactions is possible only if the reactions are studied under well-defined conditions, keeping the number of variables to a minimum. This requires single-crystal reactants and careful control of the chemical potential of the components. In addition, a knowledge of point defect equilibria in the product phase would be useful.

(iv) *Solid + liquid → products*, as in the dissolution of a solid in a liquid metal or molten salt, or in intercalation. When a solid reacts with a liquid, the products may form a layer on the solid surface or dissolve into the liquid phase. Where the product forms a layer covering the surface completely, the reaction is analogous to solid–gas reactions; if the reaction products are partly or wholly soluble in the liquid phase, the liquid has access to the reacting solid, and chemical reaction at the interface therefore becomes important in determining the kinetics.

The simplest solid–liquid reaction is the *dissolution* of a solid in a liquid. The rate at which a solid dissolves in a liquid depends on the particular crystallographic plane (face) exposed. The effect of crystallographic planes on dissolution is clear from the observation that spherical single crystals acquire polyhedral shapes while dissolving.

Like thermal decompositions, dissolution of solids is significantly influenced by dislocations. For example, etch pits are formed at sites where dislocations emerge on the crystal surface. It is for this reason that etching is a useful technique to render dislocations visible when to determine their density.

Intercalation refers to a solid-state reaction involving reversible insertion of guest species G into a host structure [Hs]. The host provides an interconnected system of accessible unoccupied sites □. The reaction can be schematically represented as

$$xG + \square_x\,[Hs] \rightleftharpoons G_x\,[Hs] \qquad (1.14)$$

The reaction is considered to be topotactic because the host matrix retains its integrity with respect to structure and composition in the course of intercalation and disintercalation.

(v) *Reactions of solid surfaces*: HTC reactions may involve one or more of the following elementary (rate-limiting) steps: (i) adsorption (and desorption) of gaseous species on the solid surface, (ii) chemical reaction on an atomic scale, (iii) nucleation of a new phase, and (iv) transport phenomena through solids. In addition, there are external factors such as temperature, ambient atmosphere, pressure, dynamic or static loads, flow velocity, irradiation, etc. that affect the reactivity.

The foregoing treatment clearly brings out the fact that HTC reactions are essentially solid-state reactions.

Solid-state reactions differ from those in homogeneous fluid media in a fundamental respect; whereas reactions in the liquid or gaseous state depend mainly on the intrinsic reactivity and concentration of the chemical species involved, solid-state reactions depend to a large extent on the arrangement of the chemical constituents in crystals. The fact that the constituents are fixed in specific

positions in crystals introduces a new dimension in the reactivity of solids, not present in other states of matter. In other words, chemical reactivity is determined more often by the crystal structure and defect structure of solids rather than by the intrinsic chemical reactivity of the constituents.

Several factors affect solid-state reactions, especially solid–solid reactions (Hannay 1976; Boldyrev 1979, 1981). Of these, particle size, gas atmosphere, and foreign additives are of importance. Increase of reactivity with decreasing particle size is well known in heterogeneous catalysis; small particle size also favors solid–solid reactions. Gas atmosphere can have significant effects on reactivity if the gas is also a component exchangeable between solid phases; the formation of a spinel such as $ZnFe_2O_4$ is favored in the presence of air (rather than nitrogen). Doping with foreign additives has been found to affect reaction rates. The reaction $ZnO + CuSO_4 \rightarrow ZnSO_4 + CuO$ is favored by doping ZnO with Li_2O. Since the reaction $Ge + 2MoO_3 \rightarrow GeO_2 + 2MoO_2$ involves electron transfer from Ge to MoO_3, n-type Ge is more reactive. Certain reactions are favored if they are carried out at the phase transition temperature of one of the reactants (*Hedvall effect*); formation of $CoAl_2O_4$ is easier at the γ–α transition of Al_2O_3. Boldyrev (1979, 1981) has examined the factors affecting the total process rate, the reaction at a specific location (and in a required direction), and the reaction mechanism in solid-state reactions. The method of preparation (prehistory) affects topochemical reactivity; the effect of mechanical treatment of solids is to introduce different types of defects, which, in turn, affect the total process rate. The ultimate aim is to control solid-state reactivity not only in time but also in space.

In summary, apart from HTC differences from the so-called room temperature and/or aqueous corrosion, reported in Section 1.1, many HTC mechanisms should also be envisaged as occurring by solid-state reactions. To be more precise, from the point of view of understanding HTC, a strong basic knowledge is required on the following elements: physical chemistry (including thermodynamics and kinetics), solid-state chemistry (including crystal chemistry, solid-state electrochemistry, defects, and diffusion processes), fused state electrochemistry, metallurgy and materials (including metal structures, alloy properties, multifunctional materials, and nanotechnologies), mechanically assisted corrosion (including failure analysis, creep, and strengthening mechanisms), and analytical techniques for HTC constituent characterization. It is instructive to examine a hypothetical corrosion situation. Accordingly, let us assume the case of a metal–gas reaction at high temperatures:

$$M(s) + \frac{n}{2} O_2(g) \rightarrow MO_n(s) \qquad (1.15)$$

To reach some mechanistic interpretation(s), it is important first to list the questions that must be answered if the oxidation mechanism is to be understood (Figure 1.13).

1. Does the oxidation proceed?

   The thermodynamic criterion that governs the tendency of a metal to become oxidized in a O_2 atmosphere is that the free energy change in the Reaction (1.15) should be negative. Let us assume that this criterion is fulfilled (ΔG for Eq. (1.15) is negative).

2. Is there any kinetic factor that impedes the reaction?

   The reaction of a metal with a gaseous reactant like oxygen first consists of a phase-boundary reaction forming product layer on the metal surface. Further reaction depends on the nature of the product layer. If the layer is porous, it does not prevent access of the reacting gas to the metal, and hence oxidation proceeds unimpeded; the reaction follows a linear law (rate constant in time), irrespective of the thickness of the product layer. If, on the other hand, a compact nonporous product is formed, the reacting gas has no direct access to the metal; further reaction can proceed only by transport of at least one of the reactants through the product. Therefore, the mechanism of metal oxidation crucially depends on whether the product layer is nonporous or porous.

   Let us assume that Reaction (1.15) forms a fairly thick (>1000 Å) product layer, and from kinetics and pressure dependence studies, it is concluded that the oxidation is controlled by diffusion through the MO_n protective oxide film. Then it is necessary to understand the preferential transport (ionic, electronic, both) through the oxide film.

3. Which is the mobile ion?

   Marker studies, electrochemical techniques, etc. may show if the oxide grows by preferential transport of oxygen, or metal ions, or both anionic and cationic ions.

4. What is the oxide defect structure?

   Studies on the conductivity of bulk MO_n at various O_2 pressures and at temperatures where electronic conduction makes a negligible contribution to the total can show if the oxide is p-type or n-type below or above a certain oxygen partial pressure. By simultaneous measurement of the lattice diffusion coefficients, it is possible to relate nonstoichiometry, conductivity, and point defect concentration in MO_n.

5. What is the macroscopic diffusion coefficient for oxygen during oxidation?

   Calculating diffusion coefficients from oxidation rates (Rosa and Hagel 1968), or from the interrupted oxidation technique of Rosenberg (Smith 1965), or from nuclear techniques, it is possible to determine

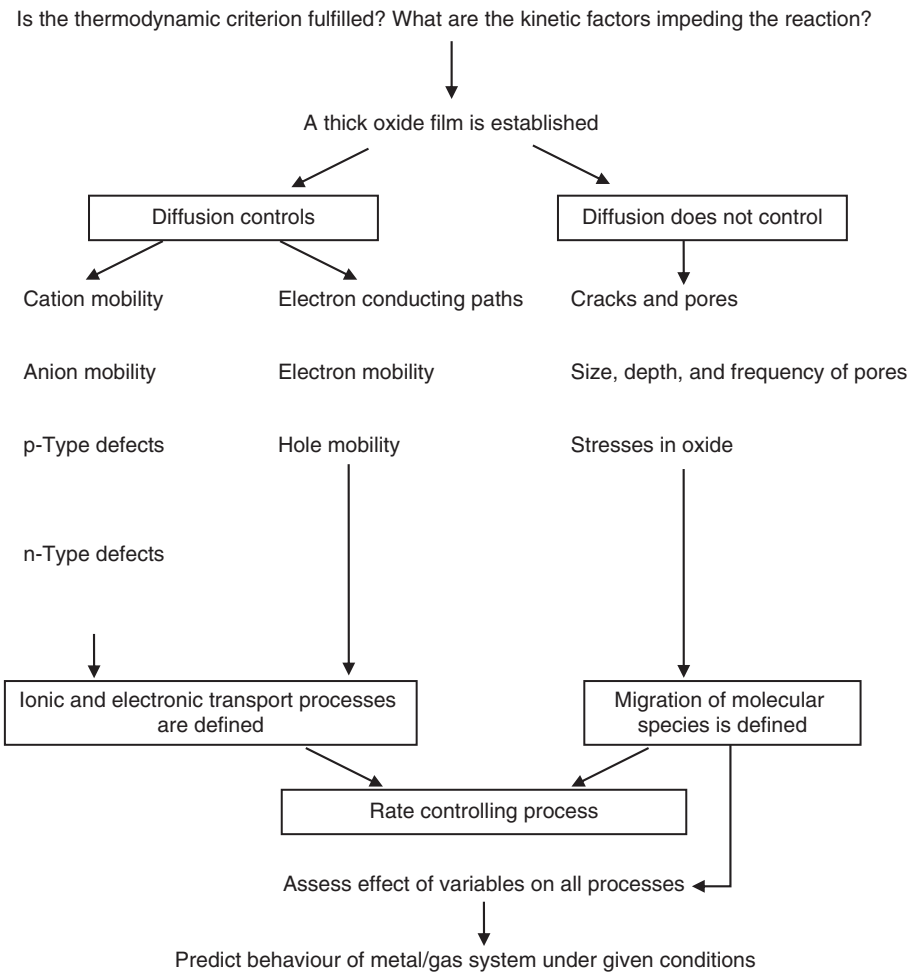


Figure 1.13 Understanding the high temperature oxidation of a metal/oxygen reaction.

the diffusion coefficient for oxygen in a growing oxide film.

6. What is the microscopic diffusion process?

Using ion bombardment mass spectrometry and other advanced techniques (Whitton 1968; Quataert and Coen-Porisini 1970; Marcus and Mansfeld 2006), it is possible to distinguish between the bulk and short-circuit diffusion coefficients in growing oxide films.

7. What really is the diffusion route?

Studies on oxide morphology (X-ray studies, oxide fractographs, etc.) can help in identifying the diffusion route. So, questions like "does the oxide product growth follow a simple rate law, or a variety of kinetic laws such as logarithmic, linear, cubic, and fourth power" can be answered in combination with observations of oxygen diffusion via crystallite boundaries and an increasing crystallite size with oxide thickness, etc.

8. What is the electron transport process?

By determining the current–voltage (*I*–*V*) characteristics for oxidizing specimens of metals and metal alloys and separating the ionic and electronic components of these, it should be possible to fit the electronic current to one of the possible *I*–*V* relationships and thereby identify the electron transport mechanism. Examination of a wider range of metal–oxide systems and oxidation conditions has shown that often the electron current is intermediate between a number of possible rate equations (Kofstad 1988; Ramasubramanian 1975; Schütze 2000). The conclusion is that there are commonly several parallel electron conducting paths (diffusion, tunneling, emission), obeying different rate equations, contributing simultaneously to the total electronic current.

9. What is the mobile electronic species?

I–*V* curves using semiconducting contacts can show if p-type (holes) or n-type (electrons) behavior predominates under different conditions.

10. What is the microscopic transport route for electrons?

It can be inferred from imaging techniques and other circumstantial evidence that high-conductivity sites (e.g. localized at intermetallic particles) may exist, which are the conduction sites at the oxidation temperature.

11. What is the contribution of surface processes?

A number of observations suggest that the conductivity of the oxide surface may be a major fraction of the total electronic resistivity during oxidation. This factor will become more important as the separation between the sites of electron transport (i.e. intermetallic particles) and ionic transport (homogeneously distributed crystallite boundaries, for example) increases. Thus, the conductivity of the environment (which will influence surface conduction) can have a bigger effect on the oxidation of metal films.

12. Is there any visual occurrence of cracks and pores?

In items 3–11, it was assumed that the oxidation Reaction (1.15) is controlled by diffusion through a protective MO_n oxide film. Let us now consider that diffusion no longer predominates. Then it is necessary to study the migration of molecular species in the oxide film. The first question is whether or not we are able to characterize cracks, pores, etc. in the oxide. Optical, electron, and scanning electron microscopy studies of specimens oxidized under a variety of conditions have enabled us to characterize the visible flaws that occur in the surface of oxide films (Marcus and Mansfeld 2006). Generally speaking, these fall into four main groups when specimens are studied at room temperature after oxidation: (i) large cracks (~1000 Å wide), usually seen at specimen edges at almost any stage in the oxidation process; (ii) fine cracks (~400 Å wide), which may be present as a network over the surface but are often absent from post-transition oxides; (iii) large pores (>1000 Å diameter), which result from the etching out of intermetallic particles during the initial surface preparation; and (iv) small pores (≤100 Å radius), which are occasionally seen in electron microscope replicas of post-transition oxide films but are at the limit of the ability of the two-stage replica technique to reveal features penetrating the surface.

13. What are the size, depth, and frequency of the pores?

Mercury porosimeter and impedance measurements, among other techniques, may indicate the presence of fine pores and gross cracks, provide information for the determination of pore sizes and depths, etc.

14. Are stresses generated in the oxide film?

Measurements of the extension or bending of thin metal foils and the plastic deformation of more massive specimens have shown that in many situations the compressive stresses in the oxide approach the compressive yield point in thin oxide films and at the oxide–metal interface in thicker oxide films. The improved plasticity of hypostoichiometric oxides, and the effect of porosity in nucleating cracking under stress (*oxide cracking*) and causing a reduction in compressive strength, would seem to be particularly relevant observations for the case of oxidation of a film and its breakdown (Ahmad and Keys 1975).

15. Does recrystallization occur in the oxide film?

The precise mechanism by which the recrystallization of the oxide films leads to pores growing at crystallite boundaries, steady increases in crystallite size, continuing changes in their texture and epitaxy, etc. is not known. Perhaps vacancy condensation, creep of the crystallites, oxide cracking, thermal cycling, and alloying additions and impurities have a large effect on those mechanisms.

It is not immediately possible to deduce from the oxidation kinetics, particularly a simple weight gain or oxide thickness versus time plot, whether or not diffusion through a protective oxide film is the rate-controlling process. Thus, adherence to a parabolic rate law shows only that the oxidation rate is inversely proportional to the oxide thickness and can be obeyed equally for oxidation controlled by ionic diffusion through a porous compact. The distinction can only be made if the porosity of the oxide film is measured.

Similarly, the observation of linear kinetics cannot be assumed to indicate control by diffusion through a constant thickness barrier oxide. It may, during oxidation at very low pressures, imply control by molecular diffusion through the oxidation apparatus from the point where the pressure is measured to the specimen. In fused salts or liquid metals, it may indicate significant dissolution of the oxide or metal. In either case, other tests such as varying the geometry of the system or performing a complete mass balance on the system will show which is the basic controlling factor.

The application of a field across the oxide could be superimposing an additional electrochemical process on what, in the absence of the applied field, could have been molecular diffusion through the film. The conclusion that the transport process is via charged species can only be reached if the charge carried across the oxide in unit time at zero applied field is determined and is shown to be equivalent to the mass of reactant (e.g. oxygen) transported in the same time, when reasonable values for the charge on the species are employed. To achieve this we need to know the complete current–voltage (*I–V*) characteristics of the system.

Measurements of the potential across a growing oxide film in fused salt are not likely to help elucidating the rate-controlling process on their own. However, if coupled with a knowledge of the detailed *I–V* characteristics of the

oxide during oxidation as a function of oxide thickness and the variable to be studied, they can be used to determine which aspect of the overall oxidation process is affected by the dependent variable, which process is then limiting the rate of oxidation, and whether the measured oxidation current is equivalent to the oxidation taking place.

With evidence available from the *I–V* characteristics of the oxide, it should also be possible to predict the effect of polarizing a specimen during oxidation, thereby confirming the conclusions about rate-controlling processes.

It emerges from the foregoing considerations that HTC deserves a deep academic interest. I have briefly dealt with some aspects of the oxidation phenomenon to point out how HTC plays a role in this crucial mode of corrosion science and technology. It was impossible to cover further important areas and unanswered questions, mainly due to gaps in my knowledge, and to the available space. But, this was a real attempt to stimulate readers to pursue their interest in these many aspects of science and engineering.

1.8 Industrial Impact of High Temperature Corrosion

As it is shown in Section 1.2, HTC has always been primarily a problem of combustion processes. In particular, if impure fuel was used for combustion, ashes and deposits on the surface of metallic structures would lead to intensive attack of the metallic materials. With advances in technology, gasification and other chemical reaction environments also entered the list of conditions where HTC occurs. A summary of the applications and processes, the temperatures, and the modes of corrosion observed is given in Table 1.17. This list may not be fully complete, but it is obvious that it is mainly in the chemical and petrochemical industries and all types of energy generation and conversion processes where it is necessary to rely on solutions concerning HTC resistance. To a lesser extent, it is also ceramics fabrication and all types of heating elements (Table 1.18). Furthermore, high temperature oxidation can be an issue for catalytic converters (e.g. automotive catalysts) and parts of automotive engines (e.g. turbo charger rotors and exhaust gas channels). In summary, although HTC is not very obvious in daily life, it is a high industrial challenge because it has economic, safety, and environmental damage consequences to a nation.

Some elements of the costs of corrosion are shown below:

Capital Costs.

- Replacement of equipment and buildings
- Excess capacity
- Redundant equipment

Control Costs.

- Maintenance and repair
- Corrosion control

Design Costs.

- Materials of construction
- Corrosion allowance
- Special processing

Associated Costs.

- Loss of product
- Technical support
- Insurance
- Parts and equipment inventory

The staggering costs of corrosion significantly affect the national economy, and it is meaningful and justified that the corrosion scientists involved should adopt corrosion control measures so that significant savings are achieved. Reference in this regard may be made to a report (NACE 1994) of the NACE Task Group T-3C-1 entitled "Economics of Corrosion," which deals with (i) economic techniques that can be used by personnel as a decision-making tool, (ii) facilitating communications between corrosion scientists and the management, and (iii) justifying the investments in corrosion preventive measures to achieve long-term benefits.

Any engineering project undertaken by a profit-motivated organization has the underlying aim of increasing the wealth of its owners (shareholders). Management in industry ultimately bases its decisions on this principle, including those related to corrosion control. The selection of optimal projects from the viewpoint of owners' wealth lies in the financial domain of capital budgeting techniques. These techniques determine how capital should be invested in the long term. Four key motives can be identified for making capital investments (expenditures) (Gitman 1991):

1. Expansion for increasing the scope and output of operations
2. Replacement for obsolete or rundown assets
3. Renewal for life extension of assets, as an alternative to replacement
4. Investment in non-tangible assets such as advertising, research, information, management consulting, etc.

The formal steps in the capital budgeting process in sequential order are (i) proposal generation, (ii) review and analysis of the proposals, (iii) decision making, (iv) implementation, and (v) monitoring of results to compare the actual project outcome with the predictions.

The next subsection will focus on the second step, namely, how to evaluate the economic feasibility of corrosion control investments. A Section 1.8.2, with which

Table 1.17 High temperature corrosion problems found in different industries

Industry	Process/production	Components	Temperature (°C)	Type of corrosion
Petrochemical processing	Ethylene cracking	Pyrolysis tube, pigtails	Up to 1100	Carburization/oxidation
	Synthesis gas production for ammonia, methanol, oxo-alcohol, and hydrogen	Pyrolysis tube, pigtails, former catalyst tubes	Up to 1100	Oxidation/carburization
	Petroleum coke calcining	Recuperators	~816	Oxidation/sulfidation
	Vinyl chloride monomer production	Electrical discharge coating (EDC) cracker tubes	Up to 650	Halide gas corrosion
	Ammonia synthesis	Converter internals, hot ammonia piping, H-P steam generator	Up to 550	Nitridation/hydrogen attack
	Carbon disulfide production	Furnace tubes	Up to 850	Sulfidation/carburization
	Styrene production	Superheater tubes	Up to 900	Steam oxidation
	Ketene and acetic anhydride production	Reactor, internals	Up to 850	Oxidation/carburization
	Melamine production from urea	Reactor, internals	450–500	Nitridation
	High temperature chlorination	Various	Up to 550	Chlorination
	Refinery plants	Flare tips	Up to 1100	Oxidation/sulfidation/chlorination/acid dew point corrosion
Oil refining	Hydrocracking	Heater tubes, reactor internals	Up to 550	H_2S/H_2 corrosion
	Hydrodesulfurization	Heater tubes, reactor linings, internals	Up to 550	H_2S/H_2 corrosion
	Hydrodealkylation	Heater tubes	Up to 750	H_2S/H_2 corrosion
	Hydrogen production	Reformer catalyst tubes	Up to 1000	Oxidation/combustion-induced corrosion
	Cat cracking	Regenerator	Up to 800	Oxidation
	General heater tube supports	Various	Up to 950	Fuel ash attack
	Flare stack tips	Various	Up to 950	Sulfidation/oxidation
	Oil-fired refinery boilers	Superheater supports	Up to 950	Ashes oxidation/fuel ash corrosion
Chemical processing	Nitric acid production	Ammonia oxidation reactor, catalyst support grid	Up to 950	Oxidation/carburization/nitridation
	Titanium oxide production/chlorine route	Oxygen heater tubes, $TiCl_4$ circuit	Up to 950	Oxidation/chlorination
	Fiberglass manufacturing	Recuperators	Up to 1100	Oxidation/sulfidation/molten salts
	Carbon regeneration in the production of corn starch, herbicides, insecticides	Kiln internals, fluidized-bed grids	Up to 980	Oxidation/carburization/sulfidation
	Various mineral, calcium sintering, and pelletizing processes	Calciners	850–1200	Oxidation/sulfidation/chlorination

(*Continued*)

Table 1.17 (*continued*)

Industry	Process/production	Components	Temperature (°C)	Type of corrosion
Nuclear power generation	Uranium refining	Hydrofluorinator and fluorinator reactors	600	HF, F_2 corrosion, radiation hazards
	Reprocessing of zirconium clad fuel elements	Hydrofluorinator	650	Molten fluoride/HF corrosion
	Engine valves	Shanks	Up to 1000	Liquid metal
Pulp and paper	Recovery boilers	Smelt spouts	820–930	Hot corrosion/molten salts
	Recovery boilers	Superheaters, internal components	Up to 820	Oxidation/hot corrosion
Metallurgical processing	Mineral chlorination, precious metals, zirconium production (Kroll process)	Chlorinator	300–900	Cl_2 corrosion
	Aluminum remelting	Recuperators	Up to 900	Oxidation/chlorination/sulfidation
	Aluminum production	Reactor vessels	Up to 700	Oxidation/chlorination
	Silicon production	Reactor vessels	Up to 540	Oxidation/chlorination
	Steel reheating furnace	Recuperators	Up to 870	Oxidation/hot corrosion
	Magnesium production (Pidgeon process)	Retorts	1100	Oxidation
	High-speed cutting tools	Various	Up to 600	Oxidation
	Resistant heaters	Various	Up to 900	Ashes oxidation
	Thermocouple elements	Various	Up to 2500	Oxidation
Heat treatment	Gas carburizing	Furnace components	850–1100	Carburization
	Gas carburizing	Furnace brick anchors, fan housing assemblies	540–820	Metal dusting
	Heat treatment	Radiant tubes	820–1100	Oxidation
Waste incineration and resource recovery	Municipal wastes	Superheaters	Up to 500	Oxidation/sulfidation/chlorination/ molten salts
	Municipal wastes	Internal components	Up to 930	Oxidation/sulfidation
	Pharmaceutical wastes	Screw conveyors, plows, rakes	Up to 815	Oxidation/sulfidation
	Chemical wastes from Si production	Recuperators	Up to 1000	Oxidation/chlorination
Coal gasification and advanced energy conversion	Gas turbine applications	Blades, disks, burner cans, vanes	Up to 950	Sulfate/chloride corrosion/ash corrosion/hot corrosion
	Oil-fired boiler superheaters	Superheaters	Up to 900	Oxidation/fuel ash corrosion
	Fuel cells	Various	Up to 800	Oxidation/molten salts
	Coal-fired boilers	Evaporator tubes, superheater tubes	450–700	Ashes oxidation/molten salts
	Coal gasification and fluidized-bed combustion	Various	Up to 1000	Ashes oxidation/sulfatic–vanadic corrosion

Table 1.18 Current uses of advanced ceramics

Application	Ceramics	Typical temperature range (°C)	Environment
Turbine engine components, combustor liners, blades, and vanes	SiC, Si_3N_4, composites	900–1400	Combustion gases; deposits: Na, Mg, Ca sulfates, Na vanadates
Piston engine components, pistons, valves	SiC, Si_3N_4, composites	900–1400	Combustion gases
Industrial furnaces, Heat exchangers	SiC, composites	900–1400	Combustion gases, various deposits
Coal combustion, particle filters	SiC, composites	700–1000	Combustion gases, slag deposits
Chemical process vessels, coal gasifiers, waste incinerators	SiC, Si_3N_4	900–1400	Various gases: Air, H_2S, HCl
Reentry shields	SiC, composites	1000–1800	Reduced pressure: N_2, O_2, CO_2, N, O
High temperature semiconductors	SiC	Use: 600 Processing: 1200	Air
Electronic substrates	AlN	Use: 600 Processing: 1200	Air
Fiber coatings for composites, crucibles, insulators	BN	900–1400	Fiber coatings: reduced pressure, combustion gases; crucibles: vacuum, inert gases
Rocket engine throats	HfC, ZrC	1500–2000	H_2/O_2 combustion products
Liquid metal containers, processing, and heat transfer	Transition metal carbides	600–1400	Vacuum or inert gas and liquid metals

we finish this chapter, briefly emphasizes the importance of safety and environment damage and then discusses corrosion management, including the people factor in corrosion failure and expert systems presently available for corrosion and related matters.

1.8.1 Corrosion Economics

Every corrosion engineering project will have a certain cash flow partner over time. Usually, there is an initial outflow of cash, when a new asset fitted with a certain corrosion control system is acquired. Subsequently, there are inflows of cash, resulting from operations and further cash outflows required for maintenance, corrosion control, upgrades, running costs, and so forth. In capital budgeting techniques, the different cash flows involved in the project are identified, estimated, and analyzed, with a view to maximizing owner's wealth.

Clearly such cash flows can be complex if all the financial implications of project options are investigated in detail. Invariably in corrosion economics calculations, a compromise has to be made between two opposing needs, the need for precision and the need for simplicity. For example, the present costs or investment in two alternative anticorrosion methods may be known with a high degree of certainty. However, the service lives, future maintenance costs, or operating costs may be estimates with only a limited degree of certainty. The need for stringent risk assessment required of many modern engineering systems may also add to complexity of estimating useful life and cost estimates.

When considering the above cash inflows and outflows over time, the *time value of money* has to be considered. This concept implies that money has a value that varies depending on when it is received or disbursed. Readers will have gained firsthand knowledge of this principle from any loans they have taken out with financial institutions. A loan received "now" has to be repaired with interest charges in the future. The following is a generalized formula between the present value (PV) and future value of cash flows:

$$\mathrm{PV} = \frac{F_n}{(1+i)^n} \tag{1.16}$$

which states that PV of a future cash flow (F_n) after (n) time periods equals the future amount (C_n) discounted to zero date at some interest rate (i). The value of n is usually specified in years and i as the annual interest rate. Several capital budgeting techniques exist that are based on the time value for money.

Factors that need to be considered in calculating the present worth (PW) capital budgeting, also referred as net present value (NPV) technique, include:

- Initial cost.
- Best estimate of expected life.
- Length of typical shutdown for emergency repair.
- Cost of planned maintenance during scheduled shutdowns.
- Effect of failure on total plant operation.

The NPV is a summation of the PV of all cash inflows and outflows minus the initial project cost (C_0). To include the effects of taxation (essentially a business expense), all actual cash flows for tax-paying organizations are deduced

by the formula given in Eq. (1.17):

$$\text{Amount after taxes} = C\,(1 - T_x) \tag{1.17}$$

All expenses allowed to be charged against income for tax purposes, but not representing actual cash flow, are modified by the formula given in Eq. (1.18). Depreciation allowances are an excellent example of where such tax savings are possible; they are treated similarly to income:

$$\text{Cash flow} = \text{noncash expense charge}\,(T_x) \tag{1.18}$$

The PV of the tax saving cash flow from a depreciation expense series (DES) of an original cost is given in Eq. (1.19):

$$\text{PV}_{\text{DES}} = C_0\,(Q, i, N_Q)\,T_{\text{x}} \tag{1.19}$$

where Q is the PV factor for a cash flow stream and N_Q is the time span of the depreciation expense stream.

Combining these definitions, one can obtain the fundamental NPV equation that includes tax effects

$$\text{NPV} = \sum_{n=1}^{N} \frac{F_n}{(1+i)^n}\,(1 - T_x) + C_0\,(Q, i, N_Q)\,T_x - C_0 \tag{1.20}$$

Verink has developed a simplified version of this complex equation to fit engineering systems (Verink 1987). This equation takes into account the influence of taxes, straight-line depreciation, operating expenses, and salvage value in the calculation of PW and annual cost. Using this equation, a problem can be solved merely by entering data into the equation with the assistance of compound interest data:

$$\text{PW} = -P + \left[\frac{t\,(P-S)}{n}\right]\left(\frac{P}{A, i\%, n}\right) - (1-t)\,(X)\left(\frac{P}{A, i\%, n}\right) + S\left(\frac{P}{F, i\%, n}\right) \tag{1.21}$$

where

A = annual end-of-period cash flow
F = future sum of money
$i\%$ = interest rate
n = number of years
P = cost of the system at time 0
S = salvage value
t = tax rate expressed as a decimal
X = operating expenses

The first term, $-P$, represents the initial project expense, at time zero. As an expense, it is assigned a negative value. There is no need to translate this value to a future value in time because the PW approach discounts all money values to the present (time zero).

The second term, $[t\,(P - S)/n]\,(P/A, i\%, n)$, in this equation describes the depreciation of a system. The portion enclosed in brackets expresses the annual amount of tax credit permitted by this method of straight-line depreciation. The portion in parentheses translates annual costs in equal amounts back to time zero by converting them to PW.

The third term, $-(1-t)\,(X)\,(P/A, i\%, n)$, in the generalized equation consists of two terms. One is $(X)\,(P/A, i\%, n)$, which represents the cost of items properly chargeable as expenses, such as the cost of maintenance, insurance, and the cost of *inhibitors*. Since this term involves expenditure of money, it also comes with a negative sign. The second part, $t(X)\,(P/A, i\%, n)$, accounts for the tax credit associated with this business expense, and because it represents a saving, it is associated with a positive sign.

The fourth term, $S\,(P/F, i\%, n)$, translates the future value of salvage to the PV. This is a one-time event rather than a uniform series, and therefore it involves the single-payment PW factors. Many corrosion measures, such as coatings and other repetitive maintenance measures, have no salvage value, in which cases this term is zero.

PW can be converted to equivalent annual cost (A) by using the following formula:

$$A = (\text{PW})\,(A/P, i\%, n) \tag{1.22}$$

One can calculate different options by referring to interest tables or by simply using the formula describing the various functions. The capital recovery function (P/A), or how to find P once given A, is

$$\left(\frac{P}{A},\ i\%, n\right) \text{ where } P_n = A\,\frac{(1+i)^n - 1}{i\,(1+i)^n} \tag{1.23}$$

The compound amount factor (P/F), or how to find P once given F, is

$$\left(\frac{P}{A},\ i\%, n\right) \text{ where } F_n = P\,(1+i)^n \tag{1.24}$$

The capital recovery factor (A/P), or how to find A once given P, is

$$\left(\frac{A}{P, i\%, n}\right) \text{ where } A_n = P\,\frac{i\,(1+i)^n}{(1+i)^n - 1} \tag{1.25}$$

Three examples illustrative of discounted cash flow calculations taken from the literature are as follows.

Example 1

A new heat exchanger is required in conjunction with a rearrangement of existing facilities. Because of corrosion, the expected life of a carbon steel heat exchanger is five years. The installed cost is $9500. An alternative to the heat exchanger is a unit made of AISI type 316 stainless steel, with an installed cost of $26 500 and an estimated life of 15 years, to be written off in 11 years. The minimum acceptable interest rate is 10%, the tax rate is 48%, and the depreciation method is straight line. Determine which unit would be more economical based on annual costs.

Solution	Option 1, carbon steel heat exchanger	Option 2, AISI type 316 heat exchanger
−P	–$9 500	–$26 500
$[t\,(P - S)/n]\,(P/A, i\%, n)$	[0.48 (9 500 − 0)/5] (3.791) = $3 457	[0.48 (26 500 − 0)/11] (6.495) = $7 510
$-(1 - t)\,(X)\,(P/A, i\%, n)$	0	0
$S\,(P/F, i\%, n)$	0	0
PW	−$6 043	−$18 989
A	−$6 043 (0.2638) = −$1 594	−$18 989 (0.15396) = −$2 924

The carbon steel heat exchanger is thus a cheaper solution

Example 2

Given the conditions in Example 1, but uncertain that a service life of five years can be obtained, determine the service life at which the carbon steel heat exchanger is economically equivalent to the type 316 stainless steel unit.

Solution	Option 1, $n = 2$ years	Option 2, $n = 3$ years
−P	−$9 500	−$9 500
$[t\,(P - S)/n]\,(P/A, i\%, n)$	[0.48 (9 500–0)/2] (1.736) = $3 958	[0.48 (9 500–0)/3] (2.487) = $3 780
$-(1 - t)\,(X)\,(P/A, i\%, n)$	0	0
$S\,(P/F, i\%, n)$	0	
PW	–$5 542	–$5 720
A	–$5 542 (0.5762) = −$3 193	–$5 720 (0.402 11) = −$2 300

Thus, a carbon steel heat exchanger must last more than two years but will be economically favored in less than three years under the conditions given.

Example 3

Under the conditions described in Example 2, it becomes interesting to evaluate how much product loss X can be tolerated after 2–5 years of anticipated life, for example, from roll leakers or a few tube failures, before the selection of type AISI 316 stainless steel could have been justified.
Solution:

$$A_{316} = A_{\text{steel}} + A_{\text{product loss}}$$

$$-\$2924 = -\$1594 + [(1–0.48)\,(X)\,(0.8264)][0.2638] \qquad \text{the third term in the generalized equation}$$

where 0.8264 is the single-payment PW factor for two years $(P/F)_{10\%,\,2y}$

Solving for X

$$-\$1330 = 0.1134\,(X) \qquad X = -\$11\,728$$

If production losses exceed $11 728 in year 2, with no losses in any other year, the AISI type 316 stainless steel heat exchanger would be the most economical solution.

Unfortunately, all too often, selection of materials for corrosion applications is still based on a comparison of initial installed costs of alternative materials. The time value of money concept including important considerations such as ease of repair, cost associated with scheduled and unplanned shutdowns, and the effect of component failure on overall plant operations is therefore inadequately accounted for or completely ignored.

1.8.2 Safety, Environment Damage, and Corrosion Management

The industries listed in Tables 1.17 and 1.18, with the associated corrosion types (and consequent problems, accidents, or failures), emphasize the importance of safety to personnel involved in the industries as the most important factor that is reflected as the impact of corrosion.

Corrosion has a tremendous effect on the environment in the sense that corrosion-related failure of high temperature systems can have very detrimental effect on the environment in various forms, leading to the demise of strong environmental damage.

Another aspect of concern is the limit of resources in the world. Some decades ago, the term recycling was almost unknown. At the present time, recycling is a household term, and recycling of material products has been recognized for the important role it plays in conserving our resources. We have reached a level of maturity to be able to recognize that our natural resources are limited and finite in our world and that methods to conserve these resources by recycling and other methods have a prominent role to play.

Corrosion prevention and protection arrests the degradation of metals/materials and contributes in a significant way to the conservation of resources with a minimum damage to the ecosystems. Since materials are prone to corrosion, it is useful to know the factors, both direct and indirect, which affect the choice of materials and their related corrosion resistance of paramount importance in the design of an engineering structure (Table 1.19).

In the design of a new plant, the first step involves selection of materials that should have reasonable corrosion resistance properties in the environment of chosen application. This requires corrosion studies of the material.

Table 1.19 Factors affecting materials selection

Direct factors	Indirect factors
Cost	Mechanical properties
Appearance	Corrosion resistance
Ease of availability	Metallurgical
Ease of fabrication	Safety
Application	
Environmental	

The corrosion framework encompasses physical chemistry, solid-state chemistry, corrosion modes, environments, metallurgical factors, coatings, design considerations, corrosion detection, monitoring, and testing and failure analysis. Within the framework of materials, knowledge of economics, safety, specifications, and corrosion management is essential.

According to Trethewey and Chamberlain (1995), corrosion management is defined to include people along with corrosion control that concerns the materials used in a particular environment. The corrosion-related failure may be due to (i) primary corrosion mechanism and/or (ii) secondary corrosion mechanism as shown in Figure 1.14.

The secondary corrosion mechanism involves the contributions of people in different ways, and the people factor should be rated as high in corrosion management. The various functions of personnel in different stages of corrosion performance systems may be identified as shown in Figure 1.15.

In the analysis of failures, it is possible to identify the failure when the failure occurs due to a simple corrosion mechanism such as oxidation, erosion–corrosion, or severe general corrosion. In all these cases, the factors involved

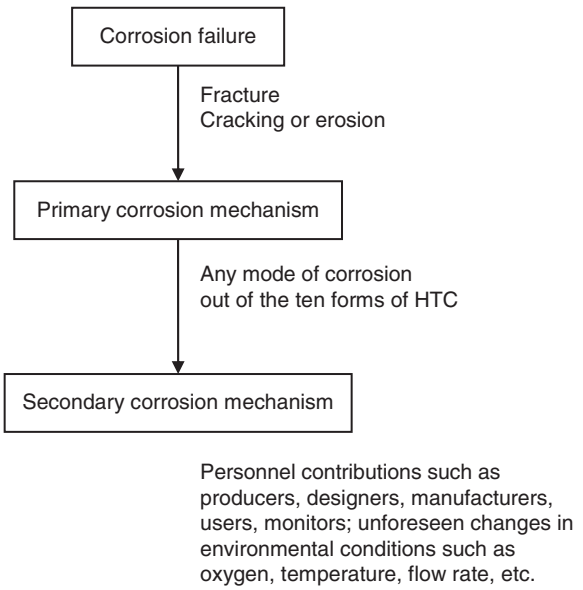


Figure 1.14 Causes of corrosion-related failure.

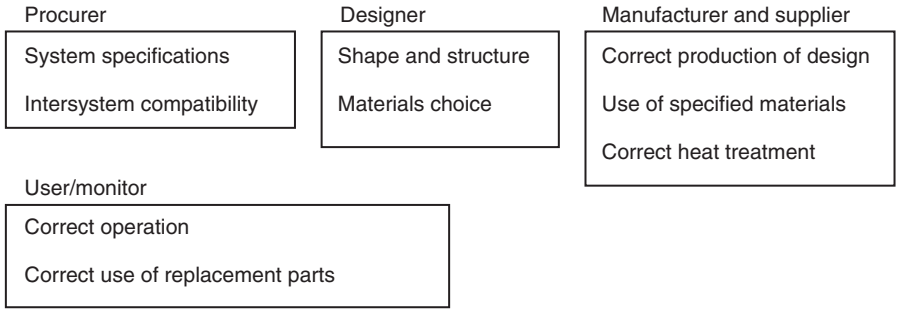


Figure 1.15 Functions of personnel in different stages of a corrosion performance of systems.

are materials, environment, flow rate of the medium, etc. These types of failure are avoidable when proper choice of materials, design, and the environment are considered. In spite of good available knowledge of various factors contributing to corrosion failures, we do encounter corrosion-related failures at remarkable frequency. In quite a few instances of corrosion-related failures such as erosion–corrosion-related failure, squarely the culprit is the improper choice of materials selected and designed by the engineer. This clearly shows the people factor involved in improper choice of materials and its use in the particular environment.

The people factor is difficult to quantify in any case of failure. It is needless to emphasize that extensive multidisciplinary knowledge in a variety of subjects such as solid-state chemistry, electrochemistry, physics, statistics, mechanical engineering, metallurgy, and management is desirable in order to reduce the people contribution factor to a minimum ($0 < \text{people factor} < 1$). An example where reliability and safety has been very high is provided by the aerospace industry. The fault-tree structure (people, materials, and environment) for corrosion failure can be programmed into a computer and used to analyze the risk of system failure.

The accounting of decisions made by people is based upon a host of disciplines such as fuzzy logic (Kosko 1992), Bayesian logic (Durkin 1994), influence diagrams (Howard and Matheson 1994), and approximate reasoning principle (Kanal and Lemmer 1986) in the course of research in artificial intelligence.

The computer-based corrosion problem-solving systems have been categorized as (i) systems for modeling corrosion/cracking processes, (ii) material selection and equipment specification programs, (iii) computer-based corrosion monitoring systems, (iv) computer-based systems for control of corrosion testing equipment, (v) databases and hypertext systems, and (vi) Internet-based databases and software programs.

Systems developed include programs for modeling corrosion and for diagnosis, failure analysis, and prediction analysis. The Selmatel (Valdes et al. 1992), for example, is an expert system for the selection of materials exposed to high temperatures in refinery furnace tubes.

The role of the Internet in corrosion science and engineering, as in any other field, has been increasingly useful in the past decade. The Internet is playing a significant role in sharing and exchanging information. The resources available to the corrosion engineer/scientist are (i) email-based, (ii) newsgroups and discussion threads, and (iii) technical resource websites. Electronic mail is a convenient mechanism for exchanging information of interest among scientists. This may also involve a mailing list of people interested in the technical topic, and an example of this is the CORROS-L list operated by the Corrosion and Protection Centre at the University of Manchester.

The web-based resources for corrosion may be classified as (i) resources for solving corrosion problems, (ii) resources for sharing information with the aid of virtual libraries and online databases, and (iii) resources for sharing information within the organizations (intranets). Some of the relevant websites for corrosion materials are:

www.Metalogic.be	Overview of corrosive environments
www.intercorr.com	A number of important papers, data, and software on corrosion materials
www.nist.gov/srd/materials.htm	NIST materials databases
www.oilonline.com	Online news, rig counts, products, and literature on oil industry
www.xs4all.nl/en/	Overview of corrosion processes

It is conceivable that most of the tasks performed by humans may be replaced by computers in the future, but the role of people in corrosion management will not be diminished in spite of the technical advances being made.

It has been said at the beginning of this subsection that within the framework of materials, knowledge of economics, safety specifications, and corrosion management is essential. It is also necessary for the corrosion scientist to have knowledge of the various modes of corrosion encountered in high temperature environments along

with the recommended solutions. To this end, efforts are made in the following chapters to discuss as succinctly as possible the required material for both students and practicing corrosion scientists and engineers.

1.9 Questions

1.1 How does high temperature corrosion differ from the so-called low temperature or room temperature corrosion?

1.2 Why is there a need to study high temperature corrosion?

1.3 What are the various forms of high temperature corrosion?

1.4 Is oxidation a degradation phenomenon alone? Under what conditions is oxidation a corrosion protection method?

1.5 What are the criteria to choose materials for high temperature applications?

1.6 What are the most corrosive high temperature environments?

1.7 Give examples of peculiar high temperature corrosion phenomena

1.8 What are the more common alloying elements used to improve the high temperature corrosion resistance in alloys?

1.9 Why are the carbon steels and low-alloyed steels widely used in high temperature service?

1.10 Why are the superalloys used for critical components in aerogas turbines as well as in the nuclear power and space industries?

1.11 Give examples of technically important refractory metals

1.12 What are the limitations of oxides as high temperature construction materials?

1.13 Why is "high temperature corrosion in combustion gases and/or deposits" a relevant theme of research?

1.14 Why is "interaction of corrosion and mechanical factors such as corrosion and fatigue" a relevant theme of research?

1.15 Why is "high temperature corrosion of ceramics" a relevant theme of research?

1.16 Why research in high temperature corrosion may result in improved energy efficiency and reduced emissions to the environment?

1.17 Note which high temperature materials exhibit ionic, covalent, metallic, hydrogen, and van der Waals bonds.

1.18 Is the thickness of an adhering scale always proportional to the square root of time?

1.19 In designing for high temperature service, is creep and eventual rupture more or less critical than yield and tensile strengths?

1.20 Note that radiation damage occurs because atoms (and electrons) are knocked out of their normal positions, then altering the basic properties. Recovery is facilitated by annealing.

1.21 Distinguish between acidic and basic refractories

1.22 What is the meaning of the spall resistance index of a refractory?

1.23 What are the materials' requirements for fuel cans?

1.24 What is the distinction between a film and a scale?

1.25 Briefly discuss film nucleation and growth

1.26 Characterize the fundamental aspects of solid-state reactions

1.27 How can cracks, pores, etc., in an oxide, be characterized?

1.28 Can the early studies on oxidation be studied by electrochemical methods? Discuss.

1.29 Discuss the economic impact of high temperature corrosion

1.30 Analyze the existing expert systems for dealing with high temperature corrosion

References

Agarwal, D.C. and Ford, M. (1998). *Corrosion/98*, Paper No. 485. Houston, TX: NACE International.

Agarwal, D.C., Herda, W.R., and Kloewer, J. (2000). *Corrosion/2000*, Paper No. 501. Houston, TX: NACE International.

Ahmad, T.H. and Keys, L.H. (1975). *J. Less-Common Met.* 39: 99.

ASM International (1985). *Metals Handbook: Metallography and Microstructures*, 9e, vol. 9. Materials Park, OH: ASM.

Baerlecken, E., Fischer, W.A., and Lorenz, K. (1961). *Stahl und Eisen* 81: 768.

Betteridge, W. (1982). *Cobalt and its Alloys*. Chichester: Ellis Horwood.

Boldyrev, V.V. (1979). *Annu. Rev. Mater. Sci.* 9: 455.

Boldyrev, V.V. (1981). *Ann. Chim. Fr.* 6: 359.

Bornstein, N.S. (1996). *JOM* 11: 37.

Bringas, J.E. (1993). *The Metals Red Book – Nonferrous Metals*, vol. 2. Edmonton: CAST Publishing.

Brooks, J.A. and Thompson, A.W. (1991). *Int. Met. Rev.* 36: 16.

Bystram, M.C.T. (1956). *Br. Weld. J.* 3: 41.

Cox, D. and Donner, A. (1973). *J. Nucl. Mater.* 47: 72.

Davis, J.R. (ed.) (1996). *ASM Specialty Handbook: Stainless Steels*. Materials Park, OH: ASM International.

DIN EN 10027 (1992). *Stahl – Bezeichnungs system, Part 1. Bezeichnung nach Kurznamen, Hauptsymbole*. Berlin-Wien-Zürich: Beuth Verlag.

Donachie, M.J. Jr. (2000). *Titanium: A Technical Guide*, 2e. Materials Park, OH: ASM International.

Donachie, M.J. Jr. and Donachie, S.J. (2002). *Superalloys: A Technical Guide*, 2e. Materials Park, OH: ASM International.

Durkin, J. (1994). *Bayesian Logic*. New York: MacMillan.

Fehlner, F.P. and Mott, N.F. (1970). *Oxid. Met.* 2: 59.

Fox, D.S. (1998). *J. Am. Ceram. Soc.* 81: 945.

Friend, W.Z. (1980). *Corrosion of Nickel and Nickel Base Alloys*. New York: Wiley.

Gesmundo, F., Viani, F., and Tassa, O. (1993). *J. Phys. (Paris)* (IVC9): 375.

Gilbert, G.N.J. (1959). *J. Res. Br. Cast Iron Assoc.* 7: 478.

Gilbert, G.N.J. and White, D.E. (1963). *J. Res. Br. Cast Iron Assoc.* 11: 295.

Gitman, L.J. (1991). *Principles of Managerial Finance*. New York: Harper Collins.

Grauer, R. and Feitknecht, W. (1966). *Corros. Sci.* 6: 301.

Gray, R.D. (1974). *Stellite – A History of the Haynes Stellite Company, 1912–1972*. Boston, MA: Cabot.

Gurrappa, I. and Gogia, A.K. (2001). *Mater. Sci. Technol.* 17: 581.

Hannay, N.B. (ed.) (1976). *Treatise on Solid-State Chemistry*, vol. 4. New York: Plenum Press.

Hasselman, D.P.H. (1969). *J. Am. Ceram. Soc.* 52: 600.

Hatfield, W.H. (1927). *J. Iron Steel Inst.* 115: 517.

Heubner, U. (1987). *Nickel Alloys and High Alloy Special Stainless Steels*. Werdohl: Krupp VDM.

Howard, R.A. and Matheson, J.E. (eds.) (1994). *Influence Diagrams in the Principles and Applications of Decision Analysis*, vol. II. Menlo Park, CA: Strategic Decisions Group.
Jacobson, N.S. (1989). *Oxid. Met.* 31: 91.
Jacobson, N.S. (1993). *J. Am. Ceram. Soc.* 76: 3.
Kanal, L.N. and Lemmer, J.F. (eds.) (1986). *Uncertainty in Artificial Intelligence*, vol. 4. Amsterdam: North Holland.
Kofstad, P. (1988). *High Temperature Corrosion*. London: Elsevier.
Kosko, B. (1992). *Neural Networks and Fuzzy Systems*. Englewood Cliffs, NJ: Prentice Hall.
Kubaschewski, O. (1982). *Iron Binary Phase Diagrams*. Dusseldorf: Springer, Verlag Stahleisen m.b.H.
Lai, G. (1990). *High Temperature Corrosion of Engineering Alloys*. Materials Park, OH: ASM International.
Leyens, C., Peters, M., Weinem, D., and Kaysser, W.A. (1996). *Metall. Mater. Trans. A* 27: 1709.
Leyens, C., Schmidt, M., Peters, M., and Kaysser, W.A. (1997). *Mater. Sci. Eng., A* 239–240: 680.
MacEwen, S.R. and Hastings, I. (1975). *Philos. Mag.* 31: 135.
Marcus, P. and Mansfeld, F. (eds.) (2006). *Analytical Methods in Corrosion Science and Engineering*. Boca Raton, FL: CRC Press.
Meier, G.H. (1996). *Mater. Corros.* 47: 595.
NACE 3C194 (1994). *Economics and Corrosion*. Houston, TX: NACE International.
Narushima, T., Goto, T., Hirai, T., and Iguchi, Y. (1997). *Mater. Trans., JIM* 38: 821.
Nichols, J.R., Leggett, J.T., and Andrews, P. (1997). *Werkst. Korros.* 48: 56.
Nohara, K., Ono, Y., and Ohashi, N. (1977). *J. Iron Steel Inst. Jpn.* 63: 5.
Perkins, R.A. and Meier, G.H. (1990). *JOM* 8: 17.
Quataert, D. and Coen-Porisini, F. (1970). *J. Nucl. Mater.* 36: 20.
Ramasubramanian, N. (1975). *J. Nucl. Mater.* 55: 134.
Rapp, R.A. (1986). *Corros. Sci.* 42: 568.
Rosa, C.J. and Hagel, K.C. (1968). *J. Nucl. Mater.* 27: 12.
Sabol, G. and Dalgaard, S.B. (1975). *J. Electrochem. Soc.* 122: 316.
Schaeffler, A.L. (1949). *Met. Prog.* 56: 680.
Schütze, M. (ed.) (2000). *Corrosion and Environmental Degradation*. Weinheim: Wiley-VCH.
Sims, C.T. and Hagel, W.C. (1972). *The Superalloys*. New York: Wiley.
Sims, C.T., Stoloff, N.S., and Hagel, W.C. (eds.) (1987). *Superalloys II*. New York: Wiley.
Smith, T. (1965). *J. Electrochem. Soc.* 112: 560.
Sullivan, C.P., Donachie, M.J. Jr., and Morral, F.R. (1970). *Cobalt-Base Superalloys-1970*. Brussels: Centre dInformation du Cobalt.
Trethewey, K.R. and Chamberlain, J. (1995). *Corrosion for Science and Engineering*. London: Longman.
Uhlig, H.H. and Revie, R.W. (eds.) (1985). *Corrosion and Corrosion Control*. New York: Wiley.
Valdes, A., Gonzalez, A., Techorrewski, R., and Hopkinson, B. (1992). *Corrosion/92*, Paper No. 275. . Houston, TX: NACE International.
Verink, E.D. (1987). *Metals Handbook: Corrosion*, 369–374. Materials Park, OH: ASM International.
Welsch, G. and Desai, P.D. (eds.) (1996). *Oxidation and Corrosion of Intermetallic Alloys*. West Lafayette, IN: Purdue Research Foundation.
Westbrook, J.H. and Fleischer, R.L. (eds.) (1994). *Intermetallic Compounds: Principles and Practice*. New York: Wiley.
Whitton, J.L. (1968). *J. Electrochem. Soc.* 115: 58.
Wojcik, C.C. (1998). *Adv. Mater. Processes* 154: 27.

Further Reading

Beddoes, J. and Parr, J.G. (1999). *Introduction to Stainless Steels*, 3e. Materials Park, OH: ASM International.
Briant, C.L., Petrovic, J.Z., Bewlay, B.P. et al. (eds.) (1994). *High-Temperature Silicides and Refractory Alloys*. Pittsburgh, PA: MRS.
Burstein, T. (2008). *High Temperature Oxidation and Corrosion*. London: Elsevier.
Dybkov, V.I. (2002). *Reaction–Diffusion and Solid-state Chemical Kinetics*. Kiev: IMPS Publications.
Fordham, R.J. (ed.) (1990). *High Temperature Corrosion of Technical Ceramics*. London: Elsevier.
Gao, W. and Li, Z. (eds.) (2008). *Developments in High-Temperature Corrosion and Protection of Materials*. Cambridge: Woodhead Publishing Limited.
Greenwood, N.N. (1968). *Ionic Crystals*. Butterworths, London: Lattice Defects and Nonstoichiometry.
Hill, V.L. and Black, H.L. (eds.) (1981). *Properties and Performance of Materials in Coal Gasification Environments*. Metals Park, OH: ASM.
Kubaschewski, O. and Hopkins, B.E. (1962). *Oxidation of Metals and Alloys*, 2e. Butterworths, London.
Lang, E. (ed.) (1983). *Coating for High Temperature Applications*. London: Applied Science Publishers.
Lai, G.Y. (2007). *High-Temperature Corrosion and Materials Applications*. Materials Park, OH: ASM International.
Marriott, J.B., Van de Voorde, M., and Betteridge, W. (1984). *Coal Conversion Processes and their Materials Requirements*, EUR 9182. EU Publications.
Meadowcraft, D.B. and Manning, M.I. (eds.) (1983). *Corrosion Resistant Materials for Coal Conversion Systems*. London: Applied Science Publishers.
Meetham, G.W. (ed.) (1981). *Developments in Gas Turbine Materials – 1*. London: Applied Science Publishers.
Nathal, M.V., Darolia, R., Liu, C.T. et al. (eds.) (1997). *Structural Intermetallics 1997*. Warrendale, PA: TMS.
Newkirk, J.B. (ed.) (1980). *High Temperature Materials*. Tel-Aviv: Freund Publishing House.
Nickel, K.G. (ed.) (1994). *Corrosion of Advanced Ceramics*. Dordrecht, The Holland: Kluwer Academic Publishers.
Norton, J.F. (ed.) (1984). *High Temperature Materials Corrosion in Coal Gasification Atmospheres*. London: Applied Science Publishers.
Philibert, J. (1991). *Atom Movements Diffusion and Mass Transport in Solids*. Les Uis: Editions de Physique.
Rapp, R.A. (ed.) (1983). *High Temperature Corrosion*. Houston, TX: NACE.
Sauthoff, G. (1995). *Intermetallics*. New York: Wiley-VCH.
Sedricks, A.J. (1996). *Corrosion of Stainless Steels*, 2e. New York: Wiley.
Sequeira, C.A.C. (2013). *Chem. Eng. Res. Des.* 91: 318.

Chapter 2

Metallurgical Structure and Metals

Since high temperature corrosion (HTC) is essentially a high temperature reaction between a metallic material and its environment, the very significant effect of crystal defects and metallurgical structure on most of HTC phenomena is to be expected. It is no longer possible to neglect the metallurgical aspects of a corrosion problem than it is to overlook the environmental and physicochemical factors. In this chapter, basic concepts of physical metallurgy are considered, outlining structural metallurgy relevant to HTC. The first section forms the basis for all the others, particularly Section 2.5. The phenomenon of diffusion, which is a subject of physical metallurgy highly important in HTC, is studied in Chapter 5.

2.1 Imperfections in an Essentially Perfect Structure

There are approximately 80 metals (Table 2.1), and it is often stated that they are all ductile and malleable and have characteristic luster. This is quite incorrect. Bismuth shatters like glass when struck with a hammer, and even copper becomes stiff and brittle after being bent a few times. The nonmetals graphite and silicon frequently have "metallic" luster. Moreover, terms such as ductile, brittle, and malleable have grown up with metallurgy over the ages and are themselves difficult to define (see Section 2.6). Metals are not necessarily strong (indium is not strong enough to support its own weight), nor are they always good conductors of electricity (manganese is a poor conductor). There is no unique mechanical property by which metals may be defined. They are, however, all elements whose electrical resistance increases with temperature, whereas that of molten ionic compounds, such as sodium chloride, decreases.

In present times, metals are being used close to their limits of strength, and it is vital to understand the practical and theoretical principles that govern their use.

2.1.1 The Essentially Perfect Structure of Pure Metals

Dalton's atomic theory (see Section 2.3) retarded the development of an understanding of the *structure* of metals. Throughout the nineteenth century, metals were considered as disordered arrangements of molecules. At the turn of the twentieth century, X-ray analysis proved that metals essentially consist of ordered arrangements of atoms. The analysis showed that for true metals there are three basic structures: the *face-centered cubic* (FCC), the *hexagonal close-packed* (HCP), and the *body-centered cubic* (BCC). Some metals such as iron (Section 2.4) exist in more than one form, each of which is exclusively stable under equilibrium conditions over a definite range of temperatures.

In both FCC and HCP structures, the atoms are said to be close-packed with each atom immediately surrounded by the maximum number of 12 neighboring atoms. On the other hand, in the BCC structure, which is not close-packed, each atom is only immediately surrounded by eight atoms. The two close-packed structures may be built up from the close-packed layers illustrated in Figure 2.1. The distribution of atoms, which are regarded as hard spheres, in the first close-packed layer A is identical to that in all others of the close-packed type. Each atom is surrounded by six others within the same plane. One set of interstitial holes between the atoms in the first layer A has been marked with a cross and the second layer B may either fit over this or the other set but not both. The difference between the FCC and HCP structures arises from the position that the third layer adopts relative to the first. The FCC structure is formed when the centers of the atoms in the third layer are directly over one of the sets of holes in the first layer. The fourth layer is then over the atoms in the first layer. If the position of the first layer is denoted as A and those of the second and third layers as B and C, respectively, then the stacking pattern of the layers is ABCABCABC … The HCP structure, however, is formed when the third layer is directly over the

High Temperature Corrosion: Fundamentals and Engineering, First Edition. César A. C. Sequeira.
© 2019 John Wiley & Sons, Inc. Published 2019 by John Wiley & Sons, Inc.

Table 2.1 Common crystal structures of metals

Metal	Structure	Metal	Structure	Metal	Structure
(Actinium)	FCC	Gold	FCC	Potassium	BCC
Aluminum	FCC	Hafnium	HCP	Praseodymium	Poly
(Americium)		Holmium	HCP	(Promethium)	
Antimony	Trig	Indium		(Protactinium)	
(Astatine)		Iridium	FCC	(Radium)	
Barium	BCC			Rhenium	HCP
(Berkelium)			αBCC	Rhodium	FCC
Beryllium	HCP	Iron	γFCC	Rubidium	BCC
Bismuth	Trig		δBCC	Ruthenium	HCP
Cadmium	HCP	Lanthanum	αHCP	Samarium	
Cesium	BCC		βFCC	Scandium	Poly
Calcium	αFCC			Silver	FCC
	γHCP	Lead	FCC	Sodium	BCC
(Californium)		Lithium	BCC	Strontium	FCC
Cerium	αHCP	Lutetium	HCP	Tantalum	BCC
	βFCC	Magnesium	HCP	(Technetium)	HCP
		Manganese	Poly	Terbium	Poly
Chromium	αBCC	(Mendelevium)			
	βHCP	Mercury	HCP	Thallium	αHCP
		Molybdenum	BCC		βFCC
Cobalt	αHCP	Neodymium	Poly		
	βFCC	(Neptunium)		(Thorium)	FCC
Copper	FCC			Thulium	HCP
(Curium)		Nickel	αHCP	Tin	Tetragonal
Dysprosium	HCP		βFCC	Titanium	HCP
(Einsteinium)				Tungsten	BCC
Erbium	HCP	Niobium	BCC	Uranium	Poly
Europium	BCC	(Nobelium)		Vanadium	BCC
(Fermium)		Osmium	HCP	Ytterbium	Poly
(Francium)		Palladium	FCC	Yttrium	Poly
Gadolinium	Poly	Platinum	FCC	Zinc	HCP
Gallium	Rhombic	(Plutonium)		Zirconium	Poly
Germanium	Poly	(Polonium)	Poly		

Radioactive metals are shown in brackets; poly = polymorphic; trig = trigonal.

atoms in the first layer and the repeated stacking pattern is ABABAB … In both structures each atom is surrounded by six atoms within the same layer and three in both of the adjacent layers.

Since the BCC structure is not a close-packed one as it does not contain any close-packed layers, it might be thought that the densities of metals with the BCC structure would always be less than those with the close-packed structure. This is not the case. Tungsten ($19.4\,\mathrm{mg\,m^{-3}}$), molybdenum (10.2), and niobium (8.57), which have each the BCC structure, are more dense than HCP titanium (4.54) and FCC aluminum (2.7).

Although each atom is surrounded by 8 as opposed to 12 others, this is compensated by the next nearest neighbors being only 1.16 times further away.

The unit cell (Figure 2.2) is the basic three-dimensional unit of pattern that, when repeated, gives the whole crystal framework. It is the simplest volume repeating unit based on a parallelepiped and includes both lengths and relative directions. The lengths are labeled a, b, and c; α is the angle between b and c, β between a and c, and γ between a and b. Of the seven unit cells, only the cubic and hexagonal ones are concerned with the ideal structures of metals. In the cubic unit cell, $a = b = c$ and each angle is 90°. The hexagonal unit cell is often but incorrectly drawn as the hexagon. This is not, however, the simplest repeating unit, which is the rhomboidal prism such that $a = b \neq c$ and $\alpha = \beta = 90°$ with $\gamma = 60°$. The ideal c/a ratio is 1.633.

The *Miller indices* are used to denote the positions of all the close-packed and other planes in the unit cell. The indices are conveniently kept as small as possible by using the reciprocals of the intercepts that the planes make with the axes in the order a, b, and finally c. Consequently, the (100) plane (Figure 2.3) makes a unit intercept at A on the α axis and is parallel to b and c. The (110) plane makes unit intercept at A and B on the a and b axes, respectively, but is

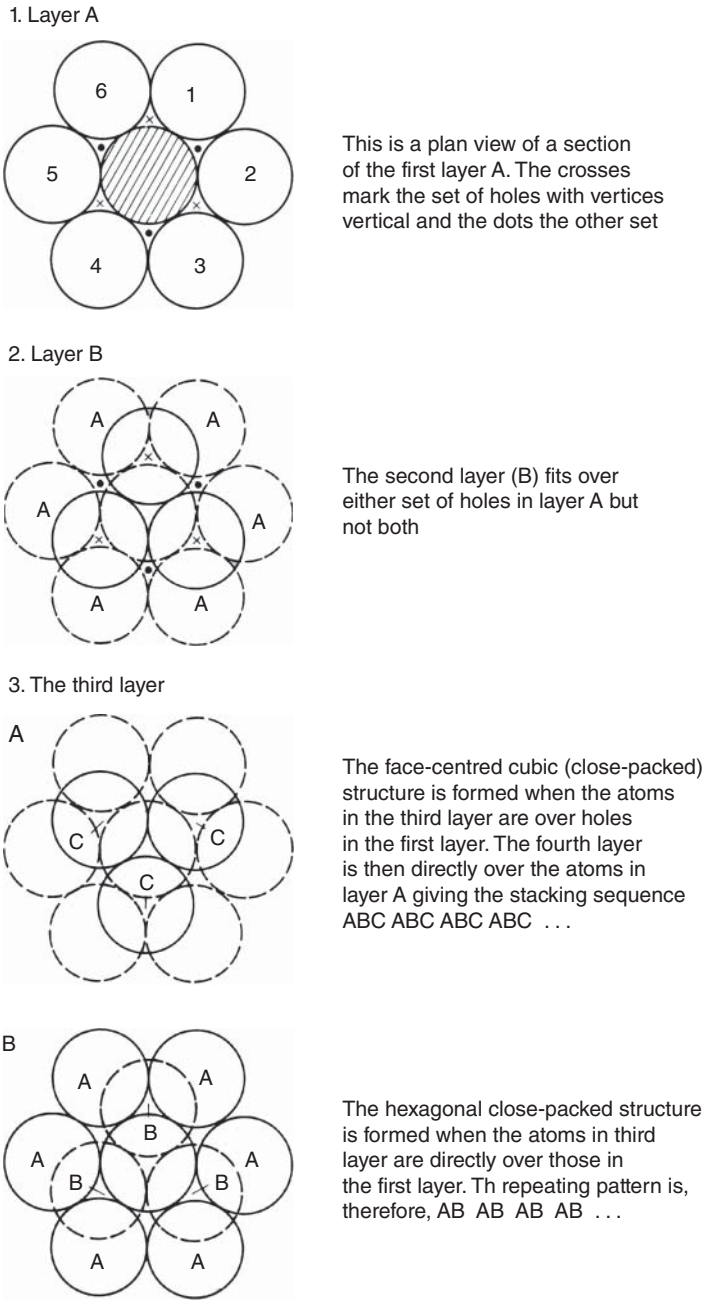


Figure 2.1 Ideal close-packed structures.

parallel to the *c* axis. The (111) plane makes unit intercepts at *A* and *B* as before but divides *OC*, where *O* is the origin into two equal parts each of length *c*/2.

There is a definite convention about the use of brackets:

(111) means a 111 plane.

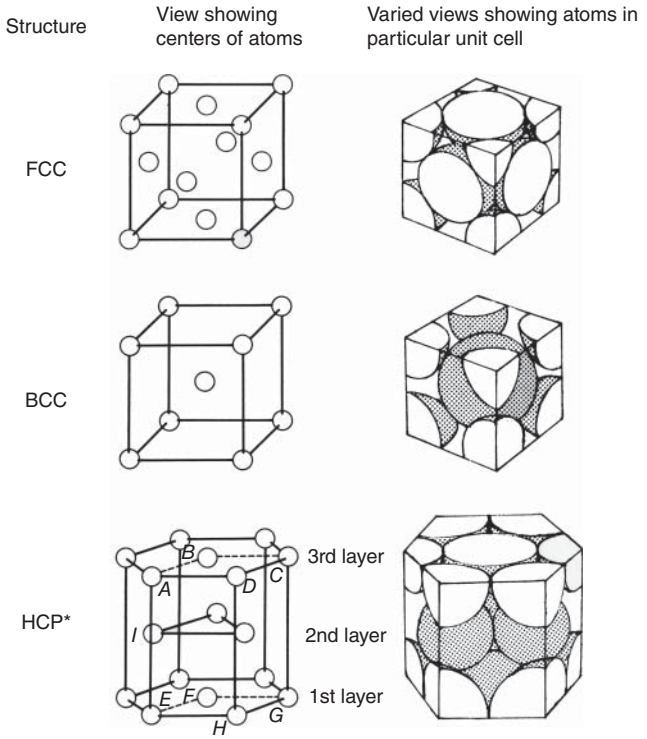
{111} means a set of planes of the (111) type, including $(1\bar{1}1)$ where $\bar{1}$ means a unit negative intercept.

[111] means a direction whose rectangular coordinates are [111] (see Figure 2.3).

⟨111⟩ means all directions of the [111] type.

The FCC metals, which include copper, are often strong and ductile at all temperatures. It will be shown later that they owe these desirable properties to sets of close-packed planes that correspond to the {111} set. There are four sets altogether, these being parallel to *ABC*, *EFO*, *AGB*, and *DFO* (Buerger 1956).

The profound influence that these close-packed planes have on the properties of metals arises partly because the distance between adjacent layers is larger than that between all others. Generally speaking, the greater the density of atoms (Figure 2.4) within a given set of layers,



* The unit cell is not the hexagon but the rhomboidal prism *A B C D E F G H* such that $\alpha = \beta = 90°$; $\gamma = 60°$ $a{=}b{\neq}c$(a is equal to side *AB*; *b* to *FG*; *c* to *CG*) to which the hexagon is closely related.

Figure 2.2 Unit cells.

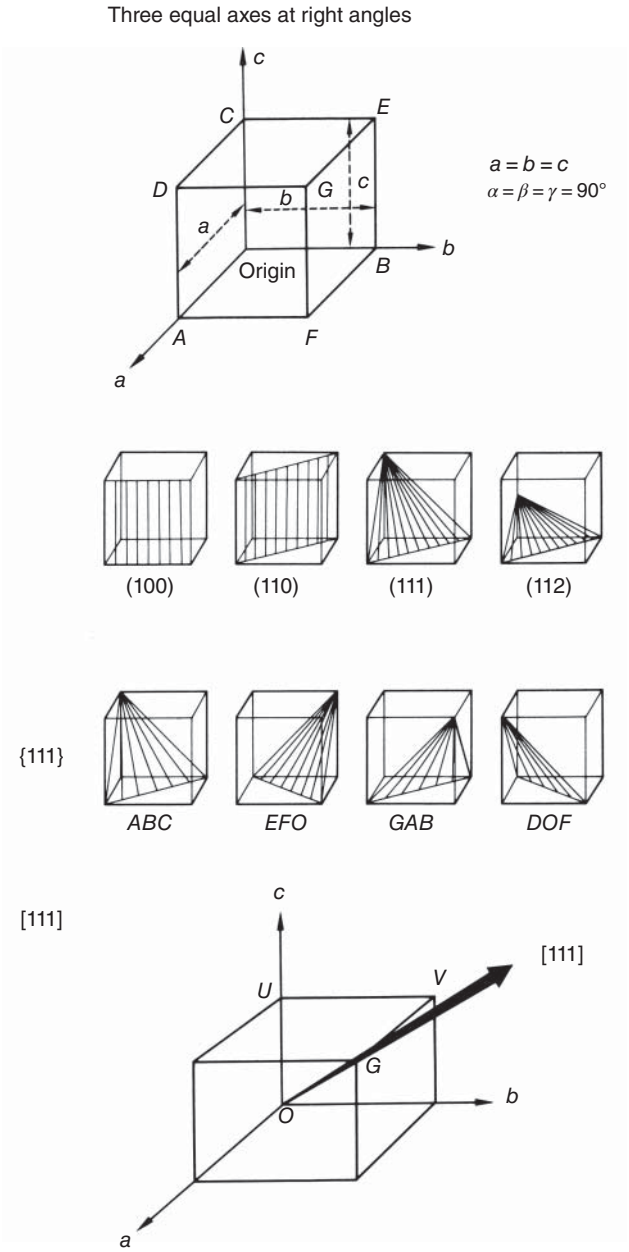


Figure 2.3 Miller indices and the cubic system.

the greater the spacing between adjacent layers of that set. The spacing between the (111) planes is much greater than that between the (110) planes, and the atomic density is greater. Long bonds are weaker than short bonds, and therefore the bonds between the close-packed planes are weaker than those between all other sets. Consequently, close-packed planes slip over one another more easily than all other sets when the metal is deformed (Section 2.5).

The position of the unit cell relative to the close-packed planes is illustrated in Figure 2.4. The name FCC is derived from the arrangement of the atoms that constitute the unit cell. There is 1 atom at each of the 8 corners and one at the center of each face, but it is incorrect to say that there are a total of 14 atoms in the unit cell. In this and in BCC structures (not HCP), the atoms at corners are shared by eight unit cells, those at the edges by four, and those on faces by two unit cells. The true number, which is exactly the same for each of FCC unit cell, is four:

There are six at sides shared by two unit cells	3
There are eight at corners shared by eight cells	1
True number	4

The point may be clarified by building the unit cell depicted in Figure 2.2.

The total volume is not totally occupied by the atoms, since there are holes or interstices between the atoms. In Sections 2.3 and 2.4 it will be shown that carbon atoms occupy these interstices in both FCC and BCC iron to form the interstitial alloy steel. The volume occupied by atoms in all FCC metals and hence the percentage free space are found as follows.

The sides of the unit cell each have length a so that the volume is a^3. The volume of the unit cell in terms of the

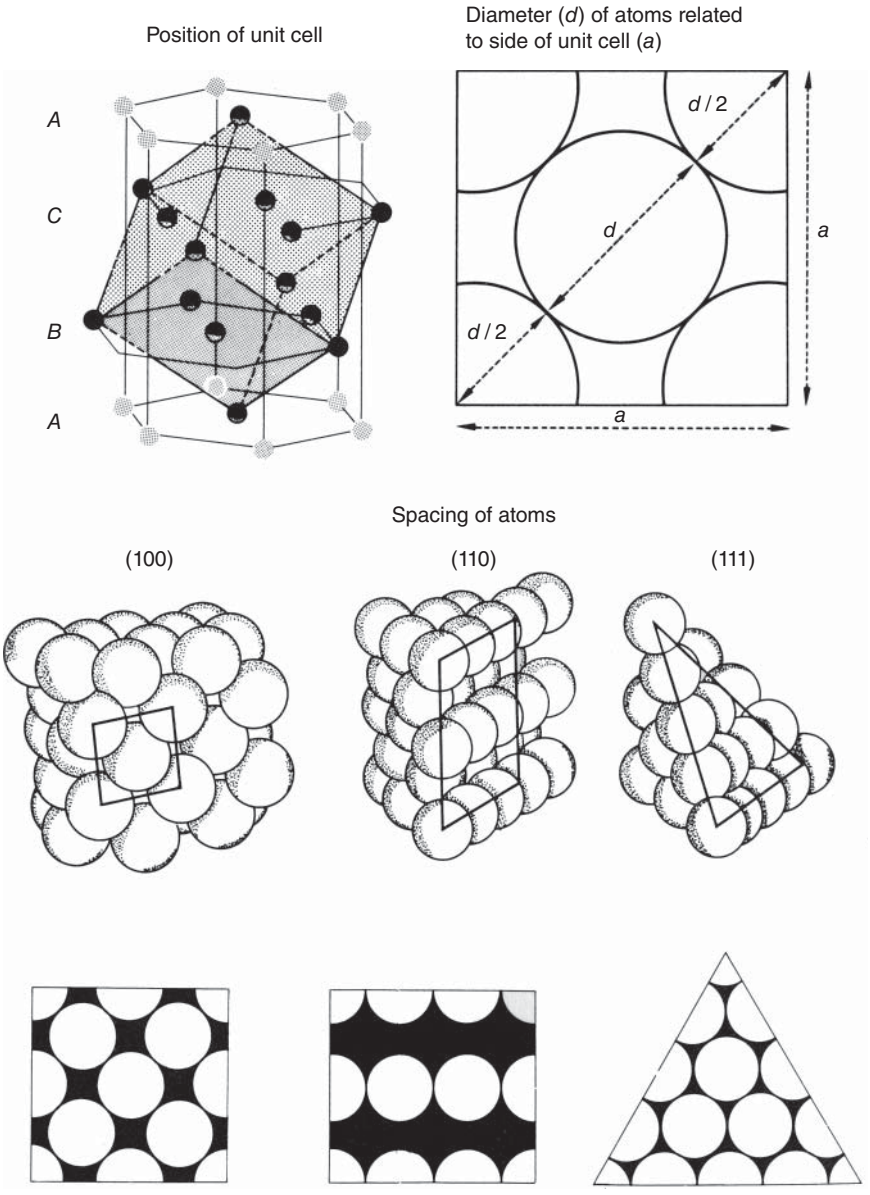


Figure 2.4 Face-centered cubic structure.

diameter (d) of the spheres is found using Figure 2.4:

$$\text{Length of side} = a = 1.41\,d$$

$$\text{Volume} = a^3 = (1.41\,d)^3$$

$$\text{Volume occupied by one atom} = \frac{4}{3}\pi\left(\frac{d}{2}\right)^3$$

Percentage volume occupied by four atoms (or atomic packing factor):

$$\text{APF} = \frac{4 \times 4 \times 3.14 \times d^3 \times 100}{3 \times 2^3 \times 1.414^3 \times d^3} = 74\% \qquad (2.1)$$

This means that in each perfect FCC structure, there is 26% free space that may be occupied by small atoms such as carbon.

HCP metals, such as magnesium, which have the hexagonal structure, are often ductile like the FCC metals. Close-packed planes form the top and bottom of the hexagon that is closely related to the unit cell (Figure 2.2). There is only one set of close-packed planes compared with four in the FCC metals, but planes in this one set can easily slip over one another. The ideal c/a ratio of 1.633 is unknown for pure metals (it is possibly known in a magnesium–cadmium alloy). In cadmium (1.88) itself and in zinc (1.86), the unit cell is extended along the c axis. In most metals, however, the ratio is lower than the ideal value (beryllium, 1.57; cobalt, 1.62; magnesium, 1.62; titanium, 1.62; and zirconium, 1.59).

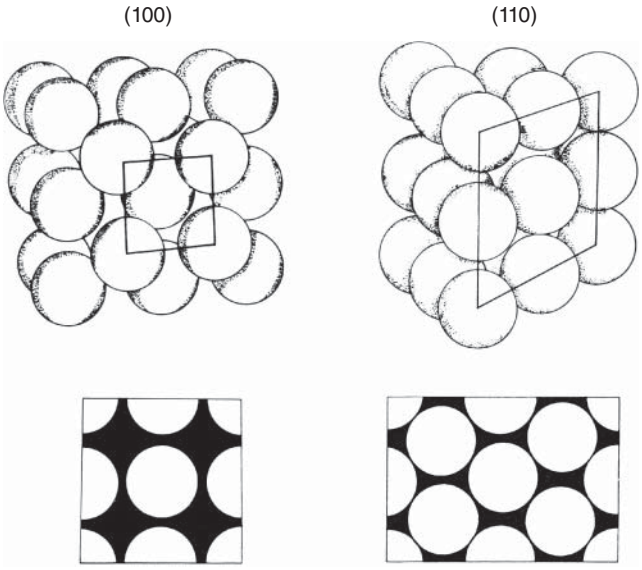


Figure 2.5 Body-centered cubic structure.

BCC metals, such as sodium or iron, which have the BCC structure, are brittle at low temperatures. Sodium is soft but brittle. It is used to be said that fractured iron rails (Section 2.6) had crystallized before fracture but metals with the BCC structure are brittle at low temperatures because they have no close-packed planes. The distance between all adjacent layers is comparatively small so that they do not move over one another with the ease of close-packed planes in FCC and HCP metals. From Figure 2.5 for the BCC structure,

$$(2d)^2 = \left(\sqrt{2} \times a\right)^2 + a^2$$

$$a = \frac{2d}{\sqrt{3}} \tag{2.2}$$

where d is the diameter of each atom and a the side of the unit cell.

Therefore, the volume of the unit cell $= \left(\frac{2d}{\sqrt{3}}\right)^3 = \frac{8d^3}{3\sqrt{3}}$.

Each cell contains two atoms:

There is one unshared atom in the center	1
There are eight at each corner shared by eight unit cells	1
True number	2

$$\text{APF(percent occupied space)} = 2 \times \frac{4}{3} \times \frac{22}{7} (d/2)^3 / \frac{8d^3}{3\sqrt{3}} = 68\% \tag{2.3}$$

There is 32% free space that is 6% more than in the FCC structure. In Section 2.4, it will be shown that the solubility of carbon in BCC iron is smaller than in FCC iron even though the percent free space is greater (Ashby and Jones 2005).

2.1.2 The Metallic Bond

The attractive (or cohesive) forces, which hold the atoms together, constitute the metallic bond. The simplest picture of the bond envisages ions embedded in a sea of electrons, and, although undoubtedly an oversimplification, this model does provide a pictorial approach applicable to the following text. Since each ion is embedded in its own particular region of the sea, the bond is nondirectional and is not localized between two atoms as are single covalent bonds. Consequently, the movement of layers of atoms over one another (Section 2.5) is not restricted by the metallic bond, as the electrons permeate the whole structure. The bond can be easily reformed. In addition, the metallic bond is unsaturated, which means that it does not limit the number of adjacent atoms. Geometry alone places the maximum number of equidistant and identical spheres at twelve. Moreover, the combination of nondirectionality and unsaturation enables atoms of comparable size to dissolve one another over the entire ratios of concentrations. Copper and gold (Section 2.3) are completely soluble in each other. In principle, it is only necessary to bring the clean surfaces together, but in practice the metals have to be heated close to their melting points to give the atoms sufficient thermal energy to enable them to diffuse (Chapter 5) through the framework of atoms. The metallic bond does not itself set the limits of solubility of carbon in iron. The limit is set by the extent to which the iron framework (Section 2.4) allows itself to be distorted because, although the carbon atoms are small, they are still larger than the interstitial holes into which they fit.

All this is in direct contrast to the properties that the covalent bond bestows on substances such as diamond because this bond is directional and saturated. The directional nature arises from the fact that the electrons that constitute the covalent bond are localized between the atoms. This means that once broken the bond cannot be easily reformed. The saturated nature of the bond results in strict ratios of atoms in all covalent compounds (for example, one to four in CCl_4).

In all solids there are repulsive forces as well as attractive ones. There must be – otherwise the atoms would collapse into each other. The magnitude of both types of forces varies with the distance that separates the atoms. Figure 2.6 illustrates the manner in which they vary for two ions of opposite charge combining to form an ion pair, but the same shape of curve is obtained for any crystalline array of atoms and is therefore applicable to metals. At large distances, the attractive force is zero, but as the ions come together, the attractive forces resulting from the charges of opposite sign

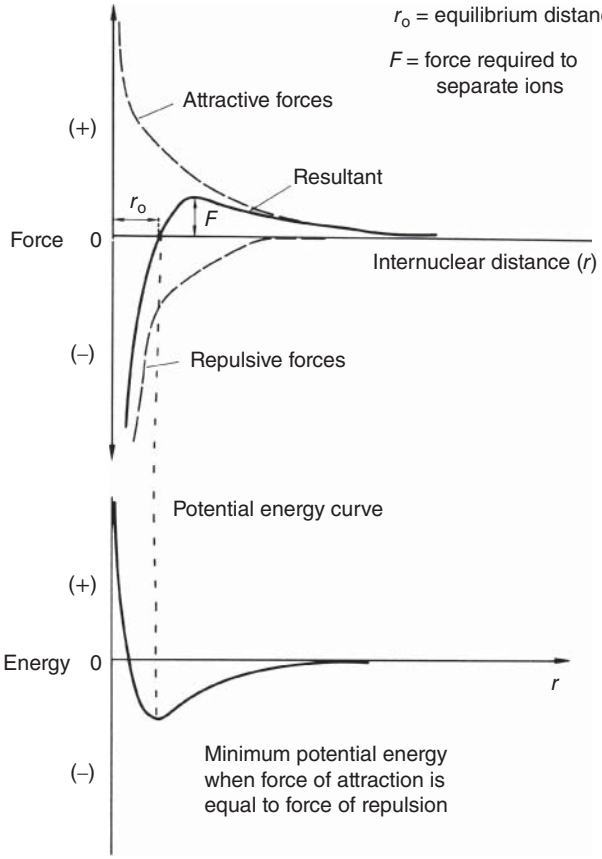


Figure 2.6 Force–distance curve.

increase in inverse proportion to r, the distance of separation. The attractive forces continue to increase, but then the repulsive forces begin to take effect. These forces vary as r^{-10} and consequently are insignificant unless the distance r is very small, but then they increase as r decreases and the negatively charged electrons on adjacent atoms repel each other. An analogy to repulsive forces is that the force required to compress two rubber spheres together increases greatly with the degree of compression.

The atoms come to rest at the equilibrium distance such that the repulsive and attractive forces are equal, that is, the potential energy is minimum (Figure 2.6; see also Figure 2.47). The shape of the force–distance curve at this point is important to the ensuing discussion. The curve is linear in this region, which means that "Force is proportional to distance."

Hooke's law can be applied to atomic bonds for either stretching (tensile) or compressive forces.

The maximum (F) in the force–distance curve gives the force required to separate the atoms. Since the maximum falls at a value of r greater than the equilibrium distance, the atoms can only be separated by tensile and not compressive forces.

2.1.3 The Real Structures of Metals

While structures of pure metals may be perfect at absolute zero, they contain *imperfections* at all finite temperatures. Calculations, for example, that assume that metals are perfect arrays of atoms give values of the above force required to separate atoms 1000–10 000 greater than needed in practice. Again it might be expected from the previous discussion on the perfect structure that all metals with the same unit cell would need the same force to separate the atoms. This is not the case. In addition, perfect structures are unable to account for solidification, melting, diffusion, the strength of alloys compared with pure metals, hardening of steel, deformation, and fracture.

Imperfections naturally occur in metals and all real metals are imperfect – indeed it is important that they should be so. Metals are undoubtedly essentially perfect (much more than 99.9%), and yet these imperfections account for all of the properties that distinguish one metal from another. The imperfections may result from the growth of metals, from the vibrations of the atoms, from contact with other materials, or from thermal and mechanical treatments. The properties of metals are always considered in relation to the imperfections that are always present and that may be altered by varying the rate of growth from the melt, alloying, heat, and mechanical treatments to produce the required combination of properties (Table 2.2), each of which has its own distinct effect on the properties of the metal. Their nature under the effect that they have on metals is discussed hereafter.

2.1.3.1 Point Imperfections: Vacancies and Interstitial Atoms

Vacancies are holes left by the absence of a metal atom, but this does not mean that vacancies are unstable because the surrounding atoms do not necessarily collapse to fill the space. There are always a finite number of vacancies at all temperatures above absolute zero. At low temperatures – below half of the melting point T_M in degrees kelvin – the number of vacancies is smaller than that at high temperatures. Near to the melting point, there is approximately one vacancy for every 10^4 atoms. As will be discussed later, vacancies provide a model for a description of diffusion (particularly at elevated temperatures), for melting, and for the extension of metals under constant stress (creep).

2.1.3.2 Line Imperfections: Dislocations

An edge dislocation is illustrated in Figure 2.7. For clarity, it has been drawn for the rare simple cubic system, that is, with atoms at the corners of the cubic unit cell but nowhere

Table 2.2 Imperfections

Type	Name	Property	Section
Point	Vacancy (interstitial atom)	Diffusion	2.2–2.6
		Solidification	2.2–2.4
		Melting	2.2
		Creep	2.3 and 2.5
Line	Dislocation	Deformation (discrepancy between observed and calculated strength)	2.5 2.3 and 2.4
		Fracture	2.6
		Crystal growth	2.2
Plane	Grain boundaries	Low temperature diffusion	2.2
		Deformation	2.5
		Fracture	2.6
		Etching patterns	2.1
(Volume)	Second component soluble	Substitutional and interstitial solid solution alloys	2.3 and 2.4 2.5 and 2.6
	Insoluble	Dispersion hardening	2.3
		Deformation	2.5
		Fracture	2.6

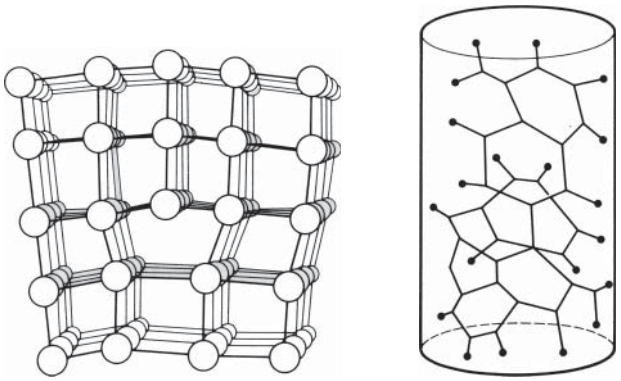


Figure 2.7 Dislocations (see also screw dislocation in Section 2.2). (a) Edge dislocation caused by introduction of an extra plane of atoms and (b) network of dislocation.

else. Only α-polonium has this structure. The edge dislocation arises when an extra plane of atoms is inserted between others, and in an undeformed metal this may occur once for every million atoms. The edge dislocation will be used throughout the ensuing discussion to describe mechanisms for deformation and fracture. They do, however, act in combination with screw dislocations that provide the mechanism of crystal growth.

In addition, *dislocations* cannot terminate in ordered regions but may do so at other imperfections such as other dislocations, and, as a result, a network (Figure 2.7) may be formed throughout the metal. Alternatively, they may run to the surface of the metal. The atoms at the dislocations have a higher energy than those in the ordered regions (Brandon and Kaplan 1999).

2.1.3.3 Plane Imperfections: Grain Boundaries

Metals are polycrystalline. That is, they consist of many separate abutting crystallites that are called *grains*. Individual grains are themselves essentially ordered arrays of atoms but normally contain vacancies and dislocations. The *grain boundaries* are regions of disorder two to three atoms thick (c. 3 Å). They limit the freedom of movement of dislocations and act as vacancy sinks but allow atoms to move through them at low temperatures. Atoms within grain boundaries have higher energy than those in the grains and are preferentially attacked by chemicals, as are those at the dislocations.

2.1.3.4 Influence of a Second Component

Pure metals are extremely difficult to prepare and often there is a second component. Frequently a second component is deliberately added to improve the properties of a metal. The second component may be soluble (copper in gold) in the matrix metal or insoluble (molybdenum in copper) or partially soluble (tin in lead). Moreover, the second component may react to produce a compound. Thus, carbon can combine with iron to form iron carbide and copper with aluminum to form the compound $CuAl_2$. Normally, second components or phases limit the movement of dislocations and improve resistance to deformation and fracture.

Direct visual evidence for imperfections comes from the microscopic study of the surface. In the past it had been very difficult to achieve convincing evidence for vacancies because they are simply absences of atoms. Developments

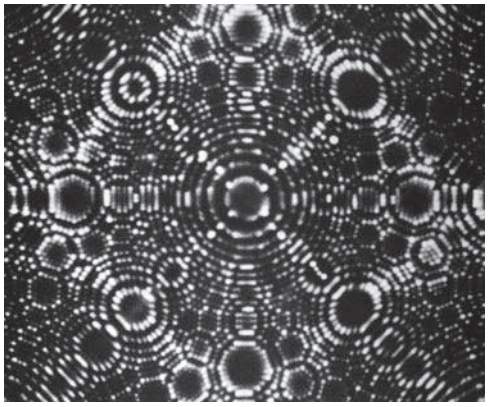


Figure 2.8 Field ion micrograph of a normal metal tip–ideal structure ($\times 10^7$).

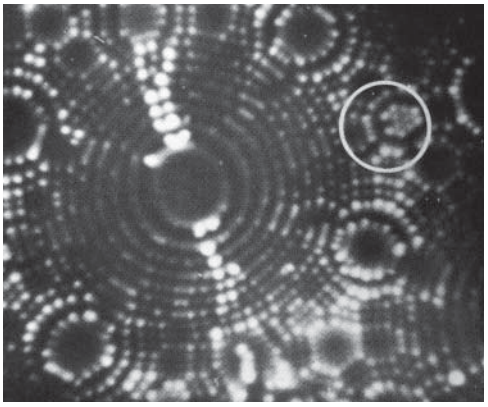


Figure 2.9 Field ion micrograph of a vacancy ($\times 10^7$).

of the technique of field ion microscopy led to magnifications of the order of 10^7, which are sufficiently large to allow individual atoms (of 10^{-7} mm diameter) to be seen as the white dots on micrographs shown in Figures 2.8–2.10. The plate is a flat projection of a hemispherical surface of the tip of a needle made from tungsten, and the mosaic pattern common to each arises from the manner in which the surface cuts the atomic planes. The evidence for vacancies and grain boundaries comes from a direct comparison of Figures 2.9 and 2.10, respectively, with the perfect structure (Figure 2.8). Therefore, vacancies are seen as the absence (dark holes) in the atomic pattern. The grain boundaries are seen as discontinuities in the atomic pattern, and each one is approximately 2–3 Å wide.

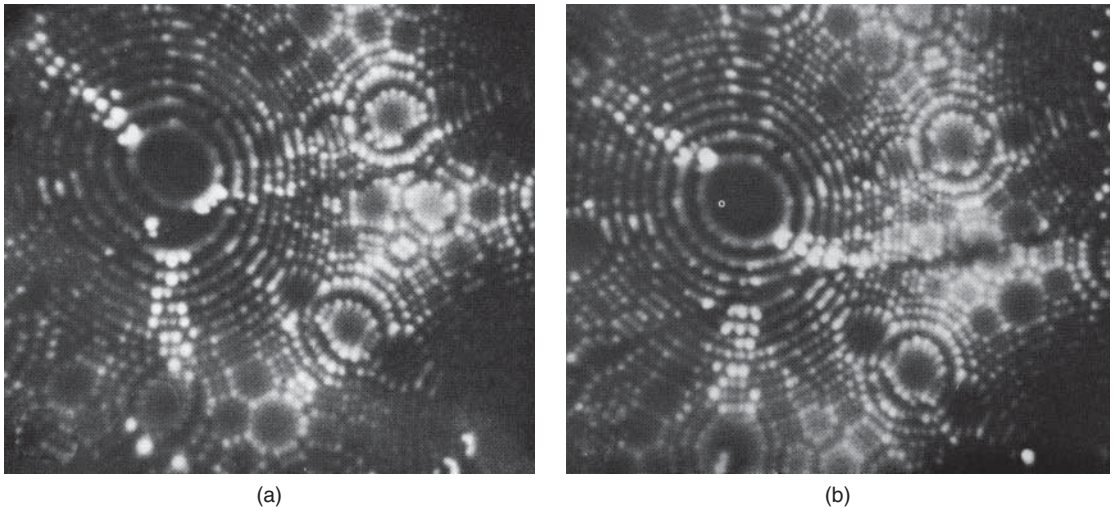
Throughout the remaining text, plates have been included that give evidence for imperfections, namely, dislocations and grains. Dislocations are seen, for example, as the dark lines in Figure 2.5, which was obtained from an electron microscope. The grains can be seen at much lower magnification with the optical microscope since they are usually about 100th of a millimeter across (Figure 2.11) (Van Bueren 1960).

2.2 Solidification

Solidification is the reverse of melting, being the study of changes that take place when a molten metal solidifies. The size, shape, and distribution of the grains in cast metals depend on the relative rates of *nucleation* and *growth*. In later sections it will be shown that grain size and shape may be changed by further heat treatment (Sections 2.3 and 2.4) and also by deformation (Section 2.5).

2.2.1 Solidification of a Pure Metal

A molten metal at *A* (Figure 2.12) slowly cools to *BC* where the temperature remains constant at the freezing point



(a) (b)

Figure 2.10 Field ion micrograph of grain boundary ($\times 10^7$). (a) Stage 1 and (b) Stage 2 – after a few layers of atoms have been removed.

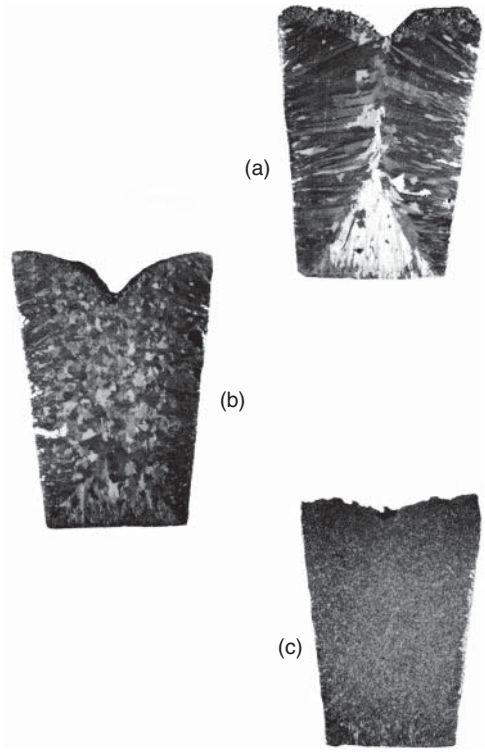


Figure 2.11 Grain structure of pure zinc cast from different temperatures (etched ×1/2). (a) 820 K, (b) 740 K, and (c) 690 K.

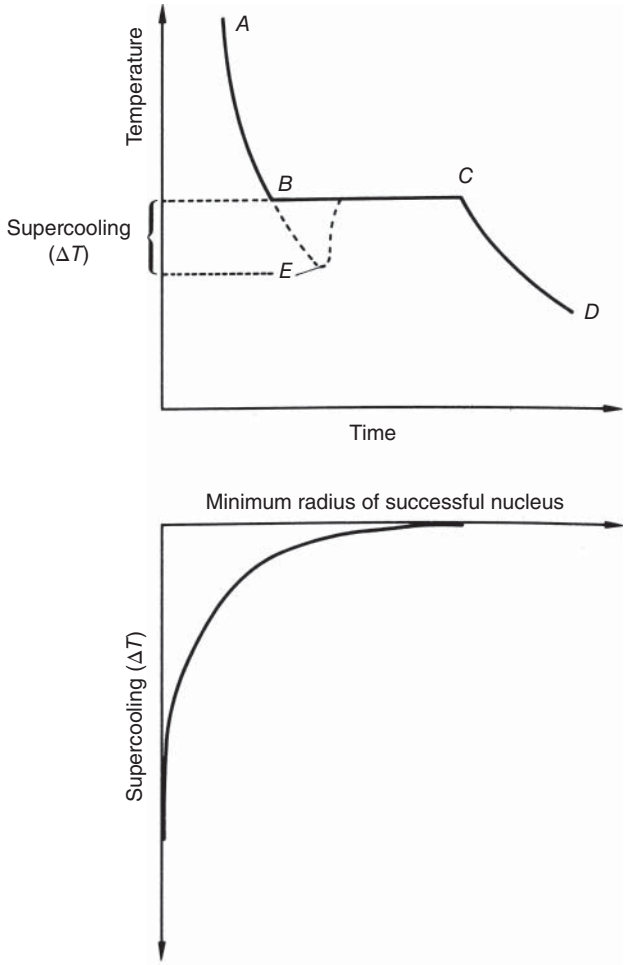


Figure 2.12 Cooling curve and the radii of successful nuclei.

while the latent heat is given out. There are no regions of solidified metal at temperatures above the freezing point as solidification starts at *B* and is completed at *C*. Thereafter the solidified metal continues to cool to the temperatures of its surroundings. This type of cooling curve in which there is equilibrium between solid and molten metal at *B* is only met when the rate of cooling is very low. There must be some heterogeneous nuclei around which the grains may grow as the atoms diffuse to them, but if the nuclei are absent, the crystals cannot form and the liquid supercools below the freezing point (point *E* on the dotted line) until the metal itself forms nuclei. This nucleation is the first stage of solidification and is followed by the second in which the nuclei grow into crystals. The rate of nucleation is related to the degree of *supercooling*, which is the temperature difference between the freezing point and that at which the nucleation begins. For small degrees of supercooling (Figure 2.12), the minimum radius of the successful nuclei is very large, and seldom do sufficient nuclei come together. At high degrees of supercooling, the minimum radius is very small, and many are formed because each successful nucleus needs only a few atoms. When there is only one successful nucleus, the resulting crystal that has only one grain is called a *single crystal*.

The final size and distribution of the grains in the solidified metal depend on the number and distribution of the nuclei together with the time in which they are allowed to grow into grains. A metal held under equilibrium conditions at *B* forms a few nuclei that may remelt or grow into grains. The grains will be large and evenly distributed throughout the metal because there are so few successful nuclei. Since a supercooled liquid forms a large number of nuclei, there are more but smaller grains in the regions where the supercooling is greatest. One is tempted to say that a high rate of nucleation always gives small grains, but the rate of nucleation must be considered in relation to the rate at which the grains grow. That is, a slow rate of nucleation may produce small grains if it is much greater than the rate of grain growth. Conversely, a high rate of nucleation may produce large grains if it is much smaller than the rate of growth.

The final shape of the grains depends on the direction of heat withdrawal because they grow in the opposite direction to that in which the heat is abstracted. If, therefore, heat is strongly abstracted in one direction, the crystals are long and thin (columnar), but if uniformly they tend to be rounded (equiaxed).

When molten zinc at 820 K, which is well above its melting point of 690 K, is subjected to casting into a cool mold, the metal that comes into contact with the surface of the mold is instantly cooled below its freezing point, whereas that in the center remains molten. The many nuclei formed around the edges may remelt or grow into grains, but no nuclei are formed in the center. At first, the nuclei grow in all directions to produce small equiaxed grains that have roughly the same size but different orientation. Sideways growth, however, only continues until the neighboring grains abutt and then the face with the favored orientation grows inward in the opposite direction to that in which heat is abstracted. The resulting long, thin columnar grains grow until they meet in the center where the rate of nucleation is very low indeed. When zinc is cast at 740 K, the columnar grains grow as previously, but some nuclei are also formed toward the center. The rate of nucleation and growth at the center is more comparable with that at the perimeter. Consequently, the columnar grains only grow inward until they come into contact with the large equiaxed grains. When zinc is cast from marginally above its melting point, the rate of nucleation is very high, much greater than the rate of growth over the whole mold. The result is that small equiaxed grains are formed throughout (Figure 2.11).

2.2.2 Casting an Alloy

The stages of nucleation and growth are applicable to alloys as well as pure metals. Columnar grains are found, for example, in alloys used for welding operations in which the molten metal is used to join separate surfaces. Figure 2.13 illustrates the grain structure that has resulted from the cooling of a stainless steel weld metal. The molten metal has cooled like zinc at 820 K from well above its melting point so that no nuclei are formed at the center. Nucleation and growth occur entirely from the perimeter with the result that long columnar grains meet at the center.

The recesses at the top of the solidified metals in Figure 2.14 (primary pipes) result from the fact that molten zinc occupies a larger volume than the same mass of solidified zinc. The change in volume that results from the solidification of metal may lead to serious failure in cast objects, particularly when they yield hidden holes (secondary pipes). These internal holes often arise when nuclei form and grow from the top surface as well as from the base and sides, with the result that molten metal remains in the center of the metal after that near the surface has solidified. As nuclei grow from all four surfaces, the adjacent layers of molten metal shrink as they solidify. The remaining metal moves toward the growing area, and as each layer shrinks on solidification, a hole is formed at the center.

It should be clear that the changes in volume from liquid metal to solid are applicable to alloys as well as pure metals.

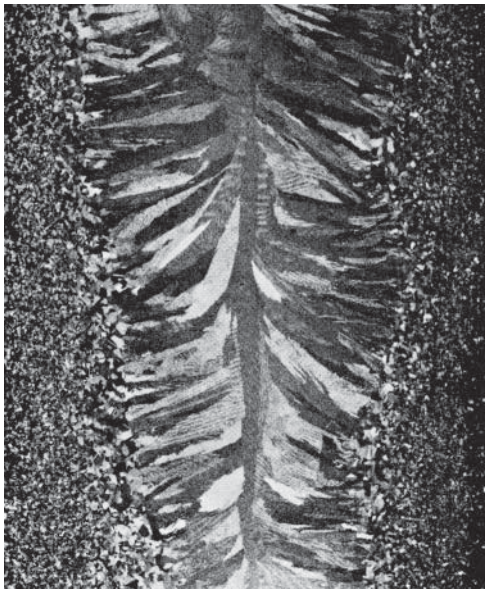


Figure 2.13 Grain structure of a weld metal (×5).

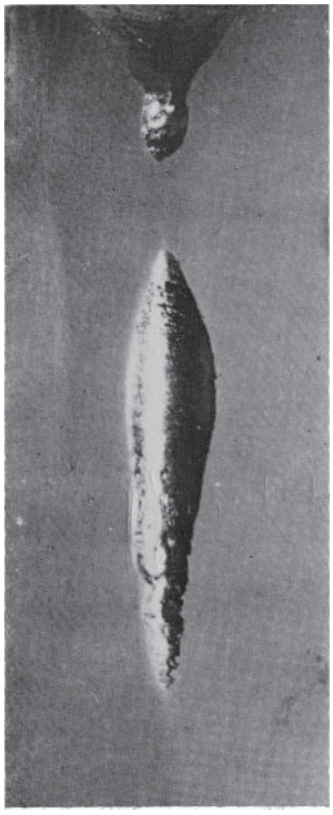


Figure 2.14 Holes in a solidified ingot (×1/3) (Hume-Rothery et al. 1969).

2.2.3 Mechanism of Crystal Growth

In Section 2.1 it was mentioned that edge dislocations act in conjunction with spiral dislocations, which provide the mechanism for crystal growth. Calculations have shown that the degree of supercooling (or supersaturation) required to deposit atoms on a completely planar surface is far in excess of that experimentally found to have been needed. The calculations also showed that the experimental degree of supercooling is compatible with a discontinuity such as a step on the surface. The problem is whether or not the step has to disappear when the layer is completed. The formation of a new step itself requires too high a degree of supercooling, and therefore steps are not continually formed and lost. In practice the step spirals through the metal as it grows, and, in Figure 2.15, the spiral can be seen emerging from a magnesium crystal. The position of the spiral is clarified by white magnesium oxide formed by preferential attack of oxygen on the atoms constituting the step that, like the edge dislocation, is a region of higher than average energy.

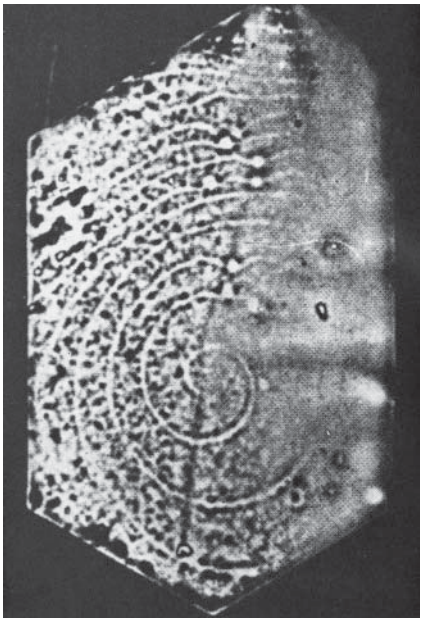


Figure 2.15 A spiral dislocation emerging from a magnesium crystal (×325) (Hume-Rothery et al. 1969).

Solidification may be studied by means of the electron microscope. In Figure 2.16, solidified metal (white) is seen growing into the molten salt (black). The curved surfaces denote the solid–liquid interfaces through which latent heat changes are transferred as the metal solidifies, resulting in partial remelting. Growth only occurs along a few favorably oriented faces, and the insoluble impurities are often pushed to the grain boundaries by the advancing

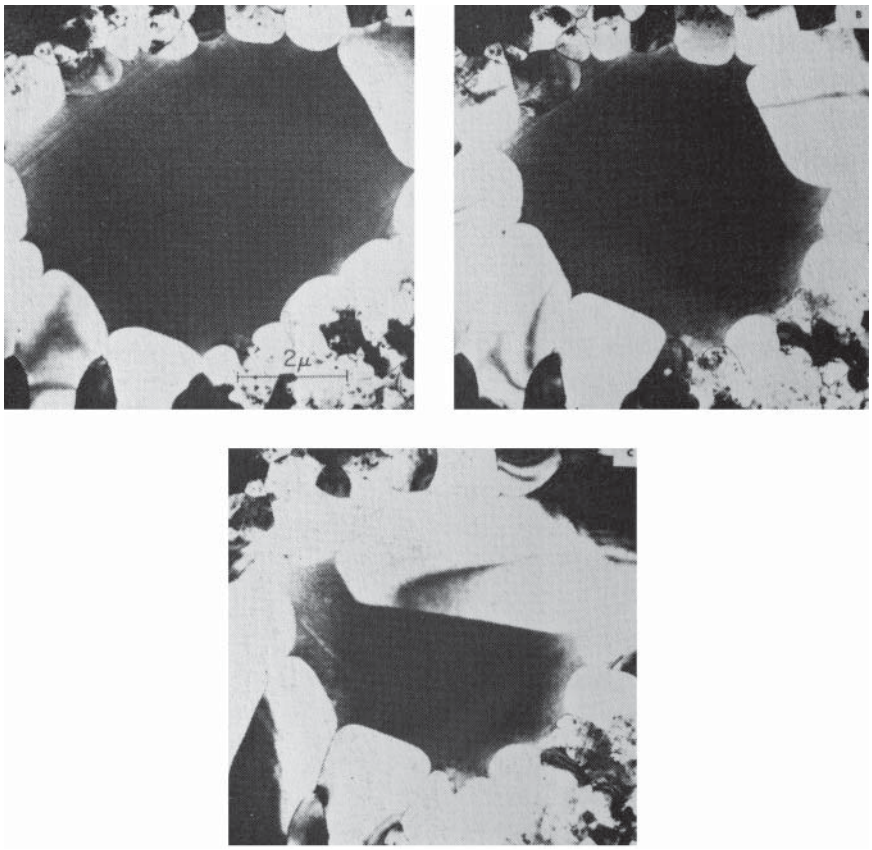


Figure 2.16 Grain growth of bismuth (×11 430).

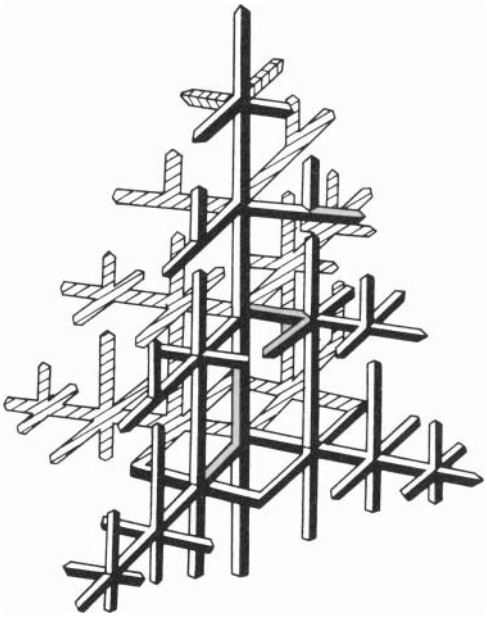


Figure 2.17 Dendrites.



Figure 2.18 Dendrites in antimony (×1).

solid–liquid interface. In the lower plate, it may be seen that the grain boundaries are the last to solidify.

The curved solid–liquid interfaces in Figure 2.16 are followed particularly in cubic metals by a dendritic or fir tree-like growth. In many cases the long arms are able to penetrate beyond the curved liquid–solid interface into the cooler regions of the liquid metal. These regions are cooler because the latent heat of fusion evolved as the metal solidifies, which only locally heats up the liquid directly in contact with the mass of the solidifying metal but not that in the bulk. In FCC or BCC metals, the dendritic arms extend along the [100] directions on which atoms are preferentially deposited as the metal solidifies. Each dendrite grows under equilibrium conditions along the mutually perpendicular directions (Figure 2.17) until it reaches the neighboring dendrite. The star of antimony, which was one of the wonders of the alchemists, is perhaps the most famous example of dendritic growth. The one illustrated in Figure 2.18 was heated to well above the melting point of antimony and allowed to cool under equilibrium conditions such that the rate of growth was much greater than the rate of nucleation. The metal was then etched.

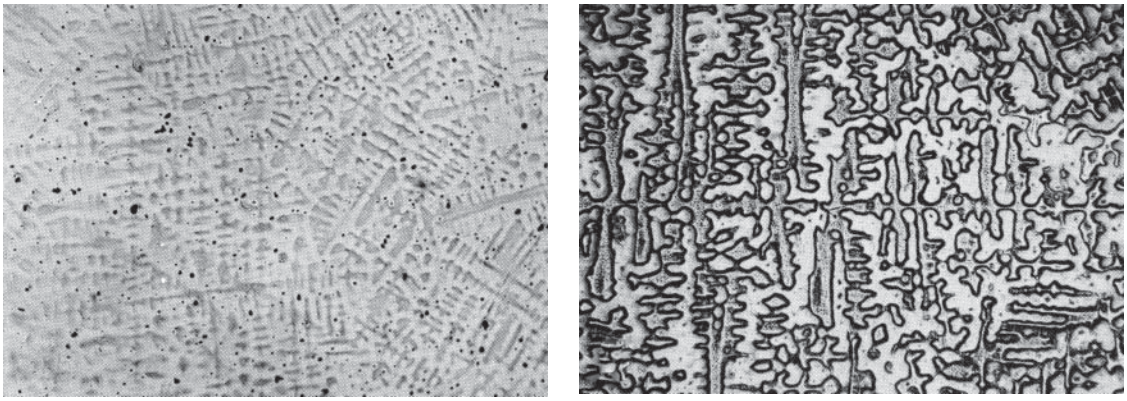
Dendrites are well known in alloys as well as pure metals. In the upper part of Figure 2.19, the lighter regions are (FCC) copper rich, and the darker ones tin rich. The heavy etch given in the lower sample illustrates that etching takes place at the grain boundaries, since these have higher energy than the atoms within the grains. Heavy etches are to be avoided because they give the appearance of a second phase even when there is only one present. The dendrites are not as well formed as in the star of antimony as the rate of cooling was greater so that the rate of growth was more comparable with the rate of nucleation. Solidification of alloys is further discussed in Section 2.3.

As indicated in Section 2.1, metals can form compounds with each other. These intermetallic compounds have definite stoichiometric ratios of atoms and have characteristic crystal structures. Copper and aluminum, for example, combine to form the compound $CuAl_2$, needle-like crystals of which are illustrated in Figure 2.20. The molten compound was cast into a mold, and the favorably oriented crystals grew into needles. The remaining molten compound was then poured off.

Alloys of iron exhibit many of the crystal forms that have been mentioned above. Some of them are illustrated in Figure 2.21. Meteoric iron with 15% nickel adopts a needle-like habit. Purified (refined) cast iron illustrates the dendrites, but the less pure cast ingot has small equiaxed grains because the impurities act as nuclei from which the grains grow in the normal manner.

2.2.4 Grain Structure and Corrosion

The grain structure of alloys, as well as intergranular precipitation, can markedly affect their corrosion behavior. For example, the corrosion resistance of certain wrought metals may be less on surfaces perpendicular to the hot or cold working direction than on surfaces parallel to this direction. Typically there may be severe localized corrosion starting on the faces perpendicular to the working direction and proceeding into the metal in the working direction, while the surfaces parallel to the working direction remain relatively



(a) (b)

Figure 2.19 Dendrites in a 9% tin bronze. (a) Normal etch (×100) and (b) prolonged etch – dendrites appear incorrectly to be a second phase (×150).

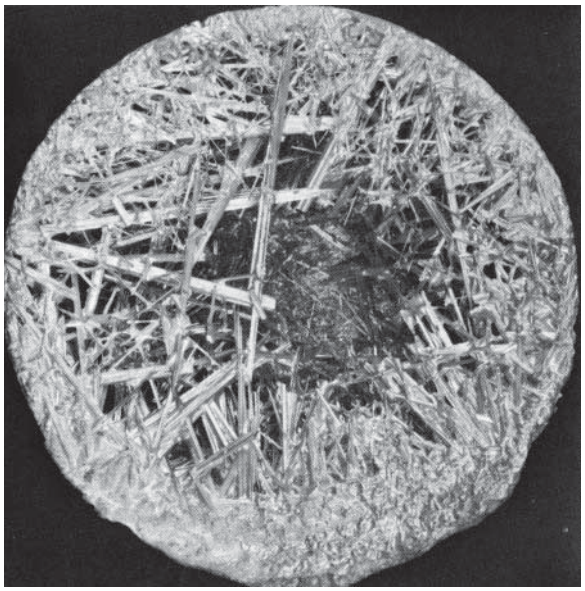


Figure 2.20 Needle crystals of $CuAl_2$ (×4/7).

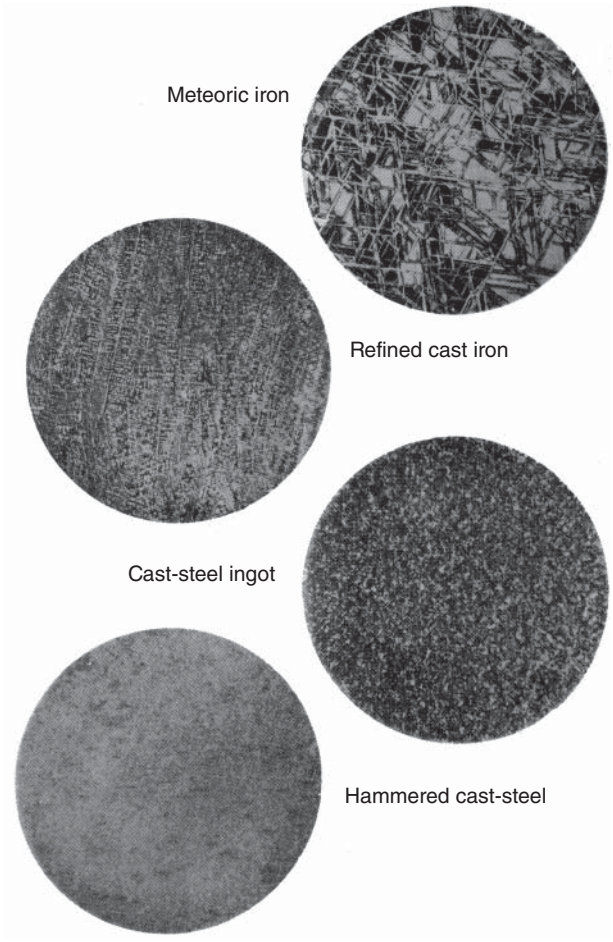


Figure 2.21 Grain structure of some iron alloys (×1).

unattacked. Such end-grain attack, which is basically the result of the grain structure being elongated in the working direction, has been observed in austenitic stainless steels, titanium alloys, and mild steel.

Grain structure also affects the stress corrosion behavior of high-strength age-hardenable aluminum alloys. Cracking in these alloys is always exclusively intergranular. When they are stressed in the short transverse direction (*a* in Figure 2.22), their highly elongated, pancake-shaped grain structure ensures that an easy path for crack propagation is readily available. On the other hand, when stressed in the long transverse or the longitudinal direction (*b* and *c*, respectively, in Figure 2.22), the possible intergranular crack paths are clearly complex and difficult. Many high-strength aluminum alloys are therefore quite susceptible to *stress corrosion cracking* when stressed in the short transverse direction but quite resistant or immune when stressed in the long transverse or longitudinal directions. This result is of considerable

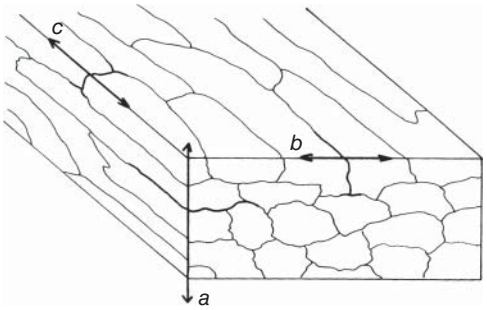


Figure 2.22 Grain structure of a wrought high-strength precipitation-hardening aluminum alloy showing potential crack growth paths.

practical importance: high-strength aluminum alloys can often be used in sheet form (when the short transverse tensile stresses are generally negligible) in tempers in which they cannot normally be used in thick sections of forgings (when the tensile stresses in the short transverse direction may be high). The distinction is, for example, between an aircraft's skin and its wing spars; with a susceptible alloy, stress corrosion cracking is likely to be a problem in the latter instance, but less so in the former.

2.3 Alloys

2.3.1 Introduction

Alloys are essential to the modern way of life because of their strength and ductility. Even a pure metal is weaker than its alloys. Indeed, the most important way of strengthening a metal is to prepare one of its alloys. The other ways include work hardening and heat treatment. Alloying, which is the purposeful addition of one metal to another, is also the most important way of improving the corrosion-resistant properties of pure metals.

Alloys always contain a primary (or base) metal that forms the bulk together with purposefully added metallic and probably nonmetallic alloying components. The properties of an alloy, such as strength, hardness, and creep resistance, depend on the elements present together with the combinations of work hardening and heat treatment to which it has been subjected. In practice, it is very difficult to obtain absolutely pure metals (see Section 2.2), but even small amounts of impurities can change the properties of metals. For example, 0.50% carbon added to pure iron may change the soft metal of melting point 1800 K to a much harder steel that melts over a range of temperatures. The exact control of the composition of alloys is a very skilled craft, and metallurgists would by no means regard 0.50% carbon as unusually difficult to control. It should be emphasized right at the start that steel is by no means a typical alloy because the alloying element (carbon in this case) fits into the holes between the atoms of the primary metal (iron). *Solid solutions*, in which the elements can occupy similar positions in the structure, are more typical.

The development of our civilization is closely linked with the improvements that have been made in alloy technology over the ages. In ancient times, the early artisans used native metals and became expert in shaping copper, silver, and gold, which were used mainly for decorative purposes. Around 4000 BCE these metals became rather scarce, but a really major advance was made when it was realized that these and other metals could be obtained by smelting. The dictionary definition of smelting is that it is a process in which a metal is extracted from its ores by heating. To be more precise, it usually involves the reduction of the oxide by carbon.

The continued demand for improved alloys, mainly for war purposes, meant that the artisans of the Near East were forced to do their work well. All of the metals that could be obtained by carbon reduction had been prepared, and all of the useful alloy compositions were available before the early Greeks. Almost in recognition of the technological experts who had preceded them, the Greeks had defined four "Ages of Man" before their own and three of these involved direct reference to metallurgy. The Ages were "Gold," "Silver," "Bronze," and "Heroic" – the first two refer to pure metals and the third to an alloy. Until the sixteenth century no new alloys were developed that were not known to the Greeks. The available alloys fulfilled most of the demands made on them until cast iron guns started fracturing with frightening rapidity.

The shortage of tin ores in part led directly to the Iron Age. The artisans undoubtedly preferred to work with bronzes, which are copper–tin alloys, than with iron, which was much more difficult to produce and the final quality much less predictable. Nevertheless, the demands of the soldiers and politicians spurred on the development of iron (steel) alloys because the ores were much more abundant than those of copper and tin.

Steel was not recognized as an alloy until 1774 CE because the diffusion of carbon into the iron was undetected. Although excellent techniques were developed for the production and shaping of steel, the iron often contained weakening impurities. When iron was needed to withstand high stresses, very large clad pieces were used in the hope that the metal would be sufficiently strong. Even so, many cannons exploded with fatal consequences.

New alloys are often developed when existing ones cannot meet the demands made on them. Titanium alloys are being developed to meet the new requirements of the aircraft and rocket industries.

For alloys of a particular primary metal, there are two general classes of alloys: wrought and cast. *Cast metals* are those that flow well when molten and as such are poured into molds of the desired shape. They are often weaker

(more brittle) than wrought metals but have the advantage that very complex shapes can be formed, thus keeping costs to a minimum. *Wrought alloys* are those that either have very high melting points or, more usually, do not flow well when molten. They are unsuitable for casting and are shaped when solid by one or a combination of techniques including hot or cold rolling, drawing, forging, extruding, pressing, or spinning. Wrought alloys have the advantage that they are stronger than cast metals, although the shaping and finishing costs are much higher.

Many objects are made from gray cast iron, which is a general-purpose casting alloy. The term "gray" was used advisedly because there is another form called *white cast iron*, which contains very hard particles or iron carbide. White cast iron is similarly hard and durable but is very brittle. *Gray cast iron*, on the other hand, contains free graphite and is suitable for piston rings in which the graphite acts as a lubricant. Figure 2.23 illustrates such a ring that is made from a standard fine gray cast iron. The black areas are graphite, and the region with parallel lines is pearlite. Iron phosphide forms the areas with the cellular structure, and manganese sulfide the gray area with an angular inclusion. In contrast, Figure 2.24 illustrates the microstructure of a Victorian wrought iron railing. The black fibers are of slag, and the equiaxed grains are of iron, which acts as a soft matrix. The grain is virtually free of carbon and other alloying elements such as phosphorus, silicon, and manganese. The fibers are formed from slag particles by a hot rolling process in which lengths of wrought iron are welded together. Any cracks that attempt to pass through the body of the wrought iron are diverted along the fibers, which thus serve to toughen the metal. Wrought iron can therefore be used for load carrying as in chains and crane hooks.



Figure 2.23 Gray cast iron (×750).

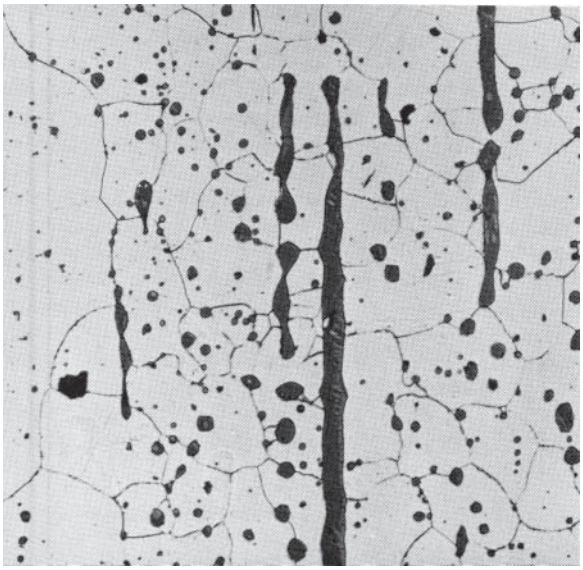


Figure 2.24 Wrought iron (×150).

Alloy steels, particularly those containing nickel and chromium, often have the added advantage that they are more corrosion resistant than cast iron.

The most popular corrosion-resistant alloy is stainless steel, the production of which has risen by over 10% per annum, which is comparable with the growth of aluminum.

The metallurgical problem with pure metals is that they are far too soft for mechanical components. They need to have a higher resistance to plastic deformation without becoming unduly brittle. To achieve this it is necessary to make heterogeneous structures so that the movement of dislocations is limited. The heterogeneity may be achieved by a combination of alloying and heat treatment called *precipitation hardening*, which is discussed later. Small finely dispersed groups of foreign atoms are deliberately introduced into the structure because the dislocations lock themselves onto them.

The search is always for new materials with the correct combinations of elastic stiffness and resistance to fracture and to plastic deformation. An entirely new approach to the problem has been adopted by the inclusion of strong but brittle fibers into a soft matrix such as a resin or a metal. Brittle substances need not be unduly fragile, for example, toffee is brittle but needs a hard blow to make it crack. Figure 2.25 illustrates a metal containing carbon fibers that has been fractured. Note the carbon fibers and the metal fracture independently and that there is no bonding between them. The combination of the two components is called a *composite*, which is lighter, stiffer, and stronger than the separate components. Moreover, composites are stronger than alloys, provided that the fibers are not scratched. Consequently, the matrix consists of a soft metal such as aluminum or copper.

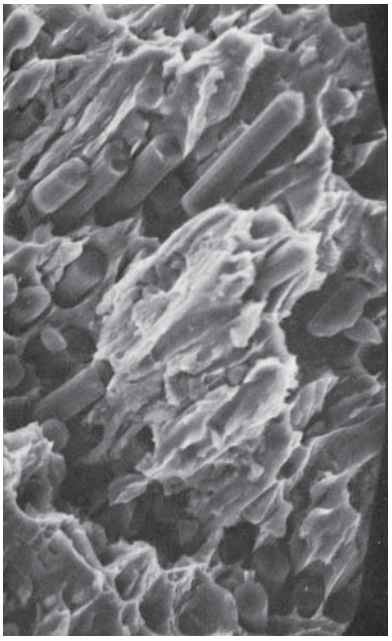


Figure 2.25 Fractured metal specimen containing carbon fibers (×100).

Composites are unique for two reasons. The first is the way in which the metal transmits the load to the *fiber*. The high-strength fibers do not elongate more than 1% or 2% of their original length, even when high stresses are applied – they have low ultimate strains. On the other hand, the metal has much higher strain, and yet in the composite there is a strong tendency for the difference in strains to be minimized.

The result is that there is a very much greater stress in the fiber. In fact, the stress in the metal is not significant at all and can be neglected when calculating properties such as the breaking strain. The second is the way that the two components render cracks formed at high stresses insignificant by a combination of mechanisms. The soft metal as usual may limit the spreading of cracks by plastic flow. The fibers do not fail in the one plane, and for cracks to spread in that plane, all of the fibers would have to be removed as they broke. The adhesion between the fibers and the matrix, which was referred to in Figure 2.25, is purposely designed to be low so that the crack is deflected along the weak interface and consequently is harmless.

One of the advantages of composites is their lightness, which offsets initially high production costs, particularly for the aircraft industry.

2.3.2 The Structure of Alloys

Alloys are formed when one element dissolves in another. In the alloy Monel, for example, copper is dissolved in the nickel. The alloy is said to be a solid solution of copper in nickel. Throughout the development of science, there seems to have been a great resistance to the idea that one solid can dissolve in another. Solid solutions were not accepted until the development of X-ray crystallography at the turn of the twentieth century.

The early Greek philosophers such as Democritus (fifth century BCE) and Lucretius (first century BCE) postulated that matter consisted of atoms but not all of them were of interest given the manner in which they were arranged. Moreover, their work was overshadowed by that of Aristotle, who believed that there were four elements – earth, air, fire, and water. His influence was such that it was not until the seventeenth century that people began to think once more in terms of atoms. It was Francis Bacon who drew attention to the Greek atomists, and as a result both Boyle and Newton were strongly influenced by them.

Later, Dalton's atomic theory did much harm to the development of the theory of the structure of alloys because it was primarily concerned with fixed ratios of atoms in molecules. Atoms, in effect, were rejected in favor of molecules. It was Berthollet who challenged the theory, as he realized that the concepts could not be applied to alloys. As a metallurgist who had worked on steel for a number of years, Berthollet observed that alloys need to have fixed compositions and that steel with as little as 1% of carbon was not a compound. Unfortunately, he did not produce a suitable alternative theory, and even he could not fully accept the concept of a solid solution. Dalton himself considered that steel consisted of carbon molecules (not atoms) dissolved in iron and allotropic changes always resulted from alterations in the arrangements of atoms within molecules rather than in the total distribution of atoms.

It is possible that physicists could have helped to solve the controversy between the chemist, Dalton, and the metallurgist, Berthollet. During the nineteenth century, however, the physicists were largely uninterested in structure. Even those who were passingly interested considered that molecules were completely randomly arranged even in crystals with pronounced symmetry. Not one single physicist attempted to build a model of a metal from an entirely disordered array of molecules. They turned a blind eye to the earlier work of Haüy, who had shown that a symmetrical crystal could be built up from a regular arrangement of smaller units. This is doubly surprising because the chemist Crum Brown has constructed a model of the correct structure of sodium chloride at the turn of the nineteenth century, 100 years before W.L. Braggs proved him to be right. The metallurgists qualitatively recognized that the structure of solid metals was identical to that of the molten metal prior to casting, and, at the turn of the twentieth century, X-ray crystallography confirmed the view that one solid metal can dissolve another just as in

the liquid phase. Essentially the atoms are arranged on regular fixed patterns such as the FCC system discussed in Section 2.1. Calculations subsequently made on the strength of alloys on the basis of this complete regularity showed that metals and alloys were often more than 1000 times weaker than theory predicted. It was the major drawback of the atomic theory. Metals are not entirely ordered, and the oversimplification of the structure introduced by crystallography made scientists blind to the idea of imperfections, although nowadays the low strength of metals and alloys is explained in terms of dislocations in an essentially ordered structure. The following is a summary of the results of X-ray crystallographic investigations.

In a *substitutional solid solution*, the solute (alloying) element replaces some of the atoms of the solvent (primary) metal. Consequently, there is only one type of crystal structure – that of the solvent. Examination with a microscope will not distinguish between the solute and solvent (Figure 2.26). The alloy is stronger, tougher, and harder than the separate elements. The atoms of the solvent are replaced randomly by those of the solute. Each set of atoms occupies equivalent sites, but one region contains more atoms of the solute than another. The replacement of the solvent atoms can result in some distortion of the structure, particularly when the atoms are of different size. In the case of the copper–nickel alloy, the atoms of nickel are smaller than those of copper. Consequently, when atoms of copper are replaced by those of nickel, the average distance is no longer that given by the minimum in the potential energy curve (Figure 2.6) when the structure becomes distorted (Figure 2.27). Note that the mean internuclear distances for pure copper and for pure nickel are twice their respective atomic radii.

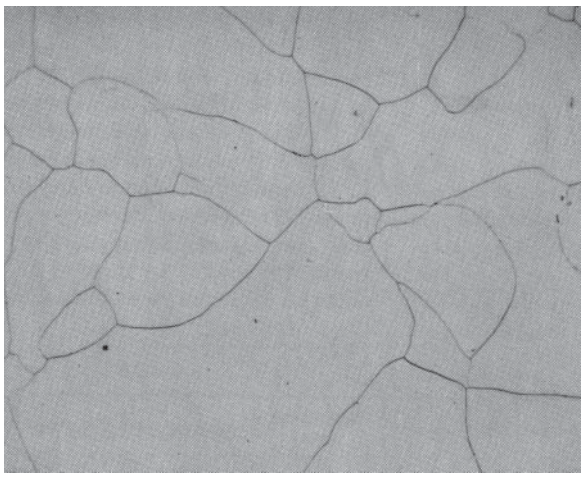


Figure 2.26 The solute and solvent are indistinguishable in a solid solution. A solution of silicon (3¼%) in iron (×500) – the specimen was polished electrolytically in chromic acid and acetic acid solution. Then it was etched in the same solution.

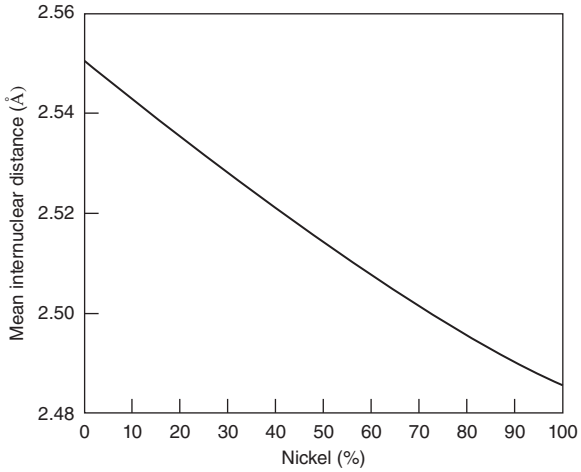


Figure 2.27 Decrease of mean interatomic distance as nickel is added to copper (the mean internuclear distances for pure copper and for pure nickel are twice their respective atomic radii).

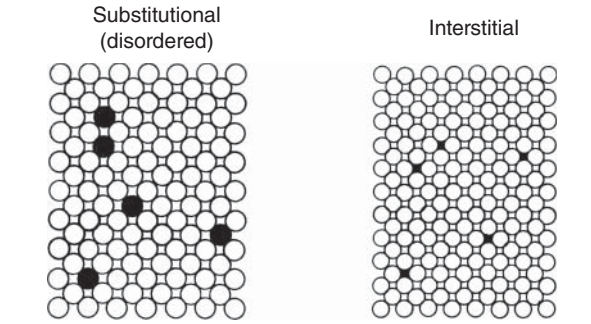


Figure 2.28 The two types of solid solution.

The extent to which two metals form substitutional solid solutions (Figure 2.28) depends on:

A. The size of atoms: Metals are only soluble over the entire range of concentrations when the atomic radii are within 15% of each other. Thus, nickel with a radius of 1.242 Å and copper with a radius of 1.275 Å form a continuous range of solid solutions. The radii of lead and antimony are outside the range, and they are "insoluble" in the solid state. The word "insoluble" must be used advisedly, because no two metals are completely so – although for our purposes lead and antimony will be taken to be mutually insoluble.

B. The crystal structure of the elements: The crystal structures must be the same. Both copper and nickel have the face-centered close-packed structure, but zinc has the hexagonal structure. Consequently, zinc has only a limited solubility in copper.

C. The chemical properties of the elements: The elements must be chemically and preferably in the same group

of the periodic table, for example, copper forms a continuous range of solid solutions with silver. In extreme cases when the elements have very different electronegativities, a compound is formed. Thus, iron (1.8) and carbon (2.5) may form the compound iron carbide.

Earlier in this section it was pointed out that steel is not a typical alloy. Steel belongs to an unusual class of alloys known as interstitial alloys because the carbon atoms are sufficiently small to fit into the holes (interstices) between the iron atoms. The carbon atoms do not replace those of iron. The whole complex history of steel is based on an *interstitial solid solution* of carbon in iron.

2.3.3 Ideal Equilibrium Diagrams

These may also be called phase or constitutional diagrams. Some *equilibrium diagrams* may be conveniently investigated by plotting cooling curves. The muffle furnace and the chromel–alumel thermocouple are suitable for the determination of these cooling curves. In addition, the solids so formed may be ground, polished, and studied under a microscope. The phases, such as a pure metal or a solid solution, can be directly related to the composition of the alloy and to the equilibrium diagram. The form of the diagram largely depends on whether the metals are insoluble, partially soluble, or completely soluble in the solid phase. Attention will be restricted to the binary systems, that is, those that contain only two metals.

The cooling curves provide a unique method of introducing equilibrium diagrams because the lines can usually be plotted directly from the results. In a number of cases, however, the exact temperature at which a solid solution starts to come out of the liquid phase is not clear. There are two main types of cooling curve: the normal and inverse-rate cooling curve. For example, a pure metal has a normal cooling curve of the type shown in Figure 2.29, but metallurgists prefer the alternative inverse-rate curve because it enables the freezing point to be determined more

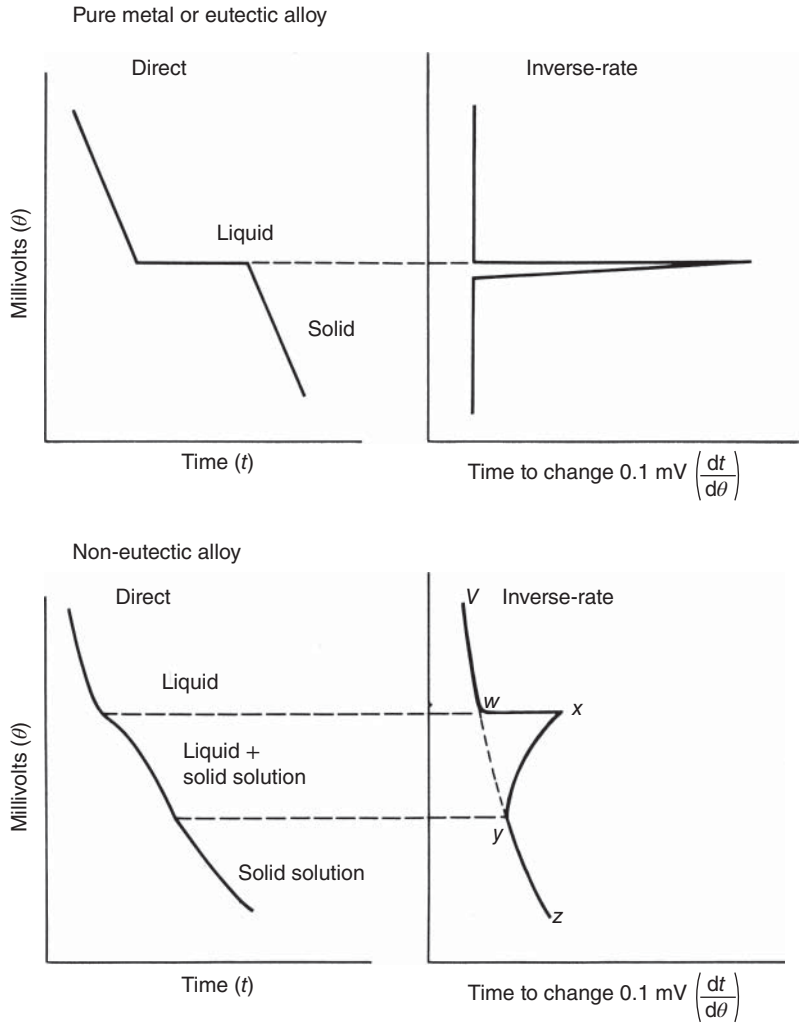


Figure 2.29 Idealized cooling curves for metals and alloys.

accurately. Instead of plotting temperature (millivolts) against time, the inverse-rate curve is drawn by plotting temperature against the reciprocal of the rate of cooling. If θ is the temperature and t the time, then $d\theta/dt$ is the rate of cooling and $dt/d\theta$ the reciprocal. The main reason why the inverse-rate method is more accurate than the normal one is because the reciprocal is large. Thus, when the rate of cooling tends to zero, the reciprocal tends to infinity.

A liquid pure metal cools at a constant rate until it reaches the melting point at which the temperature remains until all the metal has solidified. The solid then cools to room temperature. At the melting point the rate of cooling is zero, and the reciprocal has an infinite value. The melting point is taken to correspond to the temperature at which the gradient starts to change. Whereas metals have very definite freezing points, alloys usually freeze over a range of temperatures. The only case where an alloy has a definite melting point is when it has the eutectic composition. The lower pair of diagrams in Figure 2.29 illustrates the cooling curves for a non-eutectic alloy from which a solid solution separates out on cooling. (In Figure 2.31 this corresponds to the line *lms*.) The liquid alloy cools steadily until the solid solution starts to separate when the slope of the normal curve changes. The variation of the gradient in the inverse-rate curve is more noticeable at this stage. The point at which solidification starts is relatively easy to fix, but that at which solidification finishes is much more difficult to define. The technique is to continue the original slope of the curve *vw* until it joins *yz*, which has the same gradient as *vw*. The point *y* is taken as that at which solidification has finished. If the rate of cooling is too fast to allow equilibrium to be maintained throughout, then *y* may be fixed at too low a temperature.

Three cases of ideal behavior are now discussed in order that the principles may be clearly understood. In each case the metals are completely miscible in the liquid phase.

2.3.3.1 The Solid Phase Only Contains Pure Metals

The equilibrium diagram for this binary system is given in Figure 2.30. Metals A and B have different melting points, with that of B having the higher value. Nevertheless, when B is added to A, the melting point of A is lowered and not raised. The lowering of the melting point is almost proportional to the amount of B added. Similarly, when A is added to B, the melting point of B is lowered. *AC* and *BC* are called the liquidus lines and represent the compositions of liquid in equilibrium with solid A and solid B, respectively. The compositions of the liquid may be read off along the axis *FG*. Above the liquidus lines there is only liquid, and below them and between *DCE*, the liquid is in equilibrium with solid A or solid B. The line *BCD* is called the solidus line, below which only pure solid A and pure solid B can exist. The point *C* represents the lowest temperature at which liquid can be in equilibrium with either of the pure metals and was given the name *eutectic* by F. Guthrie in 1884. The word "eutectic" comes from the Greek word eutektos, which means "easily melting." The eutectic consists of an intimate mixture of pure A and pure B – in this case there is no eutectic compound. The eutectic is the alloy composition that melts at the lowest temperature, and frequently metallurgists work with alloys of eutectic composition because less heat needs to be supplied for melting prior to casting.

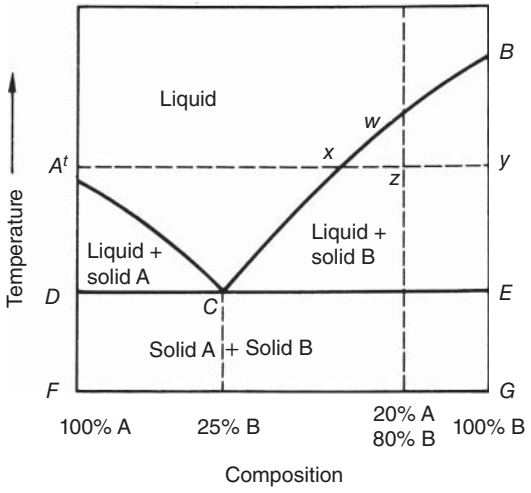
When an alloy of composition 80% B and 20% A is melted and then allowed to cool, the composition of the liquid remains unchanged until the liquidus line is reached at *w* and solid B crystallizes out. The liquid becomes richer in A as the alloy continues to cool, and the composition of the liquid can be read off along the line *BC*. At temperature *t* liquid of composition *x* is in equilibrium with pure B at *y*. The proportion of liquid and solid can be found using the *law of levers*:

$$\frac{\text{Weight of solid B}}{\text{Weight of liquid}} = \frac{zy}{xz} \tag{2.4}$$

The composition of the liquid continues to move down *BC* until it reaches *C* and then does not change further. That is, it does not start moving along *CA* since the alloy is richer in *B* than the eutectic. Similarly, the eutectic cannot contain more *B* than represented by *C*. The eutectic and pure B solidify, after which the solid continues to cool to room temperature.

The idealized inverse-rate cooling curves for this type of system illustrate how the liquidus and the solidus lines may be found experimentally. The first and fifth curves are those of pure metals, which may be used to calibrate the thermocouples. The fourth curve corresponds to the 20% A and 80% B alloy, which was discussed above. The top arrest point indicates the temperature at which pure B starts to solidify, and the lower point the temperature at which pure B and the eutectic freeze. The upper arrest point therefore gives one point (*w*) on the liquidus curve, and the lower point gives one reading for the temperature at which the solidus line *DCE* should be drawn. The second cooling curve is similar to the fourth and enables a point on the liquidus line *AC* to be fixed, together with a second reading for the solidus line.

The third curve is the cooling curve for an alloy of *eutectic composition*. This alloy freezes at one temperature like a pure metal and not over a range of temperatures. Normally the alloys freeze over a range of temperatures between the liquidus and solidus lines.



Ideal inverse-rate cooling curves for alloys in the above equilibrium diagram

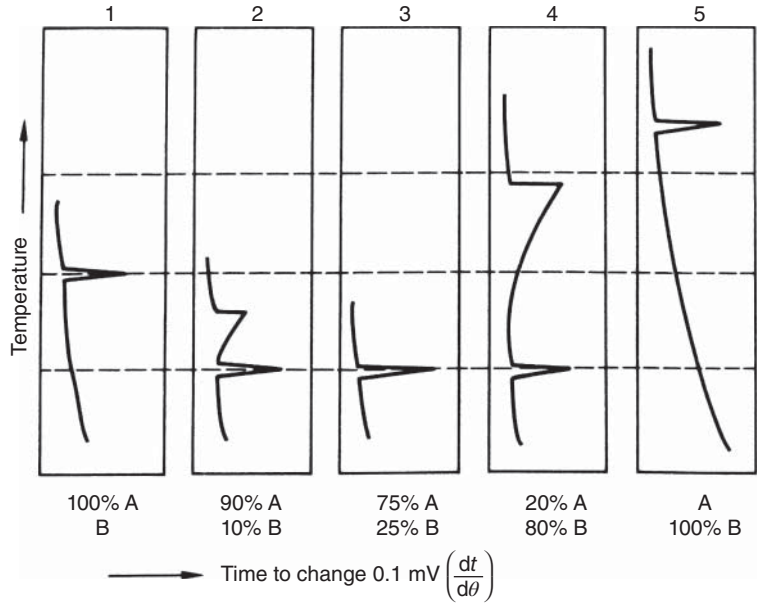


Figure 2.30 Equilibrium diagram for two metals that are completely miscible in the liquid phase, but the solid phase contains only pure metals. (The lead–antimony system is an example of this type.)

2.3.3.2 Two Metals Partially Miscible in the Solid State

It frequently happens that metals A and B can partially dissolve each other. The Greek letter α is given to the solution of B in A, and the letter β to a solution of A in B. The equilibrium diagram for this system is illustrated in Figure 2.31. The main difference between this and the last system is that *D* and *E* have been moved in to allow for the extra α and β phases but the principles are essentially the same as before. When the solubility of A in the β phase is small, *E* is close to the BB' axis, and when the solubility is higher, *E* is further away from BB'. The composition of A in the β phase is simply found by dropping a perpendicular onto the composition axis. The point *C* represents the eutectic. The liquid l_2 in the first idealized cooling curve has the eutectic composition and consequently has a sharp melting point, as before. There is only liquid above the liquidus lines *AC* and *BC* but only solid below the solidus line *DCE*. The curve *AD* represents the composition of solid α in equilibrium with liquid on *AC* at the same temperature. *BE* similarly represents the solubility of A in the β phase. Note that the solubility increases as the temperature falls until *E* is reached; thereafter the solubilities decrease along *DF* and *EG*. The lines *DF* and *EG* represent the compositions of solid α and solid β in equilibrium at a given temperature. The exact positions of these lines are very difficult to find, and they may very well be missed altogether in simple experiments because the heat changes are small and the rate

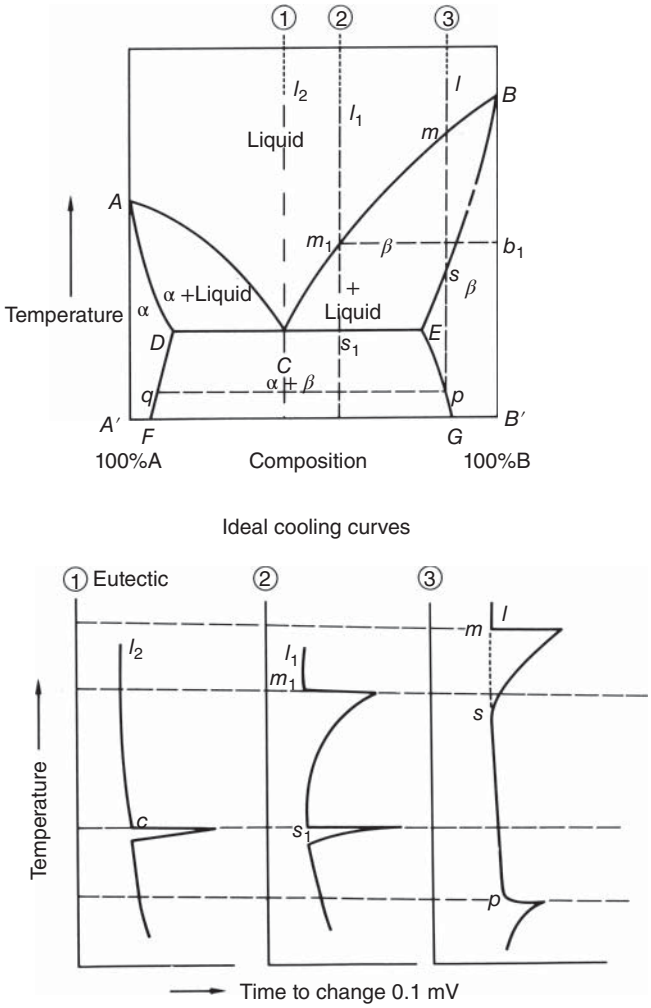


Figure 2.31 Equilibrium diagram for two metals completely soluble in the liquid phase but partially soluble in the solid phase. (The lead–tin, gold–nickel, bismuth–lead, cadmium–tin, and iron–chromium systems are examples of this type.)

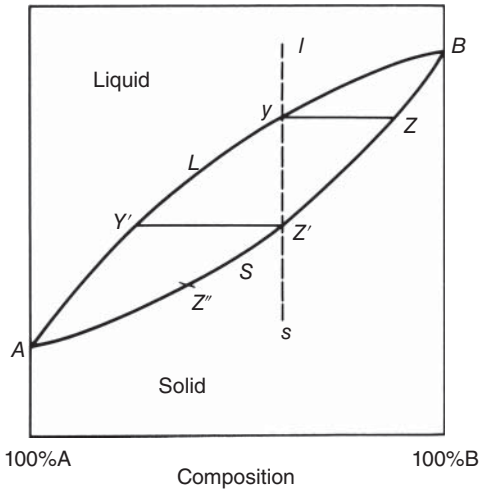
of change depends on the rate at which metal atoms diffuse in the solid state. The area *FDCEG* represents solid α in equilibrium with solid β. The area *ADC* represents solid α in equilibrium with liquid, and *BCE* solid β in equilibrium with liquid. The second idealized cooling curve represents that of liquid l_1, which is richer in β than the eutectic. Consequently, at m_1, the β phase starts to crystallize out, and the alloy is completely solidified at s_1 when the eutectic crystallizes out. The ratio of eutectic to β phase is given by

$$\frac{\text{Eutectic}}{\beta\text{-phase}} = \frac{s_1 \times \text{C}}{s_1 \times \text{E}} \tag{2.5}$$

The point s_1 is on the solidus line *DCE*, but the point s in the third idealized cooling curve is not at the same (solidus) temperature. Can you see why? Solidification of liquid *l*, which is richer in the β phase than *E*, starts at *m* and is completely finished at *s*, provided that the composition of the solid remains in equilibrium with the liquid. No eutectic is formed. The composition of the solid remains unaltered until the point *p* is reached. If the system is maintained at *p*, the solid solution represented by *q* is formed as α diffuses out of the β phase, and then, if the system cools very slowly, the compositions of the solid solutions move along *DF* and *EG*. In practice, the cooling is usually too quick to allow the slow change to *q* to occur, and a *metastable* solid solution of composition *p* may remain for a long time. The rate at which the metastable solid solution can revert to the stable one depends on diffusion phenomena.

2.3.3.3 Total Solid Solubility

When two metals form a continuous range of solid solutions, the melting point of one component is raised by alloying – in the previous examples it was always lowered. Only the solid phase exists, and, as before, there is only one liquid phase. The equilibrium diagram for such a system is given in Figure 2.32. The upper curve (*ALB*) is the liquidus and the lower the solidus. When a liquid of composition l cools, the solid that starts to come out at *y* is of composition *z* and not z'. Consequently, the solid is always richer in the component of higher melting point. As cooling proceeds, the composition of the liquid moves down the curve *BLA*, while



The copper–nickel; cobalt–nickel; gold–silver; gold–platinum systems are examples of this type

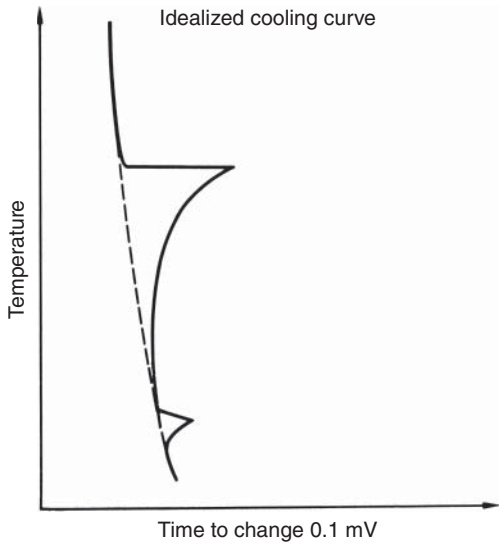


Figure 2.32 Equilibrium diagram for two metals that are completely miscible in both the solid and liquid phases.

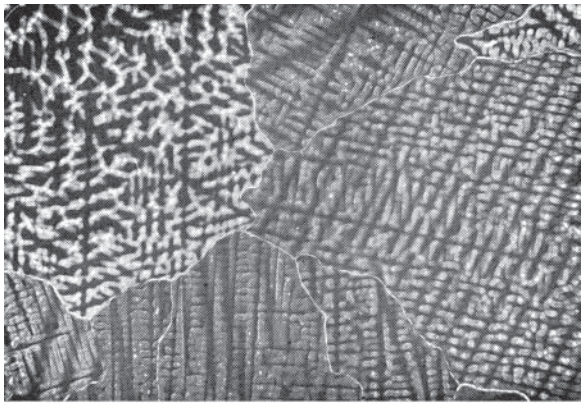
that of the liquid moves down *BSA*. The compositions continue to change until the solid reaches z', and at this point the liquid has nearly disappeared, provided that the system has remained in equilibrium. When a solid of composition s is heated slowly to z', the liquid that first melts has the composition y'. Consequently, the curve *BSA* is sometimes called the melting point curve, whereas *BLA* is the freezing point curve. The composition of the solid moves along *ASB* to z as more liquid is formed, and finally at z itself nearly all of the solid has melted. If heating is carried out too fast, there will be some solid remaining.

Readers who wish to study further may care to read about the peritectic and ternary equilibrium diagrams in more advanced texts.

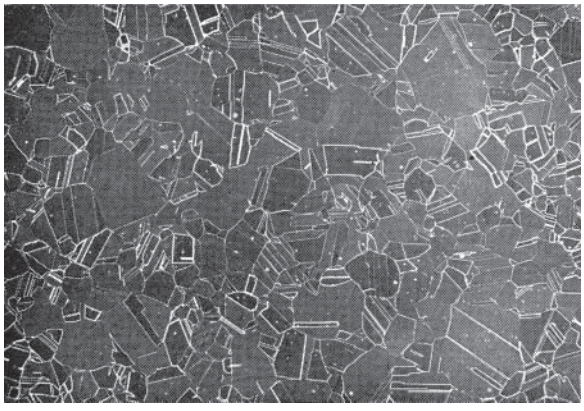
2.3.4 Nonequilibrium Conditions (Coring)

The liquid l (in Figure 2.32) that cools to the liquidus curve is in equilibrium at y with solid nuclei of composition z. Under equilibrium conditions the composition of the solid gradually changes from z to z' as more atoms of the components A and B diffuse from the liquid. If the rate of cooling is too high, the composition of the solid cannot steadily adjust along the solidus line *BSA* as there is insufficient time for the atoms to diffuse. Under these nonequilibrium conditions, the liquid y' is in contact with the solid, the composition of which varies from z to z'. The average composition of the solid phase is between z and z'. The composition of the last part of the solid phase to form is not between these points but is at z'', resulting in an average composition of z. The composition of the solid phase is inhomogeneous and is said to be *cored*.

The cored dendrites in a 70/30 copper–zinc alloy (one of the many brasses) have been revealed in Figure 2.33 by a fairly deep etch with alcoholic iron(III) chloride. The regions that appear dark are comparatively rich in zinc, and



(a)



(b)

Figure 2.33 (a) Coring in a sand cast 70/30 copper–zinc brass (×100). (b) The same alloy – cold-worked and annealed (×200).

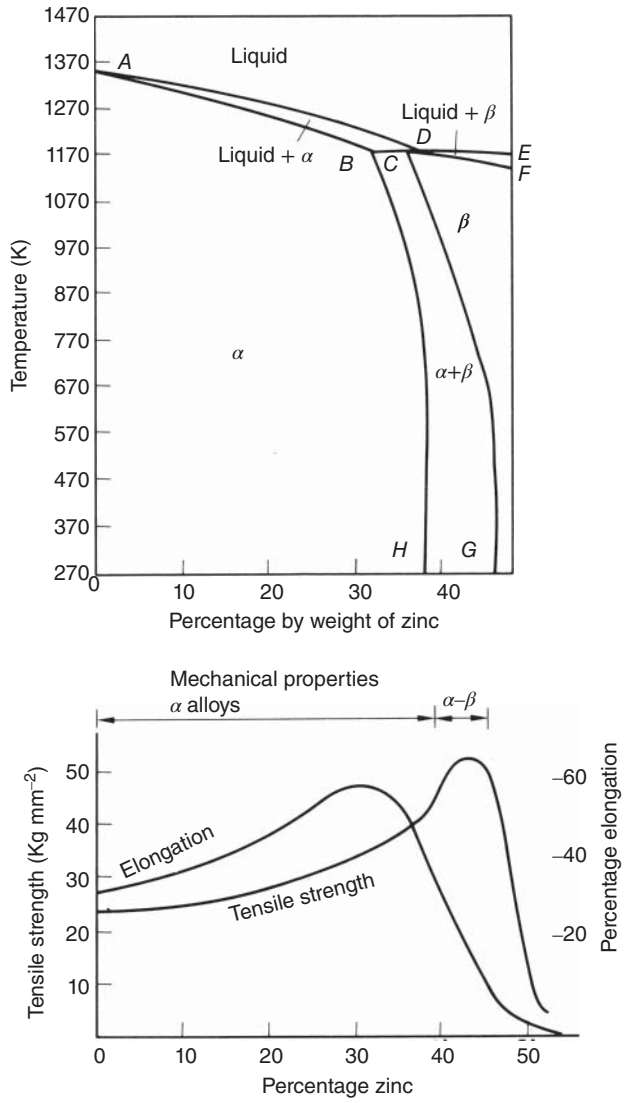


Figure 2.34 Copper–zinc equilibrium diagram (simplified).

those richer in copper appear white. When the alloy cools, copper-rich dendrites are first formed (see Figure 2.34), leaving the liquid richer in zinc. As the dendrite grows under nonequilibrium conditions, it becomes progressively poorer in copper, so that copper atoms are unable to diffuse through the solid sufficiently quickly to give a homogeneous composition.

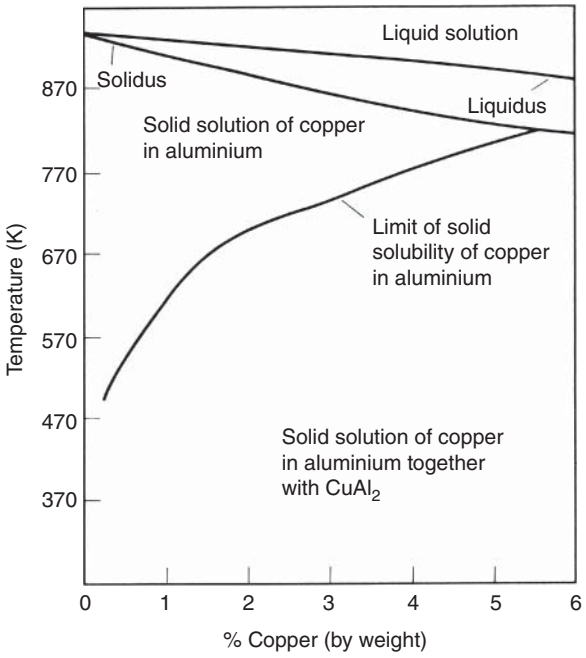
Dendritic growth continues until restricted by neighboring grains, and finally solidification of the zinc-rich liquid occurs between the grains. The inhomogeneity may be removed by *annealing*. This allows the atoms to diffuse at elevated temperatures through the solid in order to reduce the local concentration differences of the components. The rate of diffusion is not only increased by raising the temperature because previous cold working helps recrystallization to occur during annealing. Figure 2.33b illustrates the same 70/30 brass as Figure 2.33a with the exception that the alloy has now been cold-worked and annealed. The resulting alloy is homogeneous, and etching with alcoholic iron(III) chloride does not produce light and dark patches as before. The distributions of copper and zinc are uniform throughout the solid. Incidentally, this last plate illustrates annealing twins that are formed by FCC metals as copper and iron in their alloys. These annealing twins are characterized by flat surfaces about which twinning occurs, and they indicate that the alloy has been deformed prior to annealing.

2.3.5 Age-Hardening Alloys

Age-hardening alloys were discovered accidentally when Dr. Alfred Wilm of the Dürener Metallwerke was studying the influence of small additions of metals such as copper and magnesium on aluminum. The initial strength of one alloy containing 3% copper and 0.5% magnesium was discouraging but was surprisingly much improved when the alloy was retested one week later. A series of experiments involving the sequence heating, quenching, testing, storing, and retesting was carried out on this alloy, which was found to age-harden in about four days. Since Wilm's experiments the age-hardening alloys have been greatly used, for example, in the aircraft industry, although the mechanism of *age hardening* was not well understood. Investigators were severely handicapped because the instruments such as the metallurgical microscope were far too sensitive to detect small changes in the microstructure.

When an aluminum bronze containing 4% by weight of copper is heated to 800 K, the resulting solid solution is homogeneous. As the alloy cools (Figure 2.35), the solubility of the copper in the aluminum decreases, and below 500 K the aluminum holds less than 0.5% copper. The copper atoms diffuse through the aluminum to form copper-rich areas that eventually form the intermetallic compound $CuAl_2$. This separates out as a second phase. When the solid solution is quenched to room temperature, the copper does not have sufficient time to diffuse through the solid, and the second phase of $CuAl_2$ does not have time to form. The quenched solid solution is, therefore, metastable, and as it ages, the compound $CuAl_2$ slowly separates out.

The second phase serves to lock the dislocations in age-hardening alloys that are consequently both strengthened and hardened. Precipitation hardening is used wherever one (or more) component forms a solid solution at an elevated temperature but segregates at a lower one. It is widely used in industry because the alloy can be forged as a relatively soft solid solution and then the shaped article may be naturally or artificially hardened. Age-hardening alloys are not solely based on aluminum, for example, age-hardened alloys of copper with a few



Solid solubility of copper at different temperatures

Temperature (K)	Solubility (%)
821	5.65
773	4.15
723	2.60
673	1.50
523	0.50

Figure 2.35 A section of the aluminum–copper equilibrium diagram.

percent of beryllium and cobalt are used to give strong, hard tools. Age-hardened nickel-based alloys are often used for high temperature work.

2.4 Iron and Steel

2.4.1 Introduction

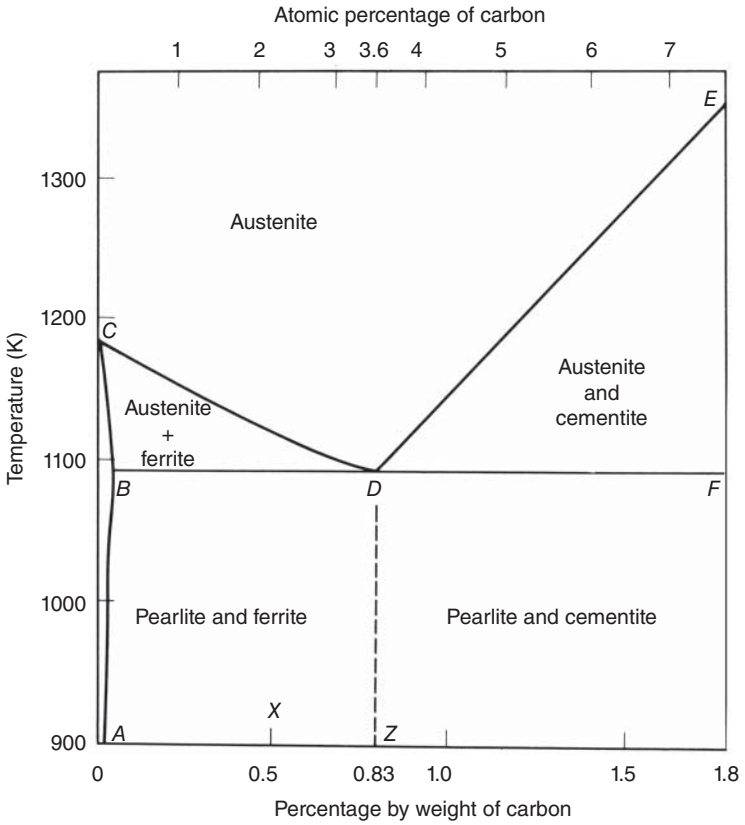
Steel deserves a special mention because it is not a typical alloy and it has made the all-important contribution to the development of our civilization.

The Iron Age did not develop until after the Bronze Age, partly because the iron blooms that the ancient artisans originally obtained were uselessly spongy and porous. Iron appeared to be nonmetallic. Moreover, it took many centuries to develop the techniques of working the useless bloom into a functional steel. It was not until 600 BCE that the techniques of smelting, carburizing, quenching, and tempering were well established. Even the art of smelting the ore was more difficult to discover and perfect for iron than for copper. Copper melted (m.p. 1356 K) under the conditions that its ore was smelted (1300–1400 K) and was easily collected in pans. The iron, however, did not so melt (m.p. 1808 K) at the temperature required (1400 K). All the iron quickly solidified as the ore was reduced and was lost in the slag and cinders. Iron was formed, incidentally, in primitive pottery kilns and never in campfires. The secrets of smelting iron ores were probably discovered in Asia Minor early in the third millennium BCE. The metal was always very expensive, for example, the best prehistoric furnaces could consume 90 kg (200 lb) of charcoal in 8–10 hours to produce about 20 kg of iron. It was the Chalybes of Armenia who discovered how to convert the useless iron into steel by repeatedly hammering the red hot bloom, followed by quenching. When the Hittites, to whom the Chalybes were subject, were overthrown (c. 1200 BCE), knowledge of the techniques quickly spread, seized upon by the foreign artisans who had previously tried without success to work the iron blooms. The Iron Age had begun.

The advent of iron as a metal suitable for weapons meant that an even greater emphasis was placed on the artisans, the great skill and ingenuity of whom may be illustrated by the example of the Indian workers who made the steel for the Damascus swords. The confused ripply pattern of the sword consists of globular cementite in a soft matrix of *pearlite*. The *cementite* (iron carbide Fe_3C) appears as white streams, and the pearlite as the dark background. The overall carbon content varies from 0.5% to 1.7%. The streaks and eddies of cementite pass through the inside of the sword in parallel bands, which are mainly produced by the very careful crystallization of the carbon-rich cast iron. The long, weak crystalline needles are broken down by forging the steel at cherry heat. There is an interesting story associated with the parallel lines that run from edge to edge. These are collectively known as Jacob's ladder and were taken to mean that the sword that had the pattern was of supreme strength. Of course, it is now well known that the pattern is produced by simply making file marks prior to the final forging.

2.4.2 The Iron–Carbon Equilibrium System

The full equilibrium diagram is complex, but a simplified portion, which is suitable for interpreting the properties of steels, is drawn in Figure 2.36. Pure iron exhibits *allotropy*, and it is iron with its BCC structure, which is the stable form at room temperature. The γ allotrope, which has the FCC structure, is formed between 1179 and 1674 K. The allotropic transition is accompanied by a decrease in volume because the atoms are more closely packed in FCC γ iron than in the BCC α form. Consequently, when an iron



Ferrite is a solid solution of carbon in BCC (α) iron
Austenite is a solid solution of carbon in FCC (γ) iron
Cementite is iron carbide (Fe_3C)
B is at 0.025% C by weight, 996 K
C is at 1179 K
D is at 0.83% C by weight (and 3.6 at.%)
CBA is ferrite

Figure 2.36 Simplified portion of iron–carbon equilibrium diagram.

wire is heated, there is normal linear expansion until 1179 K is reached, when the wire contracts. Metals do not always expand on heating. As the iron cools through this transition point, it expands and glows, while the metal loses the difference in energy between the two forms (Chipman 1972).

Iron is uselessly soft without carbon. Indeed it has been stated that the whole development of mankind has rested on the differential solubility of carbon in the two forms of iron. Surprisingly, carbon is more soluble in FCC γ iron, even though the iron atoms are more closely packed than in the BCC α form. The apparent anomaly is resolved when it is realized that the interstitial holes between the iron atoms are larger in the FCC γ form, although there are fewer of them. In this form each carbon atom in the largest set of holes is surrounded by six equidistant iron atoms at 1.82 Å. In α iron each carbon is surrounded by four atoms at 1.61 Å. Since the atomic radius of carbon is 0.77 Å and that of iron is 1.24 Å, the carbon atoms are squeezed in both structures but particularly in the BCC α form. The lines *CB* and *BA* represent the limits of the solid solubility of carbon in the α iron, and the line *DE* represents the corresponding values for γ iron. Both *CB* and *BA* are further to the left than *DE* because the solid solubility of carbon in the α form is lower.

Ferrite and austenite are the names given to the solid solutions of carbon in the BCC α and FCC γ forms, respectively. In the area *CDC*, austenite is in equilibrium with ferrite. Consequently, when steels with compositions of up to 0.83% carbon cool under equilibrium conditions to *CD* ferrite of one composition along, *CB* separates out as a second phase. In order for this separation to take place, carbon has to diffuse from ferrite forming regions into the austenite, the composition of which falls along *CD* until *D* is reached as the alloy cools. At the eutectoid point *D*, austenite, ferrite, and cementite all exist in equilibrium, but as the alloy continues to cool, austenite is converted into ferrite and cementite. Carbon-rich areas are formed by diffusion, and these ultimately become cementite nuclei as carbon moves from the neighboring ferrite forming regions. Both components grow in layers to form the lamellar structure of pearlite as the carbon continues to be

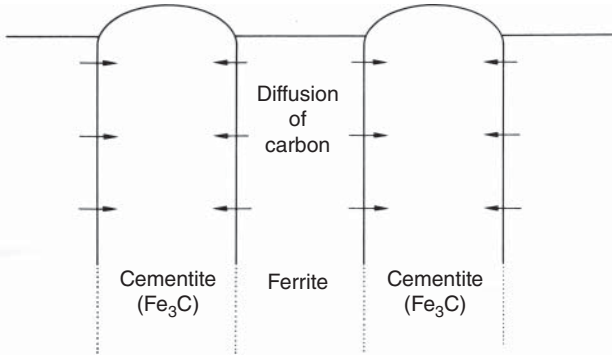


Figure 2.37 Pearlite forms as carbon diffuses from the ferrite into adjacent layers of cementite.

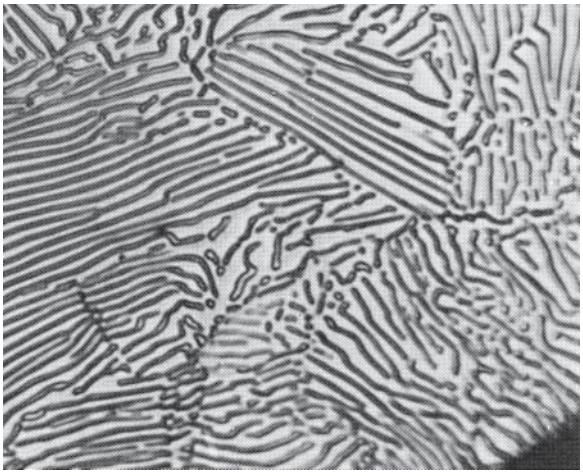


Figure 2.38 Pearlite (×225).

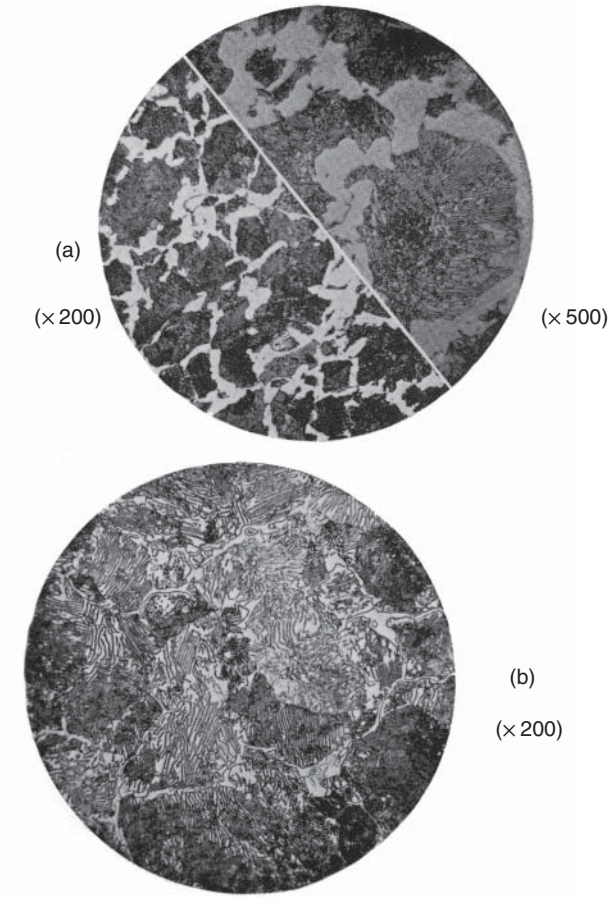


Figure 2.39 Microstructure of some annealed carbon steels. (a) 0.5–0.6% C steel and (b) 0.95–1.25% C steel.

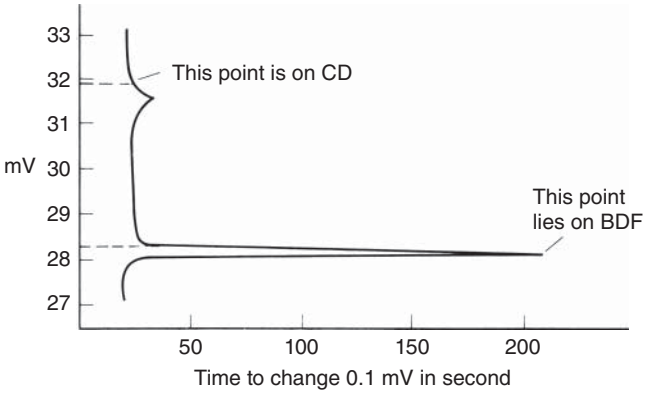


Figure 2.40 Cooling curve for a steel with 0.25–0.3% of carbon.

rejected by the ferrite (Figure 2.37). The resulting alloy is called pearlite (Figure 2.38) because it resembles mother of pearl after it has been etched. The final microstructure (Figure 2.39) contains areas of ferrite and cementite.

Within the area *DEF*, austenite is in equilibrium with cementite, which is the hard, covalent iron carbide (Fe_3C). The HB number of cementite is more than 600 compared with a value of 80 for ferrite. When an alloy with 0.8–1.8% by weight of carbon cools to *DE*, cementite separates out and the composition of the austenite moves down *ED* to *D* as carbon diffuses to the cementite forming regions. The austenite then forms pearlite at *D*. The final microstructure (Figure 2.39) of the annealed alloy contains cementite and pearlite.

The position of the line *CD* can be determined from a set of cooling curves for alloys whose compositions fall to the left of *D*. The steel is heated sufficiently to ensure that it is entirely present as the austenitic solid solution and then allowed to cool slowly in a furnace. The millivolts generated by a chromel–alumel thermocouple are plotted against the time taken to change 0.1 mV as shown in Figure 2.40 for an alloy of nominal composition 0.25–0.3% by weight of carbon. The rate of cooling must be slow, but even so the temperatures corresponding to the line *CD* are lower in simple experiments than in standard diagrams because very low rates of cooling are needed to ensure that equilibrium is completely established. The line *BDF* is theoretically constant for all carbon steels,

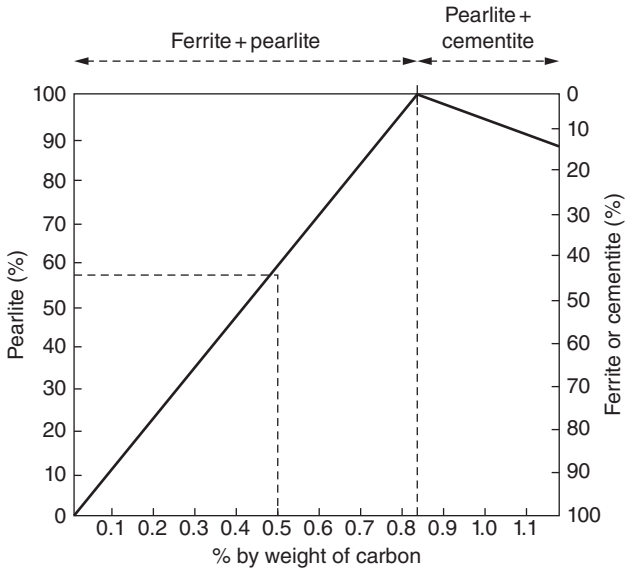


Figure 2.41 Pearlite in annealed carbon steels (at room temperature).

but in simple experiments its position is very difficult to fix, particularly when the percentage of pearlite ultimately formed is low. The solid solubility lines *BA* and *DE* cannot be established from cooling curves that nevertheless allow the area *CBD* to be established.

The proportions of the components in the microstructure may be calculated in the normal way using the law of levers.

Thus, for a 0.5% carbon steel, the percentage of pearlite is

$$\frac{AX \times 100}{AZ} = 58\% \qquad (2.6)$$

(the remainder being ferrite; see Figures 2.36 and 2.41).

Alternatively, the carbon content of annealed steels may be estimated from an experimental determination of the amount of pearlite in the microstructure.

The equilibrium diagram does not indicate the form in which the components appear in the microstructure. Ferrite, for example, forms at the grain boundaries when the steel is very slowly cooled. With higher rates of cooling, however, the ferrite is not formed at the grain boundaries but within the grains of pearlite. Moreover, in some cases, a Widmanstätten pattern, which weakens the steel, is formed as the ferrite separates out along the octahedral planes and occasionally the ferrite forms around the inclusions. Equally, cementite may separate out as hard brittle laminates as in pearlite or, alternatively, as plates in cast steels (Massalski et al. 1990).

Ductility is sacrificed for strength as the percentage of carbon increases to that in pure pearlite. The tensile strength (TS, Figure 2.42) increases from about 33 kg mm^{-2} with pure iron to 90 kg mm^{-2} with pearlite, which is the strongest carbon steel. The elongation, which

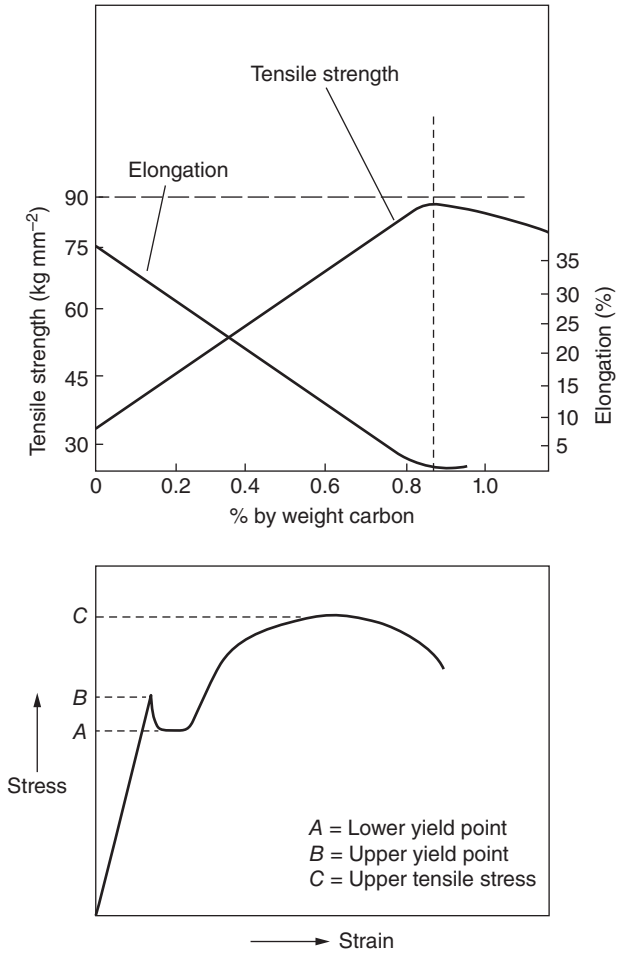


Figure 2.42 Mechanical properties of annealed carbon steels (see Figures 2.47 and 2.49).

is a measure of the ductility, correspondingly decreases from 35% to under 5%. Ferrite is ductile but weak in relation to pearlite because the interstitial carbon atoms inhibit neither the slip of atomic planes nor the movement of dislocations. Pearlite is much stronger and yet less ductile. Layers of cementite limit both slip and the movement of dislocations. Nevertheless, the intimate mixture of cementite and ferrite in pearlite results in a strong alloy because the hard but brittle cementite initially takes the load that is transmitted to the ductile ferrite matrix. The strengthening effect introduced by increasing the proportion of a hard dispersed phase is called *dispersion hardening*. Cementite is brittle because the strong covalent bonds are directional, being localized between the iron and the carbon atoms. Consequently, the bonds are difficult to break and once broken cannot easily reform. In ferrite, however, the nondirectional bonds can be broken and reformed with facility as the atomic planes slip over one another.

Low carbon steels have characteristic stress–strain curves because ferrite yields at the onset of plastic

deformation (Figure 2.42). The curves, therefore, have an upper yield point at the end of the elastic region followed by a lower point, but these merge in higher carbon steels as the proportion of ferrite decreases.

Mechanical properties depend on the grain structure, even in annealed steels. For example, the hardness of a carbon (0.75%) steel that has been heated to the austenitic region depends on the rate of cooling. When the alloy is cooled in the oven, the hardness is 200 (Figure 2.43), but when air-cooled (normalized), it is 250. The grains of the two alloys are illustrated in Figure 2.44. The size of those in the oven-cooled sample is greater than those in the air-cooled one because they have had longer to grow. The Widmanstätten pattern, which was mentioned earlier, also influences the mechanical properties. The strong pearlitic regions become separated by weak crystallites of cementite or ferrite in which cracks may be readily propagated. This and other sources of weakness may be removed by suitable heat treatment.

2.4.3 Heat Treatment

So far discussion of carbon steels has been limited to equilibrium conditions, but these are rarely used or desired in practice. When the austenitic solid solution is quenched, the hardness of the resulting alloy is greater than would be expected from the appropriate combination of ferrite and cementite. When steel with nominally 0.5–0.6% by weight of carbon, for example, is quenched, the hardness is more than 600 (Figure 2.43) compared with less than 200 for the annealed alloy. The disparity is due to a third phase called martensite, which is not present in the equilibrium diagram because it is formed under strictly nonequilibrium conditions. Martensite is a metastable interstitial solid solution of carbon in BCC iron, but, unlike ferrite, the cubic unit cell of the iron is distorted. In addition to being very hard, martensite makes steels rigid because the distorted cubes fit imperfectly into the regular cubic structures of ferrite. Martensite limits slip and movement of dislocations. It is usual to choose a combination of quenching and heat treatment to give a large proportion of martensite. The conditions are, however, largely dominated by the equilibrium diagram. Quenching a 0.5% carbon steel in water gives steels the hardness that depends on the temperature from which the steel is quenched. Quenching from 1000 K gives an alloy of roughly the same hardness as the annealed alloys (200), but from 1000 to 1050 K the hardness of the resulting alloy increases from 200 to 600. Quenching from above 1050 K results in a hardness of over 600 (Figure 2.43). Reference to the equilibrium diagram (Figure 2.36) shows that the temperatures approximate to points on *BD* and *CD*. The alloy must be present only as the austenitic solid solution prior to quenching of it is to have the maximum hardness. If the quenching temperature falls

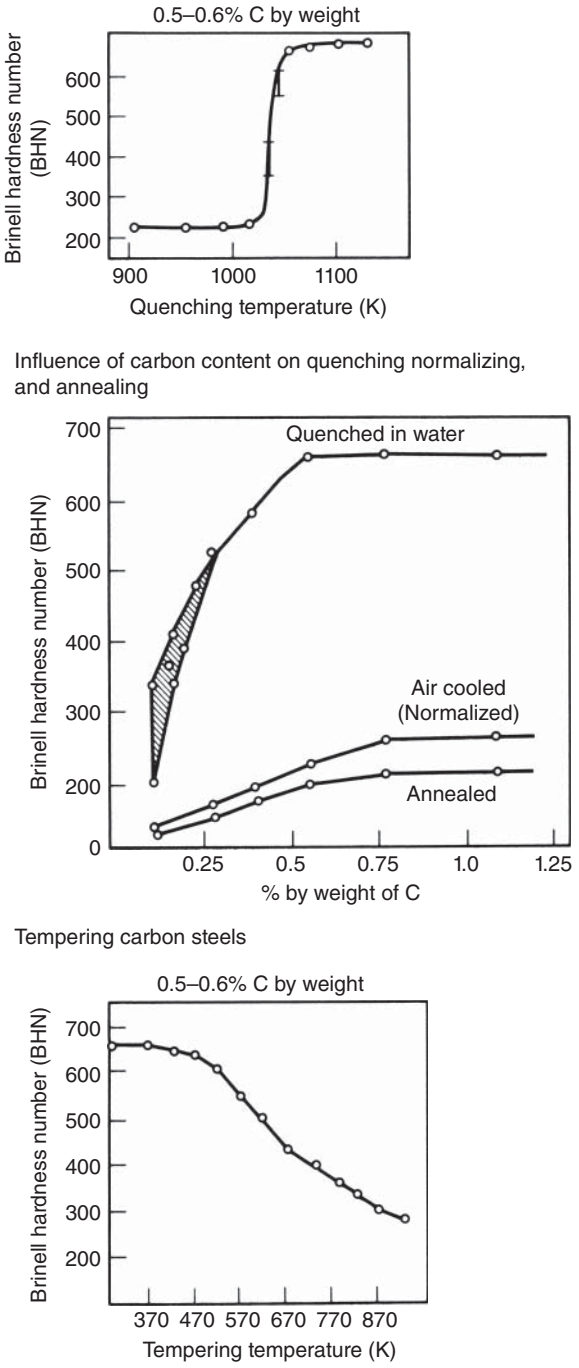


Figure 2.43 Quenching and tempering carbon steels.

in the area *CBD*, the increase is only intermediate and there is no hardening if the temperature is below that of *BD*.

The carbon content has a considerable influence on the resulting hardness of the quenched alloy because the low carbon steels do not quench harden as readily as the higher carbon ones. Even the higher carbon steels do not harden when quenched in oil. The reason is that the rate of cooling is greater when the steel is quenched in water and the carbon has less chance to diffuse out of the austenite to form

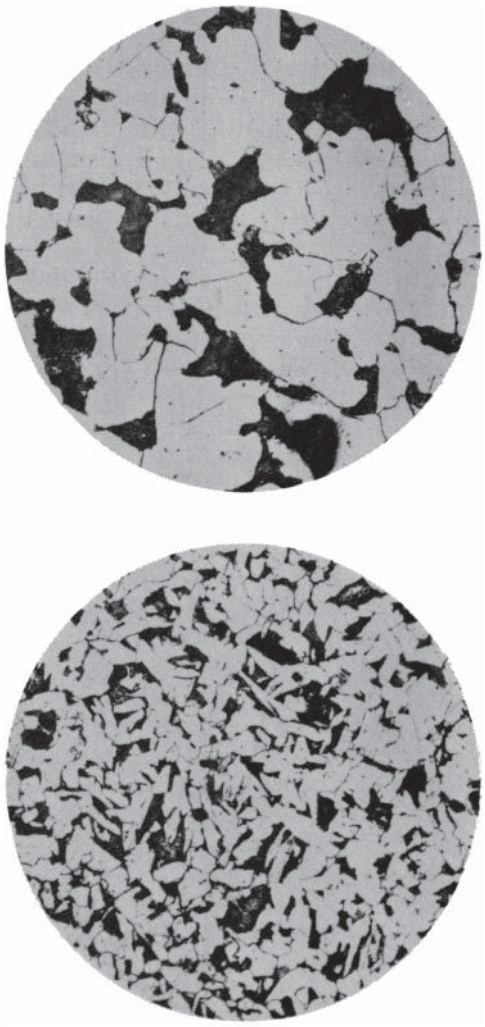


Figure 2.44 Heat treatment of carbon steels (0.07–0.15% C). (a) Annealed (×250) – cooled in the oven. (b) Air-cooled (×250) – normalized. (Coakham and Evans 1970a).

cementite nuclei. Consequently, more martensite is formed. Each carbon steel has a critical rate of quenching, which must be exceeded if the maximum amount of martensite is to form. With carbon steels this roughly corresponds to the rate of cooling produced when the steel is quenched in water but that with oils is too low.

Martensite is not formed by the usual process of nucleation and grain growth because the rate of cooling is so high that diffusion is severely limited. The rate of growth is, however, extremely rapid, and unlike diffusion-controlled growth, it is independent of temperature. Once a martensite nucleus has been formed, the whole needle-shaped crystal may grow in 10^{-7} seconds even down to 4 K as a shear wave moves through the alloy. Martensite (Figure 2.45) appears as acicular (needlelike) crystals, the size of which increases as the quenching temperature is raised.



Figure 2.45 Needlelike crystals of martensite (×1500).

Martensite, however, renders the quenched steel exceedingly brittle, which may be removed by tempering. This is a process in which the quench-hardened alloy is heated to a convenient temperature that must be below *BDF* (Figure 2.36). The carbon diffuses out of the martensite, which forms ferrite, to initiate the nucleation of cementite. The amount of ferrite and cementite formed mainly depends on the tempering temperature. Tempering colors are often used as a guide to the tempering range, which largely governs the properties of the resulting article. These colors arise from the interference patterns in thin oxide films produced during tempering. A temper in the range of 420–500 K strengthens the steel with little loss of hardness because the internal stresses are relieved and any residual austenite is decomposed. The steel is softened but toughened in the range of 470–720 K because both austenite and martensite decompose to ferrite in which minute particles of ferrite are dispersed. Between 720 and 970 K, the cementite particles reduce their surface area by coalescing or spheroidizing, particularly in the higher temperatures. The steel is rendered softer and more ductile, being sufficiently tough for use in axles and crankshafts.

Tempered steels are therefore softer but stronger than the quenched steel, provided that at least some of the hard martensite has been converted to ferrite and cementite. The degree of softening is greater at the higher temperatures because it is controlled by the rate of diffusion of carbon. Consequently, there is little softening up to 470 K because the carbon atoms are largely localized. Between 470 and 870 K (Figure 2.43), the carbon atoms become progressively more mobile, and cementite itself diffuses, particularly at the higher temperatures.

2.4.4 Graphitization

Cast irons, although common, are in fact quite complex alloys. The iron–carbon phase diagram exhibits a eutectic reaction at 1420 K and 4.3 wt% C (see Figure 2.46). One

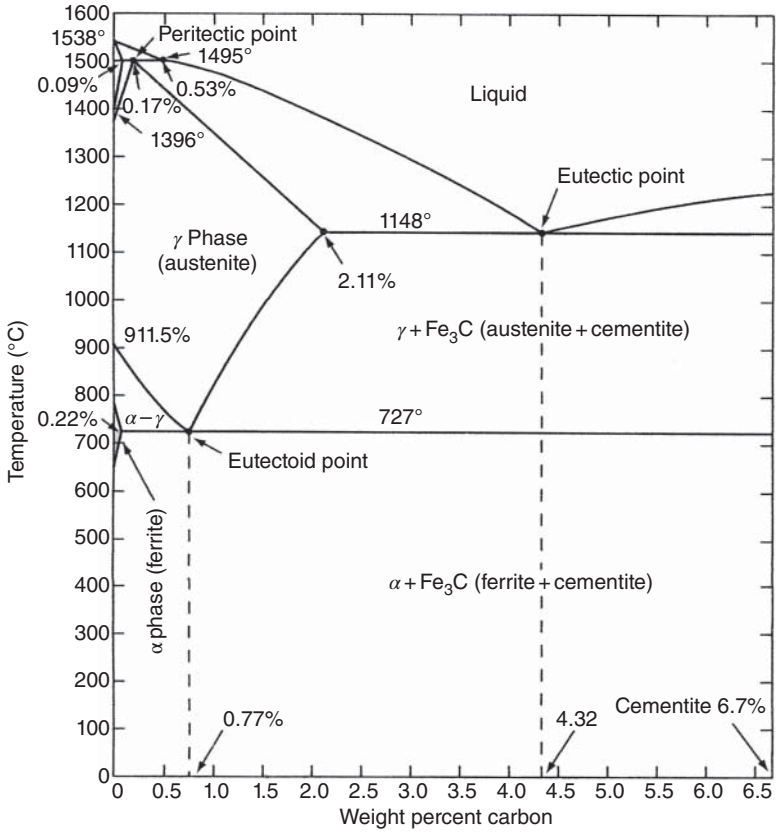


Figure 2.46 The iron–iron carbide metastable phase diagram. Source: Reprinted with permission of ASM International.

product of this eutectic reaction is always austenite; however, depending on the cooling rate and the composition of the alloy, the other product may be cementite or graphite. The graphite may be used in the form of flakes, which are all interconnected (although they appear separate on a metallographic section), or spheroids, which are all separate. The resulting alloys are known as white, gray, and spheroidal graphite cast irons, respectively. During subsequent cooling the austenite may transform to ferrite, pearlite, or martensite, or it may, in the case of high nickel irons, be retained at room temperature.

Graphite is more noble than any of the other phases in cast iron and is a very good cathode material; highly effective *galvanic cells* therefore exist between the graphite and the surrounding, less noble matrix. In gray cast irons, the matrix therefore corrodes preferentially, leaving behind a network of interconnected graphite flakes that is very porous and weak. The attack is often not readily apparent on superficial inspection. White cast irons are not susceptible to *graphitization* since they contain no graphite; spheroidal graphite cast irons are also not susceptible to graphitization, since although they contain graphite it is in the form of discrete spheroids that have a limited effect, instead of the interconnected graphite flakes in gray cast iron. Thus, not only the existence but also the distribution of a cathodic phase is important.

2.4.5 Alloy Steels for High Temperature Service

Section 2.4 has been largely devoted to carbon steels, but it must be emphasized that small additions of alloying metals (e.g. Mo, V, Nb, Ti, Al) may greatly influence the properties of the steel. The changes largely arise owing to the formation of new solid solutions or new phases. The result often is that the equilibrium diagram is modified. Thus 3% of nickel lowers the line *BDF* in Figure 2.19 by 30 K, whereas 12% of chromium changes the carbon content of pearlite to 0.33% as compared with 8.3% in ordinary carbon steels. Alternatively, the new alloying metal may form a new carbide akin to cementite. Addition of 1% of chromium to the 0.95–1.25% carbon steel enables the resulting alloy steel to be hardened (to 600 BMH) by oil quenching because the critical cooling rate is sufficiently lowered (Coakham and Evans 1970a,b).

Alloy steels are usually tougher than the carbon steels. A steel chisel containing 0.38–0.42% of carbon, 3.5% of nickel, and a maximum of 0.6% of manganese is sufficiently tough to be driven through 6 cm of mild steel without any damage to its cutting edge.

Alloy steels (Honeycombe 1982) are among the most versatile, widely used, and complex structural materials. Density-corrected strengths of steels are competitive with

nickel-based superalloys at lower temperatures and at much lower cost. However, at higher temperatures their strengths fall off below those of the superalloys.

Alloy steels are strengthened by a combination of solid solution strengthening by interstitial elements such as carbon and nitrogen, substitutional solid solutions either in the α phase or in the γ phase, precipitation hardening from carbides of Nb and V, grain size control, and processing-induced texture of grains such as by rolling. Different alloying elements stabilize different phases. The degree of solid solution strengthening by substitution is controlled by expanding (with the addition of C, N, Cu, and Zn), contracting (with the addition of Ta, Nb, and Zr), opening (with the addition of Ni, Mn, Co, Ru, Rh, Pd, Pt, etc.), or closing (with the addition of Si, Al, Be, and P) the γ phase field of Figure 2.46, which is an extended version of the diagram drawn in Figure 2.36.

The austenite phase in Figure 2.46 can dissolve as much as 2.11 wt% (∼10 at.%) carbon in a solid solution. If austenite is quenched very fast to a relatively low temperature in the vicinity of room temperature, instead of changing to ferrite and cementite as the phase diagram in Figure 2.46 shows, it transforms into a phase called martensite supersaturated with carbon.

The high carbon content distorts the crystal structure to body-centered tetragonal (BCT). The unique feature of this transformation is that it does not involve diffusion of atoms. Instead, the phase forms by shear or local displacive transformation at rates close to the velocity of sound in the alloy. The maximum temperature below which martensitic transformation occurs is known as the martensite start temperature, M_s. The martensite grains, with plate- or needlelike morphology, are hard and brittle. The presence of martensite in steels increases strength significantly, as already discussed in Section 2.4.3.

To achieve the optimum combination of microstructure, strength, and ductility of alloy steels, heat treatment regimens have been developed using *time–temperature–transformation* (TTT) diagrams (Honeycombe 1982).

Some of the commercially available alloy steels include the following:

High-strength low-alloy steel (HSLA): These low carbon (0.03–0.15 wt% C) steels derive their strengthening from a solid solution (C, Mn, Si), precipitation hardening (carbides of Nb, Ti, and V), grain size control stabilized by grain boundary carbides, and processing-induced texture. Typical TS and failure strains are 700 MPa (100 ksi) and 12–18%, respectively.

Bainite steel: Such steels consist of a fine dispersion of cementite in a strained ferrite matrix. Bainite steels are produced by suitable isothermal heat treatment of low carbon (<0.05 wt% C) steels using a TTT diagram between 250 °C (482 °F) and 550 °C (1022 °F). Typical TS and failure strains are 600–1200 MPa (86–171 ksi) and 15–20%, respectively.

Dual-phase steels: These low carbon (0.1–0.2 wt% C) steels contain two phases, a fine dispersion of 10–20 vol.% martensite in a matrix of ferrite. The microstructure and phase contents are achieved by heating the $\alpha + \gamma$ phase field (Figure 2.46) to form 10–20 vol.% austenite followed by rapid quenching to convert to martensite. These steels have moderate to high TS with high ductility.

Transformation-induced plasticity steels (TRIP): In these steels, austenite (γ phase) is retained at room temperature by fast quenching followed by mechanical deformation during processing. During use or testing under load, the austenite phase transforms to martensite, providing the strengthening mechanism. TSs in the range of 600–1300 MPa (86–171 ksi) and failure strains of 25–40% are not uncommon.

The temperature capability of steels in HTC applications is controlled by strength as well as environmental resistance and is generally limited to 650 °C (1200 °F). This temperature capability can be improved by applying a high temperature coating to the substrate alloy steel.

2.5 Deformation and Recrystallization

2.5.1 Stress and Strain

This is the study of metals when subjected to stresses, which may be tensile, compressive, shear, or torsional. In this section, tensile stresses on bulk samples are emphasized together with the accompanying shear stresses on the constituent atomic planes. The general theme that was established in Section 2.1 is continued in that the mechanical properties are always closely related to the imperfections that are present in the essentially perfect structures (Dieter 1986).

The elongation produced when a metal is subjected to a tensile (pulling) force is a function of the shape as well as the applied force. In order to compare the tensile properties of metals, force is replaced by *stress* and elongation by *strain*:

$$\sigma(\text{stress}) = \frac{\text{Force}}{\text{Cross-sectional area}} \tag{2.7}$$

$$\varepsilon(\text{strain}) = \frac{\text{Change in length}}{\text{Original length}} \tag{2.8}$$

Strain has no dimensions, as it is a ratio; the units of stress are newtons per square meters or pascals ($1\ \text{Nm}^{-2} = 1\ \text{Pa}$).

When a metal is subjected to a steadily increasing tensile stress, the strain varies as shown in Figure 2.47

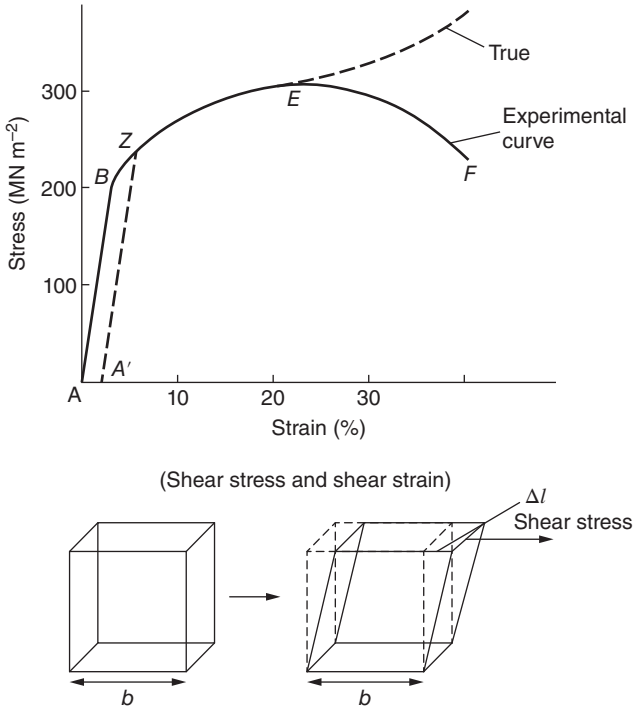


Figure 2.47 Tensile stress–strain curves.

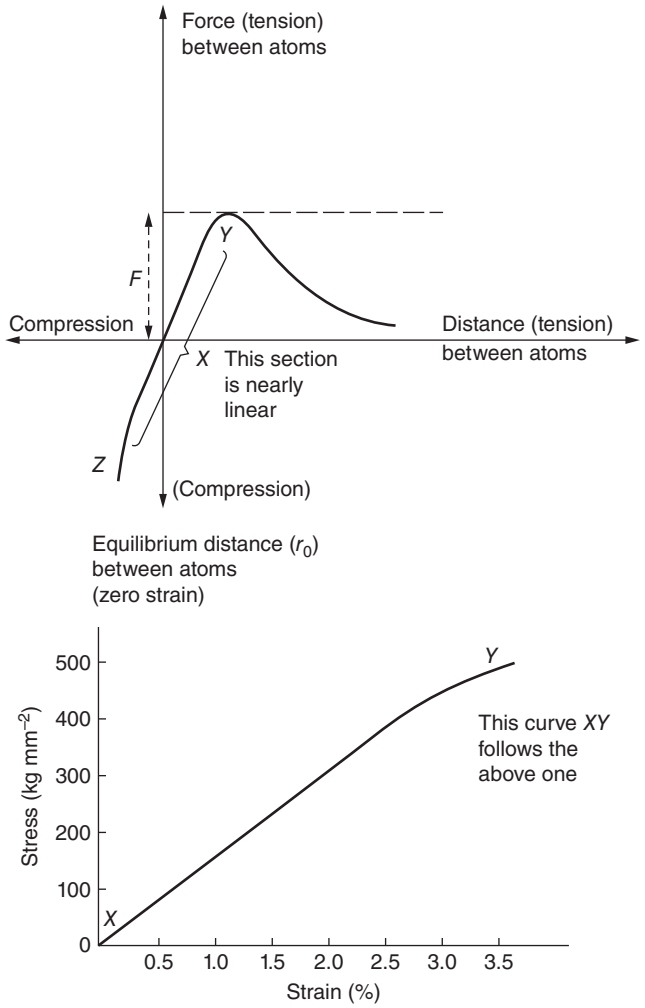


Figure 2.48 Forces between atoms and the elastic deformation of a very strong silicon whisker.

in which the figures are for a 70/30 copper–zinc brass. The curve is broadly divisible into two regions, namely, the elastic region *AB* and the plastic region *BF*, and the sample fractures at *F*. In the elastic region, once the stress is removed, the sample returns to its original dimensions, but in the plastic region it is permanently (plastically) deformed. The ill-defined stress *B* at the elastic limit is called the *yield stress* and denotes the point at which *plastic deformation* starts to dominate over *elastic deformation*. On the basis of the perfect structure of metals, B should occur in the region of 3.5% strain, but in practice it is often at about 0.2%.

In the elastic region, *Hooke's law* applies, that is, for small stresses. The deformation, which is measured by strain, is proportional to stress, and the proportionality constant is called *Young's modulus*, where

$$Y(\text{Young's modulus}) = \frac{\text{Tensile (compressional) stress}}{\text{Strain}} \tag{2.9}$$

This modulus of elasticity is closely related to (Figures 2.6 and 2.48) the slope of the force–distance curve at the equilibrium separation of r_o because the bonds themselves behave elastically for small strains. The proportionality between tensile stress and strain in the elastic region arises because the relevant portion of the force–distance curve is linear. Compressional stress and strain are proportional for the same reason. Since with normal polycrystalline metals the yield stress does not usually occur above 0.2% strain, the curved portion at *Y*, which is approximately at 3.5% strain, is not usually seen. However some strong single crystals (whiskers) are capable of elastic strain of this order. Elastic deformation of these very strong crystals indicates that the stress–strain curve (Figure 2.48) does indeed follow the force–distance one.

The slope of the curve at the equilibrium distance (zero applied stress) is unique for a particular metal, and consequently Young's modulus is a fundamental and characteristic property. Values over a large range, for example, lead has Young's modulus of 16 GN m^{-2}, whereas tungsten has a value of 390 GN m^{-2}. Moreover, the modulus is a measure of the strength, hardness, and stiffness of the metal so that lead is weaker, softer, and more pliable than tungsten.

Whereas Young's modulus is primarily a measure of resistance to elastic deformation, yield stress indicates the resistance to plastic deformation. The steel (Figure 2.49) with a yield stress of 300 MN m^{-2} is stronger than brasses

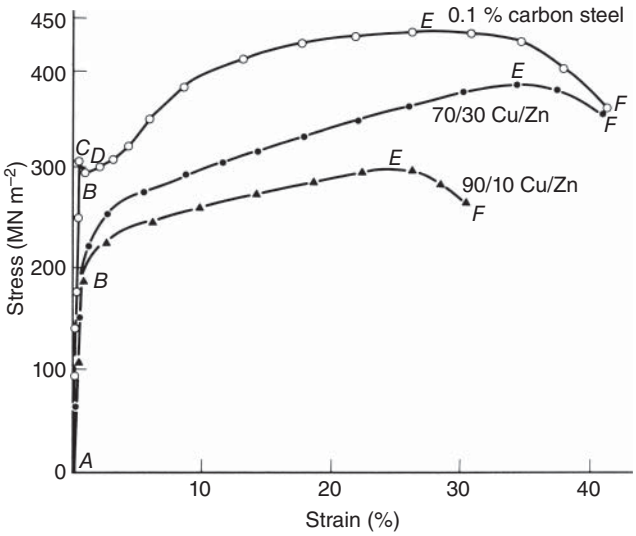


Figure 2.49 Stress–strain curves for typical alloys.

Table 2.3 Young's moduli

Element	Structure	Young's moduli
Lead	HCP	16
Magnesium	HCP	45
Cadmium	HCP	50
Zinc	HCP	90
Aluminum	FCC	71
Silver	FCC	79
Gold	FCC	80
Palladium	FCC	113
Copper	FCC	123
Platinum	FCC	168
Nickel	FCC	200
Iron	BCC	210
Tungsten	BCC	390

with a value of 200 MN m^{-2}. In addition, hardness, which is directly proportional to Young's modulus, may be a measure of strength, and it is quite common to consider hardness in conjunction with strength. Although in the age-hardened alloys discussed in Section 2.3, Young's modulus is not increased significantly. It must be realized that the values of Young's moduli quoted in Table 2.3 are really average values since metals are anisotropic. In each grain of a cubic metal, the modulus in the ⟨111⟩ direction is different to that in the ⟨100⟩ direction. In copper (FCC) the ratio

$$\frac{\text{Young's modulus along the}\langle 111\rangle\text{direction}}{\text{Young's modulus along the}\langle 100\rangle\text{direction}}$$

is 2.8 compared with a value of 1.2 for aluminum (FCC), which is much more isotropic. Nevertheless, since metals are polycrystalline and the separate grains are randomly oriented, the average values have significant meaning. Moreover, at a given temperature, the modulus of any polycrystalline metal is constant, being independent of the microstructure. Consequently, the modulus for each steel is the same whether the steel has been annealed, quenched, cold-worked, or treated in any other way.

When a horizontal shear is applied (Figure 2.47) to the upper surface of a rectangular block fixed at its base, the resulting deformation is measured as the shear strain ($\Delta l/b$ radian). The corresponding elastic *shear modulus* that has the dimensions of shear stress is given by

$$G(\text{shear modulus}) = \frac{\text{Shear stress}}{\text{Shear strain}} \qquad (2.10)$$

The importance of the concept of shear lies in the fact that a tensile stress acting on the bulk sample produces a shear stress across the planes of atoms. The magnitude of the shear stress depends on the orientation of the planes to the applied stress and is a maximum when the planes are at 45° to the direction along which the tensile stress is applied (tensile axis) and is zero for planes perpendicular or parallel to the tensile stress. If the angle is greater than 45°, the layers tend to be pulled apart, and when smaller the effectiveness of the strength is reduced because it acts over a larger area. Shear between planes of atoms is responsible for plastic deformation.

After the yield stress B, a given increase in tensile stress produces a bigger change in strain because plastic deformation is superimposed on the elastic deformation. A sample at Z contracts to A' "when the stress is removed and the permanent deformation is measured by the strain along AA'." At E, which is the *upper tensile stress* (UTS), the applied stress noticeably starts to decrease as the sample forms a neck, which is usually a region of a narrower cross section.

It should be emphasized that the UTS is calculated by dividing the stress at B by the cross-sectional area at E although there is a small but definite necking before this point:

$$\sigma(UTS) = \frac{\text{Maximum load}}{\text{Original cross-sectional area}} \qquad (2.11)$$

The UTS is another measure of strength. Thus, the 0.1% carbon steel (Figure 2.49) with a value of 450 MN m^{-2} is stronger than the 70/30 copper–zinc brass (390 MN m^{-2}) and the 90/10 brass (280 MN m^{-2}).

The percentage strain at the point of fracture F is one measure of the *ductility* of the sample. Thus the 0.1% carbon steel (40%) and the 70/30 brass (39%) are more ductile than the 90/10 brass (30%). The percentage strain is defined as

$$\%\text{EL(Percentage strain)} = \frac{\text{Increase of length} \times 100}{\text{Original length}} \qquad (2.12)$$

Although the applied stress steadily decreases after E as the sample continues to neck, the true stress increases because the further accelerated reduction in cross-sectional area is reduced. Once yielding has first occurred, the stress required to continue plastic deformation increases with strain. This is known as *work hardening*.

Another mechanical property that may be important to consider is *hardness*, which is a measure of a material's resistance to localized plastic deformation (e.g. a small dent or a scratch). The hardness is directly related to the strength because the metal yields plastically when a hardened steel ball is compressed into the surface under constant load for a few seconds. If, for example, a circular steel ball is used, the resulting Brinell Hardness (HB) is given by

$$\text{HB} = \frac{\text{Load}}{\text{Contact area between ball and metal}} = P \Big/ \frac{\pi D}{2}(D - \sqrt{D^2 - d^2}) \tag{2.13}$$

where P is the load in kg, D is the ball diameter (mm), and d is the maximum internal diameter of the impression measured between graticules on a microscope. A qualitative and somewhat arbitrary hardness indexing scheme was devised, termed the *Mohs scale*, which ranged from 1 on the soft end for talc to 10 for diamond. For steel alloys, the TS and Brinell hardness (HB) (which are indicators of a metal's resistance to plastic deformation) are related according to

$$\begin{aligned} \text{TS(MPa)} &= 3.45 \times \text{HB} \\ \text{TS(psi)} &= 500 \times \text{HB} \end{aligned} \tag{2.14}$$

Note that 145 psi = 1 MPa, where psi means pounds force per square inch.

2.5.2 Slip Mechanisms

Whereas elastic deformation is homogeneous and involves only a small reversible displacement of the atoms, plastic deformation is inhomogeneous and may involve large irreversible displacements. Elastic deformation may be interpreted in terms of the perfect structures, while plastic deformation is related to the movement of dislocations.

Plastic deformation usually takes place by a mechanism called *slip* (Figure 2.50) in which whole planes of atoms move over one another. Slip is governed by three major rules:

1. Slip occurs along the most close-packed set of planes.
2. The direction of slip is that along which the atoms are most closely packed.
3. For a given set of systems (close-packed planes and directions), the slip occurs on that system where the shear stress is a maximum that falls at 45° to the applied tensile stress.

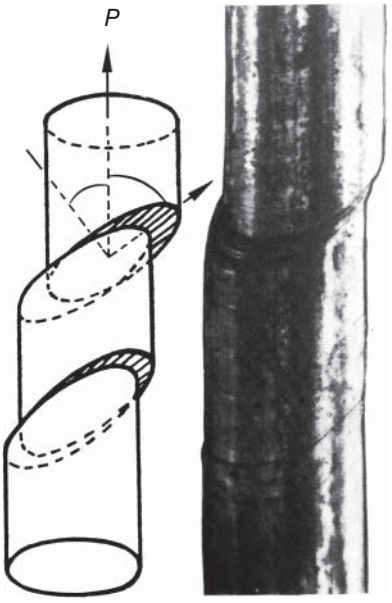
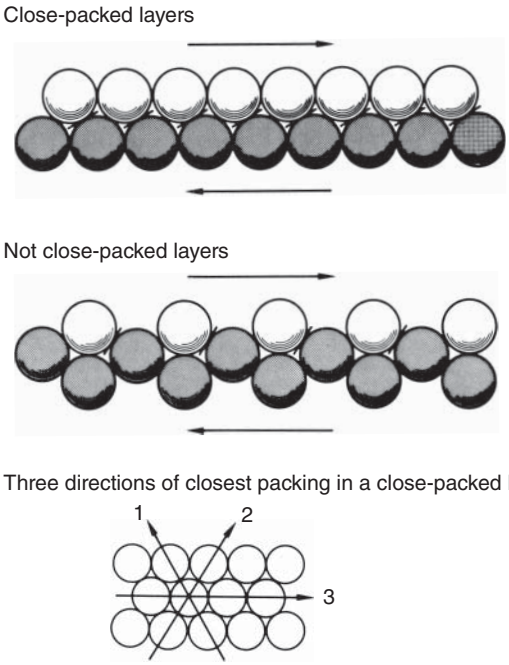


Figure 2.50 Slip (×20) (Hume-Rothery et al. 1969).

Slip always tends to occur along the set of planes that requires the least stress to move one plane over another. In Section 2.1 (see Figure 2.4), it was shown that the spacing between adjacent close-packed planes was greater than that between all other planes, and, consequently, the force between them is the least. Figure 2.51 represents two sets of planes, the upper one of which is close-packed. The shear stress needed to move the layers over one another is related to the tangent that is less for the close-packed layers, which consequently slip preferentially.

There are three directions of closest packing in each fully close-packed layer, and easy slip can place along any of these. The number of slip systems is calculated by multiplying the number of sets of close-packed planes by three. Thus, for the FCC structure in which there are four such sets, there are twelve slip systems. In the HCP structure with one set, there are three systems. In FCC metals there is a greater probability of finding a slip system at 45° to the applied stress than in HCP metals. In BCC structures there are no truly close-packed sets of planes, and slip is often seen as wavy lines because the ⟨111⟩ close-packed direction has roughly the same density of atoms in four different sets of non-close-packed planes.

Slip is best studied with single crystals because the process takes place without the interference of neighboring grains. The yield stress required to initiate slip is least for the system at 45° to the applied stress. Slip is confined to the region between the disks (Figure 2.50), and consequently slip is inhomogeneous. The considerable amount of strain that occurs when a single crystal is stressed arises from the tilting of the disks. Each individual disk retains its original shape, but a single crystal, which was of circular



Structure	Close-packed planes	Slip systems
FCC	4	12
HCP	1	3
BCC	0	0

Figure 2.51 Plastic flow – the shear stress needed to move one layer over another is proportional to the slope of the tangents.

cross section, is oval at the end of the deformation. The slip step is several thousand angstrom units high, which means that each one is composed of several thousand or so atoms.

In HCP metals such as cadmium, zinc, and magnesium, slip only occurs along the one set of close-packed planes, and it is unlikely that this one set falls at exactly 45° to the applied stress. Deviations from this angle require higher stresses to initiate slip that may still occur, provided that the shear stress is less than that required to initiate slip on other type of planes or to pull the layers of atoms apart (brittle fracture). In the case where the close-packed planes are perpendicular to the stress, the layers may separate rather than slip. In FCC metals such as copper and aluminum, there are more slip systems, and slip starts along the most favorably oriented one but may be joined by other systems at higher stresses. In BCC metals such as tungsten, there are no pure close-packed planes, and slip starts at higher stresses, and the metal may fracture rather than slip, especially at low temperatures (Figure 2.68).

Slip requires an initial higher stress in polycrystalline metals than in single crystals because the grain boundaries limit the movement of atoms that form the steps. In spite of this, slip does occur in each grain along the most favorably oriented system (Figure 2.52) and is seen under the optical

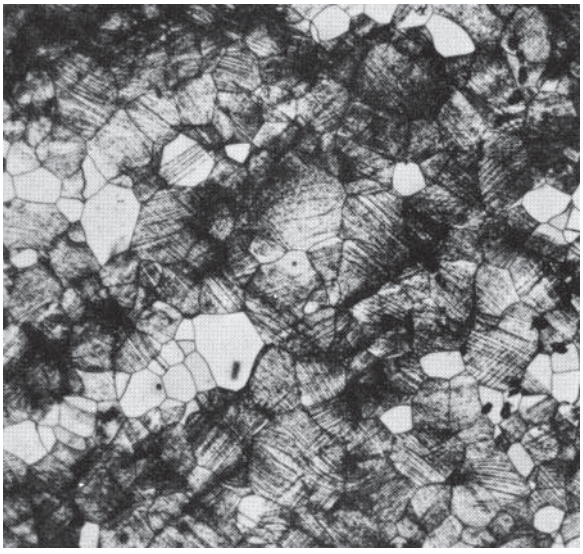


Figure 2.52 Slip planes in a polycrystalline material (×1000).

microscope as sets of approximately 3000 Å deep parallel slip lines that disappear on polishing. In certain grains there are two or more sets of parallel slip lines because slip has occurred on interlinking slip systems. The wide range of angles between the slip lines in adjacent grains arises because the grains are randomly oriented.

Slip lines may be formed by compressional as well as tensile stresses. The two cylinders of copper in Figure 2.53

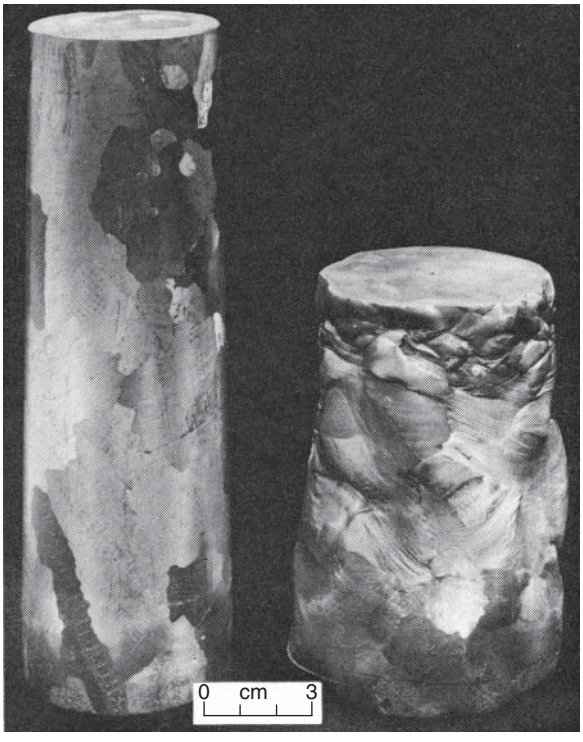


Figure 2.53 Effect of compression on soft pure copper (×1/4).

were both cast into identical molds that were slowly cooled together to allow large grains to grow. The right-hand block was compressed by 41% of its original length under a load of about 60 kg. Each grain has its own slip lines, and the zigzag portion of the central grain boundary confirms that the abutting grains have interfered with slip in each other. Other grain boundaries have clearly moved over one another. If the sample had been cooled quickly to give small grains, the deformation would have produced a barrel-like object with rounded rather than uneven sides.

Slip lines also arise from internal stresses caused by uneven expansion and contraction, particularly in metals with distorted unit cells. During the war there were two classes of bearing metals, in which hard precipitates transfer stress to the matrix metal. One class was based on lead (FCC) and the other on tin (tetragonal distorted cube). Whereas the lead ones functioned well, the tin ones failed in service, sometimes with fatal results.

The yield stress, which marks the beginning of the plastic region, is the stress required to initiate plastic deformation. Calculations based on the perfect structure of metals show that the value of the yield stress, which corresponds to F in Figures 2.6 and 2.47, should not be less than $G/30$ where G is the shear modulus. The values for aluminum in Table 2.4 are, however, representative of all metals, and the discrepancy between the theoretical and the calculated values is very large, even for the polycrystalline material. In each case the experimental value of the yield stress is much lower than the calculated one, which means that the plastic deformation starts more easily than expected if the structure was perfect. The easy initiation of slip arises because one atom plane does not move over another in one big jump but by a series of movements.

An analogy is that a train often cannot start a long line of carriages by commencing with an even pull. The driver backs carefully into the carriages so that the links are slack and then accelerates sharply, pulling the first carriage with his engine. This carriage then jolts the second into motion, and the process is completed when all the carriages are moving. Another analogy from the household is that it is very difficult to pull a large carpet in one move, but individual rucks can be moved with facility so that the whole carpet is moved by a series of easy stages.

Table 2.4 Discrepancy between theoretical and experimental yield stress (σ_L) of aluminum

	G (MPa)	σ_L (MPa)	G/σ_L
Single crystal	25 000	0.4	60 000
Polycrystalline (pure)	25 000	26	900
Polycrystalline (commercial)	25 000	99	250

2.5.3 Dislocations and Plastic Deformation

It is the line imperfections or dislocations, which were discussed in Section 2.1, that are responsible for the discrepancy between the calculated and experimental values of yield stress. The calculated stress required to move a dislocation ranges from $G/60\,000$ for single crystals to $G/200$ for polycrystalline undeformed crystals, and these values are in good agreement with the experimental values (Table 2.4).

Slip occurs at dislocations because it is at these that the interatomic forces are weakest. Dislocations, which are the regions between slipped and unslipped regions, are able to move freely through a regular structure, and, as in the above analogy, they facilitate slip in that they allow movement of a few atoms at any one time. Figure 2.54 illustrates the movement of a dislocation when a shear stress is applied. The dislocation moves from the right surface to that on the left, and the distortion, which causes the local increase in energy, is only limited to three layers of atoms, as the others are essentially undisturbed.

The model illustrates that the movement of one dislocation produces a step of one atomic diameter (c. 3 Å). Steps, however, must be 3000 Å to be seen under the optical microscope, and each one is produced by the easy passage of a thousand or so dislocations. The concentration of dislocations is represented by the dislocation density, which is defined as the length of line per unit volume (mm/mm^{-3} or mm^{-2}). The density (10^6 mm^{-2}), in annealed metals before deformation, is insufficient to account for the large steps. Dislocations may, for example, start at a surface imperfection and travel as in Figure 2.54 along the slip plane and disappear at the other surface. Dislocations are formed during slip, and the dislocation density increases with the amount of deformation.

Although dislocations are present before plastic deformation, only those that fall on the favored slip planes are used. The rest remain immobile. In the case of hexagonal crystals, for example, the plane at right angles to the tensile axis contains inactive dislocations. Where dislocations are able to move, they can only freely do so in completely ordered regions, as they are restricted by each type of imperfection discussed in Section 2.1.

When a metal such as aluminum is heated, the elongation is greater than would be expected from an increase of the crystallographic dimensions. The reason for the difference is that vacancies are produced at the higher temperatures. These vacancies may be trapped by quenching the hot metal quickly in water. The quenched metal (Figure 2.55) requires a higher yield stress to initiate slip than an identical sample cooled under equilibrium conditions when the

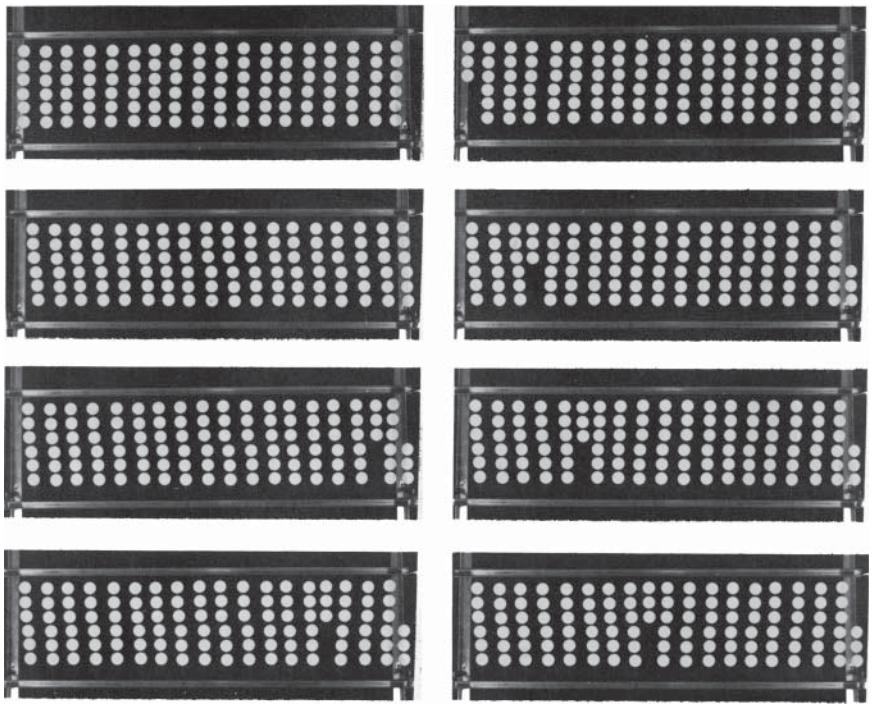
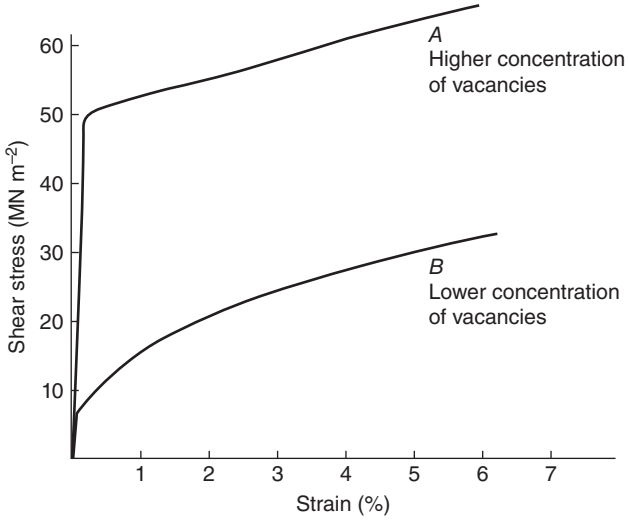


Figure 2.54 Slip and the movement of dislocations. Source: Smallman (1963). Reproduced with permission of Elsevier.



A – cooled quickly in water
B – cooled slowly under equilibrium conditions

Figure 2.55 Influence of vacancies on the deformation of aluminum.

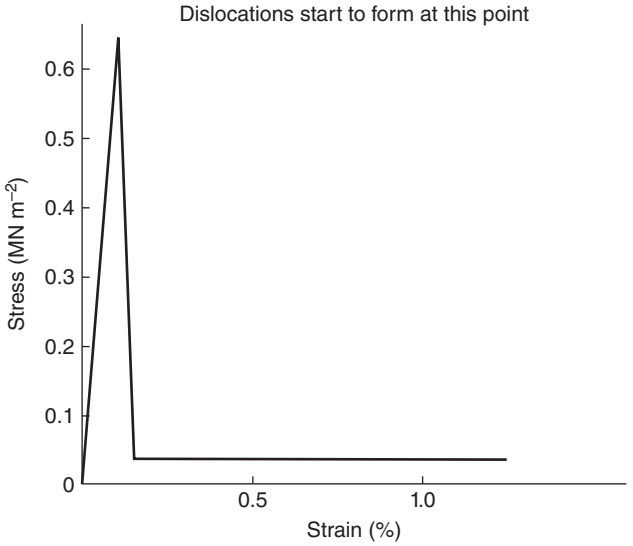


Figure 2.56 Deformation of a single crystal of copper initially free of dislocations that, once formed, move along a single plane.

vacancies have sufficient time to diffuse to the grain boundaries. This is because vacancies impede the movement of dislocations.

Figure 2.56 illustrates the stress–strain curve of a single crystal of copper (FCC) that was initially free of dislocations. These start to be formed at about $G/30$ but thereafter are formed at $G/1000$. This rather special behavior in which slip starts at one stress and then proceeds at a much lower value arises because the dislocations once formed move along parallel planes and do not become entangled. Normally, and especially in FCC metals, slip starts along one set of planes and is joined by slip on another set. Dislocations entangle because the two sets of planes cross each other (Figure 2.52) and become progressively more difficult to move. Consequently, the normal type of stress–strain curve is that in Figure 2.47, in which an ever-increasing

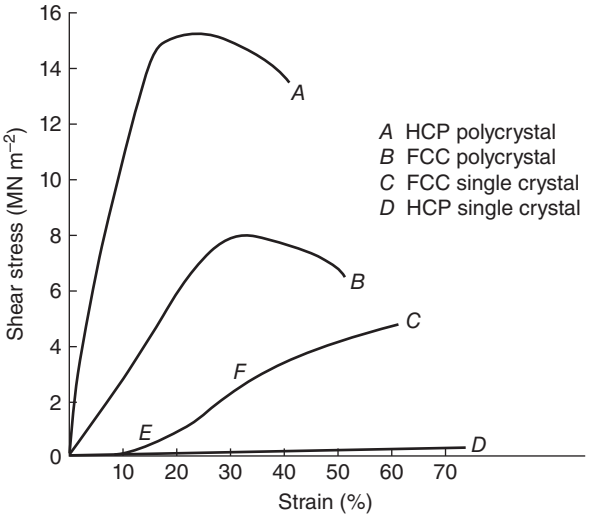


Figure 2.57 Deformation of single and polycrystalline samples of HCP and FCC metals.

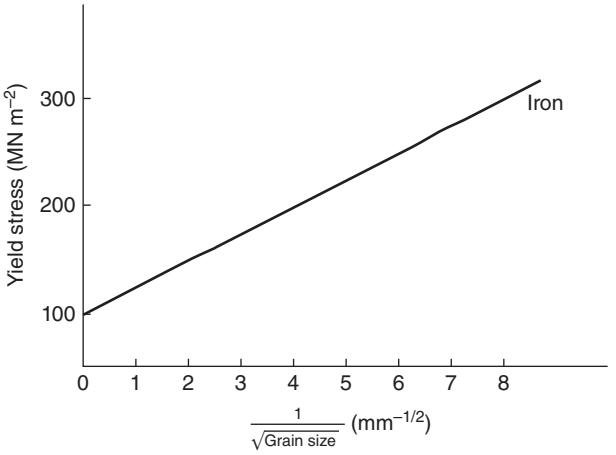


Figure 2.58 Influence of grain size on yield stress.

stress is needed to move the dislocations and the metal work hardens.

Figure 2.57 illustrates the stress–strain curve for single and polycrystalline samples of HCP and FCC metals. In a single crystal of zinc or magnesium (HCP), the dislocations do not entangle because flow is restricted to one set of parallel planes. Consequently, the gradient of the stress–strain curve is small. In FCC single crystals the curve may be divided into three regions. In the first (*OE*), which occurs up to 10% strain, slip occurs on one set, and the gradient is identical to that of the HCP metals. At higher stresses (*EF*), slip occurs on the other planes, possibly because rotation of the disks may bring new planes (Figure 2.47) into favorable orientation. Alternatively, dislocations may pile up at another imperfection such as grain boundary or a precipitate of a second phase, and the resulting knot eventually redirects others along new planes. Once the dislocations enable slip to proceed on interlinking planes, they soon become entangled, and the metal work hardens roughly a hundred times greater than the hexagonal single crystal. Beyond *F* the stress is so high that the dislocations are forced past one another. This is a form of recovery and occurs at lower stresses at elevated temperatures.

In *polycrystalline metals* the individual grains do not deform as if they were each single crystals because the grain boundaries severely interfere with the normal process of slip. Polycrystals of HCP metals only deform with difficulty because there are few favorably oriented planes in which the dislocations are mobile. In FCC polycrystals the dislocations become quickly entangled after a 0.2% strain is exceeded. Whereas the hexagonal single crystals are more ductile than single crystals of FCC metals, the order is reversed for polycrystals.

Grain boundaries limit slip and dislocations are unable to pass freely from one grain to another. Dislocations can be seen piling up at a grain boundary, and the knot so formed is called a stress concentration, the energy of which may inject dislocations through into the next grain boundary so that the yield stress depends on the grain size. With large grains that are few grain boundaries through which the dislocations have to be driven but with small grains (Figure 2.58), there are many more.

The influence that the second component has on dislocations depends on its size, solubility, and dispersion. Small solute atoms such as carbon, which form interstitial solid solutions, cause a local distortion of the iron atoms that surround them. They move rapidly to the vacancies provided by the dislocations, and consequently only a small number (1 in 10^5) of interstitial atoms are needed to pin them. The stress–strain curves of low carbon steels characteristically have an upper yield stress (*C* in Figure 2.49) and a lower value (*D*). The upper yield stress is that which is needed to unpin the dislocations from the interstitial carbon atoms and to cause the ferrite to yield along the favorably oriented bands at 45° to the tensile axis. New dislocations are formed when the ferrite layers slip and these are free from the interstitial carbon atoms so that they can move at the lower yield stresses.

Even the ancient artisans knew that the combination of two metals was stronger than either of the individual ones. Provided that the two metals are completely soluble, the yield stress increases linearly with the percentage of alloying element (up to 20%), and the gradients in the stress–composition curves in Figure 2.59 vary according to the elements involved. Silicon, for example, with a radius of 1.17 Å has an effect greater than chromium (1.25) on iron (1.24). It is tempting to say that the difference depends on the distortion produced by the inclusion of atoms of different size. This is not the complete

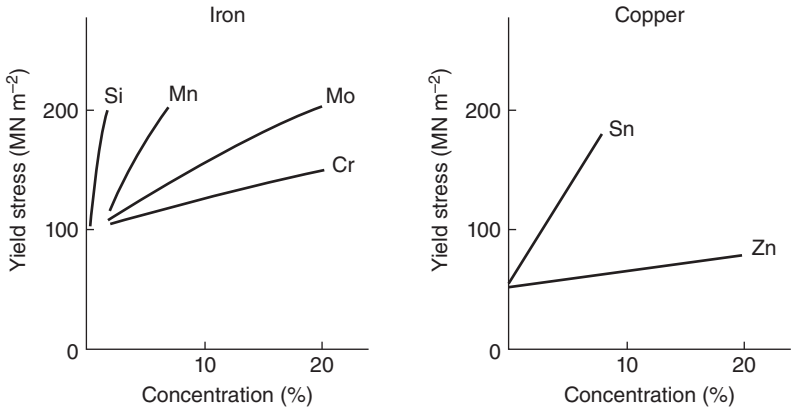


Figure 2.59 Substitutional solid solutions. The influence of solute concentration on yield stress.

answer because solute atoms are rarely individually dispersed throughout the metal and they normally form clusters, each of which is capable of limiting dislocation movement.

Precipitation hardening, which was discussed in Section 2.3, relies on very small, randomly dispersed particles limiting the movement of dislocations. The unique properties of the age-hardening aluminum–copper alloys arise from precipitates (clusters) of the compound $CuAl_2$ dispersed along the {100} matrix planes (see Figures 2.20 and 2.33). When these precipitates are very close together, the dislocations are unable to move freely between them. The dislocations, therefore, move directly through the precipitates (Figure 2.60) that are fractured, a process that requires a higher stress as bonds have to be broken. Dislocations are, however, able to move through well-spaced precipitates, but in doing so the clusters are looped by dislocation debris. The yield stress required to move the dislocations between the precipitates is less than that needed to move them through, but the two curves (Figure 2.60) approach one another at high strains, partly because the loops themselves limit further dislocation movement.

The hardness of these age-hardened alloys varies (Figure 2.60) according to the temperature at which they are annealed. When they are heated at a low temperature (T_1), the hardness slowly increases – typically over four days – until the maximum value is reached. When annealed at moderate temperature (T_2), the hardness increases faster and to a higher value because a larger number of precipitates are formed as copper and aluminum diffuse more quickly than at temperature T_1. When annealed at high temperature (T_3), the hardness increases rapidly to a high value as the forming precipitates limit the movement of the dislocations, but thereafter the hardness decreases because the precipitates break up, enabling the dislocations to move more freely.

2.5.4 Mechanisms of Strengthening in High Temperature Materials

Pure metals are weak and do not have adequate environmental resistance. Therefore, they are seldom used without strengthening by various mechanisms and protected from the environment by surface treatments. Table 2.5 summarizes a number of processes by which metals are strengthened.

Solid solution strengthening and precipitation hardening are effective at high temperatures and, therefore, are used in strengthening *high temperature alloys*. Of the other mechanisms listed in Table 2.5, grain size control is used in conjunction with solid solution and precipitation hardening. The oxide dispersion strengthening (ODS) process is sparsely used in selected cases for moderate temperature applications. Martensitic transformation and work hardening are not effective at temperatures of interest here (Weertman and Weertman 1992).

Strengthening by solid solution and precipitation involves impeding motions of dislocations in the metallic structure. In a solid solution, appropriate alloying elements (called the solute) are dissolved in a metal (called the solvent). The solute atoms randomly substitute for the solvent atoms (Figure 2.61) without altering the phase that is the crystal structure. In the vicinity of the solute atoms, compressive or tensile stresses are generated depending on whether the substituting atom is larger or smaller than the solvent atom. Motions of dislocations are impeded by the presence of the stress fields. The size differences between the solvent and the solute atoms as well as the volume fraction of the solute determine how effective the strengthening would be. For this mechanism to be useful, the solute atoms should have reasonable solubility in the solvent metal, and the atomic size difference should be significant.

In addition to substitutional solid solution in which solute atoms randomly replace the solvent atoms, the solute atoms may also enter the solvent in the interstitial sites

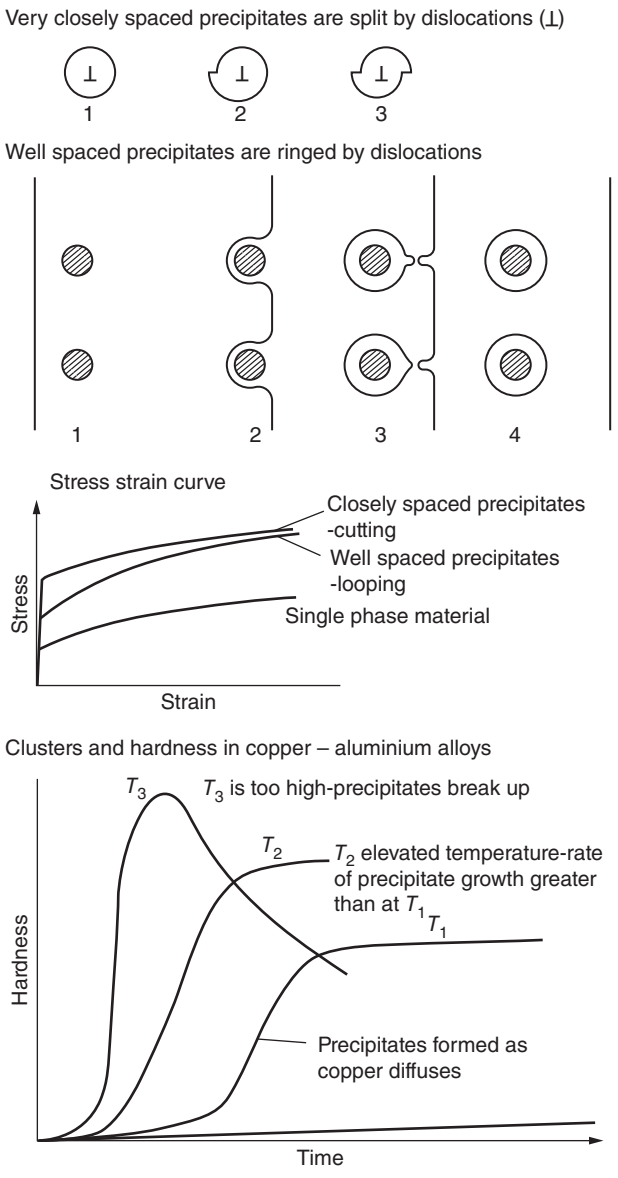


Figure 2.60 Interactions between dislocations and precipitates (e.g. of $CuAl_2$ or Fe_3C).

Table 2.5 Strengthening mechanisms for metals

Mechanisms	Effective temperature
Solid solution strengthening	High temperature
Precipitation (or age) hardening	High temperature
Grain size control	Moderate temperature
ODS	Moderate temperature
Martensitic transformation strengthening	For specific metals and at low temperature
Work hardening	Low temperature

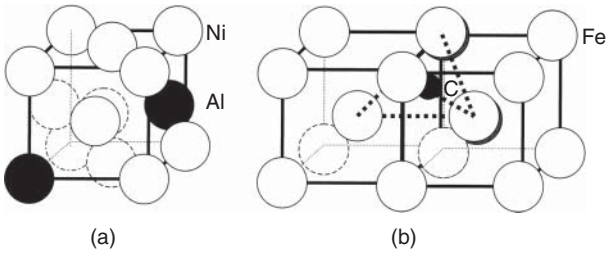


Figure 2.61 Schematic of solid solution. (a) Substitutional (Al dissolved in Ni) and (b) interstitial (C dissolved in Fe).

(Figure 2.61). For example, carbon, being a small atom, forms an interstitial solid solution with iron. The stress fields associated with the interstitial atoms also interfere with dislocation motion, thereby influencing strength.

In precipitation hardening, the solute atoms participate in creating a fine and uniformly dispersed second phase. To achieve this condition, the solvent metal needs to form a supersaturated solid solution at high temperature. On cooling, the solubility decreases, and the solute atoms are rejected from solution in the form of fine precipitates. These precipitates impede dislocation motion. The size, strength, "coherency," and volume fraction of the precipitates control the strength achieved by this process. These parameters are controlled through appropriate heat treatment of the alloys.

2.5.5 Creep

Creep is the slow plastic deformation of a metal under constant load. Figure 2.62 illustrates a typical creep curve in which strain is plotted against time at a constant temperature. The curve is divided into three regions. In the region of transient creep, the sample *AB* strains rapidly at a decreasing rate. In the steady-state region, there is a constant but slow rate of straining, and metals are not usually used in this region. In the region of accelerating creep, the rate of creep accelerates until the sample fractures.

In the first region, creep occurs by slip, and the resulting dislocations become entangled, causing the sample to work harden. Metals at low temperatures and low stresses may not move out of this region. In the steady-state region, the dislocations move only to a limited extent according to their thermal or vibrational energy. Those that have sufficient energy are able to climb over adjacent ones so that the metal softens locally. Thereafter, more dislocations pile up and entangle. The region is shortened if the temperature is raised because more dislocations are given the necessary energy to allow them to move. In the third stage, which is particularly prevalent at high temperatures, cracks form at grain boundaries as vacancies diffuse and dislocations move along slip lines to them. These cracks grow until the grains separate completely.

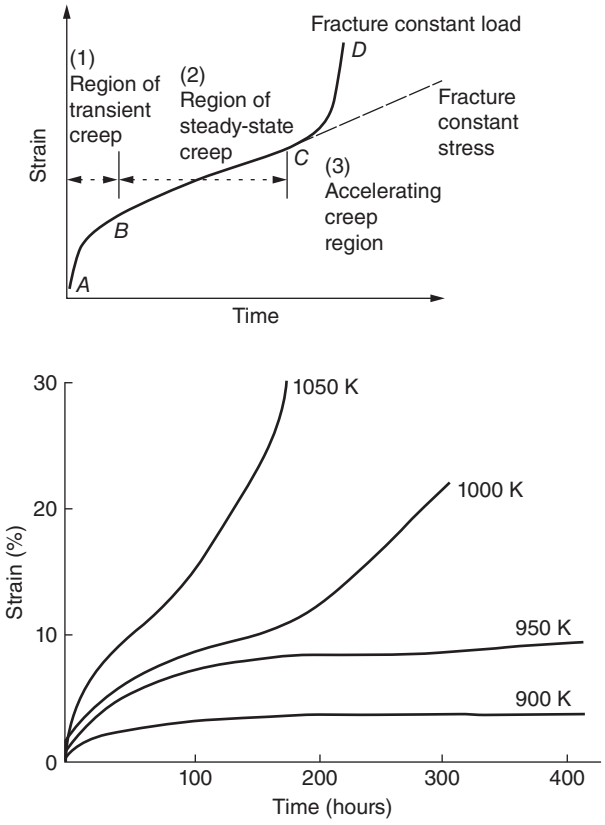


Figure 2.62 Deformation under constant load (creep).

A single crystal deforms by creep more quickly and to a greater extent than a polycrystalline sample of the same metal because there are no grain boundaries at which the dislocations can pile up. Similarly, a large-grained sample deforms more than a small-grained one. An alloy deforms by creep less than a pure metal, as the clusters of the alloying element limit the movement of dislocations. The strains produced, however, are much greater than can be explained by slip and the accompanying movement of dislocations, and there is good evidence that the local softening discussed above enables grains to slide over one another, as in viscous flow.

Creep is particularly noticeable at high temperatures since it is largely controlled by diffusion processes. The temperature range over which creep becomes important largely depends on the melting point of the metal. Thus, at temperatures below 0.3 T_M (where T_M is the melting point), the metals rarely move out of the transient creep stage. At higher temperatures (0.5 T_M), they usually move into the steady-state region and above 0.7 T_M into the final stage. With metals such as lead, creep occurs at room temperature, which is the reason why lead pipes sag. Steel pipes, however, deform by creep above (700 K), whereas those made from nickel alloys only deform above 1300 K. Creep places a limiting temperature (0.7 T_M) above which metals cannot be used.

Creep-resistant materials are often based on high-melting, precipitation-hardened alloys. The alloy must be stable, for example, the finely dispersed precipitates must not coalesce, a process that would allow dislocations too much freedom. Age-hardened alloys must, therefore, be used with extreme caution under conditions where creep may occur.

Alloys based on FCC metals are common because the dislocations are sufficiently mobile to reduce stress concentrations (Section 2.6), which are really regions of high energy. The reduction of the stress concentration spreads out energy so that few dislocations have sufficient energy to overcome obstacles.

"Very ductile" (superplastic) in this context means that the alloy can be plastically deformed to very high elongations before fracture. For example, a sample initially with a diameter of 5 mm can give a 200% elongation. The very ductile metals have very small grains (10^{-6} m across) (Figure 2.62) that move over one another by grain boundary movement in a form of viscous flow – seen particularly in the central grains. The grains do not coarsen nor do they become oriented during deformation because the alloys are composed of two quite separate phases. In the aluminum–zinc alloy, there are zinc- and aluminum-rich phases, each comprising 50% of the total volume. One phase moves through the other as if it were moving through a phase of low viscosity. The very ductile metals often have eutectic composition, and a fine grain size is produced by working the alloy just below the eutectic point. They are potentially of use in shaping processes such as those needed for car body manufacture because they deform to give very high elongation under low stresses, but unfortunately they only do so at slow rates of strain.

Stainless steels (Section 1.4.4), refractory metals (Section 1.4.9.1), and superalloys (Section 1.4.7) are especially *resilient* to creep and are commonly employed in high temperature service applications. The creep resistance of cobalt and nickel superalloys is enhanced by solid solution alloying and also by the addition of a dispersed phase that is virtually insoluble in the matrix. In addition, advanced processing techniques have been used; one such technique is directional solidification, which produces either highly elongated grains or single-crystal components. Another is the controlled unidirectional solidification of alloys having especially designed compositions wherein two-phase composites result.

2.5.6 Recovery, Recrystallization, and Grain Growth

When an annealed or a cast metal is deformed or cold-worked, the grains become elongated in the direction

of working. This change in microstructure is accompanied by an increase of strength and hardness because dislocations become entangled. Whereas in an undeformed metal the density is 10^6 cm^{-2}, in a well-deformed one, it is as much as 10^{12} cm^{-2}. Although cold working is a useful means of strengthening, the undeformed state is unstable with respect to the deformed state by approximately 10^7 J m^{-3}. At low temperatures, however, the dislocations have insufficient energy to become unlocked, and, in addition, diffusion is strictly limited to the grain boundaries so that the deformed state can exist undefinitely. Heavy cold working, however, is often followed by annealing to reduce internal stresses and to render the metal more ductile.

At higher temperatures (0.3–0.5 T_M), the grains are formed from strained ones by a process called annealing, which renders the deformed metal weaker but more ductile. Annealing occurs in the stages of recovery, recrystallization, and grain growth.

During recovery the dislocations rearrange themselves, and the dislocation density is not greatly reduced, and as a result there is little change in strength, hardness, and ductility (Figure 2.62). *Recrystallization* is characterized by a significant reduction in strength but an increase in ductility and the formation of new grains and proceeds by a process of nucleation and growth akin to that which occurred in solidification. Nuclei are especially successful in the most strained regions where the strain energy is at a maximum, being used to reorient the atoms to form unstrained grains with 120° angles. The resulting grains are often a hundred times smaller than those in cast metals.

For each metal there is a definite threshold degree of deformation or strain energy below which the metal will not recrystallize. With aluminum a 2% deformation is needed, whereas iron needs 10% and lead 1%. When a metal is deformed a fraction more than this critical value, very large grains are formed, but the grain size decreases as the strain energy moves away from this value.

During recrystallization, the dislocations have sufficient thermal energy to become mobile, and the strain-free grains are formed as a result of dislocation migration. The rate at which recrystallization proceeds depends on a number of factors, each of which influences the mobility of dislocations. A high degree of deformation accelerates the rate because the extra strain energy introduced can be used to reorient the atoms. Recrystallization is faster at higher temperatures than low because the higher thermal energy enables the dislocations to move through one another more quickly. With iron, for example, a given grain size is formed in eight minutes at 950 K, but the same size is only produced in 32 hours at 820 K. Thus, pure aluminum recrystallizes below room temperature, but commercial aluminum only does so above 500 K. There is no such thing as a recrystallization temperature, because recrystallization for any given metal commences over a range of temperatures.

After recrystallization has been completed and all of the strained grains have been removed, *grain growth*, in which large grains grow at the expense of small ones, takes place. The overall effect is to straighten and generally reduce the surface energy of the grain boundaries since the surface area of a large set of grains is less than that of an equal volume of small grains.

When a metal is hot-worked, the deformation is accompanied by recovery and possibly by some recrystallization, especially at high temperatures (0.7 T_M). Under normal manufacturing conditions, deformation is only accompanied by recovery, but, as the metal cools, it recrystallizes and the final microstructure is indistinguishable from that resulting from cold working and annealing. In Figure 2.63, the upper photograph is of an as-cast pure iron silicon alloy, and the lower photograph illustrates the same metal after it has been hot-worked. The inhomogeneous cast structure, which contains chill columna and equiaxed grains, has disappeared, and the grains are of a uniform size. A metal such as lead can be hot-worked at room temperature, whereas iron is cold-worked at 700 K. The advantage of *hot working* is that low stresses are needed, particularly when the deformation is accompanied by recrystallization. It does, however, give a poor surface finish, and the final size is difficult to control and is often

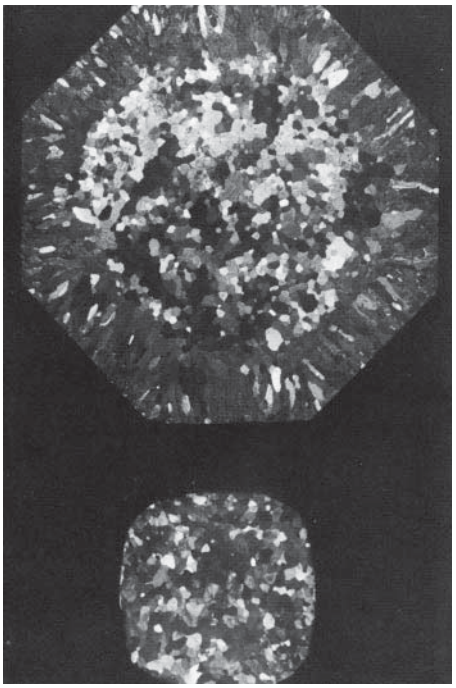


Figure 2.63 Hot working. Grain structure of cast and hot-rolled alloys (×9/10). A pure iron silicon (3%) alloy was cast, sectioned, and etched in nitric acid. The alloy was hot rolled at 1500 K and etched in nitric acid.

used prior to the more easily controlled cold working that gives a better finish.

2.6 Fracture and Fatigue

2.6.1 Brittle Fracture

In Section 2.5 the term "strength" was considered solely in the context of resistance to deformation, but there is an entirely different meaning, and that is toughness or resistance to crack propagation. Brittle metals are weak because they offer little resistance to crack propagation, that is, they fracture rather than deform plastically. Ductile metals, on the other hand, are said to be tough because they offer a high resistance to fracture in that they deform rather than allow cracks to be propagated through them. In Figure 2.47, the ductile alloy only fractured after necking, which caused the stress to be concentrated in one area.

On 15 January 1919, a molasses tank exploded with the loss of 12 lives, and at one time bridges in America were breaking at the rate of 12 a year. On 16 January 1943, an all-welded T2 tanker lying at anchor in still waters suddenly cracked without warning and with a report that was heard a mile away. These and other catastrophes have concentrated research on brittle fracture because in each case the vessel was operating well within the limits of tensile stress.

Theoretically, all brittle materials should not fail when a stress less than $E/10$ is applied where E is Young's modulus, but in practice brittle fracture can occur well below $E/1000$. This discrepancy arises from the fact that all materials contain cracks that act so as to concentrate stress. In a perfect structure (Figure 2.64), all of the bonds are intact, and the applied stress is distributed uniformly. When a crack is present, however, the absence of bonds across the cracks causes stress to be concentrated at the crack tip. The magnitude of the stress concentration increases as each overstressed bond is broken and is related to the applied stress by the approximate relationship:

$$\text{Stress concentration} = \frac{\text{Stress at the crack tip}}{\text{Applied stress}} = \left(\frac{\text{Crack length}}{\text{Crack radius}}\right)^{1/2} \qquad (2.15)$$

A crack of 10^4 Å length and 1 Å radius has a stress concentration factor of 200, which means that the stress at the crack tip is 200 times greater than the applied stress. Since the stress concentration is inversely proportional to the square root of the radius, narrow cracks are much greater stress raisers than wide ones. Also the stress at the tip of a long crack is greater than that of a short one with equal tip radius. There is, however, a critical length of crack such that those that are shorter than this value are not propagated and those longer are propagated.

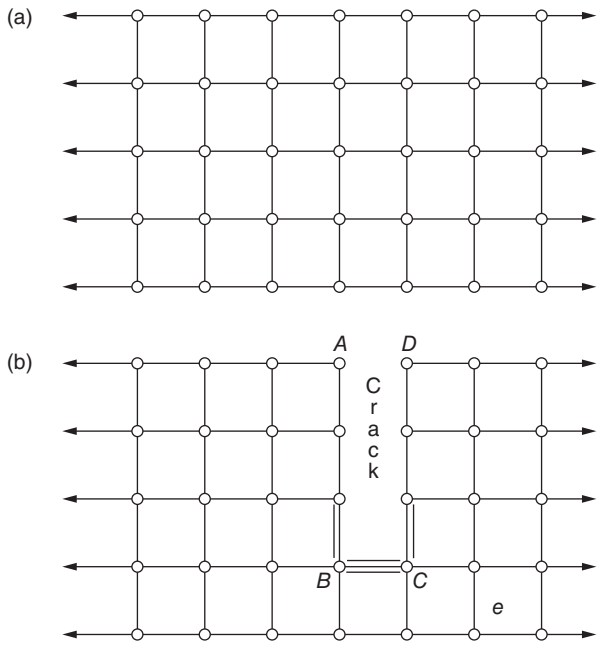


Figure 2.64 Schematic representation of stress concentrations. (a) In a perfect structure with no cracks the stresses are evenly distributed. (b) In a structure with cracks at the surface (Griffith's cracks) there is a large stress concentration at the bond which terminates the crack.

The *critical crack length* may be accurately calculated for vitreous (noncrystalline) substances in which the bonds behave elastically. The applied stress has to stretch and break bonds, but the energy required to do so is compensated by the surface energy of the two new surfaces AB and CD. (The surface energy arises because the bonds at the surface are unsaturated.) The result of the calculation is that

$$\text{Stress required to form a crack} = \left(\frac{\text{Surface energy} \times \text{Young's modulus}}{\text{Crack length}}\right)^{1/2} \qquad (2.16)$$

Using typical values, the critical crack length is 2×10^{-3} mm (10^4 Å), which corresponds to 10 000 or so atoms. Cracks of this length are frequently found on glass, and once the necessary stress is applied by a sharp blow, the cracks are propagated at about 60% of the velocity of sound. With longer cracks, the energy required to break the bonds is more than offset by the gain in surface energy.

In glass these cracks lie at the surface and are formed by contact between two surfaces. In very small perfect single crystals (whiskers) that are free from surface cracks, the strength approaches the theoretical value (Figure 2.65) of $E/10$.

The *Griffith microcrack theory* is only true for vitreous substances, but nevertheless the stress required is still inversely proportional to the square root of the crack

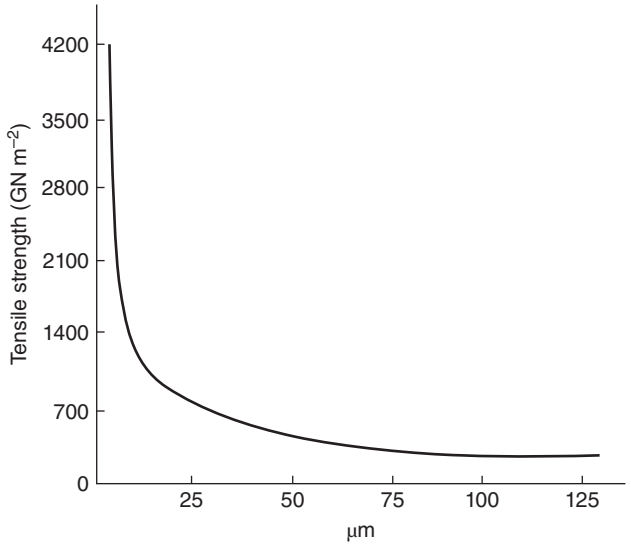


Figure 2.65 Strength as a function of radius for small glass fibers.

length. In crystalline solids, which include diamond and sodium chloride in addition to metals, the bonds are not entirely elastic, and fracture is always accompanied by plastic deformation and dislocation movement. The result is that the cracks are rounded off and the stress at the crack tip is reduced so that higher applied stresses or longer cracks are needed for fracture. Examination of Eq. (2.15) shows that the stress concentration increases with crack length, and Eq. (2.16) indicates that the stress required for crack propagation decreases as the crack becomes longer. Therefore, there is a critical crack length for all crystalline solids as well as vitreous ones. Cracks longer than the critical value may rapidly spread, with the result that crystalline solids fail by brittle fracture. Nevertheless, crystallinity does not imply brittleness.

It might be thought that crystalline solid with strong interatomic bonds would be less susceptible to brittle fracture than those with weaker bonds, but this is not the case. Diamonds in which the carbon-to-carbon bond strength is 450 kJ mol^{-1} are brittle, whereas lead (250 kJ mol^{-1}) is ductile. The reason why brittleness is not related to bond strength is that in ductile solids dislocations are able to reduce the stress concentration at the crack tip. Brittle ones are much less able to do so, and the stress concentration at the crack tip is far greater than the strength of the chemical bonds.

Brittle fracture may occur in any solid in which dislocation movement is severely restricted. Metals with the BCC structure are particularly susceptible to brittle fracture because there are no close-packed planes on which the dislocations may easily move. HCP metals, which have one set of close-packed planes, are normally less brittle but can be made so by rendering the dislocations inoperative.

Dislocation movement accompanying brittle fracture has been confirmed in a manner similar to that described in Figure 2.63, as the stress required for fracture is inversely proportional to the square root of the grain size.

Brittle fracture occurs in two stages – crack nucleation and propagation. Cracks are nucleated in one of two main ways. In the first, dislocations pile up at an imperfection such as a precipitate of a second phase (Figure 2.66). In the

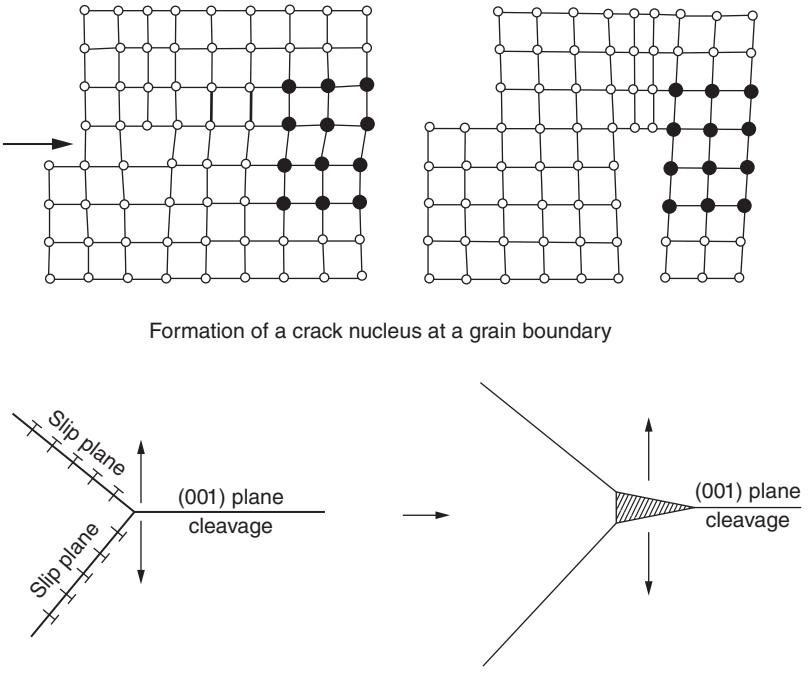


Figure 2.66 Crack nucleation.

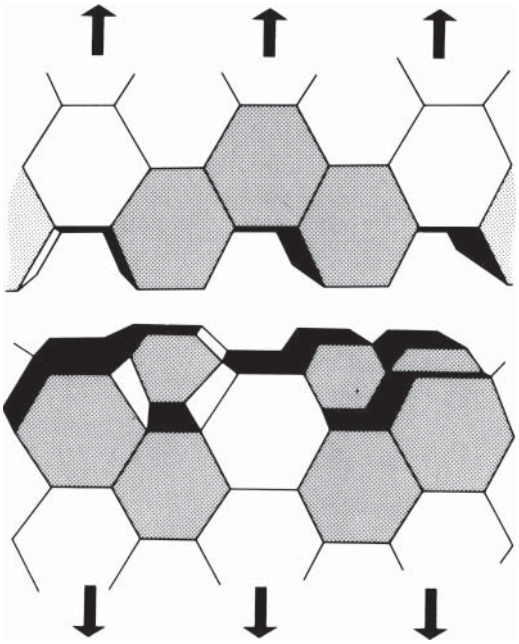


Figure 2.67 Intergranular fracture.

second, dislocations move down close-packed or other slip planes, and the cumulative effect is to form a crack.

Cracks are normally propagated along well-defined sets of cleavage planes within each grain, leaving bright smooth reflecting surfaces. There are often parallel "river" lines on these surfaces because the cracks run at different heights. Fracture that propagates through the grains is called transgranular fracture, which is well known in all pure metals and most alloys. In cases where the grain boundaries have been weakened by impurities or by precipitates of a second phase, fracture can occur between the grains (Figure 2.67) in a process called *intergranular fracture*, which has been well characterized for a number of molybdenum alloys.

2.6.2 Ductile Fracture

The point *F* in Figure 2.47 is that at which the ductile metal has fractured. The metal starts to neck after *E*, and although the applied stress decreases from *E* to *F*, the real stress at the plane of fracture continues to increase. The bulk of the fracture surface is usually at right angles to the applied tensile stress, with the rim being at 45°, and the resulting profile is known as a "cup and cone" fracture. Pure metals may, however, constrict uniformly throughout their length like the very ductile metals. Single crystals of zinc and cadmium (HCP) sometimes fracture as a result of block slip, particularly when the close-packed planes are at an angle of 45° to the applied tensile stress.

Ductile fracture normally starts at the interface between precipitates of a second phase and the metal. Small pores are formed as the metal is pulled away from the weak interface, and, as necking proceeds, adjacent pores join up so that each piece of metal may be regarded as a small tensile test specimen, each of which necks and fractures. When many of these pores have joined up, they form a large internal cavity, the rim of which fails by shear at 45° to the tensile axis.

The mechanism for brittle and ductile fractures is present in all metals at all times. They fail by whichever mechanism is the weaker. In FCC and HCP metals, the dislocations are sufficiently mobile to be able to reduce the stress concentration sufficiently so that these metals fail by ductile fracture. In BCC metals, however, the mobility of the dislocations very much depends on their thermal energy. At low temperatures, the dislocations are insufficiently mobile to affect greatly the stress concentration, so that the stress required for brittle fracture is less than that for ductile fracture. In BCC metals, however, the mobility of the dislocations very much depends on their thermal energy. At low temperatures, the dislocations are insufficiently mobile to affect greatly the stress concentration, so that the stress required for brittle fracture is less than for ductile fracture. BCC metals such as iron are therefore brittle at low temperatures, and iron rails sometimes fail by brittle fracture in winter. The old cry used to be that the rail had crystallized, but this is incorrect – it was crystalline when ductile at the higher temperatures. When the dislocations have sufficient thermal energy, they are mobile and able to climb over one another so that the stress required for brittle fracture is greater than that for ductile fracture. Figure 2.68 shows the temperature dependence of yield stress for some metals as a function of temperature. The FCC and HCP metals have a very little dependence on temperature because they fail by ductile fracture throughout, but the marked variation with temperature with the BCC metals arises because of the brittle-to-ductile transition.

2.6.3 Failure by Fatigue

In the case where a metal can withstand a tensile stress below the yield stress indefinitely, an identical stress applied alternatively with a compressive stress may result in a sudden failure. This is known as *fatigue*, which is responsible for over 90% of all metal failures. Fatigue tests involve the application of two types of curve (Figure 2.69): The upper curve *A* is typical of steels and has a horizontal section at the *fatigue limit*. Stresses below the fatigue limit do not produce fatigue failures, whereas those above this value induce failure at the number of cycles indicated on the graph. The other curve *B* is typical of all nonferrous alloys and for steels in a corrosive environment. These do not have a fatigue limit, which means that fatigue can be induced at all stresses. In practice, however, the lower the

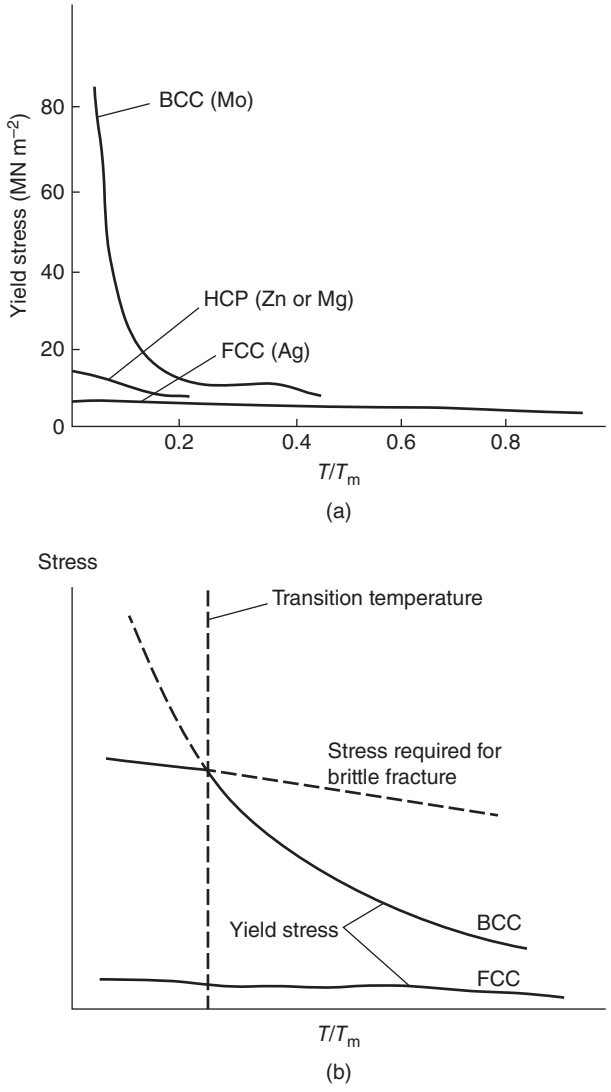


Figure 2.68 Brittle-to-ductile transition in BCC metals. (a) Yield stress of BCC metals varies greatly with temperature. (b) At low temperatures the yiels stress is higer than the stress for brittle fracture. BCC metals are brittle at low temperatures but at high temperatures they are ductile as the yield stress is below the stress required for brittle fracture.

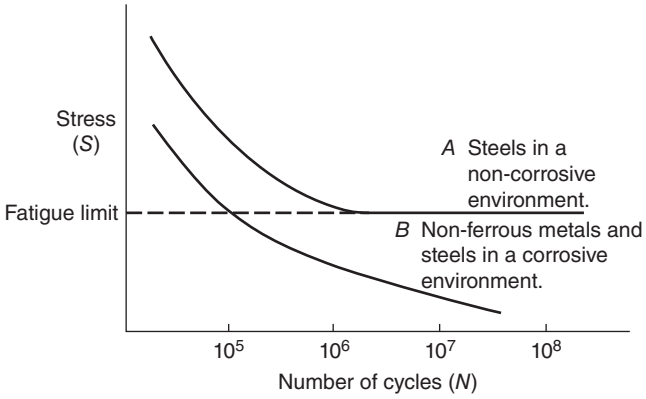


Figure 2.69 Fatigue. The metal fail by fatigue at the values of S and N indicated by the curves. Steels in a noncorrosive environment do not fail at all below the fatigue limit.

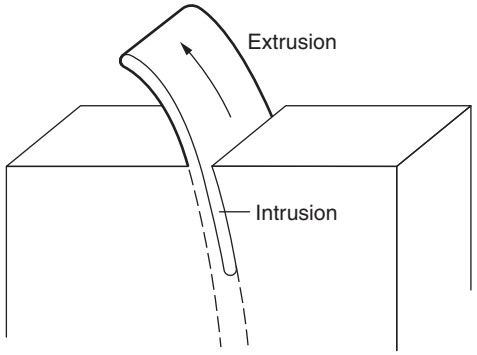


Figure 2.70 Formation of surface cracks during fatigue. Extrusions and intrusions are formed where active slip bands meet the surface.

stress, the greater the number of cycles needed for fatigue failure (Wulpi 1999).

Fatigue proceeds by a process of crack nucleation followed by propagation. Cracks are initiated at the surface of the article at the point where there is a concentration of stress (Figure 2.70). As the alternating stress is applied, dislocations move to the stress concentrator where the metal work hardens. This dislocation movement is manifested as small regions of extruded metal adjacent to intrusions, and both are formed early (10%) in *fatigue life*. Thereafter they lie dormant until they turn out of the slip plane along which dislocations initially came into a path perpendicular to the applied stress. The fatigue crack then advances quickly a step at each oscillation, giving a kind of ringed region. The crack advances until the remaining metal can no longer hold the stress and the metal fractures by brittle or ductile fracture. Since failure commences at the surface, it is vital that all forms of surface imperfections are removed by good design, correct choice of alloy, proper surface treatment, and a nonhostile environment.

The fatigue failure of the Comet 1 aircraft arose from a small rivet hole (1 mm radius) near to one of the windows, and an improvement in design soon rendered them safe. Solid solution alloys are particularly resistant to fatigue failure, provided that the alloy itself is stable and not of the age-hardening type, because stable alloys are able to limit the movement of dislocations in the manner described earlier. Fatigue, however, creates vacancies that enhance diffusion so that in age-hardening alloys, large coarse precipitates are formed, which weaken the alloy to the point where it is little stronger than the metal itself. The static strength of these alloys is much greater than their fatigue strength.

Another method of improving resistance to fatigue is to harden the surface itself, so that plastic flow is severely

restricted and the dislocations cannot pile up at the surface. In one technique available for steels, the hot metal is placed into carbonaceous material from which carbon diffuses to form a hard layer of carbide at the surface. The resulting expansion of the surface iron causes compressive stresses to be raised over the surface, with the result that crack formation is severely limited.

All metals subject to alternating stresses must be used under corrosion-free conditions because a hostile environment attacks the surface at the region of highest stress. This corrosive attack enhances crack formation and severely limits the working life. Whereas steels have a stress (fatigue limit) below which they do not fail by fatigue, this limit is entirely removed by corrosive agents. Steels subject to fatigue in a hostile environment therefore have a fatigue curve of type *B* in Figure 2.49. It is therefore important to choose the alloy that is not subject to corrosive attack under conditions of service. In alloys that are particularly resistant to corrosion, a stable oxide layer is formed over the surface. Thus, in chromium steels, there is a layer of chromium oxide.

Once a crack has formed and is being propagated through the metal, it can freely do so unless some barrier is placed in its path. In all-welded ships the hull was continuous, so that once a crack started at a stress raiser such as a hatchway, the crack freely spreads at a velocity approaching that of sound. In hulls that are composed of riveted sheets, cracks in one sheet cannot spread to another because there is a gap between them.

In fiber-containing metals it is arranged that the interface between the fiber and metal is one-fifth as strong as that of the metal alone. Weak interfaces of this type that are roughly at right angles to the direction of crack spreading serve to toughen the metal because the crack (Figure 2.71) is redirected. It may seem surprising that a weak interface can strengthen a metal, but fiber-reinforced materials are tougher than metals. The true strength at the crack tip is, as stated earlier, 10% E, and reduction of this by one-fifth still gives a value higher than that obtained by ductile mechanism in metals. The weak interface moreover reduces the stress concentration at the crack tip because the tip radius (Eq. (2.15)) is greatly increased.

2.6.4 Toughness Mechanisms

Toughness is a mechanical term that is used in several contexts; loosely speaking, it is a measure of the ability of a material to absorb energy up to fracture. Specimen geometry and the manner of load application are important in toughness determinations. For dynamic (high strain rate) loading conditions and when a notch (or point of stress concentration) is present, *notch toughness* is assessed by using an impact test, as discussed below.

Two standardized tests, the Charpy and Izod, were designed and are still used to measure the impact energy, sometimes also termed notch toughness. The Charpy V-notch (CVN) technique is the most commonly used in the United States. For both Charpy and Izod, the specimen is in the shape of a bar of square cross section into which a V-notch is machined. The load is applied as an impact blow from a weighted pendulum hammer that is released from a cocked position at a fixed height h. The specimen is positioned at the base. Upon release, a knife edged mounted on the pendulum strikes and fractures the specimen at the notch, which acts as a point of stress concentration for this high velocity impact blow. The pendulum continues its swing, rising to a maximum height h', which is lower than h. The energy absorption, computed from the difference between h and h', is a measure of the impact energy. The primary difference between the Charpy and Izod techniques lies in the manner of specimen support. Furthermore, these are termed impact tests in light of the manner of load application. Variables including specimen size and shape as well as notch configuration and depth influence test results.

One of the primary functions of Charpy and Izod tests is to determine whether or not a material experiences a *ductile-to-brittle transition* with decreasing temperature and, if so, the range of temperatures over which it occurs. The ductile-to-brittle transition is related to the temperature dependence of the measured impact energy absorption. This transition is represented for a steel by curve *A* in Figure 2.72. At higher temperatures, the CVN energy is relatively large, in correlation with a ductile mode of fracture. As the temperature is lowered, the impact energy drops suddenly over a relatively narrow temperature range, below which the energy has a constant but small value; that is, the mode of fracture is brittle.

Alternatively, appearance of the failure surface is indicative of the nature of fracture and may be used in transition temperature determinations. For ductile fracture this surface appears fibrous or dull (or of shear character). Conversely, totally brittle surfaces have a

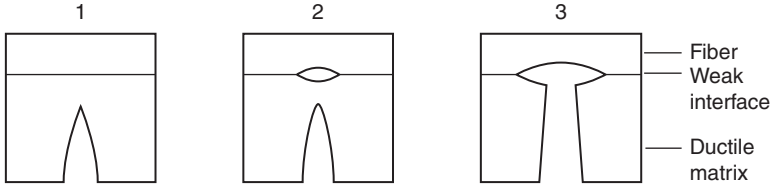


Figure 2.71 Preventing crack propagation. A crack which is a wedge shape hole, is diverted along a weak metal–fiber interface. The radius at the crack tip and hence the stress concentration is thus greatly reduced and the crack propagation stops.

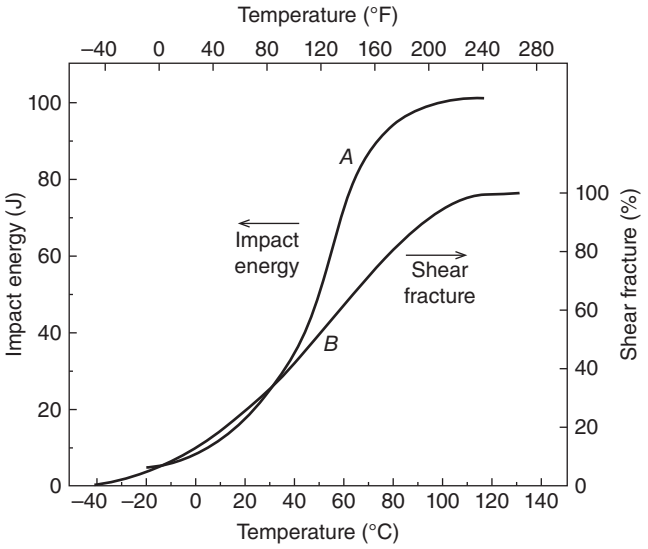


Figure 2.72 Temperature dependence of the Charpy V-notch impact energy (curve *A*) and percent shear fracture (curve *B*) for an A283 steel.

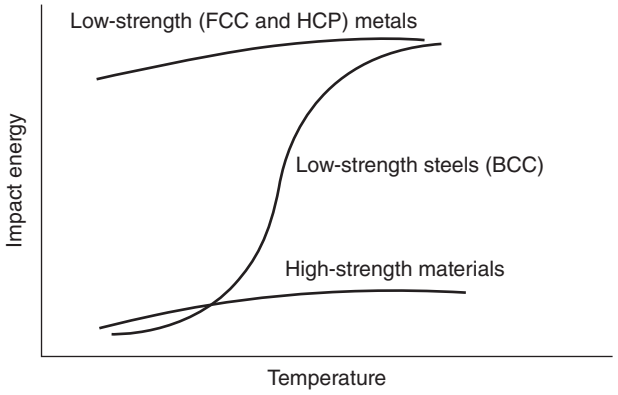


Figure 2.73 Schematic curves for the three general types of impact energy-versus-temperature behavior.

granular (shiny) texture (or cleavage character). Over ductile-to-brittle transition, features of both types will exist. Frequently, the percent fracture is plotted as a function of temperature – curve *B* in Figure 2.72.

For many alloys, there is a range of temperatures over which the ductile-to-brittle transition occurs (Figure 2.72); this presents some difficulty in specifying a single ductile-to-brittle transition temperature.

In addition to the ductile-to-brittle transition represented in Figure 2.72, two other general types of impact energy-versus-temperature behavior have been observed; these are represented schematically by the upper and lower curves of Figure 2.73. Here it may be noted that low-strength FCC metals (some aluminum and copper alloys) and most HCP metals do not experience a ductile-to-brittle transition (corresponding to the upper curve of Figure 2.73) and retain high impact energies (i.e. remain ductile) with decreasing temperature. For high-strength materials (e.g. high-strength steels and titanium alloys), the impact energy is also relatively insensitive to temperature (the lower curve of Figure 2.73); however, these materials are also very brittle, as reflected by their low impact energy values. And, of course, the characteristic ductile-to-brittle transition is represented by the middle curve of Figure 2.73. As noted, this behavior is typically found in low-strength steels that have the BCC crystal structure.

Most ceramics also experience a ductile-to-brittle transition. For ceramic materials, the transition occurs only at elevated temperatures, ordinarily in excess of 1000 °C (1850 °F). Furthermore, using fracture mechanical principles, an expression has been developed that relates critical stress for crack propagation (σ_c) and crack length (a) as

$$K_c = Y\sigma_c\sqrt{\pi a} \tag{2.17}$$

In this expression, K_c is the fracture toughness, a property that is a measure of a material's resistance to brittle fracture when a crack is present. Worth noting is that K_c has the unusual units of MPa $\sqrt{m}$ or psi $\sqrt{\text{in.}}$ (alternatively, ksi $\sqrt{\text{in.}}$). Furthermore, Y is a dimensionless parameter or function that depends on both crack and specimen sizes and geometries, as well as the manner of load application.

Relative to this Y parameter, for planar specimens containing cracks that are much shorter than the specimen width, Y has a value of approximately unity.

For relatively thin specimens, the value of K_c will depend on specimen thickness. However, when specimen thickness is much greater than the crack dimensions, K_c becomes independent of thickness; under these conditions a condition of plane strain exists. By plane strain we mean that when a load operates on a crack in a plate of infinite width, there is no strain component perpendicular to the front and back faces. The K_c value for this thick-specimen situation is known as the plane strain fracture toughness K_{Ic}; furthermore, it is also defined by

$$K_{Ic} = Y\sigma\sqrt{\pi a} \tag{2.18}$$

K_{Ic} is the fracture toughness cited for most situations. The I (i.e. Roman numeral "one") subscript for K_{Ic} denotes that the plane strain fracture toughness is for mode I crack displacement (opening or tensile mode).

Brittle materials, for which appreciable plastic deformation is not possible in front of an advancing crack, have low K_{Ic} values and are vulnerable to catastrophic failure. On the other hand, K_{Ic} values are relatively large for ductile materials. Fracture mechanics is especially useful in predicting catastrophic failure in materials having intermediate ductilities.

The plane strain fracture toughness K_{Ic} is a fundamental material property that depends on many factors, the most influential of which are temperature, strain rate, and microstructure. The magnitude of K_{Ic} diminishes with increasing strain rate and decreasing temperature. Furthermore, an enhancement in yield strength wrought by solid solution or dispersion additions or by strain hardening generally produces a corresponding decrease in K_{Ic}. Furthermore, K_{Ic} normally increases with reductions in grain size as composition and other microstructural variables are maintained constant.

For the static (low strain rate) situation, toughness may be ascertained from the results of a tensile stress–strain test. It is the area under the σ–ϵ curve up to the point of fracture. The units for toughness are the same as for resilience (i.e. energy per unit volume of material). For a material to be tough, it must display both strength and ductility; often, ductile materials are tougher than brittle ones.

Both plane strain fracture toughness and the impact tests determine the fracture properties of materials. The former is quantitative in nature, in that a specific property of the material is determined (i.e. K_{Ic}). The results of the impact tests, on the other hand, are more qualitative and are of little use for design purposes.

2.7 Questions and Problems

2.1 Describe the difference in atomic/molecular structure between crystalline and noncrystalline materials.

2.2 Draw unit cells for FCC, BCC, and HCP crystal structures.

2.3 Calculate the volume of an FCC unit cell in terms of the atomic radius R.

Answer: $V_c = 16R^3\sqrt{2}$.

2.4 Copper has an atomic radius of 0.128 nm, an FCC crystal structure, and an atomic weight of 63.5 g mol^{-1}. Compute its theoretical density and compare the answer with its measured density.

Answer: Theoretical $\rho = 8.89$ g cm^{-3}; measured $\rho = 8.94$ g cm^{-3}.

2.5 Draw a $[1\bar{1}0]$ direction within a cubic unit cell.

2.6 Indium has a tetragonal unit cell for which the a and c lattice parameters are 0.459 and 0.495 nm, respectively. (a) If the atomic packing factor and atomic radius are 0.693 and 0.1625 nm, respectively, determine the number of atoms in each unit cell. (b) The atomic weight of indium is 114.82 g mol^{-1}; compute its theoretical density.

Answer: (a) $n = 4$ atoms/unit cell; (b) $\rho = 7.31$ g cm^{-3}.

2.7 Distinguish between single crystals and polycrystalline materials.

2.8 Name the two types of solid solutions and provide a brief written definition and/or schematic sketch of each.

2.9 Describe the atomic structure within the vicinity of (a) a grain boundary and (b) a twin boundary.

2.10 Aluminum–lithium alloys have been developed by the aircraft industry to reduce the weight and improve the performance of its aircraft. A commercial aircraft skin material having a density of 2.47 g cm^{-3} is desired. Compute the required Li concentration (in wt%).

Answer: $C_{Li} = 2.38$ wt%.

2.11 What is the difference between the states of phase equilibrium and metastability?

2.12 Briefly describe the phenomenon of coring and why it occurs. Cite an undesirable consequence of coring.

2.13 Briefly explain why, upon solidification, an alloy of eutectic composition forms a microstructure consisting of alternating layers of the two solid phases.

2.14 What is the carbon concentration of an iron–carbon alloy for which the fraction of the total cementite is 0.10?

Answer: $C_o = 0.69$ wt% C.

2.15 A steel alloy is known to contain 93.65 wt% Fe, 6.0 wt% Mn, and 0.35 wt% C (a) What is the approximate eutectic temperature of this alloy? (b) What is the proeutectoid phase when this alloy is cooled to a temperature just below the eutectoid? (c) Compute the relative amounts of the proeutectoid phase and pearlite. Assume that there are no alterations in the positions of other phase boundaries with the addition of Mn.

Answer: (a) T(eutectoid) = 700 °C; (b) ferrite; (c) $W_\alpha = 0.20$, $W_p = 0.80$.

2.16 Cite two major differences between martensitic and pearlitic transformations.

2.17 In terms of heat treatment and the development of microstructure, what are two major limitations of the iron–iron carbide phase diagram?

2.18 Briefly describe the phenomena of superheating and supercooling. Why do these phenomena occur?

2.19 Briefly explain why ferrite and austenitic stainless steels are not heat-treatable.

2.20 Cite three reasons why ferrous alloys are used so extensively. Also cite three characteristics of ferrous alloys that limit their use.

2.21 What is the main difference between wrought and cast alloys?

2.22 How would you expect a decrease in the austenitic grain size to affect the hardenability of a steel alloy? Why?

2.23 Below is a list of metals and alloys:

Plain carbon steel	Magnesium	Tool steel
Brass	Gray cast iron	Tungsten
Platinum	Titanium alloy	Aluminum
Stainless steel	Cobalt alloy	Zinc

Select from this list the metal or alloy that is best suited for each of the following applications and cite at least one reason for your choice:

(a) The block of an internal combustion engine

(b) Condensing heat exchanger for steam

(c) Jet engine turbofan blades

(d) Drill bit

(e) As a pyrotechnic (i.e. in flares and firework)

(f) High temperature furnace elements to be used in oxidizing atmospheres

2.24 A piece of copper originally 305 mm (12 in.) long is pulled in tension with a stress of 276 MPa (40 000 psi). If the deformation is entirely elastic, what will be the resulting elongation?

Answer: $\Delta l = 0.77$ mm.

2.25 A cylindrical specimen of steel having an original diameter of 12.8 mm (0.505 in.) is tensile tested to fracture and found to have an engineering strength of 460 MPa (67 000 psi). If its cross-sectional diameter at fracture is 10.7 mm (0.422 in.), determine (a) the ductility in terms of percent reduction in area and (b) the true stress at fracture.

Answer: (a) % RA = 30%; (b) $\sigma = 660$ MPa (95 700 psi).

2.26 For the tensile deformation of a ductile cylindrical specimen, describe changes of the specimen profile to the point of fracture.

2.27 Define a slip system.

2.28 Briefly cite the differences between recovery and recrystallization processes.

2.29 Describe and explain solid solution strengthening for substitutional impurity atoms in terms of lattice strain interactions with dislocations.

2.30 Explain how grain boundaries impede dislocation motion and why a metal having small grains is stronger than another having large grains.

2.31 Cite three metallurgical/processing techniques that are employed to enhance the creep resistance of metal alloys.

2.32 Is it possible to produce an iron–carbon alloy of eutectoid composition that has a minimum hardness of 200 HB and a maximum ductility of 25% RA? If so, describe the continuous cooling heat treatment to which the alloy would be subjected to achieve these properties. If it is not possible, explain why.

Answer: Yes; coarse pearlite.

2.33 A cylindrical tube in a chemical plant is subjected to an excess internal pressure of 6 MN m^{-2}, which leads to a circumferential stress in the tube wall. The tube wall is required to withstand this stress at a temperature of 510 °C for nine years. A designer has specified tubes of 40 mm bore and 2 mm wall thickness made from a stainless alloy of iron with 15% by weight of chromium. The manufacturer's specification for this alloy gives the following information:

Temperature (°C)	618	640	660	683	707
Steady-state creep rate $\dot{\varepsilon}(s^{-1})$ for an applied tensile stress σ of 200 MN m^{-2}	1.0×10^{-7}	1.7×10^{-7}	4.3×10^{-7}	7.7×10^{-7}	2.0×10^{-7}

Over the present ranges of stress and temperature, the alloy can be considered to creep according to the equation

$$\dot{\varepsilon} = A\sigma^5 e^{-Q/RT}$$

where A and Q are constants, R is the universal gas constant, and T is the absolute temperature. Given that failure is imminent at a creep strain of 0.01 for the present alloy, comment on the safety of the design.

Answer: Strain over nine years = 0.00057; design safe.

2.34 An alloy tie bar in a chemical plant has been designed to withstand a stress, σ, of 25 MN m^{-2} at 620 °C. Creep tests carried out on specimens of the alloy under these conditions indicated a steady-state creep rate, $\dot{\varepsilon}$, of 3.1×10^{-12} s^{-1}. In service it was found that for 30% of the running time, the stress and temperature increased to 30 MN m^{-2} and 650 °C. Calculate the average creep rate under service conditions. It may be assumed that the alloy creeps according to the equation

$$\dot{\varepsilon} = A\sigma^5 e^{-Q/RT}$$

where A and Q are constants, R is the universal gas constant, and T is the absolute temperature. Q has a value of 160 kJ mol^{-1}.

Answer: 6.82×10^{-12} s^{-1}.

2.35 The window glass in old buildings has an uneven surface, with features that look like flow marks. The common explanation is that the glass has suffered creep deformation over the years under its own weight. Explain why this scenario is complete rubbish (why do you think the glass does appear to have "flow marks?").

2.36 Why do bolted joints in pressure vessels operating at high temperature have to be retorqued at regular intervals?

2.37 Why are creep-rupture figures useful when specifying materials for high temperature service?

2.38 Structural steelwork in high-rise buildings is generally protected against fire by a thick coating of refractory material even though a fire would not melt the steel. Explain.

References

Ashby, M.F. and Jones, D.P.H. (2005). *Engineering Materials 2: An Introduction to Microstructures, Processing and Design*, 3e. Woburn: Butterworth-Heinemann.

Brandon, D. and Kaplan, W.D. (1999). *Microstructured Characterization of Materials*. New York: Wiley.

Buerger, M.J. (1956). *Elementary Crystallography*. New York: Wiley.

Chipman, J. (1972). Thermodynamics and phase diagram of the Fe-C system. *Metall. Trans.* 3: 55–64.

Coakham, J.W. and Evans, W. (1970a). An introduction to steel. *Sch. Sci. Rev.* 177: 326–338.

Coakham, J.W. and Evans, W. (1970b). Phase diagrams and microstructures of some simple alloys. *Sch. Sci. Rev.* 177: 830–844.

Dieter, G.E. (1986). *Mechanical Metallurgy*, 3e. New York: McGraw-Hill.

Honeycombe (1982). *Steels: Microstructure and Properties (Metallurgy and Materials Science)*. American Society for Metals.

Hume-Rothery, W., Smallman, R.E., and Haworth, C.W. (1969). *Elements of Structure of Metallurgy*, Monograph and Report Series, No. 1. London: Institute of Metals.

Massalski, T.B., Okamoto, P.R., Subramanian, P.R., and Kacjrzak, L. (eds.) (1990). *Binary Phase Diagrams*, 2e. Materials Park, OH: ASM International.

Smallman, R.E. (1963). *Modern Physical Metallurgy*. London: Butterworth.

Van Bueren, H.G. (1960). *Imperfections in Crystals*. Amsterdam: North-Holland.

Weertman, J. and Weertman, J.R. (1992). *Elementary Dislocation Theory*. New York: Oxford University Press.

Wulpi, D.J. (1999). *Understanding How Components Fail*, 2e. Materials Park, OH: ASM International.

Further Reading

Cottrell, R.H. (1967). *An Introduction to Metallurgy*. London: Edward Arnold.

Courtney, T.H. (2000). *Mechanical Behaviour of Materials*, 2e. Buss Ridge, IL: McGraw-Hill Higher Education.

Cullity, B.D. and Stock, S.R. (2001). *Elements of X-Ray Diffraction*, 3e. Upper Saddle River, NJ: Prentice Hall.

Davies, D.E. (1966). *Practical Experimental Metallurgy*. London: Elsevier.

Evans, U.R. (1951). Stress corrosion: its relation to other types of corrosion. *Corrosion* 7: 238.

Henker, D.P. and Pense, A.W. (2002). *Structures and Properties of Engineering Materials*, 5e. New York: McGraw Hill.

Hertzberg, R.H. (1996). *Deformation and Fracture Mechanics of Engineering Materials*, 4e. New York: Wiley.

Okamoto, H. (2000). *Desk Handbook: Phase Diagrams for Binary Alloys*. Materials Park, OH: ASM International.

Popplewell, J.M., Procter, R.P.M., and Ford, J.A. (1972). On the relation between stress-relief annealing, ordering and stress-corrosion cracking susceptibility in three copper alloys. *Corros. Sci.* 12: 193.

Porter, D.A. and Easterling, K.E. (1992). *Phase Transformations in Metals and Alloys*. New York: Chapman and Hall.

Richardson, J.A. and Wood, G.C. (1970). A study of the pitting corrosion of Al byscanning electron microscopy. *Corros. Sci.* 10: 313.

White, M.A. (1999). *Properties of Materials*. New York: Oxford University Press.

Chapter 3

High Temperature Equilibria

3.1 Introduction

From the physical chemist's point of view, a number of factors are contributory to the phenomenon of high temperature corrosion. While the reaction kinetics will be influenced by factors such as the temperature, pressure, concentration, and mobility of the solid, liquid, and gaseous reactants, solvent power and reactivity of molten phases, and viscosity of melts and their capillary effects, the tendency for a reaction to occur is measured in terms of the stability of the reactants and the products. It would be difficult to conceive an experimental procedure that would isolate the individual effects of all these factors. For this reason, the following thermochemical and electrochemical procedures have been adopted to the problem of high temperature corrosion to provide a means of assisting in the rationalization of experimental data. These procedures provide a means of analyzing the chemical reactions that may be involved in the system under study. While the analysis described in this chapter concerns only the thermodynamics of high temperature corrosion, the experimental data reported in the literature must be considered in terms of all of the physicochemical factors.

3.2 Thermochemical Analysis

An important tool in the analysis of high temperature corrosion problems is equilibrium thermochemistry that, although not predictive of kinetics, allows to ascertain which reaction products are possible, whether or not significant evaporation or condensation of a given species is possible, the conditions under which a given reaction product can react with a condensed deposit. This standard method of thermochemical analysis is commonly used in metallurgical equilibria involving reactions between a gas and a solid as a function of temperature. The most important of these reactions is oxidation, which is an ambivalent term, i.e. it involves the formation of oxides (strict oxidation), sulfides (sulfidation), carbides (carburization), nitrides (nitridation), and halides (halogenation). The complexity of the oxidation phenomena usually dictates that the thermochemical analysis be represented in graphical form. The types of thermochemical diagrams most often used in oxidation research are:

1. Standard free energy of formation versus temperature diagrams, which allow the thermodynamic data for a given class of compounds, oxides, sulfides, carbides, etc. to be represented in a compact form (Ancy-Moret 1973; Ellingham 1944; MacKowiak 1966; Richardson and Jeffes 1948; Shatynski 1977, 1979).
2. Gibbs free energy versus composition diagrams and activity versus composition diagrams, which are used for describing thermodynamics of solutions (Aaranson 1999; Arper 1970; Darken and Gurry 1953; Gaskell 1995).
3. Two-dimensional isothermal stability diagrams, which map the stable phases in systems involving one metallic and two reactive nonmetallic components (Giggins and Pettit 1980; Jansson and Foroulis 1973; Rapp 1983).
4. Vapor species diagrams, which allow the vapor pressures of compounds to be presented as a function of conventional variables such as partial pressure of a gaseous component (Belton and Worrel 1970; Chase et al. 1975; Gulbransen and Meier 1979).
5. Two-dimensional isothermal stability diagrams, which map the stable phases in systems involving two metallic components and one reactive nonmetallic component (Jacob et al. 1979; Pelton and Schmalzried 1973).
6. Phase stability diagrams for two or more metals and two or more nonmetallic components (Barralis and Maeder 1997).

The basic concepts pertinent to the construction and analysis of those thermochemical diagrams are partial Gibbs free energy, chemical potential, free energy of mixing, Gibbs–Duhem equation, activity, Raoult's law, Henry's

High Temperature Corrosion: Fundamentals and Engineering, First Edition. César A. C. Sequeira.
© 2019 John Wiley & Sons, Inc. Published 2019 by John Wiley & Sons, Inc.

law, equilibrium state, variance (number of degrees of freedom of a system), pressure dependence of activity in the case of equilibrium between a condensed solution and a gas phase, and types of solution (ideal, dilute, concentrated). These concepts are described in numerous thermodynamics books (Gaskell 1995; Kubaschewski and Alcock 1979; Schick 1966; Swalin 1972).

Determination of the conditions under which a given corrosion product is likely to form is often required, e.g. in selective oxidation of alloys. In this regard, Ellingham diagrams, i.e. plots of the standard free energy of formation (ΔG°) versus temperature for compounds of a type, e.g. oxides, sulfides, carbides, etc., are useful in that they allow comparison of the relative stabilities of each compound. In the next subsection, these free energy/temperature diagrams will be discussed, and then our considerations on the thermodynamics of high temperature oxidation will move to the other five types of diagrams listed above.

3.2.1 Ellingham Diagrams

The Ellingham plot is a graphical representation of the standard free energies of oxidation of pure metals versus temperature. The most useful form of representation is to express the quantities in terms of 1 mol of the oxidizing species:

$$M + O_2 = MO_2 \tag{3.1}$$

At a given temperature T, the standard free energy ΔG°_T of the reaction is

$$\Delta G^\circ_T = \Delta H^\circ_T - T\Delta S^\circ_T \tag{3.2}$$

where ΔH°_T and ΔS°_T are the standard enthalpy and entropy of the reaction, respectively. At equilibrium, we can write:

$$\Delta G^\circ_T = -RT \ln K = -RT \ln \left({}^{a_{MO_2}}/_{a_M} \cdot\ p_{O_2} \right) \tag{3.3}$$

Assuming that the oxide MO_2 is stoichiometric and that there is no miscibility between metal and oxide, the activities of M and MO_2 are taken as unity. Thus

$$\Delta G^\circ_T = RT \ln p_{O_2} \tag{3.4}$$

The oxygen partial pressure at which the metal and oxide coexist is the dissociation pressure of the oxide. In Ellingham diagrams, ΔG°_T (or $RT \ln p_{O_2}$) is plotted versus temperature for the compounds of a given type, e.g. oxides, sulfides, chlorides, carbides, etc. The standard enthalpy and entropy of the formation of the compounds are also considered to be independent of temperature over large temperature ranges (the "Ellingham approximation"). For these conditions,

$$\Delta G^\circ_T = \Delta H^\circ_{298} - T\Delta S^\circ_{298} \tag{3.5}$$

Accordingly, the ΔG°_T values fall on straight lines in the diagram although changes in the slope of the lines occur in the diagram corresponding to the phase changes of the metal or the compound. Figure 3.1 is such a plot for many simple oxides. The values of ΔG°_T are expressed as kJ mol^{-1} O_2, so the stabilities of various oxides may be compared directly, i.e. the lower position of the line on the diagram, the more stable the oxide.

The values of p_{O_2} may be obtained directly from the oxygen monograph on the diagram by drawing a straight line from the origin marked O through the free energy line at the temperature of interest and reading the oxygen partial pressure from its intersection with the scale at the right side labeled p_{O_2}. Values for the pressure ratio H_2/H_2O for equilibrium between a given metal and oxide may be obtained by drawing a similar line from the point marked H to the scale labeled H_2/H_2O ratio, and values for the equilibrium CO/CO_2 ratio may be obtained by drawing a line from point C to the scale CO/CO_2 ratio.

Thus, it is possible to obtain the oxygen potential of the environment in terms of $p_{O_2}, p_{H_2}/p_{H_2O}, p_{CO}/p_{CO_2}$ and the oxygen partial pressure in equilibrium with the oxide of interest from Figure 3.1 to determine whether or not the oxide is likely to form thermodynamically.

Figure 3.1 also illustrates the relative stability of various oxides. The most stable oxides have the largest negative values of ΔG°_T, or the lowest values of p_{O_2}, or the highest values of p_{H_2}/p_{H_2O} and p_{CO}/p_{CO_2}. Table 3.1 lists the coexistence equations, temperature ranges, and standard energy changes that can be used to construct Ellingham diagrams for oxides (Gaskell 1995).

Similar free energy diagrams, which can be interpreted in exactly the same way, have been constructed for sulfides (Richardson and Jeffes 1952), carbides (Richardson and Jeffes 1953), nitrides (Pearson and Ende 1953), and chlorides (Villa 1950) (Figures 3.2–3.5).

It is clear from Figure 3.1 that oxides of iron, nickel, and cobalt, which are the alloy bases for the majority of engineering alloys, are significantly less stable than the oxides of some solutes (e.g. chromium, aluminum, silicon, etc.) in engineering alloys. When one of these solute elements is added to iron, nickel, or cobalt, internal oxidation of the solute is expected to occur if the concentration of the solute is relatively low. As the solute concentration increases to a sufficiently high level, the oxidation of the solute will be changed from internal oxidation to external oxidation, resulting in an oxide scale that protects the alloy from rapid oxidation. This process is known as *selective oxidation*. The majority of iron-, nickel-, and cobalt-based alloys rely on selective oxidation of chromium to form a Cr_2O_3 scale for oxidation resistance. Some high temperature alloys use aluminum to form an Al_2O_3 scale for oxidation resistance. Most oxides exhibit high melting

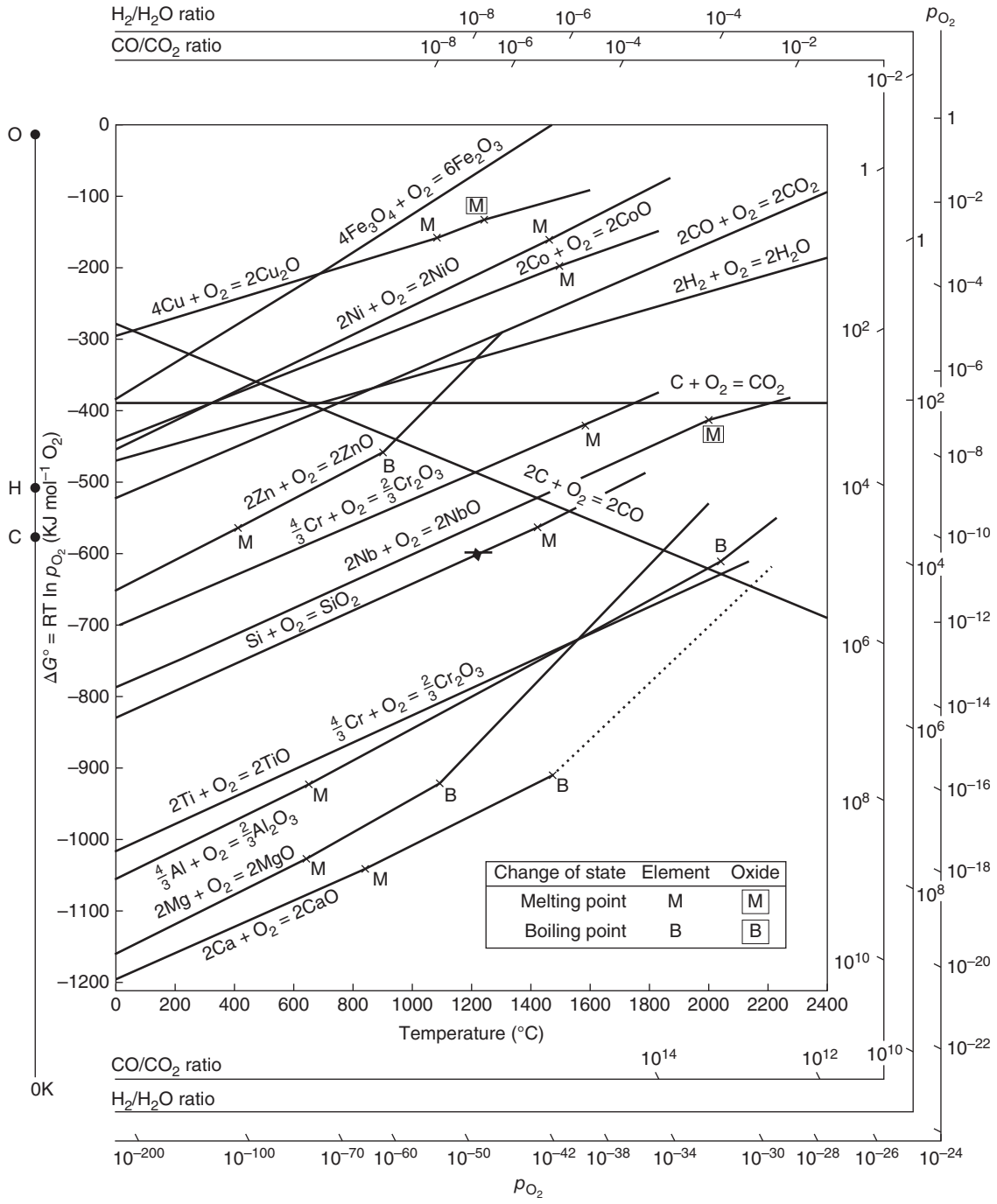


Figure 3.1 Standard free energy of the formation of selected oxides as a function of temperature (Richardson and Jeffes 1948).

points and remain in a solid state for the temperature range in which the alloys are used.

Oxides of molybdenum (MoO_3) and vanadium (V_2O_5), however, exhibit very low melting points. Vanadium (V), which is a strong carbide former, is often used in alloy steels for increasing the strength of the material. However, the amount typically used is quite small and is not likely to form V_2O_5. Molybdenum (Mo) is also a strong carbide former and is used in a small amount to strengthen low-alloy steels (e.g. Cr–Mo steels). It is unlikely that these steels will be affected by MoO_3 oxidation problems.

Industrial gaseous atmospheres may, in addition to air, consist of complex gases (CO_2, H_2O, SO_2, SO_3, etc.) or mixtures of several gases or contain the gaseous products of corrosion or of thermal decomposition of corrosion products (Pettit 1967; Rocabois et al. 1966; Yazawa

Table 3.1 Thermodynamic data for reactions involving oxygen

Temperature range (K)	Coexistence equation (oxidation reaction)	Standard free energy change (J)
900–1154	$Pd + 0.5O_2 = PdO$	$-114\,200 + 100\,T$ (°K)
884–1126	$2Mn_3O_4 + 0.5O_2 = 3Mn_2O_3$	$-113\,360 + 92.0\,T$
298–1300	$3CoO + 0.5O_2 = Co_3O_4$	$-183\,200 + 148\,T$
892–1302	$CuO_2 + 0.5O_2 = 2CuO$	$-130\,930 + 94.5\,T$
1396–1723	$1.5UO_2 + 0.5O_2 = 0.5U_3O_8$	$-166\,900 + 84\,T$
878–1393	$U_4O_9 + 0.5O_2 = 4/3\ U_3O_{7.5}$	$-164\,400 + 82\,T$
967–1373	$2Fe_3O_4 + 0.5O_2 = 3Fe_2O_3$	$-246\,800 + 141.8\,T$
1489–1593	$2Cu + 0.5O_2 = Cu_2O$	$-166\,900 + 43.5\,T$
1356–1489	$2Cu + 0.5O_2 = Cu_2O$	$-190\,300 + 89.5\,T$
924–1328	$2Cu + 0.5O_2 = Cu_2O$	$-166\,900 + 71.1\,T$
992–1393	$3\,MnO + 0.5O_2 = Mn_3O_4$	$-222\,540 + 111\,T$
1160–1371	$Pb + 0.5O_2 = PbO$	$-190\,580 + 74.9\,T$
772–1160	$Pb + 0.5O_2 = PbO$	$-215\,000 + 96.0\,T$
911–1376	$Ni + 0.5O_2 = NiO$	$-233\,580 + 84.9\,T$
1173–1373	$Co + 0.5O_2 = CoO$	$-235\,900 + 71.5\,T$
973–1273	$10WO_{2.90} + 0.5O_2 = 10WO_3$	$-279\,400 + 112\,T$
973–1273	$10WO_{2.72} + O_2 = 10WO_{2.90}$	$-284\,000 + 101\,T$
973–1273	$1.39WO_2 + 0.5O_2 = 1.30WO_{2.72}$	$-249\,310 + 62.7\,T$
973–1273	$0.5\,W + 0.5O_2 = 0.5WO_2$	$-287\,400 + 84.9\,T$
949–1273	$3FeO + 0.5O_2 = Fe_3O_4$	$-311\,600 + 123\,T$
770–980	$Sn + 0.5O_2 = SnO_2$	$-293\,230 + 108\,T$
903–1540	$Fe + 0.5O_2 = FeO$	$-263\,300 + 64.8\,T$
1025–1325	$0.5Mo + 0.5O_2 = 0.5MoO_2$	$-287\,600 + 83{,}7\,T$
1050–1300	$2NbO_2 + 0.5O_2 = Nb_2O_5$	$-313\,520 + 78.2\,T$
693–1181	$Zn + 0.5O_2 = ZnO$	$-355\,890 + 107.5\,T$
1300–1600	$0.66Cr + 0.5O_2 = 0.33Cr_2O_3$	$-371\,870 + 83.7\,T$
1050–1300	$NbO + 0.5O_2 = NbO_2$	$-360\,160 + 72.4\,T$
923–1273	$Mn + 0.5O_2 = MnO$	$-388\,770 + 76.3\,T$
1539–1823	$Mn + 0.5O_2 = MnO$	$-409\,500 + 89.5\,T$
1073–1823	$0.4Ta + 0.5O_2 = 0.2Ta_2O_5$	$-402\,400 + 82.4\,T$
1050–1300	$Nb + 0.5O_2 = NbO$	$-420\,000 + 89.5\,T$
298–1400	$0.5\,U + 0.5O_2 = 0.5UO_2$	$-539\,600 + 83.7\,T$
1380–2500	$Mg(v) + 0.5O_2 = MgO$	$-759\,600–30.83\,T \log T + 317\,T$
923–1380	$Mg(l) + 0.5O_2 = MgO$	$-608\,200–1.00\,T \log T + 105\,T$
1124–1760	$Ca + 0.5O_2 = CaO$	$-642\,500 + 107\,T$
1760–2500	$Ca(v) + 0.5O_2 = CaO$	$-795\,200 + 195\,T$

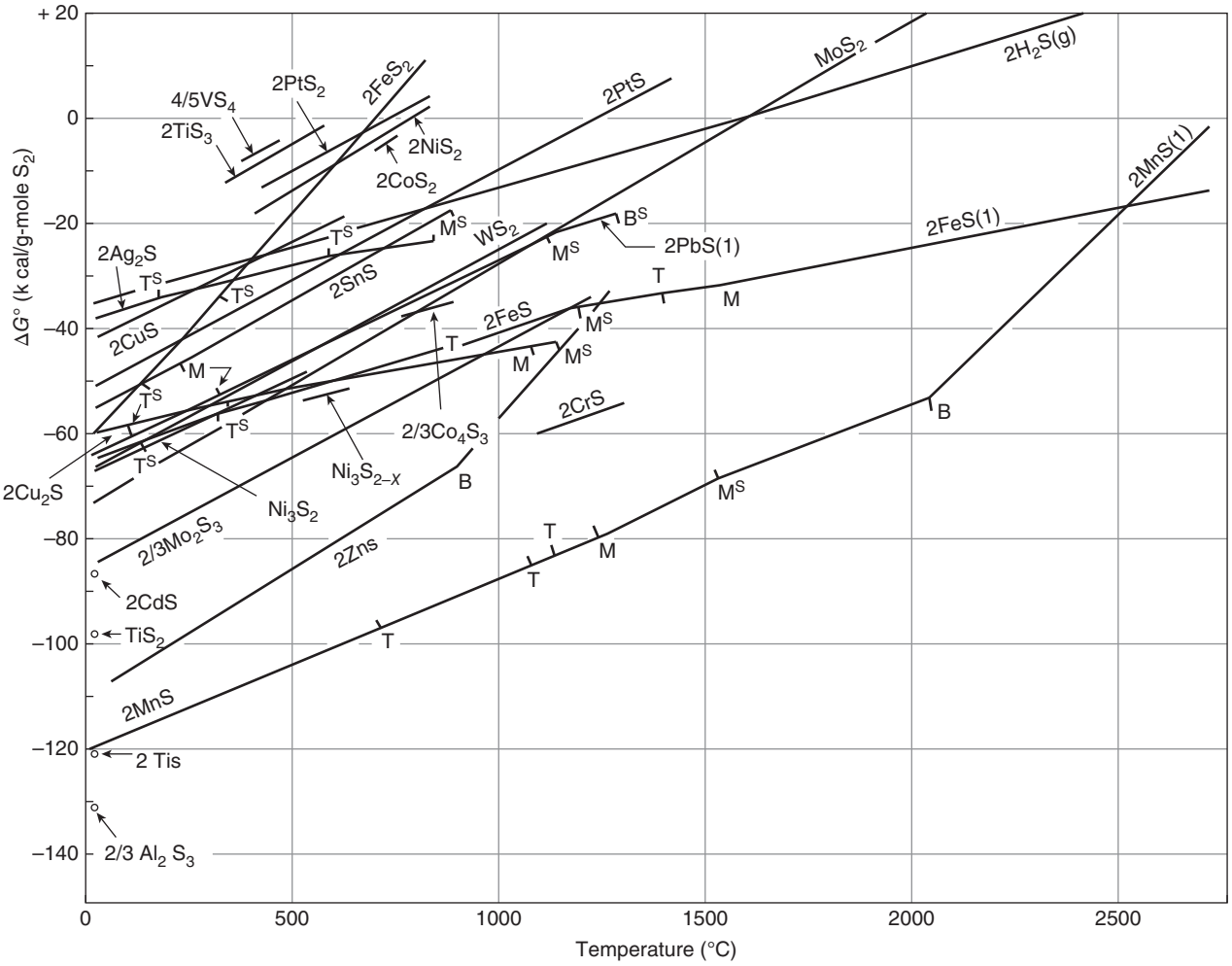
1979). Despite the complexity of corrosion phenomena, the problem can be solved, in some cases, using simple thermodynamic calculations from simplifying hypotheses. In other situations, involving numerous components, it is necessary to use a software that minimizes the total free energy of the system (Eriksson 1975; Eriksson and Hack 1990; Königsberger and Eriksson 1995; Reynolds 1986; Sundman et al. 1985).

3.2.2 Integral Free Energy–Concentration Diagrams

This type of diagram may be useful for the quantitative thermodynamic assessment of gas–metal systems, which form nonstoichiometric condensed phases and which are sensitive to relatively small stresses in the condensed phases or small changes in chemical potentials, in the gaseous phase, and in other physical or chemical effects that can be expressed in terms of energy (e.g. irradiation, vibrations, gravity, grain size, penetrating liquids, variation of surface tension, magnetic effects, etc.).

In this subsection it is intended first to outline the theoretical basis of these diagrams by considering a simple metal-A–gas-B binary system followed by a quantitative treatment of a hypothetical metal M (at. wt 50) and oxygen binary system. Finally, the application of these diagrams will be illustrated using the Ti–C, Fe(s)–Zn(v), and Fe(s)–Zn(l) systems.

The key to an efficient use of these diagrams is the understanding of the properties of a common tangent to two



General reaction is $2x/yM(s, l, or g) + S_2(g) \rightarrow 2/y\ MxSy(s, l, or g)$
The reactions for formation of the following compounds are:

CoS_2 $2CoS(s) + S_2(g) \rightarrow 2CoS_2(s)$
FeS_2 $2FeS(s) + S_2(g) \rightarrow 2FeS_2(s)$
NiS_2 $2NiS(s) + S_2(g) \rightarrow 2NiS_2(s)$
PtS_2 $2PtS(s) + S_2(g) \rightarrow 2PtS_2(s)$
TiS_3 $2TiS_2(s) + S_2(g) \rightarrow 2TiS_3(s)$
VS_4 $2/5V_2S_3(s) + S_2(g) \rightarrow 4/5\ VS_4(s)$

Courtesy Addison - Wesley Publ. Co.
and Pergamon Press.

T = Transition point of metal
T^s = Transition point of sulfide
M = Melting point of metal
M^s = Melting point of sulfide
B = Boiling point of metal
B^s = Boiling point of sulfide

Figure 3.2 Free energy of the formation of sulfides (Richardson and Jeffes 1952).

or more free energy–concentration curves and in particular the information that may be obtained from the so-called *tangency rule*. It is therefore intended to develop the tangency rule using a simple isothermal binary system of a pure solid metal A and a pure gas B at 1 atm pressure having two nonstoichiometric solid compounds denoted by phase I and phase II. Figure 3.6 shows ΔG_m-concentration diagram for this system. The vertical axis y represents the isothermal free energy changes (ΔG_m) that are obtained when one mole of a mixture having a given composition is formed. The horizontal axis gives the composition of the mixture, in mole fraction, of the gas B. On the left-hand side of the scale, we have $X_A = 1$ (i.e. pure metal) and the concentration of the gas $X_B = 0$, whereas on the right-hand side of the scale, $X_A = 0$ and $X_B = 1$ (i.e. pure gas B at 1 atm pressure) since $X_A + X_B = 1$. The integral free energy changes with concentration for phases I and II are shown as ΔG_I and ΔG_{II} curves, respectively.

Using the diagram it is now possible to predict quantitatively the equilibrium composition of the two condensed phases when in contact with each other, i.e. when growing as solid layers on the surface of the metal A. According to

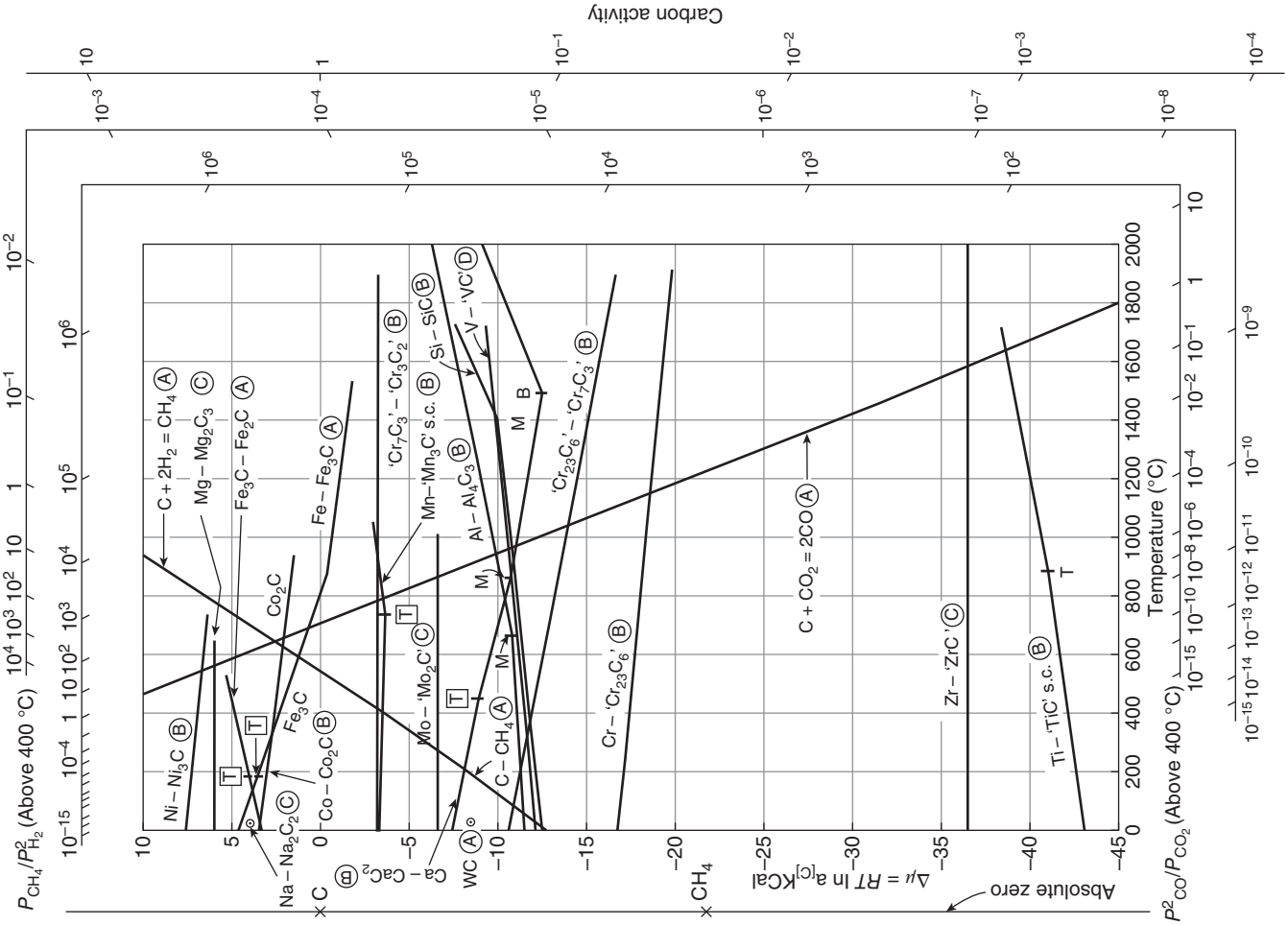


Figure 3.3 Free energy of the formation of carbides (Richardson and Jeffes 1953).

Gibbs (1961), in a two-component system any condensed phases at equilibrium will have to satisfy simultaneously two energy conditions, namely, (i) the mixture of the phases will acquire the lowest overall free energy and (ii) the chemical potential (or partial molal free energy) of a particular component must be the same in all phases that are in contact with each other. These two conditions are now sufficient to predict the exact composition of the condensed phases at equilibrium with each other.

Gibbs' definition of the *chemical potential* of the gaseous component B in a mixture at constant temperature T and pressure p is given by

$$\left(\frac{\partial \Delta G_{\mathrm{m}}}{\partial X_B}\right)_{T,p} = (\Delta \mu_{\mathrm{B}})_{T,p} = (\Delta \overline{G}_{\mathrm{B}})_{T,p} \qquad (3.6)$$

Therefore, this partial differential represents mathematically the tangent to any ΔG-concentration curve. In our case, for a common tangent to ΔG_{I} and ΔG_{II}, we must have not only a common slope

$$\frac{\mathrm{d}y_1}{\mathrm{d}x_1} = \frac{\mathrm{d}y_2}{\mathrm{d}x_2} = \mathrm{m} \qquad (3.7)$$

but also a common intercept on the ΔG_{m} axis. Thus, the equation for a common slope and intercept in Figure 3.6 must be of the form

$$y_1 - y_2 = \mathrm{m}\,(x_1 - x_2) \qquad (3.8)$$

It can be shown that the intercept of this tangent on the y-axis where $X_{\mathrm{B}} = 1$ (pure gas B at 1 atm pressure) gives the numerical value of $\Delta \mu_{\mathrm{B}} = \Delta \overline{G}_{\mathrm{B}}$ for 1 mol of B dissolved in a mixture of AB having a composition of the point of contact of the common tangent to any ΔG_{m}-concentration curve. Similarly, the intercept of the same tangent on the y-axis at $X_{\mathrm{A}} = 1$ (pure metal) gives the numerical value of $\Delta \mu_{\mathrm{A}} = \Delta \overline{G}_{\mathrm{A}}$, i.e. the chemical potential (or partial molal free energy) of 1 mol of metal A dissolved in the phase having the composition given by the point of contact of the tangent to the ΔG-concentration curve.

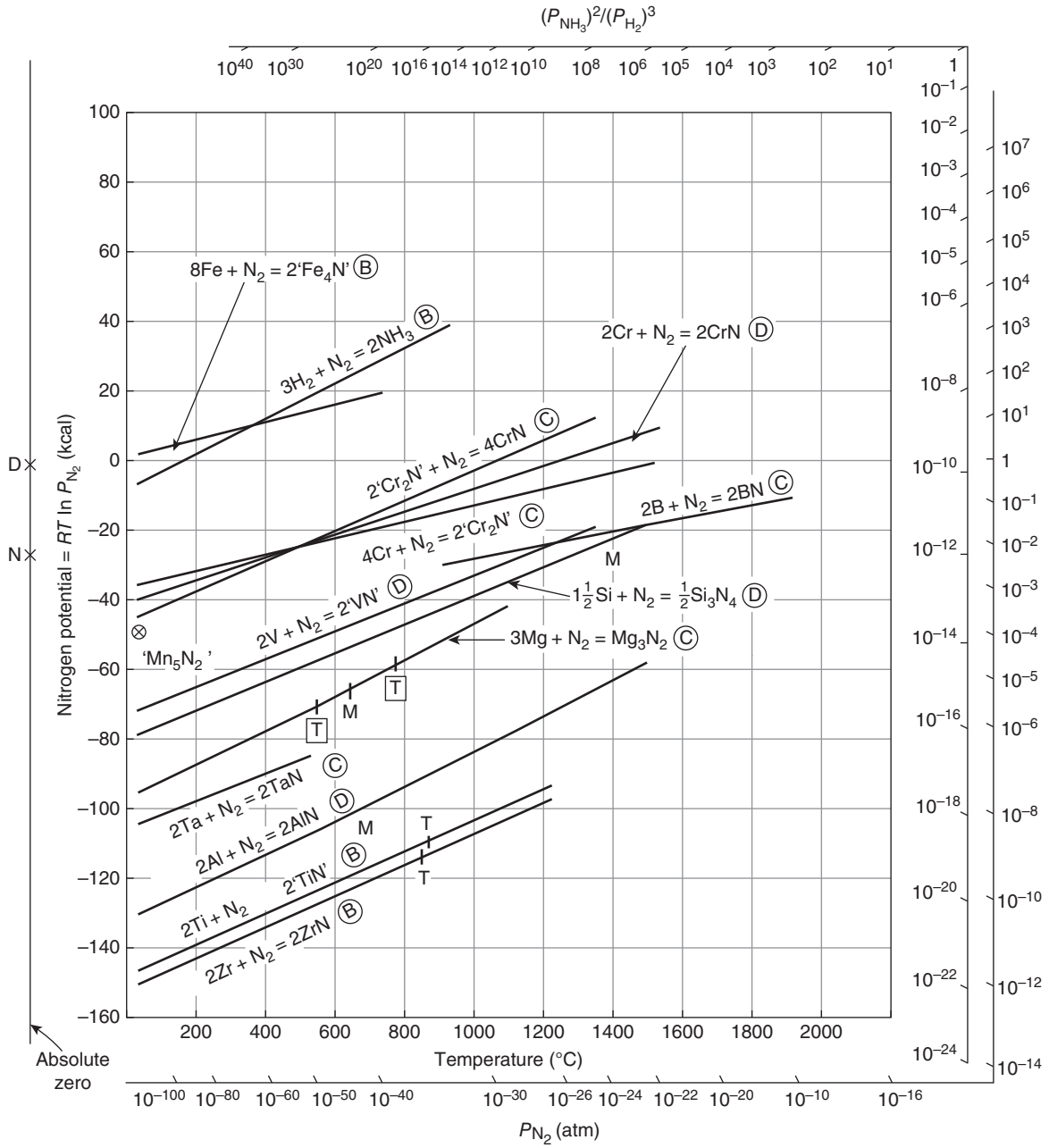


Figure 3.4 Free energy of the formation of nitrides (Pearson and Ende 1953).

In Figure 3.6, using the common tangent construction, the equilibrium compositions of phase I and phase II at their boundary are found, from the points of contact, to be $X_B = X_1$ and $X_B = X_2$, respectively.

Figure 3.7 further illustrates the above points and their relationship to the conventional phase diagram for a hypothetical binary eutectic system, clearly explained by Hillert in Aaranson's book (1999).

Figure 3.8 shows a more complicated isothermal, binary system consisting of metal M and gaseous oxygen O_2 at a temperature of 1000 K. The free energy–concentration diagram for the system shows four condensed phases, the first being a solid solution of oxygen in the metal, followed by nonstoichiometric condensed phases of nominal compositions M_2O^x, MO^x, and MO_2^x. Using the tangency rule, it will be shown that each of these oxides must have a region of homogeneity over a range of composition in which it will be the sole stable phase. In Figure 3.8, the vertical axis represents the isothermal free energy change associated with the

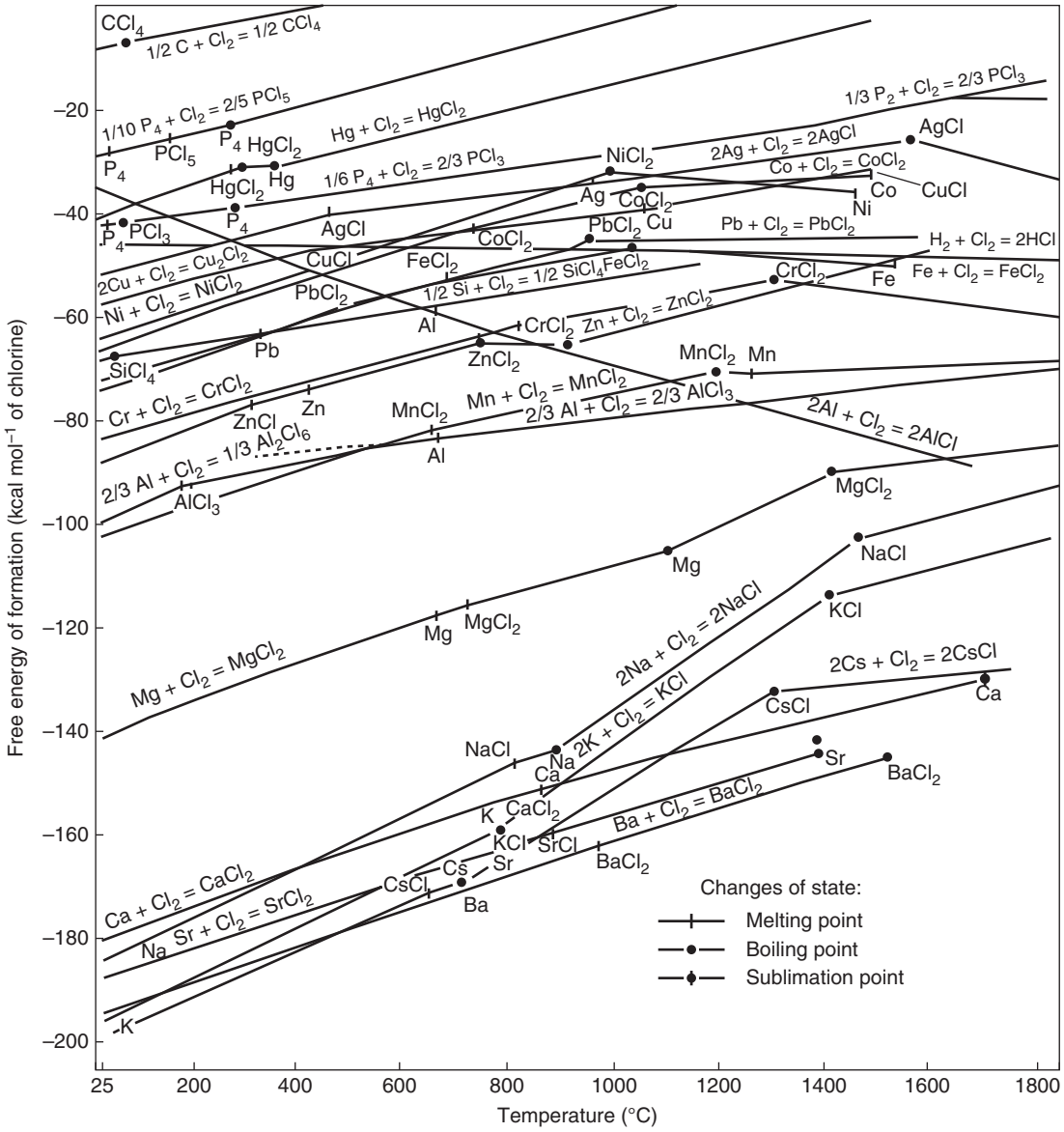


Figure 3.5 Free energy of the formation of chlorides (Villa 1950).

formation of one mole of the M–O mixture of a given composition, expressed in mole fractions of the metal (X_M) and oxygen (X_O) shown along the horizontal axis.

When a pure solid metal M is in contact with a gas containing oxygen, at first a solid solution of oxygen in the metal is formed. The Gibbs free energy of mixing (ΔG_m) for the corresponding concentrations of oxygen in the solid solution is shown by the curves a–b–c. Note that the section a–b of the curve is the only part that can be determined experimentally, whereas the section b–c, representing a supersaturated solution, is either extrapolated from the a–b section or calculated theoretically. The values of the free energies of mixing, producing any possible phase, can now be calculated using computer techniques in conjunction with the appropriate thermodynamic data coupled with the relevant phase diagram. It is worth noting that there are already a number of powerful programs that, in conjunction with stored thermodynamic data, can be used to calculate theoretically these curves for an ever-increasing number of binary, ternary, and even quaternary systems.

Once the solid solution is produced, a surface layer of M_2O^x oxide phase will be formed, having an excess of the metal. This new phase has a separate $\Delta G_{M_2O^x}$-concentration curve shown in Figure 3.8 by d–e–f–g. This curve is followed by that of ΔG_{MO^x} phase shown by h–i–j–k. Finally, a layer of MO_2^x will be formed, and its free energy composition curve is shown by l–m–n–o. Applying now the

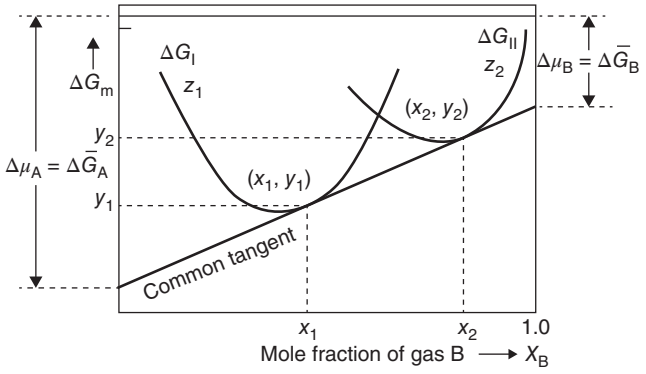


Figure 3.6 The graphical method for obtaining equilibrium compositions for free energy versus composition curves at a given temperature. Points of contact give equilibrium compositions X_1 for phase I and X_2 for phase II.

tangency rule, by drawing common tangents to neighboring ΔG_m-concentration curves, the range of stability of the oxides is determined. As the chemical potential of the oxygen $\Delta\mu_O$ or $\Delta\overline{G}_O$ is fixed by the oxygen pressure in the atmosphere, the equilibrium composition of the MO_2^x oxide layer exposed to the atmosphere is obtained by drawing a tangent to the $\Delta G_{MO_2^x}$ curve with an intercept on the ΔG_m axis when $X_O = 1$ equal to the value of the oxygen chemical potential of the atmosphere (i.e. in our case $= 1/2RT \ln p_{O_2}$ where p_{O_2} is the oxygen pressure in the atmosphere – here 1 atm and pure O_2, therefore, $\Delta\mu_O = 0$). Thus, a tangent from the point $\Delta G_O = 0$ to $\Delta G_{MO_2^x}$ gives the equilibrium composition. The mole fraction of oxygen in the MO_2^x can now be read off the composition axis. The point of contact, *n*, gives the oxygen equilibrium composition $X_O = 0.7$ in MnO_2^x. The mole fraction of the metal M is $X_M = 1 - X_O = 0.3$. Therefore, the equilibrium composition of the outermost oxide layer will be $M_{0.3}O_{0.7}$ with respect to an atmosphere consisting of oxygen at 1 atm pressure.

The common tangent between $\Delta G_{MO_2^x}$ and ΔG_{MO^x} gives points of contact for MO_2^x $X_O = 0.675$ and $X_M = 0.325$

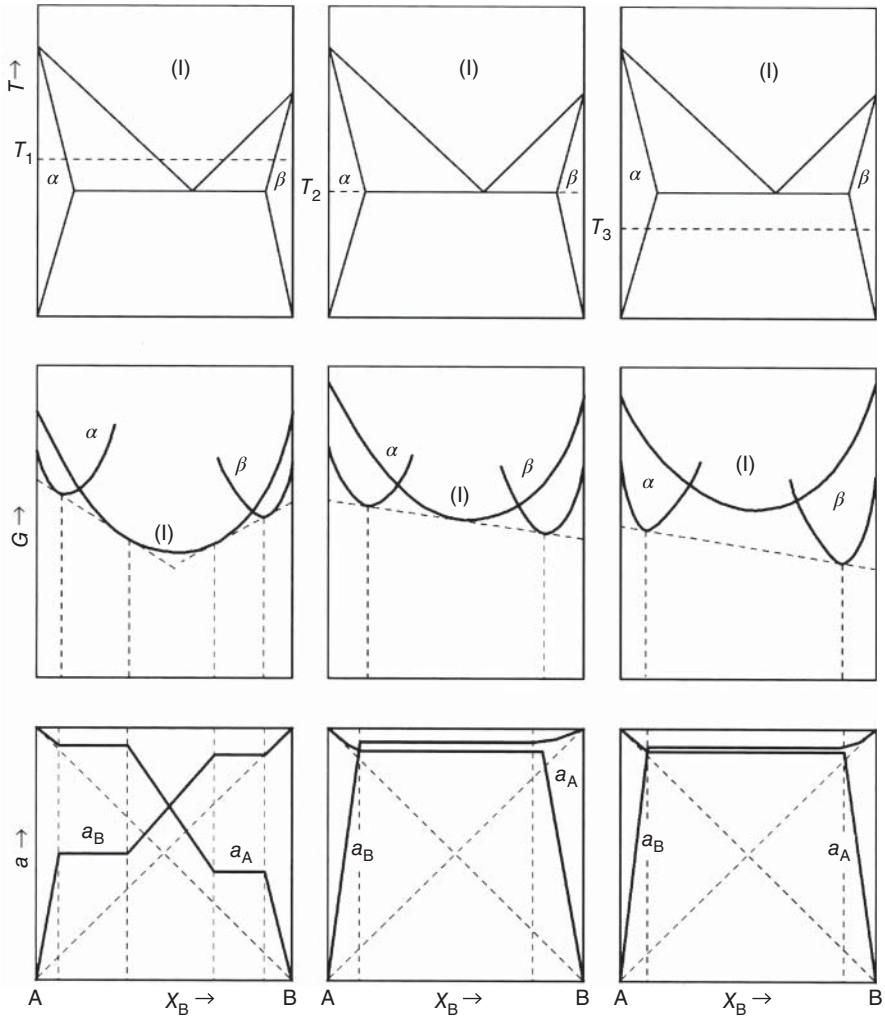


Figure 3.7 Free energy versus composition and activity diagrams for a hypothetical eutectic system (Birks et al. 2006).

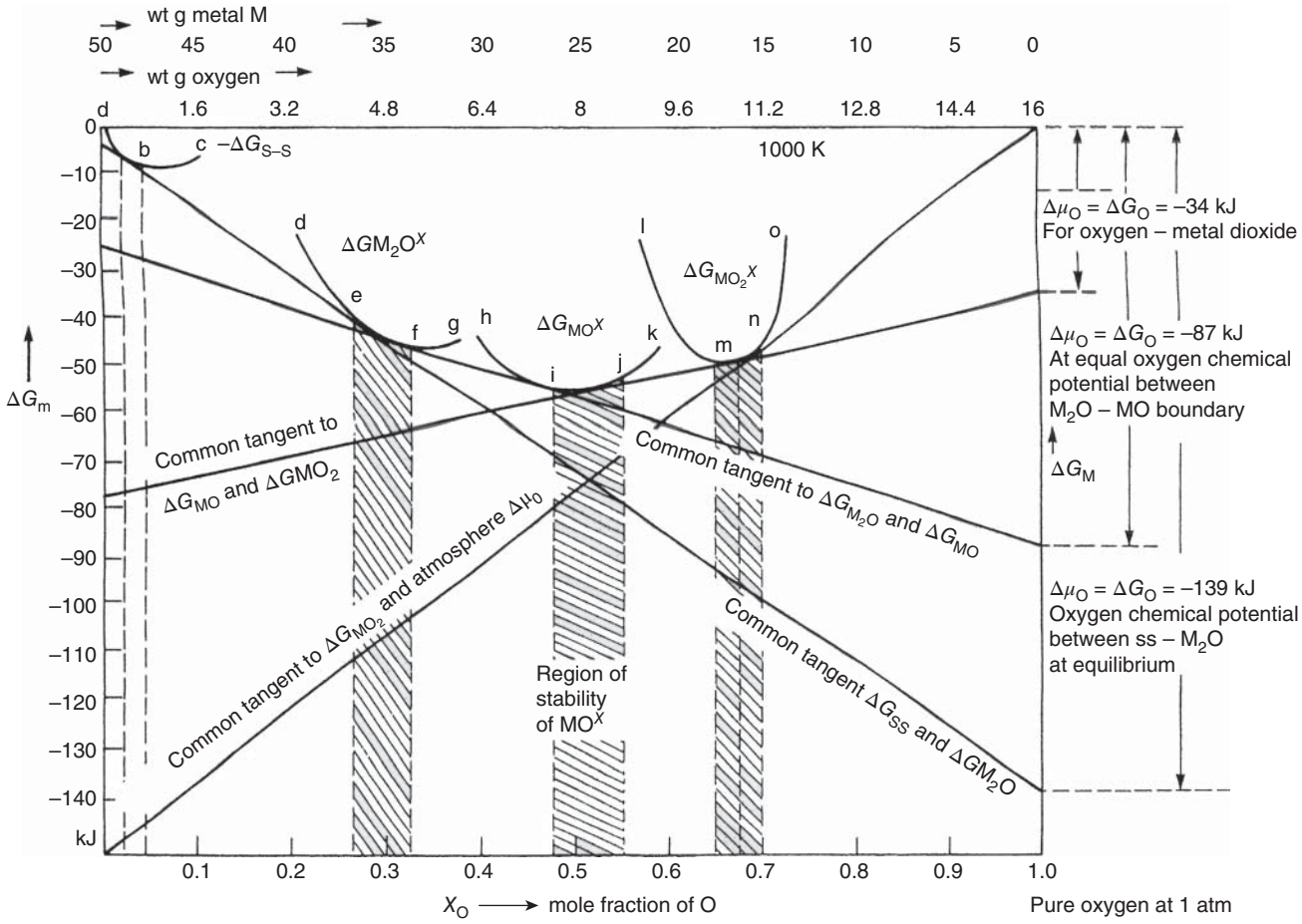


Figure 3.8 Free energy diagram for a binary system consisting of metal M and gaseous oxygen O_2 at a temperature of 1000 K.

and $X_O = 0.55$ and $X_M = 0.45$ for MO^x (see Figure 3.8). Similarly, the equilibrium compositions on the MO^x and M_2O^x boundary are found by drawing a common tangent to the ΔG_{MO^x} and $\Delta G_{M_2O^x}$ curves. The points i (on the ΔG_{MO^x} curve) and f (on the $\Delta G_{MO_2^x}$ curve) give the equilibrium compositions $M_{0.525}O_{0.475}$ and $M_{0.675}O_{0.325}$ for the two oxides at their boundary. Finally, the equilibrium compositions at the boundary between the solid solution and the adjacent oxide layer (M_2O^x) are found by drawing the common tangent to the $\Delta G_{M_2O^x}$ and ΔG_{SS}. Points b (on the ΔG_{SS} curve) and point e (on the $\Delta G_{M_2O^x}$ curve) give the respective equilibrium compositions. Thus, the maximum solubility of oxygen in the metal is found from the point b to be $X_O = 0.045$, and the composition of the M_2O^x in contact with the saturated solid solution is $M_{0.375}O_{0.265}$.

Closer examination of Figure 3.8 shows that each of the nonstoichiometric oxides has a region of homogeneity over which the compound is the sole stable phase. It has been observed, from a number of gas–metal systems, that the lower oxides (here M_2O^x and MO^x) usually show a wider region of nonstoichiometric behavior than the higher oxides (here MO_2^x).

In Figure 3.8 each oxide has two points of contact produced by common tangents. These two points predict the range composition within which each of the oxides is the sole stable phase. Thus the composition of MO_2^x oxide will vary from an oxygen mole fraction $X_O = 0.7$ on the surface of the oxide exposed to the oxygen atmosphere to $X_O = 0.675$ at the MO_2^x/MO^x boundary. It is also clear from the diagram that as long as the oxygen chemical potential remains between $\Delta\mu_O = 0$ (i.e. $p_{O_2} = 1$ atm) and $\Delta\mu_O = 34$ kJ (i.e. $p_{O_2} = 2.8 \times 10^{-4}$ atm), the outermost surface oxide layer will consist of an MO_2^x oxide phase. However, as the pressure of the oxygen is lowered to between 1 and 2.8×10^{-4} atm, the equilibrium oxygen contents in the MO_2^x surface layer decrease predictably from $X_O = 0.7$ to $X_O = 0.675$.

The exact equilibrium concentration of oxygen in the MO_2^x oxide in contact with the gas phase can be obtained by first calculating the oxygen chemical potential in the atmosphere, using the relationship $\Delta\mu_O = 1/2RT \ln p_{O_2}$,

and then drawing a tangent from the point on the $X_O = 1$ axis to the $\Delta G_{MO_2^x}$ curve. The point of contact with $\Delta G_{MO_2^x}$ curve will give the composition of the MO_2^x in contact with the atmosphere at p_{O_2}. It is also evident from Figure 3.8 that, once the pressure of oxygen falls below the critical $p_{O_2} = 2.8 \times 10^{-4}$ atm, the MO_2^x oxide phase cannot form since no common tangent can be drawn from the new oxygen potential point to $\Delta G^x_{MO_2}$ curve without intersecting other ΔG_m-concentration curves. It is also worth noting that any change in the oxygen pressure in the atmosphere from $p_{O_2} = 1$ atm to the vicinity $p_{O_2} = 2.8 \times 10^{-4}$ atm will have no effect on the compositions of the MO^x, M_2O^x and solid solution phases.

Between oxygen pressures of 2.8×10^{-4} and 8×10^{-4} atm, the outermost oxide layer will consist of the MO^x phase. Its exact surface composition can be predicted by using the common tangent in the same manner as described for MO_2^x. From Figure 3.8 it is clear that, as the oxygen pressure in the atmosphere is reduced, the composition of the surface oxide layer will vary in a predictable manner from $X_O = 0.55$ to $X_O = 0.475$.

Once the oxygen pressure falls to between 8×10^{-10} and 3.04×10^{-15} atm, the M_2O^x oxide phase will change from $X_O = 0.325$ to $X_O = 0.275$. Below an oxygen pressure of 3.04×10^{-15} atm, no oxide will be formed, and the equilibrium solubility of oxygen in the solid solution for a particular oxygen pressure can be predicted once again using the tangency rule.

The above concepts can also be applied to pseudo-binary systems where the components are taken as compounds of fixed stoichiometry. Figure 3.9 shows the activity versus composition plot for such a system, Fe_2O_3–Mn_2O_3. This type of diagram may be constructed for any of the systems encountered in high temperature corrosion, e.g. sulfides, oxides, sulfates, etc., and is useful in interpreting corrosion products and deposits formed on metallic or ceramic components.

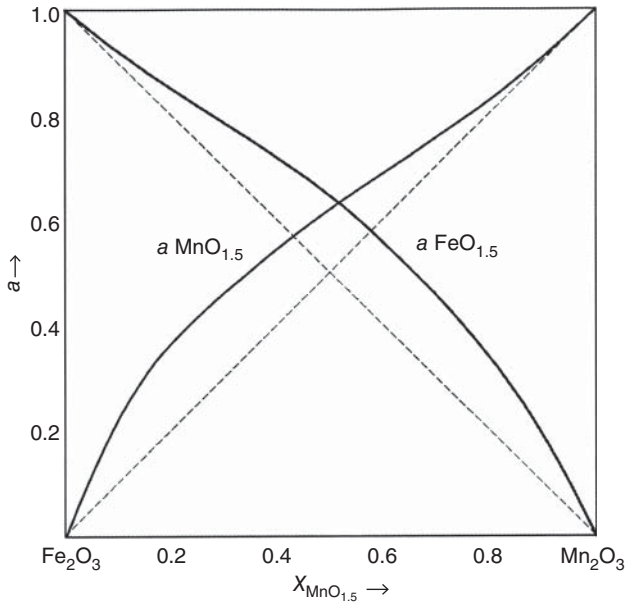


Figure 3.9 Activity versus composition diagram for Fe_2O_3–Mn_2O_3 system at 1300 °C (Birks et al. 2006).

3.2.3 Vapor Species Diagrams

Vapor species that form in any given high temperature corrosion situation often have a strong influence on the rate of attack, the rate being generally accelerated when volatile corrosion products form. Gulbransen and Jansson (1970) have shown that metal and volatile oxide species are important in the kinetics of high temperature oxidation of carbon, silicon, molybdenum, and chromium. Six types of oxidation phenomena were identified:

1. At low temperature, diffusion of oxygen and metal species through a compact oxide film.
2. At moderate and high temperatures, a combination of oxide film formation and oxide volatility.
3. At moderate and high temperatures, the formation of volatile metal and oxide species at the metal–oxide interface and transport through the oxide lattice and mechanically formed cracks in the oxide layer.
4. At moderate and high temperatures, the direct formation of volatile oxide gases.
5. At high temperature, the gaseous diffusion of oxygen through a barrier layer of volatilized oxides.
6. At high temperature, spalling of metal and oxide particles.

The diagrams most suited for presentation of vapor pressure data in oxide systems are $\log p_{M_xO_y}$ versus $\log p_{O_2}$ at constant temperature and Arrhenius diagrams of $\log p_{M_xO_y}$ versus $1/T$ a constant oxygen pressure. The following example will illustrate the construction of the first type of these diagrams by considering the Cr–O system at 1200 °C or 1473 K. Only one condensed oxide, Cr_2O_3, is formed under these conditions of high temperature oxidation. The thermodynamical data for producing the vapor equilibria diagram shown in Figure 3.10 are given in Table 3.2. The thermochemical data for Cr_2O_3(s), Cr_2O_3(g) and the four possible gaseous species Cr(g), CrO(g), CrO_2(g), and CrO_3(g) were obtained from Chase et al. (1975), Gulbransen and Meier (1979), Gulbransen and Jansson (1970), and Wicks and Block (1963).

The enthalpy (H_T), entropy (S), and heat capacity (C_p) of each species considered were calculated using Eqs. (3.9)–(3.11) in which T was set at 1473 K (Table 3.3). In these equations H_{tr} and T_{tr} represent, respectively, the enthalpy and temperature associated with any phase

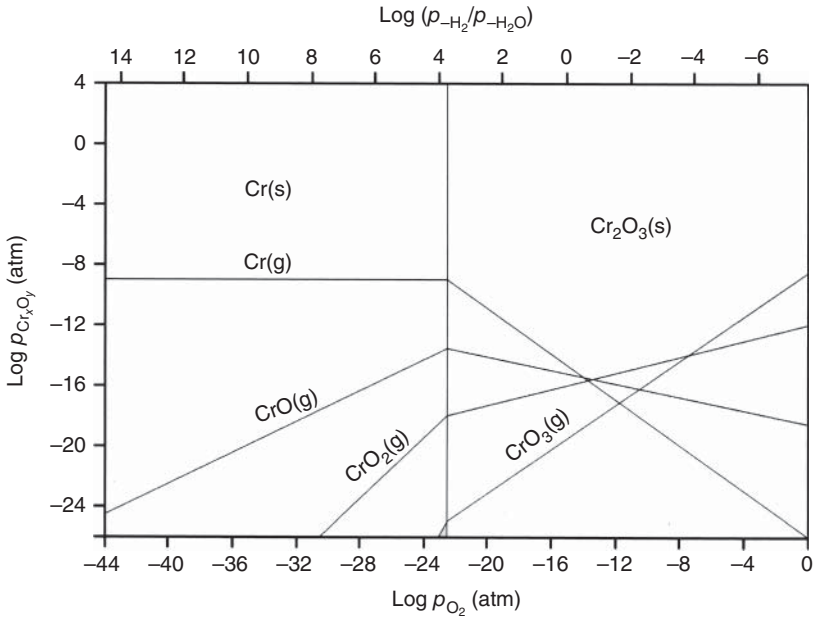


Figure 3.10 Volatile species in the Cr–O system at 1473 K (Birks et al. 2006).

Table 3.2 Thermochemical data for the Cr–O system

		Enthalpy	Entropy	Heat capacity (C_p)				Temperature range	
Species	State	H (kJ mol^{-1})	S (J mol^{-1} K^{-1})	A (J mol^{-1} K^{-1})	B	C	D	T_1 (K)	T_2 (K)
Cr	Gas	397.48	174.305	20.786	0	0	0	298.15	700
	Gas			15.456	2.556	16.828	0.874	700	3000
Cr	Solid	0	23.64	17.715	22.966	−0.377	−9.033	298.15	1000
	Solid			18.067	15.531	−16.698	0	1000	2130
	Liquid	16.933	7.95	39.33	0	0	0	2130	2945
Cr_2O_3	Solid	−1139.7	81.199	104.307	24.451	7.59	−3.807	298.15	2603
CrO	Gas	188.28	239.266	24.518	25.33	0.222	−11.201	298.15	400
	Gas			34.292	3.979	−4.351	−1.138	400	1600
CrO_2	Gas	−75.312	269.24	30.878	46.689	0	−15.782	298.15	400
	Gas			45.309	18.552	−7.222	−7.632	400	1100
CrO_3	Gas	−292.88	266.169	74.002	7.686	−18.393	−1.644	298.15	3000
O_2	Gas	0	205.146	31.321	3.895	−3.105	−0.335	298.15	5000

Table 3.3 Thermochemical data for the Cr–O system at 1473 K

Species	State	H (kJ mol^{-1})	S (J mol^{-1} K^{-1})	G (kJ mol^{-1})
Cr	Gas	422.02	207.58	116.25
Cr	Solid	36.97	70.78	−67.29
Cr_2O_3	Solid	−993.71	276.68	−1401.27
CrO	Gas	230.37	295.28	−204.57
CrO_2	Gas	−12.73	351.72	−530.81
CrO_3	Gas	−206.60	381.78	−766.96
O_2	Gas	39.67	257.73	−339.97

transition encountered between the reference temperature (298.15 K) and the temperature of interest.

$$H_{(T)} = H_{f(298.15)} + \int_{298.15}^{T} C_p \mathrm{d}T + H_{\mathrm{tr}} \qquad (3.9)$$

$$S = S^{\circ}_{(298.15)} + \int_{298.15}^{T} \frac{C_p}{T} \mathrm{d}T + \sum \frac{H_{\mathrm{tr}}}{T_{\mathrm{tr}}} \qquad (3.10)$$

$$C_p = \mathrm{A} + \mathrm{B}\ 10^{-3}T + \mathrm{C}\ 10^{5}T^{-2} + \mathrm{D}10^{-6}T^{2} \qquad (3.11)$$

The free energy (G) for each species considered was then calculated with Eq. (3.12) and used to evaluate the stability of these species and the predicted energy of reaction for each equilibrium (Table 3.4):

$$G = H - TS \qquad (3.12)$$

Vapor pressures of species at equilibrium with either the metal or its most stable oxide (i.e. Cr_2O_3) must then be determined. The boundary between these regions is the oxygen pressure for the Cr/Cr_2O_3 equilibrium in Eq. (3.13):

$$2\mathrm{Cr(s)} + 1.5\mathrm{O_2(g)} = \mathrm{Cr_2O_3(s)} \qquad (3.13)$$

Table 3.4 Standard energy of reactions for the Cr–O system at 1473 K

Reaction	ΔG° (kJ mol^{-1})
$2Cr(s) + 1.5O_2 = Cr_2O_3$	−756.72
Over Cr(s)	
$Cr(s) = Cr(g)$	183.54
$Cr(s) + 0.5O_2 = CrO(g)$	32.71
$Cr(s) + O_2 = CrO_2(g)$	−123.54
$Cr(s) + 1.5O_2 = CrO_3(g)$	−189.71
Over Cr_2O_3	
$0.5Cr_2O_3(s) = Cr(g) + 0.75O_2$	561.90
$0.5Cr_2O_3(s) = CrO(g) + 0.25O_2$	411.07
$0.5Cr_2O_3(s) + 0.25O_2 = CrO_2(g)$	254.81
$0.5Cr_2O_3(s) + 0.75O_2 = CrO_3(g)$	188.65

for which the equilibrium constant (K_p) is evaluated with Eq. (3.14), giving an equilibrium pressure of oxygen calculated with Eq. (3.15):

$$\log K_p = \frac{-\Delta G^{\circ}}{2.303\,RT} \tag{3.14}$$

$$\log (p_{O_2}) = -\frac{2}{3}\ \log\ K_p^{Cr_2O_3} = -17.90 \tag{3.15}$$

The dotted vertical line in Figure 3.10 represents this boundary. At low oxygen pressure it can be seen that the presence of Cr(g) vapor pressure may be obtained from the equilibrium expressed in Eq. (3.16):

$$0.5Cr_2O_3(s) = Cr(g) + 0.75O_2(g) \tag{3.16}$$

The other lines in Figure 3.10 are obtained by using similar equilibrium equations (Table 3.4). The vapor equilibria presented in Figure 3.10 show that significant Cr(g) vapor pressures are developed at low oxygen partial pressure (e.g. at the alloy–scale interface of a Cr_2O_3-forming alloy), but that a much larger pressure of $CrO_3(g)$ develops at high oxygen partial pressure. The high $CrO_3(g)$ pressure is responsible for the thinning of Cr_2O_3 scales by vapor pressure during exposure to oxygen-rich environments. Figure 3.11 indicates the temperature dependence of various equilibria. Similar diagrams may be constructed for other oxides, sulfides, carbides, halides, etc.

Over the years, Pourbaix and his coworkers in the Cebelcor at Brussels, founded under his direction, extended these diagrams by including lines for metastable compounds (Pourbaix 1980). Figure 3.12 illustrates such a presentation for the Fe–O system over the temperature range 830–2200 K. Pourbaix used these diagrams as a basis for a discussion on the stability of metallic iron (solid, liquid, and vapor phases), the oxides of iron as a function of oxygen pressure and temperature from which he explained the protection of iron at high temperature by immunity and passivation. He also pointed out the value of these diagrams in the fields of geology, metallurgy, corrosion, and catalysis, among others.

3.2.4 2D Stability Diagrams for One Metal/Two Nonmetals

A convenient way of representing the thermodynamic information for a given system is by means of isothermal phase stability diagrams that show the ranges of gas compositions over which a condensed phase can exist either singly or in equilibrium with another condensed phase or phases (Alcock 1976; Ingraham 1967; Rao 1985).

The method of construction of this type of diagram will be illustrated using the general case of the three-component

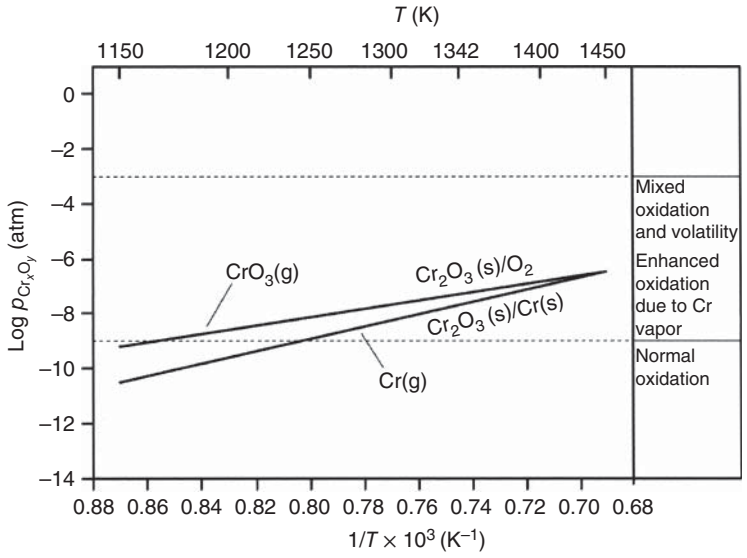


Figure 3.11 Cr–O system volatile species versus temperature. The line for Cr(g) refers to the pressure at the Cr–Cr_2O_3 interface, and the $CrO_3(g)$ line refers to the Cr_2O_3/gas interface for an oxygen partial pressure of 1 atm (Birks et al. 2006).

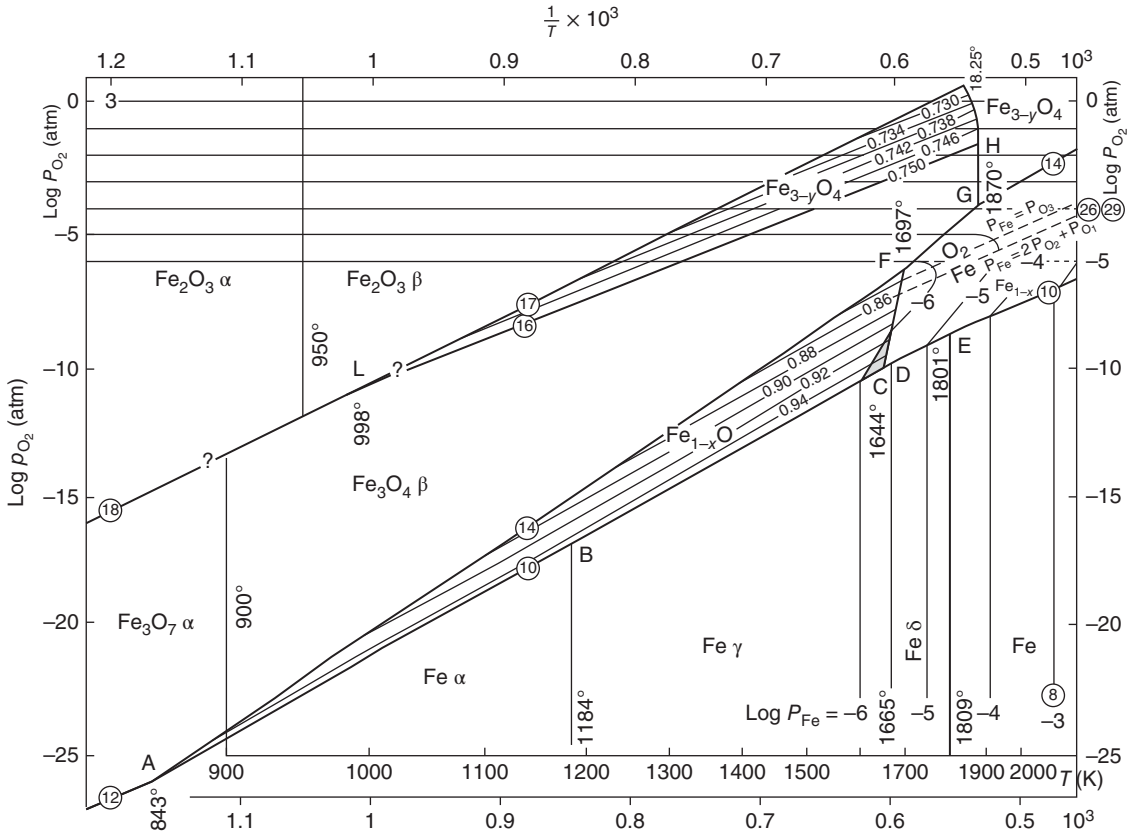


Figure 3.12 Equilibrium diagram for log $p_{O_2} = f(1/T)$ for the Fe–O system (between 830 and 2200 K (Pourbaix 1980).

system metal–sulfur–oxygen (M–S–O) whose values of ΔG_T° for the reactions between the various condensed phases are given in Table 3.5.

Assume that at the isothermal temperature of interest, the following stable condensed phases (solid or liquid) can be formed: M, MO, MS, and MSO_4. From the phase rule it is clear that the maximum number of condensed phases in contact with each other can be three, in addition to the gaseous phase (SO_2 and O_2). Following the suggestion of Kellog and Basu (1960), the phase stability diagram may be constructed by plotting the sulfiding potential $\log p_{SO_2}$ along the vertical axis and the oxidizing potential $\log p_{O_2}$

Table 3.5 Data for the construction of thermodynamic phase stability diagram M–S–O at 1000 K[a]

Boundary between phases	Reaction considered	Slope of boundary	ΔG_{1000}° (kJ)	Calculated data from ΔG_{1000}° and the appropriate equations				
				$-\log K$	$\log p_{SO_2}$	$\log p_{O_2}$	Line no.	Remarks
M/MO	$M + \frac{1}{2}O_2 \rightleftarrows MO$	Parallel to y-axis	−153.2	−16	NA	−16	1	Independent of p_{SO_2}
M/MS	$M + SO_2 \rightleftarrows MS + O_2$	1	+229.8	+12	−4	−16	2	–
MS/MO	$MS + \frac{3}{2}O_2 \rightleftarrows MO + SO_2$	$\frac{3}{2}$	−38.3	−20	−4	−16	3	–
MS/MSO_4	$MS + 2O_2 \rightleftarrows MSO_4$	Parallel to y-axis	−459.6	−24	NA	−12	4	Independent of p_{SO_2}
MO/MSO_4	$MO + SO_2 + \frac{1}{2}O_2 = MSO_4$	$-\frac{1}{2}$	−76.6	−4	+2	−12	5	–

[a]Assumed data of ΔG_{1000}° for the purpose of illustrating the calculation of the position of the boundary lines and triple points A and B (see Figure 3.13).

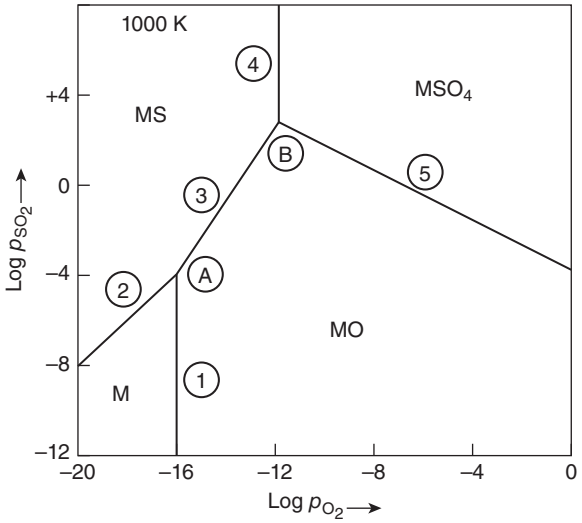


Figure 3.13 Phase stability diagram for a metal–sulfur–oxygen (M–S–O) system at 1000 K (Kellog and Basu 1960).

along the horizontal axis as in Figure 3.13. The position and the slopes of the boundary lines between the areas of stability for the condensed stable phases of the system are then calculated from the appropriate chemical equations described in the reactions, which take place when one condensed phase reacts to form the other phase. The only thermodynamic data required are either the standard Gibbs free energy change at the chosen temperature (ΔG_T°) or the equilibrium constant for the reaction at the given temperature (K_T).

Usually, the most convenient boundary to calculate first is that between the pure metal (M) and the metal–oxide (M–O), i.e. the M/MO boundary, since it will be parallel to the *y*-axis. Using the balanced reaction for the formation of the oxide

$$\mathrm{M} + \frac{1}{2}\,\mathrm{O_2} = \mathrm{MO} \quad \text{at 1000 K} \tag{3.17}$$

and the relationship between (ΔG_T°) and K_T gives

$$\Delta G^\circ_{1000} = -RT\ \ln\ K_{1000} = -RT\ \ln \frac{a_{\mathrm{MO}}}{a_{\mathrm{M}} p_{\mathrm{O_2}}^{1/2}} \tag{3.18}$$

For pure M and MO by definition, $a_{\mathrm{M}} = a_{\mathrm{MO}} = 1$.

Converting $\ln p_{\mathrm{O_2}}$ to $\log p_{\mathrm{O_2}}$, rearranging terms and substituting values for ΔG°_{1000} (Table 3.5), R, and T, the following is obtained:

$$\log p_{\mathrm{O_2}} = -16 \tag{3.19}$$

Since $p_{\mathrm{SO_2}}$ does not take part in the reaction, the boundary line between M and MO is independent of $\log p_{\mathrm{SO_2}}$ and so given by a straight vertical line at $\log p_{\mathrm{O_2}} = -16$, parallel to the *y*-axis (line 1 in Figure 3.13). It should be noted that stability areas across the boundary follow the sequence of condensed phases shown in the equation, i.e. on the left-hand side of the boundary, pure metal is the stable phase and on the right-hand side the pure metal–oxide.

To determine the position of the boundary between M and MS, the following chemical reaction is used:

$$\mathrm{M} + \mathrm{SO_2} = \mathrm{MS} + \mathrm{O_2} \tag{3.20}$$

For pure M and MS, $a_{\mathrm{M}} = a_{\mathrm{MS}} = 1$.
Using Eq. (3.21),

$$-\Delta G^\circ = RT \ln K = 19.15\, T \log K \tag{3.21}$$

$$\Delta G^\circ_{1000} = -19.15\ \log \frac{p_{\mathrm{O_2}}}{p_{\mathrm{SO_2}}} = 19.15T\ (\log\ p_{\mathrm{SO_2}} - \log\ p_{\mathrm{O_2}}) \tag{3.22}$$

Rearranging:

$$\log\ p_{\mathrm{SO_2}} = \log\ p_{\mathrm{O_2}} + \frac{\Delta G^\circ_{1000}}{19.15T} \tag{3.23}$$

This is the equation of a straight line of the form $Y = \mathrm{m}x + \mathrm{c}$ when $\log\ p_{\mathrm{SO_2}}$ is plotted against $\log\ p_{\mathrm{O_2}}$, where $Y = \log\ p_{\mathrm{SO_2}}$, m is the slope that here is unity, $x = \log\ p_{\mathrm{O_2}}$, and c is a constant that in this case is $\Delta G^\circ_{1000}/19.15T$. Substituting values for $\Delta G^\circ_{\mathrm{MS}} = 229.8 \times 10^3$ and $\log\ p_{\mathrm{O_2}} = 10^{-16}$ (where the previous line and the new line intersect) gives

$$\log\ p_{\mathrm{SO_2}} = \frac{229.8 \times 10^3}{19.15 \times 10^3} - 16 = -4 \tag{3.24}$$

Thus, the coordinates of the point of intersection (A in Figure 3.13) of the two boundary lines M/MS and M/MO are $\log\ p_{\mathrm{SO_2}} = -4$ and $\log\ p_{\mathrm{O_2}} = -16$.

These calculated data are now sufficient to draw the boundary line between the stability areas of M and MS. This is constructed by drawing a straight line having a slope of +1 from the point of intersection A. Next, the position of the boundary between MS and MO can be calculated from the reaction:

$$\mathrm{MS} + \frac{3}{2}\mathrm{O_2} = \mathrm{MO} + \mathrm{SO_2} \tag{3.25}$$

Thus,

$$\Delta G^\circ_{1000} = -19.15T\ \log \frac{p_{\mathrm{SO_2}}}{p_{\mathrm{O_2}}^{3/2}} \tag{3.26}$$

which, on rearranging, gives

$$\log\ p_{\mathrm{SO_2}} = \frac{3}{2}\ \log\ p_{\mathrm{O_2}} - \frac{\Delta G^\circ_{1000}}{19.15T} \tag{3.27}$$

The slope of the line is $+\frac{3}{2}$ and the line is drawn from point A to the MS/MSO_4 boundary to be determined next.

The boundary between the MS and MSO_4 stability areas is calculated from the reaction

$$MS + 2O_2 = MSO_4 \tag{3.28}$$

Thus

$$\log p_{O_2} = \frac{-459 \times 10^3}{19.15 \times 10^3 \times 2} = -12 \tag{3.29}$$

Since SO_2 does not take part in the above reaction, the boundary between MS and MSO_4 stability areas is independent of $\log p_{SO_2}$ and is given by a vertical line (4) at $\log p_{O_2} = -12$ parallel to the $\log p_{SO_2}$ axis. The intersection point of the MS/MSO_4 line (4) with that of MO/MS boundary line (3) at point B of Figure 3.13 completes the stability area of the MS phase (lines 2, 3, and 4).

Finally, the boundary between MO and MSO_4 is calculated from the reaction

$$MO + SO_2 + \frac{1}{2}O_2 = MSO_4 \tag{3.30}$$

Thus

$$\log p_{SO_2} = \frac{\Delta G^\circ_{1000}}{19.15 \times 10^3} + \frac{1}{2} \log p_{O_2} \tag{3.31}$$

Since this line will start at point B of Figure 3.13, i.e. when the values of $p_{O_2} = -12$ and $\Delta G^\circ_{1000} = -76.6$ kJ, one can calculate the value of $\log p_{SO_2}$ for the point B by substituting these values in the previous equation:

$$\log p_{SO_2} = \frac{-76.6 \times 10^3}{19.15 \times 10^3} - \frac{1}{2}(-12) = +2 \tag{3.32}$$

Therefore, the calculated coordinates of the triple point for the coexistence of MO, MS, and MSO_4 are $\log p_{SO_2} = +2$ and $\log p_{O_2} = -12$, and the slope of the MO/MSO_4 boundary is $-1/2$. The straight line from point B having slope $-1/2$ gives the boundary line (5) between the stability areas of MO and MSO_4. This completes the construction of the phase stability diagram for M–S–O at 1000 K.

The stability phase diagrams contain a wealth of information. The selected diagrams shown in Figures 3.14–3.18 for the Fe–S–O (Gray and Starr 1980), Ni–S–O (Giggins and Pettit 1980), AISI 316 S–O (Gray and Starr 1980), Cr–C–O (Hemmings and Perkins 1977), and U–O–Cl (Knacke 1972) found many applications, namely, in the field of high temperature corrosion.

Types of diagrams such as that shown in Figure 3.15 are used to interpret the reactions involving metals in complex atmospheres and hot corrosion (see later Chapter 15).

When significant intersolubility exists between neighboring phases on stability diagrams, solution regions may be included as shown in Figure 3.19 taken from the work of Giggins and Pettit (1980). The phase boundaries in Figure 3.19 were calculated from the equilibria, such as before for Figure 3.15, but the boundaries of the solution regions were calculated, taking the activities of the essentially pure species as unity and of the minor species as some limiting value. In constructing Figure 3.19, the activity of NiS was taken as 10^{-2} in equilibrium with essentially pure NiO, and the activity of NiO was taken as 10^{-2} in equilibrium with essentially pure NiS. Obviously, experimental data regarding the extent of intersolubility of phases and activities in solution are essential to quantify such diagrams.

For some applications, different coordinate axes become more convenient for the construction of stability diagrams. For example, the phase equilibria of the Ni–S–O system in Figure 3.15 may be equally well represented on a plot of $\log p_{O_2}$ versus $\log p_{SO_3}$ since specification of these two variables fixes $\log p_{S_2}$ because of the equilibrium shown in the equation:

$$\frac{1}{2}S_2(g) + \frac{3}{2}O_2(g) = SO_3(g) \tag{3.33}$$

The equilibria of Figure 3.15 are replotted in Figure 3.20 using these coordinates. This choice of coordinates is particularly useful in analyzing hot corrosion situations such as those that occur when a metal is oxidized while covered with a deposit of sodium–sulfate, since the

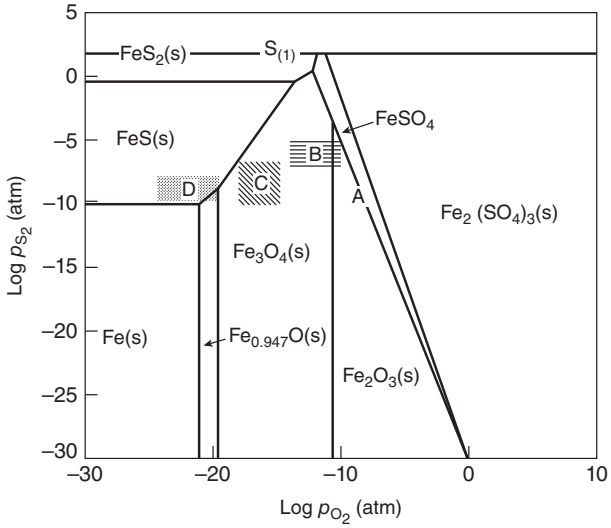


Figure 3.14 Thermochemical stability diagram for the system Fe–S–O at 1000 K showing the relative corrosion potentials of the atmospheres in conventional coal combustion (A), fluidized bed combustion (B), conventional coal gasification (C), and coal gasification using nuclear heat (D) (Gray and Starr 1980).

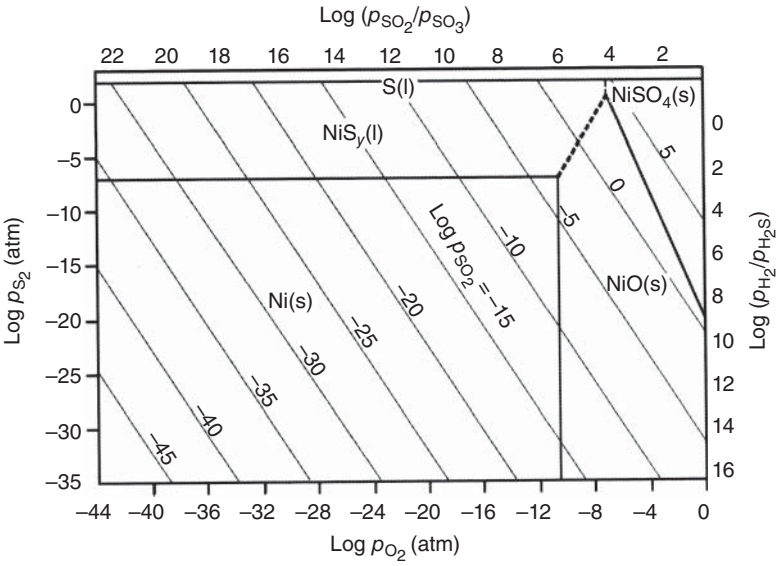


Figure 3.15 Condensed phase equilibria for the Ni–O–S system at 1250 K (Giggins and Pettit 1980).

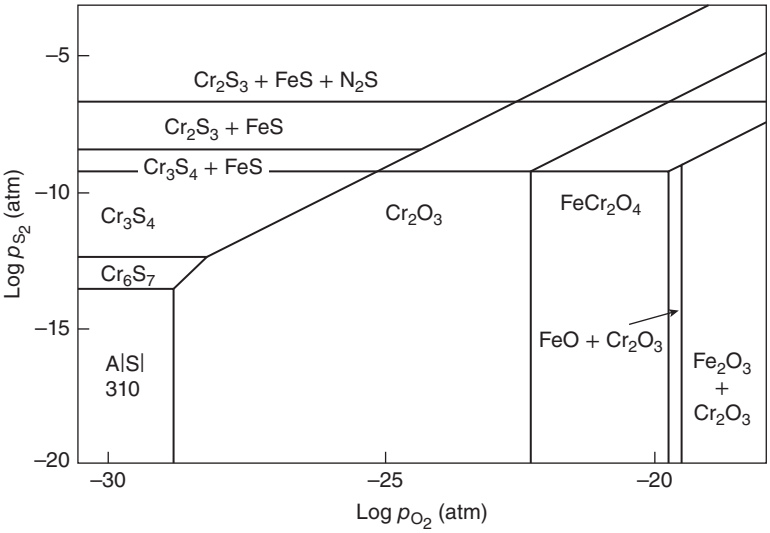


Figure 3.16 Thermochemical stability diagram for the 310 stainless-steel–S–O system at 750 °C (Gray and Starr 1980).

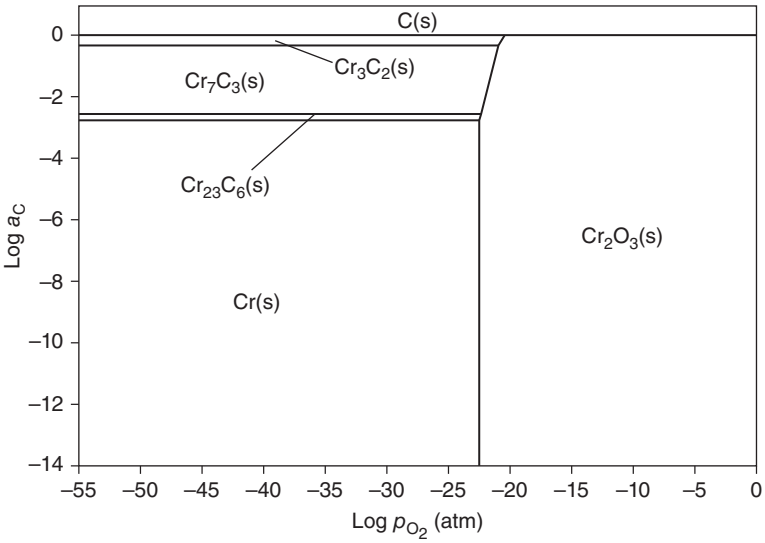


Figure 3.17 Stability diagram for the Cr–C–O system at 1250 K (Hemmings and Perkins 1977).

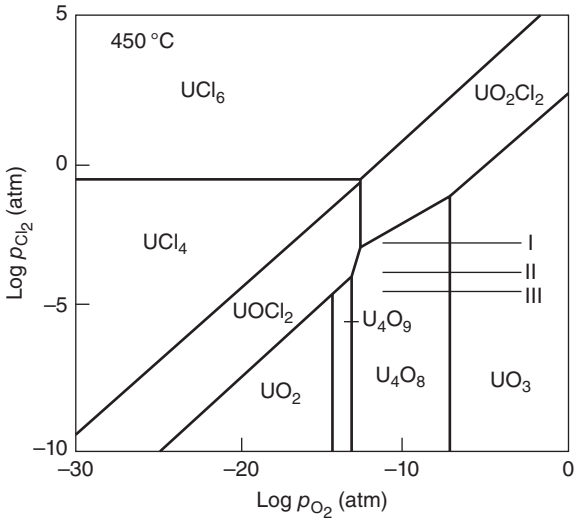


Figure 3.18 Composition ranges in the U–O–Cl system at 450 °C (Knacke 1972).

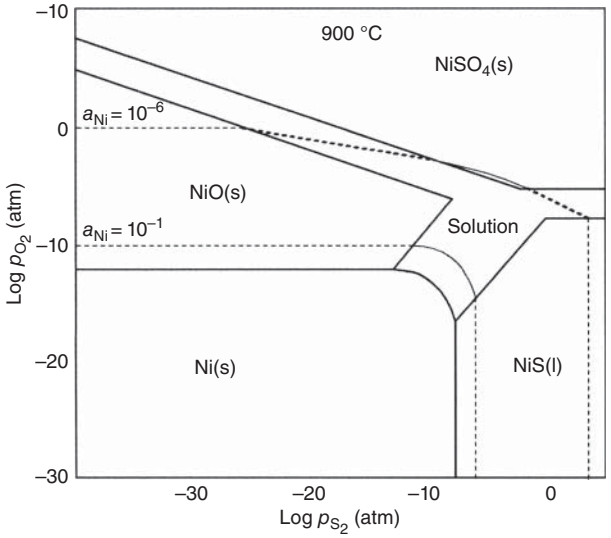


Figure 3.19 Stability diagram for the Ni–O–S system where regions of solution were assumed to exist between NiO, NiS, and $NiSO_4$ (Giggins and Pettit 1980).

components of Na_2SO_4 may be taken as Na_2O and SO_3. This phenomenon will be described in Chapter 15.

3.2.5 2D Stability Diagrams for Two Metals/One Nonmetal

The condensed phase equilibria when only one oxidant is present must now be considered. Figure 3.21, taken from the work of Sticher and Schmalzried (1975), is the stability diagram for the Fe–Cr–O system at 1300 °C. The construction of this type of diagram requires the establishment of the free energy composition behavior, as discussed in Section 3.2.2, for the system of interest and then the evaluation of the stability fields at a given temperature by minimizing the free energy of the system, i.e. applying the common tangent construction. The rules governing these types of diagrams are clearly explained by Pelton and Schmalzried (1973).

3.2.6 Phase Stability Diagrams for Two or More Metals

These include two-dimensional and three-dimensional and isothermal and non-isothermal stability diagrams, for two or more metals and two or more nonmetallic components. Figure 3.22 shows a stability diagram having phase areas for Co–S–O (solid lines) and for Cu–S–O (broken lines). From this diagram it can be clearly seen that at 950 K at certain gas mixtures, pure metals Co and Cu will be unaffected by the atmosphere, while, at other atmospheric compositions, the pure oxides will be stable. Figure 3.23 illustrates a simplified diagram at 871 °C for three metallic elements Cr/Mn/Ni–S–O in a heat-resisting alloy; the range for coal gasification is also included. It is clear that Cr_2O_3 is stable in all these atmospheres, but NiS will be stable under these atmospheric conditions above 620 °C in the form of a eutectic liquid with Ni. Thus, an alloy of Cr and Ni may produce either of these phases or their mixtures, leading to corrosion problems.

Figure 3.24 shows a diagram for the three metals Fe, Cr, and Ni as a function of sulfide potential against oxygen potential. This diagram has been used to select atmospheres in the study of high temperature corrosion in which relatively small changes in oxygen and sulfur have a marked effect on the kinetics of corrosion, scale morphology, and scale composition of 34Fe–39Ni–27Cr alloy ingots. The atmospheres selected for the study are shown in Figure 3.24 as *X*1, *X*2, *X*3, and *X*4. Figure 3.25 shows the stability diagram at 1000 K for Al, Ti, Si, Cr, and Fe sulfides at oxidizing potentials, log p_{O_2}, between −10 and −50 and sulfiding potentials, log p_{S_2}, between 0 and −25. Isobaric lines for log p_{SO_2} ranging from 0 to −40 are also included in the diagram as straight lines. The diagram was produced for a study aimed at finding improved materials that would be immune to sulfur corrosion and lead to the increased efficiency of thermal and nuclear power stations. From Figure 3.25 it is clear that the oxides are unstable under high sulfur pressure and very low oxygen pressure. It is also clear that the formation of SO_2 has to be taken into consideration as the reaction between sulfur and oxygen significantly lowers the oxygen activity; under high sulfur pressure and low SO_2 pressure, only some oxides are stable (Al_2O_3, TiO_2, and SiO_2), and the oxides of Fe, Co, Ni, and perhaps Cr are decomposed.

Tridimensional thermodynamic phase stability diagrams have also been constructed; for example, diagrams

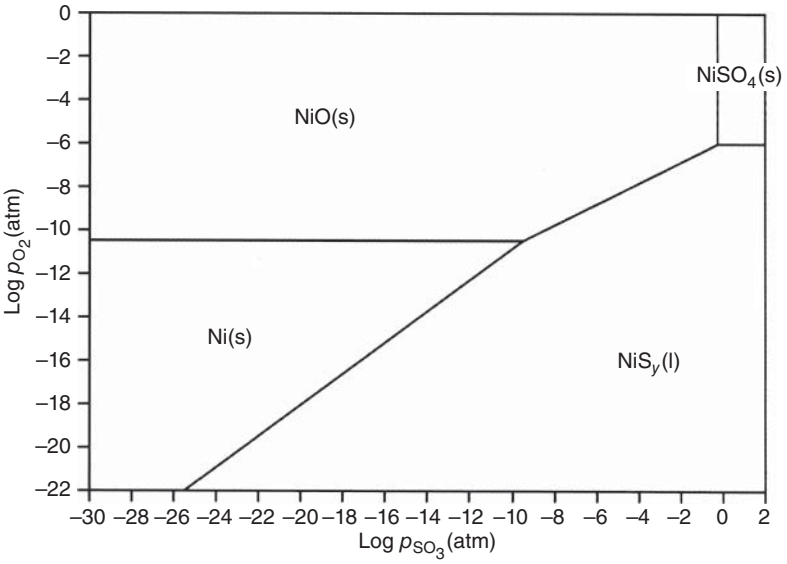


Figure 3.20 Stability data for the Ni–O–S system at 1250 K expressed as $\log p_{O_2}$ versus $\log p_{SO_3}$ (Giggins and Pettit 1980).

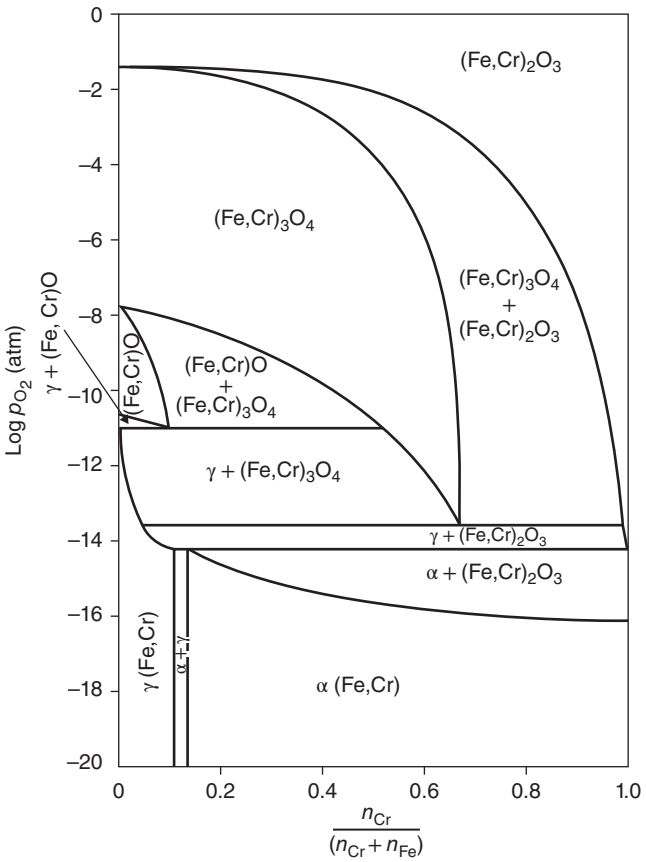


Figure 3.21 Stability diagram for the Fe–Cr–O system at 1300 °C (Sticher and Schmalzried 1975).

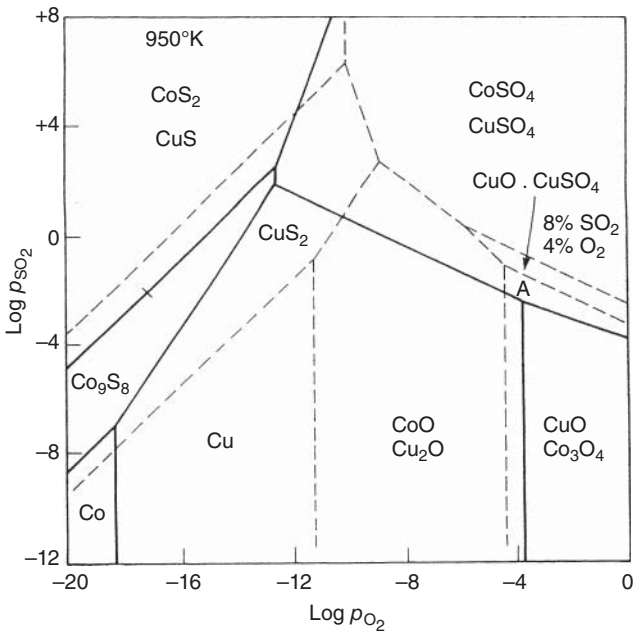


Figure 3.22 Superimposed predominance area diagrams at 950 K for the Co–S–O system (solid lines) and the Cu–S–O system (broken lines). Within the area A, $CoSO_4$ and CuO are the stable phases (Ingraham 1967).

displaying the stability zones under varying conditions of temperature, pressure, and atmosphere composition are more completely defined than in the Ellingham diagram. However, these diagrams are considered to be more complex, and it may be necessary to take advantage of specialized computer data banks and iterative routines for its automatic plotting.

Figure 3.26 shows a three-dimensional phase stability diagram for the Fe–S–O system between 800 and 1000 K. These diagrams are obtained from a knowledge of the variation of ΔG_T° for the different reactions that describe the appropriate phase boundary. In general, changes in temperature may have a significant effect on the areas of stability. These may become larger or smaller as the

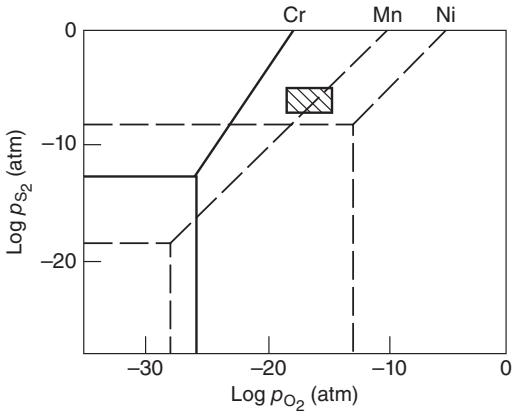


Figure 3.23 Superimposed simplified thermodynamic stability diagrams for three elements with oxygen and sulfur at 871 °C. The shaded rectangle indicates possible activity ranges in coal gasification atmospheres (Stringer 1980).

temperature is increased. A detailed description of the method for their production and interpretation may be found elsewhere (Ingraham 1966, 1967; Rao 1985).

3.3 Electrochemical Analysis

High temperature corrosion in gas turbines, steam generators, incinerators, boilers, and numerous petrochemical vessels involves contact of metallic or ceramic materials with corrosive fused salt films that effect accelerated degradation, namely, hot corrosion (Chapter 15). Perhaps the three most important facts about the problem are as follows: (i) generally, fused salts are electrolytic conductors so that the attack must be electrochemical in nature, (ii) oxyanion-fused salts (sulfates, carbonates, nitrates, etc.) exhibit an acid–base behavior that is crucial to most mechanistic aspects of corrosion, and (iii) generally, metallic engineering alloys have virtually no regimes for mutual thermodynamic stability with a fused salt such as Na_2SO_4, so that a corrosion product must form upon contact of the salt with the metallic substrate. Clearly, the avoidance of corrosion is achieved by forming a slow-growing, compact, and only slightly soluble oxide scale.

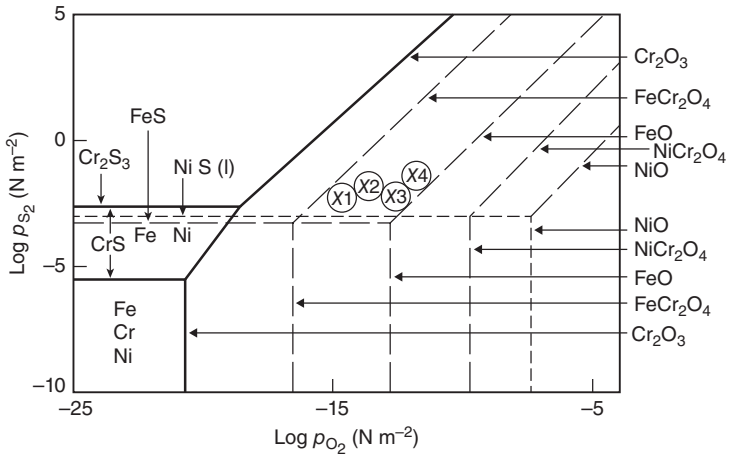


Figure 3.24 Thermodynamic stability diagram for the Fe–Ni–Cr system at 1143 K, assuming metal activities to be unity. - - - -, phase boundaries involving Fe; ----, phase boundaries involving Ni; —, phase boundaries involving Cr. The location of environments 1, 2, 3, and 4 are indicated by *X* (Stott and Smith 1980).

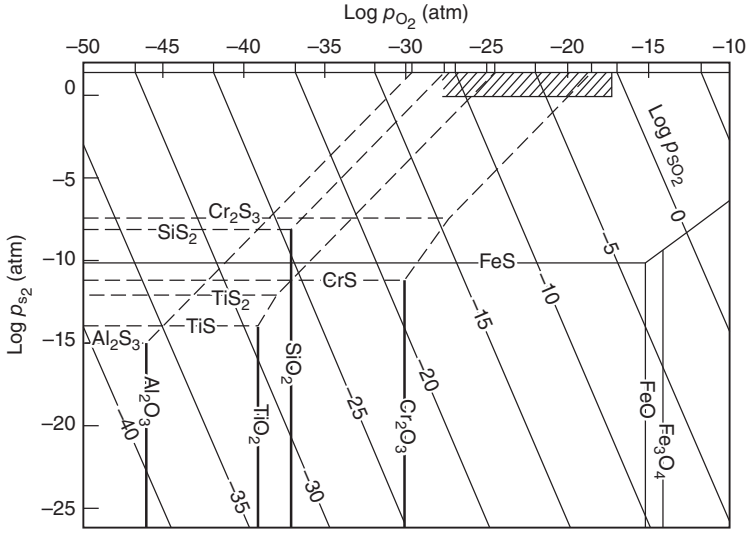


Figure 3.25 Thermodynamic stability diagram for some oxides and sulfides at 1000 K (Lions 1980).

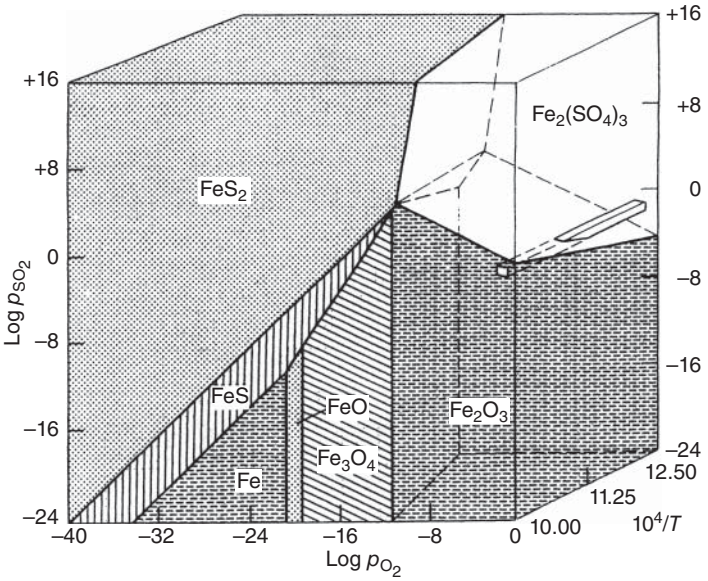


Figure 3.26 Predominance volume diagram for the Fe–S–O system for the temperature range 800–1000 K (Ingraham 1967).

The subject of thermodynamics (or phase equilibria) of metal-fused salt systems in high temperature corrosive environments has been treated in a manner exactly analogous to aqueous solutions by the formalism of Pourbaix, i.e. plots of electrode potential (oxidizing potential) versus basicity, which, for the pure Na_2SO_4 as treated here, is defined as $\log a_{Na_2O} = pO^{2-}$ (Littlewood 1962; Nishikata et al. 1991; Trémillon 1971, 1974). In the following subsection we will show its range of applications in the field of high temperature corrosion.

3.3.1 Oxidizing Potential Basicity Diagram for Fe in Molten Na_2SO_4

The information available in the open literature, in addition to our own experience, shows that iron exhibits active-to-passive transitions and other complex *polarization* behavior, which are characteristic of many corrosion-resistant industrial alloys. In order to interpret the corrosion of iron, thermodynamic diagrams for iron in molten sulfate eutectic systems at 873 K (Baudo and Tamba 1969; Rahmel 1968) and in other melts (Bale 2009; Pingfang et al. 2007; Seon 1982) have been published. Here, a thermodynamic diagram for iron/sodium–sulfate at 1173 K is constructed and properly detailed.

3.3.1.1 Conventions

An electrochemical reaction occurring in molten sulfate can be represented in half-cell form by

$$aA + bB + cR - mO^{2-} + ne^- = 0 \qquad (3.34)$$

in which A represents a reagent substance that is changed into a product, B the only other species appearing being solvent ions, R (reducible or oxidizable species resulting from the acid–base dissociation of the melt), oxide ions, O^{2-}, and electrons, e^-.

The half-cell reduction potential, E, for this reaction is given by

$$E = E^\circ + \frac{RT}{nF} \ln[(\{A\}^a\{B\}^b\{C\}^c)/\{O^{2-}\}^m] \qquad (3.35)$$

where E° is the standard electrode potential at the temperature T, F is Faraday's constant, R is the gas constant, n is the number of free electrons exchanged in the electrochemical reaction, and the notation $\{X\}$ indicates the activity of reactant, X. The acid–base equilibrium for sulfates can be expressed by the equation (Flood et al. 1952; Lux 1939)

$$SO_4^{2-} = SO_3 + O^{2-} \qquad (3.36)$$

The oxide activity depends on the presence of sulfur trioxide, and if we assume $\{SO_4^{2-}\} = 1$,

$\log\{O^{2-}\} + \log P_{SO_3} = \log K_{36}$. ($\{O^{2-}\} = 0$ implies $p_{SO_3} = \infty$, and for $\{O^{2-}\} = 1$ the assumption $\{SO_4^{2-}\} = 1$ is not valid.) The acidity of the melt may therefore be expressed either as pO^{2-} or as $-\log P_{SO_3}$, where $pO^{2-} = -\log\{O^{2-}\} = -\log a_{Na_2O}$, as seen above. Moreover, the standard electrode potential, E°, for each equilibrium is given by $E^\circ = -\Delta G^\circ/nF$. So, the reduction potential, E, can be written as

$$E = -\frac{\Delta G^0}{nF} + \frac{2.303\,RT}{nF} (a \log\{A\} + b \log\{B\} + c \log\{R\}) + \frac{2.303\,RT}{nF} mpO^{2-} \qquad (3.37)$$

In the present case, reduction potentials are referred to the sulfate electrode

$$SO_3 + \frac{1}{2}O_2 - SO_4^{2-} + 2e^- = 0 \qquad (3.38)$$

at unit SO_3 and O_2 pressure and unit sulfate ion activity at the temperature of interest (hence $E_{38} = 0 + 0.1163 \log P_{SO_3} + 0.0582 \log P_{O_2}$ at 1173 K), and therefore ΔG° is obtained by adding the term $\frac{n}{2}\Delta G^\circ_{36}$, corresponding to the standard free energy for the acid–base equilibrium described by Eq. (3.36) to the standard Gibbs energy change for the whole cell reaction:

$$aA + bB + cR + \left(\frac{n}{2} - m\right)O^{2-} - \frac{n}{4}O_2 = 0 \qquad (3.39)$$

If this reaction does not involve electron transfer, $n = 0$. In this case,

$$pO^{2-} = + \frac{1}{m}\left(\frac{\Delta G^\circ}{2.303\,RT} - a\,\log\{A\} - b\,\log\{B\} - c\,\log\{R\}\right) \qquad (3.40)$$

which defines pO^{2-} for equilibrium between components of given activities.

The free energies of the different compounds at the temperature, T, are obtained from $\Delta G^\circ_T = \Delta H^\circ_T - T\Delta S^\circ_T$, where ΔH°_T and ΔS°_T are the corresponding enthalpy and entropy changes, respectively, at the temperature, T. Data used for the calculation of the ΔG°_T values were taken from works by Kubaschewski and Alcock (1979) and by Richardson and Jeffes (1952) and are presented in Tables 3.6 and 3.7. The heats of formation and entropies of Na_2O, Na_2S, Na_2SO_4, Fe, O_2, and SO_3 at 1173 K had to be calculated, their values being obtained as shown in the tables.

3.3.1.2 Equilibria in Sulfate Melt

From the thermodynamic viewpoint, the possible reactions related with sodium–sulfate decomposition are:

$$\frac{1}{2}O_2 + 2e^- = O^{2-} \qquad (3.41)$$

$$SO_3 + 2e^- = SO_2 + O^{2-} \qquad (3.42)$$

$$SO_3 + 6e^- = \frac{1}{2}S_2 + 3O^{2-} \qquad (3.43)$$

$$SO_3 + 8e^- = S^{2-} + 3O^{2-} \qquad (3.44)$$

$$Na^+ + e^- = Na \qquad (3.45)$$

The E° values for these equilibria can be obtained from the following reactions:

$$Na_2SO_4 = SO_3 + Na_2O \quad (\Delta G^\circ = 103.1537\ \text{kcal}) \qquad (3.46)$$

$$Na_2SO_4 = SO_2 + \frac{1}{2}O_2 + Na_2O \quad (\Delta G^\circ = 100.6984\ \text{kcal}) \qquad (3.47)$$

$$3Na_2SO_4 = 2SO_3 + \frac{1}{2}S_2 + \frac{3}{2}O_2 + 3Na_2O \quad (\Delta G^\circ = 373.3212\ \text{kcal}) \qquad (3.48)$$

$$4Na_2SO_4 = 3SO_3 + 2O_2 + Na_2S + 3Na_2O \quad (\Delta G^\circ = 474.3881\ \text{kcal}) \qquad (3.49)$$

$$\frac{1}{2}Na_2SO_4 = Na + \frac{1}{2}SO_3 + \frac{1}{4}O_2 \quad (\Delta G^\circ = 84.7130\ \text{kcal}) \qquad (3.50)$$

using the procedure reported previously by Sequeira and Hocking (1977). We have decided to repeat these calculations since the thermodynamic data used before do not coincide with the most recent data selected for this construction.

From the E° values and the equilibrium for the acid–base Reaction (3.36), which may be expressed by

$$pO^{2-} - \log p_{SO_3} = -\log[\{Na_2O\}x\,p_{SO_3}] = 19.23 \qquad (3.51)$$

and taking the SO_4^{2-} activity as unity and assuming that Na_2O is an ionic compound, the Nernst equations for Reactions (3.41)–(3.45) were obtained; they are assembled in Table 3.6. As seen in this table, the value of E°_{45}, for example, differs by 0.137 V from the one reported previously, which justifies the present calculation. It is therefore possible to build up a diagram by plotting E versus pO^{2-} for Reactions (3.41)–(3.45) as is shown in Figure 3.27.

As referred to in the previous work by Sequeira and Hocking (1977), the acidity of the system plays an important role in deciding which of the cathodic Reactions (3.42)–(3.45) is most favorable thermodynamically. In acid melts ($pO^{2-} > 12.58$), the reduction of SO_3 to SO_2 is likely to occur rather than the reduction to S_2 or to S^{2-}, whereas in basic melts ($pO^{2-} < 12.58$) the sequence is reversed. Even so the reduction of SO_3 is a more favored process with respect to Na^+ cation discharge.

3.3.1.3 Iron Sulfate Equilibria

Once the equilibrium diagram for sodium–sulfate is established, those equilibria where either iron or iron compounds are involved can be considered.

The species that may be formed when molten Na_2SO_4 attacks iron are Fe^{2+}, Fe^{3+}, FeO, Fe_2O_3, Fe_3O_4, FeS, and FeS_2 (Baudo and Tamba 1969; Rahmel 1968, 1977).

Table 3.6 Thermochemical data for the species under consideration

Substance	$-\Delta H^{\circ}_{298}$ (kcal mol^{-1})	S°_{298} (cal deg^{-1} mol^{-1})	Tr. Pt. (K)	L_t (kcal mol^{-1})	M.P. (K)	L_f (kcal mol^{-1})
Fe(s)	0	6.52	1033	1.22		
$FeSO_4$(s)	222.0	28.91				
$Fe_2(SO_4)_3$(s)	617.35	73.5				
Na_2O(s)	99.2	17.94	1023	0.42		
Na_2S(s)	89.5	19.0				
$Na_2(SO_4)$(s)	333.5	35.73	522; 980	2.58; 0.08	1157	5.5
O_2(g)	0	49.0				
SO_3(g)	94.58	61.35				

Substance	$C_p = a + b + cT^{-2}$ (cal deg^{-1} mol^{-1})			Temperature range (K)
	a	$b \times 10^3$	$c \times 10^{-5}$	
Fe(s,α,γ)	8.873	1.474		298–1809
Na_2O(s,α)	13.26	16.78	−0.99	298–1023
Na_2O(s,ß)	19.67	3.05		1023–1243
Na_2S(s)	18.10	3.0		298–1251
Na_2SO_4(s,α)	23.50	31.74		298–450
Na_2SO_4(s,γ)	29.06	19.34		514–1157
Na_2SO_4(l)	47.18			1157–1850
O_2(g)	7.16	1.0	−0.40	298–3000
SO_3(g)	13.70	6.42	−3.12	298–1200

Reaction	$\Delta G^{\circ} = A + BT$ (cal)		Temperature range (K)
	A	B	
$FeO(s) = Fe(s) + \frac{1}{2}O_2(g)$	63 310	−15.62	298–1642
$Fe_3O_4(s) = 3FeO(s) + \frac{1}{2}O_2(g)$	74 620	−29.9	298–1642
$3Fe_2O_3(s) = 2Fe_3O_4(s) + \frac{1}{2}O_2(g)$	59 620	−33.62	298–1460
$2FeS(s\ ß) = 2Fe(s,\alpha) + S_2(g)$	71 820	−25.12	412–1179
$2FeS_2(s) = 2FeS(s) + S_2(g)$	73 600	−68.00	600–1200
$Na_2S(s) = 2Na(l) + \frac{1}{2}S_2(g)$	105 250	−31.45	371–1187
$S_2(g) + 2O_2(g) = 2SO_2(g)$	−173 240	34.62	298–2000
$S_2(g) + 3O_2(g) = 2SO_3(g)$	−218 440	77.34	318–1800

Conversion factor 1 cal = 4.184 J.

Therefore, only the following equilibria are considered:

$$Fe^{2+} + 2e^- = Fe \quad (3.52)$$

$$Fe^{3+} + 3e^- = Fe \quad (3.53)$$

$$FeO + 2e^- = Fe + O^{2-} \quad (3.54)$$

$$Fe_2O_3 + 6e^- = 2Fe + 3O^{2-} \quad (3.55)$$

$$Fe_3O_4 + 8e^- = 3Fe + 4O^{2-} \quad (3.56)$$

$$Fe + SO_3 + 6e^- = FeS + 3O^{2-} \quad (3.57)$$

$$Fe + 2SO_3 + 12e^- = FeS_2 + 6O^{2-} \quad (3.58)$$

$$Fe^{3+} + e^- = Fe^{2+} \quad (3.59)$$

$$FeO = Fe^{2+} + O^{2-} \quad (3.60)$$

$$Fe_2O_3 + 2e^- = 2Fe^{2+} + 3O^{2-} \quad (3.61)$$

$$Fe_3O_4 + 2e^- = 3Fe^{2+} + 4O^{2-} \quad (3.62)$$

$$Fe^{2+} + SO_3 + 8e^- = FeS + 3O^{2-} \quad (3.63)$$

$$Fe^{2+} + 2SO_3 + 14e^- = FeS_2 + 6O^{2-} \quad (3.64)$$

$$Fe^{3+} + O^{2-} + e^- = FeO \quad (3.65)$$

Table 3.7 Data for the heats and entropies of the formation of Fe, Na_2O, Na_2S, Na_2SO_4, O_2, and SO_3 at 1173 K

	$\Delta H^\circ_{1173} = \Delta H^\circ_{298} + \int_{298}^{1173} \Delta C_p dT + L_t + L_f$				ΔH°_{1173}
Substance	ΔH°_{298}	$\int_{298}^{1173} \Delta C_p dT$	L_t	L_f	(kcal mol^{-1})
Fe(s,α,γ)	0	8.7125	1.22		9.9325
Na_2O(s)	−99.2	20.8683	0.42		−77.9117
Na_2S(s)	−89.5	17.7682			−71.7318
Na_2SO_4(l)	−333.5	27.6904[a]	2.58; 0.08	5.5	−297.6496
O_2(g)	0	6.8085			6.8085
SO_3(g)	−94.58	15.3383			−79.2417

	$S^\circ_{1173} = S^\circ_{298} + \int_{298}^{1173} \frac{\Delta C_p}{T} dT + \frac{L_t}{T_t} + \frac{L_f}{T_f}$				S°_{1173}
Substance	S°_{298}	$\int_{298}^{1173} \frac{\Delta C_p}{T} dT$	$\frac{L_t}{T_t}$	$\frac{L_f}{T_f}$	(cal deg^{-1} mol^{-1})
Fe(s,α,γ)	6.52	13.46	1.18		21.16
Na_2O(s)	17.94	31.045	0.41		49.395
Na_2S(s)	19.0	27.353			46.353
Na_2SO_4(l)	35.73	56.18	4.94; 0.081	4.75	101.68
O_2(g)	49.0	10.446			59.446
SO_3(g)	61.35	22.77			84.12

Conversion factor 1 cal = 4.184 J.

[a]The heat capacity of Na_2SO_4 in the temperature range 450–514 K is assumed to be given by the equation for the temperature range 298–450 K.

$$Fe_2O_3 = 2Fe^{3+} + 3O^{2-} \quad (3.66)$$

$$3Fe^{3+} + 4O^{2-} + e^- = Fe_3O_4 \quad (3.67)$$

$$Fe^{3+} + SO_3 + 9e^- = FeS + 3O^{2-} \quad (3.68)$$

$$Fe^{3+} + 2SO_3 + 15e^- = FeS_2 + 6O^{2-} \quad (3.69)$$

$$Fe_2O_3 + 2e^- = 2FeO + O^{2-} \quad (3.70)$$

$$Fe_3O_4 + 2e^- = 3FeO + O^{2-} \quad (3.71)$$

$$FeO + SO_3 + 8e^- = FeS + 4O^{2-} \quad (3.72)$$

$$FeO + 2SO_3 + 14e^- = FeS_2 + 7O^{2-} \quad (3.73)$$

$$3Fe_2O_3 + 2e^- = 2Fe_3O_4 + O^{2-} \quad (3.74)$$

$$Fe_2O_3 + 2SO_3 + 18e^- = 2FeS + 9O^{2-} \quad (3.75)$$

$$Fe_2O_3 + 4SO_3 + 30e^- = 2FeS_2 + 15O^{2-} \quad (3.76)$$

$$Fe_3O_4 + 3SO_3 + 26e^- = 3FeS_2 + 13O^{2-} \quad (3.77)$$

$$Fe_3O_4 + 6SO_3 + 44e^- = 3FeS_2 + 22O^{2-} \quad (3.78)$$

$$FeS + SO_3 + 6e^- = FeS_2 + 3O^{2-} \quad (3.79)$$

In these equilibria, the O^{2-} potential is that in Na_2O resulting from the acid–base dissociation equilibrium (3.36).

E°_{52} can be obtained from Reaction (3.38) and the following equilibrium:

$$Fe_2SO_4 = Fe + SO_3 + \frac{1}{2}O_2 \quad (3.80)$$

assuming that ferrous sulfate is an ionic compound. As no thermal data for the ferrous sulfate at 1173 K exist, the corresponding free energy of the formation was calculated using the approximate relation, $\Delta G^\circ_T = \Delta H^\circ_{298} - T\Delta S^\circ_{298}$. Hence, $\Delta G^\circ_{80} = 31.6479$ kcal and E°_{52} is calculated from Reaction (3.38) and data for

$$\frac{1}{2}Fe_2(SO_4)_3 = Fe + \frac{3}{2}SO_3 + \frac{1}{4}O_2 \quad (3.81)$$

The free energy for the ferric sulfate was calculated using the approximate relation above. So, $\Delta G^\circ_{81} = 22.8315$ kcal and $E^\circ_{53} = -0.3300$ V.

To evaluate E°_{54}, the following reaction must be considered:

$$FeO = Fe + \frac{1}{2}O_2 \quad (3.82)$$

in addition to Reaction (3.41). Thus, $E^\circ_{54} = -3.2120$ V.

To evaluate E°_{55}, the following reaction must be considered:

$$Fe_2O_3 = 2Fe + \frac{3}{2}O_2 \quad (3.83)$$

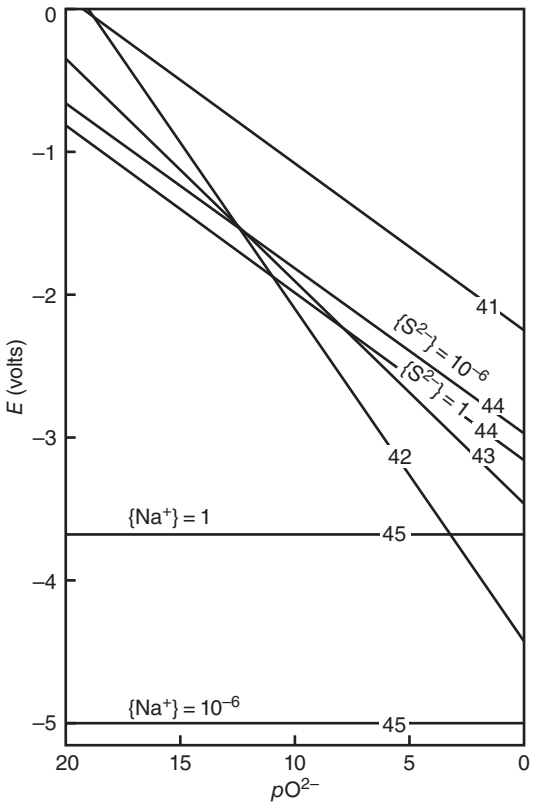


Figure 3.27 Electrochemical equilibria for Na_2SO_4 at 1173 K. The numbers correspond to the equilibria given in Table 3.8.

in addition to Reaction (3.41). Thus, $E^\circ_{55} = -3.1261$ V.

To evaluate E°_{56}, the following reaction must be considered:

$$Fe_3O_4 = 3Fe + 2O_2 \tag{3.84}$$

in addition to Reaction (3.41). Thus, $E^\circ_{56} = -3.1826$ V.

E°_{57} is calculated from Reaction (3.41) and data for

$$Fe + SO_3 = FeS + \frac{3}{2}O_2 \tag{3.85}$$

Hence, $E^\circ_{57} = -2.5451$ V.

E°_{58} is calculated from Reaction (3.41) and data for

$$Fe + 2SO_3 = FeS_2 + 3O_2 \tag{3.86}$$

Hence, $E^\circ_{58} = -2.6328$ V.

Data for Reaction (3.59) are obtained from Reactions (3.52) and (3.53). Therefore, $E^\circ_{59} = +0.3823$ V.

Data for Reaction (3.60) are obtained from Reactions (3.41), (3.52), and (3.82). From equilibrium (3.60), the activity of ferrous ion is thus obtained as

$$\log\{Fe^{2+}\} = -21.71 + pO^{2-} \tag{3.87}$$

E°_{61} is −8.0058 V as calculated from Reactions (3.52) and (3.55).

For calculating E°_{62}–E°_{65} the same procedure is followed, taking into account the Reactions ((3.52), (3.56)), ((3.52), (3.57)), ((3.52), (3.58)), and ((3.53), (3.54)). Thus, $E^\circ_{62} = -10.6716$ V, $E^\circ_{63} = -2.0804$ V, $E^\circ_{64} = -2.3547$ V, and $E^\circ_{65} = +5.4340$ V.

Data for Reaction (3.66) are obtained from Reactions (3.41), (3.53), and (3.83). From equilibrium (3.66), the activity of ferric ion is thus obtained as

$$\log\{Fe^{3+}\} = -36.06 + \frac{3}{2}pO^{2-} \tag{3.88}$$

E°_{67} is +22.4902 V as calculated from Reactions (3.53) and (3.56).

For calculating E°_{68}–E°_{79} the same procedure is followed, taking into account the Reactions ((3.53), (3.57)), ((3.53), (3.58)), ((3.54), (3.55)), ((3.54), (3.56)), ((3.54), (3.57)), ((3.54), (3.58)), ((3.55), (3.56)), ((3.55), (3.57)), ((3.55), (3.58)), ((3.56), (3.57)), ((3.56), (3.58)), and ((3.57), (3.58)), respectively. Thus, $E^\circ_{68} = -1.8067$ V, $E^\circ_{69} = -2.1722$ V, $E^\circ_{70} = -2.9541$ V, $E^\circ_{71} = -3.0941$ V, $E^\circ_{72} = -2.7118$ V, $E^\circ_{73} = -2.7155$ V, $E^\circ_{74} = -2.6743$ V, $E^\circ_{75} = -2.7388$ V, $E^\circ_{76} = -2.7314$ V, $E^\circ_{77} = -2.7412$ V, $E^\circ_{78} = -2.7327$ V, and $E^\circ_{79} = -2.7204$ V.

The reactions together with the corresponding potential $-pO^{2-}$ relationships used to drive stability diagrams for the iron/sodium–sulfate system at 1173 K are listed in Table 3.8. The Nernst equations for Fe, Fe^{2+}, Fe^{3+}, FeO, Fe_3O_4, and Fe_2O_3 species, as well as those that are independent of the redox potential (Eqs. (3.87) and (3.88)) are plotted in Figure 3.28 as a potential $-pO^{2-}$ diagram at 1173 K. The Nernst equations for Fe, Fe^{2+}, Fe^{3+}, FeS, and FeS_2 species are plotted in Figure 3.29, still as potential $-pO^{2-}$ diagram at 1173 K. For this purpose, the SO_3 term is eliminated in favor of O^{2-} and SO_4^{2-} using equilibrium (3.51) for the acid–base Reaction (3.36). It is thus assumed that the SO_4^{2-} activity is unity at all the phase boundaries, which is a reasonable approximation in high temperature corrosion, particularly if one does not go deeper into the scale.

3.3.1.4 Conclusions

Potential $-pO^{2-}$ diagrams (Figures 3.30–3.32) for the iron/sodium–sulfate system at 1173 K have been constructed from the thermodynamic properties given in Tables 3.6–3.8 and an analysis of Figures 3.27–3.29. In these diagrams, the lines bounding regions of soluble species are defined as representing activities of 10^{-6}.

The diagonal broken lines (41), (42), and (44) in the diagrams represent the limits for the thermodynamic stability of molten sodium–sulfate at 1 atm (101 kN m^{-2}) total pressure. The lower lines represent the equilibrium potentials for the production of SO_2 (p_{SO_2} = 1 atm) and S^{2-} ($\{S^{2-}\} = 10^{-6}$), respectively, as a function of pO^{2-}.

Table 3.8 Nernst equations at 1173 K

$\frac{1}{2}O_2 + 2e^- = O^{2-}$ (3.41)	$E = -2.2366 + 0.0582 \log p_{O_2} + 0.1163\, pO^{2-}$
$SO_3 + 2e^- = SO_2 + O^{2-}$ (3.42)	$E = -2.1833 + 0.1163 \log p_{SO_3} - 0.1163 \log p_{SO_2} + 0.1163\, pO^{2-}$
	$E = -4.4119 - 0.1163 \log p_{SO_2} + 0.2326\, pO^{2-}$
$SO_3 + 6e^- = \frac{1}{2}S_2 + 3O^{2-}$ (3.43)	$E = -2.6980 + 0.3876 \log p_{SO_3} - 0.01938 \log p_{S_2} + 0.1163\, pO^{2-}$
	$E = -3.4434 - 0.1938 \log p_{S_2} + 0.1551\, pO^{2-}$
$SO_3 + 8e^- = S^{2-} + 3O^{2-}$ (3.44)	$E = -2.5716 + 0.0291 \log p_{SO_3} - 0.0291 \log \{S^{2-}\} + 0.0872\, pO^{2-}$
	$E = -3.1312 - 0.0291 \log \{S^{2-}\} + 0.1163\, pO^{2-}$
$Na^+ + e^- = Na$ (3.45)	$E = -3.6735 + 0.2326 \log \{Na^+\}$
$Fe^{2+} + 2e^- = Fe$ (3.52)	$E = -0.6862 + 0.1163 \log \{Fe^{2+}\}$
$Fe^{3+} + 3e^- = Fe$ (3.53)	$E = -0.3300 + 0.775 \log \{Fe^{3+}\}$
$FeO + 2e^- = Fe + O^{2-}$ (3.54)	$E = -3.2120 + 0.1163\, pO^{2-}$
$Fe_2O_3 + 6e^- = 2Fe + 3O^{2-}$ (3.55)	$E = -3.1261 + 0.1163\, pO^{2-}$
$Fe_3O_4 + 8e^- = 3Fe + 4O^{2-}$ (3.56)	$E = -3.1826 + 0.1163\, pO^{2-}$
$Fe + SO_3 + 6e^- = FeS + 3O^{2-}$ (3.57)	$E = -2.5451 + 0.0388 \log p_{SO_3} + 0.1163\, pO^{2-}$
	$E = -3.2907 + 0.1551\, pO^{2-}$
$Fe + 2SO_3 + 12e^- = FeS_2 + 6O^{2-}$ (3.58)	$E = -2.6328 + 0.0388 \log p_{SO_3} + 0.1163\, pO^{2-}$
	$E = -3.3784 + 0.1551\, pO^{2-}$
$Fe^{3+} + e^- = Fe^{2+}$ (3.59)	$E = +0.3823 + 0.2326 \log \{Fe^{3+}\} - 0.2326 \log \{Fe^{2+}\}$
$Fe_2O_3 + 2e^- = 2Fe^{2+} + 3O^{2-}$ (3.61)	$E = -8.0058 - 0.2326 \log \{Fe^{2+}\} + 0.3489\, pO^{2-}$
$Fe_3O_4 + 2e^- = 3Fe^{2+} + 4O^{2-}$ (3.62)	$E = -10.6716 - 0.3489 \log \{Fe^{2+}\} + 0.4652\, pO^{2-}$
$Fe^{2+} + SO_3 + 8e^- = FeS + 3O^{2-}$ (3.63)	$E = -2.0804 + 0.0291 \log\{Fe^{2+}\} + 0.0291 \log p_{SO_3} + 0.0872\, pO^{2-}$
	$E = -2.6400 + 0.0291 \log \{Fe^{2+}\} + 0.1163\, pO^{2-}$
$Fe^{2+} + 2SO_3 + 14e^- = FeS_2 + 6O^{2-}$ (3.64)	$E = -2.3547 + 0.0166 \log\{Fe^{2+}\} + 0.0332 \log p_{SO_3} + 0.0997\, pO^{2-}$
	$E = -2.9931 + 0.0166 \log \{Fe^{2+}\} + 0.1329\, pO^{2-}$
$Fe^{3+} + O^{2-} + e^- = FeO$ (3.65)	$E = +5.4340 + 0.2326 \log \{Fe^{3+}\} - 0.2326\, pO^{2-}$
$3Fe^{3+} + 4O^{2-} + e^- = Fe_3O_4$ (3.67)	$E = +22.4902 + 0.6978 \log \{Fe^{3+}\} - 0.9304\, pO^{2-}$
$Fe^{3+} + SO_3 + 9e^- = FeS + 3O^{2-}$ (3.68)	$E = -1.8067 + 0.0258 \log\{Fe^{3+}\} + 0.0258 \log p_{SO_3} + 0.0775\, pO^{2-}$
	$E = -2.3028 + 0.0258 \log \{Fe^{3+}\} - 0.1033\, pO^{2-}$
$Fe^{3+} + 2SO_3 + 15e^- = FeS_2 + 6O^{2-}$ (3.69)	$E = -2.1722 + 0.0155 \log\{Fe^{3+}\} + 0.0310 \log p_{SO_3} + 0.0931\, pO^{2-}$
	$E = -2.7683 + 0.0155 \log \{Fe^{3+}\} - 0.1241\, pO^{2-}$
$Fe_2O_3 + 2e^- = 2FeO + O^{2-}$ (3.70)	$E = -2.9541 + 0.1163\, pO^{2-}$
$Fe_3O_4 + 2e^- = 3FeO + O^{2-}$ (3.71)	$E = -3.0941 + 0.1163\, pO^{2-}$
$FeO + SO_3 + 8e^- = FeS + 4O^{2-}$ (3.72)	$E = -2.7118 + 0.0291 \log p_{SO_3} + 0.1163\, pO^{2-}$
	$E = -3.2714 + 0.1454\, pO^{2-}$
$FeO + 2SO_3 + 14e^- = FeS_2 + 7O^{2-}$ (3.73)	$E = -2.7155 + 0.0332 \log p_{SO_3} + 0.1163\, pO^{2-}$
	$E = -3.3359 + 0.1495\, pO^{2-}$
$3Fe_2O_3 + 2e^- = 2Fe_3O_4 + O^{2-}$ (3.74)	$E = -2.6743 + 0.1163\, pO^{2-}$
$Fe_2O_3 + 2SO_3 + 18e^- = 2FeS + 9O^{2-}$ (3.75)	$E = -2.7388 + 0.0258 \log p_{SO_3} + 0.1163\, pO^{2-}$
	$E = -3.2349 + 0.1421\, pO^{2-}$
$Fe_2O_3 + 4SO_3 + 30e^- = 2FeS_2 + 15O^{2-}$ (3.76)	$E = -2.7314 + 0.0310 \log p_{SO_3} + 0.1163\, pO^{2-}$
	$E = -3.3275 + 0.1473\, pO^{2-}$
$Fe_3O_4 + 3SO_3 + 26e^- = 3FeS_2 + 13O^{2-}$ (3.77)	$E = -2.7412 + 0.2684 \log p_{SO_3} + 0.1163\, pO^{2-}$
	$E = -3.2573 + 0.1431\, pO^{2-}$
$Fe_3O_4 + 6SO_3 + 44e^- = 3FeS_2 + 22O^{2-}$ (3.78)	$E = -2.7327 + 0.0317 \log p_{SO_3} + 0.1163\, pO^{2-}$
	$E = -3.3423 + 0.1480\, pO^{2-}$
$FeS + SO_3 + 6e^- = FeS_2 + 3O^{2-}$ (3.79)	$E = -2.7204 + 0.0388 \log p_{SO_3} + 0.1163\, pO^{2-}$
	$E = -3.4660 + 0.1551\, pO^{2-}$

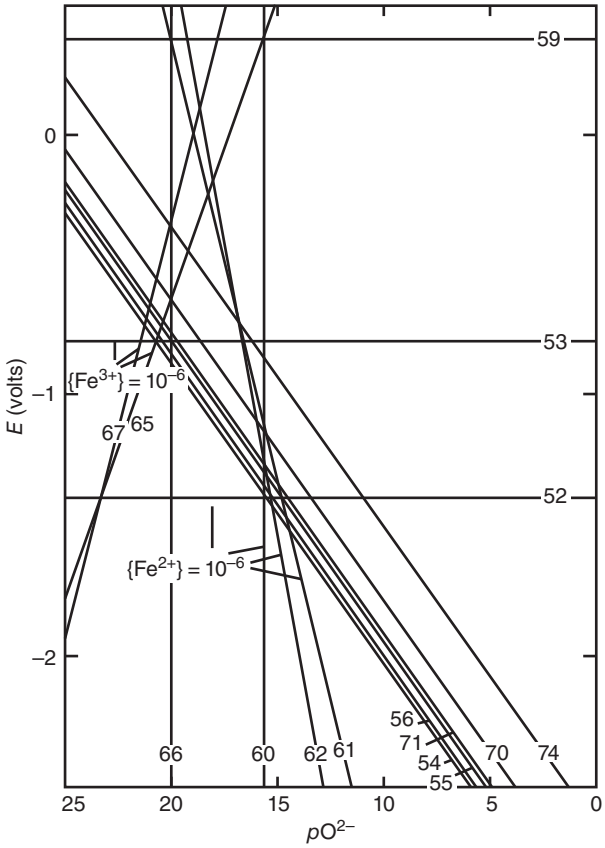


Figure 3.28 Electrochemical equilibria for Fe/Na_2SO_4 at 1173 K assuming the oxide presence only. The numbers correspond to the equilibria given in Table 3.8.

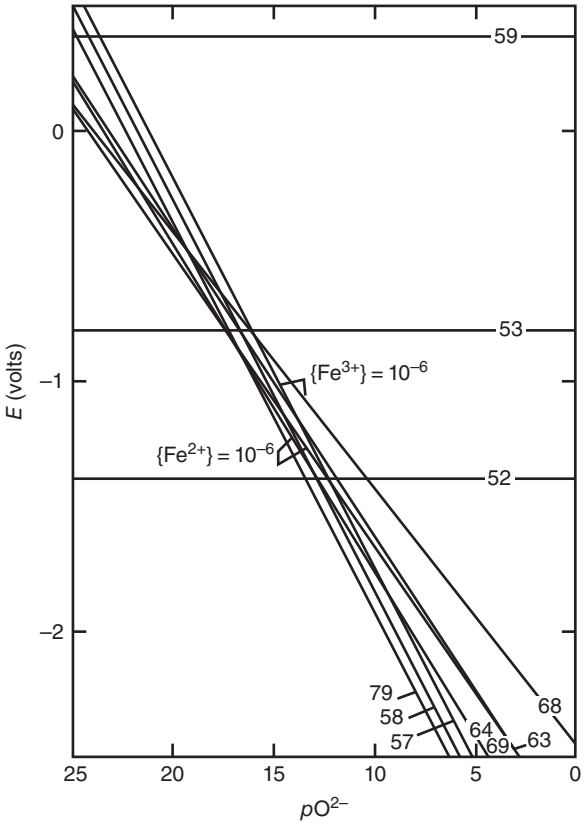


Figure 3.29 Electrochemical equilibria for Fe/Na_2SO_4 at 1173 K assuming the sulfide presence only. The numbers correspond to the equilibria given in Table 3.8.

The upper limit of sodium–sulfate stability is that for the equilibrium between sulfate and oxygen ($p_{O_2} = 1$ atm). This domain of stability provides information concerning the possible existence of mixed potentials and the probable reactions comprised therein.

As shown in Figure 3.30, assuming that sulfidation is unlikely to occur, there is a region of immunity where Fe is stable. The limits of this region are the lines defining the Fe/FeO and Fe/Fe^{2+} (in $FeSO_4$) equilibria, depending on the activity of oxide ions in the melt. A second region is distinguished at higher anodic potentials and low oxide ion activity ($pO^{2-} > 15.71$), where the stable species are Fe^{2+} or Fe^{3+} dissolved in the molten salt. This area is limited by equilibria comprising oxide or metal/ionic species. The number of these equilibria that may participate in the corrosion and passivation phenomena depends on the metal. Thus, three equilibria could be calculated for iron and only one for nickel (Sequeira and Hocking 1977). The third region corresponds to passivity, and it extends at potentials above the Fe/FeO equilibrium line and toward the region of higher oxide ion activity. This region is limited at high anodic potentials by the reversible O_2/O^{2-} electrode line. This region comprises the Fe/FeO, FeO/Fe_3O_4, and Fe_3O_4/Fe_2O_3 equilibria. It is also interesting to note that the region of existence of FeO is not so narrow as at 873 K, but even so, the higher oxides Fe_2O_3 and Fe_3O_4 continue to be the main products of corrosion reactions at 1173 K, at least for most of the E, pO^{2-} values, as may be seen from Figure 3.30.

Figure 3.31 was constructed considering the possibility of the formation of iron sulfides as corrosion products. As above, there are regions of Fe immunity, corrosion, and passivation. But, in this case, the concept of passivation is rather misleading, because sulfides are unlikely to give effective protection. Diffusion through sulfide layers will allow a significant reaction rate at 1173 K and mechanical failure of these layers may also occur (Mrowec et al. 1969). The diagram also shows two other significant changes that occur as a result of considering the iron sulfides instead of the iron oxides. First, the region of stability of iron metal effectively decreases, but the lower limit for the stability of sodium–sulfate lies well into this domain. In other words, Fe remains stable at lower anodic potentials and high oxide ion activity ($pO^{2-} < 12.25$). Second, the equilibrium line for the evolution of oxygen at $pO^{2-} < 7.5$ is lowered in relation to that for the equilibrium between iron and

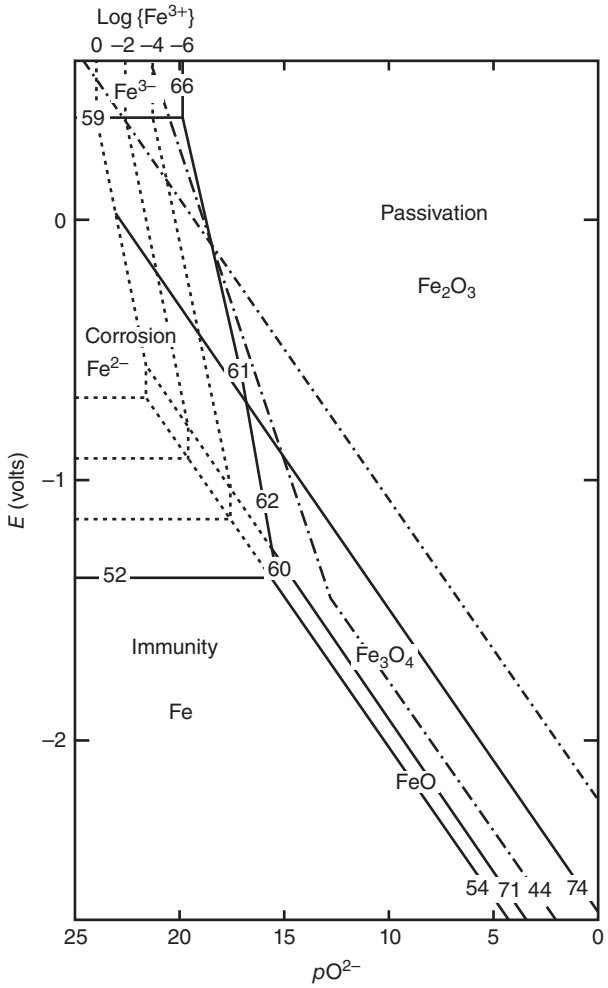


Figure 3.30 E–$p\mathrm{O}^{2-}$ diagram for the system Fe/Na_2SO_4 at 1173 K based on the assumption of oxide formation only. The numbers correspond to the equilibria given in Table 3.8.

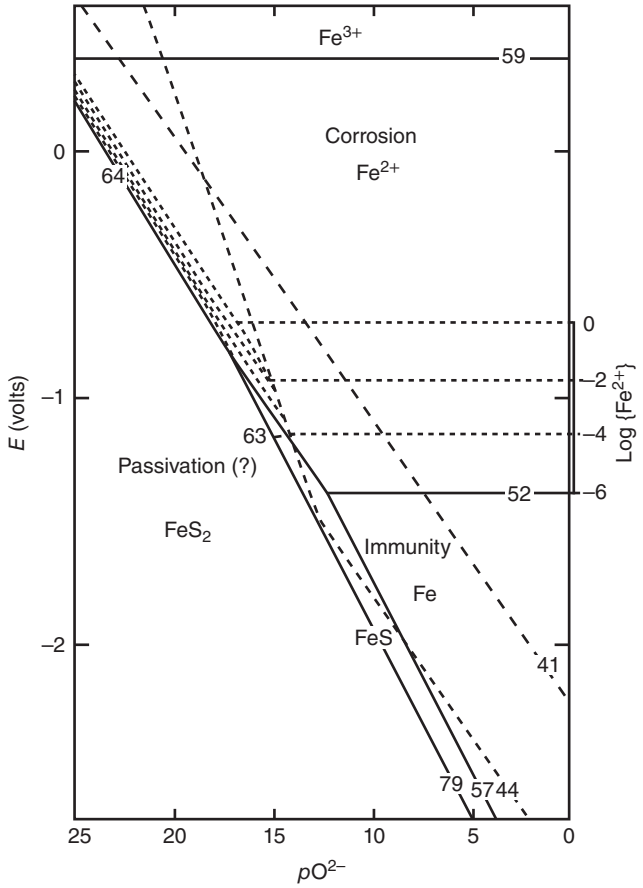


Figure 3.31 E–$p\mathrm{O}^{2-}$ diagram for the system Fe/Na_2SO_4 at 1173 K based on the assumption of sulfide formation only. The numbers correspond to the equilibria given in Table 3.8.

$FeSO_4$. Thus, the O_2/O^{2-} equilibrium line appears at more negative potentials than that of Fe^{2+}/Fe equilibrium line. Therefore, $FeSO_4$ is unstable in the presence of basic molten sodium–sulfate at 1173 K, and oxygen tends to be evolved.

The E–$p\mathrm{O}^{2-}$ diagram for the system Fe/Na_2SO_4 at 1173 K based on the assumption of sulfide and oxide formation is shown in Figure 3.32. Since this figure takes into account the possibilities of oxide and sulfide formation, the stability of the metal iron can now be discussed with some real significance; discussion is without relevance if it is based on Figures 3.30 and 3.31 because there is no exclusive oxide (sulfide) formation in the Fe/Na_2SO_4 system at 1173 K. Such a region of stability is limited by the lines defining the iron/iron oxide and iron/iron sulfide equilibria. One important feature of this region is that it lies outside the region for the stability of Na_2SO_4; therefore, the establishment of conditions for Fe immunity in Na_2SO_4 cannot be achieved without the aid of external action. The corrosion area is located at higher anodic potentials and low oxide ion activity and is limited by equilibria comprising iron oxides or iron sulfides/iron ion species. The passivity area comprises three oxide and two sulfide species, and it extends over the whole range of $p\mathrm{O}^{2-}$. In the region extending above the line of the oxygen/oxide electrode, localized corrosion may occur because of the instability of the oxide ion. These regions, in general, present common features with those found for the iron electrode in the fused sulfate system at 873 K, as well as in aqueous systems (Pourbaix 1966).

The thermodynamic diagrams of the iron/molten sodium–sulfate help one to visualize the role of acid–base equilibria in determining corrosion conditions, but they are not necessarily relevant when kinetic effects are present. When equilibrium conditions no longer prevail, the predicted picture may be strongly modified, although it is also possible that, during corrosion or passivation in the case of the molten system, equilibrium conditions are closer than in aqueous systems (Littlewood 1965).

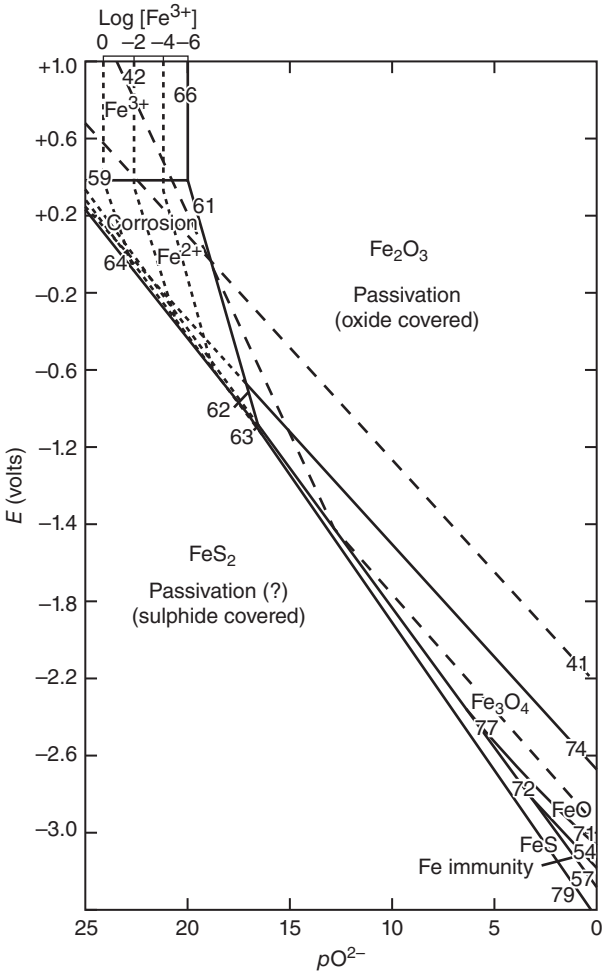


Figure 3.32 E–pO^{2-} diagram for the system Fe/Na_2SO_4 at 1173 K based on the assumption of sulfide and oxide formation. The numbers correspond to the equilibria given in Table 3.8.

In any case, on the assumption of both sulfide and oxide formation, only the simultaneous basicity of the melt and cathodic polarization by lowering the potential into the region of immunity of the metal may be an effective remedy against iron corrosion in the melt. On the other hand, this protection is much more reliable when the applied potential is only slightly more negative than the potential for the metal/metal–oxide equilibrium, as the immunity region is very narrow. It is also obvious that the possibility of controlling iron corrosion by alkalizing and cathodically polarizing is enhanced if the formation of iron sulfides occurs very slowly due to high *overpotential* for processes such as $Fe + SO_3 + 6e^- \rightarrow FeS + 3O^{2-}$.

References

Aaranson, H.I. (ed.) (1999). *Lectures on the Theory of Phase Transformations*. Warrendale, PA: The Minerals, Metals and Materials Society.

Alcock, C.B. (1976). *Principles of Pyrometallurgy*. London: Academic Press.

Ancy-Moret, M.F. (1973). *Mem. Sci. Rev. Metall.* 70: 429.

Arper, A.M. (ed.) (1970). *Phase Diagrams, Materials Science and Technology*, vol. 1. New York: Academic Press.

Bale, C.W. (2009). *CALPHAD* 33: 295.

Barralis, J. and Maeder, G. (1997). *Précis de Métallurgie: Élaboration, Structures-propriétés, Normalisation*. Paris: AFNOR-Nathan.

Baudo, G. and Tamba, A. (1969). *Br. Corros. J.* 4: 129.

Belton, G.R. and Worrel, W.R. (eds.) (1970). *Heterogeneous Kinetics at Elevated Temperatures*. New York: Plenum Press.

Birks, N., Meier, G.H., and Pettit, F.S. (2006). *Introduction to the High-Temperature Oxidation of Metals*. Cambridge: Cambridge University Press.

Chase, M.W., Curnutt, J.L., Prophet, H. et al. (1975). JANAF thermochemical tables. *J. Phys. Chem. Ref. Data* 4 (1).

Chase, M.W., Curnutt, J.L., Prophet, H. et al. (1986). *JANAF Thermochemical Tables*, 3e. Midland, MI: Dow Chemical Co.

Darken, L.S. and Gurry, R.W. (1953). *Physical Chemistry of Metals*. New York: McGraw-Hill.

Ellingham, H.J.T. (1944). *J. Soc. Chem. Ind.* 63: 125.

Eriksson, G. (1975). *Chem. Soc.* 8: 100.

Eriksson, G. and Hack, K. (1990). *Metall. Trans. B* B21: 1013.

Flood, H., Förland, T., and Motzfeld, K. (1952). *Acta Chem. Scand.* 6: 257.

Gaskell, D.R. (1995). *Introduction to the Thermodynamics of Materials*, 3e. Washington, DC: Taylor and Francis.

Gibbs, J.W. (1961). *The Scientific Papers*, vol. 1, 65. New York: Dover Publication.

Giggins, C.S. and Pettit, F.S. (1980). *Oxid. Met.* 14: 363.

Gray, J.A. and Starr, F. (1980). *Proc. Petten Int. Conf* (ed. I. Kirman), 3. London: The Metals Society.

Gulbransen, E.A. and Jansson, S.A. (1970). *Heterogeneous Kinetics at Elevated Temperatures* (ed. G.R. Belton and W.R. Warrel). New York: Plenum Press.

Gulbransen, E.A. and Meier, G.H. (1979). DOE Report on Contract No. DE-AC01–79-ET-13547. University of Pittsburgh, USA.

Hemmings, P.L. and Perkins, R.A. (1977). Report FP-539, EPRI. Palo Alto, CA, USA.

Ingraham, R.R. (1966). *Trans. Metall. Soc. AIME* 236: 1064.

Ingraham, R.R. (1967). *Applications of Fundamental Thermodynamics to Metallurgical Processes* (ed. G.R. Fitterer), 179. New York: Gordon & Breach.

Jacob, K.T., Rao, D.B., and Nelson, H.G. (1979). *Oxid. Met.* 13: 25.

Jansson, S.A. and Foroulis, Z.A. (eds.) (1973). *High Temperature Gas-Metal Reactions in Mixed Environments*. New York: American Institute of Mining, Metallurgical and Petroleum Engineering.

Knacke, O. (1972). *Metallurgical Chemistry* (ed. O. Kubaschewski), 549. London: N.P.L., H.M.S.O.

Kellog, H.H. and Basu, S.K. (1960). *Trans. Metall. Soc. AIME* 218: 76.

Königsberger, E. and Eriksson, G. (1995). *CALPHAD* 19: 207.

Kubaschewski, O. and Alcock, C.B. (1979). *Metallurgical Thermochemistry*, 5e. Oxford: Pergamon Press.

Lions, J. (1980). *Proc. Petten Int. Conf* (ed. I. Kirman), 769. London: The Metals Society.

Littlewood, R. (1962). *J. Electrochem. Soc.* 109: 525.

Littlewood, R. (1965). *Trans. AIME* 233: 772.

Lux, H. (1939). *Z. Electrochem.* 45: 303.

MacKowiak, J. (1966). *Physical Chemistry for Metallurgists*, 185. New York: George Allen & Unwin.

Mrowec, S., Walec, T., and Weber, T. (1969). *Oxid. Met.* 1: 93.

Nishikata, A., Numata, H., and Tsuru, T. (1991). *Mater. Sci. Eng.* A146: 15.

Pearson, J. and Ende, V. (1953). *J. Iron Steel Inst.* 175: 52.

Pelton, A.D. and Schmalzried, H. (1973). *Metall. Trans.* 4: 1395.

Pettit, F.S. (1967). *Trans. Metall. Soc. AIME* 239: 1296.
Pingfang, S., Engstrom, A., Hoglund, L. et al. (2007). *J. Iron Steel Res. Int.* 14: 210.
Pourbaix, M.S.N. (1966). *Atlas of Electrochemical Equilibria in Aqueous Solutions*. Oxford: Pergamon Press.
Pourbaix, M.S.N. (1980). *The Industrial Use of Thermochemical Data*, Special Publ. No. 34, 55. London: The Chemical Society.
Rahmel, A. (1968). *Electrochim. Acta* 13: 495.
Rahmel, A. (1977). *Werkstoffe Korros.* 28: 299.
Rao, Y.K. (1985). *Stoichiometry and Thermodynamics of Metallurgical Processes*. Cambridge: Cambridge University Press.
Rapp, R.A. (ed.) (1983). *High Temperature Corrosion*. Houston, TX: NACE.
Reynolds, W.C. (1986). STANJAN, version 3. Department of Mechanical Engineering, Stanford University, CA, USA.
Richardson, F.D. and Jeffes, J.H.E. (1948). *J. Iron Steel Inst.* 160: 261.
Richardson, F.D. and Jeffes, J.H.E. (1952). *J. Iron Steel Inst.* 171: 165.
Richardson, F.D. and Jeffes, J.H.E. (1953). *J. Iron Steel Inst.* 175: 33.
Rocabois, P., Chatillon, C., and Bernard, C. (1966). *J. Am. Ceram. Soc.* 79: 1361.
Schick, H. (1966). *Thermodynamics of Certain Refractory Compounds*. New York: Academic Press.
Sequeira, C.A.C. and Hocking, M.G. (1977). *Br. Corros. J.* 12: 158.
Seon, F. (1982). *J. Electroanal. Chem.* 138: 315.
Shatynski, S.R. (1977). *Oxid. Met.* 11: 307.
Shatynski, S.R. (1979). *Oxid. Met.* 13: 105.
Sticher, J. and Schmalzried, H. (1975). Report, Clausthal Institute für Theoretische Huttenkunde und Angewandte Physikalische Chemie der Technische Universität Clausthal.
Stott, F.H. and Smith, S. (1980). *Proc. Petten Int. Conf* (ed. I. Kirman), 781. London: The Metals Society.
Stringer, J. (1980). *Proc. Petten Int. Conf* (ed. I. Kirman), 739. London: The Metals Society.
Sundman, B., Jansson, B., and Andersson, J.-O. (1985). *CALPHAD* 9: 1953.
Swalin, R.A. (1972). *Thermodynamics of Solids*. London: Wiley.
Trémillon, B. (1971). *Pure Appl. Chem.* 25: 395.
Trémillon, B. (1974). *Chemistry in Non-Aqueous Solvents*. London: Reidel Publishing Company.
Villa, H. (1950). *J. Soc. Chem. Ind.* 1: 59.
Wicks, C.E. and Block, F.E. (1963). Bulletin 605. Bureau of Mines, US Government Printing Office, Washington, DC, USA, p. 408.
Yazawa, A. (1979). *Metall. Trans. B* 10B: 307.

Further Reading

Andersson, J.-O., Helander, T., Höglund, L. et al. (2002). *CALPHAD* 26: 273.
Balducci, G., Ciccioli, A., de Maria, G. et al. (2009). *Pure Appl. Chem.* 81 (2): 299.
Barin, I. (1993). *Thermochemical Data of Pure Substances*. Weinheim: Wiley-VCH.
Bender, R. and Shütze, M. (2003). *Mater. Corros.* 54: 567.
GTT-Technologies (1998). Chem. Sage, version 4.16. GTT-Technologies, Aachen, Germany.
Christ, H.J., Chang, S.Y., and Krupp, U. (2003). *Mater. Corros.* 54: 887.
Danielewski, M. (2003). *Corrosion: Fundamentals, Testing and Protection*, ASM Handbook, vol. 13A, 97. ASM International.
Davies, R.H., Dinsdale, A.T., Gisby, J.A. et al. (2002). *CALPHAD* 26: 229.
Grabke, H.J. (1998). *Mater. Corros.* 49: 303.
Grabke, H.J. (1998). *Carburization: A High Temperature Corrosion Phenomenon*, MTI Publications N° 52. St. Louis, MO: Materials Technology Institute of the Chemical Process Industries.
Hocking, M.G. and Sidky, P.S. (1987). *Corros. Sci.* 27: 205.
Hultgren, R., Desai, P., Hawkins, D. et al. (1973). *Selected Values of the Thermodynamic Properties of Elements and Binary Alloys*. Materials Park, OH: ASM.
Jansson, S.A. and Foroulis, Z.A. (eds.) (1973). *High Temperature Gas-Metal Reactions in Mixed Environments*. The Metallurgical Society of AIME.
Lambertin, D. (2005). *J. Nucl. Mater.* 341: 124.
Liu, J.C. and McNallan, M.J. (1999). *Mater. Corros.* 50: 253.
McNallan, M.J. and Opila, E. (eds.) (2001). *High Temperature Corrosion and Materials Chemistry III, Proc*, vol. 2001–12. Pennington, NJ: The Electrochemical Society, Inc.
Nishiyama, Y., Otsuka, N., and Nishizawa, T. (2003). *Corrosion* 59: 688.
Norton, J.F. (ed.) (1984). *High Temperature Materials Corrosion in Coal Gasification Atmospheres*. Amsterdam, Holland: Elsevier.
Opila, E. (2013). *Interface* 22: 69.
Pankratz, J.B. (1984). *Thermodynamic Properties of Halides*, Bureau of Mines Bulletin 672. Washington, DC: US Government Printing Office.
Pingfang, S. (2013). *Materials Corrosion Applications with Thermo-Calc Software*. Stockholm: Thermo-Calc Software.
Saunders, N. and Miodownik, A.P. (eds.) (1998). *CALPHAD (Calculation of Phase Diagrams): A Comprehensive Guide*. London: Pergamon Press.
SSUB4 (2008). SGTE substance database provided by Thermo-Calc Software, v4.1.
Schütze, M. (ed.) (2000). *Corrosion and Environmental Degradation*, Materials Science and Technology, vol. II. Weinheim: Wiley-VCH.
Stott, F.H. and Shih, C.Y. (2000). *Mater. Corros.* 51: 277.
TCSAB (2013). (Thermo-Calc Software AB): Thermo-Calc, DICTRA, and TC-PRISMA, software, databases, programming interfaces and applications. Stockholm, Sweden.
Young, D.J. (2016). *High Temperature Oxidation and Corrosion of Metals*, 2e. Amsterdam, Holland: Elsevier.
Zahs, A., Spiegel, M., and Grabke, H.J. (1999). *Mater. Corros.* 50: 561.

Chapter 4

Lattice Defects in Metal Compounds

4.1 Introduction

From the early 1900s many inorganic compounds were found to be nonstoichiometric, and later theoretical considerations by Wagner and Schöttky (1931) showed that all inorganic compounds may in principle have variable composition. In fact, the very exact stoichiometric composition is an exception rather than the rule and can only be achieved at definite sets of temperature and partial pressures of the components in a crystal.

Concurrently it also became clear that no crystals are ideally built up. At any temperature crystals contain different structural imperfections or defects. There are several types of such *structural defects*, and these are often divided into three main groups:

1. Point defects
2. Line defects
3. Plane defects

If the imperfection is limited to one structural or lattice site and its immediate vicinity, the imperfection is termed a *point defect*. Simple defects of this type include:

1. Empty sites or vacancies where constituent atoms are missing in the structure.
2. Interstitial atoms occupying the interstices between the regular sites.

In principle there may also be misplaced atoms, e.g. a cation on an anion site, but this type of defect is probably not important in oxides. The defects that are formed in pure crystals, e.g. vacancies and interstitial atoms, are commonly called native point defects. Foreign atoms are also usually considered to be point defects.

The line defects or *dislocations* are characterized by displacements in the periodic structure in certain directions. The *plane defects* comprise stacking faults, internal surfaces (e.g. grain boundaries), and external surfaces.

In addition to the structural defects, crystals also contain *electronic imperfections*, i.e. electrons and holes, that are relatively free to move in the crystal.

The different types of imperfections and deviations from the ideal structure and composition determine a number of properties of solids. For instance, it is now well established that diffusion in solids takes place because of the presence of imperfections. Point defects are responsible for lattice diffusion; dislocation or short circuit diffusion takes place along the line defects, and grain boundary and surface diffusion along the plane defects. Solid-state diffusion, in turn, determines or strongly influences a number of properties or processes in solids such as mass transport in solids, solid-state reactions, sintering, many precipitation reactions, high-temperature creep, gas–metal reactions resulting in the formation of compact layers of reaction products, etc. Electronic imperfections determine such properties as electronic conductivity, thermoelectric power, electro-optical properties, etc.

The crystal structures of many of the simple metallic oxides to be discussed later can be considered to consist of a hexagonal or cubic close-packed oxygen ions, while the metal ions occupy interstitial voids in the close-packed structures. The interstitial voids in close-packed structures are of two types:

1. Voids surrounded by four oxygen ions, the so-called tetrahedral voids.
2. Voids surrounded by six oxygen ions, the octahedral voids.

In the close-packed structure, there are two tetrahedral sites and one octahedral site per oxygen ion. In different crystal structures of simple metal oxides, the cations often occupy the tetrahedral and/or octahedral interstices in regular patterns (Wells 1950; Azaroff 1960; Naray-Szabo 1969).

As a basis for further detailed consideration of defect structures, diffusion, and defect-controlled properties to be discussed subsequently, the remainder of this section briefly discusses the notation for description of point defects and qualitative descriptions of different types of defect structures.

High Temperature Corrosion: Fundamentals and Engineering, First Edition. César A. C. Sequeira.
© 2019 John Wiley & Sons, Inc. Published 2019 by John Wiley & Sons, Inc.

4.1.1 Notation for Description of Point Defects

In order to describe the point defects and to express their formation in terms of equations, it is necessary to have a system of notation. Different systems have been set forth by Schöttky (1959), Rees (1954), Kröger and Vink (1956), and others, and these systems, with or without variations, have variously been used in the literature. The symbols and system used by Kröger and Vink will be employed in this book. In this system, the type of imperfection is indicated by a major symbol, and the site is occupied by a subscript.

In an oxide MO the metal ions on the normal and regular lattice positions are written as M_M, where the subscript M thus describes the type of lattice site that is occupied. Correspondingly, the oxygen ions on normal lattice sites are written as O_O.

The native point defects in an oxide MO include M and O vacancies and M and O interstitial atoms or ions. Vacancies are written as V with a subscript M or O referring to vacant metal or oxygen sites, respectively. Interstitial ions or sites are described with a subscript i.

Real crystals contain impurities. When a foreign Mf cation occupies a regular M site, the foreign ion is written as Mf_M, while if it occupies an interstitial site, it is described by the symbol Mf_i.

The point defects may be neutral or charged. In considering their charges, one may describe their actual charges or valence. However, in writing defect reactions, it is generally more convenient to consider the charge on the defects relative to the perfect crystal. This relative charge is termed the *effective charge of the defect*.

With the perfect crystal as reference, the normal atoms on the regular lattice site have zero effective charge. To emphasize this zero charge and that the normal atoms are neutral in this reference system, a cross, *x*, is often added as a superscript to the symbol for normal atoms. The normal cations and anions in an oxide MO are thus written as M_M^x and O_O^x.

Let us consider the formation of an oxygen vacancy. In this case an oxygen atom on a normal site is removed from the crystal. In this process, the two negative actual charges, i.e. two electrons, of the oxygen ion are left in the crystal. If both of these electrons are localized at the oxygen vacancy, the oxygen vacancy has two negative actual charges; the charge is the same as in a perfect crystal, and the oxygen vacancy then has zero effective charge; it is, as such, termed a neutral oxygen vacancy that is written as V_O^x. One or both of the localized or trapped electrons may be excited or ionized and transferred away from the neighborhood of the oxygen vacancy, and the oxygen vacancy becomes singly or doubly ionized, respectively. Since electrons are removed, the ionized oxygen vacancies will have an effective positive charge with respect to the perfect crystal. To distinguish effective from actual charges, different symbols are used. While actual charges are written as + and −, the effective positive charge is indicated by a superior dot, and the effective negative charge by a superior prime; singly and doubly ionized vacancies are, for instance, written as $V_O^{\bullet}$ and $V_O^{\bullet\bullet}$, respectively.

Quasi-free electrons and holes have effective negative and positive charges, respectively. They are written as e' and $h^{\bullet}$.

If the crystal is to be electrically neutral, the sum of all positive effective charges must equal the sum of all negative effective charges:

$$\sum \text{pos. effective charges} = \sum \text{neg. effective charges}$$

This *principle of electroneutrality* forms one of the basic equations and conditions for treating defect equilibria and for evaluating defect concentration in crystals.

4.1.2 Description of Defect Structures

The chemical formulas for oxides and other inorganic compounds are usually written to indicate that there is a definite ratio of cations to anions in the compound, e.g. M_aO_b, where *a* and *b* are usually small integers determined by the valency of the constituent atoms. When the oxide M_aO_b does not contain M and O atoms in the exact ratio *a*/*b*, it is said to have a nonstoichiometric composition.

As mentioned above, an exact stoichiometric composition in inorganic compounds is in principle the exception rather than the rule. Oxides in equilibrium with their surroundings are generally nonstoichiometric, except under specific conditions of temperature and partial pressure of the components. However, within our experimental ability to measure the ratio of the constituent atoms, many inorganic compounds may be considered to be so near stoichiometry over large temperature and pressure ranges that minor deviations from stoichiometry may often be neglected in a discussion of defect concentration and defect-controlled properties.

Seitz and Turnbell (1956) list six basic defect structures (internal atomic disorder) that are possible in a stoichiometric compound. These include:

1. Cation and anion vacancies ($V_M + V_O$).
2. Vacancies and interstitial ions of the same component, ($V_O + O_i$) or ($V_M + M_i$).
3. Misplaced atoms ($M_O + O_M$).
4. Vacancies and misplaced atoms for the same type of atom ($V_M + M_O$).
5. Interstitial and misplaced atoms ($O_i + M_O$).
6. Interstitial atoms ($M_i + O_i$).

A stoichiometric crystal with *Schöttky disorder* contains equivalent concentrations of cation and anion vacancies. Such a disorder in an oxide MO is illustrated schematically in Figure 4.1. It may be noted that formation of Schöttky defect pairs can only occur at outer and inner surfaces or dislocations and will diffuse into the crystal until equilibrium is reached.

A crystal with a *Frenkel disorder* contains the same concentrations of vacancies and interstitial ions for the same atom. A schematic illustration of this type of disorder involving the cations in an oxide MO is given in Figure 4.2. Contrary to the Schöttky defects, a Frenkel defect can be formed directly inside the crystal.

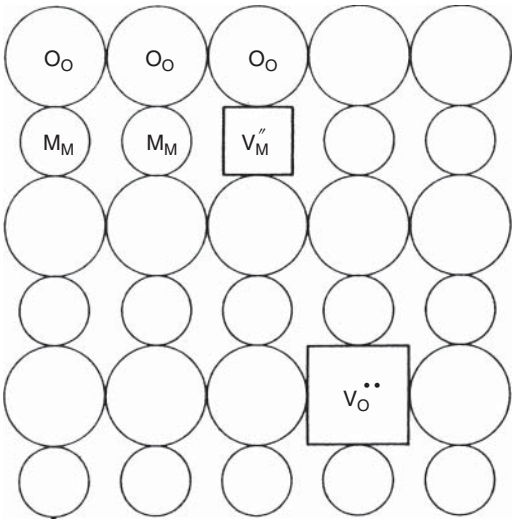


Figure 4.1 Schematic illustration of Schöttky disorder with equivalent concentrations of doubly charged vacancies, V_M'' and $V_O^{\bullet\bullet}$, in an oxide MO.

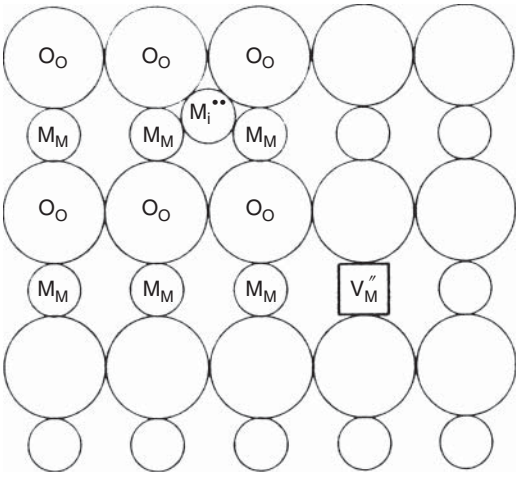


Figure 4.2 Schematic illustration of Frenkel disorder involving doubly charged cation vacancies and interstitial ions in an oxide MO.

NaCl and AgBr are well-known examples of stoichiometric inorganic compounds with Schöttky and Frenkel disorder, respectively.

Nonstoichiometry in oxides may consist of two main types:

1. Oxygen deficiency (or excess metal) with respect to stoichiometric composition.
2. Metal deficiency (or excess oxygen) with respect to stoichiometric composition.

Nonstoichiometry in a compound is equivalent to the presence of point defects, and the extent of nonstoichiometry is a direct measure of the net concentration of the corresponding defect or defects in a compound. While complementary point defects are formed in stoichiometric crystals, the electrical neutrality of nonstoichiometric compounds is conserved through formation of point defects and *complementary electronic defects*.

When a nonstoichiometric oxide is *oxygen deficient*, the predominating defects may be either oxygen vacancies (oxygen deficit) or interstitial metal ions (excess metal) or both types of defects.

Formation or annihilation of these nonstoichiometric defects can only take place at surfaces exposed to the ambient gas atmosphere or in conjunction with a higher or lower oxide or metal, e.g. at a metal/oxide interface of an oxide film.

If oxygen vacancies predominate and interstitial cations may be neglected, the formula of an oxide, say, MO_2, may be written as MO_{2-x}. A schematic illustration of this type of defect structure, involving doubly charged oxygen vacancies, is shown in Figure 4.3.

Figure 4.4 schematically illustrates the defect structure if interstitial cations predominate. In this case, the composition of the oxide may be written as $M_{1+y}O_2$ to emphasize

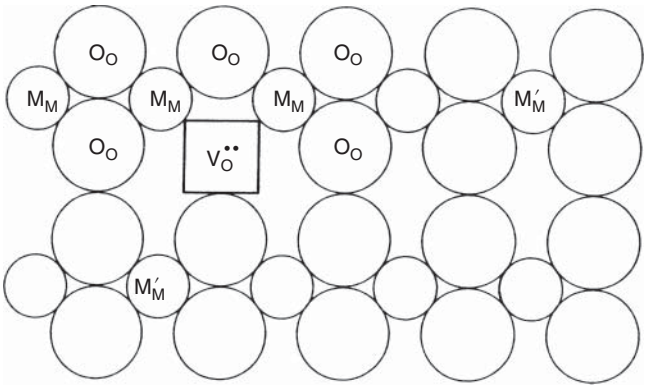


Figure 4.3 Schematic illustration of an oxygen-deficient oxide, MO_{2-x}, in which doubly charged oxygen vacancies predominate. The electrons are assumed to be localized at M atoms on regular lattice sites, M_M'.

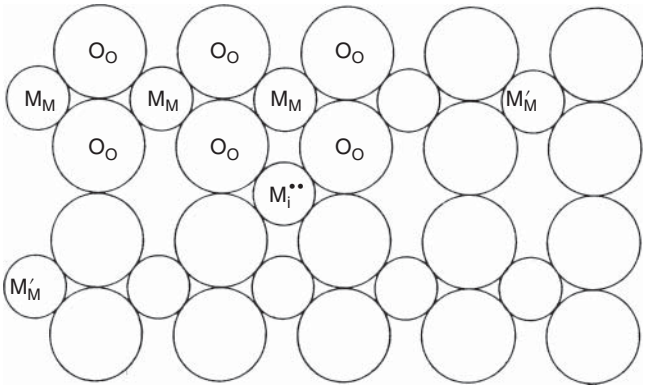


Figure 4.4 Schematic illustration of an oxygen-deficient oxide (excess metal), $M_{1+y}O_2$, in which doubly charged interstitial cations predominate. The electrons are assumed to be localized at M'_M.

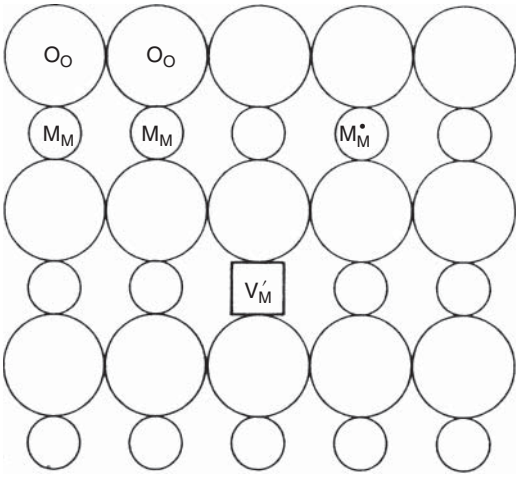


Figure 4.5 Schematic illustration of a metal-deficient oxide (excess oxygen), $M_{1-y}O$, containing singly metal vacancies. The electron holes are assumed to be localized at M atoms on regular lattice sites, $M_M^{\bullet}$.

that the defects represent an excess of metal rather than oxygen deficit relative to the stoichiometric composition.

Examples of oxides that may exhibit overall oxygen deficiency (oxygen deficit or excess metal) are TiO_2, ZrO_2, CeO_2, Nb_2O_5, etc.; their electronic conductivity is due to a transport of electrons, and they are termed *n-type conductors*.

When a nonstoichiometric oxide is metal deficient, the predominating defects may either be metal or interstitial oxygen atoms (excess oxygen).

Figure 4.5 schematically shows a defect structure predominantly involving single metal ion vacancies ($M_{1-y}O$). The formation of charged metal ion vacancies leads to the formation of complementary positive electronic defects (holes). In such oxides, the electronic conductivity involves a transport of holes, and such electronic conductors are termed *p-type conductors*.

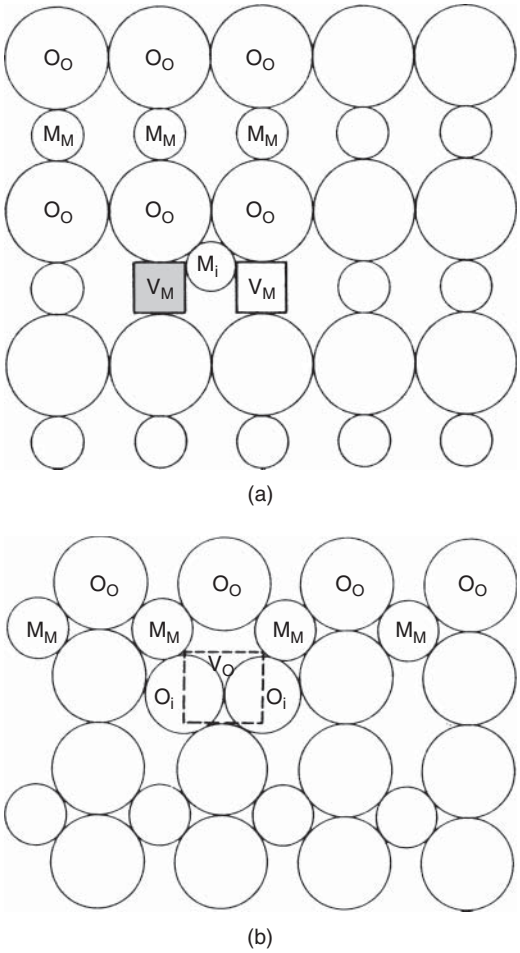


Figure 4.6 (a) Schematic illustration of a metal-deficient oxide, $M_{1-y}O$, with hypothetical complex metal vacancy defect. (b) Schematic illustration of complex oxygen interstitial defect in an oxide, $M_{2+x}O$, with excess oxygen.

In metal-deficient oxides where the disorder is limited to the cation lattice (oxygen lattice), the point defects may be more complex than that indicated by the single vacancies illustrated in Figure 4.5. This is illustrated in Figure 4.6 for two hypothetical situations of formation of $V_{Fe}Fe_iV_{Fe}$ (a) and $O_iV_OO_i$ (b).

Well-known examples of oxides with cation vacancy-type defects are MnO, FeO, CoO, NiO, Cu_2O, etc.

4.2 Defect Reactions

As discussed in the previous section, many different types of defects may be formed in inorganic compounds. In principle, all types of defects may be present in a compound, but in general, one or a small number of different defects will predominate. When defect-controlled properties of solids are to be interpreted, it is important that the defect concentrations are known. For this purpose, it is necessary

to formulate the reaction equations involving formation and mutual interaction of defects.

The defect formation may either occur internally in the solid or through reactions with the environment. In the following, the rules for formulating defect reactions will be described and applied to different defect structure systems, while in the next section, conditions for equilibrium and equations relating equilibrium defect concentrations to temperature, partial pressure of the components in a compound, impurity concentrations, etc. will be discussed.

4.2.1 Rules for Writing Defect Reactions

There are various rules that must be followed and obeyed in writing the correct defect reactions (Kröger 1964; Van Gool 1966). These rules are:

(i) The ratio of the number of regular cation and anion sites in a crystalline ionic compound is constant. Thus, in a compound M_2O_5, the ratio of regular cation to anion sites equals 2 : 5, and if 5 O-vacancy sites are created in M_2O_5 through a defect reaction, two M sites must also simultaneously be created.

(ii) The total number of regular sites may change in a defect reaction, and, therefore, the defect equation may include the creation or annihilation of sites.

(iii) The number of atoms involved in the defect reaction must be the same before and after the defect formation.

(iv) The compounds are electrically neutral. With the perfect crystal as a reference, this means that the total effective charge is the same before and after the formation of the defects.

4.2.2 Examples of Defect Reactions

4.2.2.1 Stoichiometric Oxides

The defect structures in stoichiometric compounds are also commonly termed *internal disorder*. We will consider Schöttky and Frenkel disorders.

If one starts with a pair of cations and anions on regular sites within the crystal, M_M and O_O, one must also take into account that the formation of the Schöttky pair results in the formation of two new lattice sites, and the overall equation may thus be written as

$$M_M + O_O = V''_M + V^{\bullet\bullet}_O + O_O + M_M \tag{4.1}$$

However, in this equation M_M and O_O on both sides may be canceled, and the net reaction therefore becomes

$$O = V''_M + V^{\bullet\bullet}_O \tag{4.2}$$

where O designates a perfect crystal.

In the formation of a Frenkel defect pair, a cation on a normal site is transferred to an interstitial position, and no new lattice sites are created in the process. If the interstitial ion and the resulting vacancy are, for the sake of illustration, assumed to be doubly charged, the formation of a Frenkel defect may be written as

$$M_M = M^{\bullet\bullet}_i + V''_M \tag{4.3}$$

A corresponding equation may be written for the formation of an anion Frenkel defect pair. The defect situation is also often termed an *anti-Frenkel defect* structure.

4.2.2.2 Nonstoichiometric Oxides

The extent of nonstoichiometry and the defect concentration in inorganic compounds are functions of temperature and partial pressure of their components. For an oxygen-deficient oxide, for instance, the overall nonstoichiometric reaction may be written as

$$MO = MO_{1-x} + \frac{x}{2}O_2 \tag{4.4}$$

and from this equation it is qualitatively seen that the oxygen deficit increases with decreasing oxygen pressure. For oxides with excess oxygen, the nonstoichiometry conversely increases with increasing oxygen pressure.

An oxygen vacancy is formed by the transfer of an oxygen atom on a normal site to the gaseous state. No change in the number of sites takes place. This defect reaction may be written as

$$O_O = V^x_O + \frac{1}{2}O_2 \tag{4.5}$$

In this equation, it is assumed that the oxygen vacancy is neutral, but the oxygen vacancy may act as a donor and becomes singly or doubly charged:

$$V^x_O = V^{\bullet}_O + e' \tag{4.6}$$

$$V^{\bullet}_O = V^{\bullet\bullet}_O + e' \tag{4.7}$$

The free electrons may also be considered to be associated with or localized at the cations on normal sites, and for an oxide MO, Eqs. (4.6) and (4.7) may then be written as

$$M_M + V^x_O = V^{\bullet}_O + M'_M \tag{4.8}$$

$$M_M + V^{\bullet}_O = V^{\bullet\bullet}_O + M'_M \tag{4.9}$$

The oxygen deficiency in an oxide may alternatively be equivalent to the presence of excess metal relative to stoichiometric composition, in which case the predominant defects constitute interstitial M atoms. In an oxide MO, the formation of an M^x_i atom involves the transfer of an M_M atom to an interstitial site, while an O_O atom is transferred to the gas phase:

$$M_M + O_O = M^x_i + \frac{1}{2}O_2 \tag{4.10}$$

The number of cation and anion sites is reduced by one in this reaction.

The neutral M_i atoms may be successfully ionized to singly charged or doubly charged interstitial ions:

$$M_i^x = M_i^\bullet + e', \text{etc.} \tag{4.11}$$

In metal-deficient oxides, metal vacancies may be the predominating defects. In an oxide MO, a metal may be formed through the reaction of oxygen with the oxide:

$$\frac{1}{2}O_2 = V_M^x + O_O \tag{4.12}$$

In this reaction, a pair of cation anion sites is created in MO.

The neutral metal vacancy has associated in its immediate neighborhood two real positive charges or electron holes, which may be excited yielding

$$V_M^x = V_M' + h^\bullet, \text{etc.} \tag{4.13}$$

or

$$M_M + V_M^x = V_M' + M_M^\bullet \tag{4.14}$$

This correspondingly means that the valence change is from +2 for M_M atoms to +3 for $M_M^\bullet$ atoms.

4.2.2.3 Intrinsic Ionization of Electrons

In addition to the formation of electronic defects in connection with the formation of the point defects, electronic defects are also formed through intrinsic ionization of electrons. An electron is then excited from the valence band to the conduction band, leaving an electron hole in the valence band. This process is written as

$$(e'h^\bullet) \text{ or } O = e' + h^\bullet \tag{4.15}$$

4.2.2.4 Dissolution of Foreign Cations in an Oxide

The presence of impurities may, depending on the relative valences of the ions in the parent compound and that of the impurities and what positions the impurity atoms occupy, significantly affect the concentration of the native defects.

Let us assume that the parent oxide is MO and that small amounts of an oxide Mf_2O_3 are dissolved in MO. The Mf-ions have, in this case, a valence of +3, and if it is assumed that the Mf-ions occupy normal sites in MO, the dissolved Mf-ions will have one positive effective charge. These additional positive effective charges from $Mf_M^\bullet$ must, for electroneutrality reasons, be balanced by creation of an equivalent concentration of negative effective charges. If these are electronic defects, the dissolution process may be written as

$$Mf_2O_3 = 2Mf_M^\bullet + 2e' + 2O_O + \frac{1}{2}O_2 \tag{4.16}$$

and thus the electron concentration is increased.

If MO is oxygen deficient and doubly charged oxygen vacancies predominate, an increase in the electron concentration will, as will be discussed in the next section, also simultaneously decrease the oxygen vacancy concentration. The effect of dissolved Mf_2O_3 could then alternatively be written as

$$V_O^{\bullet\bullet} + Mf_2O_3 = 2Mf_M^\bullet + 3O_O \tag{4.17}$$

If impurity Mb-ions are singly valent, they will have one effective negative charge in MO. The dissolution of Mb_2O in MO may in this case be written as

$$2e' + Mb_2O + \frac{1}{2}O_2 = 2Mb_M' + 2O_O \tag{4.18}$$

The dissolution of Mb_2O in oxygen-deficient MO will thus reduce the electron concentration (or increase the electron hole concentration). For oxygen-deficient MO with doubly charged oxygen vacancies, it may correspondingly be shown that dissolution of Mb_2O will increase the oxygen vacancy concentration.

The effect of aliovalent impurities in p-conductors (e.g. a metal-deficient oxide) is the opposite of that in n-conductors. Thus, the dissolution of Mf_2O_3 in MO will reduce the electron hole concentration according to

$$2h^\bullet + Mf_2O_3 = 2Mf_M^\bullet + 2O_O + \frac{1}{2}O_2 \tag{4.19}$$

If MO is metal deficient and predominantly contains charged metal vacancies (V_M''), the dissolution of Mf_2O_3 will simultaneously increase the concentration of metal vacancies:

$$Mf_2O_3 = 2Mf_M^\bullet + V_M'' + 3O_O \tag{4.20}$$

Substitutional dissolution of monovalent cations, on the other hand, increases the electron hole and reduces the metal vacancy concentration.

4.3 Defect Equilibria

4.3.1 Equilibrium Thermodynamics

After the correct defect equation or equations in a compound have been formulated, the next problem is to set up the equilibrium relations that correlate the equilibrium concentrations of the different defects with temperature, partial pressures of the compound components, and other parameters that affect the defect structure. The defect equilibria will generally be described by the law of mass action in the following discussion. The same problems may also be treated by statistical mechanics.

From thermodynamics (Glasstone 1947; Guggenheim 1949), we know that the free energy of a system, G, is given by the equation

$$G = H - TS \tag{4.21}$$

where T is the absolute temperature and H and S are the enthalpy and entropy of the system, respectively.

If a system is to be in equilibrium at a given temperature and pressure, the free energy of the system must be a minimum. This means that at equilibrium

$$\mathrm{d}G_{T.p} = 0 \tag{4.22}$$

when defects are created without reaction with the surrounding atmosphere, energy is required, and ΔH is positive. Therefore, it is easy to show that at any temperature ($T > 0$) all solids will contain point defects.

If a system consists of $n_1 + n_2 + \cdots + n_i$ moles of constituents 1, 2, … , i, the partial molar free energy for the "i"th constituent is given by

$$\left(\frac{\partial G}{\partial n_i}\right) T, p, n_1, \ldots = \overline{G}_i = \mu_i \tag{4.23}$$

The partial molar free energy $\overline{G}_i$ is commonly termed the chemical potential that is written as μ_i.

The free energy of a system is in terms of chemical potentials of the constituents given by

$$G = n_1\mu_1 + n_2\mu_2 + \ldots + n_i\mu_i + \ldots \tag{4.24}$$

For an open system at constant temperature and pressure, dG is given by

$$\mathrm{d}G_{T.p} = \mu_1\mathrm{d}n_1 + \mu_2\mathrm{d}n_2 + \ldots + \mu_i\mathrm{d}n_i + \ldots \tag{4.25}$$

Following Eq. (4.22), at equilibrium we then have

$$\Sigma\mu_1\mathrm{d}n_1 = 0 \tag{4.26}$$

It may also be shown that

$$n_1\mathrm{d}\mu_1 + n_2\mathrm{d}\mu_2 + \ldots + n_i\mathrm{d}\mu_i + \ldots = 0 \tag{4.27}$$

Equation (4.27) is one form of the Gibbs–Duhem equation.

In a chemical reaction, e.g.

$$a\mathrm{A} + b\mathrm{B} = c\mathrm{C} + d\mathrm{D} \tag{4.28}$$

the free energy change is given by the difference in the total free energy in the final state and the total free energy of the initial state:

$$\Delta G = (\mathrm{c}\mu_\mathrm{C} + \mathrm{d}\mu_\mathrm{D}) - (\mathrm{a}\mu_\mathrm{A} + \mathrm{b}\mu_\mathrm{B}) \tag{4.29}$$

At equilibrium, $\mathrm{d}G_{T.p} = 0$, and accordingly the fundamental condition for chemical equilibrium is that

$$\Delta G = 0 \tag{4.30}$$

The chemical potential of the constituent "i" in a mixture can be written as

$$\mu_i = \mu_i^0 + RT\ \ln\ a_i \tag{4.31}$$

where a_i is the activity of constituent "i" in the mixture and μ_i^0 is the chemical potential of constituent "i" at a chosen standard state of unit activity. In heterogeneous equilibria, the activity of pure solids or liquids is usually taken as unity at atmospheric pressure. In solutions the activity is not unity, but may be equated with the mole fraction, N_i, in ideal solutions or in real dilute solutions. The activity is related to the mole fraction, N_i, or concentration through the activity coefficient, γ_i:

$$a_i = \gamma_i N_i \tag{4.32}$$

where γ_i is equal to unity in ideal solutions.

It may be noted that in a system consisting of several phases, the condition of equilibrium implies that the chemical potential of constituent "i" is the same in all phases.

If one introduces the expression for the chemical potential (Eq. (4.31)) in Eq. (4.29), it follows that ΔG is given by

$$\Delta G = \Delta G^\circ + RT\ln\frac{\mathrm{a}_\mathrm{C}^c.\mathrm{a}_\mathrm{D}^d}{\mathrm{a}_\mathrm{A}^a.\mathrm{a}_\mathrm{B}^b} \tag{4.33}$$

where $\Delta G^\circ = (c\mu_\mathrm{C}^\circ + d\mu_\mathrm{D}^\circ) - (a\mu_\mathrm{A}^\circ + d\mu_\mathrm{B}^\circ)$ represents the free energy change in the standard state, i.e. at unit activities. ΔG° is a constant under specified standard states, and at equilibrium

$$\Delta G^\circ = -RT\ln K \tag{4.34}$$

where K is a constant given by

$$K = \frac{\mathrm{a}_\mathrm{C}^c.\mathrm{a}_\mathrm{D}^d}{\mathrm{a}_\mathrm{A}^a.\mathrm{a}_\mathrm{B}^b} \tag{4.35}$$

K is termed the equilibrium constant and relates the activities (or concentrations under ideal conditions) of products and reactants when equilibrium has been attained at a given temperature. ΔG° may, as in Eq. (4.21), be expressed in terms of the standard enthalpy change, ΔH°, and entropy change, ΔS°:

$$-RT\ln K = \Delta G^\circ = \Delta H^\circ - T\Delta S^\circ \tag{4.36}$$

Equation (4.36) may be rewritten in the form

$$K = K_o \exp\left(-\frac{\Delta H^\circ}{RT}\right) \tag{4.37}$$

where $K_o = \Delta S^\circ/R$.

The temperature dependence of K is furthermore given by

$$\frac{\mathrm{d}\ln K}{\mathrm{d}(1/T)} = -\frac{\Delta H^\circ}{R} \tag{4.38}$$

This general treatment is applicable to any mixtures whether these are gaseous, liquid, or solid solutions. As regards point defects in solids, the defects (solutes) may be considered to be dissolved in the solid (solvent).

Kröger et al. (1959) have shown that the virtual chemical potential of point defects behaves like a true chemical potential and may be written as (cf. Eq. (4.31))

$$\zeta = \zeta^\circ + RT \ln a \tag{4.39}$$

The virtual chemical potential differs from the true chemical potential by an undefined constant that is incorporated in ζ°. For this reason, the virtual chemical potentials cannot be determined experimentally.

4.3.2 Examples of Defect Equilibria

In the following discussion, concentrations will in most cases be expressed as the number of defects or atoms per molecule, i.e. in molar or site fractions. In compounds with the composition MO, the molar fraction equals the site fraction. It should be noted that the value of the equilibrium constant depends on the units of concentration that are employed, but it is a simple matter to convert the values of the equilibrium constant from one system to another.

4.3.2.1 Stoichiometric Oxides

Consider, for the sake of illustration, Schöttky defects in MO and that the defects are doubly charged. The defect equation for their formation is given by Eq. (4.2) ($\mathrm{O} = \mathrm{V}''_\mathrm{M} + \mathrm{V}^{\bullet\bullet}_\mathrm{O}$). The corresponding defect equilibrium may at low defect concentration be written as

$$[\mathrm{V}^{\bullet\bullet}_\mathrm{O}][\mathrm{V}''_\mathrm{M}] = K_s \tag{4.40}$$

where K_s is the equilibrium constant. The square brackets indicate that the structure elements are expressed in terms of concentrations.

In pure stoichiometric MO in which the Schöttky defects predominate, the electroneutrality requires that the concentrations of cation and anion vacancies are equal; thus

$$[\mathrm{V}^{\bullet\bullet}_\mathrm{O}] = [\mathrm{V}''_\mathrm{M}] = K_\mathrm{s}^{1/2} = K_o^{1/2} \exp(-\Delta H_s/2RT) \tag{4.41}$$

Under these conditions the defect concentrations are independent of the partial pressure of M and O_2. In Eq. (4.41), ΔH_s is the enthalpy of formation of pairs of doubly charged Schöttky defects.

If, for the sake of illustration, the Frenkel defects in MO are assumed to be doubly charged, the defect equation for their formation is given by Eq. (4.3) ($\mathrm{M_M} = \mathrm{M}^{\bullet\bullet}_\mathrm{i} + \mathrm{V}''_\mathrm{M}$). The defect equilibrium may accordingly be written as

$$[\mathrm{M}^{\bullet\bullet}_\mathrm{i}][\mathrm{V}''_\mathrm{M}] = K_\mathrm{F}\,[\mathrm{M_M}] \tag{4.42}$$

At low defect concentrations and thus when $[\mathrm{M}^{\bullet\bullet}_\mathrm{i}]$ and $[\mathrm{V}''_\mathrm{M}] \ll \mathrm{M_M}$, the site or molar fraction of $\mathrm{M_M}$ is approximately equal to unity, and Eq. (4.42) reduces to

$$[\mathrm{M}^{\bullet\bullet}_\mathrm{i}][\mathrm{V}''_\mathrm{M}] = K_\mathrm{F} \tag{4.43}$$

If Frenkel defects predominate in the pure stoichiometric compound, the equivalent concentrations of interstitial cations and vacancies are equal.

4.3.2.2 Oxygen-Deficient Oxides

The formation of a neutral oxygen vacancy and the excitation of the trapped electrons are described by Reactions (4.5)–(4.7), and the corresponding equilibria may be written as

$$[\mathrm{V}^x_\mathrm{O}]\, p_{\mathrm{O}_2}^{1/2} = K_1[\mathrm{O_O}] \tag{4.44}$$

$$[\mathrm{V}^\bullet_\mathrm{O}]\, n = K_a[\mathrm{V}^x_\mathrm{O}] \tag{4.45}$$

$$[\mathrm{V}^{\bullet\bullet}_\mathrm{O}]\, n = K_b[\mathrm{V}^\bullet_\mathrm{O}] \tag{4.46}$$

where $n = [\mathrm{e}']$ designates the concentration of electrons. If oxygen vacancies and the complementary electrons are the predominating defects in the oxygen-deficient oxide, the principle of electroneutrality requires that

$$n = [\mathrm{V}^\bullet_\mathrm{O}] + 2[\mathrm{V}^{\bullet\bullet}_\mathrm{O}] \tag{4.47}$$

The concentration of the electrons and the neutral, singly, and doubly charged oxygen vacancies are related through the four equations (Eqs. (4.44)–(4.47)), and by combination of these equations, expressions for each of the defects may be obtained. The electron concentration is given by

$$n^3 = K_1 K_a\, p_{\mathrm{O}_2}^{-1/2}(2K_b + n) \tag{4.48}$$

Equation (4.48) has two limiting conditions:

$$\text{if } n \gg 2K_b, \quad n = (K_1K_a)^{1/2} p_{\mathrm{O}_2}^{-1/4} \tag{4.49}$$

$$\text{while if } n \ll 2K_b, \quad n = (2K_1K_aK_b)^{1/3} p_{\mathrm{O}_2}^{-1/6} \tag{4.50}$$

Thus, in oxygen-deficient oxides where oxygen vacancies and complementary electrons predominate, the concentrations of electrons will be a function of the ambient oxygen pressure. The electron concentration will increase with decreasing oxygen pressure, and the oxygen pressure dependence may range from $p_{\mathrm{O}_2}^{-1/4}$ to $p_{\mathrm{O}_2}^{-1/6}$.

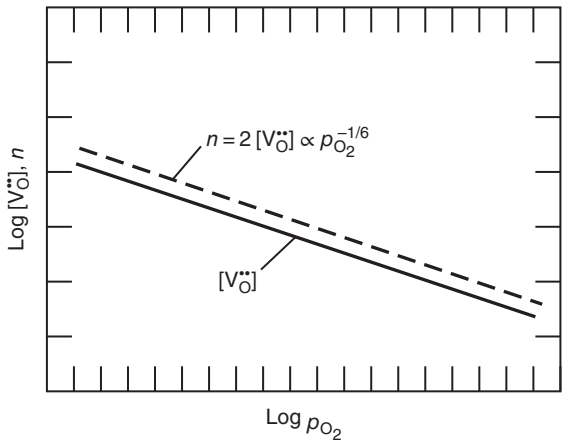


Figure 4.7 Schematic presentation of the concentration of $V_O^{\bullet\bullet}$ and e' as a function of oxygen pressure in an oxygen-deficient oxide predominantly containing doubly charged oxygen vacancies.

The latter pressure dependence applies when $[V_O^{\bullet\bullet}] \gg [V_O^x] + [V_O^{\bullet}]$, in which case the electroneutrality condition can be approximately $2[V_O^{\bullet\bullet}] = n$. A graphical presentation of n and $[V_O^{\bullet\bullet}]$ as a function of the partial pressure of oxygen under such conditions is given in Figure 4.7.

As regards the concentrations of oxygen vacancies, the following limiting conditions apply:

$$\text{if } [V_O^x] \gg [V_O^{\bullet}] + [V_O^{\bullet\bullet}], \quad [V_O]_{\text{total}} = K_1 p_{O_2}^{-1/2} \tag{4.51}$$

$$\text{if } [V_O^{\bullet}] \gg [V_O^x] + [V_O^{\bullet\bullet}], \quad [V_O]_{\text{total}} = (K_1 K_a)^{1/2} p_{O_2}^{-1/4} \tag{4.52}$$

$$\text{if } [V_O^{\bullet\bullet}] \gg [V_O^x] + [V_O^{\bullet}], \quad [V_O]_{\text{total}} = \left(\frac{1}{4} K_1 K_a K_b\right)^{1/3} p_{O_2}^{-1/6} \tag{4.53}$$

Thus, the concentration of oxygen vacancies in an oxygen-deficient oxide may have an oxygen pressure dependence that ranges from $p_{O_2}^{-1/2}$ to $p_{O_2}^{-1/6}$.

Studies of point defect equilibria in individual oxides at high temperature showed that doubly charged oxygen vacancies usually predominate relative to neutral or singly charged ones.

Similar relations apply if interstitial metal ions and complementary electrons are the predominating defects.

In an oxygen-deficient oxide, it is a priori difficult to predict whether oxygen vacancies or interstitial metal ions predominate. In principle, both types of defects may be important, at least in certain regions of nonstoichiometry. In such a case, the defect equilibria involving the interstitial ions and oxygen vacancies should be considered simultaneously. Thus, for an MO_2 oxide, it can be written as

$$O_O = V_O^{\bullet\bullet} + 2e' + \frac{1}{2}O_2 \tag{4.54}$$

$$2O_O + M_M = M_i^{\bullet\bullet} + 2e' + O_2 \tag{4.55}$$

and the defect equilibria (assuming that $[M_M]$ and $[O_O]$ are equal to units) may be written as

$$[V_O^{\bullet\bullet}]\, n^2\, p_{O_2}^{1/2} = K_{V_O^{\bullet\bullet}} \tag{4.56}$$

$$[M_i^{\bullet\bullet}]\, n^2\, p_{O_2} = K_{M_i^{\bullet\bullet}} \tag{4.57}$$

The electroneutrality condition is given by

$$n = 2[V_O^{\bullet\bullet}] + 2[M_i^{\bullet\bullet}] \tag{4.58}$$

Two limiting conditions may be considered:

1. When $[V_O^{\bullet\bullet}] \gg [M_i^{\bullet\bullet}]$, then

$$n/2 = [V_O^{\bullet\bullet}] = (K_{V_O^{\bullet\bullet}}/4)^{1/3}\, p_{O_2}^{-1/6} \tag{4.59}$$

$$[M_i^{\bullet\bullet}] = K_{M_i^{\bullet\bullet}}/(2K_{V_O^{\bullet\bullet}})^{2/3}\, p_{O_2}^{-2/3} \tag{4.60}$$

Under these conditions, $[M_i^{\bullet\bullet}]$ increases rapidly with decreasing oxygen pressure.

2. When $[M_i^{\bullet\bullet}] \gg [V_O^{\bullet\bullet}]$, then

$$\frac{1}{2}n = [M_i^{\bullet\bullet}] = (K_{M_i^{\bullet\bullet}}/4)^{1/3}\, p_{O_2}^{-1/3} \tag{4.61}$$

$$[V_O^{\bullet\bullet}] = K_{V_O^{\bullet\bullet}}/(2K_{M_i^{\bullet\bullet}})^{2/3}\, p_{O_2}^{1/6} \tag{4.62}$$

The overall situation may be illustrated as shown in Figure 4.8, in which $[M_i^{\bullet\bullet}]$, $[V_O^{\bullet\bullet}]$, and n are plotted as a function of the partial pressure of oxygen. In this diagram, it is assumed that the $[V_O^{\bullet\bullet}]$ is 10^{10} times larger than $[M_i^{\bullet\bullet}]$ at 1 atm O_2, and even with this assumption it is seen that the interstitial cations will predominate at a partial pressure of oxygen below about 10^{-20} atm. Many of the high-melting oxides are stable at such low oxygen pressures at elevated temperatures, and it is not improbable that this hypothetical situation, with oxygen vacancies predominating at high partial pressures of oxygen (and small deviations from stoichiometry) and interstitial cations predominating at low partial pressures (and relatively large deviations from stoichiometry), may generally apply to oxygen-deficient oxides at elevated temperatures. In actual cases, more than one ionization state for the defects must also be considered. The defect structures of TiO_2 and Nb_2O_5 have been interpreted in terms of this general model.

Similar models and equations may be set up when dealing with metal-deficient oxides.

4.3.2.3 Intrinsic Ionization of Electrons

For many oxides, and particularly when considering defect structure situations close to stoichiometry, it is also essential to take into account the intrinsic ionization of electrons

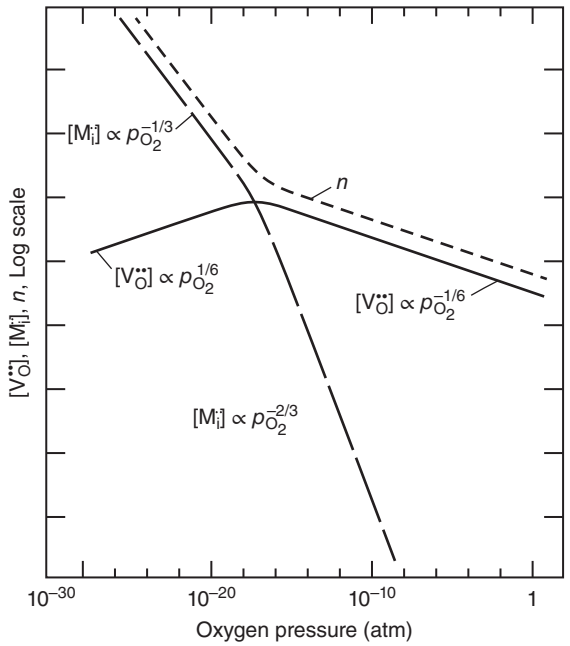


Figure 4.8 Schematic presentation of the concentrations of $V_O^{\bullet\bullet}$, $M_i^{\bullet\bullet}$,and e' as a function of oxygen pressure in an oxygen-deficient oxide MO_2 containing both doubly charged oxygen vacancies and interstitial metal ions. In this example, $[V_O^{\bullet\bullet}]$ is arbitrarily taken to be 10^{10} larger than $[M_i^{\bullet\bullet}]$ at 1 atm O_2.

from the valence to the conduction band. This equilibrium is written as

$$np = K_i \tag{4.63}$$

where p designates the concentration of electron holes.

If the intrinsic ionization is large and concentration of electron and holes according to Eq. (4.63) predominates in an oxide, then the electroneutrality condition may be approximated by

$$n = p = K_i^{1/2} \tag{4.64}$$

If this occurs in an oxide MO in which predominating point defects are doubly charged metal vacancies ($[V_M''] \gg [V_M']$), then the oxygen pressure dependence of the concentration of the vacancies can be written as

$$[V_M''] = \frac{K_3 K_e K_f}{p^2} p_{O_2}^{1/2} = \frac{K_3 K_e K_f}{K_i} p_{O_2}^{1/2} \tag{4.65}$$

4.3.2.4 Defect Structure Involving Oxygen Vacancies and Interstitials

In principle, many oxides may either have an oxygen deficit or a metal deficit depending on the partial pressure of oxygen. As an illustration of such a defect structure situation, a hypotethical case will be considered where an oxide predominantly contains oxygen vacancies at low partial pressures of oxygen and interstitial oxygen ions at high oxygen pressures. In an intermediate pressure region, the oxide will be stoichiometric or close to stoichiometric. For the sake of simplicity, it will be assumed that both the interstitial oxygen ions and the oxygen vacancies are doubly charged. In this case, it will then be necessary to consider the following defect equilibria:

$$[V_O^{\bullet\bullet}]\, n^2\, p_{O_2}^{1/2} = K_{V_O^{\bullet\bullet}} \tag{4.66}$$

$$[O_i'']\, p^2 = K_{O_i''}\, p_{O_2}^{1/2} \tag{4.67}$$

$$np = K_i \tag{4.68}$$

$$[O_i'']\,[V_O^{\bullet\bullet}] = K_F \tag{4.69}$$

It should be noted that the defect equilibria are interrelated, and through a combination of the equations, it may be shown that $K_i K_F = K_{V_O^{\bullet\bullet}}\, K_{O_i''}$.

It is useful to consider limiting conditions:

(i) *Large oxygen deficit*:

$$[V_O^{\bullet\bullet}] = \frac{1}{2} n \gg [O_i''] \tag{4.70}$$

and it may be seen that

$$p_{O_2} \ll K_{V_O^{\bullet\bullet}}^2 / 16 K_F^3 \tag{4.71}$$

(ii) *Large excess oxygen*:

$$[O_i''] = \frac{1}{2} p \gg [V_O^{\bullet\bullet}] \tag{4.72}$$

and it may be seen that

$$[O_i'']\, \frac{1}{2} p = (K_{O_i''}/4)^{1/3} p_{O_2}^{1/6} \tag{4.73}$$

$$[V_O^{\bullet\bullet}] = K_F (K_{O_i''}/4)^{1/3} p_{O_2}^{-1/6} \tag{4.74}$$

leading to

$$p_{O_2} \ll 16 K_F^3 / K_{O_i''}^2 \tag{4.75}$$

At or close to stoichiometry, again two alternative limiting conditions must be considered.

Case 1: Intrinsic ionization predominates, and thus

$$p = n = K_i^{1/2} \gg [V_O^{\bullet\bullet}] \text{ and } [O_i''] \tag{4.76}$$

p and n are independent of oxygen pressure, while the point defect concentrations are given by

$$[O_i''] = K_{O_i''} / K_i\, p_{O_2}^{1/2} \tag{4.77}$$

$$[V_O^{\bullet\bullet}] = K_{V_O^{\bullet\bullet}} / K_i\, p_{O_2}^{1/2} \tag{4.78}$$

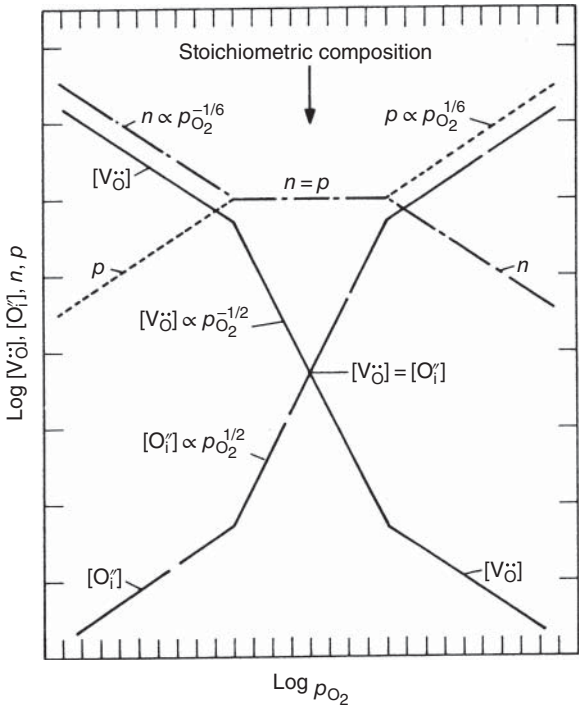


Figure 4.9 Schematic presentation of the concentration of oxygen point defects and electronic defects as a function of oxygen pressure in an oxide that, depending on the partial pressure of oxygen, may have an excess or deficit of oxygen. Intrinsic electronic equilibrium is assumed to predominate at stoichiometric composition (Case 1).

Case 2: Internal disorder (anti-Frenkel defects) predominates, and thus

$$[O_i''] = [V_O^{\bullet\bullet}] = K_{F_i}^{1/2} \gg p \text{ and } n \tag{4.79}$$

$[O_i'']$ and $[V_O^{\bullet\bullet}]$ are independent of the partial pressure of oxygen, while the concentration of electronic defects is given by

$$n = (K_{V_O^{\bullet\bullet}}^{1/2} / K_F^{1/4}) p_{O_2}^{-1/4} \tag{4.80}$$

$$p = (K_{O_i''}^{1/2} / K_F^{1/4}) p_{O_2}^{1/4} \tag{4.81}$$

A schematic diagram of the variations in point defects and electronic defects with oxygen pressure for Case 1 is shown in Figure 4.9. As it is shown later, the oxide is an essentially pure electronic conductor at all oxygen pressures.

4.3.2.5 Effects of Impurities on Defect Equilibria

In the previous considerations we have only dealt with pure crystals, and no account has so far been taken of impurities and their effects on defect equilibria. Under real conditions, it is thermodynamically impossible to produce truly pure crystals, and the impurities may, depending on their concentration, significantly affect or completely control defect concentration in crystals.

Dissolved impurities may have various effects on crystals. A difference in size between the impurity and parent atoms will cause strain in the lattice, the polarization caused by impurity will be different from that of the native atoms, and differences in valence between impurity and native atoms will affect the electroneutrality condition of a crystal.

To illustrate the effect of impurities on Schöttky equilibria, let us consider a compound MX where the cations and anions have a valence of 1 and the cation and anion vacancies are singly charged. If divalent cations, M^{2+}, are dissolved substitutionally in the lattice and occupy the normal M sites, the M^{2+} ions will have one effective positive charge, $Mf_M^{\bullet}$. When the Schöttky defects predominate and intrinsic ionization can be neglected, the electroneutrality condition becomes

$$[Mf_M^{\bullet}] + [V_X^{\bullet}] = [V_M'] \tag{4.82}$$

By combining this relation with the Schöttky defect equilibrium

$$[V_M'][V_X^{\bullet}] = [V_M']_o^2 = K_S \tag{4.83}$$

where $[V_M']_o$ represents the cation vacancy concentration in pure MX, the metal vacancy concentration can be expressed by

$$[V_M'] = \frac{1}{2}\{(4[V_M']_o^2 + [Mf_M^{\bullet}]^2)^{1/2} + [Mf_M^{\bullet}]\} \tag{4.84}$$

This equation shows that if the impurity concentration is much larger than the vacancy concentration in the pure crystal, i.e. $[Mf_M^{\bullet}] \gg 2[V_M']_o = 2K_S^{1/2}$, then the vacancy concentration in the impure crystal becomes equal to the impurity concentration, i.e. $[V_M'] = [Mf_M^{\bullet}]$. However if $2[V_M']_o \gg [Mf_M^{\bullet}]$, then $[V_M'] = [V_M']_o$, and the impurities do not affect the concentration of the Schöttky defects in the crystal.

Values of $[V_M']$ as a function of $[Mf_M^{\bullet}]$ for a value of $K_S = 25$ are illustrated graphically in Figure 4.10. The region where the native defect concentration is essentially unaffected by the impurities is also termed the intrinsic region, and where $[V_M'] \approx [Mf_M^{\bullet}]$ the extrinsic region. It may be noted that when $[V_M']$ increases, the value of $[V_X^{\bullet}]$ correspondingly decreases according to Eq. (4.83).

Such effects of impurities have been demonstrated for additions of divalent cations to alkali halides, e.g. Cd^{2+} additions to NaCl (Lidiard 1957).

Stoichiometric oxides with Frenkel defects and nonstoichiometric oxides exhibit similar qualitative effects on additions of impurities. This may be shown by setting up the appropriate electroneutrality condition combined with the defect equilibria in a manner corresponding to that discussed above.

Impurities and point defects may associate to form complex defects. A main driving force is the coulombic

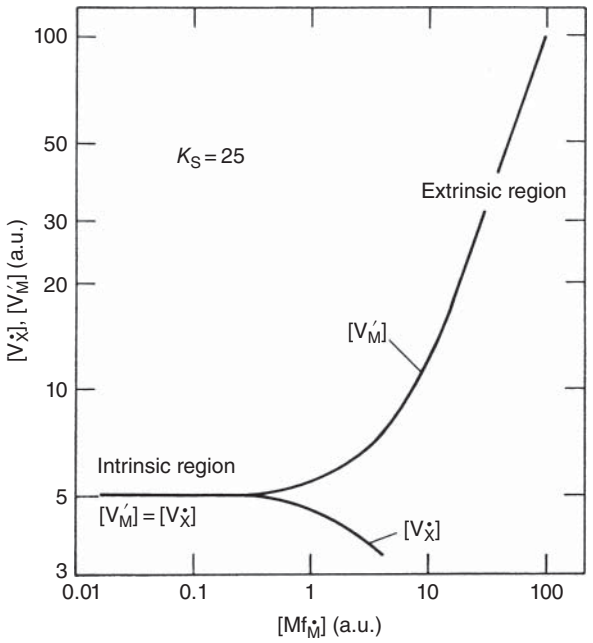


Figure 4.10 Effect of higher valent cation impurities $[Mf_M^\bullet]$ on defect structure in MX predominantly containing Schöttky defects $(V_M' + V_X^\bullet)$.

attraction between impurities and point defects having opposite effective charges.

As an illustration, it may be assumed that the predominating effects are doubly charged oxygen vacancies and that the cationic impurities have two effective negative charges, e.g. Mf_M''. The associated complex between $V_O^{\bullet\bullet}$ and Mf_M'' can be written $(V_O \cdot Mf_M)^x$, and this overall defect can be considered neutral.

The complex defect will be in equilibrium with the single defects according to the reaction

$$(V_O \cdot Mf_M)^x = V_O^{\bullet\bullet} + Mf_M'' \tag{4.85}$$

If all the species are randomly distributed in the crystal, the equilibrium can be written as

$$[V_O^{\bullet\bullet}][Mf_M''] = K_{compl}\,[(V_O \cdot Mf_M)^x] \tag{4.86}$$

where K_{compl} is the equilibrium constant.

Many other alternative examples of the effects of impurities on defect equilibria may be cited, but when necessary these will be considered in connection with actual oxide systems that are well treated in the open literature.

4.4 Equilibrium Constants

In the previous section, the interrelationships among the equilibrium concentrations of point defects, electronic defects, and the partial pressure of the oxide constituents have been treated and described in terms of the law of mass action. By analogy with aqueous solutions, such a treatment of defect chemistry in crystalline solids offers no conceptual difficulty to a physical chemist. However, a physicist is usually trained to consider crystalline solids and their properties in terms of other models such as, for instance, the band model of solids. It therefore seems useful to give a brief description of the band model and to point out the significance of the equilibrium constants for defect reactions involving electronic defects in terms of this model.

4.4.1 Band Model of Solids

In single atoms the electrons may only possess certain discrete energies. These allowed energies are designated by quantum numbers that refer to the electron shell that the electron occupies (principal quantum number), the orbital angular momentum of the electron (azimuthal quantum number), and the direction of the angular momentum vector (magnetic quantum number). In addition, and according to the Pauli exclusion principle, each energy state can only be accommodated by two electrons that have opposite spins about the electron axis (Kittell 1966).

When individual atoms are brought together in a molecule or solid, i.e. when the interatomic spacing decreases and electronic orbitals overlap, a splitting of the energy levels begins to occur, and the energy levels may be considered to form energy bands in this solid. This is illustrated in Figure 4.11, which shows the energy as a function of interatomic spacing. But the total number of discrete energy levels within a band corresponds exactly to the total number of atoms present in the solid, and

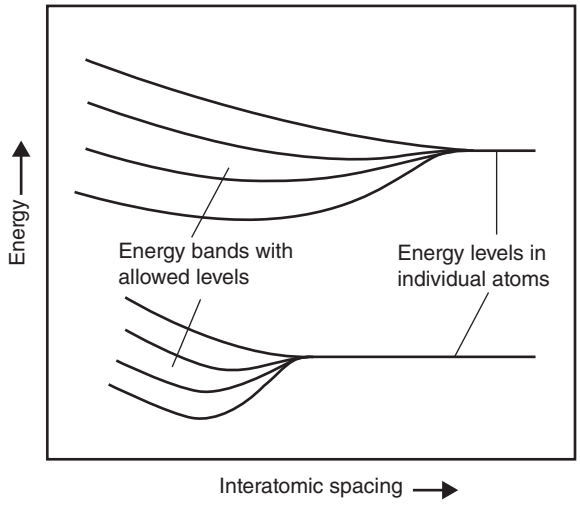


Figure 4.11 Schematic illustration of the splitting of energy levels when atoms are brought together in a solid or molecule. Energy versus interatomic spacing.

therefore the levels become more and more finely spaced the larger the number of atoms present. Because of the Pauli exclusion principle, each band can accommodate twice as many electrons as there are energy levels. Solids contain 10^{22}–10^{23} atoms per cubic centimeter, and the number of levels in each band is thus of the same order.

The energy bands may overlap or be separated by energy gaps. In pure semiconductors or insulators, the energy bands of importance to the electronic transport properties in solids are termed the valence and conduction band. As illustrated in Figure 4.12, where the vertical axis represents the electron energy and horizontal axis the distance through the solid, the valence band and conduction band are separated by an *energy gap*. In a perfect and ideal solid, the electrons may not possess energies within the energy gap, and this is therefore also often termed the forbidden energy gap. The extent of the energy gap differs for inorganic compounds (see below).

In an insulator or semiconductor at 0 K, the valence band is completely filled with electrons, while the conduction band is completely empty. In such cases, no electronic conduction takes place when an electric field is applied (Wert and Thomson 1964).

When the temperature is increased, electrons in the valence band may be excited across the forbidden energy gap to the conduction band. This is the *intrinsic ionization*. The electrons in the conduction band and the unoccupied electron sites in the valence band (electron holes) can move in an electric field. The electron holes behave as though they were positively charged and move in the opposite direction of the electrons. The intrinsic ionization thus produces pairs of electron and electron hole charge carriers.

The equilibrium constants for the intrinsic ionization and other excitation processes are determined by the electron population or distribution among the energy levels in a crystal. By Fermi statistics it may be shown that the number of electrons in any energy level "i" with an energy E_i is given by

$$n_i = \frac{g_i}{I + \exp(E_i - E_F/kT)} \tag{4.87}$$

where g_i represents the degeneracy of level i (the number of states that have the same energy). The parameter E_F is termed the *Fermi level*. It may be noted that when $E_F = E_i$, then $n_i = \frac{1}{2}g_i$, and this corresponds to the case that half of the number of states or energy E_i is filled at T (K).

When

$$\frac{E_i - E_F}{kT} \gg 1 \tag{4.88}$$

which corresponds to the situation when the "i"th level is slightly populated, Eq. (4.87) reduces to

$$n_i = g_i \exp -(E_i - E_F)/kT \tag{4.89}$$

The condition given by Eq. (4.88) represents the limit where the Fermi statistics reduces to classical statistics, and Eq. (4.89) is the classical distribution law.

The number of electrons in the conduction band corresponding to Eq. (4.89) may be written as

$$n = N_C \exp -(E_C - E_F)/kT \tag{4.90}$$

where N_C represents the number of states (degeneracy or effective density of sites) in the conduction band and E_C is the energy of the lowest level of the conduction band (Figure 4.12).

When assuming that the electrons occupy a narrow band of energies close to E_C, a parabolic relation between N_C and E may be assumed, and it may be shown that N_C is then given by

$$N_C = \left(\frac{8\pi m^x_{e'} kT}{h^2}\right)^{3/2} \tag{4.91}$$

where $m^x_{e'}$ is the effective mass of the electron.

A corresponding relation holds for the population of electron holes in the valence band:

$$p = N_V \exp -(E_F - E_V)/kT \tag{4.92}$$

where N_V represents the effective density of states in the valence band and E_V is the energy of the highest level in the valence band.

When the effective density of states is located in a narrow region close to E_V, N_V is corresponding to Eq. (4.91) given by

$$N_V = \left(\frac{8\pi m^x_{h\bullet} kT}{h^2}\right)^{3/2} \tag{4.93}$$

where $m^x_{h\bullet}$ is the effective mass of the hole.

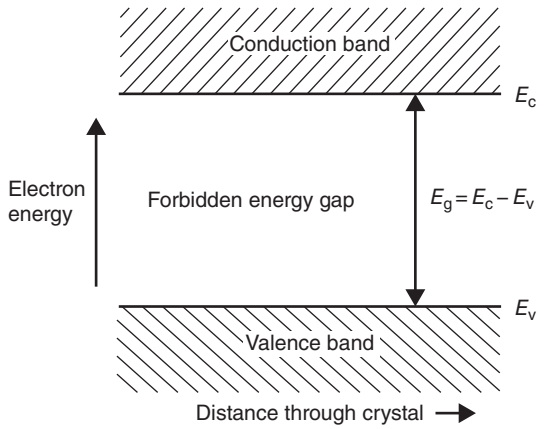


Figure 4.12 Schematic illustration of the energy band diagram for a pure semiconductor.

The equilibrium constant for the intrinsic ionization is in terms of Eqs. (4.90) and (4.92) given by

$$K_i = np = N_C N_V \exp -E_g/kT \tag{4.94}$$

where $E_g = E_C - E_V$ is the bandgap between the conduction and the valence band. E_g may thus be considered the enthalpy or heat of reaction in the intrinsic ionization.

In an intrinsic conductor, $n = p$, and by combining Eqs. (4.90)–(4.93), one may solve for E_F that is given by

$$E_F = \frac{E_V + E_C}{2} + \frac{3kT}{4} \ln \frac{m_{e'}^x}{m_{h^\bullet}^x} \tag{4.95}$$

When the effective masses of the electron and holes are equal, the Fermi level in an intrinsic conductor lies halfway between the valence and conduction band (Azaroff 1963).

If charged imperfections (impurities or native point defects) are present, these may either donate or accept electrons. The imperfections may be considered to contribute to additional localized energy levels to the total energy diagram as illustrated in Figure 4.13 (Hannay 1967).

If one considers the excitation or ionization of an electron from a donor state, D, then this may in terms of a defect reaction be written as

$$D = D^\bullet + e' \tag{4.96}$$

and the corresponding defect equilibrium is given by

$$\frac{[N_D^\bullet]\, n}{[D]} = K_D \tag{4.97}$$

where K_D is the equilibrium constant.

If the total number of donor states is N_D, then $[D^\bullet] = N_D - [D]$, and Eq. (4.97) may be rewritten to give

$$\frac{\left(l - \frac{[D]}{N_D}\right) n}{\frac{[D]}{N_D}} = K_D \tag{4.98}$$

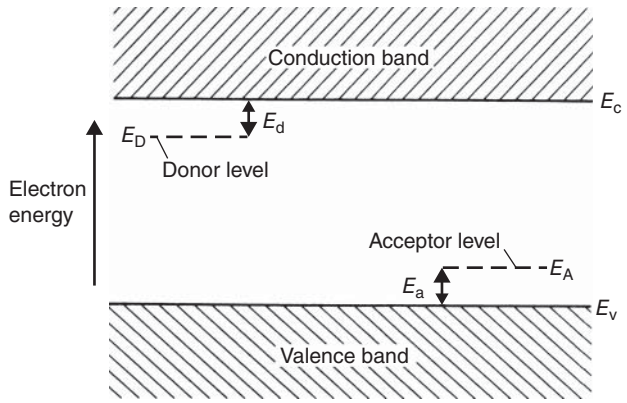


Figure 4.13 Schematic illustration of additional localized energy levels due to donors and acceptors in the energy band diagram of a pure semiconductor.

If the energy of the donor state is E_D, then $\frac{[D]}{N_D}$ is according to Fermi statistics (Eq. (4.89)) given by

$$\frac{[D]}{N_D} = \frac{l}{l + \exp\left(\frac{E_D - E_F}{kT}\right)} \tag{4.99}$$

When inserting this value of $\frac{[D]}{N_D}$ in Eq. (4.98) and combining with the expression for n (Eq. (4.90)), K_D becomes

$$K_D = N_C \exp -(E_C - E_D)/kT = N_C \exp(-E_d/kT) \tag{4.100}$$

where $E_d = E_C - E_D$ represents the ionization energy of the donor (Figure 4.13) and may be considered the enthalpy of the defect reaction (Eq. (4.96)).

A corresponding treatment may be made for ionization of acceptors, which in terms of a defect reaction may be written as

$$A = A' + h^\bullet \tag{4.101}$$

The equilibrium constant $K_A = [A']p/[A]$ may, correspondingly, be expressed as

$$K_A = N_V \exp -(E_A - E_V)/kT = N_V \exp -E_a/kT \tag{4.102}$$

where $E_a = E_A - E_V$ and E_A is the energy of the acceptor level (Figure 4.13).

In connection with the thermodynamic treatment of defect equilibria in Section 4.3, it is of interest to correlate the thermodynamic approach with the band model. As described in Section 4.3, a chemical equilibrium implies that the chemical potential of a species is the same in all phases. As regards electrons in a system, this means that their chemical potentials (or electrochemical potentials of the inner potential cannot be neglected) (Holmes 1966) must be equal, although they may have different energies. Thus, the *chemical potential of the electrons* in general, μ_e, must be equal to the chemical potential of valence electrons (Van Gool 1966):

$$\mu_{e'} = \mu\,(\text{cond.el.}) = \mu^o\,(\text{val.el.}) \tag{4.103}$$

The chemical potential of the electrons, e.g. conduction electrons, may be written in terms of the chemical potential in a standard state and a term for the entropy of mixing:

$$\mu_{e'} = \mu\,(\text{cond.el.}) = \mu^o\,(\text{cond.el.}) + kT \ln \frac{n}{N_C} \tag{4.104}$$

Equation (4.90) may be rewritten as

$$E_F = E_C + kT \ln \frac{n}{N_C} \tag{4.105}$$

A comparison between Eqs. (4.104) and (4.105) shows that the Fermi level represents the chemical potential of the electrons. For the conduction electrons, μ^o equals E_C.

Various correlations have been proposed between the bandgaps of semiconductors and insulators and various quantities such as bond energies (Manca 1961; Vijh 1968), heats of formation of the compounds (Ruppel et al. 1957; Vijh 1970), electronegativities (Hannay 1967), and atomic number (Bube 1960). As first discussed by Manca (1961), and later expanded by Vijh (1969), the correlation between the energy gap, E_g, and the bond energy appears to have a wide applicability for inorganic binary compounds, and the correlation is shown graphically in Figure 4.14. The bond energy is expressed as the atomization energy per equivalent. The atomization energy, E_{at}, is the energy needed to dissociate the compound into separate gaseous atoms of the components (Appen et al. 1965). The equivalent represents the number of a particular ion in a binary compound times the valence of the ion. In a compound Ta_2O_5, for instance, the atomization energy per equivalent equals 1/10 of the atomization energy of Ta_2O_5.

The straight-line relationship in Figure 4.14 can be represented by the equation

$$E_g = 2(E_s - b)\,(\ln \text{eV}) \tag{4.106}$$

where $E_s = E_{at}$/equiv. and b is constant approximately equal to 2.7.

Vijh (1969) has theoretically derived Eq. (4.106) for ionic compounds by applying the Madelung approach and the Born–Haber cycle.

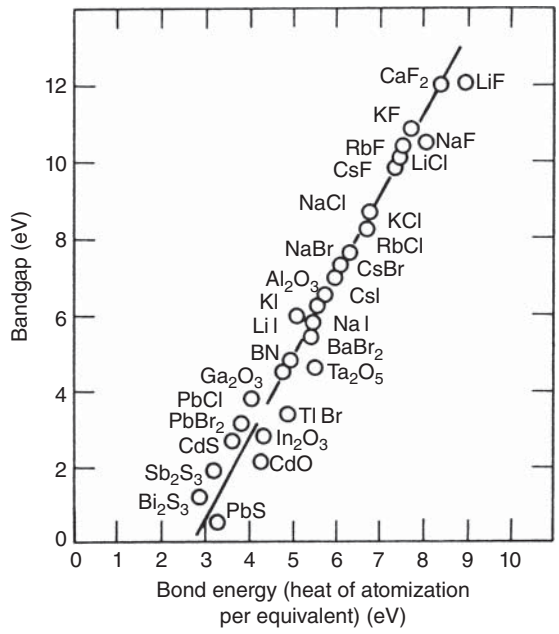


Figure 4.14 Correlation between the forbidden energy gap, E_g, and bond energy for various binary semiconductors and insulators. The bond energy represents the energy of atomization per equivalent.

4.5 Questions

4.1 Why do perfect crystals not exist at room temperature?

4.2 What is nonstoichiometry? What is it due to? How is it measured?

4.3 What types of nonstoichiometry would a p-type of oxide have?

4.4 Determine defect equilibria for an oxide of type MO_{2-x}.

4.5 What would be the pressure dependence for the defect concentrations for an oxide of type $M_{1+x}O$?

4.6 State the type of defect in an oxide of type MO_{2+x}. Derive an expression for the relationship of defect concentration with the partial pressure of oxygen. Also show this relation graphically. What is the name of such a graphical relationship between pressure and defect concentration?

4.7 Can an oxide show different kinds of defects as a function of pressure? Explain using Brouwer's diagrams.

4.8 What are Wagner Hauffe's rules? How do they explain the oxidation behavior of various oxides?

4.9 Show whether the oxidation rate of the following oxides will increase or decrease by doping Li or Cr into their metal before oxidation: ZnO, CaO, FeO, ZrO_4, Fe_2O_3, NiO.

4.10 Write defect reactions for formation of sodium vacancies in NaCl by exchange with (a) chlorine gas and (b) sodium gas.

4.11 We have in the text claimed that charges can be associated directly with ideal point defects, even if the compound is not ideally ionic, and that this normally does not affect the results of the calculations. Under what conditions will it start to matter that the charge of the defect actually extends outside the defect itself?

4.12 Write defect reactions for dissolution of CaO into the oxide ZrO_{1-x}.

4.13 Write defect reactions for dissolution of MfO into $M_{2-x}O_3$ when we assume that the foreign metal M is small and therefore dissolves interstitially.

4.14 Write defect reactions for dissolution of CaO substitutionally into the anion-Frenkel dominated Y_2O_3.

4.15 Write defect reactions for dissolution of ZrO_2 substitutionally into the anion-Frenkel dominated Y_2O_3.

4.16 Write defect reactions for dissolution of CaF_2 into CaO, assuming that F^- dissolves substitutionally and that CaO is dominated by Schöttky defects in the pure, undoped state.

4.17 Write a defect reaction for dissolution of protons in an oxide with water vapor as source and with oxygen interstitials as compensating effects.

4.18 Write defect reactions for dissolution of protons in an oxide $M_{1-x}O$ with water vapor as source.

References

Appen, A.A., Glushkova, V.B., and Kayalova, S.S. (1965). *Izv. Akad. Nauk. SSSR, Neorg. Mater.* 1: 576.

Azaroff, L.V. (1960). *Introduction to Solids*. New York: McGraw Hill.

Azaroff, L.V. (1963). *Electronic Processes in Materials*. New York: McGraw-Hill.
Bube, R.H. (1960). *Photoconductivity of Solids*. New York: Wiley.
Glasstone, S. (1947). *Thermodynamics for Chemists*. New York: Van Nostrand.
Guggenheim, E.A. (1949). *Thermodynamics*. Amsterdam, Holland: North-Holland.
Hannay, N.B. (1967). *Solid-state Chemistry*. New York: Prentice Hall.
Holmes, P.J. (ed.) (1966). *The Electrochemistry of Semiconductors*. New York: Academic Press.
Kittell, C. (1966). *Introduction to Solid-state Physics*. New York: Wiley.
Kröger, F.A., Stieltjes, F.H., and Vink, J.H. (1959). *Philips Res. Rep.* 14: 557.
Kröger, F.A. and Vink, A.J. (1956). *Solid State Phys.* 3: 307.
Kröger, F.A. (1964). *The Chemistry of Imperfect Crystals*. Amsterdam, Holland: North-Holland Publishing Company.
Lidiard, A.B. (1957). *Handbuch der Physik*, vol. 20. Berlin: Springer Verlag.
Manca, P. (1961). *J. Phys. Chem. Solids* 20: 268.
Naray-Szabo, I. (1969). *Inorganic Crystal Chemistry*. Budapest: Akademiai Kiado.
Rees, A.G. (1954). *Chemistry of the Defect Solid-state*. London: Methuen.
Ruppel, W., Rose, A., and Gerritsen, H.J. (1957). *Helv. Phys. Acta* 30: 238.
Schöttky, W. (ed.) (1959). *Halbleiterprobleme*, vol. 4. Braunschweig: Vieweg un Sohn.
Seitz, F. and Turnbell, D. (eds.) (1956). *Solid State Physics*, vol. 3. New York: Academic Press.
Van Gool, W. (1966). *Principles of Defect Chemistry of Crystalline Solids*. New York: Academic Press.
Vijh, A.K. (1968). *J. Phys. Chem. Solids* 29: 2233.
Vijh, A.K. (1969). *J. Phys. Chem. Solids* 30: 1999.
Vijh, A.K. (1970). *J. Mater. Sci.* 5: 379.
Wagner, C. and Schöttky, W. (1931). *Z. Phys. Chem.* B11: 163.
Wells, A.F. (1950). *Structural Inorganic Chemistry*. London: Oxford University Press.
Wert, C.A. and Thomson, R.M. (1964). *Physics of Solids*. New York: McGraw-Hill.

Further Reading

Hauffe, K.K. (1955). *Reaktionen in und an Fester Stoffen*. Berlin: Springer-Verlag.
Hong, J., Hu, Z., Probert, M. et al. (2015). *Nat. Commun.* 6: 6293.
Kittel, C. (1966). *Introduction to Solid-state Physics*. New York: Wiley.
Kofstad, P. (1967). *J. Phys. Chem. Solids* 28: 1842.
Kubaschewski, O., Evans, E.L., and Alcock, C.B. (1967). *Metallurgical Thermochemistry*. London: Pergamon Press.
Mott, N.F. and Guerney, R.W. (1940). *Electronic Processes in Ionic Crystals*. Oxford: Clarendon Press.
Nordlund, K. and Averback, R. (1989). *Phys. Rev. Lett.* 80 (19): 4201.

Chapter 5

Diffusion in Solid-State Systems

5.1 Introduction

Diffusion as the process of mitigation and mixing due to irregular movement of particles (atoms, ions, molecules) is one of the basic and ubiquitous phenomena in nature. As this process shows up in all states of matter over very large time and length scales, the subject is still very general involving a large variety of natural sciences such as physics, chemistry, biology, and geology and their interfacial disciplines. Besides its scientific interest, diffusion is of enormous practical relevance for industry and life, ranging from steelmaking, growth of oxide scales, sintering, and high temperature creep of metals to oxide/carbon dioxide exchange in the human lung. It therefore comes as no surprise that the early history of the subject is marked by scientists from diverse communities, e.g. the scottish botanist R. Brown (1773–1858), the scottish chemist T. Graham (1805–1869), the german physiologist A. Fick (1829–1901), the english metallurgist W.C. Roberts-Austen (1843–1902), and the german physicist A. Einstein (1879–1955). Today, exactly 162 and 112 years after the seminal publications by Fick and Einstein, respectively, the field is flourishing more than ever with more than 10 000 scientific papers per year.

The present chapter is confined, of course, to diffusion in condensed matter, namely, in metals, binary alloys, and oxides. Emphasis is on very basic fundamental aspects, the contents being roughly characterized by the headings general theory of diffusion, diffusion coefficients, Matano–Boltzmann analysis, Kirkendall effect, Darken analysis, factors influencing diffusion, impurity diffusion in metals, grain boundary (GB) diffusion in metals, diffusion in solid oxides, morphology of reaction products, and measurement of diffusion parameters.

Many references are added at the end of the chapter for readers in the forefront of the subject.

5.2 General Theory of Diffusion

5.2.1 Basic Concepts, Laws, and Mechanisms

Diffusion is defined as "a process whereby particles intermingle as the result of their spontaneous movement caused by thermal agitation."

In the solid state, this manifests itself as the migration of "solute" atoms through a host lattice via the defect structure of that lattice. Since the rate of formation of defects increases with the vibrational energy of the atoms, the diffusion process is enhanced at elevated temperatures. However, the inherently rigid structure of a solid leads to a slow diffusion process as compared with liquids and gases. The basic point defects within a crystal lattice are vacancies and interstitial atoms, and it is via these, and a combination of them, that solid-state diffusion occurs, in general.

Various atomic mechanisms of diffusion in crystals have been identified and are catalogued as follows.

5.2.1.1 Interstitial Mechanism

Solute atoms that are considerably smaller than the solvent (lattice) atoms (e.g. hydrogen, carbon, nitrogen, and oxygen) are usually incorporated in interstitial sites of a metal. In this way, an interstitial solid solution is formed. Interstitial solutes usually occupy octahedral or tetrahedral sites of the lattice. Octahedral and tetrahedral interstitial sites in the FCC and BCC lattices are illustrated in Figure 5.1. Interstitial solutes can diffuse by jumping from one interstitial site to the next as shown in Figure 5.2. This mechanism is sometimes also denoted as direct interstitial mechanism in order to distinguish it more clearly from the interstitialcy mechanism discussed below.

High Temperature Corrosion: Fundamentals and Engineering, First Edition. César A. C. Sequeira.
© 2019 John Wiley & Sons, Inc. Published 2019 by John Wiley & Sons, Inc.

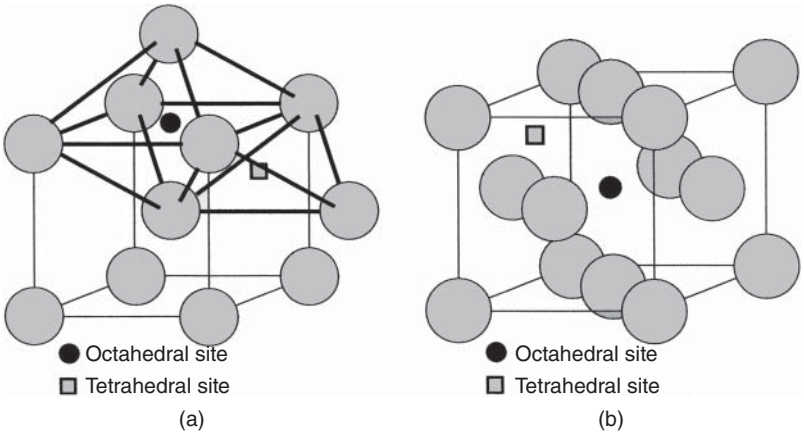


Figure 5.1 Octahedral (a) and tetrahedral (b) interstitial sites in the FCC (left) and BCC (right) lattice. Lattice atoms (open circles); interstitial sites (full circles).

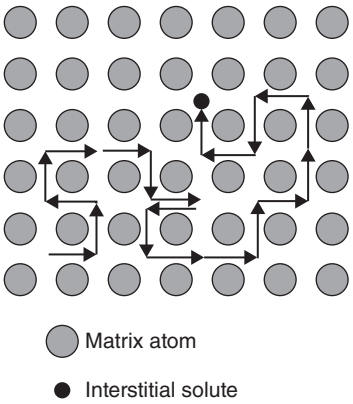


Figure 5.2 Direct interstitial mechanism of diffusion.

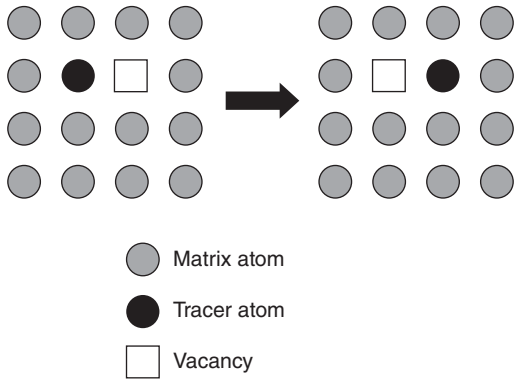


Figure 5.3 Vacancy mechanism of diffusion.

5.2.1.2 Vacancy Mechanism

Self-atoms or substitutional solute atoms migrate by jumping into a neighboring vacant site as illustrated in Figure 5.3. In thermal equilibrium, the atomic fraction of vacancies C_V^{eq} in a monoatomic crystal is given by

$$C_V^{eq} = \exp\left(\frac{S^F}{R}\right) \exp\left(-\frac{H^F}{RT}\right) \tag{5.1}$$

where S^F and H^F denote formation entropy and enthalpy of a vacancy (superscript F). Self-diffusion in metals and alloys and in many ionic crystals (e.g. alkali halides) and ceramic materials occurs by the vacancy mechanism.

5.2.1.3 Divacancy Mechanism

Diffusion of self-atoms or substitutional solute atoms can also occur via bound pairs of vacancies (denoted as divacancies or as vacancy pairs) as illustrated in Figure 5.4. At thermal equilibrium, divacancies in an elemental crystal are formed from monovacancies according to the reaction

$$V + V \rightleftharpoons 2V \tag{5.2}$$

As a consequence of the law of mass action, we have for the mole fractions C_V and C_{2V} of mono- and divacancies

$$C_{2V}^{eq} = K\,(C_V^{eq})^2 \tag{5.3}$$

The quantity K contains the Gibbs free binding energy of the vacancy pair. Since the monovacancy population under equilibrium conditions increases with temperature, the concentration of divacancies C_{2V}^{eq} becomes more significant at high temperatures. Divacancies in FCC metals have a higher mobility than monovacancies (Cahn and Haasen 1996). Therefore, self-diffusion of FCC metals usually has some divacancy contribution in addition to the vacancy mechanism. The latter is, however, the dominating mechanism at temperatures below 2/3 of the melting temperature (Seeger et al. 1970).

5.2.1.4 Interstitialcy Mechanism

In this case, self-interstitials – extra atoms located between lattice sites – act as diffusion vehicles. As illustrated in Figure 5.5, a self-interstitial replaces an atom on a substitutional site, which then replaces again a neighboring

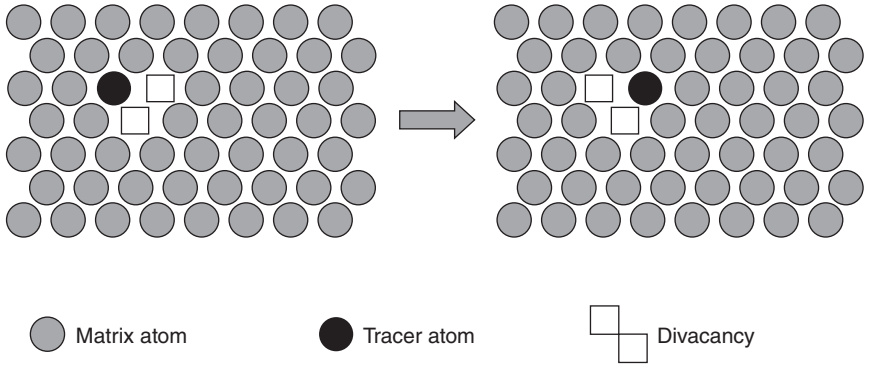


Figure 5.4 Divacancy mechanism of diffusion.

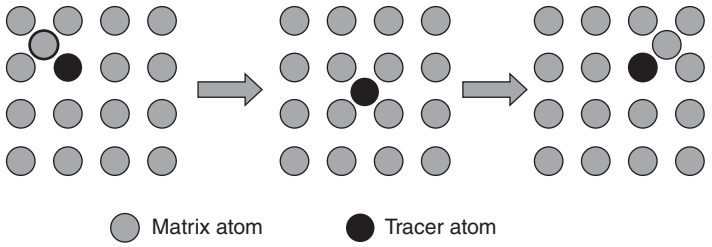


Figure 5.5 Interstitialcy mechanism of diffusion.

lattice atom. Self-interstitials are responsible for diffusion in the silver sublattice of silver halides. In silicon, the base material of microelectronic devices, the interstitialcy mechanism dominates self-diffusion and plays a prominent role in the diffusion of some solute atoms including important doping elements (Murch and Nowick 1984). This is not surprising since the diamond lattice (coordination number 4) provides sufficient space for interstitial species.

5.2.1.5 Interstitial–Substitutional Exchange Mechanisms

Some solute atoms (B) can be dissolved on interstitial (B_i) and substitutional (B_s) sites of a solvent crystal (A) and diffuse via an interstitial–substitutional exchange mechanism (see Figure 5.6). For some of these so-called hybrid solutes, the diffusivity of B_i is much higher than the diffusivity of B_s, whereas the opposite is true for the solubilities. Under

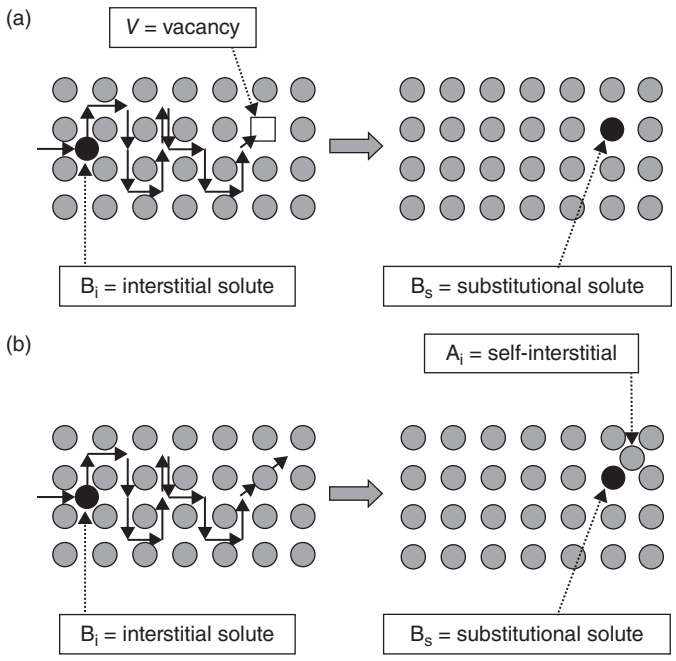


Figure 5.6 Interstitial–substitutional exchange mechanisms of foreign atom diffusion. (a) Dissociative mechanism. (b) Kickout mechanism.

such conditions, the incorporation of B atoms can occur by the fast diffusion of B_i and the subsequent changeover to B_s. Two types of interstitial–substitutional exchange mechanisms can be distinguished:

If the changeover involves vacancies (V) according to

$$B_i + V \rightleftharpoons B_s \tag{5.4}$$

the mechanism is denoted as *dissociative mechanism* (sometimes also *Frank–Turnbull mechanism* or *Longini mechanism*). The rapid diffusion of Cu in germanium and of some foreign metallic elements in polyvalent metals such as lead, tin, niobium, titanium, and zirconium has been attributed to this mechanism (see Section 5.10).

If the changeover involves self-interstitials (A_i) according to

$$B_i \rightleftharpoons B_s + A_i \tag{5.5}$$

the mechanism is denoted as *kickout mechanism*. The fast diffusion of Au, Pt, and Zn in silicon has been attributed to this mechanism (Bracht et al. 1995).

The considerations above illustrate the main diffusion mechanisms. In the case of semiconducting materials, the simple picture may be complicated to some extent by the wide range of energy values available up to the Fermi level. This range leads to the possibility that the given lattice defect may occur with different states of ionization. However, a useful consequence of this phenomenon is the opportunity to investigate diffusion processes in more detail by using electrical methods.

The equation that governs the relationship between the flux J of the diffusing species and the concentration gradient of that species at any point is

$$J = -D \operatorname{grad} C \tag{5.6}$$

where D is called the *diffusion coefficient* of that species. The negative sign indicates a flow from a region of high concentration to that one of lower concentration in an isotropic medium. D may be defined as "the quantity of substance that, in diffusing from one region to another, passes through each unit of cross-section per unit of time, when the volume-concentration gradient is unity." Equation (5.6) is the *first Fick's law*.

The actual diffusion mechanism, which is operating in a given situation, may be established by the position and the charge state of the diffused impurity, if this information can be obtained. If not, the variation of D in the particular situation may lead to a solution. In particular, the temperature dependence of D is often given by Chitraub et al. (2000)

$$D = D_0 \exp\left(-\frac{Q}{k_B T}\right) \tag{5.7}$$

where Q is the activation energy for the jump mechanism while each mechanism has a unique value of Q.

Using now the continuity equation for the flow of atoms through a given volume

$$\frac{\partial C}{\partial t} = -\operatorname{div} J \tag{5.8}$$

we have with (5.6)

$$\frac{\partial C}{\partial t} = \operatorname{div}(D \operatorname{grad} C) \tag{5.9}$$

which is known as *second Fick's law*.

For the case of diffusion in one dimension only, this becomes

$$\frac{\partial C}{\partial t} = \frac{\partial}{\partial x}\left[D\frac{\partial C}{\partial x}\right] \tag{5.10}$$

and if D is independent of x, then

$$\frac{\partial C}{\partial t} = D\frac{\partial^2 C}{\partial x^2} \tag{5.11}$$

In order to see which of the above two equations should be applied in any particular case and, further, which boundary conditions must be used in order to find a solution to that equation, it is necessary to consider the possible types of diffusion processes and the ways in which diffusion may be carried out in practical terms.

5.2.2 Diffusion at Chemical Equilibrium

In this case, diffusion occurs in a uniform chemical and defect environment. It is termed *self-diffusion* when dealing with solute atoms of the same species as the host lattice and *isoconcentration diffusion* for the case of foreign atoms. In the latter situation, the crystal must be pre-diffused to a homogeneous level of impurity concentration prior to the experimental diffusion (Huggins 2001). It is clear that in both cases the solute and solvent atoms must be mutually distinguishable, and this is best achieved by the use of radioisotopes (Section 5.12.3). Under these diffusion conditions, the concentration of the diffusing species is constant, and, consequently, if D is considered to be exclusively a function of C at a given temperature, then D will be independent of position. Therefore, in this case, Eq. (5.11) is always valid.

5.2.3 Diffusion in a Net Chemical Flux

The system is now in a nonequilibrium situation with chemical fluxes being formed by the presence of chemical potential gradients. Diffusion under these conditions is often termed *chemical diffusion*. Since, in this situation, there exists a concentration gradient $\partial C/\partial x$, Eq. (5.11) is only valid if D is independent of C. Otherwise, one must use the form of Fick's law shown in Eq. (5.10). However, if it is for the present state assumed that it is valid to use

Eq. (5.11), then the boundary conditions, necessary for a solution, are specified by the experimental conditions under which the diffusion is carried out (Vuci and Gladi 1999).

5.2.4 Condition of Limited Source

In this situation, the total amount of impurity present in the system is small, and the appropriate boundary condition is that the total number of impurity atoms in the diffused region is constant. Experimentally, the impurity is often present as a thin layer, deposited on the surface of the host crystal. The corresponding solution to Fick's law is

$$C = \frac{Q^{\mathrm{i}}}{(\pi D t)^{1/2}} \exp\left(-\frac{x^2}{4Dt}\right) \tag{5.12}$$

where Q^{i} is the number of impurity atoms, per unit area, initially contained in the layer (Labid et al. 1997).

5.2.5 Conditions of Infinite Source

Here we have the case in which the number of atoms already diffused into the lattice at any time is small compared with their number available in the source. The appropriate boundary condition is now that the number of impurity atoms per unit volume, C_0, at the surface of the crystal is constant for all diffusion times. The corresponding solution is

$$C = C_0 \ \mathrm{erfc}\left(\frac{x^2}{4Dt}\right)^{1/2} \tag{5.13}$$

To be more precise, in practice C_0 is the solubility of the impurity under the particular conditions of the experiment in question. erfc(y) is a complementary error function given by

$$\mathrm{erfc}(y) = 1 - \frac{2}{\pi^{1/2}} \int_0^y \exp(-z^2)\mathrm{d}z \tag{5.14}$$

The most common way of obtaining this condition is to diffuse from a vapor source. This is the method employed for most of the experimental diffusions described in the open literature, and hence the solution shown in Eq. (5.13) is of considerable interest. Provided that the infinite source condition is satisfied, it indicates the theoretical form of the impurity profile for all concentration experiments and those chemical diffusions, where D is independent of C. Any deviation from this profile shape is thus usually an indication that D is a function of C, and Eq. (5.10) must be solved to give the relationship between D and C. The discussion of this problem is presented in a later section.

5.3 Diffusion Coefficients

Diffusion in materials is characterized by several diffusion coefficients, which depend on the experimental situation. Our focus is on bulk diffusion in simple binary systems. In this section, we will distinguish the various diffusion coefficients by lower and upper indices. We will drop the indices in the following sections again, whenever it is clear which diffusion coefficient is meant.

5.3.1 Tracer Diffusion Coefficients

If the diffusion of A atoms in a solid element A is studied, one speaks of self-diffusion. Studies of self-diffusion use a tracer isotope A* of the same element. A typical initial configuration for a tracer self-diffusion experiment is illustrated in Figure 5.7a. If the applied tracer layer is very thin as compared to the average diffusion length, the tracer *self-diffusion coefficient* $D_{\mathrm{A}}^{\mathrm{A}*}$ is obtained from such an experiment.

The connection between the macroscopically defined tracer self-diffusion coefficient and the atomistic picture of diffusion is the famous *Einstein–Smoluchowski relation*. In simple cases, it reads

$$D_{\mathrm{A}}^{\mathrm{A}*} = f D_{\mathrm{E}} \ \text{ with } \ D_{\mathrm{E}} = \frac{l^2}{6\tau} \tag{5.15}$$

where l denotes the jump length and τ the mean residence time of an atom on a certain site of the crystal. The quantity f is the correlation factor. For self-diffusion in cubic crystals, f is a numeric factor. Its value is characteristic of the lattice geometry and the diffusion mechanism. In some textbooks, the quantity D_{E} is denoted as the *Einstein diffusion coefficient*. Equation (5.15) considers only the simplest case: cubic structure, all sites are energetically equivalent, and only jumps to nearest neighbors are allowed.

In a homogeneous binary $\mathrm{A}_x\mathrm{B}_{1-x}$ alloy or compound, two tracer diffusion coefficients for both, A* and B* tracer atoms, can be measured. A typical experimental starting configuration is displayed in Figure 5.7b. We denote the tracer diffusion coefficients by $D_{\mathrm{A}_x\mathrm{B}_{1-x}}^{\mathrm{A}*}$ and $D_{\mathrm{A}_x\mathrm{B}_{1-x}}^{\mathrm{B}*}$. Both tracer diffusion coefficients will in general be different.

This diffusion asymmetry depends on the crystal structure of the material and on the atomic mechanisms that mediate diffusion. Both diffusivities, of course, also depend on temperature and composition of the alloy or compound and for anisotropic media on the direction of diffusion.

When the diffusion of a trace solute C^* in a monoatomic solvent A or in a homogeneous binary solvent $\mathrm{A}_x\mathrm{B}_{1-x}$ (Figure 5.7) is measured, the tracer diffusion coefficients

$$D_{\mathrm{A}}^{C*} \text{ and } D_{\mathrm{A}_x\mathrm{B}_{1-x}}^{C*}$$

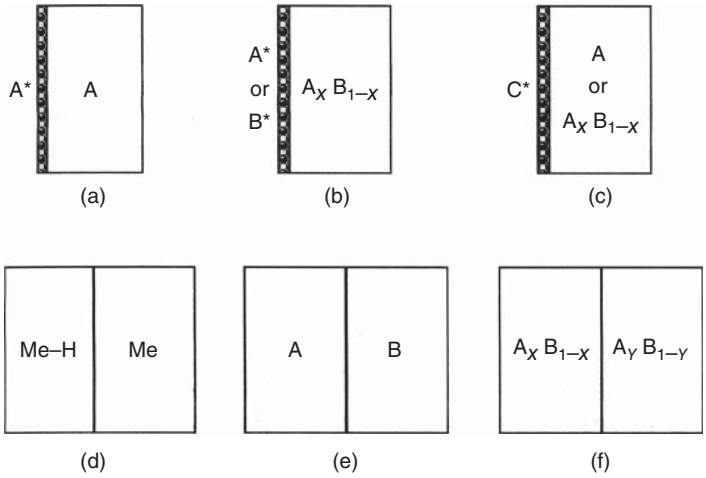


Figure 5.7 Initial configurations for diffusion experiments: (a) Thin layer of A* on A: tracer diffusion in pure elements. (b) Thin layer of A* or B* on homogeneous alloy: tracer diffusion of alloy components. (c) Thin layer of C* on element A or homogeneous alloy: impurity diffusion. (d) Diffusion couple between metal–hydrogen alloy and a pure metal. (e) Diffusion couple between pure end-members. (f) Diffusion couple between two homogeneous alloys.

are obtained. These diffusion coefficients are denoted as *impurity diffusion coefficients* or sometimes also as foreign atom diffusion coefficients.

Figure 5.8 shows collected data of self-diffusion coefficients in sulfides in relation to analogous results obtained for several metal oxides (Mrowec and Przybylski 1984). It becomes clear from this comparison that the rate of self-diffusion in metal sulfides is generally much higher than in the corresponding oxides. As chemical diffusion coefficients in metal oxides and sulfides are comparable, as shown in Figure 5.9, the significantly higher self-diffusion rates of cations in the majority of transition metal sulfides

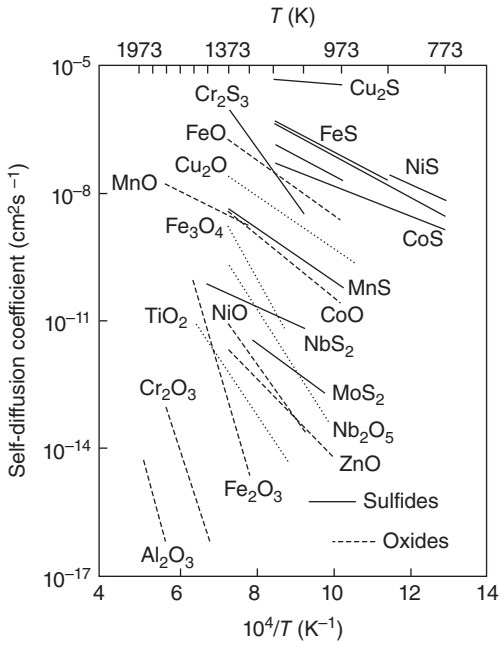


Figure 5.8 Comparison of self-diffusion coefficients in several metal sulfides and oxides.

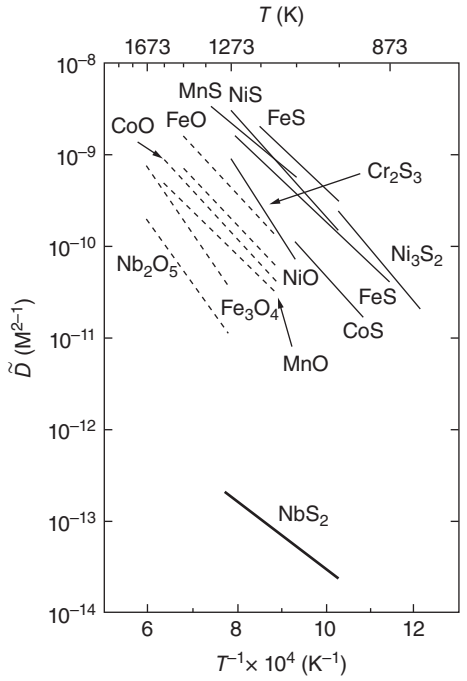


Figure 5.9 Chemical diffusion coefficient in niobium sulfide on the background of analogous data obtained for several metal sulfides and oxides.

result mainly from much higher defect concentration and not their mobilities (see Chapter 8). The only known exception is niobium sulfide.

5.3.2 Chemical Diffusion (or Interdiffusion) Coefficient

So far, we have considered in this section cases where the concentration gradient is the only cause for the flow of matter. We have seen that such situations can be studied

using tiny amounts of trace elements in an otherwise homogeneous material. However, from a general viewpoint, a diffusion flux is proportional to the gradient of the chemical potential.

The chemical potential of a species i in a binary alloy is given by

$$\mu_i = \left(\frac{\partial G}{\partial_{n_i}} \right)_{p,T,n_j \neq i} \qquad i = \mathrm{A}, \mathrm{B} \tag{5.16}$$

In Eq. (5.16), G denotes Gibbs free energy, n_i the number of moles of species i, T the temperature, and p the hydrostatic pressure. The chemical potential depends on the alloy composition. For ideal solutions, the chemical potentials are

$$\mu_i = \mu_i^0 + RT \ln \frac{n_i}{n_\mathrm{A} + n_\mathrm{B}} \tag{5.17}$$

where μ_i^0 depend on T and p only. In this case, the gradient of the chemical potential is directly proportional to the logarithmic gradient of the concentration. In nonideal solutions, the gradient of the chemical potential gives rise to an "internal" driving force. As a consequence, the *interdiffusion coefficient* is concentration dependent, and Fick's equation in the form of (5.10) must be used.

Examples of diffusion couples that entail an interdiffusion coefficient are (see Figure 5.7):

(i) Pure end-member diffusion couples consisting of two samples of pure elements joined together (e.g. Ni/Pd, Cu/Ag, etc.).

(ii) Incremental diffusion couples consisting of two samples of homogeneous alloys joined together (e.g. $Ni_{50}Pd_{50}/Ni_{70}Pd_{30}$, $Ni/Ni_{70}Pd_{30}$, etc.).

(iii) Diffusion couples that involve solutions of hydrogen in a metal (e.g. Pd-–H/Pd, $Ag_{1-x}H_x/Ag_{1-Y}H_Y$, etc.).

Binary metal–hydrogen systems are often special in the sense that hydrogen is the only mobile component.

Interdiffusion results in a composition gradient in the diffusion zone. Interdiffusion profiles are analyzed by the Boltzmann–Matano method or related procedures, as described below. It allows to deduce the concentration dependence of the interdiffusion coefficient

$$\widetilde{D} = \widetilde{D}(C) \tag{5.18}$$

from the experimental diffusion profile.

As already mentioned, the rate of chemical diffusion and thus the rate of defect mobility in the majority of transition metal sulfides are generally higher than in analogous oxides, but these differences do not exceed 1 order of magnitude (Figure 5.10). Some of the most important results concerning chemical diffusion in transition metal sulfides obtained by Grzesik and Mrowec (2006) are the data describing the mobility of predominant defects in niobium sulfide, being the main product of niobium sulfidation. As it is shown in Figure 5.8, the mobility of these defects is several orders of magnitude lower than that in all other metal sulfides and oxides. It should be noted that one of the most fascinating problems in the case of niobium sulfidation is its extremely high resistance to sulfur attack at high temperatures, in spite of very high concentration of point defects in the growing scale on this metal. The only hypothetical explanation of this unexpected phenomenon was based on the assumption that the mobility of defects in niobium sulfide scale is several orders of magnitude lower than in other transition metal sulfides (Gesmundo et al. 1992). Thus, in spite of a very high concentration of defects, the sulfide scale on niobium shows very good protective properties, comparable with those of the Cr_2O_3 scale on chromium.

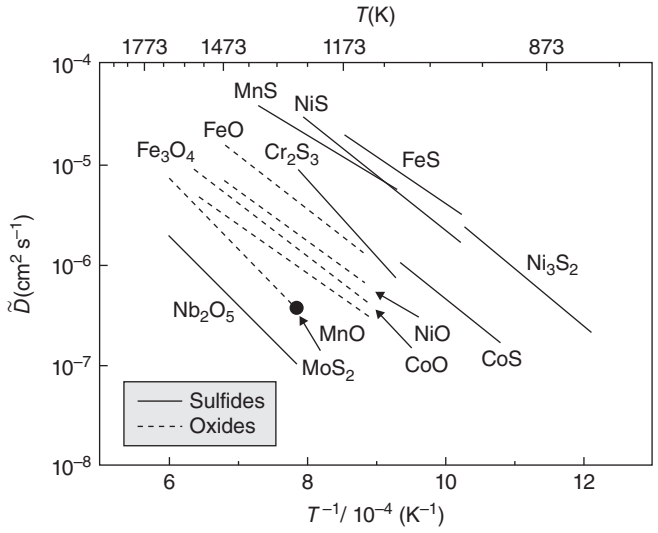


Figure 5.10 Comparison of chemical diffusion coefficients in several metal sulfides and oxides.

5.3.3 Intrinsic Diffusion Coefficients

The *intrinsic diffusion coefficients* (sometimes also component diffusion coefficients) D_A and D_B of a binary A–B alloy describe the diffusion of the components A and B in relation to the lattice planes. The diffusion rates of A and B atoms are usually not equal. Therefore, in an interdiffusion experiment, a net flux of atoms across any lattice plane exists. The shift of lattice planes with respect to a sample fixed axis is denoted as *Kirkendall effect* (see Section 5.7).

The Kirkendall shift can be observed by incorporating inert markers at the initial interface of a diffusion couple. This shift was observed for the first time for the Cu/Cu–Zn diffusion couples by Smigelskas and Kirkendall (1947). In the following decades, work on many different alloy systems and a variety of markers demonstrated that the Kirkendall effect is a widespread phenomenon of interdiffusion.

The intrinsic diffusion coefficients D_A and D_B of a substitutional binary A–B alloy are related to the interdiffusion coefficient $\tilde{D}$ and the marker velocity v_K (*Kirkendall velocity*). These relations were deduced for the first time by Darken (1948) and refined later on by Manning (1968). They will be discussed in Section 5.8. If the quantities $\tilde{D}$ and v_K are known from experiment, the intrinsic diffusion coefficients can be deduced.

We emphasize that the intrinsic diffusion coefficients and the tracer diffusion coefficients are different. D_A and D_B pertain to diffusion in a composition gradient, whereas D_{AB}^{A*} and D_{AB}^{B*} are determined in a homogeneous alloy. In a metal–hydrogen system usually only H atoms are mobile. Then the intrinsic diffusion coefficient and the chemical diffusion coefficient of hydrogen are identical.

5.4 Matano–Boltzmann Analysis

The Matano–Boltzmann analysis is used frequently by researchers to study diffusion in the solid state. By this method, one can measure interdiffusion coefficients, $\tilde{D}$, at different compositions from the concentration profile measured by microprobe analysis. However, this method is restricted to systems where the partial molar volumes of the components are constant, i.e. the total volume does not change with reaction and mixing. Consider the case when two materials with initial compositions C_B^- and C_B^+ are coupled and annealed for reasonably short time, t, such that after annealing, still some part of the end-members is not affected by the diffusion process as shown in Figure 5.11a. Boundary conditions can be written as

$$\begin{aligned} C_B &= C_B^- \quad \text{for } x < 0 \text{ at } t = 0 \\ C_B &= C_B^+ \quad \text{for } x > 0 \text{ at } t = 0 \end{aligned} \tag{5.19}$$

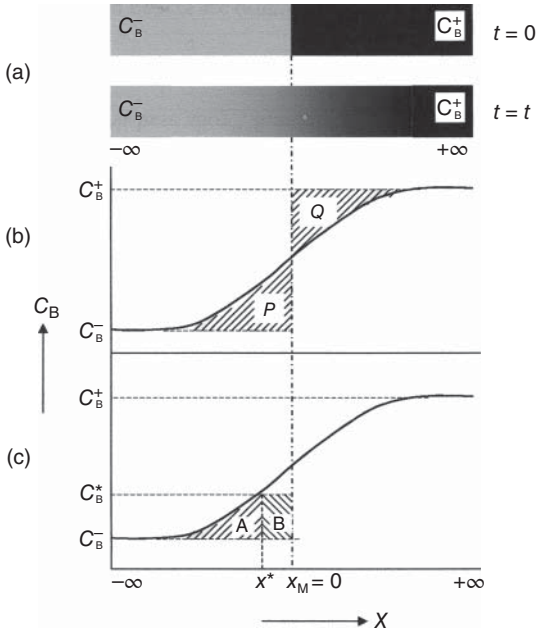


Figure 5.11 (a) Diffusion couple with end-member compositions C_B^- and C_B^+ before and after annealing for time t. (b) Matano plane $x_M = 0$ can be found by equalizing the areas P and Q. (c) The value of the integral in Eq. (5.24) is equal to the shaded area (A + B) as shown in Eq. (5.26).

where "−" and "+" represent the left- and right-hand end of the reaction couple.

Boltzmann (1894) introduced the variable

$$\lambda = \lambda(C_B) = \frac{x}{t^{1/2}} \tag{5.20}$$

which means that C_B is a function of λ only. The relation states that all compositions in a diffusion zone move parabolically in time with respect to one fixed frame of reference.

By using the definition of λ, and transforming $\partial C_B/\partial_t$ and $\partial C_B/\partial_x$ in Fick's second law, using also Eq. (5.20), one can write

$$-\frac{\lambda}{2}\frac{\partial C_B}{\partial \lambda} = \frac{\partial}{\partial \lambda}\left(\tilde{D}\frac{\partial C_B}{\partial \lambda}\right) \tag{5.21}$$

This treatment is known as the Boltzmann transformation, and this transformation was used for the first time by Matano (1933) to study interdiffusion in the solid state.

Initial conditions at time $t = 0$ can be written as, considering Eq. (5.20),

$$\begin{aligned} C_B &= C_B^- \quad \text{at } \lambda = -\infty \\ C_B &= C_B^+ \quad \text{at } \lambda = +\infty \end{aligned} \tag{5.22}$$

Equation (5.21) contains only total differentials and $\partial\lambda$ can be canceled from both sides. Integrating from initial composition C_B^- to the concentration of interest to measure

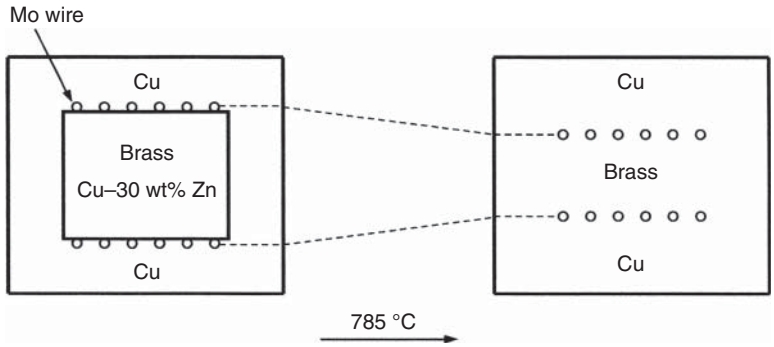


Figure 5.12 Schematic representation of a cross section of the diffusion couples prepared by Smigelskas and Kirkendall (1947) before and after annealing at 785 °C. Molybdenum wires moved closer to each other with increasing time, t.

the interdiffusion coefficient, $\widetilde{D}$, at C_B^* ($C_B^- < C_B^* < C_B^+$) leads to

$$-\frac{1}{2}\int_{C_B^-}^{C_B^*} \lambda \, dC_B = \widetilde{D}\frac{dC_B}{d\lambda}\bigg|_{C_B^-}^{C_B^*} \tag{5.23}$$

The data is always measured at some fixed time so that t is constant. If we assume that after annealing the ends of the couple are not affected, then $dC_B/dx = 0$ at C_B^- and C_B^*. Using Eq. (5.20) one can write

$$\widetilde{D}(C_B^*) = -\frac{1}{2t}\left(\frac{dx}{dC_B}\right)_{C_B^*}\int_{C_B^-}^{C_B^*} x \, dC_B \tag{5.24}$$

and

$$\int_{C_B^-}^{C_B^*} x \, dC_B = 0 \tag{5.25}$$

Equation (5.25) defines the plane $x_M = 0$, and the initial contact plane between the end-members is called *Matano plane*.

The Matano plane position, x_M, can be determined from the concentration–penetration curve of the system measured by X-ray microanalysis by equalizing the areas P and Q as shown in Figure 5.11b. After integrating by parts, Eq. (5.24) can be modified, and, from Figure 5.11c, the interdiffusion coefficient can be expressed in terms of shaded areas as

$$\widetilde{D}(C_B^*) = -\frac{1}{2t}\left(\frac{\partial x}{\partial C_B}\right)_{C_B^*}[A + B] \tag{5.26}$$

The main disadvantage of this analysis is that one has to find the position of the Matano plane, x_M. When the total volume does not change with reaction/mixing, this is easy to determine. However, when the total volume changes, determining the initial contact plane (denoted by x_0) is rather confusing.

5.5 Kirkendall Effect

By the Matano–Boltzmann analysis, one can quantify the interdiffusion coefficient, $\widetilde{D}$, which is, in fact, a kind of average diffusivity of the elements, and it does not shed light on the diffusivities of the species, separately. In the early stage, it was common belief among researchers that diffusivities of the species are the same.

Hartley (1946) was the first to use purposely foreign inert particles, titanium dioxide, in an organic acetone/cellulose acetate system to study the inequality of the diffusing species. Shortly after that, Smigelskas and Kirkendall (1947) used the same technique to examine the inequality of diffusivities of the species in the Cu–Zn system by introducing molybdenum as an inert marker. Researchers dealing with metallic systems at that time were not familiar with Hartley's work, and the effect of inequality of diffusivities on the inert marker was named the Kirkendall effect (Darken and Gurry 1953).

In the experiment by Smigelskas and Kirkendall, a rectangular bar ($18 \times 1.9\,cm^2$) of 70/30 wrought brass (70 wt%Cu/30 wt%Zn) was taken. This bar was ground and polished, and then 130 μm diameter molybdenum wires, which are inert to the system, were placed on opposite sides of the surfaces. Then a copper layer of 2500 μm was deposited on that, as shown in Figure 5.12. This couple was subjected to annealing at 785 °C. After annealing for a certain time, one small piece was cross-sectioned to examine, and the rest of the part was further annealed. Following this method, it was possible to get specimens at different annealing times. With annealing, α-brass grows in between, and after etching, the distance between the markers was measured. If the diffusivities of copper and zinc are the same and there is no change in volume during diffusion/reaction, marker should not move and stay at the original position.

However, after measuring, it was clear that with increasing annealing time, the distance between markers decreases parabolically with time. Considering the change in the lattice parameter, it was found that only 1/5 of the displacement occurred because of molar volume change. This shift was explained by Smigelskas and Kirkendall (1947), being possible to draw two conclusions of enormous impact at the time on solid-state diffusion:

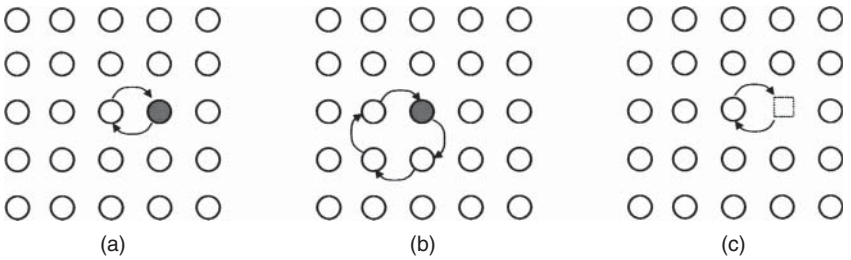


Figure 5.13 Atomic diffusion mechanisms: (a) direct exchange mechanism, (b) ring mechanism, and (c) vacancy mechanism.

1. The rate of diffusion of zinc is much greater than that of copper in α-brass.
2. When zinc diffuses more rapidly than copper in α-brass, the interface shifts to compensate, at least partially, the diffusion rate.

Till then, direct exchange or ring mechanisms were accepted as diffusion mechanism in the solid state as shown in Figure 5.13a,b. If any of these mechanisms would be true, then diffusivities of the species should be the same. However, from Kirkendall's experiment, it is evident that Zn diffuses faster than Cu, which results into the movement of the markers. When zinc diffuses away, all the sites are not occupied by the flow of Cu from opposite direction, and, because of that, vacant sites are left unoccupied. In other sense, there should be a flow of vacancies opposite to the faster diffusing species Zn to compensate for the difference between the Zn and Cu flux. Vacancies will flow toward the brass side, and excess Zn will diffuse toward the Cu side. Ultimately, this results into shrinking in the brass side and swelling in the copper side so that markers move to the brass side. In some diffusion reactions, pores can be found in the product phase. If there is not enough plastic relaxation during the process, vacancies will coalesce to form pores or voids in the reaction layer.

From this experiment, it was clear that diffusion occurs by a vacancy mechanism (Figure 5.13c), and after that the direct exchange and ring mechanisms were abandoned. At first, this work was highly criticized, but later this phenomenon was confirmed from experiments on many other systems (da Silva and Mehl 1951; Nakajima 1997; Sequeira and Amaral 2014). The impact of Kirkendall's work, at that time, can be realized from Mehl's comment on his work (Mehl 1947).

5.6 Darken Analysis

From Kirkendall's experiment, it was clear that the diffusion process in solid solutions cannot be described by one diffusion coefficient; rather one has to determine the diffusivity of both species. This was treated mathematically by Darken (1948). Almost at the same time, Hartley and Crank (1949) studied the same subject, and they named

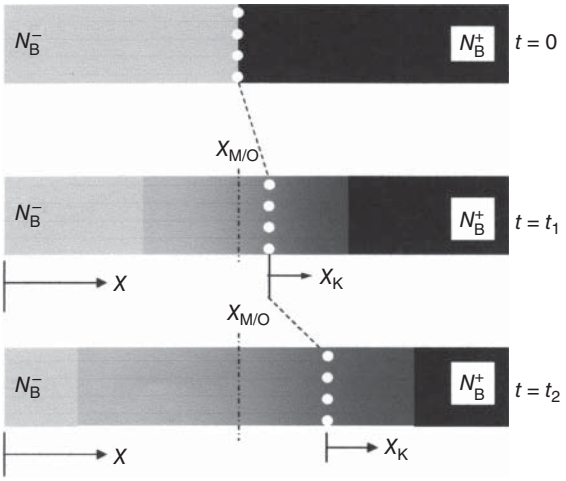


Figure 5.14 Schematic representations of a diffusion couple with the end-members N_B^- and N_B^+ demonstrating the Kirkendall effect. Inert markers (white spots) placed at initial contact interface before annealing are shifted with increasing annealing time ($t_2 > t_1$) to the right (from $x_{M/0}$) as the diffusion of the species B is higher than the species A. The Kirkendall frame of reference, x_K, moves with time, with respect to one end of the unreacted part of the specimen or with respect to $x_{M/0} = 0$.

the diffusivities of species as intrinsic diffusion coefficient. Seitz (1948) studied the solid-state diffusion process more extensively.

Let us consider a binary diffusion couple of species A and B of the compositions N_B^- and N_B^+ as shown in Figure 5.14. Before annealing fiducial (inert) markers are introduced at the initial bonding interface and annealed at elevated temperature so that interdiffusion takes place. When interdiffusion starts, the markers will be trapped at a certain fixed composition and cannot escape at a later stage so that they move along with that fixed composition. If the intrinsic diffusivity of B (D_B) is higher than the intrinsic diffusivity of A (D_A) at that marker plane (called Kirkendall plane), then the Kirkendall marker plane will move to the right-hand side from the initial contact interface, $x_{M/0}$. The Matano plane, x_M, is the initial contact interface when there is no change in total volume and is fixed with respect to the ends of the diffusion couple. This initial contact plane is denoted by x_0 when volume changes upon reaction/mixing.

The intrinsic molar flux at the Kirkendall plane can be expressed by Fick's first law as

$$J_A = -D_A\left(\frac{\partial C_A}{\partial x}\right)_K; \quad J_B = -D_B\left(\frac{\partial C_B}{\partial x}\right)_K \tag{5.27}$$

This Kirkendall reference plane, x_K, is not fixed but moves relative to the laboratory frame of reference. If we consider that this Kirkendall plane moves from $x_{M/0} = 0$ with a velocity v_K, then the relation between interdiffusion fluxes $\tilde{J}_A$ and $\tilde{J}_B$ (measured with respect to $x_{M/0}$) and intrinsic fluxes J_A and J_B (measured with respect to the Kirkendall frame of reference at the position x_K) can be written as

$$\tilde{J}_A = J_A + v_K C_A; \quad \tilde{J}_B = J_B + v_K C_B \tag{5.28}$$

where $\tilde{J}_A$ and $\tilde{J}_B$ are related by (using the relation $V_A\,dC_A + V_B\,dC_B = 0$)

$$\tilde{J}_A = -\tilde{D}\left(\frac{\partial C_A}{\partial x}\right) = \frac{V_B}{V_A}\tilde{D}\frac{\partial C_B}{\partial x} = -\tilde{J}_B\frac{V_B}{V_A} \tag{5.29}$$

In terms of volume flux (volume flux = partial molar volume of component, $V_i \times$ molar flux),

$$\begin{aligned} J_A^{vol} &= V_A\tilde{J}_A = V_A J_A + v_K V_A C_A; \\ J_B^{vol} &= V_B\tilde{J}_B = V_B J_B + v_K V_B C_B \end{aligned} \tag{5.30}$$

In an "infinite" diffusion couple (where ends of the couple are not touched by diffusion) from Eq. (5.29),

$$V_A\tilde{J}_A + V_B\tilde{J}_B = J_A^{vol} + J_B^{vol} = 0 \tag{5.31}$$

From Eqs. (5.27), (5.30), and (5.31), it follows that

$$\begin{aligned} &- V_A D_A\left(\frac{\partial C_A}{\partial x}\right)_K + V_A C_A v_K \\ &- V_B D_B\left(\frac{\partial C_B}{\partial x}\right)_K + V_B C_B v_K = 0 \end{aligned} \tag{5.32}$$

By using the standard thermodynamic relations $C_A V_A + C_B V_B = 1$ and $V_A\,dC_A + V_B\,dC_B = 0$,

$$\begin{aligned} v_K &= V_B(D_B - D_A)\left(\frac{\partial C_B}{\partial x}\right)_K = \frac{V_A V_B}{V_m^2}(D_B - D_A)\left(\frac{\partial N_B}{\partial x}\right)_K \\ &= -(V_B J_B + V_A J_A) \end{aligned} \tag{5.33}$$

Substituting Eq. (5.33) in Eq. (5.28) and comparing with equations $C_A V_A + C_B V_B = 1$ and (5.29) leads to

$$\begin{aligned} -\tilde{D}\frac{\partial C_B}{\partial x} &= J_B + v_K C_B = -D_B\frac{\partial C_B}{\partial x} + C_B V_B(D_B - D_A)\frac{\partial C_B}{\partial x} \\ &= -(1 - C_B V_B)D_B\frac{\partial C_B}{\partial x} - C_B V_B D_A\frac{\partial C_B}{\partial x} \\ &= -(C_A V_A D_B + C_B V_B D_A)\frac{\partial C_B}{\partial x} \\ \tilde{D} &= V_A C_A D_B + V_B C_B D_A \end{aligned} \tag{5.34}$$

In the special case when partial molar volumes of the components are equal and do not change with the composition so that $V_m = V_A = V_B$, Eq. (5.34) reduces to

$$\tilde{D} = N_A D_B + N_B D_A \tag{5.35}$$

Equation (5.35) is known as the *Darken equation*. It should be noted that interdiffusion coefficients can be measured at any composition in a concentration profile; however, intrinsic diffusivities can only be measured at compositions indicated by inert markers introduced in the couple prior to annealing.

5.7 Factors Influencing Diffusion

5.7.1 Temperature Dependence

It is well known that diffusion coefficients in solids generally depend rather strongly on temperature, being low at low temperatures but appreciable at high temperatures. Empirically, measurements of diffusion coefficients over a certain temperature range may be often, but by no means always, described by an Arrhenius relation:

$$D = D_0 \exp\left(-\frac{\Delta H}{RT}\right) \tag{5.36}$$

In Eq. (5.36) D_0 is denoted as pre-exponential factor and ΔH (or Q) as activation enthalpy of diffusion. The pre-exponential factor can be written as

$$D_0 = D_0' \exp\frac{\Delta S}{R} \tag{5.37}$$

where ΔS is the diffusion entropy and D_0' contains geometric factors, the correlation factor, the lattice parameter squared, and an attempt frequency of the order of the Debye frequency.

Equation (5.36) is often also written as Eq. (5.7).

If the first version of the Arrhenius equation is used, the unit ΔH is $\mathrm{kJ\,mol^{-1}}$. If the second version is used, the appropriate unit of ΔH is eV per atom. Note that 1 eV per atom = $96.472\,\mathrm{kJ\,mol^{-1}}$. The gas constant R and the Boltzmann constant k_B are related via $R = N_A k_B = 8.314 \times 10^{-3}\,\mathrm{kJ\,mol^{-1}\,K^{-1}}$, where N_A denotes the Avogadro constant. Note that the symbol Q for the activation enthalpy is also widely used in the literature.

In an Arrhenius diagram, the logarithm of the diffusivity is plotted versus the reciprocal temperature T^{-1}. For a diffusion process with a temperature-independent activation enthalpy ΔH, the Arrhenius diagram is a straight line with slope $-\Delta H/\mathrm{R}$. From its intercept for $T^{-1} \to 0$, the pre-exponential factor D_0 can be deduced. Such simple Arrhenius behavior should, however, not be considered to be universal. Departures from it may arise for many reasons, ranging from fundamental aspects of

the atomic mechanism, temperature dependence activation parameters, effects associated with impurities, or microstructural features such as GBs. For example, thermodynamics tells us that a temperature-dependent enthalpy according to

$$\frac{\partial \Delta H}{\partial T} = T\frac{\partial \Delta S}{\partial T} \tag{5.38}$$

automatically entails a temperature-dependent entropy and vice versa. If enthalpy and entropy increase with temperature, the Arrhenius diagram will show some upward curvature. Nevertheless, Eq. (5.36) provides a very useful standard.

5.7.2 Pressure Dependence

The variation of diffusivity with hydrostatic pressure p is far less pronounced than with temperature. Usually, the diffusivity decreases as the pressure is increased. Typical pressure effects range from factors of 2–10 for a pressure of 1 GPa (10 kbar). This variation is largely due to the fact that the Gibbs free energy of activation ΔG varies with pressure according to

$$\Delta G = \Delta H - T\Delta S = \Delta E - T\Delta S + p\Delta V \tag{5.39}$$

where ΔV denotes the activation volume and ΔE the activation energy of diffusion. Using Eqs. (5.37) and (5.39), the Arrhenius equation (5.36) can also be written as

$$D = D_0' \exp\left(-\frac{\Delta G}{RT}\right) \tag{5.40}$$

Thermodynamics tells us that

$$\Delta V = \left(\frac{\partial \Delta G}{\partial p}\right)_T \tag{5.41}$$

Equation (5.41) can be considered as the definition of the activation volume. Using Eqs. (5.40) and (5.41), the activation volume can be obtained from measurements of the diffusion coefficient at constant temperature as a function of pressure via

$$\Delta V = -RT\left(\frac{\partial \ln D}{\partial p}\right)_T + \underbrace{RT\,\frac{\partial \ln D_0'}{\partial p}}_{RT \text{ correction term}} \tag{5.42}$$

The term arising from the pressure dependence of D_0' can be estimated from the isothermal compressibility and the *Grueneisen constant* of the material. It is often negligibly small (a few percent of the molar volume V_m or of the atomic volume $\Omega = V_m/N_A$, respectively). Typical values for the activation volume for various metals lie between 0.5 and 0.9 Ω.

We emphasize that a complete characterization of the diffusion process requires knowledge of the three activation parameters $\Delta H = \Delta E + p\Delta V$ (valid only for p = const.), ΔS, and ΔV. For solids, the term $p\Delta V$ becomes significant only at high pressures. At ambient pressure, it is negligible and hence $\Delta H \approx \Delta E$.

5.7.3 Other Factors Dependence

The various diffusion coefficients in solid systems vary, in general, with the composition of the materials system. However, even in systems where D has a strong concentration dependence, little error is involved in assuming D as a constant, providing that diffusion occurs in a dilute solution or over a small range of concentration.

The diffusion in ferritic iron is about 100 times faster than in the austenitic form. This is mainly due to the open BCC structure in the former as compared with a close-packed FCC structure in the latter.

Another effect of crystal structure is the variation of the diffusion coefficient with crystal orientation in a single crystal of the solvent metal. Such anisotropy is nearly or completely absent in cubic metals, but bismuth (rhombohedral space lattice) has a self-diffusion coefficient about a thousand times larger in the direction parallel to the C-axis compared with that in a direction perpendicular to it. A significant effect on the diffusion constant has also been noticed if the crystal structure is distorted by plastic strains or by extensive plastic deformation.

The strong influences of alloying elements on the hardenability of steels might be the result of factors other than large changes in the rate of diffusion of carbon. That is, impurities usually have a small effect on the diffusion of solute atoms in a solvent metal.

In the usual range of grain sizes, it is not necessary to take grain size into account in making diffusion calculations. On the other hand, at lower temperatures, GB diffusion will generally dominate since the bulk or lattice diffusion rate will be small.

The arrangement of atoms is different at GBs, near a free surface and adjacent to a dislocation, from that in a regular crystal lattice. As a result, diffusion via vacancy mechanism is greatly enhanced in these regions. Both the number of vacancies and their mobility may be larger as a result of local disruption of crystal regularity. For this reason, activation energy for GB diffusion is less than that of lattice diffusion. In this context, Atkinson et al. (1982) have reported that the oxidation of Ni is controlled by the outward diffusion of Ni ions along GBs in the NiO film at temperatures below 1100 °C. From diffusion results collected for NiO, Atkinson et al. (1986) extracted the boundary diffusivities by assuming a "GB width" of 1 nm. The lattice diffusion coefficient for Ni ions is much larger than that for O ions, as would be expected from the defect structure of NiO. However, the diffusion coefficients for

Ni ions in low-single and high-single GBs are still larger. The relative contributions to scale growth of bulk and GB diffusion will depend on temperature and oxide grain size. It is generally observed that oxide scales growing on metals have rather fine grain sizes (on the order of a micrometer) so boundary diffusion can predominate to quite high temperatures. It is reported for NiO that boundary diffusion has a similar oxygen pressure dependence to bulk diffusion, which suggests that similar point defects control both processes.

In summary, the diffusion coefficient is a function of many variables, such as temperature, pressure, concentration, crystal structure, impurities, grain size, and short circuit along the GBs, dislocations, or surfaces, but also of an electric field or a local state of stress.

5.8 Impurity Diffusion in Metals

Let us now consider a very dilute substitutional binary alloy of metals A and B with the mole fraction of B atoms much smaller than that of A atoms. Then A is denoted as solvent (or matrix), and B is denoted as solute. Diffusion in a dilute alloy has always two aspects: solute diffusion and solvent diffusion. In this section we consider only solute diffusion in very dilute FCC alloys. This is often denoted as *impurity diffusion*. It implies that the solute is isolated from other solutes in the matrix. In what follows, we consider only fast solute diffusion in some polyvalent metals, which are sometimes also denoted as *open metals* (Wenwer et al. 1989). Open refers to the large ratio between atomic and ionic radius of the solvent. This solvent property leads to solutes with relatively small radii to the occurrence of fast solute diffusion.

Fast solute diffusion in metals has been attributed to the dissociative mechanism (Nowick and Burton 1975). This mechanism operates for solutes that are incorporated not only on substitutional sites but also to some extent to interstitial sites of the solvent metal. As discussed above, the dissociative reaction involves vacancies. Provided that local equilibrium is established, the concentrations of the three involved species must fulfill the law of mass action:

$$\frac{C_\mathrm{i} C_\mathrm{V}}{C_\mathrm{s}} = K(T) = \frac{C_\mathrm{i}^\mathrm{eq} C_\mathrm{V}^\mathrm{eq}}{C_\mathrm{s}^\mathrm{eq}} \tag{5.43}$$

where C_i, C_s, and C_V denote molar fractions of interstitial solute, substitutional solute, and vacancies, $K(T)$ is a constant that depends on temperature, and the superscript eq denotes thermal equilibrium.

A metal crystal with a normal density of dislocations has a sufficient abundance of vacancy sources or sinks to keep the vacancies everywhere at equilibrium. Then, the *effective diffusivity* of solutes is given by Murch and Nowick (1984):

$$D^\mathrm{eff} = \frac{D_\mathrm{s} C_\mathrm{s}^\mathrm{eq}}{C_\mathrm{i}^\mathrm{eq} + C_\mathrm{s}^\mathrm{eq}} + \frac{D_\mathrm{i} C_\mathrm{i}^\mathrm{eq}}{C_\mathrm{i}^\mathrm{eq} + C_\mathrm{s}^\mathrm{eq}} \tag{5.44}$$

where D_i denotes the diffusivity of the solute in its interstitial state and D_s its vacancy-mediated diffusivity on substitutional sites.

For solutes with dominating interstitial solubility and diffusivity ($C_\mathrm{i}^\mathrm{eq} \gg C_\mathrm{s}^\mathrm{eq}$ and $D_\mathrm{i} \gg D_\mathrm{s}$) the effective diffusivity reduces to the trivial case of interstitial diffusion:

$$D^\mathrm{eff} \approx D_\mathrm{i} \tag{5.45}$$

For so-called hybrid solutes, the substitutional solubility dominates ($C_\mathrm{s}^\mathrm{eq} \gg C_\mathrm{i}^\mathrm{eq}$), but the interstitial diffusivity is much faster than the substitutional one ($D_\mathrm{i} \ggg D_\mathrm{s}$). Then, the effective diffusivity (Eq. (5.44)) approaches

$$D^\mathrm{eff} \approx \frac{D_\mathrm{i} C_\mathrm{i}^\mathrm{eq}}{C_\mathrm{s}^\mathrm{eq}} \tag{5.46}$$

This relation contains the factor

$$\frac{C_\mathrm{i}^\mathrm{eq}}{C_\mathrm{s}^\mathrm{eq}} = \exp\left(-\frac{G_\mathrm{is}}{RT}\right) \tag{5.47}$$

where G_is denotes the Gibbs free energy difference between the interstitial and substitutional positions of the solute. The rather wide *diffusivity dispersion* of fast solute diffusers can be largely attributed to this factor.

Fast diffusion of solutes is well known for the semiconducting elements silicon and germanium (Seeger and Chik 1968). It has been also attributed to interstitial–substitutional exchange mechanisms. The kickout mechanism is dominating diffusion of Au, Pt, and Zn in silicon (Bracht et al. 1995), whereas the dissociative mechanism is operating, e.g. for Cu and germanium (Franck and Turnbull 1956). From a chemical viewpoint, these similarities are not surprising. Silicon and germanium are group IV elements such as the "open" metals lead and tin. Fast diffusion is also observed for compound semiconductors (e.g. Zn in GaAs [Stolwijk et al. 2001]). Actually, the concepts growing out from studies of fast diffusion in semiconductors have strongly influenced the interpretation of fast diffusion in metals (Murtagh et al. 2001).

5.9 Grain Boundary Diffusion in Metals

GB diffusion plays an important role in many processes taking place in engineering materials at elevated temperatures. Such processes include Coble creep, sintering,

diffusion-induced GB migration, discontinuous reactions (such as discontinuous precipitation, discontinuous coarsening, etc.), recrystallization, and grain growth.

The fact that GBs provide high-diffusivity ("short-circuit") paths in metals has been known since a few decades. First indications of enhanced atomic mobility at GBs were obtained as early as in the 1920–1930s, for example, from grain size dependence of creep and sintering rates in polycrystalline materials. However, the first direct proof of GB diffusion was obtained in the early 1950s using autoradiography: the additional blackening of autoradiographic images along GBs indicated that the radiotracer atoms penetrated into GBs much faster than in the regular lattice. These observations were immediately followed by two important events: the appearance of the nowadays classic *Fisher model* of boundary diffusion, on one hand, and the development and extensive use of the radiotracer serial sectioning technique, on the other hand. It was largely due to these events that GB diffusion studies were put on a quantitative basis and GB diffusion measurements became the subject of many investigations and publications (Kaur et al. 1989, 1995). This section presents a brief review of fundamentals of GB diffusion on metals and metallic alloys.

Most mathematical treatments of GB diffusion are based on the Fisher model (1951) describing diffusion along a single GB. In the Fisher model, a GB is represented as a high-diffusivity uniform and isotropic slab embedded in a low-diffusivity isotropic crystal perpendicular to its surface (Figure 5.15). The GB is thus described by two physical parameters: the GB width δ and the GB diffusion coefficient D_b such that $D_b \gg D$, D being the volume diffusion coefficient. In a typical diffusion experiment, a layer of foreign atoms, or tracer atoms of the same material, is created at the surface, and the specimen is annealed at a constant temperature T for a time t. During the anneal, the atoms diffuse from the surface into the specimen in two ways: directly into the grains and, much faster, along the GB. In turn, the atoms that diffuse along the GB eventually leave it and continue to diffuse in the lattice regions adjacent to the GB, thus giving rise to a volume diffusion field around the GB.

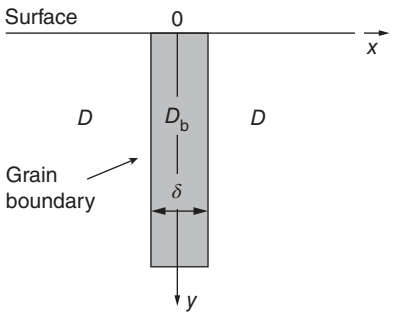


Figure 5.15 Schematic geometry of the Fisher model of grain boundary diffusion.

Mathematically, the diffusion process is described by two coupled equations:

$$\frac{\partial C}{\partial t} = D\left(\frac{\partial^2 C}{\partial x^2} + \frac{\partial^2 C}{\partial y^2}\right), \quad \text{where} \quad |x| > \frac{\delta}{2} \tag{5.48}$$

$$\frac{\partial C_b}{\partial t} = D_b \frac{\partial^2 C_b}{\partial y^2} + \frac{2D}{\delta}\left(\frac{\partial C}{\partial x}\right)_{x=\delta/2} \tag{5.49}$$

These equations represent diffusion in the volume and along the GB, respectively. $C(x,y,t)$ is the volume concentration of the diffusing atoms, and $C_b(y,t)$ is their concentration in the GB. The second term in the right-hand side of (5.49) takes into account the leakage of the diffusing atoms from the GB to the volume. Any solution of (5.48) and (5.49) should meet the surface condition, which can be different in different experiments (see below), as well as the natural initial and boundary conditions at $x \to \pm\infty$ and $y \to \infty$. The joining condition between functions $C(x,y,t)$ and $C_b(y,t)$ depends on whether we study self-diffusion of impurity diffusion. For self-diffusion, the joining condition simply reflects the continuity of the concentration across the GB:

$$C_b(y,t) = C\left(\pm\frac{\delta}{2}, y, t\right) \tag{5.50}$$

For impurity diffusion, the joining condition involves the equilibrium segregation factor s and reads

$$C_b(y,t) = sC\left(\pm\frac{\delta}{2}, y, t\right) \tag{5.51}$$

where s is the segregation factor.

The determination of the triple product $s\delta D_b$ of impurity diffusion is relatively easy if s is constant.

In the case of self-diffusion, we can only determine the product δD_b. We thus need to know δ if we want to determine the GB diffusion coefficient D_b. The assumption $\delta = 0.5$ nm introduced by Fisher (1951) seems to be a good approximation. This value of δ is well consistent with evaluations of GB width by high-resolution transmission electron microscopy, field ion microscopy, and other techniques (Howe 1997; Kaur et al. 1995). Furthermore, recent combined B-regime and C-regime measurements of self-diffusion in silver indicate that $\delta = 0.5$ nm is a very good estimate of δ in metals. Atomistic computer simulations also confirm that the enhanced diffusivity at GBs is confined to the GB core of around 0.5 nm in thickness (Keblinski and Yamakov 2003; Suzuki and Mishin 2003).

It should be noted that type B kinetics is the regime in which

$$\delta \ll (Dt)^{1/2} \ll d \tag{5.52}$$

where d is the spacing between the GBs. In this type, GB diffusion is accompanied by volume diffusion around GBs,

but volume diffusion fields of neighboring GBs do not overlap.

If, starting from the B regime, we go toward lower temperatures and/or shorter anneal times, we eventually arrive at a situation when volume diffusion is almost "frozen out" and diffusion takes place only along GBs without any leakage to the volume. In this regime, called type C, we have

$$(Dt)^{1/2} \ll \delta \tag{5.53}$$

and then the concentration profile is either a Gaussian function

$$\overline{C} \propto \exp\left(-\frac{y^2}{4D_b t}\right) \tag{5.54}$$

(instantaneous source) or an error function (constant source)

$$\overline{C} \propto \operatorname{erfc}\left[\frac{y}{2(D_b t)^{1/2}}\right] \tag{5.55}$$

Atomistic computer simulations (Sörensen et al. 2000; Suzuki and Mishin 2003) suggest that the full description of GB diffusion should include both the vacancy and interstitial-related mechanisms. Simulations also reveal that vacancies can move by "long jumps" involving a simultaneous displacement of two or more atoms.

Interstitials move by the interstitialcy mechanism in which two or more atoms jump in a concerted manner. On some (although rare) occasions, even the ring mechanism was found to operate in certain GBs (Sörensen et al. 2000). Which mechanism dominates the overall atomic transport depends on the particular GB structure. Atomistic modeling also suggests that at high temperatures, GBs can develop a significantly disordered, "liquid-like" structure (Keblinski et al. 1999). Diffusion in such GBs is believed to occur by mechanisms similar to those in liquids.

5.10 Diffusion in Solid Oxides

5.10.1 Brief Overview

Many technologically important kinetic processes occurring in systems containing oxides are dependent on the mobility of atoms and ions through the oxide phases. In order to determine the rate and the atomic mechanisms by which processes such as sintering, oxidation, creep, grain growth, and various solid-state reactions occur, it is essential to determine the nature and the rate of diffusion of the several species contributing to the process of interest.

In general, diffusion-controlled processes, such as the oxidation of metals, occur, not in homogeneous oxides, but under conditions where a chemical potential gradient exists. These gradients may result from the oxide being in contact with several different oxygen potentials, thermal energy sources, or phases of varying chemical composition. In such cases, the process is controlled by chemical diffusion, which takes into account the existing chemical potential gradient, rather than by self-diffusion.

A number of investigations have been conducted, therefore, with the goal of measuring chemical diffusion in oxides. In addition, a number of equations have been developed to relate self-diffusion to chemical diffusion.

Many of these aspects are treated in sections above, in this chapter. Moreover, in Chapter 4, the nature of the point defects in oxides is described, and examples of the relationships that exist among these imperfections are presented. The influence of stoichiometry and foreign atom concentration on the point defect disorder is also emphasized. In general, diffusion mechanisms are discussed, the various kinds of diffusion coefficients are defined, the main equations relating these diffusivities are presented, etc., but many subjects are omitted because there is a great diversity of information that has been obtained from diffusion studies. Being impossible to be further comprehensive, here we will turn to a brief overview of diffusion in oxides, and then more attention will be placed on the influence of external forces on the diffusion in oxides.

Studies of cation self-diffusion in oxides have been most fruitful when directed toward those compounds that have homogeneity regions greater than about 0.01%. In these cases, it has been possible to measure intrinsic diffusivities as a function of oxygen pressure under conditions where impurity levels were low. By comparing results obtained from studies with "pure" intrinsic crystals with those for specimens doped with aliovalent foreign atoms, it has been possible not only to establish the nature of the type and charge of the atomic point defects controlling diffusion but also to separate the enthalpies and entropies of defect formation and migration. In addition, diffusion studies, together with measurements of other defect structure-dependent properties, have revealed the complex nature of atomic disorder that occurs in many oxides. In some cases, a satisfactory interpretation of experimental results requires the invocation of defect models that include the existence of defects with several different charge levels as $V_{Co'}$, $V'_{Co'}$, and V''_{Co} in CoO. In addition, the presence of a stoichiometric imbalance must, in some cases, be attributed not simply to one kind of defect, but rather to a combination of vacancies and interstitials. The predominant kind of defects and the change of those defects are a function of the oxide purity and of the temperature and oxygen pressure at which the oxide was prepared. Cation self-diffusion studies have been particularly useful in aiding in the understanding of defect structures on the cation sublattice for oxides where cation defects are the minority atomic disorder, as

in the case of UO_{2+x}. For such oxides, little can be learned from measurements of electrical conductivity and weight change, which reflect effects due to the majority defects.

Attention has been directed toward understanding the atomic defect structures of oxides with very narrow homogeneity ranges, such as Al_2O_3. For these cases, careful studies with known aliovalent foreign atom additions can be employed to establish the nature of the diffusion mechanisms for such impurity-sensitive compounds. Conversely, it is clear that large discrepancies in diffusivities obtained by different investigators can often be traced to differences in purity of specimens used in the various studies.

It is apparent that the results of some early studies of oxygen diffusion in oxides may be in error because of the many difficulties involved in the use of the ^{16}O–^{18}O exchange method. Nevertheless, diffusion data obtained in recent years has been the single most important source of information available for the development of our understanding of the oxygen sublattice defect structure. This is particularly true for the oxygen-excess p-type conductors for which the primary disorder is on the cation sublattice. Available evidence shows that both oxygen vacancies and oxygen interstitials exist in appreciable concentrations in different oxides.

From studies on compounds such as CoO and CdO, it has been further established that the defects on the oxygen sublattice are charged and that their concentrations may be influenced by aliovalent foreign atom additions.

A subject of great importance is the role of defect complexes in anion and cation diffusion. It is clear that clusters of two or more defects must be the primary defects in oxides such as Fe_xO and UO_{2+x}, which have wide homogeneity ranges. While diffusion measurements can provide some clues regarding the nature of these defects, it is obvious that such measurements cannot provide unambiguous evidence for their specific composition.

Studies of oxygen diffusion in α-Nb_2O_5 have been taken as an indication that all changes in composition of oxides cannot be attributed to simple unassociated atomic defects. It is likely that for the oxides of niobium, titanium, and others, whole series of ordered compounds exist, each of which can tolerate only small concentrations of unassociated point defects.

Our current understanding of interphase chemical diffusion is not very good. Absolute values for chemical diffusivities are, in general, several orders of magnitude greater than tracer diffusion coefficients for either species of simple oxides. This behavior is not surprising, since interphase chemical diffusivities are equated with atomic defect diffusivities and do not include defect formation contributions.

Furthermore, tracer diffusion coefficients calculated from chemical diffusivities through Darken's equation or C. Wagner's equation are often in good agreement with experimentally determined tracer diffusivities. The observed dependence of interphase chemical diffusion rates on oxygen pressure and dopant concentration has not been satisfactorily explained, however. From first principles, it might be expected that such diffusion coefficients would be independent of oxygen partial pressure and dopant level. While this is true for some systems, such as CoO, for which excellent reproducibility has been obtained by different investigators using different experimental techniques, there is ample evidence that chemical diffusivities in other oxides, such as FeO and MnO, increase with decreasing oxygen pressure. This is opposite to the oxygen dependence observed for cation tracer diffusion in these compounds. Similarly, the chemical diffusion rates and cation tracer diffusivities have opposite dependencies on aliovalent foreign atom additions. A number of suggestions have been offered to qualitatively interpret this behavior, but more convincing quantitative analyses of the phenomena have to be presented. While some of the data may have been influenced by surface reaction control of the equilibration process, it appears that some of the apparently anomalous results represent diffusion-controlled processes.

The magnitude and dependence on defect concentration of interphase chemical diffusivities, as measured from interdiffusion of oxide couples, are well understood in relation to tracer diffusion data. Many studies have been published on those systems in which the oxygen sublattices can be assumed to be rigid, while interdiffusion occurs by coupled motion of the cation species. In such cases, interdiffusion rates have been found to increase with increasing cation vacancy concentration. If trivalent cations such as Cr^{3+} or Al^{3+} are diffused into divalent oxides such as MgO, self-doping of the trivalent diffusant results in increasing diffusivities with increasing trivalent cation concentration. Furthermore, the diffusion activation energies for interphase chemical diffusion can often be equated with the activation energy for diffusion of the more slowly diffusing species in the oxide under study. Activation energies reflecting both intrinsic and extrinsic diffusion have been found, depending on the influence of diffusant on the vacancy concentration.

In some cases, such as Fe–MgO interdiffusion, chemical diffusion activation energies are found to depend on diffusant concentration as a result of structural changes that take place in the oxide.

There have also been many careful studies of interphase or interphase chemical diffusion in oxides. Many of the still unexplained observations will undoubtedly be clarified when additional experimental data are available from which theoretical considerations can be substantiated, modified, or rejected.

5.10.2 Diffusion in External Forces

If an oxide is exposed to external thermodynamic forces, e.g. an oxygen potential gradient or an electric potential gradient, defect fluxes are induced, which again cause fluxes of the chemical components.

In oxides where the oxygen ions are much more mobile than the cations, essentially only oxygen is driven through the oxide. For pure oxygen ion conductors, this situation corresponds to an electrolyte in a solid oxide fuel cell (applied oxygen potential gradient) or an electrochemical oxygen pump (applied electrical potential gradient). For mixed conductors, this situation corresponds to oxygen permeation cells (Gellings and Bouwmeester 1996).

In oxides with dominating cation disorder, external forces act on the mobile cations. The implications for the cases of chemical diffusion in an oxygen potential gradient and for electron transport in oxides are considered below.

If an oxide $A_{1-\delta}O$ of thickness Δz is exposed to an oxygen potential gradient, established, e.g. by different gas mixtures on both sides of the disk, different concentrations of cation vacancies, C_V^1 and C_V^2, are established on both sides of the oxide disk. As a consequence, a vacancy flux, j_V, occurs from the high to the low oxygen potential side. Due to the flux coupling, $j_{A^{2+}} + j_V = 0$, cations are driven in the opposite direction. When vacancies and cations arrive at the oxide surfaces, reduction and oxidation of the oxide occur at the low and high oxygen potential side, respectively:

$$V_A'' + 2\dot{h} + AO \underset{\text{oxidation}}{\overset{\text{reduction}}{\rightleftharpoons}} A_A^x + \frac{1}{2}O_2(g) \qquad (5.56)$$

Thus, lattice planes are removed from the low oxygen potential side and added to high oxygen potential side. As a result, the crystal surfaces move relatively to the immobile oxygen sublattice to the side of the higher oxygen activity. The crystal displacement and the vacancy concentration profile can be calculated by solving the diffusion equation (Martin and Schmalzried 1990). After a short transient period, the crystal moves with a constant velocity. A steady-state solution can be calculated by transforming from the laboratory reference frame to a moving coordinate system (coordinate z) that is fixed at one surface. The steady-state vacancy fraction profile in the moving system, $x_v(z)$, is linear in position, z, to a very good approximation, and the steady-state velocity, v, is given by

$$x_v = a + b \times z, \quad v = \widetilde{D} \times b \qquad (5.57)$$

with

$$a = x_V^1, \qquad b = \frac{x_V^2 - x_V^1}{\Delta z} \qquad (5.58)$$

Experiments with the model system CoO exposed to an oxygen potential gradient confirm the shift of the crystal surfaces relatively to immobile oxygen sublattice (Martin and Schmalzried 1990).

Electron transport in oxides, i.e. the motion ions due to an external electric potential gradient, $\nabla\Phi$, will be discussed as follows. As above, where diffusion in an applied oxygen potential gradient was analyzed, the fluxes of the mobile components i (ions and electronic defects) can be written as a sum of a diffusion and a drift flux, $j_i = j_i^{\text{diff}} + j_i^{\text{drift}}$. In a chemically homogeneous oxide without any gradients in chemical potentials, the diffusion fluxes vanish, and the drift flux can be written as

$$j_i^{\text{drift}} = -L_{ii}\left(\sum_k z_k \times \frac{L_{ik}}{Lii}\right) F \times \nabla\Phi \qquad (5.59)$$

where L_{ii} and L_{ik} are transport coefficients. The sum in parentheses is usually denoted as effective charge, $z_{i,\,\text{eff}}$. It is identical to the formal charge, z_i, only if the cross coefficients L_{ik} $(i \neq k)$ are zero and, consequently, the fluxes are independent of each other.

The effective charges are thus a measure of the cross coefficients, which are again indicating defect–defect interactions. In homogeneous oxides exposed to an electric field, (radioactive) tracers can be used to measure the drift velocities of ions from which their effective charges can be calculated. During demixing experiments, however, the oxide becomes chemically inhomogeneous, resulting in drift and diffusion fluxes as well.

Figure 5.16 shows the typical experimental setup that can be used to measure the effective charges, $z_{i,\,\text{eff}}$, of the host cation A or of impurity cations B in an oxide AO using radioactive tracers, A* and B*. The tracer source is located between two single crystals of the oxide in a sandwich arrangement, and the electric potential gradient is applied by two reversible electrodes. Diffusional broadening of the tracer source results in a Gaussian profile from which the

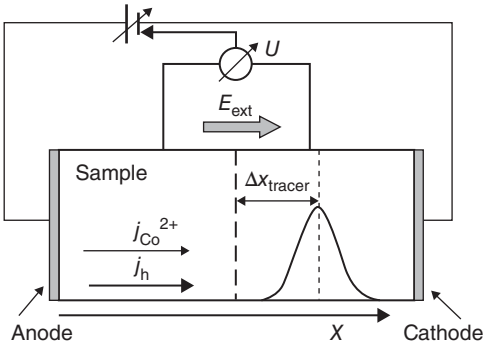


Figure 5.16 Schematic experimental setup for the measurement of the effective charge in a constant electric potential gradient (sandwich experiment). The Gaussian curve shows the broadening and shift of a tracer concentration profile that has developed from a point source located originally in the middle of the crystal.

tracer diffusion coefficient can be obtained. Superimposed is a drift of the tracer concentration profile due to the applied electric field. As shown in detail in Schroeder and Martin (1998), the drift velocity of the tracer concentration profile, v_A^{drift} or v_B^{drift}, allows the determination of the effective charges of the corresponding cations, A or B. For self-diffusion, i.e. tracers A*, we obtain

$$v_A^{drift} = \frac{D_A}{RT} \times z_{A,eff} \times F \times \nabla\Phi, \quad z_{A,eff} = z_A + \frac{L_{Ah}}{L_{AA}} \quad (5.60)$$

The effective charge of cation A, $z_{A,\,eff}$, contains the cross coefficient, L_{Ah}, which indicates the flux coupling between cations and electron holes. $z_{A,\,eff}$ is often called "charge of transport." For impurity tracer cations, B*, the result is

$$v_B^{drift} = \frac{D_B}{RT} \times z_{B,eff} \times F \times \nabla\Phi, \quad z_{B,eff} = z_B + \frac{L_{Bh}}{L_{BB}} + \frac{L_{BA}}{L_{BB}} \quad (5.61)$$

The effective charge of cation B, $z_{B,\,eff}$, contains two cross coefficients, L_{Bh} and L_{BA}, which indicate flux coupling between B and h and between B and A.

This brief analysis shows that apart from a fundamental interest, diffusion in oxides exposed to external forces is of great practical importance, e.g. for long-term degradation processes of oxides in technical applications, such as fuel cells, sensors, etc.

5.11 Morphology of Reaction Products

Initial attempts to provide theoretical models for the oxidation of metals, and the reduction of oxides, sulfides, etc., usually assumed that the reaction products formed in layers normal to the chemical potential gradient and diffusion flux (topochemical description). Microstructural examination, however, often revealed a more complex situation with extended reaction zones, and an aggregate (or lamellar) arrangement of initial and product phases often intersected with a network of pores. Any analysis of the formation of extended reaction zones must take into account such factors as nucleation and growth mechanism, interfacial stability (coherent and non-coherent), accommodation of volume changes by plastic deformation, strain, or fracture.

If the overall rate-determining step is solid-state diffusion, then in favorable situations, it is possible to predict whether a layered or aggregate morphology should be produced. For example, Wagner (1956) analyzed the diffusion processes involved in the oxidation of alloys containing noble metals and concluded that an oxide layer of uniform thickness is stable only if interdiffusion in the alloy is relatively rapid compared with diffusion in the oxide of the less noble metal. This situation is illustrated in Figure 5.17, where the alloy–oxide interface in a layered arrangement is tentatively assumed to have an uneven profile. If the growth of the Me_ν phase is limited by cation diffusion within the $Me_\nu O$ phase, then the flux of cations arriving at position I exceeds that at position II. With a higher growth rate at position I, a flat $M/Me_\nu O$ interface would be stable, and the interface would become flat. Alternatively, if the growth of the $Me_\nu O$ phase were limited by a step in advance of the $M/Me_\nu O$ interface (the relatively difficult transport of oxygen through the metal as considered here or in general a slow reaction at the M/M_xO interface), then the flux of oxygen arriving at position II would exceed that at position I. Under these conditions, the more rapid growth at position II would lead to a clefted or serrated interface, and a flat growth interface for $Me_\nu O$ would be unstable; a two-phase product zone (i.e. the aggregate morphology) would result. The oxidation of Cu–Au alloys (Wagner 1956), for example, can result in the formation of a composite scale of the lamellar type. Rapp et al. (1973) have analyzed the growth kinetics and morphology associated with simple solid-state displacement reactions of the type

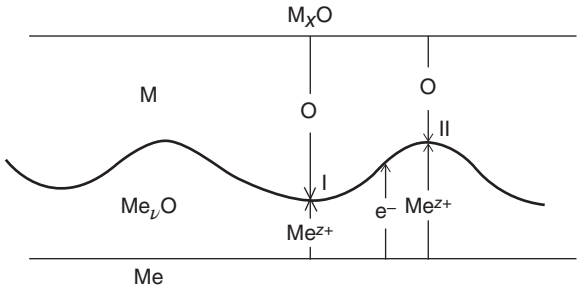


Figure 5.17 Schematic illustration of a displacement reaction with a layered morphology and a tentatively assumed uneven interface.

$$Cu_2O + Ni \rightarrow NiO + 2Cu \quad (5.62)$$

The product morphology can again be either of a layered or aggregate (e.g. lamellar) type depending upon the relative diffusion rates of oxygen in the metal M and cations in the oxide MO. If growth of M_yO is limited by diffusion of oxygen in the metal M phase, then an aggregate morphology will be produced. Available thermodynamic and kinetic data suggested that this situation should prevail for the Cu_2O/Fe reaction. Subsequent investigation confirmed this prediction.

Aggregate morphologies are also often observed in the reduction of oxide and sulfide minerals. The microstructure of hematite, for example, reduced in CO/CO_2 mixtures near 1000 °C exhibits a distinct lamellar texture (Matyas and Tighe 1972).

The fact that magnetite plates grow at an angle to the surface at a rate faster than along the surface might be attributed to the higher vacancy fluxes associated with the

faster chemical diffusion expected in magnetite (Rapp et al. 1973; Yurek et al. 1973). The situation would be similar to that with lamellar growth expected to be stabilized. As the Fe_3O_4/Fe_2O_3 interface is only semi-coherent with the misfit accommodated by plastic deformation, it is possible that the lamellar growth mechanism is also aided by relatively rapid interfacial diffusion of oxygen (Matyas and Tighe 1972).

When hematite samples are reduced at lower temperatures (400–700 °C), the growth of the magnetite phase is accompanied by the formation of tunnels (~100 Å diameter), which are well visible by transmission electron micrography. The tunnels could grow by a vacancy mechanism similar to that postulated by von Bogdandy and Engell (1971) for the formation of tunnels in wüstite and the subsequent production of porous ion. This model takes into account that, at the beginning of reduction, the vacancy content in the interior of the wüstite is greater than that which would correspond to equilibrium with iron. As the reduction of wüstite proceeds by a surface reaction of the type

$$\mathrm{Fe}_{\mathrm{Fe}}^{x} + \mathrm{O}_{\mathrm{O}}^{x} + \mathrm{V}_{\mathrm{Fe}}'' + 2\dot{h} + \mathrm{CO} \rightarrow \mathrm{Fe}_{\mathrm{Fe}}^{x} + \mathrm{CO}_2 \quad (+ \text{ two lattice sites removed}) \tag{5.63}$$

then there will be a flux of cation vacancies ($\mathrm{V}_{\mathrm{Fe}}''$) toward the surface, which will be greater in the vicinity of a surface depression because of the shorter diffusion path. The higher concentration of vacancies in this region will be accompanied by a faster surface reaction as this process is proportional to the vacancy concentration (oxygen activity) (Engell 1958). According to this self-enhanced reaction mechanism, a tunnel could readily develop from an initial depression on the surface. The enlargement of the surface area during the reduction of wüstite can proceed by this mechanism until the vacancy concentration in the wüstite approaches the value associated with the Fe/FeO equilibrium. While a similar model could be responsible for the tunnel structure produced in hematite, there is insufficient data about the surface reaction mechanism to confirm whether it would be enhanced by a flux of cation vacancies although this is probable. The reason for the change in mechanism responsible for the reduction of hematite as the temperature increases is not yet fully understood and provides an interesting problem for solid-state chemistry.

5.12 Measurement of Diffusion Parameters

Modern techniques providing useful information regarding the nature and composition of corrosion films and transport processes in corrosive thin films and scales grown at high temperature are described in Chapter 17.

The two basic parameters, which specify a given diffusion distribution, are the surface concentration, Co, and the diffusion coefficient, D, at any point within the material. This section is mainly concerned with the evaluation of these parameters. Given the specificity of the described procedures, these measurements are described here and not in Chapter 17.

5.12.1 Junction Methods

5.12.1.1 Impurity Profiles

In general, the diffusion of an impurity into a crystal will lead to a change in the physical properties of the diffused region. A definition of the boundary between the two regions so formed can lead to considerable information about the impurity distribution.

Firstly, one can consider the particular case of an impurity diffused into an n-type semiconductor, producing a p–n structure with an intrinsic region at the junction. In this case, a measurement of the junction depth, x_j, will simply lead to the value of the acceptor concentration in the n-type material. To progress further, it is necessary to assume the shape of the impurity profile and to make the measurement of C_0. This will enable the calculation of D using, for example, an equation of the form

$$C(x_j) = C_0 \,\mathrm{erfc}\left(\frac{x_j^2}{4Dt}\right)^{1/2} \tag{5.64}$$

The necessity to measure C_0 may be removed by using the two-specimen method, after Fuller (1952). He diffused two specimens of differing resistivities under identical experimental conditions. Measurement gave identical values of surface concentration and enabled the elimination of C_0 from the two equations of the above type, each with a different value of x_j. D was then calculated from the values of x_j, the diffusion time, the resistivity, and the carrier mobility of each specimen. This method does not, however, remove the need to know or assume the form of the profile. This major drawback of the technique may be overcome by simultaneously diffusing into several samples, each one having a different background donor concentration, C_B. Measurement of x_j for each sample then gives a value of C for varying depths within the crystals for a given set of experimental conditions. The plot of C versus x may now be directly made, and this is the form of the impurity profile. C_0 is determined by extrapolation of the profile to the surface, and D is directly calculated as shown in Section 5.12.5. This particular method requires the use of a large amount of semiconductor crystal to produce one profile. More importantly, the profile produced will only be a true representation of the impurity atom concentration throughout the material if there is a complete ionization with each atom being associated with one shallow acceptor over the entire range of concentration values.

In the above procedures, the important step is the measurement of the junction depth, x_j. Several methods have been used for this purpose, chemical etching being the most common. Two other ones are electrochemical displacement plating and the scanning light spot method.

5.12.1.2 Chemical Etching

This method simply requires the exposure of a surface of the diffused crystal, across which the variation in impurity concentration is evident, to a chemical solution that will distinguish between the n- and p-type materials, for example. This surface may be formed by cleaving the crystal perpendicularly to the original large area faces, parallel to the direction of diffusion. Since the junction depth is, in general, of the order of microns, a metallographic microscope is usually necessary to measure x_j in this case. Because cleavage produces a clean and sharp break, it is possible to use the line of the original surface as a reference in this technique. Care must be taken not to confuse a junction with cleavage lines on the newly produced surface. The effective width of the diffused region may be increased by using angle-lapping techniques. Here, a beveled surface is produced on the crystal at an angle θ to the horizontal plane. This increases the "width" by a factor $1/\sin\theta$. The value of θ typically lies between 1° and 5°. Problems of this method are the determination of the bevel start, measurement of the lapping angle, and a less smooth surface than that produced by cleaving. A fair degree of accuracy may still be maintained; however, the measurement of the junction depth is usually carried out with a traveling microscope. A comprehensive study of the various etches, which are suitable for a wide selection of materials, is given by Gatos and Lavine (1965). The way in which junction delineation actually takes place is, to a great extent, uncertain, but falls essentially into two categories. Some etches work at different rates on the two types of material on one side of the junction by the production of a thin layer, often an oxide or hydride.

5.12.1.3 Electrochemical Plating

This method is essentially similar to the staining technique outlined above but involves the plating out of a metal from a solution of one of its salts, preferentially onto one side of the junction.

5.12.1.4 Scanning Light Spot

By scanning a small spot of light across a beveled surface containing a p–n junction, the exact position of the junction can be determined by means of the photoinduced voltage, generated at the junction (Tong et al. 1969). Similarly, an electron beam may be used in the scan, and hence the junction may be detected using a scanning electron microscope. This general technique has the advantage of better reproducibility over the chemical methods, the latter being very sensitive to the ambient experimental conditions. Problems can occur, however, with the electrical contacting of the material. Also, the usual problems associated with the angle lapping are relevant.

5.12.2 Electrical Methods

5.12.2.1 Four-point Probe

One of the first uses of the electrical measurement on diffused layers was to produce a value for the surface concentration C_0 and hence complement the p–n junction methods of determining the diffusion coefficient D. The method involves the measurement of the sheet resistivity, ρ_s, of the diffused layer, using a four-point probe arrangement of the type shown in Figure 5.18. The p–n junction acts as an insulating boundary between the two regions. This value of ρ_s may then be used to give a value of C_0 by reference to the published curves, provided that certain conditions are satisfied. Irvin (1962) and Backentoss (1958) produced such curves for silicon and germanium by finding analytical solutions to an equation of the form

$$f(x) = \frac{1}{\rho_s x_j} = \frac{1}{x_j}\int_0^{x_j} q\mu(C + C_B)[C(x) - C_B]\,dx \quad (5.65)$$

where C_B is background donor concentration, $C(x) = C_0 f(x)$, and $\mu(C + C_B)$ is mobility as a function of total carrier concentration.

The solutions were only valid for one particular distribution function $f(x)$, and hence the use of the curves is subject to question unless the form of the impurity profile is well established. The situation is considerably simplified by assuming the value of mobility, μ, to be

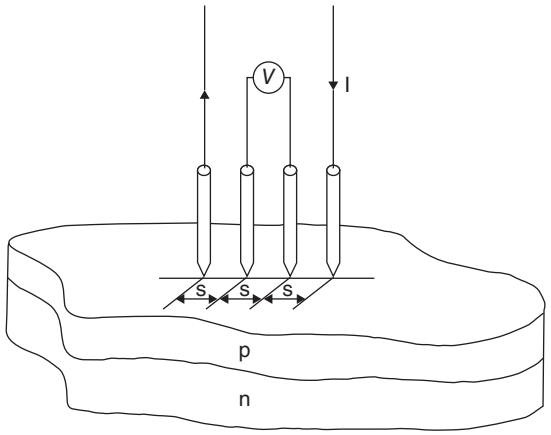


Figure 5.18 A "four-point probe" arrangement on a diffused layer.

constant throughout the layer. Busen and Shirn (1964) shown for p-type silicon and germanium that such an assumption leads to a small error in the evaluation of C_0. Since the curves of Irvin and Backentoss are plots of σ versus C_0, it is generally necessary to know the value of x_j as well as ρ_s to establish a surface concentration for a given measurement. In the mentioned plots, σ is the diffused layer conductivity. However, it has been shown that in certain cases ($\sigma_s \gg \sigma_B\ x_j$), it is possible to find C_0 directly from a measurement of ρ_s, without evaluating the junction depth. The need to make assumptions about the profile form may be eliminated by using a successive layer removal technique. Tannenbaum (1961) used a differential resistivity method to produce a profile of phosphorus in silicon by repeatedly measuring the sheet resistivity of the diffused layer at different depths, removing successive thin layers from the surface. Her technique still relied, however, on published ρ versus C curves (Irvin 1962), and so it is limited in application. The majority of such information is available only for Ge, Si, and GaAs and is generally derived from experiments using homogeneously doped materials. This makes its use, in the analysis of concentration gradient profiles, questionable. Fuller and Ditzenberger (1952) developed a technique of layer removal and four-point probe measurements, which did not rely on any empirical relationship except the variation of mobility with concentration. For simplicity, they regarded μ as a constant for all C. The analysis of their results considers that the change in sheet conductance, as each layer is removed, is dependent on the average carrier concentration in that layer. The method was later modified by Lamorte (1960) to produce more accurate results. However, this method does not completely eliminate the necessity to make certain assumptions about the profile shape. The geometrical factors affecting analysis by four-point probe techniques have been extensively studied.

5.12.2.2 Hall Effect

The dependence on "ρ versus C" information may also be removed by a change in the contact geometry from four in-line probes to a square array. This makes it possible to combine measurement of resistivity with that of Hall voltage in a magnetic field (Biggeri et al. 1997; Vickers et al. 1992). The latter leads directly to a value for carrier concentration, which, in conjunction with the measured resistivity, leads to a value for mobility.

(a) *One dominant carrier type*:

For carrier concentration, n, and mobility, μ, it holds

$$n = \frac{1}{R_H e} = \frac{IB}{V_H b e} \tag{5.66}$$

$$\mu = \frac{1}{ne\rho} \tag{5.67}$$

where I is the current in the specimen, B the magnetic field, V_H the Hall voltage, R_H the Hall coefficient, and b the specimen thickness.

(b) *Two carrier types:*

$$\sigma = \frac{1}{\rho} = e(n_h\mu_h + n_e\mu_e) \tag{5.68}$$

$$R_H = \frac{n_h\mu_h^2 - n_e\mu_e^2}{(n_h\mu_h + n_e\mu_e)^2}\ \frac{1}{e} \tag{5.69}$$

The signs of V_H and R_H in the second case are generally dependent on the type of dominant carrier, p-type material giving a positive value for R_H and n-type material a negative value. However, it can be seen from Eq. (5.69) that even if $n_h > n_e$ (p type), R_H may still be negative if $\mu_e > \mu_h$. This is particularly important in the case of III–V compounds where the ratio μ_e/μ_h is generally large and can be of the order of 100 or greater. Thus, a low concentration of uncompensated donors in a p-type region may cause a Hall voltage indicative of n-type carriers.

The fact that the two types of carriers oppose each other in producing the Hall voltage, but are additive for conduction (Eqs. (5.68) and (5.69)), can lead to an evaluation of their concentrations by measurement of both the conductivity and Hall voltage for the given specimen.

The technique is, once again, very sensitive to changes in the geometry of the specimen, and correction factors have been derived by Green and Gunn (1972) for samples of both arbitrary and given shape. A method developed by Van der Pauw (1958) enables the measurement of resistivity and Hall coefficient on a sample or arbitrary shape using only one empirical correction factor. This factor depends on the measured specimen resistance. Errors due to contact geometry are also shown to be reduced by the use of a "cloverleaf" specimen as illustrated in Figure 5.19.

Analysis of experimental results, using the above equations, is perfectly straightforward for the case of

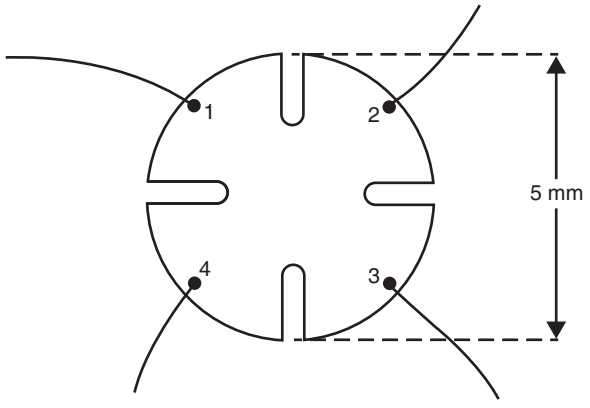


Figure 5.19 A "cloverleaf" Hall specimen. Coding 1, 2, 3, 4 describes the different contacts used in the Van der Pauw technique.

a homogeneous specimen, but more consideration is required when dealing with a diffused layer with a carrier concentration gradient. Now, the magnitude of the measured voltages is indicative of the average carrier concentration throughout the diffused region. Without assuming a particular profile form, it is therefore necessary to use a serial sectioning technique to find absolute values of concentration at any given depth. The accuracy of these values will depend on the thickness of removed layers. The situation may be further complicated by the variation of carrier mobility with concentration. If the form of this variation is not known, an iterative technique may have to be employed to calculate the values of n, ρ, and μ for a given penetration in the diffused layer, these parameters being interdependent.

5.12.2.3 Diode Capacitance

Carrier concentrations in a diffused semiconductor crystal can be calculated from the measurement of the capacitance associated with a p–n junction depletion region and its variation with applied bias. For a linearity-graded junction, an impurity carrier profile can be determined (Sze 1969), while for an abrupt junction, the carrier concentration on the "low" side of the junction can be found (Carter et al. 1972). Similarly, the formation of a metal–semiconductor junction on the crystal surface, in combination with a layer removal technique, can lead to the determination of a complete impurity profile through the crystal. The measurement penetration of these methods is limited by the possible width of the depletion region, which decreases with the carrier concentration within the semiconductor. This limits the range of the p–n junction profiling method, but, for the layer removal technique, it means that the measured value of carrier density is restricted to a thin layer beneath the surface. This negates the need to convert average values over a region to absolute values at a point. Considerable problems may arise for these techniques over suitable contacting procedures and the formation of good metal–semiconductor "Schöttky" diodes (Wartlick et al. 2000).

5.12.3 Radiochemical Techniques

If, by some means, the atoms diffusing into a crystal can be directly viewed, no assumptions need to be made about the form of the diffusion profile and D and C_0 may be found directly from the plotted distribution. Radiochemistry provides such a possibility, since atoms of interest may be "tagged" by using them in the form of radioisotopes.

5.12.3.1 Radiotracer Analysis

This method of analysis may be adopted if there exists, for the impurity of interest, a radioactive isotope with suitable half-life and emission strength. It simply consists of using the radioisotope as the diffusing species and measuring the activity present at successive points through the crystal, with some form of sectioning and counting techniques. Sectioning is most often achieved by grinding or etching, and the analysis may be performed by calculating either the activity of the removed layers or the residual activity in the crystal after the removal of each layer, by comparison with a known standard.

5.12.3.2 Neutron Activation

The methods of analysis in this procedure are basically the same as those described above (Polyakov et al. 2005). However, the radioisotope is now produced by irradiation of the entire crystal after a nonradioactive diffusion. This has the disadvantage of producing unstable isotopes in addition to those of particular interest, and the technique is therefore made essentially redundant by radiotracer analysis.

5.12.4 Other Techniques

In recent years, the detection of impurity levels in crystals has been accomplished using plasma resonance techniques and electron microprobe analysis (Bellegia et al. 2000; Dzhafarov et al. 1998). The first method relies on the resonant absorption of infrared radiation at a frequency, w_p, which is a function of the free-carrier concentration in the material. In the second case, the characteristic secondary X-ray emissions from a surface bombarded by electrons are an indication of the element present on the surface and below it. The resonance method suffers from calibration problems, and the microprobe has a limited resolution of about $10^{19}\,\mathrm{cm}^{-3}$. Certain qualitative information may be obtained by the use of autoradiographic techniques. The use of Auger spectroscopy is also being investigated.

It is very important to note at this point that in choosing a method for measuring diffusion parameters, care should be taken when assessing what physical characteristic is actually measured. For instance, radiotracer analysis measures the total amount of impurity present in the crystal, whereas a Hall effect measurement will give the concentration of free carriers. The two values may be different and, indeed, may lead to an understanding of the diffusion process by pinpointing the types of site on which the impurity atoms sit, by indicating their state of ionization.

5.12.5 Calculation of *D* from a Profile

If one is able to produce an experimentally derived diffusion profile as, for example, with radiotracer analysis, C_0 can be found by extrapolation and D evaluated quite easily.

Firstly, if the profile has a simple mathematical form as shown in Eqs. (5.12) and (5.13), D follows immediately.

For the limited source condition, a plot of ln $C(x)$ versus x^2 yields a straight line with the slope $-(4Dt)^{-1}$, and for the infinite source, D is calculated from a plot of C versus x that is a straight line on arithmetical probability paper.

However, the profile will not have a simple form if D is a function of C, and, in this situation, Eq. (5.10) must be employed to calculate the value of D. One method frequently used is known as the Boltzmann–Matano analysis (Shewmon 1963). Here, the diffusion is described in terms of a single variable $xt^{-1/2}$, and Fick's law is transformed into an ordinary homogeneous differential equation. It can then be shown that

$$D(C') = -\frac{1}{2t}\left(\frac{\mathrm{d}x}{\mathrm{d}C}\right)_{C'} \int_0^{C'} x\,\mathrm{d}C \qquad (5.70)$$

and the value of D for any value of concentration C' can be determined from the slope and area under the experimentally determined profile at point C'. This method is difficult and inaccurate to perform since steep gradients are often involved. More importantly, great care must be taken to ensure that it is valid to describe the diffusion in terms of the single variable $xt^{-1/2}$. This involves the execution of a preliminary set of experiments with time as the variable. The problem of a concentration-dependent value of D may be overcome by using the isoconcentration techniques (Hannay 1976; Manning 1968; Metselaar 1984, 1985).

5.13 Questions and Problems

5.1 Why is oxidation through short-circuit diffusion paths faster compared with that of volume diffusion?

5.2 The parabolic rate constant for the oxidation of Ni at 500 °C is several orders of magnitude greater than the calculated one; however, there is complete agreement of the two at 1000 °C. Give reasons.

5.3 State the various diffusion mechanisms in oxides. Which of these diffusion mechanisms has the lowest, and which has the highest activation energy for diffusing ions?

5.4 What is the Kirkendall effect? State its importance, giving an example of the oxidation of a particular oxide.

5.5 What is the interdiffusion coefficient?

5.6 How does grain size influence the oxidation rate? Explain why smaller grain size is beneficial for the oxidation of an alloy but is detrimental to the oxidation of a pure metal.

5.7 What is the limitation of the marker method to determine the mechanism of transporting species in an oxide?

5.8 State the principle of the tracer method for determining the mechanism of transport of oxidizing species.

5.9 What is the role of diffusion in secondary creep?

5.10 Carburization of pure iron is carried out at 950 °C. It is desirable to achieve a carbon content of 0.9% at a depth of 0.1 mm, assuming that the carbon content of the surface is maintained at 1.20% and the diffusion coefficient Dr. (iron) = 10^{-10} m^3 s^{-1}. Calculate the time necessary for this process.

5.11 Two binary alloys containing the elements A and B were intimately joined together by welding. The composition of the alloy to the right of the weld is 40% A and that to the left of the weld 60%. The couple is heated very rapidly to a temperature T_1 and held there for 20 hours. After cooling to room temperature, it was found that at a distance of 1.0 mm to the right of the weld, the alloy contains 55.0%. Estimate the general diffusivity D for the process.

5.12 The following data have been obtained for the diffusion of aluminum in a silicon crystal:

Temperature (°C)	Diffusion coefficient D (m^3 s^{-1})
1380	3.11×10^{-14}
1300	7.1×10^{-15}
1250	4.1×10^{-15}
1200	1.74×10^{-15}

(a) Plot the logarithm of the diffusion coefficient versus $1/T$ (K).

(b) Determine the constants A and E in the equation $D = A$ exp. $(-Ea/RT)$.

(c) Calculate the rate of diffusion at 800 °C.

References

Atkinson, A.A., Taylor, R.I., and Hughes, A.E. (1982). *Philos. Mag. A* 45: 823.

Atkinson, A.A., Moon, D.P., Smart, D.W., and Taylor, R.I. (1986). *J. Mater. Sci.* 21: 1747.

Backentoss, G. (1958). *Bell Syst. Techn. J.* 37: 699.

Bellegia, M., Cristofori, D., Merli, P.G., and Pozzi, G. (2000). *Micron* 31: 231.

Biggeri, V., Borchi, E., Bruzzi, M. et al. (1997). *Nucl. Instrum. Methods Phys. Res., Sect. A* 400: 113.

von Bogdandy, L. and Engell, H.J. (1971). *The Reduction of Iron Ores*, 94. Berlin: Springer-Verlag.

Boltzmann, L. (1894). *Ann. Phys.* 53: 959.

Bracht, H., Stolwijk, N.A., and Mehrer, H. (1995). *Phys. Rev. B* 52: 16542.

Busen, K.M. and Shirn, G.A. (1964). *Solid State Electron.* 7: 49.

Cahn, R.W. and Haasen, P. (eds.) (1996). *Physical Metallurgy, Part 2*. Amsterdam, Holland: North-Holland.

Carter, W.E., Gummel, H.R., and Chaula, B.R. (1972). *Solid State Electron.* 15: 195.

Chitraub, M., Scherrer, S., and Scherrer, H. (2000). *J. Phys. Chem. Solids* 61: 1963.

Darken, L.S. (1948). *Trans. Met. Soc. AIME* 175: 184.

Darken, L.S. and Gurry, R.W. (1953). *Physical Chemistry of Metals*. New York: McGraw Hill Book Company.

Dzhafarov, T.D., Akeiz, C.S., and Oren, D. (1998). *Thin Solid Films* 312: 327.

Engell, H.J. (1958). *Acta Metall.* 6: 439.

Fisher, J.C. (1951). *J. Appl. Phys.* 22: 74.

Franck, F.C. and Turnbull, D. (1956). *Physiol. Rev.* 104: 617.

Fuller, C.S. (1952). *Physiol. Rev.* 86: 136.

Fuller, C.S. and Ditzenberger, J.A. (1952). *Phys. Rev.* 87: 527.

Gatos, H.C. and Lavine, M.C. (1965). *Prog. Semicond.* 9: 1.
Gellings, P.J. and Bouwmeester, H.J.M. (eds.) (1996). *The CRC Handbook of Solid-State Electrochemistry*. Boca Raton, FL: CRC Press.
Gesmundo, F., Viani, F., and Niu, Y. (1992). *Oxid. Met.* 38: 465.
Green, M.A. and Gunn, M.W. (1972). *Solid State Electron.* 15: 577.
Grzesik, Z. and Mrowec, S. (2006). *High Temp. Mater. Process.* 25: 209.
Hannay, N.B. (ed.) (1976). *Treatise on Solid State Chemistry*. New York: Plenum Press.
Hartley, G.S. (1946). *Trans. Faraday Soc.* 46: 6.
Hartley, G.S. and Crank, J. (1949). *Trans. Faraday Soc.* 45: 801.
Howe, J.M. (1997). *Interfaces in Materials: Atomic Structure, Thermodynamics and Kinetics of Solid-Liquid and Solid-Solid Interfaces*. New York: Wiley.
Huggins, R.A. (2001). *Solid State Ionics* 143: 3.
Irvin, J.C. (1962). *Bell Syst. Tech. J.* 41: 387.
Kaur, I., Gust, W., and Kozma, L. (1989). *Handbook of Grain and Interphase Boundary Diffusion Data*. Stuttgart: Ziegler.
Kaur, I., Mishin, Y., and Gust, W. (1995). *Fundamentals of Grain and Interphase Boundary Diffusion*. Chichester, West Sussex: Wiley.
Keblinski, P., Wolf, D., Phillipot, S.R., and Gleiter, H. (1999). *Philos. Mag. A* 79: 2735.
Keblinski, P. and Yamakov, V. (2003). *Interface Sci.* 11: 111.
Labid, M., Boussetta, H., and Monty, C.J.A. (1997). *Solid State Ionics* 104: 133.
Lamorte, M.F. (1960). *Solid State Electron.* 1: 164.
Manning, J.R. (1968). *Diffusion Kinetics for Atoms in Crystals*. Princeton, NJ: van Nostrand.
Martin, M. and Schmalzried, H. (1990). *Ber. Bunsen Ges. Phys. Chem.* 94: 721.
Matano, C. (1933). *Jpn. J. Phys.* 8: 109.
Matyas, A.G. and Tighe, N.J. (1972). *Internal Report*. Imperial College, University of London.
Mehl, R.F. (1947). *Trans. AIME* 171: 135.
Metselaar, R. (1984). *J. Mater. Ed.* 6: 229.
Metselaar, R. (1985). *J. Mater. Ed.* 7: 653.
Mrowec, S. and Przybylski, K. (1984). *High Temp. Mater. Process.* 6: 1.
Murch, G.E. and Nowick, A.S. (eds.) (1984). *Diffusion in Crystalline Solids*. New York: Academic Press.
Murtagh, M.J., Hulvat, J., Dieckmann, R., and Sass, S.L. (2001). *Acta Mater.* 49: 3493.
Nakajima, H. (1997). *JOM* 49: 15.
Nowick, A.S. and Burton, J.J. (eds.) (1975). *Diffusion in Solids – Recent Developments*. New York: Academic Press.
Polyakov, A.Y., Smirnov, N.B., Gorbokov, A.V. et al. (2005). *J. Appl. Phys.* 98: 033529.
Rapp, R.A., Ezis, A., and Yurek, E.J. (1973). *Met. Trans.* 4: 1283.
Schroeder, M. and Martin, M. (1998). *Z. Phys. Chem.* 207: 1.
Seeger, A. and Chik, M.P. (1968). *Phys. Status Solidi B* 29: 455.
Seeger, A., Schumacher, D., Diehl, J., and Schilling, W. (eds.) (1970). *Vacancies and Interstitials in Metals*. Amsterdam, Holland: North-Holland.
Seitz, F. (1948). *Physiol. Rev.* 15: 1513.
Sequeira, C.A.C. and Amaral, L. (2014). *Trans. Nonferrous Met. Soc. China* 24: 1.
Shewmon, P.G. (1963). *Diffusion in Solids*. London: McGraw-Hill.
da Silva, L.C.C. and Mehl, R.F. (1951). *Trans. AIME* 191: 155.
Smigelskas, A.D. and Kirkendall, E.O. (1947). *Trans. AIME* 171: 130.
Sörensen, M.R., Mishin, Y., and Voter, A.F. (2000). *Phys. Rev. B* 62: 3658.
Stolwijk, N.S., Bösker, G., and Pöjjing, J. (2001). *Defect Diffus. Forum* 194–199: 687.
Suzuki, A. and Mishin, Y. (2003). *Interface Sci.* 11: 131.
Sze, S.M. (1969). *Physics of Semiconductor Devices*. New York: Wiley.
Tannenbaum, E. (1961). *Solid State Electron.* 2: 123.
Tong, A.H., Schumann, P.A. Jr., and Dupnok, A. (1969). *Semiconductor Silicon*. The Electrochemical Society.
Van der Pauw, L.L. (1958). *Phillips Res. Rep.* 13: 1.
Vickers, A.J., Tsui, E.S.-M., Robert, F., and Lyons, V. (1992). *Rev. Sci. Instrum.* 63: 5487.
Vuci, Z. and Gladi, J. (1999). *J. Cryst. Growth* 205: 136.
Yurek, G.J., Rapp, R.A., and Hirth, J.P. (1973). *Met. Trans.* 4: 1293.
Wagner, C. (1956). *J. Electrochem. Soc.* 103: 571.
Wartlick, B.D., Blanchard, C., and Barbot, J.F. (2000). *Mater. Sci. Eng., B* 71: 254.
Wenwer, F., Stölwijk, N.A., and Mehrer, H. (1989). *Z. Metallkd.* 80: 205.

Further Reading

Adda, Y. and Philibert, J. (1991). *Atom Movements and Mass Transport in Solids*. Les Ulis: Les Éditions de Physique.
Alnatt, R. and Lidiard, A.B. (1993). *Atomic Transport in Solids*. Cambridge University Press.
Aziz, M.G. (1997). *Appl. Phys. Lett.* 70: 2810.
Belle, J. (1961). *Uranium Dioxide: Properties and Nuclear Application*. Washington, D.C.: U.S. Government Printing Office.
Belton, G.R. and Worrell, W.L. (eds.) (1970). *Heterogeneous Kinetics at Elevated Temperatures*. New York: Plenum Press.
Bird, R.B., Stewart, W.E., and Lightfoot, J.E.N. (1960). *Transport Phenomena*. New York: Wiley.
Boettinger, W.J., Guyer, J.E., Campbell, C.E., and McFadden, G.B. (2007). *Proc. R. Soc. A* 463: 3347.
Bollmann, W. (1970). *Crystal Defects and Crystalline Interfaces*. Berlin: Springer-Verlag.
Brenner, H. (2006). *Physica A* 370: 190.
Brenner, H. (2009). *Physica A* 88: 3391.
Cornet, J.F. and Calais, D. (1974). *J. Phys. Chem. Solids* 35: 1247.
Crank, J. (1956). *The Mathematics of Diffusion*. Oxford University Press.
Dybkov, V.I. (2002). *Reaction–Diffusion and Solid-State Chemical Kinetics*. Kiev: IMPS Publications.
Ernst, F. (1995). *Mater. Sci. Eng. Rep.* R14 (3): 97.
Glicksman, M.E. (2000). *Diffusion in Solids*. New York: Wiley.
Grueneisen, E. (1912). *Ann. Phys.* 344: 257.
Haugsrud, R. (2003). *Corros. Sci.* 45: 211.
Hirth, J.P., Pieraggi, B., and Rapp, R.A. (1995). *Acta Metall. Mater.* 43: 1065.
Hobbs, L.W., Sawhill, H.T., and Tinker, M.T. (1983). *Radiat. Eff.* 74: 291.
Hobbs, L.W., Rosen Benezra, V., Mangin, S.P. et al. (2005). *Int. J. Appl. Ceram. Technol.* 2: 221.
Howard, R.E. and Lidiard, A.B. (1964). *Rep. Prog. Phys.* 27: 161.
Iijima, Y., Irano, K.-I., and Kikuchi, M. (1982). *Trans. JIM* 23: 19.
Jost, W. (1952). *Diffusion in Solids, Liquids, Gases*. New York: Academic Press.
Kirkaldy, J.S. and Young, D.J. (1987). *Diffusion in the Condensed State*. London: The Institute of Metals.
Kuazynski, G.C. (ed.) (1967). *Sintering and Related Phenomena*. New York: Gordon and Breach.
Lesena, M. and Pieraggi, B. (1985). *J. Phys.* 46 (C4): 135.
van Loo, F.J.J. (1990). *Prog. Solid State Chem.* 20: 47.
van Loo, F.J.J., Pieraggi, B., and Rapp, R.A. (1990). *Acta Metall. Mater.* 38: 1769.
Manning, M.I. (1979). *Corros. Sci.* 21: 301.
Massalski, T.B. (ed.) (1986). *Binary Alloy Phase Diagrams*, vol. 2. Metals Park, OH: American Society for Metals.
Mrowec, S. and Grzesik, Z. (2004). *J. Phys. Chem. Solids* 65: 1651.
Nalwa, H.S. (ed.) (2001). *Handbook of Surfaces and Interfaces of Materials*. San Diego, CA: Academic Press.
Paul, A., van Dal, H.J.H., Kodenstov, A.A., and van Loo, F.J.J. (2004). *Acta Mater.* 52: 623.
Peraldi, R., Monceau, D., and Pieraggi, B. (2002). *Oxid. Met.* 58: 249.

Philibert, J. (1991). *Atom Movements: Diffusion and Mass Transport in Solids*. Les Ulis: Éditions de Physique.
Pieraggi, B., Rapp, R.A., and Hirth, J.P. (1995). *Oxid. Met.* 44: 63.
Pond, R.C. and Hirth, J.P. (1994). *Solid State Phys.* 47: 287.
Rapp, R.A. (1985). *Metall. Trans. A* 15A: 765.
Shewmon, P.G. (1963). *Diffusion in Solids*. New York: McGraw-Hill.
Shimozaki, T., Ito, K., and Onishi, M. (1987). *Trans. JIM* 28: 457.
Sohn, Y.H. and Dayananda, M. (1999). *Scr. Mater.* 40: 79.
Steele, B.C.H. and Floyd, J.M. (1971). *Proc. Br. Ceram. Soc.* 19: 55.
Stringer, J. (1970). *Corros. Sci.* 10: 513.
Takashi, T. (ed.) (1989). *High Conductivity Solid Ionic Conductors*. Singapore: World Scientific Publishing Co.
Wachtman, J.B. Jr. and Franklin, A.D. (eds.) (1968). *Mass Transport in Oxides*, NBS Special Publication 296. Washington, DC.
Wagner, C. (1969). *Acta Metall.* 17: 99.

Chapter 6

High Temperature Electrochemistry

6.1 Introduction

Accelerated corrosion in gas turbine engines, boilers, and other high temperature systems is usually caused by the existence of combustion products in a liquid phase. In the chemical industry, the molten salts used as a heat transfer medium are compatible with construction materials, and corrosion is an inevitably serious problem. Thus far, there have been many reports from both theoretical and experimental viewpoints and fundamental approaches made by Simons et al. (1955), Goebel and Pettit (1970), Mamantov (1969), and others, who suggested with sufficient credibility the electrochemical mechanistic models for the observed corrosion. In fact, most of the molten salts behave as ionic or electrolytic conductors, and therefore it is easy to understand that the molten salt corrosion at high temperature is of electrochemical nature, as it happens in aqueous systems. Accordingly, high temperature electrochemistry is of great importance in understanding and controlling molten salt corrosion. But the scientists and engineers concerned with high temperature corrosion problems need also to deal with metals, alloys, ceramics, composites, and other advanced materials of difficult processing. Moreover, the diversity of interests in advanced technology applications at high temperature oblige them to be concerned with complex environments, namely, gaseous atmospheres containing oxygen, hydrogen, carbon dioxide, water vapor, sulfides, chlorides, etc. At high temperatures, these gaseous atmospheres lead to the growth of thin oxide layers, compact scales, and multilayered scales. Most of these layers and scales are ionic compounds or, at least, partially ionic compounds. Thus, the chemical reactions established at solid–solid and solid–gas interfaces during the growth of the corrosion products can be visualized as oxidation–reduction electrode processes; in other words, it is acceptable that high temperature oxidation, sulfidation, halogenation, nitridation, carburization, etc. are processes of electrochemical nature.

In summary, it is clear that the extension of electrochemistry to high temperature materials and systems (Garcia-Diaz et al. 2016) that are highly susceptible to corrosion will constitute an important tool that requires further exploration (Wildgoose et al. 2004).

In this chapter, basic aspects of molten salt electrochemistry and solid-state electrochemistry are described to show how molten salt corrosion and high temperature oxidation can be further understood and mitigated.

6.2 Electrochemical Nature of Molten Salt Corrosion

The loss of material is substantially attributed to the corrosion reaction, and therefore the material surface suffers from the homogeneous or heterogeneous attack of corrosive media. For the former case, Wagner and Traud (1938) described the fact that the occurrence of the corrosion reaction necessitates simultaneous dissolution of metals and reduction of oxidant. According to their theory, the location of the metal dissolution is not necessarily identified with that of oxidant reduction at the metal–solution interface. Therefore, the important factors in corrosion are not only impurities, defects, and other heterogeneities of the material but also the chemical nature of the oxidant involved in the liquid (i.e. impurities and by-products due to dissociation). From this viewpoint, the corrosion reaction in molten salts is a fairly complex phenomenon compared with that in an aqueous medium where only a few chemicals such as oxygen and protons might be candidates for the oxidant of the corrosion reaction.

It should be noted that while in aqueous solutions metals are virtually insoluble in the electronated state, in molten or fused salts (which can be regarded as infinitely concentrated aqueous solutions), they can be appreciably soluble and corrosion occurring, in such cases, without the de-electronation of the metal. In spite of this, the electrochemical approach for molten salt systems was put forward about 55 years ago and is finding general acceptance.

High Temperature Corrosion: Fundamentals and Engineering, First Edition. César A. C. Sequeira.
© 2019 John Wiley & Sons, Inc. Published 2019 by John Wiley & Sons, Inc.

Based on the mixed potential theory, the corrosion reaction is expressed by the combination of metal dissolution, partial anodic reaction and reduction of oxidant, and partial cathodic reaction under the restriction of electric charge neutrality: thus, for the partial anodic reaction,

$$\mathrm{M} \rightarrow \mathrm{M}^{n+} + n\mathrm{e}^- \tag{6.1}$$

$$\mathrm{M}^{n+} + \frac{1}{2}n\mathrm{O}^{2-} \rightarrow \mathrm{MO}_{n/2} \tag{6.2}$$

and for the partial cathodic reaction,

$$\mathrm{Ox} + n\mathrm{e}^- \rightarrow \mathrm{R} \tag{6.3}$$

where M, Ox, and R represent the metal, oxidant, and reductant, respectively, and n is the number of electrons. Accordingly, in a molten salt, there are several oxidants (O_2, H^+, H_2O, and OH^-) common to the molten salts, and such oxidants are associated with the dissociation reaction of molten salts themselves.

At this stage and before moving further to thermodynamic considerations, it is important to briefly describe the meaning of the electrode potential, which is the central electrochemical parameter.

6.3 The Single Potential of an Electrode

In the most general sense of the word, an electrode is a system consisting of two phases in contact with each other, which can be the seat of an electrode reaction, i.e. a reaction in which certain constituents of the two phases participate and by which a transfer of charge takes place from the bulk of one phase to the bulk of the other. In a more restricted sense, an electrode is defined as a metal–electrolyte or metal–solution system of one or several electrolytes.

It has been shown over the last 100 years that at the interface of two phases, one finds an electrical double layer with a characteristic potential (Adam 1938; Butler 1940).

The origin and the characterization of the electrochemical double layer on a metal immersed in an aqueous electrolyte have been extensively studied. Similar studies in melts have been carried out only more recently. This section is not intended to deal with this aspect in detail, but the subject is mentioned because of its importance. Very good reviews on the subject have been published by Devanathan and Tilak (1965), Graves et al. (1966), and Ukshe et al. (1964).

Returning to the subject of this section, let the inner electric potential of the metal be Φ_M and that at a remote point in the molten electrolyte be Φ_S. Moreover, let $\Delta\Phi$ represent the Galvani electric potential across the electrochemical double layer, i.e. $\Delta\Phi = \Phi_\mathrm{M} - \Phi_\mathrm{S}$. When a dynamic equilibrium across the double layer is set up, the electrochemical energy of 1 mol of metal in the surface will be equal to the electrochemical free energy of 1 mol of ions on the melt side of the double layer:

$$\widetilde{\mu}_\mathrm{M} = \widetilde{\mu}_\mathrm{S} \tag{6.4}$$

or

$$\mu_\mathrm{M} + nF\Phi_\mathrm{M} = \mu_\mathrm{S} + nF\Phi_\mathrm{S}$$

and

$$\mu_\mathrm{M} - \mu_\mathrm{S} = -nF\Delta\Phi \tag{6.5}$$

where $\mu_\mathrm{M} - \mu_\mathrm{S}$ is the chemical energy balanced by the electrical energy liberated as M^{n+} ions traverse the double layer, F is Faraday's constant, and n is the number of free electrons exchanged at the M^{n+}/M interface. It is impossible to measure $\Delta\Phi$ directly, but if the metal–melt electrode system is coupled "back to back" with a second arbitrarily chosen electrode system, it is possible to obtain a relative potential difference. If a zero potential and a convenient reference scale of potentials is defined, the combined system acts as a cell between those electrodes and there exists an electromotive force (e.m.f.) given by

$$E_{0.4} = \Delta\Phi - \Delta\Phi_\mathrm{R} \quad \text{(assumed zero)} \tag{6.6}$$

where $E_{0.4}$ is called the single potential of the M^{n+}/M electrode on the chosen standard reference scale. Considering now a more concise electrode reaction,

$$\sum_i \upsilon_i \mathrm{M}_i + n\mathrm{e}^- = 0 \tag{6.7}$$

where M_i represents the constituents of the electrode taking part in the reaction and e^- represents the electron; the corresponding conditions of dynamic equilibrium can be expressed in the general form

$$\sum_i \upsilon_i \mu_i - nFE_{0.7} = 0 \tag{6.8}$$

Relating the chemical potentials, μ_i, to the standard chemical potential, μ_i^0, Eq. (6.8) can be put into the form

$$RT \sum \upsilon_i \log \{\mathrm{M}_i\} = \sum_i \upsilon_i \mu_i^0 + nFE_{0.7} \tag{6.9}$$

Changing from natural to Briggsian logarithms, the last relation can be rewritten in the form

$$E_{0.7} = E_{0.7}^0 + \frac{2.3026\,RT}{nF} \sum_i \upsilon_i \log \{\mathrm{M}_i\} \tag{6.10}$$

in which $E_{0.7}^0$ has the following value in terms of the standard chemical potentials of the reactants:

$$E_{0.7}^0 = \frac{\sum_i \upsilon_i \mu_i^0}{nF} \tag{6.11}$$

Equation (6.10) is the Nernst equation. $E^0_{0.7}$ is the single potential of the electrode measured when the activity of every constituent is equal to unity and is known as the normal or standard potential. Once the normal electrode potential on the standard reference scale is known, the Nernst equation allows a calculation of what the equilibrium electrode potential will be when the system has any $\{M_i\} \neq 1$. Extensive analytical treatments of this subject are given by Conway (1965), de Groot (1951), Grahame (1947), Guggenheim (1929), Parsons (1954), and Prigogine (1947). Experimental proof of the validity of the Nernst equation in molten media is given by Blander et al. (1959), Duke and Garfinkel (1961), Gordon (1899), Ranford and Flengas (1965), and many other workers.

6.4 Equilibrium Diagrams

Thermodynamic considerations can predict whether a metal is stable or whether it will corrode when it coexists with the oxidants common to molten salts. When the metal dissolution in Eq. (6.1) and the oxidant reduction in Eq. (6.3) are taken into account, the free energy of the global reaction associated with them can be negative, i.e. the potential difference $\Delta E(= E_{0.3} - E_{0.1})$ is positive, and therefore corrosion proceeds spontaneously. Since the metal reacts with chemical species such as oxide ions and oxyanions that constitute the molten salts, the equilibrium potential varies with the activity of the oxide ion in the melts. Hence, the diagram of chemical entities in the melt as a function of the electrode potential and the basicity is helpful in a comprehensive understanding of the corrosion behavior. The basicity of the melt is defined as $p\mathrm{O}^{2-}$ $(= -\log a_{\mathrm{O}^{2-}})$ on the basis of the Lux–Flood regulation (Flood and Förland 1947; Lux 1939) (see also Section 3.3.1). It is recognized that each molten salt has an appropriate acid–base equilibrium involving its anion in the case of the oxyanion system. For example, the basicity expressed as the logarithm p_{SO_3}, assuming an acid–base equilibrium in the alkali sulfate melt:

$$\mathrm{SO}_4^{2-} = \mathrm{SO}_3 + \mathrm{O}^{2-} \tag{6.12}$$

$$\begin{aligned} p\mathrm{O}^{2-} &= -\log a_{\mathrm{O}^{2-}} = -\log\left(\frac{K_T}{p_{\mathrm{SO}_3}}\right) \\ &= -\log K_T + \log p_{\mathrm{SO}_3} \end{aligned} \tag{6.13}$$

where K_T indicates the equilibrium constant of Eq. (6.12). Table 6.1 shows typical acid–base equilibria and the $p\mathrm{O}^{2-}$ equation for these molten salts.

The equilibrium diagrams E–$p\mathrm{O}^{2-}$ and its construction are fully described in Section 3.3.1 for the iron/sodium sulfate system at 1173 K. Similar diagrams for molten salts including single, binary, and ternary salt mixtures are also published in the open literature (Ingram and Janz 1965; Kunst and Duke 1963; Littlewood 1962; Marchiano and Arvia 1972; Rahmel 1968; Sequeira and Hocking 1977).

Thermodynamically calculated E–$p\mathrm{O}^{2-}$ diagrams have resulted in remarkable progress in understanding corrosion, but this method has several (qualitative) disadvantages for the realistic requirements of design engineers. In particular, the domains of thermodynamic stability considered in the diagrams give only a theoretical possibility of existence, not a certainty. Further on, as far as passivation is concerned, it must be pointed out that a proper passivity in molten media has not been obtained up to date, perhaps due to special properties of the film involved, mainly adherence, coherence, and deviation from stoichiometry. Therefore, elaborate kinetic techniques for obtaining precise corrosion rates are needed.

6.5 The Tafel Relationship

Considering now the dynamic side of the corrosion phenomenon, particular importance will be attached to electrochemical kinetic studies. A classic relationship precisely relating a characteristic parameter of the electrode, its electrode potential, and the current density traversing it is that found by Tafel in 1905. Therefore this semiempirical law enables us to establish a connection between the "thermodynamic electrode potential" and the current density that defines the kinetic character of the phenomenon.

The Tafel equation may be written as

$$E = a + b \log i \tag{6.14}$$

Table 6.1 Basicities $p\mathrm{O}^{2-}$ of various molten salts where p_{gas} is the partial pressure of the gas

Molten salt	Temperature (°C)	Equilibrium reaction	$p\mathrm{O}^{2-}$
KCl–LiCl, KCl	800		$-\log a_{\mathrm{O}^{2-}}$
$(\mathrm{Na, Li, K})_2\mathrm{SO}_4$	600	$2\mathrm{SO}_4^{2-} \rightleftarrows \mathrm{S}_2\mathrm{O}_7^{2-} + \mathrm{O}^{2-}$ $2\mathrm{SO}_7^{2-} \rightleftarrows 2\mathrm{SO}_3 + \mathrm{O}^{2-}$	$19.7 + \log p_{\mathrm{SO}_3}$
$(\mathrm{Na, Li, K})_2\mathrm{CO}_3$	600	$\mathrm{CO}_3^{2-} \rightleftarrows \mathrm{CO}_2 + \mathrm{O}^{2-}$	$11 - p_{\mathrm{CO}_3}$
$(\mathrm{Na, K})\mathrm{NO}_3$	250	$\mathrm{NO}_3^- \rightleftarrows \frac{1}{2}\mathrm{NO}_2 + \frac{1}{2}\mathrm{O}_2 + \frac{1}{2}\mathrm{O}^{2-}$	$75.6 - \log p_{\mathrm{NO}_2} + \frac{1}{2}p_{\mathrm{O}_2}$

where E is the relative electric potential of the electrode at a current density i (also called "reaction-electrode potential"), a is a constant characteristic of the electrode, and b is the Tafel slope, which is one of the parameters indicating the mechanism of the electrode reaction.

Thus, a definition of overpotential for the reaction can be introduced by the expression

$$\eta = E - E_0 \tag{6.15}$$

where E_0 is the reversible or equilibrium electric potential possessed by the electrode at electrochemical equilibrium (i.e. at zero imposed current) or, more generally, the equilibrium potential of the electrochemical reaction of the type (Eq. (6.7)). Equation (6.15) defines the overpotential, and considering Eq. (6.14), it is seen that the Tafel equation is itself closely related to the overpotential (η). These problems of electrochemical kinetics are discussed in more detail later.

The brief discussion given above is significant enough for the present purpose of showing that the Tafel relationship leads to the experimental polarization curves. Figures 6.1 and 6.2 represent the anodic and cathodic potential–current curves for two typical electrochemical reactions, with either an arithmetic scale for the reaction current (Figures 6.1a and 6.2a) or with a logarithmic one (Figures 6.1b and 6.2b). The exchange current density (i_0), which is defined as the exchange rate per unit area of the potential-determining electrode process at equilibrium, is represented in Figures 6.1b and 6.2b. The aspect of the polarization curves is very important because it gives an account of the degree of irreversibility of the reactions. In fact, in the case of a reversible reaction (Figure 6.1), the application of very small polarizing potentials is sufficient for producing significant current densities. In the case of irreversibility (Figure 6.2), on the contrary, the existence of high overpotentials is a measure of the extent of irreversibility. The reversible or fast electrode processes exhibit high exchange current densities; on the other hand, the irreversible or slow ones exhibit low exchange current densities. Thus, if an electrode is more likely to behave

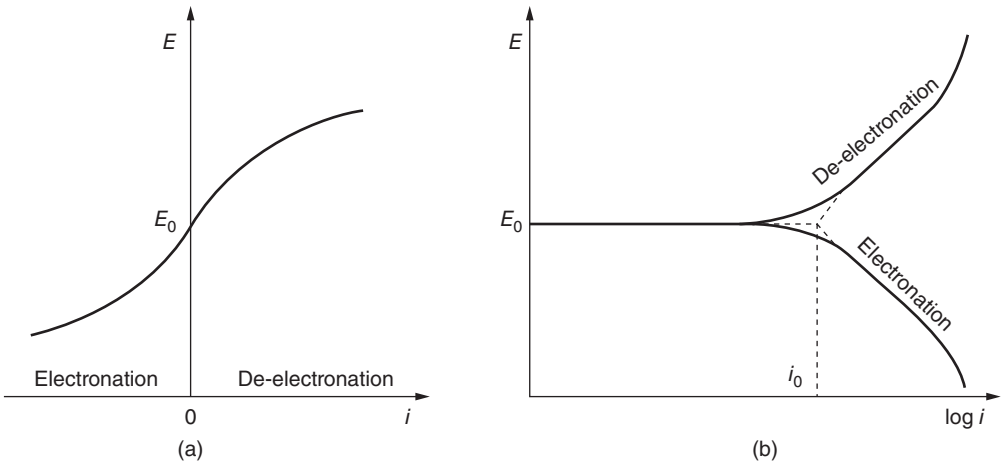


Figure 6.1 Polarization curves of a fast electrochemical reaction. (a) Arithmetic scale for i. (b) Logarithmic scale for i.

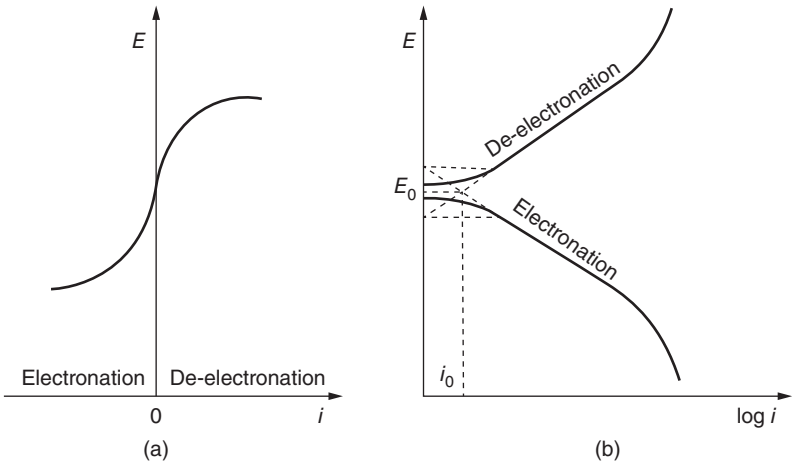


Figure 6.2 Polarization curves of a slow electrochemical reaction. (a) Arithmetic scale for i. (b) Logarithmic scale for i.

reversibly, the higher is its intrinsic exchange current density.

The Tafel curves giving E as the function of $\log i$ also provide interesting results about the kinetics of the phenomena. In fact, the plot of E against $\log i$ is not usually a straight line, i.e. the kinetics of the reaction does not obey the Tafel relation. The experimental curves obtained can be considered as built up of rectilinear portions or, on the contrary, as showing systematic departures from the linear Tafel relation for certain current densities reached. It is well established in electrochemistry that the Tafel relation does not apply precisely for small and large current densities. One reason for this is that the Tafel equation is derived purely by considering the overpotential due to polarization caused by charge transfer requirements, which assumes that a cation moves away from the metal-fused electrolyte interface as soon as it is dissolved. This is generally not the case. The removal of the anodic product does not increase in the same proportion as the current density and the concentration of these products will increase and cause a back e.m.f. This effect is particularly relevant in the case of fast electrode processes as observation of Figures 6.1 and 6.2 shows: the difficulty in obtaining a pure Tafel slope, i.e. unaffected by double layer and mass transfer effects, increases with kinetics of the electrode processes (i.e. with high i_0) due to increasing overlapping of the diffusion zones over the Tafel one. Polarization measurements also include ohmic overpotential that arises from an IR drop through a portion of the electrolyte and between the test electrode and the reference one, but this term is not significant in molten media as compared with an aqueous system. The validity of the Tafel equation has been verified by Laitinen and Gaur (1957), Randles and White (1955), and others for many fused systems.

The facts mentioned above are very important especially due to their repercussion on the interpretation of electrochemical phenomena. So, it is seen, by this simple enumeration, that it is possible to connect thermodynamic considerations to kinetic ones.

6.6 Corrosion Potential–pO^{2-} Relationship

In the section above, where some concepts of electrode kinetics were discussed, a quantity of crucial importance to electrodics was defined: the overpotential (η). In electrochemical kinetics, the only reaction directly affected by the potential is the charge transfer reaction, i.e. the reaction in which charge carriers are transferred across the electrochemical double layer at a phase boundary. The rate of the charge transfer reaction determines the charge transfer or activation overpotential. This kind of overpotential has been treated in detail by Audubert (1942), Bard and Faulkner (1998), Bockris (1954), Butler (1924), Conway (1965), Erdey-Gruz and Volmer (1930), Gerischer (1960, 1961), and others.

Prior to discussion, it is noted that only the basic electrodic equations will be considered.

Considering the conversion of M^+ ions into metallic M, the number of moles of positive ions reacting per second by crossing unit area of the melt–metal interface is proportional to the electronation current density i and as a first approximation (Erdey-Gruz and Volmer 1930):

$$\begin{aligned} i_- &= -K'_- \{M^+\} \exp(-\Delta\widetilde{G}^*_-/RT) \\ &= -K'_- \{M^+\} \exp(-\Delta G^*_-/RT) \exp -[(1-\alpha)FE/RT] \\ &= -K_- \{M^+\} \exp[-(1-\alpha)FE/RT] \end{aligned} \tag{6.16}$$

where $\Delta\widetilde{G}^*_-$ is the activation energy required for the electronation process at the potential E, K_- and K'_- are constants, $\{M^+\}$ is the activity of cations M^+ on the metal side of the interface, ΔG^*_- is the chemical activation free energy barrier when there is zero electric field acting on the ion, and α is the transfer coefficient for the de-electronation reaction introduced by Erdey-Gruz and Volmer (1930) that has values ranging from zero to unity ($0 < \alpha < 1$) (Vetter 1952). K_- is dependent on the reference potential chosen since $K_- = K'_- \exp(\Delta G^*_-/RT)$. Moreover, positive ions can move from the melt to the electrode and also in the opposite direction. Thus, there is an electronation reaction

$$M^+ + e^- \rightarrow M \tag{6.17}$$

and also a de-electronation reaction

$$M \rightarrow M^+ + e^- \tag{6.18}$$

In this case, the total current density passing through the double layer is

$$\begin{aligned} i &= i_+ + i_- \\ &= K_+\{M\} \exp(\alpha FE/RT) \\ &\quad - K_-\{M^+\} \exp[-(1-\alpha)FE/RT] \end{aligned} \tag{6.19}$$

where $\{M\}$ is the activity of the metallic atoms immediately at the electrode surface (unity). If the metal–melt interface reaches its equilibrium state, there is no net current ($i = 0$), but there is an exchange current. The electronation and de-electronation reactions continue to occur but at the same rate. The current densities corresponding to these individual reactions become the exchange current density i_0 ($i_0 = i_+ = |i_-|$). Hence,

$$\begin{aligned} i_0 = i_+ &= K_+\{M\} \exp(\alpha FE_0/RT) \\ &= i_- = K_-\{M^+\} \exp[-(1-\alpha)FE_0/RT] \end{aligned} \tag{6.20}$$

where E_0 is the potential difference across the interface at equilibrium. On dividing Eq. (6.19) by the corresponding

expressions in Eq. (6.20) and taking into consideration the definition for overpotential η, the following important relationship is obtained (Erdey-Gruz and Volmer 1930):

$$i = i_0\{\exp(\alpha F\eta/RT) - \exp[-(1-\alpha)F\eta/RT]\} \quad (6.21)$$

For higher charge transfer overpotentials, $|\eta| \gg RT/F$, the first or second term on the right-hand side (r.h.s.) of Eq. (6.21) can be neglected depending on the sign of the current so that if this Eq. (6.21) is put into a logarithmic form, a linear relationship results between η and $\log|i|$ similar to the Tafel equation:

$$\eta_+ = -\frac{2.3026\,RT}{\alpha F}\log i_0 + \frac{2.3026\,RT}{\alpha F}\log i_+$$

or (6.22)

$$\eta_- = +\frac{2.3026\,RT}{(1-\alpha)F}\log i_0 + \frac{2.3026\,RT}{(1-\alpha)F}\log|i_-|$$

Here, the subscripts "+" and "−" to the overpotential denote anodic and cathodic polarization, respectively.

Let us now consider the following reaction of a metal M in a molten sulfate (Burrows and Hills 1966):

$$M + \frac{1}{2}SO_3 = M^+ + \frac{1}{2}SO_2 + \frac{1}{2}O^{2-} \quad (6.23)$$

This overall reaction can be considered as the sum of the two half-reactions:

$$M = M^+ + e^- \quad (6.24)$$

$$\frac{1}{2}SO_3 + e^- = \frac{1}{2}SO_2 + \frac{1}{2}O^{2-} \quad (6.25)$$

For these two processes to take place simultaneously, it is necessary and sufficient that the potential difference across the interface be more positive than the equilibrium potential for the reaction (6.24)

$$E_{0.24} = E^0_{0.24} + \frac{2.3\,RT}{F}\log\{M^+\} \quad (6.26)$$

and more negative than the equilibrium potential of the electronation reaction (6.25) involving electron acceptors (such as SO_3) contained in the melt:

$$E_{0.25} = E^0_{0.25} + \frac{2.3\,RT}{2F}\log\frac{p_{SO_3}}{p_{SO_2}} - \frac{2.3\,RT}{2F}\log\{O^{2-}\} \quad (6.27)$$

The behavior for the potential–current curve $E(I)$ that can be envisaged for the process Eq. (6.23) is illustrated in Figure 6.3 by the continuous thick line. (I) E is composed additively of the metal dissolution current I_{24} (E) and the electronation current I_{25} (E), and the two are independent of each other at the same potential value. The principle of additive combination of all partial processes at an electrode surface to obtain the total potential–current curve was first formulated by Wagner and Traud (1938). The potential E at zero current is neither $E_{0.25}$ nor $E_{0.24}$, but a so-called mixed potential (E_M) for which the total potential–current curve gives $I(E_M) = 0$. The total metal dissolution current I_{24} and electronation current I_{25} are then equal in magnitude but opposite in sign, i.e.

$$I_{24} = -I_{25} \quad (6.28)$$

The rate of corrosion of the metal is obviously given directly by the rate of metal dissolution; hence, the free corrosion current I_c (i.e. the rate at which the metal destroys itself) is given by

$$I_c = I_{24} = -I_{25} \quad (6.29)$$

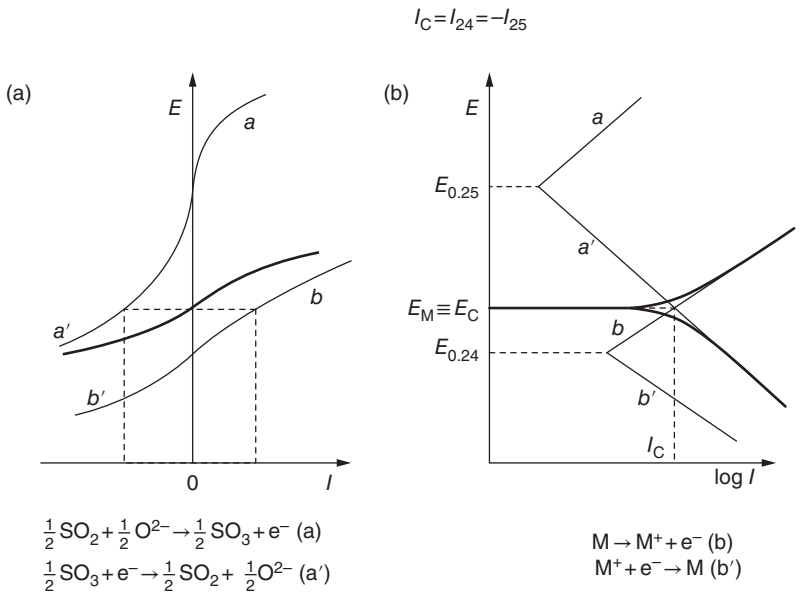


Figure 6.3 Corrosion of a metal M in a molten sulfate with SO_2 evolution. Anodic and cathodic polarization curves. Corrosion potential and corrosion current. (a) Representation with an arithmetic scale for the reaction current. (b) Representation with a logarithmic scale for the reaction current.

Considering the electrode kinetics, we can thus write

$$I_c = I_{24} = A_{24} i_{24} = A_{24}(i_{+,24} + i_{-,24}) = A_{24} K_{+,24}\{M\} \exp(\alpha_{24} F E_c / RT) - A K_{-,24}\{M^+\} \exp[-(1-\alpha_{24}) F E_c / RT] \quad (6.30)$$

$$I_c = -I_{25} = -A_{25} K_{+,25} P_{SO_2}^{1/2} \{O^{2-}\}^{1/2} \exp(\alpha_{25} F E_c / RT) + A_{25} K_{-,25} P_{SO_3}^{1/2} \exp[-(1-\alpha_{25}) F E_c / RT] \quad (6.31)$$

where A_{24} is the sink area and A_{25} is the electron-source area (at the metal–electrolyte interface). Assuming that overpotentials are sufficiently large, Eqs. (6.30) and (6.31) become

$$I_c = I_{24} = A_{24} K_{+,24}\{M\} \exp(\alpha_{24} F E_c / RT)$$
$$I_c = -I_{25} = A_{25} K_{-,25} p_{SO_2}^{1/2} \exp[-(1-\alpha_{25}) F E_c / RT] \quad (6.32)$$

The free corrosion potential, E_c, i.e. the uniform potential difference over the surface of the corroding metal, can be evaluated from the expressions above. It follows that

$$E_c = \frac{2.3RT}{[\alpha_{24} + (1-\alpha_{25})]F} \log \frac{A_{25} K_{-,25}}{A_{24} K_{+,24}\{M\}} + \frac{2.3\,RT}{[\alpha_{24} + (1-\alpha_{25})]F} \log p_{SO_3}^{1/2} \quad (6.33)$$

It is clear from this that the free corrosion potential and the mixed potential are identical.

In accordance with the theory of Lux (1939) and Flood et al. (1952) who assign a definite acid–base equilibrium to all oxyanionic melts, the acid–base equilibria for sulfates can be expressed by the Eq. (6.12) and by the equilibrium constant

$$K_{12} = p_{SO_3}\{O^{2-}\}\{SO_4^{2-}\}^{-1} \quad (6.34)$$

Assuming $(SO_4^{2-}) = 1$, it follows that

$$\log p_{SO_3}^{1/2} = \frac{1}{2} \log K_{12} + \frac{1}{2} pO^{2-} \quad (6.35)$$

where $pO^{2-} = -\log\{O^{2-}\}$ is a nonprotonic function that measures the acidity of the melt, as already reported. The expression (6.35) for the active species SO_3 can be introduced into Eq. (6.33), giving

$$E_c = \frac{2.3RT}{[\alpha_{24} + (1-\alpha_{25})]F} \log \frac{A_{25} K_{-,25} K_{12}^{1/2}}{A_{24} K_{+,24}\{M\}} + \frac{2.3\,RT}{2[\alpha_{24} + (1-\alpha_{25})]F} pO^{2-} \quad (6.36)$$

Assuming that the ratio of A_{25} and A_{24} as well as α_{24} and α_{25} is constant during the overall corrosion reaction (which is not free from error), Eq. (6.36) becomes

$$E_C = a + b\, pO^{2-} \quad (6.37)$$

with a and b being two constants. Thus, we attain a linear relationship between the corrosion potential and the function pO^{2-}, which should be valid for all oxyanionic melts.

What has been presented above is a very elementary account of electrodics of corrosion under quite ideal conditions. The details of the complex corrosion phenomena in real systems are out of the scope of this chapter.

6.7 Electrochemical Polarization and Monitoring

In this section, an account is given of several available methods for obtaining the potential–current curves, the free corrosion rates, and the electrochemical monitoring of corrosion. It is customary to classify the electrochemical methods for obtaining such potential–current curves into potential-sweep, current-sweep, potential-step, and current-step methods. The former method, sometimes called potentiodynamic (or potentiokinetic) polarization, is accomplished by continuously changing the applied electrode potential (with feedback control) at a constant rate and simultaneously recording current. In the current-sweep (intensiokinetic) method, the electrolysis current (with feedback control) is varied with time according to a given program, and the electrode potential is recorded as a function of current. In the potential-step method, electrode potential is rapidly changed over a finite increment, and current measured after a predetermined time interval, and this process is repeated. In the last (above) method, a current step is applied, and the resulting variation of potential with time is recorded. These two-step methods are also referred to as potentiostatic and galvanostatic (or intensiostatic), respectively, to indicate that at any instant E (or I) is held constant, by means of feedback control.

All the polarization methods described above are well established in the ambient temperature range (Edeleanu 1958; Greene 1962; Greene and Leonard 1964; Pourbaix and Vandervelden 1965; Prazak 1963) for electrochemical studies of metals, the best or most accurate of them depending, of course, on its intended use: if the purpose is to study the kinetics phenomena, the methods in which the electrode potential is controlled are the best; when the permanent physicochemical modifications, due to applied current, are the objective, the methods in which the electrolysis current is controlled are preferable. Generally speaking, however, potential-step and potential-sweep methods will be more useful for the study of corrosion phenomena than current-step and current-sweep methods because they give more precise indications concerning the quality of the passivation and concerning the conditions of activation. The investigation of corrosion processes in melts by these standard electrochemical techniques was pioneered by a reasonable number of researchers

(Arvia et al. 1971, 1972a,b; Baudo et al. 1970; Davis and Kinnibrugh 1970; Kazantsev et al. 1968; Sequeira and Hocking 1978a,b, 1981), and, in general, it can be said that almost all workers in the field of high temperature agree that the polarization methods appear to be quite suitable in corrosion studies at high temperature in molten electrolytes.

The polarization curves have several shapes, but near the potential axis their character is similar to that shown by the curves plotted in Figures 6.1 and 6.2.

A potentiodynamic polarization curve provides a graphic summary of the corrosion characteristics of tested material so that its plot and evolution can be used as a very rapid and practically nondestructive corrosion test. However, the corrosion characteristics obtained are accurate only for the medium in which the curve was obtained. Therefore, the importance of the method does not lie in any final evaluation of the rates of corrosion in a particular medium, but rather in the rapid evaluation of fundamental corrosion properties with the possibility of sensitive relative comparison (Prazak 1963). Another feature of the method is that analysis of such potential–current curves, together with $E - pO^{2-}$ diagrams, enables us to predetermine those reactions theoretically possible and impossible for each electrode potential value.

One of the most important electrochemical values for the determination of the kinetics and mechanisms of primary corrosion processes is the value of the free corrosion current. When the primary corrosion process is slow (absence of concentration polarization), the free corrosion current can be obtained by potentiodynamically polarizing the alloy electrode at a very slow sweep rate in the neighborhood of the free corrosion potential. The alloy dissolution rate is obtained by plotting potential versus log current, and extrapolating the linear anodic and cathodic branches is the free corrosion potential, the intercept giving the free corrosion current. This method can also be applied when some (relatively small) concentration polarization is present; the latter can be taken into account by using the approximate expression

$$I = \frac{I_{\text{meas.}} \times I_{\text{d}}}{I_{\text{d}} - I_{\text{meas.}}} \tag{6.38}$$

where $I_{\text{meas.}}$ is the measured current in the presence of concentration polarization and I_{d} is the diffusion current (of course this correction implies the exact knowledge of the diffusion current). When the primary corrosion processes are sufficiently fast, other methods, namely, relaxation methods, must be used. The objective of these methods is the study of the electrode processes before they become diffusion controlled. The experimental techniques associated with these methods are very complex, but they are the most important ways allowing accurate determination of fast charge transfer corrosion rates. Several relaxation methods for these measurements have been considerably revised by Graves and Inman (1970), and useful exposition of the "classical" relaxation methods is that of Damaskin (1967). The selection of the method to measure the free corrosion currents, depending precisely on rate phenomena, is obviously difficult (because the values of these corrosion rates are not known *a priori*).

In general, the high temperatures of fused salt systems cause most corrosion processes to be rapid (reversible with respect to the non-relaxation methods). Generally speaking, therefore, relaxation methods will be the most appropriate for the determination of corrosion rates in melts.

The measurement of free corrosion rates in molten salts was pioneered by Baudo et al. (1970) and Cutler (1971), among others. The first workers determined the corrosion rates using the conventional method, extensively and successfully applied at low temperatures in aqueous systems; they presented the results in the form of Tafel plots, but they do not give information on the current–potential measured values from which the plots of E versus log i were obtained. It is rather surprising in view of the relatively high corrosion rates quoted that it had been possible to obtain pure Tafel zones. It is certain that this method enables the measurement of rough values (more of qualitative than quantitative value) of the free corrosion rates, but it is advisable to put into practice LaQue's opinion that new and more accurate tests should be introduced for a better understanding of the corrosion mechanisms (LaQue 1969). A cyclic potential-sweep method is used by Cutler (1971) to determine the free corrosion rates that seems scientifically more appropriate than the conventional one.

The search for accurate methods for the determination of the kinetics and mechanisms of corrosion processes in molten salt systems has led to the study of newer electrochemical methods suitable for corrosion studies in aqueous systems. As a result, DC polarization curves, linear polarization resistance methods, AC impedance, and electrochemical noise/galvanic coupling are continually increasing their application to molten salts, and it can be concluded that apart from being useful additions to investigate high temperature corrosion processes in molten salts, they have demonstrated feasibility for use in online monitoring and for estimating corrosion under realistic operational conditions in boilers, gas turbines, and other high temperature equipment (Mu et al. 1995; Pardo et al. 1992; Rapp and Zhang 1994; Ratzer-Scheibe 1991; Sequeira 1998). It should be noted that the techniques widely used for the electrochemical monitoring of corrosion in aqueous solutions have not been applied to molten salt corrosion very often because of the limitations of the experimental technique under high temperature conditions. Nishikata and coworkers have investigated the possibility of electrochemical monitoring of molten salt corrosion by the linear polarization resistance and AC impedance

techniques (Nishikata and Haruyama 1986; Nishikata et al. 1981; Numata et al. 1983).

The correlation between the polarization resistance and corrosion rate was first derived by Stern and Geary (1957), assuming that both the anodic and cathodic partial reactions obey the Tafel relation. The polarization resistance R_p is written as

$$R_p = \left(\frac{\Delta E}{\Delta I}\right)_{E_c} = \frac{K}{I_c} \tag{6.39}$$

where I_c indicates the corrosion rate and K is a constant that depends on the temperature and corrosion mechanisms. The K value could be determined theoretically from the Tafel slopes of the partial anodic and cathodic polarization curves. However, it is very difficult to measure the Tafel slopes, especially in molten salts because of extremely fast charge transfer rates (Laitinen et al. 1960; Nishikata et al. 1983).

According to the generalized derivation presented by Ohno and Haruyama (1981), the value of K is expressed as

$$\frac{1}{K} = \left[\left\{\frac{\partial \ln I_+}{\partial E}\right\}_{E_c} - \left\{\frac{\partial \ln I_-}{\partial E}\right\}_{E_c}\right] \tag{6.40}$$

The terms in parentheses in Eq. (6.40) are the slopes of the partial anodic and cathodic polarization curves on a semilogarithmic scale at a corrosion potential. According to Eqs. (6.39) and (6.40), the polarization conductance I/R_p is proportional to I_c even if a distinct Tafel region is not observed on the polarization curves. The K value can be determined practically by plots of $\log(I/R_p)$ measured from the electrochemical method versus $\log I_c$ calculated from weight loss measurements. The polarization resistance R_p is determined from the slope of the straight portion of the polarization curve in the vicinity of the corrosion potential as shown in Figure 6.3.

In general, K values differ significantly, and K depends on the natures of the metal and molten salt. For example, in molten chloride, the K value in the absence of oxygen is approximately half that in the presence of oxygen. This is caused by the difference between the cathodic polarization curves (Nishikata et al. 1984).

As a result, if the K value in the molten salt of interest is measured in advance, the instantaneous corrosion rates can be obtained by polarization resistance measurements. For example, as the polarization resistance is possible to measure continuously and to record using an AC corrosion monitor (Mansfeld and Bertocci 1981), the corrosion rates can be precisely determined by the Stern–Geary equation. By this method, the effects of alloying metals and other elements on the corrosion rates have been investigated in diverse molten salts.

6.8 Electrochemical Nature of Metal Oxidation

In the sections above, the basic fundamentals of molten salt electrochemistry are described, and it is shown how high temperature electrochemistry can be applied to understand and mitigate corrosion in molten media. The reader should also give attention to Chapters 3 and 17, where further electrochemical descriptions relevant to molten salt corrosion are presented. Nowadays, high temperature electrochemistry, and its unique electrolyte features to process materials in nonaqueous environments, provides many opportunities including concentrated solar power systems, nuclear fuel reprocessing, tritium recovery in fusion energy technologies, light metal production, and others. Although high temperature solid-state electrochemistry and its applications are less well known, namely, in the area of corrosion, it is a fact that the evidence of ionic or electrolytic conductivity in many corrosion products found in high temperature oxidation systems led to the conclusion that corrosion in these dry (or wet) oxide systems is also an electrochemical phenomenon that is important to understand and mitigate by electrochemical means. One specific area of high temperature solid-state electrochemistry that has been increasing in importance is concerned with the electrochemical behavior of ionic or quasi-ionic solid oxides. Here, we will begin to show that the metal–oxide systems can be viewed as systems where oxidation occurs by electrochemical processes. Then, particular attention will be given to the electrochemistry of ionic solid oxides or oxide solid electrolytes and the relationships that govern their properties, namely, ionic and electronic conductivities, chemical diffusion coefficients, transport numbers, mobilities, stoichiometry, and thermodynamic factor, among others. More specifically the equations that allow the characterization of the total conduction process in an oxide electrolyte, over a wide range of oxygen partial pressures in both electronic and ionic conduction regimes, are to be examined. These equations are applied in several electrochemical situations, namely, that where current is supplied to reversible electrodes at the interfaces of an oxide conductor and that of the ionic conductor with ohmic contacts but no current supply. Mathematics are presented that will allow one to calculate the electron and hole conductivities, as well as ionic transport numbers, directly from polarization measurements.

To easily demonstrate the electrochemical nature of the metal–oxide systems, let us recall from Chapter 1 that the chemical reaction between a metal and oxygen is called oxidation, which takes place at low and high temperatures. This reaction is heterogeneous, as it involves different phases – solid (metal) and a gas – that take place depending on different factors at different interfaces. The result of

heterogeneous reactions is usually the formation of a new phase as they occur between two immiscible phases.

If no natural oxide can be found on the surface, oxidation starts with the adsorption of oxygen (O_2) on the surface, followed by O_2 splitting into O atoms, and – as the reaction proceeds – oxygen is dissolved in the metal, and the oxide is formed.

The chemical reaction can be written as

$$aM + \frac{b}{2}O_2 = M_aO_b \tag{6.41}$$

Equation (6.41) can be determined by the second law of thermodynamics, which can be written in terms of Gibbs' free enthalpy ΔG° (Eq. (3.2)) at high temperature, as the temperature and pressure are constant. The reaction is spontaneous if $\Delta G^\circ < 0$, or in equilibrium if $\Delta G^\circ = 0$, and thermodynamically impossible if $\Delta G^\circ > 0$.

It should also be noted that the oxide will also be thermodynamically formed only if the ambient oxygen pressure is greater than the dissociation pressure of the oxide in equilibrium with the metal. If we consider the formation of MO according to Eq. (6.41) for simplicity, it can be assumed that the oxide is simply divalent and ΔG° (MO) as the standard free energy of the reaction at a certain temperature, the oxidation of M is only possible if the following inequality holds:

$$p_{O_2} \geq \exp\left\{-\frac{2\Delta G^\circ(\mathrm{MO})}{RT}\right\} \tag{6.42}$$

The different dissociation pressures of the oxide and the corresponding standard free energies of formation of some oxides are summarized in the well-known Ellingham diagrams, which do not take the kinetics into account. In Section 3.2.1, the Ellingham diagrams are deeply analyzed.

After the scale becomes continuous, the metal is separated from the gas, and the further reaction is carried on through diffusional transport of the reactants through the oxide scale. The difference between a thin (or anodically) and a thick grown oxide is in the driving force, which is known to be the electric field for the thin film and the chemical potential for the second category.

The resistance of materials at high temperature is defined by the formation of a continuous, adherent, slow growing, and thermodynamically stable oxide. The reaction takes place at both metal–oxide and oxide–oxygen interfaces as shown in Figure 6.4. There are several reactions occurring at the different interfaces:

Metal–oxide interface:

$$\begin{aligned} M &\rightarrow M^{2+} + 2e^- \\ M + O^{2-} &= MO + 2e^- \end{aligned} \tag{6.43}$$

which represents the two possible reactions at this interface – the oxidation of the metal and the reaction between the metal and the ionized oxygen, respectively.

Oxide–gas interface:

$$\begin{aligned} M^{2+} + \frac{1}{2}O_2 + 2e^- &= MO \\ \frac{1}{2}O_2 + 2e^- &\rightarrow O^{2-} \end{aligned} \tag{6.44}$$

At this interface, the two possible mechanisms are the reaction of the metal cations with oxygen and the reduction of O_2 in oxygen anions, respectively.

Figure 6.4 shows that the scale can grow either at the metal–oxide or oxide–gas interface, implying that the growth can be limited by the diffusion of the species through the oxide. In this case, the rate of the reaction can be expressed as

$$x\mathrm{d}t = k_p t \tag{6.45}$$

where x is the scale thickness, k_p is the parabolic rate constant, and t is the reaction time, considering that the process leads to parabolic rates. The oxidation rate can be either linear, logarithmic (inversely logarithmic) at low temperatures, or parabolic, which is the ideal case at high temperatures, but in reality a combination of different laws is observed. The reaction rate can be calculated using Eq. (6.45) as oxidation is oxygen enrichment. The rates of different oxides are shown in Figure 6.5 where alumina shows the lowest growth rate.

After integrating Eq. (6.45), the following expression of the oxide scale can be obtained:

$$x^2 = 2k_p t \tag{6.46}$$

where $x = 0$ and $t = 0$.

The diffusion rate can be expressed with the first Fick's law, Eq. (6.47), which describes the flux of species through the oxide scale (see also Eq. (5.6)):

$$j = -D\frac{\partial c}{\partial x} \tag{6.47}$$

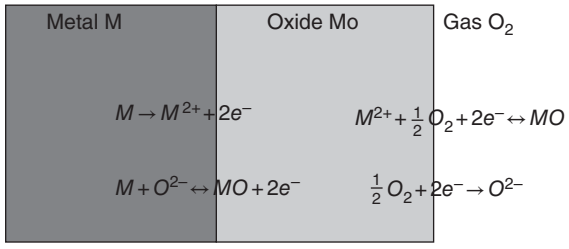


Figure 6.4 Schematic representation of the different reactions occurring at the metal–oxide and oxide–gas interfaces.

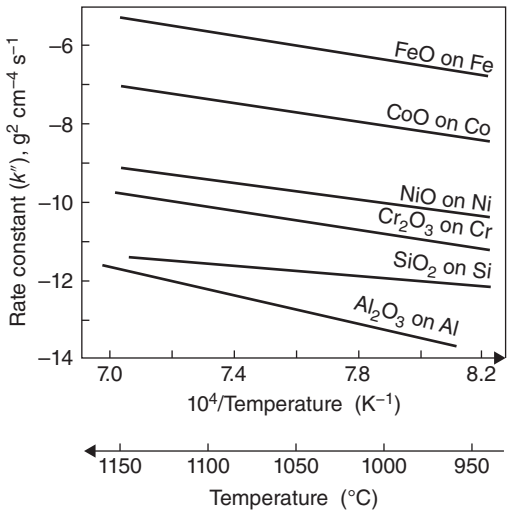


Figure 6.5 Rate constants for the growth of selected oxides.

where j is the flux defined as the rate at which the moving species pass through unit area; D is the diffusion constant, which is material specific; and c is the concentration. This equation shows that the diffusion takes place from the higher to the lower concentration region.

Equation (6.46) may also be expressed in terms of mass change per area, $\Delta m/A$:

$$\left(\frac{\Delta m}{A}\right)^2 = 2k_w t \tag{6.48}$$

$$k_w = \frac{k_p}{2} \cdot \left(\frac{V_{ox}}{A_O}\right)^2 \tag{6.49}$$

where V_{ox} is equivalent to the volume of the oxide, which can be calculated as the molecular weight/density of the oxde, and A_O is the atomic weight of oxygen.

A parabolic growth rate is required mostly for a continuous and adherent scale, which can be assumed for metals at high temperature. In this case, the rate-controlling factor is the migration of ions and/or electric charge (electrons) through the layer.

The transport of species is supported by defects in the scale (vacancies, interstitial atoms) or short-circuit paths, such as grain boundaries. Several mechanisms have been proposed to explain the role of defects during diffusion. It has been shown that the cation vacancy concentration in metal-deficient oxide MO depends on the oxygen partial pressure p_{O_2}:

$$\frac{1}{2}O_2 = O_0 + 2h^{\bullet} + V_M'' \tag{6.50}$$

From the above, we can determine the vacancy concentration $[V_M]$ that is strongly dependent on the oxygen partial pressure and can be calculated as

$$[V_M] = k_p p_{O_2}^{1/6} \tag{6.51}$$

For a more general case (neutral, single or double charged vacancies), we can write

$$[V_M] = k_p p_{O_2}^{1/n} \tag{6.52}$$

Therefore, the parabolic rate constant varies with the oxygen partial pressure across the scale, as given below:

$$k_p \alpha [p_{O_2^1} - p_{O_2^2}]^{1/n} \tag{6.53}$$

where $p_{O_2^1}$ and $p_{O_2^2}$ are the oxygen partial pressures at the oxide–gas and metal–oxide interfaces, respectively. As the partial pressure of oxygen is strongly decreased at the metal–oxide interface, it can be neglected. Thus, Eq. (6.54) can be written as

$$k_p \alpha (p_{O_2^1})^{1/n} \tag{6.54}$$

Oxides are generally ionic or semiconductors at elevated temperatures; therefore they are either solid electrolytes of n- or p-type oxides. For a p-type oxide, the parabolic constant rate depends on the oxygen partial pressure in the gas phase. In the case of an n-type oxide with nonmetal deficit or metal excess, the exponent of the oxygen partial pressure is found to be negative after calculations, and k_p is insensitive to the pressure in the gas phase:

$$k_p \alpha (p_{O_2})^{-1/6} \text{ or } (p_{O_2})^{-1/4} \tag{6.55}$$

Deeper fundamentals of oxidation are described in Chapter 7, but the above considerations seem to be enough convincing of the electrochemical nature of high temperature oxidation, as shown long time ago for metal-aqueous solutions and not so long time ago for metal-fused salt systems.

6.9 Usefulness of Electrochemical Cells

As far as electrochemical cells relevant for applications or electrochemical measurements are concerned, we must distinguish between polarization cells, galvanic cells, and open-circuit cells, depending on whether an outer current flows and, if so, in which direction this occurs. Table 6.2 provides examples of the purposes for which such cells may be used. In terms of application, we can distinguish between electrochemical sensors, electrochemical actors, and galvanic elements such as batteries and fuel cells. These applications offer a major driving force for dealing with solid-state electrochemistry.

Electrochemical cells can also be used for the precise determination of kinetic and thermodynamic parameters that may be used in studies of corrosion mechanisms. Such cells can be classified according to the combination of reversible and blocking electrodes. Cell types and

Table 6.2 An overview of electrochemical devices and measurement techniques based on various cell types

Cell type	Measurement technique	Technological application
Polarization cell	Measurement of kinetic data by polarization	Electrochemical composition actors (electrolyzers, pumps, electrochromic windows), electrochemical composition sensors (amperometric, conductometric)
Current-generating cell	Measurement of kinetic data by depolarization	Electrochemical energy storage and conversion devices (batteries, fuel cells, supercapacitors)
Open-circuit cell	Measurement of thermodynamic formation data, transport number of electrons	Potentiometric composition sensors

Table 6.3 Combination of reversible (O^{2-}, e^-|, typically porous Pt) and blocking electrodes (e^-|, i.e. only reversible for e^-, a typical example being graphite); or (O^{2-}|, i.e. only reversible for O^{2-}, a typical example being a Pt-contacted zirconia electrolyte) leads to a variety of measurement techniques applied to the oxide MO

Cell	Quantities to be determined
(O^{2-}, e^-|MO|e^-, O^{2-})	Resistances and capacitances
(O^{2-}, e^-|MO|e^-, O^{2-}) [a]	Transport numbers, chemical diffusion coefficients
(O^{2-}, e^-|MO|e^-)	Electronic conductivities as a function of activity, chemical diffusion coefficients
(e^-|MO|e^-)	Electronic conductivities, chemical diffusion coefficients
(O^{2-}, e^-|MO|O^{2-})	Ionic conductivities as a function of activity, chemical diffusion coefficients
(O^{2-}|MO|O^{2-})	Ionic conductivities, chemical diffusion coefficients
(O^{2-}|MO|e^-)	Stoichiometry, thermodynamic factor, chemical diffusion coefficients

[a] A different oxygen partial pressure was used on the right-hand side.

parameters to be determined are compiled in Table 6.3. The determination of kinetic parameters makes use of the condition that, in an experiment with a mixed conductor, the flux densities are composed of a drift and stoichiometric term:

$$j_{\{\}} = -\frac{\sigma_{\{\}}}{\sigma}\frac{i}{z_{\{\}}F} - D^{\delta}_{\{\}}\nabla c_{\{\}} \tag{6.56}$$

In Eq. (6.56) only the total current i and the total conductivity σ carry no indices, but the other quantities do ({}). If associates do not play an important role, the indices simply refer to ions or electrons or the respective component (in j, D^{δ}, c) (Wagner 1975). If associates, however, play a substantial role, the respective "conservative ensemble" must be considered (Maier and Schwitzgebel 1982).

If, for example, oxygen vacancies ($V_O^{\bullet\bullet}$ denoting a missing O^{2-}) and electrons are present and then also associates such as $V_O^{\bullet}$ (one electron trapped by an oxygen vacancy) and V_O^{x} (two electrons trapped by an oxygen vacancy), the flux and conductivities in Eq. (6.56) address the total oxygen ensemble, $\sigma_{\{O\}} \equiv \sigma_{V_O^{\bullet\bullet}} + 2\sigma_{V_O^{\bullet}}$ (V_O^{x} does not contribute being effectively neutral). The ensemble diffusion coefficient $D^{\delta}_{\{O\}}$ is essentially composed of $\sigma_{e'} - \sigma_{V_O^{\bullet}}$ and $\sigma_{V_O^{\bullet\bullet}} + 2\sigma_{V_O^{\bullet}}$, as well as of respective differential trapping factors. Of course, interaction can also formally be put on Onsager's cross coefficient, but this does not provide any mechanistic insight (Onsager 1931).

6.10 Current–Potential Measurements on Solid Electrodes

Since the fundamental electrochemical thermodynamic relationships do not depend on the type of electrolyte, we still expect the Nernst equation to be valid and hence to obtain thermodynamic data from appropriate measurements. As an example, we can consider the oxygen concentration cell:

$$O_2(P_1)|Pt|ZrO_2 \cdot 0.15\, Y_2O_3|Pt|O_2(P_2) \tag{6.57}$$

The electrochemical equilibrium at both electrodes has the form

$$\frac{1}{2}O_2 + 2e^- = O^{2-} \tag{6.58}$$

We find for each electrode

$$E = E^0 + \frac{RT}{2F}\ln\frac{(p_{O_2})^{1/2}}{\{O^{2-}\}} \tag{6.59}$$

where $\{O^{2-}\}$ is the activity of the oxide ion in the ceramic. The e.m.f. of the cell (Eq. (6.57)) can then be written as

$$E = \frac{RT}{4F} \ln \frac{P_2}{P_1} \tag{6.60}$$

Above c. 650 °C, this equation is often found to be accurately obeyed since above this temperature the reaction rate for oxygen reduction is sufficiently fast for equilibrium to be established. In practice, a thin layer of porous platinum is deposited on both sides of a ceramic disk to form the electrodes, and the arrangement can be modified to measure the partial pressure of oxygen with considerable precision.

If hydrogen replaces oxygen at the anode, we have a fuel cell of the form

$$H_2(P_1)|Pt|ZrO_2 \cdot 0.15\ Y_2O_3|Pt|O_2 \tag{6.61}$$

with the anode reaction being

$$H_2 + O^{2-} = H_2O + 2e^- \tag{6.62}$$

The overall cell reaction is now

$$H_2 + \frac{1}{2}O_2 = H_2O \tag{6.63}$$

and placing a load between the anode and cathode allows us to generate electrical energy. If, instead, the e.m.f. of this cell is measured under conditions of zero current flow, the free energy, enthalpy, and entropy of reaction (6.63) can be obtained above c. 650 °C.

By contrast, kinetic measurements with solid electrolytes are much more difficult. It is obviously not possible to control mass transport to the electrode through hydrodynamic means, and there are frequently rather high resistances that build up between electrode and ionic conductor, such that in the worst case all that can be measured is an ohmic response. Perhaps most serious is the fact that the solid–solid phase boundary undergoes changes during current flow (including the formation of cavities and dendrites), and impurities accumulating at the boundary cannot be removed by simple electrode activation as in the liquid–solid cell.

These difficulties have severely inhibited high-quality electrode kinetic studies in solid electrolytes, but one example, that of oxygen reduction on $Pt|ZrO_2$, has been carried out with the experimental setup shown in Figure 6.6, with high precision. The working electrode was a platinum needle, designed to eliminate diffusion within the Pt pores of a conventional porous electrode and to prevent any alteration in the morphology of the interface. Studies between 800 and 1000 °C showed that the rate-limiting processes in this region were either the dissociative adsorption of O_2 or the surface diffusion of O^{2-} ions to the $Pt|ZrO_2$ contact point. Neither electron transfer nor oxide ion transport in the solid electrolyte was rate limiting at any temperature in this range. Note that the reference electrode in Figure 6.6 is identical to the counter electrode.

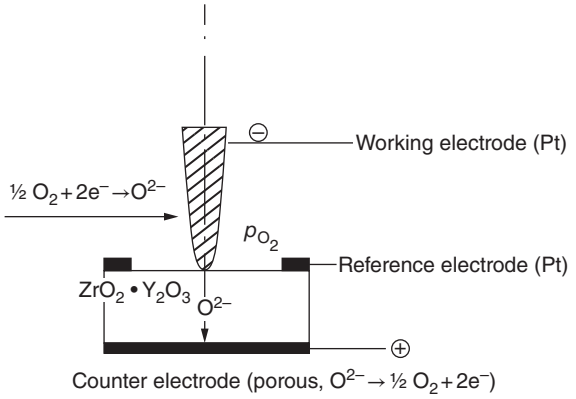


Figure 6.6 Experimental setup for the investigation of the oxygen reduction reaction at an electrode/solid electrolyte interface.

6.11 Simple Concepts of Oxide Semiconductors

It has been reported in Section 6.10 that many oxides of interest in high temperature corrosion are *semiconductors*; therefore they are n- or p-type oxides. To understand their main characteristics, which explain several times their application as *semiconductor electrodes*, we must discuss here some simple concepts of electrochemistry of semiconductors. These oxide semiconductors are also called *network solids*. These are formed from an essentially infinite array of atoms covalently bonded together. A consequence of the extended bonding network is that electrons in the solid occupy *energy bonds* rather than *energy levels*. Consider the energy level diagram of an atom, A, shown in Figure 6.7. The atomic energy levels are

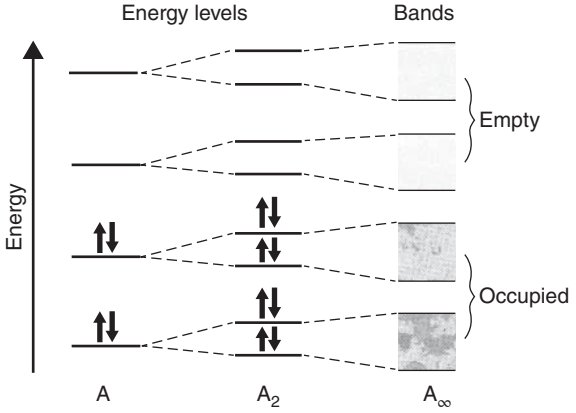


Figure 6.7 Energy bands of solids. A represents the atom of an element.

represented by lines, and occupancy by a pair of electrons is indicated by the paired arrows. If two A atoms are bonded together, simple molecular orbital theory dictates that each atomic level is split into two molecular energy levels, grouped as shown in Figure 6.7. There are as many molecular energy levels as there are atomic energy levels in the isolated atoms. When a very large number of atoms are bonded into a solid (e.g. Avogadro's number, a quantity typical of a macroscopic solid), each atomic energy level now splits into Avogadro's number of energy levels. The energy levels are grouped into energy bands. Within each band the energy separation between two energy levels becomes so minute that the energy band can be regarded as a continuum of energy levels. Each energy band also has a definite upper and lower limit, called *band edges*.

Of particular interest are the highest occupied and the lowest empty energy bands. If, for a given solid, these two bands are separated by a gap devoid of energy levels, called the *bandgap*, then the solid is either a semiconductor or an insulator. On the other hand, if the highest occupied and lowest empty energy bands overlap, then the solid is a metal. A second situation giving rise to metallic properties occurs when an energy band is partially filled with electrons. The juxtaposition of occupied and empty energy levels (i.e. no bandgap) is a necessary condition for the electrical conductivity of metals (see below).

From now on we shall consider just these two energy bands. In the language of solid-state physics, the highest occupied energy band is called *valence band*, and the lowest empty energy band the *conduction band* (Figure 6.8a). The upper edge of the valence band is marked by E_v and the lower edge of the conduction band by E_c. An extremely important parameter is the *bandgap energy*, E_{bg}, defined as the separation between the conduction and valence band edges. It is usually expressed in the energy unit electron volts. The bandgap energy distinguishes semiconductors from insulators. In general, solids and bandgap energies less than 3 eV are considered to be semiconductors, while insulators have bandgap energies larger than 3 eV.

Silicon and germanium comprise the only two important monoatomic semiconductors, but many useful binary compounds exist. They may be broadly classified according to group number combinations. Several metal oxides also behave as semiconductors; typical examples include TiO_2, ZnO, SnO_2, Fe_2O_3, and Cu_2O. Ternary combinations are known but are less commonly used.

In order for electrons to be mobile in a solid (the essence of electrical conductivity), they must be able to occupy a partially empty energy level within an energy band. In metals, empty levels are available immediately above the filled ones, and at room temperature it is easy for electrons to hop up to the empty levels and move under the impetus of an applied voltage. However, in semiconductors and insulators, the filled energy levels are separated from the empty ones by the bandgap. In this simple description, conduction is not possible.

Semiconductors can be made conductive either by putting extra electrons into the conduction band or by removing electrons from the valence band. Consequently, there are two modes of conduction in a semiconductor. The first is the movement of electrons through the (mostly empty) conduction band (Figure 6.8a). The second mode is an electron flow in the valence band, but its description differs in solid-state physics. Removal of an electron from the valence band creates a positively charged vacancy called a *hole* (Figure 6.8a). The hole can be regarded as the mobile entity because annihilation of a hole by a nearby electron effectively moves the hole over in space. So electrical current can be carried by either electrons in the conduction band or holes in the valence band, or by both types of charge carriers.

Mobile charge carriers can be generated by three different mechanisms: *thermal excitation*, *photoexcitation*, and *doping*. If the bandgap energy is sufficiently small, thermal excitation can promote an electron from the valence band to the conduction band (Figure 6.8a). Both the electron and the accompanying hole are mobile. As the average thermal energy at room temperature is 0.026 eV ($= kT$), this mechanism is important only for narrow bandgap semiconductors ($E_{bg} < 0.5$ eV).

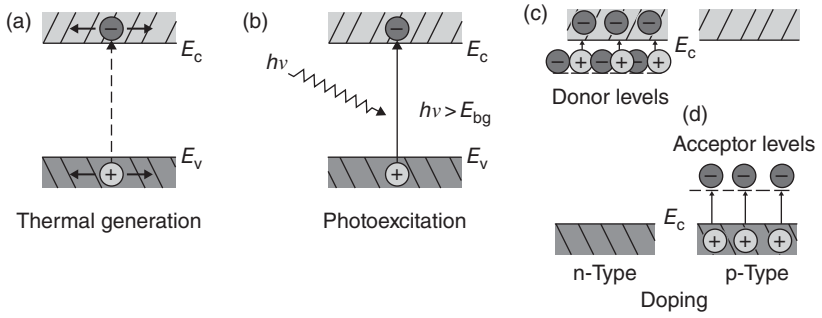


Figure 6.8 Mechanisms of charge carrier generation. (a) Thermal generation. (b) Photoexcitation. (c) Doping, n-type. (d) Doping, p-type.

In a similar manner, an electron can be promoted from the valence band to the conduction band upon the absorption of a photon of light (Figure 6.8b). A necessary condition is that the photon energy exceeds the bandgap energy ($h_\nu > E_{bg}$). This is the primary event in the conversion of sunlight to usable forms of energy. The bandgap energy therefore sets the condition for photon absorption. Defining λ_{bg} according to Eq. (6.64), wavelengths greater than λ_{bg},

$$\lambda_{bg}(\text{nm}) = \frac{1240}{E_{bg}}(\text{eV}) \tag{6.64}$$

are not absorbed by the semiconductor; it is transparent at those wavelengths. At wavelengths shorter than λ_{bg}, photons are adsorbed within a short distance of the semiconductor surface. The semiconductor thus exhibits a *threshold response* to light. One consideration in choosing a useful semiconductor is the range of solar wavelengths that are absorbed by the semiconductor. Theoretical calculations of the wavelength–intensity distribution of sunlight combined with the maximum power output by the solar cell have led to the prediction that maximum solar energy conversion efficiency will be obtained for $E_{bg} = 1.5 \pm 0.5$ eV (600 nm $< \lambda_{bg} <$ 1100 nm).

The third mechanism of generating mobile charge carriers is doping. Doping is the process of introducing new energy into the bandgap. Doping can be effected by either disturbing the stoichiometry of the semiconductor (such as partially reducing a metal oxide) or by substituting a foreign element into the semiconductor lattice. The classic example of the latter method is the introduction of group III or group V elements into group IV semiconductors. Two types of doping can be distinguished. For n-type doping, occupied donor levels are created very near the conduction band edge (Figure 6.8c). Electrons from the donor levels are readily promoted to the conduction band by thermal excitation. Electrons in the conduction band outnumber the few thermally generated holes in the valence band; hence, current is carried mainly by negative charge carriers. Likewise, p-type doping corresponds to the formation of empty acceptor levels near the valence band edge (Figure 6.8d). The acceptor levels trap electrons from the valence band, creating positive charge carriers. The donor and acceptor levels become charged due to loss or gain of electrons, but they are not charge carriers because they are fixed within the crystal lattice. Semiconductors are commonly described as *n-type* or *p-type* to indicate the dominant charge carrier; undoped semiconductors are referred to as *intrinsic semiconductors*.

A discussion of the Fermi level (alternatively called the Fermi energy) is crucial in electrochemistry of semiconductors because of the following key point: changes in the electrode potential correspond to changes in the position of the Fermi level with respect to a reference energy. The reference energy can be the energy of an electron in a vacuum, or it can be the Fermi level of a reference electrode. To keep the discussion qualitative, we will use the probability definition of the Fermi level. The *Fermi level* is the energy (E_f) at which the probability of an energy level being occupied by an electron is exactly 1/2. In metals, the Fermi level can be considered to be the tidemark of electrons in the energy band. Above the Fermi level the probability of occupancy drops to zero, and the energy levels are empty, while below E_f the energy levels are filled (probability $\rightarrow$ 1). However, in a semiconductor the Fermi level occurs in the bandgap (the definition does not require an energy level at E_f; it merely depends on a probability if an energy level were present). For an intrinsic (undoped) semiconductor, E_f occurs approximately midway between the conduction and valence band edges (Figure 6.9).

A second key point is that doping shifts the Fermi level with respect to band edges. N-type doping results in a shift of E_f toward E_c (Figure 6.9). The shift is consistent with the fact that the probability of occupancy of energy levels at E_c has increased; there are more electrons in the conduction band. Thus the energy at which the probability equals 1/2 must be closer to E_c. Likewise, p-type doping shifts E_f nearer to E_v (Figure 6.9).

As the doping level increases (as measured by the number of mobile charge carriers per cm^3), E_f shifts closer and closer to the band edges. A very high doping level causes E_f to move into the conduction or valence band; at this point the semiconductor becomes a metal.

For a given semiconductor with a fixed doping level, the Fermi level can be manipulated by the applied potential.

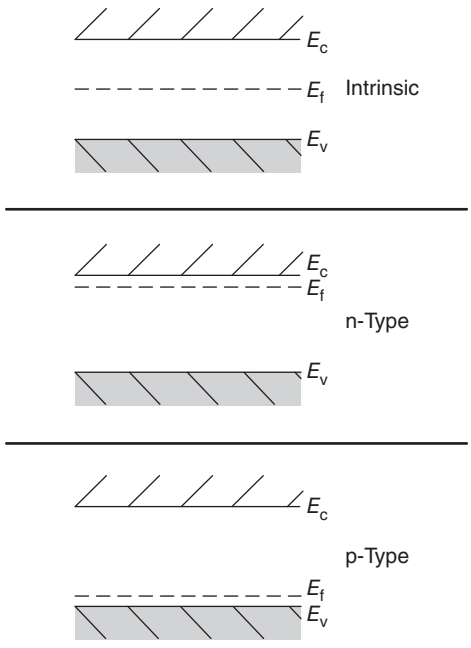


Figure 6.9 The Fermi level and the effects of doping.

Consider a semiconductor electrode connected externally to a reference electrode; both electrodes are immersed in the same electrolyte. In such a situation, $E_f^{sc} = E_f^{reference}$, i.e. the Fermi levels of the two electrodes match in energy. Now if the semiconductor electrode is biased (by means of a battery or a potentiostat) at a potential one volt positive with respect to the reference electrode, the Fermi level of the semiconductor shifts down in energy with respect to the reference Fermi level. The downward shift arises from the lower energy of electrons in a region of more positive (less negative) potential. Furthermore, the energy difference between the Fermi levels ($E_f^{sc} = E_f^{reference}$) is exactly one electron volt (by definition). Biasing the semiconductor negative raises the semiconductor Fermi level above the reference Fermi level. Thus, it is possible to control the semiconductor Fermi level with respect to solution energy levels by means of the applied potential. In the bulk of the semiconductor, the Fermi level remains fixed relative to E_c and E_v, but the situation is different near the electrolyte interface.

We have developed here some simple concepts of solid-state physics that apply to a particular class of solids. The reader should note that although the terminology is foreign to corrosion, the concepts are not. These concepts will be useful in explaining how a semiconductor electrode responds to perturbations of light and potential as well as how its electronic structure and excited-state kinetic scheme aids to understand several corrosion mechanisms and their effects.

6.12 Conduction Processes in Ionic Oxides

The design of new oxide solid electrolytes, processing, and development of their applications require that careful consideration be given to the electrical properties of the electrolyte chosen for the study. In an oxide conductor, the electrical conductivity can be the result of either mobile electronic or ionic charge carriers. In general, both types of conduction processes will occur simultaneously, and so the total conduction process needs to be characterized in terms of the partial conductivity of each of the mobile species. Oxide conductors are different from electronically conducting semiconductors (such as Si- or Ge-based semiconductors) in that the composition of the oxide can be affected by variations in the surrounding environment, which, in turn, can modify the magnitude of the conductivity for some or all of the mobile charge-carrying species. It then becomes important to properly define the oxygen activity at which any particular conductivity is used or measured.

In this section, we shall first consider the quasi-chemical description of the defect structure and see how variations in the environment give rise to variations in the concentrations of defects that participate in the conduction processes of the oxide. Second, we shall develop some transport equations that describe conduction processes that occur in oxide solid electrolytes. These equations are useful to characterize processes and devices in which oxide solid electrolytes are applied (e.g. high temperature fuel cells, solid oxide electrolyzers, resistance elements in high temperature electrical furnaces, electrodes in magnetohydrodynamic power generators, electrically renewable oxygen getters, solid oxide auto exhaust sensors, etc.) and to give information on the high temperature processes occurring in aggressive environments in which ionic oxide corrosion products play a key role.

We will chose as an example for our quasi-chemical defect discussion a generalized material that is similar in behavior to those used as electrolytes in oxide galvanic cell applications. The compound of interest will be MO_2 that has been doped with a significant amount of another oxide, AO. It will be assumed that the intrinsic defects in pure MO_2 are of the Schöttky type, i.e. vacancies on the anion and cation sublattices (Sequeira 1984). It should be noted that fundamentals of lattice defects in metal compounds are deeply described in Chapter 4, and the reader should take it into account when reading this and the next section.

Kröger–Vink notation (1956) will be used to describe the various defects. Therefore, V_M will represent a metal vacancy and V_O an oxygen vacancy. Brackets are used to indicate concentrations. Charges are attributed relative to the perfect lattice, i.e. V'_M is a metal vacancy singly negatively charged relative to the lattice, and $V_O^{\bullet\bullet}$ is an oxygen vacancy doubly positively charged relative to the lattice. Concentrations of holes or electrons are denoted by p or n, respectively.

The incorporation of the dopant, AO, into the oxide structure of MO_2 may be described by the following reaction:

$$AO \rightarrow A''_M + V_O^{\bullet\bullet} + O_O \tag{6.65}$$

The above reaction describes the generation of a cation with an A atom occupying it, being doubly negatively charged relative to a normal M atom occupying the site. It also includes the generation of the two anion sites necessary to maintain the crystal structure. One of these sites is occupied by an oxygen ion; the other is vacant, leaving a net positive charge relative to the lattice.

The incorporation of oxygen from the gas phase into the solid MO_2 is given as follows:

$$\left(\frac{1}{2}\right) O_2 + V_O^{\bullet\bullet} + 2e^- \rightleftharpoons O_O; \quad k_1 = \frac{1}{P_{O_2}^{1/2}[V_O^{\bullet\bullet}]n^2} \tag{6.66}$$

where k_1 is the quasi-chemical equilibrium constant for the reaction. The intrinsic Schöttky equilibrium of the compound MO_2 is given by the following null reaction:

$$\text{null} \rightleftharpoons V_M'''' + 2V_O^{\bullet\bullet}; \quad k_s = [V_M''''][V_O^{\bullet\bullet}]^2 \tag{6.67}$$

The null reaction describing the intrinsic electronic equilibrium is

$$\text{null} \rightleftharpoons h^{\bullet} + e'; \quad k_i = np \tag{6.68}$$

Charge neutrality must be maintained throughout the crystal; therefore, the electroneutrality condition (ENC) is

$$n + 4[V_M''''] + 2[A_M''] = p + 2[V_O^{\bullet\bullet}] \tag{6.69}$$

We now have five equations describing interrelationships between the five predominant defect species in the structure of the oxide. These equations can, in general, be solved rigorously to determine the oxygen pressure dependence of the concentration of the various defect species. However, a simpler method will be employed (Brouwer 1954; Sequeira 1983). We shall look at p_{O_2} regions in which the ENC can be approximated by a pairwise equality between two defects. The strength of this method lies in its application to practical situations where, over wide p_{O_2} regions, there are generally orders of magnitude differences between the concentrations of a predominant defect pair and the minority defects.

Firstly, let us take the case of p_{O_2}. In this situation

$$[V_O^{\bullet\bullet}] \gg [V_M''''] \tag{6.70}$$

so that the ENC may be approximated by

$$n = 2[V_O^{\bullet\bullet}] \tag{6.71}$$

The above ENC is the result of the incorporation reaction for oxygen into the oxide, the Schöttky equilibrium, and the intrinsic electronic equilibrium. As p_{O_2} goes down, k_1 requires that $[V_O^{\bullet\bullet}]$ increase. In turn, this increase requires, through the Schöttky constant k_s, that $[V_M'''']$ decrease, thus leaving e' and A_M'' as the two negatively charged species. Eventually, the concentration of oxygen vacancies exceeds that of A_M'', which is fixed by the dopant level, and electrical neutrality must be maintained by increasing n. The intrinsic electronic equilibrium requires p to decrease as n increases.

If we put the approximated ENC into Eq. (6.66), we have for the oxygen pressure dependence of oxygen vacancies

$$[V_O^{\bullet\bullet}] = \frac{1}{(4k_1)^{1/3}} p_{O_2}^{-1/6} \tag{6.72}$$

Since $n = 2[V_O^{\bullet\bullet}]$, there is the same pressure dependence for the electrons, their concentration being just twice that of the oxygen vacancies. Using the Schöttky equilibrium, the p_{O_2} dependence of the metal vacancy concentration is

$$[V_M''''] = k_s(4k_1)^{2/3} p_{O_2}^{1/3} \tag{6.73}$$

The intrinsic electronic equilibrium and Eq. (6.72) are combined to give

$$p = (2k_i k_1)^{2/3} p_{O_2}^{1/6} \tag{6.74}$$

for the p_{O_2} dependence of the hole concentration.

At some intermediate pressure range, it is possible, due to the level of doping and the method of incorporation of A into the MO_2 lattice, to approximate the ENC with

$$[V_O^{\bullet\bullet}] = [A_M''] \tag{6.75}$$

The result of equating the concentrations of dopant and oxygen vacancies is that, over this pressure range, the concentration of oxygen vacancies is independent of oxygen pressure, fixed only by the dopant level.

By applying procedures similar to that for the previous case, the pressure–concentration dependences of the other defects are evaluated for this region. These are given by

$$[V_M''''] = \frac{k_s}{[A_M'']^2} \tag{6.76}$$

$$n = \frac{1}{(k_1[A_M''])^{1/2}} p_{O_2}^{-1/4} \tag{6.77}$$

$$p = k_i(k_1[A_M''])^{1/2} p_{O_2}^{1/4} \tag{6.78}$$

As the oxygen pressure continues to rise, we see that the concentration of holes continues to rise; however, the metal vacancy concentration is independent of oxygen pressure. The magnitude of $[V_M'''']$ is determined solely by the Schöttky constant and the oxygen vacancy concentration. At some sufficiently high p_{O_2}, it is then possible to approximate the ENC in the following manner:

$$p = 2[A_M''] \tag{6.79}$$

A marked change is noted in the behavior of the anion and cation vacancy pressure dependences. These are

$$[V_O^{\bullet\bullet}] = \frac{4[A_M'']^2}{k_1 k_i^2} p_{O_2}^{-1/2} \tag{6.80}$$

$$[V_M''''] = \frac{k_s k_1^2 k_i^4}{16[A_M'']^2} p_{O_2} \tag{6.81}$$

During this pressure region, the electron concentration is constant, determined by the interaction with holes through the intrinsic equilibrium

$$n = \frac{k_i}{2[A_M'']} \tag{6.82}$$

Finally, at some very high p_{O_2}, the situation occurs where

$$[V_M''''] \gg [A_M''] \tag{6.83}$$

and ENC can be approximated by

$$p = 4[V_M''''] \tag{6.84}$$

For this very high p_{O_2} pressure region, the various defect concentrations are described by

$$[V_O^{\bullet\bullet}] = \frac{(4k_s)^2}{k_1 k_i^2} p_{O_2}^{-1/10} \tag{6.85}$$

$$[V_M''''] = \frac{(k_1 k_i^2)^2}{(4^4 k_s^3)} p_{O_2}^{1/5} \tag{6.86}$$

$$p = \frac{(k_1 k_i^2)^2}{(4k_s)^3} p_{O_2}^{1/5} \tag{6.87}$$

$$n = k_1 \left(\frac{k_i}{4k_s} \right)^3 p_{O_2}^{-1/5} \tag{6.88}$$

The defect concentrations for the various pressure regions are schematically given in Figure 6.10.

The important result of this discussion comes from an examination of the intermediate pressure region. Across this region, hopefully an extended p_{O_2} range, the majority defect is ionic, and the concentrations of electronic defects can be substantially depressed below the level of majority defect. If the mobility of the ionic defect is sufficiently high, then it would be expected that the conduction process in the intermediate pressure range would be primarily ionic in nature.

It is well known that for a material to be suitable as an electrolyte in galvanic cell measurements, its conductivity must be primarily ionic. As such, a material similar to that of MO_2 doped with AO might be capable of being used as an electrolyte for a high temperature solid-state galvanic cell that is operated in an environment equivalent to the intermediate oxygen partial pressure range.

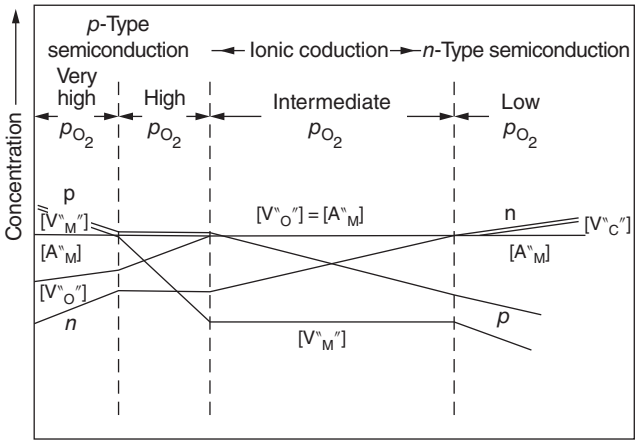


Figure 6.10 Defect concentration versus p_{O_2} for an oxide solid electrolyte (logarithmic scale).

The above discussion can be readily applied to a material that contains Frenkel instead of Schöttky defects as the intrinsic atomic defect structure (Sequeira 1983). In either case, the analysis predicts a region where the atomic defects are independent of oxygen pressure.

The total conduction process that occurs in an oxide solid electrolyte is, in general, mixed in nature, i.e. contributions from electronic and ionic carriers. The mixed nature of the process can be inferred from the results above where we saw that over all pressure ranges except the intermediate one, the concentration of an electronic species is equal to or greater than the concentration of the predominant ionic species. It is then necessary to describe the partial current density for each of the participating species in order to characterize the overall conduction process.

A procedure that largely follows that of Heyne (1968) will be used to describe the conduction processes in an oxide. The description of the partial current densities will be done by first considering a general transport equation. Then, specific cases will be examined describing the partial electronic, ionic, and total current densities.

6.12.1 General Partial Current Density

Let us define the partial current density, j_k, which is the contribution to the total current that is carried out by species k. The species has charge $z_k q$, where z_k is the valence of the species and q is the absolute electronic charge. The concentration of the species will be described by n_k, and the mobility of the species will be v_k. The diffusion coefficient associated with the species will be D_k.

As such, the partial current density may be expressed as

$$j_k = -n_k |z_k| q v_k (\text{grad}\, \psi) - D_k |z_k| q \,\text{grad}\, n_k \tag{6.89}$$

Here, ψ is the electrical potential.

The *electrochemical potential* for species k is given by

$$\tilde{\mu}_k = \mu_k + |z| q\psi \tag{6.90}$$

where

$$\mu_k = \mu_k^0 + k_B T \ln n_k \tag{6.91}$$

The Einstein relationship between mobility and the diffusion coefficient is given by

$$D_k = \frac{k_B T}{|z_k| q} v_k \tag{6.92}$$

where k_B is the Boltzmann constant and T the absolute temperature.

Here it should be noted that the expression for the partial current density contains (by assumption) no interaction or cross-terms as would be expected from the generalized descriptions of forces and fluxes as given by irreversible thermodynamics. The only interactions that are allowed are those that occur through the electrical potential, which means that apart from fluxes under electrical fields, the movement of one species does not influence the flow of another.

The gradient in the electrochemical potential is

$$\operatorname{grad} \widetilde{\mu}_{\mathrm{k}} = k_{\mathrm{B}} T \frac{\operatorname{grad} n_{\mathrm{k}}}{n_{\mathrm{k}}} + |z_{\mathrm{k}}|\, q \operatorname{grad} \psi \tag{6.93}$$

Putting the Einstein equation into the expression for the partial current density yields

$$j_{\mathrm{k}} = -n_k\, |z_{\mathrm{k}}|\, q v_{\mathrm{k}} (\operatorname{grad} \psi) - \nu_{\mathrm{k}} kT \operatorname{grad} n_{\mathrm{k}} \tag{6.94}$$

which may be simplified to

$$\frac{j_{\mathrm{k}}}{n_{\mathrm{k}}} = -v_{\mathrm{k}} \left[\operatorname{grad} \psi\, |z_{\mathrm{k}}|\, q + \frac{k_{\mathrm{B}} T}{n_{\mathrm{k}}} \operatorname{grad} n_{\mathrm{k}} \right] \tag{6.95}$$

Recognizing that the term in brackets is just the gradient of the electrochemical potential, we have

$$\frac{j_{\mathrm{k}}}{n_{\mathrm{k}}} = -v_{\mathrm{k}} \operatorname{grad} \widetilde{\mu}_{\mathrm{k}} \tag{6.96}$$

Rewriting the above equation we obtain

$$j_{\mathrm{k}} = -n_{\mathrm{k}} v_{\mathrm{k}} |z_{\mathrm{k}}|\, q \frac{\operatorname{grad} \widetilde{\mu}_{\mathrm{k}}}{|z_{\mathrm{k}}|\, q} \tag{6.97}$$

Defining the conductivity of species k as

$$\sigma_{\mathrm{k}} \equiv n_{\mathrm{k}} v_{\mathrm{k}} |z_{\mathrm{k}}|\, q \tag{6.98}$$

and putting the conductivity into Eq. (6.97) gives us the desired result

$$j_{\mathrm{k}} = \frac{-\sigma_{\mathrm{k}}}{|z_{\mathrm{k}}| q} \operatorname{grad} \widetilde{\mu}_{\mathrm{k}} \tag{6.99}$$

The partial current density for some particular species is proportional to the gradient of the electrochemical potential for that species.

6.12.2 Electronic Current Density

Let us now apply the expression for the partial current density to the case of current being carried by electronic species, i.e. hole or electron current. The total electronic current density is

$$J_{\mathrm{e}} = j_{\mathrm{n}} - j_{\mathrm{p}} \tag{6.100}$$

Using the general expression for a partial current density, we have

$$J_{\mathrm{e}} = -\frac{\sigma_{\mathrm{n}}}{q} \operatorname{grad} \widetilde{\mu}_{\mathrm{n}} + \frac{\sigma_{\mathrm{p}}}{q} \operatorname{grad} \widetilde{\mu}_{\mathrm{p}} \tag{6.101}$$

The electrochemical potential of the holes or electrons is equivalent to the Fermi energy that is commonly used in semiconductor physics. Expanding and simplifying Eq. (6.101) gives

$$J_{\mathrm{e}} = -\frac{(\sigma_{\mathrm{n}} + \sigma_{\mathrm{p}})}{q} \operatorname{grad} \widetilde{\mu}_{\mathrm{n}} + \frac{\sigma_{\mathrm{p}}}{q} (\operatorname{grad} \widetilde{\mu}_{\mathrm{n}} + \operatorname{grad} \widetilde{\mu}_{\mathrm{p}}) \tag{6.102}$$

Excluding processes such as injection and extraction that occur at or near p–n junctions or electrodes, we shall consider that the thermodynamic equilibrium between electrons and holes is not disturbed by the flow of particles. As such, we see that

$$\operatorname{grad} \widetilde{\mu}_{\mathrm{n}} + \operatorname{grad} \widetilde{\mu}_{\mathrm{p}} = 0 \tag{6.103}$$

so that

$$J_{\mathrm{e}} = \frac{-(\sigma_{\mathrm{n}} + \sigma_{\mathrm{p}})}{q} \operatorname{grad} \widetilde{\mu}_{\mathrm{n}} \tag{6.104}$$

or

$$J_{\mathrm{e}} = -\frac{\sigma_{\mathrm{e}}}{q} \operatorname{grad} \widetilde{\mu}_{\mathrm{n}} = \frac{\sigma_{\mathrm{e}}}{q} \operatorname{grad} \widetilde{\mu}_{\mathrm{p}} \tag{6.105}$$

where $\sigma_{\mathrm{e}} = \sigma_{\mathrm{p}} + \sigma_{\mathrm{n}}$. We have the result that the total electronic current density is proportional to the gradient in either the hole or electron electrochemical potentials.

6.12.3 Ionic Current Density

Consider the transport of electric charge by two ionic species. The total ionic current density is given by

$$J_{\mathrm{I}} = j_2 - j_1 \tag{6.106}$$

where j_1 and j_2 are the partial ionic current densities of the anions and cations, respectively. By expressing the partial ionic currents in terms of the general Eq. (6.99), expanding, and simplifying, the total ionic current density is determined to be

$$J_{\mathrm{I}} = \frac{-(\sigma_1 + \sigma_2)}{|z_2|\, q} \operatorname{grad} \widetilde{\mu}_1 + \frac{\sigma_2}{q} \left(\frac{1}{|z_1|} \operatorname{grad} \widetilde{\mu}_1 + \frac{1}{|z_2|} \operatorname{grad} \widetilde{\mu}_2 \right) \tag{6.107}$$

Again, it will be postulated that a steady-state current flow does not disturb the thermodynamic equilibrium of the ions. Let us consider this equilibrium by first describing a reaction between a cation, anion, and their resulting neutral combination in a crystal:

$$|z_2|\, \mathrm{M}^{z_1} + |z_1|\, \mathrm{X}^{z_2} \leftrightharpoons \mathrm{MX} \tag{6.108}$$

where $MX = M_{|z_2|}X_{|z_1|}$. Equilibrium requires that

$$|z_2|\,\widetilde{\mu}_1 + |z_1|\,\widetilde{\mu}_2 = \mu_{MX} \tag{6.109}$$

where $1 \equiv M$ and $2 \equiv X$. Taking the gradient of the above expression gives

$$|z_2|\,\text{grad}\,\widetilde{\mu}_1 + |z_1|\,\text{grad}\,\widetilde{\mu}_2 = \text{grad}\,\mu_{MX} \tag{6.110}$$

For the case of small defect concentrations, $\text{grad}\,\mu_{MX} \approx 0$. Therefore,

$$|z_2|\,\text{grad}\,\widetilde{\mu}_1 + |z_1|\,\text{grad}\,\widetilde{\mu}_2 = 0 \tag{6.111}$$

Combining this result with Eq. (6.107), it comes that the total ionic current density is proportional to the gradient in the electrochemical potential of one ion:

$$J_I = \frac{-(\sigma_1 + \sigma_2)}{|z_2|\,q}\text{grad}\,\widetilde{\mu}_2 = \frac{\sigma_1 + \sigma_2}{|z_1|\,q}\text{grad}\,\widetilde{\mu}_1 \tag{6.112}$$

6.12.4 Total Current Density

Let us now combine the previous results and describe the total current through an oxide solid electrolyte. The total current may be expressed as

$$J_{tot} = J_I + J_e = \frac{\sigma_e}{q}\text{grad}\,\widetilde{\mu}_p - \frac{\sigma_i}{|z_2|\,q}\text{grad}\,\widetilde{\mu}_2 \tag{6.113}$$

in terms of the anion and hole electrochemical potential gradients. If a current flow does not disturb the thermodynamic equilibrium between the various species in the specimen, the equilibrium is expressed by

$$X^{z_2} + |z_2|\,h^{\bullet} \leftrightharpoons X \tag{6.114}$$

or, in terms of chemical potentials,

$$\widetilde{\mu}_2 + |z_2|\,\widetilde{\mu}_p = \mu_X \tag{6.115}$$

By combining the above equilibrium with Eq. (6.113), we arrive at the expression describing the total conduction process through the oxide solid electrolyte:

$$J_{tot} = \frac{\sigma_{tot}}{q}\text{grad}\,\widetilde{\mu}_p - \frac{\sigma_i}{|z_2|\,q}\text{grad}\,\widetilde{\mu}_X \tag{6.116}$$

where $\sigma_{tot} = \sigma_i + \sigma_e$.

The equations examined in this section that allow the characterization of the total conduction process in an oxide electrolyte, over a wide range of oxygen partial pressures in both electronic and ionic conduction regimes, can be applied in several electrochemical situations, namely, that where current is supplied to reversible electrodes at the interfaces of an oxide conductor and that of the ionic conductor with ohmic contacts but no current supply. In the next section, we analyze these situations.

6.13 Common Solid-State Electrochemical Situations

In the previous section, the quasi-chemical description of the defect structure in an oxide solid electrolyte was considered. It was shown how variations in the environment give rise to variations in the concentration of defects that participate in the conduction process of the oxide. Then, the relevant transport equations that describe the conduction processes that occur in oxide solid electrolytes were developed.

To use the electrical transport equations, the nature of the interfaces between the oxide conductor and the applied electrodes must be considered since the transfer of holes, electrons, or ions at interfaces is not always easy. In general, there are two types of interfaces: ohmic, i.e. those that have the same potential drop independent of current flow, and blocking or rectifying, i.e. those that allow significant current of some type to pass in only one direction.

Not only must the physical nature of the interface be considered, but the chemical environment that the electrodes define for the oxide is also important. The conductivity that was defined for an arbitrary species in the description of the transport equation was a function of both the concentration and its mobility. We shall assume here that as long as the defect concentrations are low and there is no significant interaction between defects, the mobility of any particular species will be independent of its concentration. This may be expressed as

$$\sigma \equiv \upsilon_k n_k |z_k|\,q \approx K' n_k \tag{6.117}$$

or

$$\upsilon_k \neq \upsilon(n_k) \tag{6.118}$$

We have seen that the oxygen partial pressure has a significant effect on the concentrations of the various defects: if the above assumption is correct, then the conductivity of a particular species under various boundary conditions is defined by changing oxygen pressure and should behave in a manner similar to the dependence of the concentration under pressure.

Let us now apply the electrical transport equations to some common electrochemical cases, namely, that where current is supplied to reversible electrodes at the interfaces of an oxide conductor and that of the ionic conductor with ohmic contacts but no current supply. Moreover, let us see what information may be obtained from this application. This is the purpose of this section.

6.13.1 Ohmic Contacts with a Current Supply

The first situation to be examined is that of ohmic contacts, reversible electrodes, and a defined oxygen pressure.

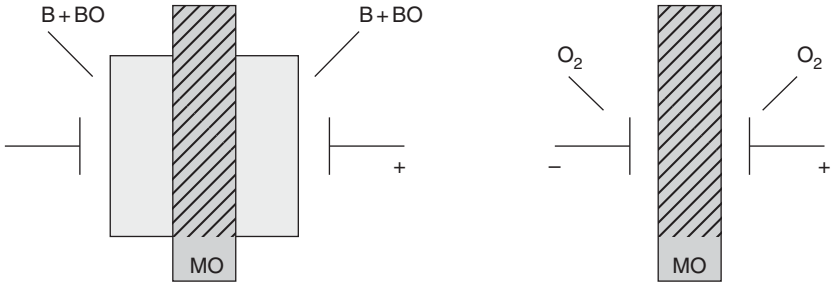


Figure 6.11 Ionic conductor with ohmic contacts.

Experimental geometries that meet these requirements are given in Figure 6.11. Figure 6.11a shows a case in which both electrodes are composed of a coexistence mixture of a metal B and its oxide BO. Case b in Figure 6.11 is that where inert contacts are made with the oxide and the general environmental oxygen pressure is controlled. In either case, the oxide of interest will be MO_2 that has been doped with a significant amount of another oxide, AO.

For the above condition, the oxide is everywhere in equilibrium with a defined oxygen pressure; as such, no concentration gradients exist in the oxide. We have seen that the electrochemical potential for the participating species 1 is given by

$$\breve{\mu} = \mu_1 + |z_1|\, q\psi \tag{6.119}$$

and

$$\mu_1 = \mu_1^0 + kT \ln n_1 \tag{6.120}$$

where k is the Boltzmann constant, T the absolute temperature, and n_1 the concentration of species 1.

The gradient of the electrochemical potential is

$$\operatorname{grad} \widetilde{\mu}_1 = \frac{kT}{n_1} \operatorname{grad} n_1 + |z_1|\, q \operatorname{grad} \psi \tag{6.121}$$

but the condition of equilibrium requires that grad $n_1 = 0$. Therefore,

$$\operatorname{grad} \widetilde{\mu}_1 = |z_1|\, q \operatorname{grad} \psi = -|z_1| qE \tag{6.122}$$

where E is the electric field given by

$$E = -\operatorname{grad} \psi \tag{6.123}$$

As such, the electronic current density may be written as

$$J_e = -\frac{\sigma_e}{q} \operatorname{grad} \widetilde{\mu}_n = \sigma_e E \tag{6.124}$$

which is just ohmic behavior. Likewise, for the ionic contribution to the conductivity (charge transported by two ionic species),

$$J_I = -\frac{\sigma_1 + \sigma_2}{|z_1|\, q} \operatorname{grad} \widetilde{\mu}_1 = (\sigma_1 + \sigma_2)\, E \tag{6.125}$$

The above expressions indicate that as long as the electrodes do not become current limiting due to material transport problems, the current through the oxide is linearly proportional to the applied voltage.

The determination of the relative magnitudes of the partial ionic or electronic current densities could be accomplished by measuring the uptake or output of oxygen at the cathode or anode, and comparing this, through the Faraday constant, to the total current flowing in the external circuit. The measurement could be easily done by monitoring the weight change of the metal–metal oxide electrodes, the cathode losing weight, and the anode gaining weight. The relationship between the magnitudes of the various current densities may be expressed in terms of the transference number. Let us define the *transference number* of a species as that fraction of the total current carried by that species. As such, the transference number for species of type k is expressed by

$$t_k = \frac{J_k}{\sum_k J_k} = \frac{\sigma_k}{\sum_k \sigma_k} \tag{6.126}$$

Transfer numbers are subject to the constraint $\sum_K t_k = 1$.

6.13.2 Ohmic Contacts with no Current Supply

Let us now consider the geometry defined by Figure 6.12.

In this case, the oxide specimen is between two fixed chemical potentials of oxygen, defined by the coexistence of the two different metal–metal oxide mixtures, and there is no current supplied by an external source. As such, the total current through the specimen is zero so that

$$J_{tot} = 0 = \frac{\sigma_T}{q} \operatorname{grad} \widetilde{\mu}_p - \frac{\sigma_i}{|z_2|\, q} \operatorname{grad} \widetilde{\mu}_X \tag{6.127}$$

or

$$\operatorname{grad} \widetilde{\mu}_p = \frac{\sigma_i}{\sigma_T} \frac{1}{|z_2|} \operatorname{grad} \widetilde{\mu}_X \tag{6.128}$$

in terms of the anion and hole electrochemical potential gradients.

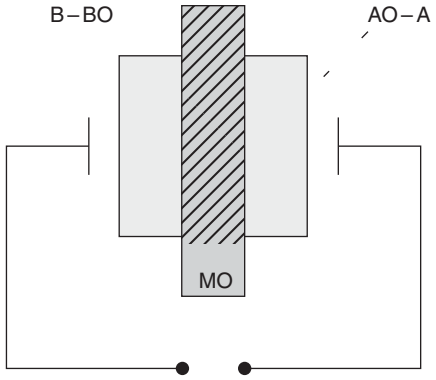


Figure 6.12 Ionic conductor with ohmic contacts but no current supply.

Using the intrinsic electronic equilibrium,

$$\text{grad}\,\tilde{\mu}_n = -\text{grad}\,\tilde{\mu}_p \tag{6.129}$$

to express Eq. (6.128) in terms of all negatively charged species, we have

$$\text{grad}\,\tilde{\mu}_n = -\frac{1}{|z_2|}t_{ion}\,\text{grad}\,\tilde{\mu}_X \tag{6.130}$$

having remembered that $\sigma_i/\sigma_T = t_{ion}$.

Assuming that no injection or extraction processes are occurring at the boundaries, we can write for grad $\tilde{\mu}_n$

$$\text{grad}\,\tilde{\mu}_n = q\,\text{grad}\,\psi \tag{6.131}$$

Substituting this in Eq. (6.130), converting to planar geometries so that there is only a one-dimensional variation to $\tilde{\mu}_X$, and integrating between the boundaries, we have

$$\int_I^{II} d\psi = -\frac{1}{|z_2|q}\int_I^{II} t_{ion}\,d\tilde{\mu}_X \tag{6.132}$$

However, the left-hand integral

$$\int_I^{II} d\psi = \psi^{II} - \psi^{I} = \varepsilon \tag{6.133}$$

is just the difference in electrical potential between the two boundaries. As such, Eq. (6.132) is given by

$$\varepsilon = -\frac{1}{|z_2|q}\int_I^{II} t_{ion}\,d\tilde{\mu}_X \tag{6.134}$$

In terms of an oxide conductor with $|z_2| = 2$ and $\tilde{\mu}_X = \tilde{\mu}_0 = \frac{1}{2}\mu_{O_2}$, we arrive at the well-known equation of Wagner (1935) for electrolytes of mixed conduction:

$$\varepsilon = -\frac{1}{4q}\int_{p_{O_2}^{I}}^{p_{O_2}^{II}} t_{ion}\,d\mu_{O_2} \tag{6.135}$$

If the potential difference is small so that t_{ion} is approximately constant and can be replaced with an average value, we can integrate the r.h.s. to give

$$\varepsilon = -\frac{\bar{t}_{ion}}{4q}\left(\mu_{O_2}^{II} - \mu_{O_2}^{I}\right) \tag{6.136}$$

Using for the chemical potential of oxygen

$$\mu_{O_2} = \mu_{O_2}^0 + kT\ln p_{O_2} \tag{6.137}$$

we write for the e.m.f. generated by a chemical potential difference

$$\varepsilon = -\frac{\bar{t}_{ion}}{4q}kT\ln\frac{p_{O_2}^{II}}{p_{O_2}^{I}} \tag{6.138}$$

Equation (6.138) now affords another possibility for determining the relative magnitudes of the electronic and ionic conductivities. If one were to use two metal–metal oxide mixtures with known thermodynamic potentials, an expected ε, based upon the assumption that t_{ion} was unity, could be calculated. By then comparing this with the actually measured ε, the transference number for ionic conduction could be calculated from

$$t_{ion} = \frac{\varepsilon_{meas}}{\varepsilon_{theor}} \tag{6.139}$$

However, we again encounter the problem that when $t_{ion} \gg 0.99$, errors in the thermodynamic potential determinations can negate the ability to accurately determine transference numbers of low-level electronic conduction.

6.13.3 Blocking or Polarizing Electrodes

The direct determination of electronic conductivities can be accomplished by use of a geometry employing a blocking or polarizing electrode. Such a geometry is shown in Figure 6.13.

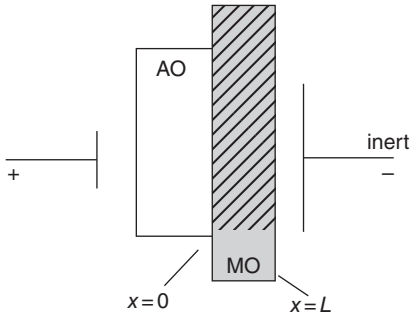


Figure 6.13 Blocking or polarizing electrode.

In the blocking electrode case, a potential less than the decomposition potential of the specimen is applied between an inert polarizing electrode and one that behaves reversibly at a fixed chemical potential of oxygen. Initially, some ionic current flow exists as the interface between the polarizing electrode and the electrolyte is depleted of oxygen and as a shift occurs in the ionic distribution within the electrolyte. However, as the ionic charge redistribution occurs, a reverse potential builds up to eventually prevent any further ionic current; at this time, the steady-state current flowing in the external circuit will be due to electron or hole conduction through the electrolyte.

The decomposition voltage for an oxide electrolyte is that voltage corresponding to the energy for the reaction

$$O_O \rightarrow V_O^{\bullet\bullet} + 2e' + \frac{1}{2} O_2 \tag{6.140}$$

For the case of calcia-stabilized zirconia, for example, the decomposition voltage is approximately 2.16 V.

We shall now develop an expression for the voltage–current relationship during steady-state polarized conduction for an oxide electrolyte. The method used shall be similar to that first put forward by Patterson et al. (1967).

The partial current density for a species is given by

$$j_i = -\frac{\sigma_i}{|z_1|q} \text{grad}\, \tilde{\mu}_1 \tag{6.141}$$

At steady state in the polarized condition, the current of ions is zero, i.e. $j_{ion} = 0$, so that $\tilde{\mu}_{O''} = 0$. As such, the steady-state current is given by the sum of the partial current densities of the holes and electrons:

$$J_{ss} = j_p - j_n = \frac{\sigma_n}{q} \text{grad}\, \tilde{\mu}_n - \frac{\sigma_p}{q} \text{grad}\, \tilde{\mu}_p \tag{6.142}$$

From the equilibrium of the oxide electrolyte with its environment, we can write

$$\frac{1}{2} O_2 + 2e' \rightarrow O'' \tag{6.143}$$

giving

$$\frac{1}{2} \mu_{O_2} + 2\tilde{\mu}_n = \tilde{\mu}_{O''} \tag{6.144}$$

and

$$\frac{1}{2} \text{grad}\, \mu_{O_2} + 2 \text{grad}\, \tilde{\mu}_n = -\text{grad}\, \tilde{\mu}_{O''} \tag{6.145}$$

However, due to the polarized condition, we have seen

$$-\frac{1}{4} \text{grad}\, \mu_{O_2} = \text{grad}\, \tilde{\mu}_n = -\text{grad}\, \tilde{\mu}_p \tag{6.146}$$

The last term in Eq. (6.146) arises from the intrinsic equilibrium that states

$$\text{grad}\, \tilde{\mu}_n + \text{grad}\, \tilde{\mu}_p = 0 \tag{6.147}$$

Putting Eq. (6.146) into the expression for steady-state current (Eq. (6.142)), we have

$$J_{ss} = -\frac{\sigma_n}{4q} \text{grad}\, \mu_{O_2} - \frac{\sigma_p}{4q} \text{grad}\, \mu_{O_2} \tag{6.148}$$

If we now consider planar geometries with only an x component to the gradient, then

$$J_{ss} = -\frac{\sigma_n}{4q} \frac{d\mu_{O_2}}{dx} - \frac{\sigma_p}{4q} \frac{d\mu_{O_2}}{dx} \tag{6.149}$$

$$J_{ss} = -\frac{(\sigma_n + \sigma_p)}{4q} \frac{d\mu_{O_2}}{dx} \tag{6.150}$$

Since, at steady state, the current density is independent of position, the above is integrated to give

$$J_{ss}(L) = -\frac{1}{4q} \int_{p_{O_2}}^{\mu_{O_2}^{L}} (\sigma_n + \sigma_p) d\mu_{O_2} \tag{6.151}$$

where L is length of the specimen and the limits of integration are the chemical potentials of oxygen at the two boundaries. Equation (6.146) may be written in terms of a one-dimensional variation,

$$d\tilde{\mu}_n = -d\tilde{\mu}_p = -\frac{1}{4} d\mu_{O_2} \tag{6.152}$$

and if one considers the case of no external field and low concentration of defects, then the above may be expressed as follows:

$$d\tilde{\mu}_n = kT\, d\ln n = -\frac{1}{4}\, d\mu_{O_2}$$

$$d\tilde{\mu}_p = kT\, d\ln p = \frac{1}{4}\, d\mu_{O_2} \tag{6.153}$$

These may be integrated between limits corresponding to the concentrations and oxygen potentials at the boundaries; then, if the concentration of the upper limit is expressed as a function of the oxygen potential, we have

$$C_n = C_n^0 \exp\left[-\frac{1}{4kT} (\mu_{O_2}^{L} - \mu_{O_2}^{O})\right]$$

$$C_p = C_p^0 \exp\left[\frac{1}{4kT} (\mu_{O_2}^{L} - \mu_{O_2}^{O})\right] \tag{6.154}$$

If we assume the mobility of the carriers to be independent of concentration, the partial conductivities of the two species are proportional to their concentrations so that the sum of the conductivities is expressed by

$$\sigma_n + \sigma_p = \sigma_n^0 \exp\left[-\frac{\mu_{O_2}^{L} - \mu_{O_2}^{O}}{4kT}\right] + \sigma_p^0 \exp\left[\frac{\mu_{O_2}^{L} - \mu_{O_2}^{O}}{4kT}\right] \tag{6.155}$$

This may now be put in the expression for the steady-state current (Eq. (6.151)), and the integral evaluated to yield

$$J_{ss}(L) = \frac{kT}{q}\,\sigma_n^0\left[\exp\left(-\frac{\mu_{O_2}^L - \mu_{O_2}^O}{4kT}\right) - 1\right] + \sigma_p^0\frac{kT}{q}\left[1 - \exp\left(\frac{\mu_{O_2}^L - \mu_{O_2}^O}{4kT}\right)\right] \quad (6.156)$$

From the previous example of no ionic current flowing through the electrolyte, we have Eq. (6.136), which describes the e.m.f. generated by a partial pressure gradient. Assuming that $t_{ion} = 1.0$ and imposing an e.m.f. such that $J_{ion} = 0$, i.e. making the reversible electrode positive, the above also describes an imposed oxygen potential generated by an applied cell potential. For this situation, the oxygen potential at the polarized interface is lower than that at the reversible electrode. For our case, this oxygen potential difference may be written as

$$\mu_{O_2}^L - \mu_{O_2}^O = -4\varepsilon q \quad (6.157)$$

Putting the above in Eq. (6.156) and converting to practical units for the constants gives the desired result:

$$J_{ss}(L) = \frac{RT}{LF}\,\sigma_n^0\left[\exp\left(\frac{\varepsilon F}{RT}\right) - 1\right] + \frac{RT}{LF}\,\sigma_p^0\left[1 - \exp\left(-\frac{\varepsilon F}{RT}\right)\right] \quad (6.158)$$

which is identical to the result by Patterson et al. (1967).

Equation (6.158) may be simplified by combining some of the constants

$$U = \frac{\varepsilon F}{RT}$$
$$K = \frac{RT}{LF} \quad (6.159)$$

so the steady-state polarization current may be written as

$$J_{ss} = K\sigma_n^0\left[(\exp U - 1)\right] + K\sigma_p^0[1 - \exp(-U)] \quad (6.160)$$

where σ_n^0 and σ_p^0 are the partial electron and hole conductivities that are defined for the oxide when it is equilibrated with an oxygen chemical potential defined by the reversible electrode. A polarizing electrode technique allows us to measure the partial electrical conductivities directly and, for the case of $t_{ion} \gg 0.99$, avoids the necessity of taking the difference between two large numbers to arrive at a value for the low-level electronic contribution to the total conductivity.

In summary, we have seen that under situations where current is supplied to reversible electrodes at the interfaces of an oxide conductor, the current is ohmic in nature. If a chemical potential gradient is applied across the oxide conductor and no external conduction circuit is employed, an e.m.f. will be generated by the electrolyte that is proportional to the chemical potential difference across the conductor. Brief discussions were given describing methods of determining the transference number for ions in either the current supply or open-circuit case. Finally, mathematics were presented that allow one to calculate the electron and hole conductivities directly from polarization measurements.

A combination of these various applications and techniques will allow the conduction processes of an oxide conductor to be characterized over a wide range of oxygen partial pressures in both electronic and ionic conduction regimes. This, of course, will help in understanding the transport properties of various combinations of oxides, which can be universally used at low and high temperatures, as smartly emphasized by Goto (1988) and others in many recent materials science monographs, as listed in "Further Reading."

References

Adam, N.K. (1938). *Physics and Chemistry of Surfaces*, 2e. London: Oxford University Press.

Arvia, A.J., Podestá, J.P., and Piatti, R.C.V. (1971). *Electrochim. Acta* 16: 1797.

Arvia, A.J., Podestá, J.P., and Piatti, R.C.V. (1972a). *Electrochim. Acta* 17: 33.

Arvia, A.J., Podestá, J.P., and Piatti, R.C.V. (1972b). *Electrochim. Acta* 17: 889.

Audubert, M.R. (1942). *J. Phys. Radium* 3: 81.

Bard, A.J. and Faulkner, L.F. (1998). *Electrochemical Methods*. New York: Wiley.

Baudo, G., Tamba, A., and Bombara, G. (1970). *Corrosion-NACE* 26: 193.

Blander, M., Blankenship, F.F., and Newton, R.F. (1959). *J. Phys. Chem.* 3: 1259.

Bockris, J.O.'.M. (1954). *Modern Aspects of Electrochemistry*, vol. 1. London: Butterworths.

Brouwer, G. (1954). *Philips Res. Rep.* 9: 366.

Burrows, B.W. and Hills, G.J. (1966). *J. Inst. Fuel* 39: 168.

Butler, J.A.V. (1924). *Trans. Faraday Soc.* 19: 729.

Butler, J.A.V. (1940). *Electrocapillarity: The Chemistry and Physics of Electrodes and Other Charged Surfaces*. London: Methuen and Co.

Conway, B.E. (1965). *Theory and Principles of Electrode Processes*. New York: The Ronald Press Co.

Cutler, A.J.B. (1971). *J. Appl. Electrochem.* 1: 19.

Davis, H.J. and Kinnibrugh, R.R. (1970). *J. Electrochem. Soc.* 117: 392.

Damaskin, B.B. (1967). *The Principles of Current Methods for the Study of Electrochemical Reactions*. New York: McGraw-Hill.

De Groot, S.R. (1951). *Thermodynamics of Irreversible Processes*. Amsterdam: North Holland Publishing Co.

Devanathan, M.A.V. and Tilak, B.V.K.S.R.A. (1965). *Chem. Rev.* 65: 635.

Duke, F.R. and Garfinkel, H.M. (1961). *J. Phys. Chem.* 65: 1627.

Edeleanu, C. (1958). *J. Iron Steel Inst.* 188: 122.

Erdey-Gruz, T. and Volmer, M. (1930). *Z. Phys. Chem. A* 150: 203.

Flood, H. and Förland, T. (1947). *Acta Chem. Scand.* 1: 592.

Flood, H., Förland, T., and Motzfeldt, K. (1952). *Acta Chem. Scand.* 6: 257.

Garcia-Diaz, B.L., Olson, L., Martinez-Rodriguez, M. et al. (2016). *J. S. C. Acad. Sci.* 14: 11.
Gerischer, H. (1960). *Z. Phys. Chem. (Frankfurt)* 26: 223, 326.
Gerischer, H. (1961). *Z. Phys. Chem. (Frankfurt)* 27: 48.
Goebel, J.A. and Pettit, F.S. (1970). *Metall. Trans.* 1: 1943.
Gordon, C. (1899). *Z. Phys. Chem.* 28: 302.
Goto, K.S. (1988). *Solid-state Electrochemistry and Its Applications to Sensors and Electronic Devices*. New York: Elsevier Publ. Co.
Grahame, D.C. (1947). *Chem. Rev.* 41: 441.
Graves, A.D., Hills, G.J., and Inman, D. (1966). *Advances in Electrochemistry and Electrochemical Engineering*, vol. 4, 117. New York: Interscience.
Graves, A.D. and Inman, D. (1970). *J. Electroanal. Chem.* 25: 357.
Greene, N.D. (1962). *Corrosion-NACE* 18: 136t.
Greene, N.D. and Leonard, R.B. (1964). *Electrochim. Acta* 9: 45.
Guggenheim, E.A. (1929). *J. Phys. Chem.* 33: 842.
Heyne, L. (1968). *Proceedings of a Symposium Mass Transport in Oxides*. Washington, D.C.: NBS Special Publication 296.
Ingram, M.D. and Janz, G.J. (1965). *Electrochim. Acta* 10: 783.
Kazantsev, G.N., Nichkov, I.F., and Raspopin, S.P. (1968). *Sov. Electrochem.* 2: 466.
Kröger, F.A. and Vink, J.H. (1956). *Solid-State Physics*, vol. 3. New York: Academic Press.
Kunst, R.N. and Duke, F.R. (1963). *J. Am. Chem. Soc.* 85: 2225.
Laitinen, H.A. and Gaur, H.C. (1957). *J. Electrochem. Soc.* 104: 730.
Laitinen, H.A., Tischer, R.P., and Roe, D.K. (1960). *J. Electrochem. Soc.* 107: 546.
LaQue, F.L. (1969). *J. Electrochem. Soc.* 116: 73C.
Littlewood, R. (1962). *J. Electrochem. Soc.* 109: 525.
Lux, H. (1939). *Z. Elektrochem.* 45: 303.
Maier, J. and Schwitzgebel, G. (1982). *Phys. Status Solidi B* 113: 535.
Mamantov, G. (1969). *Molten Salts: Characterization and Analysis*. New York: Marcel Dekker.
Mansfeld, F. and Bertocci, U. (eds.) (1981). *Electrochemical Corrosion Testing*, 167. Philadelphia, PA: ASTM, ASTM Spec. Tech. Pub 727.
Marchiano, S.L. and Arvia, A.J. (1972). *Electrochim. Acta* 17: 25.
Mu, D., He, Y., and Zhu, R. (1995). *Trans. Nonferrous Met. Soc. China* 5: 41.
Nishikata, A. and Haruyama, S. (1986). *Corrosion-NACE* 42: 578.
Nishikata, A., Numata, H., and Haruyama, S. (1981). *J. Jpn. Inst. Met.* 45: 610.
Nishikata, A., Numata, H., and Haruyama, S. (1983). *J. Jpn. Inst. Met.* 47: 198.
Nishikata, A., Shamatani, Y., and Haruyama, S. (1984). *J. Jpn. Inst. Met.* 48: 705.
Numata, H., Nishikata, A., and Haruyama, S. (1983). *Proceedings of the 3rd Japan Institute Metals International Symposium*, 303. Transactions of the Japan Institute of Metals Supplement.
Ohno, I. and Haruyama, S. (1981). *Surf. Technol.* 13: 1.
Onsager, L. (1931). *Phys. Rev.* 37: 405; (1931). 38, 2265.
Pardo, A., Otero, E., Perez, F.J., and Saenz, E. (1992). *Rev. Metal. (Madrid, Spain)* 28: 313.
Parsons, R. (1954). *Modern Aspects of Electrochemistry*, vol. 1. London: Butterworths.
Patterson, J.W., Bogren, E.C., and Rapp, R.A. (1967). *J. Electrochem. Soc.* 114: 752.
Pourbaix, M.J.N. and Vandervelden, F. (1965). *Corros. Sci.* 5: 81.
Prazak, M. (1963). *Corrosion-NACE* 19: 75t.
Prigogine, I. (1947). *Thermodynamic Study of Irreversible Phenomena*. Liège: Deoser.
Rahmel, A. (1968). *Electrochim. Acta* 13: 495.
Randles, J.E.B. and White, W. (1955). *Z. Elektrochem.* 59: 666.
Ranford, R.E. and Flengas, S.N. (1965). *Canad. J. Chem.* 43: 2879.
Rapp, R.A. and Zhang, Y.S. (1994). *JOM* 46: 47.
Ratzer-Scheibe, H.J. (1991). *Mater. Sci. Forum* 73–75: 513.
Sequeira, C.A.C. (1983). *Rev. Port. Quím.* 25: 155.
Sequeira, C.A.C. (1984). *Portgal. Phys.* 15: 111.
Sequeira, C.A.C. (1998). *Molten Salt Forum* 5–6: 417.
Sequeira, C.A.C. and Hocking, M.G. (1977). *Br. Corros. J.* 12: 156.
Sequeira, C.A.C. and Hocking, M.G. (1978a). *J. Appl. Electrochem.* 8: 145.
Sequeira, C.A.C. and Hocking, M.G. (1978b). *J. Appl. Electrochem.* 8: 179.
Sequeira, C.A.C. and Hocking, M.G. (1981). *Corrosion-NACE* 37: 392.
Simons, A.L., Browning, G.V., and Liebhafsky, H.A. (1955). *Corrosion* 11: 505t.
Stern, M. and Geary, A.L. (1957). *J. Electrochem. Soc.* 104: 56.
Ukshe, E.A., Bukan, N.G., Leikis, D.I., and Frumkin, A.N. (1964). *Electrochim. Acta* 9: 431.
Vetter, K.J. (1952). *Z. Naturforsch.* 7: 328.
Wagner, C. (1935). *Z. Phys. Chem.* B21: 25.
Wagner, C. (1975). *Prog. Solid State Chem.* 10: 3.
Wagner, C. and Traud, W. (1938). *Z. Elektrochem.* 44: 391.
Wildgoose, G.G., Giovanelli, D., Lawrence, N.S., and Compton, R.G. (2004). *Electroanalysis* 16: 421.

Further Reading

Alnatt, A.R. and Lidiard, A.B. (1993). *Atomic Transport in Solids*. Cambridge: Cambridge University Press.
Bruce, P.G. (1995). *Solid-State Electrochemistry*. Cambridge: Cambridge University Press.
Geller, S. (ed.) (1977). *Solid Electrolytes*. Berlin: Springer-Verlag.
Gellings, P.J. and Bouwmeester, H.J. (eds.) (1997). *CRC Handbook of Solid-State Electrochemistry*. Boca Raton, FL: CRC Press.
Hagenmuller, P. and Van Gool, W. (eds.) (1978). *Solid Electrolytes-General Principles, Characterization, Materials, Applications*. New York: Academic Press.
Kharton, V.V. (ed.) (2009). *Solid-State Electrochemistry I: Fundamentals, Materials and their Applications*. Weinheim: Wiley-VCH.
Lantelme, F. and Groult, H. (eds.) (2013). *Molten Salt Chemistry: From Lab to Applications*. Amsterdam, Holland: Elsevier.
Lvov, S.N., Zhou, X.Y., Ulyanov, S.M., and MacDonald, D.D. (2000). *Power Plant Chem.* 2: 5.
Maier, J. (2004). *Physical Chemistry of Ionic Materials. Ions and Electrons in Solids*. Chichester: Wiley.
Metaxas, A.C. (1996). *Foundations of Electroheat*. New York: Wiley.
Morrison, S.R. (1980). *Electrochemistry at Semiconductor and Oxidized Metal Electrodes*. New York: Plenum Press.
Rickert, H. (1982). *Electrochemistry of Solids*. Berlin: Springer-Verlag.
Seitz, F. and Turnbull, D. (eds.) (1956). *Solid-State Physics. Advances in Research and Applications*, vol. 3. New York: Academic Press.
Smith, R.A. (1978). *Semiconductors*, 2e. Cambridge: Cambridge University Press.
Subbarao, F.C. (ed.) (1980). *Solid Electrolytes and their Applications*. New York: Plenum Press.
Wallace, W., Nozik, A., and Deb, S. (eds.) (1982). *Photoelectrochemistry: Fundamental Processes and Measurement Techniques*. Princeton, NJ: Electrochemical Society.

Chapter 7

Oxidation

7.1 Introduction

7.1.1 Historical Perspective

Oxidation is an important high temperature corrosion phenomenon. Metals or alloys are oxidized when heated to elevated temperatures in air or in highly oxidizing environments, such as combustion atmospheres with excess air or oxygen. Many metallic components are subject to oxidation in engineering applications.

The first paper that expressly addressed high temperature oxidation was written by Gustav Tammann in 1920. He articulated the "parabolic law," i.e. the rate of oxidation of metal decreases as oxide layer thickness increases. In 1922 he established the logarithmic law of oxidation of metals. However, the first paper that laid out the basics of the problem as we know it was that by N.B. Pilling and R.E. Bedworth in 1923. They defined "high temperature" as that at which the transport of the reactive components through the protective layer was the principal determinant of the reaction rate (as opposed to the situation in aqueous corrosion processes at close to ambient temperatures). They showed that under these circumstances it could be expected that the rate of reaction would diminish as the protective scale thickened, leading to a "parabolic rate law." They also highlighted the problems associated with forming an adherent crack-free protective oxide layer on the oxidizing surface because of the volume changes associated with the oxidation process. The discussion to this seminal paper shows that others were thinking along similar lines at the time. Six years later, Leonard B. Pfeil introduced the concept of movement of metal outward rather than oxygen inward into the oxide layer, and in 1934 Portevin, Prétet, and Jolivet carried out extensive studies on the oxidation of iron and its alloys. At the same time, the discovery that oxides contained lattice defects and that the transport processes within them are determined by the motion of these defects allowed a more quantitative approach. This was recognized by Carl Wagner, who produced an important body of work over the course of the next 20 years largely defining how we now look at the basic theory of the bulk transport processes in oxides. Of significance was the derivation of Wagner's equation by Hoar and Price in 1938. In recent years, however, the recognition that in many cases the transport processes involve short-circuit paths, such as grain boundaries, has introduced further complications into this elegant picture.

The problem of the integrity of the protective oxide was not part of Wagner's contribution, and its practical solution for the high temperature alloys that were developed for applications mentioned above was discovered essentially by accident in the early 1940s. It was found that very small amounts of what are now called "reactive elements" added to the alloys introduced a remarkable improvement in the apparent integrity of the protective oxide, particularly in its resistance to thermal cycling. The reasons for this effect are still a matter of considerable debate.

Other important contributions in the 1939–1948 period were those of Cabrera and Mott (1948), postulating that oxide film growth is controlled by ions jumping from site to site over intervening energy barriers. Mott's theory was then highly criticized by Hauffe, who studied the oxidation of alloys (Mott 1940). During the 1920–1940 period, other relevant studies on oxidation at high temperature deserve reference: these are the interference method of obtaining thickness of oxide films (Tammann 1920–1926), the spectroscopic method to obtain thickness of oxide film (Constable 1927), and the X-ray and electron diffraction methods to study oxide films (Finch Quarrell 1933).

The earliest treatments of oxidation problems considered simple systems, with a single oxidant (usually oxygen) and a pure metal, although in practice high temperature-resistant materials were always alloys. More recently, approaches such as in multicomponent diffusion theory have been applied, and the growth of oxides on polyphase materials have been analyzed. These approaches have been greatly assisted by the development of modern characterization techniques.

High Temperature Corrosion: Fundamentals and Engineering, First Edition. César A. C. Sequeira.
© 2019 John Wiley & Sons, Inc. Published 2019 by John Wiley & Sons, Inc.

7.1.2 Purpose of the Chapter

The oxidation of metals is usually a reaction between a gas and a solid that produces a solid reaction product. At a first glance, this would seem to be a very simple process, but, actually, it is considerably more complex. The metal is usually not pure but contains, in addition to metallic impurities, O, N, H, C, S, etc. The gas atmosphere is also usually complex, containing (in addition to O_2), N_2, H_2, CO_2, H_2O, etc. One would think that the reaction product, i.e. the scale that formed on the metal, acts as a physical barrier between the reactants, and thus the reaction should cease after the barrier is established. We know that this is not the case, because transport of matter through the scale causes the reaction to continue. We also know that the scale may not be dense and adherent to the substrate, but it may be cracked, partially spalled, partially detached (wrinkled), or even very porous. In some extreme cases, the scale may be a liquid that simply drips from the surface, or it may volatilize at very high temperatures. Indeed, the reaction between a gas and a metal is very complicated.

Our interest in this multidisciplinary field of physical chemistry, solid-state chemistry, metallurgy, materials science, and engineering arises from the fact that the chemical activity of a metal in various environments is an important factor in the winning, processing, and use of the metal. Demands are pressing from aerospace/gas turbine, chemical processing, refining and petrochemical, fossil-fired power generation, coal gasification, waste-to-energy industry, pulp and paper, heat treating, mineral and metallurgical processing, nuclear power, space exploration, molecular electronics, and other sides for better metals and alloys for high temperature service in special reactive atmospheres and for metals with special physical properties.

The science of gas–solid reactions, oxidation referred to in the generic sense, can involve reactions with, for example, sulfur, nitrogen, carbon dioxide, and water vapor and has greatly evolved in the past 60 years. Numerous symposia and colloquia (Steinmetz et al. 2004; Taniguchi et al. 2006) have been held on the subject and have been widely attended by researchers from all over the world. One of the many factors enabling advancement of our understanding of the field is the creation and evolution of new, sophisticated instruments and techniques that allow a much better analysis of scale compositions and structures. Details regarding this subject have led to thousands of publications and the writing of several books. Of the more recent books on oxidation, those indicated in references (Birks et al. 2006; Fromm 1998; Khanna 2002; Kofstad 1988, Lai 2007; Sarrazin et al. 2008) have been very useful.

The present chapter summarizes the main factors for determining the nature and extent of gas–metal reactions, which are of paramount importance to understand the subject.

7.2 Thermodynamic Considerations

An important tool in the analysis of oxidation problems is equilibrium thermodynamics, which, although not predictive of kinetics, allows one to ascertain which reaction products are possible, whether or not significant evaporation or condensation of a given species is possible, the conditions under which a given reaction product can react with a condensed deposit, and so on. The complexity of the oxidation phenomena usually dictates that the thermodynamic analysis be represented in graphical form. The types of thermodynamic diagrams most often used in oxidation research are listed in Section 3.2 on high temperature equilibria.

The basic concepts pertinent to the construction and analysis of those thermodynamic diagrams are described in numerous thermodynamics books (Gaskell 1995; Kubaschewski and Alcock 1979).

Determination of the conditions under which a given corrosion product is likely to form is often required, e.g. in selective oxidation of alloys. In this regard, Ellingham diagrams, i.e. plots of the standard free energy of formation (ΔG°) versus temperature for the compounds of a type, e.g. oxides, sulfides, carbides, etc., are useful in that they allow comparison of the relative stabilities of each compound. In Section 3.2.1 these free energy/temperature diagrams are properly discussed; here our considerations on the thermodynamics of high temperature oxidation will finish with a brief reference to the volatility of oxides.

7.2.1 Volatility of Oxides

Some oxides exhibit high vapor pressures at very high temperatures (e.g. above 1000 °C). Oxide scales become less protective when their vapor pressures are high. Chromium, molybdenum, tungsten, vanadium, platinum, rhodium, and silicon are metals for which volatile species are important at high temperature. Vanadium is typically used in small quantities as a carbide former in alloy steels. Thus, the volatility of VO_2 is generally of no concern in oxidation of alloys.

The oxidation of Pt, and Pt-group metals, at high temperatures is influenced by oxide volatility in that the only stable oxides are volatile. This results in a continuous mass loss. Alcock and Hooper (1960) studied the mass loss of Pt and Rh at 1400 °C as a function of oxygen pressure.

The gaseous species were identified as PtO_2 and RhO_2. These results have an extra significance because Pt and Pt–Rh wires are often used to support specimens during high temperature oxidation experiments. If these experiments involve mass change measurements, it must be recognized that there will be a mass loss associated with volatilization of oxides from the support wires.

The oxidation of pure Cr is, in principle, a simple process since a single oxide, Cr_2O_3, is observed to form.

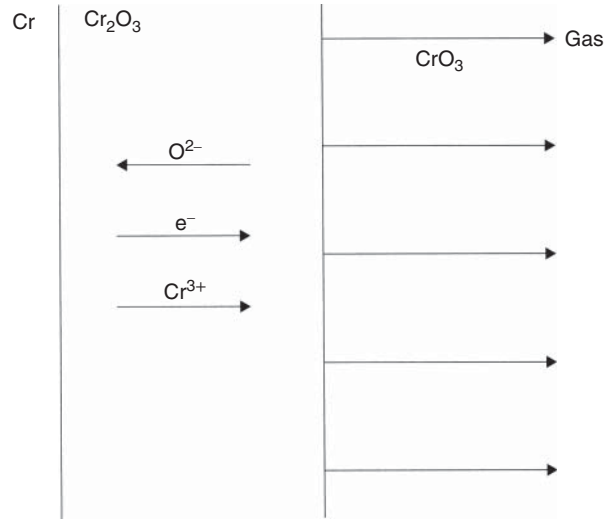


Figure 7.1 Schematic diagram of combined scale growth and oxide volatilization from Cr (Birks et al. 2006).

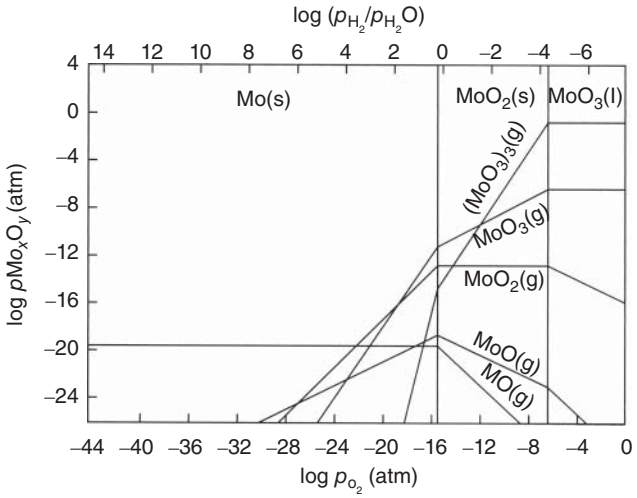


Figure 7.2 The Mo–O system volatile species diagram for 1250 K (Birks et al. 2006).

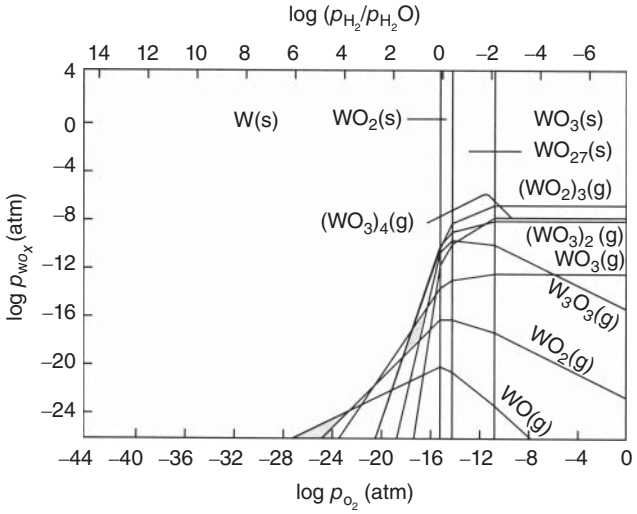


Figure 7.3 The W–O system volatile species diagram for 1250 K (Birks et al. 2006).

However, under uncertain exposure conditions, several complications arise, which are important both for the oxidation of pure Cr and for many important engineering alloys that rely in a protective Cr_2O_3 layer for oxidation protection. The two most important features are scale thinning by CrO_3 evaporation and scale buckling as a result of compressive stress development (Asteman et al. 1999).

The formation of CrO_3 by the reaction

$$Cr_2O_3 + \frac{3}{2}O_2 = 2CrO_3 \qquad (7.1)$$

becomes significant at high temperatures and high oxygen partial pressures. The evaporation of CrO_3, shown schematically in Figure 7.1, results in the continuous thinning of the protective Cr_2O_3 scale, so the diffusive transport through it is rapid. The effect of the volatilization on the oxidation kinetics has been analyzed by Tedmon (1966).

Caplan and Cohen (1961) also observed that resistance promoted volatilization of Cr_2O_3. Asteman et al. (1999) indicated that high vapor pressure of $CrO_2(OH)_2$ can form by reacting Cr_2O_3 with H_2O in O_2-containing environments.

The volatilization of oxides is particularly important in the oxidation of Mo and W at high temperatures and high oxygen pressures. Unlike Cr, which develops a limiting scale thickness, complete oxide volatilization can occur in these systems. The condensed and vapor species for the Mo–O and W–O systems have been reviewed by Gulbransen and Meier (1979a,b), and the vapor species diagrams for a temperature of 1250 K are presented in Figures 7.2 and 7.3. The effects of oxide volatility on the oxidation of Mo have been observed by Gulbransen and Wysong (1948) at temperatures as low as 475 °C, and the rate of oxide evaporation above 725 °C was such that gas-phase diffusion became the rate-controlling process (Gulbransen et al. 1963). Naturally, under these conditions, the rate of oxidation is catastrophic. Similar behavior is observed for the oxidation of tungsten, but at higher temperatures because of the lower vapor pressures of the tungsten oxides. The oxidation behavior of tungsten has been reviewed in detail by Kofstad (1966).

The formation of SiO_2 on silicon-containing alloys and Si-based ceramics results in very low oxidation rates. However, this system is also one that can be influenced markedly by oxide vapor species. Whereas the oxidation of Cr is influenced by such species at high oxygen pressures, the effects for Si are important at low oxygen partial pressures. The reason for this may be seen from the volatile

species diagram for the Si–O system (Rocabois et al. 1966). A significant pressure of SiO is seen to be in equilibrium with SiO_2 (s) and Si (s) at oxygen pressures near the dissociation pressure of SiO_2. This can result in a rapid flux of SiO away from the specimen surface and the subsequent formation of a non-protective SiO_2 smoke. This formation of the SiO_2 as a smoke, rather than as a continuous layer, allows continued rapid reaction (Wagner 1958, 1965).

7.3 Kinetic Considerations

Consider the oxidation reaction

$$\mathrm{M} + \frac{1}{2}\,\mathrm{O_2} = \mathrm{MO} \tag{7.2}$$

A similar reaction involving a metal phase and a gas phase was used in Section 6.8 to demonstrate the electrochemical nature of metal oxidation. Simple expressions for the growth of the MO oxide scale were also associated to support the transport of ionic and electronic species through the oxide layer. In this section, the kinetics of reaction (7.2) is discussed in more detail than it was possible in that overview chapter on high temperature electrochemistry.

The progress, W, of this reaction can be characterized using several definitions of the reaction rate. It can, for example, be defined as the rate of oxygen pickup, $\mathrm{d}n_\mathrm{o}/A\mathrm{d}t$, where $\mathrm{d}n_\mathrm{o}$ corresponds to the number of moles of oxygen consumed during time $\mathrm{d}t$ and A the sample area. From an experimental point of view, though, it is easier to use the sample weight gain Δm. The reaction rate can then be expressed as $\mathrm{d}\Delta m/A\mathrm{d}t$, where $\mathrm{d}\Delta m$ is the weight change occurring during time $\mathrm{d}t$. These expressions are linked by the equation

$$\frac{\mathrm{d}n_\mathrm{o}}{\mathrm{d}t} = \frac{1}{16}\,\frac{d\Delta m}{\mathrm{d}t} \quad \text{where } \Delta m \text{ is expressed in grams.} \tag{7.3}$$

Integration of the rate equation leads to the rate law corresponding to the corrosion process and defines the progress, W, of the reaction with time. We obtain either an implicit form:

$$f(W) = k \times t \tag{7.4}$$

where k is the rate constant for the reaction process, or an explicit form:

$$W = g(t) \tag{7.5}$$

In any fundamental study of the oxidation mechanism of a metal or an alloy, one of the main factors that needs to be determined is the variation of the oxidation rate with temperature and with the pressure of the oxidizing gas.

This type of investigation has sometimes been neglected because of difficulties controlling precisely the gas pressure in thermobalances. However, for some years, it has been possible to couple such thermogravimetric equipment to devices capable of controlling and monitoring the oxygen partial pressure in a gas (e.g. an electrochemical oxygen pump, oxygen sensor). The oxygen pressure then can be precisely controlled between 1 and 10^{-25} bar in gas mixtures, e.g. inert gas–oxygen, CO–CO_2, or H_2–H_2O mixtures (ASM 2003).

The rate constants of the kinetic laws often obey, under constant pressure, an Arrhenius-type equation:

$$k = k^0 \exp\left(-\frac{E_\mathrm{a}}{RT}\right) \quad (\text{at given } P) \tag{7.6}$$

where E_a is the apparent activation energy of the process, R the gas constant, and T the absolute temperature. The apparent activation energy can be easily determined by plotting k as a function of $1/T$. The slope of the straight line obtained is equal to $-E_\mathrm{a}/2.303R$. A change in the activation energy could indicate a corresponding change in the limiting process for the corrosion reaction.

The main kinetic laws are of linear, parabolic, logarithmic, or cubic types, but it should be noted these are limiting cases and deviations from them are often encountered. In some cases, it is difficult, or even impossible, to obtain such simple kinetic laws from the experimental results (Evans 1960; Hauffe 1965; Kofstad 1988).

At high temperatures, the oxidation kinetics of numerous metals obey a parabolic law:

$$W^2 = k_\mathrm{p} t \tag{7.7}$$

where k_p is the parabolic constant. Such a law corresponds, as will be shown later, to a corrosion rate limited by diffusion through the compact scale that is formed.

The reaction rate constant may be expressed in different units depending on the actual parameter used to define the progress of the reaction. For example, if the extent of reaction is characterized by the mass gain per unit surface area of the metal during the exposure period, t, the kinetic law is given by $(\Delta m/A)^2 = k_\mathrm{p} \times t$, and the rate constant is expressed in $\mathrm{kg^2\ m^{-4}\ s^{-1}}$. If the reaction rate is defined by the increase in thickness, y, of the scale, the kinetic law has the form $y^2 = k'_\mathrm{p}\, t$, and the parabolic rate constant k'_p is expressed in $\mathrm{m^2\ s^{-1}}$. On the other hand, if the reaction rate is defined by the number of moles of the compound MX formed per unit area during the exposure period, t, the kinetic law has the form $(\Delta n_\mathrm{MX}/A)^2 = k''_\mathrm{p}\, t$. In this case, the rate constant k''_p is expressed in $\mathrm{mol^2\ m^{-4}\ s^{-1}}$. There is a simple relationship between the rate constants k_p, k'_p, and k''_p:

$$k'_\mathrm{p} = \Omega^2\, k''_\mathrm{p} = \left(\frac{\Omega}{\mathrm{M}_x}\right)^2 k_\mathrm{p} \tag{7.8}$$

where Ω is the molar volume of compound MX and M_x is the atomic weight of the nonmetallic element (oxygen, sulfur, etc.).

In some cases, the oxidation rate is constant, which means that the kinetic law is linear:

$$W = k_l t \quad (k_l \text{ is the linear rate constant}) \tag{7.9}$$

As will be shown later, the oxidation rate is then governed by an interfacial process such as sorption, reaction at the metal–oxide interface, etc. Using similar nomenclature as for the parabolic rate constants, k_l characterizes the reaction measured by the mass gain per unit surface area during time t and k_l' if the rate is defined by the increase in thickness of the growing scale.

The cubic law ($W^3 = k_c t$) has been observed during the oxidation of several metals, for example, copper, nickel, and zirconium.

Logarithmic laws are observed typically in the case of many metals at low temperatures (generally below 673 K). The initial oxidation rate, corresponding to the growth of oxide layers of thickness generally less than a few tens of nanometers, is quite rapid and then drops off to low or negligible values. This behavior can be described by a direct logarithmic law:

$$W = k_{\log} \log (at + 1) \tag{7.10}$$

or by an inverse logarithmic law:

$$\frac{1}{W} = B - k_{\text{inv}} \log t \tag{7.11}$$

The evaluation of the kinetic parameters in the case of the logarithmic law is, generally, not very precise, and this makes it difficult to validate experimentally proposed mechanisms.

The oxidation rate is frequently found to follow a combination of rate laws.

As an example, at low temperatures, a logarithmic law followed by a parabolic rate equation can be observed. At high temperature, oxidation reactions are often described by a parabolic rate equation followed by a linear law ("paralinear" regime) or a linear rate equation followed by a parabolic law (Pettit and Wagner 1964).

Typical kinetic laws characteristic of the oxidation of a large number of metals as a function of temperature were fully analyzed by Kubaschewski and Hopkins (1967), Kofstad (1988), and others. Table 7.1 gives some examples.

As an example, the kinetic laws characteristic of chromium oxidation are shown in Figure 7.4. It can be seen that at 1000 °C, a parabolic law is observed but that at 1075 °C the experimental curve is characteristic of the formation of compact scales that crack at a critical thickness due to high mechanical stresses between the metal

Table 7.1 Kinetic laws characteristic of the oxidation of several metals as a function of temperature (from Kubaschewski and Hopkins 1967)

T (°C)	200	400	600	800	1000	1200
Mg	*log*	*par*	*paralin*	*lin*		
Ca	*(log)*	*par*		*lin*		
Ce	*log*	*log-lin*	*lin*	*break*		
Th		*par*	*lin*	*lin*		
U	*par*	*paralin*	*lin*			
Ti		*log*	*cub*	*cub*	*paralin*	*paralin*
Zr		*log*	*cub*	*cub*	*cub*	*cub-lin*
Nb		*par*	*par*	*parlin*	*lin*	*lin*	*break*
Ta	*log*	*inv. log*	*par*	*paralin*	*lin*	*lin*	
Mo		*par*	*paralin*	*paralin*	*lin*	*lin*	
W			*par*	*par*	*paralin*	*paralin*	*paralin*
Fe	*log*	*log*	*par*	*par*	*par*	*par*	*par*	*par*
Ni		*log*	*log*	*cub*	*par*	*par*	*par*
Cu	*log*	*cub*	*(par)*	*par*	*par*	*par*	
Zn		*log*	*log*	*par*	*par*		
Al	*log*	*inv.log*	*(log)*	*par*	*(asym)(lin)*		
Ge				*par*	*paralin*		

par: parabolic law, *log*: logarithmic law, *lin*: linear law, *cub*: cubic law, *paralin*: paralinear law, *break*: "breakaway" corrosion.

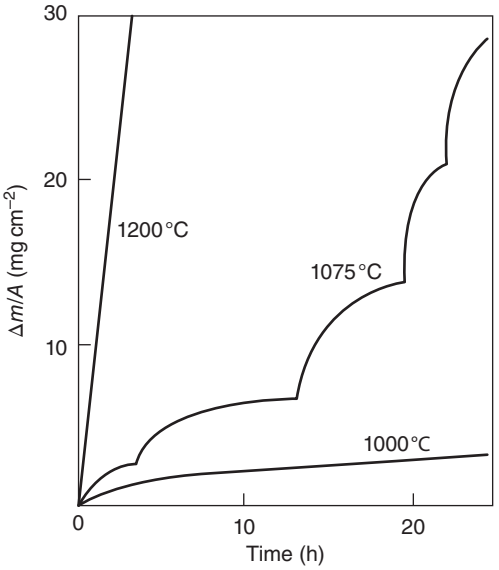


Figure 7.4 Chromium oxidation, between 1000 and 1200 °C, under 1 bar of oxygen (Kofstad 1966).

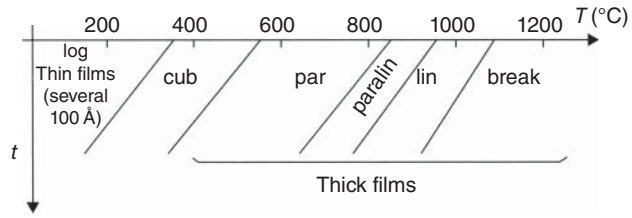


Figure 7.5 Successive kinetic laws observed for the oxidation of a given metal as function of temperature and time.

and the growing scale; at 1200 °C, a linear rate equation is observed, with a noticeable increase in corrosion rate.

Besides the variation of the kinetic laws with temperature, a change of these rate equations with time can sometimes occur. A typical example, characteristic of the changes that may be observed as functions of temperature and time, is given in Figure 7.5. At 800 °C, for example, the following rate equations are successively observed: parabolic, paralinear, and finally linear after extended oxidation.

In many cases, it may be difficult to fit experimental data to simple rate equations, but a first approach can be to plot the $W = f(t)$ curve using double logarithmic coordinates. In the case of a law of type $W^n = kt$, the slope of the straight line then gives the value of n, i.e. 1, 2, and 3 for linear, parabolic, and cubic laws, respectively.

Some authors, using computer software, fit the data to a third-degree polynomial in W:

$$AW^3 + BW^2 + CW + D = t \qquad (7.12)$$

Difficulties in evaluating the proper kinetic law are particularly important in the case of changes in the oxidation behavior during the corrosion process.

An elegant method consists of continuously monitoring the kinetic curves with exposure time and calculating, for each experimental point, the rate constant appropriate to the expected model. Deviations from this model can be readily identified (Monceau and Pieraggi 1998).

7.4 Defect Structures

The formation of an oxide scale starts with the adsorption of oxygen gas on the metal surface. During adsorption, oxygen molecules of other gaseous species in the environment dissociate and are adsorbed as atoms. These atoms initially adsorb at sites where the atom is in contact with the maximum number of surface atoms in the metal substrate. Therefore, in polycrystalline materials, grains of preferential orientation exist where the number of adsorbed atoms from the gaseous atmosphere is highest. The result of this process is a two-dimensional adsorption layer. The presence of adsorbed layers may increase the rates of surface diffusion by orders of magnitude compared with those for surfaces with none or small amounts of adsorbate.

When the metal surface that is saturated with adsorbed oxygen atoms or atoms from other gaseous species is further exposed to the gas, the gaseous species may dissolve in the metal, and nuclei of the corrosion product are formed on the surface. These nuclei grow laterally and form a continuous film on the surface. Generally nucleation and growth of the nuclei are dependent on the composition of the substrate, the grain orientation, the temperature, and the gas partial pressure. The nuclei grow in thickness and lateral direction and the reaction rate increases with time. As soon as the nuclei impinge on each other, the growth rate decreases. Therefore, the general reaction kinetics can be described by an S-shaped curve (Kofstad 1988).

Nuclei of all potential corrosion products can be formed on alloys initially, i.e. those that are possible from thermodynamic stability considerations. After the initial stage of oxidation, which is determined by the behavior of the nuclei, growth of the continuous scale occurs in the thickness direction. In dense oxide scales, the growth is determined by solid-state diffusion through the scale. Corrosion products, which include the oxide scales, are ionic structures, and diffusion in such structures requires lattice disorder, i.e. the corrosion products need to be non-stoichiometric compounds. Therefore, an understanding of reaction mechanisms in high temperature conditions requires a precise knowledge of defect structures in solids. Extensive studies of defect theory have been provided by Kröger et al. (1956), Kröger (1975), Philibert (1985), Kofstad (1972), Mrowec (1980), and others, but here

only an oversimplified discussion will be presented. It should also be noted that Chapter 4 of this book gives a general treatment of lattice defects in metal compounds and includes descriptions of point defects, defect reactions, defect equilibria, and equilibrium constants. It was considered desirable to include these more general aspects so that the book could be read as a self-contained text without the need for repeatedly consulting other books or publications.

Various types of defects may affect scale growth, but we shall only consider the crystalline defects that determine the growth of a compact layer and the three-dimensional defects, such as cracks and pores, that determine the growth of a porous scale. The crystalline defects represent departures from the perfect crystalline array and include point defects (imperfections in the distribution of ions within the lattice), line defects (displacements in the periodic structure of the crystal in certain directions or dislocations), and planar defects or grain boundaries (regions of lattice mismatch).

The point defects comprise either empty crystallographic sites (vacancies) or atoms occupying the interstices between the regular lattice sites (interstitial atoms). Their mole fraction in each sublattice, i.e. either the cation or anion sublattice, generally does not exceed 10^{-3}–10^{-2} and is frequently much less. For point defect mole fractions sufficiently high, the defects may associate or cluster to form complex defects such as extended defects or aggregates of point defects (clusters). Point defects strongly influence the growth of compact scales and will be briefly treated hereafter.

7.4.1 Point Defects

7.4.1.1 Real Oxide Structures

A complete development of defect chemistry of inorganic compounds requires a system of notation to describe all the elements of the crystal or "structural elements," that is, not only regular crystallographic sites but also lattice imperfections. The Kröger and Vink notation (Kröger et al. 1956), recommended by IUPAC because of its great simplicity, will be used here. Thus, in a crystal MO, a structural element of the cation sublattice has a normal charge of +2 and, consequently, an effective charge equal to zero. The electronic defects may be considered as structural elements. The electronic defect with positive charge will be written $h^{\bullet}$ (h with a superscript dot). This defect corresponds to the removal of an electron from a regular site of the cation sublattice and can also be written as M'_M (a superscript prime ($'$) is used for a negative charge). These rules must be followed in writing defects in equilibrium reactions:

- Electroneutrality of the total charges of the structural elements, i.e. involving normal charges, actual charges, and effective charges.
- Mass balance, i.e. the number of atoms of each chemical species involved in the defect reaction must be the same before and after the defect formation.
- Ratio of regular lattice sites, i.e. for a crystal M_pX_q: number of M sites/number of X sites should be equal to p/q.

Following these rules, it is possible to write equilibrium reactions that occur internally without involving the external environment and external equilibria involving mass exchange with the environment. The equilibrium constants will then be evaluated assuming that the activities of atoms on their normal lattice positions can be considered as unity and the activities of point defects will be approximated by their concentration, usually indicated by a double bracket [ ], and expressed as the number of moles per mole of compound.

7.4.1.2 Stoichiometry

Alkali halides, silver halides, and several oxides (Al_2O_3, MgO, etc.) are stoichiometric compounds. Some of them are characterized by vacancies and interstitials in one sublattice (e.g. AgBr, with Frenkel disorder); others possess defects in both sublattices (e.g. NaCl, with Schottky disorder). However, it is apparent that neither of these defects can be used to explain material transport during oxidation reactions, because neither defect structure provides a mechanism by which electrons may migrate.

Considering a diagrammatic representation of the oxidation process shown in Figure 7.6, it is seen that either neutral atoms or ions and electrons must migrate in order for the reaction to proceed. In these cases, the transport step of the reaction mechanism links the two phase-boundary reactions as indicated. There is an important distinction between scale growth by cation migration and scale growth by anion migration in that cation migration leads to scale formation at the scale/gas interface, whereas anion migration leads to scale formation at the metal/scale interface.

In order to explain simultaneous migration of ions and electrons, it is necessary to assume that the oxides that are formed during oxidation are nonstoichiometric compounds. From a macroscopic viewpoint, two alternative classes of nonstoichiometric compounds can be considered:

1. M_aX_b compounds for which $\frac{\text{atom number of M}}{\text{atom number of X}} > \frac{a}{b}$. These compounds are ionic semiconductors with metal excess ($M_{a+\delta}X_b$, where δ is the deviation from stoichiometry in comparison with the stoichiometric composition M_aX_b) or with nonmetal deficit ($M_aX_{b-\delta}$). ZnO is a typical n-type semiconductor with a metal excess; TiO_2, Nb_2O_5, MoO_3, and WO_3 are typical n-type semiconductors with nonmetal deficit.

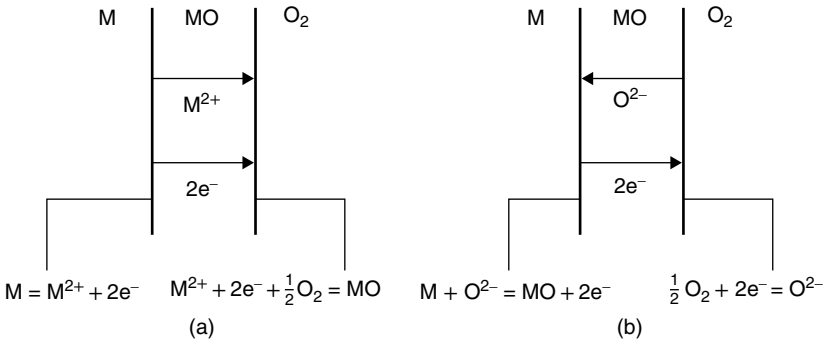


Figure 7.6 Interfacial reactions and transport processes for high temperature oxidation mechanisms: (a) cation mobile and (b) anion mobile (Birks et al. 2006).

2. M_aX_b compounds for which $\frac{\text{atom number of M}}{\text{atom number of X}} < \frac{a}{b}$. These include the p-type semiconductors with metal deficit (FeO, NiO, Cr_2O_3, Al_2O_3) or with an excess of non-metal (UO_2).

In order to allow extra metal in ZnO, it is necessary to postulate the existence of interstitial cations with an equivalent number of electrons in the conduction band. The structure may be represented as shown in Figure 7.7. Here, both Zn^+ and Zn^{2+} are represented as possible occupiers of interstitial sites. Cation conduction occurs over interstitial sites, and electrical conductance occurs by virtue of having the "excess" electrons excited into the conduction band. These, therefore, are called "excess" or "quasi-free" electrons.

The formation of this defect may be visualized, conveniently, as being formed from a perfect ZnO crystal by losing oxygen: the remaining unpartnered Zn^{2+} leaving the cation lattice and entering interstitial sites and the two negative charges of the oxygen ion entering the conduction band. In this way, one unit of ZnO crystals is destroyed, and the formation of the defect may be represented by

$$\mathrm{ZnO} = \mathrm{Zn}_i^{\bullet\bullet} + 2\mathrm{e}' + \frac{1}{2}\mathrm{O}_2 \tag{7.13}$$

for the formation of $Zn_i^{\bullet\bullet}$, doubly charged Zn interstitials, or

$$\mathrm{ZnO} = \mathrm{Zn}_i^{\bullet} + \mathrm{e}' + \frac{1}{2}\mathrm{O}_2 \tag{7.14}$$

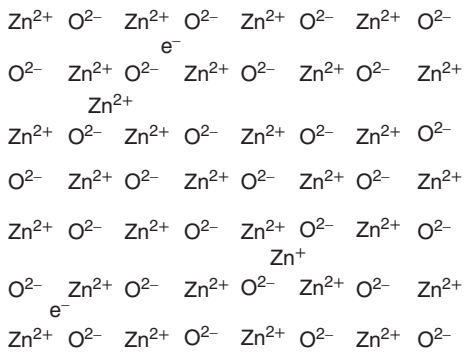


Figure 7.7 Interstitial cations and excess electrons in ZnO – an n-type metal excess semiconductor (Birks et al. 2006).

for the formation of $Zn_i^{\bullet}$, singly charged Zn interstitials.

The two equilibria shown above will yield to thermodynamic treatment, giving Eq. (7.15) for the equilibrium in Eq. (7.13):

$$K = a_{\mathrm{Zn}_i^{\bullet\bullet}} a_{\mathrm{e}'}^2 p_{\mathrm{O}_2}^{1/2} \tag{7.15}$$

or, since the defects are in very dilute solution, we may assume that they are in the range obeying Henry's law, when the equilibrium may be written in terms of concentrations $[Zn_i^{\bullet}]$ and $[e']$ as in Eq. (7.16):

$$K' = [\mathrm{Zn}_i^{\bullet}]\,[\mathrm{e}']\,p_{\mathrm{O}_2}^{1/2} \tag{7.16}$$

If Eq. (7.13) represents the only mechanism by which defects are created in ZnO, then Eq. (7.17) follows:

$$2[\mathrm{Zn}_i^{\bullet\bullet}] = [\mathrm{e}'] \tag{7.17}$$

Hence, putting Eq. (7.17) into Eq. (7.16), we obtain Eq. (7.18),

$$K' = 4[\mathrm{Zn}_i^{\bullet\bullet}]^3\, p_{\mathrm{O}_2}^{1/2} \tag{7.18}$$

or Eq. (7.19), and therefore we obtain Eq. (7.20):

$$[\mathrm{Zn}_i^{\bullet\bullet}] = (K'/4)^{1/3} p_{\mathrm{O}_2}^{-1/6} = \text{const.} p_{\mathrm{O}_2}^{-1/6} \tag{7.19}$$

$$[\mathrm{e}'] \infty p_{\mathrm{O}_2}^{-1/6} \tag{7.20}$$

Similarly, applying the same analysis to the reaction shown in Eq. (7.14), the result shown in Eq. (7.21) is obtained:

$$[\mathrm{Zn}_i^{\bullet}] = [\mathrm{e}'] \propto p_{\mathrm{O}_2}^{-1/4} \tag{7.21}$$

Measurement of electrical conductivity as a function of oxygen partial pressure carried out between 500 and 700 °C (von Baumbach and Wagner 1933) indicated that the conductivity of ZnO varied with oxygen partial pressure having exponents between 1/4.5 and 1/5. This result indicates that neither defect mechanism predominates and the actual structure could involve both singly and doubly charged interstitial cations (Kofstad 1972).

Similar approaches can be applied to nonstoichiometric compounds with cation vacancies ($Cu_{2-\delta}O$-type oxide),

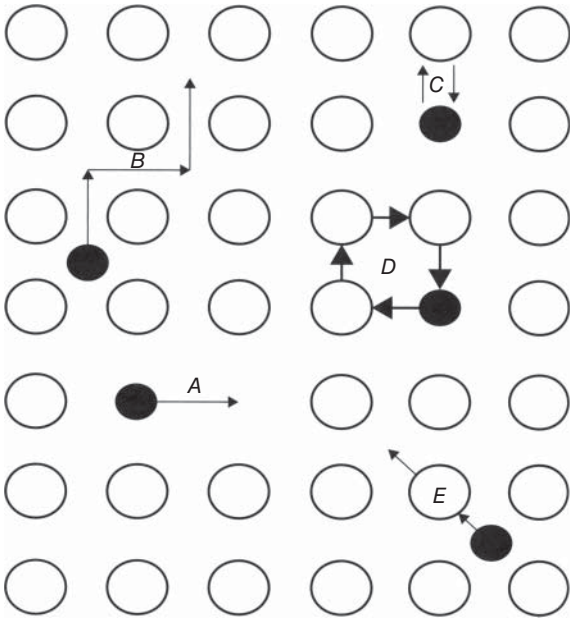


Figure 7.8 Schematic illustration of transport mechanisms in crystalline solids (Sequeira and Santos 2006).

oxygen interstitials ($UO_{2+\delta}$-type oxide), etc. (Farhi and Petot-Ervas 1978; Pope and Birks 1977).

7.4.1.3 Mass and Electrical Transport

Intragranular or volume diffusion in crystalline compounds takes place through crystal imperfections and mainly through the movement of point defects. Several types of mechanisms may be considered, as shown schematically in Figure 7.8, but mass transport generally occurs by hopping mechanisms from a well-defined site of the crystal into another adjacent site.

Consider a one-dimensional flux of particles (atoms, ions, point defects, or electrons) in the Ox direction. Let $C(x, t)$ be the defect concentrations (number of particles per unit volume) at the coordinate x and at time t. In a chemical potential gradient and without an electrical potential gradient or other type of driving force, a flux, J, of particles occurs in the Ox direction:

$$J = -\frac{CD}{RT}\frac{\partial \mu}{\partial x} \quad \text{(generalized Fick's law)} \tag{7.22}$$

where D is the diffusion coefficient of the particle.

Under an additional electrical potential gradient, the particle flux would obey the following general equation:

$$J = -\frac{CD}{RT}\frac{\partial \widetilde{\mu}}{\partial x} \tag{7.23}$$

where $\widetilde{\mu}$, termed the electrochemical potential, is related to the chemical potential μ by the equation

$$\widetilde{\mu} = \mu \pm zF\phi \tag{7.24}$$

where z is the particle charge number, F the Faraday constant, ϕ the electrical potential, and $\pm zF$ the electrical charge.

If the ion movements within one sublattice of the binary compound M_aX_b produce displacements of ions only in that sublattice, M or X diffusion is termed self-diffusion, and the self-diffusion coefficient D_j of component j will obey the following equation:

$$J_j = -\frac{C_j D_j}{RT}\frac{\partial \mu_j}{\partial x} \tag{7.25}$$

where C_j is the concentration of component j.

Let J_δ be the flux of the defect, δ, in the j sublattice at the coordinate x and in the absence of an electric field. The diffusion coefficient D_δ of the defect δ is defined by equation

$$J_\delta = -\frac{C_\delta D_\delta}{RT}\frac{\partial \mu_\delta}{\partial x} \tag{7.26}$$

where C_δ is the concentration of the defect δ.

As a general rule, the relationship between D_j and D_δ may be written as

$$C_\delta D_\delta = C_j D_j \tag{7.27}$$

If N_δ is the mole fraction of defects δ in the j sublattice, we may write

$$D_j = N_\delta D_\delta \quad \text{since } N_\delta = \frac{C_\delta}{C_\delta + C_j} \approx \frac{C_\delta}{C_j} \tag{7.28}$$

This relationship shows that the self-diffusion of component j is proportional to the mole fraction of defect δ contained in the j sublattice.

A comparison of the self-diffusion coefficients of anions and of cations may allow identification of the component that provides the majority of mass transport within the crystal. Thus, nonstoichiometric oxides such as NiO, FeO, and Cu_2O contain metal vacancies; this observation is in agreement with the order of magnitude of the diffusion coefficients, i.e. $D_M \gg D_O$ ($D_M/D_O \approx 10^2$–10^4). In contrast, in some oxides such as TiO_2 that have an oxygen deficit, it has been observed that $D_O \approx D_{Ti}$. This result is not in contradiction with the assumption of several authors who postulate that both oxygen vacancies and titanium interstitials are simultaneously present in this oxide.

Electrical transport in ionic compounds does not necessarily occur by means of point defects. Electrical conductivity due to a charge carrier is given by

$$\sigma = C\,U\,z\,F \tag{7.29}$$

where C is the molar concentration of charge carriers per unit volume and U is the electrical mobility (expressed in $m^2\ s^{-1}\ V^{-1}$). The mobility U corresponds to the velocity of the charged particles under an electric field equal to unity.

In ionic crystals, the total conductivity σ_t is generally written in terms of ionic and electronic conductivities as

$$\sigma_t = \sigma_{ionic} + \sigma_{electronic} \tag{7.30}$$

Let σ_δ be the partial conductivity relevant to the defect δ, and considering the definition of the electrical mobility U_δ, we obtain

$$\sigma_\delta = zFC_\delta U_\delta = z^2F^2\frac{C_\delta D_\delta}{RT} \tag{7.31}$$

If σ_j is the contribution to the total conductivity of the charged species j, we can write

$$\sigma_j = \sigma_\delta \tag{7.32}$$

Since

$$C_\delta D_\delta = C_j D_j \tag{7.33}$$

we obtain the *Nernst–Einstein equation*:

$$\sigma_j = z^2F^2\frac{C_j D_j}{RT} \tag{7.34}$$

In this equation, σ_j is the ionic contribution of species of type j to the total conductivity, D_j is the self-diffusion coefficient of particles j, and C_j is the volume concentration of regular sites in the sublattice that contain species j.

Since the mobility of electronic defects is much higher than that of point defects ($U_\varepsilon \gg U_\delta$), it can be said that the total electrical conductivity is essentially electronic. Also, it is easy to show that the conductivity varies with oxygen pressure in the same way as does the concentration of the predominant ionized defect (although the current is carried by electronic defects).

The temperature dependence of the conductivity is determined by both the charge carrier mobility and concentration terms.

When ion movements involve jumps between definite sites of the crystal, an energy barrier ΔG_m has to be overcome. The defect mobility then increases strongly with temperature according to an exponential law (*activated process*):

$$U_\delta = U_\delta^0 \exp\left(-\frac{\Delta G_m}{RT}\right) \tag{7.35}$$

where ΔG_m is the free energy of migration of the defect.

The temperature dependence of electron mobility is a function of the electronic structure of the crystal. The electron movement is an activated process, and the electronic mobility obeys the following equation:

$$U_\varepsilon = U_\varepsilon^0 \exp\left(-\frac{E_\varepsilon}{RT}\right) \tag{7.36}$$

where E_ε is the overall activation energy for polaron migration in the periodic field within the crystal or, in other words, for polaron (electron and distortion field) scattering by lattice vibrations and/or imperfections, also known as *polaron hopping* and usually treated as a diffusion process.

The determination of the variation of the electronic mobility with temperature may allow us to identify the migration mechanism of electrons in the lattice. Whatever the nature of the charge carrier (ionic or electronic defects), the concentration increases with temperature according to

$$[\text{defect}] = [\text{defect}]_0\left(-\frac{\Delta G_f}{RT}\right) \tag{7.37}$$

where ΔG_f is the free energy of formation of defects.

Whatever the nature of the conduction mechanism, the electrical conductivity is proportional to the product of the drift mobility and the charge carrier concentration, which varies exponentially with temperature. The crystal conductivity always increases with increasing temperature due to the exponential increase in the number of charge carriers. This characteristic differentiates covalent/ionic compounds from metallic conductors, which exhibit a decrease of the electrical conductivity with increasing temperature (Kröger 1975; Mrowec 1980; Philibert 1985).

7.4.2 Line and Planar Defects

As diffusion along line and surface defects, including dislocations, grain boundaries, internal and external surfaces, etc., is generally more rapid than lattice diffusion, they are termed high-diffusivity or easy diffusion paths. This type of diffusion is often called *short-circuit diffusion*. The contribution of grain boundary diffusion to the total diffusion flux decreases as the temperature increases for two main reasons:

- The grain size is larger and the temperature is higher because of grain growth.
- The activation energy for grain boundary diffusion is less than that for intracrystalline diffusion (from 20% to 30% smaller).

The *effective diffusion coefficient* may be defined by the *Hart equation*:

$$D_{eff} = fD_{gb} + (1-f)\,D_v \tag{7.38}$$

where f is the volume fraction of short-circuit paths, D_v the lattice diffusion coefficient, and D_{gb} the short-circuit diffusion coefficient. D_{eff} may be identified with D_v, the intracrystalline diffusion coefficient, at high temperatures, but at low temperatures, the short-circuit contribution to diffusion can become significant. In general, in accordance with Tamann's empirical law, grain boundary diffusion would be expected to dominate at lower temperatures, say, below a transition temperature of between 1/2 and 2/3 of the absolute melting temperature of the crystal. Conversely,

the contribution made by short-circuit diffusion processes will be negligible at higher temperatures. Grain boundary diffusion in growing oxide scales has been reported for NiO (Atkinson et al. 1986), Cr_2O_3 (Hussey and Graham 1996), Al_2O_3 (Prescott and Graham 1992), and other product films.

7.4.3 Three-Dimensional Defects

Stress generation in the oxide layer and the underlying metal may cause through-scale cracking, spalling of the oxide, stratification phenomena, or even detachment of the scale. These phenomena lead to loss of protective properties and faster degradation of metals and alloys. The sources of stress may be either internal (scale growth) or external (mechanical and/or thermal stresses). Often, due to mechanical stresses, a porous layer may develop after the oxide scale has reached a critical thickness. The two main sources of stress are growth stresses, which develop during isothermal formation of the scale, and thermal stresses, which arise from differential thermal expansion between the oxide scale and the metal or alloy during temperature changes.

7.4.3.1 Growth Stresses

Observed stresses depend on the oxidation mechanism and on the physicochemical properties of the alloy and of the oxide. The most important causes of growth stresses are (Béranger et al. 1987) the volume difference between the oxide and the metal (Pilling and Bedworth rule), the oxidation mechanism (for example, internal or external oxidation of alloys), oxygen dissolution in alloys, epitaxial constraints, physicochemical changes in the alloy or scale during the growth, specimen geometry, etc.

Two different types of growth stresses can be distinguished: geometrically induced growth stresses caused by the surface curvature of components and the intrinsic growth stresses. As can often be seen in oxidation experiments, the oxide scales crack at the edges of the specimens, initially leading to a locally increased attack at these sites. Such cracking is usually due to geometrically induced growth stresses that arise at edges and corners due to the small surface curvature radius. This situation has been dealt with quantitatively by Manning (1981).

With the help of models, the tangential and radial stresses can be calculated for the ideal case of curved surfaces with a constant radius of curvature. Introduction of the oxide displacement vector M is helpful here; M lies perpendicular to the oxide–metal interface and describes the displacement of a reference point in the film resulting from the oxidation. The magnitude and sign of M are incorporated in M, which is calculated as follows:

$$M = \mathrm{PBR}\,(1-a) - (1-V) \tag{7.39}$$

where a is the fraction of oxide formed on the scale surface, $(1-a)$ is the fraction of oxide formed at the metal–oxide interface, V is the volume fraction of metal consumed in the oxidation by injecting vacancies into the metal, $(1-V)$ is the volume fraction of metal consumed in the oxidation that originates directly from the metal surface, and PBR is the *Pilling–Bedworth ratio* (see later in this section).

Oxidation leads to an increase in the strain in the circumferential direction (tangential strain $\varepsilon^{\mathrm{t}}_{\mathrm{Ox}}$) with a rate of

$$\frac{\mathrm{d}\varepsilon^{\mathrm{t}}_{\mathrm{Ox}}}{\mathrm{d}t} = \left(\frac{M}{R_{\mathrm{s}}}\right)\frac{\mathrm{d}h}{\mathrm{d}t} = \frac{M}{R_{\mathrm{s}} \times \mathrm{PBR}}\,\frac{\mathrm{d}x}{\mathrm{d}t} \tag{7.40}$$

where R_{s} is the radius of curvature of the surface (concave $R_{\mathrm{s}} < \mathrm{O}$, convex $R_{\mathrm{s}} > \mathrm{O}$) and h is the metal recession (increase in oxide film thickness $\mathrm{d}x = \mathrm{PBR}\ \mathrm{d}h$). Equation (7.40) allows the tangential stresses $\sigma^{\mathrm{t}}_{\mathrm{Ox}}$ to be calculated assuming linear elastic behavior. The magnitude of the maximum radial stresses, $\sigma^{\mathrm{r}}_{\mathrm{Ox}}$, is given by

$$\sigma^{\mathrm{r}}_{\mathrm{Ox}} = \frac{\mathrm{PBR} \times h}{R_{\mathrm{s}}}\sigma^{\mathrm{t}}_{\mathrm{Ox}} \tag{7.41}$$

The relationship between the signs of the tangential and radial strains and stresses in the scale and at the metal–oxide interface, respectively, are

$$\mathrm{sign}\ \varepsilon^{\mathrm{t}}_{\mathrm{Ox}} = \mathrm{sign}\ (-\varepsilon^{\mathrm{r}}_{\mathrm{Ox}} R_{\mathrm{s}}) \tag{7.42}$$

$$\mathrm{sign}\ \sigma^{\mathrm{t}}_{\mathrm{Ox}} = \mathrm{sign}(-\sigma^{\mathrm{r}}_{\mathrm{Ox}} R_{\mathrm{s}}) \tag{7.43}$$

A plus sign indicates tensile stress, and a minus sign means compressive stress. The sign and level of the stresses in the scale depend on its growth direction and on the radius of service curvature, as well as the PBR. The latter was introduced in 1925 in order to explain the formation of growth stresses during oxidation and describes the volume change that is involved in the transition from the metal lattice to the cation lattice of the oxide when only the oxygen anions are diffusing. In other words, the PBR corresponds to the ratio of the volume per metal ion in the oxide to the volume per metal atom in the metal (Fromm 1998):

$$\mathrm{PBR} = \frac{1}{a} V_{\mathrm{eq}}(\mathrm{M}_a\mathrm{O}_b)/V_{\mathrm{eq}}(\mathrm{M}) \tag{7.44}$$

It was argued that if the PBR was less than 1, the growth stresses would be tensile and the oxide would crack and not cover the entire metal surface. As indicated in Table 7.2, alkali and alkaline earth metals belong to this class of materials. On the other hand, if the PBR was higher than 1, compressive stresses would develop and the oxide could be protective, at least during the early stages of oxidation. The majority of metals fall into this category.

We now know that the Pilling–Bedworth rule regarding protective behavior exhibits several exceptions. Important examples are tantalum or niobium where, even though the

Table 7.2 Pilling–Bedworth ratios for some metal–oxygen systems

Oxide	K_2O	CaO	MgO	CeO_2	Na_2O	CdO	Al_2O_3	ZnO	ZrO_2
PBR	0.45	0.64	0.8	0.90	0.97	1.21	1.28	1.55	1.56
Oxide	Cu_2O	NiO	FeO	TiO_2	CoO	SiO_2	Cr_2O_3	Ta_2O_5	Nb_2O_5
PBR	1.64	1.65	1.7	1.73	1.86	1.9	2.07	2.5	2.7

PBR is substantially larger than unity, cracks develop in the oxide scale after extended exposure and these produce non-protective conditions. Whereas the Pilling–Bedworth paper (1923) was a significant advance at the time, it is now recognized that the approach was incomplete and that the influence of the difference between the molar volume of metal and oxide depends on the oxide growth mechanism. However, the Pilling–Bedworth approach may be of great help for the assessment of the geometrically induced growth stresses, as shown earlier.

7.4.3.2 Thermal Stresses

In most applications, high temperature alloys are subjected to temperature fluctuations even under nominally isothermal conditions. In this case, though, the resultant stresses in the oxide layer, resulting from the difference in the *coefficient of thermal expansion* (CTE) of the metal and oxide (see Table 7.3), are small and may be neglected. This will not be the case, however, for large thermal cycles or during cooling to room temperature when large stresses, perhaps of 1 GPa order, are produced in the oxide layer. Metals have, generally, a higher CTE than oxides (Table 7.3), and consequently, tensile stresses are induced in the oxide scale on heating and compressive stresses during cooling.

The thermally induced stresses can be calculated from the CTE according to the following equation (Cathcart 1975):

$$\sigma_{\text{therm}} = \frac{-E_{\text{Ox}}\Delta T(\alpha_{\text{M}}\alpha_{\text{Ox}})}{\left(1 + 2\,\frac{E_{\text{Ox}}}{E_{\text{M}}}\,\frac{d_{\text{Ox}}}{d_{\text{M}}}\right)(1-\upsilon)} \tag{7.45}$$

where α is the CTE for the metal and the oxide, E is *Young's modulus* for the metal and the oxide, d is the thickness for the metal and the oxide, and υ is *Poisson's ratio*. ΔT stands for the temperature change. The CTEs for technical materials can be found in many of the materials producers' brochures, and those for corrosion products are given in the literature (Schütze 1997). In most cases, the CTEs can be approximated by linear behavior in the temperature range concerned, but in some cases, where phase changes occur in the scale during the temperature change, nonlinear temperature dependence is found for the CTE. This is, for example, the case for several sulfide layers (Schulte and Schütze 1999) and is particularly important for magnetite and some iron-based spinels (Armilt et al. 1978), affecting stresses in oxide scales on low-alloy steels. This naturally decisively affects the stress situation in the oxide scales on low-alloy steels (Christl et al. 1989). In the temperature range between about 600 and 450 °C, the magnetite partial layer is under tensile stress when cooling from 600 °C. At lower temperatures, this oxide partial layer may come under compressive stresses, depending on the metallic substrate and its CTE. In the hematite layer, the stresses are always compressive, as the CTE always lies below that of the low-alloy steel (the exception is 9% chromium steel at temperatures below 150 °C).

Table 7.3 Linear coefficients of thermal expansion of metals and oxides, 1/°C (Schütze 1997)

System	Oxide: $10^6 \cdot \alpha_{\text{ox}}$	Metal: $10^6 \cdot \alpha_{\text{M}}$	Ratio: $\alpha_{\text{M}}/\alpha_{\text{ox}}$
Fe/FeO	12.2	15.3	1.25
Fe/Fe_2O_3	14.9	15.3	1.03
Ni/NiO	17.1	17.3	1.03
Co/CoO	15.0	14.0	0.93
Cr/Cr_2O_3	7.3	9.5	1.30
Cu/Cu_2O	4.3	18.6	4.32
Cu/CuO	9.3	18.6	2.0

7.4.3.3 Mechanical Scale Failure

Growth stresses and thermal stresses may be relieved through various mechanisms that could operate simultaneously:

- Plastic deformation of the oxide scale.
- Plastic deformation of the metal substrate.
- Spalling of the oxide from the alloy.
- Cracking of the scale.

When plastic deformation is not sufficient for stress relief, cracking may develop in the scale. It is the more efficient relaxation mechanism but will result in a sudden increase in corrosion rate. The metal oxidation may exhibit repeated regular sequences of cracking and healing of the scale.

Under tensile stresses (heating to temperatures higher than the oxidation temperature or over convex regions of a nonplanar surface), cracks appear as soon as the elastic fracture strain is reached. This critical value will be significantly less than 1% even at high temperatures.

Under compressive stresses, the degradation leads to spallation and the mechanisms are more complex. Two

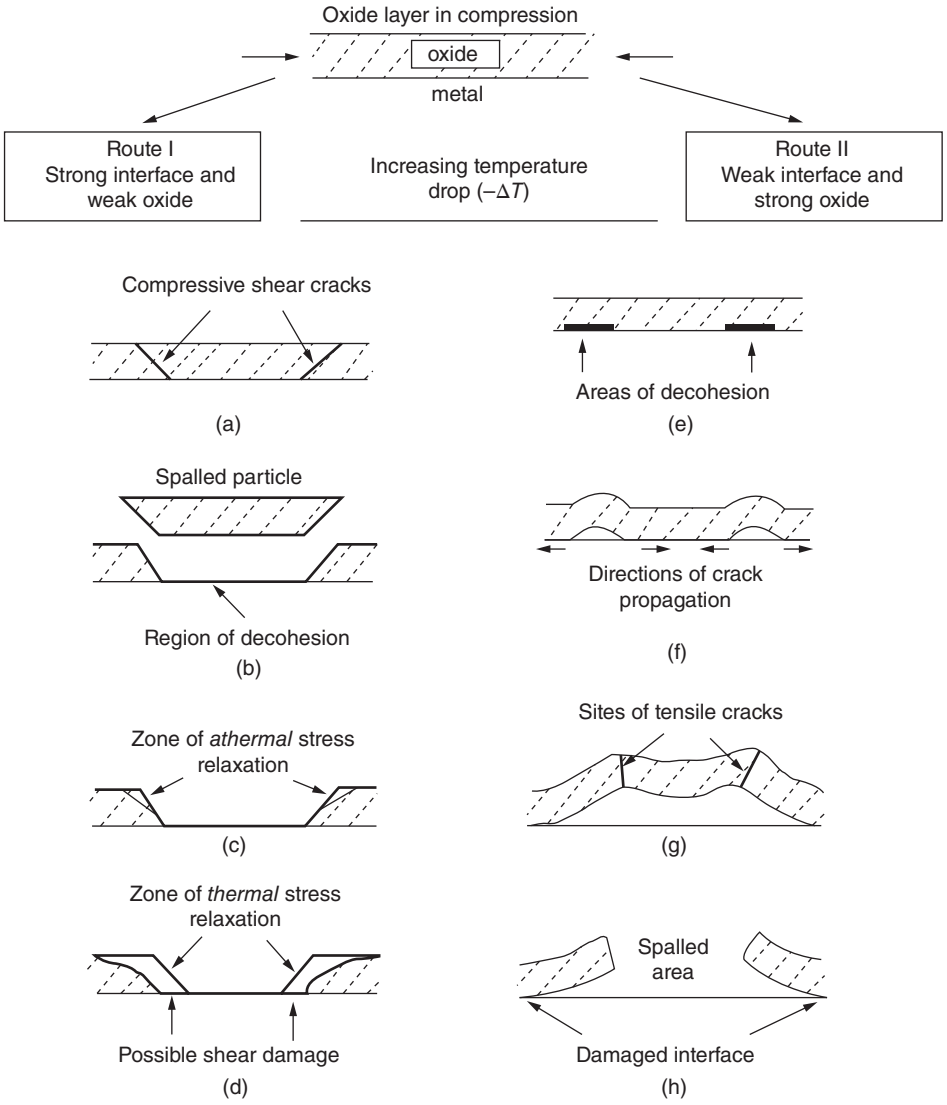


Figure 7.9 Cracking and spallation by compressive oxide stresses (Evans 1995).

processes are necessary to produce spalling: transverse cracking through the oxide and decohesion along the metal–oxide interface. Two routes of spallation have been identified: the case corresponding to a low cohesive strength of the oxide and a high adhesive strength of the scale on the substrate surface (route 1: cracking of the oxide before decohesion) and the case corresponding to a high cohesive strength of the oxide and poor adhesion of the oxide to the metal (route 2: decohesion before metal cracking). Figure 7.9 illustrates these two distinct mechanisms.

7.5 Compact Scale Growth

7.5.1 Elementary Chemical Steps

The overall oxidation reaction of a metal M may be written as shown in Eq. (6.41) (Section 6.8). The reaction can proceed only if diffusion of matter (oxygen or metal) occurs through the solid scale M_aO_b. If the scale is porous, mass transport occurs by oxygen diffusion; if the scale is compact, mass transport occurs by means of solid-state diffusion. In the latter case, the oxidation mechanism consists of at least four steps (Barret 1975; Mrowec and Stoklosa 1971; Yang et al. 1998):

- Surface step – Oxygen adsorption on the oxide.
- External step – Matter exchange at the adsorbed phase/oxide interphase.
- Diffusion step – Ionic transport through the oxide scale.
- Internal step – Matter exchange at the oxide–metal interface.

Of course, mass transport by migration of ionized point defects is accompanied by simultaneous electrical

transport, which complicates the process. In this section, the kinetics of the oxidation process leading to the growth of a compact scale are analyzed.

Let a chemical elementary step be a local reversible reaction that occurs without the formation of a distinct intermediate product, i.e. the reaction proceeds in a single step, and let an interphase elementary step be a chemical process involving matter exchange between two distinct phases. The main difficulty encountered for the formulation of these steps relates to the conditions required for the application of classical theories (Eyring theory) for the calculation of the step rates (Glasstone et al. 1941).

We will have to choose, for the adsorbed phase as well as for the oxide, structural models that exhibit ideal behavior for the reacting species in their own phase. Moreover, we will assume that the theory of absolute rates can, under these conditions, be extended to heterogeneous elementary steps involving matter exchange between two different phases.

On a solid surface, the atomic environment is modified in comparison with that in the bulk. The resulting imbalance of the forces in the surface of solids produces attractive forces for gas molecules or atoms. The phenomenon of adsorption can then produce an excess of gas atoms or molecules on the surface compared with the concentration in the adjacent gas phase. For adsorption to occur spontaneously, the process must produce a decrease in free energy, but since that is also a decrease in system entropy, adsorption is always an exothermic process. Consequently, the amount of adsorbed gas at equilibrium at constant pressure (the *adsorption isobar*) decreases with increasing temperature.

Depending on the nature of the forces involved, adsorption processes may be classified as physical adsorption (also termed *van der Waals adsorption* or *physisorption*) or chemical adsorption, usually abbreviated to chemisorption (Brunauer et al. 1938; Langmuir 1918). Physisorption is generally quasi-instantaneous, while *chemisorption* often proceeds slowly, involving an activation energy E_a. Thus, the chemical adsorption rate becomes appreciable only at sufficiently high temperature.

Many theories and models have been proposed to explain the shape of adsorption isotherms that represent the variation of adsorbed volume as a function of gas pressure or of the p/p_0 ratio (p_0 is the saturation vapor pressure at the experimental temperature). The description of monolayer adsorption can be made using as variable the fraction of the available adsorption sites that are occupied by adsorbed atoms or molecules, $\theta = s/s_0$, where s_0 is the number of adsorption sites that are initially available per unit surface area and s the number of occupied surface sites per surface area unit (thus, θ is the fraction of occupied sites).

Chemisorption involves partial electronic transfer between adsorbed molecules and the substrate. The solid surface appears inhomogeneous and exhibits specific "active" sites on which chemisorption takes place preferentially. When temperature is increased, the amount of adsorbed gas by chemisorption increases because it is an activated process; then the adsorption isobar passes through a maximum because chemisorption is an exothermic process. Since the establishment of high temperature oxidation requires at least the presence of one monolayer on the surface, it can be assumed that a chemisorbed phase is produced as a surface step.

In this discussion, this adsorbed phase is considered as a two-dimensional solution (i.e. sorption of a monolayer) of free surface sites, s, and of occupied sites, leading to the formation of a superficial compound referred to as O-s (atomically chemisorbed oxygen) where O is a particle of the gas phase (O_2). Such a solution may be considered as ideal since it is assumed that no interaction occurs between the free and occupied sites. The sorption process may then be described by an equation representing the balance between two opposite reactions with rate constants K'_a and K''_a, respectively:

$$O_2 + 2s = 2O\text{-}s \tag{7.46}$$

with $K_a = K'_a/K''_a$ denoting the equilibrium constant of the elementary step of sorption.

Under these conditions, if p denotes the partial pressure of the p_{O_2} species, θ^{eq} the fractional surface coverage, the law of mass action applied to the equilibrium leads to

$$\theta^{eq} = \sqrt{K_a p_{O_2}}\left(1 + \sqrt{K_a p_{O_2}}\right) \tag{7.47}$$

indicating that the sorption is governed by the *Langmuir equation* (dissociation occurs on chemisorption, which is likely at high temperature). If $dn_{O\text{-}s}$ is the number of O-s particles formed by adsorption per unit area during the time dt, the rate of the sorption process can be given by the equations

$$\frac{dn_{O\text{-}s}}{dt} = K'_a(1-\theta)^2 p_{O_2} - K''_a\theta^2 \tag{7.48}$$

or

$$\frac{dn_{O\text{-}s}}{dt} = K'_a\frac{\theta^2}{K_a}\left[\left(\frac{1-\theta}{\theta}\right)^2 K_a p_{O_2} - 1\right] \tag{7.49}$$

with

$$K_a p_{O_2} = \left(\frac{\theta^{eq}}{1-\theta^{eq}}\right)^2 \tag{7.50}$$

The proposed model to account for the external and internal steps uses the concept of point defects, and, for simplicity, it can be assumed that only one defect is predominant in the lattice, that is, either the metal vacancy V''_M or the oxygen interstitial O''_i for the case of a p-type semiconductor and either the oxygen vacancy $V^{\bullet\bullet}_0$ or the metal interstitial $M^{\bullet\bullet}_i$ for the case of an n-type semiconductor.

The defects are then generated at the external interphase (cationic diffusion, p-type semiconductor) or at the internal interphase (anionic diffusion, n-type semiconductor) (see Figure 7.6).

Then, in the case of an n-type semiconductor with metal vacancies, the external step can be described by

$$\text{O-s} = \text{O}_0 + \text{V}''_\text{M} + 2\text{h}^\bullet + \text{s} \tag{7.51}$$

with $K_\text{e} = K'_\text{e}/K''_\text{e}$ denoting the equilibrium constant of the external step of matter exchange. The external reaction rate is given by

$$\frac{\text{d}n_\text{e}}{\text{d}t} = K'_\text{e}\,\theta - K''_\text{e}[\text{V}''_\text{M}]_\text{e}[\text{h}^\bullet]^2_\text{e}(1-\theta) \tag{7.52}$$

Under equilibrium conditions, for a given value of θ, we have

$$\frac{\text{d}n_\text{e}}{\text{d}t} = K'_\text{e}\,\theta\,\left[1 - ([\text{V}''_\text{M}]_\text{e}/[\text{V}''_\text{M}]^\text{eq}_\text{e})^3\right] \tag{7.53}$$

with

$$[\text{V}''_\text{M}]^\text{eq}_\text{e} = \frac{1}{4}\,K_\text{e}\theta/(1-\theta) \tag{7.54}$$

Again for a p-type semiconductor with metal vacancies, we have for the internal step

$$\text{V}''_\text{M} + 2\text{h}^\bullet + \text{M} = \text{M}_\text{M} \tag{7.55}$$

$$\frac{\text{d}n_\text{i}}{\text{d}t} = 4K'_\text{i}[\text{V}''_\text{M}]^3_\text{i} - [\text{V}''_\text{M}]^{\text{eq}3}_\text{i} \tag{7.56}$$

with

$$[\text{V}''_\text{M}]^\text{eq}_\text{i} = \left(\frac{1}{4}\frac{1}{K_\text{i}}\right)^{1/3} \tag{7.57}$$

In a thick, growing oxide scale, a positive space charge can appear in contact with the metal balanced by a negative space charge localized near the external interphase. This charge distribution induces, at any point within the scale, an electric field that both accelerates the positively charged ionic defects and slows down the negatively charged electronic defects until no net electrical current flows through the scale. Consequently, stationary concentration profiles are established in the MO scale, the electrically neutral zone extending over practically all of the scale thickness (Wagner 1933a,b).

Taking into account the possible electrical potential gradient through the scale, the particle fluxes are given by

$$J_z = -\left[D_\delta\frac{\partial c_\delta}{\partial x} + C_\delta U_\delta\frac{\partial\phi}{\partial x}\right] \tag{7.58}$$

$$J_\varepsilon = -D_\varepsilon\left[\frac{\partial c_\varepsilon}{\partial x} \pm C_\varepsilon U_\varepsilon\frac{\partial\phi}{\partial x}\right] \tag{7.59}$$

In these expressions, C_δ (C_ε) is the volume concentration of point (electronic) defects with z degree of ionization, D_δ (D_ε) is the diffusion coefficient, U_δ (U_ε) is the electric mobility of these charge carriers, and ϕ is the electric potential at the coordinate x. C_δ and $[\delta]$ are linked by the relationship $C_\delta = [\delta]/\Omega$, Ω being the volume of one mole of oxide. A positive sign (+) has to be used if the defects are positively charged and a negative sign (−) for negatively charged defects.

A brief kinetic analysis of the four elementary steps for reaction (6.41) has been presented in this section. The rate expressions of the elementary steps were expressed in a form involving the deviation from equilibrium, i.e. within the framework of the thermodynamics of irreversible processes. The general system of equations relating to the growth of an oxide scale MO can then be established by expressing the mass balance at both sides of each interphase in the adsorbed phase and within the scale. These equations being differential cannot be solved analytically. However, it is possible to make the simplifying assumption that the concentrations tend to become time independent, i.e. a quasi-steady state develops. On this basis, the system of differential equations allowing calculation of the reaction rate can be solved analytically, leading to considerable simplifications. It should be recalled that if one of the rate constants or the diffusion coefficient has a finite value, all the other constants having very large values, we deal with what is called a pure regime (Gesmundo and Viani 1981; Graham et al. 1972). In all other cases, it is called a mixed regime (Deal and Grove 1965; Pettit and Wagner 1964). Hereinafter, we describe pure diffusional regimes.

7.5.2 Diffusion-Controlled Oxidation

Assuming that cationic transport across the growing oxide layer controls the rate of scaling and that thermodynamic equilibrium is established at each interphase, the outward cation flux, $J_{\text{M}^{2+}}$, is equal and opposite to the inward flux of cation vacancies, and we can write

$$J_{\text{M}^{2+}} = -J_{\text{V}''_\text{M}} = D_{\text{V}''_\text{M}}\frac{[\text{V}''_\text{M}]'' - [\text{V}''_\text{M}]'}{y} \tag{7.60}$$

where y is the oxide thickness, $D_{\text{V}''_\text{M}}$ is the diffusion coefficient for cation vacancies, and $[V''_\text{M}]'$and $[V''_\text{M}]''$ are the vacancy concentrations at the scale/metal and scale/gas interphases, respectively.

Since there is thermodynamic equilibrium at each interphase, the volume of $([\text{V}''_\text{M}]'' - [\text{V}''_\text{M}]')$ is constant, and we have

$$J_{\text{M}^{2+}} = \frac{1}{\Omega}\frac{\text{d}y}{\text{d}t} = \frac{1}{\Omega}\frac{K'}{y} \tag{7.61}$$

where

$$K' = D_{\text{V}''_\text{M}}\,\Omega\,([\text{V}''_\text{M}]'' - [\text{V}''_\text{M}]') \tag{7.62}$$

Integrating and noting that $y = 0$ at $t = 0$, we obtain

$$y^2 = 2K't \tag{7.63}$$

which is the common parabolic rate law. Furthermore, since it has been shown that the cation vacancy concentration is related to the oxygen partial pressure by the equation

$$[V''_M] = \text{const. } p_{O_2}{}^{1/n} \tag{7.64}$$

the variation of the parabolic rate constant with oxygen partial pressure can be predicted by

$$K'\alpha \left[(p''_{O_2})^{1/n} - (p'_{O_2})^{1/n}\right] \tag{7.65}$$

and since p'_{O_2} is usually negligible compared with p''_{O_2}, we have

$$K'\alpha\, (p''_{O_2})^{1/n} \tag{7.66}$$

Clearly, the concentration gradient in the scale never equals zero, and, therefore, scale growth never stops.

Originally, Eq. (7.63) was derived by Wagner in a theoretical detailed analysis of the electrochemical potential situation and the transport conditions in the scale. Figure 7.10 gives a summary of the conditions for which the theory is valid.

Assumptions are as follows:

- The oxide layer is a compact, perfectly adherent scale.
- Migration of ions or electrons across the scale is the rate-controlling process.
- Thermodynamic equilibrium is established at both the metal/scale and scale/gas interfaces.
- The oxide scale shows only small deviations from stoichiometry, and, hence, the ionic fluxes are independent of position within the scale.
- Thermodynamic equilibrium is established locally throughout the scale.
- The scale is thick compared with the distances over which space charge effects (electrical double layer) occur.
- Oxygen solubility in the metal may be neglected.

This model led to the final equation of the parabolic rate constant, which is (Kofstad 1988; Wagner 1975)

$$K'_p = \frac{1}{2}\int_{p'_{O_2}}^{p''_{O_2}} \left\{ \frac{z_c}{|z_a|} D_M + D_O \right\} d\ln p_{O_2} \tag{7.67}$$

where K'_p, D_M, and D_O are given in units of $cm^2\ s^{-1}$, with D_M and D_O the self-diffusion coefficients for random diffusion of the respective ions (metal and oxygen) and z the valence of the respective ion (anion and cation).

The parabolic rate law that was derived for thickness growth can also be modified for weight gain by oxidation. In this case, K'_p has to be replaced by K''_p according to the equation

$$K''_p = 2\int_z^2 K'_p \tag{7.68}$$

Values of $\int_z$ are given in Table 7.4 for several oxides. These values are, however, based on the assumption that the scale is free of pores and cavities and consists of only one phase. Under practical conditions, this is not usually the case, and therefore these values should only be used as estimations.

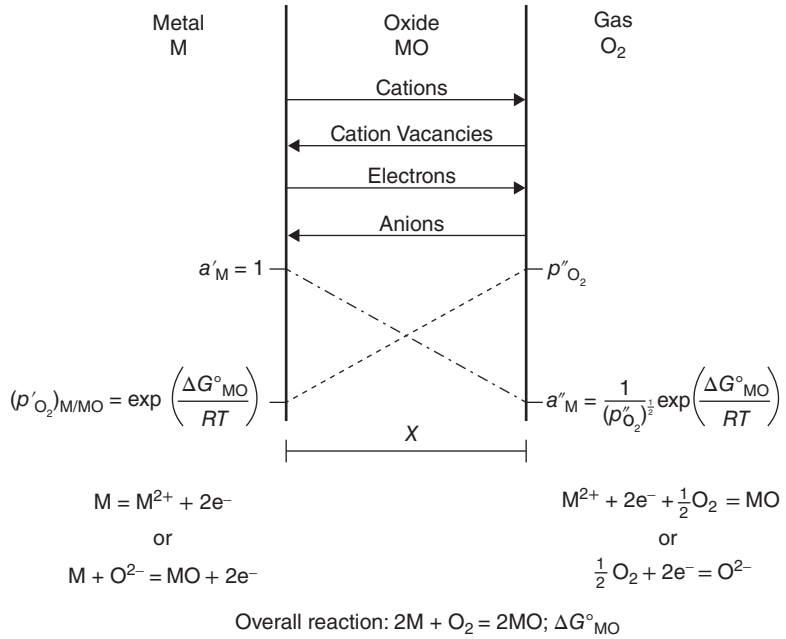


Figure 7.10 Diagram of scale forming according to Wagner's model (Birks et al. 2006).

Table 7.4 Calculation factor $\int_z$ for the conversion of mass gain data into scale thickness data using Eq. (7.68) for several oxides and sulfides (Rahmel and Schwenk 1977)

Corrosion product	$\int_z$ (g cm^{-3})
FeO	1.28
Fe_3O_4	1.43
Fe_2O_3	1.57
Cr_2O_3	1.64
$FeCr_2O_4$	1.45
FeS	1.76
FeS_2	2.60

The *oxidation rate constant* K_p is the most important parameter for describing oxidation resistance. If K_p is low, the overall oxidation rate is low and metal consumption occurs at a very low rate. This is typical for protective oxidation. If K_p is high, metal consumption occurs at a high rate and the case of non-protective oxidation exists. From K_p the metal consumption rate can also be calculated (Heitz et al. 1992). This requires knowledge of the stoichiometry of the oxide and the specific weight values, as well as the molar weights of the reactants. Then the metal consumption can be calculated.

The real value of Wagner's analysis lies in providing a complete mechanistic understanding of the process of high temperature oxidation under the conditions set out. The predictions of Wagner's theory for n-type and p-type oxides have been extensively examined by several workers (Heitz et al. 1992; Mrowec and Przybylski 1977a,b; Sarrazin and Besson 1973). For many systems, the obtained rate constants are generally several orders of magnitude larger than those that one would calculate from lattice diffusion data from Eq. (7.67). This discrepancy indicates that "short-circuit transport" is contributing to growth of the oxide film.

7.5.3 Short-Circuit Diffusion

Lattice diffusion is the dominant process of mass transport at high temperature, provided there is a sufficiently high defect concentration, but mass transport can also occur along dislocations or grain boundaries. Thus, the overall transport in polycrystalline oxide scales generally results from two fluxes of matter in parallel: an intragranular flux J_V and a flux along grain boundaries J_{gb}.

The oxidation rate may be expressed as a function of the effective diffusion coefficient defined by Eq. (7.38) (see Section 7.4.1). The scale growth rate obeys the differential equation

$$\frac{dy}{dt} = \Omega D_{eff} \frac{\Delta C}{y} \tag{7.69}$$

where ΔC is the defect concentration difference through the oxide scale and Ω the molar volume of the oxide. Integration of Eq. (7.69) leads to

$$y^2 = 2D_{eff}\Delta C t = K'_{p(eff)} t \tag{7.70}$$

where $K'_{p(eff)}$ is the *effective parabolic constant*.

Assuming that the oxide is dense and pure and the grains are spherical, the following rate equation can be obtained (Caplan et al. 1972; Graham et al. 1972; Khoi et al. 1975):

$$y^2 = 2\Omega\,\Delta C \left[D_v t + 4D_{gb} \frac{1}{K} (Kt + r_0^2)^{1/2} \right] \tag{7.71}$$

where R_0 is the initial grain radius and K is a constant, which is a function of, among others, the surface energy of grain boundaries and their thickness and of the diffusion coefficient of matter across the grain boundaries. Further numerical development of this simple model has allowed a grain size distribution, different grain boundary widths, or different laws of grain growth to be taken into consideration.

7.6 Multilayered Scale Growth

The formation of several corrosion scales on metals or alloys is often observed. In order to understand clearly the growth mechanisms of these scales, it is of major importance to know whether they form concurrently or sequentially.

7.6.1 Compact Subscales

The theory of multilayered scale growth on pure metals has been treated by Yurek et al. (1974). The hypothetical system treated is shown in Figure 7.11. It is assumed that the growth of both scales is diffusion controlled with the outward migration of cations large relative to the inward migration of anions. The flux of cations in each oxide is assumed to be independent of distance. Each oxide exhibits predominantly electronic conductivity, and local equilibrium exists at the phase boundaries. The total oxidation reaction is

$$2V_{M_2} + M_{M_1} = 3V_{M_1} + M_{M_2} + O_{O_1} \tag{7.72}$$

The cation vacancies are assumed to be neutral. The cation flux in subscale (1) is

$$J_M = \frac{1}{\Omega_1} \frac{K'_{p1}}{y_1} \tag{7.73}$$

and the amounts, Q, of metal consumed per unit area to form layers (1) and (2) are, respectively,

$$Q_1 = 2y_1/\Omega_2; \quad Q_2 = y_2/\Omega_2 \tag{7.74}$$

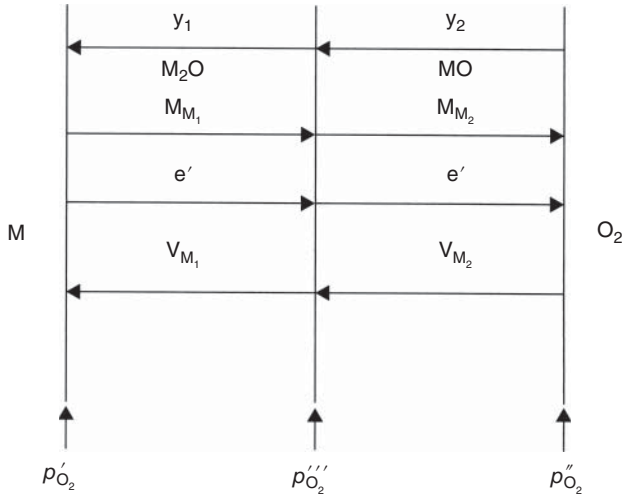


Figure 7.11 Schematic diagram of hypothetical two-layered scale.

The fractions of the cation flux involved in the growth of subscales (1) and (2) are, respectively.

$$J_{M_1} = \frac{Q_1}{Q_1 + Q_2} J_M = \frac{2y_1}{\Omega_1} \cdot \frac{K'_{p_1}/\Omega_1 y_1}{(2y_1/\Omega_1) + (y_2/\Omega_2)} \quad (7.75)$$

$$J_{M_2} = \frac{Q_2}{Q_1 + Q_2} J_M = \frac{y_2}{\Omega_2} \cdot \frac{K'_{p_2}/\Omega_2 y_2}{(2y_1/\Omega_1) + (y_2/\Omega_2)} \quad (7.76)$$

with $J_M = J_{M_1} + J_{M_2}$.

With this model, it is not possible to express simply the ratio of the thickness of both subscales. However, the ratio of parabolic rate constants can be obtained as

$$\frac{K'_{p_2}}{K'_{p_1}} = \left(\frac{y_2}{y_1}\right)^2 \frac{1 + (\Omega_1 y_1/2y_2\Omega_2)}{1 + (2\Omega_2 y_2/\Omega_1 y_1)} \quad (7.77)$$

When one of the layers is much larger than the other, this expression simplifies to

$$\frac{y_2}{y_1} = \frac{K'_{p_2}}{K'_{p_1}} \times \frac{\Omega_1}{\Omega_2} \quad (7.78)$$

for example, if $y_2 \ll y_1$. It appears that this ratio is directly proportional to the ratio of parabolic rate constants for the growth of each layer alone, i.e. roughly proportional to the ratio of the self-diffusion coefficients of the mobile species.

This theory has been shown by Garnaud (1977) to describe the growth of CuO and Cu_2O on Cu, by Garnaud and Rapp (1977) to describe the growth of Fe_3O_4 and FeO on Fe, and by Hsu and Yurek (1982) to describe the growth of Co_3O_4 and CoO on Co.

7.6.2 Paralinear Oxidation

Generally, experience shows that the oxidation of a metal is often protective during the early stages but that the protective properties of the scale can be partially or totally lost during later stages. For example, according to the *Haycock–Loriers model* (Haycock 1959; Loriers 1950), the oxidation process involves the concurrent growth of an inner compact layer of MO, controlled by a diffusion mechanism, and its progressive transformation at its outer interface into an external porous layer MO′. The rate of growth of the inner compact layer controlled by diffusional transport is given by

$$d(\Delta m_1)/dt = (K_p/2\Delta m_1) - K_1 \quad (7.79)$$

where Δm_1 is the mass of oxygen in the compact scale, K_p is the parabolic rate constant for growth of the layer, and K_1 is the rate constant for its transformation. The growth rate of the outer porous layer controlled by the reaction at its interface with the inner compact layer is given by

$$d(\Delta m_2)/dt = fK_1 \quad (7.80)$$

where f is the ratio of the oxygen content in the oxide MO′ to that in the oxide MO. If the scale consists of two layers of the same oxide, $f = 1$, and the weight gain Δm is given by the rate equation

$$\Delta m + \frac{K_p}{2K_1} \ln\left[1 - \frac{2K_1}{K_p}(\Delta m - K_1 t)\right] = 0 \quad (7.81)$$

where the rate constant K_1 is characteristic of a transformation in the solid state that does not depend on the oxygen pressure. The function $\Delta m = \Delta m_1 + \Delta m_2 = F(t)$ can be approximated by the equation

$$\Delta m = \sqrt{K_p t} + f K_1 t \quad (7.82)$$

which describes *paralinear oxidation* for which parabolic kinetics predominate during the early stages of oxidation becoming linear at longer times. This is illustrated in Figure 7.12. Paralinear oxidation is observed during the oxidation of a wide range of metals, especially if mechanical damage occurs to the scale during thermal cycling (Chang et al. 1990; Rapp and Colson 1966). This is more likely to be the case if the CTE of the oxide is much less or greater than unity. The simultaneous oxidation and evaporation leads to the formation of porous and partially porous scales (Tedmon 1966).

7.6.3 Stratified Scales

Several metals, particularly in columns IV and V (Ti, Zr, Nb, Ta) of the periodic table, form *stratified scales* during their oxidation at high temperatures as a result of periodic cracking of the growing oxide. From a kinetic point of view, such cracking leads to two types of rate laws (Figure 7.13): the first one is described by successive parabolic or cubic

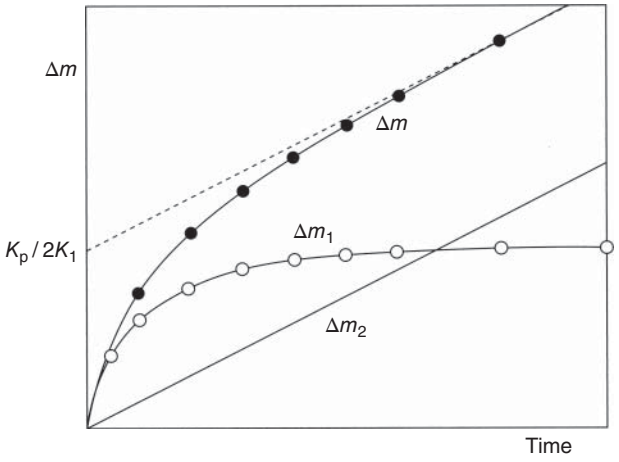


Figure 7.12 Schematic representation of total weight gain Δm illustrating paralinear rate equation.

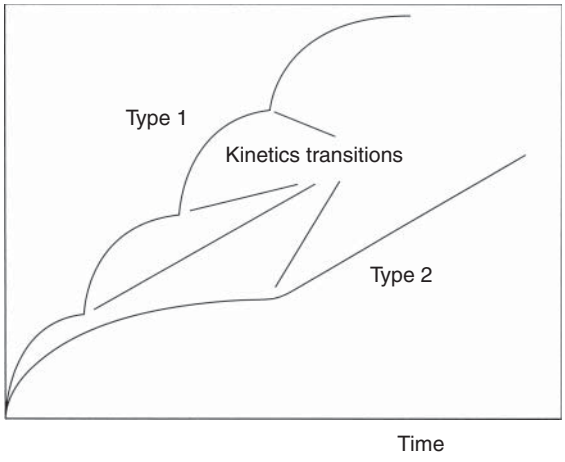


Figure 7.13 Schematic rate laws associated with formation of stratified scales.

periods (type 1), and the second one by an initial parabolic or cubic period followed by a near-linear period.

Examination of the scale formed on such specimens, either on fractured or polished cross sections, shows that for both type 1 and type 2 rate laws,

- A compact and adherent scale is formed before the first transition.
- After the first transition, a porous scale exists that consists of well-defined layers formed essentially parallel to the metal surface; these may be separated by isolated cracks, also parallel to the metal surface, or by connected pores.

Mass transport through the oxide occurs by oxygen, mainly by vacancies V_0 (diffusing from the internal to the external interface). Since the scale grows in a confined space at the internal interface, the increase in volume on oxide formation, associated with a PBR greater than unity, may generate large compressive stresses in the oxide (several gigapascals have been measured). The metal is concurrently submitted to tensile stresses of smaller magnitude (several tens of megapascals) due to its larger thickness. The high compressive stresses in the oxide are probably responsible for the observed tendency for the kinetics to approach a cubic rate law due to an associated reduction in the oxygen diffusion flux. In all cases, oxygen pressure has no influence on the rate constants.

As oxide thickness increases, compressive stresses may also increase and result in localized spallation and/or cracking (Stringer 1960a,b). Then, free access of the gas to a bare metal surface occurs and reoxidation results. Two cases can be envisaged. In the first, the bare metal is unchanged compared with that at the beginning of oxidation, in terms of composition, microstructure, or mechanical properties. Reoxidation occurs exactly as in the initial period, and the rate law is the exact repetition of the first pre-transition curve. Kinetics of type 1 (Figure 7.13) are then observed with a succession of parabolic-type periods.

In the second example, the bare metal differs from the initial state, for example, dissolution of oxygen may have occurred, leading to increased hardness and lower creep relaxation rates. The second oxide layer that forms does not then reach the thickness of the first since stress increases at a higher rate and early separation occurs from the metal. In the case of TiO_2 growth on titanium at 850 °C, for example, the second and all subsequent layers have a thickness of 1–2 μm, whereas the first attains 10–15 μm. The spallation or cracking of these scales does not occur at the same time for all locations on the specimen surface, and the resulting law is approximately linear with an increased rate compared with that in the pre-transition period. The system can be described as a metal covered by an oxide of statistically constant thickness (Munir and Cubicciotti 1983; Newcomb and Bennett 1993).

7.7 Oxidation Resistance

The oxidation of alloys and other metallic materials is a complex process consisting of a large number of phenomena that may, themselves, depend on material composition and environment, i.e. temperature, mechanical stress, gas composition, etc. To obtain effective protection of a metallic material, the oxide formed must lead to a continuous scale (external oxidation) and not to precipitates within the alloy (internal oxidation).

Although numerous studies have been devoted to oxidation of alloys, the oxidation mechanisms are often still not fully understood. In fact, the models have usually been developed for the oxidation of the relatively simple

example of pure metals and are inadequate to describe alloy oxidation. In order to do this, additional factors have to be taken into account, e.g. the different affinity for oxygen of each of the alloy's constituents, dissolution of oxygen into the alloy, solid solubility between the oxides formed, formation of complex oxides, different mobilities of the various metal ions in the oxide phases, etc. Moreover, alloy oxidation involves complex processes for which the equilibrium state is reached very slowly or may never be reached. It is unrealistic to try to classify all the various types of alloy oxidation using simple criteria. However, several classification systems have been proposed (Bénard 1962; Gesmundo and Niu 1998) to account for the diverse morphologies of oxidation scales. They use thermodynamic diagrams and kinetic considerations, and, for simplicity, we can consider that three methods are available to protect metals and alloys from high temperature oxidation: (i) control of the atmosphere, (ii) alloying addition of species more easily oxidized than the base metal (chromium, aluminum) and which form a protective scale during oxidation, and (iii) use of protective coatings deposited by various methods (cementation, plasma spraying, ion bombardment, etc.). Some considerations of these three approaches are presented in the following paragraphs.

7.7.1 Atmosphere Control

When a process is considered for use in industry, it must be effective, reliable, and economical. For most applications these requirements rule out systems based on high vacuum, and the general practice is to use atmospheres derived from fuels. The gases used are therefore mixtures of N_2, CO, CO_2, H_2, H_2O, and CH_4, which make up the products of combustion of fuels. More recently, atmospheres based on nitrogen have been increasingly used.

Starting from the fuel and air, various types of atmospheres can be produced. The main, or common, differentiation is between "exothermic" and "endothermic" atmospheres. The nomenclature is ambiguous and it is as well to be clear about its meaning. An exothermic atmosphere is produced exothermically by burning the fuel with measured amounts of air. This type of atmosphere has the highest oxygen potential. An endothermic atmosphere is produced by heating, by external means, a mixture of fuel gas with air over a catalyst to provide a gas containing reducing species. This atmosphere has a low oxygen potential, and heat is absorbed during its preparation; hence the atmosphere is described as endothermic. A glance at the analysis of dried, stripped, exothermic atmospheres will confirm that they are predominantly pure nitrogen. Basically, the fuel has been used to remove oxygen from the air.

The economics of using nitrogen as a controlled-atmosphere source become more attractive when such factors as safety, reliability, and productivity are considered. Furthermore, the present tendency is to move away from oil toward electricity, in which case nitrogen atmospheres will be particularly attractive.

Modern techniques are currently available using carburizing and nitriding systems under vacuum. In these processes of vacuum carburizing and plasma carburizing, the components are heated under vacuum to around 950 °C. Methane is leaked into the chamber to a pressure of between 3 and 30 mbar to add carbon to the system. In the absence of a plasma, the methane will only decompose to the extent of about 3%, probably on the surface of the components according to a sequence such as that shown in the following equation:

$$CH_4 \rightarrow CH_3 + H \rightarrow CH_2 + 2H \rightarrow CH \rightarrow 3H \rightarrow C + 4H \tag{7.83}$$

These reactions may be stimulated to provide 80% decomposition by using a plasma process to excite the methane molecule. In this case, the molecular breakdown may occur in the plasma to produce charged species. Hydrocarbons other than methane may be used as the feedstock. The usual operating sequence involves flushing and evacuation, heating to a temperature under the inert atmosphere, and carburizing for a predetermined time followed by a diffusion anneal in a carbon-free atmosphere. This cycle is designed to provide optimum surface carbon content and carburized depth (Birks et al. 2006; Fromm 1998; Grabke and Meadowcroft 1995).

The main application of controlled atmospheres is in the area of heat treatment of finished machined components or of articles of complex shape, which cannot easily be treated subsequently for the removal of surface damage. In this context, the atmosphere is controlled for one of two reasons: to prevent surface reaction or to cause a surface reaction, such as carburizing or nitriding.

Prevention or control of oxide layer formation is primarily a matter of controlling the oxygen partial pressure of the atmosphere at a value low enough to prevent oxidation, as described in Section 7.2.1. For a metal that undergoes oxidation according to the reaction shown in Eq. (7.2) (Section 7.3), where MO is the lowest oxide of M, the oxygen partial pressure must be controlled so as not to exceed a value p_{O_2}:

$$p_{O_2} = \exp\left(\frac{2\Delta G^\circ}{RT}\right) \tag{7.84}$$

where ΔG° is the standard free energy of reaction (7.2).

Unfortunately, $(p_{O_2})_{\text{M-MO}}$ is a function of temperature and has lower values at lower temperatures. Thus, if an atmosphere is designed to be effective at high temperatures, it may become oxidizing as the temperature is reduced during cooling. A surface oxide layer may, therefore, form as the metal is cooled. Although the metallurgical damage to the surface will be negligible, the surface

may be discolored, i.e. not bright. This condition can be overcome to some extent by rapid cooling or by changing the atmosphere to a lower oxygen partial pressure just before or during cooling.

For alloys, the most critical reaction must be considered when deciding on the composition of the atmosphere to be used. For this purpose, the activities of the alloy components must be known since, if the metal M in Eq. (7.2) exists at an activity a_M, the corresponding equilibrium oxygen partial pressure will be given by p'_{O_2}:

$$p'_{O_2} = \frac{1}{a_M^2} \exp\left(\frac{2\Delta G^\circ}{RT}\right) \tag{7.85}$$

If the metal activities in the alloy are not known, then, by assuming the solution to be ideal, mole fractions may be used instead of activities to give a value of the oxygen partial pressure at which experiments must be performed to establish the correct atmosphere composition.

Low oxygen partial pressures can be provided and, more importantly, controlled by using "redox" gas mixtures. These mixtures consist of an oxidized and a reduced species, which equilibrate with oxygen, e.g.

$$CO + \frac{1}{2}O_2 = CO_2$$

$$\Delta G^{\circ\prime} = -282\,200 + 86.7T\ J \tag{7.86}$$

from which p''_{O_2} or, more importantly, p_{CO_2}/p_{CO} can be obtained:

$$p''_{O_2} = \left(\frac{p_{CO_2}}{p_{CO}}\right)^2 \exp\left(\frac{2\Delta G^{\circ\prime}}{RT}\right) \tag{7.87}$$

$$\frac{p_{CO_2}}{p_{CO}} = p_{O_2}^{1/2} \exp\left(\frac{-\Delta G^{\circ\prime}}{RT}\right) \tag{7.88}$$

Thus, from Eq. (7.87), the ratio of carbon dioxide to carbon monoxide may be calculated for any oxygen partial pressure and temperature.

Further discussion of protective atmospheres can be found in references by Jansson and Foroulis (1973) and Kofstad (1966, 1988).

7.7.2 Alloying

For engineering applications, metals are strengthened and their environmental resistance improved by appropriate alloying. The basic mechanisms operating in pure metal oxidation are also operative in the oxidation of alloys with added complications. These complications include the formation of multiple oxides, mixed oxides, internal oxides, and diffusion interactions within the metals. The effect of alloying on oxidation behavior can be understood first by considering binary and ternary alloy systems, upon which so many commercial high temperature materials are based.

Alloy components have different affinities for oxygen and do not diffuse at the same rate in the oxide or the alloy. Consequently, the simple kinetic rate equations are often not followed, and the scale and the alloy compositions change in a complex way with time. The second component may enter the scale, affecting its lattice defect structure, or may accumulate as metal or as oxide beneath the main scale. Also, if oxygen diffuses into the alloy in atomic form, precipitation of the oxide of the less noble metal may occur as internal oxide. When it is considered that scales can crack, contain voids, spall, sinter, and give multiple layers of irregular thickness, it is clear that the general situation is complex. It is important to attempt to break alloy oxidation down into certain limiting cases, applicable specifically to binary alloys but in a more general way to commercial alloys, which can be treated quantitatively or at least semiquantitatively.

Thermodynamics, usually in the form of ternary equilibrium diagrams involving two alloying components and oxygen (or sulfur, etc.), are useful in predicting the alloying element likely to be preferentially oxidized and sometimes the likely steady-state scale. They can also provide information on subsequent reactions, such as the changes occurring when internal oxide is incorporated into the main scale. The application of thermodynamic concepts is exemplified here for a binary alloy AB, based on metal A, which is less reactive than the alloying element B. The oxides formed will be referred to as AO_a and BO_b.

7.7.2.1 Basic Thermodynamic Approach

Let AB be an alloy for which, at temperature T, A and B form an ideal solid solution but two immiscible oxides, AO_a and BO_b. Let $\Delta_r G_1^\circ$ be the standard Gibbs free energy, at this temperature, of the following reaction:

$$A + \frac{a}{2}O_2 = AO_a \tag{7.89}$$

For a binary alloy AB in which N_B is the mole fraction of the solute B, the equilibrium oxygen pressure obeys the following relationship:

$$\log p_{O_2} = -\frac{2}{a}\log(1 - N_B) + \frac{2\Delta_r G_1^\circ}{a\,RT\ln 10} \tag{7.90}$$

The variation of the oxygen pressure of the alloy composition, at a given temperature, is plotted in Figure 7.14 (curve (1)) (Gesmundo and Niu 1998). Likewise, the variation of the oxygen pressure of the following equilibrium ($\Delta_r G_2^\circ$ is the standard Gibbs free energy of the reaction)

$$B + \frac{b}{2}O_2 = BO_b \tag{7.91}$$

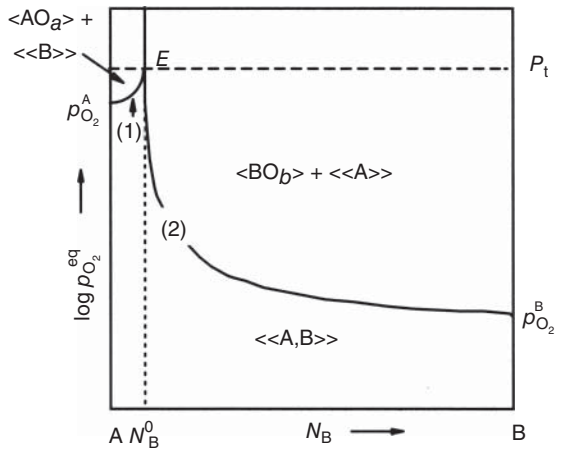


Figure 7.14 Diagram of condensed phases in the case of the oxidation of a binary alloy for which solute B is much more reactive with oxygen than component A, i.e. $p^{B}_{O_2} \ll p^{A}_{O_2}$.

obeys the equation

$$\log p_{O_2} = -\frac{2}{b}\log N_B + \frac{2\Delta_r G^\circ_2}{b\,RT\ln 10} \qquad (7.92)$$

The corresponding variation of the oxygen pressure with the alloy composition is also drawn in Figure 7.14 (curve (2)).

The point of intersection between curves (1) and (2) (point E in Figure 7.14) corresponds to equilibrium between both oxides AO_a, BO_b and the alloy (at an equilibrium pressure termed P_t). The mole fraction N^0_B of component B, corresponding to point *E*, depends on the standard Gibbs free energy of reactions (7.89) and (7.90), according to

$$\log \frac{(N^0_B)^{1/b}}{(1-N^0_B)^{1/a}} = \frac{a\Delta_r G^\circ_2 - b\Delta_r G^\circ_1}{a\,b\,RT\ln 10} \qquad (7.93)$$

Figure 7.14 was drawn assuming that the solute B is much more reactive with oxygen than the base component A. In that case, $\Delta_r G^\circ_2 \ll \Delta_r G^\circ_1$ and the mole fraction N^0_B corresponding to point *E* is very much less than 0.5.

It is necessary to plot the diagrams of condensed phases to check the compatibility of the proposed models with the experimental results.

In Chapter 3, many thermodynamic diagrams for high temperature corrosion situations are considered in detail, and here most emphasis is being placed upon factors affecting the spatial distribution of components in the scale and alloy and the influence of these factors on overall scaling behavior.

When an alloy is oxidized, the oxides of the components may be completely miscible, producing an oxide solid solution, or they may be completely or partly immiscible, producing multiphase scales. In the case of partially or completely immiscible oxides, a crude categorization for a range of alloys AB, in which A is the more noble metal and B the less noble metal, is as follows:

1. A relatively narrow composition range near pure A where AO is produced almost exclusively, at least in the external scale.
2. A relatively wide composition range near pure B where BO is produced exclusively.
3. An intermediate composition range where both AO and BO are produced.

In composition ranges (1) and (3), it is often possible to get doping of the major oxides. For example, if AO is produced almost exclusively, small concentrations of B may dissolve in the oxide, even if B is of a different valency to A and BO of different crystallographic type to AO, thereby changing its defect structure and growth rate. Furthermore, in the intermediate composition range, AO and BO may combine to give partial or complete layers of a more complex oxide compound.

There are two distinct possibilities of binary alloy oxidation. Initially, the special case of the exclusive oxidation of one alloy component is considered before procedure to the more general case where both components oxidize (Figure 7.15).

Group I

Only one of the following elements oxidizes under the prevailing conditions, giving BO.

1. The addition (minor) element B oxidizes under the given conditions:
   (a) Internally, giving BO particles in a matrix of A, e.g. Ag–Si alloys dilute in silicon, producing SiO_2 particles in a silver matrix (Figure 7.15a). The oxygen pressure in the atmosphere is less than the equilibrium dissociation pressure of AO.
   (b) Exclusively externally, giving a single layer of BO above an alloy matrix depleted in B, e.g. Ag–Si alloys richer in silicon, producing an external SiO_2 layer (Figure 7.15b). The oxygen pressure in the atmosphere is again generally less than the dissociation pressure of AO. A special case of this situation exists, however, where both alloying elements can oxidize, but the kinetic and geometrical conditions allow B to be highly selectively oxidized, e.g. Fe–Cr and Ni–Cr alloys reasonably rich in chromium produce essentially Cr_2O_3 scales, especially when oxidized at low partial pressures of oxygen. In practice, small amounts of iron or nickel enter the Cr_2O_3 scales, producing solid solutions of doping effects.
2. The element B is now the major element and oxidizes exclusively:

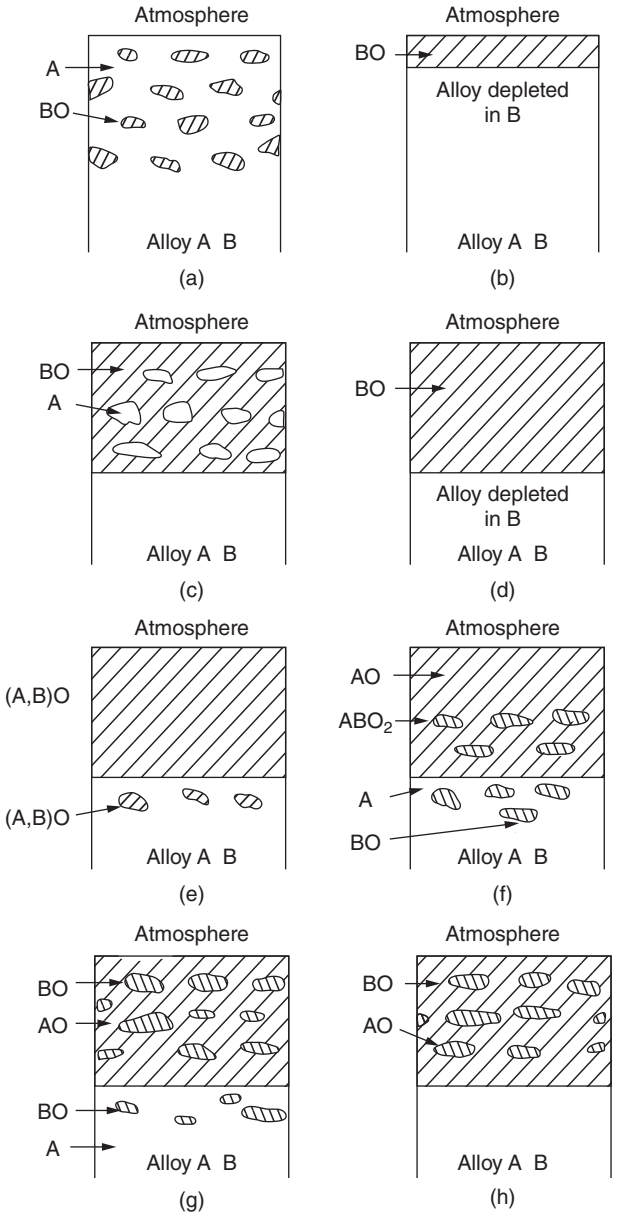


Figure 7.15 Schematic representation of modes of oxidation of alloy AB of variable composition, where B is the less noble metal. (a) Minor element B only oxidizes, giving internal oxide BO in a matrix of A. (b) Minor element B only oxidizes, giving external oxide BO above alloy depleted in B. (c) Major element B only oxidizes giving particles of A in a matrix of BO. (d) Major element B only oxidizes, giving external oxide BO above alloy depleted in B. (e) A and B oxidize to give single solid solution or compound of variable composition, (A, B)O. (f) A and B oxidize to give compound ABO_2 dispersed in a matrix of AO. (g) A and minor component B oxidize to give insoluble oxides, with BO in a matrix of AO. (h) A and major component B oxidize to give insoluble oxides, with AO in a matrix of BO.

(a) Leaving the non-oxidizable metal A dispersed in BO, e.g. Cu–Au alloys rich in copper (Figure 7.15c).

(b) Leaving the non-oxidizable metal A in an A-enriched zone beneath the BO scale, e.g. Ni–Pt alloys (Figure 7.15d), Fe–Cr alloys richer in chromium than those in group I (a)(2) come in this category, as do certain Fe–Ni alloys under appropriate conditions.

Group II

Both alloying elements oxidize simultaneously to give AO and BO, the oxygen pressure in the atmosphere being greater than the equilibrium dissociation pressures of both oxides.

1. AO and BO react to give a compound:

(a) AO and BO give a single solid solution (A, B)O, e.g. Ni–CO alloys (Figure 7.15e). In practice, some internal (A, B)O richer in B than the surface scale is found in the alloy.

(b) A double oxide is formed, often as a spinel, which may give a complete surface layer of variable composition (Figure 7.15e), as for certain Fe–Cr alloys, or particles incorporated into a matrix of AO if the reaction is incomplete, as for certain Ni–Cr alloys (Figure 7.15f).

2. AO and BO are virtually insoluble in each other:

(a) The less noble metal B is the minor component. An internal oxide of BO lies beneath a mixed layer of AO and BO, e.g. certain Cu–Ni, Cu–Zn, Cu–Al alloys, and many other examples (Figure 7.15g).

(b) The less noble metal is the major component so that no internal oxidation is now observed (Figure 7.15h). In practice, the second-phase oxidation in Figure 7.15g may not be present in the outer regions of the scale because AO may grow rapidly to produce outer regions exclusively of this oxide. The outer regions may be oxidized to higher oxides, e.g. a CuO layer is found outside Cu_2O on Cu–Si alloys. Conditions may develop so that the internal oxide particles link up to give a complete healing layer of BO at the scale base. This can apply to alloys that begin scaling as in Figure 7.15g.

It is therefore apparent that there is not, and never can be, a single comprehensive theory of alloy oxidation. Rather, there is a sequence of special cases. Furthermore, it must be recognized that in certain alloy systems several classifications of behavior are possible, depending on the composition and oxidation atmosphere, temperature, pressure, time, etc. Changes from one type of behavior to another may occur on a single specimen.

The case of alloys AB, such as Ag–In or Ag–Si, in which only one of the components can be oxidized at

elevated temperature, is considered first. The component B on the alloy surface produces nuclei of BO in a matrix of A. If B can diffuse up to the alloy surface sufficiently rapidly, a complete surface layer of BO is produced, but if this condition is not met, atomic oxygen diffuses into the alloy, precipitating BO internal oxide particles at appropriate locations. So, the formation of BO internally or externally depends on the balance between the outward flux of B and the inward flux of oxygen in the alloy.

The process of internal oxidation occurs in the following manner. Oxygen dissolves in the base metal (either at the external surface of the specimen or at the alloy–scale interface if an external scale is present) and diffuses inward through the metal matrix containing previously precipitated oxide particles. The critical activity product, $a_B a_O$, for the nucleation of precipitates is established at a reaction front (parallel to the specimen surface) by the inward-diffusing oxygen and the outward diffusion of solute (reaction B + O = BO). Nucleation of the oxide precipitate occurs, and a given precipitate grows until the reaction front moves forward and depletes the supply of solute B arriving at the precipitate. Subsequent precipitate growth occurs only by capillarity-driven coarsening (*Ostwald ripening*).

In summary, the main conditions that favor internal oxidation are as follows:

(i) The alloying element is less noble than the base alloy.

(ii) Oxygen permeability within the base alloy is sufficiently high. Note that the measurement of the depth, δ (of the subsurface zone where particles of the oxide BO are dispersed within the metal matrix A), for an alloy with a known concentration of element B allows us to estimate the product $C_O^s D_O$, which is the oxygen permeability within the alloy. Here, C_O^s is the oxygen concentration (moles/unit volume) at the alloy surface in equilibrium with the gaseous atmosphere ($C_O = C_O^s$ at $t = 0$), and D_O is the oxygen diffusion coefficient.

(iii) Oxygen dissolution within the alloy is not inhibited by a surface layer of oxide.

(iv) The mole fraction of alloying element B is sufficiently low.

In this model of internal oxidation and under steady-state conditions, with a stable BO oxide formed, the number of moles of element B that react under unit area of the specimen surface is equal to the number of moles of diffusing oxygen:

$$\frac{d\delta}{dt} = D_O C_O^s / C_B^0 \delta \tag{7.94}$$

where C_B^0 is the value of C_B for $x \geq 0$ (at $t = 0$) and $x \to \infty$ (for whatever t). By integration, a parabolic law for the depth, δ, of oxidation is obtained:

$$\delta^2 = 2 D_O C_O^s / C_B^0 \, t \tag{7.95}$$

which shows that the depth of oxidation zone at a given time is inversely proportional to the square root of the concentration of element B in the alloy. The penetration rate of the oxidation zone decreases with increasing concentration of element B and decreasing oxygen concentration, C_O^s, at the alloy surface produced, for example, by decrease in the oxygen partial pressure of the oxidizing gas. It can be appreciated that there is a limiting concentration of element B above which a continuous blocking oxide scale is formed. This corresponds to the transition from internal to external oxidation and a consequent decrease in the oxidation rate. The main conditions that favor external oxidation are as follows:

(i) The mole fraction of alloying component B is sufficiently high, and/or the diffusion coefficient D_B is high.

(ii) Oxygen permeability within the base alloy is low.

Wagner has proposed a criterion based on the comparison of both the diffusion coefficients and the equilibrium concentrations of B and O in the alloy. For an oxide BO the criterion is expressed, in a simplified form, as the ratio between the depths of the B-depleted zone (external oxidation) and the internally oxidized zone:

$$\gamma = \frac{\delta'}{\delta} = \left(2 \frac{D_B}{D_O} \times \frac{C_B^0}{C_O^s} \right)^2 \tag{7.96}$$

$\gamma > 1$ leads to external oxidation, whereas internal oxidation occurs when $\gamma < 1$.

The transition is the basis for the design of alloys based on iron, nickel, and cobalt and containing elements such as Cr, Al, and Si, which give highly stable oxides, e.g. Cr_2O_3, Al_2O_3, and SiO_2. With a sufficiently high content of alloying component, a complete external scale of oxide is formed, which protects the alloy from further oxidation. It should be pointed out that with alloying concentrations around the critical value, mechanical damage of the protective scale may result in transient non-protective oxidation of the solute-depleted zone.

The process described above in which a solute oxidizes preferentially to the parent element and forms a continuous layer on the surface is referred to as *selective oxidation*. The selective oxidation of elements that form a slowly growing protective layer is the basis for the oxidation protection of all alloys and coatings used at high temperature. The only elements that consistently result in protective scales are Cr (chromia scale), Al (alumina scale), and Si (silica scale). However, SiO_2 is not stable at low pressures. It decomposes to gaseous species such as SiO. It also reacts with water vapor at high temperatures, forming $Si(OH)_4$

gas. The use of Cr_2O_3 scale-forming alloys as well as Al_2O_3 scale-forming alloys requires a further analysis.

7.7.2.1.1 Chromia-Forming Alloys There are three composition (in weight %) regimes, with distinct oxidation characteristics for each family of Ni–Cr forming a chromia scale:

- Ni–Cr < 10%: Such alloys form a NiO external scale and internal Cr_2O_3.
- Ni-30% > Cr > 10%: In such alloys the outer scale consists of NiO on grains and Cr_2O_3 in grain boundaries.
- Ni–Cr > 30%: For such alloys the external scale consists of Cr_2O_3, which is maintained because of the large Cr reservoir.

The oxidation of Fe–Cr and Co–Cr alloys is similar to the Ni–Cr oxidation, leading to chromia scales, apart from Fe_2O_3, Fe_3O_4, and other oxides (Gesmundo and Viani 1986; Wood and Chattopadhyay 1970; Wood and Stott 1987; Wood et al. 1970).

7.7.2.1.2 Alumina-Forming Alloys There are also three composition regimes, with distinct oxidation characteristics for each family of Ni–Cr forming an alumina scale:

- Ni–Al < 6%: Such alloys form a NiO external scale and internal Al_2O_3 and $NiAl_2O_4$.
- Ni-17% > Al > 6%: In such alloys the outer scale initially consists of Al_2O_3. However, on continuous exposure, Al depletion occurs in the alloy adjacent to the oxide scale. In the depleted zone, the Al activity is well below the requirement to form continuous Al_2O_3. NiO, therefore, overtakes Al_2O_3. The overall result is the formation of a mixture of NiO and $NiAl_2O_4$ spinel formed by the combination of NiO and Al_2O_3.
- Ni–Al > 17%: For such alloys, the external scale of Al_2O_3 is maintained because of the large Al reservoir.

The oxidation of Fe–Al, Fe–Cr–Al, Ni–Cr–Al–Y, Co–Cr–Al–Y, and Fe–Cr–Al–Y alloys is similar to the Ni–Al oxidation, leading to alumina scales, apart from other Fe_2O_3, Fe_3O_4, Y_2O_3, and other oxides (Pint and Hobbs 1994; Pint et al. 1997; Westbrook and Fleischer 1994).

Alumina, Al_2O_3, exhibits a very low deviation from stoichiometry, much lower than chromia, Cr_2O_3, therefore ensuring more protective behavior (Table 7.5).

The addition of Cr to Ni–Al alloys results in a remarkable synergistic effect that is of great technological interest. For example, chromium additions of about 10 wt% can enable external Al_2O_3 formation on alloys having aluminum levels as low as 5 wt%. This phenomenon has allowed the design of more ductile alloys and coatings.

The oxidation resistance of high temperature materials is so dependent on the formation of a chromia or alumina layer that it seems appropriate to further discuss the characteristics of these protective oxides.

7.7.2.1.3 Chromia and Alumina Characteristics Cr_2O_3 has the corundum crystal structure (Figure 7.16) consisting of a hexagonal lattice, close packed with oxygen anions with 2/3 of the octahedral holes occupied by Cr. It is the only relevant oxide stable at high temperatures and is protective against both corrosion and oxidation at elevated temperatures. The Cr(III) oxide is an intrinsic semiconductor above 1250 °C that, depending on the temperature, can be p- or n-type.

Lillerud and Kofstad (1980) showed that the oxide has an equal concentration of holes and electrons at temperatures above 1000 °C, depending on the oxygen partial pressure, whereas at lower temperature chromia is p-type or n-type (at low partial pressures). Cr_2O_3 is cation deficient, and it increases at $a(O_2)^{1/8}$ rate (Stott 1987). Cr interstitials are the predominant ionic defect at low p_{O_2} (Young et al. 1985), whereas Cr vacancies are predominant (Stott 1987). Certainly, most studies of chromium oxidation indicate that the scale grows largely by chromium diffusion outward, as confirmed by oxygen tracer studies in the growing scale. However, oxygen isotrope exchange measurements (Lees and Calvert 1976) have inferred that anion transport by mechanisms other than lattice diffusion does not occur during growth of Cr_2O_3 scales on alloys at high temperature. Rapid-diffusion paths, such as grain boundaries, have a significant influence on the oxidation behavior of chromium at high temperature, as they enhance

Table 7.5 A comparison of the deviation from stoichiometry, self-diffusion coefficients, and parabolic rate constants for the growth of alumina and chromia scales

	Al_2O_3	Cr_2O_3
Deviation from stoichiometry	10^{-4} (at 1000 °C)	10^{-3} (at 600 °C)
Cation self-diffusion coefficient in oxide at 1000 °C ($cm^2\ s^{-1}$)	10^{-15}	10^{-12}
Parabolic rate constant at 1000 °C (on Fe–25Cr–5Al for Al_2O_3, on Fe–20Cr for Cr_2O_3) ($g^2\ cm^{-4}\ s^{-1}$)	2.7×10^{-13}	2.0×10^{-11}

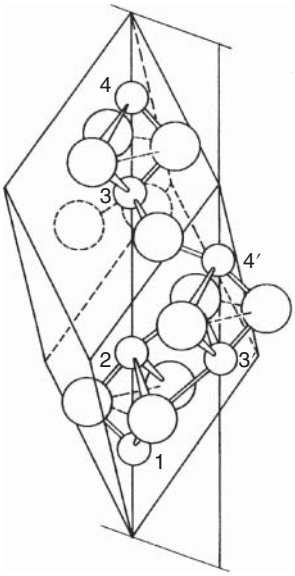


Figure 7.16 Crystal structure of Cr_2O_3 – the bigger atoms are Cr^{3+} and the smaller are O^{2-}.

the transport of cations and perhaps anions (Caplan and Sproule 1975). The scale microstructure is also determined for the chromia oxidation rate, as the fine-grained structure increases the number of short diffusion paths, therefore allowing higher oxidation rate to be achieved. The addition of reactive elements, such as yttrium, hafnium, cerium, zirconium, etc., improves the oxidation behavior as well as scale adhesion of Cr_2O_3 (Ecer and Meier 1979) and their oxides, present as fine dispersed particles in the alloy prior to oxidation (Hindam and Whittle 1982). At very high temperatures, chromia reacts with oxygen to form the volatile species CrO_3, which induces oxide thinning and a metal recession, when the diffusion through the scale is low. This effect becomes significant at 1000 °C. Therefore, alumina is a suitable candidate, as there is no vapor in the Al–O_2 system with significant vapor pressures.

Aluminum oxide exists in various modifications, depending on the temperature and the exposure time. These phases (γ-Al_2O_3, θ-Al_2O_3, and δ-Al_2O_3) are mostly metastable and are called transition oxides, as they are all transformed to the stable α-alumina after prolonged exposure. α-Al_2O_3 is also known as corundum, as its crystal structure is corundum, such as chromia (Figure 7.16). In this case, the Cr ions are replaced by Al cations located in octahedrally coordinated interstitial sites in the anion sublattice and fill 2/3 of the interstices in order to maintain electrical neutrality.

The resistance of materials at high temperature is defined by the diffusion of the species through the oxide as the kinetics depends on the mobility of the ions. It has been shown that alumina grows from both outward diffusion of Al^{3+} and inward diffusion of oxygen with a similar diffusion rate. The protection given by α-Al_2O_3 scales at high temperatures is due to the low concentrations and mobility of ionic and electronic defects. The concentrations of intrinsic point defects are probably so low that all reported properties relating to point defects and transport have been dominated by impurity dopants. It is believed that ionic defects are the major species, with electrons and holes as minorities. The concentrations of all defects depend on doping and oxygen pressure, but the nature of the dominant native ionic defects is not well established (Kröger 1981). The diffusion of aluminum occurs through bulk lattice and oxide at the grain boundaries, which represents the major short-circuit path (Reddy et al. 1982), whereas the oxygen diffusion in the scale is less prominent. The scale formed has a dual morphology, whereby the outer region usually consists of small and equiaxed grains, while the grains are columnar and coarser in the inner region (Felton and Pettit 1976; Smialek 1978). The scale morphology changes with temperature: at 900 °C whiskers are observed on the grown oxide at the oxide–gas interface extending from the substrate surface, which may be due to the formation of the unstable θ-Al_2O_3, whereas an almost flat layer (α-Al_2O_3) is observed at 1200 °C (Prescott and Graham 1992). The scale growth mechanisms depend strongly on the exposure temperature.

One of the major concerns for protective oxides at high temperatures is their adhesion to the alloy. The adhesion is mostly lost due to stresses induced during scale growth. Generally, the thermal expansion between metal and oxide is large enough to cause compressive stresses (Hindam and Whittle 1983) at room temperature, causing an interfacial shear stress and subsequent scale buckling (Hindam and Whittle 1982; Sadique et al. 2000). In the case of chromia, the addition of reactive elements ($\leq$0.01%) improves the oxidation behavior and scale adhesion of alumina (Anderson et al. 1985). The effects of rare earth elements on the oxidation resistance at high temperature are various. Reactive elements react with sulfur and form stable sulfide (Smeggil 1987), and sulfur tends to weaken the surface (Sigler 1988). They also promote faster formation of alumina.

From the above considerations, it is clear that native and doped ionic defects in compact and multilayered scales represent important factors controlling the oxidation rate of binary and multicomponent alloys at high temperature. In particular, there is now evidence that doping is the most likely rate-controlling factor in many complex oxidation processes. Therefore, a short reference is now given to doping and the *Wagner–Hauffe rules*.

7.7.2.1.4 Doping on Oxide Defect Structure The various types of defects in oxides have been well described by Kofstad (1966) and neglecting rare oxides; it can be said

that the commonly found nonstoichiometric, semiconducting oxides are normally divided into two general classes:

1. Oxides with cation defects:
   (a) Metal deficient, with cation vacancies on the cation sublattice (p-type semiconductor), e.g. NiO, CoO, and FeO.
   (b) Metal excess, with interstitial cations (n-type semiconductor), e.g. possibly ZnO.
2. Oxides with anion defects:
   (a) Oxygen deficient, with oxygen ion vacancies on the anion sublattice (n-type semiconductor), e.g. Nb_2O_5 or Ta_2O_5.
   (b) Oxygen excess, with interstitial oxygen ions (p-type semiconductor), e.g. UO_2.

In actuality, the defect structures are often more complex, the oxides containing several types of defects, sometimes linked with impurities.

When a foreign ion or dopant is added to a nonstoichiometric oxide, electroneutrality must be maintained by a redistribution of electronic and ionic defects. For example, with a metal-deficient p-type oxide like NiO, addition of trivalent ions such as Cr^{3+} increases the concentration or activity of cation vacancies but decreases the concentration of electron holes. Since transport of cations through the cation vacancies is rate determining in scale growth, there is an observed increase in oxidation rate. Additions of monovalent ions such as Li^+ have the reverse effect and reduce the oxidation rate. Comparable rules would apply to oxygen-excess p-type semiconductors. For n-type oxides of either type, additions of cations of a higher valency than those of the parent oxide decrease the respective concentrations or activities of anion vacancies or cation interstitials, thereby generally reducing the oxidation rate. Lower valency additions increase the oxidation rate. Addition of ions of the same valency should have little effect at such low levels.

The Wagner–Hauffe rules should, in principle, apply to individual matrix and precipitate phases in multiphase oxides as well as to single-phase oxides, as long as blocking effects of precipitates and certain other general rules regarding the nature of the solution of the dissolving ions are obeyed. The overoptimistic application of the rules has led to disappointment in their lack of generality, but closer scrutiny often shows that obedience could not reasonably be expected in real oxidation situations. For the rules to be obeyed, the true defect structure of the parent oxide must be fully understood (many oxides really contain several defects, possibly in association), the foreign cations are assumed to enter normal cation positions in the parent oxide at their anticipated valency, and a Wagner-type parabolic growth relationship must hold rather than a mechanism involving, say, grain boundary diffusion. Ions often have only limited solubility in the parent oxide, so the rules would not necessarily hold progressively at high addition levels. The ionic radius is a pertinent parameter in such considerations. In ideal cases, it is assumed that the dopant is homogeneously distributed through the scale, i.e. the parent and dopant oxidize at the same rate, and the rates of diffusion of the two cations in the scale are equal. In practice this probably rarely, if ever, occurs, and, except in special circumstances, concentrations of ions at the alloy–oxide and oxide–oxygen interfaces may change with time. Recently several cases of obedience and disobedience to the rules are being summarized.

Recent examples that were once considered classical cases of such doping, including the increase in oxidation rate of nickel and cobalt by additions of chromium, are now known to be much more complex. The increase in oxidation rate is a result of a very soluble interplay of doping, or other alloying effects in the semiconducting oxide, possibly electric field effects, internal and external oxidation, effects on vacancy consumption by the alloy and hence the activity gradient across the scale, pore formation in the inner and possibly the outer regions of the scale, and finally the reduction of cross-sectional area within the scale and at the alloy–oxide interface caused by Cr_2O_3 or $NiCr_2O_4$ or $CoCr_2O_4$ spinel particles (Kofstad and Hed 1969; Wood and Hodgkiess 1966).

Commercial superalloys contain many alloying elements of significance over and above chromium and aluminum. The oxidation behavior of these alloys is very complex, and oxidation resistance varies widely, although the general mechanisms described earlier still apply. The complexities arise from significant influence of the individual elemental constituents. Nickel-based superalloys containing elements such as Co, Cr, Al, Ti, W, and Ta exhibit general behavior similar to simple NiCrAl alloys. These superalloys are the most common materials used for high temperature applications. NiCrAlY-type superalloy coatings also exhibit two interesting properties: they can be adjusted to have compositions near that of the substrate, avoiding differential strain problems and possible loss of adhesion, and they provide high resistance to oxidation due to the combined effects of Al and Y. This subsection on alloying finishes by reporting basic aspects of nickel-based superalloys, taking into account their increasing importance as industrial alloys for high temperature applications.

7.7.2.1.5 Ni-Based Superalloys Superalloys belong to the category of high temperature materials with excellent mechanical properties and oxidation resistance at room and elevated temperatures. They also possess a structural stability at high temperature. In 1973, a superalloy was defined as “an alloy developed for elevated temperature service, usually based on group VIIIA elements, where

relatively severe mechanical stressing is encountered, and where high surface stability is frequently required" (Sims and Hagel 1972). This definition is still applicable. Superalloys are widely used in aerospace, power generation, aircraft, marine, petrochemical processing, gas and oil extraction as rocket engines, nuclear reactors, and steam power plants, just to name a few of their applications.

The main superalloys are Fe-, Ni-, and Co-based alloys. At temperatures up to around 700 °C, ferritic Fe-based superalloys are used. With the highest strength, Co-based superalloys can be used at very high temperatures but have poor corrosion resistance at high temperatures.

Ni-based superalloys can be applied at higher temperatures, whereas single crystalline materials can be used at $0.8T_m$ (slightly below the melting point) and for durations of up to 100 000 hours (Sims et al. 1987) and even for 200 000 hours for special alloys (Reed 2006) at somewhat lower temperatures. These materials are generally used in the hottest areas, such as the hottest part of turbines, due to their very high strength. Their metallurgy is very complex as they can be fabricated as either wrought alloys, cast alloys, or directionally solidified alloys. The chemical composition of Ni-based superalloys is very complex as up to 12 elements can be alloyed to Ni, owing to its high alloying tolerance. Furthermore, the "tramp" elements – such as sulfur, phosphorus, oxygen, and nitrogen – can be carefully controlled through appropriate melting practice. Trace elements, such as selenium, bismuth, thallium, tellurium, and lead, should be held at very low levels. With the addition of chromium and aluminum, these alloys can form continuous and adherent scales – alumina at very high temperatures and chromia at somewhat lower temperatures. Cr_2O_3 is also very effective against hot corrosion. The former polycrystalline alloys have very high Cr content (10–20% Cr), which has been decreased with the increasing use of alloys at higher temperatures. In contrast, Al content has been maintained at around 6%. The quantity of elements, such as molybdenum, tungsten, tantalum, columbium, and hafnium, depends on the strength that might be reached. With the advent of single crystalline materials, the grain boundary strengtheners – boron, zirconium, and carbon – have been removed, or their content has been reduced, carbon in particular, as is the case in, for example, the single crystalline superalloy PWA 1483. Boron and zirconium are known to retard the generation of boundary cracking, as they segregate at the grain boundaries. Zr is also a "getter" center for trace and *tramp elements*. Hafnium has taken the role of Zr in the new generation of alloys.

Superalloys have a close-packed FCC (face-centered cubic) austenite lattice. The lattice consists generally of a γ′-phase (strengthening phase Ni_3Al or Ni_3Ti with Al or Ti positioned at the corners and Ni on the faces), which are represented in Figure 7.17.

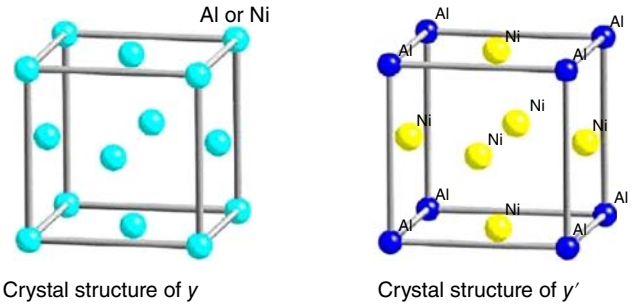


Figure 7.17 Lattice structures of the matrix *y* and the intermetallic phase *y′* (AG 2011).

Other phases such as γ″, carbides, borides, TCP (*topologically closed packed phases*) should also be mentioned. The alloying elements are selectively distributed in the crystal.

The γ-matrix usually contains a high percentage of solid solution elements, such as Co, Cr, Mo, W, Ta, Ti, and Al, strengthening the matrix.

The γ′ phase usually consists of $(Ni, Co)_3(Al, Ti)$ with a higher amount of Al or Ti. The superlattice of Ni_3Al is the Cu_3Au ($L1_2$)-type structure. This phase precipitates coherently with gamma. This intermetallic phase has the particular characteristic of increasing its creep with increasing temperature, whereby its ductility prevents cracks. A small misfit between γ/γ′ is of importance, as it lowers the total surface energy, therefore stabilizing the microstructure at high temperatures.

Carbides are more important for polycrystalline materials (low content 0.05–0.2% carbon) as they precipitate at grain boundaries and react with refractory elements (Ti, Ta, and Hf) to form strong carbides (MC, M is the metal), which strengthen the grain boundary, prevent or retard grain boundary sliding, or allow stress relaxation. They may also tightly bind some elements that favor phase instability.

Borides may also have a similar role as carbides. Boron (50–500 ppm) is located at grain boundaries and provides enhancement of the grain boundary cohesion, thus reducing grain boundary tearing under creep-rupture loading.

TCP phases, which are platelike phases, including σ, μ, and Laves forms, result from excessive alloying of elements, such as Mo, W, Re, and Cr. They are undesirable in Ni-based superalloys as they detrimentally affect the properties of the alloys. Due to their morphology, they are an excellent source for crack initiation and propagation, leading to low temperature brittle failure, especially sigma, which contains a high amount of refractory metals sapped from the γ-matrix, causing the loss of solution strengthening.

The development of new metallurgical processes (directional solidification and single-crystal formation) has improved the performances of gas turbines. Single crystals, which are widely used in the hottest part of turbine (e.g.

in aircraft turbines), are based on the γ/γ' constituent. The volume fraction of γ' is generally in the range of 40–70%. This phase is either distributed in spherical shape, if the lattice mismatch is around 0–0.2%, or cubical, occurring at 0.5–1.0% lattice mismatch (Sims and Hagel 1972), or plates become perpendicular to the load at mismatch about 1.25% (Fedelich 1999). Needles aligned with the load, as well as plates, have also been observed by Bressers (1996) as a consequence of anisotropic coalescence due to extreme temperatures and loading conditions.

Some elements, such as the grain boundary strengtheners – boron, zirconium, and carbon – are removed in single crystalline materials, as these do not have grain boundaries. Both Zr and Hf tend to lower the solidus temperature of the alloy, preventing the complete dissolution of γ' during solution heat treatment. Hf is, however, added in very low quantities (0.01–0.05%), as it reacts with sulfur (the presence of which is undesirable) to form stable sulfides, therefore improving the scale adhesion of the oxides. In addition, it prevents cracking during the solidification cool-down cycle in cored columnar-grained alloys.

After service, some elements accumulate at the dendritic core or in interdendritic regions during cooling. Al, Ti, and Ta tend to segregate in the interdendritic parts, whereas Re and W, for example, join the dendritic core (Fuchs 2001, 2002), which can be reduced by an appropriate solution treatment. The amount of refractory metals in superalloys, such as W, Ta, and Re, has been steadily increasing in the past few years, as they increase the creep resistance as well as strength due to solid solution strengthening, strengthening of γ', and slower diffusion rate. The new generation of superalloys also contains rhenium, which not only increases the mechanical properties of the alloy (Pollock 2000) but also leads to the formation of TCP phases (Feng et al. 2003).

Superalloys, just as most of high temperature alloys, owe their good oxidation resistance to the formation of a protective scale, which is slow growing, has a low defect concentration, and is adherent. This is achieved by the selective oxidation of either Cr or Al, depending on the service temperature. Therefore, a minimum amount of these elements is required to ensure the growth of this external scale. Due to its volatility at around 1000 °C, Cr_2O_3 is replaced by α-Al_2O_3, which is stable from about 950 °C. On the other hand, the presence of Cr decreases the amount of Al needed to form alumina rapidly (Prescott and Graham 1992). The oxides formed separate the substrate with the corrosive medium, therefore preventing the formation of fast-growing oxides, such as Ni, Co, or Fe oxides. A better adherence of the scales is mostly achieved by addition of reactive elements, such as hafnium, yttrium, and zirconium, as alumina tends to be very brittle. The selective oxidation of Cr and Al lead to their depletion under the alloys, causing the degradation of the mechanical properties especially if the substrate is very thin.

7.7.3 Protection by Coatings

The focus on the development of substrate alloys discussed in this chapter is generally to achieve high strength, high ductility, and efficient production. Oxidation resistance may not be consistent with achieving these goals. For example, increased Al and Cr result in improved oxidation resistance; however, beyond a certain level, these elements reduce creep strength of the resulting alloys. To achieve both strength and resistance to environmental degradation, the two functions are separated. The load capability is provided by the application of thin coatings with adequate Al and Cr. The thickness of the coating is controlled so that it does not carry any significant load. Depending on the temperature of use, many high temperature alloys require coatings compatible with its composition and structural (modulus) and thermal (CTE) properties. Diffusion, overlay, and thermal barrier coatings were described a few years ago in a chapter on high temperature oxidation that we have published in *Uhlig's Corrosion Handbook*, 3rd ed., edited by R. Winston Revie. Recently, surface coatings are gaining high potential industrial applications in the field of high temperature corrosion protection, Therefore, it was felt that protective coatings should be discussed in more detail deserving a chapter on the subject, as it is done in Chapter 18 of this book. Here, surface coatings are considered in terms of coating systems, coating processes, and coating degradation and are extended for cyclic oxidation, hot corrosion, sulfidation, carburization, erosion–corrosion, etc.

7.8 Oxidation of Engineering Materials

There is a large spectrum of engineering materials available for applications subject to oxidation in different temperature ranges. This section focuses on laboratory and field experience of many materials that are being considered for applications in various temperature regimes. They range from carbon and Cr–Mo steels to advanced superalloys.

At temperatures below 550 °C, carbon steel in air shows very little weight gain after exposure for nearly one month. As the temperature is increased to 700 °C, the oxidation rate is significantly increased, exhibiting a linear rate of oxidation attack. Test results by John (1999) showed that carbon steel exhibited about 0.25 mm/year (10 mpy) of oxidation at 604 °C; at 650 °C, carbon steel exhibited oxidation rates of the order of 1.25 mm/year (50 mpy). The beneficial effects of chromium and silicon additions to carbon steel were reported by Zeuthen (1970). Cr–Mo

steels are used at higher temperatures than carbon steel because of higher tensile and creep-rupture strengths as well as better microstructural stability. Molybdenum and chromium provide not only solid solution strengthening but also carbide strengthening.

Silicon is very effective in improving the oxidation resistance of Cr–Mo steels, but the most important alloying element for improving oxidation resistance is chromium.

The superior oxidation resistance of martensitic and ferritic stainless steels to that of carbon and Cr–Mo steels is well illustrated in the open literature (McGarrow 1971). The 25Cr steel (Type 446 = S44600) is the most oxidation resistant among the 400 series stainless steels due to the development of a continuous Cr_2O_3 scale on the metal surface. In Fe–Cr alloys, a minimum of approximately 18 wt% Cr is needed to develop a continuous Cr_2O_3 scale against further oxidation attack (Wright 1987). Cyclic oxidation studies conducted by Grodner (1956) also revealed that Type 446 was the best performer in the 400 series stainless steels, followed by Type 430 (S43000; 14–18Cr), 416 (S41000; 12–14Cr), and 410 (S41000; 11.5–13.5Cr). The growth of a thin, adherent $(Fe,Cr)_2O_3$ scale as a function of the accumulated isothermal hold time up to 1000 hours was observed by Walter et al. (1993) at 650 °C in air, during cycling from 650 to 300 °C.

The 300 series austenitic stainless steels have been widely used for high temperature components because they exhibit higher elevated temperature strength than ferritic stainless steels. Furthermore, they do not suffer 475 °C embrittlement or ductility-loss problems in thick sections and in heat-affected zones as do ferritic stainless steels. Nevertheless, some austenitic stainless steels can suffer some ductility loss upon long-term exposure to intermediate temperatures (e.g. 540–800 °C) due to sigma-phase formation (Sherby 1962). Moccari and Ali (1979) observed the beneficial effects of nickel in improving the oxidation resistance of austenitic stainless steels.

In evaluating materials for automobile emission-control devices, such as thermal reactors and catalytic converters, Kado et al. (1978) carried out cyclic oxidation tests on various stainless steels. In cyclic oxidation tests performed in still air at 1000 °C for 400 cycles (30 minutes in the furnace and 30 minutes out of the furnace), types 409 (S40900; 12Cr), 420 (S42000, 13Cr), and 304 (S30400; 18Cr–8Ni) suffered severe attack. Type 420 (S42000; 13Cr) was completely oxidized after only 100 cycles, although the sample did not show any weight changes. Alloys that performed well under these conditions were types 405 (S40500; 14Cr), 430 (S43000; 17Cr), 446 (S44600; 25Cr), 310 (S31000; 25Cr–20Ni), and DIN 4828 (19Cr–12Ni–2Si).

When cycled to 1200 °C for 400 cycles (30 minutes in the furnace and 30 minutes out of the furnace), all alloys tested except F-1 alloy (Fe–15Cr–4Al) suffered severe oxidation attack. This illustrates the superior oxidation resistance of alumina formers (i.e. alloys that form Al_2O_3 scales when oxidized at elevated temperatures). Their data also illustrate that for temperatures as high as 1200 °C, Cr_2O_3 oxide scales can no longer provide adequate oxidation resistance.

Oxidation data generated in combustion atmospheres is relatively limited. No systematic studies have been reported that varied combustion conditions, such as air-to-fuel ratios. In combustion atmospheres, the oxidation of metals or alloys is not controlled by oxygen only. Other combustion products, such as H_2O, CO, CO_2, N_2, hydrocarbon, and others, are expected to influence oxidation behavior. When air is used for combustion, nitride formation in conjunction with oxidation can occur in combustion atmospheres under certain conditions.

The presence of water vapor can also be an important factor in affecting oxidation behavior of alloys, as discussed later in this section.

Manufacturing processes can greatly influence the surface chemistry of an alloy product. Stainless steels can be finished into the final product by bright annealing (i.e. annealing is performed in a protective atmosphere, such as hydrogen environment or dissociated ammonia environment). This process generally produces a product with minimal depletion of chromium at or near the surface. On the other hand, when the alloy product is finished by black annealing (i.e. annealing is performed in air or combustion atmosphere in the furnace) and followed by acid pickling, there is a good chance that the alloy product may exhibit surface depletion of chromium. This is particularly important for thin-gage sheet products or thin tubular products (Ruther and Grunberg 1964).

Some stainless steel producers may manufacture stainless steels at the bottom of the specification range for key alloying elements, such as chromium, to reduce material cost. Accordingly, the chromium content can be insufficient to maintain a continuous chromium oxide scale during prolonged service or when subjected to thermal cycling or overheating conditions, thus promoting breakaway oxidation. The oxidation resistance of these "lean" stainless steels can be further degraded by the surface depletion of chromium resulting from manufacturing processes that may involve excessive pickling after "black" annealing (annealing in air or combustion atmosphere), during successive reductions in cold rolling in flat product manufacturing, or pilgering in tubular manufacturing. The chromium concentration at the surface of such a product, particularly a thin-gage sheet or tube, may be too low to form or maintain a continuous chromium oxide scale during service. As a result, iron oxides and isolated non-protective Fe–Cr oxide nodules can develop on the metal surface, thus resulting in breakaway oxidation, as discussed later.

Some commercial electrical resistance heating elements are made of Fe–Cr–Al alloys, such as Kanthal® alloys, which rely on the formation of the Al_2O_3 scale for applications up to 1400 °C (Kanthal 1995). For example, some of the Kanthal alloys that are available in wire, strip, and ribbon product forms are Kanthal A-I (K92500; Fe–22Cr–5.8Al), AF (Fe–22Cr–5.3Al), and D (Fe–22Cr–4.8Al). Since these wrought alloy products are essentially ferritic alloys, they exhibit low creep-rupture strengths when the temperature exceeds 650 °C and cannot be used for high temperature structural components. Thus, the electrical resistance heating elements made of these alloys must be properly supported to avoid creep deformation, such as sagging. These Kanthal wires can be used in arc or flame spraying to produce an oxidation-resistant coating or in weld overlay cladding by using a gas metal arc welding (GMAW) process. A powder metallurgy (P/M) process was used to produce a new alloy product, Kanthal APM, reported to exhibit improved creep-rupture strength (Berglund and Jonsson 1989). Other commercial Fe–Cr–Al alloys include ALFA-I™ (Fe–13Cr–3Al), ALFA-II™ (Fe–13Cr–4Al), and ALFA-IV™ (Fe–20Cr–5Al–Ce) developed by Allegheny Ludlum (1990) and Fecralloy® (Fe–16Cr–4Al–0.3Y) developed by Atomic Energy Authority (Moseley et al. 1984).

As the nickel content in the Fe–Ni–Cr system increases from austenitic stainless steels to a group of iron-based alloys with 20–25Cr and 30–40Ni, the alloys become more stable in terms of metallurgical structure and more resistant to creep deformation (i.e. higher creep-rupture strengths). In general, this group of alloys also exhibits better oxidation resistance. Some of the wrought alloys in this group are 800H/800HT (Fe–21Cr–32Ni–Al–Ti), RA330 (NO8330; Fe–19Cr–35Ni–1.2Si), HR120 (Fe–25Cr–37Ni–0.7Nb–N), AC66 (N53228; Fe–27Cr–32Ni–0.8 Nb–Ce), 353MA (Fe–25Cr–35Ni–1.5Si–Ce), and 803 (Fe–26Cr–35Ni–Al–Ti) (Smith et al. 1997).

In many Ni–Cr alloys, many alloying elements, such as those for solid solution strengthening (e.g. Mo, W) and precipitation strengthening (e.g. Al, Ti, Nb), are added to the alloys to provide strengthening of the alloy at elevated temperatures. Many of these alloys are commonly referred to as "superalloys." The superalloys also include oxide dispersion strengthened (ODS) alloys, which are briefly discussed later.

Similar to Fe–Cr–Al alloys, aluminum is also used as an alloying element in Ni–Cr alloys to improve the oxidation resistance. Although a Ni–Cr alloy generally requires a minimum of 4% Al to form a protective Al_2O_3 scale, the addition of less than 4% Al can significantly improve the oxidation resistance of the alloy. Alloy 601 (NO6601), with only about 1.3% Al, shows excellent oxidation resistance (Ganesan et al. 1993).

Ni–Cr alloys containing about 4% Al or higher form a very protective Al_2O_3 scale when heated to very high temperatures; for example, Lai (1985) compared Alloy 214 (Ni–16Cr–4.5Al–Y) with Alloy 601 and Alloy 800H in cyclic oxidation tests performed in still air at 1150 °C with specimens cycling to room temperature once a day except weekends. Alloy 214 showed essentially no weight loss after 42 days of testing, whereas Alloy 601 showed a linear weight loss.

For applications at high temperatures, many superalloys contain numerous alloying elements for increasing the elevated temperature strength of the alloy. Molybdenum and tungsten are common alloying elements for providing solid solution strengthening for increasing the creep-rupture strength of the alloy. Two iron-based superalloys, Multimet alloy (R30155; Fe–20Ni–20Co–21Cr–3Mo –2.5W–1.0Nb+Ta) and Alloy 556 (R30556; Fe–20 Ni–18Co–22Cr–3Mo–2.5W–0.6Ta–0.02La–0.02Zr), are good examples. However, the oxides of both molybdenum and tungsten (MoO_3 and WO_3) exhibit high vapor pressures at very high temperatures. Multimet alloy showed rapid oxidation attack at 1150 and 1200 °C, with specimens completely consumed at both temperatures. However, formation of the volatile oxides of MoO_3 and WO_3 can be minimized by modification of some key alloying elements in Multimet alloy. The development of Alloy 556 was aimed at improving the oxidation resistance of Multimet alloy without losing the elevated temperature strength by modifying the Multimet alloy composition. The modification involved a slight increase in chromium, a decrease in cobalt, replacement of niobium with tantalum, and addition of a rare earth element, lanthanum, and a reactive element, zirconium, but the concentrations of molybdenum and tungsten were not changed. The result was a much more oxidation-resistant alloy, Alloy 556, at 1095 and 1150 °C, although rapid oxidation nevertheless occurred at 1200 °C.

Cobalt-based alloys with tungsten, such as Alloy 188 (R30188; Co–22Cr–22Ni–14W–0.04La), Alloy 25 (R30605; Co–20Cr–10Ni–15W), and Alloy 6B (Co–30Cr–4.5W–1.2C), showed rapid oxidation at 1205 °C. A cobalt-based alloy, Alloy 150 (Co–27Cr–18Fe), containing no tungsten, also showed rapid oxidation attack at 1205 °C.

Again, the oxidation of a cobalt-based alloy can be significantly improved with some modification of alloying elements. Alloy 25 with 15% W exhibits excellent creep-rupture strength at high temperatures. However, because of the high level of tungsten, the alloy shows high oxidation rates at very high temperatures, such as 1095 and 1150 °C. With a slight increase in chromium and nickel along with the addition of lanthanum, the result of the modification was Alloy 188, which has significantly better oxidation resistance than Alloy 25 at 1095 and 1150 °C.

ODS alloys use very fine oxide particles that are uniformly distributed throughout the matrix to provide excessive strengthening at very high temperatures. These oxide particles, typically yttrium oxide, do not react with the alloy matrix, and so no coarsening or dissolution occurs during exposure to very high temperatures, thus maintaining the strength of the alloy. This group of superalloys is produced using specialty powders that are manufactured by the mechanical alloying process. These powders are essentially composite powders with each particle containing a uniform distribution of submicron oxide particles in an alloy matrix. The process of producing these ODS powders involves repeated fracturing and rewelding of a mixture of powder particles in vertical attritors or horizontal ball mills (Lowell et al. 1982). A vertical attritor is a high-energy ball mill (like the conventional horizontal ball mill), in which the balls and the metal powders are charged into a stationary vertical tank and are agitated by impellers rotating from a central rotating shaft. The shaft turns, but the jar stays put. As the balls are stirred, they fall on the contents and grind whatever is between the balls. Alloy powders are then canned, degassed, and hot extruded, followed by hot working and annealing to produce a textured microstructure. Alloys are available in mill products, such as bar, plate, sheet, and so forth, or custom forgings.

Oxidation of alloys can significantly increase under high velocity gas streams, as in, for example, combustors and transition ducts in gas turbines. These components are also subject to severe thermal cycling, particularly gas turbines in airplane engines. Laboratory burner rigs have been developed to evaluate the type of oxidation, often referred to as "dynamic oxidation," under conditions of very high gas velocities. Some of these dynamic oxidation burner rigs are described elsewhere (Lai 1988; Lowell et al. 1982, Schütze 2000).

Hicks (1987) performed dynamic oxidation tests with $170\,m\,s^{-1}$ gas velocity, at 1100 °C with 30 minutes cycles for several wrought chromia-forming superalloys and an ODS alumina former (MA956). Alumina former MA956 was found to be considerably better than chromium formers, such as alloys 191, 86, 617, 188, and 263.

MA956, along with some ODS alloys, was studied by Lowell et al. (1981) with 0.3 Mach gas velocity at 1100 °C with 60 minutes cycles. ODS alloys included in the study were MA956 (Fe–19Cr–4.4Al–0.6Y_2O_3), HDA8077 (Ni–16Cr–4.2Al–1.6Y_2O_3), TD-NiCr (Ni–20Cr–2.2ThO_2), and STCA264 (Ni–16Cr–4.5Al–1Co–1.5Y_2O_3). Also included in the study was a physical vapor deposition (PVD) coating of Ni–15Cr–17Al–0.2Y on MAR-M200 alloy (Ni–9Cr–10Co–12W–1Nb–5Al–2Ti).

MA956 and HDA8077 as well as PVD Ni–Cr–Al–Y coating were found to perform well. No explanation was offered for STCA264, which did not perform as well as HDA8077 although both alloys had similar chemical compositions.

In Fe–Cr, Fe–Ni–Cr, Ni–Cr, and Co–Cr alloy systems, the formation of an external Cr_2O_3 oxide scale provides the oxidation resistance for the alloy. The growth of the Cr_2O_3 oxide scale follows a parabolic rate law as the exposure time increases. As the temperature increases, the oxide scale growth rate also increases. The growth of the Cr_2O_3 scale requires that a continuous supply of chromium from the alloy interior diffuses to the oxide–metal interface. Continued oxidation can eventually deplete chromium in the alloy matrix immediately under the oxide scale. When the chromium concentration in the alloy matrix immediately beneath the oxide scale is reduced to below a critical concentration, the alloy matrix no longer has adequate chromium to reform a protective Cr_2O_3 oxide scale when the scale cracks or spalls due to oxide growth stresses or thermal cycling. Once this occurs, fast-growing, non-protective iron oxides, or nickel oxides, or cobalt oxides (i.e. oxides of base metal) form and grow on the alloy surface. Breakaway oxidation initiates, and the alloy begins to undergo oxidation at a rapid rate. The alloy thus requires the level of chromium immediately under the chromium oxide scale to reheal (Evans et al. 1980; Gleeson and Harper 1998; Hicks 1987; Quadakkers and Bongartz 1994; Schütze 2000).

To prolong the time for initiation of breakaway oxidation, it is necessary to have an adequate reservoir of chromium immediately below the oxide scale to provide adequate chromium to maintain a protective chromium oxide scale or to reheal the oxide scale after local cracking or failure.

For alumina formers, such as Fe–Cr–Al alloys, and Fe–Cr–Al-based and Ni–Cr–Al-based ODS alloys, breakaway oxidation occurs when aluminum concentration under the Al_2O_3 scale has been reduced to a critical level such that healing of the Al_2O_3 is no longer possible, thus resulting in the formation of non-protective, fast-growing oxides of base metals (e.g. iron oxides or nickel oxides). The breakaway oxidation due to rapid growth of iron oxides or nickel oxides becomes essentially a life-limiting factor. This critical aluminum concentration was found to be about 1.0–1.3% for Fe–Cr–Al-based ODS alloys (e.g. MA956, ODM751) at 1100–1200 °C (Gurrappa et al. 2000; Quadakkers and Bongartz 1994). These values were obtained from foil specimens (0.2–2 mm thick) tested in still air at 1100–1200 °C. For the non-ODS Fe–20Cr–5Al alloy, this critical aluminum concentration was found to be higher (about 2.5%) at 1200 °C (Quadakkers and Bongartz 1994). Since breakaway oxidation is related to the aluminum reservoir in the alloy, this reservoir is a critical issue when the component is made of thin sheet or foil. Because of excellent oxidation resistance at very high temperatures, there is increasing interest in considering

alumina formers for products that require thin foils, such as honeycomb seals in gas turbines, metallic substrates for automobile catalyst converters, and recuperators in microturbines.

For alumina formers to improve their resistance to breakaway oxidation, yttrium is frequently used to increase the adhesion of the aluminum oxide scale. Other alloying elements that are known to increase the adhesion of the aluminum oxide scale include zirconium and hafnium. Quadakkers (1990) shows that both MA956 (Fe–20Cr–4.5 Al–0.5Y_2O_3) and Aluchrom (Fe–20Cr–5Al–0.01Y) exhibited much more cyclic oxidation resistance than Fe–20 Cr–5Al when tested at 1100 °C in synthetic air with an hourly cycle to room temperature.

Addition of Y_2O_3 to an alumina former has a similar beneficial effect as yttrium added as an alloying element. Klower and Li (1996) studied the oxidation resistance of Fe–20Cr–5Al alloys in 10 different compositions containing various amounts of yttrium ranging from 0.045% to 0.28%. All 10 compositions contained 0.002% S, and eight compositions contained 0.04–0.06% Zr with two compositions containing no zirconium. The cyclic oxidation tests were performed at 1100 and 1200 °C, respectively, with each cycle consisting of 96 hours at temperature and rapid air cooling to room temperature. These authors concluded that the yttrium addition of about 0.045% was sufficient to prevent the oxide scales from spalling, and when the yttrium concentration was increased to more than 0.08%, substantial internal oxidation could occur, resulting in rapid metal wastage (Klower and Li 1996).

Sulfur in the alloy is known to play a very significant role in adhesion of the aluminum oxide scale to the alloy substrate for alumina formers. The role of yttrium is believed to prevent the preferential segregation of sulfur in the alloy to the scale/metal interface to weaken the adhesion of the oxide scale (Funkenbusch et al. 1985; Smeggil et al. 1985, 1986). Reducing the concentration of sulfur in a Ni–Cr–Al alloy can significantly improve the oxidation resistance of the alloy. Smeggil (1987) compared cyclic oxidation resistance between the normal purity Ni–Cr–Al alloys (approximately 30–40 ppm S) with the high purity Ni–Cr–Al alloys (approximately 1–2 ppm S), showing a significant improvement in cyclic oxidation resistance when sulfur in the alloy was significantly reduced. Also demonstrated was the beneficial effect of yttrium addition to the normal purity Ni–20Cr–12Al alloy, showing significant improvement in the cyclic oxidation resistance of the alloy without reducing the sulfur content in the alloy. Sulfur was found to segregate to the oxide–alloy interface during oxidation in Fe–Cr–Al alloys (Hou 2000; Hou and Stringer 1992). Yttrium is believed to tie up sulfur at the oxide–metal interface, thus improving the oxide scale adhesion (Smeggil 1987).

There are some industrial applications that require thin-gage sheet materials or thin foils for construction of critical components. As the component thickness decreases, oxidation becomes a major factor that limits service life. When the component is made of thin foil, prolonging the incubation time before initiation of breakaway oxidation is the controlling factor for extending the service life of the component. Thus, as applications are being pushed toward higher and higher temperatures, alloys that form aluminum oxide scales can offer significant advantages in performance over those alloys that form chromium oxide scales (Klower 1998; Pint 2006; Simms et al. 2003).

In high temperature combustion atmospheres, water vapor is invariably present in the environment. The effect of water vapor on the oxidation of alloys is an important factor in the alloy selection process. Most oxidation data are generated in laboratory air, which generally contains low levels of water vapor (Segerdahl et al. 2002a,b; Tuck et al. 1966). The effect of water on oxidation, and its detrimental effect, has been established by Onal et al. (2003) and many others (Béranger et al. 1987; Birks et al. 2006; Fleming et al. 1987; Streiff et al. 1989, 1997; Thoma 1986; Zeuthen 1970).

As temperature increases, metals and alloys generally suffer increasingly higher rates of oxidation. When the temperature is excessively high, metals and alloys can suffer rapid oxidation. There is, however, another mode of rapid oxidation that takes place at relatively low temperatures, often referred to as "catastrophic oxidation," associated with the formation of a liquid oxide that disrupts and dissolves the protective oxide scale, causing the alloy to suffer rapid oxidation at relatively low temperatures. This phenomenon has been observed by, for example, Meijering and Rathenau (1950), Brennor (1955), Sawyer (1961), Brasunas and Grant (1950), and Sequeira (2003). The most effective way to alleviate the potential catastrophic oxidation problem is to avoid a stagnant condition of the gaseous atmosphere.

7.9 Conclusions

This chapter is a summary of the main factors for determining the nature and extent of gas–metal reactions, the comprehension of which is of paramount importance to understand the subject. Some of these factors are metal structure, oxide structure, metal diffusion, oxygen or metal diffusion at grain boundaries or on the surface, metal and oxide volatility, oxygen solution in metal, cracking, spalling, blistering, sintering, oxide nucleation, electronic conductance, oxide adhesion, and oxide plasticity.

It starts with the basics of thermodynamics, followed by the usual topics, such as defect structures, growth of

compact scales, formation of multilayered scales, oxidation studies of metals and engineering alloys, and corrosion protection, and ending with pertinent references on the subject.

7.10 Questions

7.1 What is a clean surface?

7.2 Why is low temperature oxidation based upon empirical relations rather than actual experimentation?

7.3 How does the Mott theory differ from the Cabrera–Mott theory? What are the migrating species in both theories?

7.4 Does structure play an important role in low temperature oxidation? State the answer with a suitable example.

7.5 What is place exchange mechanism? Under which stage is it applicable?

7.6 What are the deleterious effects of oxygen dissolution in metals? Which metal has the highest solubility in oxygen?

7.7 How strictly are Wagner's assumptions valid in practical cases of metal oxidation?

7.8 What is mobility of an ion?

7.9 Why is cobalt the best example of Wagner's model of oxidation?

7.10 What is a practical method of measuring the transport of diffusion species?

7.11 What is catastrophic oxidation? How can it be avoided?

7.12 State the oxidation of Zr. Under what conditions can it undergo breakaway oxidation?

7.13 Which classification of metals best explains the oxidation behavior of metals?

7.14 How does the oxidation behavior of iron differ below 570 °C from that above this temperature?

7.15 Which is the most detrimental oxide in the case of iron and why? How can this be overcome?

7.16 In multilayer oxides, (a) what is the relationship between the thickness and their individual parabolic rate constants? (b) Which oxide is next to a metal–oxide interface and which is next to an oxide–gas?

7.17 Why can stainless steel, which forms a very protective chromia oxide layer on oxidation, not be used above 900 °C?

7.18 Why are refractory metals, in spite of high melting point and excellent mechanical properties, not used for high temperature applications?

7.19 How does oxidation of alloys differ from the oxidation of pure metal?

7.20 Under what conditions does internal oxide formation change to external scale formation?

7.21 What is selective oxidation? What is its importance?

7.22 What is one limitation of selective oxidation and how can it be overcome?

7.23 Al like Cr is an important alloying addition to form a selective oxide layer for corrosion resistance. Why, like Fe–Cr alloys, are binary alloys of Fe–Al not known, but instead alumina-forming alloys are always Fe–Cr–Al alloys?

7.24 What is the basic difference between catastrophic and breakaway oxidation?

7.25 What are oxide maps? How can we make use of these maps to design an oxidation-resistant alloy?

References

Alcock, C.B. and Hooper, G.W. (1960). *Proc. R. Soc.* 254A: 551.

Allegheny Ludlum Data Sheet (1990). Allegheny Ludlum. Pittsburgh, PA.

Anderson, A.B., Mehandru, S.P., and Smialek, J.L. (1985). *J. Electrochem. Soc.* 132: 1695.

Armilt, J., Holmes, D.R., Manning, M.I. et al. (1978). *The Spalling of Steam-Grown Oxide from Super-Heater and Reheater Tube Steels*: Final Report. EPRI Report Nr FP 686. Palo Alto, CA: Electric Power Research Institute.

ASM International (2003). *Corrosion: Fundamentals, Testing and Protection*, vol. 13A. ASM Handbook.

Asteman, H., Svensson, J.E., Johansson, L.G., and Norell, M. (1999). *Oxid. Met.* 52: 95.

Atkinson, A., Moon, D.P., Smart, D.W., and Taylor, R.I. (1986). *J. Mater. Sci.* 21: 1747.

Barret, P. (ed.) (1975). *Reaction Kinetics in Heterogeneous Chemical Systems*. Amsterdam: Elsevier.

von Baumbach, H.H. and Wagner, C.Z. (1933). *Phys. Chem.* 22: 199.

Bénard, J. (1962–1964). *Oxydation des Métaux*, vol. 1/2. Paris: Gauthier-Villars.

Béranger, G., Colson, J.C., and Dabasi, F. (1987). *Corrosion des Matériaux à Haute Température*. Les Ulis: Les Éditions de Physique.

Berglund, R. and Jonsson, B. (1989). Industrial Heating (21 October).

Birks, N., Meier, G.H., and Pettit, F.S. (2006). *Introduction to the High Temperature Oxidation of Metals*, 2e. Cambridge: Cambridge University Press.

Brasunas, A.d.S. and Grant, N.J. (1950). *Trans. ASM* 44: 1133.

Brennor, S.S. (1955). *J. Electrochem. Soc.* 102: 16.

Bressers, J. (1996). *Mater. Sci. Eng., A* A220: 147.

Brunauer, S., Emmett, P.H., and Teller, E. (1938). *J. Am. Chem. Soc.* 60: 309.

Cabrera, N. and Mott, N.F. (1948). *Rep. Prog. Phys.* 12: 163.

Caplan, D. and Cohen, M. (1961). *J. Electrochem. Soc.* 108: 438.

Caplan, D. and Sproule, G.I. (1975). *Oxid. Met.* 9: 459.

Caplan, D., Graham, M.J., and Cohen, M. (1972). *J. Electrochem. Soc.* 119: 1205.

Cathcart, J.V. (ed.) (1975). *Stress Effects and the Oxidation of Metals*. New York: TMS-AIME.

Chang, S.L., Pettit, F.S., and Birks, N. (1990). *Oxid. Met.* 34: 23.

Christl, W., Rahmel, A., and Schütze, M. (1989). *Oxid. Met.* 31: 1.

Deal, B.E. and Grove, A.S. (1965). *J. Appl. Phys.* 36: 3770.

Ecer, G.M. and Meier, G.H. (1979). *Oxid. Met.* 13: 159.

Evans, U.R. (1960). *The Corrosion and Oxidation of Metals*. London: Edward Arnold.

Evans, H.E. (1995). *Int. Mater. Rev.* 40: 1.

Evans, H.E., Hilton, D.A., Holm, R.A., and Webster, S.J. (1980). *Oxid. Met.* 14: 235.

Farhi, R. and Petot-Ervas, G. (1978). *J. Phys. Chem. Solids* 39: 1169.

Fedelich, B. (1999). *Comput. Mater. Sci.* 16: 248.

Felton, E.J. and Pettit, F.S. (1976). *Oxid. Met.* 10: 184.

Feng, Q., Nandy, T.K., and Pollock, T.M. (2003). *Mater. Sci. Eng., A* 373: 239.

Fleming, R.H., Meeker, G.P., and Blattner, R.J. (1987). *Thin Solid Films* 153: 197.

Fromm, E. (1998). *Kinetics of Metal-Gas Interactions at Low Temperature – Hydriding, Oxidation, Poisoning*. Berlin: Springer-Verlag.
Fuchs, G.E. (2001). *Mater. Sci. Eng., A* A300: 52.
Fuchs, G.E. (2002). *J. Mater. Eng. Perform.* 11: 19.
Funkenbusch, A.W., Smeggil, J.G., and Bornstein, N.S. (1985). *Metall. Trans. A* 16: 1164.
Ganesan, P., Smith, G.D., and Tassen, C.S. (1993). Corrosion/93, Paper No. 234. Houston, TX: NACE International.
Garnaud, G. (1977). *Oxid. Met.* 11: 127.
Garnaud, G. and Rapp, R.A. (1977). *Oxid. Met.* 11: 193.
Gaskell, D.R. (1995). *Introduction to Thermodynamics of Materials*, 3e. Washington DC: Taylor & Francis.
Gesmundo, F. and Niu, Y. (1998). *Oxid. Met.* 50: 1.
Gesmundo, F. and Viani, F. (1981). *J. Electrochem. Soc.* 128: 470.
Gesmundo, F. and Viani, F. (1986). *Oxid. Met.* 25: 269.
Glasstone, S., Laidler, K.J., and Eyring, H. (1941). *Theory of Rate Process*. New York: McGraw-Hill, Booth Company.
Gleeson, B. and Harper, M.A. (1998). *Oxid. Met.* 49: 373.
Grabke, H.J. and Meadowcroft, D.B. (eds.) (1995). *Guidelines for Methods of Testing and Research in High Temperature Corrosion*. London: The Institute of Materials.
Graham, M.J., Caplan, D., and Cohen, M. (1972). *J. Electrochem. Soc.* 119: 1265.
Grodner, A. (1956). Welding Research Council Bulletin No 31.
Gulbransen, E.A. and Meier, G.H. (1979a). Proceedings of the 10th Materials Research Symposium, 1639. National Bureau of Standards Special Publications 561.
Gulbransen, E.A. and Meier, G.H. (1979b). *Thermochemical Stability Diagrams for Condensed Phases and Volatility Diagrams for Volatile Species Over Condensed Phases in Twenty Metal-Sulfur-Oxygen Systems Between 1150 and 1450 K*. DOE Report on Contract nr DE-AC01-79-ET-13547. University of Pittsburgh.
Gulbransen, E.A., Andrew, K.F., and Brassart, F.A. (1963). *J. Electrochem. Soc.* 110: 952.
Gurrappa, I., Weinruch, S., Naumenko, D., and Quadakkers, W.J. (2000). *Mater. Corros.* 51: 224.
Hauffe, K. (1965). *Oxidation of Metals*. New York: Plenum Press.
Haycock, G.W. (1959). *J. Electrochem. Soc.* 106: 771.
Heitz, E., Henkhaus, R., and Rahmel, A. (1992). *Corrosion Science – an Experimental Approach*. New York: Ellis Horwood.
Hicks, B. (1987). *Mater. Sci. Technol.* 3: 772.
Hindam, H. and Whittle, D.P. (1982). *Oxid. Met.* 18: 245.
Hindam, H. and Whittle, D.P. (1983). *High Temperature Corrosion*. Japan: Transactions of the Japan Institute of Metals, JIMIS-3.
Hou, P.Y. (2000). *Mater. Corros.* 51: 329.
Hou, P.Y. and Stringer, J. (1992). *Oxid. Met.* 38: 323.
Hussey, R.J. and Graham, M.J. (1996). *Oxid. Met.* 45: 349.
Jansson, S.A. and Foroulis, Z.A. (eds.) (1973). *High Temperature Gas-Metal Reactions in Mixed Environments*. New York: American Institute of Mining Metallurgical and Petroleum Engineering.
John, R.C. (1999). Corrosion/99, Paper No. 73. Houston, TX: NACE International.
Kado, S., Yamazaki, T., Yamazaki, M. et al. (1978). *Trans. Iron Steel Inst. Jpn.* 18: 387.
Kanthal Alloys Data Sheet (1995). Sandvik, Sweden.
Key to Metals AG (2011). *Nickel-Based Superalloys, Part One, 1999–2011*. Key to Metals AG.
Khanna, A.S. (2002). *High Temperature Oxidation and Corrosion*. Materials Park, OH: ASM International.
Khoi, N.N., Smeltzer, W.W., and Embury, J.D. (1975). *J. Electrochem. Soc.* 116: 1495.
Klower, J. (1998). *Mater. Corros.* 49: 758.
Klower, J. and Li, J.G. (1996). *Mater. Corros.* 47: 545.
Kofstad, P. (1966). *High Temperature Oxidation of Metals*. New York: Wiley.
Kofstad, P. (1972). *Non Stoichiometry, Diffusion and Electrical Conductivity in Binary Metal Oxides*. New York: Wiley.
Kofstad, P. (1988). *High Temperature Corrosion*. London: Elsevier Applied Science.
Kofstad, P. and Hed, A.Z. (1969). *J. Electrochem. Soc.* 116: 224–229.
Kröger, F.A. (ed.) (1975). *The Chemistry of Imperfect Crystals*. Amsterdam, Holland: North Holland Publishing Co.
Kröger, F.A. (1981). *High Temperature Corrosion* (ed. R.A. Rapp), 89. Houston, TX: National Association of Corrosion Engineers, NACE.
Kröger, F.A., Vink, H.J., Seitz, F., and Turnbull, D. (1956). *Solid-State Physics*, vol. 3. London: Academic Press.
Kubaschewski, O. and Alcock, C.B. (1979). *Metallurgical Thermochemistry*, 5e. Oxford: Pergamon Press.
Kubaschewski, O. and Hopkins, B.E. (1967). *Oxidation of Metals and Alloys*. London: Butterworths.
Lai, G.Y. (1985). *J. Miner. Met. Mater. Soc.* 37: 14.
Lai, G.Y. (1988). Haynes International, Inc., unpublished results.
Lai, G.Y. (2007). *High Temperature Corrosion and Materials Applications*. Materials Park, OH: ASM International.
Langmuir, I. (1918). *J. Am. Chem. Soc.* 40: 1361.
Lees, D.G. and Calvert, J.M. (1976). *Corros. Sci.* 16: 767.
Lillerud, K.P. and Kofstad, P. (1980). *J. Electrochem. Soc.* 127: 2397.
Loriers, J. (1950). *C.R. Acad. Sci.* 231: 522.
Lowell, C.E., Deadmore, D.L., and Whittenberger, J.D. (1982). *Oxid. Met.* 17: 205.
Manning, M.I. (1981). *Corros. Sci.* 21: 301.
McGarrow, H.E. (ed.) (1971). *The Making, Shaping and Treating of Steel*. United States Steel Corp.
Meijering, J.K. and Rathenau, G.W. (1950). *Nature* 165: 240.
Moccari, A. and Ali, S.L. (1979). *Br. Corros. J.* 14: 91.
Monceau, D. and Pieraggi, B. (1998). *Oxid. Met.* 50: 477.
Moseley, P.T., Hyde, K.R., Bellamy, B.A., and Tappin, G. (1984). *Corros. Sci.* 24: 547.
Mott, N.F. (1940). *Trans. Faraday Soc.* 3: 472.
Mrowec, S. (1980). *Defect and Diffusion in Solids*. London: Elsevier Science Publications.
Mrowec, S. and Przybylski, K. (1977a). *Oxid. Met.* 11: 365.
Mrowec, S. and Przybylski, K. (1977b). *Oxid. Met.* 11: 383.
Mrowec, S. and Stoklosa, A. (1971). *Oxid. Met.* 3: 291.
Munir, Z.A. and Cubicciotti, D. (eds.) (1983). *High Temperature Materials, Chemistry*. New York: The Electrochemical Society.
Newcomb, S.B. and Bennett, M.J. (eds.) (1993). *Microscopy of Oxidation*, vol. 2. London: The Institute of Materials.
Onal, K., Maris-Sida, M.C., Meier, G.H., and Pettit, F.S. (2003). *High Temp.* 20: 327.
Pettit, F.S. and Wagner, J.B. (1964). *Acta Metall.* 12: 35.
Philibert, J. (1985). *Diffusion et Transport de Matière dans les Solides*, Monographie de Physique. Les Ulis: Les Éditions de Physique.
Pilling, N.B. and Bedworth, R.E. (1923). *J. Inst. Met.* 1: 529.
Pint, B.A. (2006). *J. Eng. Gas Turbines Power* 128: 1.
Pint, B.A. and Hobbs, L.W. (1994). *Oxid. Met.* 41: 203.
Pint, B.A., Treska, M., and Hobbs, L.W. (1997). *Oxid. Met.* 47: 1.
Pollock, T.M. (ed.) (2000). *Superalloys 2000*, 737. The Minerals, Metals and Materials Society (TMS).
Pope, M.C. and Birks, N. (1977). *Corr. Sci.* 17: 747.
Prescott, R. and Graham, M.J. (1992). *Oxid. Met.* 38: 233.
Quadakkers, W.J. (1990). *Werkst. Korros.* 41: 659.
Quadakkers, W.J. and Bongartz, K. (1994). *Werkst. Korros.* 45: 232.
Rahmel, A. and Schwenk, W. (1977). *Korrosion und Korrosionsschutz von Stahlen*. Weinheim: Verlag Chemie.
Rapp, R.A. and Colson, H. (1966). *Trans. Metall. Soc. AIME* 236: 1616.
Reddy, K.P.R., Smialek, J.L., and Cooper, A.A.R. (1982). *Oxid. Met.* 17: 429.
Reed, R.C. (2006). *The Superalloys: Fundamentals and Applications*, 1e. Cambridge: Cambridge University Press.

Rocabois, P., Chatillon, C., and Bernard, C. (1966). *J. Am. Ceram. Soc.* 79: 1361.
Ruther, W.E. and Grunberg, S. (1964). *J. Electrochem. Soc.* 111: 1116.
Sadique, S.E., Mollah, A.H., Islam, S. et al. (2000). *Oxid. Met.* 54: 385.
Sarrazin, P. and Besson, J. (1973). *J. Chim. Phys.* 1: 27.
Sarrazin, P., Galerie, A., and Fouletier, J. (2008). *Mechanisms of High Temperature Corrosion: A Kinetic Approach*. Zürich: Trans. Tech. Publications Ltd.
Sawyer, J.W. (1961). *Trans. TMS-AIME* 221: 63.
Schulte, M. and Schütze, M. (1999). *Oxid. Met.* 51: 55.
Schütze, M. (1997). *Protective Oxide Scales and Their Breakdown*. Chichester: Wiley.
Schütze, M. (ed.) (2000). *Corrosion and Environmental Degradation*. Weinheim: Wiley-VCH.
Segerdahl, K., Svensson, J.E., and Johansson, L.G. (2002a). *Mater. Corros.* 53: 247.
Segerdahl, K., Svensson, J.E., and Johansson, L.G. (2002b). *Mater. Corros.* 53: 479.
Sequeira, C.A.C. (ed.) (2003). *High Temperature Corrosion in Molten Salts*. Uetikon-Zürich: Trans. Tech. Publications.
Sequeira, C.A.C. and Santos, D.M.F. (2006). *Czech. J. Phys.* 56: 549.
Sherby, O.D. (1962). *Acta Metall.* 10: 135.
Sigler, D.R. (1988). *Oxid. Met.* 29: 23.
Simms, N.J., Newton, R., Norton, J.F. et al. (2003). *Mater. High Temp.* 20: 439.
Sims, C.T. and Hagel, W.C. (1972). *The Superalloys*. New York: Wiley.
Sims, C.T., Stoloff, N.S., and Hagel, W.C. (eds.) (1987). *Superalloys II, High-Temperature Materials for Aerospace and Industrial Power*. New York: Wiley.
Smeggil, J.G. (1987). *Mater. Sci. Eng.* 87: 261.
Smeggil, J.G., Funkenbusch, A.W., and Bornstein, N.S. (1985). *High Temp. Sci.* 16: 163.
Smeggil, J.G., Funkenbusch, A.W., and Bornstein, N.S. (1986). *Metall. Trans. A* 17: 923.
Smialek, J.L. (1978). *Metall. Trans. A* 9A: 309.
Smith, F.N., McGurn, J.F., Lai, G.Y., and Sastri, V.S. (eds.) (1997). Applications and materials performance. Proceedings of the Nickel-Cobalt 97 International Symposium, The Metallurgical Society of CIM, Montreal, Canada.
Steinmetz, P., Wright, I.G., Meier, G. et al. (eds.) (2004). *High Temperature Corrosion and Protection of Materials*, vol. 6. Zürich: Trans. Tech. Publications Ltd.
Stott, F.H. (1987). *Rep. Prog. Phys.* 50: 861.
Streiff, R., Stringer, J., Krutenat, R.C., and Caillet, M. (eds.) (1989). *High Temperature Corrosion 2: Advanced Materials and Coatings*. London: Elsevier Science Publishing.
Streiff, R., Stringer, J., Krutenat, R.C. et al. (eds.) (1997). *High Temperature Corrosion and Protection of Materials*, vol. 4. Zürich: Trans. Tech. Publications Ltd.
Stringer, J. (1960a). *Acta Metall.* 8: 758.
Stringer, J. (1960b). *Acta Metall.* 8: 810.
Taniguchi, S., Maruyama, T., Yoshiba, M. et al. (eds.) (2006). *High Temperature Oxidation and Corrosion 2005, Materials Science Forum*, vol. 522–523. Zürich: Trans. Tech. Publications Ltd.
Tedmon, C.S. (1966). *J. Electrochem. Soc.* 113: 766.
Tuck, C.W., Odgers, M., and Sachs, K. (1966). Anti-Corrosion, June 1966, p. 14.
Wagner, C. (1933a). *Z. Phys. Chem. Abt.* B21: 25.
Wagner, C. (1933b). *Z. Elektrochem.* 39: 543.
Wagner, C. (1958). *J. Appl. Phys.* 29: 1295.
Wagner, C. (1965). *Corros. Sci.* 5: 751.
Wagner, C. (1975). *Prog. Solid State Chem.* 10: 3.
Walter, M., Schütze, M., and Rahmel, A. (1993). *Oxid. Met.* 39: 389.
Westbrook, J.H. and Fleischer, R.L. (eds.) (1994). *Intermetallic Compounds: Principles and Practice*. New York: Wiley.
Wood, G.C. and Chattopadhyay, B. (1970). *Corros. Sci.* 10: 471.
Wood, G.C. and Hodgkiess, T. (1966). *Nature (London)* 211: 685.
Wood, G.C. and Stott, F.H. (1987). *Mater. Sci. Technol.* 3: 519.
Wood, G.C., Wright, I.G., Hodgkiess, T., and Whittle, D.P. (1970). *Werkst. Korros.* 21: 900.
Wright, I.G. (1987). *Corrosion*, Metals Handbook, vol. 13, 97. ASM International.
Yang, J.C., Yeadon, M., Kolasa, B., and Gibson, J.M. (1998). *Scr. Mater.* 38: 1237.
Young, E.W.A., Stiphout, P.C.M., and de Wit, J.H.W. (1985). *J. Electrochem. Soc.* 132: 884.
Yurek, G.J., Hirth, J.P., and Rapp, R.A. (1974). *Oxid. Met.* 8: 265.
Zeuthen, A.W. (1970). *Heat. Pip. Air Cond.* 42: 152.

Further Reading

Aaronson, H.I. (ed.) (1999). *Lectures on the Theory of Phase Transformations*. Warrendale, PA: The Minerals, Metals and Materials Society.
Arper, A.M. (ed.) (1970). *Phase Diagrams, Materials Science and Technology*, vol. 1. New York: Academic Press.
Ashby, M. and Jones, D.R.H. (2005). *Engineering Materials 1: An Introduction to Properties, Applications and Design*, 3e. London: Elsevier.
Baboian, H. (ed.) (1995). *High-Temperature Gases (Corrosion Tests and Standards: Applications and Integration)*. Washington, DC: ASTM.
Bak, T., Nowotny, J., and Sorell, C.C. (1997). *Key Eng. Mater.* 125–126: 1.
Barralis, J. and Maeder, G. (1997). *Précis de Métallurgie: élaboration, structures-proprietés, normalisation*. Paris: AFNOR-Nathan.
Belton, G.R. and Worrell, W.L. (1970). *Heterogeneous Kinetics at Elevated Temperatures*. New York: Plenum Press.
Böhm, G. and Kahlweit, M. (1964). *Acta Metall.* 12: 641.
Bose, S. (2007). *High Temperature Coatings*. Amsterdam, Holland: Elsevier.
Dahotre, N.B. and Hampikian, J. (eds.) (1999). *Elevated Temperature Coatings: Science and Technology III*. San Diego, CA: TMS.
Darken, L.S. and Gurry, R.W. (1953). *Physical Chemistry of Metals*. New York: McGraw-Hill.
Donachie, M.J. Jr. and Donachie, S.J. (2002). *Superalloys: A Technical Guide*, 2e. Materials Park, OH: ASM International.
Douglass, D.L. (ed.) (1971). *Oxidation of Metals and Alloys*. Materials Park, OH: ASM.
Douglass, D.L. (1995). *Oxid. Met.* 44: 81.
Ellingham, H.J.T. (1944). *J. Soc. Chem. Ind.* 63: 125.
Gao, W. (ed.) (2008). *Developments in High Temperature Corrosion and Protection of Materials*. Cambridge: Woodhead Publ. Ltd.
Glaser, B., Rahts, K., Schorr, M., and Schütze, M. (1994). *Sonderband des Praktischen Metallographie*, vol. 25, 75. Frankfurt, M.: MAT-INFO, Werkstoff-Informationsges.
Hauffe, K. and Ilschner, B. (1954). *Z. Elektrochem.* 58: 382.
Hauffe, K. (1957). *Oxydation von Metallen und Metallegiesungen*. Berlin: Springer-Verlag.
Herman, H. (ed.) (1971). *Advances in Materials Research*. New York: Wiley.
Hocking, M.G., Vasantasree, V., and Sidky, P.S. (1989). *Metallic and Ceramic Coatings: Production, High Temperature Properties and Applications*. Essex: Longman Scientific & Technical.
JANAF Thermochemical Tables (1975). *J. Phys. Chem. Ref. Data* 4: 1.
Khanna, A.S., Quadakkers, W.S., and Wasserfuhr, C. (1988). The influence of sulfur and its interaction with yttrium on the composition,

growth and adherence of oxide scales on alumina-forming alloys. Conference on the Role of Active Elements in the Oxidation Behaviour of High-Temperature Metals and Alloys.
Kofstad, P. (1968). *Corrosion* 24: 379.
Landolt, D. (1993). *Traité des Matériaux, N° 12, Corrosion et Chimie des Surfaces des Métaux*. Presses Polytechniques Romandes.
Lang, E. (ed.) (1989). *The Role of Active Elements in the Oxidation Behaviour of High Temperature Metals and Alloys*. Amsterdam: Elsevier.
Marcus, P. and Mansfeld, F. (eds.) (2006). *Analytical Methods in Corrosion Science and Engineering*. Boca Raton, FL: CRC Press, Taylor & Francis Group.
Mitchell, D.F., Hussey, R.J., and Graham, M.J. (1983). *J. Vac. Sci. Technol., A* 1: 1006.
Mrowec, S. and Werber, T. (1978). *Gas Corrosion of Metals*. Varsovie, Poland: Foreign Scientific Publications Department of the National Center for Scientific, Technical and Economic Information.
Nicholls, J. (ed.) (1999). *High Temperature Surface Engineering*. London: Institute of Materials.
Nowotny, J. (1992). *Diffusion in Solids and High Temperature Oxidation of Metals*. Zürich: Trans. Tech. Publications Ltd.
Nowotny, J. and Sorrell, C.C. (1997). *Electrical Properties of Oxide Materials*. Zürich: Trans. Tech. Publications Ltd.
Psaras, P.A. and Langford, H.D. (eds.) (1987). *Advancing Materials Research*. Washington, DC: National Academy Press.
Rahmel, A. (ed.) (1982). *Aufbau von Oxidschichten auf Hochtemperaturwerkstoffen und ihre technische Bedeutung*. Oberursel: Oberursel, Deutsche Gesellschaft für Metallkunde.
Rapp, R.A. (1965). *Corrosion* 21: 382.
Rickert, H. (1960). *Z. Phys. Chem.* NF21: 432.
Sato, Y., Onay, B., and Maruyama, T. (eds.) (1992). *High Temperature Corrosion of Advanced Materials and Protective Coatings*. Amsterdam, Holland: Elsevier.
Schick, H. (1966). *Thermodynamics of Certain Refractory Compounds*. New York: Academic Press.
Schütze, M. and Quadakkers, W.J. (eds.) (1999). *Cyclic Oxidation of High Temperature Materials, EFC27*. London: Maney Publishing.
Schütze, M. and Quadakkers, W.J. (eds.) (2008). *Novel Approaches to Improving High Temperature Corrosion Resistance*. Cambridge: Woodhead Publ. Ltd.
Sequeira, C.A.C., Chen, Y., Santos, D.M.F., and Song, X. (2008). *Corros. Prot. Mater.* 27: 114.
Stern, K.H. (1996). *Metallurgical and Ceramic Protective Coatings*. London: Chapman and Hall.
Streiff, R., Stringer, J., Krutenat, R.C., and Caillet, M. (eds.) (1987). *High Temperature Corrosion of Materials and Coatings for Energy Systems and Turboengines*. Sequoia, Lausanne, Switzerland: Elsevier.
Streiff, R., Stringer, J., Krutenat, R.C., and Caillet, M. (eds.) (1993). *High Temperature Corrosion and Protection of Materials*, vol. 3. Les Ulis: Les Éditions de Physique.
Streiff, R., Wright, I.G., Krutenat, R.C. et al. (eds.) (2001). *High Temperature Corrosion and Protection of Materials*, vol. 5. Zürich: Trans. Tech. Publications Ltd.
Swalin, R.A. (1972). *Thermodynamics of Solids*. London: Wiley.
Wagner, C. (1956a). *J. Electrochem. Soc.* 99: 369.
Wagner, C. (1956b). *J. Electrochem. Soc.* 103: 571.
Wagner, C. (1959). *Z. Elektrochem. Soc.* 63: 772.
Wood, G.C. (1978). *Oxid. Met.* 2: 11.

Chapter 8

Sulfidation

8.1 Introduction

Because of the widespread natural occurrence of sulfur in fuels (whether solid, liquid, or gaseous), severe corrosion may arise when materials come into contact with hot combustion atmospheres derived from these fuels, as in superheaters, heat exchangers, gas turbines, etc. Sulfur contamination problems also arise in processing plants in the petroleum and chemical industries.

In these situations, the main concern is the interaction between metals and alloys and hydrogen sulfide, sulfur dioxide, sulfur trioxide, or elemental sulfur itself.

Metal/alloy reactions with other sulfur-containing compounds such as carbon disulfide are also a source of concern.

Interaction with sulfur dioxide (and/or trioxide) may produce scales consisting of the oxide alone, or oxide plus sulfide, or even sulfate, but in the present review, the reactions that lead to the formation of sulfide scales on metals and alloys only will be considered.

The sulfidation behavior of metals and alloys is also a subject of academic interest, since it would be hoped that fundamental studies of these phenomena might ultimately lead to a more complete understanding of the process involved and to the development of better sulfidation-resistant materials.

The present chapter is confined to a brief theoretical consideration of the sulfidation behavior of metals and alloys, discussing the basic phenomena involved in the processes. Accordingly, first, an overall picture of the sulfidation process is given, which is more amplified in three further sections concerning the kinetics of sulfidation of metals, the sulfidation behavior of alloys, and the defect structure of metal sulfides. Reference to published papers covering many aspects of sulfidation is also included.

8.2 The Process of Sulfidation

For the formation of a metal sulfide, MS, from a divalent metal and sulfur vapor containing S_2 molecules as the main species, according to a scheme of the type

$$M + \frac{1}{2}S_2 \rightarrow MS \tag{8.1}$$

the driving force is the decrease in free energy (ΔG°) attending the reaction. Provided that $\Delta G^\circ_{8.1}$ is less than 0, i.e. is negative, then it is reasonable to assume on the basis of the usual thermodynamic arguments that the reaction will occur spontaneously. In fact, since the standard free energy of formation of most metal sulfides is often negative at the elevated temperatures relevant to many environments containing sulfur, then corrosion may be expected as a natural consequence.

Thermodynamic considerations of this type, as discussed adequately in Chapter 3, are of only limited use since the corrosion product either partially or completely covers the metal surface. The subsequent reaction is then governed entirely by the physicochemical properties of this sulfide scale, and the corrosion problem becomes one of reaction kinetics and not thermodynamics. If we assume that the layer is compact, dense, and pore-free, affording a protective covering to the underlying metal surface, as may reasonably be expected since the volume of metal consumed in producing that volume of sulfide, according to the principles established by Pilling and Bedworth (see Chapter 7), then the rate of continued scaling will be governed by one of several possible mechanisms, which together constitute the overall process, viz.:

1. Adsorption and dissociation of sulfur molecules into atoms at the sulfide/sulfur interface

$$S_2(g) \rightarrow 2S(g) \rightarrow 2S(ads) \tag{8.2}$$

High Temperature Corrosion: Fundamentals and Engineering, First Edition. César A. C. Sequeira.
© 2019 John Wiley & Sons, Inc. Published 2019 by John Wiley & Sons, Inc.

2. Ionization of the metal atoms into ions and electrons at the metal/sulfide interface

$$M \rightarrow M^{2+} + 2\,e^{-} \tag{8.3}$$

followed by flow of the electrons toward the sulfide/sulfur vapor interface to allow production of sulfur ions

$$S(ads) + 2e^{-} \rightarrow S^{2-} \tag{8.4a}$$

or

$$S(ads) \rightarrow S^{2-} + 2 \oplus \quad \text{electron hole} \tag{8.4b}$$

3. A diffusion either of cations, M^{2+}, outward through the sulfide lattice toward the sulfide/sulfur interface (see Figure 8.1a) or alternatively of anions, S^{2-}, inward through the lattice toward the metal/sulfide interface (Figure 8.1b), either process allowing the formation of the corrosion product

$$S^{2-} + M^{2+} \rightarrow MS \tag{8.5}$$

but at different interfaces.

It should be emphasized, however, that even when such a favorable potentially protective sulfide/metal volume relationship exists within a given reaction system, often in practice, because of the large stresses that are produced within the system by virtue of this large volume ratio, the protective scale breaks down mechanically and develops porosity, leading to an enhanced reaction rate (Hauffe 1965; Kubaschewski and Hopkins 1962).

Of these three reaction products (1)–(3), one will be the slowest and will therefore control the overall rate of reaction. It should be noted that processes (1) and (2) also involve incorporation of S^{2-} ions and M^{2+} ions into the sulfide layer, respectively. Again, the ionization of metal atoms (process 2) may require a simultaneous injection of vacancies into the underlying metal. When considering the individual mechanisms constituting processes (1) and (2), it is important to recognize that these are all phase-boundary reactions, in contrast to process (3). Which of these processes is rate controlling will normally be reflected in the scaling kinetics; if process (1) or (2) is rate controlling, linear kinetics will prevail, while if process (3) is the slowest overall mechanism, then diffusion-controlled (often parabolic) kinetics may be expected.

Thus, although at first sight we have in sulfidation an essentially simple chemical interaction, involving the normal thermodynamic considerations, the process is, in fact, complex. It should be emphasized that the foregoing description of some of the main features of the sulfidation process has been limited to a consideration of the formation of compact sulfide scales of a single chemical composition. In practice, the unrestricted natural growth of a physically and mechanically perfect scale, according to the mechanisms outlined above, is rare. Often the scales formed on metals and alloys develop imperfections (cracks, voids, porosity) and lose adhesion to the metal surface, leading to the development of non-protective scales that may seriously modify the normal processes, particularly (3).

To enable the outline description of the sulfidation process to be amplified, it is convenient to further discuss the subject matter under three headings: sulfidation kinetics, sulfidation behavior, and defect structures.

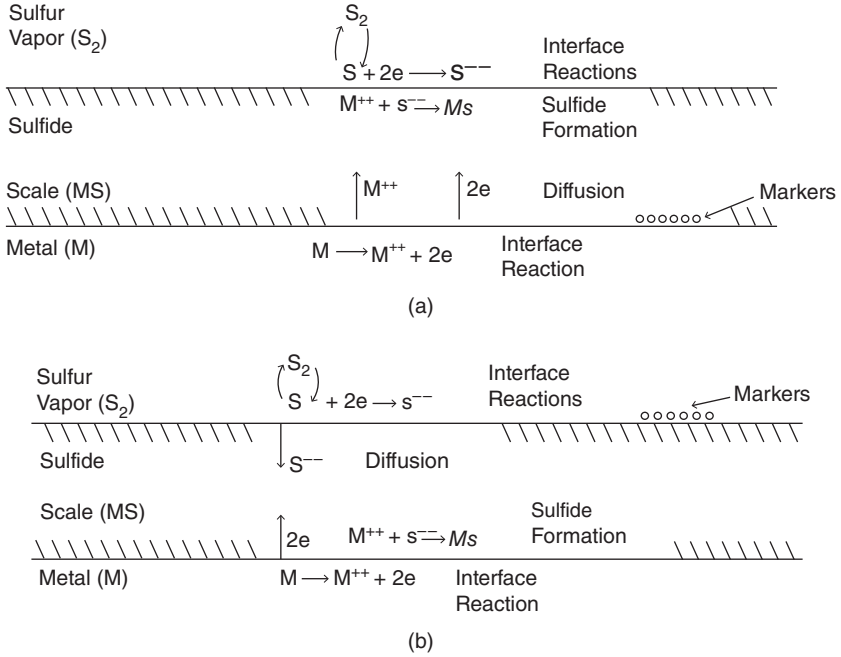


Figure 8.1 Summary of the various mechanisms leading to the formation of sulfide scales on metals involving (a) an outward diffusion of cations and (b) an inward diffusion of anions.

8.3 Sulfidation Kinetics

Two types of reaction kinetics – linear and parabolic – have been observed during the sulfidation of metals under isothermal exposure conditions that lead to a formation of sulfide scales. Of these two kinetic types, the parabolic relationship between weight gain and exposure time has been most commonly observed. If we consider an increase in weight per unit area of sample, Δm, due to sulfidation after an exposure time t, the parabolic relationship is defined as $(\Delta m)^2 = k_p \cdot t$ where k_p is the parabolic reaction-rate constant. The linear scaling law is defined by the expression $(\Delta m) = k_l \cdot t$ where k_l is the linear rate constant.

Occasionally, sulfidation reactions are initially parabolic, but linear kinetics is observed to succeed as a second reaction stage ("paralinear" kinetics). This transition in behavior appears to be associated with the development of mechanically imperfect, porous, or partially fused scales (Davin and Coutsouradis 1962; Dravnieks 1951; Haycock 1959a,b).

The mechanism of parabolic scaling of metals (whether involving oxidation or sulfidation) was fully described over 75 years ago by Wagner (1933a,b).

The main features of the Wagner model may be conveniently illustrated with reference to the parabolic sulfidation of silver, a reaction system that has been studied in some considerable detail. The interaction between silver and liquid sulfur leads to the formation of the scale of silver sulfide, Ag_2S (Figure 8.2), and the growth of this scale depends on the physicochemical properties of the scale and involves three reaction mechanisms, as defined earlier. Of these mechanisms (1)–(3), the Wagner model is concerned only with the diffusion-controlled reaction, i.e. mechanism (3); it is assumed that the phase-boundary reactions described in mechanisms (1) and (2) are sufficiently rapid not to be rate controlling and that a volume diffusion of the reacting ions (Ag^+) and transport of electrons across the growing scale controls the overall rate of reaction. Electrons and ions are considered to migrate independently of each other through the n-type defect silver sulfide lattice. The part played by a possible counter diffusion of S^{2-} ions in forming the Ag_2S scale is considered negligible. It is assumed that thermodynamic equilibrium is established between the metal and the sulfide at the metal/sulfide interface and between the sulfide and the sulfur at the sulfide/sulfur interface; in this way, the boundary conditions for diffusion are established.

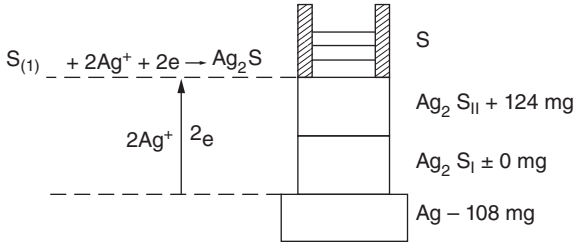


Figure 8.2 The reaction between silver and liquid sulfur to form silver sulfide (Wagner 1951).

The driving force for the sulfidation process is the free energy change associated with the formation of the sulfide Ag_2S from metallic silver and the sulfur, and a chemical-potential (concentration) gradient exists across the scale. The partial pressure of sulfur at the metal/sulfide interface is equal to the equilibrium dissociation pressure of the sulfide in contact with the metal, while at the other interface, it corresponds to the sulfur activity in the liquid sulfur in equilibrium with the sulfide. More generally, for gaseous sulfur corrosion, this sulfur activity would correspond to the partial sulfur pressure of the surrounding atmosphere.

The rate of growth of the sulfide scale at the outer sulfide/sulfur interface is determined by this chemical concentration gradient through the scale and the rate of diffusion of silver ions under the influence of the gradient. The mobilities or the diffusion coefficients of the cations and electrons are, however, not equal, and, as a result, an electrical-potential difference exists across the scale, which draws the silver ions through the scale to the outer interface. The transport of ions and electrons through the scale is then described in terms of diffusion due both to the chemical-potential and electrical-potential differences across the scale.

On the basis of this model, Wagner derived an expression for the rate of thickening ($d\eta/dt$ equivalents per second) of a scale of thickness Δx:

$$\frac{d\eta}{dt} = \left\{ \frac{300}{FNe} \int_{\mu x'}^{\mu x''} \left| \frac{I}{Z_2} \right| (t_1 + t_2) t_3 K \, d\mu x \right\} \frac{I}{\Delta x} = K_r \frac{I}{\Delta x} \tag{8.6}$$

where K is the electrical conductivity of the scale (Ω^{-1} cm^{-1}) and t_1, t_2, t_3 are the transport numbers of the cations (Ag^+), the anions (S^{2-}), and electrons, respectively – properties that can be measured. In practice we may note that $t_2 \simeq 0$ and $t_3 \simeq 1$, i.e. the contribution of the S^{2-} ion to the total conductivity is negligible and the conductivity of Ag_2S is considered to be mainly electronic, with a small cationic contribution. Z_2 is the valency of the negatively charged nonmetal (sulfur) ion; $\mu x'$ and $\mu x''$ are the chemical potentials of the nonmetal for the equilibria between the sulfide reaction product and the metal (i.e. at the inner interface) and between the sulfide reaction product and the nonmetal (i.e. sulfur at the outer interface). F is the Faraday (96 500 C), N is Avogadro's number, and e is the charge on the electron in e.s.u.; K_r, the expression within the braces was termed the rational rate constant by Wagner, indicating the reaction rate in equivalents/cm^2 s for a scale layer of unit thickness (1 cm).

Since the chemical potential of the nonmetal is by definition related to the activity, a_x, of the nonmetal, and if the activity is approximated to partial pressure, we may write

$$\mathrm{d}\mu_x = RT\,\mathrm{d}\,\ln\,a_x = RT\,\mathrm{d}\,\ln p_x = \frac{1}{2}\,RT\,\mathrm{d}\,\ln\,p_{\mathrm{s}_2} \qquad (8.7)$$

Normally, it is common practice to measure parabolic sulfidation rates gravimetrically; when the units of k_p are $(\mathrm{gS})^2/\mathrm{cm}^4\ \mathrm{s}$, k_r is proportional such that

$$k_\mathrm{r} = \frac{1}{2}\,V_\mathrm{eq}\left(\frac{Z_2}{A}\right)^2 k_\mathrm{p} \qquad (8.8)$$

for a sulfide M_2S (e.g. Ag_2S), where V_eq is the volume of 1 g equivalent of the sulfide, Z_2 is the valency of the sulfur ion, and A is the atomic weight of sulfur.

Wagner was, in fact, able to show experimentally that the growth of silver sulfide was indeed governed mainly by silver-ion migration and at the same time demonstrated the validity of expression (8.6).

The experimental arrangement used is shown in Figure 8.2. Two silver sulfide tablets (I and II) were placed on the top of a cylinder of metallic silver. A glass tube containing sulfur was placed on the top surface of tablet II. The complete unit was then heated at 220 °C in an atmosphere of nitrogen for one hour. During this period silver sulfide was observed to form at the bottom of the glass tube, i.e. at the sulfur/silver sulfide interface. The gain in weight of tablet II (including the freshly formed sulfide) was equal to the weight loss of the silver cylinder together with the equivalent weight of (combined) sulfur.

Thus, Wagner showed that the reaction

$$2\mathrm{Ag} + \mathrm{S} \rightarrow \mathrm{Ag_2S} \qquad (8.9)$$

took place mainly at the sulfur/sulfide interface and involved only silver-ion migration. By observing the growth rate of the silver sulfide, a rational rate constant of 1.6×10^{-6} equiv. $\mathrm{cm}^{-1}\ \mathrm{s}^{-1}$ was calculated. The corresponding values of $2\text{–}4 \times 10^{-6}$ calculated from Eq. (8.6) using available transport numbers and electrical-conductivity data were in reasonable agreement with the experimentally determined value, thus confirming the validity of the reaction model.

Sulfidation experiments reported by Hauffe and Rahmel (1952), Meussner and Birchenall (1957), and many others would appear in general to support the validity of the Wagner model. But, when considering these results, it is important to realize that the reaction model does not assume larger molecular species such as S_4, S_6, and S_8 in the vapor phase; also idealized sulfide scale growth is uncommon, marker experiments are difficult to interpret, the sulfide defect model does not consider the degree of association of the ionic and electronic defects, etc. In summary, practical analysis of the kinetics of sulfidation of metals is by far really a complicated situation.

8.4 Sulfidation of Selected Materials

Studies on the sulfidation of pure metals have yielded useful information regarding the fundamental mechanism(s) of the process. In general, it has been concluded that there are many similarities but also differences between the kinetics and mechanisms of oxidation and sulfidation. One of the most important conclusions is that both sulfide and oxide scales on common metals grow by outward diffusion of cations. On the other hand, in the case of the sulfidation of some refractory metals, e.g. molybdenum, tantalum, and tungsten, inert markers were found on the scale surface, strongly suggesting that the MoS_2, TaS_2, and WS_2 scales, like the ZrO_2 scale, grow by inward diffusion of anions. This important similarity in the growth mechanism of sulfide and oxide scales on metals results from the same type of predominant disorder in transition metal sulfides and oxides. However, the sulfidation rates of common metals are usually many times higher than their oxidation rates, which results mainly from a very high concentration of point defects in the sulfides. In other words, sulfidation rates are primarily determined by lattice diffusion, grain boundary diffusion being less important in sulfides than in the case of metal oxidation.

It is also very important to note that very small solubility of sulfur in metals as well as rapid scale formation makes the formation of an internal sulfidation zone, which plays an important role in oxide corrosion, impossible. Furthermore, small or even trace amounts of impurities may dramatically influence the rate of sulfide corrosion due to the doping effect that will be discussed later.

Since pure metals are not generally suitable for high temperature structural engineering applications on account of their lack of strength, for practical purposes the development of sulfidation-resistant alloys is of interest.

There are two possible approaches to this problem. First, on theoretical grounds, according to the principles established by Wagner, it should be possible to reduce the number of defects present in a semiconducting sulfide scale by the incorporation into that scale of a suitable alloying element. This in turn might be expected to reduce the rate of sulfidation, provided the reaction was controlled by a diffusional process.

Accepting the application of this Wagner alloying theory to sulfidation phenomena (which was originally postulated and proved with reference to metal oxidation), there are certain practical limitations that unfortunately severely restrict its application.

The second approach to the problem of developing sulfidation-resistant alloys is to consider alloying the basis metal with another metal that reacts very readily to form a stable sulfide, i.e. sulfidizes preferentially. This might be expected to result in the formation of a protective

layer over the underlying alloy and so reduce the rate of sulfidation. A low defect concentration in the preferentially formed sulfide is clearly implicit for effective protection.

The Wagner theory of alloying as a method for reducing the rate of sulfidation of metals may be explained as follows. Briefly, the effect depends upon whether the ions of the solute (i.e. alloying addition) increase or decrease the number of defects in the surface compound (semiconducting sulfide) of the solvent. Consider the formation of silver sulfide, Ag_2S. If we accept that silver sulfide is an n-type (metal-excess) semiconductor, the defect equilibrium may be considered as follows:

$$Ag_2S = 2Ag_i^+ + 2e^- + \frac{1}{2}(S_2) \tag{8.10}$$

which, applying the law of mass action, gives

$$[Ag_i^+]^2 \times [e]^2 = \text{const.}(p_{S_2})^{-1/2} \tag{8.11}$$

The substitution of a metal of higher valency than unity into the sulfide lattice would increase the number of excess electrons and bring out a decrease in the number of the interstitial monovalent silver ions, in accordance with the law of mass action. Since, as we have seen, the sulfidation of silver is parabolic, and the rate of reaction is controlled by the rate of diffusion of silver ions through the defect lattice, the reaction rate would be expected to decrease following this decrease in the Ag_i^+ concentration. An opposite effect might be expected for additions of metals of lower valency than that of the metal constituting the parent sulfide, e.g. the addition of silver to cadmium sulfide.

Experimental evidence in support of these theoretical predictions has been given in the open literature along the last 30 years.

It is now necessary to compare the application of the Wagner theory of alloying to p-type (metal-deficit) sulfide semiconductors. As an important industrial example, one might consider the formation of ferrous sulfide, FeS, during the sulfidation of iron. The defect structure of FeS has been discussed earlier. Here, the opposite effect to that observed for n-type Ag_2S would be expected, i.e. addition of metals exhibiting a valency of >2 should increase the number of vacant cation sites. Thus, in a situation where the growth of FeS is diffusion controlled, the rate of reaction would be expected to increase over that for pure iron for an iron-based alloy containing such addition elements. On the other hand, addition of monovalent metals as alloying elements to iron should decrease the number of cation vacancies and slow down the reaction rate relative to the pure metal.

However, when one considers the selection of metals that fulfill this valency requirement, other difficulties become apparent. First, it is implicit in the Wagner theory that the alloying addition, which must be present as a minor addition (i.e. in amounts insufficient to form a separate sulfide phase), must be freely soluble in the parent sulfide.

A proper idea of the solubility, i.e. the ease of incorporation of the foreign ion, depends on the availability of appropriate phase diagrams or of other data that is not reported yet. Sulfidation experiments trying to reproduce the theoretical predictions led to complex results. By reviewing the works of Hauffe and Rahmel (1952), Foley et al. (1953), Lichter and Wagner (1960), Mrowec et al. (1966), and Spauschus et al. (1954), we notice that many of the reported data are in disagreement with the theoretical predictions of Wagner.

It will be clear therefore that the successful development of sulfidation-resistant alloys on the basis of rational theoretical considerations is limited. However, it would seem that even if the required data were available, often the theoretical analysis of the particular system would prove to be inadequate and oversimplified, so that in practice only a partial success could be expected. For all these reasons, a somewhat empirical approach to alloy development is unavoidable. Nevertheless, the development of sulfidation-resistant alloys, based on the premise of the formation of a stable protective sulfide by selective sulfidation, would appear to be fairly successful, certainly when compared with the alternative approach based on the principles of Wagner.

Following this avenue, Davin and Coutsouradis (1962), Hancock (1962), Setterlund and Prescott (19611), and others carried out sulfidation experiments on Ni–Cr, Fe–Cr, Co–Cr, Fe–Al, and Fe–Cr–Al alloys and others, but no satisfactorily accounted improvement results were obtained. Due to these difficulties, it is very important to select candidate materials to be used in $S + H_2S + RSH$, $H_2 + H_2S$, and other high temperature sulfidation environments by monitoring their behavior in real industrial situations during their operation life. It seems to be appropriate now to review some of these materials that are used in calcining of mineral and chemical feedstock, petrochemical processing, fossil-fired boilers, petroleum refining, coal gasification, waste incineration, fluidized-bed coal combustion, and oil-fired boilers (Hill and Black 1981; Lai 1985; Norton 1984; Rapp 1981; Sorell et al. 1986; Stringer 1986).

Sulfidation behavior of metals and alloys in sulfur vapor environments has been studied generally at sulfur pressures higher than 10^{-3} atm. Studies of H_2–H_2S mixtures have been typically carried out at sulfur partial pressures less than 10^{-2} atm. Mrowec and Przybylski (1984) and Young (1980) gave excellent reviews on sulfidation in sulfur vapor and H_2–H_2S environments. Data generated in these types of environments (iron at 250–980 °C, nickel at 400–640 °C, cobalt at 500–1000 °C, chromium at 700–800 °C, iron-, nickel-, and cobalt-based alloys in S_2 and H_2–H_2S mixtures) are applicable only to industrial environments where sulfides, but not oxides, are thermodynamically stable. Improved sulfidation resistance for alloys with less than 40 at.% Cr at sulfur potentials

greater than 10^{-2} atm was attributed to the formation of an inner sulfide layer: $Fe(Fe_{2-x}Cr_x)S_4$ for Fe–Cr alloys, chromium sulfides with nickel for Ni–Cr alloys, and chromium sulfides with cobalt for Co–Cr alloys. In alloys with higher chromium (40 at.%), a single layer of chromium sulfide (Cr_2S_3) was observed.

In refineries, sulfidation, which is commonly referred to as a *sulfidic corrosion* in refinery industry, is a common materials problem, at temperatures between 260 and 540 °C. Sulfur compounds originating from crude oils include polysulfides, hydrogen sulfide, mercaptans, aliphatic sulfides, disulfides, and so forth (Foroulis 1985). The crude distillation units that process mostly sweet crude oils (<0.6% total sulfur, with essentially no hydrogen sulfide) experience relatively less sulfidation problems. More sulfidation problems are encountered in the distillation units that process mostly sour crudes (Gutzeit et al. 1987). The corrosion rates of the crudes and their liquid fractions can be predicted by the so-called modified McConomy curves. Figure 8.3 shows the modified McConomy curves for liquid hydrocarbon streams containing 0.6 wt% (Gutzeit 1986). For hydrocarbon streams containing more than 0.6 wt% sulfur, the corrosion rate multiplier (Gutzeit 1986) can be used in conjunction with the data shown in Figure 8.3 for making the prediction of the corrosion rate of the various steels at different temperatures.

Hydrogen in hydrotreating, hydrocracking, and hydrosulfurizing processes is used to remove sulfur (to convert it to hydrogen sulfide) and nitrogen (to ammonia) for separation from the hydrocarbon stream. Hydrocracking processes combine desulfurization and cracking operation that can convert hydrocarbon feedstocks into various products. Sulfidation in these processing units is dictated by the H_2S concentration in the H_2–H_2S environment. Sulfidation in H_2–H_2S environments is severe since the corrosion products are sulfides with no protection by oxide scales in these environments. Materials issues related to hydrogen attack are discussed in Chapter 12. *Couper–Gorman curves* are generally believed to provide the most practical correlation among corrosion rates, temperature, and concentration of H_2S for various steels. These curves were based on a survey conducted by NACE Committee T-8 on Refining Industry Corrosion (Couper and Gorman 1971). The modified Couper–Gorman curves (i.e. the original curves were extended to higher concentrations of H_2S with dashed lines) for 5Cr–0.5Mo steels (also applicable to carbon steels) and 18Cr–8Ni steel are shown in Figures 8.4 and 8.5, respectively. It was found that total pressure between 1 and 18 MPa was not a significant variable. Gutzeit, Couper, and Gorman also observed that no sulfidation occurred at very low H_2S concentrations and at temperatures above 315 °C because formation of iron sulfides in that regime is not feasible thermodynamically.

Sulfidation behavior of alloys in environments containing H_2, CO, CO_2, H_2O, and H_2S, and their gaseous

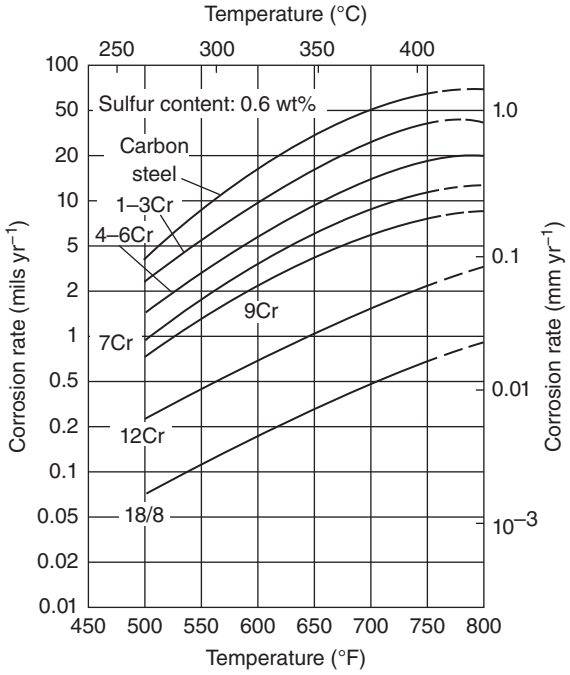


Figure 8.3 Modified McConomy curves providing predicted corrosion rates as a function of temperatures for various steels in a liquid hydrocarbon stream containing 0.6% S (Gutzeit 1986).

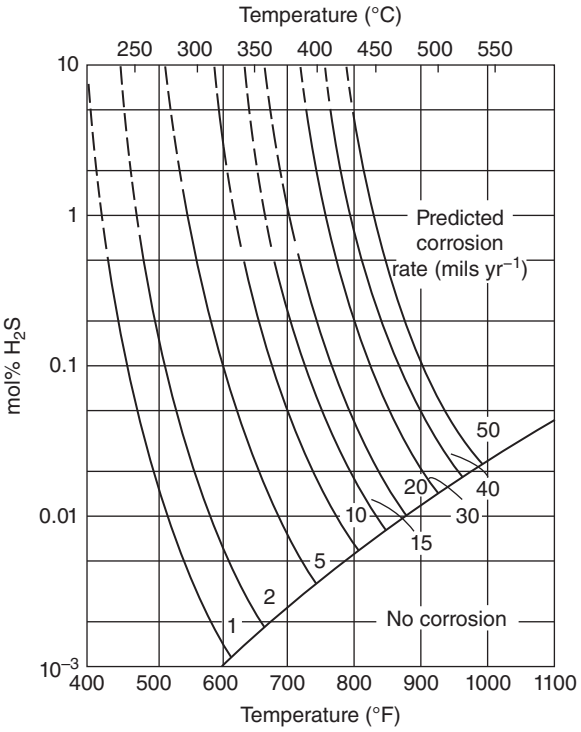


Figure 8.4 Modified Couper–Gorman curves showing corrosion rates as a function of H_2S concentration (mol%) and temperature for 5Cr–0.5Mo steel. The data is also applicable to carbon steels and alloy steels with less than 5% Cr (naphtha desulfurizers (Gutzeit 1986).

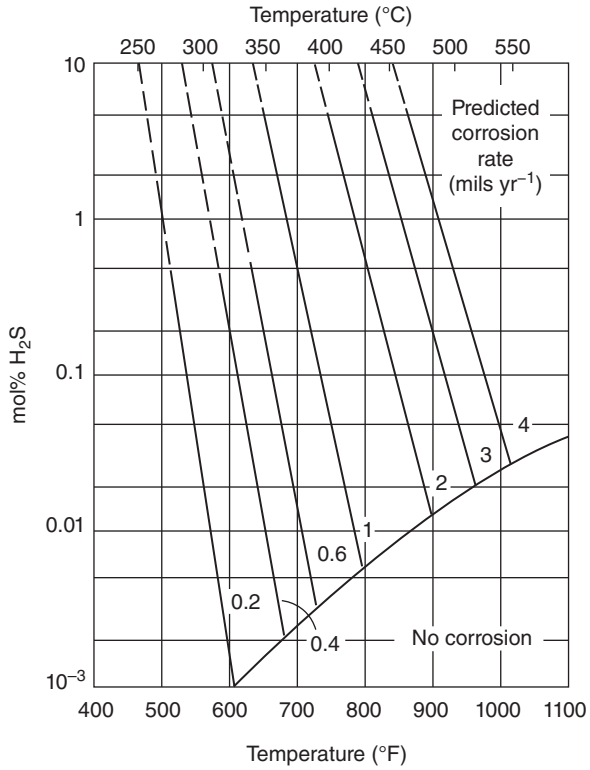


Figure 8.5 Modified Couper–Gorman curves showing corrosion rates as a function of H_2S concentration (mol%) and temperatures for 18Cr–8Ni steel (Gutzeit 1986).

components with oxygen and sulfur potentials high enough to form oxides and sulfides for most high temperature alloys, has been extensively studied during the 1970s, 1980s, and early 1990s when coal gasification programs have been actively pursued. Significant understanding of corrosion reactions in these coal gasification atmospheres having sulfur potentials of 10^{-5}–10^{-10} atm and oxygen potentials of 10^{-15}–10^{-20} atm has been achieved (Hill and Black 1981; Howes 1987; Humphreys and Schaefer 1983; Kneeshaw et al. 1987; Rothman 1985). In addition, a large engineering database on more than 80 commercial alloys has been generated. Many of these alloys were discussed by Verma (1985) who observed that chromium was the most important alloying element in resisting sulfidation attack. Breakdown of the protective chromium oxide scale resulted from the sulfides formed over it (Perkins 1980). Formation of liquid sulfide slag over the chromium oxide scale is most damaging. Manganese, iron, cobalt, nickel, and other alloying elements diffuse through the chromium oxide scale and react with the environment on top of the oxide scale to form external sulfides. This was proposed by Perkins (1980) as a possible mechanism for breakaway corrosion, schematically illustrated in Figure 8.6. In addition to outward diffusion of alloying elements to form external sulfides, the corrosion reaction also involves sulfur penetrating through the oxide scale to form discrete particles of sulfides in the matrix. Natesan (1983) showed that, for a given sulfur potential, there exists a threshold value for oxygen potential beyond which a continuous protective oxide scale is developed. This threshold oxygen partial pressure (kinetic boundary) is about 10^3 times the oxygen partial pressure for chromium oxide and chromium sulfide equilibrium (thermodynamic boundary).

John et al. (1993) reported the corrosion data generated at 700 °C and 1 atm pressure for various commercial alloys in syngas environments that were rich in CO and H_2 with low water. The data for various Fe-, Ni-, and Co-based alloys at 700 °C and lower in CO–$26H_2$–$1.0CO_2$–$0.9H_2S$–$2H_2O$–$10N_2$ shows that Co-based alloys, such as alloys 25 (CO–20Cr–10Ni–11.5W) and 150 (Co–27Cr–18Fe), were not significantly better than Type 310 and but not as good as Type 446. Natesan (1993) found that molybdenum and TZM (molybdenum with 0.5Ti and 0.04Zr) formed very thin adherent sulfide scales when tested at 871 °C in a sulfidizing environment with low oxygen and high sulfur potentials. The beneficial effect of molybdenum in improving the alloy sulfidation resistance in the environments with low oxygen, high sulfur potentials would be of interest since molybdenum has been used in many high temperature nickel-based alloys to provide solid solution strengthening for the alloy. Some of these wrought alloys include alloys X, S, 617, 625, and R-41. Furthermore, molybdenum is also a major alloying element in Ni–Cr–Mo corrosion-resistant alloys, such as C-276, C-12, 59, C-2000, and 686. These Ni–Cr–Mo alloys contain molybdenum in a range of 13–16%. High levels of molybdenum in these Ni–Cr–Mo alloys can cause a thermal stability issue when used at high temperatures because of the formation of intermetallic phases during the long-term, high temperature exposures.

Most corrosion studies of SO_2-bearing environments have been conducted in either SO_2 or O_2–SO_2 mixtures. Materials investigated include nickel, iron, cobalt, chromium, Co–Cr alloys, Ni–Cr alloys, and so forth (Hocking and Sidky 1987; Hocking and Vasantasree 1976; Sidky and Hocking 1987; Strafford et al. 1989; Vasantasree and Hocking 1976). Kofstad (1988) reviews the corrosion of pure metals and binary alloys in SO_2 and SO_2–O_2, which form oxides and/or sulfides as corrosion products, strongly depending on temperature. The reaction rate generally peaks at a certain temperature and then decreases with increasing temperature. The highest corrosion rate is normally related with the formation of sulfides. Sulfides provide paths for rapid outward diffusion of metals, such as nickel, iron, chromium, and so forth, resulting in rapid corrosion attack. Chromium does not form sulfides in SO_2 at temperatures from 700 to 1000 °C, but instead forms a Cr_2O_3 scale. Thus, chromium as an alloying element improves resistance in Co–Cr and Ni–Cr alloys.

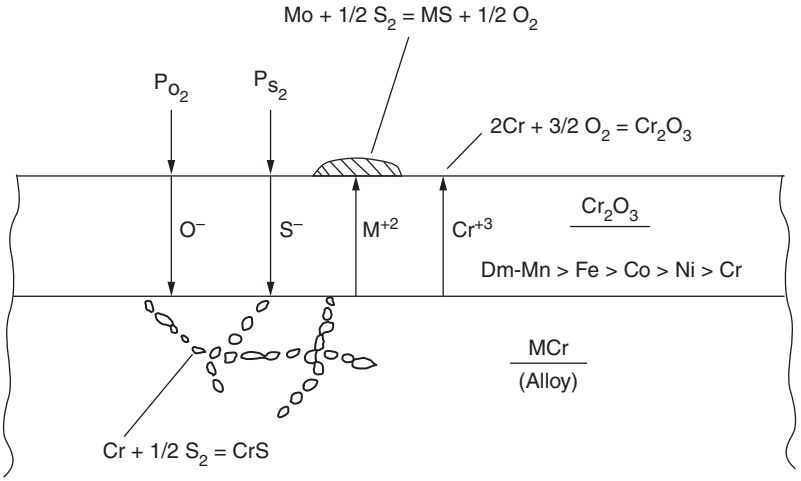


Figure 8.6 Formation of external sulfides on top of the chromium oxide scale and the formation of internal sulfides (Verma 1985).

Many industrial processes that generate SO_2-bearing environments are generally at temperatures lower than 900 °C. Yates et al. (1994) tested alloys X (identified as HX Ni–22Cr–9Mo–18Fe), 617 (Ni–22Cr–12Co–9Mo–1.2Al), 230 (Ni–22Cr–14W–La), 198 (Co–22Cr–20Ni–14W–La), and 214 (Ni–16Cr–3Fe–4.5Al–Y) at 704 °C in O_2–4% SO_2 for more than 40 days. Based on their test results, Ni–Cr and Co–Cr alloys containing about 22% Cr are considered to have adequate corrosion resistance in O_2–4% SO_2 at 704 °C. All four 22Cr alloys (X, 617, 188, and 230) exhibited a parabolic reaction kinetics with low mass changes over more than 40 days of exposure, indicating the formation of protective chromium-rich oxide scales. On the other hand, Ni–Cr–Al alloy 214 with only about 16% Cr showed some indication of breakaway corrosion.

Not many investigators have tested commercial alloys in SO_2-bearing environments, particularly at low SO_2 level (<1%), but these oxidizing environments generated by combustion of a sulfur-containing fuel of feedstock with excess air or oxygen are generally less corrosive than reducing environments.

Before concluding this section, it is worth noting that the Co–Cr alloys exhibited better resistance to corrosion than the other alloys, and it was suggested that it was due to the smaller molecular volume of the cobalt sulfide, the slow outward diffusion of cobalt ions, and the fairly high melting point of the cobalt–sulfur eutectic (Co–Co_4S_3 eutectic at 880 °C). It may be noted that the superior corrosion resistance exhibited by the Co–Cr alloys relative to the Ni–Cr alloys is of considerable interest in the context of gas turbine development. While the creep-rupture strength of Ni-based high temperature alloys is superior to that for Co-based alloys at the intermediate temperatures of 900–950 °C, the cobalt alloys offer equal, if not slightly better, strength properties at high temperatures (950–1100 °C). However, it seems that the better sulfidation resistance of Co–Cr alloys may be the limiting factor and could finally influence the choice of material for turbine blades to attain the desired higher operating temperatures, depending upon the required operating life of the turbine.

8.5 Defect Structures of Metal Sulfides

In Section 8.2, it was emphasized that the physicochemical properties of the sulfide scale formed on a metal entirely govern the process of sulfidation. Of particular importance is the defect structure of the sulfide, i.e. whether the surface-layer compound is an n-type (metal-excess) or p-type (metal-deficit) semiconductor, since this largely dictates – certainly during the formation of a dense compact scale – the basic growth processes of the scale. When comparing the available data relating to the defect structures of metal sulfides, on the one hand, and of metal oxides, on the other, it becomes apparent that more fundamental studies have been attempted with oxides than with sulfides. In this section, a brief attention is given to the experimental methods used to provide these data. Then, the role of the defect structures and doping effect in modifying corrosion rate and protective properties of sulfide scales will be discussed with good examples of such situations.

Information concerning the defect nature of oxide or sulfides may be obtained by carrying out specific experiments to provide various physical and chemical data, which, if viewed separately and in isolation, are insufficient, but which when considered collectively and as a whole yield a picture of the defect state of the material. It is possible to classify the methods that have been used and that are cited in the literature into two main groups: (A) those concerned with property measurements on the actual compounds themselves, i.e. detached from the metal

and in fact often prepared "artificially," for example, by the sintering of powders to produce pellets of the required material, and (B) those concerned with observing the manner in which the compound (the scale) is formed on the metal (essentially oxidation of sulfidation experiments under specific exposure conditions). The various experimental procedures within these two groups that may be used, together with the expected observations and the conclusions that may be drawn from such observations, are summarized in Table 8.1. Techniques involved in group A provide direct evidence regarding the defect nature of a compound, while those in group B can only be considered as providing indirect, complementary supporting evidence to that derived from group A experiments and involve the inherent assumptions required with the invocation of the Wagner model of scaling (see Section 8.2).

In Table 8.1, x is the term associated with the charge on the vacancies (equal numerically to 3, 2, or 1), and n is the number of atoms associated with the dominant molecular species. The stoichiometry of certain sulfides has also been established by the experimental techniques known as coulometric titration, whose underlying principles have already been covered by many investigators (Wagner 1953; Wagner and Wagner 1957; Wehefritz 1960). Concerning the nature of electronic defects in sulfide semiconductors, the measurement of the sign of the *Hall coefficient* or of the *Seebeck or Peltier coefficient* (the so-called thermoelectric power) (Hannay 1959; Wagner 1933a,b) is sufficient to allow distinction between n- and p-type semiconductors. These R and π coefficients shown in Table 8.1 are explained in the Glossary of the selected terms used in high temperature corrosion.

To demonstrate that the defect structures and the doping effect may not only improve but also considerably worsen the protective properties of sulfide scales, changing simultaneously the temperature and pressure dependence of the sulfidation reaction, let us analyze a few of these phenomena. A first example is the case of Al–Mo alloy sulfidation.

From Wagner's theory of metal oxidation, it follows that, if the concentration of the predominant defects in the growing scale on a given metal is low enough that their mobility is concentration independent, the self-diffusion coefficient of diffusing species depends in the same way on oxidant pressure as the parabolic rate constant of scale growth (Kofstad 1988). Thus, in the cases of Mo and Al–Mo alloys (e.g. Al–34Mo), sulfidation K_p ($g^2\ cm^{-4}\ s^{-1}$) should be given by

$$K_p = \text{const.}\ D_S = \text{const.}\ D_i[S_i'] = \text{const.}\ D_S^0\, p_{S_2}^{1/4} = \text{const.}\ p_{S_2}^{1/4} \tag{8.12}$$

as found by Mrowec (2003). Here D_S is the self-diffusion coefficient of sulfide ions, D_i is the defect diffusion coefficient, and $[S_i']$ are single ionized interstitial sulfide ions. Note that D_i is a direct measure of defect mobility (Kofstad 1972; Mrowec 1980). In the case of Al-doped MoS_2, not only lower defect concentrations (Rau 1980) but also different pressure and temperature dependences are to be expected. Thus, assuming that the Al^{3+} ions are dissolved

Table 8.1 Experimental methods for assessing sulfide defect structures

Experimental procedure	Observations	Conclusions
Group A: Physicochemical property measurements		
(1) Determination of stoichiometry by:		
(a) Chemical analysis		
(b) X-ray diffraction and density measurements		
(c) Coulometric titration	See Wagner (1953)	See Wehefritz (1960)
(2) Electrical-conductivity (K) measurements:		
(a) On pure sulfides, as a function of sulfur activity	(a) $K \propto (a_{S_n})^{1/xn}$ or $\propto (a_{S_n})^{-1/xn}$	p-Type or n-type
(b) On sulfide doped with addition of element A, at various (constant) temperatures	(b) Valency of A > valency of M K increased or decreased	n-Type or p-type
	Valency of A < valency of M K increased or decreased	p-Type or n-type
(3) Hall coefficient (R) measurement at various (constant) temperatures	R negative or positive	n-Type or p-type
Seebeck coefficient (π)	π negative or positive	n-Type or p-type
Group B: Sulfidation experiments		
(1) Assessment of the variation of k_p with sulfur activity at constant temperature	$k_r \propto (a_{S_n})^{1/xn}$ or $\propto (a_{S_n})^{-1/xn}$	p-Type or n-type
(2) Observation of the effects on k_p of additions of alloying element (A) to basis metal M at constant temperature	Valency of A > valency of M k_p increased or k_p decreased	p-Type or n-type
	Valency of A < valency of M k_p increased or k_p decreased	n-Type or p-type

on regular Mo sites, the following defect equilibria may be described (Kröger 1974):

$$Al_2S_3 + \frac{1}{2}S_2 = 2Al'_{Mo} + 2h^{\bullet} + 4S_S \tag{8.13}$$

$$Al_2S_3 + 2S'_i = 2Al'_{Mo} + 4S_S + \frac{1}{2}S_2 \tag{8.14}$$

Neglecting other defects, the electroneutrality condition is given by

$$[h^{\bullet}] = [S'_i] + [Al'_{Mo}] \tag{8.15}$$

If $[S'_i] \gg [Al'_{Mo}]$, $[S'_{Mo}] = [h^{\bullet}]$, which corresponds to the defect situation for pure MoS_{2+y}; in other words the native (intrinsic) defect equilibrium in the sulfide is not affected:

$$[S'_i] = [h^{\bullet}] = K^{1/2} p_{S_2}^{1/4} \tag{8.16}$$

where K is the defect equilibrium constant for the sulfidation quasi-chemical reaction of defects formation:

$$\frac{1}{2}S_2 = S'_i + h^{\bullet} \tag{8.17}$$

If $[S'_i] \ll [Al'_{Mo}]$, $[h^{\bullet}] = [Al'_{Mo}]$; in other words the point defect concentration decreases, and the electron hole concentration is fixed by the dissolved amount of aluminum ions. From the simplified form of the electroneutrality condition and the value of K, it results

$$[S'_i] = (K/[Al'_{Mo}]) p_{S_2}^{1/2} \tag{8.18}$$

Under these conditions, a very low point defect concentration in Al-doped MoS_2 increases more rapidly with increasing sulfur pressure than in the case of pure molybdenum disulfide (Eq. 8.16). Thus, similarly to Eq. (8.12), the parabolic rate constant of alloy sulfidation should be the following function of sulfur activity:

$$K_p = \text{const.}\ p_{S_2}^{1/2} \tag{8.19}$$

From Eq. (8.13) it follows also that the effect of dopants depends not only on its concentration but also on sulfur activity. Concentration of native defects increases with increasing sulfur pressure, and consequently at any constant aluminum concentration, both limiting cases of the electroneutrality condition for the doped molybdenum disulfide (MoS_2–Al_2S_3 solid solution) may theoretically be realized by appropriate changes of equilibrium sulfur pressure. At higher sulfur activities, the concentration of dopant may be too low to affect the defect structure of MoS_2. With decreasing sulfur activity, the concentration of point defects in the sulfide decreases, and at sufficiently low sulfur pressure, an extrinsic region may be reached, in which foreign ions determine the electron hole concentration. The lower the dopant concentration, the less sulfur pressure is needed to pass from the intrinsic to the extrinsic region.

A second example is the case of Mn–Cr alloy sulfidation. The predominant defects in manganous sulfide ($Mn_{1-y}S$) are doubly ionized cation vacancies, and, consequently, three-valent foreign ions (for example, chromium) incorporating substitutionally into the cation sublattice of the sulfide will increase the concentration of ionic defects and decrease electronic defects (Mrowec and Grzesik 2002):

$$Cr_2S_3 = 2Cr^{\bullet}_{Mn} + V''_{Mn} + 3S_S \tag{8.20}$$

$$Cr_2S_3 + 2h^{\bullet} = 2Cr^{\bullet}_{Mn} + 2S_S + \frac{1}{2}S_2 \tag{8.21}$$

It follows that the concentration of cation vacancies in chromium-doped $Mn_{1-y}S$ is higher than that in pure manganous sulfide, and the concentration of electron holes is lower. In other words, the growth rate of Cr_2S_3–$Mn_{1-y}S$ solid solution scale on Mn–Cr alloy should be higher than that of $Mn_{1-y}S$ scale on pure manganese metal.

The electroneutrality condition for Cr_2S_3–$Mn_{1-y}S$ solid solution

$$[Cr^{\bullet}_{Mn}] + [h^{\bullet}] = 2[V''_M] \tag{8.22}$$

shows that when $[Cr^{\bullet}_{Mn}] \gg [h^{\bullet}]$, $[Cr^{\bullet}_{Mn}] = 2[V''_M]$, that is, the higher sulfidation rate of Mn–Cr alloy should be pressure independent and the activation energy of this reaction must be lower than that of pure manganese sulfidation. In summary, in the case under discussion, the doping effect was negative. However, doping the same scale ($Mn_{1-y}S$) by monovalent addition (for instance, lithium) may play a positive role. For the growing MnS scale on Mn–Li alloy, the quasi-chemical reversible reactions (Grzesik and Mrowec 2006) are

$$Li_2S + V''_{Mn} = 2Li'_{Mn} + S_S \tag{8.23}$$

$$Li_2S + \frac{1}{2}S_2 = 2Li'_{Mn} + 2h^{\bullet} + 2S_S \tag{8.24}$$

and the electroneutrality condition can be written as

$$[Li'_{Mn}] + 2[V''_M] = [h^{\bullet}] \tag{8.25}$$

Thus, if $[Li'_{Mn}] \gg [V''_M]$, $[Li'_{Mn}] = [h^{\bullet}]$, and the very low concentration of cation vacancies in $Mn_{1-y}S$–Li_2S solid solution, and therefore the sulfidation rate of Mn–Li alloy, would increase much more rapidly with increasing sulfur pressure than that of pure manganese sulfidation. This results from replacing in the equilibrium constant K_v of the defect reaction of pure $Mn_{1-y}S$

$$\frac{1}{2}S_2 = V''_M + 2Li^{\bullet} + S_S \tag{8.26}$$

the electron hole concentration by that of dopant

$$[V''_M] = (K_v/[Li'_{Mn}])\, p_{S_2}^{1/2} \tag{8.27}$$

When $[Li'_{Mn}] \ll [V''_M]$, $2[V''_{Mn}] = [h^\bullet]$, which implies that in this case the rate of sulfidation of such a very diluted Mn–Li alloy should be virtually the same as that of pure manganese sulfidation. It follows that in agreement with Hauffe–Wagner theory (Kofstad 1988; Mrowec 1982), as already discussed for oxidation processes in Section 7.7.2, the protective properties of the sulfide scale on Mn–Li alloy are considerably better than on pure manganese due to the doping effect.

8.6 Questions

8.1 Why are the sulfidation rates of metals much higher than the corresponding oxidation rates?

8.2 How is sulfidation prevented?

8.3 Write the three thermodynamic conditions under which only sulfide, only oxide, and a mixed oxide + sulfide will form.

8.4 How is the behavior of chromia-forming alloys different from that of alumina-forming alloys in a sulfidizing environment?

8.5 What are phase stability diagrams? How can one use them to predict the behavior of metals and alloys in a mixed environment?

8.6 Why does the corrosion behavior of metals and alloys differ in pure SO_2 compared with that in an $SO_2 + O_2$ mixture?

8.7 Why does maximum corrosion occur when the SO_2:O_2 ratio is 2 : 1?

8.8 Why does Ni have the highest corrosion rate at 635 °C, after which the rate goes on decreasing with increase in temperature?

8.9 Comment: Ni-based alloys are best for high temperature sulfidation compared with Co-based and Fe-based alloys.

8.10 Sulfides follow Wagner's model more closely than oxides; explain.

References

Couper, A.S. and Gorman, J.W. (1971). *Mater. Prot. Perform.* 10: 31.

Davin, A. and Coutsouradis, D. (1962). *Cobalt* 17: 23.

Dravnieks, A. (1951). *Ind. Eng. Chem.* 43: 2897.

Foley, R.T., Bolton, M.J., and Morrill, W. (1953). *J. Electrochem. Soc.* 100: 538.

Foroulis, Z.A. (1985). *Anti-Corrosion* 32: 4.

Grzesik, Z. and Mrowec, S. (2006). *Corros. Sci.* 48: 3186.

Gutzeit, J. (1986). *Process Industries Corrosion – The Theory and Practice*. Houston, TX: NACE.

Gutzeit, J., Merrick, R.D., and Scharfstein, L.R. (1987). *Metals Handbook*, Corrosion, 9e, vol. 13, 1262. ASM International.

Hancock, P. (1962). *First International Conference on Metallic Corrosion* (10–15 April 1961), , 193. Butterworth: London.

Hannay, N.B. (ed.) (1959). *Semiconductor Principles*, American Chemical Society Monographs. New York: Reinhold.

Hauffe, K. (1965). *Oxidation of Metals*. New York: Plenum Press.

Hauffe, K. and Rahmel, A. (1952). *Z. Phys. Chem.* 199: 152.

Haycock, E.W. (1959a). *J. Electrochem. Soc.* 106: 764.

Haycock, E.W. (1959b). *J. Electrochem. Soc.* 106: 771.

Hill, V.L. and Black, H.L. (eds.) (1981). *The Properties and Performance of Materials in the Coal Gasification Environments*. Metals Park, OH: American Society for Metals.

Hocking, M.G. and Sidky, P.S. (1987). *Corros. Sci.* 27: 205.

Hocking, M.G. and Vasantasree, V. (1976). *Corros. Sci.* 16: 279.

Howes, H.A.H. (1987). *High Temperature Corrosion in Coal Gasification Systems*, Final Report GRI-8710152. Chicago, IL: Gas Research Institute.

Humphreys, A. and Schaefer, A.O. (1983). *Annual Report 1982*. New York: The Metal Properties Council.

John, R.C., Fort, W.C. III, and Tait, R.A. (1993). *Mater. High Temp.* 11: 124.

Kneeshaw, J.A., Menzies, I.A., and Norton, J.F. (1987). *Werkst. Korros.* 38: 473.

Kofstad, P. (1972). *Nonstoichiometry Diffusion and Electrical Conductivity of Binary Metal Oxides*. New York: Wiley.

Kofstad, P. (1988). *High Temperature Corrosion*. London: Elsevier Applied Science.

Kröger, F.A. (1974). *The Chemistry of Imperfect Crystals*. Amsterdam: North-Holland.

Kubaschewski, O. and Hopkins, H.H. (1962). *Oxidation of Metals and Alloys*. London: Butterworths.

Lai, G.Y. (1985). *J. Met.* (July): 14.

Lichter, B.D. and Wagner, C. (1960). *J. Electrochem. Soc.* 107: 168.

Meussner, R.A. and Birchenall, C.E. (1957). *Corrosion* 13: 677t.

Mrowec, S. (1980). *Defects and Diffusion in Solids*. Amsterdam: Elsevier.

Mrowec, S. (1982). *An Introduction to the Theory of Metal Oxidation*. Washington, DC: National Bureau of Standards and National Science Foundation.

Mrowec, S. (2003). *High Temp. Mater. Processes* 22: 1.

Mrowec, S. and Grzesik, Z. (2002). *Bull. Pol. Acad. Sci., Chem.* 50: 37.

Mrowec, S. and Przybylski, K. (1984). *High Temp. Mater. Processes* 6: 1.

Mrowec, S., Werber, T., and Zastawnik, M. (1966). *Corros. Sci.* 6: 47.

Natesan, K. (1983). *High Temperature Corrosion* (ed. R.A. Rapp), 336. Houston, TX: NACE.

Natesan, K. (1993). *Mater. High Temp.* 11: 36.

Norton, J.F. (ed.) (1984). *High Temperature Materials Corrosion in Coal Gasification Atmospheres*. Amsterdam: Elsevier.

Perkins, R.A. (1980). Sulfidation of high temperature alloys, In: *Environmental Degradation of High Temperature Materials*, Series 3, vol. 2 (No. 13), p. 5. London, UK: Institution of Metallurgists.

Rapp, R.A. (ed.) (1981). *High Temperature Corrosion*. Houston, TX: NACE.

Rau, H. (1980). *J. Phys. Chem. Solids* 41: 765.

Rothman, M.F. (ed.) (1985). *High Temperature Corrosion in Energy Systems*. The Metallurgical Society of AIME.

Setterlund, R.B. and Prescott, G.R. (1961). *Corrosion* 17: 277t.

Sidky, P.S. and Hocking, M.G. (1987). *Corros. Sci.* 27: 183.

Sorell, G., Humphries, M.J., Bullock, E., and Van de Voorde, M. (1986). *Int. Met. Rev.* 31: 216.

Spauschus, H.O., Hardt, R.W., and Foley, R.T. (1954). *J. Electrochem. Soc.* 101: 6.

Strafford, K.N., Datta, P.K., Hampton, A.F., and Mistry, P. (1989). *Corros. Sci.* 29: 673.

Stringer, J. (1986). *Corrosion/86*, Paper No. 90. Houston, TX: NACE International.

Vasantasree, V. and Hocking, M.G. (1976). *Corros. Sci.* 16: 261.

Verma, S.K. (1985). *Corrosion/85*, Paper No. 336. Houston, TX: NACE International.

Wagner, C. (1933a). *Z. Phys. Chem.* B21: 25.

Wagner, C. (1933b). *Z. Phys. Chem.* B32: 195.

Wagner, C. (1951). *Atom Movements*, 153. Cleveland, OH: American Society for Metals.
Wagner, C. (1953). *J. Chem. Phys.* 21: 1819.
Wagner, J.B. and Wagner, C. (1957). *J. Chem. Phys.* 26: 1602.
Wehefritz, V. (1960). *Z. Phys. Chem.* 26: 22.
Yates, D.H., Ganesan, P., and Smith, G.D. (1994). *Advanced Materials and Coatings for Combustion Turbines Conference Proceedings* (ed. V.P. Swaminathan and N.S. Cheruvu), 89. Materials Park, OH: ASM International.
Young, D.J. (1980). *Rev. High Temp. Mater.* 4: 299.

Further Reading

Bar-Cohen, Y. (2014). *High Temperature Materials and Mechanisms*. Boca Raton, FL: CRC Press.
ChemSage (1998). Version 4.16, Aachen, Germany: GTT-Technologies.
Jiang, S. and Wagner, J.B. Jr. (1995). *J. Phys. Chem. Solids* 56: 1101.
Khanna, A.S. (ed.) (2016). *High Temperature Corrosion*. Hackensack, NJ: World Scientific Publishing Company.
Kleinert, H. (1989). *Gauge Fields in Condensed Matter*, Stresses and Defects, vol. II, 743–1456. Singapore: World Scientific.
McNallan, M., Opila, E., Maruyama, T., and Narita, T. (eds.) (2000). *High Temperature Corrosion and Materials Chemistry, Proceedings*, vol. 99–38. Pennington, NJ: The Electrochemical Society.
Newkirk, J.B. (ed.) (1980). *High Temperature Materials*. Tel Aviv: Freund Publishing House.
Norton, J.F. (ed.) (1984). *High Temperature Materials Corrosion in Coal Gasification Atmospheres*. Amsterdam: Elsevier.
Revie, R.W. (ed.) (2011). *Uhlig's Corrosion Handbook*, 3rde. Hoboken, NJ: Wiley.
Saito, Y., Onai, B., and Maruyama, T. (eds.) (1991). *High Temperature Corrosion of Advanced Materials and Protective Coatings*. London: North Holland.
Schmalzried, H. (1991). *Solid-State Reactions*. Weinheim: Verlag Chemie.
Schmalzried, H. (1995). *Chemical Kinetics of Solids*. Weinheim: Wiley-VCH.
Schroeder, M. and Martin, M. (1998). *Z. Phys. Chem.* 207: 1.
Schütze, M. (ed.) (2000). *Corrosion and Environmental Degradation*, vol. II. Weinheim: Wiley-VCH.
Schütze, M. and Quadakkers, W. (eds.) (2008). *Novel Approaches to Improving High Temperature Corrosion Resistance*, EFC 47. . London: Woodhead Publishing.
Wolf, D. and Yip, S. (eds.) (1992). *Materials Interfaces. Atomic-Level Structure and Properties*. London: Chapman & Hall.
Young, D.J. (2008). *High Temperature Oxidation and Corrosion of Metals*. Amsterdam: Elsevier.

Chapter 9

Carburization and Metal Dusting

9.1 Introduction

Metals and alloys are susceptible to *carburization* when exposed to an environment containing CO, or CH_4 or other hydrocarbon gases, such as ethane (C_2H_6), propane (C_3H_8), and so forth, at elevated temperatures. Carburization involves the formation of internal carbide precipitates. Severe carburization occurs in the cracking tubes used in ethylene and other olefin plants, in the heat treatment of components associated with carburizing furnaces (e.g. baskets, trays, retorts, and fans), and for reformer tubes used in the steam reforming of natural gas. Furnace equipment and many other components repeatedly subjected to carburizing environments at 850–950 °C frequently suffer brittle failures as a result of carburization attack. Examples of studies and reviews of material carburization have been presented by Catlow and Mackrodt (1987), Grabke and Wolf (1987), Kane and Cayard (1995), and Rahmel et al. (1998).

Metal dusting (MD) is a catastrophic carburization that occurs at temperatures of 430–900 °C when a process gas stream consists of primarily H_2, CO, and CO_2 along with some hydrocarbons with high carbon potentials ($a_C > 1$). Metals or alloys can suffer rapid metal wastage in a form of *pitting* or general thinning of the cross-sectional thickness of a metallic component. Materials failures associated with MD have been encountered in refining and petrochemical processing, such as production of syngas in hydrogen, ammonia, nitric acid, and methanol plants, plants producing iron ores, heat treating, and other industrial processes (Lai 2007). Relevant aspects of MD have been reviewed by Hochman (1977), Grabke (1998a,b, 2003), and more recently by Nishiyama et al. (2006).

9.2 Carburization

Whether an alloy is likely to be carburized or decarburized depends on the carbon activity (a_C) in the environment and that of the alloy. The thermodynamic condition dictates either carburization, $a_{C\ environment} > a_{C\ metal}$, or decarburization, $a_{C\ environment} < a_{C\ metal}$. Thus one needs to know the carbon activities of both the environment and the alloy.

Carburization can proceed by one of the following reactions when the environment contains CH_4, CO, or H_2 and CO:

$$CO + H_2 = C + H_2O \tag{9.1}$$

$$2CO = C + CO_2 \tag{9.2}$$

$$CH_4 = C + 2H_2 \tag{9.3}$$

Assuming that carburization follows Reaction (9.1), the carbon activity in the environment can be calculated by

$$a_C = \exp(-\Delta G^\circ/RT) \cdot (p_{CO} \quad p_{H_2}/p_{H_2O}) \tag{9.4}$$

Similarly, if carburization follows Reaction (9.2), known as *Boudouard reaction*, the carbon activity of the environment can also be calculated:

$$a_C = \exp(-\Delta G^\circ/RT) \cdot \left(p_{CO}^2/p_{CO_2}\right) \tag{9.5}$$

When carburization follows Reaction (9.3), the carbon activity in the environment is

$$a_C = \exp(-\Delta G^\circ/RT) \cdot \left(p_{CH_4}/p_{H_2}^2\right) \tag{9.6}$$

Data for carbon activities of commercial alloys at temperatures below 1200 °C are relatively limited. Natesan (1976) reported that a_C for 2.25Cr–1Mo steel is in the range of 1×10^{-1} to 10^{-2} from 550 to 750 °C. Natesan and Kassner (1973) reported the carbon activities of Fe–18Cr–8Ni alloys.

For carbon steels, carbon activity can be estimated by assuming that it is in equilibrium with cementite (Fe_3C):

$$3Fe + C = Fe_3C \tag{9.7}$$

$$a_C = \exp(-\Delta G^\circ/RT) \text{ (assuming } a_{Fe_3C} = a_{Fe} = 1) \tag{9.8}$$

Environments containing gas mixtures such as CO/CO_2 or H_2/H_2O are very significant in terms of

High Temperature Corrosion: Fundamentals and Engineering, First Edition. César A. C. Sequeira.
© 2019 John Wiley & Sons, Inc. Published 2019 by John Wiley & Sons, Inc.

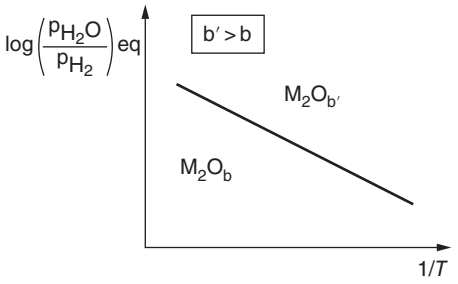


Figure 9.1 Stability domains of M_2O_b and $M_2O_{b'}$ in a H_2/H_2O gas mixture.

carburization/oxidation phenomena. Let us, for example, consider the following reaction:

$$M_2O_b + (b' - b)\,H_2O = M_2O_{b'} + (b' - b)\,H_2 \qquad (9.9)$$

The variance of the equilibrium is equal to 2 in this case of condensed phases without miscibility since there are three independent components and three phases in equilibrium. At equilibrium, we have

$$\begin{aligned}\Delta G^\circ &= -(b' - b)RT \ln (p_{H_2}/p_{H_2O}) \\ &= -(b' - b)RT \ln (N_{H_2}/N_{H_2O}) \end{aligned} \qquad (9.10)$$

where N_{H_2} and N_{H_2O} are the mole fractions of hydrogen and water vapor in the gas mixture, respectively. Assuming that the activities of the condensed phases are unity and that the gases show ideal behavior, ΔG° is independent of the total pressure p, and the gas composition is a function of temperature only. Under these conditions, the equilibrium is considered as pseudo-invariant.

The stability domains of the condensed phases are represented in N_{H_2} (or N_{H_2O}) versus f(T) plots (*Chaudron diagram*) or as $\log p_{H_2}/p_{H_2O}$ (or $\log p_{CO}/p_{CO_2}$) versus $1/T$. In effect, Eq. (9.10) can be written as

$$\log \frac{p_{H_2O}}{p_{H_2}} = [2.3R(b' - b)]^{-1} \cdot [(\Delta H^\circ/T) - \Delta S^\circ] \qquad (9.11)$$

Assuming that ΔH° and ΔS° are independent of temperature, $\log p_{H_2O}/p_{H_2}$ is a linear function of $1/T$, as represented in Figure 9.1. The straight line marks the boundary between the stability domains of each oxide, i.e. M_2O_b and $M_2O_{b'}$.

If several oxides of the same metal can be formed, it is necessary to proceed in the same way as described in Chapter 3 for the case of equilibrium with a simple gas.

The stability domains of iron and iron oxides, i.e. FeO, Fe_2O_3, and Fe_3O_4, as functions of gas composition and temperature are represented in Figures 9.2 and 9.3. Figure 9.2 corresponds to a Chaudron diagram and Figure 9.3 to the plot of $\log p_{H_2O}/p_{H_2}$ or $\log p_{CO_2}/p_{CO}$ versus $1/T$.

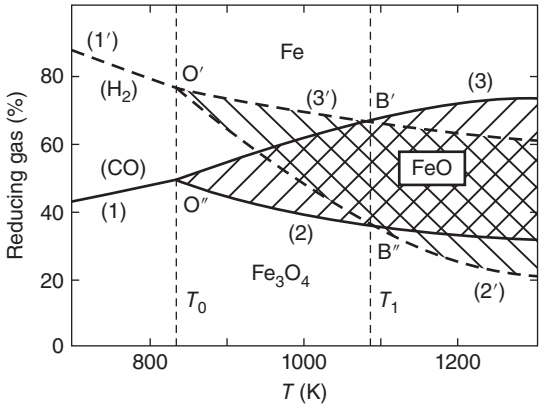


Figure 9.2 Stability domains of iron and iron oxides as functions of temperature and gas composition according to the Chaudron diagram (CO/CO_2 and H_2/H_2O mixtures). The hatched areas indicate the stability domains of FeO according to the gas mixture, i.e. CO/CO_2 or H_2/H_2O (COACH data bank 2002).

Note that both diagrams exhibit a triple point, $T_0 = 830\,K$, O', and O'', respectively, in Figure 9.3, corresponding to a pseudo-invariant system, insofar as the pressure is not a factor in the equilibrium since there are three independent components and four phases. Also note that B' and B'' in Figure 9.2 (intersection of, respectively, the curves (2) and (2′) and (3) and (3′)) correspond to the inversion temperature of the following equilibrium:

$$CO + H_2O = CO_2 + H_2 \qquad (9.12)$$

that is, $T_1 = 1100\,K$. Moreover, for $T < 1100\,K$, CO is more reducing than hydrogen, whereas the reverse applies for $T > 1100\,K$.

A more general treatment of high temperature equilibria for oxidation, and carburization or decarburization of iron or steel, requires the consideration of the equilibria H_2O/H_2, CO_2/CO, and CH_4/H_2. Therefore, the reactions chiefly responsible for this corrosion at high temperature are

$$Fe + H_2O = FeO + H_2 \qquad K_{13} = p_{H_2}/p_{H_2O} \qquad (9.13)$$

$$Fe + CO_2 = FeO + CO \qquad K_{14} = p_{CO}/p_{CO_2} \qquad (9.14)$$

$$Fe_3C + CO_2 = 3Fe + 2CO \qquad K_{15} = p_{CO}^2/p_{CO_2} \qquad (9.15)$$

$$3Fe + CH_4 = Fe_3C + 2H_2 \qquad K_{16} = p_{H_2}^2/p_{CH_4} \qquad (9.16)$$

The data presented in Figures 9.4–9.6 show the variation with temperature of the equilibrium constant for each of the four Reactions (9.13)–(9.16).

The constants are given in terms of the partial pressure of each gas, that is, the total pressure multiplied by the volume fraction (not weight percentage) of the gas in question. For example, in a gas mixture containing 45% CO, 15% CO_2, and 40% N_2 at a total pressure of 1 atm, the partial pressure of CO is 0.45, and that of CO_2 is 0.15.

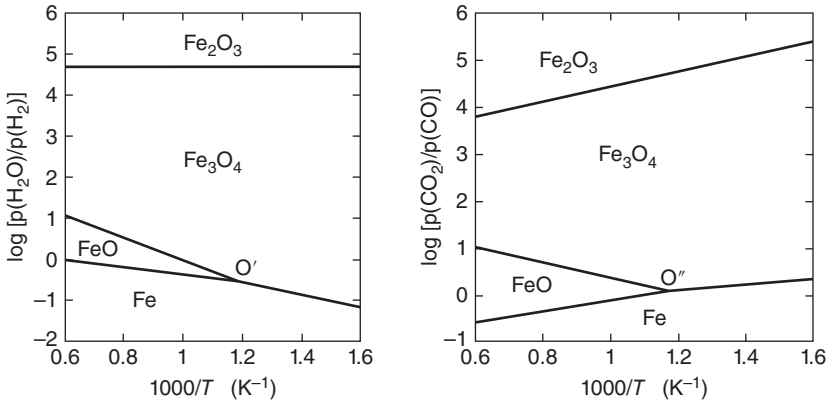


Figure 9.3 Stability data domains of iron and iron oxides as functions of temperature and of the p_{H_2O}/p_{H_2} ratio or of the p_{CO_2}/p_{CO} ratio (COACH data bank 2002).

The curves presented in the several figures enable one to predict the way in which a mixture containing CO and CO_2 or H_2 and H_2O tends to react with iron or iron oxide. (They do not indicate the rate at which this tendency may be followed.) As an illustration, for the gas mixture described above, the pCO/pCO_2 ratio is 0.45/0.15 or 3. Figure 9.4 shows that this ratio is equal to the equilibrium constant at 1130 °C; hence at this temperature this mixture is inert to iron or iron oxide, at higher temperature it cannot reduce iron oxide and tends to oxidize iron, and at a lower temperature it tends to reduce iron oxide and cannot oxidize iron.

To ascertain whether this mixture tends to carburize or to decarburize steel at 800 °C, the value of the equilibrium constant for Reaction (9.3) is computed; it is $p^2CO/pCO_2 = (0.45)^2/0.15 = 1.35$. Figure 9.5 shows that at 800 °C this gas is decarburizing toward steel of any carbon content. A ratio of 6 instead of 1.35 would indicate (see Figure 9.5) that at 800 °C the gas mixture tends to decarburize steel containing less than 0.8% carbon and to carburize steel containing a higher concentration of carbon.

The use of these charts for mixtures of hydrogen and methane (Figure 9.6) is analogous to that for carbon monoxide and carbon dioxide.

Note that at high temperatures the oxide that first forms is FeO, and if the partial pressure of oxygen is low, this is the only oxide that forms. At somewhat higher oxygen pressures, a layer of Fe_3O_4 forms on the top of FeO, and at still higher pressures, a layer of Fe_2O_3 forms over Fe_3O_4.

Below about 600 °C, FeO is unstable and decomposes into iron and Fe_3O_4 so that high temperature scales on iron examined at room temperature show only iron, Fe_3O_4, and possibly Fe_2O_3.

Even though in cases where the gas mixture may not reach an equilibrium condition, it will be of great benefit to better understand the gas–metal reaction in terms of thermodynamic equilibrium in multicomponent gas environments. The thermodynamic equilibrium gaseous composition along with its thermodynamic potentials, such as carbon activity, a_C, oxygen potential, p_{O_2}, hydrogen potential, p_{H_2}, methane potential, p_{CH_4}, and other potentials, can be determined using a commercial software program such as HSC Chemistry for Windows (HSC 2006, Finland), ChemSage/FactSage (GTT 2015, Germany), and Gemini (Thermodata 2002, France).

The environment is also being characterized in terms of a_C, and $p_{O_2}, p_{H_2S}, p_{H_2}$, etc., and in complex gas mixtures such as H_2–CH_4–H_2S, H_2–CO–H_2O–H_2S, as well as reported in the open literature (Barralis and Maeder 1997; Christ 1998; Coltters 1985; Forseth and Kofstad 1998; Grabke 1998a,b, Jakobi and Gommans 2003; Nishiyama et al. 2003; Rocabois et al. 1996; Yazawa 1979).

As reported above, carburization depends on the carbon activity in the environment and that of the alloy. The phenomenon refers to ingress of carbon into the material in the presence of carbonaceous gases such as CO, CO_2, CH_4, and other hydrocarbons. Carbon is transferred to the material surface, diffuses through it, and forms various carbides with the alloying elements. Usually, it happens at $T > 800$ °C and $a_C < 1$. Apart from carbon inward diffusion and carbide precipitation, MD is also observed for lower temperatures and greater a_C ($a_C > 1$). But, during metallic carburization, other effects may occur, namely, discontinuous precipitation, microcrack formation, and volume expansion, as will be discussed next.

The growth of discontinuously precipitated carbides was described by Cahn (1959) and Hillert (1969) during the 1950–1960s. Many solid-state reactions such as eutectoid transformations like pearlite formation and discontinuous precipitation result in a lamellar structure. In the case of discontinuously precipitated carbide in austenite, Cr diffusion occurs in the austenite/austenite grain boundary as the boundary of the growing cell moves through the supersaturated austenite. In the alloy 602CA (alloy type NiFeCrAl), a fine substructure of carbides (probably M_7C_3) and a new Ni-enriched, Cr-depleted austenite were formed from the carbon-saturated austenite.

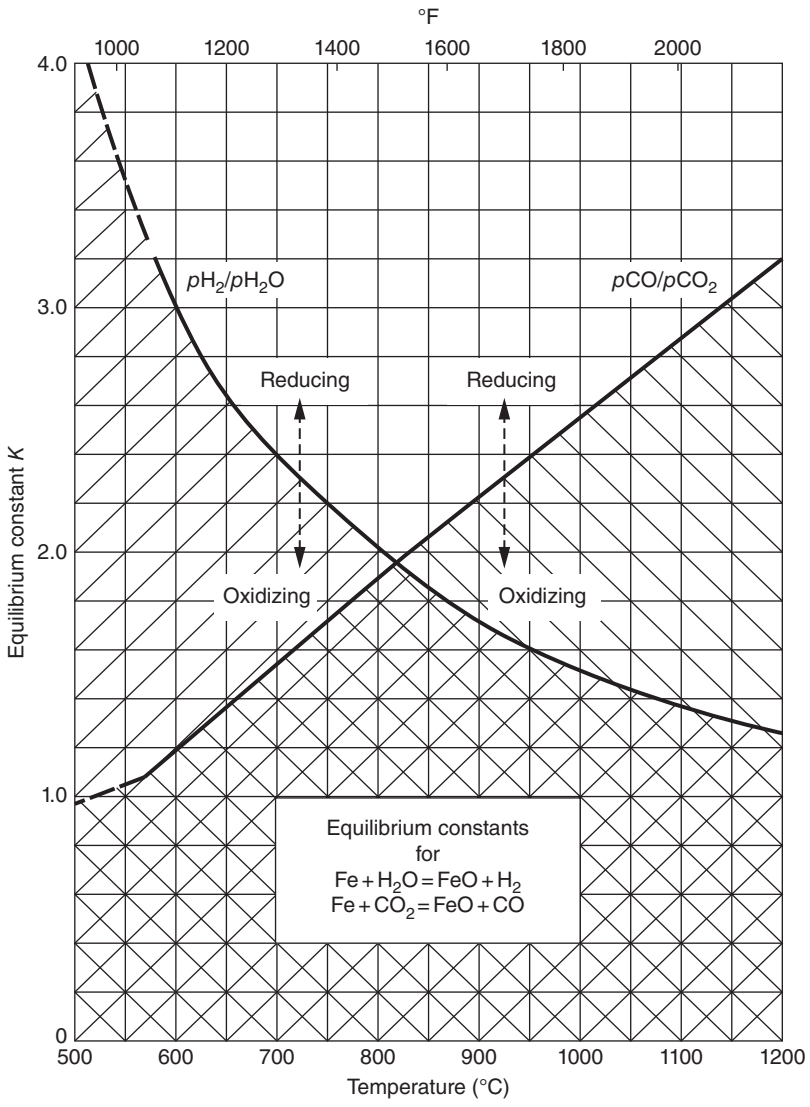


Figure 9.4 Chart illustrating the variation with temperature of the equilibrium constant for the reaction between iron and water vapor or carbon dioxide.

The carbon supersaturation decreases discontinuously as the carburized austenite/newly formed austenite cell boundary advances. The carburization thus constitutes the driving force for the phase transformation, which occurs by a discontinuous cooperative growth of carbide and Cr- and C-depleted austenite. This type of reaction represents a fast precipitation process at lower temperatures where bulk diffusion is slow. It has been suggested that the force, actually pulling the cellular boundary of discontinuous precipitation, is the difference in atomic size, which gives rise to strain energy in the concentration gradient ahead of the growing new austenite grain. This mechanism was originally proposed by Sulonen (1994).

Two different morphologies of the discontinuously precipitated carbides were also detected in AISI 304L as well as in nanosized carbon filament formation during MD of stainless steel (Lin and Tsai 2003; Szakálos et al. 2002).

In the case of the alloy 602CA, the cellular growth rate of discontinuous precipitated carbides means that the advancement of the cellular boundary is governed by the rate at which a sufficient amount of Cr can move to the carbide phase via the cellular boundary.

Every Ni atom has a short diffusion distance between the carburized bulk (old austenite) and the newly formed low-alloyed austenite, while Cr has orders of magnitude longer diffusion distances toward the nearest Cr carbide. This means that the average Ni atom has a very short dwell time, and, as a consequence, the average Cr fraction in the boundary could be much higher than the bulk fraction of 0.25. The cellular growth in this case is characterized by a small fraction of discontinuous precipitates, and both the new phases formed are close to equilibrium, i.e. the Cr-diffusion process, and, subsequently, the Cr-carbide formation, is almost accomplished.

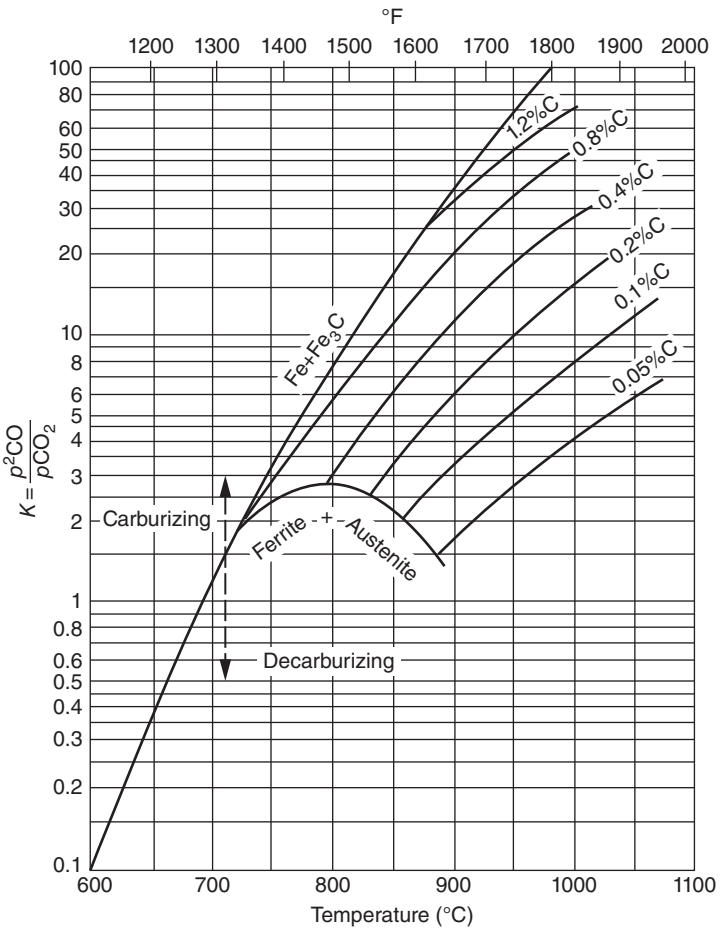


Figure 9.5 Equilibrium constants for the reaction $Fe_3C + CO_2 = 3Fe + 2CO$ as a function of temperature and carbon content.

It is possible to estimate the cellular growth rate based on diffusion limitations. It is assumed that the cellular boundary can move forward in steps of the boundary thickness and before it moves forward, all metal transport needed to reach equilibrium must be accomplished. Consider a segment of the cellular boundary, with S the lamellar spacing in the cellular structure and $S/2$ the characteristic diffusion distance.

Using an approximation of Fick's first law, we can write

$$\Delta m/\Delta t = \delta\, D_{GB}/LA\rho\, \Delta C_{Cr}/\Delta x \qquad (9.17)$$

where Δm is the amount of Cr metal in the segment that diffuses and forms carbide $\Delta x(S/2)$ is the diffusion length, Δt is the time for one segment of cellular growth ΔC_{Cr} $(2X_{Cr})$ is the Cr content in the cellular boundary, which may be much higher than the bulk content (X_{Cr}) (and the difference in Cr concentration toward the carbide may therefore be estimated as $\Delta C_{Cr} = 2X_{Cr}$) A is the diffusion cross-sectional area or $A = \delta$ per unit length ρ is the density of the diffused metal, i.e. Cr $\delta\ D_{GB}$ is the effective grain boundary diffusion coefficient of the Cr atoms with $LA\rho$ as a characteristic size of the structure, in this case $L = \delta$, which is the cellular boundary thickness or segment thickness.

The growth increment or movement of the cellular boundary is set to the grain boundary thickness, δ, and thus the diffusion-controlled velocity of the cellular boundary v_1 may be written as

$$v = \delta/\Delta t = 8\delta\, D_{GB}/S^2 \qquad (9.18)$$

Using the model for cellular growth proposed by Hillert (1969), it gives the maximum growth rate:

$$v' = 16\delta\, D_{GB}/S^2 \qquad (9.19)$$

The constant 16 in Eq. (9.19) is directly comparable with the constant 8 in Eq. (9.18). This means that Hillert's model predicts two times faster growth rate of the discontinuously precipitated carbide structure. This implies that the MD corrosion rate could be much higher if the atmosphere was more aggressive, i.e. with higher carbon activity. The cellular structure is thus of vital importance and facilitates the relatively fast MD kinetics at lower temperatures.

Carburization during MD conditions may result in low ductility and microcracks, which form flat metal fragments on the surface in different sizes up to 200 μm × 60 μm × 10 μm, where 10 μm represents the typical crack depth. Crack configuration suggests

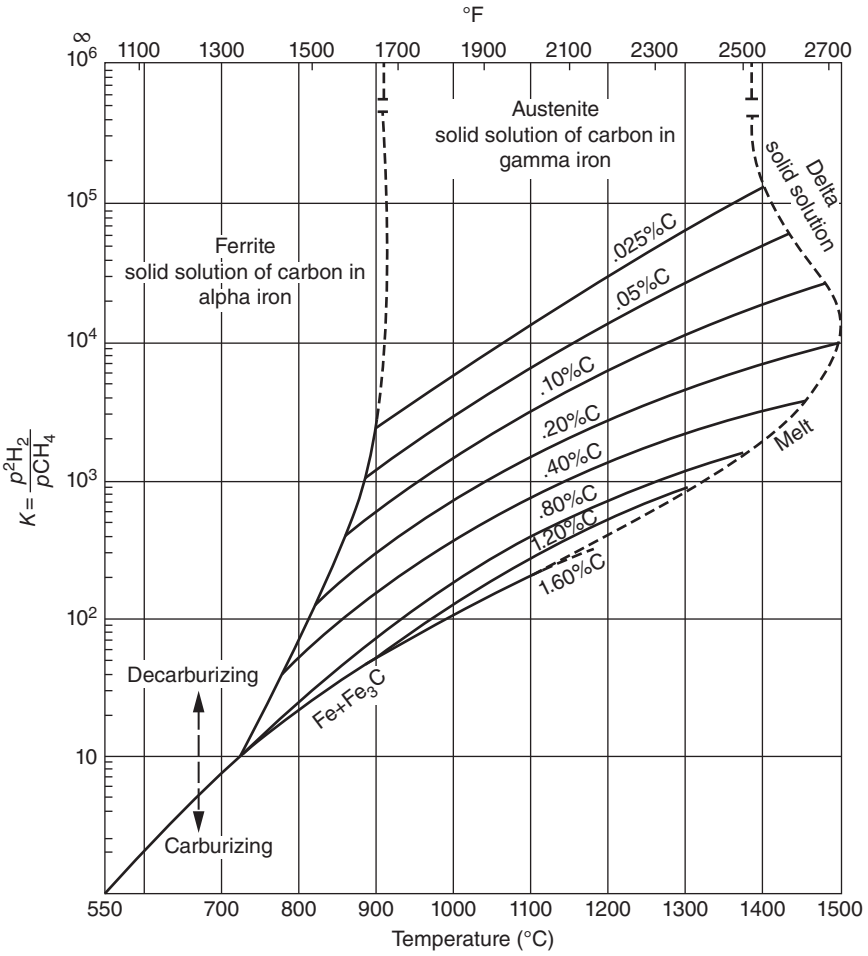


Figure 9.6 Equilibrium constants for the reaction $3Fe + CH_4 = Fe_3C + 2H_2$ as a function of temperature and carbon content.

that the carburized surface metal developed compressive stresses, which could result in shear cracks parallel to the surface, favored by a ductility drop. Distribution of the microcracks all over the carburized surface, revealing the crack propagation path through the carbide network, shows that general surface carburization can be simultaneously involved with oxidation and microcrack formation, as revealed by cross sections of 602CA at 540 °C.

Carburization gives rise to compressive stresses due to volume expansion (Schnaas and Grabke 1978), but at higher temperatures, such as 650 °C, stress relaxation may take place fast enough to avoid crack formation. An additional effect may be that microcracks form during cooling because of different thermal expansion in the carburized layer and the bulk. If the uncarburized bulk "shrinks" somewhat more during cooling than the carburized surface layer, the result would be cracks parallel to the surface.

The microcrack formation during cooling may explain the surprisingly low metal attack resistance for 602CA during cyclic conditions as pointed out by Toh et al. (2003).

Several phases such as oxides and carbides, which will form in an AISI 304L steel during metal carburization/dusting conditions, give rise to a substantial volume expansion. This may contribute to the rather rapid degradation process that characterizes the metal aggression phenomenon. Some possible phases and calculated volume expansions, when formed in the steel matrix, are given in Table 9.1. These *extended Pilling–Bedworth ratios* (EPBR) for different phases are based on density changes for the metal during phase transformation. The phase stability conditions are calculated with Thermo-Calc.

The EPBR are calculated by virtual volume expansion or density change of the metal component during phase transformation, i.e. if C, O, or N had zero mass:

$$\text{E.PBR} = \frac{\rho_{304}}{\rho_{\text{Phase}'}} = \frac{\rho_{304}}{\rho_{\text{Phase}} - \rho_{\text{Phase}}\left(\frac{m_i}{m_{\text{me}}+m_i}\right)} = \frac{\rho_{304}(m_{\text{me}} + m_i)}{\rho_{\text{Phase}} m_{\text{me}}} \tag{9.20}$$

where ρ_{304} is the density of the AISI 304L steel; ρ_{Phase} the density of the phase formed in the steel; $\rho_{\text{Phase}'} = \rho_{\text{Phase}}$

Table 9.1 Possible phases formed in AISI 304L at 650 °C during carburization and metal dusting conditions and calculated volume expansion

Phase formed in the steel matrix	Phase stability conditions regarding carbon and/or oxygen content	Phase density ($g\,cm^{-3}$)	Calculated volume expansion when the phase is formed in a AISI 304L steel, EPBR
Reference (304L)		7.9	1.00
304 + 1 at.% C		7.9	1.0087[a]
$M_{23}C_6$	≤2.3 wt% C	6.97	1.20
M_7C_3	≥1.2 wt% C	6.9	1.25
Graphite	≥3.5 wt% C ($a_c \geq 1$)	2.26	∞ or 1.06[b]
$(Fe,Cr)_3C$	$a_c \geq 2.1$	7.66	1.11
Ni_3C	$a_c \geq 39$	7.96	1.06
Cr_3C_2	$a_c \geq 600$	6.68	1.35
Cr_2O_3	$10^{-31} \leq pO_2 \leq 10^{-28}$ ($a_c \leq 1800$)	5.21	2.17
$(Cr_2Fe)O_4$	$pO_2 \geq 10^{-28}$ ($a_c \leq 190$)	4.8	2.28
FeO	$pO_2 \approx 10^{-23}$ ($a_c \leq 2.1$)	5.7	1.79
NiO	$pO_2 \geq 10^{-18}$ ($a_c \leq 39$)	6.67	1.53
$(Fe_2Ni)O_4$	$pO_2 \geq 10^{-22}$ ($a_c \leq 10^{16}$)	5	2.19
Cr_2N	≤1.8 wt% C	6.8	1.31
CrN	≥1.8 wt% C	6	1.65

[a]Lattice spacings and structures of metals and alloys (Pearson 1958).

[b]When related to M_7C_3.

with reduction of the mass contribution of the element C, N, or O; $m_i = n_i M_i$ = (number of C, O, or N atoms in the empirical phase formula) × (molar weight); and $m_{me} = n_{me} M_{me}$ = (number of metal atoms in the empirical phase formula) × (molar weight).

Once formed, chromia or spinel oxide is very stable even at extremely high carbon activities, as seen in Table 9.1. As the carbide content in the different phases grows, volume expansion becomes visible. It is obvious that these volume expansions will create stresses and finally eject the corrosion products, which most likely accelerate the metal corrosion process. An especially detrimental "grain pick out" process occurs when the grain boundaries are selectively attacked and complete grains are ejected as observed by de Bruyn et al. (2001) in reformer plants at 540 °C. This effect was also observed at higher temperatures as "green rot" by Dovey and Jenkins (1950) (see Section 1.5.11).

9.3 Alloy Resistance to Carburization

Carburization attack generally results in the formation of internal carbides in the alloy matrix as well as at grain boundaries. The measurement of the carbon concentration profile as a function of distance from the metal surface is an excellent method for characterizing the carburized alloy, but it will be certainly beneficial to use as many evaluation methods (gravimetric, metallographic, etc.) as possible for characterizing the carburized alloys.

Figure 9.7 illustrates three possible carbon concentration profiles to analyze the impact of carburization on an alloy's performance (Krikke et al. 1976). Krikke et al. considered profile A with a steep concentration profile to be the most damaging. Further analysis showed that for carburization, the real issue is the effect of carburization on the alloy's mechanical properties, such as creep-rupture properties and toughness or ductility, but for making an informed material selection, it is necessary to review and analyze the carburization data in terms of mass gain, mass carbon absorption, carburization depth, and concentration profile of the carburized layer (Klower and Heubner 1998). When the environment is such that no protective oxide scale (e.g. Cr_2O_3 scale) is formed on the metal surface, carburization is controlled by diffusivity and solubility, carbon permeation through the oxide layer being possible only if the layer contains pores and fissures (Wolf and Grabke 1985). Pyrolysis furnace tubes typically constructed of Fe–Cr–Ni cast alloys, such as HK (Fe–25Cr–20Ni or 25/20) and HP (Fe–25Cr–35Ni or 25/35), show improved carburization resistance as well as creep-rupture strengths when modified with additions of Nb, W, Mo, Si, Ti, Ni, or Cr (*microalloyed castings*) (Hall et al. 1985).

Fe–Ni–Cr alloys, including commercial and experimental alloys, were tested at Petten laboratories, at fixed carbon activities (a_C of 0.3 and 0.8) and spread temperatures (825–1050 °C), with various additions of Si,

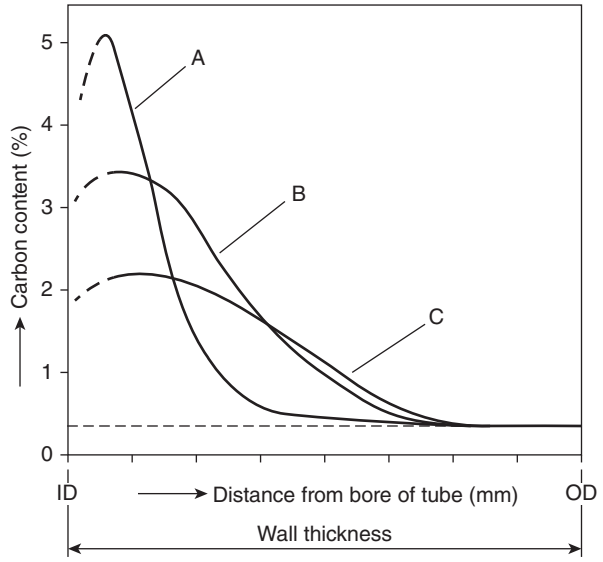


Figure 9.7 Three possible carbon concentration profiles of carburized alloys (Krikke et al. 1976).

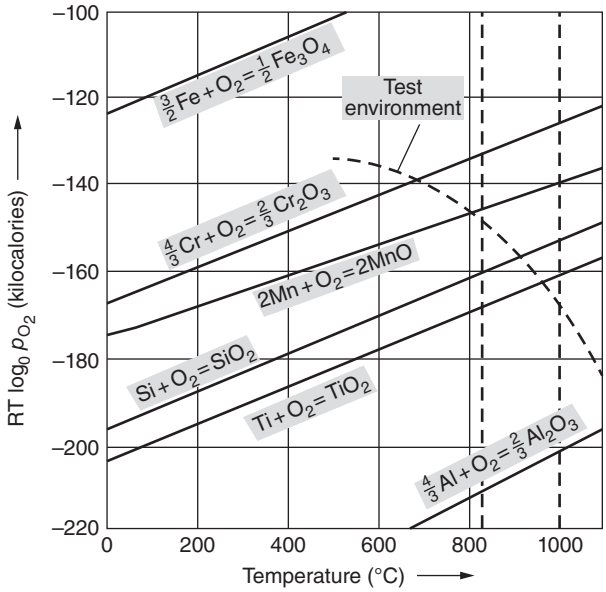


Figure 9.8 Oxygen potentials of the test environments used in carburization studies at Petten laboratories (Harrison et al. 1979).

Nb, Cr, and Fe and various oxygen potentials (Harrison et al. 1979). The oxygen potentials of the test environment were below that in equilibrium with Cr_2O_3 (Figure 9.8), that is, no chromium oxide scales should have formed on the metal surface. The test results at 825 °C showed that type 314 stainless steel (2.04% Si) was significantly more carburization resistant than HK-40 (1.35% Si), HP-40 Nb (1.29% Si), and 800H (0.4% Si). The beneficial effect of Si on carburization resistance was clearly demonstrated. Both chromium and iron are carbide formers, constituting the major elements in M_7C_3 and $M_{23}C_6$ carbides resulting from carburization. Nickel reduces the diffusivity of carbon in Fe–Ni–Cr alloys and also decreases the solubility of carbon in Fe–Ni alloy system. Bose and Grabke (1978) observed that increasing nickel improved carburization resistance in Fe–Ni–Cr alloys, with the maximum resistance achieved when the ratio of Ni to Fe was 4 : 1. This is in general agreement with the product of carbon solubility and diffusivity. High nickel alloys are generally more resistant to carburization than Fe–Ni–Cr alloys.

Small additions of some minor elements, such as Ti, Nb, W, and rare earth elements, may also improve an alloy's resistance to carburization in test environments of H_2–8.6% CH_4–7% H_2O and H_2–12% CH_4–10% H_2O (Khandros et al. 1984). The superior carburization resistance of TMA 4750 alloy (0.50C–0.70Mn–1.84Si–25.1Cr–38.4Ni–0.13Ti–0.28Nb–0.27W-REM, this denoting rare earth metals) to HK-40 2.0% Si (0.41C–0.60Mn–1.98Si–25.0Cr–20.7Ni) can be attributed to small additions of Ti, Nb, W, and REMs. In both test environments, the oxygen potentials are believed to be high enough to form oxide scales. Thus, improvements in carburization resistance may be partly due to the improved oxide scale.

Ando et al. (1989) concluded that a critical concentration of c. 2.7 Al in Fe–Al alloys is required for good carburization resistance at 930 °C. They suggested that an incomplete and/or non-protective Al_2O_3 film forms at aluminum concentrations below this critical value. A drawback to the use of wrought alumina formers such as 214 and 602CA is their relatively poor creep strength at the higher operating temperatures when carburization is often a problem ($T > 950$ °C). Despite this, these alloys can be used effectively in carburizing applications involving lower temperatures and/or lower stresses.

Adjusting the composition of the process environment can also reduce the rate of carburization attack. For instance, injection of steam into the environment reduces the carbon activity and increases the tendency for oxide formation. Alternatively, carburization attack in the absence of oxide-barrier formation can be reduced by introducing very small amounts of sulfur or sulfur compounds into the environment (Grabke et al. 1977); the sulfur blocks the transfer of carbon into the steel. Sulfur levels higher than 1.4×10^{-10} atm at 1000 °C reduce the extent of carburization, but overall corrosion increases because of the growth of sulfide scales (Corish et al. 1987; Rahmel et al. 1998). In general, the solubility of carbon in nickel alloys is low; therefore, the choice of nickel alloys to resist carburizing environments is widespread. However, heat-resistant alloys invariably contain many alloying elements such as chromium, aluminum, silicon, and so on. Carburization thus always leads to the formation of various chromium carbides. Nickel alloys are protected from carburization by stable oxide scales. Whether an alloy will undergo oxidation or carburization in a gas mixture at

a given temperature is determined by the partial pressure of oxygen (oxygen potential) and the carbon activity at that temperature.

At higher temperatures, typically greater than 1050 °C, oxide scales are stable in the following order: $Al_2O_3 > SiO_2 > Cr_2O_3$.

For service below 1050 °C, chromia-forming alloys offer satisfactory life. For service above 1050 °C, silica- or alumina-forming alloys are preferred.

If the processing conditions alternate between carburizing and oxidizing, then chromium in the alloy would alternately oxidize and carburize. The carburization of oxides releases CO for subsequent oxidation, and the cycle continues. This phenomenon leads to what is known as "green rot," named for the greenish chromium oxides on the fracture surface (see Sections 1.5.11 and 9.2).

High temperature oxidation performance of austenitic stainless steels in oxidizing or hazardous atmospheres has been one of the main scientific and engineering interests in the large field of environmentally induced degradation of materials over the past 25 years (Rouillard et al. 2009). It is well known that parts of the boiler system are exposed to high temperature oxidation and hot corrosion that are recognized as the main factors for degradation of boiler parts. In general, most of the metals are thermodynamically unstable with respect to ambient gases such as CO, O_2, and CO_2 at elevated temperature. Finally, the gas reacts with the surface of the boiler part to form different compounds such as oxide or spinel. Certain compounds may protect the underlying metals or may also thicken into a non-protective scale with various defects such as cavities, microcracks, and porosities.

Many service environments contain combustion products, such as water vapor and carbon dioxide compounds. All have a harmful influence on oxidation resistance of the underlying metals. Furthermore, it is well recognized that oxide films are ductile at high temperature and are often brittle at lower temperature. Most oxide films have different coefficient of thermal expansion of those of the underlying metals from which they are formed. Therefore, the oxide films formed at high service temperature may lose adherence to the underlying metals when cooled to lower temperature and turn into the non-protective films. These are the major reasons for breakaway oxidation and degradation of the underlying metals (Othman et al. 2010).

In the process of oxy-fuel combustion, the oxygen is required to separate from air prior to combustion, and the fuel is combusted in oxygen diluted with recycled flue gas rather than by air. The oxygen-rich, nitrogen-free atmosphere results in the final flue gases consisting mainly of CO_2 and H_2O (water). Specific concern for corrosion in the presence of water vapor is identified to increase the corrosive tendency of the environment. Water vapor can affect this process in various ways. It has been well known that the presence of water vapor in oxidizing environments can accelerate the degradation process for many different metals including austenitic stainless steel (Kumar et al. 2011).

In order to understand the effect of dry and wet CO_2 gas environments at high temperatures (≅700 °C) on high temperature carburization/oxidation behavior of austenitic stainless steels, many studies have been described (Chia and Wen 2009; Grabke 1998a,b; Szakálos et al. 2002; Wuchina et al. 2009; Young 2008).

In the presence of CO_2 at 700 °C, oxidation takes place instead of carburization due to dissociation of CO_2. The process can be split into several steps at the scale interface. The reactant-gas molecule must move toward the surface and become adsorbed there. The adsorbed molecules then split to form adsorbed oxygen, which finally attracts electrons from the oxide lattice to become initially chemisorbed and eventually integrated into the lattice (Freund and Robert 1996). These processes can be expressed as follows:

$$\frac{1}{2}\,O_2(g) \rightarrow \frac{1}{2}\,O_2(ad) \rightarrow O\,(ad) \rightarrow O\,(chem) \rightarrow O^{2-}(latt) \tag{9.21}$$

$$CO_2(g) \rightarrow CO_2(ad) \rightarrow CO\,(ad) \rightarrow O\,(ad) \rightarrow O^{-}\,(chem) \rightarrow O^{2-}(latt) \tag{9.22}$$

From Eq. (9.22), CO_2 adsorbs onto the oxide surface and there dissociates to adsorb CO and O species. In fact, the adsorbed oxygen then goes through the ionization stages. Oxygen turns into dominant and reacts with the substrate (Liu et al. 2012). The oxide phases found were wustite (FeO), magnetite (Fe_3O_4), and hematite (Fe_2O_3) in iron after exposure to CO_2 gas (Huenert et al. 2008). It can be explained by the following reactions:

$$2Fe + O_2 = 2FeO \tag{9.23}$$

$$6FeO + O_2 = 2Fe_3O_4 \tag{9.24}$$

$$4Fe_3O_4 + O_2 = 6Fe_2O_3 \tag{9.25}$$

In dry (Ar–75% CO_2) environments, protective oxide scale, which is Cr_2O_3 layer, was developed. The capability of the austenitic stainless steel to form protective oxide scale is based on Cr content (Francis 1966). The oxide scale of austenitic stainless steel was found to be adhesive and dense in dry CO_2 especially between metal–oxide interfaces. From the cross-sectional observation, it can be seen that diffusion of oxygen through the scale was less in dry CO_2, which showed that the corrosion attack was slower in dry condition.

The aim of this characterization was to obtain a better understanding of the effect of water vapor in flowing CO_2 gas on samples as well. The presence of water vapor in the CO_2 environment accelerated the oxidation of austenitic

stainless steel alloys. This indicates that non-protective scale growth occurs in the Ar–75% CO_2–12% H_2O. The presence of water vapor causes acceleration of the oxide growth from protective oxide to non-protective oxide scale. It leads to a significant increase in oxidation rates and thickening of the oxide scale due to the formation of non-protective Fe_3O_4 oxides.

Silicon has also been found to be very effective in improving carburization resistance, as reported by Kane (1983), Steinkusch (1979), Van der Bruck and Schillmoller (1985), Wolfe (1978), and Wright (1983). The focus thus far has been primarily on alloys used in ethylene cracking and steam hydrocarbon reforming operations. Most of the alloys are cast alloys used for furnace tubes. A variety of wrought alloys of stainless steels, Fe–Ni–Cr alloys, and Ni–Cr alloys have been widely used in various industries, including heat treating and chemical processing. Silicon was again noted for its beneficial effect as illustrated by type 304 versus type 302B. Chromium was found to be beneficial in Fe–Cr alloys, as shown by type 446 versus type 430. Small additions of titanium or niobium appeared to be beneficial when comparing type 321 and type 347 to type 304.

Aluminum is the most effective alloying element in improving an alloy's carburization resistance at high temperature. Lai (1985a,b) showed that when tested at 870, 930, and 980 °C, alloy 214 (Ni–16Cr–3Fe–4.5Al–Y) was the most carburization-resistant alloy among more than 20 commercial wrought alloys, ranging from stainless steels and Fe–Ni–Cr alloys to nickel- and cobalt-based superalloys in the test environments, which were characterized by a unit carbon activity and oxygen potentials such that Cr_2O_3 was not expected to form on the metal surface. Oxides of silicon, titanium, and aluminum were expected to be stable under the test conditions. The excellent carburization resistance of this alloy was attributed to the Al_2O_3 oxide scale formed on the metal surface.

Kirchheiner et al. (2005) developed a commercial, centrifugally cast nickel-based alumina-forming alloy, alloy 60HT, containing approximately 25% Cr, 11% Fe, 0.4% C, and Al. No carburization data were reported. However, the resistance to coking was studied on alloy 60HT containing three levels of aluminum (i.e. 2.35, 3.55, and 4.81%). They found significant reduction in coking rates for the samples containing 3.55 and 4.81% Al, with the samples containing 2.35% Al exhibiting only slight reduction of coking rates compared with the conventional HP-40 alloy (4852). Coking, which is an important phenomenon in ethylene cracking, develops on the internal surface of the pyrolysis tube and reduces the heat transfer. The ethylene cracking operation has to be interrupted to allow decoking, typically with steam and air to remove the coked layer. This decoking operation can have detrimental effects on the tube properties, thus reducing the tube's service life.

Other factors such as surface finish have been found to be very important in affecting carburization reactions. Machining the metal surface to improve the surface finish can significantly increase an alloy's carburization resistance. It is common practice to bore or hone the internal diameter of a centrifugally cast tube to remove surface shrinkage pores (Pons and Hugo 1981; Thuillier 1976).

A cast metal surface with shrinkage pores can generate stagnant conditions in crevices, which are very conductive to carburization attack. In addition, a machined surface exhibits a cold-worked layer, which tends to accelerate the diffusion process and results in rapid formation of oxide scale or film, thus slowing subsequent carbon ingress.

Injecting sulfur compounds into the carburization gas stream can significantly reduce the carburization kinetics. Sulfur compounds, such as H_2S, can retard carburization kinetics. This was observed by many workers, namely, Ramanarayanan et al. (1998) and Wright (1983).

It was shown that carburization of HK-40 alloy was significantly reduced when 100 ppm H_2S was injected into the test environment. The effect of different levels of H_2S injection on the carburization of HK-40 was also observed. The carburization of alloy 800H in H_2–CH_4 ($a_C = 1.0$) with injection of different levels of H_2S (H_2S/H_2) was also studied by Grabke et al. (1979). When this approach is used for controlling carburization, it is important to determine the optimum level of sulfur compounds needed to achieve maximum effectiveness. Too much can lead to accelerated corrosion due to sulfidation, which may be worse than carburization. In fact, a low H_2S injection failed to reduce carburization, and a high H_2S injection caused sulfidation attack for alloy 800H. It has been proposed by Grabke et al. (1977) and Ramanarayanan and Srolovitz (1985) that sulfur absorbed on the metal surface blocks the potential sites for carbon absorption from the carburizing gas, thus significantly reducing the carbon concentration in the metal surface layer and retarding the overall carbon transfer into the metal.

The room temperature ductility or toughness of an alloy can be severely degraded when the alloy is heavily carburized (Klower and Heubner 1998). For high temperature components that are subjected to severe carburizing environments at very high temperatures, such as ethylene pyrolysis furnace tubes, the component can be carburized through the thickness of the component with significant amount of carbon pickup. Grabke and Jakobi (2002) performed a metallurgical analysis of a failed ethylene pyrolysis furnace tube made of HP-40 Nb and found that the tube was carburized throughout the tube wall with 3.14–3.3% C, as opposed to the original carbon content of about 0.5%. Furthermore, carburization can increase the volume of the carburized zone, thus developing internal stresses. When the alloy is severely carburized, these internal stresses can be significant enough to develop

cracking when the carburized alloy is cooled to room temperature. The effect of carburization on the mechanical properties of high temperature materials has also been studied in terms of their creep-rupture behavior. Marriott et al. (1987) edited an excellent book documenting these and related aspects of carburization corrosion.

9.4 Metal Dusting Problem

MD deterioration as a concept was first reported by Camp et al. in 1945. The corrosion problem was initially detected in a superheater for reforming naphtha. Several laboratory exposures were performed on 18/8 stainless steel in order to minimize the newly detected corrosion phenomenon, and it was concluded that different forms of sulfur additions eliminate the corrosion.

More focused studies on the mechanisms of MD were initiated by Prange (1959) during the 1950s with studies on the effects of carbon-bearing gases on alloys in petrochemical applications and were a major feature at the 1959 NACE conference. Several excellent conference papers on the subject were published by Prange and other authors.

A statement by Prange summarizes the state of the art of MD research on high-alloyed materials during the time period: "While a few aspects are discernible (regarding MD), the picture as a whole is hazy. At first glance it might seem that oxidation phenomena govern the entire problem . . . ." This seems to anticipate, 50 years later, the lively debate on effect and role of oxygen in MD of high-alloyed materials, which is thoroughly described in recent literature.

Pure carbon-induced MD on binary Fe–Ni alloys was described during the 1950s by Hultgren and Hillert (1953). Today, this disintegration by graphitization is considered to be one of the major degradation mechanisms of MD. This paper has not been referred to until recently, perhaps because, in the words of one of the authors (Hillert), "At that time, we did not know that the phenomenon was denoted metal dusting."

In the 1960s, Hochman and Burson (1966) identified an additional mechanism that operates on iron and low-alloyed steels, which includes decomposition of metastable cementite. However, the steady-state situation and driving force of this mechanism were never elucidated.

A statement by Zeng et al. (2002) may summarize the situation of MD research a few years ago: "Metal dusting has been studied for more than 50 years, but the mechanisms are not fully understood." Obviously, there are still several gaps in the understanding of MD mechanisms, especially concerning high-alloyed materials.

The Hochman proposal for the MD corrosion of iron, which has been further elaborated and confirmed by Grabke et al. (1998), Pippel et al. (1998), and Chun et al. (2003), involves the initial formation of a metastable Fe_3C carbide layer on the iron surface in environments that are supersaturated with carbon. The carbide subsequently dissociates into carbon and metal particles when it is destabilized by carbon deposition, leading to the formation of "dust." Often the metastable Fe_3C does not decompose, but instead constitutes the dust by the rupture of surface Fe_3C layer.

The stresses generated during the formation and growth of Fe_3C appear to be rather large, and above a critical stress level, the surface Fe_3C layer breaks up, with fractured Fe_3C migrating upward through the carbon deposit. The presence of Fe_3C in the carbon deposit has also been reported by Toh et al. (2002), Zeng et al. (2002), and Zhang et al. (2003).

Nickel and cobalt are also subject to MD; however, their disintegration leads to larger metal particles, the overall rate of metal wastage is lower, and the amount of carbon deposition is less. Previous work (Chun et al. 2003) indicated that the mechanism of MD of Ni and Co is different from that of iron and steel because the metastable surface carbide layer that typifies Fe corrosion is not observed. However, Ni and Co still corrode by a combination of atom migration through surface carbon deposits and carbon intrusion and precipitation in the bulk metal.

Schneider et al. (1999) have also carried out some studies on the MD of nickel-based alloys. It is believed that MD can be suppressed by the formation of a protective stable oxide layer. However, the breakup of surface oxide films initiates localized attack. Corrosion then leads to the formation of hemispherical pits and holes, from which coke grows in various forms such as cones, worms, leeches, etc. The following sequence of steps has been proposed by Grabke (2003): (i) carbon transfer from the carbon-supersaturated environment to the alloy surface and dissolution in the alloy, (ii) deposition of graphite on the alloy surface in different orientations, (iii) growth of graphite into the alloy interior by addition of dissolved carbon to graphite basal planes normal to the alloy surface, (iv) destruction of the alloy by inward-growing graphite and dislodgement of metal particles into the coke layer, and (v) further coke formation on these metal particles that act as catalyst.

Zhang et al. (2005) have studied the effect of copper additions to nickel on the rate of MD. Because copper is noncatalytic to carbon deposition from the gas atmosphere, the addition of ~20 wt% copper to nickel was able to suppress or greatly retard the MD of the alloy without the need for a protective oxide scale on the surface. This concept was originally used by Ramanarayanan et al. (2004) to propose MD corrosion-resistant coatings. High temperature MD is treacherous since when initiated, the MD pit growth rate may reach at least a millimeter per month on stainless steels and an order of magnitude higher

on low-alloyed steels. It is a widespread problem in the petrochemical industry, particularly in cracker furnaces and reforming units, i.e. in hydrocarbon synthesis gas containing predominantly CO and H_2 with some water vapor. This means that basically all production of monomers, which are the raw materials for polymer production, like polyethylene, may be subjected to MD. Other chemical processes where organic compounds are reacting, such as in butane dehydrogenation, hydrodealkylation, acetic acid cracking, and pyridine production, are also subjected to MD (Grabke 1995). Industrial processes within the heat treating industry, energy production (coal gasification plants), and ammonia plants are other examples. During the recent years, MD has attracted considerable attention due to development of new processes in the petrochemical industry as well as in electric power generation.

In the important context of energy production, it is fairly safe to say that mankind will not stop the usage of fossil fuel until all of the Earth's reservoirs of oil, gas, and coal have been emptied. However, their exploitation via today's technology at the current rate is also associated with negative ecological and climatic consequences. The solution of these problems is believed to be in new technology, where only the hydrogen part of the fossil fuels is used for energy production or by using CO_2 sequestration techniques.

A more immediate problem is that the global production of conventional oil is predicted to peak toward the end of next decade. However, it is possible to compensate the forthcoming decrease in oil production with natural gas, but it requires more efficient techniques.

The prevailing circumstances have recently increased the interest in *Fischer–Tropsch gas-to-liquid* (GTL) hydrocarbon processing technologies and the pursuit of maximum efficiency in steam reforming technologies. Another important future technique for energy production is represented by *solid oxide fuel cell* (SOFC) and *molten carbonate fuel cell* (MCFC) technologies. Significant progress on reducing the operating temperatures of an SOFC has already been achieved, from ~1000 °C down to 550–800 °C intermediate temperature solid oxide fuel cell (ITSOFC). However, the Achilles' heel in all these techniques is the development of equipment, i.e. metallic materials capable of operating at increased carbon activities across the temperature range of 450–850 °C, where MD can cause severe damage to alloy components.

Even today's technology suffers significant problems with MD. The US Department of Energy (DOE) has calculated that savings of more than US$ 300 million could be made annually in hydrogen production alone if the limitations caused by the MD phenomenon could be circumvented.

A solution to the MD problem without lowering the carbon activity or introducing inhibitors, i.e. by development of a new generation of engineering alloys immune to MD corrosion, would represent an important contribution toward a more durable and environmentally nondestructive society – the hydrogen society.

9.5 Metal Dusting Mechanisms

The phenomenon of MD may be divided into three main mechanisms denoted type I, type II, and type III.

Type I, first described by Hochman (1972) and further detailed by Grabke (1995, 1998a), involves decomposition of metastable cementite.

Type II may be described as disintegration of a carbon-supersaturated phase by internal graphitization and was first described by Hultgren and Hillert (1953) and studied in detail by Pippel et al. (1995, 1998).

Type III, which operates on high-alloyed steels and Ni-based alloys, was first proposed and further detailed by Szakálos et al. (2002, 2006) and involves selective oxidation of alloyed carbides, i.e. not pure Fe carbides.

9.5.1 Type I Mechanism

Pure metals like Fe, Ni, and Co do not form any protective oxides in synthesis gas mixtures since the oxygen partial pressure is typical in the range of 10^{-20} to 10^{-24} bar depending on the content of oxygen-bearing gases such as H_2O and CO_2. This means that their MD behavior is likely to be poor. Nevertheless, these metals are of principal importance since the alloys used today in MD environments are based on Fe, Ni, and Co.

MD mechanism on iron and low-alloy steels has been studied in recent times by Grabke and coauthors. The suggested mechanism may be summarized as formation of metastable cementite and its subsequent decomposition into graphite and iron during MD conditions (Figure 9.9).

Based on the model, the prerequisite for MD to occur is a high carbon activity environment ($a_C > 1.0$) that causes the oversaturated metal with the carbon activity being more than 1. This condition promotes the formation of cementite (Fe_3C) on the metal surface. Constructed thermodynamic graphs of carbon activity as a function of gaseous composition in terms of ($p_{CO} \cdot p_{H_2}/p_{H_2O}$) ratios for various temperatures (400–1000 °C) show that the carbon activities in equilibrium with cementite are higher than 1.0 at 700 °C and lower temperature. Figure 9.10 shows a metastable Fe–C–O phase diagram at 600 °C, indicating that metastable cementite forms at $a_C > 1.0$ (Bonnet et al. 2003). Once graphite deposits on the cementite with the carbon activity of the graphite at 1, cementite in contact with graphite becomes unstable and then decomposes into iron and carbon with iron migrating outward into the graphite layer. As a result, metal wastage takes place as a

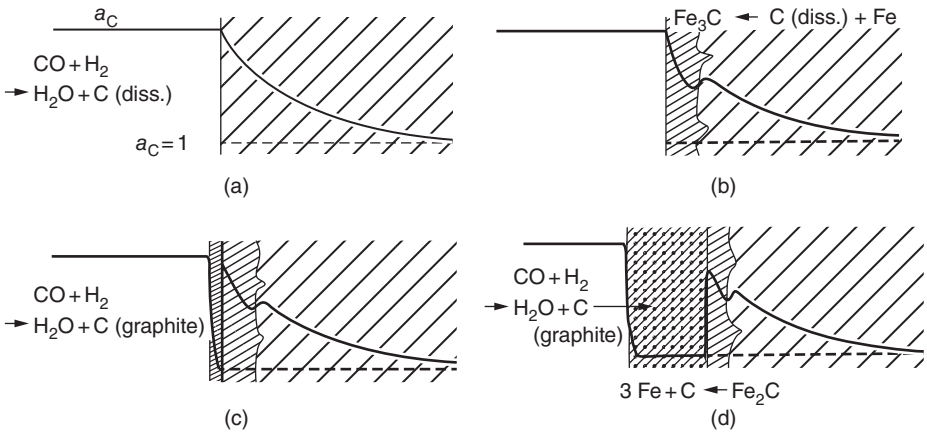


Figure 9.9 Schematic illustration of the metal dusting mechanism on iron and low-alloy steels from Grabke (1995): (a) supersaturation of the metal matrix by carburization, (b) formation of Fe_3C at the surface with growth from the interior, (c) deposition of graphite onto the Fe_3C surface, and (d) Fe_3C decomposition and outgrowth of coke by carbon deposition on the metal particles from the Fe_3C decomposition.

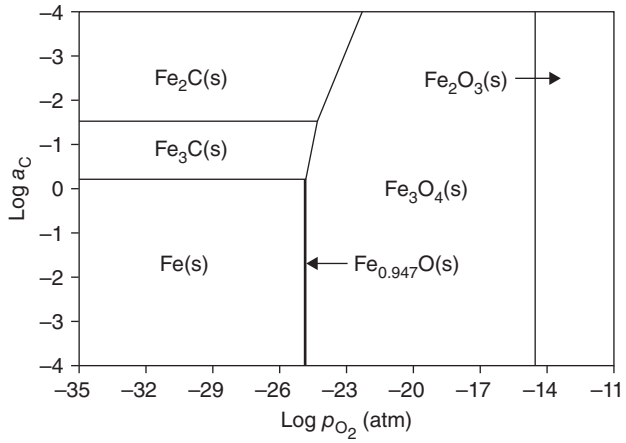


Figure 9.10 Fe–C–O metastable phase stability diagram showing that metastable cementite (Fe_3C) forms under high carbon activities ($a_C > 1$) at 700 °C and lower (Bonnet et al. 2003).

repeated reaction of formation of metastable cementite and decomposition of cementite into iron and carbon. For iron and low-alloy steels with no protective oxide scales, metal wastage attack in general follows uniform metal thinning (Grabke 1998a). A layer of cementite (Fe_3C) was found to occur on 1Cr–0.5Mo steel after exposure to MD conditions with a layer of coke on top of the cementite (Grabke 1995).

9.5.2 Type II Mechanism

The mechanism of MD on Ni and Co is predicted to be the same and involves formation of neither carbides (Chun et al. 2003) nor oxides in typical MD environments. Instead, a direct fragmentation takes place by graphitization, i.e. type II mechanism (Chun et al. 2003; Pippel et al. 1998).

This mechanism was first described by Hultgren and Hillert during the 1950s in a study of binary Fe–Ni alloys (1953).

Ni and Co have similar properties in typical MD environments (Hochman 1972; Olsson and Turkdogan 1974; Smalley et al. 2002):

- No formation of protective oxides.
- No formation of carbides.
- Dissolve carbon and stabilize graphite.
- Have strong catalytic properties on CO dissociation.

These properties promote type II mechanism – disintegration of a carbon-supersaturated matrix by internal graphite formation. Initially, larger metal fragments may be released from the MD front. These larger metal pieces are subjected to continued fragmentation until they finally may be too small for inward growth of graphite or graphite nucleation in their interior and the continued formation of solid carbon will occur on their surface. The final metal dust is typically in the nanometer scale, resulting in carbon nanotube formation.

The mechanism for MD on chromia-forming alloys is considered to be similar for austenitic iron-based alloys and Ni-based alloys. In publications by Grabke (1995, 2003), the MD of high-alloyed steels and CrFeNi alloys were described with the schematic in Figure 9.11.

The proposed mechanism includes the following main steps:

(i) Carburization and formation of very fine Cr-rich M_7C_3 carbides (gray zone) and $M_{23}C_6$ carbides in the grain boundaries.

(ii) Formation of metastable (?) $(Fe,Ni)_3C$ cementite in the Cr-depleted matrix, followed by cementite decomposition (type I) and/or direct fragmentation by graphitization (type II). The corrosion products would thus be cementite or Fe/Ni particles, graphite, and Cr-rich carbide particles.

(iii) Oxidation of the corrosion products in the coke, i.e. oxidation of the very fine Cr-rich carbides, which

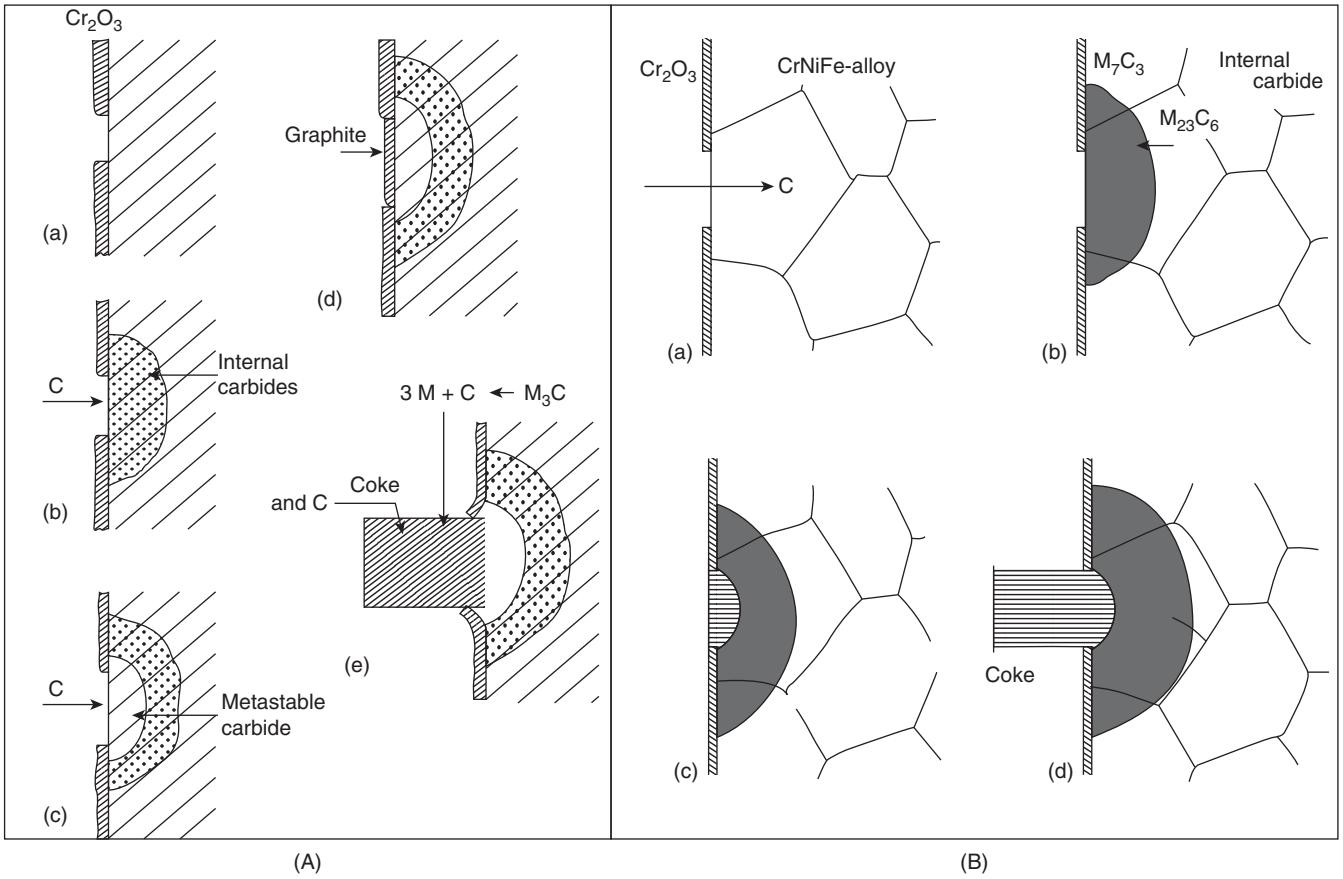


Figure 9.11 Schematic representation of the MD mechanism on high-alloyed steels and CrFeNi alloys taken from (A) Grabke (1995) and (B) Grabke (2003).

subsequently would give very fine spinel/chromia particles in the coke.

The above proposed mechanism implies that oxidation is not involved in the MD process, only in the subsequent breakdown of the corrosion products. This is contradicted by a number of metallographic observations on CrFeNi alloys such as stainless steels alloy 800 and Inconel 600 (Baker and Smith 2001; de Bruyn et al. 2001; Levi et al. 2001; Strauss et al. 1999; Toh et al. 2002).

All these observations indicate that oxygen is active in the MD process. Pippel et al. (1995) and Schneider et al. (1999) propose a somewhat modified mechanism for Cr-containing Ni-based alloys as shown in Figure 9.12.

This modified mechanism includes the following main steps:

(i) Chromia formation on the surface with subsequent formation of a Cr-depleted Ni layer underneath.

(ii) Carburization and direct fragmentation of the Ni layer by graphite tubes, i.e. type II mechanism.

(iii) The graphite tubes show an oriented growth perpendicular to the surface, and a metal dissolution mechanism in the graphite planes is suggested. The metal atoms diffuse to the graphite–gas interface, where they agglomerate to small particles.

(iv) The corrosion products would thus be Ni/Fe fragments, Ni/Fe atoms/nanoparticles, graphite, and chromia particles.

Again, the oxygen is not taking part in the suggested MD mechanism, and it is unclear what happens to the Cr atoms in the steady-state corrosion process. It should be mentioned that nickel-based alloys, typically of composition around 20Cr80Ni, may also be attacked by another high temperature corrosion phenomenon denoted "green rot"; the term has been coined because the fractured surfaces have a green appearance due to the formation of Cr_2O_3. Although green rot is a very old problem, it is described in only a few literature references. This is largely because its occurrence is limited to a narrow range of environmental parameters and to temperature range of 900–1150 °C (Betteridge 1959; Kofstad 1988; Naumann and Spies 1977; Skarda 1986). The gas environment must be reducing or at least periodically reducing with respect to the bulk metal (Ni and/or Fe) although oxidizing for Cr (Skarda 1986).

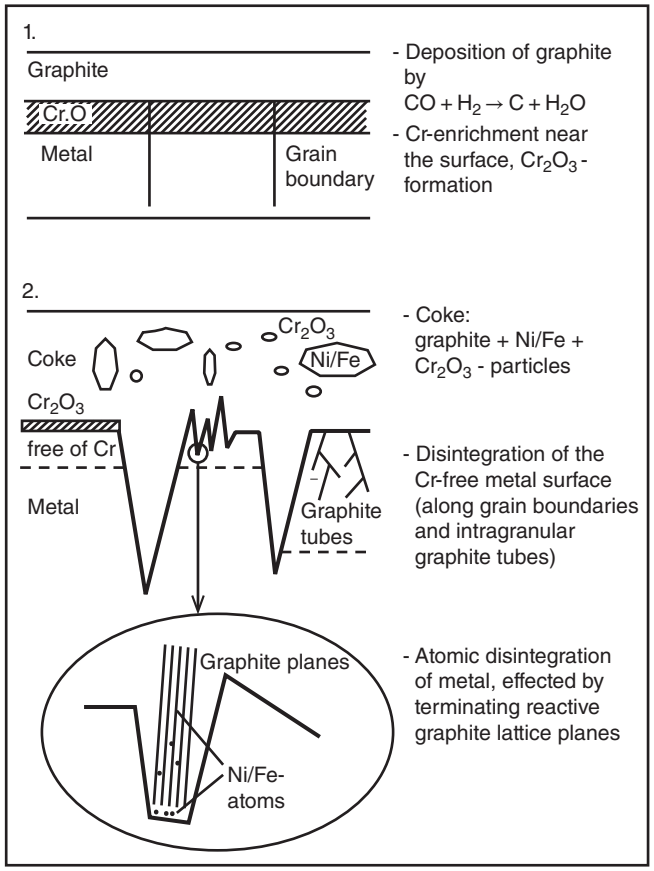


Figure 9.12 Schematic representation of the processes and reaction layers involved in metal dusting on Cr-containing nickel-based alloys (Inconel 600) from Schneider et al. (1999).

The term "green rot" has also been applied to alloys exposed to oxidizing and carburizing atmospheres, which result in internal oxidation of previously formed grain boundary Cr carbides, giving the same appearance with green chromia on the fractured surfaces (Kofstad 1988). This form of green rot may thus show some similarities with MD. However, in synthesis gas mixtures in the temperature range of 540–650 °C, the overall corrosion process is far more complex. The corrosion attack described here, with hemispherical pit formation and dark/black corrosion products, consisting of metal particles, graphite and spinel oxides, is typical of MD.

9.5.3 Type III Mechanism

Type III mechanism was first identified on an AISI 304L-type stainless steel exposed at 650 °C in a CO-containing gas mixture (Szakálos et al. 2002; Szakálos 2003). Scanning electron microscopy (SEM) images of MD reactions in AISI 304L stainless steel led to the sketch in Figure 9.13 that shows 6 MD steps (Szakálos 2003):

1. Carburized bulk with $M_{23}C_6$ carbides, which forms at lower carbon activities.
2. Carburized bulk with M_7C_3 carbides.
3. Dissolving carbide front with M_7C_3 and M_3C.
4. Cr-depleted zone ("white phase"), Fe–Ni austenite border with graphite flakes.
5. Corrosion products: Cr–Fe oxides, metal fragments in μm size, and carbon.
6. Coke – continued corrosion on the corrosion products by type II mechanism, i.e. disintegration of the metal fragments in smaller and smaller metal dust and finally nanometer-sized particles under formation of carbon nanotubes.

The main reactions of type III mechanism are presented below. In order to point out the main solid-state reactions, intermediate reactions in the gas phase are excluded.

Consider 10 atoms of AISI 304L steel of composition 18Cr–10Ni–72Fe in wt%, i.e. an approximate atomic ratio of 2Cr–1Ni–7Fe. The following reactions show the steps involved in a fully equilibrated carburization and MD process in a CO/H_2-containing gas ($a_C \geq 1.0$). Schematically, the mechanism reactions may be divided into two stages:

Carburization (zones 1 and 2 in Figure 9.13)

$$(2\mathrm{Cr}-\mathrm{Ni}-7\mathrm{Fe})\gamma_{304\mathrm{L}} + 1.29\mathrm{CO(g)} \rightarrow (6\mathrm{Fe}-\mathrm{Ni})\gamma_{\mathrm{matrix}} + 0.43[(\mathrm{Cr}_{14/3}\mathrm{Fe}_{7/3})\mathrm{C}_3] + 1.29\mathrm{O(ad)} \quad (9.26)$$

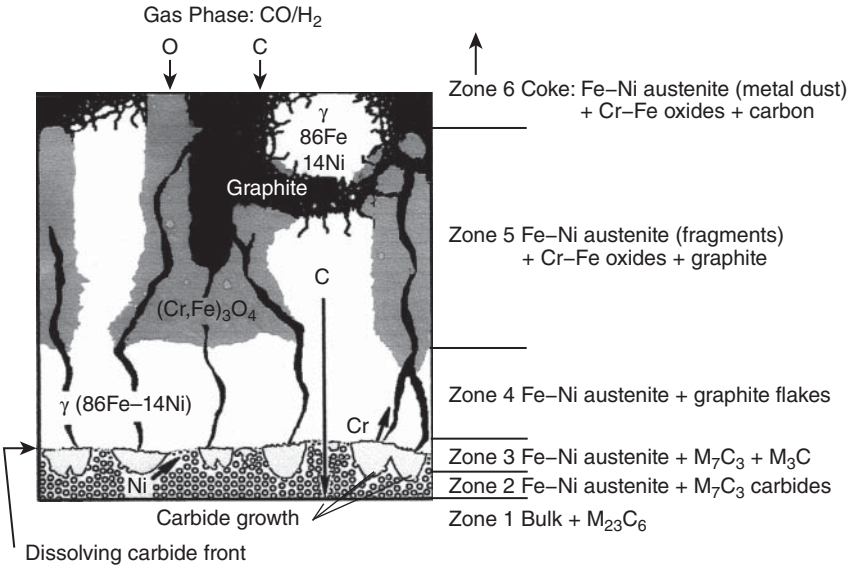


Figure 9.13 The mechanisms of metal dusting as they appear on stainless steels. They include an active corrosion process with carbon and oxygen (type III), in combination with fragmentation by graphitization (type II). The fine-grained austenite/graphite layer (zone 4) promotes the Cr diffusion and consequently oxide formation. The corrosion products consist of Fe–Ni austenitic metal dust, spinel oxides, and elementary carbon, but no carbides.

and carbide dissolution by selective oxidation (zones 3–5)

$$(6\text{Fe}-\text{Ni})\gamma_{\text{matrix}} + 0.43[(\text{Cr}_{14/3}\text{Fe}_{7/3})\text{C}_3] + 4\text{CO(g)} \rightarrow (6\text{Fe}-\text{Ni})\gamma_{\text{dust}} + (\text{Cr}_2\text{Fe})\text{O}_4 + 5.29\text{C(s)} \quad (9.27)$$

where γ_{dust} is austenitic particles, i.e. metal dust. As shown in Figure 9.13, carbides do not oxidize directly, but they dissolve first and Cr diffuses through the carbide-free austenite (zone 4) and reacts with oxygen. The equilibrium corrosion products are thus austenitic (Fe–Ni) metal particles, Cr–Fe spinel oxides, and elementary carbon. The carbide is a necessary reaction intermediate, and the overall reaction simplifies to

$$(2\text{Cr}-\text{Ni}-7\text{Fe})\gamma_{304\text{L}} + 4\text{CO(g)} \rightarrow (6\text{Fe}-\text{Ni})\gamma_{\text{dust}} + (\text{Cr}_2\text{Fe})\text{O}_4 + 4\text{C} \quad (9.28)$$

The summary reaction will be identical in the case of oxidation of cementite or $M_{23}C_6$ carbides instead of M_7C_3 carbides; it is only the carbon and CO content in Reactions (9.26) and (9.27) that differ. From the overall reaction alone, it seems that MD of stainless steels by CO is basically degradation by oxidation, but, as discussed above, a more correct description is to see MD as active corrosion by carbon since carbon reacts and is then released but not consumed. There is one major difference between the two active corrosion processes. In the case of chlorine-induced corrosion, virtually all metal atoms react chemically to form corrosion products. In the case of MD, according to the above reactions, only around 30 at.% of the steel reacts chemically to form corrosion products, and the remaining 70% forms metal particles or dust without any chemical reaction. These proportions correspond surprisingly well to SEM observations in the active reaction front in an MD pit.

In fact, in some cases only a fraction of 30 at.% have to react when the attack (type III) penetrates subgrain boundaries.

9.6 Alloy Resistance to Metal Dusting

Process equipment failures due to MD were reported in the refinery industry during the 1950s. Eberle and Wylie (1959) reported metal wastage of uncooled components, such as soot-blower elements, made of types 347SS and 310SS in the waste heat boiler of a synthesis gas reactor. The synthesis gas, predominantly CO and H_2 with some water vapor and carbon particles, was produced by combustion of methane and oxygen. The wastage took place at temperatures between 480 and 900 °C. Both 347SS and 310SS suffered severe metal wastage after only three weeks of service.

MD problems were also encountered in reforming plants where a synthesis gas (i.e. $H_2 + CO$) for methanol manufacturing was produced. Type 304SS and 310SS reformer outlet tubes were perforated by severe pitting attack at 650–725 °C.

Hydrodealkylation units, acetic acid cracking furnaces, and coal gasification plants were reported to suffer MD problems. Perkins et al. (1976) reported pitting attack of alloy 800 tubes in a preheater for gasifier recycle gas rich in H_2 and CO with some H_2O. The tubes, with a wall thickness of 0.38 cm (0.15 in.), were perforated in a few thousand hours. The attack occurred at 540–870 °C.

MD has also been encountered in the heat treating industry (Lai 1985a,b). Refractory anchors, fan housing assemblies, and other components in carburizing furnaces frequently suffer MD problems. Alloys typically used include stainless steels, such as type 310; nickel-based alloys, such as alloys X and 333; and iron-based alloys, such as Multimet alloy (or N-155). MD typically occurred at temperatures between 540 and 820 °C.

Severe attack frequently took place after one year of service and at locations where the gaseous environment became stagnant.

Ferritic Fe–Cr alloys are more resistant to MD than austenitic Fe–Ni–Cr alloys presumably due to much faster chromium diffusion rates, thus resulting in faster formation of chromium oxide scales, and then better MD resistance. Rapid diffusion of chromium to the metal surface to form a protective chromium oxide scale is important in retarding MD attack. Accordingly, for the same alloy, a fine-grained material can form a surface oxide scale more readily than a coarse-grained material – thus better MD resistance (Grabke et al. 1998).

Types 304, 310, and 800H – which are Fe–Ni–Cr alloys – were found to suffer MD attack (i.e. the reaction rates in weight loss), while two nickel-based alloys (alloy 601 and RA333) showed no MD attack (i.e. the reaction rates in weight gain). This was due to beneficial effect of silicon along with aluminum in the alloy. The beneficial effects of silicon and aluminum are demonstrated by additions of these two elements to alloy 800 (Fe–20Cr–32Ni), as shown by Strauss and Grabke (1998); also in this study, other alloying elements such as niobium, molybdenum, and tungsten were found to have some beneficial effects as well.

In reviewing data on Ni–Cr alloys, Grabke (2003) found that Ni–50Cr alloy was very resistant to MD, showing a thin chromium oxide scale (about 3 μm thick) after testing in H_2–49CO–2H_2O at 650 °C ($a_C = 18.9$) for 10 000 hours with no evidence of MD or carburization. Only minute amounts of coke were observed on the specimen surface. Under this test condition, alloy 601 had already suffered MD attack after only 1993 hours of exposure. Similarly, a very thin chromium oxide scale was observed in Cr–5Fe–1Y_2O_3 after 10 000 hours of exposure in the same test, showing no evidence of MD attack.

From the discussion so far on MD, formation of a good protective chromium oxide scale is a very effective way to provide protection against MD attack. Since the temperature range for MD attack is quite low and chromium diffusivities are relatively low at these temperatures, rapid formation of a good protective chromium oxide scale is critical. Accordingly, the concentration of chromium at the surface of the metal becomes important. Higher chromium concentration at the metal surface provides faster formation of a protective chromium oxide scale. Thus, alloys with higher bulk chromium concentration (higher surface chromium concentration) are more resistant to MD. Also, for the same alloy, the fine-grained structure exhibits better MD resistance than the coarse-grained structure. This is because grain boundaries provide fast diffusion paths for chromium to reach to the metal surface. A fine-grain-sized material will have more grain boundaries and, thus, more chromium reaching to the metal surface to form a better chromium oxide scale faster than a coarse-grained material, thereby resisting MD attack much better.

The surface of the metal can also be prepared by grinding or machining to produce a thin cold-worked layer with high density of dislocations, which also provide fast diffusion paths for chromium to reach to the metal surface to form a protective chromium oxide scale. As a result, MD is greatly improved when the surface is ground or machined. The beneficial effect of the ground surface condition is illustrated in a thermogravimetric study by Grabke (2003). For both alloy 800 and type 310SS, the as-ground specimen was most resistant to MD compared with the as-received surface (cold rolled) and electropolished surface. Electropolished surface condition was the worst because of possible surface depletion in chromium during electropolishing.

Selection of an appropriate filler metal for MD environments is also critical since not every wrought alloy has a matching filler metal. Thus, it is necessary to select a filler metal that is, at least, as good as but preferably better than the wrought alloy selected for the application. The suitable filler metal requires not only good resistance to MD but also good weldability. Also, in many cases, machining or grinding the weld joint may not be possible, particularly in tubular butt welds where inside diameter (ID) grinding or machining is not feasible after joining. Furthermore, alloys that resist MD contain high aluminum or silicon along with high chromium, as discussed previously. If matching filler metals are available for these alloys, the weldability of these high aluminum or high silicon filler metals can be an issue.

Sulfur that has a strong tendency to segregate to the surface and grain boundaries can act as an inhibitor to MD. Hochman (1977) first reported the beneficial effect of sulfur against MD attack. Extensive investigations on the effect of sulfur on MD behavior of iron were carried out by Grabke and Muller-Lorenz (1995, 1998), Schneider and Grabke (2003), and others. The mechanism for sulfur to inhibit MD attack, as proposed by Grabke and Muller-Lorenz (1995), is that the absorption of sulfur on the surface of cementite suppresses the nucleation of graphite, thus inhibiting MD attack.

Grabke (2000) avoided MD by sulfur injection under certain p_{H_2S}/p_{H_2} ratios at temperatures from about 500 to 1000 °C. Injecting a right amount of sulfur into the environment to retard MD without causing accelerated sulfidation attack is a balancing act.

References

Ando, S., Nakayayama, Y., and Kimura, H. (1989). *IZIJ Int.* 29: 511.

Baker, B.A. and Smith, G.D. (2001). *International Workshop on Metal Dusting*. Illinois: ANL, Argonne.

Barralis, J. and Maeder, G. (1997). *Précis de Métallurgie, Élaboration, Structures-Propriétés, Normalisation*. Paris: AFNOR-Nathan.

Betteridge, W. (1959). *The Nimonic Alloys*. London: Edward Arnold.

Bonnet, F., Ropital, F., Berthier, Y., and Marcus, P. (2003). *Mater. Corros.* 54: 870.

Bose, S.K. and Grabke, H.J. (1978). *Z. Metallkde* 69: 8.

de Bruyn, H.J., Edwin, E.H., and Brendryen, S. (2001). *Corrosion/2001*, Paper No. 01383. Houston, TX: NACE International.

Cahn, J.W. (1959). *Acta Metall.* 7: 18.

Camp, E., Phillips, C., and Gross, L. (1945). *Corrosion* 1: 149.

Catlow, C.R. and Mackrodt, W.C. (eds.) (1987). *Nonstoichiometric Compounds*, Advances in Ceramics, vol. 23, 3–26. Westerville, OH: The American Ceramic Society, Inc.

Chia, H.C. and Wen, T.T. (2009). *Mater. Chem. Phys.* 116: 426.

Christ, H.J. (1998). *Mater. Corros.* 49: 258.

Chun, C.M., Mumford, J.D., and Ramanarayanan, T.A. (2003). *J. Electrochem. Soc.* 150: B76.

COACH data bank (2002). Thermodata, BP 66, 38402 Saint Martin d'Hères Cédex, France.

Coltters, R.G. (1985). *Mater. Sci. Eng.* 76: 1.

Corish, J., Barnes, J., and Smith, P.J. (1987). *Nonstoichiometric Compounds*, Advances in Ceramics, vol. 23 (ed. C.R. Catlow and W.C. Mackrodt), 210. Westerville, OH: The American Ceramic Society, Inc.

Dovey, D.M. and Jenkins, I. (1950). *J. Inst. Met.* 76: 581.

Eberle, F. and Wylie, R.D. (1959). *Corrosion* 15: 622t.

Forseth, S. and Kofstad, P. (1998). *Mater. Corros.* 49: 266.

Francis, J.M. (1966). *J. Iron Steel Inst.* 204: 910.

Freund, H.J. and Robert, M.W. (1996). *Surf. Sci. Rep.* 25: 225.

Grabke, H.J. (1995). *Corrosion* 51: 711.

Grabke, H.J. (1998a). *Mater. Corros.* 49: 303.

Grabke, H.J. (1998b). *Carburization: A High Temperature Corrosion Phenomenon*. St. Louis, MO: Materials Technology Institute of the Chemical Process Industries, MTI Publications, No. 52.

Grabke, H.J. (2000). *Mater. High Temp.* 17: 483.

Grabke, H.J. (2003). *Mater. Corros.* 54: 736.

Grabke, H.J. and Jakobi, D. (2002). *Mater. Corros.* 53: 494.

Grabke, H.J. and Muller-Lorenz, E.M. (1995). *Steel Res.* 66: 252.

Grabke, H.J. and Muller-Lorenz, E.M. (1998). *Mater. Corros.* 49: 317.

Grabke, H.J. and Wolf, I. (1987). *Mater. Sci. Eng.* 87: 23.

Grabke, H.J., Petersen, E.M., and Srinivasan, S.R. (1977). *Surf. Sci.* 67: 501.

Grabke, H.J., Meller, R., and Schnaas, A. (1979). *Werkst. Korros.* 30: 794.

Grabke, H.J., Muller-Lorenz, E.M., Strauss, S. et al. (1998). *Oxid. Met.* 50: 241.

Grabke, H.J., Muller-Lorenz, E.M., and Zinke, M. (2003a). *Mater. Corros.* 54: 785.

Grabke, H.J., Martinez, H.P., and Muller-Lorenz, E.M. (2003b). *Mater. Corros.* 54: 860.

GTT Technologies. (2015). Kaisersstrasse 100, D-52134, Herzogenrath, Germany.

Hall, D.J., Hossain, M.K., and Jones, J.J. (1985). *Mater. Perform.* 24: 25.

Harrison, J.M., Norton, J.F., Derricott, R.T., and Marriott, J.B. (1979). *Werkst. Korros.* 30: 785.

Hillert, M. (1969). *Inst. Met. Monogr. London* 33: 231.

Hochman, R.F. (1972). *Proceedings of 4th International Congress on Meterials Corrosion*, 258. Houston, TX: NACE.

Hochman, R.F. (1977). *Properties of High Temperature Alloys*, PV77-1 (ed. Z.A. Foroulis and F.S. Pettit), 715. Princeton, NJ: The Electrochemical Society.

Hochman, R.F. and Burson, J.H. (1966). *Proc. API Div. Refin.* 46: 331.

HSC (2006). Chemistry for Windows. version 6.0, A. Roine, Outokurupa Technology, Finland.

Huenert, D., Schulz, W., and Kranzmann, A. (2008). *Ageing and Corrosion of Steels in CO_2 Rich Flue Gas*. Berlin: Federal Institute of Materials Research and Testing.

Hultgren, A. and Hillert, M. (1953). *Jernkont. Ann.* 137: 7.

Jakobi, D. and Gommans, R. (2003). *Mater. Corros.* 54: 881.

Kane, R.H. (1983). *Corrosion/83*, Paper No. 266. . Houston, TX: NACE International.

Kane, R.D. and Cayard, M.S. (1995). *Chem. Eng. Prog.* 91: 83.

Khandros, I.Y., Bayer, R.G., and Smith, C.A. (1984). *Corrosion/84*, Paper No. 10. . Houston, TX: NACE International.

Kirchheiner, R., Young, D.J., Becker, P., and Durham, R.N. (2005). *Corrosion/2005*, Paper No. 5428. . Houston, TX: NACE International.

Klower, J. and Heubner, V. (1998). *Mater. Corros.* 49: 237.

Kofstad, P. (1988). *High Temperature Corrosion*. London: Elsevier Applied Science.

Krikke, R.H., Horing, J., and Smit, K. (1976). *Mater. Perform.* 15: 9.

Kumar, V., Arora, N., and Singh, S. (2011). *MIT Int. J. Mech. Eng.* 1: 79.

Lai, G.Y. (1985a). *Proceedings of the TMS-AIME Symposium* (ed. M.F. Rothman), 551. The Metallurgical Society of AIME.

Lai, G.Y. (1985b). *J. Met.* 37: 14.

Lai, G.Y. (2007). *High-Temperature Corrosion and Materials Applications*. Materials Park, OH: ASM International.

Levi, T.P., Briggs, N., Minchington, I., and Thomas, C.W. (2001). *Corrosion/2001*, Paper No. 01375. . Houston, TX: NACE International.

Lin, C.-Y. and Tsai, W.-T. (2003). *Mater. Chem. Phys.* 82: 929.

Liu, L., Zhao, C., and Li, Y. (2012). *J. Phys. Chem.* 116: 7904.

Marriott, J.B., Merz, M., Nihoul, J., and Ward, J. (eds.) (1987). *High Temperature Alloys: Their Exploitable Potential*. Elsevier Applied Science.

Natesan, K. (1976). *Nucl. Technol.* 28: 441.

Natesan, K. and Kassner, T.F. (1973). *Metall. Trans.* 4: 2557.

Naumann, F.K. and Spies, F. (1977). *Prakt. Metallogr.* 14: 160.

Nishiyama, Y., Otsuka, N., and Nishizawa, T. (2003). *Corros. Sci.* 59: 688.

Nishiyama, Y., Otsuka, N., and Kudo, T. (2006). *Corros. Sci.* 48: 2064.

Olsson, R.G. and Turkdogan, E.T. (1974). *Met. Trans.* 5: 21.

Othman, N.K., Othman, N., and Zhang, J. (2010). *Sains Malaysiana* 39: 249.

Pearson, W.B. (1958). *Lattice Spacings and Structures of Metals and Alloys*. New York: Pergamon Press.

Perkins, R.A., Coons, W.C., and Radd, F.J. (1976). *Proc. Fall Meeting Electrochem. Soc.* PV76: 217.

Pippel, E., Woltersdorf, J., Grabke, H.J., and Strauss, R. (1995). *Steel Res.* 66: 217.

Pippel, E., Woltersdorf, J., and Schneider, R. (1998). *Mater. Corros.* 49: 309.

Pons, J. and Hugo, M. (1981). *Corrosion/81*, Paper No. 272. . Houston, TX: NACE International.

Prange, F.A. (1959). *Corrosion* 619t: 15.

Rahmel, A., Grabke, H.J., and Steinkusch, W. (1998). *Mater. Corros.* 49: 221.

Ramanarayanan, T.A. and Srolovitz, D.J. (1985). *J. Electrochem. Soc.: Solid-State Sci. Technol.* 132: 2268.

Ramanarayanan, T.A., Petkovic, R.A., Mumford, J.D., and Ozekin, A. (1998). *Mater. Corros.* 49: 226.

Ramanarayanan, T.A., Chun, C.M., and Munford, J.D. (2004). Metal dusting resistant alloys. US Patent 6, 737, 175.

Rocabois, P., Chatillon, C., and Bernard, C. (1996). *J. Am. Ceram. Soc.* 79: 1361.

Rouillard, F., Cabet, C., Wolski, K., and Pijolat, M. (2009). *Corros. Sci.* 51: 752.

Schnaas, A. and Grabke, H.J. (1978). *Werkst. Korros.* 29: 635.

Schneider, A. and Grabke, H.J. (2003). *Mater. Corros.* 54: 793.

Schneider, R., Pippel, E., Woltersdorf, J. et al. (1999). *Steel Res.* 7: 326.

Skarda, J. (1986). *Conference of Industrial Combustion Technologies* (29–30 April 1986), 279. Chicago, IL: ASM.
Smalley, R.E., Grosboll, M.P., Willis, P.A., and Kittrel, W.C. (2002). Process utilizing two zones for making single-wall carbon nanotubes. US Patent 0, 202, 682.
Steinkusch, W. (1979). *Werkst. Korros.* 30: 837.
Strauss, S. and Grabke, H.J. (1998). *Mater. Corros.* 49: 321.
Strauss, S., Krajak, R., and Grabke, H.J. (1999). *Mater. Corros.* 50: 622.
Sulonen, M.S. (1994). *Conference PTM'94, Solid-to-Solid Phase Transition, Minerals, Metals and Materials Society* (7–22 July 1994), 517. Farmington, PA: AIME.
Szakálos, P. (2002). A new corrosion mechanism for metal dusting on 304L stainless steel. SIMR report IM-2002-536.
Szakálos, P. (2003). *Mater. Corros.* 54: 752.
Szakálos, P., Pettersson, R., and Hertzman, S. (2002). *Corros. Sci.* 44: 2253.
Szakálos, P., Lundberg, M., and Pettersson, R. (2006). *Corros. Sci.* 48: 1679.
Thermodata (2002). INPG-CNRS, BP 66, 38402 Saint Martin d'Hères Cédex, France.
Thuillier, J.A. (1976). *Mater. Perform.* 15: 9.
Toh, C.H., Munroe, P.R., and Young, D.J. (2002). *Oxid. Met.* 58: 1.
Toh, C.H., Munroe, P.R., Young, D.J., and Foger, K. (2003). *Mater. High Temp.* 20: 129.
Van der Bruck, U. and Schillmoller, C.M. (1985). *Corrosion/85*, Paper No. 23. . Houston, TX: NACE International.
Wolf, I. and Grabke, H.J. (1985). *Solid State Commun.* 54: 5.
Wolfe, L.H. (1978). *Mater. Perform.* April: 38.
Wright, I.G. (ed.) (1983). *Corrosion in Fossil Fuel Systems*. Pennington, NJ: The Electrochemical Society.
Wuchina, E., Opila, E., Fergus, J. et al. (eds.) (2009). *High Temperature Corrosion and Materials Chemistry*. Pennington, NJ: The Electrochemical Society.
Yazawa, A. (1979). *Metall. Trans. B* 10B: 307.
Young, D.J. (2008). *High Temperature Oxidation and Corrosion of Metals*. Amsterdam: Elsevier.
Zeng, Z., Natesan, K., and Maroni, V.A. (2002). *Oxid. Met.* 58: 1.
Zhang, J., Schneider, A., and Inden, G. (2003). *Corros. Sci.* 45: 1329.
Zhang, J., Cole, D.M.I., and Young, D.J. (2005). *Mater. Corros.* 56: 756.

Further Reading

Colowell, J.A. and Rapp, R.A. (1986). *Metall. Trans. A* 17A: 1065.
Grabke, H.J. (1998). *Carburization: A High Temperature Corrosion Phenomenon: Parts I and II*. St. Louis, MO: Materials Technology Institute of the Chemical Process Industries, MTI Publications No 52, Elsevier Science, Amsterdam, Holland.
Grabke, H.J. and Schütze, M. (eds.) (2007). *Corrosion by Carbon and Nitrogen: Metal Dusting, Carburization and Nitridation*, EFC 41. Cambridge: Woodhead Publishing Ltd.
Grabke, H.J. and Spiegel, M. (eds.) (2007). *High Temperature Corrosion in Aggressive Environments*. Weinheim: Wiley-VCH.
Harston, J. (2007). *Corrosion in Refineries*, EFC 42. London: Woodhead Publishing.
Kane, R.H. (1986). *Process Industries Corrosion* (ed. B.J. Moniz and W.I. Pollock), 45. Houston, TX: NACE.
Khatak, H.S. and Raj, B. (eds.) (2002). *Corrosion of Austenitic Stainless Steels: Mechanism, Mitigation and Monitoring*. Cambridge: Woodhead Publishing Ltd.
Mitchell, D.R.G., Young, D.J., and Kleemann, W. (1998). *Mater. Corros.* 49: 231.
Tillack, D.J. and Guthrie, J.E. (1998). *Wrought and Cast Heat-Resistant Stainless Steels and Nickel Alloys for the Refining and Petrochemical Industries*, Technical Series No. 10, 071. Toronto: Nickel Development Institute.

Chapter 10

Nitridation

10.1 Introduction

Nitridation is a process that results in the formation of nitrides in a material. It results from exposure to reducing high temperature environments with high nitrogen activity. These environments can be relatively simple, containing N_2, NH_3–H_2O, and H_2–N_2–NH_3, or can be very complex, originating mixed corrosion processes of nitridation, oxidation, and carburization. Since nitrides are inherently hard, brittle phases, nitridation can produce local or widespread loss of material strength and possible metal wastage. A beneficial form of this phenomenon, *nitriding*, is a controlled metallurgical process whereby the nitrides are formed on the surface of a material to increase hardness and improve wear resistance (Pye 2003).

There have been a number of studies directed toward the effects of nitrogen on high temperature corrosion of metals (Aydin et al. 1980; Giggins and Pettit 1980; Grabke et al. 2003; Lai 2007; Pettit et al. 1969). Pettit et al. (1969) oxidized pure chromium in air at 1200 °C and found an external scale of chromia to be formed together with a layer of chromium nitride, Cr_2N, which formed immediately on top of the metal. This structure is consistent if the nitrogen is transported through the chromia layer to form nitride at the metal surface. Perkins (1971) observed similar results for a series of chromium alloys oxidized in air at 1150 °C. Most of the alloys also showed internal nitridation. It was found that alloy surface preparation could influence the rate of transport of nitrogen through the chromia scales.

When iron-, nickel-, and cobalt-based alloys containing chromium were oxidized in air at 900 °C for 25 hours (Giggins and Pettit 1980), only oxide scales were formed, and nitride formation was observed only on a Co-35 wt% Cr alloy. Presumably the inward diffusion of nitrogen through the chromia scale occurred in all cases, but only the Co-35 wt% Cr alloy has a high enough Cr activity to form the nitride. The presence of nitrogen did not alter the isothermal behavior of the alloys, but extensive internal precipitation occurred on cyclic oxidation of Ni-25 wt% Cr-6 wt% Al and Co-25 wt% Cr-6 wt% Al alloys. It appears that the inclusion of nitrogen into the metal substrate, with resulting nitride precipitation and, perhaps, embrittlement, may be the main causes of a detrimental effect of nitrogen.

Commercial processes where nitridation is encountered are those involving reducing process environments that contain ammonia or other reactive nitrogen-containing species. Examples of these processes are found in the production of nitric acid and nylon. Since these environments are typically reducing and consequently do not have high oxygen activity, Cr content is not important. The most effective alloying element for resistance to nitridation is Ni. Up to 600 °C, it is common to use stabilized stainless steels such as AISI 347. However, for more severe conditions involving higher temperatures, Ni- and Co-based alloys are employed. These include alloys B through B-3 and N that use large additions of Ni, Mo, and/or W to promote resistance to nitride formation. In some cases, alloying with Al to over 4% has been reported to improve corrosion performance.

In some chemical processes involving exposure to very high temperature and/or very severe nitriding conditions, nitrogen-based ceramic material may be an attractive alternative. Such materials include silicon nitride and other highly stable nitrogen-containing refractory materials. They are inherently more resistant to nitridation than metallic materials but are also less ductile and require special fabrication methods. These ceramic materials can also be applied as coatings to metal substrates in some cases to promote resistance to particular components (see also Chapter 18).

10.2 Nitridation Mechanisms

When a metal is exposed to nitrogen gas at high temperatures, nitridation proceeds according to

$$\frac{1}{2}\,N_2\,(\text{gas}) = [\text{N}]\,(\text{dissolved in metal}) \tag{10.1}$$

$$[\%\text{N}] = K\,p_{N_2}^{1/2} \tag{10.2}$$

High Temperature Corrosion: Fundamentals and Engineering, First Edition. César A. C. Sequeira.
© 2019 John Wiley & Sons, Inc. Published 2019 by John Wiley & Sons, Inc.

where K is the equilibrium constant and p_{N_2} is the partial pressure in the atmosphere. Increasing the nitrogen partial pressure (or nitrogen concentration) increases the thermodynamic potential for nitridation.

Under oxidation/nitridation conditions, nitrogen molecules permeate through cracks and pores and reach the metal underneath the oxide scales when the oxide scale is no longer protective. Nitridation then proceeds by dissociation of nitrogen molecules and absorption of nitrogen atoms by the metal following reaction (10.1). Nitridation often takes place in the metal at the vicinity of cracks developed under creep conditions in air or N_2-containing combustion atmospheres. In this case, oxides are often associated with the crack deformation in air. Oxidation consumes the oxygen molecules from air, which penetrates into the crack, thus depleting oxygen and increasing nitrogen potential (or concentration) around the crack. As a result, nitridation takes place in the vicinity of the creep crack.

At temperatures below 600 °C, and at high gas flow rates, the production of nitrogen is minimized, and the nitrogen solubility at the surface of iron is determined by

$$NH_3 = \frac{3}{2} H_2 + [N] \text{ (dissolved in Fe)} \tag{10.3}$$

$$[\%N] = K (p_{NH_3}/p_{H_2})^{3/2} \tag{10.4}$$

where K is the equilibrium constant and p_{NH_3} and p_{H_2} are partial pressures of NH_3 (ammonia) and H_2, respectively.

The nitriding potential is proportional to $(p_{NH_3}/p_{H_2})^{3/2}$. Increasing ammonia partial pressure (or concentration) in the atmosphere increases the thermodynamic potential for nitridation. When nitrogen in the metal exceeds its solubility limit, nitrides will then precipitate out.

Nitrogen solubility in the material is important in affecting the nitridation resistance of the material. The solubility of nitrogen in the material is also very affected by temperature. For example, the solubility of nitrogen in stainless steels largely increases with increasing temperature (e.g. for AISI 304, 0.125 wt% N_2 at 538 °C and 0.281 wt% N_2 at 981 °C). Alloys with higher nitrogen solubilities generally exhibit less resistance to nitridation attack.

Thermodynamic and kinetic considerations on the mechanisms of nitridation, like the brief ones reported above, follow the avenues used to discuss the mechanisms for oxidation, sulfidation, halogenation, and carburization. The interested reader can find further information on these aspects in articles by Cao and Norell (2013), Christ et al. (2003), Douglass (1991), Han and Young (2001), Jack and Jack (1973), Parascandola and Möller (2000), Tjokro and Young (1995), Welker et al. (1989), and more recently in the book by Schütze and Grabke (2007).

10.3 Nitridation in Industrial Media

Many different alloys in industrial media are normally inclined to nitridation attack when subjected to environments containing nitrogen; when the temperature is below 500 °C, usually nitrogen attack (nitrogen diffusion) is nominal, but at higher temperatures surface nitrides or internal nitrides are produced, damaging the material. This is common with stainless steels when they are subjected to ammonia-based conditions at high temperatures.

Although nitridation attack is more common in reducing environments, oxidation dominating in air, or oxidizing combustion environments, under certain conditions, alloys can suffer internal nitridation attack along with oxidation. Internal nitridation attack, when it occurs, can penetrate farther into the metal interior than oxidation, thus significantly affecting the creep-rupture behavior of the alloy by accelerating the creep crack growth. In an air oxidation study for two nickel-based alloys, Litz et al. (1989) observed internal titanium nitrides (needle shape) formed in front of internal aluminum oxides that formed underneath the external oxide scales. Lai (2007) observed internal aluminum nitrides (needle shape) that formed underneath the external oxide scale and internal oxides in alloy 601 exposed to a furnace oxidizing atmosphere for about five years at about 800 °C.

Several thermal cycling that causes cracking and spalling of oxide scales can also result in severe internal nitridation. Han and Young (2001) conducted cyclic oxidation tests by heating the specimens to 1100 °C (2010 °F) in still air for one hour, followed by cooling to room temperature for 15 minutes and then repeating the cycle again for 260 cycles. The alloys investigated were Ni-24–38% Cr-14–25% Al. The specimens suffered severe oxide scale spallation. The internal nitridation attack was found to be extensive, and the nitridation zone consisted of AlN beneath Cr_2O_3 and Al_2O_3, then AlN + Cr_2N, and then AlN in the deepest region.

During creep testing in air, extensive internal nitridation can develop in the vicinity of cracks. Brickner et al. (1965) found that types 302, 304, and 310 stainless steels showed significant nitridation after creep-rupture testing in air at 870 °C in less than 1000 hours. Acicular nitrides (believed to be chromium nitrides) in a Widmanstätten pattern were found to form extensively in the vicinity of microcracks. Extensive nitridation was confirmed by the chemical analysis of the tested specimens for nitrogen, which showed that the nitrogen content was increased from about 0.058% before testing to 0.30–0.53% after creep-rupture testing. Extensive internal nitrides were also observed in the vicinity of creep cracks in alloy 253MA (Fe–21Cr–11Ni) (Yu et al. 1987), alloy 800H (Guttmann and Burgel 1983; Welker et al. 1989), and alloy 800HT (Hoffman and Lai 2005).

When creep cracks initially develop at the metal surface during creep testing in air, oxidation occurs at the crack surface including the crack tip. The oxide scales formed on the crack surface become non-protective due to creep deformation, thus causing the oxygen potential to decrease significantly with concurrent increase in nitrogen potentials at the oxide–metal interface. As a result, nitrogen is absorbed by the metal and is diffused into the metal in the vicinity of cracks to form internal nitrides.

High temperature alloys that are exposed to a high velocity oxidizing combustion gas stream at high temperatures are susceptible to internal nitridation attack (Hoffman and Lai 2005; Lai 1994, 1995; Swaminathan and Lukezich 1994).

A model for oxidation/nitridation reactions for chromia formers (Ni–Cr and Fe–Ni–Cr alloys) in oxidizing combustion atmospheres was proposed by Lai (1994). This model, as schematically illustrated in Figure 10.1, involves the following reaction steps:

1. Chromium oxides form a protective scale initially on the alloy surface in oxidizing combustion atmospheres.
2. Cracks, pores, and other defects develop in the chromium oxide scales after thermal cycling and/or long-term exposure.
3. Chromium oxide scales become porous and non-protective with nickel oxides forming in Ni–Cr alloys and iron oxides forming iron-based alloys.
4. Both O_2 and N_2 molecules from the combustion gas stream permeate through the oxide scales and reach the metal underneath.
5. Oxidation of the metal surface results in lower oxygen potential with a concurrent increase in nitrogen potential.
6. Nitridation then occurs following the reaction – $\frac{1}{2}N_2$ (gas) = N (solution); the concentration of nitrogen absorbed in the metal is then proportional to the nitrogen potential (p_{N_2}) (Eq. (10.2)).
7. Nitrogen dissolves into the alloy and diffuses into the metal interior. Increasing nitrogen concentration in the alloy with increasing exposure times eventually leads to the formation of nitrides in the alloy once the solubility limits for CrN, Cr_2N, AlN, and/or TiN are exceeded.

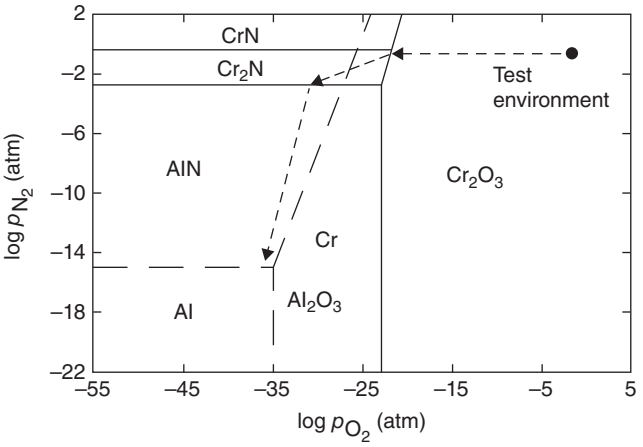


Figure 10.1 Schematic showing a model for internal nitridation attack in high temperature alloys in a simulated combustion environment (Lai 1994).

The N_2 or N_2–H_2 atmosphere is commonly used as a protective atmosphere in heat treating and sintering operations, and these atmospheres can also originate nitridation corrosion. For example, in this context, Barnes and Lai (1993) conducted an extensive nitridation study in pure nitrogen atmosphere for iron-, nickel-, and cobalt-based alloys at 1090 °C for 168 hours. Test results in terms of nitrogen absorption (mg cm^{-2}) and the depth of nitridation are summarized in Table 10.1. As a result of rapid nitridation kinetics under the test condition, nitridation attack penetrated through the thickness of the test specimen for many alloys. Due to different thicknesses for different alloys, the ranking of alloy performance in terms of nitridation depths became difficult for most alloys tested. (The thickness of the test specimen varied from alloy to alloy, because of the use of whatever sheet products that were available for the preparation of test specimens.) Iron-based alloys, the last group from RA330 to type 310SS, suffered the worst nitridation attack. Two cobalt-based alloys, alloys 188

Table 10.1 Nitrogen absorbed (mg cm^{-2}) and the average depth of internal nitridation for iron-, nickel-, and cobalt-based alloys after exposure in 100% N_2 at 1090 °C for 168 hours (Lai 1994)

Alloy	Nitrogen absorbed (mg cm^{-2})	Depth of internal nitridation (mm)
214	0.2	0.0
600	1.1	0.41
230	2.7	0.46
HR160	3.9	1.19
X	6.0	0.63
617	5.1	> 0.58
601	7.2	> 0.59
188	3.7	> 0.51
150	9.0	> 0.80
RA330	6.6	> 1.52
RA85H	8.5	> 1.44
556	9.0	> 1.52
HR120	9.6	> 0.86
253MA	10.0	> 1.50
800H	10.3	> 1.50
800HT	11.4	> 1.46
Type 310 SS	12.3	> 0.79

(Co–22Cr–22Ni–14W–La) and 150 (Co–27Cr–18Fe), exhibited poor resistance, with alloy 150 (high Cr and no Ni) showing extremely poor nitridation resistance similar to iron-based alloys. Nickel-based alloys were, in general, more resistant to nitridation attack than iron-based alloys.

Ammonia is a widely used nitriding gas for case hardening of steel material that is used at temperatures from 500 to 590 °C. The furnace units and components that are repeatedly subjected to such service conditions broadly receive brittle damages due to nitridation attack.

Carbonitriding, another way of case hardening, develops a surface layer of carbides and nitrides. The process is conducted at 700–900 °C in ammonia with inclusions of carbonaceous gases, for example, methane. Hence, the heat treat retort, fixtures, and other furnace systems are subjected to nitridation and carburization.

Engineering alloys in NH_3–H_2O environments were also found to suffer severe nitridation attack. For example, Grabke et al. (2003) investigated the corrosion behavior of a number of commercial alloys in the NH_3-30% H_2O gas mixture at 500 °C. Several interesting results were obtained from this investigation. One of the most interesting observations was that significant nitridation attack and severe intergranular cracking were observed in alloy 600 (Ni–16Cr–8Fe) after only 200 hours of exposure. Alloy 600 has been known to be one of the most nitridation-resistant alloys in ammonia environments, and the alloy has been widely used in ammonia plants. Alloy 800 (Fe–22Cr–32Ni–Al–Ti) was also found to suffer severe nitridation attack and intergranular cracking. For the ferritic stainless steel, Fe–18Cr (Sicromal), a combination of severe intergranular nitridation, cracking, and oxidation attack caused rapid disintegration of the alloy in 200 hours. An austenitic stainless steel (Fe–18Cr–9Ni) was also found to suffer severe nitridation attack. However, no cracking was observed in the austenitic stainless steel. They found formation of very fine CrN precipitates in these alloys. Grabke et al. (2003) pointed out that in these tests (low pressure), NH_3 should decompose largely to N_2 and H_2, while under high pressures, such as in the Kalina process, decomposition of NH_3 is considered to be negligible.

The production of ammonia is another source of nitridation attack. Ammonia is developed by combining nitrogen and hydrogen over a catalyst, normally at temperatures of 500–650 °C and pressures of about 800–1000 atm. The "heart" of the process is the *ammonia converter*, where hydrogen and nitrogen combine. Significant corrosion issues are associated with the converter and the internal components inside the converter. Cihal (1962) discussed the major corrosion problems – hydrogen attack and nitridation – for the ammonia converter. The converter usually consists of a vessel with a catalyst basket and an interchanger inside the vessel. Because of high pressure, high temperature hydrogen in the converter, early converters were constructed out of a thick-walled steel with an inner carbon steel lining and vent holes through the vessel wall. Thus, the inner carbon steel lining was the only part suffering hydrogen attack, while the main thick-walled vessel was unaffected by high pressure, high temperature hydrogen.

Hydrogen attack is the damage of steel by the reaction of hydrogen with cementite (Fe_3C) in steel to form methane gas (CH_4), resulting in the formation of microcracks and fissures as well as decarburization in steel. (Hydrogen attack is reviewed and discussed in Chapter 12.) Later designs of the converter allowed the cold inlet gas flowing along the vessel wall to keep the vessel cold, thus eliminating the potential hydrogen attack problem for the vessel.

Cihal indicated that the internal components made of carbon steel exhibited a short life due to hydrogen attack. Alloy steels containing chromium were more resistant to hydrogen attack but had suffered severe embrittlement problems due to nitridation attack.

An alloy steel containing a strong nitride former like titanium, such as alloy steel with 0.05% C, 2.9% W, and 0.54% Ti, exposed to the same converter environment under the same test conditions as 0.12C–5.6Cr–0.42Mo steel was found to show no cracking.

The nitridation resistance of various alloys was examined in ammonia converter and preheater lines (Barnes and Lai 1989; Jack 1973; Moran et al. 1961; Rorbo 1980; Schenck et al. 1963). Average outcomes are described in Table 10.2.

Corrosion rates were observed to be firmly based on ammonia content. Stainless steel 304 is attacked at the rate of 0.02–2.5 mm yr^{-1} with a 5–6% to 99% increase in concentration of ammonia at 500 °C. In ammonia converter containing 5–6% ammonia at 490–550 °C, the stainless steel grades tested are 304, 316, 309, 310, 321, and 330; they showed nominal nitridation attack at the rate of 0.03 mm yr^{-1} or less. For an ammonia line plant that

Table 10.2 Corrosion behavior of various alloys in an ammonia converter and ammonia line plant

	Corrosion rate (mm yr^{-1})	
Alloy	Ammonia converter	Ammonia line plant
SS 304	0.015 (0.59)	2.53 (99.5)
SS 316	0.012 (0.47)	>13.21 (520)
SS 321	0.012 (0.47)	—
SS 309	0.006 (0.23)	2.41 (95)
SS 310	0.004 (0.14)	—
SS 330	0.002 (0.02)	0.43 (17.1)
Inconel 600	—	—
Nichrome 80	—	—
Nickel	—	2.01 (79)

Table 10.3 Corrosion performance of various alloys/components in an ammonia converter

Component	Alloy	Temperature (°C)	Ammonia (%)	Operation times (yr)	Thickness of nitrides (μm [mils])	Average nitriding (μm yr^{-1} [mils yr^{-1}])
Lining	SS 304	525	15–20	4	1000 (39.4)	250 (9.8)
Plate, second bed	SS 304	475	15–20	7	100 (3.9)	14 (0.6)
Bolt	302	—	—	7	375 (14.8)	54 (2.1)
Wire mesh, second bed	Inconel 600	520	—	7	8 (0.3)	1 (0.04)
Perforated plate, first bed	SS 304	500	13	5	270 (10.6)	54 (2.1)
Inner shell, second bed	SS 304	440	8–10	5	45 (1.8)	9 (0.4)
Perforated plate, second bed	SS 304	440	8–10	5	60 (2.4)	12 (0.5)
Center tube, second bed	SS 304	485	16	5	440 (17.3)	88 (3.5)
Nuts, bottom	SS 304	480	16	5	260 (10.2)	52 (2)
Bolt, bottom	403	480	16	5	540 (21.3)	108 (4.3)
Wire mesh	Inconel 600	500	—	4	6 (0.2)	1.5 (0.06)
Thermowell	304	500	3.5	8	200 (7.9)	25 (1)

was subjected to 99% NH_3, stainless steel grades 309 and 316 suffered from intense nitridation attack with corrosion rates about 2.54 mm yr^{-1} or above. SS 304 offered better performance than 316.

Many components constructed from steel grade 304 subjected to temperatures of about 500 °C with ammonia concentrations of about 20% attained nominal nitridation attack at a rate of 0.01–0.1 mm yr^{-1}. A grade 304 described nominally higher corrosion rate of 0.25 mm yr^{-1} or 10 mils yr^{-1} due to elevated temperature limits. Inconel 600 offered better corrosion resistance as compared with stainless steel grades, showing nominal attack rates as described in Table 10.3.

McDowell Jr. (1962) reported field test results performed in a Casale converter (540 °C and 11 ksi) for one and three years. These results are summarized in Table 10.4. AISI 502 (5Cr steel) was extremely susceptible to nitridation attack, with more than 2.54 nm (0.1 in. or 100 mils) of nitridation depth in a year. Results showed a general trend of increased resistance to nitridation as nickel content in the alloy increased. One striking observation was that after three years of exposure, the alloys showed essentially similar depths of nitridation attack as they did after one year.

Verma et al. (1978) reported that an ammonia cracker unit used to develop nitrogen and hydrogen, failed after 100 hours of operation. The preheater tubes (operating at 350–400 °C) were made of Type 304SS, while the furnace tubes (operating at about 600 °C) were made of Type 310SS. Both suffered severe nitridation attack. To select an alternate alloy, nitriding tests were performed on various alloy samples at 600 °C in an environment consisting of 6–8% NH_3, 75.77–77.5 wt% N_2, and 16.25–16.5 wt% H_2. Test results are summarized in Table 10.5. The alloys that performed well include types 347, 316, 321, SLX-254, and HV-9A. Type 347 was the best performer, having a linearly extrapolated penetration rate of about 0.13 mm yr^{-1} (5 mpy). Alloy 800, which contains more nickel than any of the above stainless steels, did not perform as well. Furthermore, type 304 was found to suffer attack of 2 orders of magnitude higher than that of type 316L. The results also showed that titanium suffered severe nitridation attack, which resulted in severe sample cracking. Both carbon steel and 1Cr–0.5Mo steel suffered decarburization after only 50 hours.

Table 10.4 Depth of nitridation for various alloys after one and three years in a Casale ammonia converter (McDowell 1962)

Alloy	Nitridation depth (mm [mils])	
	1 yr	3 yr
502 (5Cr steel)	2.88 (113.2)	Completely nitrided
446	1.06 (41.7)	1.15 (45.3)
304	1.08 (42.7)	1.12 (44.0)
316	0.46 (18.2)	0.48 (18.7)
321	0.46 (18.3)	0.60 (23.6)
347	0.49 (19.2)	0.45 (17.6)
309	0.24 (9.5)	0.24 (9.6)
310	0.22 (8.8)	0.23 (9.2)
800	0.14 (5.4)	0.13 (5.3)
804 (30Cr–42Ni)	0.03 (1.2)	0.03 (1.2)
600	0.16 (6.4)	0.16 (6.4)
Nickel 200	None	None

The pollution of the atmosphere by nitrogen oxides has been a subject of growing concern during the past decade. Photochemical smog, to which nitrogen oxides contribute and which causes respiratory and eye damage, was first recognized as a problem and characterized in Los Angeles and Tokyo and has led to control of emissions

Table 10.5 Nitridation attack of various alloys in an ammonia-bearing environment at 600 °C for indicated exposure times (Verma et al. 1978)

Alloy	Penetration depth of nitridation attack (mm [mils])					
	50 h	100 h	300 h	600 h	1000 h	1500 h
Carbon steel	Decarb.	Decarb.	Decarb.	Decarb.	Decarb.	Decarb.
1Cr–0.5Mo steel	Decarb.	Decarb.	0.033 (1.3)	0.033 (1.3)	0.033 (1.3)	0.3 (11.8)
Titanium	0.0066 (0.3)	0.0133 (0.5)	0.233 (9.2)	0.266 (10.5)	Cracked[a]	Cracked[a]
304	—	0.013 (0.5)	0.013 (0.5)	0.03 (1.2)	0.06 (2.4)	4.2 (165)
316L	0.02 (0.8)	0.02 (0.8)	0.02 (0.8)	0.03 (1.2)	0.04 (1.6)	0.04 (1.6)
329	—	0.066 (2.6)	0.10 (3.9)	0.10 (3.9)	0.20 (7.9)	0.40 (15.7)
310	—	0.03 (1.2)	0.13 (5.1)	0.16 (6.3)	0.33 (13.0)	0.40 (15.7)
321	0.013 (0.5)	0.013 (0.5)	0.013 (0.5)	0.016 (0.6)	0.06 (2.4)	0.06 (2.4)
347	—	0.013 (0.5)	0.013 (0.5)	0.013 (0.5)	0.02 (0.8)	0.02 (0.8)
SLX-254[b]	0.013 (0.5)	0.013 (0.5)	0.026 (1.0)	0.026 (1.0)	0.06 (2.4)	0.06 (2.4)
HV-9A[c]	0.01 (0.4)	0.10 (3.9)	0.10 (3.9)	0.10 (3.9)	0.10 (3.9)	0.10 (3.9)
800	0.02 (0.8)	0.10 (3.9)	0.20 (7.9)	—	0.20 (7.9)	0.20 (7.9)

Decarb: decarburized.

[a]Nitridation through thickness.

[b]SLX-254: Fe–19.7Cr–24.5Ni–4.35Mo–1.43Cu.

[c]HV-9A: Fe–21.2Cr–24.6Ni–3.8Mo–1.5Cu.

from motor vehicles in the United States, Japan, and Australia. Vehicle emissions legislation, requiring tight control of nitrogen oxides, has been proposed recently in all European countries. In the European context, the major perceived problem is that of "acid rain," which has been implicated in vegetation damage, acidification of freshwater lakes and rivers, corrosion, and the weathering of buildings. Nitrogen oxides can also be a problem in the food industry where they are formed in direct fired drying and baking operations. The interaction of nitrogen oxides with proteins and foodstuffs can cause the formation of *N*-nitrosamines that are hepatotoxic and carcinogenic. To avoid this, the food industry now widely uses indirect methods of heating even though it is generally accepted that these can increase the energy consumption by as much as 15%.

Man-made emissions of nitrogen oxides can be divided conveniently into those arising from stationary sources and those from mobile sources, where the primary noncombustion source is nitric acid manufacture.

Various approaches to the problem of nitrogen oxide control may be envisaged; these are:

1. Fuel switching.
2. Fuel pretreatment.
3. Combustion (or chemical process) modification.
4. Flue (or tail) gas denitrification.

Gas denitrification from a combustion or chemical process includes *selective catalytic reduction* (SCR), noncatalytic reduction, wet chemical scrubbing, adsorption on a solid, and electron beam irradiation (Siddiqi and Tenini 1981).

Combustion modification is the first approach in controlling nitrogen oxides from combustion processes, in view of its low cost, this being put at only 20–33% of the cost of installing SCR equipment. Nevertheless, if high levels of nitrogen oxide reduction are required to meet stringent legislation, as existed in many countries, then it also becomes necessary to apply flue gas denitrification. SCR has been shown to be the most cost-effective option available. For combined nitrogen oxide and sulfur oxide control in modern power plants, it is significantly cheaper to apply SCR combined with wet flue gas desulfurization than it is to use wet methods for controlling both pollutants simultaneously.

Table 10.6 shows possible mechanisms for the catalytic control of nitrogen oxide emissions; these can be nonselective catalytic reduction (NSCR), using hydrogen, carbon monoxide, or hydrocarbons as the reducing agent, or SCR employing urea. A schematic of the SCR system is shown in Figure 10.2.

Table 10.6 Reaction mechanisms of the catalytic reduction of nitrogen oxides

$$NO_2 + R \xrightarrow{\text{catalyst}} RO + NO$$
$$2NO + O_2 \xrightarrow{\text{catalyst}} 2NO_2$$
$$NO + R \xrightarrow{\text{catalyst}} RO + N_2 \text{ or } N_2O$$
$$NO_2 + NH_2 \xrightarrow{\text{catalyst}} NH_4NO_{2/3}$$
$$NH_4NO_{2/3} \xrightarrow{\text{catalyst}} N_2 \text{ or } N_2O + H_2O$$

R = hydrocarbon, hydrogen, carbon monoxide.

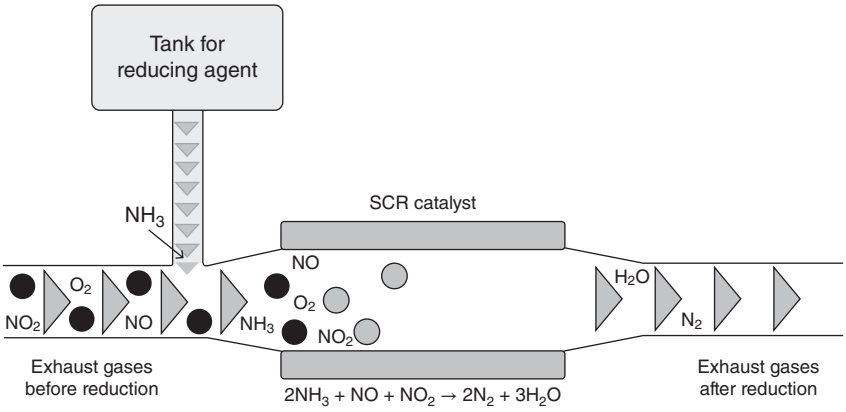


Figure 10.2 Model of the SCR system.

Urea is a solid compound for ammonia, which is the reducing agent that directly reacts with NO_x on a catalyst surface.

For applications in mobile diesel engines, the direct use of ammonia is not possible since storage and transport would be complicated and dangerous. The problem was solved by using an aqueous urea solution (32.5% by weight) stored in a tank on the outside of the truck beside the diesel tank. Firstly, the urea solution is pumped into a dosing unit and then sprayed through a nozzle into the exhaust flow, just before the muffler. The temperatures inside the exhaust flow can reach 250–600 °C depending on the engine workload. Below 250 °C the catalyst does not work. For this reason, no urea is used as the engine heats up.

When the urea solution is sprayed into the exhaust flow, water is vaporized and the urea starts to decompose. It is generally accepted that urea decomposes in two different steps. Firstly, there is the thermolysis of the urea molecules into ammonia and isocyanic acid:

$$(NH_2)_2CO \rightarrow NH_3 + HCNO \tag{10.5}$$

which occurs within the exhaust pipe, before the catalyst, and then there is the hydrolysis of isocyanic acid, which occurs on the catalyst surface and leads to the formation of ammonia and carbon dioxide:

$$HCNO + H_2O \rightarrow NH_3 + CO_2 \tag{10.6}$$

According to the two reactions above, each mole of urea generates 2 mol of ammonia, which directly react with NO or NO_2 on the catalytic surface. The main SCR reactions between ammonia and NO_x are shown below (Fang and Da Costa, 2003):

$$4NO + 4NH_3 + O_2 \rightarrow 4N_2 + 6H_2O \text{ (standard SCR)} \tag{10.7}$$

$$2NO_2 + 4NH_3 + O_2 \rightarrow 3N_2 + 6H_2O \text{ (standard SCR)} \tag{10.8}$$

$$NO + NO_2 + 2NH_3 \rightarrow 2N_2 + 3H_2O \text{ (fast SCR)} \tag{10.9}$$

The presence of O_2 molecules in the standard SCR reaction is needed to reoxidize the catalyst surface. The NO_2 molecules play a similar role in the fast SCR reaction. The faster reaction suggests that NO_2 can reoxidize the catalyst faster than O_2.

In addition to the desirable reactions that occur in a SCR system, there are several secondary reactions that are undesirable:

$$2SO_2 + O_2 \rightarrow 2SO_3 \tag{10.10}$$

$$2NH_3 + SO_3 + H_2O \rightarrow (NH_4)_2\,SO_4 \tag{10.11}$$

$$NH_3 + SO_3 + H_2O \rightarrow NH_4HSO_4 \tag{10.12}$$

These reactions do not lead to a lowering of the NO_x content in the exhaust gases and are also detrimental for the system. For example, the oxidation of NH_3 with oxygen should be removed, since it not only consumes the ammonia required for SCR process but also generates NO_x. Other undesirable reactions are sulfation and nitration of NH_3. Ammonia can react with SO_2 or NO_2 when there is water and the temperature is low. Anyway, the concentration of SO_2 and NO_2 in exhaust gases is much smaller than urea concentration, so the loss of ammonia due to the formation of NH_4NO_3 and $(NH_4)_2SO_4$ can be ignored. The major losses of urea are due to the polymerization reactions that occur during urea decomposition and can lead to the formation of polymers such as polymeric melamine (Fang and Da Costa, 2003).

The undesirable reaction for urea, instead of either anhydrous or aqueous ammonia, is

$$4NO + 2(NH_2)_2CO + O_2 \rightarrow 4N_2 + 4H_2O + 2CO_2 \tag{10.13}$$

The ideal reaction has an optimal temperature range between 630 and 720 K but can operate from 500 to 720 K with longer residence times. The minimum effective temperature depends on the various fuels, gas constituents, and catalyst geometry. Other possible reductants include cyanuric acid and ammonium sulfate.

Briefly, it can be said that, ideally, if the exhaust temperature is sufficiently high and the AdBlue injector (32.5% aqueous urea solution) and SCR system geometry have been well designed to have fast AdBlue evaporation rate and sufficiently long exhaust gas residence time between the AdBlue injector and the SCR catalyst, 100% urea to ammonia conversion can be expected at the very beginning part of the SCR catalyst.

The use of urea within the diesel exhaust aftertreatment systems, in addition to the high temperatures reached, generates a particular detrimental environment from the corrosion point of view. Although the urea has been used for some years in stationary combustion plants, not many investigations regarding the influence of urea on corrosion in diesel exhaust system can be found. The majority of articles related with urea corrosion refer to the fertilizer production industry. Although the operating conditions in these plants are far from those in exhaust aftertreatment systems, a quick survey could be in any case useful to understand the corrosion behavior in these environments.

Urea is produced at high pressure and at temperatures in the range of 200 °C (Demuzere, 1991). The two basic raw materials used are liquid ammonia (NH_3) and gaseous carbon dioxide (CO_2). The reaction takes place in two steps, since carbonic acid does not form a stable ammonium salt. The reaction between ammonia and CO_2 has to be carried out under high temperature and pressure to form the intermediate product ammonium carbamate. The compound that is the most corrosive species is formed only at high pressures, so it is not present in the exhaust system.

Nowadays, the main market that lies in fitting SCR units is becoming larger and larger, and the need to limit nitrogen oxide emissions is expected to become widespread in the future. Clearly, the high temperatures in the exhaust system, together with the products of the reduction reactions, produce a particularly corrosive environment, strongly detrimental for the corrosion resistance of the materials used. The demand for improved materials, capable of providing adequate resistance to nitridation and high temperature corrosion in general, has led to the examination of various stainless steels, namely, austenitic and ferritic stainless steels that have better engineering properties than austenitic grades and are typically less expensive because of the very low nickel content. In this context, we will be focused on the work of Cao and Norell (2013) that studied the role of the substitutional uptake of N in connection with corrosion of the 304L and 904L austenitic stainless steels at the urea injection in diesel exhaust systems. Four alloy coupons were nitrided, two of them with high N content and the other two with low N content; the nitrogen was induced in the steels by plasma nitriding (Fewell et al. 2000; Nii and Nishimoto 2012; Peng et al. 2010). Table 10.7 lists the chemical compositions of the two alloys studied. The samples nitrided with low N content were considered as-received samples. The samples were then annealed and oxidized to see how the distribution of N develops in the structure and how this affects the oxidation.

Cao and Norell found that plasma nitriding at about 400 °C deteriorates the oxidation resistance of both the austenitic steels studied in the temperature range 450–600 °C. As can be seen in Table 10.8, the deterioration was very marked for the 304L. The oxide scales were 70–100 times thicker than on the as-received 304L. Also, the nitrided 904L was more oxidized than the as-received 904L, but the oxide scales were only two to five times thicker. The X-ray diffraction (XRD) results showed the formation of expanded austenite phase on the surface of both the as-nitrided alloys. Precipitation of chromium nitrides was not detected on the as-nitrided samples.

Table 10.7 Chemical composition of AISI 304L and 904L austenitic stainless steels

	Fe	C	Mn	Cr	Ni	Mo	Si	S	P	N	Cu	Ti
304L	Balance	0.019	1.63	18.25	8.05	0.43	0.28	0.001	0.028	0.072	0.33	0
904L	Balance	0.011	1.62	20.3	24.26	4.37	0.33	0.001	0.023	0.054	1.41	0.007

Table 10.8 Oxide thicknesses for as-received and nitrided austenitic 304L and 904L oxidized for 24 hours in humid air containing 10% H_2O

	Temperature		450 °C	600 °C	450 °C	500 °C	550 °C	600 °C
Time (h)	Nitriding		None	None	X	X	X	X
24	304L	XPS/AES (nm)	28	37	2500	4500	470/4000	560/2600
	904L	XPS/AES (nm)	32	50	150	210	135	110

Regarding the austenitic 304L, there is formation of both thin and thick oxide layers at 550 and 600 °C (Cao and Norell 2013).

X-ray photoelectron spectroscopy (XPS) and Auger electron spectroscopy (AES) depth profiles showed the general formation of an outer Fe oxide layer and an inner (Fe, Cr) oxide layer on all as-received and nitrided samples, oxidized for 24 hours, except for the 904L exposed at 500 °C. In this case, no clear enrichment of chromium was found. Enrichment in manganese was observed in the outer oxide layer for both the as-received and nitrided samples of 304L oxidized for 24 hours at 600 °C. The XRD analyses of the nitrided 304L samples oxidized for 24 and 168 hours showed formation of mostly hematite and spinel phase (possibly as magnetite) at all temperatures. Only hematite was detected for the nitrided 904L samples exposed for 24 and 168 hours.

Precipitation of CrN was detected on the 304L samples at all the exposure temperatures. The XRD patterns of the samples showed the presence of a weak and broad CrN peak at 450 °C. The CrN peaks became narrower and more intense by increasing temperature, consistent with the increase of nitride precipitation and grain size. Regarding the 904L, the most intense CrN peak was found at 500 °C, whereas no CrN peaks were detected at 450 and 600 °C.

The decomposition of the S-phase was observed for both 304L and 904L samples during oxidation at higher temperatures. At higher temperatures and longer times of exposure, the diffraction peaks of the S-phase were shifted to higher 2θ angles and partially merged into the austenite peak. In 304L, formation of body-centered cubic (BCC) phase during oxidation was observed. At 500–600 °C, the S-phase was almost completely transformed to BCC phase, face-centered cubic (FCC) phase, and CrN. For 904L, formation of BCC phase was not detected. It should be noted that plasma nitriding at low temperatures (about 400 °C) produces a single phase that is known as the S-phase or expanded austenite supersaturated with N.

The austenitic stainless steels are generally more used for applications at high temperatures since they are characterized by superior oxidation resistance. The addition of nickel in these grades transforms the iron from a ferritic to an austenitic phase, which has FCC structure and is more stable at high temperatures. It has also been suggested that nickel influences the adhesion and mechanical properties of the scale and retards the breakaway transformation (Sedriks 1979).

Looking at the chemical composition of the two alloys (Table 10.7), it can be seen that the alloying element content is higher for the 904L. Particularly, chromium, nickel, and molybdenum contents are higher in this alloy. Consequently, the 904L shows an improved oxidation resistance compared with the other alloy analyzed. Also, the detrimental effect of the nitridation on oxidation is less serious for 904L than for 304L. Both nickel and molybdenum contents stabilize the S-phase and decrease the Cr nitride precipitation during the exposures. Although the 904L shows the best oxidation resistance in the temperature range 450–600 °C, the high cost limits its use. The lower alloying element content in austenitic 304L stainless steel compared with 904L austenitic grade makes this alloy cheaper and more interesting for the application in exhaust aftertreatment systems. The oxide scales formed on the 304L are about 70–100 times thicker than on as-received 304L. The strong effect of nitridation on the oxidation of austenitic 304L can be explained considering both the formation of expanded phases supersaturated of nitrogen and the further precipitation of Cr nitrides during the exposures. These two factors reduce the activity of chromium, preventing its diffusion from the alloy toward the surface and consequently the formation and maintenance of protective oxides (Gontijo et al. 2010a,b; Sung et al. 2007; Yun-tao et al. 2008). For 304L grade, the oxides formed are less homogeneous in thickness, and areas of thin and thick oxides are observed in this alloy.

AES/XPS depth profiles on nitride 304L show a general deterioration of the oxidation resistance at low temperatures. The thickest oxide scale is observed for the 304L alloy after exposure at 500 °C, which is about 4.5 μm. For the 304L, the improved oxidation resistance is observed at the highest exposure temperature. At this temperature, the values obtained for thin and thick oxides are 0.56 and 2.6 μm, respectively (AES depth profiles).

It is then concluded by Cao and Norell (2013) that:

- The surface layers on plasma-nitrided alloys 304L and 904L were dominated by expanded austenite supersaturated with N or S-phase.
- The oxides formed at 450–600 °C on nitrided samples of 304L were about 70–100 times thicker than on as-received material, and those on 904L were about 2–5 times thicker. Thus, N was detrimental for the oxidation properties.
- It is proposed that short range ordering between Cr and N in the S-phase reduces the activity of Cr and hinders the formation of a protective Cr-rich oxide.
- For 304L, the surface fraction of thick oxides decreases with increasing temperatures, consistent with an improved corrosion resistance. In parallel, CrN and BCC are formed. Though the nitrides may decrease the activity of Cr, the high diffusivity in BCC is suggested to contribute to the improved corrosion resistance at higher temperature.
- For 904L, the S-phase is more stable and the corrosion less severe due to the alloying content. At 500 °C, formation of CrN is proposed to enhance the oxidation as compared with higher and lower temperatures.

Most studies regarding the nitriding of stainless steels have been carried out with austenitic stainless steel

(Gil et al. 2006; Liang 2003; Samandi et al. 1993). But also a few have focused on ferritic and austenitic stainless steels, as briefly reviewed here.

Gontijo et al. (2010a,2010b) studied the S-phases formed on plasma-nitrided AISI 304L and AISI 316L austenitic stainless steels and AISI 409L ferritic stainless steel. The alloys were plasma nitrided between 350 and 500 °C. The presence of similar S-phase layers was observed in both the austenitic (BCC) and ferritic (FCC) stainless steels. The 409L series showed the formation of a layer with high amount of nitrogen, designed in the study as expended ferrite or ferritic S^{α}-phase. The strain state was higher for the expanded ferritic phase in comparison with the expanded austenitic phases.

Sung et al. (2007) studied the phase changes of the AISI 430 ferritic stainless steel after high temperature gas nitriding. The gas nitriding was performed at 1050–1100 °C. The relatively high chromium content of the ferritic 430 stainless steel enables the nitrogen to permeate into the interior. This effect is due to strong affinity between nitrogen and chromium. The surface layer was changed into martensite plus ferrite and Cr_2N at 1050 °C, while martensite plus a rectangular-type retained austenite appeared at 1100 °C by high temperature gas nitriding. The high temperature gas nitriding improved the wet corrosion resistance, while the precipitation of Cr_2N at the outmost surface area deteriorated the corrosion resistance.

Corengia et al. (2007) investigated the microstructure and corrosion behavior of DC-pulsed plasma-nitrided AISI 410 martensitic stainless steel. The DC-pulsed plasma nitriding was carried out at 350 and 500 °C. At the lower nitriding temperatures, α-Fe and a small amount of γ'-Fe_4N are detected on the surface. CrN nitrides were not detected since the CrN precipitation takes place at higher temperature. The shift and broadening of α-Fe peaks, observed on the XRD patterns, were associated with the formation of a nitrogen oversaturated phase, called expanded martensite. The presence of these expanded phases, in addition to the small Fe_4N nitride precipitates, produces the high surface hardness observed. At higher DC-pulsed plasma nitriding temperatures, the nitrogen solid solution decomposed into α and CrN. The precipitation of CrN depletes chromium of the expanded phase and deteriorates the corrosion resistance of the alloy. The plasma-nitrided AISI 410 was also investigated by Li and Bell (2007). After plasma nitriding at 450 °C for 20 hours, the surface consisted of mainly γ'-Fe_4N and ϵ-$Fe_{2-3}N$ iron nitrides. CrN precipitation was observed on the XRD spectrum. The formation of expanded martensitic nitrogen solid solution into the surface was also suggested in this study. However, it could not be confirmed since the outmost nitrided layer was too thick to allow the penetration of the X-ray through to the substrate. The cross-sectional microstructure of the plasma treated 410 showed the formation of two distinct layers. The outer layer was considered to be a "nitrided" case rich in nitrogen and the inner one a "carburized" layer rich in carbon.

In summary, nitridation behavior of metals and alloys in nitrogen environments is analyzed. Internal and surface nitridation attack can occur in air and oxidizing combustion environments. In NH_3 and N_2 environments, alloys behave slightly differently under nitridation attack. Industrial cases as those concerning nitriding of stainless steels and nitridation/oxidation in urea SCR systems are presented.

10.4 Questions and Problems

10.1 Is nitridation a degradation phenomenon alone? Under what conditions is nitridation a corrosion protection method?

10.2 What is nitridation potential?

10.3 How does one determine nitridation potential from Ellingham diagrams?

10.4 How can equilibrium pressure such as 10^{-24} Torr be achieved for nitridation of some metals at a particular temperature?

10.5 Using the Ellingham diagram, find the equilibrium partial pressure of nitrogen for the nitridation of Cr at 1000 °C.

10.6 For the above problem, what ratio of NH_3/H_2O or NH_3/H_2 is required to achieve such a low partial pressure?

10.7 From the Ellingham diagram, calculate the free energy of NO_2 reduction with ammonia.

10.8 Under what conditions are linear kinetics followed by nitridation of some metals?

10.9 Why is the parabolic rate considered to be followed by many industrial metals and alloys in a carbonitridation environment?

10.10 What is the principle of an electromagnetic balance? How does it measure continuous weight change with time?

10.11 Why is the carbonitridation test, carried out under cyclic conditions, considered more stringent than the corresponding test under isothermal conditions?

10.12 Why do double log plots not always give the correct value of the exponent n in equation $x = kt^n$? How then is the correct law confirmed?

10.13 On what principle is the interference color technique to measure scale thickness during oxidation/nitridation based? How thick should the scale layer be to be measured using this technique?

10.14 Why does an oxide spall? And a nitride?

10.15 What is the Pilling–Bedworth (PBR) ratio? PBR for K_2O is 0.45 – how will this metal behave under normal oxidizing conditions?

10.16 How do thermal stresses influence scale spallation? What is the most important factor to avoid spalling of an oxide scale? And of a nitride scale?

10.17 Enumerate the various stress-generating mechanisms during a metal oxide growth. Which of these factors is most important in your opinion? Is it the same during a metal nitride growth?

10.18 A metal is oxidizing by outward diffusion of cations; explain on which surface (concave or convex) would the spalling be more severe. Is it the same during metal nitriding?

10.19 What is Stoney's method of measuring stress on growing oxide/nitride scales? How would you predict whether these stresses are tensile or compressive?

10.20 How is scale spallation detected?

10.21 What is the principle of the acoustic emission method? How does it detect and identify microcracking and spalling?

10.22 How much stress will be generated when a steel tube, which was at 900 °C for several days, is suddenly cooled to 300 °C due to sudden power break? On removal, it was found that the oxide thickness was 100 μm, while the initial tube thickness was 1.5 mm. The coefficients of thermal expansion of the oxide and metal are 10 and $11.5 \times 10^{-6}\,k^{-1}$, respectively, and Young's moduli are 193 and 163 GPa, respectively.

10.23 What is the main condition for an element in the periodic table to act as an active element to enhance the spalling resistance of oxide/nitride scales?

10.24 What are the various mechanisms proposed for the active element effect to improve the oxidation behavior? And for the nitridation behavior?

10.25 How is the active element effect on chromia-forming alloys different from that on alumina-forming alloys?

10.26 What is the sulfur effect? And the nitrogen effect?

10.27 In what way do active elements improve the nitridation behavior?

10.28 What are the various ways by which active elements are added to the metal?

10.29 An alumina (Al_2O_3) crucible contains molten copper and oxygen (O_2) at 600 °C. Determine if the crucible will corrode; if so, calculate the oxygen pressure. If, instead of oxygen, the crucible contains nitrogen, would it deteriorate?

10.30 In the case of thick scale formation at high temperature, the Pilling–Bedworth theory may have a limited applicability. Explain why this may be the case.

10.31 If the protective nature of an oxide film at room temperature is lost at relatively high temperatures, explain the sequence of the oxide thickening process. Would nitride film be protective, either at room or high temperature?

10.32 Calculate (a) the equilibrium constant K and (b) the dissociation nitride pressure p_{N_2} for the nitridation of aluminum at 1100 °C.

10.33 A chromium bar is exposed to oxygen gas at 900 °C. Calculate (a) the oxygen partial pressure and (b) the oxygen activity. What are the nitrogen partial pressure and the nitrogen activity if, instead of oxygen gas, the bar is exposed to nitrogen gas?

References

Aydin, I., Bühler, H.E., and Rahmel, A. (1980). *Werkst. Korros.* 31: 675.

Barnes, J.J. and Lai, G.Y. (1989). Corrosion and particle erosion at high temperatures. In: *Proceedings of the TMS-ASM Symposium* (ed. V. Srinivasan and K. Vedula), 167. London: The Minerals, Metals and Materials Society.

Barnes, J.J. and Lai, G.Y. (1993). *J. Phys. III* 3: 167.

Brickner, K.G., Ratz, G.A., and Domagala, R.F. (1965). *Advances in the Technology of Stainless Steels and Related Alloys*, vol. 369, 99. ASTM STP.

Cao, Y. and Norell, M. (2013). *Oxid. Met.* 80: 479.

Christ, H.J., Chang, S.Y., and Krupp, U. (2003). *Mater. Corros.* 54: 887.

Corengia, P., Ybarra, G., Moina, C. et al. (2007). *Surf. Coat. Technol.* 23: 355.

Demuzere, R. (1991). High alloying welding products for the urea synthesis process, *Stainless Steel Europe*, 3 (9): 55–62.

Douglass, D.L. (1991). *JOM* 43: 74.

Fang, H.L. and Da Costa, H.F. (2003). *Appl. Catal.* 46: 17.

Fewell, M.P., Priest, J.M., Baldwin, M.J. et al. (2000). *Surf. Coat. Technol.* 131: 284.

Giggins, C.S. and Pettit, F.S. (1980). *Oxid. Met.* 14: 363.

Gil, L., Brühl, S., Jiménez, L. et al. (2006). *Surf. Coat. Technol.* 201: 4424.

Gontijo, L.C., Machado, R., Castelletti, L.C. et al. (2010a). *Surf. Eng.* 26: 265.

Gontijo, L.C., Machado, R., Castelletti, L.C. et al. (2010b). *Mater. Sci. Forum* 638–642: 775.

Grabke, H.J., Strauss, S., and Vogel, D. (2003). *Mater. Corros.* 54: 895.

Guttmann, V. and Burgel, R. (1983). *Met. Sci.* 17: 549.

Han, S. and Young, D.J. (2001). *Oxid. Met.* 55: 223.

Hoffman, J.J. and Lai, G.Y. (2005). *Corrosion/2005* , Paper No. 5402. Houston, TX: NACE International.

Jack, K.H. (1973). Physics and chemistry of carbides and nitrides in stainless steels. In: *High Temperature Gas-Metal Reactions in Mixed Environments* (ed. S.A. Jansson and Z.A. Foroulis), 182. The Metallurgical Society of AIME.

Jack, D.H. and Jack, K.H. (1973). *Mater. Sci. Eng., A* 11: 1.

Lai, G.Y. (1994). Nitridation of several combustor alloys in a simulated gas turbine combustion environment. In: *Advanced Materials and Coatings for Combustion Turbines* . Proceedings of the ASM 1993 Materials Congress Materials Week, Pittsburgh, PA (October 1993) (ed. V.P. Swaminathan and N.S. Cheruvu), 113. Materials Park, OH: ASM International.

Lai, G.Y. (1995). *Oxidation/nitridation reactions in combustion atmospheres*, Unpublished results. Haynes International, Inc.

Lai, G.Y. (2007). *High-Temperature Corrosion and Materials Applications*. Materials Park, OH: ASM International.

Li, C.X. and Bell, T. (2007). *Mater. Sci. Technol.* 23: 355.

Liang, W. (2003). *Appl. Surf. Sci.* 211: 308.

Litz, J., Rahmel, A., Schorr, M., and Weiss, J. (1989). *Oxid. Met.* 32: 167.

McDowell, D.W. Jr. (1962). *Mater. Protect.* 1: 18.

Moran, J.J., Mihalisin, J.R., and Skinner, E.N. (1961). *Corrosion* 17: 191t.

Nii, H. and Nishimoto, A. (2012). *J. Phys. Conf. Ser.* 379: 012052.

Parascandola, S. and Möller, W. (2000). *Appl. Phys. Lett.* 76: 2194.

Peng, D.Q., Kim, T.H., Chung, J.H., and Park, J.K. (2010). *Appl. Surf. Sci.* 256: 7522.

Perkins R.A. (1971). Alloying of chromium to resist nitridation. NASA Report NASA-CR-72892.

Pettit, F.S., Goebel, J.A., and Goward, G.W. (1969). *Corros. Sci.* 9: 903.

Pye, D. (2003). *Practical Nitriding and Ferritic Nitrocarburizing*. Materials Park, OH: ASM International.

Rorbo, K. (1980). *Environmental Degradation of High Temperature Materials*, Series 3, No. 13, , vol. 2, 147. London: The Institution of Metallurgists.

Samandi, M., Shedden, B.A., and Smith, D.I. (1993). *Surf. Coat. Technol.* 59: 261.
Schenck, H., Frohberg, M.G., and Reinders, F. (1963). *Stahl Eisen.* 83: 93.
Schütze, M. and Grabke, H.J. (2007). *Corrosion by Carbon and Nitrogen; Metal Dusting, Carburization and Nitridation*, EFC 41. . Cambridge: Woodhead Publishing Ltd.
Sedriks, A.J. (1979). *Corrosion of Stainless Steels*. London: Wiley.
Siddiqi, A.A. and Tenini, J.W. (1981). *Hydrocarbon Process.* 60: 115.
Sung, J.H., Kong, J.H., Yoo, D.K. et al. (2007). *Mater. Sci. Eng.* 489: 38.
Swaminathan, V.P. and Lukezich, S.J. (1994). Degradation of transition duct alloys in gas turbines. In: *Advanced Materials and Coatings for Combustion Turbines* . Proceedings of the ASM 1993 Materials Congress Materials Week (Pittsburgh, PA), October 1993 (ed. V.P. Swaminathan and N.S. Cheruvu), 99. Materials Park, OH: ASM International.
Tjokro, K. and Young, D.J. (1995). *Oxid. Met.* 44: 453.
Verma, K.M., Ghosh, H., and Rai, J.S. (1978). *Br. Corros. J.* 13: 173.
Welker, M., Rahmel, A., and Schütze, M. (1989). *Metall. Trans. A* 20A: 1541.
Yu, M., Sandstrom, R., Lethinen, B., and Westman, C. (1987). *Scand. J. Metall.* 16: 154.
Yun-tao, X., Dao-xin, L., and Dong, H. (2008). *Appl. Surf. Sci.* 254: 5953.

Further Reading

Franck, W., Hüthwohl, G., and Maurer, B. (2005). *SCR Systems for Heavy-Duty Trucks: Progress Towards Meeting EUR04 Emission Standards*. Unna: PUREM Abgassystem GmbH and Co.
Harrison, B., Cooper, B.J., and Wilkins, A.J.J. (1981). *Platinum Met. Rev.* 25: 14.
Oddershede, J., Christiansen, T.L., Stahl, K., and Somers, M.A.J. (2010). *Scr. Mater.* 62: 290.
Schneider, T. and Grant, L. (1982). *Air Pollution by Nitrogen Oxides*. Amsterdam, Holland: Elsevier.
Tooze, S. and Walgate, R. (1984). *Nature* 307 (5949): 308.
Totten, G.E. and Howes, M.A.H. (1997). *Steel Heat Treatment Handbook*. London: Marcel Dekker Inc.
Zurek, J., Michalik, M., Schmitz, F. et al. (2005). *Oxid. Met.* 63: 401.

Chapter 11

Halogenation

11.1 Introduction

Halogens and many halogen compounds are very corrosive. In fact, iodine was discovered when, as an impurity in soda ash, it caused corrosion of copper vessels. Hence, materials for containing and handling halogens and corrosive halogen compounds must be selected with particular care. In this chapter, oxidation and corrosion theories are applied to the problems of destructive metal and alloy *halogenation*.

Consideration of halogenation mechanisms is necessary because of the large number of variables involved, including temperature, flow rate, laminar or turbulent nature of flow, halogen partial pressure, diluent gases, active impurity gases such as oxygen, water and halide vapors, abrasion, thermal and mechanical stresses, metal impurities and microstructures, vibration, and radiation. In fact, the practical variations of alloy compositions and environmental conditions are virtually infinite, so that one cannot possibly evaluate all of them in laboratory or pilot-plant studies. But from some basic laboratory data on reaction kinetics and observations of product morphologies and phases, coupled with an understanding of the scaling and vaporization processes involved, one can anticipate unforeseen problems, determine the cause of existing problems, and design better laboratory tests to evaluate materials for commercial service.

Although the corrosion of metals and alloys by pure halogens receives predominant attention in this chapter, we also consider related problems of corrosion by interhalogens, gas mixtures, hydrogen halides, metal halides, and other halogenation agents. Metals may be passivated against halogen attack by deposition of solid reduction products on the metal surfaces:

$$M + MX_6(v) \rightarrow MX_2(v) + MX_4(s) \qquad (11.1)$$

where $MX_4(s)$ further blocks rapid M–MX_6(v) reaction. On the other hand, such product compounds could accelerate reaction rates. For example, if liquid or volatile oxyhalides or hydrates are formed, they may prevent *passivation*. The halogen-metal reaction kinetics is largely influenced by a few pertinent properties of the metal halides, namely, the relative coefficients of thermal expansion for halide and parent metal, the thermodynamic stabilities of condensed and volatile halide species, and halide melting points, vapor pressures, plasticities, electrical conductivities, and ionic diffusion coefficients (Canterford and Colton 1968, 1969). The thermodynamic properties for the halogen–metal reaction can be determined from a knowledge of the standard free energies of formation such as those described in Chapter 3 for several chemical reactions relevant to high temperature corrosion, using *JANAF Thermochemical Tables* and other sources (Kubaschewski et al. 1967; Reed 1971; Weast 1970). Concerning the melting temperature for the metal halides, one must use a binary phase diagram for ascertaining minimum liquidus temperatures when the reaction products comprise multiple scales, e.g. FeX_2 and FeX_3 upon the reaction of pure Fe on X_2. Likewise, upon the reaction of a binary alloy in an X_2 environment, the mixtures of product compounds for each component can establish a liquidus temperature far below those of the constituent compounds. Then, one must consult the pertinent ternary or quasi-binary phase diagrams (see, for example, the phase diagram for ceramists published by the American Ceramic Society) to establish liquidus temperatures. Concerning the relative diffusion rates, at temperatures above one-half the melting point, bulk diffusion of halogen and metal ions through the halide scale will be very significant. Using this 0.5 T_M–diffusion coefficient relationship, at 150 °C one would expect much more rapid SnF_2 (T_M = 212 °C) scale formation on tin than MgF_2 (T_M = 1263 °C) scale formation on magnesium, providing that scale growth rates are diffusion limited in both cases. Concerning the vapor pressures, there are recommended *Turkdogan's and Kellogg's methods* (Turkdogan 1964; Kellogg 1966) for the analysis of equilibrium vapor pressures for vapor species that differ in composition from the condensed phase.

High Temperature Corrosion: Fundamentals and Engineering, First Edition. César A. C. Sequeira.
© 2019 John Wiley & Sons, Inc. Published 2019 by John Wiley & Sons, Inc.

In general, the methods used to study metal halogenation kinetics are the same as those used to study metal oxidation kinetics. These include a manometric or pressure-drop method, several gravimetric methods, the photometric procedure, the electrical resistance method, and the quartz crystal microbalance. The Royal Society of Chemistry (RSC, UK) and the American Chemical Society (ACS, USA) provide good monographs on the topic, which also contain extensive bibliographies on chlorine and other halogens handling procedures and precautions.

11.2 Metal–Halogen Reactions

When a metal or alloy reacts with halogen gas to form a solid product, the product may physically separate the two reactants. This circumstance acts to slow the reaction rate if the product phase is compact and free of macroscopic cracks and voids. On the other hand, cracked or porous scales allow ingress of halogen molecules and reduce the degree of protection. One must also account for dissolution of the nonmetal into the metal and the evaporation of the scale. Thus, the rate of scale growth or metal recession depends greatly upon chemical, physical, and mechanical properties of the intervening product scale.

The sealing behavior of pure metals and alloys in oxygen (and air) environments is available in Chapter 7, and this can be used to interpret scale growth in metal-halogen systems. Theoretical and experimental studies described in the literature will help in the understanding and control of metal-halogen reactions.

As a base metal surface is exposed to an oxidant, an adsorbed film of a specific structure is set up. With a highly efficient capture of incident molecules, the adsorbed state progresses rapidly to a stable film (several angstroms thick), at which time the growth rate slows because either (i) cations, anions, or electrons are effectively immobile in the film or (ii) cations or anions are hindered at the metal/film or at the film/gas interface, respectively, from entering the scale.

At the film/gas interface, dissociated oxidant molecules (i.e. atoms) are reduced when tunneling electrons are trapped to provide an excess of negative surface charge. The resulting electric field across the growing film provides (i) a reduction in the potential energy barriers required for the diffusion of ions or for the tunneling of electrons across the film and/or (ii) a reduction in potential energy barriers for the insertion of ions into the oxide. Various authors differ on the selection of the rate-limiting step.

If the rate of ionic or electronic diffusion or ionic insertion depends upon the electric field ($\mathrm{d}\phi/\mathrm{d}x$) provided by adsorbed oxygen ions, then for a constant, equilibrium-adsorbed state, the driving force (reduction in barriers) of the electric field decreases in importance as the film thickens to become a thin scale (from tens to hundreds of angstroms). But at the same time, the morphological restructuring of the scale is contributing in a similar manner. Theories based on these considerations lead either to a logarithmic rate equation [$y = k_e\ (t_e + at)$] or to an inverse logarithmic kinetic expression [$(l/y) = b - k_{i,l.}\ \ln t$]. In the plotting of the kinetic data, one cannot usually distinguish between these rate "laws." Data for halogenation of metals at low temperatures can frequently be fit to logarithmic expressions. Wagner (1973) has treated the more difficult cases of scale growth in the thin-film range whereby an electrical charge localized to one interface is compensated by a diffuse charge distributed throughout the scales (as opposed to compensation by an opposing charge at the opposite interface). This treatment provides complicated expressions for the expected kinetics.

During the early stages of scale formation and for intermediate temperatures such that $T/T_M \leq 0.6$, the incoherent crystalline boundaries and line defects set up *short-circuit diffusion* of ions through the thin scale, and these can account for scaling rates that are higher by several orders of magnitude than those expected from the extrapolation of kinetic data from higher temperatures.

Support for the importance of short-circuit diffusion in the intermediate temperature range is gained from the response of scaling kinetics to *vacuum* "*aging*" *of the scale*, i.e. the interruption of the steady-state, rapid scale growth by the removal of the oxidant to allow annealing and grain growth in the scale.

When the predominant ionic defects in a compact scale are cation vacancies, the growth of a protective layer occurs by the outward diffusion of cations with a counterflow of vacancies and positive holes. Likewise, scale also forms at the scale/gas interface when the diffusion of interstitial cations and electrons predominate. If the predominant defects were anion interstitials (plus positive holes) or anion vacancies (plus electrons), a compact scale would grow at the metal/scale interface. At high temperatures of corrosion, Wagner (1933, 1936) has described the diffusion-controlled parabolic growth of a compact one-phase layered scale on a pure metal to obtain the result

$$\frac{\mathrm{d}n}{\mathrm{d}t} = \frac{1}{\xi}\,\frac{RT}{2FF' z_x^2}\int_{P^i_{x_2}}^{P^0_{x_2}} t_e(t_M + t_X)\sigma\,\mathrm{d}\,\ln P_{x_2} \qquad (11.2)$$

where $\mathrm{d}n/\mathrm{d}t$ is the rate of growth of an MX scale in $\mathrm{mol\,cm^{-2}\ s^{-1}}$; ξ is the instantaneous scale thickness; z_x is the valence of the anion; t_e, t_M, and t_X are the electrical *transference numbers* of electrons, cations, and anions; σ is the total electric conductivity of the scale formed; $P^i_{x_2}$ and $P^0_{x_2}$ are the nonmetal activities at the metal/scale and scale/gas interfaces, respectively; and F and F' are differing values for the Faraday constant having their

appropriate units. Equation (11.2) shows that the growth of a compact scale can essentially be limited by the transport of electrons when $(t_M + t_X) \gg t_e$ (when the scale is a solid electrolyte) or by the transport of ions when the scale exhibits predominant electronic conduction. For many halides, the partial electrical transference numbers have been established as a function of P_{x_2}.

To explain the growth of a compact one-phase layered scale that exhibits predominant electronic conduction, $t_e \gg (t_M + t_X)$, Wagner (1951) has converted Eq. (11.2) as follows:

$$\frac{dn}{dt} = \frac{1}{\xi}\frac{1}{2V_{MX}}\int_{P^i_{x_2}}^{P^0_{x_2}} \frac{Z_M}{Z_X}(D^*_M + D^*_X)d\ \ln P_{x_2} \qquad (11.3)$$

where V_{MX} is the molar volume of the product compound and D^*_M and D^*_X are the self-diffusion coefficients for the cation and anion, respectively. These expressions for instantaneous scaling rate can be used for comparison with k_p, the gross parabolic scaling rate constant, defined by

$$\xi^2 = 2k_p t \qquad (11.4)$$

through the relation

$$k_p = k_m V_{MX} \qquad (11.5)$$

where k_m represents the quantities in parentheses in either Eq. (11.2) or (11.3).

While the validity of Wagner's theory for the growth of oxide scales has been frequently checked by comparison of experimental values of k_p with calculated values of k_m through Eqs. (11.2) and (11.5), comparable use of this possibility has not been made for the analysis of halogenation reactions. Obviously, these equations provide the basis to predict the dependence of k_p on both temperature and $P^0_{x_2}$ (Wagner 1936). For the formation of compact oxide scales on copper, nickel, cobalt, iron, and manganese, good agreement between k_p and the calculated k_m has been found at sufficiently high temperatures, i.e. at about 1000 °C or T/T_M (scale) > 0.75. Experimental activation energies and p_{O_2} dependencies for parabolic oxidation also agree with the predicted values.

Because a number of halides exhibit predominant ionic conduction (Rapp 1970), the phenomenon of local cell action can contribute to the consumption of a metal by halide scale formation as observed by Ilschner-Gench and Wagner (1958). The established electronic short circuit leads to an overgrowth formation that should be anticipated whenever the corrosion product is a predominant ionic conductor.

The relatively high vapor pressures of the halide compounds that form as surface products cause the loss of molecules from the scale to the vapor at the same time that the scale is growing by diffusional transport.

Tedmon (1966) described the oxidation rates of pure chromium and Cr_2O_3 forming Fe–Cr alloys at temperatures greater than 1100 °C as the sum of a parabolic diffusion-controlled scale thickening and a time-dependent vaporization loss. The rate equation for the thickening of the scale is

$$\frac{d\xi}{dt} = \frac{k_p}{\xi} - k_v \qquad (11.6)$$

where ξ is the scale thickness, k_p is the parabolic rate constant for the diffusion step, and k_v is the linear rate constant for the vaporization step.

For short times or thin films, Eq. (11.6) predicts parabolic behavior; however, with continued growth, the two terms on the right-hand side of Eq. (11.6) approach each other so that a steady-state scale thickness, $\xi_{s.s.}$, equal to k_p/k_v, is approached. The integration of Eq. (11.6) for $\xi = 0$ at $t = 0$ yields the result

$$t = \frac{k_p}{k_v^2}\left[-\frac{k_v\xi}{k_p} - \ln\left(1 - \frac{k_v\xi}{k_p}\right)\right] \qquad (11.7)$$

This functional dependence of ξ on t is schematically illustrated in Figure 11.1.

In the consideration of *metal recession*, y, the metal is consumed both by an increase in ξ and by scale vaporization:

$$\frac{dy}{dt} = \frac{V_M}{V_{MX_v}}\left(\frac{d\xi}{dt}\right) + \frac{V_M}{V_{MX_v}}k_v = \frac{V_M}{V_{MX_v}}\left(\frac{k_p}{\xi}\right) \qquad (11.8)$$

where V_M and V_{MX_v} are the molar volumes of the metal and the MX_v scale, respectively.

To interpret gravimetric kinetics for the growth of an MX_v compound scale, the rate equation must account for the weight gain for the net scale present minus the weight loss resulting from metal recession:

$$\frac{d(\Delta m/A)}{dt} = \rho_{MX}\frac{d\xi}{dt} - \rho_M\frac{dy}{dt} \qquad (11.9)$$

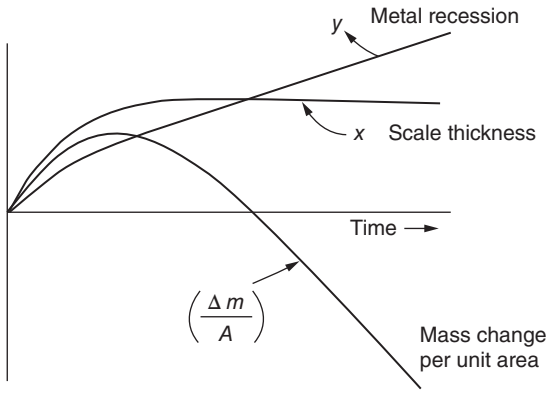


Figure 11.1 Parabolic scale growth with linear evaporation of halide scales.

where ρ_M and ρ_{MX_υ} are the bulk densities of the metal and the scale, respectively. The combination of Eqs. (11.6), (11.8), and (11.9) gives

$$\frac{d(\Delta m/A)}{dt} = \frac{\upsilon N_X}{V_{MX_\nu}}\left(\frac{k_p}{\xi}\right) - \rho_{MX_\upsilon} k_\upsilon \qquad (11.10)$$

where N_X is the atomic weight of the nonmetal.

A quantitative evaluation of recession of gravimetric kinetics to obtain the fundamental rate constants k_p and k_υ must proceed via numerical methods through integration of Eq. (11.8) or (11.10) after substitution of ξ from Eq. (11.7). In any case, as $\xi_{s.s.}$ is attained, the rates of both metal recession and weight gain correspond solely to the linear rates of evaporation. This behavior is schematically illustrated in Figure 11.1.

Another important process that occurs during scale growth at high temperatures concerns the simultaneous evaporation of scales and the reactive evaporation of metal. But many factors complicate the morphological and kinetic behavior of scale formation in this condition; therefore we will not review it here.

When the predominant ionic defects in a scale are vacant cation sites, then a compact protective layer grows by outward diffusion of cations with a counterflow of vacancies and positive holes. As the scale thickens, its resistance to plastic deformation increases, particularly at points of constraint such as the edges and corners of a specimen. With the continual arrival of vacancies through the scale to the metal/scale interface, the reduced plasticity of the scale can lead to the condensation of vacancies to form voids and ultimately a porous zone at the metal/scale interface.

The formation of this duplex scale morphology, with compact columnar grains at the external surface and a porous zone at the metal/scale interface, is favored: (i) at lower temperatures where scale plasticity is lower; (ii) for impure metals (or dilute alloys) containing more reactive solutes, because the formation of a product compound as an internal precipitate within the metal matrix could occur; (iii) for metals containing impurities that form volatile compounds with the reactant gas (e.g. hydrogen or carbon in halogenation reactions); and (iv) at specimen corners and edges where geometrical constraints oppose plastic deformation of the scales. The principal detriment of duplex scale formation is the resulting poor scale/metal adhesion, which leads to scale cracking and exfoliation particularly upon thermal cycling.

When the predominant ionic defects in a scale are vacant anion sites or anion interstitials (as in the case for FeF_2, for example), then the diffusional growth of a product scale occurs by the inward diffusion of anions with an equivalent transport of positive holes or electrons. The new scale forms at the metal/scale interface beneath the previously formed scale. Because the products of reaction generally comprise more volume than the consumed metal, the scale must deform plastically to accommodate the volume increase, or else tensile stresses are introduced into the external surface of the outer scale and cause it to fracture. Particularly at corners and edges, plastic deformation is restricted as the scale thickens, such that fractures occur and lead to a porous scale through which the molecular reactants can diffuse.

11.3 Alloy–Halogen Reactions

As a clean surface of an A–B alloy is first exposed to the reacting X_2 gas at elevated temperatures, there is too little time for selecting product formation, and the alloy simply forms the product compounds of each of the alloy components in a molar proportion equal to that in the bulk alloy (Chattopadhyay and Wood 1970). Then the reaction kinetics at short times are likely to be higher than those subsequently experienced during the steady-state growth of the protective $B_\nu X$ scale. At short times, the tiny grains of the thin initial duplex scale each grow according to their individual transport rates such that the faster-growing product (often the less stable $A_\chi X$ compound) overgrows the slower-growing product (usually the more stable $B_\nu X$ compound). As a result of the depletion of A, the underlying $B_\nu X$ grains grow laterally to ultimate impingement at the metal/scale interface. In this way, the steady-state protective scale of $B_\nu X$ may be found beneath an external $A_\chi X$ scale whose supply and growth are stopped after the underlying scale is established.

When scale vaporization is important, as in the halogenation of alloys, the transient reaction stage might be used to place a less volatile, more noble compound on top of a more volatile, but slower-growing, less noble compound. After sufficient time, of course, the outer scale could be lost completely by vaporization.

Concerning the selective oxidation of metal alloys, let us consider a binary solid solution alloy A–B for which the lowest compound $B_\nu X$ of component B is more stable (has a more negative $\Delta G_{B_\nu X}$) than the lowest compound $A_\chi X$ of component A. Generally, the selective oxidation of the less noble component B is manifested in one of two limiting product morphologies (Douglass 1971; Rapp 1965; Wagner 1959): (i) for sufficiently dilute concentrations of B in A–B (often less than about 10 at.% B), tiny precipitates of $B_\nu X$ are formed at an internal reaction front in the alloy beneath a scale of $A_\chi X$ if the permeability (solubility times diffusivity) of X dissolved in A is much greater than the product of the diffusivity times the bulk content of the reactive solute, or else (ii) for greater solute B contents (often greater than about 20 at.% B) or for alloys in which the nonmetal atoms are essentially insoluble, the compound $B_\nu X$

will form the predominant external scale layer on the A–B alloy. Intermediate behavior, e.g. internal precipitation, is several times observed and can be important to the science and technology but will not be detailed here.

Data on alloy oxidation show that the steady-state parabolic growth of a protective scale can be quite dependent upon the presence of *aliovalent solutes* (dopants) dissolved in the scale. Such solute ions differ in ionic charge (or lattice position) from the cations or anions of the host compound and are therefore electrically active. Because gross electrical neutrality is required for a growing scale, the summation of the relative charges for negative ionic defects (cation vacancies or anion interstitials) and electrons and negative dopants equals the summation of the relative charges for positive ionic defects (interstitial cations and anion vacancies) and positive holes and positive dopants. Obviously in this electrical neutrality condition, the concentration of the ionic defect whose transport accounts for scale growth is a prominent term that is balanced by the defects of opposite charge. By the introduction into the host compound (scale) of a soluble aliovalent dopant of the same sign of charge as the most mobile ionic defect, the concentration of this defect will be reduced drastically according to well-established defect equilibria conditions (Kröger 1964). Reduction of the concentration of the fastest ionic defect species obviously reduces the diffusive flux of this species and the scaling rate of the alloy as well. This discussion presumes that the scale is a predominant electronic compound. When the scale is a solid electrolyte, the scaling rate should be lowered as the concentration of the predominant electronic species is lowered through doping.

To design alloys intended for service in halogens on the basis of the doping effect, one must know at least the identities (and hopefully the concentrations) of the predominant ionic and electronic defects in the compound (scale) of the pure metal. One must know that the intended dopant ion is sufficiently soluble and has a certain electrical charge in the host lattice. Finally, for the reaction scheme under consideration, the dopant must reach the scale in a manner such that dissolution should occur.

More detail of the response of alloys to atmospheres based on Cl_2, O_2–Cl_2, and corresponding fluorine atmospheres is given by Lai (1990).

11.4 Laboratory Studies

Because nickel, copper, iron, aluminum, and their alloys are commonly used structural materials, studies of halogen attack on these metals are largely reported in the literature (Fontana and Staehle 1980; Han and Cho 2002). Laboratory studies of halogen attack on other metals (chromium, silicon, etc.) and alloys (low-alloyed ferritic steels, ferritic–martensitic steels, austenitic stainless steels, nickel-based alloys, etc.) are also being reported including observed reaction kinetics, postulated reaction mechanisms, and important experimental parameters such as temperature, halogen gas pressure and flow rate, and metal and gas purities (Kuiry et al. 1996; Maloney and McNallen 1983; Oh et al. 1986; Stott and Shih 2000).

The halogenation of many metallic materials covers wide temperature ranges and is identified in many industrial environments for the processing of metallurgical ores, calcining operations, chemical processing streams, manufacture of fluorine-containing compounds, production of uranium, and so on. In many high temperature industrial processes where fuels and/or feedstocks are often contaminated with impurities, such as alkaline metals, halogen may readily react with these metals to form halide salts. Corrosion reactions under these conditions are discussed in chapters dealing with high temperature corrosion in gas turbines, coal-fired boilers, oil-fired boilers, and so forth. Waste-fired boilers suffer severely from corrosion of critical components such as superheater tubes, when operating in high temperature environments exposed to alkali, chlorine, sulfur, and other gaseous species, in the temperature range 400–700 °C. This is a pertinent case requiring a review here, due to the large application of superheater tubes and the know-how that we can require, under the point of view of materials, corrosion, and its mitigation, when studying such a situation. A number of different materials are commonly used for superheater tubes, and these include 13CrMo44 (1Cr–0.5Mo–Fe) and 13CrMo910 (2.25Cr–1Mo–Fe) low-alloyed ferritic steels, 9–12% Cr ferritic–martensitic steels, HCM 12A that is a martensitic 12%-Cr steel containing about 35% delta ferrite, standard 304 austenitic stainless steel with 18% Cr–8% Ni–Fe, other steels in the AISI 300 series, nickel-based alloys such as Inconel 625 with 22% Cr–9% MoNi, etc. The superheater tubes face a highly complex atmosphere with both corrosive flue gas and deposits. In studies by Grabke et al. (1995) and Zahs et al. (1999, 2000), the main reason for alloy breakdown was considered molecular chlorine, formed from hydrochloric acid in the flue gas. In addition to the gaseous species, impaction of various solid particles and condensation of gaseous compounds onto the slightly cooler heat exchangers adversely affect alloy performance. Deposit formation is a topic on its own (Baxter 1993) but cannot be ignored since these deposits are a major cause for corrosion breakdown. Studies by Grabke (1995), Pettersson et al. (2006a), and Kawahara (2002) identified the following crystalline compounds within the deposit by XRD (X-ray diffraction): NaCl, KCl, $CaSO_4$; NaCl, KCl, $CaSO_4$, SiO_2; and (K, Na)Cl, K_2SO_4, Na_2SO_4, (K, Na)$_2Ca_2(SO_4)_3$, $Ca_2MgSi_2O_7$. These corrosion products clearly show that the superheaters suffer from deposit-induced corrosion,

involving oxide degradation in the presence of molten salts, the effect of sulfur/chlorine ratio in the fuel, and the effect with the chlorine-containing compounds as the major reason for rapid attack (Asteman et al. 2000; Ebbinghaus 1993; Giggins and Pettit 1980; Young 2008).

During combustion of waste and some types of biomass, high levels of HCl, NaCl, and KCl are released. In atmospheres containing both HCl and O_2, accelerated corrosion has also been observed, and a common opinion is that Cl_2 forms according to the *Deacon reaction* (Nieken and Watzenburger 1999):

$$2HCl(g) + \frac{1}{2}O_2(g) = Cl_2(g) + H_2O(g) \qquad (11.11)$$

This is normally a very slow reaction but could be catalyzed by the oxidized metal surface. During combustion of waste, alkali chlorides are deposited on the superheater tubes, and chlorine formation may take place according to

$$2NaCl(s) + Fe_2O_3(s) + \frac{1}{2}O_2(g) = Na_2Fe_2O_4(s) + Cl_2(g) \qquad (11.12)$$

Considering the thermodynamics of the M–Cl–O system, metal oxides are stable at high oxygen partial pressures, while metal chlorides can be expected in regions with low oxygen partial pressures. Chemical analyses of corrosion products formed in oxidizing–chlorinating environments have confirmed this behavior in that metal chlorides are usually observed at the metal/scale interface (low oxygen partial pressure), while the outer part of the scale (high oxygen partial pressure) contains mainly metal oxides. In other words, there seems to be an inward diffusion of chlorine through the scale and a subsequent accumulation at the metal/scale interface. It has been suggested that this implies a molecular transport in order not to have chlorine diffusion across a chlorine activity gradient (Kofstad 1988). In this case, the molecular chlorine must diffuse through the oxide layer, presumably through cracks and pores. In an O_2–Cl_2 environment, the stability of metal oxides and chlorides depends on the partial pressure of oxygen and chlorine. At the metal–oxide interface, the oxygen pressure is low and metal chlorides are stabilized. These are formed according to

$$M + \frac{x}{2}Cl_2(g) = MCl_x(s, g) \qquad (11.13)$$

At elevated temperatures, the vapor pressure of metal chlorides can be significant, and volatile chlorides will diffuse toward the oxygen-rich outer part of the scale where they are destabilized according to

$$2MCl_2(g) + \frac{3}{2}O_2(g) = M_2O_3(s) + 2Cl_2(g) \qquad (11.14)$$

The detrimental effect of chlorine and how it accelerates corrosion has been frequently studied, and the degradation process is often termed *active oxidation*. The name refers to the loose porous layer that is created, providing little or no protection. In this reaction, metal oxides are formed while chlorine is released, as Eq. (11.14) shows, and may again penetrate the oxide scale, creating a cycle. The essence of this is the continuous transport of metals away from the metal surface while little, or no, chlorine consumption exists. This is often referred to as the *chlorine cycle*, schematically illustrated in Figure 11.2 (Rees and Grabke 1992).

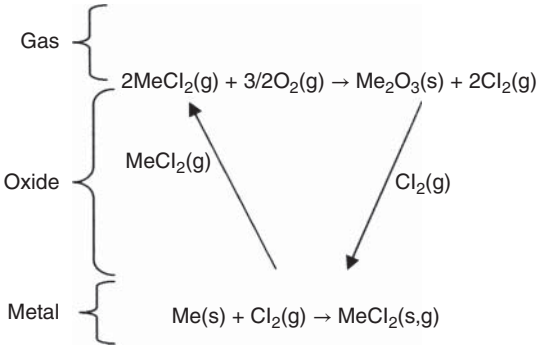


Figure 11.2 Schematic drawing of chlorine cycle as described by Reese and Grabke (1993).

Although the chlorine cycle is frequently used for describing corrosion in oxidizing–chlorinating environments, there are concerns with this model. For example, Folkesson et al. (2007) suggested that the transport could be ionic and electrochemically driven. The mechanism would then be explained by HCl dissociating at the scale/gas interface according to the cathodic process:

$$2HCl\,(ads) + \frac{1}{2}O_2\,(ads) + 2e^- \rightarrow 2Cl^- + H_2O(g) \qquad (11.15)$$

A corresponding anodic process at the metal–oxide interface creates outward diffusing cations. The transport of chlorine through the oxide scale would thus be ionic rather than gaseous, at least during the initial stages.

Although the metal chloride is thermodynamically unstable at the scale/gas interface, studies have shown the presence of metal chlorides at the surface. Jacobson et al. (1989) performed work with mass spectroscopy showing that volatile metal chlorides and metal oxychlorides are lost to the gas flow during exposure in chlorine-rich environments. Stott and Shih (1966) proposed that Tedmon (2000) behavior is evident with a weight gain due to metal oxide formation in simultaneous with a weight loss due to vaporization of volatile metal chlorides.

It is evident that chlorine interferes with the oxide formation, creating volatile corrosion products as well as porous and poorly protective oxide scales. Breakdown of metal oxides due to formation of other thermodynamically more stable corrosion products is also possible. Alkali chlorides, sulfates, and carbonates are constantly being deposited on the superheater tubes during operation.

Pettersson et al. (2006b) have studied the reaction between solid and gaseous potassium chlorides with an oxide. The authors found that a protective chromia scale will react with the alkali-forming potassium chromate according to

$$2KCl(s) + \frac{1}{2}Cr_2O_3(s) + H_2O(g) + \frac{3}{4}O_2(g) = K_2CrO_4(s) + 2HCl(g) \quad (11.16)$$

Chromates are very stable compounds and may also form by the reaction between Cr_2O_3 and NaCl or K_2CO_3. The formation of chromate may deplete the oxide in chromium and cause the formation of iron-rich oxides and mixed spinel oxides, which are considered poorly protective. The breakdown of chromia scale may thus initiate accelerated corrosion attack by facilitating, for example, chlorine ingress through the scale.

11.5 Conclusions

Several metal halogenation studies have been conducted along the last decades, but most of the information about halogen resistance of the metals comes from cursory comparisons of commercial metals and alloys. Scale morphologies, defect structures, impurity doping effects, self-diffusion coefficients, solubilities and diffusivities of the halogens in metals, and even kinetics (extensively studied in metal oxidation research) have been much neglected in studies of metal halogenation. Some studies have, in part, been discouraged by the highly toxic and corrosive nature of halogens.

A knowledge of the above-discussed metal and metal-halide scale properties and an understanding of corrosion mechanisms provide the basis for the designing and engineering of corrosion-resistant alloys. This idea of *alloy design* (used, for example, to develop alloys resistant to high temperature oxidation and hot corrosion) rather than simple alloy evaluation has not generally been applied to develop halogen-resistant alloys. Such alloy design could be very productive.

Long-term forecasting of the behavior of halogen-metal systems and the development of halogen-resistant alloys are facilitated by a knowledge of metal-halide defect structures, self-diffusion coefficients, thermodynamic properties, electrical conductivities, and physical properties and a knowledge of alloy self-diffusion and fluorine solubilities. Considerable thermodynamic data are already available, but other data are particularly sparse. It is hoped that future studies of metal halogenation will provide this information along with more detailed observations of scale morphology than have been provided in the past.

In the present chapter, some important aspects of high temperature halogenation during waste combustion have also been identified.

On a fundamental level, the corrosion breakdown in chlorinating–oxidizing atmosphere is interesting to study. HCl-induced corrosion could be analyzed in more detail with some advanced techniques such as high temperature mass spectroscopy to analyze different volatile species and quantify their impact on the corrosion attack. More detailed post-exposure analyses with scanning electron microscopy (SEM) and transmission electron microscopy (TEM) may be helpful in understanding the interaction between chlorine and the various alloying elements and how this affects the scale growth. In full-scale boilers, optimizing the alloy performance and therefore the efficiency is the main goal, and here the beneficial effect of changing alloy composition as well as flue gas composition was shown. Combining these strategies could possibly further improve alloy performance. With better control of flue gas chemistry, the deposition of aggressive compounds onto superheater tubes can be better controlled and as a consequence makes suitable alloy selection less challenging. However, this requires large test campaigns in full-scale boilers with long-term exposures under various conditions.

11.6 Questions

11.1 Describe the high temperature corrosion problems during waste incineration in waste-fired boilers.

11.2 How does the presence of chlorides in the flue gas affect the corrosion behavior?

11.3 What are the reducing and oxidizing conditions in power plants? How do they affect the corrosion of superheater tubes?

11.4 What is the main cause of corrosion in waste incinerators? What kind of materials are recommended to overcome this problem?

11.5 What is halogenation corrosion? How does it differ when oxygen and sulfur dioxide are present?

11.6 What is active oxidation? And what is the chlorine cycle?

11.7 In which way does sulfur addition mitigate the halogenation behavior?

References

Asteman, H., Svensson, J.-E., Norell, M., and Johansson, L.-G. (2000). *Oxid. Met.* 54: 11.

Baxter, L.L. (1993). *Biomass Bioenergy* 4: 85.

Canterford, J.H. and Colton, R. (1968). *Halides of the Transition Elements: Halides of the Second and Third Row Transition Metals*. London: Wiley.

Canterford, J.H. and Colton, R. (1969). *Halides of the Transition Elements: Halides of the First Row Transition Metals*. London: Wiley.

Chattopadhyay, B. and Wood, G.C. (1970). *Oxid. Met.* 2: 373.

Douglass, D.L. (ed.) (1971). *Oxidation of Metals and Alloys*. Materials Park, OH: American Society for Metals.

Ebbinghaus, B. (1993). *Combust. Flame* 93: 119.

Folkesson, N., Johansson, L.-G., and Svensson, J.-E. (2007). *J. Electrochem. Soc.* 154: 515.
Fontana, M.G. and Staehle, R.W. (eds.) (1980). *Advances in Corrosion Science and Technology*. New York: Plenum Press.
Giggins, C.S. and Pettit, F.S. (1980). *Oxid. Met.* 14: 363.
Grabke, H.J. (1995). *Corrosion NACE* 51: 711.
Grabke, H.J., Reese, E., and Spiegel, M. (1995). *Corros. Sci.* 37: 1023.
Han, G. and Cho, W.D. (2002). *Oxid. Met.* 58: 390.
Ilschner-Gench, C. and Wagner, C. (1958). *J. Electrochem. Soc.* 105: 198.
Jacobson, N.S., McNallen, M.J., and Lee, Y.Y. (1989). *Metall. Trans. A* 20A: 1566.
Kawahara, Y. (2002). *Corros. Sci.* 44: 223.
Kellogg, H.H. (1966). *Trans. Metall. Soc. AIME* 236: 602.
Kofstad, P. (1988). *High Temperature Corrosion*. London: Elsevier Applied Science.
Kröger, F.A. (1964). *The Chemistry of Imperfect Crystals*. Amsterdam, New York: North-Holland, Interscience.
Kubaschewski, O., Evans, E.L., and Alcock, C.B. (1967). *Metallurgical Thermochemistry*. Oxford: Pergamon Press.
Kuiry, S.C., Roy, S.K., and Bose, S.K. (1996). *Oxid. Met.* 46: 399.
Lai, G.Y. (1990). *High Temperature Corrosion of Engineering Alloys*. Materials Park, OH: ASM International.
Maloney, M.J. and McNallen, M.J. (1983). *Metall. Trans. B* 16: 751.
Nieken, H.P. and Watzenburger, O. (1999). *Chem. Eng. Sci.* 54: 2619.
Oh, J.M., McNallen, M.J., Lai, G.Y., and Rothman, M.F. (1986). *Metall. Trans. A* 17: 1087.
Pettersson, C., Pettersson, J., Asteman, H. et al. (2006a). *Corros. Sci.* 48: 1368.
Pettersson, J., Pettersson, C., Folkeson, N. et al. (2006b). *Mater. Sci. Forum* 522–523: 563.
Rapp, R.A. (1965). *Corrosion* 21: 382.
Rapp, R.A. (ed.) (1970). *Techniques of Metals Research*, vol. IV, Pt. 2. New York: Wiley.
Reed, T.B. (1971). *Free Energy of Formation of Binary Compounds*. Cambridge, MA: MIT Press.
Reese, E. and Grabke, H.J. (1992). *Mater. Corros.* 43: 547.
Reese, E. and Grabke, H.J. (1993). *Mater. Corros.* 44: 41.
Stott, F.H. and Shih, C.Y. (2000). *Mater. Corros.* 51: 277.
Tedmon, C. Jr. (1966). *J. Electrochem. Soc.* 113: 766.
Turkdogan, E.T. (1964). *Trans. Metall. Soc. AIME* 230: 740.
Wagner, C. (1933). *Z. Phys. Chem.* 11: 25.
Wagner, C. (1936). *Z. Phys. Chem.* B32: 447.
Wagner, C. (1951). *Atom Movements*, 153. Cleveland, OH: American Society for Metals.
Wagner, C. (1959). *Z. Elektrochem.* 63: 772.
Wagner, C. (1973). *Corros. Sci.* 13: 23.
Weast, R.C. (ed.) (1970). *Handbook of Chemistry and Physics*. Cleveland, OH: Chemical Rubber Co.
Young, D. (2008). *Mater. Sci. Forum* 595, 1189–598.
Zahs, A., Spiegel, M., and Grabke, H.J. (1999). *Mater. Corros.* 50: 561.
Zahs, A., Spiegel, M., and Grabke, H.J. (2000). *Corros. Sci.* 42: 1093.

Further Reading

Bar-Cohen, Y. (ed.) (2014). *High Temperature Materials and Mechanisms*. Boca Raton, FL: CRC Press.
Belton, G.R. and Worrell, W.L. (1970). Proceedings of an International Conference on Metallurgy and Materials Science, University of Pennsylvania (September 1969). New York: Plenum Press.
Bender, R. and Schütze, M. (2003). *Mater. Corros.* 54: 567.
Craig, B.D. (ed.) (1989). *Handbook of Corrosion Data*. Materials Park, OH: ASM International.
Elliott, P., Ansari, A.A., Prescott, R., and Rothman, M.F. (1988). *Corrosion* 44: 544.
Ihara, Y., Ohgame, H., and Sakiyama, K. (1982). *Corros. Sci.* 22: 901.
Holmes, D.R. (ed.) (1991). *Protective Oxide Scales and Their Breakdown*. Chichester: Wiley.
Karlsson, S., Amand, L.-E., and Liske, J. (2015). *Fuel* 139: 482.
Kawahara, Y., Nakamura, N., Tsuboi, H., and Yukawa, K. (1998). *Corrosion* 54: 576.
Kawahara, Y. (2005). *Corros. Eng.* 54: 213.
Lai, G.Y. (2007). *High Temperature Corrosion and Materials Applications*. Materials Park, OH: ASM International.
Lantelme, F. and Groult, H. (eds.) (2013). *Molten Salt Chemistry. From Lab to Applications*. Amsterdam: Elsevier.
Mansfeld, F.I. (ed.) (1987). *Corrosion Mechanisms*. New York: Marcel Dekker.
Rao, Y.K. (1985). *Stoichiometry and Thermodynamics of Metallurgical Processes*. Cambridge: Cambridge University Press.
Rothman, M.F. (ed.) (1985). *High Temperature Corrosion in Energy Systems*. New York: The Metallurgical Society of AIME.

Chapter 12

Corrosion by Hydrogen and Water Vapor

12.1 Introduction

The lifetime of materials exposed to high temperatures is significantly decreased by high temperature oxidation, as it affects the mechanical properties of these materials. Several alloys, namely, Ni-based superalloys are frequently used at high temperatures, due to their excellent mechanical properties and oxidation resistance. Depending on the temperatures required, different alloy classes are used. As high temperature oxidation takes place in an oxidizing environment, Ni-based superalloy is a suitable choice of material, due to its capability to resist this type of corrosion, which stems from the formation of a slow-growing, homogeneous, adherent, and low defect concentration oxide film.

The atmosphere in which the materials are used is generally not dry, as there is always a certain amount of moisture in air, with the highest content of 100% reached in steam generators. The water vapor is known to affect the oxidation behavior of metals by increasing their oxidation rate. Therefore, the presence of water vapor may influence the oxidation behavior of Ni-based superalloys at high temperature. It has been shown that steels oxidize faster in air or combustion gases containing water vapor, particularly in the case of low Cr-containing steels. The presence of water vapor as reported in the literature to cause the cracking and spalling of oxides changes the transport processes in oxides and modifies the selective oxidation processes.

The effect of water vapor on the oxidation behavior of metals and alloys at high temperature has been summarized in many reviews by Saunders et al. (2008).

Hydrogen is also a gas that causes serious industrial problems, particularly in refinery vessels and other high temperature equipment, many times associated with water and/or water vapor (Alvorado 1995). Steels, carbon, and Cr–Mo steels, low-alloy steels, and other materials can suffer hydrogen attack (HA) or hydrogen damage at high temperature, which results in rupture failures of steel components and/or microfissures in boiler tubes and other industries. The purpose of the current chapter is to provide a brief discussion of the corrosion reactions involving H_2 and/or H_2O, which are really an important subject of high temperature corrosion.

12.2 Corrosion by Hydrogen

12.2.1 Concept, Mechanism, Detection, and Prevention

Since the early ages of industrial usage of hydrogen, the selection of appropriate materials has been a concern for industrial gas operators. These operators have paid special attention to the issues raised by the specific interaction of this molecule with metallic materials, specifically with steel, in order to ensure safety and reliability of hydrogen from manufacture to cylinder filling, to distribution, and to usage at the customer site.

Hydrogen energy development will face the same constraints of material compatibility, with even stricter requirements, as the equipment will be owned and partially operated by a wide range of nonspecifically trained users and will be operated at very high pressures, 700 bar or more.

The phenomenon of *internal hydrogen embrittlement* due to excessive amounts of hydrogen introduced during the manufacture of steels has been known since the end of the nineteenth century. The phenomenon of internal hydrogen embrittlement when welding steels was discovered later. These two problems are now well mastered and are not covered here. This chapter only concerns the phenomenon of *external hydrogen embrittlement* caused by pressurized *gaseous hydrogen* in contact with steels, essentially at high temperatures. The hydrogen penetrates into the steel (during operation in the case of pressurized tanks) and diminishes local or overall mechanical

High Temperature Corrosion: Fundamentals and Engineering, First Edition. César A. C. Sequeira.
© 2019 John Wiley & Sons, Inc. Published 2019 by John Wiley & Sons, Inc.

properties of the steel. This can lead to bursting of these pressurized tanks under certain conditions.

The hydrogen that penetrates into steels can be found either in metallic solution or in combined state (H_2, CH_4 molecules).

When hydrogen is found in metallic solution, the phenomenon of steel deterioration is called *gaseous hydrogen embrittlement*; this phenomenon generally takes place at temperatures close to ambient, and the penetration or transport of the hydrogen takes place essentially by transport by dislocations when the material is undergoing deformation. This phenomenon therefore occurs essentially in areas with local plastic deformations.

When hydrogen is present in a combined state, it is a matter of hydrogen attack (HA) or *hydrogen damage*. The hydrogen reacts with the carbon in the steel to form molecules of methane; this leads to the formation of microcavities in the steel and to a lack of carbon in the steel, which lead to a reduction in the overall strength of the material. Hydrogen is therefore transported by diffusion. This is why this phenomenon mainly takes place at high temperature. In addition, contrary to the phenomenon of hydrogen embrittlement, this phenomenon is reversible as long as microcavities have not formed.

One of the most important parameters to be considered here is temperature; and, indeed, hydrogen embrittlement of steels mainly occurs around ambient temperature and tends to disappear at high temperature. On the contrary, HA only takes place at high temperature. Depending on whether the operating temperature is higher or lower than 300 °C, one or the other of the two phenomena mentioned above should be taken into account. In other words, HA is not to be confused with *hydrogen embrittlement* or other forms of low temperature hydrogen corrosion. Surface decarburization and internal decarburization are important effects of HA.

Surface decarburization results in a decrease in hardness and increase in ductility of the material near the surface. This is usually only a minor concern for these types of application. However, internal decarburization, and in particular the formation of methane and consequent development of voids, can lead to substantial deterioration of mechanical properties due to loss of carbides and formation of voids and catastrophic failure.

The main factors influencing HA are the hydrogen partial pressure, the temperature of the steel, and the duration of the exposure. Damage usually occurs after an incubation period, which can vary from a few hours to many years depending on the severity of the environment. High temperatures and low hydrogen partial pressures favor surface decarburization, while the opposite conditions (lower temperature, high hydrogen partial pressure) favor fissuring. In addition, the composition of the steel influences the resistance to HA; in particular elements that tie up carbon in stable precipitates, such as Cr, Mo, and V, are very important. Increasing content of such elements increases the resistance to HA, and Cr–Mo steels with more than 5% Cr, and austenitic stainless steels, are not susceptible to HA.

Aside from Cr and Mo, other elements that tend to bind carbon in the form of stable metallic carbide, such as Ti, W, etc., have the same favorable effect.

On the contrary, a high carbon content is detrimental. Similarly, the addition of Al, Ni, or excess of Mn has a detrimental effect on the behavior of welds.

The residual elements that lead to the formation of nonmetallic inclusions have a detrimental effect. To prevent risks of HA, stress relief treatment at temperatures equal to or greater than 650 °C is needed. These types of treatment are covered by standards and/or should be carried out in accordance with the stipulations of the local code or the code of the manufacturer.

It also appears that the risk of HA increases when the level of mechanical stresses increases. The hydrogen partial pressure should not be considered alone. Total pressure and additional stresses during operation or residual stresses, if not completely eliminated by heat treatment, should also be taken into account. In addition to the treatment following welding recommended above, it is better to limit the hardness of the weld bead and the heat affected zone.

The operating limits for steels can be empirically described using the operating temperature and hydrogen partial pressure, as originally discussed by Nelson (1949) and in the American Petroleum Institute (API) recommended practice 941, "Steels for Hydrogen Service at Elevated Temperatures and Pressures in Petroleum Refineries and Petrochemical Plants" (Das 1996; Parthasarathy 1985).

Since the 1970s, empirical data have been collected from operating plants and tests to establish operating limits of carbon steel and low-alloy steel equipment in hydrogen service at elevated temperatures. API 941 provides guidance on those limits.

Using API 941, if a piece of equipment or piping is operated above the API 941 *Nelson curve*, then the material is not suitable for service under those conditions. For example, if the normal operating conditions are a temperature of 488 °C (900 °F) and 2.23 MPa (323 psig) hydrogen partial pressure, as illustrated in Figure 12.1, then the carbon steel in this case and even the 1.0Cr–0.5Mo steel are not suitable for service under those conditions. There would be a risk of premature failure in a relatively short time of exposure. Either the temperature or the pressure would have to drop below the carbon steel curve, or chromium alloyed steel should be considered for use instead. The selection of a 1 1/4Cr–1/2Mo material would be the preferred choice.

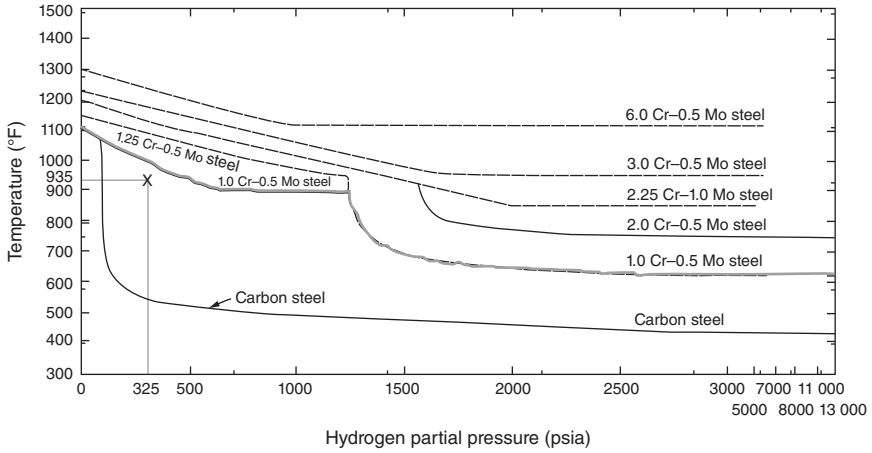


Figure 12.1 Illustration of API 941 Nelson curve – material selection for equipment exposed to hydrogen at elevated temperatures and pressures should follow API 941 guidelines.

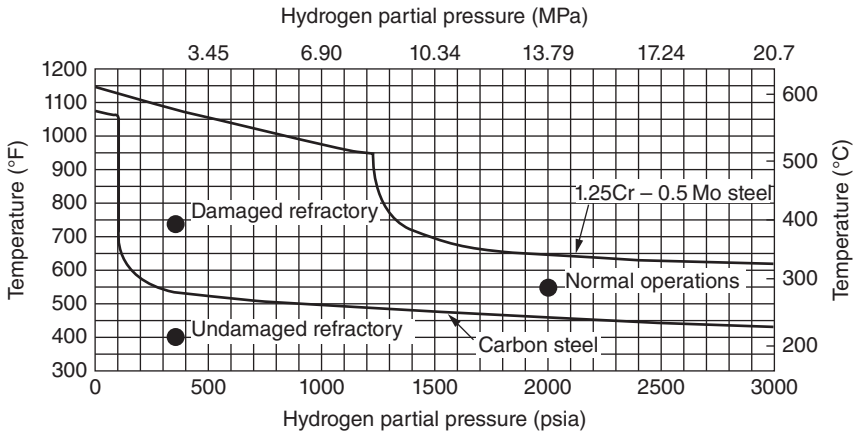


Figure 12.2 Illustration of API 941 Nelson curve – damaged refractory can result in an increase in the metal temperature that, if above the recommended limits, could result in HA failure.

Using API 941, the following practices should be considered:

1. Selecting the proper material for the operating conditions, and for increased temperatures, considering the use of alloys with higher weight percents of chromium and molybdenum.
2. Using actual operating temperatures for assessing HA susceptibility and validating that the actual operating temperatures and pressures are below API 941 curve by a defined amount.
3. Employing experienced individuals who understand the HA phenomenon as well as the API 941 recommended practices.

For corrosion purposes, sometimes vessels are clad, lined, or weld overlaid to protect the vessel surface. This can provide initial protection, provided hydrogen does not diffuse through the liner or migrate behind the lining or cladding. If that occurs, then the vessel may be susceptible to HA.

Refractory lining is often used to insulate a pipe or vessel to lower the metal wall temperature and is an effective way to reduce the effects of HA. However, the refractory can degrade, crack, or deteriorate due to operating conditions or even flexure of the refractory, allowing hot spots to form, which would elevate the metal wall temperature and possibly result in exceeding the HA operating limits of the equipment. Figure 12.2 illustrates how a degraded refractory hot spot could result in exceeding the operating temperature limit for a carbon steel line.

One way to monitor the condition of the refractory is to perform regular infrared imaging of the equipment.

For clad, lined, or overlaid equipment, the following practices should be considered:

1. Ensuring that proper foundation support for refractory-lined equipment is in place to reduce flexure of the refractory.
2. Performing regular infrared inspections, especially on the refractory-lined equipment.
3. Ensuring that the operating limit is understood and appropriate actions are taken if the limit is exceeded.

There is increasing concern that the Nelson curves may not be relevant for the newer steels being used in high

temperature hydrogen service, or may be overly conservative, and there are increasing trends toward risk-based inspection of items in hot hydrogen service.

In this context, unsatisfactory service experience with the carbon–1/2Mo steel has led to consideration of the Nelson curves. Currently, API 941 warns against new construction with the alloy and urges inspection and monitoring of existing equipment.

There are a number of inspection methods available. Most of them are based on ultrasonics:

1. Ultrasonic echo attenuation method.
2. Amplitude-based backscatter.
3. Velocity ratio.
4. Creeping waves/time-of-flight measurement.
5. Pitch-catch mode shear wave velocity.
6. Ultrasonic method based on backscatter and velocity ratio measurement.
7. AUBTs – advanced ultrasonic backscatter techniques.
8. Method based on time-of-flight diffraction (TOFD), thickness mapping, backscatter, and velocity ratio.
9. *In situ* metallography – replicas.

The overview of these techniques is given in Table 12.1.

In summary, in this section we have introduced the concept of HA and described the influence of various parameters on HA of materials, namely, steels. In order to safely use such materials in the presence of hydrogen, it is recommended to have an internal specification. This specification must cover:

- The "scope," i.e. the hydrogen pressure, the temperature, and the hydrogen purity.
- The "material," i.e. the mechanical properties, chemical composition, and heat treatment.
- The stress level of the equipment.
- The surface defects and quality of finish.
- The welding procedure, if any.

The two main sources of hydrogen that contribute to HA of steels in industries are from the corrosion of steel by boiler water in the waterwall tube for coal-fired boilers and from high pressure, high temperature hydrogen-containing atmospheres used in petroleum refining. HA problems related to these two separate areas are briefly discussed in Section 12.2.2.

12.2.2 Attack in Coal-Fired Boilers and Petroleum Refining

Subcritical drum boilers that use a recirculating steam-generating system are prone to high temperature corrosion, particularly if the water chemistry is not properly controlled. Control requires (i) removal of impurities to purify the water and (ii) chemical treatments to control pH, electrochemical potential, and dissolved oxygen concentration. With adequate control, the waterwall steel tube forms a protective magnetite (Fe_3O_4) scale when steel is corroded by water under normal operating conditions (Cohen 1989):

$$3Fe + 4H_2O \rightarrow Fe_3O_4 + 4H_2 \qquad (12.1)$$

whose by-product is hydrogen. Growth of magnetite follows a parabolic rate law with the scale growth rate diminishing with time. Accordingly, the generation of hydrogen likewise diminishes with time once a steady state is reached. The atomic hydrogen produced combines with other hydrogen atoms to form molecular hydrogen that is then dispersed in the boiler water as a gas or in solution. However, when water chemistry is poorly controlled, the boiler deposits formed on the surface of the waterwall tube may lead to acidic corrosion attack on the tube under the deposits, leading to large atomic hydrogen absorption by the steel. Hydrogen atoms in the steel then react with iron carbide (Fe_3C) to form methane (CH_4):

$$Fe_3C + 4H \rightarrow 3Fe + CH_4 \qquad (12.2)$$

Methane gas then accumulates at grain boundaries and other interfaces due to its low diffusivity. Microcracks and microfissures are eventually developed by increasing local gas pressure created by the increasing amount of methane gas produced by the iron carbide/hydrogen reaction. Furthermore, because of iron carbides being reduced to iron by reaction (12.2), the affected area is decarburized. The locations that are often susceptible to HA in the boiler are the burner zone and the bull nose area (Stultz and Kitto 1992). Monitoring and controlling boiler water chemistry is critical in preventing internal tube deposits and HA (Dooley 1987).

HA is also a serious materials issue in the design and operation of refinery equipment, such as reactors in hydrotreating, reforming, and hydrocracking units. The mechanism for HA of steels in petroleum refining is essentially the same as that described in the waterwall tube that suffers HA in the boiler. As discussed earlier, adding Cr and/or Mo to the steel to increase the stability of iron carbides can increase the resistance of the steel in HA. But concerns have been raised as discussed by Parthasarathy (1985). Thus, Cr–Mo steels are much more resistant to HA than carbon and C–0.5Mo steels. The conditions under which carbon and Cr–Mo steels can be used in high temperature hydrogen service are described in detail in API 941 (Parthasarathy 1985). The behavior of carbon and Cr–Mo steels with respect to their resistance to HA is summarized in Nelson curves, as shown in Figures 12.1 and 12.2 (Chiba et al. 1985; Merrick and Ciuffreda 1982; Sorell and Humphries 1978; Turnbull 1995).

Table 12.1 Inspection methods to detect and quantify hydrogen attack

Inspection method	Equipment required	Principle	Advantages	Limitations	Remarks
Ultrasonic echo attenuation method	Ultrasonic flaw detector or pulser/receiver and oscilloscope, longitudinal wave transducer	This technique measures the loss of back-wall echo amplitudes as an indication of hydrogen damage	Low cost, simple to use	It has no ability to discriminate hydrogen attack from abnormal grain size, inclusions, laminar cracks, rough surfaces, internal surface geometry, cladding, disbondment between cladding and base metal	Not recommended as a stand-alone method for detection of hydrogen attack
Amplitude-based backscatter	Ultrasonic flaw detector or pulser/receiver and oscilloscope, longitudinal wave transducer	This technique measures the amplitude of backscattering signals and uses high backscattering amplitude as the indication of hydrogen damage	Low cost, simple to use	It cannot differentiate hydrogen attack from internal flaws such as laminar cracks and inclusions. The validity of the technique also depends on the surface condition of the calibration material under examination as well as on the pressure applied on the ultrasonic transducer	Not recommended as a stand-alone method for detection of hydrogen attack
Velocity ratio	Ultrasonic flaw detector or pulser/receiver and oscilloscope, longitudinal and shear wave transducers	This technique measures the shear-to-longitudinal wave velocity ratio of the entire wall thickness to assess the extent of hydrogen damage	Low cost, relatively simple to use	Cladding materials influence the result. It cannot identify hydrogen damage less than 15% of the wall thickness	Not recommended as a stand-alone method for detection of hydrogen attack
Creeping waves/time-of-flight measurement	Ultrasonic flaw detector or pulser/receiver and oscilloscope, creeping wave transducer	This technique measures the reduction of creeping wave velocity as the indication of hydrogen damage	Low cost, relatively simple to use	It is applicable only to partially damaged steel and only to thin-walled vessels	Not recommended as a stand-alone method for detection of hydrogen attack
Pitch-catch mode shear wave velocity	Ultrasonic flaw detector or pulser/receiver and oscilloscope, set of shear wave transducers	The relative change in shear wave velocity is measured and correlated to the extent of hydrogen damage	Low cost, relatively simple to use	This technique cannot differentiate hydrogen attack from change of material thickness. Its sensitivity to hydrogen damage is low	Not recommended as a stand-alone method for detection of hydrogen attack

Ultrasonic method based on backscatter and velocity ratio measurement	Ultrasonic flaw detector or pulser/receiver and oscilloscope, set of shear and longitudinal wave transducers	To detect suspect areas (areas affected by hydrogen attack), the backscatter technique is used. To confirm the findings of the backscattering measurement, the sound velocity measurement method is employed	Relatively simple to use and accurate method	Cannot be used to its full extent on clad and complicated geometry areas (see velocity ratio and scatter method limitations)	Recommended method for detection of hydrogen attack
AUBTs – advanced ultrasonic backscatter techniques	Ultrasonic flaw detector or pulser/receiver and oscilloscope, set of shear and longitudinal wave transducers, plotter	A pattern-based backscattering technique is used as the initial screening method. Depending on the backscatter pattern observed, one of the several follow-up techniques, including frequency-dependent backscatter, direction-dependent backscatter, velocity ratio, spectral analysis, and spatial averaging can be used to determine the cause of backscattering signal	Determines the distance of hydrogen attack progression, can be used to determine the material mechanical properties of the hydrogen-damaged region	Requires some degree of skill in interpreting pulse-echo patterns	Recommended method for detection of hydrogen attack
Method based on TOFD, thickness mapping, backscatter and velocity ratio	TOFD equipment, thickness mapping equipment	The backscatter technique is used as an initial scanning; then velocity technique and thickness mapping techniques are used to confirm and provide picture of the extend of the damage	Gives permanent record of test results. Relatively accurate	Requires some degree of skill in interpreting TOFD and pulse-echo patterns	Recommended method for detection of hydrogen attack
In situ metallography replicas	Grinding disc, abrasive papers. Final cleaning chemicals and polishing suspensions. Acetate films, microscope	Detects microstructure changes in tested areas, degradation of material, microcracking and their causes (e.g. creep, hydrogen damage)	Can be carried out *in situ*. Gives permanent high-resolution record. Relatively fast and cost effective	Requires high degree of skill in preparing and interpreting microstructure images. Sensitive to surface contamination. This technique samples small areas only, and it is not able to measure the depth of the damage	Recently, the replication microscopy technique has become an important non destructive evaluation (NDE) method for oil and power industry. Recommended method

12.3 Corrosion by Water Vapor

Water is present in almost all environments where alloys and superalloys are used at elevated temperatures. Combustion of fossil and biofuels produces a high amount of water vapor. Steam is injected in stationery gas turbines to lower the flame temperature and is also formed during combustion.

The presence of moisture in an oxidizing medium affects the oxidation behavior of metals at high temperatures. The effect of water vapor can be linked to the following processes:

- An enhancement of the reaction at the oxide–gas interface due to fast transport of gases, thereby modifying the scale/gas interface or even producing volatile hydrated species.
- Transport of oxygen through voids at the metal–oxide interface, affecting the scale microstructure and properties.
- Changes in the concentration of point defects in the oxide scale, followed by changes in the transport properties of the scale, which are due to the possible dissolution of hydrogen in the oxide.

The kinetics during oxidation in the presence of water vapor is different of those obtained in dry air or oxygen, which is generally true, although the thermodynamic activity of oxygen is the same, as the dissociation of the water molecule is very stable.

As parameters, such as grain size, grain boundary, and porosity of the oxide layer, which may be induced by the presence of water in the atmosphere, affect the mechanical properties of oxide scales, the understanding of the effects of steam on the oxidation resistance of alloys is important.

In the case of high temperature materials, the effect of water vapor depends strongly on the nature of the formed protective scale, the exposure temperature, and water vapor pressure. Alumina-forming materials are widely used at elevated temperatures; therefore, their interaction with water vapor is of technical importance in many fields, such as heterogeneous catalysis, corrosion, and microelectronics. The scale surface morphology and properties may be altered by the presence of moisture. It is therefore necessary to understand what effects parameters such as the amount of water vapor and the partial pressure have on the resistance of oxides particularly alumina scales (see also Section 7.7.2).

12.3.1 Kinetics and Mechanisms of Oxidation

It has been suggested that the presence of water vapor affects the oxidation behavior of metals; therefore, the morphology of the scales is also affected (Rahmel and Tobolski 1965). Depending on the type of metal, the oxidation is, in some cases, enhanced or does not change the oxidation rates of alloys compared with the oxidation in dry air. For example, iron oxidizes 1.6 times faster at 950 °C in H_2/H_2O and O_2/H_2O mixtures than in dry air. The oxidation rate of a MCrAlY coating is 25 times greater in H_2/H_2O than in dry air at 1080–1100 °C (Leyens et al. 1996). The growth rates of chromia formers are proved to be higher in moisture-containing gases (Schütze et al. 2005; see also Section 7.7.2). However, water vapor has generally little effect on alumina-forming alloys (Saunders et al. 2008). The oxidation rate of Fe–21.5Cr–5.6Al is even slightly decreased in wet air compared with dry air at 1000 °C, whereas the growth rate of PM 2000, a mechanical alloyed material, is slightly increased during isothermal oxidation. Moisture has little effect on the oxidation of commercial Ni-based superalloys and coatings, as shown by Onal et al. (2003), but is detrimental for the scale adhesion.

The presence of water vapor affects the selective oxidation of species responsible for the formation of a protective scale. Kvernes et al. (1977) reported a decrease in the duration of the initial oxidation stage with water content in the ambient gas and an increase in the subsequent reaction rate under the same conditions for the high temperature oxidation of Fe–13Cr–*x*Al alloys. Though thicker scales formed, they were also less protective, including spinel in the inner part of the scale. Buscail et al. (1997) found that the water vapor decreases the isothermal oxidation rate of Fe–Cr–Al at 1000 °C. Although the effect was not significant, the study proposed that the initial transient oxidation processes were affected by the wet conditions and that water vapor might have significant effects on the cyclic oxidation of certain alloys.

It is well known that most technical steels oxidize faster in water vapor or in air or combustion gases containing water vapor than in dry air, but, according to Kofstad (1988), the mechanisms are not well understood. Therefore, it is important to know the composition and defect structure of the surface as they play an important role in the diffusion process.

Anghel et al. (2004) found that upon addition of water to CO gas, the dissociation rate of CO on Cr decreased, and after subsequent removal of water, the dissociation rate increased again. In this case, the surface activity for CO dissociation should be a key factor for carbon uptake in certain applications and can be reduced by adsorbed water. These results suggest the following adsorption ranking: $N_2 < H_2 < CO < H_2O$. Increased dissociation of oxygen ($O_2 \rightarrow 2O$) and complete dissociation of molecular water ($H_2O \rightarrow 2H + O$) on surfaces of metal–oxide promote an increased transport of both O and O^{2-} in the oxide due to

increased concentration gradient of O and O^{2-} over the oxides (Hultquist 1997).

Cation sites are Lewis acids and may interact with electron donor molecules, such as water that has a lone pair of electrons, while oxide ions may act as basic sites interacting with acceptor ions, such as proton to produce a hydroxyl group. Where selective oxidation occurs, oxygen may be added to the adsorbate, not as O^{2-}, but as a neutral oxygen atom. There will be a corresponding reduction of the substrate in the form of electrons that might be free carriers, but more often this will lead to a localized decrease in the oxidation state of the metal at the surface. Hydrogen is a nonpolar molecule with low polarizability and has a weak donor or acceptor properties. Water has a large dipole moment and lone pair of electrons and is therefore a good donor. Adsorption occurs by acid–base process through interaction with metal ions; non-dissociative molecular adsorption also occurs. Oxygen is a very powerful electron acceptor and can be reduced in several steps. Nitrogen and argon are generally inert, as expected.

The presence of water in the oxidizing atmospheres causes the formation of various defects, such as pores and whiskers. Whiskers are generally formed on the surface at the end of a dislocation by diffusion through a hollow void (Raynaud and Rapp 1984). This process is possible due to faster dissociation of water compared to oxygen, which leads to surface reaction as rate determinant for their growth and therefore their linear kinetics; however, as the oxide thickens, diffusion becomes the rate-controlling mechanism. Rahmel and Tobolski (1965) stated that pores occur at the iron/wustite interface during the oxidation of iron at 850 °C. In the presence of water vapor or carbon, a H_2/H_2O or CO/CO_2 mixture is formed, respectively, in these pores, which transports oxygen to the iron surface by an oxidation/reduction mechanism. Therefore, oxide bridges are built upward, from the metal to the scale, which enables the further oxidation of the metal without substantial inhibition. For this mechanism to take place, water vapor should penetrate the scale, and this occurs through microcracks or by proton transport. The pores are generally formed at the scale/oxide interface due to vacancies coalescence, especially for scale growing by outward transport of cations. The enhanced plasticity (ability to creep), possibly due to the incorporation of hydrogen in the lattice observed by Tuck et al. (1969), allows the scale to maintain the contact with the substrate. Quadakkers et al. (2005) showed that the scale spallation of oxides formed on Fe/12–19% Cr in steam is accompanied by the formation of a rapidly growing magnetite layer and an inner scale consisting of Cr_2–O_3 precipitates in a FeO matrix, whereby the two layers are separated by a gap due to pores. Additionally, molecular gas transport occurs through the outer scale. As the overall scale thickness increases, the Fe activity at the scale/gas interface gradually decreases due to an increasingly difficult transport of Fe cations to the oxide surface due to the presence of the large gap that develops. The purity of the alloy and exposure temperature plays an important role as they determine how the vacancies coalesce within the scale and/or at the interface scale/metal to form pores.

Porosity is observed at metal/scale interface during oxidation in dry air of chromia-formed alloys, while the pores are distributed through the entire scale. The effect of water vapor on transport mechanisms within chromia scales is to increase cation vacancies, and thus chromium diffusion is enhanced, leading to vacancy condensation and pore formation. At the same time, however, there is an increase in inward diffusion of oxidant due to the effective diffusion of OH^-, and Henry et al. (2000) suggest that the pores become incorporated in the growing scale. If wet gas is exchanged with dry gas during the oxidation, the scale remains permeable, indicating that water vapor is preferentially adsorbed in the internal surfaces, preventing further reaction with oxygen, as well as closure, as observed by Ehlers et al. (2006) during the oxidation of 9% Cr steels.

12.3.2 Protons Incorporation

Oxidation of metals in water vapor-containing atmospheres at high temperature is accompanied by the formation of hydrogen defects, which are mainly dissolved protons (Norby 1993; Tveten et al. 1999). The reaction can be written as

$$\frac{1}{2}H_2O(g) = H_i^{\bullet} + \frac{1}{4}O_2(g) + e' \tag{12.3}$$

or

$$\frac{1}{2}H_2\,(g) + h^{\bullet} = H_i^{\bullet} \tag{12.4}$$

As water reacts with oxygen to form hydroxyl ions, the following equation can be written:

$$H_2O\,(g) + 2O_0^x = 2HO_0^{\bullet} + 2e' + \frac{1}{2}O_2(g) \tag{12.5}$$

From this equation, it can be assumed that the concentration of dissolved proton depends on the activities of water as well as oxygen. Relatively large hydrogen concentrations may be dissolved in oxides doped with lower valence cations and with oxygen vacancies as the predominant native point defects. In this case, the interaction with water can be written as

$$H_2O(g) + V_O^{\bullet\bullet} = HO_0^{\bullet} + h^{\bullet} + \frac{1}{2}H_2(g) \tag{12.6}$$

One can see from Eq. (12.6) that oxygen vacancies are gradually filled while protons dissolve in the oxide. The literature demonstrates that hydrogen dissolves as protons and is bound to the oxide ions to form the substitutional ($OH_0^{\bullet}$) that

can be simply written as interstitial proton $H_i^{\bullet}$. It has been demonstrated that the concentration of interstitial protons is increased with $p(H_2O)$ and decreasing temperature. Thus, the dissolution of protons in the oxide may be written as

$$\frac{1}{2}H_2(g) = H_i^{\bullet} + e' \tag{12.7}$$

or considering the equilibrium of gases:

$$\frac{1}{2}H_2O(g) = H_i^{\bullet} + e' + \frac{1}{4}O_2 \tag{12.8}$$

Therefore, the incorporation of hydrogen protons in the oxide can be written as

$$H_2O(g) + V_O^{\bullet\bullet}(\text{crystal}) = 2H_i^{\bullet}(\text{crystal}) + O_0^x(\text{crystal}) \tag{12.9}$$

If this equation determines the dissolution, then the relationship with the partial pressure of water is given by

$$[H_i^{\bullet}] \cdots \alpha \cdots [V_O^{\bullet\bullet}]^2\, p(H_2O)^{1/2} \tag{12.10}$$

At high $p(H_2O)$ or $p(O_2)$, protons may become the dominant defect, compensated by defect electrons, metal vacancies, oxygen interstitials, or acceptor dopants. It is generally agreed that the Grotthuss mechanism allows transport of "water" in oxide scales by a proton "hopping" process in which protons localized at oxide ions move by transfer from one oxygen atom to another. Since oxygen is available everywhere, the net effect of proton diffusion is diffusion of water, and since proton diffusion rates are high compared with metal or oxygen, diffusion of "water" is easy (Saunders et al. 2008).

In close-packed structures, such as alumina and chromia, the dissolution of molecular water is less favored as, for example, in silica.

12.3.3 Volatility of Metal Hydroxides

Metal oxides generally react with water to form hydroxides and oxyhydroxides, which are sometimes volatile. The volatilization of several metals was studied by Opila (2004). The reactions of the most important oxides with water vapor for protection of metals at high temperature, to form volatile species, are

$$\frac{1}{2}Cr_2O_3 + H_2O(g) + \frac{3}{4}O_2(g) = CrO_2(OH)_2(g) \tag{12.11}$$

$$\frac{1}{2}Al_2O_3 + \frac{3}{2}H_2O(g) = Al(OH)_3(g) \tag{12.12}$$

$$SiO_2 + 2H_2O(g) = Si(OH)_4(g) \tag{12.13}$$

$$SiO_2 + H_2O(g) = Si(OH)_2(g) + \frac{1}{2}O_2(g)$$

$$SiO_2 + \frac{1}{2}H_2O(g) = SiO(OH)(g) + \frac{1}{4}O_2(g)$$

Volatilization generally induces an accelerated consumption of the scale-forming metal and, therefore, its depletion in the substrate.

The presence of water vapor is known to accelerate the degradation of chromia-forming alloys (Schütze et al. 2005). Asteman et al. (2000) showed that fast oxidation of the stainless steel 304L in the presence of water vapor was due to lower Cr/Fe ratios in the scales and consequently more rapid diffusion, where the changes in the Cr/Fe ratios were essentially attributed to the volatilization of chromium. $CrO_2(OH)_2$ is the most stable species compared with $CrO_2(OH)$ (Johnson and Panas 2000).

The influence of water vapor on the oxidation of alumina formers is not significant below 100 °C; however, the effect is much pronounced at 1400 °C, with $Al(OH)_3$ as the most stable of aluminum hydroxides (Hashimoto 1992). Thus, the rates of evaporation increase in the following order: $Al(OH)_3 < Si(OH)_4 < CrO_2(OH)_2$ (Opila 2004).

12.3.4 Plasticity of Oxide Scales

During the growth of oxide scales in the presence of water, the scale plasticity can change. The results reported by various studies are in contradiction; some workers found a decrease of oxides plasticity in the presence of water vapor, which induces spalling, whereas improvement of scale adhesion was observed as a result of increased plasticity by others. Through iron oxidation at 950 °C, Tuck et al. (1969) found that the scale thickening was accelerated with the introduction of moisture into the atmosphere. Their explanation was that water vapor, especially hydrogen, is incorporated into the lattice and prevents the loss of contact between the substrate and the scale, which is possible due to the increased plasticity (ability to creep) of the oxide in wet conditions, but not to the accelerated vacancy diffusion within the oxide. The water vapor (hydrogen) increases the concentration of dislocations and/or their sources and sinks or the mobility of already existing dislocations.

Rounded and spalled edges were observed on Fe specimens (Rahmel and Tobolski 1965) cycled in wet air, suggesting a lowering of the oxide plasticity due to moisture. The degradation manifested first at the specimen edges, where plastic deformation and accommodation of the surface oxide are required during thermal cycling in order to avoid spallation. This was observed in comparison with dry air exposure where the oxide was sufficiently plastic to deform at the edges and maintain adherence to the substrate during cycling.

Another result from this study (Atkinson 1985) was the rapid weight loss of oxide that was initiated much earlier in air containing water vapor.

12.4 Conclusions

The source of atomic hydrogen at elevated temperatures can be from the rapid waterside corrosion at the internal diameter of the waterwall tubes in a coal-fired boiler when water chemistry is not properly controlled and can also occur in some refinery equipment, such as reactors in hydrotreating, reforming, and hydrocracking units, which is exposed to a high temperature, high pressure hydrogen atmosphere. The atomic hydrogen reacts with iron carbide in the steel to form methane gas. Continued ingress of atomic hydrogen into the metal causes an increasing amount of methane gas to be generated and accumulated at grain boundaries and other interfaces, resulting in the formation of microcracks and microfissures in the steel. In addition, the steel is decarburized. Continued growth of damage and decarburization of steel result in its rupture. The water vapor addition to air affects the isothermal oxidation of the different alloys in different ways. Materials as alumina, for example, in these conditions, show a gross growth rate, and the observed mass gain may be due to the transformation of γ-AlO(OH) to formation of metastable δ-Al_2O_3, which is transformed gradually to α-Al_2O_3 at higher temperatures as shown by the following sequence:

$$\gamma\text{-AlO(OH)} \rightarrow \gamma\text{-}Al_2O_3 \rightarrow \delta\text{-}Al_2O_3 \rightarrow \theta\text{-}Al_2O_3 \rightarrow \alpha\text{-}Al_2O_3 \quad (12.14)$$

The increased mass gain during oxidation in moisture can be due to faster dissociation of water compared to oxygen, which lead to surface reaction as rate determining for their growth and therefore to linear kinetics; however, as the oxide thickens, diffusion becomes the rate-controlling mechanism, i.e. the kinetics should have been changed.

There are also more defects in the oxides formed in wet air – especially pores. This may be due to the reaction of water with the oxide to form hydrogen defects (protons), which modifies the defect structure and therefore the formal nature of the defect (Douglass et al. 1996). The other explanation may be that the oxide microstructure change leads to different diffusion processes in the scale. The pores are observed in the scale and not at the former substrate surface that, if present, should induce scale spalling. The fast diffusion of species induces thicker scales. As the water vapor amount increases, the effects are more severe, especially for alloys on which a continuous alumina layer could not be formed.

The formation of transient oxides can also be influenced by water vapor addition, as the transient oxide scale usually thickens with higher humidity. For instance, NiO growth could be faster than in dry air, as NiO is known to react with Al_2O_3 to form the spinel $NiAl_2O_4$ (Huang et al. 2006), and, as a result, the time dependence of different oxide formation may be affected. If hydrogen is incorporated as interstitial in NiO, which is a p-type semiconductor with cation vacancies (Birks et al. 2006), the following defect reaction occurs:

$$H_2O(g) = 2H_i^{\bullet} + O_0^x + V_{Ni}'' \quad (12.15)$$

The equation shows that the vacancy concentration is increased, which could lead to an increase of NiO growth rate. Hultquist et al. (2001) suggest that an enhancement of metal cation transport in alumina-forming materials, such as the alloy FeCrAlY, during high temperature oxidation can be achieved by adding hydrogen to the substrate, either by electrolysis of water or from the gas phase. Maris-Sida (2004) showed that for longer times of cyclic exposure (up to 500 hours) in wet air (air + 0.1 atm water vapor) compared with dry air, the scale formed on CMSX 4 at 1100 °C is thicker and exhibits a multilayered structure containing an appreciable, dense, and continuous layer of α-Al_2O_3 formed at the alloy surface at some early stage. This layer is maintained, while subsequent layers of $NiAl_2O_4$, $Ni(Al, Cr)_2O_4$, and NiO grow sequentially on top of the alumina. These results show that nickel may be diffusing through the alumina scale, although the possibility that these oxides formed initially as transient oxides cannot be ruled out. This increased NiO rate induces greater internal oxidation depths, which would increase the critical amount of aluminum required to form a continuous scale on the metal (Gesmundo and Viani 1986). Thus, the thicker transient oxide scale observed on several alloys and superalloys must be caused by the increased NiO and possibly chromium oxide growth rate. The accelerated oxygen transport in the presence of water vapor may be of significance too, as hydrogen can be easily incorporated into NiO and Cr_2O_3 – hence the faster diffusion of Ni and Cr ions through the scale, resulting in rise outward growth of their oxides.

The formation of spinels is also influenced by the water vapor presence and content. The spinel formation and stability depends strongly on the activities of the alloying elements in the alloy as shown in Figure 12.3 for the Ni–Al–O system. If we consider the formation of a spinel on α-Al_2O_3, which is on a Ni–Al alloy, the formation reaction can be written as follows:

$$Ni + Al_2O_3 + \frac{1}{2}O_2 = NiAl_2O_4 \quad (12.16)$$

This reaction could occur either at the α-Al_2O_3/gas or at the α-Al_2O_3/metal interface. As the oxygen pressure is very low at the oxide–metal interface, the Ni activity must be very high; in contrast, the Ni activities should be extremely low at the oxide–gas interface for the spinel to be formed. Sahin et al. (1992) suggested that Ni diffused through α-Al_2O_3; hence, Maris-Sida also proposed that the spinels are formed at the oxide–gas interface.

Ni must diffuse through defects to reach the oxide–gas interface. It is established that the growth of α-Al_2O_3 is controlled by the inward diffusion of oxygen through the

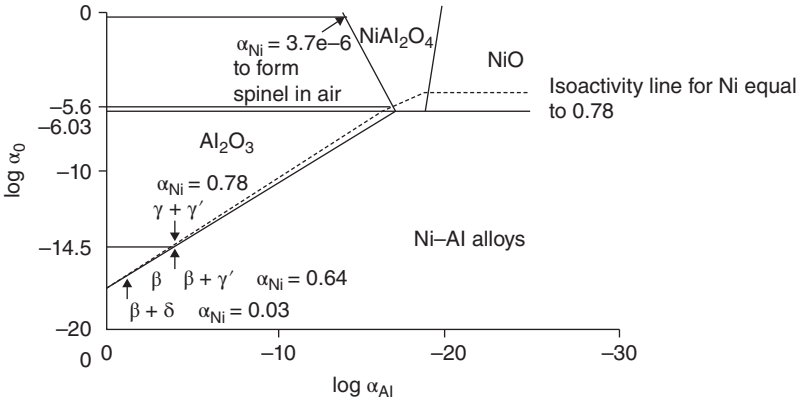


Figure 12.3 Schematic of Ni–Al–O stability diagram at 1000 °C with the activities of nickel indicated for various equilibria (Maris-Sida 2004).

oxide grain boundaries (Palladino and Kingery 1962). The proposed defects in α-alumina are Schöttky defects (Kröger 1983) involving alumina vacancies V'''_{Al} and oxygen vacancies $V^{\bullet\bullet}_{O}$. It is thus possible that Ni diffuses through these defects and reacts at the spinel/gas or at the $NiAl_2O_4/Al_2O_3$ interface. Ni^{2+} cation is slightly larger than Al^{3+} ($r_{Ni^{2+}} = 0.07$ nm and $r_{Al^{3+}} = 0.05$ nm), and the largest interface in α-alumina is 0.06 nm; it is, therefore, also possible that Ni can still diffuse through grain boundaries. Al is known to generally diffuse through grain boundaries in α-Al_2O_3 (Toplygo and Clarke 1999). For example, at 1000 °C, the activity of NiO in α-Al_2O_3 at the α-Al_2O_3-γ-γ' equilibrium is 4.3×10^{-10}, whereas the activity of NiO in α-Al_2O_3, as well as transport of nickel through α-Al_2O_3, becomes more favorable as the metallic substrate becomes depleted of aluminum or, in other words, as the oxygen reaches levels sufficient to ionize nickel. The diffusion of the species can also occur through microcracks. The formation of the other spinels can also be explained by the same mechanism as proposed for the formation of $NiAl_2O_4$. Akhtar et al. (2006) proposed that a phase transformation occurs in nickel-based single-crystal superalloys (CMSX 4 and CMSX 10) as a result of the oxidation that creates the external NiO scale. This transformation, which is the precursor to internal oxidation, creates the β phase (NiAl) first followed by the δ phase (Ni_2Al_3) prior to the formation of the spinel Ni(Cr, $Al)_2O_4$ and Al_2O_3 in succession.

References

Akhtar, A., Hedge, S., and Reed, R.C. (2006). *J. Miner. Met. Mater. Soc.* 58: 37.

Alvorado, G. (1995). *Inspectioneering J.* 1 (5).

Anghel, C., Hornlund, E., Hultquist, G., and Limbäck, M. (2004). *Appl. Surf. Sci.* 233: 392.

Asteman, H., Svensson, J.-E., Norell, M., and Johansson, L.-G. (2000). *Oxid. Met.* 54: 11.

Atkinson, A. (1985). *Rev. Mod. Phys.* 57: 437.

Birks, N., Meier, G.H., and Pettit, F.S. (2006). *Introduction to High Temperature Oxidation of Metals*, 2e. Cambridge: Cambridge University Press.

Buscail, H., Heinze, S., Dufour, P., and Larpin, J.P. (1997). *Oxid. Met.* 47: 445.

Chiba, R., Onishi, K., Ishii, K., and Maeda, K. (1985). *Corrosion* 41: 415.

Cohen, P. (ed.) (1989). *ASME Handbook on Water Technology for Thermal Power Systems*. ASME.

Das, A.K. (1996). *Metallurgy of Failure Analysis*. New Delhi: Tata McGraw-Hill.

Dooley, R.B. (1987). *Corrosion*, Metals Handbook, 9e, vol. 13, 990. Materials Park, OH: ASM International.

Douglass, D.L., Kofstad, P., Rahmel, A., and Wood, G.C. (1996). *Oxid. Met.* 45: 529.

Ehlers, J., Young, D.J., Smaardijk, E.J. et al. (2006). *Corros. Sci.* 48: 3428.

Gesmundo, F. and Viani, F. (1986). *Oxid. Met.* 25: 269.

Hashimoto, A. (1992). *Geochim. Cosmochim. Acta* 56: 511.

Henry, S., Mougin, J., Wouters, Y. et al. (2000). *Mater. High Temp.* 17: 231.

Huang, L., Sun, X.F., Guan, H.R., and Hu, Z.Q. (2006). *Oxid. Met.* 65: 391.

Hultquist, G. (1997). *Oxid. Met.* 47: 117.

Hultquist, G., Tveten, B., Hörnlund, E. et al. (2001). *Oxid. Met.* 56: 313.

Johnson, J.R.T. and Panas, I. (2000). *Inorg. Chem.* 39: 3181.

Kofstad, P. (1988). *High Temperature Corrosion*. London: Elsevier Applied Science.

Kröger, F.A. (1983). *High Temperature Corrosion*, vol. 6, 89. NACE.

Kvernes, I., Oliveira, M., and Kofstad, P. (1977). *Corros. Sci.* 17: 237.

Leyens, C., Fritscher, K., Gehrling, R. et al. (1996). *Surf. Coat. Technol.* 82: 133.

Maris-Sida, M.C. (2004). *Materials Science and Engineering*, 216. Pittsburgh, PA: University of Pittsburgh.

Merrick, R.D. and Ciuffreda, A.R. (1982). *Proc. API* 61 (III): 101.

Nelson, G.A. (1949). *Proc. API* 29M (III): 163.

Norby, T. (1993). *J. Phys. IV* 3: 99.

Onal, K., Maris-Sida, M.C., Meier, G.H., and Pettit, F.S. (2003). *Mater. High Temp.* 20: 327.

Opila, E.J. (2004). *Mater. Sci. Forum* 461–464: 765.

Palladino, A.E. and Kingery, W.D. (1962). *J. Chem. Phys.* 37: 957.

Parthasarathy, T.A. (1985). *Acta Metall.* 33: 1673.

Quadakkers, W.J., Ennis, P.J., Zurek, J., and Michalik, M. (2005). *Mater. High Temp.* 22: 47.

Rahmel, A. and Tobolski, J. (1965). *Corros. Sci.* 5: 333.

Raynaud, G.M. and Rapp, R.A. (1984). *Oxid. Met.* 21: 89.

Sahin, O., Nourbakhsh, S., Rhee, W.H., and Margolin, H. (1992). *Metall. Mater. Trans. A* 23: 3151.

Saunders, S.R.J., Monteiro, M., and Rizzo, F. (2008). *Prog. Mater. Sci.* 53: 775.
Schütze, M., Renusch, D., and Schorr, M. (2005). *Mater. High Temp.* 22: 113.
Sorell, G. and Humphries, M.J. (1978). *Mater. Perform.* 17: 33.
Stultz, S.C. and Kitto, J.B. (eds.) (1992). *Steam and Its Generation and Use*, 40e, 42. Babcock & Wilcox.
Toplygo, V. and Clarke, D.R. (1999). Per Kofstad Memorial Symposium, Honolulu, Hawaii. Pennington, NJ: The Electro-chemical Society.
Tuck, C.W., Odgers, M., and Sachs, K. (1969). *Corros. Sci.* 9: 271.
Turnbull, A. (1995). Proceedings of a Conference on Hydrogen Transport and Cracking in Metals, National Physical Laboratory, Teddington (April 1994). Cambridge: The University Press.
Tveten, B., Hultquist, G., and Norby, T. (1999). *Oxid. Met.* 52: 221.

Further Reading

Atkinson, A. (1982). *Corros. Sci.* 22: 347.
van der Burg, M.W.D. and van der Giessen, E. (1996). *Mat. Sci. Eng.* A220: 200.
van der Burg, M.W.D., van der Giessen, E., and Brouwer, R.C. (1996). *Acta Mater.* 44: 505.
van der Burg, M.W.D. and van der Giessen, E. (1997). *Acta Mater.* 45: 3047.
van der Burg, M.W.D., van der Giessen, E., and Tvergaard, V. (1998). *Mat. Sci. Eng.* A241: 1.
Garverick, L. (ed.) (1994). *Corrosion in the Petrochemical Industry*. Materials Park, OH: ASM International.
Hänsel, M., Quadakkers, W.J., and Young, D.J. (2003). *Oxid. Met.* 59: 285.
Hausgrud, R. (2003). *Corros. Sci.* 45: 211.
Hultquist, G., Tveten, B., and Hörnlund, E. (2000). *Oxid. Met.* 54: 1.
Janakiraman, R., Meier, G.H., and Pettit, F.S. (1999). *Metall. Mat. Trans. A* 30: 2905.
Jedlinski, J. (2006). *Mater. Sci. Forum* 513: 149.
Mrowec, S. (1985). *Oxid. Met.* 23: 266.
Niu, Y. and Gesmundo, F. (2006). *Oxid. Met.* 65: 329.
Parthasarathy, T.A. and Shewmon, P.G. (1984). *Metall. Trans. A* 15: 2021.
Prillieux, A. (2017). *Hydrogen and Water Vapour Effects on Oxygen Solution and Diffusivity in High-Temperature Fe-Ni Alloys*, Ph D Thesis. France: University of Toulouse.
Ropital, F. (2010). *Corrosion and Degradation of Metallic Materials: Understanding of the Phenomena and Applications in Petroleum and Process Industries*. Paris: IFP Publications, Editions TECHNIP.
Schakerford, J.S. (1996). *Introduction to Material Science for Engineers*. London: Prentice Hall International.
Settle, F.E. (ed.) (1997). *Handbook of Instrumental Techniques for Analytical Chemistry*. New York: Prentice Hall.
Stott, F.H. (1987). *Rep. Prog. Phys.* 50: 861.
Sundararajan, G. and Shewmon, P.G. (1981). *Metall. Trans. A* 12: 1761.
Timmins, P.F. (1997). *Solutions to Hydrogen Attack in Steels*. Materials Park, OH: ASM International.
Viswanathan, R. (1995). *Damage Mechanisms and Life Assessment of High Temperature Components*. Materials Park, OH: ASM International.
Young, D.J. (2008). *High Temperature Oxidation and Corrosion of Metals*, vol. 1. Oxford: Elsevier.

Chapter 13

Corrosion in Molten Salts

13.1 Introduction

Interest in the use of molten or fused salts in industrial processes is continually increasing, and these media are gradually becoming accepted as a normal field of chemical engineering. The change is being accelerated by the increasing demand for the production of refractory metals, actinides, lanthanides, transition, and light metals; by processes involving fused salts, the use of molten salts in high temperature batteries and fuel cells; and also by the novel chemical engineering techniques that have been developed in the nuclear energy industry (Lovering 1982). For example, a nuclear reactor using molten fluorides as a fluid fuel has operated, and this has involved the use of pumps, heat exchangers, and similar equipment to circulate the high temperature melt. Table 13.1 summarizes the general applications of molten salt technology in several industries.

In certain applications it has not always been easy to find suitable metallic container materials, particularly in the nuclear energy industry, where, for certain applications, corrosion resistance of the same order as that required by the fine chemical industry has to be achieved in order to prevent contamination of the process stream. Such difficulties have stimulated the study of corrosion in fused salts and have led to a fairly high degree of understanding of corrosion reactions in these media.

The subject is also closely related to fuel-ash corrosion observed in oil-fired refinery boilers, hot corrosion observed in gas turbines, other molten or semi-molten deposit corrosion observed in waste incineration systems, etc. Attention has been focused on the electrochemistry of these types of deposit corrosion (Burrows and Hills 1966) and the relevant thermodynamic data summarized in the form of diagrams (Rahmel 1968; Sequeira 2003). Fluxing and descaling reactions also resemble, in some aspects, reactions occurring during the corrosion of metals in fused salts.

There are two cases in which a metal can be attacked by a salt melt: if it is soluble in the melt or if it is oxidized to metal ions. In the first case, attack occurs by direct dissolution without oxidation of the metal, and the mechanism is likely to be closely similar to attack by liquid metals.

If the solubility is appreciable, excessive corrosion can be expected, but with few exceptions metals appear to be appreciably soluble only in their own salts. Most of the metals of the first and second groups of the periodic table are soluble in their own halides, and, in certain cases, there is complete miscibility at high temperatures (Mamantov 1969).

Many hundreds of molten salt–metal corrosion studies have been documented. Some helpful publications are listed in Section 13.14. Although the literature related to studies of corrosion in molten salts is extensive, there is still a strong need for intensive research in this field. The present chapter focuses on key aspects of molten salt corrosion processes and on corrosion data useful in selecting high temperature materials. Of course, since little information on corrosion involving only metal solubility effects is available, the present study will be confined to corrosion arising as a result of oxidation of the metallic material to ions.

13.2 Corrosion Process

Molten salts are a class of high temperature liquids that range from the low-melting systems such as the $LiNO_3$–KNO_3 eutectic (m.p. 120 °C) and molten organic salts to the high-melting systems of molten metal oxides, some of which have melting points in excess of 1400 °C. Three broad classes of molten salts may be distinguished. These are the simple ionic liquids such as molten halides and halide mixtures; the simple oxyanionic liquids such as molten nitrates, sulfates, and carbonates; and the complex polymeric oxyanionic liquids such as molten phosphates, borates, and silicates. Molten halides and oxysalts are the most interesting melts with regard to their occurrence in molten salt corrosion processes.

Molten salts are liquids with some characteristics that are different from those of liquids at room temperature.

High Temperature Corrosion: Fundamentals and Engineering, First Edition. César A. C. Sequeira.
© 2019 John Wiley & Sons, Inc. Published 2019 by John Wiley & Sons, Inc.

Table 13.1 General applications of molten salt technology in several industries (Lovering 1982)

Power	Metals/materials	Chemicals
Solar/thermal: collection, storage, transfer	Extraction: refractory metals, actinides, lanthanides, transition, and light metals	Fuels: cracking, catalysts
Nuclear: homogeneous reactors, reprocessing	Processing: heat treatment, annealing, quenching, cleaning, cementation, electroforming	Plastics: curing, etching, vulcanizing
Batteries	Surface finishing: anodizing, plating	Pyrolysis: recycling, scrap treatment, hazardous material disposal
Fuel cells	Joining: fluxes and slags for welding, brazing, soldering, and electroslag refining	Synthesis: organics, gases
	Composites: glasses, ceramics, slags	Special applications: liquid crystals, single-crystal growing, matrix
	Recycling	

Molten salt studies are very important for understanding the liquid state because molten salts consist of ions and the principal forces between particles are coulombic interactions. The existence of coulombic interactions in molten salts is demonstrated by very high melting and boiling points, surface tensions, and electrical conductivities, in comparison with these properties of other liquids. Other properties of the pure molten salts, or ionic liquids, or molten electrolytes, are of the same order of magnitude as for nonpolar liquids, although many ionic liquids exist only at high temperatures. These properties are density, viscosity, refractive index, compressibility, vapor pressure, heat of vaporization, heat of fusion, heat capacity, etc. (Blander 1964; Galasiu et al. 1999; Sundheim 1964).

In general, the ionic character of the solid crystalline form persists in the molten state, although local association reactions may take place. The range of coexistence of metal–molten salt systems depends on two simple factors, namely, the relative electronation–de-electronation potentials of the various constituents and their relative basicities. A measure of the basic or acidic strength of the system is given by

$$pO^{2-} = -\log\{O^{2-}\} \tag{13.1}$$

where pO^{2-} is equivalent to the pH for protolytic solvents. A high value of pO^{2-} indicates an acidic (and corrosive to metals) melt and a low value a basic melt. The self-dissociation constants of pure oxyanionic melts indicate the acidic strengths of the liquids. pO^{2-} for $CO_3^{2-} < SO_4^{2-} < NO_3^-$. This shows that molten nitrates are more acidic than molten carbonates (at comparable temperatures). pO^{2-} values for oxyanionic species in dilute solution provide a useful means for predicting acid–base reactions between different species. The numerical value of the term pO^{2-} will depend upon the units of concentration employed: convenient ones are molarities, molalities, mole fractions, or mole ratios.

Many studies have been published on the corrosion in fused salts in terms of acid–base properties of the melts (Lewis 1971). There have been many different methods used in the determination of pO^{2-} values. Most of the measurements have been restricted to the low temperature systems of molten nitrates and chlorides. Acid–base reactions in molten sulfates are not so well documented.

The high electrical conductivity of many molten salts makes them particularly suitable as media for electrochemical investigation (Galasiu et al. 1999).

Electrochemical studies in oxyanion melts have been initially confined to nitrate and carbonate systems. Nitrates, being low melting, are convenient media to work with, and carbonates have considerable technological importance as electrolytes for high temperature fuel cells. Molten sulfates have low vapor pressure and high melting points, and their thermal stability depends on the nature of cations, alkali sulfates being the more stable. They appear to be convenient media for electrochemical studies, and they have received much attention due to their practical importance. For example, the sulfate–chloride provides a molten salt system over a wide range of temperatures relevant to gas turbine conditions, thus promoting many studies (Hocking et al. 1989). It follows from what has been said that effects analogous to "electrochemical" or "oxygen concentration" corrosion in aqueous systems can occur in salt melts. Accordingly, in metal/melt systems one possible way of ensuring adequate corrosion resistance is to choose conditions such that the metal is passive, which requires that it should become covered with an adherent, compact, insoluble film or deposit, preventing direct contact of the metal with its environment. Any melt that reacts with a metal to give a corrosion product insoluble in the melt is in principle capable of passivating the metal, e.g. passivity can be expected to occur in oxidizing salts in which metal oxides are sparingly soluble. Thus, iron is highly resistant to alkali nitrate melts because it becomes passive, and passivity has also been observed by electrode potential measurements of an iron electrode in chloride melts containing nitrates (Littlewood and Argent 1961), although in this case the oxide corrosion product is not particularly protective. In general, fused salts are "good"

solvents for inorganic compounds so that passivity is not likely to be a widely encountered phenomenon.

"*Wash-line*" *attack* is also a common feature of corrosion by molten salts in contact with air, because the anodic and cathodic reactions will not necessarily occur at the same metal site, and "anodic" and "cathodic" areas can develop as in aqueous solutions.

When a temperature gradient exists in a system containing metal in contact with molten salt, thermal potentials are set up, causing removal of metal at high temperature points and deposition of metal at cooler places. This mass transfer is essentially different in nature from that met in liquid metal corrosion, which is simply a temperature-solubility effect. In fused salts, both the corrosion and deposition reactions are electrolytic, and it has been shown that an electrical path is necessary between the hot and cold regions of the metal. Edeleanu and Gibson suggest that this type of mass transfer be called "Faradaic mass transfer" to indicate that it requires an electrolytic current (Edeleanu and Gibson 1960).

Mass transfer deposits can lead to blockages in non-isothermal circulating systems, as in the case of liquid metal corrosion. In fused salts, the effect can be reduced by keeping contamination of the melt by metal ions to a minimum, e.g. by eliminating oxidizing impurities or by maintaining reducing conditions over the melt.

Corrosion of alloys at high temperatures is complicated by effects due to diffusion, particularly where the alloy components have different affinities for the environment, and corrosion of an alloy in a fused salt at high temperature often exhibits features similar to those of internal oxidation. Selective removal of the less noble component occurs, and as it diffuses outwards, vacancies move inward and segregate to form visible voids (*Kirkendall effect*) (Sequeira and Amaral 2014). Since diffusion rates are faster at grain boundaries than in the grains, voids tend to form at the grain boundaries, and specimens often have the appearance of having undergone ordinary intercrystalline corrosion. More careful examination has shown, however, that in the case of Fe–18Cr–8Ni corroding in a fused 50–50 NaCl–KCl melt at 800 °C in the presence of air, the attack is not continuous at the boundaries, and the voids formed are not in communication with each other. In high nickel alloys, a greater proportion of voids is formed within the grains, and the appearance of intercrystalline attack is less marked. When Inconel is exposed to fused sodium hydroxide, a two-phase corrosion product layer is formed, resulting from growth of the reaction product – a mixture of oxides and oxysalts – into the network of channels.

Selective removal of the less noble constituent has been demonstrated by chemical analysis in the case of nickel-rich alloys in fused caustic soda or fused fluorides and by etching effects and X-ray microanalysis for Fe–18Cr–8Ni steels in fused alkali chlorides. This type of excessive damage can occur with quite small total amounts of corrosion, and in this sense its effect on the mechanical properties of the alloy is comparable with the notorious effect of intercrystalline disintegration in the stainless steels.

13.3 Thermodynamic Diagrams

The thermodynamic diagrams of Pourbaix (1949) have been particularly useful in understanding the behavior of metals in contact with aqueous solutions. Pourbaix plots equilibrium potential against pH, and the diagrams divide themselves into regions of stability at different solid phases (compounds of the metal in question).

In molten salts also, free energies can be expressed as equilibrium potentials, and there are a number of functions of composition that might be used as the other variable. In this context, available thermodynamic data (Glushko 1984; JANAF 1971; Kelley 1949; Kubaschewski and Evans 1985) support the calculations. The oxygen ions are generally quite important in matters of molten salt corrosion, so the function pO^{2-} (defined by the expression (13.1)) is often used as the equivalent to the pH in aqueous environments. A typical E versus pO^{2-} diagram for cobalt in molten sodium sulfate at 900 °C is shown in Figure 13.1

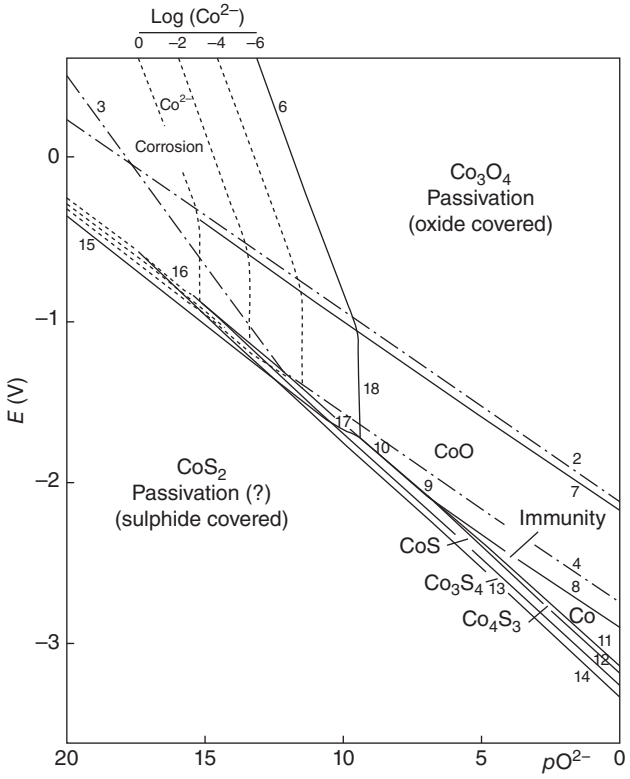


Figure 13.1 Typical E versus pO^{2-} diagram for cobalt in molten sodium sulfate at 900 °C (Sequeira 2003).

(Sequeira 2003). Areas of corrosion, immunity, and passivation are evident. More recent investigation on the thermodynamics of the molten salts is not only academic but also of practical interest (Barin 1993; Berkani and Gaune-Escard 2011; Gaune-Escard 2002). These studies are being used to further understand the behavior of metallic materials in molten salts (see also Section 3.3).

In the construction of E/pO^{2-} diagrams, there are two basic requirements, a reference scale of potential and a suitable standard state for oxidation activity. The first requirement has been satisfied by setting $E^\circ = 0$ and $dE^\circ/dT = 0$ for an appropriate reference electrode in the melt under consideration. For example, for nitrate and sulfate melts, the following electrode processes were assumed as basis for corresponding reference electrodes in these melts:

$$NO_2 + \frac{1}{2}O_2 - NO_3^- + e^- = 0 \qquad (13.2)$$

$$SO_3 + \frac{1}{2}O_2 - SO_4^{2-} + 2e^- = 0 \qquad (13.3)$$

The second requirement is rather more difficult to fulfill since a satisfactory and unambiguous oxygen electrode of the type

$$\frac{1}{2}O_2 + 2e^- = O^{2-} \qquad (13.4)$$

is not yet experimentally established in oxyanionic melts. In fact, apart from other difficulties, peroxide and superoxide ions have been identified in the melt (Mamantov 1969; Sequeira 1989), which enhances the problem.

Actually, the E versus pO^{2-} diagram is probably more useful than the Pourbaix diagram because of the absence of kinetic limitations at elevated temperatures. The following problems, however, do exist:

- Molten salt electrode reactions and the concomitant thermodynamic data are not readily available.
- Products from the reactions are often lost by vaporization.
- Diagrams based on pure component thermodynamic data are unrealistic because of departure from ideality.
- Lack of passivity even where predictions would show passive behavior.
- The stable existence of oxides other than the O^{2-} species.

13.4 Corrosion Rate Measurements

From what has been said already, it is clear that determinations of "corrosion rates" from small-scale experiments must be treated with great caution. If the metal cannot passivate, it will corrode until it becomes immune, at which point the corrosion rate will fall to zero; between initial exposure and the attainment of immunity, the corrosion rate will be continually changing. If, on the other hand, it is impossible for the metal to come to equilibrium with the melt, then the rate of corrosion, although probably constant, will be primarily controlled by diffusion and interphase mass transfer rates, and the geometry of the system will be an overriding factor. For this reason, it is not always possible to correlate the results of different workers under apparently similar conditions, nor can such results be expected to correspond particularly closely to the amount of corrosion encountered in larger-scale apparatus (Ozeryanaya 1985; Skelton and Horton 1999; Zeng et al. 2001).

It is not worthwhile, therefore, to give a digest of experimentally determined corrosion rates, but the reader is referred to typical data (Delong et al. 2002; Evans 1960; Janz and Tompkins 1979) for further information on this topic.

One interesting feature of comparative experiments with a series of salts having a common anion is that the aggressiveness of the salts toward metals is dependent on the nature of the cation. The aggressiveness of chloride melts in contact with air is in the order

$$LiCl \sim MgCl_2 \sim CaCl_2 \gg NaCl > KCl$$

In the case of $CaCl_2$ and NaCl, the order corresponds with the corrosion behavior expected from cathodic polarization curves. The order of aggressiveness of chlorides can also be explained on the basis of redox potentials of the melts, calculated on thermodynamic grounds from the free energies of formation of the appropriate oxides and chlorides. The order of aggressiveness of nitrates is complicated by passivity effects, while that of alkalis in contact with air is

$$KOH > NaOH > LiOH$$

This is the reverse order of the aggressiveness of chlorides and indicates that the mechanism of corrosion in the two systems is different, i.e. in the latter case it involves the discharge of hydrogen as in acid aqueous solutions.

13.5 Test Methods

A number of kinetic and thermodynamic studies have been carried out in capsule-type containers. These studies can determine the nature of the corroding species and the corrosion products under static isothermal conditions and do provide some much needed information. However, to provide the information needed for an actual flowing system, corrosion studies must be conducted in thermal convection loops or forced convection loops, which will include the effects of thermal gradients, flow, chemistry changes, and surface area effects. These loops can also include electrochemical probes and gas monitors (Koger 1987).

The corrosion process is mainly electrochemical in nature because of the excellent ionic conductivity of most molten salts. Therefore, the techniques and processes used in the electrochemical area to study processes in molten electrolytes (e.g. galvanostatic computational, chronoamperometry, chronopotentiometry, linear, cyclic, and square wave voltammetry, scanning electrochemical microscopy) also apply to studies of molten salt corrosion. Furnaces, cells, electrodes, and purification are particularly important aspects and deserve the following information.

Furnace and controls: The general experimental procedures in molten salt electrochemistry are common to most high temperature measurements and have been extensively reviewed by Bockris et al. (1959).

The most common type of high temperature apparatus is based on the conventional vertical wire wound furnace, which is cheap to build and simple and safe to operate up to 1600 °C. The heating element of Nichrome, Kanthal, molybdenum strip, etc. is wound on a refractory tube and embedded in thermal insulant. Metallic shields should be placed inside the refractory tube primarily to reduce electrical noise and also to smooth out temperature gradients within the hot zone of the furnace. Temperatures are measured by chromel–alumel or platinum–platinum 13% rhodium thermocouples sheated in pyrex, supremax, or alumina, depending on temperature. Proportional or high–low controllers usually control furnace temperatures.

Electrochemical cell: Molten salt systems are normally contained in sealed envelopes of glass, silica, or alumina, depending on the temperature. Electrodes can be introduced through ground glass joints placed on the cold side of the cell, without losing the controlled atmosphere in the envelope. The choice of materials directly in contact with the melt is particularly important since "acidic" materials like silica can modify the pO^{2-} of the melt through their buffering action; hence metallic (platinum, gold) containers are preferable. However, nonmetallic containers (especially of recrystallized alumina) have been widely used (Brown et al. 1970; Galasiu et al. 1999; Hocking et al. 1989). A typical high temperature cell assembly is shown in Figure 13.2 (Sequeira and Hocking 1978a).

Electrodes: Gold, silver, and, most commonly, platinum, as foil or wire, are employed for redox (electronation–de-electronation) electrodes as well as for counterelectrodes. When the melt container is metallic, it may also act as the counterelectrode. The working metal electrodes may be in form of rod, foil, or wire; their adequate insulation, at lower temperatures, can be obtained with a refractory insulator (e.g. boron nitride insulating shield), and above 800 °C, it is thought that the use of cordierite will avoid the triple contact metal–melt–atmosphere, will suppress possible crevices on the edges of the metal electrode, and would keep constant the exposed area of the specimen. Cordierite bodies of general formula $2MgO{\cdot}2Al_2O_3{\cdot}5SiO_2$ in addition to imperviousness to moisture, high surface resistance, high mechanical strength, and high puncture strength are characterized by a low glassy constant and a low amount of alkali so as to ensure negligible ionic conductivity. In our laboratory, cordierite specimens were tested for sulfate attack at $T > 800$ °C, and crucible experiments still being used. These tests showed cordierite to be completely insoluble and highly thermal shock resistant in Na_2SO_4–NaCl melts, so the production of a cordierite gasket was developed, and a specimen holder was proposed as illustrated in Figure 13.3.

Reference electrodes: The behavior of a working electrode, either anode or cathode, is usually studied by measuring its potential with reference to a third electrode at constant potential, and the main problem in carrying out such electrochemical measurements in molten salts has been the development of a suitable reference electrode.

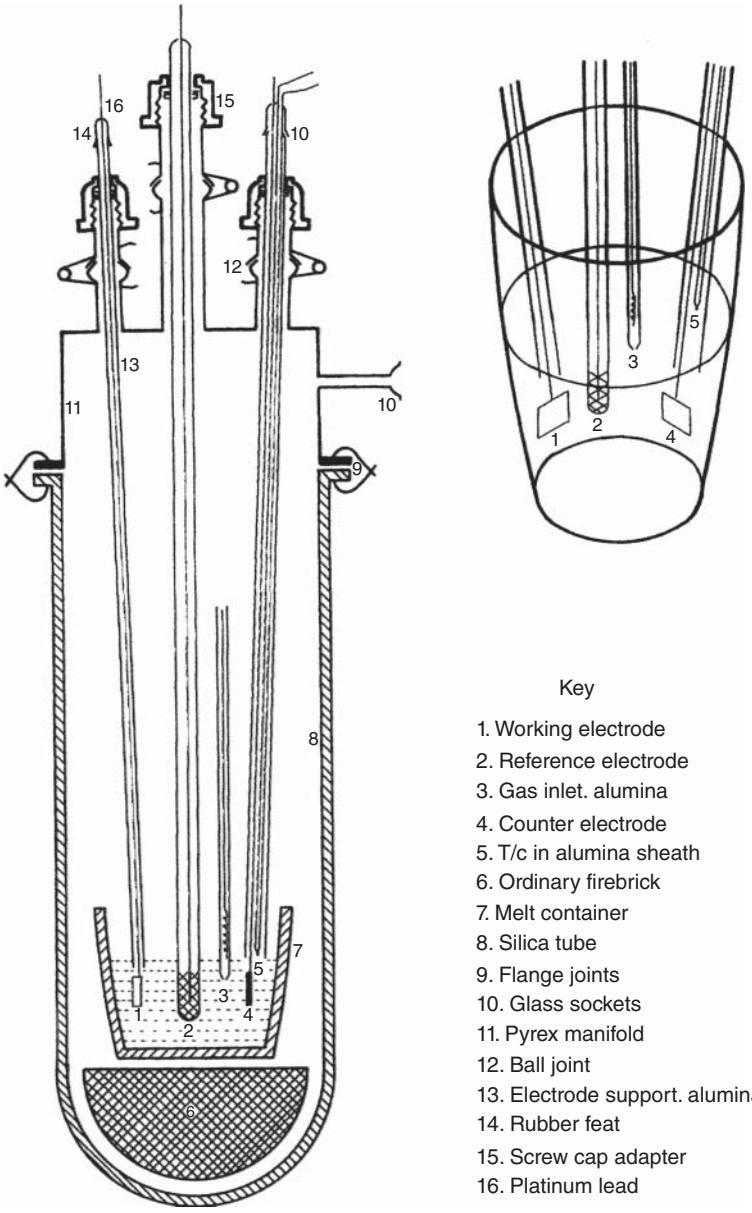
Minh and Redey (1987) have published an extensive chapter on molten salt reference electrodes. The commonest type of reference electrode in fused salts is a silver wire in contact with a solution of silver ions of known concentration in the solvent and separated from the bulk melt by a conductive barrier.

A paper by Danner and Rey (1961) describes a silver–silver sulfate reference electrode system useful to 1300 °C. Above the melting point of silver, a liquid silver pool was employed. This electrode was found to be the most satisfactory reference electrode for use in sulfate melts at temperatures up to 1000 °C.

It consists of a silver wire dipped into a solution of silver sulfate in Li_2SO_4–K_2SO_4 eutectic (m.p. 535 °C) in concentration ranging from 1 to 10 mol% and isolated from the melt by a pythagoras sheath:

$$\text{Ag} \mid \text{1–10\%solution of } Ag_2SO_4 \text{ in } Li_2SO_4 - K_2SO_4\text{eutectic} \mid \text{pythagoras sheath} \mid$$

The pythagoras porcelain acts as a solid K^+-ion conducting membrane. Pythagoras may be replaced by mullite ($2Al_2O_3{\cdot}SiO_2$), pyrex, or supremax glass at lower temperatures. The mullite sheath is conductive to sodium ions, and it was verified that it stood up well to the melt (Brown et al. 1970). Pyrex or supremax glass rapidly develops a brown coloration, and corresponding reference electrode potentials drift with time. Dissolved silver sulfate may be obtained either through *anodic dissolution* of a silver wire (which sometimes is difficult because no satisfactory container for the cathode compartment can easily be found)



Key

1. Working electrode
2. Reference electrode
3. Gas inlet. alumina
4. Counter electrode
5. T/c in alumina sheath
6. Ordinary firebrick
7. Melt container
8. Silica tube
9. Flange joints
10. Glass sockets
11. Pyrex manifold
12. Ball joint
13. Electrode support. alumina
14. Rubber feat
15. Screw cap adapter
16. Platinum lead

Figure 13.2 Typical high temperature cell assembly (Sequeira and Hocking 1978a).

or by simple dissolution of silver sulfate. A white precipitate of silver sulfate may be prepared by the addition of Analar sulfuric acid to an aqueous solution of Analar silver nitrate. Addition of silver ions to the solution by dissolution of silver oxide must be avoided because it decomposes thermally at 340 °C. The concentration of Ag_2SO_4 must be large enough to buffer the system but not so large as to cause a significant liquid junction potential.

For measurements over the longer periods of time, it is recommended to use electrodes with more than 1 mol% Ag_2SO_4 because of their higher potential stability. The atmosphere inside the reference half-cell may or may not be controlled and maintained in static or dynamic (slow bubbling) conditions. A criterion of the thermodynamically reversible e.m.f. properties of such reference electrodes is the micro-polarization test (Ives and Janz 1961). The relatively poor performance of these electrodes may be discerned in the local recrystallizations of the silver wire as well as in the decrease of the resistivity of the diaphragm over a period of days.

A reference electrode (Figure 13.4) has been developed by Sequeira and Hocking (1978a) that is similar to that described by Danner and Rey (1961) but differs in that the pythagoras capsule used by them is replaced by a mullite capsule conductive to sodium cations. Mullite has relatively poor thermal shock resistance, and the capsules fractured if brought from 900 °C to room temperature in much less than one hour, with Na_2SO_4. Crucible tests showed that mullite

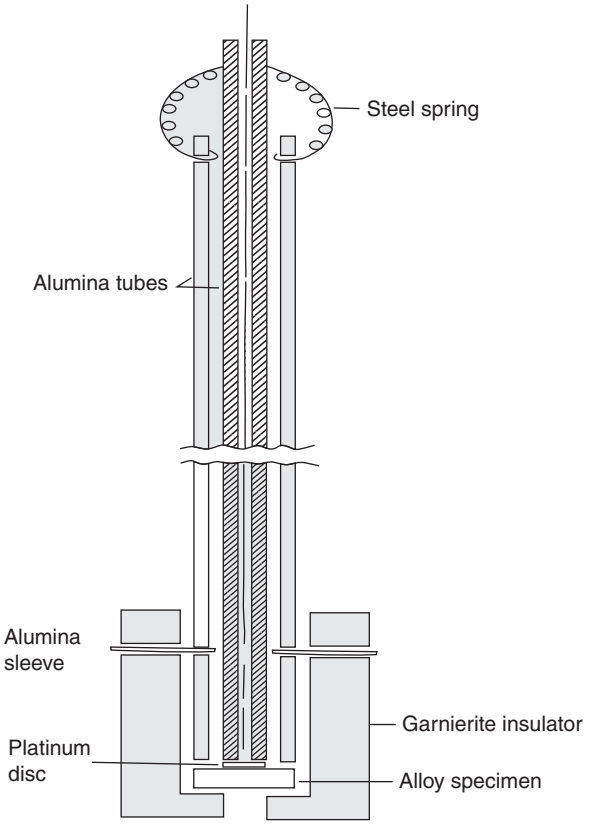


Figure 13.3 Proposed specimen holder for corrosion studies in sulfate melts.

is slightly dissolved in molten Na_2SO_4 (see Table 13.2), but the weight loss decreases strongly with time (as it is shown in Table 13.3) so that the mullite sheaths are useful, after aging, as membrane junctions for the reference half-cells. Therefore, the main advantages of the mullite electrode are that it is not so reactive with the molten Na_2SO_4 as the pythagoras electrode and it is reversible to sodium ions in the melt under study. In common with the Danner electrodes, it also has the advantage that salts in the sheath cannot intermix with those outside the sheath.

The potential of this reference electrode is the same whether evacuated or merely closed at the top by a PVC bulb through which the wire passes; closing is essential to prevent SO_3 escape from Ag_2SO_4 ($p_{SO_3} = 0.012$ atm at 900 °C). Reference electrodes are best stored at a red heat; long cooling times to ambient are necessary to prevent cracking. Against an Au wire electrode at 900 °C, an "ideal" reference electrode has a potential of −160 mV. Its reproducibility, stability, reversibility, and unpolarizability was tested by Sequeira (1979) and found satisfactory for corrosion studies.

Purification: Molten salts, whether used for experimental purposes or in actual systems, must be kept free of contaminants. This task, which includes initial makeup, transfer, and operation, is specific for each type of molten salt. For example, for nitrates with a melting point of approximately 220 °C purging with argon flowing above and through the salt at 250–300 °C removes significant amounts of water vapor. Another purification method used for this same type of salt consisted of bubbling pure dry oxygen gas through the 350 °C melt for two hours and then bubbling pure

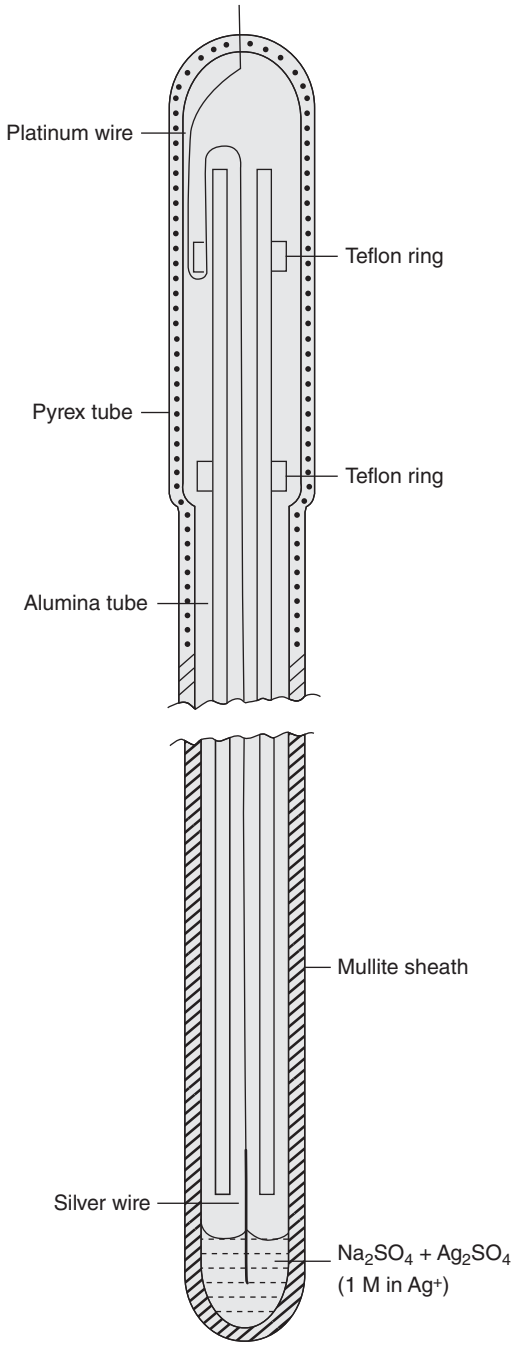


Figure 13.4 Reference electrode for molten sulfates (Sequeira and Hocking 1978a).

Table 13.2 Weight change and visual evidence of attack in Na_2SO_4-immersed ceramics (three hours tests at 900 °C, in air)

Type of material	Weight change (mg cm^{-2}) and observed corrosion					
	Sample 1	Repeat sample 1	Sample 2	Repeat sample 2	Sample 3	Repeat sample 3
Pythagoras (sillimanite) (Anderman Ltd.)	−1.86 surface roughened	Severely cracked	−2.24 surface roughened	Severely cracked	−1.04 slightly rough	Few small fragments
Alsint (sintered alumina 99.7%) (Anderman)	−0.48	−0.64 two large fragments	−0.18	−0.28	−0.22 three large fragments	
Morgan purox alumina	−0.24	−0.24	−0.20		−0.24	
Pythagoras 1800 (Anderman Ltd.)	−0.12	Severely cracked	−0.38		Severely cracked	Severely cracked
Degussit AL 23 alumina	−0.46	−0.40	−0.20	−0.36	−0.24	
Silica (thermal syndicate)	−2.66 extremely rough	−3.06 severely dissolved	−3.14 extremely rough			
Mullite (Morgan Ref. Ltd.)	Large fragments		−0.30	−0.24	Large fragments	Large fragments

Table 13.3 Weight versus time of mullite in molten Na_2SO_4 at 900 °C, in air (a mullite fragment was used)

Time (h)	Weight (g)	
	Sample 1	Sample 2
0	1.0658	0.8086
24	1.0637	0.8031
48	1.0634	0.8020
72	1.0632	0.8014
96	1.0631	0.8010

dry nitrogen for 30 minutes to remove the oxygen. All metals that contact the molten salt during purification must be carefully selected to avoid contamination from transfer tubes, thermocouple wells, the makeup vessel, and the container itself. This selection process may be an experiment in itself (Bratland 1987; Reavis 1987; White 1983).

More recently other electrochemical techniques have been largely used to study corrosion and other electrode processes in molten salts (Hamel et al. 2004; Keppert et al. 2008; Kerridge and Polyakov 1998; Polovov et al. 2008; Sarou-Kanian et al. 2009; Sørlie et al. 1995).

13.6 Fluorides

Interest in molten fluorides stems from their importance in nuclear technology and their use in the production of fluorine, electrodeposition of refractory metals, formation of corrosion-resistant diffusion coatings, and fluorination by electrochemical techniques. Most studies in alkali metal fluorides and other fluorides are rather recent and in connection with the development of molten salt reactors (Naumov and Bychkov 1996) and electrodeposition of silicon and the refractory metals. Corrosion in many fluoride molten salt melts is accelerated because protective surface films are not formed. In fact, the fluoride salts act as excellent fluxes and dissolve the various corrosion products (Lantelme and Groult 2013; Wang et al. 2014; Yaxin and Chaolin 2014). The design of a practicable system using molten fluoride salts, therefore, demands the selection of salt constituents, such as lithium fluoride (LiF), beryllium fluoride (BeF_2), uranium tetrafluoride (UF_4), and thorium fluoride (ThF_4), which are not appreciably reduced by available structural metals and alloys (Koger 1987).

Corrosion data reveal clearly that in reactions with structural metals, M:

$$2UF_4 + M = 2UF_3 + MF_2 \qquad (13.5)$$

Chromium is much more readily attacked than iron, nickel, or molybdenum.

Nickel-based alloys, more specifically Hastelloy N (Ni–6.5Mo–6.9Cr–4.5Fe) and its modifications, are considered the most promising for use in molten salts and have received the most attention. Stainless steels, having more chromium than Hastelloy N, are more susceptible to corrosion by fluoride melts but can be considered for some applications (Keiser et al. 1979).

Table 13.4 Results of corrosion test in $LiF–19.5CaF_2$ at 797 °C for 500 h (Misra and Whittenberger 1987)

Alloy	Depth of attack, μm (mils)	
	General[a]	Grain boundary[b]
Mild steel	—	155 (6.1)
304	—	185 (7.3)
310	—	130 (5.1)
316	—	165 (6.5)
RA330	—	270 (10.6)
B	30 (1.2)	—
N	15 (0.6)	15 (0.6)
S	90 (3.5)	—
X	—	140 (5.5)
600	90 (3.5)	30 (1.2)
718	45 (1.8)	120 (4.7)
75	30 (1.2)	135 (5.3)
25	—	95 (3.7)
188	—	105 (4.1)

Tests were conducted in alumina crucibles under argon.

[a]Intragranular voids near surface.

[b]Intergranular voids.

Misra and Whittenberger (1987) reported corrosion data for a variety of commercial alloys in molten $LiF–19.5CaF_2$, which was being considered for a heat storage medium in an advanced solar space power system, at 797 °C for 500 hours. The tests were conducted in alumina crucibles with argon as a cover gas. Results are tabulated in Table 13.4. For nickel-based alloys, chromium was detrimental. No influence of chromium, however, was noted in iron-based alloys.

Moisture, a common impurity in fluoride salts, can produce gaseous HF and increase corrosion attack (Tasaka et al. 1998). Therefore, it is important to reduce its level in the salt, resulting in decreased corrosion rates.

Recently, corrosion of Cu and Mg was also investigated in HF–KF mixtures (Germanaz et al. 1989) because of their use as conducting busbars in fluorine electrowinning. Copper busbars are preferred in low acidic mixtures, while magnesium is a more corrosion-resistant material in high acidic and low temperature mixtures.

13.7 Chlorides

Molten chlorides are widely used for electrowinning of metals, alloys, and gases, for annealing and normalizing of steels in high temperature batteries, etc.

Colom and Bodalo have investigated the corrosion of mild steel (1971) and Armco iron (1972) in molten LiCl–KCl eutectic as a function of the water content of the melt and of the temperature. Corrosion rates fell rapidly to a constant value with time (i.e. a passivating film is formed) and increased with rising temperature between 400 and 800 °C. The oxidation kinetics followed first a parabolic and then a linear rate law. The corrosion rate seemed to be scarcely affected by traces of water in the melt in the case of mild steel (it was enhanced by traces of water in the case of Armco iron), but, whereas the corrosion product in the dry melt was found to be Fe_2O_4, in the humid bath, both Fe_2O_3 and Fe_2O_4 were formed. Cathodic polarization waves indicate that the corrosion reaction is diffusion controlled and the diffusing species is Fe^{3+}. This interpretation requires further support in view of the known electrochemistry of iron in LiCl–KCl eutectic mixture. The rate of corrosion is lowered by cathodic protection.

Hoff (1971) has developed the theory for the corrosion of metals in molten salts under a temperature gradient. Dissolution of a metal on hot parts and recrystallization on the colder parts are caused by the thermoelectric effect. The equations of electrode kinetics can be used to obtain the theoretical relations. The temperature dependence of diffusion and of complex formation leads to a current distribution along the surface of the metal, showing a distinct maximum at the point where recrystallization occurs. The theory is tested using an aluminum wire in $AlCl_3$–NaCl–KCl in the temperature range of 215–420 °C.

Feng and Melendres (1982) have shown that Fe, Co, Ni, Cu, and Mo are considerably less corroded in molten LiCl–KCl eutectic when this melt contains lithium oxide that is due to oxide film formation.

Lai et al. (1985) evaluated various wrought iron-, nickel-, and cobalt-based alloys in a NaCl–KCl–$BACl_2$ salt bath at 840 °C for one month. Surprisingly, two high nickel alloys (alloys 600 and 601) suffered more corrosion attack than stainless steels such as Types 304 and 310. Co–Ni–Cr–W, Fe–Ni–Co–Cr, and Ni–Cr–Fe–Mo alloys performed best. Laboratory testing in a simple salt bath failed to reveal the correlation between alloying elements and performance. Tests were conducted at 840 °C for 100 hours in a NaCl salt bath with fresh salt bath for each test run.

Similar to the field test results, Co–Ni–Cr–W and Fe–Ni–Co–Cr alloys performed best.

Smyrl and Blackburn (1975) have been concerned with the stress corrosion cracking phenomena of the Ti–8Al–1Mo–1V alloy in molten LiCl–KCl at 350 °C.

More recently, Atmani and Rameau (1987) have described a tensile apparatus suitable for corrosion tests in molten salts. The behavior of 304L stainless steel was studied in molten NaCl–$CaCl_2$ at 570 °C using either a constant strain rate or a constant load technique. Intergranular corrosion fracture was shown, and the role of $M_{23}C_6$ precipitation in the crack propagation was evidenced.

Coyle et al. (1985) conducted corrosion tests on various commercial alloys at 900 °C in the molten 33NaCl–21.5KCl–45.5$MgCl_2$ eutectic. After 144 hours of exposure, 8 of the 15 Fe-, Ni-, Co-based alloys evaluated were consumed. The remaining seven alloys disintegrated after a total of 456 hours of exposure. The authors concluded that the chloride salt was too aggressive to be used at 900 °C for a solar thermal energy system (Table 13.5).

Corrosion mechanisms in chloride-based salts were also reviewed to better understand the practical implications of using these salts in thermal solar power systems (Abramov 2010; Indacochea 2001; Masset 2010; Oryshich and Kostyrko 1985). They are susceptible to high corrosion rates in the presence of moisture and oxygen, but they can be used for high temperature heat transfer fluids (HTFs) primarily due to economic considerations and for the thermal stability in the region of 700–800 °C. In other words, they may be used to increase operating efficiency in the solar systems in which high turbine inlet temperatures must be achieved. Investigation of this chloride salt family helped to understand the involved corrosion mechanisms and suggested metal alloys for use in containment vessels, piping, pumps, valves, and tanks, as exemplified in Table 13.6.

An overview of experimental observations and results of liquid Li and LiCl corrosion at 725 °C of engineering nonferrous materials has been explained by Olson et al. (1998). It has been observed that oxygen contamination is particularly harmful for the tantalum- and niobium-based refractory metal alloys, whereas nitrogen is deleterious to iron-based alloys. Materials tested included RA333, Hastelloy X, Airesist 213, Ta–2.5W, and Nb–1Zr. The corrosion and protection mechanism of molten salt electrodeposited chromium coatings in a LiCl–KCl eutectic at 450 °C has been studied by Emsley and Hill (1987). Factors influencing the optimum coating thickness on 20Cr–25Ni–Nb-stabilized stainless steel to achieve a satisfactory lifetime were discussed.

The corrosion behavior of Mo–Al_2O_3–Cr_2O_3 cermets in $BaCl_2$ molten salt has been shown to be mainly due to the electrochemical corrosion of the component Mo (Wang et al. 1991). It was also found that the other component (Cr_2O_3) is beneficial to the corrosion resistance of the *cermets* investigated.

The corrosion behavior of mild steel (St35.8), boiler steel 13Cr–Mo44, and stainless steel X 10Cr–Ni–Mo18 in contact with the eutectic salt mixtures $AlCl_3$–NaCl, LiCl–$LiNO_3$–NaCl, NaCl–$NaNO_3$, and KCl–LiCl has been investigated by Heine (1985). The test conditions were adapted to the operating conditions of latent heat storage systems. Only pure salts were used. Good corrosion resistance was observed.

Intergranular corrosion is the major corrosion morphology by molten chloride salts.

Another frequently observed corrosion morphology is internal attack by void formation. Voids tend to form at grain boundaries as well as in the grain interior. The continuing formation and growth of chromium compounds at the metal surface causes outward migration of chromium and inward migration of vacancies, thus leading to internal void formation (Koger and Pohlman 1987).

Alloying elements, specifically refractories, are thought to improve corrosion resistance in chlorides by stable spinel layer formation that tend to slow diffusion of Cr from the base alloy to the melt.

Table 13.5 Results of corrosion tests in molten eutectic NaCl–KCl–$MgCl_2$ salt at 900 °C (Coyle et al. 1985)

Alloy	Weight change (mg cm^{-2})	
	144h	456h
304	Disintegrated	—
316	Disintegrated	—
800	Disintegrated	—
800H	−310	Disintegrated
556	−250	Disintegrated
Nickel	Disintegrated	—
600	−280	Disintegrated
214	−120	Disintegrated
X	Disintegrated	—
N	Disintegrated	—
S	−400	Disintegrated
230	−300	Disintegrated
X-750	Disintegrated	—
R-41	−150	Disintegrated
188	Disintegrated	—

N_2–(0.1–1H_2O)–(1–10O_2) was used for the cover gas.

13.8 Nitrates/nitrites

Molten nitrates are commonly used for heat treatment baths; therefore, a great deal of material compatibility information exists. Plain carbon and low-alloy steels form protective iron oxide films that effectively protect the metal surface to approximately 500 °C. Chromium additions to the melt further increase the corrosion resistance of the steel, and hydroxide additions to the melt further increase the resistance of chromium-containing steels. Aluminum and aluminum alloys should never be used to contain nitrate melts, because of the danger of explosion.

Nitrate–nitrite mixtures are also widely used to heat treat salt baths at temperatures ranging from 160 to 590 °C, as well as a medium for heat transfer or energy storage.

Electrode potential oxygen partial pressure diagrams for the iron-molten $NaNO_3$ system at 600 and 700 K and for

Table 13.6 Alloys considered for molten chloride salts

Alloy	Cr	Mo	Ni	Mn	Si	C	Fe	Co	Al	B	Cu	S	Zr	Y	W	La	N	Ta	Cb
Haynes 242	7–9	24–26	65	0.8	0.8	0.03	2	2.5	0.5	0.006	0.5	—	—	—	—	—	—	—	—
Alloy was designed for resistance to halides in general due to the low Cr content and elevated Mo content. It is close in composition to Hastelloy N, but it is available, while Hastelloy N is currently not available																			
Inconel600	15.5	—	72	1	0.5	0.15	8	—	—	—	0.5	0.015	—	—	—	—	—	—	—
Low Cr content may aid in corrosion performance. Outperformed In 625 (20–25% Cr) in high temperature tests (Indacochea 2001)																			
HR 224	20	—	48.7	—	—	—	27.5	—	3.8	—	—	—	—	—	—	—	—	—	—
High Al content may help to provide resistance by formation of stable aluminum oxide																			
HA 214	16	—	75	0.5	0.2	0.05	3	—	4.5	0.001	—	—	0.1	0.001	—	—	—	—	—
High Al content may help to provide resistance by formation of stable aluminum oxide. This alloy also has lower Cr an Fe content, which were found to dissolve preferentially more readily than Ni (Abramov 2010)																			
Haynes 230	22	2	57	0.5	0.4	0.1	3	5	0.3	0.015	—	—	—	—	14	0.02	—	—	—
High alloying with refractory materials, in the presence of Ni–Cr alloys, were found to provide better resistance to corrosion (Oryshich and Kostyrko 1985)																			
HA 556	22	3	20	1	0.4	0.1	31	18	0.2	—	—	—	0.02	—	2.5	0.02	0.2	0.6	—
3% Mo + 2.5% W + 18% Co may indicate better performance (Oryshich and Kostyrko 1985) despite the high concentration of Fe																			
HR 120	25	2.5	37	0.7	0.6	0.05	33	3	0.1	0.004	—	—	—	—	2.5	—	0.2	—	0.7
2.5% Mo + 2.5% W + 3% Co may indicate better performance (Oryshich and Kostyrko 1985) despite the high concentration of Fe																			

iron, cobalt, and nickel in molten sodium nitrite have been constructed 40 years ago. In both cases, four well-defined regions, corresponding to metal corrosion, immunity, passivity, and passivity breakdown, are observed.

The oxidation kinetics of iron in molten alkali metal nitrates has also been investigated between 350 and 470 °C. The parabolic rate law, with a temperature-dependent constant, appears to be followed. The activation energy for corrosion is found to be greater in KNO_3 than in $NaNO_3$. X-ray studies show that the oxidation product is Fe_3O_4. The results are comparable with the oxidation kinetics of iron in air or oxygen. The effects of alkali metal and alkaline earth halides on the oxidation kinetics of iron and low carbon steels in molten KNO_3–$NaNO_3$ at 400 °C have also been studied. The corrosion of iron in these melts appears to begin with pitting corrosion that eventually spreads to the entire surface. The rate of attack increases with halide concentration and seems to depend on both the anion and the cation, aggressiveness increasing in the order KCl < KBr < Kl for the anion and $CaCl_2$ < $BaCl_2$ < LiCl < NaCl < KCl for the cation; halide is found to be incorporated in the oxide film formed. It is found that low carbon steels are more resistant to corrosion than pure iron. It is suggested that the corrosion behavior is similar to that in atmospheres containing halogens at high temperatures.

Ishikawa and Sasaki (1981) have carried out immersion and electrical resistance tests in alkali nitrate melts of 350–450 °C to elucidate the corrosion behavior of iron wire specimens. A parabolic law was verified for the iron specimens. Moreover, the sensitive resistometry has been shown to be a useful technique for the continuous determination of the corrosion behavior in various salt systems. Nitrate–nitrite mixtures and corrosion of iron and stainless steels by these melts were extensively studied (as a function of temperature and oxoacidity) in relation to their use as a coolant and storage fluid in solar thermal electric power plants (Picard et al. 1987). In particular, passivation of iron is observed only in a narrow acidity domain where $NaFeO_2$ can be formed. It was also demonstrated that a nitriding process appears only as a consequence of the oxidation process.

The corrosion resistance of Al, Ni, Ti, Ta, Nb, carbon steel, and stainless steel was studied in molten $LiNO_3$–$NaNO_3$–KNO_3 eutectic for the chemical open-circuit oxidation and for conditions of cathodic polarization. Experiments were carried out at 632 K under an argon atmosphere during 100 hours. By using X-ray diffraction (XRD), electron spectroscopy for chemical analysis (ESCA), secondary ion mass spectroscopy (SIMS), scanning electron microscopy (SEM), and gravimetric method, the metals under study show relatively high corrosion resistance in nitrate melts. Oxide films of predominantly higher oxidation state were formed on their surfaces. The effect of cathodic polarization on their corrosion behavior was insignificant. Only in the case of Ni, a decrease in oxidation rate was observed under the conditions of cathodic polarization (Yurkinsky et al. 1998).

Molten salt corrosion behavior of heat transfer plant materials, SS41, 2.25Cr–1Mo steel, SUS304, and Inconel 625, was studied in temperatures of 450 and 550 °C. The corrosion rate in the molten salt decreased in the decreasing order of SS41, 2.25Cr–1Mo steel, SUS304, and Inconel 625. And the corrosion resistance of SS41, 2.25Cr–1Mo steel, and SUS304 strongly depended on the temperature and Cl-exp content of the molten salt, while Inconel 625 showed high corrosion resistance in the molten salt environment. The morphology of corrosion products was examined by electron probe microanalysis (EPMA), XRD, SEM, and Auger electron spectroscopy (AES). Corrosion products of SS41 and 2.25Cr–1Mo steel consisted of porous and easy-pearling multilayer films of α-Fe_2O_3, $KFeO_2$, NO_2O–Fe_2O_3, and Fe_3O_4, while the corrosion products of SUS304 and Inconel 625 consisted of compact and well-sticked iron oxide films that contain Ni and Cr. The materials containing much more than 10 wt% Cr showed high corrosion resistance against the molten salt (Ebara et al. 1988).

Electropolished iron spontaneously passivates in molten sodium nitrate–potassium nitrite in the temperature range of 230–310 °C at certain potentials. A magnesite (Fe_3O_4) film is formed, along with a reduction of nitrite or any trace of oxygen gas dissolved in the melt. At higher potentials, all reactions occur on the passivated iron. Above the passivation potentials, dissolution occurs with ferric ion soluble in the melt. At even higher potentials, nitrogen oxides are evolved, and nitrate ions dissolve in the nitrite melt. At higher currents, hematite (Fe_2O_3) is formed as a suspension, and NO_2 is detected. Carbon steel in molten sodium nitrate–potassium nitrate ($NaNO_3$–KNO_3) at temperatures ranging from 250 to 450 °C forms a passivating film consisting mainly of Fe_3O_4.

Iron anodes in molten alkali nitrates and nitrites at temperatures ranging from 240 to 320 °C acquire a passive state in both melts. In nitrate melts, the protective Fe_3O_4 oxidizes to Fe_2O_3, and the gaseous products differ for each melt.

An interesting study was conducted on the corrosion characteristics of several eutectic molten salt mixtures on such materials as carbon steel, stainless steel, and Inconel in the temperature range of 250–400 °C in a nonflowing system. As expected, the corrosion rate was much higher for carbon steel than for stainless steel in the same mixture. Low corrosion rates were found for both steels in mixtures containing large amounts of alkaline nitrate. The nitrate ions had a passivating effect.

Electrochemical studies showed high resistance to corrosion by Inconel. Again, the sulfate-containing mixture

caused less corrosion because of passivating property of the nitrate as well as the preferential adsorption of sulfate ions.

Surface analysis by AES indicated varying thicknesses of iron oxide layers and nickel and chromium layers. The Auger analysis showed that an annealed and air-cooled stainless steel specimen exposed to molten lithium chloride (LiCl)–potassium chloride (KCl) salt had corrosion to a depth five times greater than that of an unannealed stainless steel specimen. Chromium carbide precipitation developed during slow cooling and was responsible for the increased corrosion. The mechanism of corrosion of iron and steel by these molten eutectic salts can be described by the following reactions:

$$Fe = Fe^{2+} + 2e^{-} \tag{13.6}$$

$$LiCl + H_2O = LiOH + HCl \tag{13.7}$$

$$H^{+} + e^{-} = \frac{1}{2}H_2 \tag{13.8}$$

$$H_2O + 2e^{-} = O^{2-} + H_2 \tag{13.9}$$

$$\frac{1}{2}O^2 + 2e^{-} = O^{2-} \tag{13.4}$$

$$Fe^{3+} + e^{-} = Fe^{2+} \tag{13.10}$$

$$Fe^{2+} + O^{2-} = FeO \tag{13.11}$$

$$3FeO + O^{2-} = Fe_3O_4 + 2e^{-} \tag{13.12}$$

$$2Fe_3O_4 + O^{2-} = 3Fe_2O_3 + 2e^{-} \tag{13.13}$$

In an actual flowing operating system of KNO_3–NaO_2 –NaO_3 (53, 40, and 7 mol%, respectively) at temperatures to 450 °C, carbon or chromium–molybdenum steels have been used (Sorokin and Tseitlin 1965).

For higher temperatures and longer times, nickel or austenitic stainless steel are used. Weld joints are still a problem in both cases.

Alloy 800 and Types 304, 304L, and 306 stainless steels were exposed to thermally convective $NaNO_3$–KNO_3 salt (*draw salt*) under argon at 375–600 °C for more than 4500 hours. The exposure resulted in the growth of thin oxide films on all alloys and the dissolution of chromium by the salt. The weight change data for the alloys indicated that the metal in the oxide film constituted most of the metal loss; that the corrosion rate, in general, increased with temperature; and that, although the greatest metal loss corresponded to a penetration rate of 25 μm yr^{-1}, the rate was less than 13 μm yr^{-1} in most cases. These latter rates are somewhat smaller than those reported for similar loops operated with the salt exposed to the atmosphere but are within a factor of 2–5. Spalling had a significant effect on metal loss at intermediate temperatures in the Type 304L stainless steel loop. Metallographic examinations showed no evidence of intergranular attack or of significant cold-leg deposits. Weight change data further confirmed the absence of thermal gradient mass transport processes in these draw salt systems (Carling et al. 1983).

Slusser et al. (1985) evaluated the corrosion behavior of a variety of alloys in molten $NaNO_3$–KNO_3 (equimolar volume) salt with an equilibrium nitrite concentration (about 6–12 wt%) at 675 °C for 336 hours. A constant purge of air in the melt was maintained during testing. Nickel-based alloys were generally much more resistant than iron-based alloys. Increasing nickel content improved alloy corrosion resistance to molten nitrate–nitrite salt. However, pure nickel suffered rapid corrosion attack.

Silicon-containing alloys, such as RA330 and NICROFER 3718, performed poorly. A long-term test (1920 hours exposure) at 675 °C was performed on selected alloys, showing corrosion rates similar to those obtained from 336 hour exposure tests. Alloy 800, however, exhibited a higher corrosion rate in the 1920 hour test than in the 336 hour test. As the temperature was increased to 700 °C, corrosion rates became much higher, particularly for iron-based alloy 800, which suffered an unacceptably high rate. Boehme and Bradshaw (1984) attributed the increased corrosion rate with increasing temperature to higher alkali oxide concentration. Slusser et al. (1985) found that adding sodium peroxide (Na_2O_2) to the salt increased the salt corrosivity.

Energy storage for *concentrating solar power* (CSP) is nowadays a major area of research that seeks to lower the levelized cost of electricity within the aggressive SunShot goals. One viable approach is sensible *thermal energy storage* (TES), which currently uses molten nitrate binary salt, stored at 575 °C in the hot tank of a two-tank system. Increasing the temperature limit within the hot tank requires a detailed understanding of materials corrosion behavior, in addition to salt thermal stability properties (Kruizenga et al. 2013; Siegel 2012).

High temperature nickel-based alloys are the logical choice for strength and corrosion resistance as elevated temperatures will increase corrosion kinetics; however the cost of nickel-based alloys is nearly four times more expensive than iron-based steels. For this reason, iron-based stainless steels, specifically 321SS or 347SS (nominally Fe–17Cr–9Ni), were chosen at Sandia National Laboratories, USA, for investigation at several temperatures in nitrate salt. 316SS, an elementally similar alloy, was susceptible to stress corrosion cracking while tested at Solar Two. It was suggested that alloys with stabilizing additions of niobium (347SS) or titanium (321SS) would mitigate the deleterious behavior (Federsel et al. 2015; Kruizenga and Gill 2014).

One of the most important lines of research to reduce the high cost associated with the operation and maintenance

of CSP plants is the study, design, and characterization of the salts that are used as energy storage fluids. The thermal properties of the HITEC® mixture, a molten salt composed of 40 wt% $NaNO_2$ + 7 wt% $NaNO_3$ + 53 wt% KNO_3, are highly suited to its use as storage fluid in CSP plants (Ho and Pan 2014). It is worth noting that one of the disadvantages of this ternary mixture is the need to use a protective layer of inert gas at temperatures above 350 °C to avoid oxidation of the nitrites upon contact with the oxygen in the atmosphere. This is the main reason that prevents at present the widespread use of this salt on thermoelectric solar plants. However, the use of the HITEC mixture in solar technology is once again under consideration, albeit for specific applications only. A number of research projects are currently seeking to improve the physical properties of the mixture to a point in which the mixture-enhanced properties could compensate costs (Fernández et al. 2015).

13.9 Hydroxides

The reaction of metals with molten sodium hydroxide (NaOH) leads to metal oxide, sodium oxide, and hydrogen (Gunnarsson and Johannesson 2011; Roger et al. 2014; Yurkinsky et al. 2010). Nickel is most resistant to molten NaOH, particularly low carbon nickel such as Ni 201. Gregory et al. (1956) reported corrosion rates of several nickel-based alloys obtained from static tests at 400–680 °C. Molybdenum and silicon appear to be detrimental alloying elements in molten NaOH salt. Iron may also be detrimental. Molybdenum and iron were found to be selectively removed from nickel-based alloys with less than 90% Ni, leading to the formation of internal voids (Smith and Hoffman 1957).

Molten sodium hydroxide becomes increasingly aggressive with increasing temperature. Coyle et al. (1985) evaluated a variety of alloys for a possible containment material for molten sodium hydroxide operating at 900 °C for a solar power generation system.

Many iron-, nickel-, and cobalt-based alloys disintegrated in 84 hours. Samples of the alloys that survived the 84 hour exposure test were severely corroded. Scales that formed on these samples were reportedly cracked and spalled. The weight gain or weight loss data of surviving samples are no longer indicative of alloy performance ranking. No metallographic examination was performed on these samples. The authors concluded that no further studies on molten sodium hydroxide were necessary, because the salt was too aggressive to metallic materials operating at 900 °C. The marked influence of temperature on the corrosiveness of molten sodium hydroxide has been fully demonstrated.

Corrosion of metals and alloys in molten NaOH depends strongly on the velocity of the salt. Gregory et al. (1956) showed that corrosion of nickel under dynamic conditions was enhanced by as much as several times at 540 °C and higher. The corrosion rate for nickel at 680 °C, for example, varied from about 1 mm yr^{-1} under static conditions to about 8 mm yr^{-1} at a rotational speed of 600 rpm.

Metals or alloys in molten sodium hydroxide are susceptible to mass transfer due to thermal gradients in the melt. This causes corrosion in the hot zone, and potential tube plugging in the cold zone, of a circulating system. For example, 6.35 mm diameter nickel tubing was plugged after 5000 hours at 440–480 °C and after 50 hours at 690–730 °C.

Corrosion studies in molten oxidizing salts containing hydroxides, chlorides, nitrates, and carbonates are also widely reported in the open literature stressing the effect of hydroxides in the corrosiveness of the mixed melts (Coyle et al. 1985; Klěcka et al. 2015).

13.10 Carbonates

An important parameter in understanding carbonates is the basicity of the melt, which is defined on the basis of the *Lux–Flood model* (akin to pH in an aqueous system), where an acid is an oxide (O^{2-}) acceptor and where a base is defined as the oxide donor. Therefore, the activity of oxide ions in the melt is extremely important to understand the fundamental behavior of the melt. The electrode potential, as suggested by Nishikata et al. (1991), can be calculated as

$$E = E^0 + \frac{RT}{2F} \ln \frac{p_{CO_2} p_{O_2}^{1/2}}{\{CO_3^{2-}\}} \tag{13.14}$$

Most systems were studied under molten carbonate fuel cell (MCFC) conditions, where $p_{CO_2} = p_{O_2}^{1/2} = 0.3$ atm and E^0 is calculated to be near zero. T is temperature, F is Faraday's constant, and R is the gas constant. There have been numerous electrochemical studies performed to gain a thermodynamic understanding of the system (Keijzer 2003; Keijzer et al. 1999; Nishikata et al. 1991; Vossen et al. 1994, 1996). Many other molten carbonate systems are being investigated for solar applications, but the MCFC conditions are not typical of TES conditions for several reasons.

First, MCFC requires a mixture of oxygen and carbon dioxide for the cathodic electrode in order to sustain the following reaction (Frangini et al. 2011):

$$CO_2 + \frac{1}{2} O_2 + 2e^- \rightarrow CO_3^{2-} \tag{13.15}$$

whereas the anode requires hydrogen to sustain (Vossen et al. 1994)

$$H_2 + CO_3^{2-} \rightarrow H_2O + CO_2 + 2e^- \qquad (13.16)$$

Thus, the anode will experience a mixture of hydrogen, moisture, and carbon dioxide atmospheres. Many of the works reported in the open literature on solar applications were found to be under either a representative anodic or cathodic atmosphere.

Second, the MCFC is set up as an electrochemical cell with a galvanic couple. TES will not intentionally have a driven electrochemical cell where preferential reactions are taking place. The exception to this is if an anodic or cathodic corrosion protection scheme, similar to what is done in many industries, is used. Despite both the differences identified, insight into typical chemistry processes, influences of alloying, and identifiable impurities, among others, are important for performance issues.

Austenitic stainless steels perform well in carbonate melts up to 500 °C. If temperatures to 600 °C are required, nickel-based alloys containing chromium are needed. For temperatures to 700 °C, high chromium alloys containing at least 50% Cr are required. Above 700 °C, the passive films that form at lower temperatures will break down and preclude the use of metals. Aluminum coatings on steel structures perform well to 700 °C. For higher temperatures, alumina is required. Nickel does not provide adequate protection because of intergranular attack caused by the formation of nickel oxides.

Coyle et al. (1985) report exploratory corrosion tests that were conducted on 16 commercial Ni and Fe alloys in carbonate, chloride, and hydroxide molten salts at 900 °C for up to three weeks. Corrosion information, including weight change, observations of the coupons, metallographic examination, and evaluation of the corrosion product by SEM, was obtained on the coupons exposed to these salts. These tests indicated that a number of the alloys showed significant resistance to metal loss in the carbonate molten salt with corrosion rates on the order of several millimeters per year. The corrosion product is an interpenetrating structure of metal from the more noble alloy ingredients and of an oxide made up of the reaction between melt components and oxidizable metals from the alloy.

In the molten eutectic alkali metal carbonate, Grantham et al. (1970) found that many commercial alloys, including Types 304L, 310, and 347 and alloys 600, C, N, X, and 25, exhibited low corrosion rates (about 0.01 mg cm^{-2} h^{-1} or less) at 600 °C. Non-oxidizing N_2 was used for the cover gas in their corrosion tests, which may also have contributed to low corrosion rates. The temperature dependence of corrosion rate can also be seen in results generated in the eutectic Li_2CO_3–Na_2CO_3–K_2CO_3 (about equal weight) at 500, 600, and 700 °C. The cover gas in this case was not known. Corrosion rates were found to be less than 0.025, 0.025, and 2.54 mm/yr^{-1} at 500, 600, and 700 °C, respectively.

Laboratory tests, aimed at reproducing certain industrial corrosion processes, were carried out in a gas-tight cell under an Ar atmosphere with a molten mixture at 900 °C containing approximately 20% Na_2S + 80% Na_2CO_3. A study of the corrosion behavior of various steels in this extremely corrosive medium showed that Cr and Al are beneficial in ferritic steels but that low C austenitic steels are not superior to ordinary stainless grades. Impurities, such as Na_2SO_4, in the melt influence the corrosion rate. In the case of C steels, the corrosion layer contains Fe sulfides and oxides, while for steels with 13% Cr, it consists mainly of Fe and Cr oxides. For the C steels, good agreement is noted between observations in the laboratory and in industrial tubes.

Instantaneous rates of the corrosion of Ni, Fe, and their alloys (Inconel 600, Incoloy 800, Rene 77, Hastelloy B, Hastelloy C, and Hastelloy N) were measured in molten alkali chlorides, carbonates, and sulfates at 973 K by the electrochemical polarization resistance method. The stability of the oxide films formed on the surfaces was evaluated from steady-state anodic polarization curves. The polarization resistances varied proportionally to the corrosion currents measured by weight loss in all of the melts and obeyed the Stern–Geary equation. From polarization resistance measurements, it was found that alloying with Cr increased the corrosion resistances of Ni and Fe in all of the melts and especially in molten sulfates. Alloying with Mo increased the corrosion resistance in molten chlorides but decreased that in molten carbonates and sulfates. These results correspond well with those obtained from anodic polarization curves. It was concluded that the polarization resistance method is useful for assessing the corrosion resistance of alloys in molten salts (Nishikata and Haruyama 1986).

Hsu et al. have investigated the corrosion resistance of chromium and iron (1987) in the presence of carbonate melts (Na_2CO_3–K_2CO_3) at 650 °C, in connection with their use as current collector materials in MCFCs. Thermochemical calculations were carried out to establish phase stability diagrams for the (Fe and Cr)–Li–K–C–O systems, and good agreement was observed between the predicted (deduced from calculated phase stability diagrams) and the experimentally observed corrosion products. Interesting studies of molten carbonates for MCFCs and hybrid direct carbon fuel cells were recently carried out by Frangini (2008), Ni and Lu (2014), and Xu et al. (2014).

Two types of corrosion tests were carried out for 99.9% Co sheet of 1 mm thickness: immersing and corrosion with carbonate melt coating (Kim et al. 1994). The corrosion tests were executed at 923 K in CO_2–O_2 atmosphere with

$(Li_{0.62}K_{0.38})_2CO_3$ melt. The formation of CoO and Co_3O_4 occurred mainly in the first stage of the corrosion. Once the formation of $LiCoO_2$ started, the corrosion rate decreased. It was concluded that the low solubility of $LiCoO_2$ might affect the corrosion rate.

The high temperature corrosion of Ta with the presence of molten carbonate has been studied in CO_2–O_2 atmosphere from 873 to 1123 K by measuring the weight gain of a specimen. A severe corrosion of Ta took place with the formation of unprotective Ta_2O_5 (Ota et al. 1996) at high temperature, and the corrosion reaction obeyed the linear rate law. The corrosion rate was greatly suppressed with the presence of sufficient molten carbonate. The corrosion reactions obeyed the parabolic rate law if a specimen was in the melt or coated with the coating amount $>3\,mg\,cm^{-2}$. The corrosion rate was very close to that of Ti and much smaller than those of Ni, Cr, and Fe. If the coating amount was $<3\,mg\,cm^{-2}$, the reaction changed from the parabolic rate law to the linear rate law and proceeded to severe corrosion. In order to form a protective scale, a certain amount of molten carbonate was necessary.

Corrosion tests of Type 310S stainless steel coated with $5\,mg\,cm^{-2}$ of Li–Na carbonate (52–48 mol%) have been carried out at 873, 923, and 973 °C under the simulated cathode environment CO_2–O_2 (≅2–1 vol%) of MCFC in out-of-cell tests for up to 500 hours. Corrosion products were almost the same under this temperature and consisted of two layers of $LiFeO_2$ as the outer layer and $LiCrO_2$ as the inner layer. Only Cr dissolved from the specimen into the melt. Though Na content in the melt was independent of the test duration and the temperature, Li content was decreased with increasing the test duration and increasing the temperature. On the other hand, dissolved Cr content in the melt was increased with increasing the test duration and increasing the temperature. Up to 500 hours, the amount of Cr dissolution followed the parabolic rate law.

The corrosion of iron in Na_2CO_3–K_2CO_3 (58–42 mol%) at 800 °C was studied by potentiometry at zero current and by weight loss measurements. The surface analysis by XRD and SEM showed the formation of a porous oxide layer when the melt was in contact with pure CO_2 atmosphere. When the oxygen partial pressure increased, corrosion rate increased due to peroxide ions formation according to the equilibrium

$$\frac{1}{2}O_2 + O^{2-} \rightarrow O_2^{2-} \tag{13.17}$$

Chronopotentiometric and voltammetric studies showed that peroxide ions reduction was

$$O_2^{2-} + 2e^- \rightarrow 2O^{2-} \tag{13.18}$$

The *galvanic corrosion* behavior of a platinum and nickel couple in molten Na_2CO_3 at 1173 K was investigated by Hara et al. (1997). Particular attention was given to the influence of O_2 gas on the corrosion behavior. The galvanic current passed from platinum to nickel under atmospheres of both O_2 and Ar. Nickel and platinum became the anode and cathode, respectively. The galvanic current passed under an O_2 atmosphere was larger than that under the Ar atmosphere, indicating that O_2 gas dissolved in the molten salt and hastened the galvanic corrosion. During the galvanic corrosion test under an O_2 atmosphere, the masses of platinum and nickel, respectively, decreased and increased greatly. After the corrosion test, extensive attack was observed on the platinum surface, whereas the formation of NiO and metallic platinum crystals was observed on the nickel specimen. On the basis of these results, the cathodic reaction on platinum and the anodic reaction on nickel during the galvanic corrosion test were proposed.

The high temperature corrosions of stainless steels (SUS316L and SUS310S) with the presence of molten carbonate [$(Li_{0.62}K_{0.38})_2CO_3$ and $(Li_{0.52}Na_{0.48})_2CO_3$] have been studied in CO_2–O_2 atmosphere by measuring the weight gain of the specimens.

SUS310S is generally more stable in oxygen-containing atmosphere than SUS316L due to the higher content of Cr. The corrosion of SUS316L significantly depended on the reaction conditions, although the difference between the steels was small at the present operating condition of an MCFC (Li–K carbonate melt and 923 K). With the carbonate coating (both Li–Na and Li–K carbonates), the severe corrosions occur at the initial period of the corrosion test below 923 K. The severe corrosion occurred more clearly with Li–Na coating than Li–K coating. The corrosion became severe at higher pressures of CO_2 and lower pressures of O_2 (Ota et al. 1998).

Stainless steel separator plates in MCFCs need to be protected against corrosion preferably by a coating. A suitable coating material should be corrosion resistant, electronically conducting, and high temperature resistant. Keijzer et al. (1998) selected a suitable coating material by an elimination procedure covering the whole periodic table. First, they argue that non-oxide metal/nonmetal ceramic coatings are preferred. Then, they select the metal and nonmetal components for the ceramic coating. Selected nonmetal components are B, C, N, Si, and P. Metals disregarded in the elimination procedure have oxides or mixed oxides with eutectics below the maximum MCFC operating temperature of 700 °C. Selected metal components are Ti, Y, Nb, La, Ce, Nd, Hf, and Ta. The stability of ceramics composed of the selected metals and nonmetals was tested in the eutectic Li–K carbonate at 650 °C. Stability experiments showed that TiN, TiC, NbB_2,

Al-infiltrated TiB_2 (TiBAl), and Ce-based ceramics are promising coating materials.

Corrosion tests of Type 316L stainless steel coated with mixed carbonate, $(Li_{0.51}Na_{0.49})_2CO_3$, have been carried out under ambient simulated cathode gas environment at the temperature in the range of 600–700 °C up to 500 hours in out of cell (Yanagida et al. 1998). Weight gains with time due to corrosion were observed and follow parabolic rate equation. In the first 500 hours of exposure, there is no significant difference between corrosion behavior with the Li–Na carbonate and that with $(Li_{0.62}K_{0.38})_2CO_3$. Apparent activation energy of corrosion in both systems calculated from parabolic rate constants and temperature had little difference. Corrosion mechanism is seemed to be similar between $(Li_{0.51}Na_{0.49})_2CO_3$ and $(Li_{0.62}K_{0.38})_2CO_3$.

The corrosion behavior of Ni, Ni–5Ti, Ni–10Ti, and Ni–15Ti (mass fraction, %) in molten $(Li_{62}–K_{38})_2CO_3$ at 650 °C under air was studied by Zeng and Wu (2000). The corrosion of Ni–5Ti is slightly slower than that of pure Ni, yielding a mixed scale of Ni and Ti oxides. The corrosion rate of Ni–10Ti and Ni–15Ti is significantly higher than that of pure Ni, with the formation of an external scale containing Ni and Ti oxides and a wide internal oxidation zone of Ti along the intermetallic compound phase $TiNi_3$ in the original alloys.

Compared with pure Ni, the growth of the external scale developed on Ni–Ti alloys is obviously reduced. The corrosion mechanism of the alloys was also discussed.

The corrosion behavior of pure Fe, Fe–5Cr, Fe–10Cr, Fe–20Cr, and Fe–25Cr in molten $(Li_{0.62}–K_{0.38})_2CO_3$ at 650 °C in air was studied by Zeng et al. (2000). Pure Fe, Fe–5Cr, and Fe–10Cr suffered from fast corrosion, and the addition of 5% and 10% Cr could not improve the corrosion resistance of Fe. The addition of 20% and 25% Cr greatly improved the corrosion resistance of pure Fe. The corrosion mechanism of the alloys was also discussed (Zeng et al. 2000).

As reported initially, current technology in concentrated solar power plants is considering molten carbonates as a HTF and as TES media. Carbonate salts form protective oxide layers, which inhibit corrosion from the base alloy. Since different atmospheric conditions and temperatures exist for MCFCs and thermal solar power, large amounts of work are actually being carried out for solar applications. Recent findings suggest a few promising corrosion-resistant alloys suitable for solar technology, as listed in Table 13.7.

13.11 Vanadates

The presence of organic vanadium compounds in many industrial environments is very common, and these compounds may be converted to V_2O_5 and vanadates that can originate severe corrosion attack known as *vanadic corrosion*.

All vanadates melt at temperatures below 650 °C down to even 550 °C (Rahmel and Schwenk 1977). Vanadate corrosion is mainly due to the formation of low-melting eutectics between the oxide scale, the underlying metal, and the vanadium compounds. For the system $Co_2O–V_2O_5$, a eutectic is found that melts at 530 °C. In a standard laboratory experiment where a piece of copper is introduced into V_2O_5 powder in the lower part and air in the upper part, severe attack with the formation of a liquid phase is observed at the phase boundary copper–air–V_2O_5 powder (Heitz et al. 1992). For heat-resistant steels, this problem is well known for temperatures from 600 °C upward. Again, a eutectic is formed between the steels and the V_2O_5 deposits. If sodium is present in the environment, a eutectic of $Na_2O–V_2O_5$ may be formed, which melts at 535 °C. When both Na_2SO_4 and sodium vanadates were present, melting points as low as 400 °C have been reported for slags on valves of diesel engines. Contrary to the situation for pure sulfates where the corrosive attack passes through a maximum with increasing temperature, there is a continuous increase of the corrosion rate for vanadium-induced corrosion.

In order to explain the observed kinetics of vanadic corrosion of pure metals, a mechanism involving a sequential and interdependent inward diffusion of oxygen (or other active species) and an outward diffusion of the corrosion products has been invoked: surface, grain size, and other intrinsic properties of the metal are irrelevant to the mechanism. The ease of diffusion is related to the nonstoichiometry of vanadium pentoxide, and because it has transition semiconductance, the diffusivity of the melt cannot be reduced unless its melting point is sharply raised by the corrosion products or additives. Metals that show some resistance to the attack act by forming an adherent and coherent layer of very low diffusivity with respect to the active agent: it appears that this barrier cannot be generated by external means (Sequeira and Marquis 1993).

Rahmel (1972) has investigated the corrosion of silver and copper in vanadium pentoxide melts. The rate of the reaction seems to be controlled by diffusion through a solid layer formed on the metal surface; this layer does not, however, appear to afford much protection, and its composition is unknown. In contrast, a very good protective layer is formed on nickel in V_2O_5 melts, and this metal corrodes at a very much lower rate than does silver or copper. The oxygen pressure appears to have no direct influence on the corrosion velocity. High cathodic current densities are observed, but these are believed to refer to the reduction of V^{5+}, not of oxygen. V_2O_5 is an extremely stable redox system and this seems to render cathodic protection impracticable. Even potentials of several volts between the silver

Table 13.7 Alloys considered for molten carbonate salts

Alloy	Cr	Mo	Ni	Mn	Si	C	N	Fe	Co	W	Al	Ta	La	Zr	Cu	S	P	Ti	Cb	B	Y	Ce
HA 556	22	3	20	1	0.4	0.1	0.2	31	18	2.5	0.2	0.6	0.02	0.02	—	—	—	—	—	—	—	—
Additions of minor alloying elements such as Al, La, and Zr, coupled with large additions of Ni, provide stable oxidation layers (Ozeryanaya et al. 1984)																						
In 600	15.5	—	72	1	0.5	0.15	—	8	—	—	—	—	—	—	0.5	0.015	—	—	—	—	—	—
High Ni content coupled with moderate Cr content																						
HR 224	20	—	48.7	—	—	—	—	27.5	—	—	3.8	—	—	—	—	—	—	—	—	—	—	—
High aluminum content (Oryshich and Kostyrko 1985)																						
In 625	20–23	8–10	58	0.5	0.5	0.1	—	5	1	—	0.4	—	—	—	—	0.015	0.015	0.4	3.15–4.15	—	—	—
High Ni content coupled with moderate Cr and Mo content, and minor alloying elements, may provide good resistance to corrosion																						
Haynes 230	22	2	57	0.5	0.4	0.1	—	3	5	14	0.3	—	0.02	—	—	—	—	—	—	0.015	—	—
Minor alloying element La coupled with large additions of Ni, may provide stable oxidation layers (Ozeryanaya et al. 1984). Shown to have superior cycle fatigue performance is also favorable for solar applications																						
HA 214	16	—	75	0.5	0.2	0.05	—	3	—	—	4.5	—	—	0.1	—	—	—	—	—	0.001	0.01	—
High nickel content, with high aluminum and small amounts of Zr (Oryshich and Kostyrko 1985) and Y (Wee and Lee 2006)																						
253 MA	20–22	—	10–12	0.8	1.4–2	0.05	0.14–0.2	63–68	—	—	—	—	—	—	—	—	0.04	—	—	—	—	0.03
High Si (Kruizenga 2012) and trace amounts of Ce (Wee and Lee 2006)																						
HR 120	25	2.5	37	0.7	0.6	0.05	0.2	33	3	2.5	0.1	—	—	—	—	—	—	—	0.7	0.004	—	—
2.5% Mo + 2.5% W + 3% Co may indicate better performance (Oryshich and Kostyrko 1985) despite the high concentration of Fe																						

electrode to be protected and the counterelectrode do not change the corrosion rate. The electronic contribution to the conduction in V_2O_5 implies that the reduction of oxygen, if it plays a part in the corrosion process, could take place in the bulk of the melt, making possible a high corrosion rate even in systems that have a small oxygen solubility. In V_2O_5, however, reduction of V^{5+} is thought to take the place of oxygen reduction.

The corrosive properties of mixtures of sodium salts and vanadium compounds in the molten state have been widely investigated (Martinez et al. 1998; Yoshiba et al. 1990). All mixtures of sodium sulfate or sodium chloride with vanadium pentoxide decompose at as low temperature as 500 °C by sintering and solid-state reactions. Sulfur trioxide and chlorine are evolved. These gases are themselves powerful corrosive agents at such low temperatures, whereas vanadic corrosion occurs significantly only when there is a molten phase. The decompositions of the sodium salts are very fast when the vanadium pentoxide is molten, particularly in an inert atmosphere. Existence of undecomposed free salt is observed in mixtures of >50 mol% of sodium sulfate or >25 mol% of sodium chloride with vanadium pentoxide; these limits correspond to the reactions

$$Na_2SO_4 + V_2O_5 \rightarrow Na_2O \cdot V_2O_5 + SO_3 \qquad (13.19)$$

and

$$2NaCl + 6V_2O_5 \rightarrow Na_2O \cdot V_2O_4 \cdot 5V_2O_5 + Cl_2 \qquad (13.20)$$

The sodium oxide/vanadium pentoxide melt (the residue after decomposition) solidifies with evolution of oxygen, and the solid reabsorbs the same amount of oxygen on fusion, the amount depending on the composition. The cycle can be repeated indefinitely. Chemical analysis of the solidified mixture showed that it contained vanadium tetroxide exactly equivalent to the oxygen evolved. The structure of solid sodium oxide/vanadium pentoxide "bronzes" is reported to contain about 0.4% of oxygen sites vacant in the lattice. The order–disorder transformation on fusion makes possible the absorption of oxygen to fill the vacant sites. The oxygen is highly labile and is unlike the oxygen anions in pure molten vanadium pentoxide. Consequently the oxygen transport properties of the melt and its corrosive nature are profoundly enhanced. In fact, the corrosive activity of the melt toward iron can be correlated with its oxygen absorption capacity or the corresponding amount of vanadium tetroxide. The decrease of corrosion rates in mixtures with a large excess of sodium oxide or salt is probably due to a combination of the dilution effect and the reduced activity and fluidity due to increased melting points.

13.12 Sulfates

13.12.1 General Aspects

Corrosion reactions will proceed at a metal surface in molten sulfate environments, in conjunction with the reduction of oxidizing species in the sulfate melt, when the potential at the metal surface is negative in relation to the redox potential of the melt. The initial reaction at the metal surface leads to the formation of metal ions, or metal oxyanions, dissolved in the melt, but an oxide layer will then be formed on the metal when the solubility limit is exceeded at the surface. The major components of the principal commercial alloys have relatively negative values for their reversible metal–metal ion couples.

The initial rate of the corrosion reaction is relatively fast, and the corrosion resistance of the alloy depends on the protectiveness of the oxide layer as in the case of gas-phase oxidation. However, the thermodynamic data for the corrosion reactions in molten sulfates (Rahmel 1968) show that a redox potential gradient must be established between the value defined by the metal–metal oxide equilibrium at the interface between the metal and the oxide layer and the value determined by the oxygen and SO_3 partial pressures in the gas phase in equilibrium with the sulfate melt. The gradient for the oxygen potential will increase the sulfur potential adjacent to the metal surface as a consequence of the local equilibrium for the oxy-sulfur species and thus allow the formation of the metal sulfide as well as the oxide. Under the oxidizing conditions that are generally established in combustion plant, at least outside the combustion zone, the oxidizing potential defined by the residual oxygen partial pressure in the combustion gas favors the formation of the metal oxide rather than the sulfide and the oxygen, and sulfur potential gradients will then cause the formation of the sulfide phase at the interface between the metal and the oxide layer. This arrangement is confirmed by metallographic studies of the corrosion morphology. The formation of the sulfide phase is one of the major causes of the enhanced corrosion that occurs in molten sulfate environments, since the growth of the sulfide phase will cause mechanical damage to the protective oxide layer. Under the more reducing conditions that may be experienced in the combustion zone or in a coal gasification plant, the thermodynamic relationships will favor the reverse arrangement with the oxide formed at the interface between the metal and the outer sulfide layer (Foroulis and Smeltzer 1975).

The effect of molten sulfates on the corrosion of commercial alloys at high temperatures has also been attributed to the acid and basic fluxing reactions between the molten sulfate and the protective oxide layer. These reactions are most important when a temperature gradient is established normal to the metal surface, as, for example,

at the heat transfer surfaces in boilers. In this situation, as a consequence of the temperature dependence of the solubility of the oxide, which is related to the thermal stability of the solute species, the solubility of the protective oxide layer at the metal surface will be greater than the solubility at the higher temperatures in the outer regions of the molten sulfate deposit. The concentration gradient for the solute species that is thus established will cause continued dissolution of the protective oxide and the precipitation of non-protective oxide at the outer surface of the molten sulfate deposit. The rate for this process, which then determines the rate of corrosion, can be calculated from the data for the solubility of the metal oxide and the diffusion coefficient for the solute species (Sequeira 1998).

Electrochemical methods, analogous to those that have been widely used in aqueous corrosion studies, have been used in molten sulfates to investigate the corrosion mechanisms and to measure corrosion rates. Qualitative comparisons of the corrosion behavior can be obtained from potential measurements at a test electrode as a function of time or from measurements of the anodic current as a function of time at the test electrode maintained at a constant potential. The corrosion potential initially assumes a large negative value relative to the redox potential of the melt, but the magnitude of this potential gradually decreases as the protective oxide layer is formed and provides an indication of the corrosion resistance of the alloy. Similarly, the anodic current density at the electrode polarized at a constant potential, positive with respect to the corrosion potential, is initially relatively large and decreases progressively as the protective oxide layer is formed providing a further indication of the corrosion resistance.

The current at the polarized electrode is described as a function of the potential, E, by the equation

$$i = i_{\text{corr}} \left[\exp\, b_{\text{a}} (E - E_{\text{corr}}) - \exp\, b_{\text{c}} (E - E_{\text{corr}})\right] \quad (13.21)$$

where b_{a} and b_{c} are constants for the anodic and cathodic charge transfer reactions that are involved in the corrosion process. E_{corr} is the corrosion potential for the unpolarized test electrode, and i_{corr} is the corrosion current corresponding to the balanced rates of the anodic and cathodic parts of the corrosion reaction at the unpolarized electrode. The corrosion rate can thus be determined in terms of the corrosion current from an analysis of the current as a function of the potential imposed on the test electrode in terms of this equation. The corrosion rate can be measured in this manner at intervals during a test by applying a transient potential sweep to the electrode and recording the current using a potentiostat in conjunction with a potential-sweep generator connected to a conventional three-electrode electrochemical cell. Comparisons of the corrosion rates from the polarization curves, determined over a range of ± 100 mV relative to the corrosion potential at a sweep rate of $3.3\,\text{mV}\,\text{s}^{-1}$, with estimates of the corrosion rate based on the subsequent metallographic examination of the specimens, have shown good agreement.

A modification of the electrochemical polarization method, using a smaller polarization range (± 10 mV), has been described. The exponential terms in Eq. (13.21) can then be approximated by the first term in the series expansion, and the current is described as a linear function of the potential over this small potential range. The corrosion rate is described in terms of the polarization resistance defined by the equation

$$R = \frac{\partial E}{\partial i} = \frac{1}{i_{\text{corr}}\ (b_{\text{a}} - b_{\text{c}})} \quad (13.22)$$

and the corrosion rate can be calculated if the anodic and cathodic constants, b_{a} and b_{c}, are known. This method has the advantage of applying a smaller perturbation to the corrosion reaction, but there may be some uncertainty in the values assumed for the constants b_{a} and b_{c}.

Corrosion tests have shown that the corrosion rate decreases progressively during the initial period after the metal is exposed to the molten sulfate and the protective oxide layer is formed; however, this favorable trend is not necessarily maintained indefinitely. Degradation of the protective oxide layer may eventually occur as a result of factors such as the mechanical stress, which is created during the growth of the oxide and by the formation of the sulfide phase. This will lead to an accelerated corrosion rate that may be observed only after an extended incubation period of 1000 hours or longer. Assessment of the corrosion resistance of alloys in molten sulfate environments therefore requires not only that the plant-operating conditions be adequately simulated but also that the corrosion tests be continued for an adequate period of time.

After discussing the above key aspects of the corrosion of metals in sulfate melts, it seems to be helpful to pass further attention to the following topics that are fundamental to understand corrosion in molten sulfates and summarize important results on the investigations concerning corrosion reactions in sulfate melts.

13.12.2 Metal–Metal Ion Systems

Table 13.8 lists metal–metal ion equilibrium standard potentials for a number of metals. Attempts to measure equilibrium metal–metal ion electrode potentials for metals such as iron, nickel, chromium, and magnesium were unsuccessful because all of these metals reduce the sulfate anion.

The instability of the Fe^{2+}–Fe, Ni^{2+}–Ni, Cr^{3+}–Cr, and Mg^{2+}–Mg couples in sulfate melts can also be explained in terms of the acidity of these metal ions. As they are very

Table 13.8 Standard potentials on the molal scale in sulfate melts

System	Li_2SO_4–K_2SO_4, 625 °C (mV)	Li_2SO_4–K_2SO_4–Na_2SO_4, 550 °C (mV)	Li_2SO_4–K_2SO_4–Na_2SO_4, 625 °C (mV)
Pd^{2+}–Pd	+541	+518	+530
Rh^{3+}–Rh	+387	+370	
Cu^{2+}–Cu^{+}	+51	+55	
Ag^{+}–Ag	0	0	0
Cu^{+}–Cu	−202	−220	−206
Co^{2+}–Co		−689	−714
Fe^{2+}–Fe			−930

acidic, they neutralize the oxide ion deriving from the dissociation

$$SO_4^{2-} = SO_3 + O^{2-} \tag{13.23}$$

promoting finite concentrations of SO_3 through equilibria of the type

$$M^{2+} + SO_4^{2-} = MO + SO_3 \tag{13.24}$$

and thus the potential of the metal would be determined by competitive processes such as

$$SO_4^{2-} + M = SO_2 + M^{2+} + 20^{2-} \tag{13.25}$$

and

$$SO_4^{2-} + M = SO_3 + MO + 2e^- \tag{13.26}$$

It is obvious that the criterion for the reduction of sulfate by a metal is not merely the reduction of the metal sulfate (e.g. $NiSO_4$) occurring at a potential close to the sulfate potential but also that of the metal oxide that has a low solubility product, given by $K_s = \{M^{2+}\} \times \{O^{2-}\}$. The significance of the equilibrium given by Eq. (13.23) in the hot corrosion of nickel alloys by sulfatic turbine deposits strongly depends on the fact that it will control the solubility of the protective oxide film on the surface of the metal. Therefore, corrosiveness of molten sulfates appears to be controlled only by repressing their acidity.

13.12.3 The Oxygen Electrode

Since the oxide ion is the characteristic species for basic behavior in sulfate melts, the development of an electrode on which the potential is determined by a reaction like

$$\frac{1}{2}O_2 + 2e^- = O^{2-} \tag{13.4}$$

therefore becomes the object of considerable interest.

The investigations of Lux (1939) are the first that directly aim at establishing an oxygen electrode in a melt, in order to determine the "oxygen ion concentration." He tried to establish a cell of the type

$$\underbrace{Pt, O_2\,|Na_2SO_4, K_2SO_4,\ Na_2O}_{(t=950^\circ C)}||Na_2SO_4, K_2SO_4,$$
$$\underbrace{Na_3PO_4, NaPO_3|O_2,}_{\text{Reference electrode}}$$

His results are in doubt because soda evaporated from the melt so that it was necessary to extrapolate the e.m.f. values to zero time (that is, the point of time when a known amount of sodium oxide was added to the melt). Lux's work has been critically reviewed and extended by Flood et al. (1952). These workers found a Nernst slope of $RT/2F$ at a platinum wire surrounded by oxygen and immersed in a sodium sulfate melt containing Na_2CO_3 at known CO_2 and O_2 pressures. Thus, the equilibrium of $CO_3^{2-} = CO^2 + O^{2-}$ controls the oxide ion concentration in this case. Flood and Forland investigated the overpotential associated with the anodic evolution of oxygen in fluoride melts containing sulfate, carbonate, orthophosphate, and silicate using an O_2|Pt electrode. At high temperature (900 °C) and low current densities, a Tafel slope of $RT/3F$ was found; at high c.d. at 700 °C, steady-state measurements gave a Tafel slope of RT/F. The activation overpotential was found to decrease in parallel with the X—O bond strength in the order

$$SO_4^{2-} > PO_4^{3-} > CO_3^{2-} > SiO_4^{4-}$$

Baudo et al. (1970) measured the oxygen electrode potential in a neutral Li_2SO_4–K_2SO_4 eutectic melt at 600 °C while either decreasing the O_2 pressure inside the cell or, under a constant O_2 pressure, varying the O^{2-} concentration by adding LiOH to the base melt. The Nernst expression

$$E = E^0 + \frac{2.3\,RT}{4F} \log p_{O_2}/\{O^{2-}\}^2 \tag{13.27}$$

for Reaction (13.4) was verified.

Burrows and Hills (1970) investigated the oxygen electrode by observing the e.m.f. of both bright and platinized platinum electrodes when CaO additions to the melt were

made. The results suggest a Nernst slope of *RT*/*F* and not of *RF*/2*F*. Attempts to account for this anomaly have been made admitting the formation of peroxide ion in the melt by the route

$$2O^{2-} = O_2^{2-} + 2e^- \tag{13.18}$$

Other measurements in which the oxide ion concentration was changed by adding Li_2O to the melt (Brown et al. 1970) indicated a potential change according to the Nernst equation for the Reaction (13.27). The system Pt, O_2/O^{2-} in Li_2SO_4–K_2SO_4 at temperatures of 600–700 °C has also been used to measure standard formation potentials of various metal oxides.

A metal–metal oxide electrode to investigate acid–base equilibria in molten salts has also been employed. Because of the fact that oxygen and oxide ions interact appreciably in unbuffered melts, according to the reaction

$$\frac{1}{2}O_2 + O^{2-} = O_2^{2-} \tag{13.17}$$

only relative equilibrium constants for "dibasic" acids (e.g. PO_3 and $H_2PO_4^-$) were determined.

The oxygen electrode Au, O_2/O^{2-} is also an indicator electrode for O^{2-}-ion determination and has been used for studying oxide complexes in the Na_2SO_4–K_2SO_4 eutectic melt.

Further work was undertaken by Sequeira and Hocking (1977) and Sequeira (1989) to reexamine the behavior of the anodic reactions at platinum and gold electrodes in molten Na_2SO_4 and Na_2SO_4 containing CaO in the presence of oxygen (1.0 atm) at 900 °C. Experimental data indicated that oxide ions react slowly with oxygen to form superoxide ions in accordance with the equilibrium reaction

$$2O^{2-} + 3O_2 = 4O_2^- \tag{13.28}$$

Corrosion effects were observed when CaO remained in the melt for long periods of time. In addition, it was illustrated that the results are affected by the length of time the electrodes are left unpolarized in the melts, the pretreatment of the electrodes, and the geometry of the salt/noble metal electrodes (Sequeira 1989).

13.12.4 Electronation of Sulfate Species

Several workers have investigated the limiting cathodic processes in molten sulfates. Liu (1962) investigated the electrolytic decomposition of Li_2SO_4–K_2SO_4 eutectic at 625 °C. Both sulfite and sulfide were obtained and the following reactions were suggested:

$$SO_4^{2-} + 2e^- = SO_3^{2-} + O^{2-} \tag{13.29}$$

$$SO_4^{2-} + 8e^- = S^{2-} + 4O^{2-} \tag{13.30}$$

Sulfate ion and elemental sulfur have been identified as intermediate products at low current densities by electrolysis of Li_2SO_4–Na_2SO_4–K_2SO_4 at 550 °C (Delimarski and Markov 1961). It then appeared probable that sulfate is first reduced to sulfite that then disproportionates to form sulfate and sulfide or is further reduced directly to yield sulfur. When working at a somewhat higher temperature, 900 K, in the binary sulfate eutectic, it was found that sulfur dioxide, oxide ion, and elemental sulfur were the products of the cathodic reduction of the melt. Reduction of the sulfate to sulfite, sulfide, and sulfur occurred at −1.6 V versus Ag(0)–Ag(I) reference electrode. The reduction of the alkali cations was suggested from thermodynamic considerations as the limiting cathodic process. Investigation of the anodic process that occurs during the discharge of sulfate on carbon in sodium sulfate at 700 °C led to the following reaction that was postulated:

$$SO_4^{2-} + C - 2e^- = SO_2 + CO_2 \tag{13.31}$$

More detailed investigations of the mechanism have been carried out by several workers in terms of cathodic potential-sweep studies. They observed that the sulfate ion is not directly reduced at inert metal cathodes and suggested as the first step in the cathodic reduction process the electronation of SO_3 derived either from gas phase in equilibrium with the melt or from the dissociation of SO_4^{2-} anions. Attempts to demonstrate sulfate reducibility via its acid (SO_3) component proved difficult because the dissociation of sulfate ions into sulfur trioxide and oxide is negligible and a further complication results from the dissociative equilibrium

$$SO_3 = SO_2 + \frac{1}{2}O_2 \tag{13.32}$$

which is significant at temperatures higher than 900 K.

More recently, from thermodynamic considerations, it was shown that the discharge of the alkali or alkaline earth cations is not expected to occur in these systems and so the lower limit of stability of sulfate melts may be supposed to be determined by the reduction of sulfur trioxide or of sulfur dioxide. The end products of this reduction – either SO_2, or S_2, or S^{2-} – strongly depend on the acidity of the system.

It is apparent from this survey that the limiting cathodic processes have been the subject of much discussion and more information is required for their complete understanding.

13.12.5 De-electronation of Sulfate Species

The limiting anodic process in sulfate melts is not so complex as the cathodic process, and with inert electrodes, like

platinum and gold, in alkali metal sulfate eutectic melts, it has been attributed to the de-electronation of the SO_4^{2-} anion represented by the charge transfer equation:

$$SO_4^{2-} = SO_3 + \frac{1}{2}O_2 + 2e^- \qquad (13.3)$$

The potential at which this process takes place is about +0.7 V versus the standard silver (I)–silver (0) electrode; thus the available voltage span in fused sulfates is about 2.3 V, significantly smaller than that in other fused salts, e.g. chlorides. At temperatures of 1200 K or above, the reaction

$$SO_4^{2-} = SO_2 + O_2 + 2e^- \qquad (13.33)$$

should be used due to the decomposition of SO_3 according to the equilibrium (13.32).

Further assessment of the stability ranges of sodium sulfate and sodium sulfate–sodium chloride melts was reported by Sequeira and Hocking (1978a,b). They showed that the limiting reactions that occur during electrolysis of fused Na_2SO_4 at 900 °C are the SO_3 reduction to S^{2-} and O^{2-} and the SO_4^{2-}oxidation to SO_2 and O_2 at the cathode and anode, respectively. Addition of NaCl into the sulfate did not reduce its stability range.

13.12.6 Corrosion Potential Measurements

Systematic electrochemical corrosion potential measurements on steels and other alloys in molten sulfates were reported for the last 40 years. It was verified that the electrode potential is determined by the balance that is established between the metal–metal ion and the metal–metal oxide formed on the surface by the metal oxide ion electrode process.

Free corrosion potentials versus time recorded for 0.3Mo, 1Cr–0.5Mo, 2.25Cr–1Mo, and 12Cr ferritic steels dipped in neutral Li_2SO_4–K_2SO_4 eutectic melt at 600 °C showed that the extent to which the potential of the ferritic steel electrode approaches the redox potential of the melt, as measured by a Pt electrode, could be interpreted as strictly connected to the screening action of the oxide film. Half-cell potentials were also measured on high temperature superalloys in the presence of hot corrosive Na_2SO_4 and Na_2SO_4–5 wt% NaCl melts at 900 °C to study the behavior of their normally protective surface oxide coatings. A typical potential–time curve for a nickel alloy electrode immersed in the Na_2SO_4–NaCl mixture is shown in Figure 13.5. Clearly the intermittent peaks are associated with the presence of NaCl in the molten salt.

13.12.7 Polarization Studies

A further investigation of the electrochemical corrosion behavior of materials to be employed in molten sulfates has been made in terms of the currents measured when a potential sweep was applied to the electrode in order to simulate the "corrosion potential" of real environments. From these polarization measurements valuable indications appear. For example, the protectivity of the oxide film formed on steel immersed in molten sulfates to the anodic current flowing from the metal maintained at a potential equal to the melt redox potential has been referred. Should the rate of corrosion be controlled by the transport processes through a coherent oxide film or other barrier layer formed on the surface of the metal, the corrosion rate would approach a parabolic function with time. The experimental current–time curve obtained is, in fact, of the parabolic type, although on increasing time a positive deviation from the ideal theoretical curve and a series of sharp peaks, attributed to the formation of cracks in the thickening protective oxide layer, takes place. The electrokinetic curves also revealed that chromium is beneficial in retarding the corrosion process on iron–chromium and ferritic steel alloys in molten sulfates. Also, studies on the effect of oxygen and SO_3 on corrosion of steels and nickel-based and cobalt-based gas turbine alloys in molten sulfates by means of a cyclic potential-sweep technique must be mentioned. In Figure 13.6 the corrosion rates for the range of nickel-based alloys studied as a function of time are reproduced.

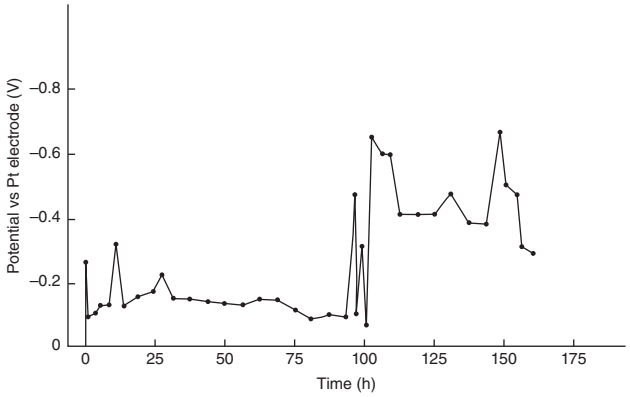


Figure 13.5 Experimental potential versus time of AMS 5384 nickel-based superalloy in molten Na_2SO_4–5 wt% NaCl at 900 °C under air (Wheatfall et al. 1967).

Casino et al. (1971) have studied the electrochemical behavior of pure iron anodes in $KHSO_4$ at 250 °C and observed typical passivation phenomena under potentiostatic as well as galvanostatic conditions. The passive film that formed was found, by XRD, to comprise Fe_3O_4 (actually a mixture of $KHSO_4$, α-Fe, and iron oxides, averaging out at Fe_3O_4). The mechanisms for passivation and for the corrosion of passivated iron are discussed in terms of the behavior of passive iron in aqueous solutions.

Sulfate melts have also been investigated in the presence of aluminum ions or ferric ions that make the melts

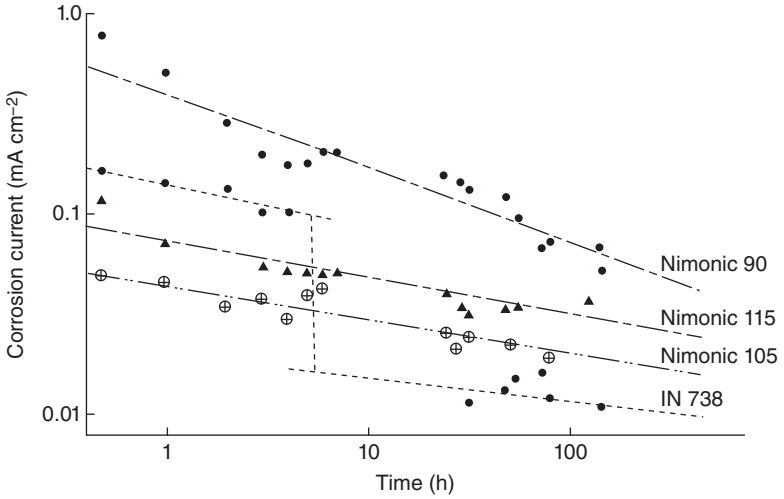


Figure 13.6 Corrosion data for nickel-based gas turbine alloys in molten sulfate at 1000 K under 1 atm O_2 and 3.23×10^{-4} atm SO_3 (Cutler and Grant 1972).

more aggressive, e.g. a deleterious effect of the salt was observed for low concentrations of this ion (<12 mol%) (Numata 1988).

The corrosion resistance, at 1000 °C, of commercially available SiC and Si_3N_4 ceramics against pure Na_2SO_4 and NaCl and their eutectic mixture was also reported. The corrosiveness of these salts decreases in the following sequence, $Na_2SO_4 > Na_2SO_4 + NaCl \gg NaCl$, showing the dependence of the corrosion effects on the free oxide ion activity. Si_3N_4 is much less reactive than SiC. It was also reported that in addition to corrosive etching, contaminant ion (Na, Cl, and S) penetration was noticeable, and hence mechanical properties might be altered. The severe attack on SiC by Na_2SO_4 (and also by Na_2CO_3) was later confirmed by Jacobson and Smialek (1986).

Further, Sequeira's studies reported in 1998, on the corrosion of nickel-based alloys in $(Na,Li)_2SO_4$ melts at 973 K, must also be mentioned.

The anodic polarization curves of Ni and Ni–Cr alloys in $(Na,Li)_2SO_4$ at 973 K after five hours immersion are shown in Figure 13.7a (O_2 atmosphere) and Figure 13.7b (O_2/H_2O atmosphere, $p(H_2O) = 2 \times 10^3$ Pa). These curves suggest that after five hours immersion, the specimens are partly or totally covered by an oxide film, the anodic dissolution taking place through the surface oxide film. This "active–passive" behavior is modified by the Cr content of the alloy and the water in the environment. The water increases the free corrosion potentials and the anodic dissolution currents, but the most remarkable effect showed by the polarization curves is the increase of the corrosion resistance of the alloys with their Cr content; particularly, for alloys containing more than 20% Cr, the passive state prevails over the active state of the specimen, and its corrosion potential moves toward the more noble values.

Figure 13.7c,d shows the time-dependent variation of the potentials for the Ni specimens in O_2 and $O_2 + H_2O$ atmospheres. In Figure 13.7c, the corrosion potentials of all specimens in O_2 atmospheres shift to the more noble direction with the time of immersion, but a negative deflection is observed for Ni, Ni–5Cr, and Ni–15Cr, with the elapse of time, which is certainly due to the breakdown of the protective film formed in the initial periods. Stable protective films, probably Cr_2O_3, seem to be characteristic of alloys with higher Cr content, whose E_{corr} values always shift to noble values. Under H_2O vapor, E_{corr} also increases, but the shift is essentially observed in the initial periods of immersion, being followed by negative/positive deviations that are attributable to rupture/passivation of unstable oxide layers, this effect being stimulated by the water/sulfate partial cathodic reduction

$$SO_4^{2-} + H_2O + 2e^- \rightarrow SO_2 + 2OH^- + O^{2-} \qquad (13.34)$$

whose validity was supported by experiments not reported here.

Figure 13.7e,f shows the time course of the polarization conductance. Again the effects of Cr/H_2O are reflected by a general increase of Rp^{-1} with time in the presence of H_2O, and the exhibition of relatively small values of Rp^{-1} for the alloys containing more than 20% Cr.

AC impedance diagrams for Ni, Ni–5Cr, Ni–20Cr, and Ni–50Cr, measured after five hours immersion in the melts under water vapor, are shown in Figure 13.7g,h. The Nyquist diagrams exhibited a dominant capacitive component. Bode diagrams exhibited phase angles with value near 90°. The reciprocal of the charge transfer resistance determined from the impedances in the low frequency regimes correlated with the i_{corr} estimated from the weight loss in the melts. Passivation/depassivation events for five time records of 2048 discrete elements

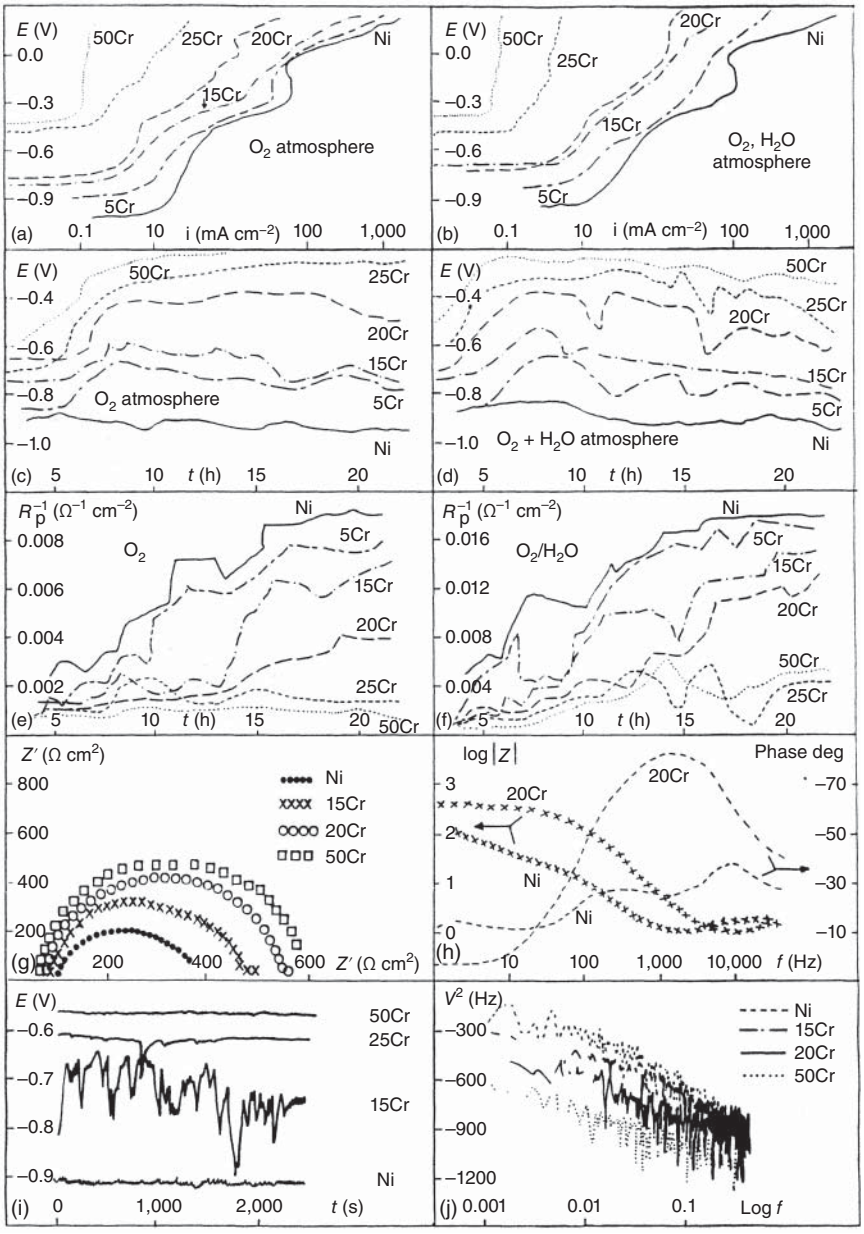


Figure 13.7 Electrochemical behavior of Ni–Cr alloys in $(Li,Na)_2SO_4$ melts at 973 K (Sequeira 1998).

each were examined in H_2O conditions for Ni, Ni–15Cr, Ni–25Cr, and Ni–50Cr.

Figure 13.7i shows a typical potential–time record. Less transient potentials were exhibited by the alloys with more than 20% Cr. Ni–50Cr was practically passive and intact, so did not exhibit a transient potential; pure Ni was almost completely depassivated or under an external potential control (dissolution products), again resulting in a lack of transient potential. Spectral analysis of the transients for the four specimens is provided in Figure 13.7j.

The flat line $E(t)$ data from Figure 13.7i for 50Cr is consistently shown here as extremely low noise at both high and low frequencies; the other specimens are slightly more noisy, with roll-offs higher than the roll-off value for 50Cr. Further examination of the noise results including stochastic analysis was also performed but is not reported here. Considering the above results, it was concluded that electrochemical impedance spectroscopy and electrochemical noise are useful complementary techniques to conventional DC polarization studies for metallic corrosion in molten salts.

The corrosion of Ni–Cr alloys in fused Li,Na sulfates is controlled by simultaneous dissolution and passivation events.

The acceleration of corrosion by water is attributable to SO_2 generated by the reaction of H_2O with SO_4^{2-}. The

passive state of the studied specimens, accompanied by the enhancement of their film stability, predominates when the alloys contain more than 20% Cr. Microscope, electron probe, and X-ray studies, not reported here, showed that the principal corrosion products are NiO, Cr_2O_3, Ni_3S_2, and CrS (Sequeira 1998).

13.12.8 Other Measurements

Sulfate–chloride mixtures have been studied both as media where the chloride ion is the reacting species and in dilute solutions of SO_4^{2-} in chloride molten salts. The investigation of the reducibility of sulfate ions was made by several workers by studying solutions of sodium sulfate in the LiCl–KCl eutectic. A chronopotentiometric study of the dissociation of sulfate ions in molten equimolar NaCl–KCl at 750 °C was also carried out. Moreover, K/Na/Mg and Zn/K chlorides containing sulfate have also been used as reaction media for electrochemical studies.

An attempt to investigate the electrochemical behavior of oxide films on nickel-based superalloys in the presence of dilute solutions of NaCl in Na_2SO_4 was made by Wheatfall et al. (1967). The response of inert platinum electrodes to the SO_2/O_2 ratio above sulfate melts was also observed. It was shown that the values of the electrode potentials are in agreement with the Nernst equation

$$E = E^0 + \frac{2.3\mathrm{RT}}{2F} \log p_{\mathrm{SO}_2} \times p_{\mathrm{O}_2} \tag{13.35}$$

derived from the Nernst expression for the sulfur trioxide electrode process given by equation

$$\frac{1}{2}\,\mathrm{SO}_3 + \mathrm{e}^- = \frac{1}{2}\,\mathrm{SO}_2 + \frac{1}{2}\,\mathrm{O}^{2-} \;:\; E = E^0 + \frac{2.3RT}{2F}\,\log \frac{p_{\mathrm{SO}_3}}{p_{\mathrm{SO}_2}}\,\{\mathrm{O}^{2-}\}^{-1} \tag{13.36}$$

by assuming that the equilibria (13.23) and (13.32) are established in the melt. Studies on the O_2, SO_3, Pt/(Na, Li,K)$_2$ SO_4 electrode showed that the electrode exhibits Nernstian behavior, being basically controlled by the O_2/O^{2-} equilibrium in the melt. Similar experiments using a gold electrode were also carried out confirming that the platinum electrode is not completely inert in the sulfate melt. At present, a large amount of corrosion studies continue to be pursued, both in molten sulfates and sulfate-based melts (Guillot et al. 2012; Tomeczek 2007; Zahrani and Alfantazi 2012) for gas turbines, boilers, furnaces, incinerators, and other high temperature corrosive environments, as described in Chapters 15, 16, 18, and 19 and referenced in Sections 13.13 and 13.14.

13.13 Prevention of Molten Salt Corrosion

There is a lack of reliable data for molten salts on structural material under industrial conditions, but several general rules should be observed. A material should be selected that will form a passive non-soluble film in the melt if possible. Material selection is the key to successful containment. Minimizing the entry of oxidizing species such as oxygen and water into the melt is very important. The oxidizing power of the melt or its redox potential should be kept as low as possible, which can be accomplished by additives. These additives are known as *regenerators*.

In "neutral" chloride salt baths (i.e. those causing neither carburization nor decarburization of steel), regenerators fall into two classes, viz alkalis and reactive metals. Alkali additions raise the O^{2-} ion activity in the melt, and since the oxygen partial pressure over the melt is constant, this results in a fall in redox potential. Reactive metals combine with oxidizing impurities in the melt, and in general the more base the metal the greater its effectiveness. The baser metals, such as sodium or potassium, are the most reactive but would be inconvenient in practice. Magnesium is sometimes used, but slightly more noble metals with volatile chlorides, such as silicon, are commoner. Evaporation of the $SiCl_4$ as it is formed drives the reaction to completion. Besides reducing the aggressiveness of salt baths, certain regenerators also affect the carburizing tendency of salt baths, but the subject is outside the scope of this discussion.

The temperature of the salt bath should be kept as low as possible. The lower temperature not only decreases the diffusion rates of the ions into the melt but also lowers the solubility of potentially passive surface films. Temperature gradients should be eliminated within the melts to decrease the selective dissolution and plating at hot and cold sides.

Significant improvement of the corrosion resistance of a material can also be obtained by the use of *inhibitors*. In this case, good results seem to be achieved with rare earths employed in low amounts as alloying metals or as protective dense oxide coatings. The use of coatings often means the research into the best compromise between mechanical properties and corrosion resistance of the material.

13.14 Summary

Molten salt corrosion can be identified as an intermediate form of corrosion between molten metal and aqueous corrosion.

The concept of acid and base behavior of the melt is very similar to its aqueous counterpart. The corrosion process is mainly electrochemical in nature because of the excellent ionic conductivity of most molten salts. Even

though there are many similarities between corrosion in molten salts and corrosion in aqueous solutions, there are also many disparities in particular due to the fact that molten salts are partially electronic conductors as well as ionic conductors. This fact allows for reduction reactions to take place in the melt as well as at the metal/melt interface. In other words, the interface reaction becomes a "volume reaction," and this can explain a substantial increase in corrosion rate over a similar electrochemically controlled aqueous system. Also, because of property differences between water and molten salt, the rate-controlling step in most molten metal systems is ion diffusion into the bulk solution, not the charge transfer reaction that is typical of aqueous systems.

Thermal gradients in the melt can cause dissolution of metal at hot spots and metal deposition at cooler spots. The result is very similar to aqueous galvanic corrosion, and like aqueous galvanic corrosion, a continuous electrical path is necessary between the hot and cold areas. Crevice corrosion has been observed, and wash-line attack caused by oxygen concentration corrosion is not uncommon at the metal/molten salt/air interface.

High temperature corrosion in molten salts often exhibits selective attack and internal oxidation.

Specific examples of the types of corrosion expected for the different metal-fused salt systems are also provided in this chapter. It is hoped that this vast amount of information will provide an appreciation of the problems involved and the material that can be obtained from various experimental procedures, namely, capsule and flow experiments.

References

Abramov, A.V. (2010). *218th ECS Meeting*. Philadelphia, PA: Electrochemical Society, Inc.

Atmani, H. and Rameau, J.J. (1987). *Mater. Sci. Eng.* 88: 247.

Barin, I. (1993). *Thermochemical Data for Pure Substances*. New York: VCH Publishers.

Baudo, G., Tamba, A., and Bombara, G. (1970). *Corrosion-NACE* 26: 193.

Berkani, M. and Gaune-Escard, M. (2011). *JEEP 2011* (ed. M. Aillerie, M. Cochez and M. Ferriol), 95. Saint-Avold: JEEP.

Blander, M.I. (ed.) (1964). *Molten Salt Chemistry*, New York: Interscience.

Bockris, J.O.'.M., White, J.L., and MacKenzie, J.D. (1959). *Physicochemical Measurements at High Temperatures*. London: Butterworths.

Boehme, D.R. and Bradshaw, R.W. (1984). *High Temp. Sci.* 18: 39.

Bratland, D. (1987). *Molten Salt Techniques*, vol. 3 (ed. D.G. Lovering and R.J. Gale), 73. New York: Plenum Press.

Brown, C.T., Bornstein, N.S., and DeCrescente, M.A. (1970). *High Temperature Metallic Corrosion of Sulphur* (ed. Z.A. Foroulis), 170. Pennington, NJ: The Electrochemical Society.

Burrows, B.W. and Hills, G.J. (1966). *J. Inst. Fuel* 39: 168.

Burrows, B.W. and Hills, G.J. (1970). *Electrochim. Acta* 15: 445.

Carling, R.W., Bradshaw, R.W., and Mar, R.W. (1983). *J. Mater. Energy Syst.* 4: 229.

Casino, R.G., Podestá, J.J., and Arvía, A.J. (1971). *Electrochim. Acta* 16: 121.

Colom, F. and Bodalo, A. (1971). *Collect. Czech. Chem. Commun.* 36: 674.

Colom, F. and Bodalo, A. (1972). *Corros. Sci.* 12: 731.

Coyle, R.T., Thomas, T.M., and Lai, G.Y. (1985). *High Temperature Corrosion in Energy Systems* (ed. M.F. Rothman), 627. Warrendale, PA: The Metallurgical Society of AIME.

Cutler, A.J.B. and Grant, C.J. (1972). *Proceedings, Conference on Deposition and Corrosion in Gas Turbines*. London: CEGB.

Danner, G. and Rey, M. (1961). *Electrochim. Acta* 4: 274.

Delimarski, Y.K. and Markov, B.F. (1961). *Electrochemistry of Fused Salts, Trans*. New York: Sigma Press.

Delong, H.C., Bradshaw, R.W., and Matsunaga, M. (eds.) (2002). *Proceedings of the XIII International Symposium on Molten Salts*. Philadelphia, PA: The Electrochemical Society, Inc.

Ebara, R., Nakajima, H., Shouzen, D., and Yamada, T. (1988). *J. Jpn. Inst. Met.* 52: 508.

Edeleanu, C. and Gibson, J.G. (1960). *J. Inst. Met.* 88: 321.

Emsley, A.M. and Hill, M.P. (1987). *J. Appl. Electrochem.* 17: 283.

Evans, U.R. (1960). *The Corrosion and Oxidation of Metals*. London: Edward Arnold and Co.

Federsel, K., Wortmann, J., and Ladenberger, M. (2015). *Energy Procedia* 69: 618.

Feng, X.K. and Melendres, C.A. (1982). *J. Electrochem. Soc.* 129: 1245.

Fernández, A.G., Cortes, M., Fuentealba, E., and Pérez, F.J. (2015). *Renewable Energy* 80: 177.

Flood, H., Förland, T., and Motzfeldt, K. (1952). *Acta Chem. Scand.* 6: 257.

Foroulis, Z.A. and Smeltzer, W.W. (eds.) (1975). *Metal-Slag-Gas Reactions and Processes*. Pennington, NJ: The Electrochemical Society.

Frangini, S. (2008). *J. Power Sources* 182: 462.

Frangini, S., Masci, A., and Zaza, F. (2011). *Corros. Sci.* 53: 2539.

Galasiu, I., Galasiu, R., and Thonstad, J. (1999). *Nonaqueous Electrochemistry* (ed. D. Aurbach), 461. New York: Marcel Dekker.

Gaune-Escard, M. (ed.) (2002). *Molten Salts: From Fundamentals to Applications*, NATO Science Series II, vol. 52. Dordrecht, Holland: Kluwer Academic Publishers.

Germanaz, P., Nicolas, F., Rouquette, S. et al. (1989). *Mater. Sci. Eng., A* 120: 329.

Glushko, V.P. (ed.) (1984). *Thermodynamic Properties of Individual Substances, The Handbook*, vol. 1. Moskow, USSR: Nauka.

Grantham, L.F., Shaw, P.H., and Oldenkamp, R.D. (1970). *High Temperature Metallic Corrosion of Sulphur and Its Compounds* (ed. Z.A. Foroulis), 253. New York: The Electrochemical Society.

Gregory, J.N., Hodge, N., and Iredale, J.V. (1956). AERE-C/M-273, UK.

Guillot, S., Faik, A., Rakhmatullin, A. et al. (2012). *Appl. Energy* 94: 174.

Gunnarsson, G. and Johannesson, B. (2011). *J. Am. Ceram. Soc.* 94: 988.

Hamel, C., Chamelot, P., and Taxil, P. (2004). *Electrochim. Acta* 49: 4467.

Hara, M., Shinata, Y., and Hashimoto, S. (1997). *Corros. Sci.* 39: 627.

Heine, D. (1985). *Corrosion of Steels in Contact with Molten Salt as Latent Heat Storage Materials*. Report DE86753181/GAR. Stuttgart, Germany: Stuttgart University.

Heitz, E., Henkhaus, R., and Rahmel, A. (1992). *Corrosion Science – An Experimental Approach*. New York: Ellis Horwood.

Ho, M.X. and Pan, C. (2014). *Int. J. Heat Mass Transfer* 70: 174.

Hocking, M.G., Vasantasree, V., and Sidky, P.S. (1989). *Metallic and Ceramic Coatings: Production, High Temperature Properties and Applications*. Essex, England: Longman Scientific and Technical.

Hoff, H. (1971). *Electrochim. Acta* 16: 1357.

Hsu, H.S., De Van, J.H., and Howell, M. (1987). *J. Electrochem. Soc.* 134: 3038.

Indacochea, J.E. (2001). *Oxid. Met.* 55: 1.

Ishikawa, T. and Sasaki, T. (1981). *Proceedings of the 8th International Congress on Metallic Corrosion*, vol. I, 803. Frankfurt: Dechema.

Ives, D.J.G. and Janz, G.J. (1961). *Reference Electrodes*. New York: Academic Press.

Jacobson, N.S. and Smialek, J.L. (1986). *J. Electrochem. Soc.* 133: 2615.
JANAF (1971). *Thermochemical Table, NSRDS-NBS*, 2nde, vol. 37. Washington, DC: US Government Printing Office.
Janz, G.J. and Tompkins, R.P.T. (1979). *Corrosion* 35: 485.
Keijzer, M. (2003). *Molten Salt Forum* 7: 15.
Keijzer, M., Au, S.F., Hemmes, K. et al. (1998). *Molten Salt Forum* 115: 5–6.
Keijzer, M., Lindberg, G., Hemmes, K. et al. (1999). *J. Electrochem. Soc.* 146: 2508.
Keiser, J.R., DeVan, J.H., and Lawrence, E.J. (1979). *J. Nucl. Mater.* 85/86: 295.
Kelley, K.K. (1949). *Contributions to the Data on Theoretical Metallurgy, X. High Temperature Heat-Content, Heat Capacity and Entropy Data for Inorganic Compounds*, United States Bureau of Mines, Bulletin 476. . Washington, D.C.: U.S. Government Printing Office.
Keppert, M., Rakhmatullin, A., and Simco, F. (2008). *Magn. Reson. Chem.* 46: 803.
Kerridge, D.H. and Polyakov, E.G. (1998). *Refractory Metals in Molten Salts*. Dordrecht, Holland: Kluwer Academic Publishers.
Kim, B., Takeishi, Y., Yoshitake, H. et al. (1994). *Proceedings of the 9th International Symposium Molten Salts*, 757. Pennington, NJ: The Electrochemical Society.
Klěcka, A., Langová, S., Raška, P. et al. (2015). *Chem. Papers* 69: 1312.
Koger, J.W. (1987). *Metals Handbook: Corrosion*, 9the, vol. 13, 50. Materials Park, OH: ASM International.
Koger, J.W. and Pohlman, S.L. (1987). *Metals Handbook: Corrosion*, 9the, vol. 13, 88. Materials Park, OH: ASM International.
Kruizenga, A.M. (2012). *Corrosion Mechanisms in Chloride and Carbonate Salts*. SAND 2012–7594. Livermore, CA: Sandia National Laboratories.
Kruizenga, A.M. and Gill, D.D. (2014). *Energy Procedia* 49: 878.
Kruizenga, A.M., Gill, D.D., and Laford, M. (2013). *Materials Corrosion of High Temperature. Alloys Immersed in 600°C Binary Nitrate Salt*. SAND 2013–2526. Livermore, CA: Sandia National Laboratories.
Kubaschewski, O. and Evans, E.L. (1985). *Metallurgical Thermochemistry*, 3rde. London: Pergamon Press.
Lai, G.Y., Rothman, M.F., and Fluck, D.E. (1985). *Proceedings Corrosion/85*, Paper No. 14. . Houston, TX: NACE International.
Lantelme, F. and Groult, H. (2013). *Molten Salts Chemistry: From Lab to Applications*. London: Elsevier.
Lewis, D. (1971). *J. Inorg. Nucl. Chem.* 33: 2121.
Littlewood, R. and Argent, E.J. (1961). *Electrochim. Acta* 4: 155.
Liu, C.H. (1962). *J. Phys. Chem.* 66: 164.
Lovering, D.G. (ed.) (1982). *Molten Salt Technology*. New York: Plenum Press.
Lux, H. (1939). *Z. Elektrochem.* 45: 303.
Mamantov, G. (ed.) (1969). *Molten Salts*. New York: Marcel Dekker.
Martinez, L., Amaya, M., Porcayo-Calderon, J., and Lavernia, E.J. (1998). *Mater. Sci. Eng., A* 258: 306.
Masset, P.J. (2010). *ECS Trans.* 25: 155.
Minh, N.Q. and Redey, L. (1987). *Molten Salt Techniques*, vol. 3 (ed. D.G. Lovering and R.J. Gale), 105. New York: Plenum Press.
Misra, A.K. and Whittenberger, J.D. (1987). Fluoride salts and container materials for thermal energy storage applications in the temperature range 973 to 1400 K. NASA Technical Memo 89913. Cleveland, OH: NASA Lewis Research Center.
Naumov, V.S. and Bychkov, A.V. (1996). *Environ. Res. Forum* 1–2: 189.
Ni, C.S. and Lu, L.Y. (2014). *Int. J. Corros.* 2014: 13.
Nishikata, A. and Haruyama, S. (1986). *Corrosion* 42: 578.
Nishikata, A., Numata, H., and Tsuru, T. (1991). *Mater. Sci. Eng., A* 146: 15.
Numata, H. (1988). *Corros. Sci.* 44: 724.
Olson, D.L., Mishra, B., and Eberle, C.S. (1998). *Proceedings Light Metals 1998*, 1349. Warrendale, PA: Minerals, Metals and Materials Society/AIME.
Oryshich, I.V. and Kostyrko, O.S. (1985). *Metal Science and Heat Treatment*, vol. 27, 740.
Ota, K.I., Toda, K., Kojima, T. et al. (1996). *Proceedings Molten Salts X*, 406. Pennington, NJ: The Electrochem Society.
Ota, K.I., Toda, K., Motohira, N., and Kamiya, N. (1998). *Molten Salt Forum* 5–6: 111.
Ozeryanaya, I.N. (1985). *Met. Sci. Heat Treat.* 3: 184.
Ozeryanaya, I.N., Manukhina, T.I., and Sannikov, V.I. (1984). *Proceedings of the International Congress Metallic Corrosion*. Toronto, Ontario, Canada: National Research Council Canada.
Picard, G.S., Lefebvre, H.M., and Trémillon, B.L. (1987). *J. Electrochem. Soc.* 134: 52.
Polovov, I.B., Volkovich, V.A., and Charnock, J.M. (2008). *Inorg. Chem.* 47: 7474.
Pourbaix, M.J.N. (1949). *Thermodynamics of Dilute Aqueous Solutions*. London: Edward Arnold and Co.
Rahmel, A. (1968). *Electrochim. Acta* 13: 495.
Rahmel, A. (1972). *Corros. Sci.* 12: 307.
Rahmel, A. and Schwenk, W. (1977). *Korrosion un Korrosionsschutz von Stählen*. Weinheim: Verlag Chemie.
Reavis, J.G. (1987). *Molten Salt Techniques*, vol. 3 (ed. D.G. Lovering and R.J. Gale), 5. New York: Plenum Press.
Roger, F., Carreau, J.-L., Ghaboné, L. et al. (2014). *Nucl. Eng. Des.* 273: 119.
Sarou-Kanian, V., Rollet, A.L., and Salanne, M. (2009). *Phys. Chem. Chem. Phys.* 11: 11501.
Sequeira, C.A.C. (1979). *Rev. Port. Quím.* 21: 117.
Sequeira, C.A.C. (1989). *J. Electrochem. Soc.* 136: 2909.
Sequeira, C.A.C. (1998). *Molten Salt Forum* 5–6: 417.
Sequeira, C.A.C. (2003). *Molten Salt Forum* 7: 41.
Sequeira, C.A.C. and Amaral, L. (2014). *Trans. Nonferrous Met. Soc. China* 24: 1.
Sequeira, C.A.C. and Hocking, M.G. (1977). *Electrochim. Acta* 22: 1161.
Sequeira, C.A.C. and Hocking, M.G. (1978a). *J. Appl. Electrochem.* 8: 145.
Sequeira, C.A.C. and Hocking, M.G. (1978b). *Electrochim. Acta* 23: 381.
Sequeira, C.A.C. and Marquis, F.D.S. (1993). *Progress in the Understanding and Prevention of Corrosion*, vol. 1 (ed. J.M. Costa and A.D. Mercer), 730. London: The Institute of Materials.
Siegel, N.P. (2012). *Wiley Interdiscip. Rev. Energy Environ.* 1: 119.
Skelton, R.P. and Horton, C.A.P. (1999). *Mater. High Temp.* 16: 87.
Slusser, J.W., Titcomb, J.B., Heffelfinger, M.T., and Dunbobbin, B.R. (1985). *JOM* 24.
Smith, G.P. and Hoffman, E.E. (1957). *Corrosion* 13: 6276.
Smyrl, W.H. and Blackburn, M.J. (1975). *Corrosion-NACE* 31: 375.
Sørlie, M., Østvold, T., and Huglen, R. (eds.) (1995). *The International Harald A. Øye Symposium*. Trondheim, Norway: NTNU.
Sorokin, Y.I. and Tseitlin, K.L. (1965). *Khim. Prom.* 41: 64.
Sundheim, B.R. (ed.) (1964). *Fused Salts*. New York: McGraw-Hill.
Tasaka, A., Tsukuda, Y., Yamada, S. et al. (1998). *Molten Salt Forum* 5–6: 437.
Tomeczek, J. (2007). *Corros. Sci.* 49: 1862.
Vossen, J.P.T., Plomp, L., and de Wit, J.H.W. (1994). *J. Electrochem. Soc.* 141: 3040.
Vossen, J.P.T., Makkus, R.C., and de Wit, J.H.W. (1996). *J. Electrochem. Soc.* 143: 66.
Wang, K., Cui, C., and Yang, Y. (1991). *Proceedings of RASELM'91*, 593. Tokyo, Japan: Japan Institute of Light Metals.
Wang, Y., Liu, H., and Zeng, C. (2014). *J. Fluorine Chem.* 165: 1.
Wee, J.H. and Lee, K.-Y. (2006). *J. Mater. Sci.* 41: 3585.
Wheatfall, W.L., Doering, H., and Danek, G.J. Jr. (1967). *Hot Corrosion Problems Associated with Gas Turbines*. ASTM STP 421, 206. American Society for Testing and Materials.
White, S.H. (1983). *Molten Salt Techniques*, vol. 1 (ed. D.G. Lovering and R.J. Gale), 19. New York: Plenum Press.

Xu, X., Zhou, W., and Zhu, Z. (2014). *RSC Adv.* 4: 2398.
Yanagida, M., Tanimoto, K., Kojima, T. et al. (1998). *Molten Salt Forum* 5–6: 149.
Yaxin, X. and Chaolin, Z. (2014). *J. Chin. Soc. Corros. Prot.* 34: 211.
Yoshiba, M., Wada, H., Sasaki, T., and Kato, M. (1990). *J. Jpn. Inst. Met.* 54: 794.
Yurkinsky, V.P., Firsova, E.G., and Makarov, D.V. (1998). *Molten Salt Forum* 5–6: 421.
Yurkinsky, V.P., Firsova, E.G., and Baturova, L.P. (2010). *Russian J. Appl. Chem.* 83: 1816.
Zahrani, E.M. and Alfantazi, A.M. (2012). *Corros. Sci.* 65: 340.
Zeng, C. and Wu, W. (2000). *Jinshu Xuebao* 36: 517.
Zeng, C., Wang, W., and Wu, W. (2000). *Jinshu Xuebao* 36: 651.
Zeng, C.L., Wang, W., and Wu, W. (2001). *Corros. Sci.* 43: 787.

Further Reading

Allen, C.B. and Janz, G.T. (1980). *J. Hazard. Mater.* 4: 145.
Birks, N. and Meier, G.H. (1983). *Introduction to High Temperature Oxidation of Metals*. London: Edward Arnold.
Gale, R.J. and Lovering, D.G. (eds.) (1981). *Molten Salt Techniques*, vol. 2. New York: Plenum Press.
Gaune-Escard, M. and Haarberg, G.M. (eds.) (2014). *Molten Salts Chemistry and Technology*. Chichester: Wiley.
Inman, D. and Lovering, D.G. (1983). *Comprehensive Treatise of Electrochemistry*, vol. 7 (ed. B.E. Conway, J.O.'.M. Bockris, E. Yeager, et al.). New York: Plenum Press.
Kofstad, P. (1988). *High Temperature Corrosion*. London: Applied Science.
Lai, G.Y. (1990). *High Temperature Corrosion of Engineering Alloys*. Materials Park, OH: ASM International.
Lai, G.Y. (2007). *High Temperature Corrosion and Materials Applications*. Materials Park, OH: ASM International.
Numata, H., Nishikata, A., and Haruyama, S. (1984). *Boshoku Gijutsu* 33: 103.
Rahmel, A. (1982). *Molten Salt Technology* (ed. D.G. Lovering), 266. New York: Plenum Press.
Rameau, J.J., Duret, C., Morbioli, R., and Steinmetz, P. (1985). *Corrosion des Matériaux à Haute Température* (ed. G. Béranger, J.C. Colson and F. Dabosi), 527. France: Les Éditions de Physique.
Rapp, R.A. (ed.) (1983). *High Temperature Corrosion*. Houston, TX: NACE.
Rapp, R.A. (1986). *Corros. Sci.* 42: 568.
Schütze, M. (1997). *Protective Oxide Scales and their Breakdown* (ed. D.R. Holmes). Chichester: Wiley.

Chapter 14

Corrosion in Molten Metals

14.1 Introduction

Molten metals, or liquid metals, are frequently used as heat transfer medium because of their excellent heat transfer properties. Due to their characteristics, namely, high thermal conductivity, high heat capacity, low vapor pressure, etc., most of their corrosion studies have been carried out in conjunction with nuclear reactor applications (Borgstedt 1982; Marchbanks et al. 1976), heat treatment baths, power generation, and others that the reader can find in articles and books listed in Further Reading. Sodium, for example, has been used as a coolant in fast breeder nuclear reactors. Molten aluminum is also one of the most aggressive metals to a number of metals and ceramics due to its engineering applications in die coating, containment materials, and semisolid processing (Tipping 2010).

Molten aluminum can cause considerable corrosion of the handling and container materials, leading to an insufficient and, above all, unpredictable lifetime. In the aluminum industry, refractory performance against corrosion is an important factor affecting the quality of metal produced and the durability of furnace lining. The tolerance of aluminum alloy castings may be affected by the wear of dies caused by aluminum flow. The search for materials compatible with molten aluminum is of great importance in the service environment of semisolid processing of aluminum, where components are subject to complex stress conditions. Under such complex stress conditions, materials should possess not only enough erosion resistance but also high fatigue resistance, satisfactory creep strength, and toughness. Consequently, those materials usually used for containment of molten aluminum, such as graphite and aluminosilicate refractories, cannot be used, and few materials have been characterized and qualified (Yu et al. 1995).

The coating of steel sheet by continuous hot dipping in a molten metal bath of zinc or in a Zn–Al melt is the most efficient and economical method of providing corrosion protection to most steel sheet compositions. Reliable performance of galvanizing pot hardware is essential to the productivity of a hot-dip galvanizing line and the quality of coatings produced. As shown in Figure 14.1, the pot hardware in galvanizing bath includes the snout, sink roll, stabilizing rolls, and the bearings supporting them. The most frequent cause of galvanizing line stoppage is pot hardware problems that are related to one or more of the following three issues: (i) wear of bearings supporting the stabilizer roll and sink roll, (ii) corrosion of the pot hardware in molten Zn–Al bath, and (iii) the nucleation and growth of dross (intermetallic compound) on roll surfaces.

Corrosion of the hardware by molten Zn–Al alloys is one of the most important reasons to cause downtime of production lines; thus the corrosion resistance becomes the primary criterion for the selection of pot hardware materials. Besides corrosion resistance, there are other properties required for pot hardware materials, among which the resistance to intermetallic dross buildup on the surface for roll materials, wear resistance for bearing materials, and ductility are the most important ones. Since corrosion resistance is the primary criterion for the pot hardware materials and each candidate material needs to show good corrosion resistance, usually corrosion studies of stainless steels and intermetallic materials are receiving further consideration (Seong et al. 2001).

A significant industrial problem related with the handling of molten metals is their storage, even at relatively low temperature, because of their elevated corroding activity against metallic containers. For example, in the case of liquid aluminum, zinc, and tin, kettles are made of low carbon, low silicon steel and deep-drawn in U-form in order to avoid welding. However, total protection of the metallic container cannot be achieved, and the steel is heavily corroded, although the iron solubility in liquid Zn, Al, and Sn at temperatures close to their melting point is low because the abovementioned molten metals react with iron, forming several intermetallic compounds that precipitate in the molten bath.

By contrast, ceramics are rather inert under the same conditions. However, kettles entirely built of ceramics are very expensive due to their dimensions. In general,

High Temperature Corrosion: Fundamentals and Engineering, First Edition. César A. C. Sequeira.
© 2019 John Wiley & Sons, Inc. Published 2019 by John Wiley & Sons, Inc.

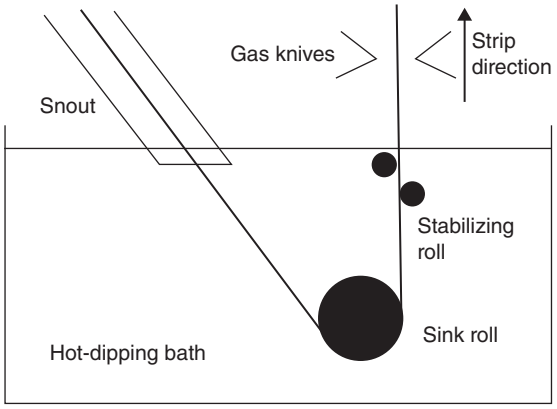


Figure 14.1 Sketch of a hot-dip bath.

ceramics prevent heating of the molten metal as they are thermal insulators. For these reasons, instead of kettles, ceramic coatings on ferrous substances are often used.

For the suitability assessment of ceramics or refractory materials for tools, crucibles, or handling aids in metallurgy and metals processing, e.g. for thixoforming or rheocasting, besides properties such as wetting behavior, wear resistance, thermal conductivity, and thermal shock resistance, mainly the corrosion behavior against the processed alloy influences the service life of a tool material. Therefore, testing strategies to characterize the corrosive interactions of ceramics with semisolid and molten metal alloys is receiving a lot of interest (Meyer-Rau and Telle 2005).

The corrosion behavior of metals, alloys, and ceramics in liquid metals is a complex problem involving simple dissolution (chemical corrosion), electron transfer processes (electrochemical corrosion), physical erosion (when there is a swift flow of melt relative to the surface of the solid), fouling, embrittlement, and stress corrosion, and this brief introduction shows that these phenomena have a real impact on many industrial applications. This chapter discusses several types of corrosion attack of materials by liquid metals and also examines reported interactions of important engineering materials with molten aluminum, zinc, lead, lithium, sodium, magnesium, mercury, and other metals.

14.2 Corrosive Processes

To define the destruction of a solid material by a liquid metal as corrosion, this word denotes solution and intermetallic compound formation, and the corrosion process for the most part simply depends on the solution rate and the extent of solubility of the solid material in the liquid metal. However, many complicating factors can influence the solution rate or the attainment of the solubility limit. The formations of surface intermetallic compounds and of oxide or nitride films are good examples of such factors. Other factors are impurities in the liquid metals (which may involve electron transfer processes, modifying or even overriding the simple dissolution process) and temperature gradients and multimetallic systems that can cause an increase in the amount of attack over that expected to saturate the liquid metal because of the mass transfer of material under the driving force of the temperature gradient or the concentration gradient.

Several variables affecting liquid metal corrosion must be considered, and they are (i) temperature; (ii) temperature gradient; (iii) cyclic temperature fluctuation; (iv) surface area to volume ratio; (v) purity of liquid metal; (vi) flow velocity, or Reynolds number; (vii) surface condition of container material; (viii) number of materials in contact with the same liquid metal; and (ix) condition of the container material, such as the presence of a grain boundary precipitate, the presence of a second phase, the state of stress of the metal, and the grain size. These variables influence the observed corrosion process, and it is appropriate to discuss six types of corrosion attack that have been frequently reported in the open literature (Borgstedt 1982).

14.2.1 Simple Dissolution

The solubility of metals in molten metals and its variation have not been explained properly up to the present days. Stratchan and Harris (1956) and Kerridge (1961) noted that plotting the solubilities of metals (at.%) in a number of solvent metals showed a periodic variation with the solute and not the solvent, i.e. a given metal such as manganese showed a consistently high solubility in molten magnesium, tin, bismuth, and copper, compared with iron or chromium, and this variation was correlated with the solute lattice energy and hence the latent heat of fusion.

In the more practical sense, dissolution may be uniform or localized. Preferential solution can take two forms:

1. *Leaching*: One component of an alloy is preferentially dissolved, an example being nickel, which is leached from stainless steels by molten lithium or bismuth, sometimes to such an extent that voids are left in the steel.
2. *Intergranular attack*: The liquid penetrates along the grain boundaries, owing either to the accumulation of soluble impurities in the boundaries or to the development at the junction of a grain boundary with the metal surface of a low dihedral angle to satisfy surface-energy relationships.

When this process is accompanied by stress, catastrophic failure can occur, a classical example being the action of mercury on brass.

The situation may be described in terms of the surface-energy changes when a crack propagates through a solid metal as shown in Figure 14.2 where γ_S is the

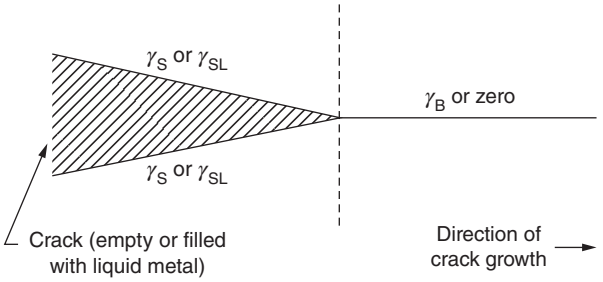


Figure 14.2 Energies involved in the growth of a crack.

solid–gas interfacial energy, γ_{SL} is the solid–liquid interfacial energy, and γ_B is the grain boundary energy.

Tabulated below are the energy changes involved for different cracking modes, with numerical values for the case of copper in contact with liquid lead with a dihedral angle at a copper grain boundary of 90° and $\gamma_S = 1.8\,\mathrm{J\,m^{-2}}$, $\gamma_B = 0.6\,\mathrm{J\,m^{-2}}$, and $\gamma_{SL} = 0.4\,\mathrm{J\,m^{-2}}$:

$$\begin{aligned}
&\text{Transgranular: } 2\gamma_S = 3.6\,\mathrm{J\,m^{-2}}\\
&\text{Grain boundary cracking: } 2\gamma_S - \gamma_B = 3.0\,\mathrm{J\,m^{-2}}\\
&\text{Grain boundary cracking in the presence}\\
&\quad\text{of liquid metal: } 2\gamma_{SL} - \gamma_B = 0.2\,\mathrm{J\,m^{-2}}\\
&\text{Transgranular cracking with the crack filled}\\
&\quad\text{with liquid metal: } 2\gamma_{SL} = 0.8\,\mathrm{J\,m^{-2}}
\end{aligned} \tag{14.1}$$

It is seen that the presence of the liquid metal greatly lowers the surface-energy change for grain boundary cracking (Rostoker et al. 1960).

A good example of the even removal of metal from the surface to saturate the liquid metal can be that of a titanium specimen after being exposed to lead at 1000 °C for 40 hours. In the case of a complex alloy, the attack can also be a simple dissolution type as it can be shown by the corrosion of Type 304 low carbon stainless steel in sodium after 40 hours at 1000 °C. Another attack that might be termed simple dissolution is the decarburizing action of lithium and sodium, as it happens with Type 430 stainless steel after 40 hours at 1000 °C in lithium.

If all the phase diagrams of liquid metal–solid metal systems were available, an ascertainment could be made of the depth of attack that would occur in a static system as a result of simple solution by examining the solubility limit of the solid metal in the liquid metal at the operating temperature. However, there would be no conception of the rate at which the solubility limit was achieved. Thus, upon looking at the Fe–Li phase diagram in Figure 14.3, it can be seen that the amount of attack of iron by lithium should be quite small in a static isothermal system, and corrosion tests have proved this. Therefore, in simple solution-type attack, the amount of damage that the solid metal will receive depends on the ratio of surface area to volume of the system, but the rate at which the attack occurs can be greatly influenced by other variables, such as impurities in the system.

It is well established that the dissolution of a solid metal in a liquid metal can be described by Eq. (14.2) (Dybkov 1990):

$$\ln\left(\frac{c_s - c_0}{c_s - c}\right) = k\frac{St}{V} \tag{14.2}$$

where c is the concentration of the solute element in the melt, c_s the saturation concentration, c_0 the initial concentration of the solute, k the dissolution rate constant, S the solid metal surface, V the melt volume, and t the time. For a fixed volume of melt, when the dissolution proceeds, the concentrations of the elements rise, resulting in a decrease in the rate of further dissolution.

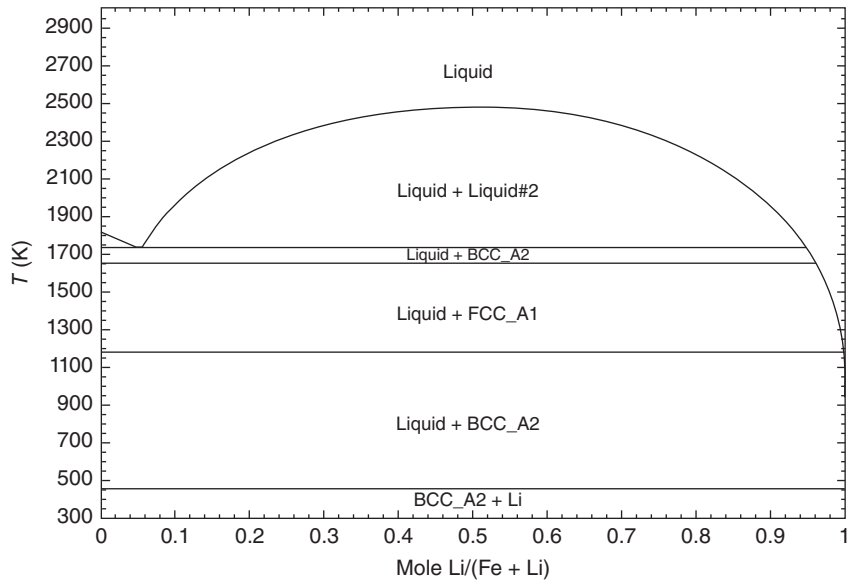


Figure 14.3 Fe–Li phase diagram.

When stirring is present in the melt, the dissolution rate constant, k, can be calculated by the equations below (Dybkov 1990):

$$k = 0.62D^{2/3}\upsilon^{-1/6}\omega^{1/2}\left(Sc = \frac{\upsilon}{D} > 1000\right) \qquad (14.3)$$

and

$$k = 0.554I^{-1}D^{2/3}\upsilon^{-1/6}\omega^{1/2}(4 < Sc \leq 1000) \qquad (14.4)$$

Here ω is the angular rotating speed of the solid metal, ν the kinematic viscosity of melt, D the diffusion coefficient of the solute across the interfacial zone, and $I = f(Sc)$.

From the above equations it can be seen that the presence and intensity of agitation affect the dissolution rate of solids in liquid. Another important loss mechanism from agitation is that it may damage the protective layer or accelerate the wear by the detachment of the reaction product, such as protuberances. The effect of melt agitation is much more drastic for those materials that form thick reaction layers that do not adhere well to substrate and are not hard enough.

Temperature is one of the most important variables affecting liquid metal corrosion, because the higher the temperature, the higher the solubility of the solid metal in the liquid phase. Also, as the temperature increases, diffusion rates increase, which is quite important in certain types of liquid metal corrosion, namely, simple dissolution. In general, the solubility, S, of a metal in molten metal varies with the temperature according to

$$\log S = A - \left(\frac{B}{T}\right) \qquad (14.5)$$

where A and B are constants for a given system. It is therefore possible for more material to dissolve from a container at its highest temperature end than at the low temperature end, and if the melt flows around the container by natural or forced convection, the liquid arriving at the cold region will be supersaturated and will precipitate solute until equilibrium is attained. If it is then recycled

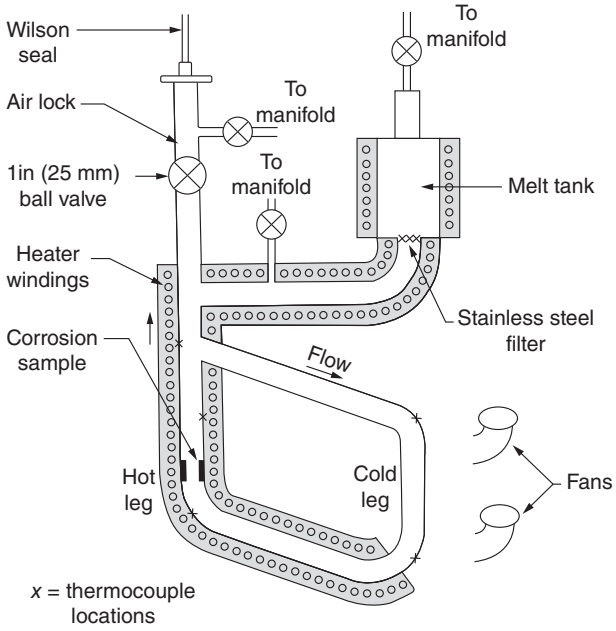


Figure 14.4 Thermal-convection loop.

to the hot end, it dissolves more metal until saturated and then returns to the cold end to precipitate this excess. This thermal-gradient mass transfer is illustrated in Figure 14.4, which shows a convection loop being circulated by a corrosive metal such as bismuth. Ward and Taylor (1957–1958) analyzed this process in some detail as shown in Figure 14.5. They found that the solution of solid copper in liquid lead and bismuth obeyed the following equations.

Under static conditions, at temperature T

$$c_t = c_0\left[1 - \exp\left(-k\frac{S}{V}\right)\right] \qquad (14.6)$$

where c_t = concentration of solute after time t, c_0 = saturation concentration of solute, S = surface area of solid exposed to liquid of volume V, $K = k_0$ exp. $(-\Delta E^{\neq}/RT)$ ($\Delta E^{\neq}$ = activation energy for solution).

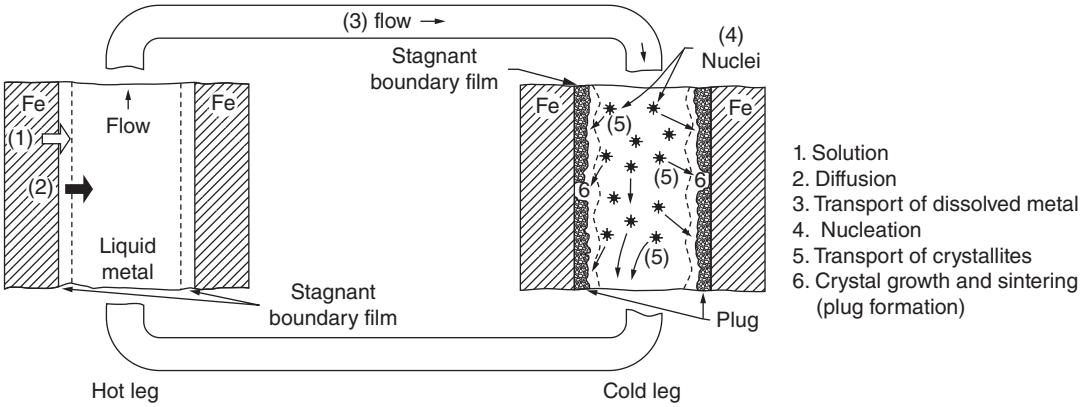


Figure 14.5 Stages in thermal-gradient mass transfer.

Under flowing conditions

$$\frac{dn_t}{dt} = k\left(\frac{S}{V}\right)(c_0 - c_t) \tag{14.7}$$

If, therefore, the solute atoms can be prevented from entering the boundary film from the solid, the process will be halted. A method for doing this was discovered by workers at the US General Electric Company 60 years ago (Frost 1958).

They found that small quantities of dissolved titanium, zirconium, chromium, nickel, and aluminum were effective as inhibitors of the corrosion of steels by hot mercury, the first two being particularly so. Later interest in the use of liquid bismuth as a carrier of uranium in a liquid metal-fueled reactor led to the extension of the use of zirconium inhibitor to bismuth in steel circuits and to an elucidation of the inhibiting mechanism. The zirconium reacts with the nitrogen, which is always present in steel to the extent of about 100 ppm, to form a surface layer of ZrN, which is thermodynamically a very stable compound and is an effective diffusion barrier. Furthermore, as long as there is residual zirconium in solution in the bismuth (or mercury) and dissolved nitrogen in the steel, the film is self-healing. Mercury boilers have operated successfully for thousands of hours relying on this principle.

The cyclic temperature fluctuation is helpful in explaining erroneous static corrosion results since under a supposedly isothermal condition in a poorly controlled furnace, the liquid metal–solid metal interface temperature can fluctuate quite appreciably around a mean temperature. Thus, at the high temperature, material goes into solution and subsequently at the lower temperature comes out of solution and precipitates in the bulk liquid or forms dendrites or a uniform layer on the container wall. The Cu–Bi system is an example of this, at 500 ± 0.5 °C.

Purity of the liquid metal can also have quite an effect on the rate at which the solubility limit is reached and can markedly affect the wetting tendency of the liquid metal on the solid metal.

14.2.2 Alloying Between Liquid Metal and Solid Metal

The next type of corrosion to be discussed is the alloying that occurs between liquid metals and solid metals. For this to result, there must be some solubility of the liquid metal in the solid metal. The Ag–Pb phase diagram (Figure 14.6) is an example of a system in which the liquid metal is soluble in the solid metal. In some experiments, the liquid metal dissolves considerably in the solid metal with the formation of an intermetallic compound. When vanadium is tested for 400 hours in lead at 1000 °C, an intermetallic compound is formed between the vanadium and lead.

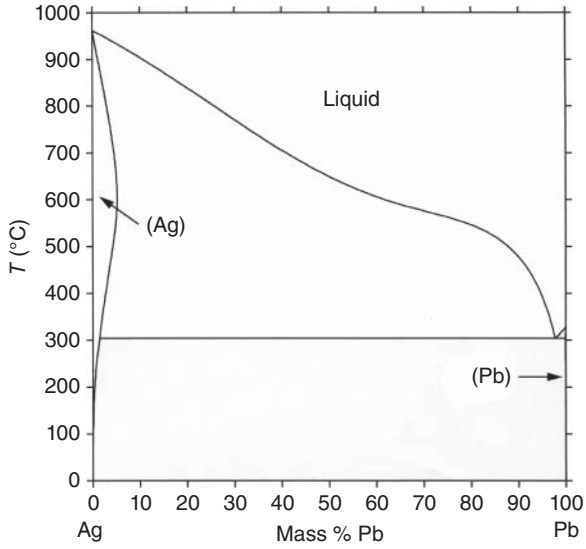


Figure 14.6 Ag–Pb phase diagram.

When Type 446 stainless steel is tested in lead at 1000 °C, it is found that after 400 hours, lead has diffused into the alloy predominantly at the grain boundaries and has formed a compound. Sodium will penetrate solid copper at the grain boundaries and will form an intermetallic compound, which is considerably harder than the base metal, copper.

14.2.3 Intergranular Penetration

One of the most serious types of corrosion that can occur is the deep intergranular penetration brought about by the removal of one constituent from an alloy. The best example of this is the selective removal of nickel from austenitic stainless steels, for example, a Type 347 stainless steel after 400 hours of testing in lead at 800 °C. Other examples of this type of corrosion are the attack on Type 304 low carbon stainless steel after 400 hours in lead and in lithium at 1000 °C. A considerable portion of the attack is attributed to the removal of nickel caused by the alloying of the nickel with the iron container wall, and it is assumed that the attack would have been less if the specimens and containers had been of the same material. The selective removal of nickel from a 75% Ni–25% Mo alloy also occurred in a sample from the hot leg of a thermal-convection loop (TCL), which operated for 200 hours with lead at 800 °C and with a 300 °C temperature gradient. In this case, the nickel was preferentially removed from the hot zone and deposited in the cold zone of the loop.

14.2.4 Impurity Reactions

In liquid metals, impurities such as oxygen, nitrogen, and carbon can have an appreciable effect upon the rate of

attack, and, in some cases, the whole mode of attack can be changed because of the effect of the impurity on the surface tension or because of the reactivity of the impurity. An example is the attack of stainless steels by lithium when nitrogen is the principal contaminant. However, the lithium is contaminated with a small quantity of nitrogen, the complete tube wall, comprising 0.89 mm, will be penetrated by the lithium during the same type of test (Casteels 1984). This is due to the nitrogen-contaminated lithium reacting with the carbides that form the grain boundary network, since a test in Type 316 stainless steel with lithium that was contaminated with nitrogen resulted in shallow attack when the testing temperature was above the solution temperature of the carbides. The true effect of nitrogen on corrosion by lithium is not understood. High temperature alloys can be severely carburized by liquid metals, especially sodium and lithium, if the liquid metals have been stored under kerosene or have acquired carbonaceous material from some other source.

In corrosion by sodium, oxygen impurities can have an appreciable effect on the rate at which the solubility limit is attained (Thorley and Tyzack 1967). In lead, the oxygen contamination, if any, decreases the rate of corrosion since most of the constituents of high temperature alloys can reduce the lead oxide and form a film that will act as a diffusion barrier between the solid metal and the liquid.

The solubility of carbon in sodium has been measured; it is considered lower than the corresponding value for oxygen (2 ppm of carbon at 520 °C) but is sufficiently high to give rise to undesirable effects. Carburization of refractory metals and of austenitic stainless steels has been observed in sodium contaminated with carbon, e.g. oil, grease, or a low-alloy ferritic steel, the source of which can be either decomposed organic material, e.g. oil or a ferritic steel of low- or zero-alloy content. The latter is an example of chemical-gradient transfer against the temperature gradient since the activity of carbon in Fe–18Cr–12Ni, possibly stabilized with titanium or niobium, is clearly lower than that in a plain carbon steel and there is, therefore, a driving force for carbon transfer. A deterioration in properties of both steels occurs, the austenitic becoming embrittlement and the ferritic softened. The effect can be minimized if the carbon activity in the ferritic steel is reduced to that in the stainless steel by the incorporation in the steel of a "carbon stabilizer" such as titanium. Hot trapping with zirconium removes carbon as well as residual oxygen, but generally carbon sources should be kept from liquid metal circuits containing materials sensitive to carburization effects.

In summary, for the transfer of a nonmetal along an activity gradient (chemical gradient), chemical thermodynamics is a useful guide to probable behavior. The transfer of a nonmetal, X, dissolved in a molten metal, M′, to another metal, M″, will depend on the relative free energies of formation of M′X and M″X. Thus, sodium will give up oxygen to Zr, Nb, Ti, and U, as the free energy of oxide formation of these metals is greater than that for sodium; on the other hand, sodium will remove oxygen from oxides of Fe, Mo, and Cu unless double oxides are formed.

Impurity reactions can be controlled or eliminated by adequate purification of the liquid metals, and in pumped loop systems, this can be achieved by using techniques known as cold trapping or hot trapping. Cold trapping involves taking a small percentage of the main loop flow and bypassing it through a container that is cooled to the required temperature to precipitate out the impurities. Hot trapping, on the other hand, involves removal of impurities by chemical reaction between the soluble species and a material that has a higher thermodynamic affinity for the impurity than the liquid metal or its containment.

In certain systems where metal solubilities are relatively high (e.g. Ni in liquid lithium), the use of cold traps can encourage thermal-gradient mass transfer; consequently, under these circumstances, other methods of purification may be required.

14.2.5 Temperature-Gradient Mass Transfer

The most damaging type of liquid metal corrosion is temperature-gradient mass transfer. The even removal of a slight amount of a container wall will not adversely affect its load-carrying abilities; however, the collection of this material in the colder regions of heat exchanger tubes as dendritic crystals would cause a cessation of flow. An example of mass-transferred material is seen in Figure 14.7, which is a plug from a Type 446 stainless steel

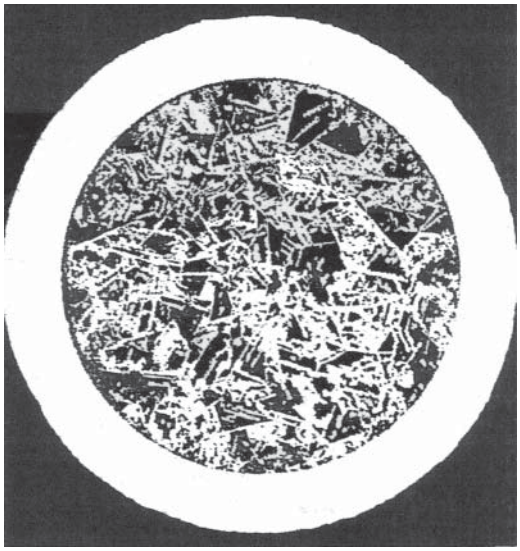


Figure 14.7 Plug from a Type 446 stainless steel thermal-convection loop that operated for 200 hours at 800 °C with a temperature gradient of 200 °C. These crystals were primarily alpha iron.

TCL that operated 200 hours at 800 °C with a temperature gradient of 200 °C. These crystals were primarily alpha iron. Note that a plug is a precipitate that eventually blocks the pipe to liquid flow. Another example is the massive matte of mass transfer material that can be observed as a plug from an Inconel-lead TCL that operated for 125 hours at 800 °C. In some loop experiments the crystals do not grow from nuclei in the bulk liquid, but mass-transferred material nucleates on the wall, and the crystals grow out into the stream as revealed by iron crystals formed on a Type 410 stainless steel TCL after 40 hours at 1000 °C with lithium. The driving force for temperature-gradient mass transfer is the difference in the solubility of the dissolved metal in the liquid metal at the temperature extremes of the heat transfer system. In examining the Cu–Pb phase diagram (Figure 14.8), it can be seen that there is considerable solubility of copper in lead at 900 °C, whereas at 500 °C it is much lower. Thus, by examining the phase diagram, the driving force for this phenomenon can be determined, but no information concerning the rate of the process can be determined.

If there is selective removal of one element from an alloy, these atoms must diffuse to the surface and then go into solution. The atoms must then diffuse through the lamellar layer into the bulk liquid stream and are finally carried to the cold portion of the system where supersaturation will occur. A collection of such atoms can accumulate and form a nucleus that will grow to a stable size and then drop from the liquid. On the other hand, the atom may supersaturate close to the wall, diffuse through the lamellar layer, and then nucleate on the metallic wall and form a dendritic crystal, or it may diffuse into the wall. As yet, the rate-controlling step in temperature-gradient mass transfer has not been found.

To obtain more data on mass transfer in liquid lead, a series of quartz TCL were operated at Oak Ridge National Laboratory (ORNL) with various alloys and the elements comprising the alloys. Results of these tests have indicated that the rate-controlling step for mass transfer by lead at the velocities used in the TCL takes place in the hot leg and is probably a solution step. For example, it was found that the formation of an intermetallic compound, or other type of diffusion barrier, in the hot zone greatly increases the time that elapses before a plug occurs in the loop.

In diffusion-controlled mass transfer situations involving turbulent fluids, Epstein (1957) has suggested that mass transfer equations can be derived from heat transfer analogies and expressions relating corrosion rate to the dimensionless groups. Reynolds number (*Re*) and Schmidt number (*Sc*) have been found to have some application where corrosion rates are sensitive to changes in flow velocity or diffusivity in the liquid phase. The equation suggested by Epstein to meet this situation is of the form

$$\text{Rate} = 0.023 \left(\frac{D}{d}\right) C_{\text{w}} (Re)^{0.8} Sc^{0.33} \tag{14.8}$$

in which C_{w} is the concentration of the dissolved species at the wall, D is the liquid-phase diffusivity for the soluble species, and d is the pipework diameter. The velocity term is incorporated in the *Re* number expression.

14.2.6 Concentration-Gradient Mass Transfer

The last type of liquid metal corrosion to be discussed is dissimilar-metal mass transfer or concentration-gradient mass transfer. One of the best examples that have been reported in the open literature is the interalloying between

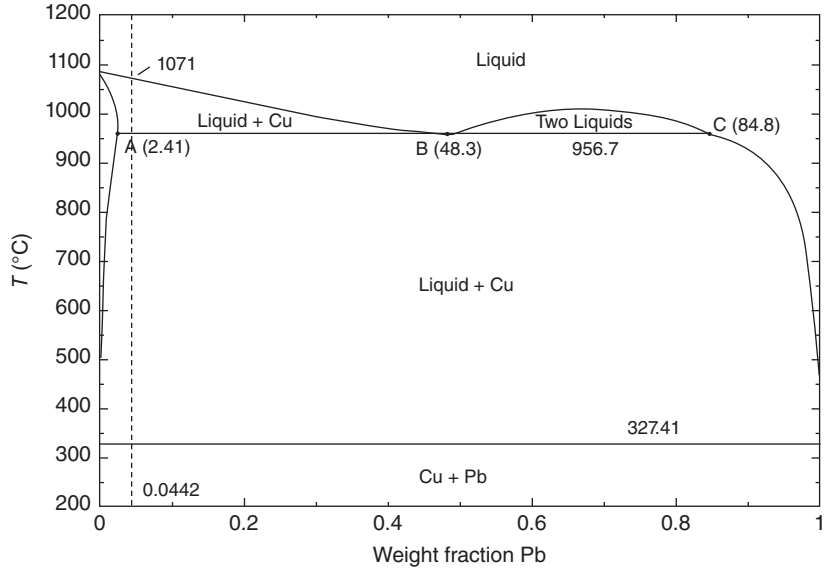


Figure 14.8 Cu–Pb phase diagram.

molybdenum and nickel. In this case, the molybdenum sample was being tested in sodium contained in a nickel crucible, and after 100 hours at 1000 °C, a sufficient quantity of nickel had transferred through the sodium and deposited and alloyed on the molybdenum surface to produce the Ni–Mo intermetallic compound and solid solution. Another example of this phenomenon resulted in the course of testing silicon with lithium in an iron capsule. It was shown that all the silicon has gone into solution in the lithium and has been carried to the wall of the iron container where alloying of the iron with the silicon occurred. Dissimilar-metal transfer can cause many misleading results as can be seen by the difference in the depth of corrosion when Type 304 stainless steel was tested with lithium in two types of containers. In one case, the Type 304 stainless steel specimen was placed in a Type 304 stainless steel container, and the attack was rather shallow. In the second case, the Type 304 stainless steel was tested in an iron container, and the attack was much more severe, which was caused by the selective removal of nickel that was transported to the iron wall where it alloyed.

In this case, atoms of metal A go into solution and move to the surface of metal B either by diffusion or by movement of the liquid. When they reach the surface of metal B, they come out of solution, alloy with metal B, and diffuse inward. The driving force for dissimilar-metal transfer is the decrease in the free energy that is achieved through the alloying of the two metals.

The greater the difference in the chemical potentials of A and B in the two solid phases, the greater will be the driving force for the occurrence of mass transfer. The rate of mass transfer is dependent on the temperature since an increase in temperature will, of course, increase the diffusion rate in both the liquid and the solid phases. A high solubility of metal A in B, or B in A, or both, will also facilitate mass transfer.

A last example is given by Covington and Woolf (1961), who have investigated, among other systems, aluminum and molybdenum in molten lead, tin, and bismuth. In bismuth, three of the four intermetallic compounds were identified in the layer on the molybdenum in the following order from the molybdenum surface: Al_3Mo, Al_5Mo, and $Al_{12}Mo$. In tin, only Al_3Mo was observed, while in lead two compounds were formed, the controlling process probably being the rate of diffusion through the layers of the different compounds and the rate of solution of the more soluble metal (aluminum) in the liquid metal.

14.3 Industrial Liquid Metals

In Section 14.2, the various types of liquid metal corrosion have been explained, and examples have been given; the driving forces for the various types of liquid metal corrosion have been discussed. Liquid metal corrosion has been described as mainly the solution of the solid metal in the liquid metal. The rate-controlling step for the various types of liquid metal corrosion has not been determined. For the successful containment of the liquid metals, the amounts of impurities, such as oxygen, nitrogen, and carbon, should be carefully controlled. Future work in the field of liquid metal corrosion must be directed toward increasing the understanding of the rate-controlling steps of dissimilar-metal transfer and temperature-gradient mass transfer. When this has been accomplished, corrective measures can then be taken to keep these types of corrosion to a minimum.

In this section, we will examine interactions of engineering materials with some molten metals.

14.3.1 Molten Aluminum

The durability of metals and ceramics in molten aluminum is a great concern in engineering applications such as die casting, containment of liquid metals, and semisolid processing. Chemical corrosion and physical erosion are the main mechanisms of materials failure in molten aluminum. Chemical corrosion refers to penetration by the melt as well as the formation of interphase layers, prevailing when relative motion between the solid materials and the melt is negligible. Erosion is dominant when there is a swift flow of melt relative to the surface of the solid and becomes more severe when there are hard particles in the melt, where mechanical wear occurs on the material surface.

Interactions of metallic materials with molten aluminum possess some common features. They all form intermediate layers of intermetallic compounds between the metal substrates and molten aluminum. These layers usually consist of either one phase or several phases, depending on the composition of the substrate and the reaction conditions. If different phases are formed, the zone consists of successive layers of intermetallic compounds. The layer adjacent to the substrate contains the highest content of the base element of the substrate, while the layer next to the molten aluminum is always aluminum rich. However, the corrosion or erosion rate in molten aluminum varies from metal to metal. Major metallic materials investigated are ferrous, nickel, and titanium alloys.

Most of the dies for production of aluminum components in the casting industry are made of ferrous alloys, especially alloy steels. Various morphologies of the intermetallic compounds, formed between the ferrous substrate and molten aluminum, have been reported. It is believed that the different morphologies, porosities, and thicknesses of the intermetallic layers are associated with alloy additions and melt agitation. Intermetallic layers are significantly harder than the steel substrate. For example,

the microhardness of a layer of 18C–8Ni stainless steel (in pure Al) is 1.8 ± 0.2 GPa (Dybkov 1990), and that of a nonporous layer of $FeAl_3$ type (in liquid A380 alloy) is 1096 GPa (1 GPa ≈ 100 kg mm^{-2}) (Sundqvist and Hogmark 1993; Yan and Fan 2000). The high hardness of interfacial layers is beneficial to wear resistance. However, the intermetallic layers on ferrous alloys do not provide good protection for the substrate. Due to the dissolution of iron and loss of interfacial compounds, the erosion rates of ferrous alloys in liquid aluminum alloys are usually high. The attack is further intensified when any relative motion exists between the solid ferrous alloy and molten aluminum. Nickel has been characterized as active with both liquid and solid aluminum (Yan et al. 1999). The high loss rates of nickel-based alloys are primarily due to the high solubility of nickel in liquid aluminum. The solubility of nickel at different temperatures is given in Table 14.1, compared with that of other metallic elements. Moreover, penetration of molten aluminum into the depth of nickel-based alloys can cause alloy loss in blocks (Yan et al. 1999). The high reactivity of nickel with molten aluminum is used in the production of alumina-reinforced aluminum matrix composites. Nickel plating of the alumina phase overcomes the non-wetting. In stainless steel, nickel preferentially dissolves in liquid aluminum from the intermediate zone (Dybkov 1990). Titanium is the least soluble in liquid aluminum among the elements listed in Table 14.1. The low solubility makes the liquid layer surrounding the solid titanium more readily saturated with titanium solute. The saturation inhibits the further dissolution of titanium. However, the high hardness of titanium makes it advantageous in the erosion environment. The growth of the intermediate layer between solid titanium and pure molten aluminum is controlled by the diffusion rate. Additions of alloying elements, such as Si, Mg, Ge, Cu, Li, Sb, Fe, Mn, Ti, Zr, and Ni, into liquid aluminum suppress the growth of the intermediate layer. Among them silicon is the most effective element, while nickel has the least effect (Takemoto and Okamoto 1988). Other metallic alloys investigated in terms of corrosion or dissolution in molten aluminum include Cr, Mo, Nb, and Y. The solubility of Cr, Mo, and Nb in liquid aluminum is relatively high, but Nb has a much lower solubility than Cr and Mo. For the Al–Y system, the solubility of yttrium in molten aluminum is found to be drastically affected by impurities in yttrium matrix and the occurrence of intermetallic phase at the Al–Y interface (Tunca et al. 1990).

A Nb-based alloy (Nb–30Ti–20W) is selected for fabrication of components like barrel and screw in a patented equipment for semisolid Al-alloy processing. This alloy is found to be the best and superior to Ti alloys in resisting erosion by molten aluminum.

The substantially reduced erosion rate is connected with the low solubility of niobium in molten aluminum and the high bulk hardness of the alloy (HV600).

Extremely high corrosion rates of iron-, nickel-, and cobalt-based alloys in molten aluminum are illustrated by the laboratory test results shown in Table 14.2 (Berry 1971). Samples of carbon steel and iron- and nickel-based alloys were consumed in four hours at 760 °C. Cobalt-based alloys, which appeared to be better than iron- and nickel-based alloys, were corroding at rates too high to be considered for containment materials. In addition, titanium, although exhibiting a corrosion rate lower than iron-, nickel-, and cobalt-based alloys, should not be considered for use as a containment material because of its rapid corrosion rate.

The corrosion resistance and mechanical properties of ceramics are affected by the chemical compositions and processing conditions, such as firing temperature and pressing pressure. To avoid infiltration by aluminum, the ceramic should be free of porosity and any constituent component that is prone to dissolve in molten aluminum. It is noteworthy that the reactivity of ceramics with molten metals other than aluminum cannot be used as indicators of their chemical reactivity with molten aluminum due to different phase relationships. For example, Si_3N_4 is found to be prone to degradation in ferrous alloy, but as will be discussed later, it is quite inert in aluminum (Yeomans and Page 1990).

Table 14.1 Solubility of elements in pure liquid aluminum

Temperature (°C)	Fe (%)	Cr (%)	Ni (%)	Ti (%)
700	3.2	0.7	9.0	0.2
750	4.9	1.3	13.2	0.3
800	6.8	2.4	17.3	0.5
850	7.9	4.2	26.2	0.7

Table 14.2 Results of static immersion tests in molten aluminum at 760 °C for four hours (Berry 1971)

Alloy	Maximum depth of corrosion attack, mm (mils)
Titanium	0.22 (8.5)
6B	0.43 (16.8)
188	0.51 (20.2)
150	0.73 (28.9)
556	>0.5 (20.6)[a]
X	>0.6 (23.8)[a]
671	>0.7 (26.3)[a]
Carbon steel	>1.6 (63.1)[a]

[a]Sample was consumed.

So far, ceramics that have been characterized chemically inert in liquid aluminum include graphite, aluminosilicate refractories, AlN, Si_3N_4, Al_2O_3, and sialons. The carbide Al_4C_3 is the only intermediate compound reported in the Al–C system (Qiu and Metselaar 1994) through the following reaction:

$$4Al + 3C = Al_4C_3 \tag{14.9}$$

The result of Al_4C_3 solubility in molten aluminum in the temperature range of 950–1000 °C calculated by Qiu and Metselaar (1994), and extrapolated to the lower temperature range below 700 °C, which normally applies in semisolid processing of aluminum, shows that the solubility of Al_4C_3 is extremely low. As one of the most cost-effective material, graphite has been well known for its compatibility with aluminum melt and the case of fabrication. However, its brittleness makes it impossible for the fabrication of components where stress bearing is a requirement. Aluminosilicate refractories are well known for their applications in melting and holding furnaces.

It is generally believed that molten aluminum alloys attack aluminosilicate refractories by redox reactions in which silica and silicates in the refractory are reduced to form elemental silicon while metallic aluminum forms aluminum oxide. The rate of attack is known to be proportional to the silica content in the refractory and especially that of the matrix phase. The mechanism of attack depends on the transport of elemental species and also on the redox reaction. While aluminum and alloying elements diffuse into the refractory, silicon is released by the redox reaction and counterdiffuses into the molten alloy (Figure 14.9). As a result, a reaction layer containing alumina is present after an incubation period and acts as a barrier against further melt penetration.

As a high temperature structural ceramic and hard refractory material, AIN is a candidate refractory container for molten metals. It possesses an intrinsic inertness and a high hardness. However, during the processing of AlN by Al in vacuum at 1220–1280 °C, it is found to occur with a relatively high activation energy, suggesting a chemical interaction between AlN and aluminum. It reveals that the inertness of AlN in molten aluminum may need some conditions, and a reducing atmosphere is favorable. Al_2O_3 is one of the most widely applied crucible materials. It is not wetted by molten aluminum below 1000 °C and considered to be inert in molten iron and nickel. Si_3N_4 has been considered to be corrosion resistant in aluminum.

Sialons are generally synthesized through sintering at high temperature above 1600 °C in nitrogen atmosphere. The main raw materials are Si_3N_4 and Al_2O_3. Al_2O_3 is an intermediate glass former capable of forming a network with silica and other network formers. This binding phase surrounding Si_3N_4 grains can be either glassy silicate or crystalline phases, or a mixture of both, depending on the composition and the cooling rate. The special network makes the sialon matrix more difficult to disrupt physically and more chemically stable, and this has been largely observed.

In molten aluminum, SiC, B_4C, TiC_x, Cr_2O_3, etc. are active and corrode at relatively high rate. SiC can react with molten aluminum, producing Al_4C_3 and silicon, according to the following reaction (Viala et al. 1993):

$$4Al + 3SiC = Al_4C_3 + 3Si \tag{14.10}$$

Silicon produced through the above reaction dissolves in aluminum, giving rise to an Al–Si alloy.

Viala et al. systematically investigated the chemical interaction of SiC with molten aluminum. It is found that from 657 to 827 °C, α-SiC interacts with aluminum via a dissolution–precipitation process. This mechanism involves the migration of carbon atoms from places where the SiC surface is in direct contact with the aluminum to the growing faces of Al_4C_3 crystals located at or close to the aluminum–SiC interface. The decomposition rate greatly depends on the polarity of the SiC surface exposed to aluminum.

It is found that the interaction between SiC and aluminum alloy intensifies when introducing 3–7% Si into aluminum.

B_4C has a high hardness just below that of diamond, has excellent thermal stability, and is considered to have significant chemical inertness. However, it has been observed that B_4C can react not only with liquid aluminum but even with solid aluminum (Viala et al. 1997). Carbon and boron atoms can diffuse into liquid aluminum from the surface of B_4C. In the temperature range of 660 (melting point of aluminum) to 868 °C, the reaction products of

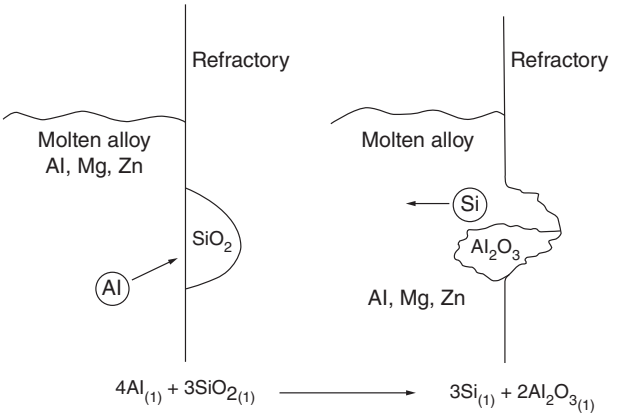


Figure 14.9 Schematic diagram showing the mechanisms of molten aluminum alloy attack on a silica-containing refractory. Alloy is lost by penetration and reaction with the refractory, while silicon is released into the alloy. Source: O'Brien and Akinc (1989). Reproduced with permission from John Wiley & Sons.

Al–B_4C mixture are Al_3BC and AlB_2, which are the same as those observed through reaction of solid B_4C and solid aluminum. Above 868 ± 4 °C AlB_2 is replaced by $Al_3B_{48}C_2$, while Al_3BC remains stable. A continuous layer of Al_3BC, once formed, may constitute an efficient diffusion barrier and provide protection for B_4C.

In Viala et al.'s work (1990), a quasi-protective reaction occurs at 812 ± 15 °C between TiC_x ($x < 0.9$) and liquid aluminum:

$$6Al + TiC_3 = Al_2Ti + Al_4C_3 \qquad (14.11)$$

Through this reaction, TiC_3 is decomposed by aluminum. Cr_2O_3 is also not inert with aluminum; in fact, it is observed to be attacked by aluminum alloys at temperatures even below 750 °C. Further research on the attack mechanisms of TiC_3 and Cr_2O_3, as well as of other metals and ceramics in molten aluminum, has been conducted nowadays.

14.3.2 Molten Zinc

Hot-dip zinc-coated steel production has increased dramatically over the past decade due to its relative economic benefits over other corrosion-resistant materials. As a result of this increased demand, the need for greater manufacturing efficiency in the galvanizing process has also gained prominence. Numerous projects have investigated the molten metal corrosion aspects of materials and designs used for the submerged pot rolls and other hardware of continuous sheet galvanizing operations. The degradation and frequent failure of these structures results in significant production downtime and leads to high maintenance costs due to extensive repair and replacement.

In order to prolong the service life of these rolls, many studies have attempted to obtain a better understanding of the corrosion behavior of the hardware materials in a variety of compositional coating baths. However, the test conditions and focus of each of the projects have been quite broad, encompassing ferrous alloys, cobalt alloys, coatings, and weld materials. Concurrently, extensive research has been carried out to define the equilibrium phase diagrams relevant to galvanizing applications. Advanced zinc phase diagrams involving Al, Fe, Cr, Ni, Co, and others are concurrently being formulated. However, with this array of research focused on materials for continuous galvanizing pot rolls, minimal effort has been directed toward understanding the molten metal reactions of hardware and containment kettles employed in general (batch) galvanizing, which uses zinc possessing very low levels of aluminum and, hence, vastly different corrosion properties.

To enrich our knowledge of these issues, corrosion tests of 316L stainless steel, 410 stainless steel, 1015 carbon steel, Fe_3Al, FeCrSi, and other alloys have been conducted in pure zinc bath and zinc–aluminum baths (Liu et al. 2005; Xu et al. 2007). It was found that, in general, both metallurgical composition and lattice structure played important roles in the molten metal corrosion behavior of these alloys. High contents of nickel combined with the influence of chromium improved the resistance to molten zinc corrosion. An increased bath temperature played an important role in molten metal corrosion by accelerating the dissolution process and changing the nature of intermetallic layers. A small amount of aluminum reduces the corrosion rate by reducing the activity of Zn in the Zn–Al baths and forming an inhibition layer. However, after aluminum content reaches the critical point, the dominant corrosion process changes from Zn–Fe reaction to Al–Fe reaction, and, therefore, the corrosion process is accelerated by increasing aluminum content in the bath.

The results of static tests in molten zinc for selected iron-, nickel-, and cobalt-based alloys are summarized in Table 14.3. Nickel-based alloys suffered the worst attack, followed by austenitic stainless steels, Fe–Ni–Cr alloys, and Fe–Cr alloys. Cobalt-based alloys generally performed better. However, an Fe–Ni–Co–Cr alloy (556 alloy) performed as well as cobalt-based alloys.

14.3.3 Molten Lead

Lead melts at 327 °C. Nickel and nickel-based alloys generally have poor resistance to molten lead corrosion. The solubility of nickel in molten lead is higher than that of iron-casting steels, and stainless steels are commonly used for handling molten lead. For example, cast iron centrifugal pumps are used to pump liquid lead. The compatibility of steels with liquid lead and liquid lead–bismuth is a critical issue for the development of accelerator-driven system. Fazio et al. (2001) carried out a set of tests in stagnant molten lead and lead–bismuth at several temperatures. Two tested martensitic steels (mod. F82H and MANET II)

Table 14.3 Results of static immersion tests in molten zinc at 455 °C for 50 hours (Lai 2007)

Alloy	Depth of corrosion attack, mm (mils)
556	0.04 (1.6)
25	0.06 (2.3)
188	0.06 (2.5)
446SS	0.24 (9.3)
800H	0.28 (11.0)
304SS	0.36 (14.1)
625	>0.61 (24.0)[a]
X	>0.61 (24.0)[a]

[a]Complete alloying.

underwent oxidation phenomena at the higher testing temperature (476 °C), due to oxygen dissolved in the melts. At a lower test temperature (300 °C) and higher exposure time (5000 hours), the oxidation rate of the martensitic steels studied seemed to be lower, and the developed oxide layer protective against liquid metal corrosion. The tested austenitic steel (573 K), in turn, exhibited an acceptable resistance to corrosion/oxidation under the test conditions. Li (2002) examined the thermodynamic basis for controlling oxygen level in lead–bismuth eutectic systems to prevent steel corrosion and coolant contamination. By using mixtures of H_2 and H_2O (steam) to obtain low oxygen partial pressure ($<10^{-24}$ atm or around 10^{-6} wt% in lead–bismuth), and calculating the potential signals of one type of oxygen sensors with a solid electrolyte and molten bismuth reference electrode, they obtained results that provide the guidance to implement the oxygen control technique in a nuclear energy system. This is an interesting application of solid-state electrochemistry to high temperature nuclear technology.

14.3.4 Molten Sodium

One important and perhaps unique feature of corrosion in the alkali metals is the formation of corrosion products based on complex ternary oxides. For example, oxides of the type $(Na_2O)_2$ FeO can form when iron is corroded in sodium under conditions where the standard state binary oxides FeO, Fe_2O_3, and Fe_3O_4 are thermodynamically unstable.

It has also been shown that many transition metals form complex oxides with Na_2O and corrosion products based on the ternary oxide Na_3NbO_4 have been identified on the surfaces of niobium after exposure to the sodium containing oxygen (Thorley and Tyzack 1973). This type of oxide is mechanically unstable in flowing sodium environments, and therefore it is relatively easy to promote fresh surfaces for further attack by oxygen impurities. Complex oxides of the type $NaCrO_2$ also feature in the corrosion of stainless steels in alkali metals. $NaCrO_2$, for example, may exist either as an oxide film on the surface of the steel during the initial stages of corrosion, or it may, under more adverse conditions, penetrate the grain boundaries and become a precursor for grain detachment.

In cold-trapped sodium containing only a few ppm of oxide, refractory metals such as Nb, V, Ta, and Zr can suffer severe oxidation. Their behavior is much the same as in oxidizing gases at high temperature, forming nonadherent oxide films. Oxygen can also diffuse into the metal to produce solid solutions with consequent embrittlement. To prevent this occurrence, the oxygen level in the sodium is brought down below the ppm level with a "hot trap."

Nitrogen is virtually insoluble in pure sodium (10^{-4} ppm at 500 °C and 1 MN m^{-2}).

A large corrosion database for a wide variety of alloys has been published in "Nuclear Systems Materials Handbook" to provide guidance to corrosion allowance for design calculation. For the alloys in liquid sodium at higher temperatures, it is said that corrosion is very severe. Ferritic and austenitic stainless steels suffered rapid corrosion attack at 1000 °C. A nickel-based alloy (Alloy 600) also exhibited a rapid corrosion rate. Borgstedt et al. (1989) investigated the corrosion behavior of several Fe–Ni–Cr and nickel-based alloys in liquid sodium at 1000 °C. Their results are summarized in Table 14.4. Nickel-based alloys suffered more attack than Fe–Ni–Cr alloys.

Table 14.4 Corrosion of several iron–nickel–chromium and nickel-based alloys in liquid sodium at 1000 °C (Borgstedt et al. 1989)

Test	Alloy	Cr	Ni	Fe	Others	Weight change (mg cm^{-2})
Run no. 1 (1000 hours)	Thermon	22	Balance	30	W, Nb	−13.0
	617	21	Balance	1.5	Co, Mo, Al	−13.0
	X	21	Balance	18	Mo	−4.5
	AC-66	27	32	Balance	Nb, Ce	−2.35
	ASL71	20	20	Balance	Co, W	−1.94
	Pyrotherm	20	33	Balance	Nb	−2.0
	800	20	33	Balance	Al, Ti	−0.7
Run no. 2 (1100 hours)	625	22	Balance	2.5	Mo, Nb	−36.01
	625	22	Balance	2.5	Mo, Nb	−35.35
	617	21	Balance	1.5	Co, Mo, Al	−25.11
	X	21	Balance	18	Mo	−16.32
	Pyrotherm	20	33	Balance	Nb	+1.43
	253-MA	21	11	Balance	Si	+9.95

14.3.5 Molten Lithium

Liquid lithium is an attractive candidate blanket material for fusion reactors. Numerous studies have evaluated the compatibility of various containment materials with liquid lithium. Among them, let us refer to Chopra et al. (1985) that summarized the data generated from different circulating loops (forced circulation loop (FCL) and TCL) at different laboratories. The data illustrated in Figure 14.10 are presented in terms of an Arrhenius plot of dissolution rates for ferritic steels (HT-9 and 9Cr–1Mo) and austenitic stainless steels (Type 316, cold-worked Type 316, and Type 304). HT-9 exhibits excellent compatibility with molten lithium.

Nitrogen is quite soluble in molten lithium (2000 ppm at 300 °C and 100 KN m^{-2}) and can accelerate the already corrosive action of lithium, particularly on steels. Zirconium and yttrium have been used to "getter" nitrogen.

14.3.6 Other Molten Metals

Corrosion data for other liquid metals, such as magnesium (melting point of 651 °C), cadmium (melting point of 321 °C), mercury (melting point of −39 °C), tin (melting point of 232 °C), antimony (melting point of 631 °C), bismuth (melting point of 271 °C), and silicon (melting point of 1414 °C) are relatively limited, but phase diagrams and other data help in determining which metals may react readily with the liquid metal. More than 50% Ni, for example, can be in solution with magnesium in liquid at 800 °C. Nickel and nickel-based alloys are therefore not suitable for use as a containment material for molten magnesium. Cobalt also forms a low-melting-point eutectic, but with a much smaller liquid-phase field. The solubility of iron in liquid magnesium is very low. It is thus reasonable to assume that iron-based alloys with low

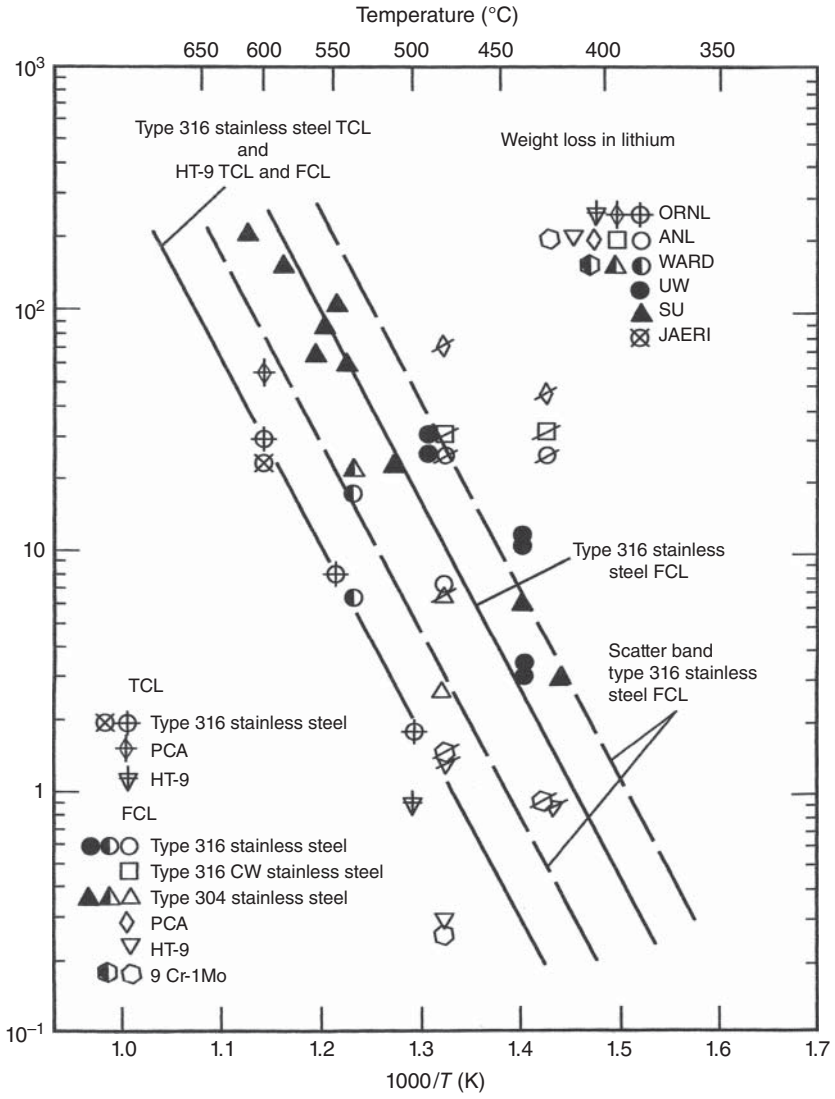


Figure 14.10 Corrosion rates of Types 304 and 316, primary candidate alloy (PCA), and HT-9 and 9Cr–1Mo steels in flowing lithium. CW, cold worked; FCL, forced-convection loop; TCL, thermal-convection loop. Source: Chopra et al. (1985). Reproduced with permission from Taylor & Francis.

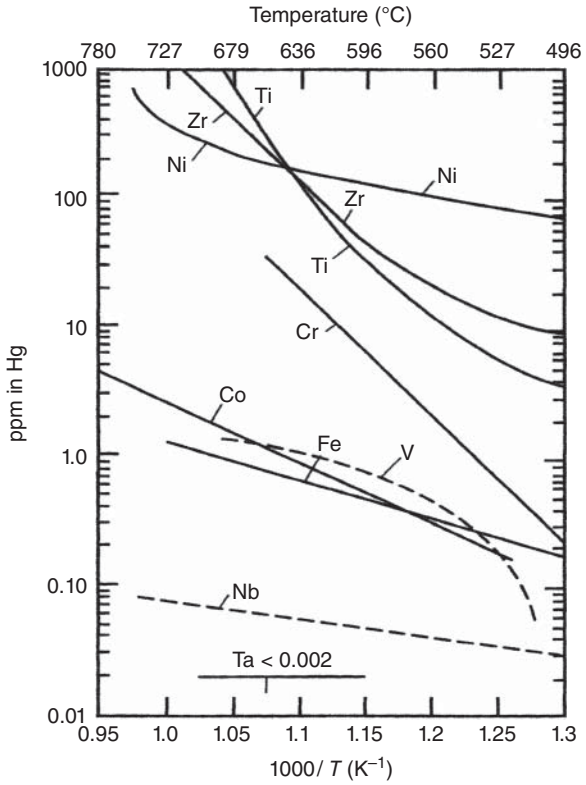


Figure 14.11 Solubilities of some metals in liquid mercury (Weeks 1967). Note: Columbium is the former (pre-1968) name of niobium.

nickel are more suitable than cobalt- and nickel-based alloys to handle molten magnesium.

The solubility of iron in molten cadmium is low. It has been indicated that cast iron has frequently been used for handling molten cadmium. Nickel and nickel-based alloys are not suitable for handling molten tin because of relatively high solubilities of nickel in molten tin. Cast iron is often used in the laboratory for handling molten tin. Cobalt, nickel, and iron have high solubilities in molten antimony. These metals, as well as their alloys, are expected to have poor corrosion resistance in molten antimony.

The solubilities of a number of metals in liquid mercury are illustrated in Figure 14.11 (Weeks 1967). Both iron and cobalt have low solubilities in liquid mercury.

For edged-defined film-fed growth (EFG) silicon ribbon growth (Swartz et al. 1975), graphite is generally used as a die material with either a graphite or quartz crucible to contain the melt. Since various reactions are possible between oxygen, silicon, and carbon, an effort was made to measure the dissolution rate of silica in the presence of carbonaceous atmosphere. After exposure to liquid silicon, tested quartz samples were examined by X-ray diffraction. In addition to α-cristobalite, β-SiC was detected. The following reactions are possible between quartz and carbon depending upon the melt temperature and the partial pressure of the gas species:

$$2C + SiO_2 \rightarrow SiC + CO_2 \tag{14.12}$$

$$3C + 3SiO_2 \rightarrow SiC + 2CO_2 + 2SiO \tag{14.13}$$

$$4C + 2SiO_2 \rightarrow SiC + 3CO + SiO \tag{14.14}$$

$$3C + SiO_2 \rightarrow SiC + 2CO \tag{14.15}$$

$$C + SiO_2 \rightarrow SiO + CO \tag{14.16}$$

$$C + 2SiO_2 \rightarrow 2SiO + CO_2 \tag{14.17}$$

Among these reactions, (14.15) and (14.16) are thermodynamically favorable. Schmidt et al. (1979) have made a complete thermodynamic analysis of these reactions and established the regions of stability of these reactions as a function of pressure and temperature. On the basis of the experimental evidence and thermodynamic analysis, we conclude that the presence of carbon in the melt enhances the dissolution of silica.

14.4 Conclusions

The corrosion of metals, alloys, and ceramics in liquid metal is for the most part due to the dissolving of the various constituents of these materials by the liquid metal. The manner in which this dissolution proceeds gives rise to many types of attack, ranging from a simple dissolution-type attack to a deep intergranular attack with the preferential leaching of one constituent of a material. Examples of many types of corrosion experienced with solid material–liquid metal systems are illustrated. The role of impurities on the corrosion is discussed. Particular attention is given to metal/alloy/liquid metal systems. In a static one-metal system, the solution step stops when the solubility limit is reached; however, in more complex systems, the corrosion of metals can be continued because of removal of the dissolved materials from the liquid metal by a temperature gradient and/or by dissimilar-metal transfer. Thus, the transfer of metal from the hot region of a plumbing system and its subsequent deposition in the cold zone and the transfer of material from one part of the system and its alloying with a metal of different composition in another part of the system will greatly increase the corrosion as compared with the results obtained in static systems. Examples of simple dissolution, alloying between liquid metal and solid metal, intergranular penetration, impurity reactions, temperature-gradient mass transfer, and dissimilar-metal transfer or concentration-gradient mass transfer are reviewed, and factors governing the occurrence of these phenomena are outlined. In addition, interactions of engineering materials with some industrial liquid metals are examined. Liquid aluminum, zinc, lead,

sodium, lithium, and other molten metals are reviewed in terms of their relevance to the corrosion of containment materials.

References

Berry, W.E. (1971). *Corrosion in Nuclear Applications*. New York: Wiley.

Borgstedt, H.U. (ed.) (1982). *Materials Behaviour and Physical Chemistry in Liquid Metal Systems*. New York: Plenum Press.

Borgstedt, H.U., Frees, G., and Jesper, H. (1989). *Werkst. Korros.* 40: 525.

Casteels, F. (1984). Liquid metal engineering and technology. In: *Proceedings of the 3rd International Conference*, (9–13 April 1984), vol. 3, 73. Oxford: British Nuclear Energy Society.

Chopra, O.K., Smith, D.L., Tortorelli, P.F. et al. (1985). *Fusion Technol.* 8: 1956.

Covington, A.K. and Woolf, A.A. (1961). *Reactor Technol.* 3.

Dybkov, V.I. (1990). *J. Mater. Sci.* 25: 3615.

Epstein, L.F. (1957). Liquid Metal Technology, 20, 67.

Fazio, C., Bernamati, G., Martini, C., and Palombarini, G. (2001). *J. Nucl. Mater.* 296: 243.

Frost, B.R.T. (1958). *Proceedings of the 2nd Conference on the Peaceful Uses of Atomic Energy*, paper P270 (1–13 September 1958), vol. 31, 7. Geneva: United Nations.

Kerridge, D.H. (1961). *Reactor Technol.* 1: 15.

Lai, G.Y. (2007). *High-Temperature Corrosion and Materials Applications*. Materials Park, OH: ASM International.

Li, N. (2002). *J. Nucl. Mater.* 300: 73.

Liu, X., Barbero, E., Xu, J. et al. (2005). *Metall. Mater. Trans. A* 36: 2099.

Marchbanks, M.F., Moen, R.A., and Irvin, J.E. (1976). *Nuclear Systems Materials Handbook*. Richland, WA: Hanford Engineering Laboratory.

Meyer-Rau, S. and Telle, R. (2005). *J. Eur. Ceram. Soc.* 25 (7): 1049.

O'Brien, M.H. and Akinc, M. (1989). *J. Am. Ceram. Soc.* 72: 896.

Qiu, C. and Metselaar, R. (1994). *J. Alloys Compd.* 216: 55.

Rostoker, W., McCaughey, J.M., and Markus, H. (1960). *Embrittlement by Liquid Metals*. New York: Reinhold.

Schmidt, F., Kattak, C., Digges, T.G., and Kaufman, L. (1979). *J. Electrochem. Soc.* 126: 935.

Seong, B., Hwang, S., Kim, M.C., and Kim, K.Y. (2001). *Surf. Coat. Technol.* 138: 101.

Stratchan, J.F. and Harris, N.L. (1956–1957). *J. Inst. Met.* 85: 17.

Sundqvist, M. and Hogmark, S. (1993). *Tribol. Int.* 26: 129.

Swartz, J.C., Surek, T., and Chalmers, B. (1975). *J. Electron. Mater.* 4: 255.

Takemoto, T. and Okamoto, I. (1988). *J. Mater. Sci.* 23: 1301.

Tipping, P.G. (ed.) (2010). *Understanding and Mitigating Ageing in Nuclear Power Plants*. Oxford: Woodhead Publishing.

Thorley, A.W. and Tyzack, C. (1967). *Proceedings of the Symposium on Alkali Metal Coolants, Vienna 1966*. Vienna, Austria: International Atomic Energy Agency.

Thorley, A.W. and Tyzack, C. (1973). 5th European Congress of Corrosion, Paris 1973, paper 56.

Tunca, N., Delamore, C.W., and Smith, R.W. (1990). *Met. Trans. A* A21: 2919.

Viala, J.C., Vincent, C., Vincent, H., and Bonix, J. (1990). *Mater. Res. Bull.* 25: 457.

Viala, J.C., Bosselet, F., Laurent, V., and Lepeticorps, Y. (1993). *J. Mater. Sci.* 28: 5301.

Viala, J.C., Bonix, J., Gonzalez, G., and Esnouf, C. (1997). *J. Mater. Sci.* 32: 4559.

Ward, A.G. and Taylor, J.W. (1957–1958). *J. Inst. Met.* 86: 36.

Weeks, J.R. (1967). *Corrosion* 98.

Xu, J., Bright, M.A., Liu, X., and Barbero, E. (2007). *Metall. Mater. Trans. A* 38: 2727.

Yan, M. and Fan, Z. (2000). *J. Mater. Sci.* 35: 1661.

Yan, M., Fan, Z., and Bevis, M.J. (1999). *Scr. Metall.* 40: 1255.

Yeomans, J.A. and Page, T.F. (1990). *J. Mater. Sci.* 25: 2312.

Yu, M., Shivpuri, R., and Rapp, R. (1995). *J. Mater. Eng. Perform.* 4 (2): 175.

Further Reading

Draley, J.E. and Weeks, J.R. (eds.) (1970). *Corrosion by Liquid Metals*. New York: Plenum Press.

Huang, Q., Zhang, M., Zhu, Z. et al. (2007). *Fusion Eng. Des.* 82: 2655.

Lou, D.C., Akselsen, O.M., Onsøien, M.I. et al. (2006). *Surf. Coat. Technol.* 200: 5282.

Park, J.J., Butt, D.P., and Beard, C.A. (2000). *Nucl. Eng. Des.* 196: 315.

Sapundjeev, D., van Dyck, S., and Bogaerts, W. (2006). *Corros. Sci.* 48: 577.

Sequeira, C.A.C. and Santos, D.M.F. (2011). *Nucl. Eng. Des.* 241: 4903.

Tsipas, D.N., Triantafyllidis, G.K., Kipkemoi Kiplagat, J., and Psillaki, P. (1998). *Mater. Lett.* 37: 128.

Vourlias, G., Pistofidis, N., Psillaki, P. et al. (2009). *J. Alloys Compd.* 483: 382.

Yang, N.Y. (1995). *Metall. Mater. Trans. A* 26: 1699.

Zhang, K. (2003). *Wear* 255: 545.

Zhang, J. and Li, N. (2007). *Corros. Sci.* 49: 4154.

Zhang, J., Hosemann, P., and Maloy, S. (2010). *J. Nucl. Mater.* 404: 82.

Chapter 15

Hot Corrosion

15.1 Introduction

Alloys for high temperature application usually contain appreciable quantities of nickel: in particular, alloys based on the 80–20 nickel–chromium system have proved extremely successful because they can combine strength with good oxidation resistance at high temperatures. However, in gas turbine applications, where the products of combustion of the fuel used condition the atmospheres, oxidation resistance alone is insufficient, and the resistance of the alloys to carburization, sulfur attack, and corrosion by ash must also be considered.

Three main types of gas turbine may be listed: (i) aeroengine, (ii) industrial, and (iii) marine. Aeroengines burn clean fuel but ingest impurities in the air intake. This is aggravated in the marine gas turbines since the air intake includes sea salt. Industrial engines burn inferior fuel containing vanadium and sodium, but the air intake can be filtered. Turbine components are made of Ni- or Co-based alloys. The blades and vanes are subject to cyclic temperature corrosion in alkali sulfate oxide ±chloride ±vanadic environment. Advanced turbines operate at high inlet temperatures (1350 °C) and the industrial turbines at 1150 °C. The blades are cooled to 850–900 °C. Catastrophic corrosion occurs at lower temperatures: 610–750 °C for Ni-based alloys and 750–850 °C for Co-based alloys. Coatings have been tested extensively in the field of gas turbines, and these include multicomponent alloy compositions and alloy-ceramic formulas as well as thermal barrier coatings (TBCs). Superalloys form 50 wt% of gas turbine engines, the rest being about equal parts of Ti alloys, steels, and composites. Development trends in the superalloy systems tend toward directional solidification (DS), powder metallurgy (PM), and mechanical alloy processing (MAP).

In gas turbines used for aircraft applications, where highly refined fuels are used, corrosion, although still a problem, is usually secondary to stress considerations, but where turbines are used for marine and chemical plant or for production of cheap electrical power, it is often necessary for economic reasons to run on lower-grade fuels, and these can introduce severe hot corrosion problems. Table 15.1 provides the relevance and importance of hot corrosion in various energy fields and the associated contaminants, which are responsible for the degradation of components during service.

Thus, on studying corrosion under turbine conditions, the effects may be broadly divided into two categories, the first being the effect of the gaseous products of combustion and the second the effects of deposits. Sulfur present in the fuel and salt in the marine environment would lead to the formation of sodium sulfate. So it is sodium sulfate with or without sodium chloride (or nitrate) that has been most extensively investigated. However, internal sulfidation called *green rot* that occurs in a carburizing environment was reported by Hancock (1968) and Strochi et al. (1969), while *black plague* corrosion found on high-strength nickel-based turbine alloys was produced when a very dilute salt solution was injected into downstream air in minute quantities. Fuel quality does not cause "black plague," which is primarily metallurgical in origin, and is regarded as an oxidation phenomenon as Belcher et al. (1967) report.

The object of the present chapter is to review some fundamental aspects of hot corrosion and the behavior of gas turbine materials in the presence of sodium sulfate (with or without sodium chloride), oxygen, and sulfur-containing gases, which are the contaminants most likely to be commonly encountered in gas turbine environments.

15.2 Engine Description and Materials

The principle of the gas turbine is as follows. Air is drawn into the engine and compressed. Fuel is mixed with the compressed air and burned in a combustion chamber with the object of heating the gas. The hot compressed gas is then expanded through a turbine that extracts the energy from it; part of this energy is used to drive the compressor

High Temperature Corrosion: Fundamentals and Engineering, First Edition. César A. C. Sequeira.
© 2019 John Wiley & Sons, Inc. Published 2019 by John Wiley & Sons, Inc.

Table 15.1 Relevance and importance of hot corrosion in energy systems

Energy systems	Mixed oxidant reactions	Hot corrosion
Batteries and fuel cells	SO_2, SO_3, O_2, H_2, H_2S, and H_2O attack of alloys	Fused halides and carbonate cells
Coal conversion and combustion systems	CO, CO_2, H_2, H_2S, and H_2O attack of alloys	Slag films, residue films, fly ash films in MHD[a], salt film-assisted coal combustion
Solar energy and energy storage	—	Salt spillage or leakage from thermal storage tanks
Nuclear energy	H–O–C in HTGR Steam reactions with zircaloy	Fission product, salt condensation on cladding
Gas turbines	SO_2, SO_3, and O_2 attack of alloys	Na_2SO_4, NaV_xO_y, and NaCl attack of alloys
Gas and oil recovery and magma energy	H_2, H_2S, and H_2O attack of alloys	—

[a]Magnetohydrodynamic.

and the remainder is available for useful work. The maximum temperature in the cycle is the temperature of the gas entering the turbine, and this temperature is determined by the capability of the turbine to accept it. The hottest part of the turbine is the first stage, which consists of a ring of stationary airfoils, called the inlet nozzle guide vanes, and a ring of rotating blades called the first-stage rotor blades or buckets.

The turbine inlet temperature in aircraft gas turbines rose progressively to a maximum of the order of 900 °C. Further increases in turbine inlet temperature were achieved as a result of the introduction of cooling of the vanes and blades using air drawn from the high-pressure compressor.

The earliest alloys used for gas turbines, developed in the 1940s, were based on Nichrome (Ni–20%Cr) heater alloys and the Stellite (Co–10%Ni–35%Cr) supercharger alloys. The strength of the nickel-based alloys was increased as a result of the introduction of the $Ni_3(Al,Ti)$ ordered phase, gamma prime. Increasing the volume fraction of gamma prime in the alloy required that the chromium content be reduced. No phase equivalent to gamma prime exists for cobalt-based alloys, and the modern cobalt-based superalloy has changed relatively little from its origins.

These early alloys owed their oxidation resistance to the formation of a protective layer of chromia, Cr_2O_3, on the metal surface. However, a number of the nickel-based alloys with lower chromium contents also exhibited excellent oxidation resistance due to the formation of protective alumina scales. The components of the first stage of modern gas turbines are now generally coated with an alumina-rich layer designed to develop an Al_2O_3 scale.

A major corrosion problem with the lower chromium nickel-based gas turbine alloys was encountered in the early 1960s in aircraft that were being used in missions at low altitudes close to the sea. Under these conditions, a rapid corrosion of the blades and vanes was sometimes encountered, leading to severe destruction of the involved materials.

The increasing cost of fuel has resulted in a renewed interest in improving the efficiency of gas turbine systems. In most cases, this involves the modification of the properties of the existing alloys and the production of new materials. A partial listing of companies producing and supplying high temperature alloys is given below. The alloys referred to in this chapter that are produced by a specific company are given in parentheses. Each company produces a more extensive range of high temperature alloys, and a complete listing can be found at the web addresses provided:

Avesta Sheffield (253MA): www.avesta-sheffield.com

Carpenter Technology (309, 310, 600, 625, 718, Waspaloy): www.cartech.com

Haynes International (HR-120, HR-160, 214, 230, 556, 625, 718, Waspaloy, X): www.haynesintl.com

Inco Alloys International, Inc. (330, 600, 601, 617, 625, 718, 738, MA754, 800, 800H, 800 T): www.incoalloys.com

Krupp VDM Technologies Corp. (330, 600, 601, 602CA, 617, 625, 718, 800H, 800HT, 800 L, X): www.kruppvdm.de

Rolled Alloys (253MA, 309, 310, 330, 600, 601): www.rolledalloy.com

Sandvik Steel (309, 310, 330): www.sandvik.com

15.3 Early Studies

15.3.1 General

It has been known for many years that at high temperatures in the presence of salt, heat-resisting alloys undergo rapid

corrosion. This problem was greatly intensified in the 1950s by development in jet engines and the application of nuclear energy. The extremely high temperatures (800 °C and above) encountered in jet engines and gas turbines required the development of new alloys with sufficient resistance to corrosion by the hot combustion gases as well as adequate mechanical properties at the high temperatures encountered. Alloys based on nickel and chromium are well known for their good resistance to oxidation at temperatures in the range of 800–1200 °C. With the demand for improvement in creep properties at elevated temperatures (≈900 °C), alloy compositions have been modified in order to attain these properties. This has been achieved by reducing the chromium content of the alloys, increasing the amounts of some of the elements already present, and introducing new elements. The alloy series – Inconel, Nimonic, Hastelloy, MELCO, and DISCO – are a result of this. Betteridge and Heslop (1974) and Sims and Hagel (1972) have discussed the Nimonic alloys in detail. Rather unexpectedly, these changes in composition have resulted in a susceptibility to a form of high temperature oxidation in which sulfur acts as a promoter and a propagator. This new phenomenon, most severe than the normal sulfur attack and generally referred to as *hot corrosion* (1967), has been encountered in gas turbines operating in marine environments. It is acknowledged that this form of attack is associated with the unfavorable operating environment.

Much research has been carried out on the chemical nature of the deposits and the mechanism of attack that results, but it is apparent from the diversity of opinions held by various workers in the field that the phenomenon was not adequately understood in 1970s (Jaffee and Stringer 1971; Stringer 1977; Seybolt et al. 1967).

However, there was general agreement that the corrosion proceeds in three steps:

1. Deposition of a molten sulfur-bearing slag on the surface of the superalloy engine components.
2. Breakdown of the protective oxide film.
3. Reaction between the sulfur from the deposit and the base alloy.

The mechanisms that have been postulated mainly differ in the explanation for the processes occurring in stages 2 and 3.

The slag that promotes sulfidation corrosion in a marine gas turbine is formed by the reaction of sulfur in the fuel and sodium from the sea salt ingested through the intake air (DeCrescente and Bornstein 1968). Under the oxidizing or de-electronizing operating conditions, sulfur in the presence of a sodium salt such as sodium chloride (NaCl) is then capable of forming Na_2SO_4 via Na_2O and SO_2/SO_3. The ability of NaCl to form sodium monoxide (Na_2O) is well demonstrated by Quets and Dresher (1969). As it is known that sulfur dioxide is more effective in converting sodium chloride to sodium sulfate than sulfur trioxide, several workers (Birks et al. 2006) suggested that the transformation of NaCl to Na_2SO_4 involves the Hargreaves type of reaction, which is the basis of an old process for the manufacture of sodium sulfate (salt cake). The equations for the formation of Na_2SO_4 might then be

$$4NaCl + 2H_2O = 2Na_2O + 4HCl \quad (15.1)$$

$$2Na_2O + 2SO_3 = 2Na_2SO_4 \quad (15.2)$$

$$O_2 + 2SO_2 = 2SO_3 \quad (15.3)$$

or combining these equations

$$4NaCl + 2SO_2 + O_2 + 2H_2O = 2Na_2SO_4 + 4HCl \quad (15.4)$$

As it has been shown by DeCrescente and Bornstein (1968), this reaction, besides being thermodynamically favorable in the temperature range of interest, is quite rapid. Sodium sulfate produced by this means, together with that already present in the sea spray (Schirmer and Quigg 1967), can condense as a slag on the hot engine parts. This concept is supported by the detection of sodium sulfate on parts corroded in service.

NaCl itself is almost never found in the deposits, due to its high dew point, but this does not rule out the possibility that impacting NaCl particles onto the alloy surface may play a significant part in the corrosion process. Therefore, as discussed by Condé (1972), NaCl may be one of the principal agents responsible for Na_2SO_4 hot corrosion.

15.3.2 Alloy–Na_2SO_4 Reaction

Reaction of a metal surface with its environment can occur only after the protective film is penetrated. In the case of the nickel-based superalloys, this film is normally a mixture of Al–Ni–O and Cr–Ni–O phases composed mainly of chromium and/or aluminum oxides (Cr_2O_3 and Al_2O_3), and, in addition, a pure NiO type of oxide or $NiCr_2O_4$ spinel oxide may form (Bergman 1967). Whether Al_2O_3, Cr_2O_3, or $NiCr_2O_4$ is responsible for protection is the subject of much controversy (see above), but it is widely believed that the major contribution comes from Cr_2O_3 (Viswanathan 1968).

In the presence of a sodium sulfate slag, the oxide film is penetrated, bringing into direct contact the metal surface and the molten salt.

The mechanism of film penetration is uncertain, but several possibilities exist (Farrel et al. 1970). One explanation that has enjoyed wide acceptance suggests that chromium oxide (Cr_2O_3) is dissolved by reactions of the type

$$Na_2SO_4 + Cr_2O_3 = Na_2Cr_2O_4 + SO_3 \quad (15.5)$$

The events that occur after film destruction are not well understood. Earlier studies on this aspect have been mainly empirical. But, in the 1970s, Condé (1972) suggested that once the protective oxide film is penetrated, sodium sulfate may be reduced, or electronated, according to the following equations:

$$Na_2SO_4 + 3R = Na_2O + 3RO + S \qquad (15.6)$$

and

$$M + S = MS \qquad (15.7)$$

and

$$Na_2SO_4 + 3MS = 4S + 3MO + Na_2O \qquad (15.8)$$

where R is an electronizing agent and M, in the case of complex superalloys, is composed of several elements including chromium. NaCl acts as the reducing agent.

Early in the 1950s, it was also proposed that Na_2SO_4 had to be chloride-contaminated to promote rapid sulfidation attack. Waddams et al. (1969) proposed that Na_2SO_4 reacts with the base metal at cracks and pores where micro-electronizing conditions may exist. Many other workers (Birks et al. 2006) report that neither the chloride ion nor externally introduced reducing conditions are prerequisites for hot corrosion. Bergman (1967) and Seybolt (1968) suggest that the depletion of chromium in surface zones through the formation of oxides and sulfides reduces the corrosion resistance of Cr-depleted zones (nickel-rich zones), thereby promoting gross oxidation and/or sulfidation. Quets and Dresher (1969) suggest that in order for hot corrosion to occur, there must be a simultaneous reaction between the nickel of the alloy and the oxide of one or more of the alloy ingredients, with sodium sulfate. The equations for the corrosion of a nickel–chromium alloy might then be

$$Na_2SO_4 + 9/2\,Ni = Na_2O + 3NiO + 1/2\,Ni_3S_2 \qquad (15.9)$$

$$2Na_2SO_4 + 3Cr \rightarrow CrS + Na_2O + Na_2Cr_2O_4 + SO_3 \qquad (15.10)$$

Bornstein and DeCrescente (1969, 1971) and Bornstein et al. (1972) show that the accelerated rates of oxidation associated with sulfidation attack are not related to preferential oxidation by sulfur in the alloy-depleted zone and relate the rapid corrosion to the presence of oxide ions in the Na_2SO_4 melt.

The most reasonable models available in the seventies for the Na_2SO_4 hot corrosion of nickel-based alloys were essentially those due to Goebel et al. (1973). In order to make progress toward discovery of the mechanism of hot corrosion, they constructed thermodynamic diagrams describing the stability and composition of pure Na_2SO_4 as well as the phases that may be formed during the exposure of nickel or aluminum to the sulfate environment. It was then necessary to consider reactions between oxides that are formed during the exposure of nickel or aluminum to the sulfate environment. It was then necessary to consider reactions between oxides that are formed on the surfaces of alloys and Na_2SO_4 and in addition reactions between the protective oxides and other components that are introduced into the modified Na_2SO_4 as a result of the oxide contaminant. Such studies indicated two types of hot corrosion.

The less severe type, referred to as Na_2SO_4-induced accelerated oxidation, runs along the following lines:

(i) An oxide layer is formed on the alloy surface, the oxygen required for its formation coming from dissociation of Na_2SO_4 (see below).

(ii) As a consequence of this, the sulfur activity at the oxide scale/Na_2SO_4 interface increases to a level at which metal sulfides can be formed in the alloy beneath the oxide scale, providing that sulfur can migrate through the oxide.

(iii) Sulfide formation increases the oxide ion activity of the Na_2SO_4, eventually allowing the dissolution of the oxide as higher ions, for example, AlO_2^-, in the case of aluminum.

(iv) Accelerated oxidation of the alloy occurs until the oxidation activity of the melt is no longer capable of fluxing the oxide scale.

This model assumes that when Na_2SO_4 comes into contact with nickel, the equilibrium oxygen pressure in Na_2SO_4 is sufficient to oxidize Ni to NiO. The oxygen consumed because of NiO formation will displace the following dissociation equilibrium reaction existing in sodium sulfate to the right:

$$SO_4^{2-} = O^{2-} + 1/2\,S_2 + 3/2\,O_2 \qquad (15.11)$$

Thus, the Na_2O and S activities rise at the NiO–Na_2SO_4 interface. This sulfur then migrates through the NiO layer to the Ni–NiO interface where, due to the lower oxygen activities, nickel sulfide phases can be formed. Removal of sulfur from the sulfate increases the Na_2O activity to Na_2SO_4 in the vicinity of the alloy surface. In this Na_2O-rich layer, formation of nickelate (NiO_2^{2-}) ions following the reaction

$$NiO + O^{2-} = NiO_2^{2-} \qquad (15.12)$$

is likely to take place. Since the oxide ion activity of the unmodified Na_2SO_4 is not sufficient for nickelate formation, NiO_2^{2-} decomposes as soon as it moves out into the Na_2SO_4. Consequently, a porous non-protective nickel oxide scale is formed, and accelerated oxidation proceeds.

For the other type of hot corrosion, referred to as Na_2SO_4-induced catastrophic oxidation, the following features are believed to be applicable:

(i) Oxide phases are developed on the alloy surface.

(ii) Specific oxides (for example, MoO_3, WO_3, or V_2O_5) of the alloy scale form higher oxides by taking oxide ions from the Na_2SO_4, reducing its oxide ion content to a low enough level so that the protective oxide layer is thermodynamically unstable in the melt.

(iii) Consequently, decomposition by ionic dissolution into the melt occurs, thereby allowing the salt to come into contact and react with the metal alloy substrate.

(iv) Rapid oxidation ensues, being self-sustained because the metal oxides responsible for this type of attack are continually formed in the Na_2SO_4 adjacent to the alloy surface.

Goebel et al. (1973) have schematically illustrated this model for a Ni–31Al–Mo alloy, as reproduced in Figure 15.1 where the abovementioned basic features are well documented.

In summary, the essential point to be emphasized is the crucial role of Na_2O on the Na_2SO_4 hot corrosion of nickel-based alloys: if the oxide ion activity of Na_2SO_4 increases to the point where oxide scales can partially dissolve in the melt, induced accelerated oxidation is to be expected; if the Na_2O activity of the melt is so small that they are efficient dissociative fluxes for oxide scales, catastrophic oxidation occurs. In addition, the formation of sulfides beneath the oxide scales in some alloys can cause the specimens to swell, which results in increased oxidation (Birks et al. 2006).

15.3.3 Effect of Sodium Chloride

The previous discussion has been confined to molten sodium sulfate as a cause for metal destruction in gas turbines. Sodium chloride was shown to be a source of sodium for reaction with fuel sulfur to form Na_2SO_4. It is also possible that NaCl by itself could be responsible for

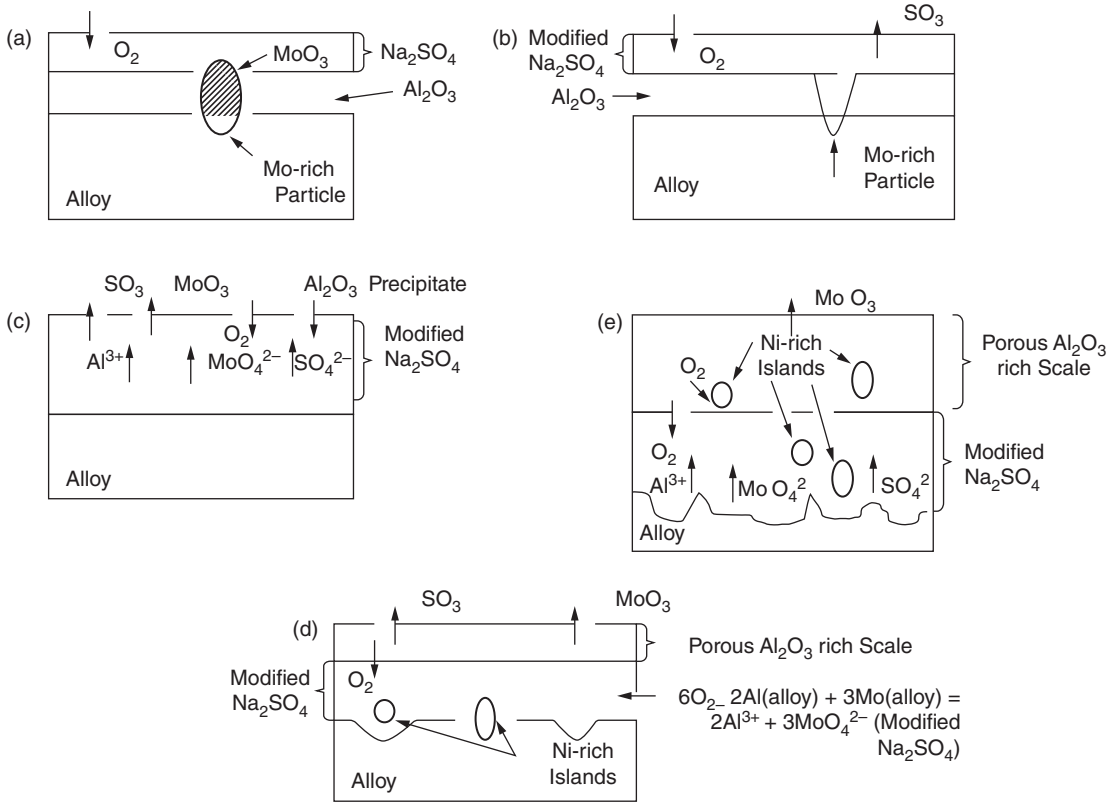


Figure 15.1 Model for the Na_2SO_4-induced catastrophic oxidation of a Ni–31Al–Mo alloy. (a) Oxygen moves from the gas through Na_2SO_4 to the alloy surface where metal oxides are developed. (b) MoO_3 reacts with Na_2SO_4 that decreases the oxide ion activity of Na_2SO_4. (c) The modified Na_2SO_4 layer reacts with the protective Al_2O_3 scale that results in its destruction. However, vaporization of MoO_3 causes the Al_2O_3 to precipitate as a porous network at the Na_2SO_4/gas interface. (d) Rapid oxidation ensues and aluminum is preferentially removed from the alloy, and the alloy–scale interface becomes irregular. (e) The nickel-rich islands developed because of preferential oxidation of aluminum are converted to NiO. The rapid oxidation is self-sustaining because MoO_3 is continually added to Na_2SO_4 by oxidation of molybdenum in the alloy (Goebel et al. 1973).

corrosion by flue gas deposits. It is widely reported, as a result of laboratory studies, that mixed sulfate–chloride slags produce a higher corrosion rate than sulfate alone (El-Dashan et al. 1972).

Although a condensate of Na_2SO_4 containing NaCl is unlikely to be formed above the dew point (the temperature at which salt species will condense on an inert solid surface) for NaCl (~730 °C) under normal situations, its formation in the case of nonequilibrium conditions may occur (Farrel et al. 1970).

Corrosion by additive NaCl may be due in part to the formation of a low-melting-point mixture between these two sodium salts and also to the action of the chloride in causing a breakdown of the film. The Na_2SO_4–NaCl phase diagram illustrating the influence of NaCl on the melting characteristics of the mixture was constructed by Danek (1965). He concludes that since a molten slag is required for sulfidation, the melting point of the salt mixture and hence the NaCl content exerts a serious influence on turbine operating temperature and thus efficiency and fuel economy. Later, Halstead (1970) reviewed the general behavior of oxides in the presence of sodium chloride. This review emphasizes that in gas turbines the nickel oxide/NaCl reaction may be better described by a general equation:

$$NiO + 2NaCl + SO_3 = NiCl_2 + Na_2SO_4 \qquad (15.13)$$

Since the $NiCl_2$ equilibrium pressure for the preceding reaction is significantly lower than the vapor pressure of $NiCl_2$ at temperatures of about 900 °C, such a reaction could lead to a loss of nickel by vaporization. This loss would lead to an appreciably less protective oxide film than one produced directly by de-electronation. Destruction of the protective chromium oxide film can also occur by the following reaction:

$$24NaCl + 10Cr_2O_3 + 9O_2 = 12Na_2CrO_4 + 8CrCl_3 \qquad (15.14)$$

The chloride may also have a catalytic effect on the following reaction:

$$4Ni + SO_4^{2-} = 4NiO + S^{2-} \qquad (15.15)$$

to cause the internal sulfur penetration observed. In an attempt to develop a picture of the role of chloride in the corrosion caused by flue gases and their deposits, Cutler et al. (1971) carried out some studies and concluded that the chloride may be especially harmful in those cases in which the deposit environment fluctuates between electronizing and de-electronizing conditions because in these situations the alloy is never capable of building up a protective layer. Other workers have considered that NaCl may possibly accelerate the Na_2SO_4-induced hot corrosion, but its influence has not been examined. Sequeira and Hocking (1978a,b, 1981) studied the corrosion behavior of nickel and Nimonic 105 in molten Na_2SO_4, NaCl, and mixtures of these two salts, at 900 °C, in laboratory air and under $O_2 + SO_2/SO_3$ atmospheres. The following conclusions were drawn from their electrochemical results, which were further supported by topochemical examinations of the corroded samples (Figure 15.2):

1. Three different regions characterize the electrokinetic behavior of nickel electrodes in molten sodium sulfate at 900 °C in air. The first region corresponds to the onset of passivity and consists of simultaneous nickel dissolution and passivation, the second is related to the dissolution of passive nickel, and the third corresponds to the local oxidation of passive nickel and sulfate discharge. The passive film on Ni is mainly NiO. It should be noted that these three regions are only observed if the anodic polarization of Ni takes place immediately after the maximum negative potential is reached, i.e. at about five minutes after insertion of the Ni electrode into the melt. If the anodic polarization of Ni is recorded after 20-60 minutes of its immersion into the melt, then auto-passivation occurs, and the polarization curves are characteristic of a passive metal electrode (i.e. $E_{i=0} > E_p$ and only passive–transpassive behavior is observed).

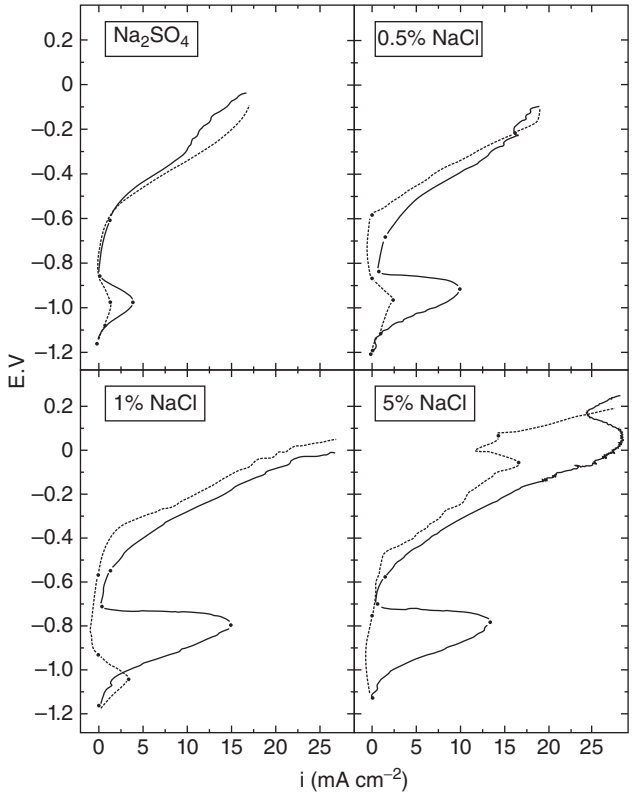


Figure 15.2 Potentiodynamic polarization curves for nickel in Na_2SO_4, Na_2SO_4–0.5% NaCl, Na_2SO_4–1% NaCl, and Na_2SO_4–5% NaCl at 900 °C in air.

2. The *E*/*I* curves for nickel in Na_2SO_4–NaCl melts, in air, in the range of 0–80% NaCl, which are similar to the anodic polarization curve for Ni in pure Na_2SO_4, show that halide additions (especially those up to 25%) strongly affect the anodic behavior of Ni in the active region and have practically no effect on the passive region. The higher dissolution rates are represented by the equation

$$Ni_3S_2 + 4NaCl + 1/2\,O_2 = 2NiCl_2 + 2Na_2S + NiO \quad (15.16)$$

which also suggested being a critical factor in the Ni passivation. Careful analysis of the transpassive part of the polarization curves also showed that the overpassive dissolution current is smaller in Cl^- melts than in SO_4^{2-} alone. This was further evidenced by particular experiments that have been concerned with determining the inhibiting role of NaCl on Ni in the passive–transpassive area.

Micrography studies and electron probe microanalyses of potentiodynamic specimens polarized in Na_2SO_4–15%NaCl at 900 °C, in air, are shown in Figures 15.3–15.6. Uniform field and the presence of scratches indicating more dissolution of the surface corrosion products were observed; along the scratch lines, the growth of oxides could also be observed; moreover, there was heavy internal grain boundary attack, plus a few pits. Figure 15.3 shows a typical Ni section. No S, Cl, or Na was detected either in the voids or in the external NiO porous fragile layer (which is almost always green). Ni_3S_2 was identified (see Figure 15.3). NiO and Ni_3S_2 are, therefore, the main corrosion products. Absorbed electron images (AEI) of a corrosion pit are shown in Figures 15.4–15.6; a sulfur X-ray image of the region shown in Figure 15.4 is shown in Figure 15.5. The Ni, S, and O contents of this region were determined. The oxygen content was below the detection limit of the electron probe. S and Ni countings were made using CdS and pure Ni as standards. The results showed that the material was not homogeneous, being higher in sulfur near the outer surface (Figure 15.3), so the measurements were split into two (outer and inner) before calculating the corrected values. The outer zone consists, therefore, of a network of Ni_3S_2, and the inner zone consists of a mixture of Ni and Ni_3S_2; it is probably this Ni–Ni_3S_2 liquid eutectic structure at 900 °C that undermines the exposed metal surface, making the corrosive process more extensive and, consequently, originating deep perforations.

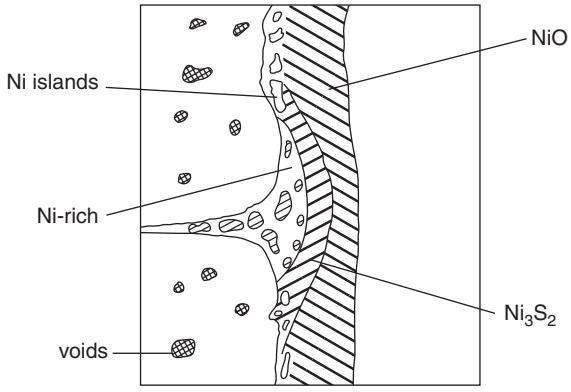


Figure 15.3 Diagram of a typical Ni section.

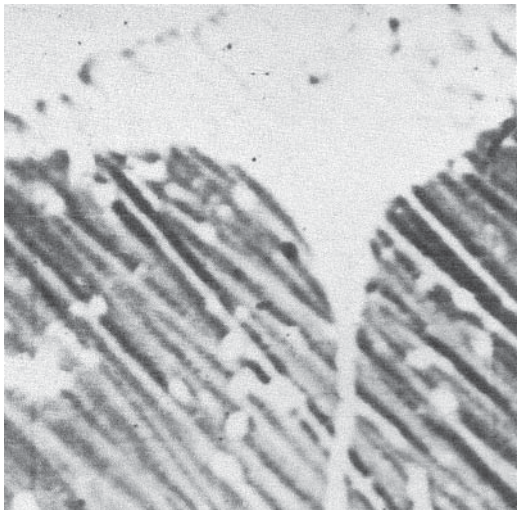


Figure 15.4 Ni, 900 °C, Na_2SO_4–15% NaCl in air after potentiodynamic sweep AEI (×1200): close view of one end of a corrosion pit.

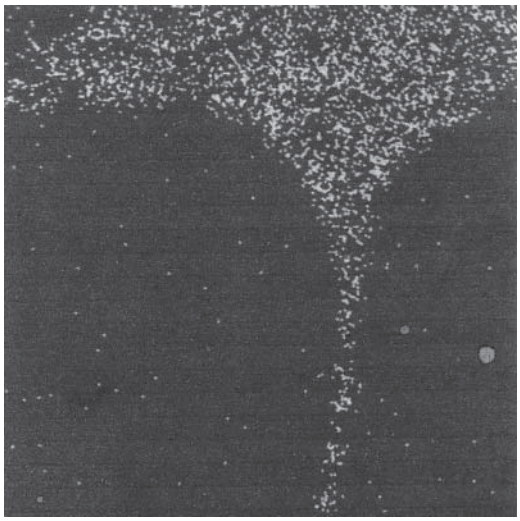


Figure 15.5 Conditions as in Figure 15.4, X-ray image (×1200): distribution of S.

3. Further examination of the *E*/*I* curves for Ni in sulfate–chloride melts at 900 °C leads to the conclusion that the rate-determining step of nickel dissolution

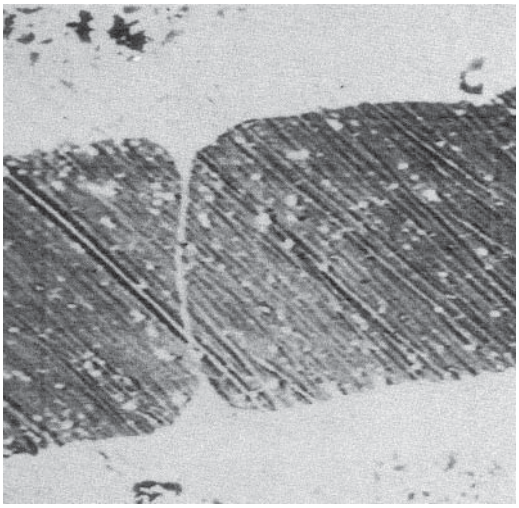


Figure 15.6 Conditions as in Figure 15.4, AEI (×300): complete view of corrosion pit.

in the melts is mainly the diffusion process into the melt.

4. SO_3 atmospheres destroy the passive capability found for Ni in Na_2SO_4–NaCl melts in air. The high rates of corrosion observed at high partial pressures of SO_3 are shown to be mainly due to the effect of SO_3 on the solubility of the corrosion products. More specifically, this corrosion stimulation is due to the SO_3 role in promoting dissolution attack of species like NiS with the appearance of Ni^{2+} until these ions precipitate or the conjugate oxygen cathodic process (O_2/O^{2-}) takes place.
5. Nimonic 105 does not exhibit the active–passive transition characteristic of nickel in sulfate media. In the presence of pure Na_2SO_4 at 900 °C, in air, two different regions characterize the *E*/*I* curve. The first region corresponds to the onset of passivity and dissolution of passive Nimonic; it is characterized by a small dissolution rate and is really an "active–passive" zone, as suggested by the physical appearance of the electrode surface polarized within its limits. The second region is a transpassive area and corresponds essentially to the sulfate discharge.
6. Additions of NaCl, up to 15%, to the sulfate melt hardly affected the forward sweep for Nimonic 105 in pure Na_2SO_4, but severely affected the reverse one. This non-repair capability of reforming a passive corrosion layer is due to the Al and Cr depletion at the Nimonic surface by NaCl attack, which is observed at high anode potential values and may be explained by reactions of the form

$$2Cr_2O_3 + 5O_2 + 8NaCl \rightarrow 4Na_2CrO_4 + 4Cl_2 \quad (15.17)$$

and

$$Al_2O_3 + 1/2\,O_2 + 2NaCl \rightarrow 2NaAlO_2 + Cl_2 \quad (15.18)$$

NaCl addition greater than 15% increased the c.d. recorded in the portion of *E*/*I* curve representing the passive potential range, mixtures of about 15–35% NaCl being the most aggressive. It seems that the Cl^- ions crack the Cr_2O_3 oxide layer, subsequently enabling reactions of the type

$$Ni(Co) + SO_4^{2-} \rightarrow Ni^{2+}(Co^{2+}) + SO_2 + 2O^{2-} \quad (15.19)$$

$$Ni^{2+}(Co^{2+}) + 2Cl^- = Ni(Co)Cl_2 \quad (15.20)$$

$$Ni(Co)Cl_2 + 2Cl^- \rightarrow Ni(Co)Cl_4^{2-} \quad (15.21)$$

and

$$9/2\,Ni + Na_2SO_4 \rightarrow Na_2O + 3NiO + 1/2\,Ni_3S_2 \quad (15.22)$$

$$x/2\,Ni_3S_2 + Cr \rightarrow CrS_x + 3x/2\,Ni \quad (15.23)$$

to occur. Evidence for these reactions is substantiated by the topochemical studies.

7. SO_3 pressures below 5×10^{-3} atm do not affect the electrokinetic behavior of Nimonic 105; SO_3 pressures above 5×10^{-3} atm produce higher corrosion rates, which may be related to the acid fluxing of the sulfate melt, either leading to ionic dissolution of the alloy scale constituents or favoring sulfur diffusion through the oxide scale and, consequently, enhancing the sulfidation process.

   A cross section from a freely corroded Nimonic 105 sample in Na_2SO_4 at 900 °C under 1 atm O_2 and 0.00005 atm SO_3, for 100 hours, showed severe penetration of the base alloy by sulfur. Figure 15.7 shows the resulting external scale morphology. Ni, Cr, and S microprobe traces (Figure 15.8) across the affected alloy zone enabled the micro-characterization of five zones of distribution of the corrosion products (base metal → scale) as schematically drawn in Figure 15.9. Zone I consists of a network of sulfides predominantly of nickel but containing 7–17%Cr. Zone II also contains a network of sulfides but mainly of chromium. Zone III is found to consist predominantly of NiS and some Cr_2O_3. Zone IV possibly consists of $NiCr_2O_4$ and small sulfide particles. In Zone V (at surface), there is a matrix of pure nickel particles associated with a thin layer of nickel oxide.
8. The high dissolution rates and the shape of the polarization curves for Ni and Nimonic 105 in pure NaCl at 900 °C in air indicate that these materials are typically in the NaCl electrolyte. Metal dissolution must

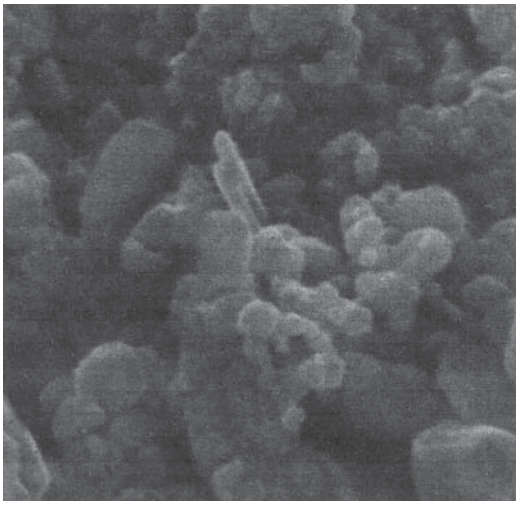


Figure 15.7 Nimonic 105 after immersion in Na_2SO_4 for 100 hours at 900 °C under 1 atm O_2 and 0.00005 atm SO_3. Surface (SEM) 5350X.

occur at the expense of a simultaneous reduction of Na^+ ions to Na_2^+ subions, accompanied by the corrosion of the metal interacting with the dissolved oxygen and the chloride ions, as well as with the chlorine and oxide ions formed in the reaction of oxygen with chloride ions.

9. The potential-decay curves for Ni in Na_2SO_4–NaCl melts show that thin passive films are very sensitive to Cl^- attack, but once a thick oxide film forms on the specimen, the Cl^- addition is accompanied by an increase in the film stability. Hence, there appears to be no simple correlation between the ease of achieving passivity (more likely in pure Na_2SO_4) and the stability of the passive film (enhanced in Cl^- melts).
10. The potential-decay curves for Nimonic 105 in Na_2SO_4 and in Na_2SO_4–15%NaCl mixtures followed a similar pattern, showing absence of passivity breakdown.
11. The *E*/*I* curves in Cl^- melts up to 15% NaCl as well as the film breakdown studies of passive Nimonic 105 suggested the feasibility of anodic protection of this material in the melts at 900 °C over a wide passive range. This is, however, not feasible as the free corrosion potential measurements indicate. The breakdown of the oxide film that occurs after some hours of immersion in the Cl^- melts suggests that a

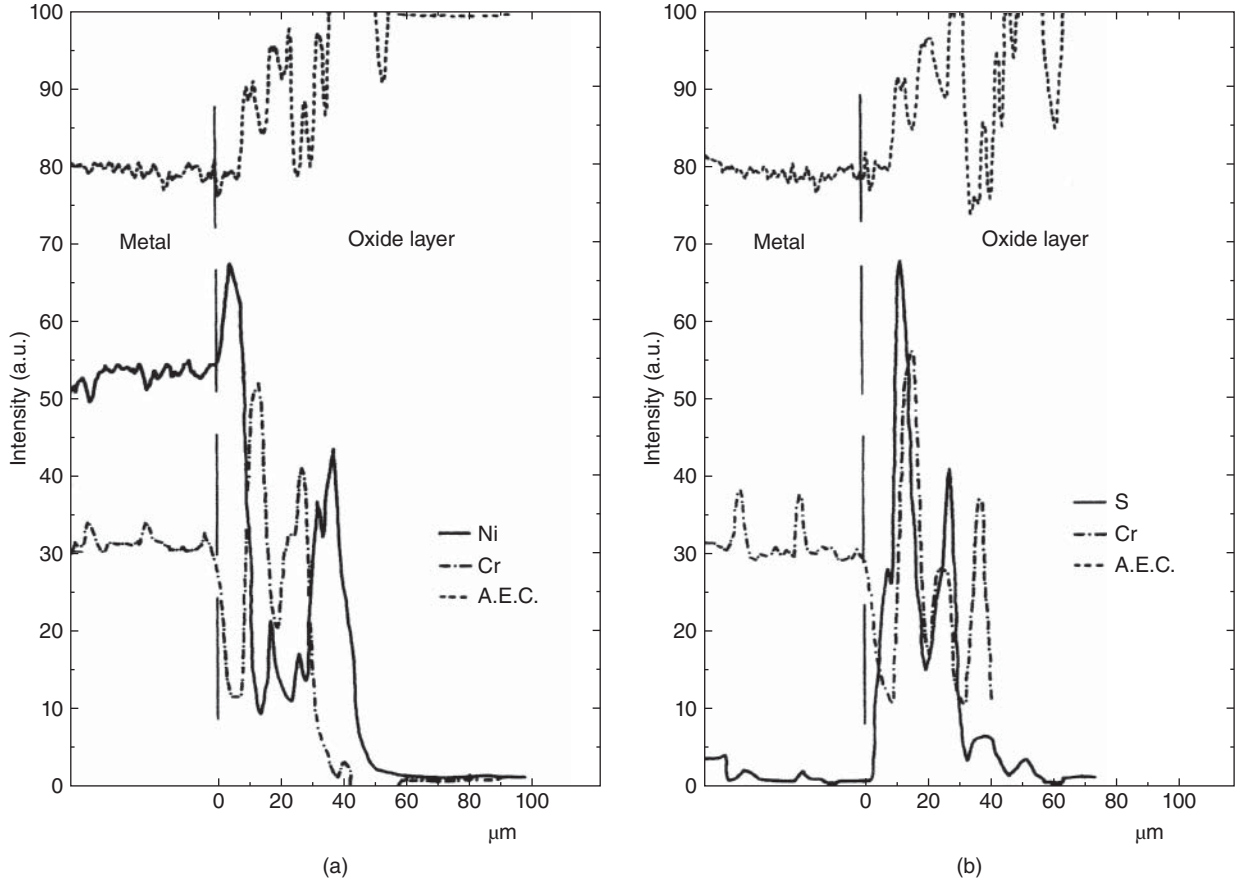


Figure 15.8 Electron microprobe analysis of the scale formed on Nimonic 105 immersed in molten Na_2SO_4 for 100 hours at 900 °C, under 1 atm O_2 and 5×10^{-5} atm SO_3: (a) Ni and Cr spectrometer traces and (b) Cr and S spectrometer traces.

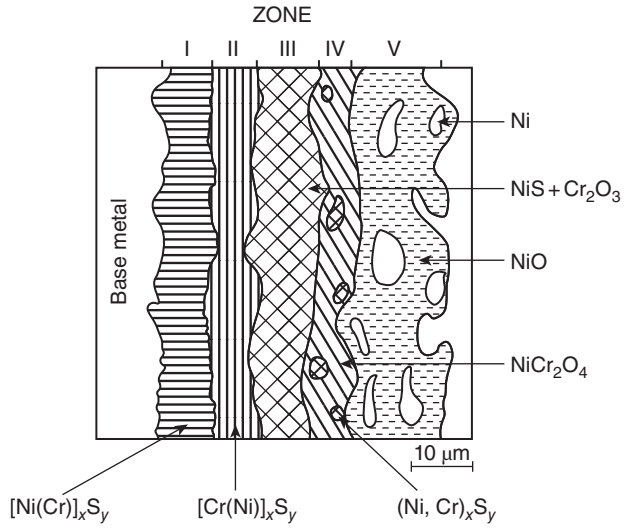


Figure 15.9 Schematic view of Nimonic 105 after corrosion in Na_2SO_4 at 900 °C for 140 hours under air.

period of incubation is required for the halide ions to accelerate the sulfidation.

Considering the early studies just presented, there could be no doubt that chloride exists in those areas of the turbine where hot corrosion is found. The processes of condensation and/or impaction required further investigation, but in general terms it could be assumed that chloride plays a crucial role in the mechanism of hot corrosion. Quite apart from providing a source of sodium for the formation of sodium sulfate, it seemed highly probable that the major role of chloride is in destroying the integrity of protective scale layers.

Thermal cycling is a normal phenomenon in the gas turbine, and thermal shock, combined with chloride effects, could be assumed to result in inhibition of the formation of protection layers. Although chloride must have a transient existence if deposited on nozzles or blades, its intermittent or continuous replenishment might also provide secondary effects in promoting reduction in the melting point of deposited salts and also in increasing wetting properties. These effects may result in hot corrosion at lower temperatures and over more extensive areas of components. This, combined with the volatility of deposits, might control the lower and upper temperatures at which the sulfidation/accelerated oxidation effect was found.

15.4 Mechanisms of Hot Corrosion

The early theories developed to explain the general appearance of the corrosion corresponding to the practical experience are now called type I hot corrosion (HTHC) (Rapp 1986; Rapp and Zhang 1998). In laboratory tests, this type appears to be absent below a lower threshold temperature and above an upper threshold temperature; these temperatures vary with the alloy and with the detailed conditions, but they are usually close to 800 and 950 °C, respectively. The primary factor in viewing molten Na_2SO_4 with respect to HTHC is that of the availability of the melt and not its mass. An attack will be self-sustaining as long as the melt can participate in the exchange and remain as the intermediate means by which alloy component elements will eventually react to solid corrosion products. In the turbine operating conditions, melt can form as and when the component particles are deposited. Products can remain in solution with the melt, form a eutectic, precipitate out, or form a solid complex with the total mass of available melt.

The following reactions will clarify the various points noted above:

$$Na_2SO_4 = Na_2O + SO_3 \tag{15.24}$$

$$SO_4^{2-} = O^{2-} + SO_3 \ (\equiv 1/2S_2 + 3/2O_2)$$
(Acidic) (Basic) (Acidic)

Now, if one expresses the above equilibrium equation in terms of activity of various components as

$$[Na_2O] \cdot [SO_3] = \text{constant} \cdot [Na_2SO_4] \tag{15.25}$$

with the assumption that for pure Na_2SO_4, $[Na_2SO_4] = 1$, one finds that the activity of Na_2O, the basic component, is inversely related to the activity of SO_3. At sufficiently low sulfur activities, Na_2O is the only stable phase, and SO_3 has sufficiently low oxygen activity. The acid and basic fluxing models depend upon whether the oxide is being dissolved by Na_2O, the basic component of Na_2SO_4, and by SO_3, the acidic component. For example, the oxidation of Ni gives NiO. The solubility of NiO in Na_2SO_4 at 1200 K goes to a minimum at $\log [Na_2O] = -10.3$. At higher values of $[Na_2O]$, Ni dissolves as NiO_2^{2-} ($NiO + O^{2-} \rightarrow NiO_2^{2-}$) and at lower values as Ni^{2+} ($NiO \rightarrow Ni^{2+} + O^{2-}$). Logically, these two types of dissolution are termed as basic and acid dissolution, respectively. It should be noted that the hot corrosion process, especially with acidic fluxing mechanism, strongly depends on the temperature. As described earlier, if the temperature of exposure is lower than the melting point of the melt, the corrosion would not occur unless a complex mixture of salts is formed. In the case of Ni, a mixture of $NiSO_4$ and Na_2SO_4 is formed, which, according to the phase diagram given in Figure 15.10, has a eutectic temperature of 671 °C. Thus, at temperatures lower than 884 °C, the melting point of Na_2SO_4, hot corrosion would result only when the eutectic mixture is formed.

The salt fluxing processes have received most attention in recent years, and a brief description of the two proposed processes – one in which the salt is displaced in a basic (Na_2O-rich) direction and the oxide is dissolved as

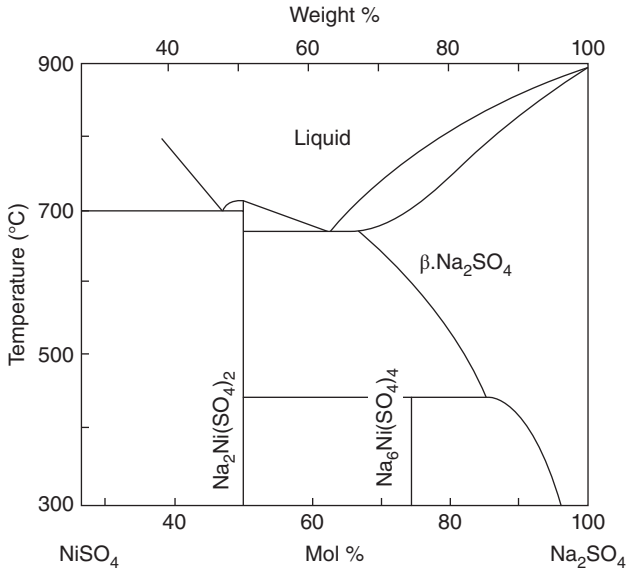


Figure 15.10 Na_2SO_4–$NiSO_4$ phase diagram showing the eutectic temperature of 671 °C.

an anionic species and one in which the salt is displaced in an acidic (SO_3-rich) direction and the oxide or the metal dissolves as a cationic species – is as follows.

15.4.1 Acidic Fluxing

Hot corrosion reactions occur where SO_4^{2-} participates with the S_2, SO_2, and SO_3 species from the gas or dissociated melt in converting the alloy to corrosion products either by chemical thermodynamic reaction or electrochemically transported as an ion for a subsequent reaction with the gaseous medium. Thus, for an alloy AB,

$$A\,(\text{alloy}) + SO_3 + (1/2)O_2 = A^{2+} + SO_4^{2-} \qquad (15.26)$$

For a continuous solution of ASO_4 in Na_2SO_4, SO_3 and O_2 must be available, e.g. $CoSO_4 + Na_2SO_4$:

$$A^{2+}(\text{alloy}) + SO_4^{2-}(\text{melt}) = AO(\text{solid}) + SO_3 \qquad (15.27)$$

AO can remain in solution with Na_2SO_4 melt if there is a negative solubility gradient (note this cannot happen in a small mass or thin layer of melt):

$$B(\text{alloy}) + SO_4^{2-} + (3/2)O_2 = BO_4^{2-} + SO_3 \qquad (15.28a)$$

or

$$A(\text{alloy}) \cdot B(\text{alloy}) + 2O_2 = A^{2+} + BO_4^{2-} \quad (\text{solution in melt}) \qquad (15.28b)$$

$$A^{2+} + BO_4^{2-} = AO + BO_3 \qquad (15.29)$$

The melt remains as a via media; very small amounts of Na_2SO_4 allow a substantial alloy-to-alloy metal oxide conversion.

In practical systems virtually all alloys are susceptible to acidic fluxing depending on the level of pSO_3 or the amount of V_2O_5 formed or deposited. The condition is prevalent when chloride is present and induces alloy depletion in gas turbine environment and in carburizing conditions when oxygen starvation occurs. Alloys containing Mo, W, or V are very vulnerable because they can be auto-generative to acidic oxides, e.g. B-1800, IN 100, MAR M-200, etc. High chromium alloys present a reasonably good resistance, as well as silica formers. IN-738 and some Hastelloys are found to outperform the above listed alloys. A refractory metal addition has to be restricted to avoid acidic degradation. Hot-pressed Si_2N_4 performs well in acidic fluxing conditions (Hocking et al. 1989).

15.4.2 Basic Fluxing

Basic fluxing of the reaction product occurs when the alkali Na_2O or the O^{2-} part of the oxyanionic melt participates in the reaction process:

$$A(\text{alloy}) + O^{2-} + (1/2)O_2 = AO_2^{2-} \qquad (15.30)$$

Na_2SO_4 is converted to Na_2AO_2 and ceases unless fresh melt Na_2SO_4 is available:

$$A(\text{alloy}) + O^{2-} + (1/2)O_2 = AO_2^{2-} = AO(\text{solid}) + O^{2-} \qquad (15.31)$$

Melt can act as a transport–precipitation reaction medium as long as it is balanced by a SO_3 supply; else, it will stifle the reaction when sufficiently basic. This means that for this reaction to be possible, there should be a negative solubility gradient of the oxide in the melt (Rapp and Zhang 1998). Viewing melt fluxing in the context of protective oxide scale formation, it may be generalized that Cr_2O_3 is more resistant under low pSO_3 conditions (i.e. a basic condition), SiO_2 has minimal solubility in high pSO_3 (i.e. it is good to resist acidic fluxing), and Al_2O_3 has a lower solubility at low pSO_3 than Cr_2O_3.

Degradation due to basic fluxing can be resisted effectively by promoting continuous scale growth of Al_2O_3 under Cr_2O_3. Since it requires an oxygen gradient for promotion, the best means of counteracting it is by formation of oxide scales that grow at a slow rate and need very low pO_2. In Ni–Cr-based superalloys, it is better not to have any Al at all than Al in a low level since the chloride effect is particularly marked in low Al Ni–Cr–Al alloys. Deposits of carbon are observed to hasten the onset of basic fluxing as it creates local reducing conditions, while a 5 μm surface topcoat of Pt inhibits basic fluxing.

Susceptibility to basic fluxing occurs with Ni and Co and their alloy systems, e.g. binary Ni–Al and Co–Al, ternary Ni–Cr–Al, or multi-element system where Cr and Al levels are lower than is required to form their stable oxides (Rapp 2002). Alloys with 20Cr or more and 10–12Al with reactive elements such as Y have good resistance in basic fluxing media. If Al has to be lowered for mechanical purposes, then the preference is given to a CoCrAl system rather than a NiCrAl alloy. Alloy depletion caused by chloride reactions and carbon-induced oxygen depletion are, once again, the contributory factors (Hocking et al. 1989).

The fluxing mechanisms obviously only operate in the presence of a molten salt layer, and this is quite restrictive: pure sodium sulfate melts at 884 °C and pure potassium sulfate at 1069 °C. The two form an extended range of solid solutions, with a minimum melting point of 823 °C, and further reductions are possible in the presence of such stable sulfates as those of calcium and magnesium. For example, in the Na_2SO_4–$MgSO_4$ system, there is a eutectic between the solid solution of $MgSO_4$ in Na_2SO_4 and $Na_2SO_4 \cdot 3MgSO_4$ at approximately 660 °C. There is also a eutectic in the Na_2SO_4–NaCl system at 630 °C and other in the Na_2SO_4–$NiSO_4$ system at 671 °C. Various other more complex phase systems are partially reported, which imply that other reductions may be possible. However, the group of compounds of most current interest is those involving the alkali sulfates and the sulfates of the transition metals.

In the late 1970s, a new form of hot corrosion was encountered at the resulting lower temperatures. The character of the corrosion was significantly different from that of HTHC. Localized pits developed, with relatively smooth metal–scale interfaces; there was usually little or no sulfidation within the metal, and there was no depletion of the more reactive alloy elements in the metal ahead of the interface (Giggins and Pettit 1980). It proved to be difficult to duplicate the attack in the laboratory until it was realized that it was necessary to control the SO_3 partial pressure in the gas stream. The upper and lower threshold temperatures for this attack, which is called type II (originally "low-power") hot corrosion (LTHC), are less well defined than the limits for type I hot corrosion, because they depend on the SO_3 partial pressure and data from service are less well characterized. However, it appears that the attack is seldom observed above 775 °C or below 700 °C. The molten salt in this case is believed to be a mixed alkali sulfate-base-metal sulfate. In general, it appears that cobalt-based alloys are somewhat more sensitive to this form of attack than nickel-based alloys, and increasing the chromium content of the alloy increases its resistance to the corrosion even when the alloy forms an alumina scale. The effect of other elements and the metallurgical structure is not clear, although it is generally accepted that coarse carbides containing refractory metals are deleterious and should be avoided by optimizing the heat treatment (Luthra and LeBlanc 1987).

A third form of high temperature corrosion is encountered in gas turbines burning low-grade petroleum-based fuels with high vanadium contents. The vanadium is present as an organic species and, during combustion, oxidizes to form V_2O_4, which is present in the combustion gas stream as an aerosol. Later, this oxidizes further to pentoxide, V_2O_5, which has a low melting point, close to 710 °C; other species, particularly sodium sulfate, can lower the melting point still further. This melt is very aggressive and is capable of dissolving most protective oxides and indeed most metals. Alloys with very high chromium levels, in excess of 35%, have some resistance to vanadium attack, but the problem is usually combated in practice by using fuel additives, which are largely based on magnesium oxide: magnesium vanadate has a relatively high melting point (Lai 1990; Stringer 1987).

Several authors, notably Rahmel (1972) and Kawakami et al. (1980), have suggested that the corrosion is essentially electrochemical in nature, with local cells established in the system, and certainly many of the features of the corrosion can be duplicated electrochemically, since the oxide ion concentration of the salt can be controlled in this way. It is difficult to decide to what extent such local cell action may be involved because, as indicated above, such a mechanism is not necessary; concentration gradients induced chemically can also account for the observations.

15.5 Hot Corrosion of Gas Turbine Alloys

Some of the laboratories that have contributed to gas turbine hot corrosion research in the last 40 years are listed hereinafter by quoting the group leaders and/or main workers:

> Agarwall, Alcock, Armijo, Barrett, Bennett, Birks, Booth, Bornstein, Carew, Condé, Coutsouradis, Cutler, Davin, DeCrescente, Douglass, Duret, Elliott, Erdos, Fairbanks, Foster, Fryburg, Gadomski, Galsworthy, Giggins, Goebel, Goward, Grabke, Hancock, Hart, Hed, Hocking, Hussain, Jacob, Jones, Khama, Kedward, Kofstad, Kohl, Kubaschewski, Lai, Lambertin, Luthra, Lloyd, McGll, McCreath, McKee, Meadowcroft, Mévrel, Misra, Mrowec, Natesan, Nichols, Nicoll, Numata, Pettit, Pichoir, Prakash, Rahmel, Ramanarayanan, Rapp, Restall, Rhys-Jones, Romeo, Rothman, Saunders, Sequeira, Shinata, Shores, Sidky, Smeggil,

Stearns, Stephenson, Stern, Stott, Strafford, Stringer, Swidzinski, Smeltzer, Taylor, Vasantasree, Wallwork, Wagner, Whitte, Wood, Worrell, Wright.

Many of their publications are listed and can be used for further reference. It should be noted that the list is not exhaustive and several more investigators have published significant works in this area. A number of papers discussing the corrosion behavior of high temperature alloys and coatings for gas turbines are discussed here.

Clelland et al. (1974) studied hot corrosion resistance of various nickel- and cobalt-based alloys in a marine environment and found that alloy X-40 (Co–25Cr–10Ni–7.5W) was the most resistant among the tested alloys. Zetmeisl et al. (1984) also found that alloy X-40 was significantly better than nickel-based alloys, such as B-1900, U-700, U-500, and IN-738. After 240 hours, alloy X-40 hardly showed any corrosion attack, while alloy B-1900 (Ni–10Co–8Cr–6Mo–4.3Ta–6Al–1Ti) suffered severe attack. Alloys U-500 (Ni–18Co–19Cr–4Mo–2.9Al–2.9Ti) and IN-738 (Ni–8.5Co–16Cr–1.7Mo–2.6W–1.7Ta–0.9Cb–3.4Al–3.4Ti) were similar, suffering only mild attack. Surprisingly, alloy U-700 (15%Cr) was found to be slightly worse than alloy B-1900 (8%Cr). Stringer (1976) considered alloy B-1900 along with IN-100 (10%Cr) and Nimonic 100 (11%Cr) to be poor in hot corrosion and suggested that they not be considered for use without coatings, even in mildly corrosive environments.

Beltran (1970) conducted burner rig tests using residual oil, which contained 3%S and 325 ppm NaCl (equivalent to 5 ppm NaCl in air), at 870 °C for 600 hours on several cobalt-based alloys with chromium varying from 20 to 30%. All tested cobalt-based alloys suffered little corrosion attack (about 0.04–0.12 mm). These values were of the same order of magnitude as those produced under natural gas combustion. Under the same test conditions, alloy U-700 suffered as much as about 0.76 mm of attack.

Wagenhein (1970) conducted an alloy development program with two goals:

1. Develop and test Co-based alloys (MELCO alloys) for service as a vane material in a typical marine gas turbine having a firing temperature of 1750 °F and a 5000 hours life between overhauls. This could mean that first-stage vane metal temperature may approach 1900 °F. For this design criterion, a Co-based alloy with the strength of WI-52 at 1900 °F and hot corrosion resistance superior to that of the X-45/X-40 type alloys was needed.
2. Investigate Co-based matrix compositions resistant to hot corrosion/oxidation atmospheres that could subsequently be used as an alloy matrix for dispersion strengthening (DISCO alloys). This alloy would be suitable for vane applications well above the 1900 °F service temperature goal ascribed to the MELCO alloys.

The response of the alloys to hot corrosion attack was apparently dependent upon the salt concentration and test temperature. At the high salt level, subsurface sulfides were observed beneath the surface oxide or in front of the leading intergranular oxide fingers at both test temperatures. At low salt concentrations, it appeared that the oxidation mechanism played a more prominent role as the test temperature was raised.

The environmental tests indicated that Cr up to 30% and Y were beneficial, while Ta was detrimental above 2000 °F. As mentioned above, the response of the alloys to hot corrosion is dependent on the test parameters. Alloys MELCO-2, MELCO-9, MELCO-10, MELCO-14, and MELCO-16 appeared best in low-salt tests, while MELCO-5 and X-45 were superior in high-salt environments.

The abovementioned goals have been successfully met by MELCO-14. Although MELCO-14 does not offer the best hot corrosion resistance or the highest stress-rupture strength capability, it was the only alloy that met both the environmental and strength requirements simultaneously.

Based on short-time/high-salt tests, the DISCO alloys did not show much change from the competitive commercial or MELCO alloys. However, the alloys appear to have promise as a matrix for dispersion strengthening. The corrosion resistance varied somewhat as a function of heat treatment and test temperature. It also appeared that lower Ni contents and addition of Y improved corrosion resistance (Wagenhein 1970).

Condé et al. (1977) performed studies that led to the conclusion that expendable or sacrificial chromium in the form of chromium oxide would inhibit hot corrosion by converting aggressive chloride and sulfate to innocuous products. They describe experiments to assess the efficacy of additions of Cr_2O_3 as a disperse phase in alloys and coatings, as well as combustion rig corrosion studies on conventional alloys and coatings in which the inhibitor was added as fuel-soluble organic chromium compounds and produced significant reductions in the extent of hot corrosion.

The effect of zigzag grain boundaries on the creep-rupture properties of a nickel-based superalloy Inconel 751 in hot corrosive environment induced by Na_2SO_4–NaCl (90%:10%) molten salt at 800 °C in static air was studied by Miyagawa and Yoshiba (1981). It is suggested that the rupture life of alloys subjected to hot corrosion is mainly determined by the intergranular penetration behavior of sulfides followed by oxides, which depends strongly upon the grain boundary configuration and the morphology of boundary carbides. Since the

straight boundaries provide extremely activated paths for rapid penetration of sulfides and oxides, a decrease in the rupture life due to hot corrosion is remarkable. On the contrary, the zigzag boundaries and the existence of coarse titanium-rich boundary carbides control the intergranular penetrations to obey a given kinetics, and, therefore, a decrease in the rupture life is sufficiently restrained.

High temperature corrosion tests in 80%Na_2SO_4–20% NaCl was made by Okanda et al. (1983) on five Fe30%–Cr5% Al alloys containing various amounts of Ce up to 0.68%. After the corrosion tests, samples were examined metallographically, by X-ray diffraction and X-ray microanalysis. It was found that the surface scale formed on each sample decreased in thickness as the Ce content increased. Electron probe microanalyses suggested that this retarding behavior is related to the early formation of a Ce-induced protective scale of α-Al_2O_3. The role of Ce in promoting the formation of the α-Al_2O_3 scale was discussed.

Wu et al. (1983) studied the resistance of Ni-based superalloys to acidic and basic fluxing in a 90Na_2SO_4–10K_2SO_4 melt at 1173 K by determining the potential dependence of the corrosion behavior. The following conclusions could be drawn from their studies:

1. The corrosion behavior of Ni-based superalloys in sulfate melts strongly depends on the corrosion potential because structure and composition of the scale are influenced by the potential.
2. Alloys with high chromium contents, such as IN-738LC, IN-939, IN-597, and IN-657, exhibit a potential region of stable protective scale formation. In this region, the melt at the specimen surface is neutral or nearly neutral. Such protective scales are not formed on alloys with low chromium and rather high aluminum and molybdenum contents such as IN-100 and IN-713LC.
3. Acidic fluxing occurs above a critical potential, leading to severe external and internal corrosion. This critical potential is slightly affected by the alloy composition.
4. Basic fluxing starts below a second critical potential that again leads to severe corrosion. This potential depends on the scale composition. Scales rich in Cr_2O_3 have a more negative breakdown potential than scales rich in Al_2O_3.
5. In addition to acidic and basic fluxing, scale cracking seems to be another mechanism of hot corrosion initiation that seems to occur preferentially with the alloys IN-100 and IN-713LC having lower corrosion resistance.
6. Potentiostatically controlled corrosion tests are a means to study acidic and basic fluxing phenomena and to compare the resistance of different materials to this kind of corrosion.
7. According to these measurements, the corrosion resistance increases in the order IN-100, IN-713LC < IN-738LC < IN-657 < IN-939, IN-597. This series agrees fairly well with the results of other tests (Dean test, rig test) and with the behavior in gas turbines.

Sodium sulfate-induced hot corrosion of pre-oxidized B-1900 and NASA-TRW VIA has been studied at 900 °C with special emphasis placed on the chemical reactions occurring during and immediately after the induction period (Fryburg et al. 1982). Thermogravimetric tests were run for predetermined periods of time after which one set of samples was washed with water. Chemical analysis of the wash solutions yielded information about water-soluble metal salts and residual sulfate. A second set of samples was run, cross-sectioned dry, and polished in a nonaqueous medium. Element distributions within the oxide layer were obtained from electron microprobe X-ray micrographs. A third set of samples was subjected to surface analysis by ESCA. Evolution of SO_2(g) was monitored throughout many of the thermogravimetric tests. Results were interpreted in terms of acid–base fluxing mechanisms.

More specifically, it was indicated that hot corrosion is initiated by acid fluxing of the protective Al_2O_3 scale. The attack is localized but spreads over the sample until Na_2SO_4 has all reacted. Since the supply of Na_2SO_4 is limited, the basic fluxing decreases as the sulfate is consumed, leading to a near parabolic rate corrosion.

The sequential, catastrophic corrosion of these alloys results from their molybdenum content. The molybdenum forms a low-melting phase (Na_2MoO_4/MoO_3) that removes the protective scales by acidic fluxing. The molybdenum phase migrates across the sample beneath the scale, resulting in a linear reaction rate and finally in complete consumption of the sample. The self-sustaining feature is a consequence of the cyclic nature of the acidic fluxing.

Hot corrosion studies were conducted at 900 °C in a simulated combustion gas atmosphere containing sulfur trioxide at a partial pressure of 750 Pa on a Ni-based superalloy (Nimocast 713) partially immersed in various $ZnSO_4$–10 wt%NaCl–Na_2SO_4 molten salt mixtures. Weight changes were measured thermogravimetrically with time, and it was found that the overall effect of the zinc sulfate addition was to reduce the degree of hot corrosion. Quantitative scanning electron microscopy (SEM) investigations revealed no evidence of Zn in the attacked zone. It is postulated that Zn reduces the chlorine activity in the system by forming a volatile chloride, thereby reducing the corrosive effect of the gas phase/molten salt mixtures (Kanary et al. 1987).

The effect of pre-oxidation on hot corrosion for Ni–20 mass % Cr–5 mass % Al alloy in molten Na_2SO_4–25 mass

% NaCl at 1173 K has been examined by the measurement of corrosion loss, the electrochemical measurement, and the analysis of the surface oxide film formed on the alloy by pre-oxidation (Hara et al. 1995). Particular attention was given to the influence of pre-oxidation temperature. The pre-oxidation at 1173 and 1273 K led to a stop of the vigorous corrosion for the alloy in the molten salt, whereas the pre-oxidation at 1373 K did not lead to an inhibition of the corrosion. The anodic polarization curve measured in the alloy after pre-oxidation, which stopped the vigorous corrosion of the alloy, showed the spontaneous passivation behavior, while that measured for the alloy without pre-oxidation showed a large current peak due to the active dissolution reaction. This suggests that the pre-oxidation treatment inhibits the electrochemical corrosion reaction of the alloy. Such an inhibition effect on the corrosion was investigated by the analysis of surface oxide film formed by pre-oxidation. The formation of oxide films consisting mainly of Cr_2O_3 was observed for the alloy after pre-oxidation at 1173 and 1273 K, while that consisting mainly of Al_2O_3 was observed on the alloy after pre-oxidation at 1373 K. Consequently, it was found that the difference in inhibition effect on the hot corrosion due to pre-oxidation temperature resulted from a difference in the kind of oxide constituting the oxide film formed by pre-oxidation.

Hara et al. (1998) prepared a Ni silicide layer on Ni substrate by electrodepositing Si and alloying it with Ni in molten salt. It was shown that nickel covered by the electrodeposit was more resistant than bare Ni to hot corrosion by molten Na_2SO_4.

Tiwari and Prakash (1996, 1997) and Tiwari (1997) have also reported studies on superalloys in the temperature range of 700–900 °C in pure Na_2SO_4, Na_2SO_4–15%V_2O_5, and Na_2SO_4–60%V_2O_5. They observed accelerated corrosion rates for Na_2SO_4–60%V_2O_5 composition, i.e. eutectic with melting point of 500 °C.

Oxidation and hot corrosion in sulfate, chloride, and vanadate environments of a cast nickel-based superalloy have been reported by Deb et al. (1996). Weight gain studies were carried out in air for uncoated samples and for samples coated with 100% Na_2SO_4, 75% Na_2SO_4 + 25% NaCl, and 60% Na_2SO_4 + 30% $NaVO_3$ + 10% NaCl. The presence of sulfur in the form of sulfates was reported to cause internal sulfidation of the alloy beneath the external oxide layer. Deb et al. observed the formation of volatile species by chlorides, which further led to the formation of voids and pits at grain boundaries that reportedly provide an easy path for flow of corrodents. The presence of vanadate in conjunction with sulfate and chloride is proposed to provide additional fluxing action. According to Deb et al. this destroys the integrity of the alloy and weakens its mechanical properties.

Almeraya et al. (1998) carried out electrochemical studies of hot corrosion of AISI-SA-213-TP-347H steel in 80 wt% V_2O_5 + 20 wt% Na_2SO_4 at 540–680 °C and reported corrosion rate values of about 0.58–7.14 mm yr^{-1}. They further observed an increase in corrosion rate with time. However, they also observed that corrosion potential decreases with increase in temperature from 540 to 680 °C.

Lee and Lin (1999) studied the oxidation, mixed oxidation–sulfidation, and hot corrosion of ductile aluminide Fe_3Al with Cr addition at temperatures of 605–800 °C. They observed that hot corrosion of iron aluminide was significantly more severe than oxidation and mixed oxidation–sulfidation. According to Lee and Lin, this can be attributed to the formation of aluminum sulfide at the metal–salt interface as a result of high sulfur potential in the molten salt at the oxide–metal interface.

The proven success of Haynes HR-120, HR-160, 230, 556, 214, and 242 modern superalloys in several high temperature industrial applications (industrial heating, chemical processing, petroleum refining, and power generation), whose key corrosion properties are resistance to hot corrosion, is reviewed by Paul et al. (1997). At present, it can be said that Ni-based alloys and coatings continue to be largely employed in gas turbine components, with emphasis on Waspaloy, IN-100, CMSX-2, Waspaloy/NiCoCrAlY, and LC022. Increasing chromium in alloys or coatings will improve the resistance of the material to both type I and type II hot corrosion attack.

Many other references have evaluated the corrosion resistance of different materials in simulated gas turbine environments and actual engine conditions (Elliott 1989; Sequeira 1998; Shifler and Kohler 1999).

15.6 Methods of Evaluating Hot Corrosion

As in all corrosion testing, the procedure that most nearly duplicates the conditions anticipated in service will provide the most satisfactory and useful information for those aspects of corrosion under consideration here. In fact, considering the extraordinary sensitivity of fused salt corrosion phenomena to minimal variations in operating conditions and purity of components, failure to reproduce these conditions with considerable accuracy may well make any test results completely unrealistic and worthless. Then, it should be understood, if not explicitly stated, that all extraneous matter must be carefully excluded from the system and that only materials closely simulating those to be employed in service (including prior history and surface preparation of the metals) should be used. Other factors affecting the corrosion in fused salts include the heat flux of the corroding surface, the volume of liquid to the surface area of the solid, and the liquid flow rate. If, however,

screening tests to establish the compatibility of a relatively large number of metals with a given molten salt are to be run, it is often useful to commence with static tests even though the ultimate application involves a dynamic system. This is desirable because static tests are comparatively simple to conduct and interpret, and considerably more economical to operate, and because experience has shown that a metal that fails static tests is not likely to survive the more severe dynamic test.

The following five hot corrosion techniques are in use for assessing a variety of materials/coatings for gas turbine engine applications: (i) burner rig test, (ii) furnace test, (iii) crucible test, (iv) thermogravimetric test, and (v) electrochemical methods. The advantages and disadvantages of each technique are presented in Table 15.2. It is important to mention here that no established ISO standard testing procedure is available until now for evaluation of materials and coatings for their hot corrosion resistance and hence the need to establish such standards in the near future. In fact, it is an important issue that needs special attention by all researchers in the field.

Static tests have been carried out in crucibles and even electrochemical measurements, with the aim of investigating the fundamentals of hot corrosion using electrochemical cells (Rahmel 1987; Wu et al. 1992).

Dynamic tests have been carried out by means of spin tests, rotating disks, and loop test installations.

Figure 15.11 illustrates the principle of the thermal convective loop widely used in liquid salts. The dynamic burner rig test is the best available test method for assessing hot corrosion characteristics of materials (Saunders and Nichols 1984). The rig burns fuel with excess air to produce combustion gases with continuous injection of a synthetic sea-salt solution. A special issue of High Temperature Technology, published in 1989, contains a number of papers discussing burner rig test procedures. Further description of these tests can be found in a specialty handbook published in 1997 (Davis 1997).

In recent years, numerous activities have also focused on the interaction between corrosion and mechanical

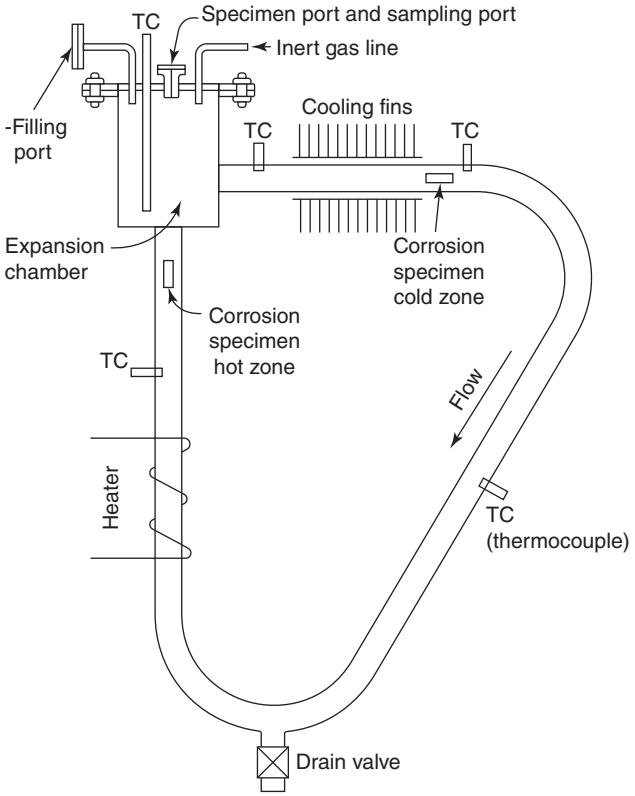


Figure 15.11 Loop test for studying the corrosion produced by molten salts.

Table 15.2 Comparison of hot corrosion evaluation techniques

Technique	Advantages	Disadvantages/limitations
Burner rig test	Simulates gas composition, pressure, velocity, and temperature of gas turbine engines	Complex process and requires long running time. Difficult to control accurately all the parameters
Furnace test	Corrosion conditions can be controlled depending upon the requirements, i.e. severe or mild corrosion	Difficult to maintain salt deposition rate for longer times
Crucible test	Most simple and highly useful for preliminary screening of the materials and coatings	Corrosion is severe for alloys or coatings having low or intermediate resistance to hot corrosion
Thermogravimetric test	Precise weight gain measurement possible under different test conditions, i.e. gas composition, temperature, salt composition, etc.	Not useful for predicting the life of materials and coatings
Electrochemical test	Fast and useful for ranking the materials and coatings based on oxidation–reduction phenomenon	Yet to be fully established

stresses from the viewpoint of cracking and spalling of the protective scales or the acceleration of internal corrosion and final materials failure. In particular, for this type of testing, the acoustic emission technique has been shown to be invaluable (Guttmann and Merz 1981; Saunders et al. 1994, 1995) (see also Chapter 17).

The large variety of tests shows that, in the meantime, a good experimental basis exists for the investigation of the complex processes occurring in hot corrosion. However, there are not many standards for hot corrosion testing, which makes it difficult to compare the data measured at different laboratories. At present, efforts are underway to establish guidelines, with the aim to transfer these into standards in the near future. The results of these efforts have been largely published (Grabke and Meadowcroft 1995), and workers should adhere to these recommendations when performing hot corrosion tests.

15.7 Prevention of Corrosion

Research over the past 35 years has led to better definition of the relationships among temperature, pressure, salt concentration, and salt vapor–liquid equilibria so that the location and rate of salt deposition in an engine can be predicted. In addition, it has been demonstrated that a high chromium content is required in an alloy for good resistance to HTHC. The trend toward lower chromium levels with increasing alloy strength has therefore rendered most superalloys inherently susceptible to this type of corrosion. The effects of other alloying additions, such as tungsten, molybdenum, and tantalum, have been documented; their effects on rendering an alloy more or less susceptible to hot corrosion are known.

In particular, the design of superalloy compositions based on phase stability predictive techniques by balancing the levels of critical elements (Cr, Mo, Co, Al, W, and Ta) is optimal for modern gas turbine applications. In this context, different superalloys of varied categories, namely, forged alloys (such as Nimonic 75, Nimonic 105, Inconel 718, etc.), conventional casting (CC) alloys (like Inconel 713, Inconel 100, etc.), and directionally solidified (DS) alloys (such as CM 247 LC, MAR-M200, MAR-M247, etc.), were reported for their hot corrosion resistance in different environments. Single-crystal superalloys of different generations such as the first generation (namely, CMSX-2, TMS-12, TMS-26, PWA 1480, Rene N4, etc.), second generation with up to 3 mass % rhenium (CMSX-4, Rene N5, TMS-82+, etc.), third generation with up to 6 mass % rhenium (CMSX-10, TMS-75, TMS-80+, etc.), and fourth generation with rhenium and ruthenium (TMS-183) have been developed recently. The third- and fourth-generation superalloys, which contain a large amount of rhenium (Re) as mentioned above and a lower amount of chromium, exhibit good hot corrosion resistance but are susceptible to oxidation. As one of the DS superalloys, CM 247 LC alloy exhibits comparable properties as the single-crystal alloy. Table 15.3 presents different superalloys for which hot corrosion characteristics have been reported in the literature (Gurrappa 2015).

The modification of the superalloy composition by addition of oxide inhibitors is also being used for protection against high temperature hot corrosion. For example, MgO-, CaO-, $ZnSO_4$-, PbO-, and SnO_2-based inhibitors are reported to be effective to decreasing the extent of hot corrosion pertaining to molten salt environment of Na_2SO_4–60%V_2O_5 for iron-, nickel-, and cobalt-based superalloys by Gitanjaly and Prakash (1999), Gitanjaly et al. (2002), and Gitanjaly (2003). The near standardization of alloys such as IN-738 and IN-939 for first-stage blades and buckets, as well as FSX-414 (Co–0.25C–29.5Cr–10.5Ni–7W–2maxFe–1maxMn–1max

Table 15.3 Typical superalloys characterized for their hot corrosion resistance

Alloy	Al	Ti	Cr	Co	Ni	W	Ta	Re	Mo	Hf	Ir	Others
Nimonic 75	—	0.4	20	—	Bal	—	—	—	—	—	—	Fe, C
Nimonic 105	4.7	1.3	15	20	Bal	—	—	—	5.0	—	—	C
Inconel 100	5.5	5.0	10	15	Bal	—	—	—	3.0	—	—	Zr, C, B, V
Inconel 713	6.0	0.8	12.5	—	Bal	—	1.75	—	4.2	—	—	Zr, C, B, Nb
MAR M-200	5.0	2.0	9.0	10	Bal	12.5	—	—	—	—	—	Zr, B, C, Nb, Fe
IN-738	3.4	3.4	16	8.3	Bal	2.6	1.75	—	1.75	—	—	Cb, Fe, C
CMSX-4	5.3	1.0	6.5	10.4	Bal	6.1	4.9	0.8	—	—	—	—
MAR M-247	5.5	1.0	9.0	10.0	Bal	10.0	3.0	—	0.6	1.5	—	B, Zr, C
MAR M-509	—	0.2	23.5	55	10	7	3.5	—	—	—	—	Zr, C
CM 247 LC	5.6	0.7	8.1	9.2	Ba	8.5	3.2	—	0.5	1.4	—	B, Zr, C
Inconel 718	—	—	18	—	Bal	—	—	—	3.0	—	—	Fe, Cb
CMSX-10	5.7	0.2	2.0	3.0	Bal	5.0	8.0	6.0	0.4	0.03	—	—
TMS-75	6.0	—	3.0	12.0	Bal	6.0	6.0	5.0	2.0	0.1	—	—
TMS-80	5.8	—	2.9	11.6	Bal	5.8	5.8	4.9	1.9	0.1	3.0	—

Si–0.012B) for first-stage vanes and nozzles, implies that these are the accepted best compromises between high temperature strength and hot corrosion resistance. It has also been possible to devise coatings with alloying levels adjusted to resist HTHC. The use of such coatings is essential for the protection of most modern superalloys intended for duty as first-stage blades or buckets.

Modern high temperature coating applications are largely intended to the aerospace industry, but it presently exists as an enormous challenge to develop and apply these techniques to other high temperature applications (Hidalgo et al. 2000; Li et al. 2003).

The best way to ensure maximum life of a given turbine must be with stringent control of fuel specifications and good air filtration. The life limitation is then the creep strength and thermal fatigue strength of the first-stage blades or vanes.

Historically, the development of corrosion-resistant coatings was aimed at combating high temperature hot corrosion. The earliest coatings were the diffusion aluminides. It was found that chromium-modified aluminides offered little additional protection against high temperature hot corrosion compared with basic aluminides but that the platinum aluminides offered superior protection compared with the basic aluminides. The chromium-modified aluminides have since been found to be particularly beneficial against low temperature hot corrosion, giving results equivalent to those of the platinum aluminides; both modified aluminides performed better than the basic aluminides.

Although these diffusion aluminides have been successful in reducing hot corrosion, the chemistry of these coatings is not really modified for further improvement in corrosion resistance. Thus, increased attention has been given to the development of overlay coatings, which offer significant compositional flexibility.

The actual compositions of these coatings depend on their intended use. Because Al_2O_3 is used for protection against high temperature hot corrosion, coatings that exhibit the greatest high temperature protection are generally high in aluminum (11%) and low in chromium (<23%). Low temperature hot corrosion, on the other hand, depends primarily on Cr_2O_3 for protection; therefore, coatings exhibiting the greatest low temperature corrosion protection are high in chromium (>30%) and low in aluminum. Other elements, such as silicon, hafnium, tantalum, and platinum, are added to these coatings in an attempt to improve resistance to corrosion and spalling. High chromium MCrAlY coatings have been developed to offer superior low temperature protection without sacrificing high temperature protection because industrial gas turbines sometimes operate under varying load conditions that could result in exposures to both low and high temperature conditions.

The lifetime of the MCrAlY system has been found to be considerably improved by aluminizing or incorporating platinum into the system (Table 15.4). MCrAlY-based bond coatings play a significant role in providing rough surface for the applications of TBCs and to provide protection for the alloy from oxidation and/or hot corrosion. Due to proven performance of these coatings for a variety of superalloys for over two decades in different applications, MCrAlY coatings have been extensively studied.

It is important to mention that the durability of the MCrAlY coating also depends on the coating technique employed. The life of coating applied by arc ion plating is significantly lower as the attack occurs at the edges due to large variation in thickness, i.e. about six times less than the coating thickness at the middle. Different degradation mechanisms proposed are oxidation followed by scale cracking and spallation, mixed oxidant attack, erosion, and molten salt-induced attack.

Overlay coatings have been applied by such techniques as electron beam physical vapor deposition, plasma spray, and sputtering (Hocking et al. 1989).

Table 15.4 Lifetimes of some coatings for aero, industrial, and marine gas turbines

System	Coating	Relative lifetime
Land-based aircraft	Uncoated	≪0.5
DS MAR M-200 + Hf	Standard aluminide (PWA 73)	1.0
	Rh–Al (BB)	<1.5
	Gas-phase aluminide (PWA 275)	<1.5
	Modified aluminide (PWA 263)	1.5
	Pt–Al (RT 22)	1.5
	NiCoCrAlY overlay (PWA 271)	2.75
Marine aircraft	Standard aluminide	1
MAR M-002	Pt–Al	2.5–3
	CoCrAlY	2
Industrial	Uncoated	1
IN-738	PtCrAl	>3
	CoCrAlY (plasma sprayed)	>2
	CoCrAlY (clad) plus Al diffusion coating	>6
	FeCrAlY	2
Marine	Standard aluminide	1
Rene 80	Rh–Al	1–2
	CoCrAlHf	2
	CoCrAlY	1
	CoCrAlY+Pt/Hf	2
	CoCrAlHfPt	2.3

Apart from overall material wastage due to hot corrosion, an additional concern has been the degradation of mechanical properties, particularly creep and fatigue resistance.

Studies are needed to understand the mechanism and implications of the environmentally induced mechanical property degradation in the context of the field performance of components.

15.8 Conclusions

A general survey has been made of a number of aspects of high temperature corrosion in relation to combustion conditions in gas turbines. It is believed that attention has been directed to those features that are most likely to be commonly encountered. It is also obvious that no single material can be recommended as able to meet all the conditions at the gas turbine; any selection must be related as closely as possible to the precise service conditions and, wherever possible, to previous experience of a relevant nature.

All the types of corrosion that have been discussed have in common the ability to disrupt, often locally, the protective oxide films generated by simple oxidation at the surface of practically serviceable heat-resisting alloys. Extrapolation to longer times of data obtained before such breakdown is clearly a dangerous procedure since, once breakdown occurs, the mechanism of corrosion is changed. The corrosion expert who is called upon to advise for 10 or 20 years' operation is, in effect, forced to take a chance that immunity that he has observed during some short period offers sufficient probability of continued freedom from attack to warrant consideration of the material concerned. If, on the other hand, he sees it as his duty to present all the possibilities at their worst, the outlook will often be unduly pessimistic.

Clearly the choice of materials for particular applications or the development of new gas turbine superalloys and coatings with some degree of reliability must await more precise determination of the thermochemical data that are lacking, further elucidation of the part processes leading to sulfidation and accelerated oxidation, and more detailed information on the environment and deposition processes within the gas turbine. In addition to sulfur oxygen, sodium, and chloride, there are clearly other chemical species present in the environment that may play an important role and require further examination.

Issues in which we should be focused are the urgent need to establish ISO standard procedures and the development of high performance aerospace structures or potential candidate materials to replace superalloys by intermetallic compounds, monolithic and composite ceramics, and refractory alloys. This developmental work should take place concurrently with the coating system. Improved understanding of interfacial behavior of TBCs and a more compatible hot corrosion/oxidation-resistant bond coating, either by modification of chemistry or more stringent control of undesirable elements to control coating properties and to predict their performance, is highly essential. Hence, the development of constructive life prediction modeling under simulated gas turbine engine conditions is necessary. Improved online control to ensure reproducible coated structures and within the service limits is also required as increased improvements to current coating technologies are unlikely to meet the goals of future generation high performance turbine engines. Then, development of smart coatings to combat type I and type II hot corrosion and high temperature oxidation for gas turbines is a challenging task to the corrosion engineer.

15.9 Questions

15.1 Why are chromium-based alloys not suitable for low temperatures compared with high temperatures in hot corrosion environments?

15.2 Describe the important difference between type I and type II hot corrosion.

15.3 Which method would you consider the best method for testing hot corrosion and why?

15.4 Are Ni–Al alloys better in hot corrosion resistance than Ni–Cr alloys? Give reasons.

15.5 How does basic fluxing differ from the acidic fluxing? Which is more severe?

15.6 How does hot corrosion behavior in a coal-based power plant differ from corrosion in a gas turbine?

15.7 Is the electrochemical measurement technique of hot corrosion reliable? Comment.

15.8 In both sulfidation and hot corrosion, it is sulfur that is diffusing down the grain boundaries. What is then the difference between hot corrosion and sulfidation?

15.9 What is green rot?

15.10 What is black plague?

15.11 Typically, a high temperature alloy might change 1/4 in./ft from ambient to 1000 °C. Would this thermal expansion/contraction affect the hot corrosion resistance of the alloy?

15.12 Describe the important differences between hot corrosion, fuel-ash corrosion, and vanadic slag corrosion.

15.13 Is hot corrosion an oxidation–sulfidation mixed process?

15.14 Does halogenation, carburization, or nitriding affect hot corrosion?

15.15 How can we screen candidate alloys for hot corrosion environments?

References

Almeraya, C.F., Martinez, V.A., and Gonzalez, R.J.G. (1998). *Br. Corros. J.* 33: 288.

Belcher, P.R., Bird, R.J., Wilson, R.W., and ASTM STP 421 (1967). *Hot Corrosion Problems Associated with Gas Turbines*, 123. Philadelphia, PA: American Society for Testing and Materials.

Beltran, A.M. (1970). *Cobalt* 46: 3.

Bergman, P.A. (1967). *Corrosion* 23: 72.

Betteridge, W. and Heslop, J. (1974). *The Nimonic Alloys*. London: Edward Arnold.

Birks, N., Meier, G.H., and Pettit, F.S. (2006). *Introduction to the High Temperature Oxidation of Metals*, 2e. Cambridge: Cambridge University Press.

Bornstein, N.S. and DeCrescente, M.A. (1969). *Trans. Metall. Soc. AIME* 245: 1947.

Bornstein, N.S. and DeCrescente, M.A. (1971). *Metall. Trans.* 2: 2875.

Bornstein, N.S., DeCrescente, M.A., and Roth, H.A. (1972). Conference on HTC in Gas Turbines, CEGB, Sudbury House, London.

Clelland, J., Taylor, A.F., and Wortley, L. (1974). *Proceedings of the 1974 Gas Turbine Materials in the Marine Environment Conference*, MCIC-75-27 (ed. J.W. Fairbanks and I. Machlin), 397. Columbus: Battelle Columbus Laboratory.

Condé, J.F.G. (1972). Specialist meeting on high temperature corrosion of aerospace alloys. In: *34th Meeting of the Structures and Materials Panel*. Lyngby, Denmark: AGARD.

Condé, J.F.G., Wareham, B.A., Hancock, P. et al. (1977). *Bib. High Temp. Chem. Phys. Mater.* 21: 41.

Cutler, A.J.B., Halstead, W.D., Laxton, J.W., and Stevens, C.G. (1971). *J. Eng. Power* 93: 307.

Danek, G.J. Jr. (1965). *Nav. Eng. J.* 77: 859.

Davis, J.R. (1997). *Heat Resistant Materials*. Materials Park, OH: ASM International.

Deb, D., Iyer, S.R., and Radhakrishnan, V. (1996). *Mater. Lett.* 29: 19.

DeCrescente, M.A. and Bornstein, N.S. (1968). *Corrosion* 24: 127.

El-Dashan, M.E., Stringer, J., and White, D.P. (1972). *Cobalt* 57: 182.

Elliott, P. (1989). *Mater. Perform.* 29 (4): 57.

Farrel, R.M., Hayman, C., and Dewey, M.A.P. (1970). *Colloquium*. Poole, Dorset: Admiralty Materials Laboratory.

Fryburg, G.C., Kohl, F.J., Stearns, C.A., and Fielder, W.L. (1982). *J. Electrochem. Soc.* 129: 571.

Giggins, C.S. and Pettit, F.S. (1980). *Oxid. Met.* 14: 739.

Gitanjaly, M. (2003). Role of high velocity spray coatings on hot corrosion of some superalloys. PhD thesis. Roorkee, India: Department of Metallurgical and Materials Engineering, IIT.

Gitanjaly, M. and Prakash, S. (1999). 5th NACE Proceedings, New Delhi, India (22–24 November), p. 174.

Gitanjaly, M., Prakash, S., and Singh, S. (2002). *Br. Corros. J.* 37: 56.

Goebel, J.A., Pettit, F.S., and Goward, G.W. (1973). *Metall. Trans.* 4: 261.

Grabke, H.J. and Meadowcroft, D.B. (eds.) (1995). *Guidelines for Methods of Testing and Research in High Temperature Corrosion*. London: The Institute of Materials.

Gurrappa, I. (ed.) (2015). *Gas Turbines-Materials, Modeling and Performance*. London: InTech Publishers Ltd.

Guttmann, V. and Merz, M. (eds.) (1981). *Corrosion and Mechanical Stress at High Temperatures*. London: Applied Science.

Halstead, W.D. (1970). *Colloquium*. Poole, Dorset: Admiralty Materials Laboratory.

Hancock, P. (1968). *Corrosion of Alloys at High Temperatures in Atmospheres Consisting of Fuel Combustion Products and Associated Impurities*. London: HMSO.

Hara, M., Honma, A., and Sato, Y. (1998). *J. Surf. Finish. Soc. Jpn.* 49: 507.

Hara, M., Okumura, H., Nakagawa, T. et al. (1995). *J. Jpn. Inst. Met.* 59: 1259.

Hidalgo, V.H., Varela, F.J.B., de la Calle, J.M., and Menendez, A.C. (2000). *Surf. Eng.* 16: 137.

High Temperature Technology (1989). Special issue on Hot-salt corrosion standards, test procedures and performance, 7 (4) November.

Hocking, M.G., Vasantasree, V., and Sidky, P.S. (1989). *Metallic and Ceramic Coatings: Production, High Temperature Properties and Applications*. Essex: Longman Scientific and Technical.

Jaffee, R.I. and Stringer, J. (1971). *High Temp. High Pressures* 3: 121.

Kanary, L.E., Caley, W.F., Hancock, H.A., and Hollingshead, R.S. (1987). *Mater. Sci. Technol.* 3: 571.

Kawakami, M., Goto, K.S., and Rapp, R.A. (1980). *Trans. Iron Steel Inst. Jpn.* 20: 646.

Lai, G.Y. (1990). *High-Temperature Corrosion of Engineering Alloys*. Materials Park, OH: ASM International.

Lee, W.H. and Lin, R.Y. (1999). *Mater. Chem. Phys.* 58: 231.

Li, M.H., Zhang, Z.Y., Sun, X.F. et al. (2003). *Surf. Coat. Technol.* 165: 241.

Luthra, K.L. and LeBlanc, O.H. Jr. (1987). *Mater. Sci. Eng.* 87: 329.

Miyagawa, O. and Yoshiba, M. (1981). *Proceedings of the 8th International Congress on Mettalic Corrosion*, vol. I, 662. Frankfurt: Dechema.

Okanda, Y., Fukusumi, M., Nenno, S., and Newkirk, J.B. (1983). *Metall. Trans. A* 14: 2131.

Paul, L.D., Ishwar, V.R., and Lai, G.Y. (1997). *Proceedings of CORCON-97*, vol. II, 493. Amsterdam: Elsevier Science.

Quets, J.M. and Dresher, W.H. (1969). *J. Mater. JMSLA* 4: 583.

Rahmel, A. (1972). *Corros. Sci.* 12 (265): 307.

Rahmel, A. (1987). *Mater. Sci. Eng.* 87: 345.

Rapp, R.A. (1986). *Corrosion* 42: 568.

Rapp, R.A. (2002). *Corros. Sci.* 44: 209.

Rapp, R.A. and Zhang, Y.S. (1998). *Molten Salt Forum* 5–6: 25.

Saunders, S.R.J. and Nichols, J.R. (1984). *Thin Solid Films* 119: 247.

Saunders, S.R.J., Evans, H.E., and Stringer, J.A. (eds.) (1994). *Mechanical Properties of Protective Oxide Scales*. London: Butterworth-Heinemann, 1995.

Schirmer, R.M., Quigg, H.T., and ASTM STP 421 (1967). *Hot Corrosion Problems Associated with Gas Turbines*, 270. Philadelphia, PA: American Society for Testing and Materials.

Sequeira, C.A.C. (1998). *Molten Salt Forum* 5–6: 417.

Sequeira, C.A.C. and Hocking, M.G. (1978a). *J. Appl. Electrochem.* 8: 145.

Sequeira, C.A.C. and Hocking, M.G. (1978b). *J. Appl. Electrochem.* 8: 179.

Sequeira, C.A.C. and Hocking, M.G. (1981). *Corrosion* 37: 392.

Seybolt, A.U. (1968). *Trans. Metall. Soc. AIME* 242: 1955.

Seybolt, A.U., Beltran, A., and ASTM STP 421 (1967). *Hot Corrosion Problems Associated with Gas Turbines*, 21. Philadelphia, PA: American Society for Testing and Materials.

Shifler, D.A. and Kohler, L.K. (1999). *Electrochemical Society Proceedings*, vol. 99-38, 282. Princeton, TX: The Electrochemical Society.

Sims, C.T. and Hagel, W.C. (1972). *The Superalloys*. London: Wiley.

Stringer, J. (1976). *Proceedings of the Symposium Properties of High Temperature Alloys with Emphasis on Environmental Effects* (ed. Z.A. Foroulis and F.S. Pettit), 513. Princeton, NJ: The Electrochemical Society.

Stringer, J. (1977). *Annu. Rev. Mater. Sci.* 7: 477.

Stringer, J. (1987). *Mater. Sci. Technol.* 3: 482.

Strochi, P.M., Vicentini, B., and Mosca, V. (1969). *Electrochim. Met.* 4: 339.

Tiwari, S.N. (1997). Investigations on hot corrosion of some Ni-,Fe- and Co base superalloys in environment under cyclic conditions. PhD thesis. Roorkee, India: Department of Metallurgical and Materials Engineering, UOR.

Tiwari, S.N. and Prakash, S. (1996). *Proceedings of Symposium on Metals and Materials Research*, 4–5 July, , 107. Madras, India: IIT.

Tiwari, S.N. and Prakash, S. (1997). Proceedings of SOLCEC, Kalpakkam, India, 22–24 January, Paper C33.
Viswanathan, R. (1968). *Corrosion* 24: 359.
Waddams, J.A., Wight, J.C., and Gray, P.S. (1969). *J. Inst. Fuel* 32: 246.
Wagenhein, N.T. (1970). *Cobalt* 48: 129.
Wu, W.T., Rahmel, A., and Schorr, M. (1983). *Oxidat. Met.* 19: 201.
Wu, C.X., Nishikata, A., and Tsuru, T. (1992). *High Temperature Corrosion of Advanced Materials and Protective Coatings* (ed. Y. Saito, B. Onay and T. Maruyama), 221. Elsevier Science.
Zetmeisl, M.J., Lawrence, D.F., and McCarthy, K.J. (1984). *Mater. Perform.* 23: 41.

Further Reading

Agarwal, A., Katipelli, L.R., and Dahotre, N.B. (2000). *Metall. Mater. Trans. A* 31A: 461.
Braunstein, J. and Selman, J.R. (eds.) (1981). The electrochemical society. Proceedings of 2nd International Symposium On Molten Salts. Princeton, New Jersey, USA.
Chatterjee, U.K., Bose, S.K., and Roy, S.K. (2001). *Environmental Degradation of Metals*. New York, NY: Marcel Dekker.
Haugsrud, R. (2003). *Corros. Sci.* 45: 211.
Hocking, M.G. (1993). *Surf. Coat. Technol.* 62: 460.
Johannesen, O. and Andersen, A.G. (eds.) (1989). *Studies in Inorganic Chemistry*, vol. 9. Amsterdam: Elsevier.
Rahmel, A. and Holmes, D.R. (eds.) (1978). *Materials and Coatings to Resist High Temperature Oxidation and Corrosion*. London: Applied Science Publishers.
Rapp, R.A. (1987). *Mater. Sci. Eng.* 87: 319.
Rapp, R.A. (1990). *Pure Appl. Chem.* 62: 113.
Rapp, R.A. and Zhang, Y.S. (1994). *JOM* 46: 47.
Rothman, M.F. (ed.) (1989). *High Temperatures Property Data: Ferrous Alloys*. Materials Park, OH: ASM International.
Schütze, M. (1997). *Protective Oxide Scales and Their Breakdown*. Chichester: Wiley.
Sims, C.T., Stoloff, N.S., and Hagel, W.C. (eds.) (1987). *Superalloys II*. New York, NY: Wiley.
Streiff, R., Stringer, J., Krutenat, R.C., and Caillet, M. (eds.) (1987). *High Temperature Corrosion of Materials and Coatings for Energy Systems and Turboengines*. Sequoia, Lausanne: Elsevier.

Chapter 16

Fireside Corrosion

16.1 Introduction

The problem of high temperature fireside corrosion in coal- and oil-fired steam generating plants, and generally in heat-recovery units, has been well recognized over the past decades.

Its practical importance is easily understood considering that damages are not always limited to the replacement of corroded tubes and to the consequent interruption of steam production. Indeed, the blowdown may cause well heavier losses as, for instance, the breaking off of steel production should the damage occur in a heat-recovery unit of a steel plant.

Since the end of World War II, when the first cases of fireside corrosion were experienced, a great deal of research has been conducted in order to elucidate corrosion mechanisms and to assess methods of preventing it. Soon it became apparent that corrosion was primarily due to the condensation from the flue gases, on the comparatively cool metal tubing surfaces, of highly aggressive deposits that, at the operating tube temperature, were soft or liquid. Whether such deposits come entirely from the flue gases or are formed through a reaction between flue gas component and tube metal has been a matter of speculation, and some issues have not yet been fully resolved. Nevertheless, the important point is that whatever the origin of deposits, their aggressiveness largely depends on their physical state, i.e. the molten or semi-molten state.

Deposits from fireside areas that have suffered external corrosion almost invariably contain appreciable quantities of alkali sulfates. The amount of such constituents largely depends on the nature of the burning fuel; it ranges from 35% to 50% sulfur reported as SO_3 in coal-fired furnaces to 25–45% in oil-fired units. In every case, such deposits are water soluble, with a pH as low as 3, the acidity being due to the excess of SO_3 in alkali sulfates released by hydrolysis. The nature of these complex deposits has been investigated since their existence was recognized more than 70 years ago. These sulfates are reported as complex trisulfates whose chemical stability depends primarily on temperature and SO_3 content of the atmosphere. Actually, their formation could be explained by the following reaction:

$$3K_2SO_4 + Fe_2O_3 + 3SO_3 \Longleftrightarrow 2K_3Fe(SO_4)_3 \quad (16.1)$$

Of the three reagents, at least two come from the flue gas and therefore from the fuel, the third, iron oxide, from the tube oxide scale. On the other hand, the formation of aluminum trisulfates, for example, may be entirely caused by reagents coming from the environments: that is the case of coal-fired furnaces where larger bulks of aluminosilicate materials come from combustion residues.

Obviously enough, the early investigations attempted to reproduce in the laboratory the corrosion phenomena encountered in the field. These investigations helped to understand the fundamental role of SO_3 in the progression of Reaction (16.1) as well as the importance of temperature level in deciding the stability of complex trisulfates. Their occurrence and hence their aggressiveness is restricted to a relatively narrow temperature range. Furthermore it was recognized that the SO_3 concentrations usually encountered in flue gases (25–35 ppm) were insufficient to progress Reaction (16.1) in laboratory experiments where a SO_3 concentration as high as 250 ppm was found necessary. Actually, the slow attainment of equilibrium of reaction

$$SO_2 + 1/2\,O_2 \Longleftrightarrow SO_3 \quad (16.2)$$

causes SO_3 to be only about 1% of the SO_2 in the flue gas. Thus, a good deal of research has been conducted to establish the catalytic effect of iron oxide surfaces to speed up the formation of SO_3 in Reaction (16.2) in order to explain the practical occurrence of complex trisulfates.

It has been a matter of controversy the mechanism through which the tube wastage by molten complex sulfates takes place. Some authors maintain that the metal loss is essentially due to the scale-destroying Reaction (16.1) in which complex sulfates are formed. Its progression depends on periodic tube deslagging and subsequent thermal decomposition of trisulfates to provide

High Temperature Corrosion: Fundamentals and Engineering, First Edition. César A. C. Sequeira.
© 2019 John Wiley & Sons, Inc. Published 2019 by John Wiley & Sons, Inc.

the necessary SO_3. Others believe that losses are due to a direct redox reaction of complex sulfates on the tube metal through a scale-creating irreversible pattern:

$$3Fe + SO_4^{2-} = Fe_3O_4 + S^{2-} \qquad (16.3)$$

Reactions (16.1) and (16.3) are somewhat different, the latter taking place at higher temperatures and its progression generating in addition to iron oxide also iron sulfate as corrosion product. Furthermore, the complex sulfates are generated in the ash deposits, and the contact between the tube metal and the corrodent is provided by migration of molten deposits under a thermal gradient.

Previous discussion has been confined to molten sulfates as cause of metal wastage in boilers. Actually in oil-fired units, deposits contain appreciable amounts of vanadium compounds. Vanadium comes from the oil, and vanadate formation takes place through an acid–base reaction in the flue gas with alkali metal species also coming from the fuel; vanadates subsequently condense on superheater tubes as liquid aggressive layers.

Other components that could be responsible for corrosion by flue gas deposits are chlorides. These can be found in both coal- and oil-fired boilers; the conditions of their occurrence, as well as their general behavior, are well described by Lai (2007). The conclusions are that excepting the case of nonequilibrium conditions in which anomalous situations may arise, chlorides entering the system with fuel will remain mostly in the gas phase without participating in the corrosion process. Therefore, as written previously, high temperature fireside corrosion in coal or oil burning boilers is best outlined by admitting the presence of molten or semi-molten deposits. Obviously, corrosion is affected by transport processes across deposits and by reactions occurring at gas–deposit interfaces and deposit-metal surfaces. The presence of a molten phase is a sufficient prerequisite to stimulate both transport processes and heterogeneous reactions, providing a more intimate contact between metal and corrodents. An additional factor is the presence of SO_3 (either as "excess" sulfate in complex sulfates or as dissolved sulfur trioxide) that, besides stabilizing the physical state of deposits, enhances corrosion by increasing the metal oxide solubility in the molten phase and, acting as oxygen carrier, by increasing the oxidizing power of deposits.

It is the aim of this chapter to briefly delineate mechanisms, remedies, materials problems, and other current views related with this field of high temperature fireside corrosion. A brief summary of industrial experience of fireside corrosion in Denmark, Germany, Holland, the United Kingdom, and Japan is also included.

16.2 Coal-Fired Boilers

The principle of a thermal power plant is to produce electricity by burning a fuel generally consisting of coal, biomass, or waste. Electricity is produced by the process of heating water in a boiler to yield steam. The steam under pressure, heated to high temperature in the superheater part, flows into a turbine, which drives a generator to produce electricity (Figure 16.1).

In today's conventional coal-fired power plants, the steam is brought to above 22 MPa and above 540 °C in a supercritical state.

Since the energy crisis in the 1970s, there has been a constant need for increasing the efficiency of thermal power plants. In other words, the development aimed at increasing the amount of electricity produced for the

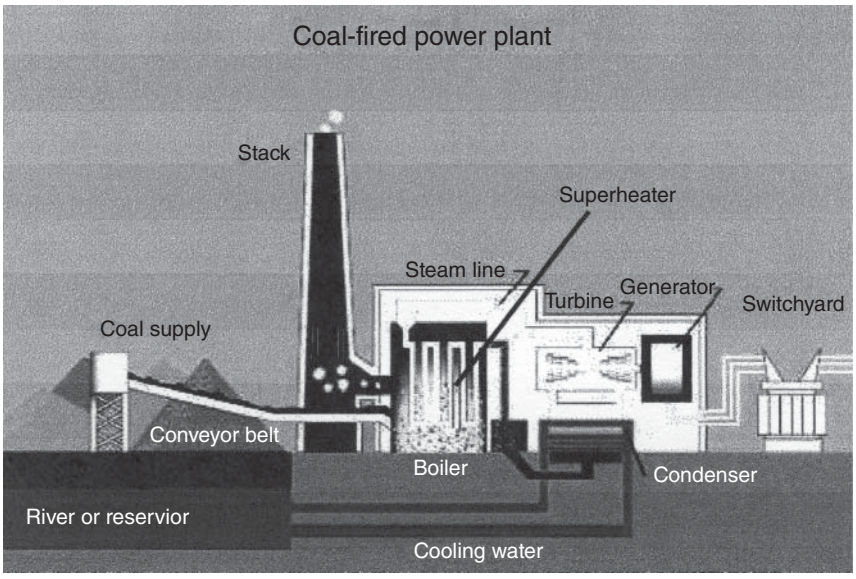


Figure 16.1 Principle of a coal-fired power plant.

same fuel consumption. The general route that has been followed consists of increasing the steam parameters, temperature, and pressure in the plant. As an example, the total efficiency of a plant increases by nearly 6% when changing the steam parameters from 538 °C/18.5 MPa to 593 °C/30 MPa. It could even reach an 8% increase at 650 °C (Viswanathan and Bakker 2000). One of the most modern coal-fired power plants commissioned in 2002 in Niederaussem in Germany demonstrates quite well the current state of the development with a fuel conversion efficiency of 43% and steam parameters up to 580 °C and 28 MPa (Heitmüller and Kather 1999). Furthermore, the Kyoto Protocol ratified in 1997 by many countries, including the European Union, plans a significant reduction of greenhouse effect gas emissions. These include first of all CO_2 but also NO_x (Kyoto Protocol 1997).

At the same time, predictions indicate that the global electricity demand will continue to increase at an average of 2% per year until 2020 (Parker 2002). To cover these new capacity demands, the global coal consumption is planned to increase by 60% between 2000 and 2020 (Figure 16.2). Coal is a cost-effective fuel, which will have a significant role at least until the efficiency of renewable energy products is improved in the next 20 years.

The electricity production from waste or biomass is also planned to increase. Waste firing offers a solution for reducing the increasing amount of waste, especially municipal waste. Biomass, like wood or straw, is a renewable fuel that can be considered as a long-term alternative to the decreasing amount of fossil sources.

Meeting both the Kyoto requirement and the increase of the electricity production leads to the need of improving the efficiency of the fuel to power conversion processes, which by extension means an increase of the steam parameters. For coal-fired systems, temperatures up to 720 °C or even 760 °C with a pressure of 35 MPa are currently under consideration in Europe and in the United States, respectively. The aim is to achieve a thermal efficiency of 60% by the year of 2020 (Ruth 2003).

The superheater tube temperatures often exceed the steam temperature by as much as 30 °C (Viswanathan 2004). This application thus requires a material with high temperature creep resistance. During the last decades, high temperature steels or more recently nickel-based alloys have demonstrated their potential with regard to high temperature creep strength. Nevertheless, metallic materials are well known for expanding when increasing the temperatures. The use of materials with low coefficient of thermal expansion is thus required in order to minimize the generated mechanical stresses. Moreover, the thermal conductivity of the superheater components has to be kept as high as possible in order to maximize the efficiency of the energy conversion. For building a superheater, several tubes must be welded together. Therefore, the weldability of the materials involved has also to be optimized.

Depending on the type of fuel, the combustion produces hot gases of various concentrations but is usually composed of O_2, CO_x, SO_x, HCl, H_2O, and NO_x. Furthermore, depending on the tube temperature, solid or liquid ashes and salts are deposited on the superheater tube surfaces. Table 16.1 gives the typical species found in various deposits. For coal-fired plants, the deposits contain usually sodium or potassium sulfates, whereas for waste-fired plants, the deposits are rather composed of alkali or heavy metal chlorides, due to the unceasing

Table 16.1 Typical salt deposits found on superheater tubes

Type of fuel	Typical salt deposits
Waste	$ZnCl_2$, $PbCl_2$, KCl, NaCl
Straw	KCl, K_2SO_4
Wood	KCl, K_2SO_4, NaCl, Na_2SO_4
Coal	Na_2O_4, K_2SO_4, $(Na,K)_2Fe(SO_4)_3$

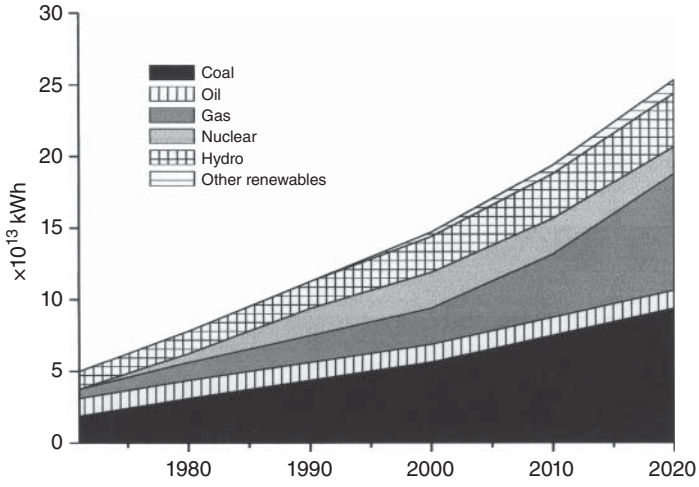


Figure 16.2 Trends in global electricity production from 1971 to 2020 (Parker 2002).

increase of the polyvinyl chloride (PVC) plastic content in refuses. Concerning biomass firing, the deposits are usually composed of potassium chlorides or potassium sulfates.

Molten sulfates and chlorides, as well as the gases mentioned earlier, are known for provoking corrosion damage at high temperature (Kofstad 1988). Moreover, on the inner side of the tube, the high temperature steam can lead to rapid oxidation. As a consequence, in addition to high creep strength, low thermal expansion, high thermal conductivity, and good weldability, the superheater tubes have to resist high temperature corrosion.

The mechanisms describing this form of corrosion are various and complex with strong dependence on the type of material and environment. They involve reactions such as oxidation, chlorination, carburization, sulfidation, and chemical/electrochemical in molten or semi-molten salt deposits. The reader can find detailed explanations on these reactions in Chapters 7 (oxidation), 8 (sulfidation), 9 (carburization), 11 (chlorination), and 13 (molten salts).

A major piece of the equipment in the power plant is the boiler, which generates steam that is then delivered to the turbine for generation of electricity. This section reviews materials issues and corrosion problems associated with utility boilers. Therefore, the boiler basics, including its description and types of coal and coal ash, are now presented to help readers to better understand these matters. Then, important high temperature materials and corrosion problems in coal-fired power plants will be discussed.

A large utility boiler consists of a large firebox, within which the combustion takes place. A number of burners are installed in the walls, through which the pulverized coal is blown. The walls of the firebox are manufactured with vertical tubes, typically between 70 and 100 mm of outside diameter, joined by webs of the order of 30 mm width. This is "membrane wall" construction. Preheated water enters the bottom of these walls, which are usually called the waterwalls, and boils at some location usually a little above the top of the burner array. The effective temperature in the combustion zone is in the range of 1200–1800 °C. As the combustion gases rise in the furnace, they cool; at the top of the furnace, the temperature is of the order of 1000–1200 °C, and the gas turns into a horizontal section. In this section, and sometimes at the top of the furnace itself, there are tubular platen heat exchangers hanging down into the combustion gas stream: these are commonly superheaters, and the principal corrosion problems are in the superheaters and the waterwalls (Meadowcroft 1987).

The majority of the utility boilers are subcritical recirculating boilers with a main steam pressure of approximately 16 MPa. The boiling point at this pressure is about 350 °C, and the outer surface of the waterwall tubes will be about 50 °C above this. The superheat temperature is 538 °C, and the maximum outer metal temperature in the superheater may be as much as 100 °C above this because of nonuniformities in the temperature distribution across the superheater bank.

The materials for the pressure parts are selected on the basis of their mechanical properties. For the lower temperature parts, the tensile strength is limiting; for the higher temperature parts, the creep strength is critical. The majority of the tubes, pipes, and drums are manufactured with plain carbon steel or low-alloy ferritic steels; the highest ferritic alloy normally used is T (or P) 22, which is essentially 2Fe–1/4Cr–1Mo. The very last sections of the superheater and reheater exchangers may be manufactured with austenitic steel (Meadowcroft and Manning 1983).

There are two main high temperature corrosion problems that may be identified in utility boilers:

1. The fireside corrosion of the superheaters and reheaters.
2. The fireside corrosion of waterwalls.

Figure 16.3 indicates the typically affected regions in a fuel-fired boiler.

There are several methods for burning coal. Firing with pulverized coal has been the most dominant method for utility boilers. Coal is burned as fine powders suspended in the furnace and almost all types of coal from anthracite to lignite can be burned by pulverized firing. Pulverized coal in particle sizes of 50 μm diameter or smaller can be completely combusted in a matter of one to two seconds.

Stultz and Kitto (1992) developed the cyclone furnace for firing coal grades that have a low fusion temperature and are not suitable for pulverized coal firing because of potentially forming a molten slag, thus developing a severe slagging problem in superheaters. In cyclone boilers, the cyclone barrels burn coal in such a way that most of the coal ash is captured to form a molten slag that coats the inside surface of the cyclone barrels. The combustion flue gas from the cyclone barrels then enters the main furnace to generate steam (Stultz and Kitto 1992).

There are four different types of coal. The youngest, or lowest-rank coal, is lignite, which is then followed by an older, or higher-rank subbituminous coal, then bituminous coal, and then anthracite coal. Heating values, moisture content, volatile matter content, ash content, and sulfur content can be different among these different types of coal. Bituminous coal is the most commonly used coal for utility boilers in the United States. Subbituminous coal in the United States generally contains very low sulfur, with many deposits containing less than 1%. Table 16.2 shows the properties of some US coal. There is a great variation in moisture, ash content, ash softening temperatures, and sulfur content from various grades of coals. The material factors associated with coal can directly or indirectly affect the boiler tube material performance at different locations in the boiler.

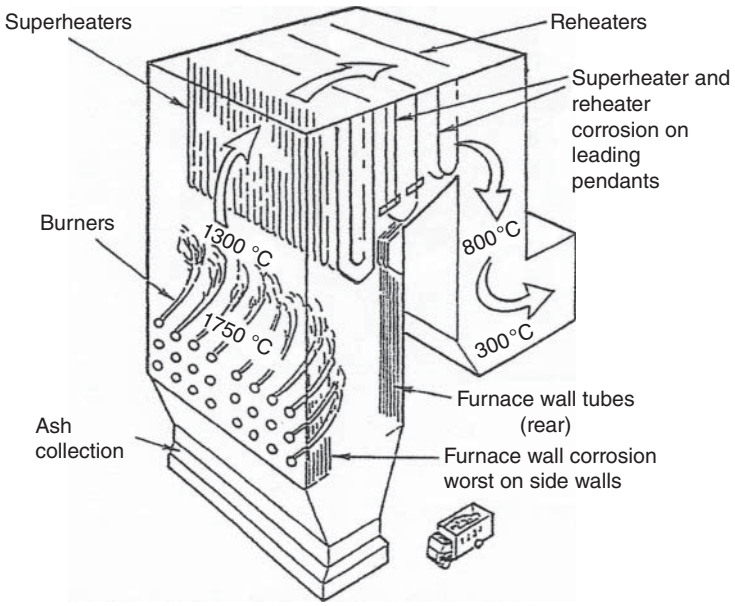


Figure 16.3 Schematic of a typical fuel-fired boiler showing areas of corrosion.

Table 16.2 Properties of several types of US coal (Stultz and Kitto 1992)

	Coal type			
Property	Anthracite	Illinois #6 bituminous, Illinois	Spring Creek subbituminous, Wyoming	Bryan lignite, Texas
Approximate composition (%)				
Moisture	7.7	17.6	24.1	34.1
Volatile matter, dry	6.4	44.2	43.1	31.5
Fixed carbon, dry	83.1	45.0	51.2	18.1
Ash, dry	10.5	10.8	5.7	50.4
Composition (%)				
Carbon	83.7	69.0	70.3	33.8
Hydrogen	1.9	4.9	5.0	3.3
Nitrogen	0.9	1.0	1.0	0.4
Sulfur	0.7	4.3	0.4	1.0
Oxygen	2.3	10.0	17.7	11.1
Ash	10.5	10.8	5.7	50.4
Thermal properties				
Heating value (as received) Btu/lb	11 890	10 300	9 190	3 930
Ash fusion temperatures (reducing atmosphere) (°F)				
Initial deformation	—	1 930	2 100	2 370
Softening	—	2 040	2 160	2 580
Fluid	—	2 700	2 700	2 900+
Ash analysis[a] *(%)*				
SiO_2	51.0	41.7	32.6	62.4
Al_2O_3	34.0	20.0	13.4	21.5
Fe_2O_3	3.5	19.0	7.5	3.0
TiO_2	2.4	0.8	1.6	0.5
CaO	0.6	8.0	15.1	3.0
MgO	0.3	0.8	4.3	1.2
Na_2O	0.7	1.6	7.4	0.6
K_2O	2.6	1.6	0.9	0.9
P_2O_5	—	—	0.4	—
SO_3	1.4	4.4	14.6	3.5

[a]Elements present in the ash are determined and reported as oxides.

Sulfur is the most important impurity in coal for causing high temperature corrosion in the boiler. Sulfur is present in coal in the form of organic sulfur, pyritic sulfur (i.e. pyrite), and iron sulfate. High sulfur coals also cause SO_x emission problems and require expensive air pollution control equipment. As a result of the US Federal Clean Air Act emissions issues, the low sulfur Powder River Basin (PRB) coal (a subbituminous coal) has become extremely popular in the past years. The PRB coal, which is from mines in southern Montana through northern Wyoming, contains less than 0.6 kg of sulfur per million Btu, making it compliant with the Clean Air Act emissions limits without air pollution control equipment.

One of the important characteristics of ash is its fusion temperature. Table 16.2 lists the ash fusion temperatures of several coals under reducing conditions. These fusion temperatures can affect the nature of the ash deposits, whether in the form of "dust" or a tenacious slag. If ash reaches the heat-absorbing surface at a temperature near its softening temperature, the resulting deposits are likely to be porous and can be easily removed by sootblowing. Also, if such a deposit is subjected to high gas temperature, the ash deposit can reach its melting point (due to the thermal insulating properties of the ash) and run down the furnace wall surface. This solidified slag is tightly bonded and is difficult to remove. This slag may require water lances or water cannons to create thermal shock for the removal of this slag deposit. The furnace walls that are subject to radiant heat are likely locations for developing this *slagging* problem.

The analyses of ash for several types of US coal are shown in Table 16.2. The compositions shown in Table 16.2 are presented as oxides. However, most ash constituents in coal are minerals. Typical minerals found in coal are shown in Table 16.3. When these minerals are exposed to oxidizing environments at appropriate high temperatures, oxides and/or complex salts are formed as stable phases. This is illustrated in Table 16.4.

If the ash constituents are present as oxides, the ratio of basic oxides (e.g. Fe_2O_3, CaO, MgO, Na_2O, and K_2O) to acidic oxides (e.g. SiO_2, Al_2O_3, and TiO_2) may determine the fusion (fusibility) temperature of the reaction product. It was reported that the ash may exhibit low fusibility temperature with higher slagging potential when its base–acid ratio is in a range of 0.4–0.7. Many other parameters, such as SiO_2/Al_2O_3 ratio, Fe_2O_3/CaO ratio, $Fe_2O_3/(CaO + MgO)$ ratio, $(Na_2O + K_2O)$, and so forth, are also used for predicting the fusibility temperature of the coal ash. It has been suggested that SiO_2 is more likely than Al_2O_3 to form lower-melting species. The fusibility temperature of coal ash will be lowered when the Fe_2O_3/CaO ratios are in a range of 0.2–10. Alkalis are important in affecting the fusibility of coal ash and the furnace slagging potential. Many sodium compounds melt at temperatures below 900 °C, playing an aggressive role in fireside corrosion.

Chlorine content is also an important indication for *fouling* potential. When chlorine in coal is greater than 0.3%, fouling potential becomes high. Alkali metals and chlorine can also play a significant role in high temperature corrosion in boilers.

Table 16.3 Typical mineral species found in coal

Mineral species	Formula
Kaolinite	$Al_2O_3 \cdot 2SiO_2 \cdot H_2O$
Illite	$K_2O \cdot 3Al_2O_3 \cdot 6SiO_2 \cdot 2H_2O$
Biotite	$K_2O \cdot MgO \cdot Al_2O_3 \cdot 3SiO_2 \cdot H_2O$
Orthoclase	$K_2O \cdot Al_2O_3 \cdot 6SiO_2$
Albite	$Na_2O \cdot Al_2O_3 \cdot 6SiO_2$
Calcite	$CaCO_3$
Dolomite	$CaCO_3 \cdot MgCO_3$
Siderite	$FeCO_3$
Pyrite	FeS_2
Gypsum	$CaSO_4 \cdot 2H_2O$
Quartz	SiO_2
Hematite	Fe_2O_3
Magnetite	Fe_3O_4
Rutile	TiO_2
Halite	NaCl
Sylvite	KCl

Source: Singer (1991).

Table 16.4 Melting points of coal-ash constituents

Element	Oxide	Melting point, °C (°F)	Compound	Melting point, °C (°F)
Si	SiO_2	1715 (3120)	Na_2SiO_3	877 (1610)
Al	Al_2O_3	2043 (3710)	K_2SiO_3	977 (1790)
Ti	TiO_2	1838 (3340)	$Al_2O_3 \cdot Na_2O \cdot 6SiO_2$	1099 (2010)
Fe	Fe_2O_3	1565 (2850)	$Al_2O_3 \cdot K_2O \cdot 6SiO_2$	1149 (2100)
Ca	CaO	2521 (4570)	$FeSiO_3$	1143 (2090)
Mg	MgO	2799 (5070)	$CaO \cdot Fe_2O_3$	1249 (2280)
Na	Na_2O	Sublimes at 1277 (2330)	$CaO \cdot MgO \cdot 2SiO_2$	1391 (2535)
K	K_2O	Decomposes at 349 (660)	$CaSiO_3$	1540 (2804)

Source: Singer (1991).

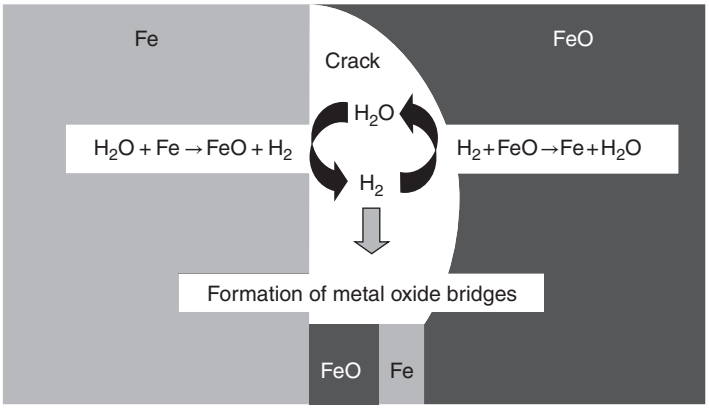


Figure 16.4 Acceleration of the oxidation mechanism by the formation of metal oxide bridges due to the presence of H_2/H_2O in a crack between iron and wustite (Rahmel and Tobolski 1965). The same mechanism applies for CO/CO_2.

We have been discussing complex corrosion phenomena and other issues in typical boilers being evident that to help the reader's understanding, the important high temperature corrosion aspects in coal-fired power plants should be rapidly summarized at this stage.

In coal-fired power plants, besides corrosion damage due to molten salts, corrosion can occur by oxidizing flue gas and other reactions as already reported. Depending on the way the combustion is carried out, the gases emanating from the combustion can be either reducing or oxidizing. The typical gaseous species encountered in oxidizing conditions are O_2, NO_x, HCl, SO_x, H_2O, and CO_x.

With respect to the high sulfur content in some types of coals, particular attention has to be given to sulfur-containing gases. Indeed, it is well known that in most cases, sulfidation kinetics are much faster than those of oxidation and that sulfides are usually non-protective other than oxides.

The second corrosive element is chlorine, which is usually found as HCl in combustion products. Chlorine is particularly detrimental because of the formation of low temperature eutectic melts and high volatile metallic chlorides that can form at high temperature and lead to rapid metal loss. Furthermore, Rahmel and Tobolski (1965) proposed a mechanism explaining the acceleration of the oxidation of pure iron in the presence of water vapor or CO_2. This mechanism is based on the formation of cracks within the oxide scale. After some time, these cracks are filled with H_2O/H_2 or CO_2/CO, respectively. As shown in Figure 16.4 for H_2O-affected oxidation, a repeated reduction of H_2O at the metal surface and oxidation of H_2 at the gas–oxide interface is put in place within the crack. As a consequence, the presence of H_2O or CO_2 enables further oxidation of the metal without substantial inhibition. This mechanism is still accepted nowadays. Many studies focused on the corrosion mechanisms of one or two types of corrosive species, for example, SO_x or SO_x combined with O_2 as reviewed by Kofstad (1988). Others focused on the effect of chlorine, in particular HCl combined with O_2 (Zahs et al. 1998). On the other hand, in-plant studies are generally governed by molten salt corrosion and are hardly comparable due to differences in plant operation and the difficulty for precisely analyzing the combustion gases. In fact, there seems to be only a limited number of studies addressing the corrosion resistance of 9–12% Cr steels in simulated coal firing flue gas, containing three or more oxidizing species, as will be presented later.

Fireside corrosion of the steam-containing superheater and reheater tubes due to the deposition of fuel impurities from the flue gas at its highest temperature is a significant problem, and considerable research has been carried out concerning this corrosion process. Since it has been shown that accelerated wastage of superheater and reheater tubes occurred under an ash deposit, much research work has involved exposing metals and alloys to molten salt baths, building up a thin sulfate film of around 1–2 mm thickness, to replicate typical deposits found on the tubes (Figure 16.5).

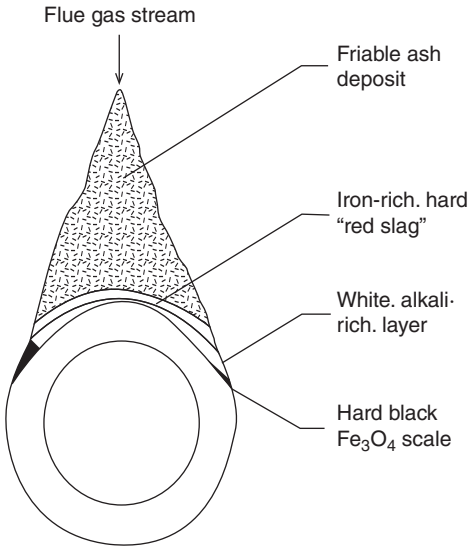


Figure 16.5 Section showing deposit layers on a leading superheater or reheater tube.

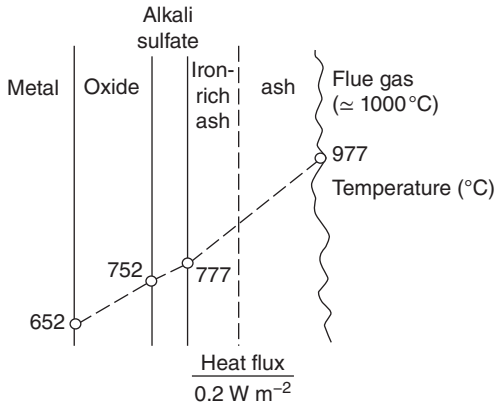


Figure 16.6 Schematic of a typical thermal gradient through a deposit from flue gas to superheater metal.

The black inner layer is iron oxide, essentially Fe_3O_4, and is typically 2.20 μm thick. The white layer contains majorly sulfates of Na, K, and Al, with some Fe. This is the molten sulfate layer and is usually around 1 mm thick. The "red slag" layer is high in Fe, low in alkali, and with a sulfate content intermediate between that of the white deposit and the ash. The adhering fly ash is rich in Fe_2O_3 and remains porous, even if sintered. Dissolution of both white and red layers in water produces acidic solutions.

Figure 16.6 shows the temperature distribution through the system for a typical set of conditions. This diagram is however oversimplified. The overall heat flux to a superheater tube is of the order of 0.2 MW m^{-2}. It is however evident from Figure 16.5 that the thickness of the insulating ash layer is greater at the front, leading, position of the tube than the rear, trailing, area. This results in a variation in the heat flux around the tube. Wastage takes place at the "2 o'clock" and "10 o'clock" positions relative to the flow of the flue gases, the "12 o'clock" position. The heavy buildup of ash on the front surface reduces the temperature flux within the deposit below that required for the salt layer to be molten. The thinner ash levels at the side of the tube allow for a higher heat flux, and a molten layer beneath, at the deposit–metal interface.

The origin and role of the molten salt layer, and its associated fly ash, may be summarized as follows. The cations arise largely from the clay component of the coal, and the sulfate ions from the oxidation of the sulfur in the fuel to SO_2. The air entering the combustion chamber contains about 10% more oxygen than necessary for stoichiometric combustion, and Fe_2O_3 in the fly ash acts as a catalyst to convert the SO_2 to SO_3. Fuels containing vanadium, such as fuel oil, often used in the start-up process in boilers, provide an even more effective catalyst for SO_3 formation. SO_3 readily dissolves in the molten sulfate, forming essentially pyrosulfate ions $[S_2O_7]^{2-}$: SO_3 and O_2 are the main oxidants and SO_2 is insoluble in sulfate melts.

The SO_3 present in the flue gas has the major effect on the corrosion of metal tubes, since this determines the oxidizing potential of the sulfate deposit, in terms of the redox equilibria:

$$SO_3 + 2e^- \Longleftrightarrow SO_2 + O^{2-} \tag{16.4}$$

The corrosion process is thus two separate reactions. First, an anodic oxidation, by

$$M \rightarrow M^{n+} + ne^- \tag{16.5}$$

to form metal ions in the corrodant (n may be 2 or 3 but here will be assumed as 2). Thus

$$Fe \rightarrow Fe^{2+} + 2e^- \tag{16.6}$$

Second, the cathodic reaction is transfer of electrons to the oxidizing agent

$$Ox + ne^- \rightarrow Ox^{n-} \tag{16.7}$$

More specifically, for the reduction of SO_4^{2-} and/or SO_3, we can write

$$SO_4^{2-} + 8e^- \rightarrow S^{2-} + 4O^{2-} \tag{16.8}$$

$$SO_3 + 8e^- \rightarrow S^{2-} + 3O^{2-} \tag{16.9}$$

These equations are oversimplified and the reaction mechanism is better understood by considering a steady state in which SO_2 and O_2 from the flue gas enter the porous fly ash. The catalytic action of Fe_2O_3 then produces equilibrium concentrations of SO_3. SO_3 dissolves in the melt and migrates to the oxide–melt interface. Then, it diffuses through the porous oxide to the oxide–metal interface.

$$2SO_3 + 8e^- \rightarrow SO_4^{2-} + S^{2-} + 2O^{2-} \tag{16.10}$$

This is regarded as the overall result of the electrode Reactions (16.6) and (16.7). Solid metal oxides and sulfates result from the subsequent oxidation of the metal together with metal ions in the sulfate melt. Dissolution of the metal oxides at the oxide–melt interface takes place, viz.

$$MO(S) \rightarrow M^{2+}(l) + O^{2-}(l) \tag{16.11}$$

with some of the metal sulfide being converted to the oxide, introducing imperfections in the oxide scale as it forms.

The solubility and stability of the dissolved metal ions in the melt is dependent upon both SO_3 partial pressure and temperature, increasing with increase in SO_3 content, but decreasing with increasing temperature. A mutual opposition is thus seen for the effects of SO_3 partial pressure and temperature on traversing from the oxide–melt to the melt–fly ash interface such that a temperature is reached

where the dissolved metal ion is precipitated as the oxide. A resulting concentration gradient of dissolved metal ions across the melt was thus envisioned and has been shown (Griffiths et al. 1982).

The corrosion process is therefore considered as the continuous dissolution of metal and metal oxide, reprocessing to form a non-protective layer at the melt–fly ash interface. Considering all the factors involved, the rate-determining step for the dissolution of the protective layer that the steel tubes generate, the overall rate of corrosion process, is that of the diffusion of metal ions away from the metal–metal oxide interface.

The transition metal ions from the steel tubes in the sulfate melt do not behave like the alkali metal ions Na^+ and K^+ – they form complexes with the sulfate ions:

$$M^{2+} + 3SO_4^{2-} \rightarrow [M(SO_4)_3]^{4-} \qquad (16.12)$$

The evidence for this comes from the electronic absorption spectra of such melt systems. The spectra obtained all correspond to the presence in solution of the metal ions surrounded octahedrally by six oxygen atoms. It is therefore concluded that each of the metal ions has three bidentate sulfate ions coordinating to it.

In 2002, Masuyama presented a review of the last 50 years of alloy development for power plant applications. Four generations of the evolution of ferritic steels since the 1950s are distinguished on the basis of their creep properties. The alloy development has indeed been motivated by the enhancement of the creep strength. The 10^5 hour creep-rupture strength at 600 °C is the parameter typically used for alloy classification (Figure 16.7). It reaches 140 MPa in the current state of the art. But among the commercialized 9% Cr steels, the P91 has been extensively used for heaters and steam pipes in plants operating at temperatures up to 593 °C.

From a metallurgical point of view, the steels presented in Figure 16.7 are either called ferritic or martensitic steels. In fact, both designations are correct depending on the heat treatment. For instance, P91 results from a specific heat treatment that consists of an austenitization step followed by rapid cooling for the martensitic transformation. A subsequent tempering is then required to transform part of the martensite into ferrite and allow carbides to precipitate homogeneously within the martensite.

The steel development shown in Figure 16.7 has mainly consisted of adding alloying elements with strengthening effects (Viswanathan and Bakker 2000). W, Cr, Mo, and Co are used for solid solution strengthening, and the latest tendency was to replace Mo by the more beneficial W. W, Cr, and Mo also contribute to precipitation strengthening by formation of carbides, whereas V and Nb used in junction with N contribute to precipitation strengthening by forming carbonitrides. Although carbon is required for the fine carbide precipitation, the carbon content remains limited, below 0.12 wt%, in order to obtain a good weldability. Nickel additions improve the toughness but are detrimental to creep strength. Therefore, some developments, such as for HCM12A, consisted of replacing part of the Ni by Cu. Finally, Cr additions have been rather motivated by the enhancement of the corrosion resistance, which will be discussed.

The oxidation resistance of 9–12% Cr steels, especially the P91, has been extensively studied in various environments including air in order to simulate fireside corrosion.

It was demonstrated that changes of the surface conditions of the 9% Cr steels influence the formation of a protective chromia layer (Grabke et al. 1997), in

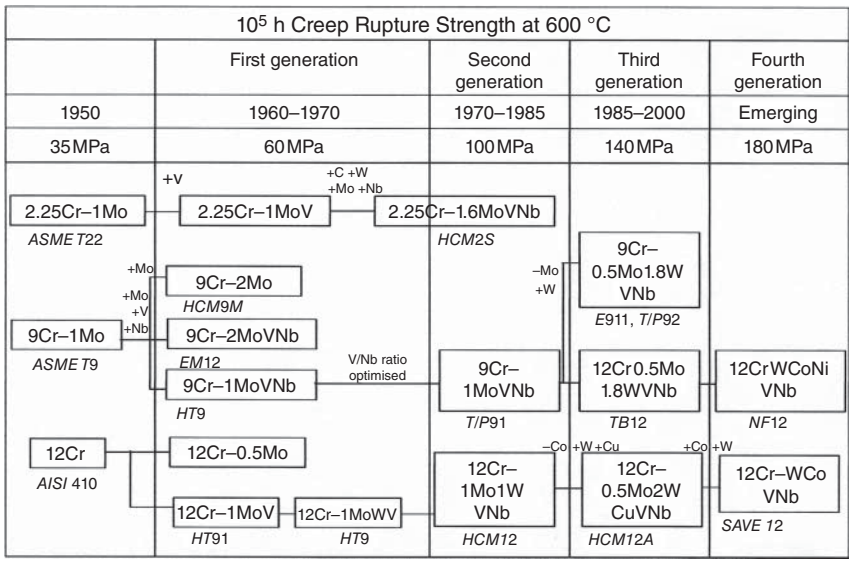


Figure 16.7 Development progress of ferritic steels (Masuyama 2002). Some commercial steels are indicated in italics.

particular during the very early stage of oxidation. First of all, the early formation of chromia is strongly influenced by the Cr diffusivity toward the surface. This is enhanced when the dislocation density is increased by previous deformation of the subsurface zone, using sandblasting, for instance (Ostwald and Grabke 2004). Moreover, in the first 10–15 minutes of oxidation, local effects are of great importance. Fast Cr diffusion along grain boundaries lead to the nucleation and growth of chromia. However, in other areas, formation of less protective Fe-rich oxides was reported for 9% Cr, whereas a Cr content higher than 11% is more favorable for the formation of Cr-rich oxides without local differences (Grabke et al. 2004).

By considering exposure times of several thousand hours, the minimum Cr content required for the formation of a protective chromia scale was estimated to about 7.2 wt% (Vossen et al. 1997).

Obviously, a little drop in the Cr content completely changes the nature of the oxide scale. As a consequence, the evolution with time of the Cr content in the subsurface zone has to be considered with care. Indeed, the oxidation is consuming Cr; thus, after some time, the Cr concentration falls under the level required for forming the protective oxide layer. This can be particularly detrimental in the case of scale cracking, because the Cr-depleted metal is then directly in contact with the corrosive environment. The resulting oxide scale is thus not protective anymore. This phenomenon explains the high corrosion rates observed for cyclic oxidation (Pillai et al. 2004). In this case, scale cracking is accelerated due to the repeated cooling process and leads to accelerated Cr depletion.

Grünling et al. (1979) reviewed the corrosion mechanisms that can lead to a decrease in creep resistance. A few examples of these mechanisms are pore formation near the surface due to the growth of an oxide scale by cationic diffusion, depletion of the matrix in solid solution-hardening elements as a result of selective oxidation, decomposition of hardening precipitates, and enhanced grain boundary slip by diffusion of noxious elements into the grain boundaries. More recently, it has also been suggested that injection of vacancies deep into the metal due to cationic oxidation may also play a role in the reduction of creep resistance due to oxidation (Dryepondt et al. 2005).

As mentioned before, the heat exchanger tubes are submitted to several constraints, resulting in creep, e.g. due to the high pressures inside the tube or other operational parameters. The formation of thick oxide scales has therefore several consequences for the service behavior of components:

1. The loss of material reduces the availability load-bearing cross section, so that as oxidation proceeds, the stresses acting on the component increase. The magnitude of the effect will, of course, depend on the initial wall thickness and the oxidation rate. By considering creep data measured in air as well as the oxidation rates mentioned earlier for steam and simulated coal firing, Ennis et al. (1993) and Nickel et al. (1998) evaluated the influence of oxidation on the creep resistance. For example, for a thin-walled heat exchanger tube of about 5 mm wall thickness, the reduction of the load-bearing cross section due to corrosion would have severe consequences for service life.
2. The thermal insulation effect of a thick oxide scale, which reduces the heat transfer across the component wall, can lead to overheating. A small increase in component operating temperature can reduce the stress-rupture life considerably.
3. The matrix becomes depleted in those elements that are selectively oxidized to form the thick oxide scales, leading to microstructural changes and associated potential effects on the long-term strength. This effect has been investigated in particular by comparing the creep-rupture time in air of specimens preoxidized in steam with heat-treated specimens (Ennis et al. 1993).

By the same method of testing the creep resistance in air of specimens preoxidized in steam, Schütze et al. (2004) investigated the effect of load on the oxidation behavior. This method particularly allowed comparing the healing properties of the oxide scale. Indeed, the imposed load brings the oxide scale to crack. The ability of the material to reform a protective scale will thus be crucial for its lifetime. For 9% Cr steels, it was shown that silicon offers some advantages for healing the protective oxide scale, but this effect is spoiled in the presence of Mo in dry environment.

The preceding description of the properties of 9–12% Cr steels shows that further increasing the heat exchanger temperatures will require higher corrosion resistance and creep strength. If this has to be achieved with chromia-forming alloys, higher Cr contents are required (Staubli et al. 2002; Viswanathan et al. 2002). Table 16.5 shows the benefit of higher Cr contents with regard to corrosion resistance.

Furthermore, steam oxidation tests showed that depending on the grain structure, a minimum of 20–25 wt% is recommended for forming protective Cr_2O_3 oxide scale at 650 °C (Otsuka et al. 1989). This amount lies clearly above the limit of martensitic steels, and since body-centered cubic ferritic steels have poor mechanical properties, the ferritic–martensitic steels are preferentially replaced by austenitic steels or Ni-based alloys. However, at higher temperature, the low Cr diffusivities in austenitic steels limit the Cr supply toward the metal–oxide interface and therefore the ability of the alloys for healing a cracked oxide scale. In austenitic steels, increasing the Ni content

Table 16.5 Comparison of the properties of the ferritic–martensitic steel P91 (Haarmann et al. 2002), the austenitic steels AISI 347H (Wegst 1995), Incoloy Alloy 800, and the nickel-based Inconel Alloy 617

Type of material	Concentration in wt%		Coefficient of thermal expansion (10^{-6} K^{-1})[a]	Thermal conductivity at 650 °C (W m^{-1} K^{-1})	10^5 h Creep rupture stress		Hot corrosion weight loss at 650 °C/5 h[b]
	Cr	Ni			650 °C	550 °C	
Ferritic–martensitic P91	9	—	12.7	30	48	162	>40
Austenitic AISI 347H (1.4961)	17	13	18.6	24	64	170	17
Austenitic Alloy 800	20	32	17.3	22	60	200	10
Ni-based IN617	22	Bal.	14.4	23	160	–	10

[a]Coefficient of linear thermal expansion from room temperature to 650 °C (10^{-6}/°C).

[b]The corrosion data is taken from Ikeshima for simulated coal firing tests with molten salts (Ikeshima 1983).

seems to have a beneficial effect on the resistance to water vapor oxidation (Peraldi and Pint 2004). However, when comparing other properties of these materials, not only the higher costs are a drawback for the replacement of ferritic–martensitic steels. Firstly, the lower thermal conductivities of austenitics and nickel-based materials limit the heat transfer (Table 16.5). Secondly, a higher thermal expansion has to be taken into account for plant design. This also means that the thermal expansion mismatch between the alloy and the oxide scale is higher, resulting in a higher tendency for oxide spallation. Thus, even though some austenitic steels form a thin protective Cr_2O_3 layer, with a thermal expansion of about 8×10^{-6} K^{-1} (Robertson and Manning 1990), this might spall off due to temperature changes. For comparison, up to 400 °C, the thermal coefficient for magnesite lies between 11 and 14×10^{-6} K^{-1} (Armilt et al. 1978), which is close to the expansion of P91. The tendency for oxide scale spallation is thus higher on austenitic steels compared with ferritic–martensitic ones. The concern is that spalled flakes appearing inside the exchanger tube lead to erosion and blocking of the steam turbine components. Yet, Peraldi and Pint (2004) observed that increasing the Ni content in austenitic steels reduces spallation. A minimum of 20 wt% Ni is nonetheless recommended for observing a significant effect at 650 °C.

Eventually, from a mechanical point of view, ferritic–martensitic steels offer the best creep properties at low temperature. The most recent modifications could be used up to 650 °C. Furthermore, austenitic steels can be used in a small range up to 670 °C. Higher temperatures require the use of Ni-based alloys (Smith and Shoemaker 2004; Viswanathan et al. 2002).

16.3 Coal-ash Corrosion

Corrosion in coal-fired boilers is frequently referred to as *coal-ash corrosion* particularly when the aggressive phenomena are mainly due to the nature of the ash that deposits on the heat-absorbing surfaces of metallic components (waterwalls, superheater, and reheater tubes of boilers and furnaces).

The waterwall tubes can undergo a very rapid wastage even though the metal temperature may have been over 400 °C and sometimes would have been cooler than this. In the vicinity of the combustion zone, much of the ash will still be molten, and some of this is deposited on the waterwalls as a slag layer. The combustion zone is designed to be located in the center of the furnace enclosure, at a distance from the walls. Poor adjustment of the burners, wear of the burner nozzles, a change in the combustion characteristics of the coal, or several other factors can result in the combustion zone being displaced, or simply being larger than had been expected. In this case, the slag deposit in the region where the combustion zone approaches the walls contains unburnt carbon and unoxidized pyrite. It is under these circumstances that rapid wastage can result.

Early investigators thought that this wastage was also associated with alkali sulfate species. In fact, alkali sulfates deposited on the waterwalls may react with SO_2 or SO_3 to form pyrosulfates, such as potassium pyrosulfate ($K_2S_2O_7$) and sodium pyrosulfate ($Na_2S_2O_7$), or possibly complex alkali iron trisulfate. The latter compounds are formed in thicker deposits after long periods of time at about 480 °C. The K_2SO_4–$K_2S_2O_7$ system forms a molten salt mixture at 407 °C when SO_3 concentration is 150 ppm. The corresponding sodium system can become liquid at about 400 °C, but it requires about 2000 ppm SO_3 for this to occur; such levels of sulfur oxides are likely only under deposits. Thus, molten salt attack on the tube metal by $K_2S_2O_7$ is more likely and occurs according to the reaction

$$K_2S_2O_7 + 3Fe \rightarrow FeS + Fe_2O_3 + K_2SO_4 \qquad (16.13)$$

By such a mechanism, $K_2S_2O_7$ can react aggressively with any protective iron oxide scales on the tubes and lead to accelerate wastage through fluxing of the oxides and attack of the substrate metal. Differential scanning calorimetry (DSC) of samples of deposits taken from

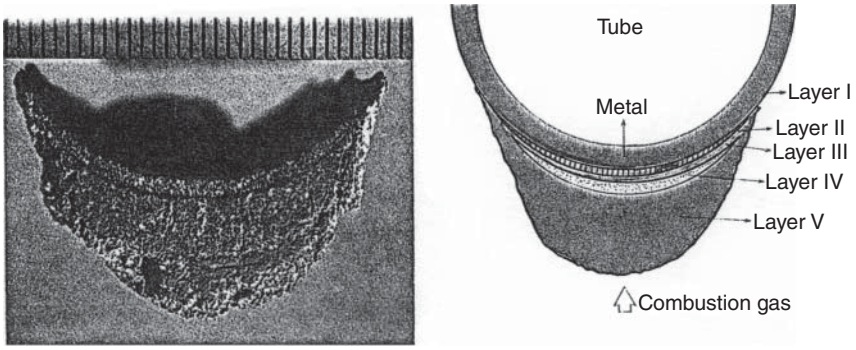


Figure 16.8 Profile of a scale and deposit formed on the test probe after 6000 hours' exposure.

waterwall tubes typically indicates melting points in the range of 335–410 °C.

There is also general agreement that the waterwall fireside corrosion is caused by localized reducing conditions.

Laboratory corrosion test and probe test in actual coal-fired boiler were made to clarify the corrosion mechanism and evaluate corrosion resistance of commercial alloys in coal combustion atmosphere of ultra-supercritical units (Rothman 1984).

Picture and illustration of scale and deposit formed on 17–14CuMo steel test probe are shown in Figure 16.8. The scale and deposit is recognized as five different layers by the chemical compositions as shown in Table 16.6. The main corrosion product was iron oxide (layer 3) formed on the internal Cr sulfide and oxide (layers 1 and 2). Alkali sulfates were involved in these porous scales. Based on the analysis of the scale in the above probe test and laboratory tests, the coal-ash corrosion mechanism by the sequence illustrated in Figure 16.9 was suggested. It was concluded that the corrosion was a catastrophic oxidation explained by acidic–basic fluxing model mediated with molten alkali iron sulfate.

Consequently, it was clarified that the potential for coal-ash corrosion is expressed as functions of temperature, SO_2 content in the flue gas, and alkali sulfate content in the ash. However, the degree of dependence on each varies with material. Therefore, *isocorrosion diagrams* as a function of SO_2 and alkali sulfates at various temperatures for various material types are useful for obtaining the practical corrosion rate. In the task for coal-ash corrosion of EPRI research project "Boiler R&D for Improved Coal-Fired Plants," isocorrosion diagrams for many candidate materials were made. An example of isocorrosion diagram is shown in Figure 16.10. Note that the isocorrosion curves are well coincident with the result of the probe test in an actual boiler.

Table 16.6 Summary of the analysis of the scale and deposit formed on the Cu/Mo steel test probe

Designation	Elements detected	Remarks
Layer I	Cr, Fe, Ni, Mo, O, S, K	Cr sulfide is predominant Mo is concentrated K is penetrated between slides and scales
Layer II	Cr, Ni, Fe, O, Mo, S (Mo and S exist only in the interface of Layer I)	Cr oxide is predominant Ni sulfide is formed in the interface of Layer I
Layer III	Fe, O, K, Ni, S, Al	Fe oxide is predominant
Layer IV	Ca, Fe, Mg, Al, Si, K, O, S	Ca sulfate is predominant
Layer V	Fe, Al, Si, Ca, Mg, K, O, S	Fe, Al, and Si oxides are predominant

The comparison of corrosion resistance for 12 commercial alloys under the condition simulating a high sulfur coal combustion atmosphere is shown in Figure 16.11. It suggests that the alloys containing over 25% Cr show satisfactory corrosion resistance.

Solutions to fireside corrosion of furnace waterwalls are available from changes in operating procedures and changes in tube materials. Where the corrosion results from the presence of reducing conditions near the waterwalls, operational actions include adjusting the air and fuel distribution to individual burners and among burners in order to promote better mixing and more uniform combustion conditions, as well as resetting to design specification the coal fineness delivered to burners from the milling plant. Flame impingement can be rectified by changing the characteristics of the offending burners through adjustment of secondary air registers to control airflow and degree of swirl.

Another method of countering reducing conditions near the waterwalls is to introduce a flow of air along the walls through openings in the membrane between waterwall tubes. This is often referred to as air blanketing of curtain air, and it should also be implemented and adjusted in conjunction with local monitoring of the gas composition.

Furnace wall corrosion can also be lessened by reducing the levels of the chemical species in the coal that are responsible for corrosion. Approximately one-half of the sulfur and alkali metal content of coal can be removed by standard coal-washing procedures. However, washing generally does not remove the chlorine-containing species from

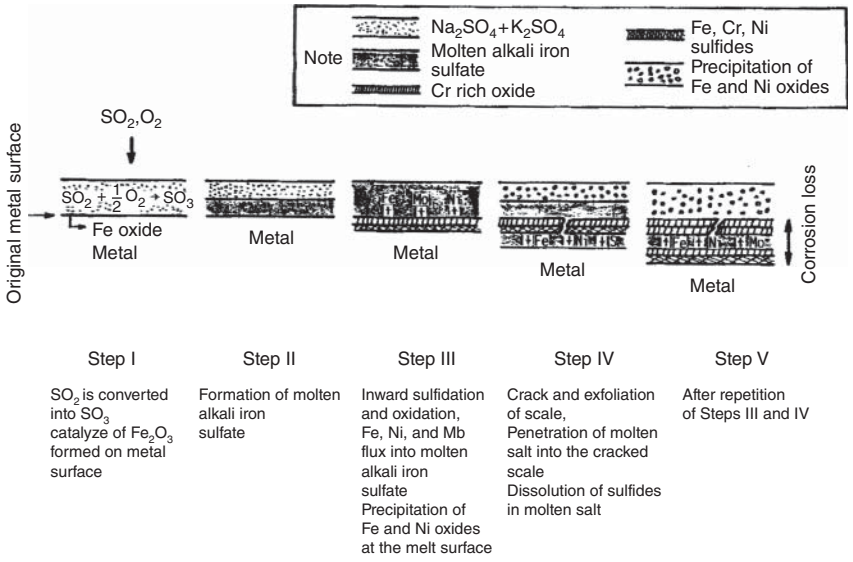


Figure 16.9 Schematic illustration of coal-ash corrosion sequence.

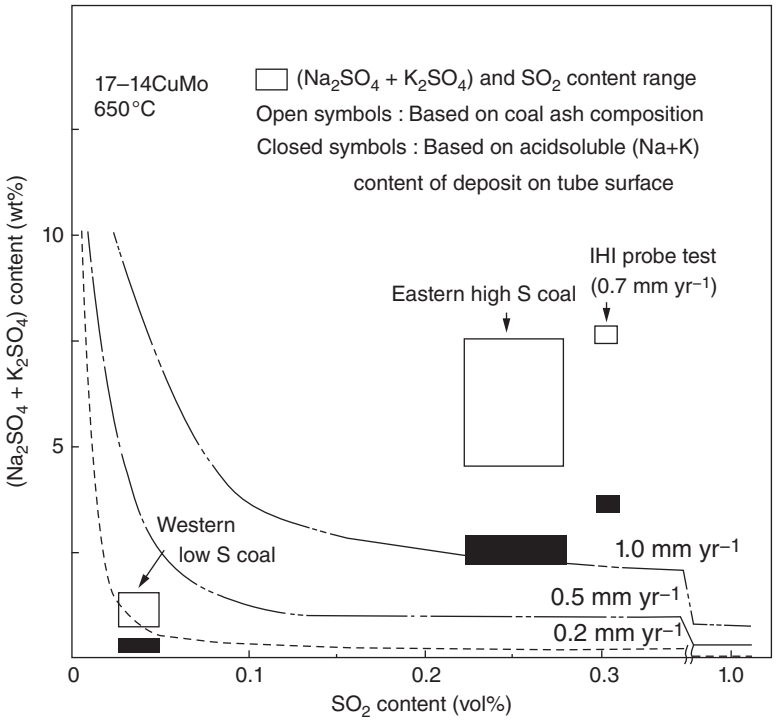


Figure 16.10 Isocorrosion diagram of 17Cu–14Mo steel in coal combustion atmosphere at 650 °C.

coal; therefore, the net effect is that the chlorine content of washed coal is increased.

16.4 Oil-Fired Boilers

Fireside corrosion can present a serious problem in oil-fired boilers or refinery/petrochemical furnaces fired with low-grade fuels with high concentrations of vanadium, sulfur, and sodium. This corrosion is frequently referred to as *oil-ash corrosion*. Accelerated attack by oil-ash corrosion is related with the formation of low-melting-point molten vanadium pentoxide and sodium sulfate eutectics, which flux the protective oxide scale from the metal surface. In boilers, superheater and reheater tubes are susceptible to oil-ash corrosion attack. Uncooled components in the boilers, such as tube supports and spacers, can suffer severe corrosion attack because of higher temperatures. Oil-ash corrosion can also occur in refinery and petrochemical furnaces burning low-grade fuels. The resistance of

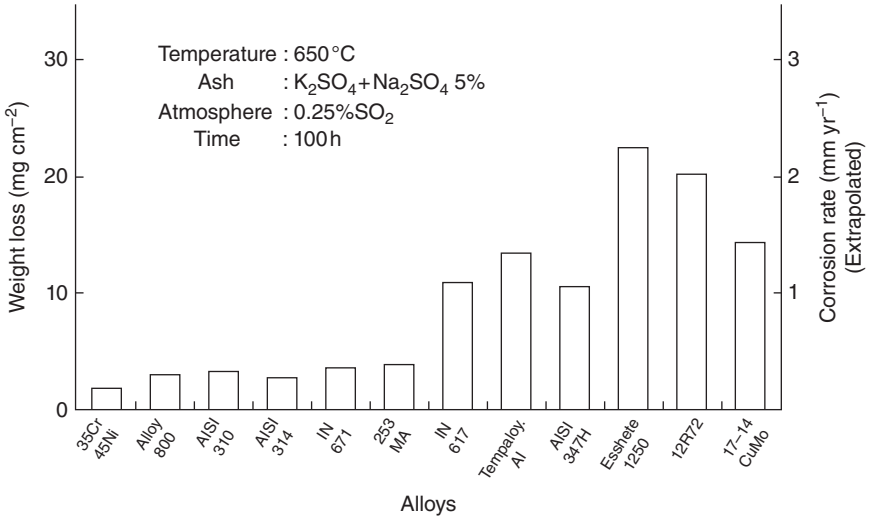


Figure 16.11 Comparison of corrosion resistance of commercial alloys in coal combustion atmosphere.

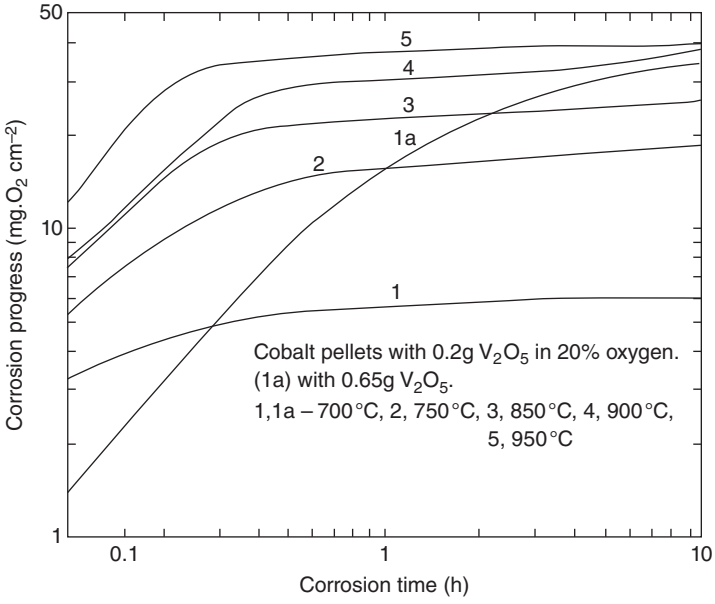


Figure 16.12 General nature of the vanadic corrosion of cobalt in the presence of small quantities of vanadium pentoxide.

oil-ash corrosion for various alloys in both boilers and refinery/petrochemical furnaces is also reviewed in this section.

One of the main elements responsible for the oil-firing corrosion is vanadium, which appears in the deposits as complex vanadates. The appearance of vanadium is not so common both in coal-fired boilers and in gas turbines (hot corrosion). Therefore, it seems appropriate here to discuss with some detail the nature of vanadic corrosion, in other words, the corrosiveness of metals in the presence of sufficient quantities of molten vanadium oxides, particularly vanadium pentoxide.

There are two distinct classes of metals with regard to their behavior toward vanadic corrosion. Metals such as vanadium, tungsten, and molybdenum form low-melting acidic oxides that offer no appreciable resistance to vanadic corrosion, whereas metals like iron, cobalt, nickel, and chromium possess oxides or form complex vanadates that do influence the corrosion rate, the extent depending on the conditions. Cobalt is a median example of the second class, and Figure 16.12 represents its behavior in the presence of a small amount of vanadium pentoxide. With moderate excess of molten vanadium pentoxide, corrosion progress is generally linear with respect to time except for (i) accelerated stage following the main linear process and (ii) the final deceleration. In fact, corrosion of most metal specimens by molten vanadium pentoxide shows a gradual but persistent divergence from any simple rate law when viewed as a whole. Generally, the complete sequence of vanadic corrosion is not explicitly expressed by linear, parabolic, or logarithmic time functions. However, the

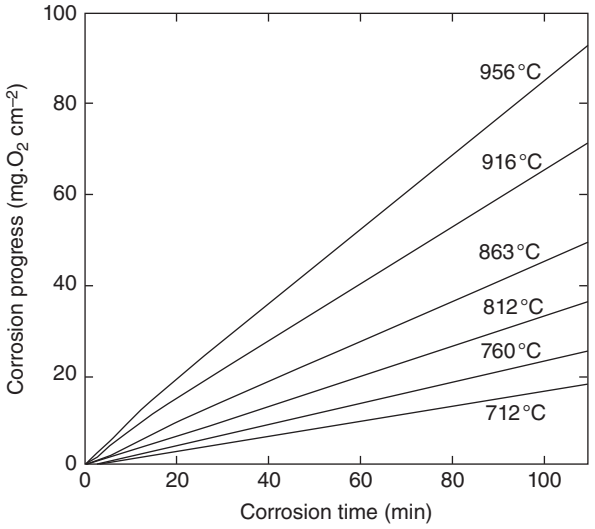


Figure 16.13 Corrosion of vanadium in oxygen with 0.4 cm depth of molten vanadium pentoxide.

initial state of corrosion adheres closely to a linear rate law (except for chromium and nickel), and the later divergence is to be attributed to secondary effects developed in the melt. The ideal case is the one with absence of a corrosion barrier together with absence of a change in the transport properties of the melt. Invariably a smooth, linear corrosion rate is observed (Figure 16.13), i.e.

$$\Delta w = kt \tag{16.14}$$

where Δw is the weight change per square centimeter at time t and k is the velocity constant. This relation, derived for a diffusion-controlled corrosion process, holds good for the initial stages of corrosion of iron, cobalt, titanium, molybdenum, and tungsten in the presence of moderate excess of molten vanadium pentoxide. Nickel is found to obey a simple semilogarithmic law, as might be expected for a process governed by diffusion through the corrosion layer. Chromium is the most resistant of all metal studies reported in the open literature.

In all cases, the velocity constants obey Arrhenius relationships in their temperature variation:

$$k = A \exp\{-E/RT\} \tag{16.15}$$

Apparently, corrosion under molten vanadium pentoxide follows a single mechanism over a reasonably wide temperature range.

In the presence of molten vanadium pentoxide (not contaminated with sodium sulfate), only a general surface attack and slag thickening have been observed (Logan 1961). Electron probe microanalysis shows the presence of a sharp boundary between the metal and slag and the absence of any vanadium in the grain boundaries at the metal surface; this proves that only general surface oxidation occurs. Moreover, the corrosion rates under otherwise exactly similar conditions are not altered by more than 1% over the range of grain sizes – from single crystal to grain dia. 0.02 mm – for iron, cobalt, nickel, and molybdenum. This is conclusive evidence for general rather than intergranular corrosion.

Diffusion-controlled corrosion processes are characterized by velocity constants inversely proportional to the depth of melt. Even for small depths of melt covering the tablet specimens, this relationship was found to hold. So, if the rate constants for the corrosion of vanadium, molybdenum, and iron, for example, are plotted against the reciprocal depth, the plots are linear, demonstrating inverse proportionality between the velocity constant and depth of melt.

If the effect of the corrosion layer or of the diffusion of metal ions is to be minimized so that oxygen diffusion through the melt column alone determines the corrosion, the velocity of corrosion ($v = \mathrm{d}w/\mathrm{d}t$) is given by

$$\frac{\mathrm{d}w}{\mathrm{d}t}.l = D_8 C_\mathrm{o} \tag{16.16}$$

where l is the depth of melt, D_8 the diffusion coefficient in the melt, and C_o the oxygen concentration at the surface of the melt (proportional to the oxygen partial pressure). This means that the product of depth of melt and velocity of corrosion under constant oxygen pressure should be constant and independent of the nature of the metal. Moreover, in principle it is possible to evaluate from it and from its change with temperature the diffusion coefficient (and its "activation energy") of oxygen or other active species.

Changes in oxygen pressure have a marked effect on vanadic corrosion rates, and there is a sharp change of power dependence at pressures near 0.05 atm, varying slightly with temperature and with the corroding metal (Figure 16.14). With the exception of nickel, the power varies between 0.08 and 0.12 for the higher pressures and between 0.6 and 0.9 for the lower region: details are given in Table 16.7. A generalized theoretical treatment of the mechanism of oxygen transport in molten vanadium pentoxide is that the rate would be dependent on a low power of oxygen pressure, at higher pressures, and dependent on approximately the square root of oxygen pressure, at the lower values. Until the constants in the equations relating short-order defect structure of the melt to oxygen pressure have been evaluated, a rigid treatment is impossible, and even then it will be difficult to predict the exact effect of the minor additions of other metal ions on the relationship. Nevertheless, it is reasonable to assume that the effects stem from the semiconductivity of the melt, analogous to those in the conductivity and rate of oxidation of vanadium dioxide. All three effects of oxygen pressure are closely interdependent.

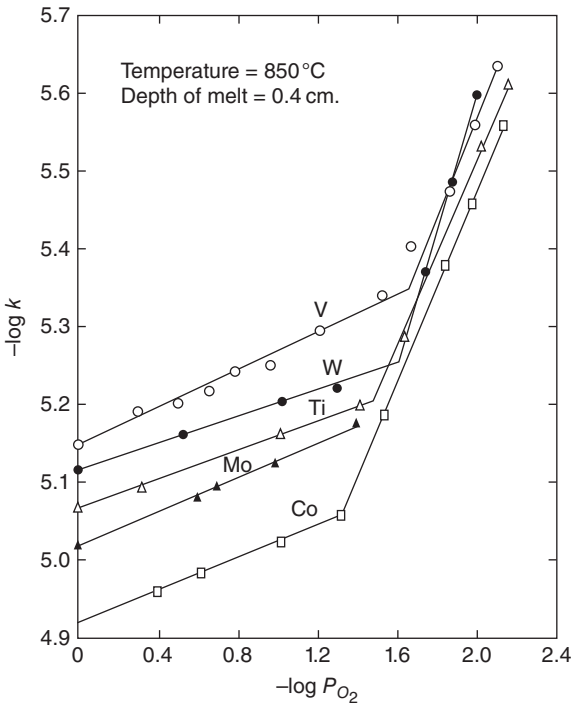


Figure 16.14 Effect of oxygen pressure on the corrosion of metals at 850 °C with 0.4 cm depth of molten vanadium pentoxide.

At higher oxygen pressure, low power dependence would be expected, but at lower pressures, where defects are greater in number, transport by anion vacancies or dependence on Sieverts' law would predominate. Quantitatively, it is reasonable to expect divergences from predicted simple relationships, since the effect of corrosion products on vacancies is likely to be appreciable and exact obedience to the mass action law is an optimistic approximation.

A better insight into the mechanism of vanadic corrosion can be gained by a comparison of the energies of activation for the various processes, since it is this that can characterize the processes, especially in determining whether the rate-controlling step is chemical or physical (diffusional).

In view of the inverse proportionality between the depth (l) of melt and the corrosion rate, as well as of the fact that the corrosion rate varies with the nth power of the oxygen pressure, the simple Arrhenius relation (Eq. (16.15)) has to be modified to

$$k = A_k \frac{1}{l} . p_{O_2}^n . \exp\{-E/RT\} \qquad (16.17)$$

where A_k is the characteristic and measured action constant of the system. With these modifications, the necessary data on the corrosion and other rate processes are collected in Table 16.7.

Table 16.7 Comparison of various rate processes (700–950 °C)

Process	p_{O_2}	Depth of melt (cm)	Activation energy (kcal)	Experimental action constant A_k (corrected)	Exponent of oxygen pressure	
					High pressure	Low pressure
$VO_{2.5} \Longleftrightarrow VO_2 + 1/4\ O_2$	—	—	25.6	—	—	—
$VO_2 + 1/4\ O_2 \rightarrow VO_{2.5}$	1.0	—	16.8	(0.754)	0.083	0.83
					0.098	0.91
					0.102	0.91
	0.1	—	16.3	—	—	—
	0.05	—	16.3	—	—	—
	0.01	—	3.4–9.8	—	—	—
Conductance	1.0	—	17.2–25.9	—	0.24	0.59
Viscous flow	1.0	—	10.1	—	—	—
Diffusional corrosion	1.0	—	14.7	—	—	—
Corrosion of Co	1.0	0.4	27.0	1.150	0.083	0.71
	0.2	0.3	26.5	1.189	—	—
Corrosion of Fe	1.0	0.4	21.2	0.069 4	0.11	0.91
	0.008 69	0.4	7.4	2.67×10^{-6}	—	—
Corrosion of Ti	1.0	0.4	24.0	0.143	0.091	0.59
Corrosion of W	1.0	0.4	28.2	0.796	0.077	0.83
Corrosion of Mo	1.0	0.4	18.3	0.012 76	0.1	0.77
	0.2	0.4	18.4	0.017 01	—	—
Corrosion of V	1.0	0.4	16.5	0.004 56	0.12	0.71
	1.0	0.8	16.5	0.004 58	—	—
	0.008 69	0.4	8.9	4.81×10^{-6}	—	—
Corrosion of Ni	0.2	0.4	27.9	(2971)	0.15	1.67

Table 16.8 Volume ratio and free energy of formation of the metal oxides in relation to vanadic corrosion

Metal	Rate law	Velocity constant ($g\,cm^{-2}\,s^{-1}$) (850 °C; O_2; 0.4 cm depth of melt)	Primary oxidation product	Volume ratio	Free energy of formation ΔG_{1123} (kcal)	Activation energy (kcal)	
						Vanadic corrosion	Corrosion in pure oxygen
Fe	Linear	12.3×10^{-6}	FeO	1.7	−45.3	21.2	22.4
Co	Linear	12.0×10^{-6}	CoO	1.86	−36.9	27.0	20.0
Ti	Linear	8.6×10^{-6}	TiO	1.20	−98.4	24.0	24.3
Mo	Linear	9.3×10^{-6}	MoO_3	3.3	−94.2	18.0	—
W	Linear	7.6×10^{-6}	WO_3	3.35	−133.5	28.2	44.0
V	Linear	7.2×10^{-6}	V_2O_5	3.19	—	16.5	—
Ni	Logarithmic	1.4×10^{-6}	NiO	1.65	−42.0	27.9	34.7

In view of the results, it would be an obvious temptation to consider vanadic corrosion as a chemically controlled process. However, the following observations lead to the conclusion that vanadic corrosion is definitely a diffusion-controlled process:

(a) Different metals obey the same rate law deduced for a diffusion-controlled corrosion process.

(b) Corrosion rates are remarkably consistent from metal to metal (Table 16.8).

(c) Corrosion is independent of the nature of the surface, particularly with respect to grain size.

(d) An inverse proportionality is observed between the depth of melt and the corrosion rate, and convection, set by temperature gradients, has a marked effect on the rate.

(e) The action constants and the activation energies for vanadic corrosion at very low oxygen pressures are small.

(f) During corrosion, sample disks, especially under small depths of vanadium pentoxide, and rods dipping into large depths, show a distinct rounding off at the upper perimeter and a marked "necking" at the melt–atmosphere interface, respectively (Figures 16.15 and 16.16). The activity of oxygen (or of the corresponding reactive species) at the bottom of the crucible would be less than at the top if it were a diffusion-controlled step; the greater corrosion of the rod at the oxygen–melt interface and the rounding off of the tablet specimens at the top are therefore to be expected.

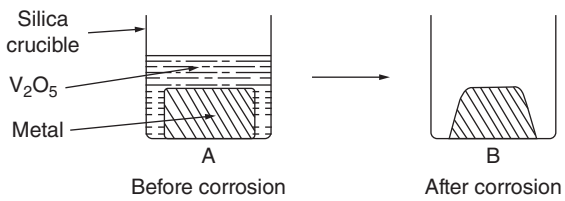


Figure 16.15 Shape of corroded metal disks.

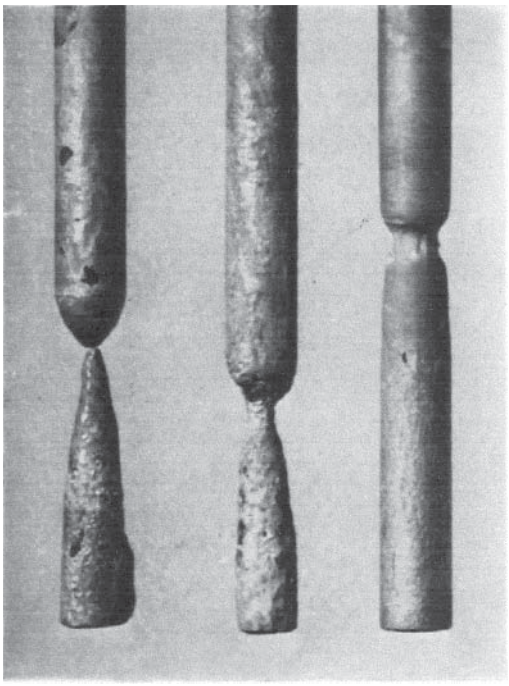


Figure 16.16 Corrosion of iron electrodes immersed in vanadium pentoxide.

(g) There are reports where the activation energies for self-diffusion have been found to be as high as those observed for vanadic corrosion.

It would therefore be reasonable to conclude that vanadic corrosion is a diffusion-controlled process.

But to be more in agreement with issues not yet solved (e.g. marked divergence between activation energies and action constants for the corrosion of different metals), it is necessary to view vanadic corrosion as a two-stage diffusion process, viz. an inward diffusion of oxygen (common to all metals) and an outward diffusion of the corrosion products away from the surface (different from metal to metal). For either process, the entropy should be small and should not differ appreciably between metals, since there are no significant divergences of the changes

Table 16.9 Action constants characteristic of the outward diffusion of the products of oxidation during vanadic corrosion of metals

Metal	Action constant (A_k)	Action constant for inward diffusion of oxygen (A_1)	Action constant for outward diffusion of oxidation products (A_2)
V	0.004 57	0.004 57	—
Co	1.150	0.004 57	0.004 58
Fe	0.069 4	0.004 57	0.004 88
Ti	0.143	0.004 57	0.004 71
W	0.796	0.004 57	0.004 59
Mo	0.012 76	0.004 57	0.007 1

in disorder. The values of the individual action constants (Table 16.9) are in remarkable conformity with this view. The highest and slightly abnormal value of the action constant is for molybdenum. But this is to be expected because the oxidation product, e.g. molybdic oxide, has a considerable vapor pressure in the temperature range studied (700–900 °C) and, *inter alia*, increases the effective diffusion owing to vapor formation.

As constituents of residual fuel oil ash, the effect of sodium sulfate and chloride on the corrosive properties of vanadium pentoxide has been widely investigated but piecemeal and largely empirically (Phillips and Wagner 1961; Sequeira et al. 2003). All mixtures of sodium sulfate or sodium chloride with vanadium pentoxide decompose at as low a temperature as 500 °C by sintering and solid-state reactions. Sulfur trioxide and chlorine evolved, respectively. These gases are themselves powerful corrosive agents at such low temperatures, whereas vanadic corrosion occurs significantly only when there is a molten phase. The decompositions of the sodium salts are very fast when the vanadium pentoxide is molten, particularly in an inert atmosphere. Existence of undecomposed free salt is observed in mixtures of >50 mol% of sodium sulfate or >25 mol% of sodium chloride with vanadium pentoxide; these limits correspond to the reactions

$$Na_2SO_4 + V_2O_5 \rightarrow Na_2O \cdot V_2O_5 + SO_3 \qquad (16.18)$$

and

$$2NaCl + 6V_2O_5 \rightarrow Na_2O \cdot V_2O_4 \cdot 5V_2O_5 + Cl_2 \qquad (16.19)$$

The sodium oxide/vanadium pentoxide melt (the residue after decomposition) solidifies with evolution of oxygen, and the solid reabsorbs the same amount of oxygen on fusion, the amount depending on the composition. The cycle can be repeated indefinitely. Chemical analysis of the solidified mixture showed that it contained vanadium tetroxide exactly equivalent to the oxygen evolved. The structure of solid sodium oxide/vanadium pentoxide *bronzes* is reported (Ozerov and Kildisheva 1959) to contain about 0.4% of oxygen sites vacant in the lattice. The order–disorder transformation on fusion makes possible the absorption of oxygen to fill the vacant sites. This oxygen is highly labile and is unlike the oxygen anions in pure molten vanadium pentoxide. Consequently, the oxygen transport properties of the melt and its corrosive nature are profoundly enhanced.

After invoking relevant aspects concerning vanadic corrosion, it is necessary to consider other aspects of fireside corrosion in oil-fired boilers and furnaces, described as follows.

Residual fuel oils contain between 50 ppm w/w and 300 ppm of sodium present as the chloride and vanadium as organic compounds in amounts depending on the origin of the crude. Nickel and iron compounds in the oil appear on the tubes; so do clay-mineral components, but these ash-forming materials are in relatively small proportion compared with coal. Typically, the deposit on the tubes will be 1–2 mm thick after a year in service. Sodium appears on the tube as sulfate, and vanadium as complex vanadates. These two elements are responsible for the corrosiveness of the deposits. The ratio between them (i.e. V/Na weight ratio in the fuel) can be a useful guide to corrosiveness (Coats 1969). Other factors mentioned previously apply equally to oil and coal, except that the temperatures at which corrosion occurs are perhaps lower for oil, particularly for austenitic steels (Parker et al. 1972); a "bell-shaped" corrosion/temperature curve has been found to apply for oil as for coal, and a sharp increase in the corrosion rate occurs at 600 °C with a peak between 700 and 720 °C. The rate then falls until at 800–850 °C the curve is almost coincident with that obtained in air oxidation without deposit. There is less firm evidence on corrosion resistance at 9% and 12% Cr ferritic steels at metal temperatures above 600 °C; the reason for this is that the corrosion of ferritic steel follows a parabolic rate law and very long times are required to observe specific effects. Stainless steels follow a rectilinear corrosion/time curve.

Many comprehensive studies of corrosion in oil-fired plant are available, and the reader is referred to the extensive tests made at Marchwood Power Station where the gas temperature was 1100 °C. Corresponding tests have been carried out at Bankside Power Station with a flue gas temperature below 1000 °C. On the basis of this work, the Central Electricity Generating Board (CEGB) has concluded that the temperature conditions are so critical at a metal temperature above 590 °C (metal temperature c. 580 °C) and not increased to 565 °C, as in common practice in coal-fired plants. At present, high reliability of modern plants is usually worth more than a marginal increase in overall efficiency.

Oil-ash corrosion problems are best controlled by proper alloy selection. Severe materials problems due

to oil-ash corrosion were illustrated by numerous case histories presented in a 1958 NACE Technical Committee Report.

Extensive field rack tests in boilers fired with Bunker "C" oils containing high concentrations of vanadium (150–450 ppm) were conducted 50 years ago. Test racks were exposed in the superheater section. Alloys ranging from low-alloy steels to iron- and nickel-based alloys suffered severe corrosion attack. Even the best performer (50Ni–50Cr alloy) suffered a corrosion rate of 3.1 mm yr^{-1}.

Spafford (1982) reported good performance of the 50Ni–50Cr alloy in refinery heaters for coking and catalytic reformer units. The heaters were fired with heavy fuel oil containing 2.5–40% S and 50–70 ppm V (occasionally up to 150 ppm). The hangers and tube supports made of cast HH alloy (25Cr–12Ni steel) suffered severe corrosion attack. Metal temperatures were in the range of 730–890 °C. The highest corrosion rates were 6.4–9.5 mm yr^{-1}. Replacement of Alloy 657 (a 50Ni–50Cr alloy) was reported to perform very well, with minimal maintenance and repair. In a field rack test in crude oil heater at 700 °C, Alloy 657 performed 10 times better than HH and HK alloys. Swales and Ward (1979) reported numerous field experiences for Alloy 657 as tube supports in refinery heaters. They concluded that the alloy provided satisfactory service at temperatures up to 900 °C. At temperatures higher than 900 °C, Alloy 657 has often suffered severe corrosion attack.

Superheaters and reheaters with much lower temperatures than tube supports are also susceptible to oil-ash corrosion. Bolt (1988) evaluated various superheater and reheater materials in an experimental boiler firing with heavy oil containing 2.2% S, 200 ppm V, and 50 ppm Na. The test was conducted on Type 347H tubes and several coextruded tubes, including Type 310 over Esshete 1250, Type 446 over Alloy 800H, CR35A over Alloy 1714 CuMo, and Alloy 671 over Alloy 800H. Type 347H suffered the worst corrosion attack, followed by Type 310, with maximum corrosion rates occurring at about 670 °C. Both alloys showed unacceptably high corrosion rates (>1 mm yr^{-1}) at 630–675 °C. Three high chromium cladding materials – Type 446 (27Cr), Cr35A (a new Japanese cladding material, 35Cr–45Ni-Fe), and Alloy 671 (47Cr) – performed significantly better than Types 347H and 310.

In a 10 000-hour field test in a boiler fired with fuel oil containing 2.65% S, 49 ppm V, and 44 ppm Na, Parker et al. (1972) reported that ferritic steels were significantly better than austenitic steels because of sulfidation involved. At 500–650 °C, 2.25Cr–1Mo, 9Cr, and 12Cr steels performed significantly better than Types 316, 321, 347, and 310 and Esshete 1250. Among the austenitic stainless steels tested, however, Type 310 was the most resistant to the environment.

Another effective method of combating oil-ash corrosion problems is to inject additives (high-melting-point compounds) into the fuel to raise the melting point of the oil-ash deposit (Kawamura and Harada 1980).

The additive reacts with vanadium compounds to form reaction products with higher melting points. When magnesium compounds are used, some of the reaction products and their melting points are:

- $MgO{\cdot}V_2O_5$: 671 °C
- $2MgO{\cdot}V_2O_5$: 835 °C
- $3MgO{\cdot}V_2O_5$: 1191 °C

When the injection involves magnesium compounds, increasing the Mg/V ratio increases the melting point of the oil-ash deposits (Fichera et al. 1987). Increasing the melting point of oil-ash deposits results in lower corrosion rates. Disadvantages of the additive injection approach include additional operating costs and a substantial increase in ash volume, which may require additional furnace downtime for tube cleaning (Wilson 1976).

Reducing the excess air levels for combustion is also effective in mitigating the oil-ash corrosion problems. This tends to favor the formation of high-melting-point vanadium oxides, such as V_2O_3 and V_2O_4, and to reduce the amount of low-melting-point V_2O_5. This approach was reported to have received greater success in Europe.

16.5 Corrosion in Waste Incinerators

The corrosion problems experienced in boilers fueled with municipal refuse are different from those encountered with fossil fuels in that chlorine rather than sulfur is primarily responsible for the attack. The average chlorine content of municipal solid waste is 0.5%, of which about one-half is present as PVC plastic. The other half is inorganic, principally NaCl. The chlorine in the plastic is converted to hydrochloric acid (HCl) in the combustion process. The inorganic chlorides are vaporized in the flame and ultimately condense in the boiler deposits or pass through the boiler with the flue gases. Zinc, lead, and tin in the refuse also play a role in the corrosion process by reacting with the HCl to form metal chlorides and/or eutectic mixtures with melting points low enough to cause molten salt attack at wall tube metal temperatures. Investigation of an incinerator wall tube that was corroding at a rate of 2 mm yr^{-1} showed that zinc and sodium were both associated with chlorine in the deposit. The presence of NaCl was confirmed by X-ray diffraction. However, the high corrosion rate could not be accounted for in terms of attack by NaCl or HCl. Consequently, laboratory tests were conducted to demonstrate that the corrosion could

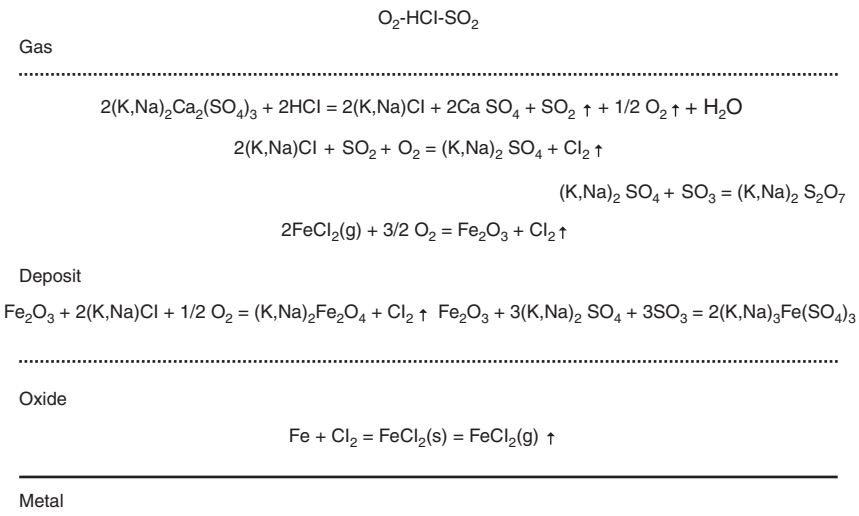


Figure 16.17 Schematic of the main reactions in the system gas/fly ash deposit/oxide scale/steel, representing superheater tubes in waste-fired power plants (Grabke et al. 1998).

be caused by the eutectic mixture of 84% $ZnCl_2$ and 16% NaCl, which has a melting point of 262 °C. After a 336 hour exposure to this mixture at 315 °C, carbon steel had a corrosion rate of 23 mm yr^{-1}, indicating that such molten salt attack was the likely mechanism in the incinerator. There is as yet no evidence for participation of $SnCl_2$ in the incinerator corrosion reactions. However, its low melting point and the possibility of forming a eutectic mixture with NaCl that melts at 199 °C make it a likely contributor to molten salt corrosion.

Figure 16.17 gives a schematic picture of the main reactions in the system gas/fly ash deposit/oxide scale/steel, representing superheater tubes in waste-fired power plants.

Most of the methods for preventing incinerator wall tube corrosion exert some penalty in boiler efficiency. The practice of studding the tubes and covering them with silicon carbide refractory has been widely used in European incinerators, but this remedy reduces heat transfer. Increasing overfire air or blanketing the walls with air to prevent reducing conditions in the flue gas has been effective, but either approach will reduce boiler efficiency. Lowering tube metal temperatures by operating at lower steam pressure also has a cost in efficiency.

However, upgrading the boiler tube material to a corrosion-resistant alloy does not involve an efficiency penalty. Although capital costs will be greater, the extended tube life resulting from the use of more resistant alloys can offset the initial expense and can be a cost-effective solution to the problem. Extensive corrosion probe studies in municipal incinerators showed that in the temperature range of 150–315 °C, a number of alloys provided good performance in resisting high temperature corrosion. In decreasing order, the better alloys were Incoloy 825, AISI Type 446, 310, 316L, 304, and 321 stainless steels, and Inconel alloys 600 and 601. However, when subjected to moist deposits, simulating boiler downtime conditions, all of the austenitic stainless steels underwent chloride stress corrosion cracking (SCC). The Type 446 stainless steel, Inconel 600, and Inconel 601 suffered pitting. Consequently, unless the boilers were to be maintained at a temperature above the HCl dew point during downtime, only Incoloy 825 was recommended.

Many other materials were evaluated in waste incinerators, and several references shown in the section on further reading give a good account of the reported results.

16.6 Plant Experience with Fireside Corrosion

This section briefly reviews fireside corrosion experience in some European and Japanese plants. The numbers and operating conditions of the plants are summarized, and the range of materials used in the boilers is indicated. Experience of furnace wall and superheater/reheater corrosion in coal-fired plants is also summarized, emphasizing the need to "control" fireside corrosion rather than being able to eliminate it and the importance of more corrosion-resistant materials, particularly as coextruded tube. Tube life prediction techniques in use at some plants are outlined, and some current areas of research are described.

16.6.1 British Experience

The CEGB is the nationalized company responsible for the integrated electricity generation system in England and Wales. At present, it operates more than 100 power stations with a declared net capacity of over 75 MW. All the large units have high pressure turbine steam pressures of about 180 bar with single reheat at about 50 bar, the coal-fired units being operated at 570/570 °C and coal/oil-fired units at 540/540 °C. There are also 260 MW supercritical units with steam conditions of 250/55 bar and 600/570 °C. The coals are practically all mined in England and Wales,

Table 16.10 Range of ash analyses in CEGB coals (%)

SiO_2	46–53
Al_2O_3	24–33
Na_2O	0.7–3.3
K_2O	2.4–3.9
MgO	1.0–2.0
Fe_2O_3	7.6–12.0
TiO_2	0.9–1.1
CaO	1.0–6.0
SO_3	0.3–2.0

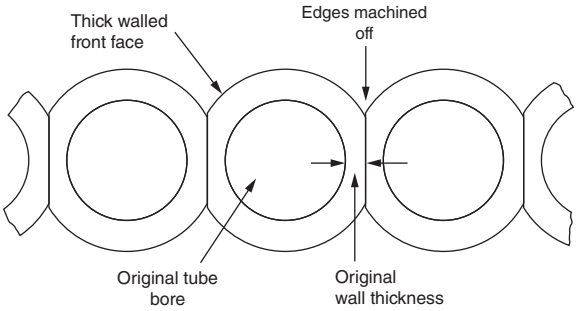


Figure 16.18 The use of faceted mild steel tube to fit in a tangent waterwall construction to give a greater thickness for corrosion.

typical sulfur levels being 1–3% and, quite uniquely, chlorine levels from 0.1% to 0.8%, with a current average burn of about 0.25%. The range of ash compositions is given in Table 16.10.

Furnaces are constructed of vertical mild steel tubes, either tangential or with a membrane construction in the most recent units. Typical dimensions are 50–70 mm outside diameter and 6–8 mm wall thickness. Superheaters in coal-fired plants are low chromium ferritic steels (1 and 2 1/4Cr) for the primary superheat conditions with austenitic tubes for the final stage of superheat and reheat. 316, 321, 347, and Esshete 1250 are all used. In oil-fired plants, the final superheaters are 2 1/4Cr with final steam temperatures limited to 560 °C. Final stage metal temperatures in coal-fired plants range up to 660 °C, depending on station design, with gas temperatures of 900–1100 °C. The maximum design operating metal temperature for 2 1/4Cr tubes is 580 °C. In the furnace surface, metal temperatures approach 450 °C for 160 bar units and 375 °C for the older and smaller (<200 MW) 100 bar lower pressure units.

In this short description, attention is restricted to coal-fired furnace wall and superheater/reheater corrosion. Typical affected regions are indicated in Figure 16.3.

If during units operation the combustion is not altered, the coal-fired furnace walls affected by corrosion remain localized and constant in position, so materials "solutions" have proved to be the prime control method of fireside corrosion.

Depending on the corrosion rate and plant involved, three strategies result:

1. Replace mild steel tubes with identical tubes.
2. Replace mild steel tubes with thicker-walled tubes. To fit them in tangent wall constructed furnaces, the sides of the tubes are removed or are extruded thinner (Figure 16.18).
3. Replace mild steel tubes with coextruded tubes having an AISI 310 (Nb) outer layer and mild steel inner layer. Coextruded tubes are necessary to avoid the susceptibility of austenitics to chloride stress corrosion. Corrosion rates are two to three times lower than for mild steel. The niobium addition to 310 is to reduce intergranular corrosion.

Major overhaul periods occur only every three years in modern CEGB plants. An important factor in the economic analysis to choose the optimum materials strategy is to be able to guarantee freedom from tube failures between major overhauls.

Superheater/reheater corrosion is now well under control, both by the use of improved materials and by having a good predictive tube life capability in terms of gas and metal temperature, steam conditions, and coal quality.

It has been found that austenitics are more corrosion resistant than 2 1/4Cr steels and that there is no significant difference in behavior between 316, 321, 347, and Esshete 1250. In practice, "significant" here means within ±25% for given conditions. By analysis of the plant corrosion rates, the corrosion rates of these alloys can now be predicted to this accuracy.

CEGB documents concerning fireside corrosion in power station boilers detail the procedure for combining corrosion behavior and mechanical property data to predict lifetime of tubes by either creep failure or exceeding the proof stress. The procedure is amenable to personal computer program calculation, summing the fraction of creep life expired in each exposure temperature and suitable time interval, checking at each stage as the tube loses wall section by corrosion whether proof stress failure is then predicted.

Concerning research, work on several major topics is in progress, namely:

(a) *Furnace wall corrosion*: Materials such as 310 Nb and similar are not adequate for the most severe conditions, so alternative materials, primarily high chromium ferritics, are being evaluated. While a simple laboratory simulation of the combustion gas atmosphere (10% CO, 10% H_2O, 0.3% H_2S, N_2) gives rapid rates of corrosion for mild steel comparable with plant, highly alloyed materials have a very low rate; in particular, 310 gives a rate far below that experienced in plant. Reasons for this and more advanced alloys are

being studied; possibilities are the effects of deposits, heat flux, and the free radicals present in a flame and not in an isothermal gas mixture.

(b) *Superheater materials*: The 10-fold reduction in corrosion rate offered by 50Cr–50Ni compared with the austenitic boiler steels is more than sufficient to deal with any expected corrosive situation. However, 50Cr–50Ni is not an attractive material metallurgically. It is two phase and a powder metallurgy production route has to be followed, making it very expensive. Probe trials of single-phase alloys with chromium contents of 30–40% are therefore being undertaken. These should have better corrosion resistance than AISI 310 (25Cr–20Ni–Fe) and be more commercially attractive than 50Cr–50Ni. Other materials being studied are 9–12% Cr steels (P91, P92), austenitic Alloy 800, and Ni-based IN-617.

(c) *Factory and in situ plasma spraying*: The development of factory and *in situ* plasma spraying are being pursued as possible complements to coextruded tube for corrosion control. For corrosion resistance, 100% integrity of a coating is essential, and in the past this has proved impossible. Developments in plasma spraying and other coating processes, and experience gained from station trials over the past 10 years, are proving very encouraging.

16.6.2 Danish Experience

Most of the power plants in Denmark are located near the bigger cities, being able to produce both electricity and district heating. The power plants went through different generation, starting with 30 MW generation in 1945. The newest plants are over 350 MW supercritical units. Natural circulation and once-through boilers are manufactured by Babcock & Wilcox, Steinmüller, Burmeister, and Deutsche Babcock; turbines are manufactured by Skoda, Stal-Laval, AEG/Siemens/KWV, and BBC. Just before the oil crisis in 1973, 70% of the units were oil fired and 30% coal fired. After 1973, the oil burning units were rebuilt. In 1977 the consumption of coal was c. 80%. Today it is about 98% coal fired.

Denmark imports all the coal. The qualities cover the whole world spectrum. The power plants are normally optimized for one or two coal qualities; but nearly all qualities will be used. Nowadays coal is imported from Colombia (30%), Australia (40%), China (10%), England (10%), Russia, Poland, etc. (10%). The most corrosive coal used up to now is the English. Most materials used in the power plants are ferritic steels (Table 16.11). Since 1970, the final stage of superheaters and reheaters are made of x20Cr MoV (12% Cr 1% Mo 0.25% V), which has showed excellent behavior. Maximum steam temperature is about 560 °C. In the new units where the steam temperature is supposed to be 570–590 °C, the superheater/reheater material is austenitic in the final stage. Fireside corrosion has only been seen in few units. Research studies showed that there normally will be no problem with superheaters and reheaters if the following is considered in the design of the boilers:

1. Steam temperature profile in the superheater/reheater.
2. Where and how the superheater/reheater is placed in the boiler (steam or metal/temperature versus gas/temperature).

Nowadays, the final superheater will be placed after a high pressure heater with lower steam/temperature and the final reheater will be placed after the superheater.

Steam/temperature measurements in the individual superheater tube have normally given temperatures up to 590 °C. At this temperature, the lifetime of 10CrMo910 will be about 80–100 000 hours and about 150 000 hours with the x20CrMoV12.1.

Very aggressive corrosion has only been seen in units, where the boiler for different reasons has been badly designed and/or constructed. Redesign has solved all

Table 16.11 Materials used in Danish power plants

Equipment		Material	Steam temperature
Furnace		Mild steel/15Mo 3	<400 °C
Superheater	1st stage	13Cr Mo44 ≈ 1Cr 1/2Mo	<510 °C
	2nd stage	10Cr Mo910 ≈ 2 1/4Cr 1Mo x20Cr Mo V12.1 ≈ BS 762 (x9Cr Mo91 ≈ 9Cr 1Mo) (AISI 316)	Up to 545 °C
Reheater	1st stage	13Cr Mo44 ≈ 1Cr 1/2Mo	<510 °C
	2nd stage	10Cr Mo910 ≈ 2 1/4Cr 1Mo x20Cr Mo V12.1 ≈ BS 762 (x9Cr Mo91 ≈ 9Cr 1Mo) (AISI 316)	Up to 545 °C

major problems. All Danish power plants are examined after 100 000 hour service. Superheater/reheater tubes are inspected after sandblasting. Tube samples are collected from the worst exposed areas, and measurements of the magnesite thickness, inner–outer diameter, wall thickness, and structure characterization are carried out. All new units are also equipped with temperature measurement devices. The lifetime is then assessed based on these results.

A few years ago, the steam temperature was about 550 °C, but the new units attain 580 °C or more. Also, the tube materials changed from ferritic to austenitic steels. To choose the right quality of austenitic alloy or other advanced material, the coal quality has to be considered. At present, data collections correlating material behavior at the operation temperature in various fly ashes are being established. Clearly, the final decision is pragmatic because the future coal quality is uncertain.

16.6.3 Dutch Experience

The total power capacity installed in the Netherlands today amounts to 20 000 MW. The main fuels are natural gas, coal, and uranium. After the first oil crisis of 1973, the share of heavy oil increased drastically at the cost of natural gas. In this period, corrosion, fouling, and fuel additive experiences have been gathered. Nowadays, heavy oil is not used, and the fireside corrosion, fouling, slagging, and additive aspects concern the coal-fired boilers. The Dutch coal-fired boilers are dual fuel units: besides coal, they are suited for gas or oil firing.

All the coal used in the Netherlands is imported from various regions. Australian and US coals are covering about three-fourths of the supplies, while the remaining coal is of Polish, Ruhr, and Colombian types. In general, the coals are fired as blends. The blends are composed on the basis of firing and slagging experiences in the respective boiler. In general, a new blend is fired every two weeks.

Materials in use for boiler tubing vary over a wide range of compositions. Creep strength and oxidation resistance in relation to maximum service temperatures are parameters governing the choice of material type. Table 16.12 summarizes the materials most frequently used, particularly in the traditional installations.

In some cases 9Cr–1Mo steel is used for intermediate tubing between low-alloy ferritic steel and austenitic steel tubing.

Materials for strips and spacers usually have higher alloy contents than the tube materials they are connected to because they reach higher service temperatures. An example is Type A351 CH20, a cast austenitic steel with about 30% Cr and 20% Ni, used between 12Cr–1MoV steel tubes. Welding materials are usually of composition similar to the tube material compositions. For dissimilar metal welds between ferritic and austenitic tubing, iron-based austenitic or nickel-based Inconel alloys have been used.

Table 16.12 Boiler tube materials in use in many boilers of Dutch electricity supply undertakings and their maximum service temperatures

Steel type	Maximum allowable service temperature (°C)
0.5Mo	530
1Cr 0.5Mo	550
2.25Cr 1Mo	580
12Cr 1MoV	615
347H	> 615

Unforeseen plant unavailability amounts to about 10% of the theoretical production capacity. Almost half of this is caused by disturbances in the steam generating parts of the units. The largest group among these disturbances is the group called “high pressure parts inside the gas stream” (economizers, evaporators, superheaters, and reheaters). This group caused an unforeseen loss of theoretical production capacity of about 1.1% in the last decades. On average, this means that about one unplanned stop per unit per year, with an average duration of 117 hours, is caused by problems with high pressure parts inside the gas stream.

Although only a part of these problems is related to fireside corrosion, the phenomenon still merits attention for economic reasons.

A review of databases on failure analysis shows that sulfidation has occurred in all of the ferritic and austenitic materials mentioned in Table 16.12. In one case, a part of the high temperature corrosion was attributed to the chlorine content of the flue gases of an incinerator plant.

In most cases, sulfidation has occurred together with creep damage. In some of these cases, it is hard to say which predominant factor is causing the damage. Sometimes either mechanism could occur because the material actually used was less alloyed than the material planned in the drawing.

In some cases, fireside corrosion was confined to the neighborhood of strips connecting the superheater tubes. This was attributed to the fact that these zones reached higher temperatures than uninfluenced tube wall material. In several cases, sulfidation has also been found to occur in deflector and impellers around oil burners and in oil atomizers.

Countermeasures proposed after sulfidation damage usually include the application of materials containing more chromium and/or less nickel and a reduction of service temperatures, e.g. by reducing the direct heat radiation or flame impingement. In some cases, the use of coextruded tubing has been proposed.

In may periods of oil firing, about three-fourths of the oil-fired boilers used additives based on MgO or

$Mg(OH)_2$. Dosage took place in suspensions of water or light oil in the fuel supply rod or, more frequently, directly in the boiler. The additive dosage was, in principle, inspired by economic motives: by reacting with SO_3 at low flue gas temperatures to dry magnesium sulfate powder, the sulfuric acid dew point decreased, and the outlet flue gas temperature could be lowered to 115–120 °C, thereby increasing the overall efficiency. An important beneficial side effect was apparently the decreasing fouling tendency in the superheater and reheater sections: a dry brittle deposit was formed, easy to remove by means of sootblowing. It was found that in additive-dosed boilers, less fireside superheater and reheater damage occurred than in boilers without additive dosage. With some types of additives problems occurred due to white coloring of the waterwalls, leading to a decreasing heat transfer at the waterwall tubes and an undesirable increased heat transfer in the superheater sections. By applying additive types with iron oxide additions, the waterwall deposit assumed a dark color, and more heat could be absorbed.

In some smaller coal-fired boilers, permanent slagging problems are found. It concerns older boilers with relatively high flue gas temperatures. Dosage of copper oxychloride appeared to be very effective. An evaluation test with this additive was carried out in 1986 by Babcock under contract to EPRI.

To prevent slagging, fouling, and corrosion problems and to create a stable flame pattern, the coal in the Netherlands is generally fired in blends. Besides coal properties, such as reactivity, caloric value, volatile matter content, and maceral composition contributing to the flame pattern and heat load, the macro ash composition also plays a role in boiler slagging. The traditional slagging tendency formulas for the most frequently used coals in the Netherlands are mentioned in Table 16.13.

It may be seen that the coal types fired in the Netherlands show very low slagging tendency. The chlorine content is, in general, about 0.1% with a maximum of 0.2%, while the sulfur content amounts to approximately 1%. Possible extreme values are averaged by blending. It can be concluded that the coal (blends) as fired in the Netherlands displays a relatively low fireside corrosion tendency.

Table 16.13 Slagging tendency of coals fired in the Netherlands

Origin	SR	B/A	ST (°C)	Slagging tendency
Australia	90–99	0.05–0.09	1475–1650	Very low
US	78–87	0.12–0.21	1450–1550	Low
Germany	80	0.21	1475	Low
Poland	71	0.32	1275–1300	Moderate

SR, silica ratio; B/A, base–acid ratio; ST, softening temperature predictable by KEMA formula: ST (°C) = 1326−20.0 $(Fe_2O_3 + CaO + MgO) + 14.4\ Al_2O_3$, standard deviation: 29 K.

KEMA is the Mechanical and Testing Division of Arnhem Institutions of the Dutch Electricity Supply Undertakings.

At KEMA, the remnant life of creep-loaded boiler components is assessed by means of iso-stress, increased temperature creep tests. This means that five test specimens are loaded to service stress at five different temperatures that are higher than the service temperature. During these tests, the strain rates and rupture times are measured. The test results are extrapolated in the inversed temperature versus logarithmic rupture time domain, giving an estimate of the rupture time under service conditions.

This system presupposes constant service stress. However, if high temperature corrosion causes a reduction of the pipe wall thickness, the stress in the remaining wall thickness increases during plant life, and the normal remnant life prediction might be no longer conservative. Some systems have been developed in which this phenomenon is taken into account. But these systems presuppose general or homogeneous attack of the wall thickness. However, in KEMA's experience on some materials, high temperature corrosion can cause highly local effects whereby wall thickness is locally reduced several times more than elsewhere. The reason for this phenomenon is not completely clear, but its consequences are that the minimum wall thickness varies over a wide range and that the wall thickness reduction rate is not a single value for all locations.

These factors make a remnant life estimate under these conditions very uncertain and call for the application of very conservative values.

Based on a failure analysis of the attack of reheater tubes of 347H material in an oil-fired 540 MW unit after 20 000 hours, and on the results of 2000 hour tests in the oil-fired KEMA experimental boiler, the following was found:

- At metal temperatures below 600 °C, the corrosion rates of 347H material show a parabolic behavior in accordance with $(\Delta W)^2 = Kt$, in which ΔW represents the loss in wall thickness, t stands for time, and $K = 4.2 \times 10^{-15}\ m^2\ s^{-1}$.
- At metal temperatures between 630 and about 670 °C, the corrosion rate of 347H material shows a linear behavior in accordance with $\Delta W = Kt$, with $K = 3.7 \times 10^{-11}\ m\ s^{-1}$. This behavior applies in both cases to flue gas temperatures of 1120–1150 °C (under oil-fired circumstances).

The details of the difference in corrosion rate behavior are further explained in this subsection.

In the KEMA oil-fired experimental boiler with a steam production of $3\ t\ h^{-1}$, candidate superheater materials are exposed under severe corrosion conditions, with metal temperatures of up to 700 °C and flue gas temperatures of about

Table 16.14 Coextruded materials tested in the oil-fired KEMA boiler

Type	Manufacturer	Main composition		
		%Cr	%Ni	%Si
347H (reference)	Sandvik	18	10	0.6
Esshete 1250/AISI 310 (outside)	T.I.	26	20	1.2
800H/Tp 446 (outside)	Sandvik	27	—	0.5
1714CuMo/NAC 35CrA (outside)	Nippon Kokan	35	45	0.03
Inco 800H/Inconel 671 (outside)	INCO	46	54	—

1150 °C. The aim of the ongoing activities is to improve turbine efficiency by raising the steam temperature and pressure and, by doing so, to improve the overall unit efficiency. In Table 16.14, some of the materials tested up to now are mentioned.

The corrosion rates of 347H and Esshete 1250/AISI 310 at a continuous thermal load (540–680 °C) and a discontinuous load (500–670 °C) for heavy fuel oil (200 ppm V, 50 ppm Na, 2% S) and flue gas temperatures of 1150 and 1000 °C, respectively, showed that the rate:

- Is found to be low at metal temperatures below 600 °C because of the presence of a relatively thick oxide layer and the absence of a molten sulfate layer.
- Reaches a maximum at metal temperatures of about 670 °C because of the presence of a 50 µm thick molten sulfate layer situated directly near the oxide layer.
- Decreases at metal temperatures above 680 °C because of the absence of a molten sulfate layer. On the basis of differential thermal analysis (DTA) – and DSC – experiments with simulated deposits, it was confirmed that $Fe_2(SO_4)_3$ decomposed into Fe_2O_3 and SO_3 at about 670 °C, while the remaining high-melting calcium and sodium sulfates recrystallize. The corrosion rate is then governed by the diffusion transport rate through solid matter.

Therefore, the corrosion mechanism can be described as a continuously proceeding ~10 µm thick sulfidation front under the iron–chromium oxide layer.

It has been demonstrated that at metal temperatures in the 625–670 °C range, the corrosion rate behavior follows the SO_3 flux behavior (see Figure 16.19). In this model, the (diffusion-controlled) SO_3 supply through the deposit is assumed to be the rate-determining step. The model was originally developed for coal-fired conditions (Hendry and Lees 1980).

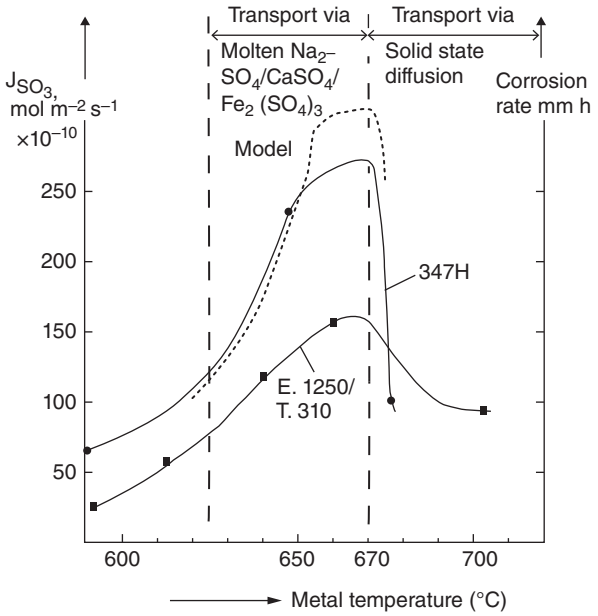


Figure 16.19 SO_3 flux (dashed line) calculated in superheater deposits from the KEMA experimental boiler (Hendry and Lees 1980).

From 1990 onward, besides more similar corrosion tests as in the oil-fired boiler, research experiments concerning the reactivity of coal blends, slagging and fouling, flue gas desulfurization and denitrification, and bag filters were carried out.

In addition to the exposure to corrosive environments in the test boiler, several other tests have been performed with coextruded material.

Welding procedures for both shop and construction welds have been qualified, and the existing CEGB bending procedure for Esshete 1250/Type 310 tubes has been adjusted for small radius bends.

Medium length creep tests have been performed on coextruded tubes with circumferential welds. During these tests, tube specimens have been loaded by means of both an internal pressure and a bending load.

Through reactions of oxygen with nitrogen from the coal and with nitrogen from the combustion air (fuel and thermal, respectively), NO_x is formed. There is an exponential relation between the reaction rate of thermal NO_x and the flame temperature, while the formation of fuel NO_x is governed by the oxygen supply. The contribution of fuel NO_x to the total emission is relatively large: measures for NO_x reduction primarily concern the decrease of the oxygen supply in the primary combustion zone.

Nowadays, some Dutch units use the so-called overfire air (OFA) ports. Above the burners, two air supplies are present through which about 15% of the air can be added. In 1987, two units started up building in license of Mitsubishi Heavy Industries (MHI). The main features of these boilers are their relatively large fire room volume (20–25% larger

than conventional ones) and the set of measures for retarded air supply. Provisions are made to ensure that an air-rich zone is present close to the waterwall to prevent corrosion accelerating conditions due to a reducing atmosphere.

For more recent techniques, there are demonstration projects planned for existing conventional boilers. This concerns the high temperature NO_x reduction (HTNR) in which volatilization under reducing conditions will be relatively great and the in-furnace NO_x reduction (IFNR), in which the burn-out occurs in three stages. NO_x formed in the primary zone will be partly reduced to N_2 in the planetary burning zone.

Corrosion problems of the waterwall tubes with OFA techniques and MHI burners are not expected. In the case of staged firing and IFNR reduction, the reducing conditions in combination with the aggressive hydrogen sulfide gas may lead to corrosion. A mechanism proposed for carbon steel is as follows:

- Directly on the steel surface, a thin layer of Fe_3O_4 is present, followed by a mixed layer of Fe_3O_4 and FeS. Adjacent to this, a FeS layer was found. The outer FeS layer grows through outward diffusion of iron cations, and the inner Fe_3O_4 layer (containing FeS) grows through inward diffusion of oxygen and sulfur to the base metal.

If unacceptably high corrosion rates in (local regions of) the waterwall tubes are found ($>0.1\,mm\,yr^{-1}$), the application of more corrosion-resistant materials can be considered, e.g. coextruded tubes with carbon steel inside (little susceptibility for chloride SCC on the water side) and high chromium containing Type 310 (25Cr–20Ni) outside.

Many corrosion test programs are now being started or prepared to evaluate the change in corrosion conditions of the waterwalls due to different low NO_x burning techniques.

16.6.4 German Experience

The fossil fuel fired in German power plants is usually low in salts and chlorine and low to medium in sulfur content.

Concerning temperature, German power plant design is rather conventional. The typical main steam temperature is about 570 °C. Temperatures in the evaporator area depend on the pressure. They are usually below 500 °C.

For evaporator tubing, unalloyed and low-alloy steels ($15Mo_3$ and 13Cr–Mo44) are used. The materials used in the final sections of conventional superheaters and reheaters are 10Cr–Mo910 and sometimes the 12% Cr steel x20CrMoV121.

Because of the comparable low wall temperatures, corrosion rates observed in the evaporator section are usually low, i.e. below $10\,nm\,h^{-1}$. Increased corrosion rates could frequently be traced back to incomplete combustion and direct particle or flame impingement. Some other cases were investigated where chlorine or chlorides were involved in the corrosion mechanism. With this mechanism, corrosion rates up to $500\,nm\,h^{-1}$ can be observed. From the appearance of the oxide layer and the ash deposit, it is concluded that a non-protective oxide layer is formed by gas-phase transport of iron as chloride from the tube wall to the outer parts of the layer.

The examination of a great number of superheater and reheater tubes supports the meaning of Effertz that *fireside corrosion* in the temperature range in question is caused by a solid/gas-phase reaction and, despite great differences in the composition of the *ash deposit*, it is similar for *coal-fired* and *oil-fired units*. However, the corrosion rates given by Effertz are considerably higher than those that can be expected from the results of the VGB laboratories for normal boiler operation.

Fireside corrosion at the rear side of the tubes (not facing the gas stream) is usually low and not significantly higher than oxidation by steam. That means that oxidation by flue gas probably obeys a parabolic law. At the front side of the tubes, the corrosion rates are 5–15 times higher. This increase in corrosion rate cannot be explained by higher temperatures and a different chemical load only. There is strong evidence that the integrity of the oxide layers is destroyed again and again by mechanical and thermal stresses. This would result in direct access of the flue gas to the metal surface and in time-independent corrosion rates.

By the high chromium content of the material x20CrMoV121, fireside corrosion is not decreased in the same extent as steam oxidation. In certain circumstances, the 12% Cr steel does not perform significantly better than low-alloyed steels. This can be traced back partly to carburization of the steel and depletion of the metallic matrix by the formation of chromium carbide.

16.6.5 Japanese Experience

In Japan, most of the fuel of thermal plants is LNG and coal. In oil-fired boilers, low sulfur oil has been used for the last 40 years due to the environmental regulations.

Since vanadium content is generally low in sulfur, oil and excess air combustion has been applied to suppress NO_x; recently catastrophic oxidation by vanadium compounds (V attack) is hardly observed, and sulfidation is frequently observed for fireside corrosion. Since sodium and sulfur compounds are dominant components of the deposit on the superheater and reheater tube surface in the low vanadium oil combustion, sulfidation inevitably occurs. Moreover, low O_2 and high S potential atmosphere by low excess air combustion promotes the occurrence of sulfidation.

On the other hand, a recent tendency for diversity in fireside corrosion is noted because high sulfur oil is being used again. However, it seems that the research work on

fireside corrosion in oil-fired boiler is inactive and the tube replacement by monitoring the tube wall thickness has recently been established as the countermeasure of fireside corrosion in Japan.

Concerning the tube materials, carbon steel, low-alloy steels (1.25Cr–1Mo and 2.25Cr–1Mo), and austenitic stainless steels (316H, 321H, and 347H) have been widely used for superheater and reheater tubes. Also, 9Cr–1Mo steel (SA213-T91) is being used for new plant and tube replacement due to an excellent high temperature strength and low price.

Research work for improvement of coal-fired plants aiming at a high efficiency has been very active in these last decades, as demonstrated by reports on coal-ash corrosion and development of novel materials technology including coextruded and coating tubes, published in the open literature.

Since low corrosive coals such as the Australian coal have been widely used in Japan, fireside corrosion has seldom occurred in superheater and reheater areas of Japanese coal-fired boilers. On the other hand, corrosion in a reducing atmosphere has occurred in furnace waterwall area by the application of two-stage (sub-stoichiometric) combustion for suppressing NO_x.

Heavy corrosion occurred in furnace waterwall tubes of coal-fired boilers in which the same quality coal was fired. The specification of the boilers, where the fireside corrosion was investigated, is shown in Table 16.15. Table 16.16 shows the characteristics of coal fired. The tube wall thickness was measured in a whole furnace waterwall area after two years' service. The maximum surface recession was estimated to be about 3 mm. The chemical composition of deposits from the front wall tubes of the left-side wall heavily corroded is shown in Table 16.17. The deposits mainly consist of iron sulfide and contain almost no Na, K, and Cl. Concerning the corrosion of furnace waterwall tube, the corrosion by molten pyrosulfate ($Na_2S_2O_7$, $K_2S_2O_7$) and the corrosion by HCl are well known. However, judging from the chemical composition of the deposit, the corrosion in the boiler is not explained by the above mechanisms. The results of DTA and thermogravimetry (TG) measurements also show that the deposition includes FeS and no alkali sulfates. Electron and X-ray images of deposit and scale certify that the main component of the deposit is iron sulfate.

Pyrite (FeS_2) involved in coal is converted into SO_2 in the combustion atmosphere. But the pyrite melts and deposits on furnace waterwall tube as Fe_2S of FeS in the local reducing atmosphere. FeS_2 corrodes metal (Fe) by the following equation:

$$FeS_2 \rightarrow FeS + S(g) \tag{16.20}$$

Table 16.15 Specification of the boiler

Capacity	550 ton h^{-1}
Steam pressure	173.5 kg cm^{-2}
Steam temperature	569 °C (superheater outlet)
	541 °C (reheater outlet)
Type	Single drum, natural circulation

Table 16.16 Coal and ash characteristics

Approximate analysis (%)		Ultimate analysis (%)		Ash fusion temperature (°C) Reducing atmosphere		Ash composition (%)	
Inherent moisture	1.6	Carbon	54.3	Initial def.	1170	SiO_2	51.5
Fixed carbon	33.3	Hydrogen	4.0	Softening	1200	Al_2O_3	23.6
Volatile matter	33.5	Nitrogen	0.8	Hemisphere	1240	Fe_2O_3	8.23
Ash	31.6	Oxygen	6.1	Fluid	1340	TiO_2	1.96
		Sulfur	3.2			CaO	9.82
						MgO	1.57
						Na_2O	2.34
						K_2O	1.18
						SO_3	2.87

Table 16.17 Deposit characteristics

	Tube no. 28	Tube no. 49
Chemical composition (%)		
SiO_2	3.30	4.07
Al_2O_3	1.62	1.70
Fe_2O_3	19.6	15.4
CaO	0.40	0.50
MgO	0.07	0.09
Na_2O	0.12	0.16
K_2O	0.09	0.10
TiO	0.07	0.08
SO_3	2.48	2.49
FeS	68.7	70.8
Ash fusion temperature (°C)		
Initial def.	1100	1130
Softening	1260	1240
Hemisphere	1320	1305
Fluid	1340	1335

$$S(g) + Fe\,(\text{metal tube}) \rightarrow FeS \tag{16.21}$$

Reducing atmosphere is easily formed in the furnace side wall area because the boiler was operated by two-stage combustion to reduce NO_x, hydrogen, hydrocarbon, carbon monoxide, and hydrogen sulfide gases, which are possibly involved in the reducing atmosphere. Sulfidation occurs under the coexistence of SO_2 and CO by the following equations:

$$3CO + SO_2 \rightarrow COS + 2CO_2 \tag{16.22}$$

$$COS + Fe \rightarrow FeS + CO \tag{16.23}$$

or

$$2CO + SO_2 + Fe \rightarrow FeS + 2CO_2 \tag{16.24}$$

$$7CO + 2SO_2 + Fe_2O_3 \rightarrow 2FeS + 7CO_2 \tag{16.25}$$

The above corrosion mechanisms suggest that the corrosion in these units was possibly generated by the deposit of FeS or CO–SO_2 atmosphere.

Therefore, laboratory corrosion tests under simulating atmospheres were carried out to clarify the corrosion mechanism. In the first experiment, test coupons coated with FeS powder were exposed in reducing and oxidizing atmosphere at 500 °C. The test results showed that the corrosion was accelerated by FeS in both reducing and oxidizing atmospheres. In the other experiment, test coupons were exposed to the flowing gas involving CO and SO_2. It was confirmed that SO_2 addition to reducing atmosphere ($CO + CO_2$) accelerated the corrosion.

Since the advanced steam cycle (ASC) boilers are operated at higher temperature and pressure than conventional boilers, higher creep strength is required for superheater and reheater tube materials. Furthermore, in coal-fired ASC boilers, a high resistance to coal-ash corrosion is needed. But creep strength and corrosion resistance are generally incompatible. Therefore, composite tubes, such as coextruded and coating tubes, are technically and economically promising. Itoh (1986) reported the results of an extensive program of metallurgical, mechanical property, creep strength, corrosion, and manufacture testing for coextruded and diffusion coating tubes. In this study, 17Cu–14Mo, fine-grained TP347H, Tempaloy A-1, Alloy 800H, and conventional TP347H were selected as inner tube materials, and 310SS, 35Cr–45Ni steel with chromizing coatings were selected as the outer corrosion-resistant layers of the composite tubes. The results demonstrated the following: coextruded tubes and chromized tubes can be produced by normal manufacturing procedures without affecting the tube strength; the tubes may be designed by assuming that only the inner tube contains the pressure; resistance to coal-ash corrosion is greatly improved by both cladding and chromizing; the cladding (coating)/tube interface remains stable in service; welding and bending composite tubes can be obtained with no significant difficulty.

New alloys possessing high creep strength and corrosion resistance have been developed with the purpose of being used as mono-wall tubes. The following four alloys gave good results: 23Cr–34Ni–1.25Mo–0.4Nb (Alloy 800H), 30Cr–50Ni–2Mo–0.2Ti–0.02Zr (CR30A), 23Cr–43Ni–6W, 20Cr–25Ni–1.5Mo–0.25Nb–0.05Ti–0.15N (NF709). It has been confirmed that the boiler tubes of the above developed alloys could be manufactured by existing procedures. Moreover, judging from the Cr contents of these alloys, satisfactory resistances to coal-ash corrosion were expected as it was later observed.

In summary, fireside corrosion in Japan, accompanied with sulfidation, is predominant in recent oil-fired boilers due to using low V oil and applying low excess air combustion. Despite the use of low V content oil, the fireside corrosion has not been completely suppressed. For example, the corrosion rates of 347H in the units firing 0.24% S, 4 ppm V contents oil and 0.96% S, 10.8 ppm V contents oil were 0.10 and 0.4 mm yr^{-1}, respectively. Moreover, the application of two-stage combustion for low NO_x operation brought the new type of corrosion in reducing atmosphere for the furnace waterwall tube of coal-fired boilers.

As countermeasures of the above processes, the usefulness of newly researched colored fuel additive and the increase of reliability for evaluating the local corrosion by probabilistic approach have been reported. Furthermore, coextruded tubes, chromized tubes, and newly developed alloys are applicable for the various kinds of corrosion mentioned above. Therefore, accumulation of test results of these new materials installed in actual boilers is desired.

16.7 Conclusions

This chapter covers high temperature corrosion involving ash/salt deposits in fossil-fired boilers, furnaces, and waste incinerators. Fireside corrosion in coal-fired boilers is reviewed in terms of the corrosion of furnace walls and superheaters/reheaters. Corrosion of furnace wall tubes is believed to be enhanced by the establishment of localized reducing conditions in the vicinity of furnace walls. Corrosion of superheater/reheater tubes may be related with the formation of molten alkali metal iron trisulfate $(Na,K)_3Fe(SO_4)_3$. Fireside corrosion can be a severe problem in oil-fired boilers or furnaces when low-grade fuels with high concentration of vanadium, sulfur, and sodium are used for firing. Accelerated attack by oil-ash corrosion is related with the formation of low-melting-point molten vanadium pentoxide and sodium sulfate eutectics, which

flux the protective oxide scale from the metal surface. The corrosion processes generated by incineration of municipal, hospital, industrial, chemical, and low-level radioactive wastes are not very well understood, but sulfidation, chloride attack, and molten salt deposit attack are frequently responsible for the corrosion reaction. Furthermore, industrial experience of fireside corrosion in some European countries and in Japan is described.

References

Armilt, J., Holmes, D.R., Manning, M.I. et al. (1978). *The Spalling of Steam Grown Oxide from Superheater and Reheater Tube Steels. EPRI Report FP686*. Palo Alto, CA: EPRI.

Bolt, N. (1988). *Proceedings of the 10th International Conference on Metallic Corrosion*, 3593. New Delhi: Oxford and IBM Publishing.

Coats, A.W. (1969). *J. Inst. Fuel* 42: 75.

Dryepondt, S., Monceau, D., Crabos, F., and Andrieu, E. (2005). *Acta Mater.* 53: 4199.

Ennis, P.J., Quadakkers, W.J., and Schuster, H. (1993). *J. Phys. IV* Coll. C9, Supplément au Journal de Physique III 3: 979–986.

Fichera, M., Leonardi, R., and Farina, C.A. (1987). *Electrochim. Acta* 32: 955.

Grabke, H.J., Müller-Lorenz, E.M., Eltester, B. et al. (1997). *Steel Res. Int.* 68: 179.

Grabke, H.J., Reese, E., and Spiegel, M. (1998). *Molten Salt Forum* 5–6: 405.

Grabke, H.J., Tökei, Z., and Ostwald, C. (2004). *Steel Res. Int.* 75: 38.

Griffiths, T.R., King, K., and Mortimer, D. (1982). *High Temp. Technol.* 1: 43.

Grünling, H.W., Ilschner, B., Leistikow, S. et al. (1979). *Proceedings of the Petten International Conference* (15–18 October), 869. The Metals Society.

Haarmann, K., Vaillant, J.C., Vandenberghe, B. et al. (2002). *The T91/P91 Book*. Vallourec and Mannesmann Tubes.

Heitmüller, R.J. and Kather, A. (1999). *VGB Kraftwerkstechnik* 5: 75.

Hendry, A. and Lees, D.J. (1980). *Corros. Sci.* 20: 383.

Ikeshima, T. (1983). *Bull. Jpn. Inst. Met.* 22: 389.

Itoh, M. (1986). ASME 86-JPGC-FACT-8.

Kawamura, T. and Harada, Y. (1980). *Mitsubishi Tech. Bull n° 139*. Tokyo: Mitsubishi Heavy Industries.

Kofstad, P. (1988). *High Temperature Corrosion*. London: Elsevier Applied Science.

Kyoto Protocol (1997). 3rd Conference Parties United Nations Framework Convention on Climate, Kyoto, Japan.

Lai, G.Y. (2007). *High-Temperature Corrosion and Materials Applications*. Materials Park, OH: ASM International.

Logan, H.L. (1961). *Corrosion* 17: 185t.

Masuyama, F. (2002). Proceedings of the 7th Liège Conference on Materials for Advanced Power Engineering, Energy Technology, 21, Part I–III, p. 1767.

Meadowcroft, D.B. (1987). *Mater. Sci. Eng.* 88: 313.

Meadowcroft, D.B. and Manning, M.I. (eds.) (1983). *Corrosion Resistant Materials for Coal Conversion Systems*. London: Applied Science.

NACE Technical Committee (1958). Report on the Present Status of the Oil Ash Corrosion Problems. Pub 58-11. Houston, TX.

Nickel, H., Wouters, Y., Thiele, M., and Quadakkers, J. (1998). *J. Anal. Chem.* 361: 540.

Ostwald, C. and Grabke, H.J. (2004). *Corros. Sci.* 46: 1113.

Otsuka, N., Shida, Y., and Fujikawa, H. (1989). *Oxid. Met.* 35: 13.

Ozerov, R.P. and Kildisheva, E.V. (1959). *Russ. J. Inorg. Chem.* 4: 476.

Parker, J.D. (2002). *Mater. High Temp.* 2: 47.

Parker, J.C., Rosborough, D.F., and Virr, M.J. (1972). *J. Inst. Fuel* 45: 95.

Peraldi, R. and Pint, B.A. (2004). *Oxid. Met.* 61: 463.

Phillips, N.D. and Wagner, C.L. (1961). *Corrosion* 17: 102.

Pillai, S.R., Sankar, P., and Khatak, H.S. (2004). *High Temp. Mater. Processes* 23: 195.

Rahmel, A. and Tobolski, J. (1965). *Corros. Sci.* 5: 333.

Robertson, J. and Manning, M.I. (1990). *Mater. Sci. Technol.* 6: 81.

Rothman, M.F. (ed.) (1984). *High Temperature Corrosion in Energy System*. New York: The Metallurgical Society of AIME.

Ruth, L.A. (2003). *Mater. High Temp.* 3: 11.

Schütze, M., Schorr, M., Renusch, D. et al. (2004). *Mater. Res.* 7: 111.

Sequeira, C.A.C., Chen, Y., and Marquis, F.D.S. (2003). *Molten Salt Forum* 7: 335.

Singer, J. (1991). *Combustion-fossil Power Systems*. Windsor, CT: Combustion Engineering Inc.

Smith, G. and Shoemaker, L. (2004). *Adv. Mater. Processes* 23.

Spafford, B.F. (1982). *UK Corrosion'83, Conference Proceedings*, 67. Birmingham: Institution *of* Corrosion Science and Technology.

Staubli, M., Mayer, K.H., Giselbrecht, W. et al. (2002). Proceedings of the 7th Liège Conference on Materials for Advanced Power Engineering, Energy Technology, 21, Part I–III, p. 1065.

Stultz, S.C. and Kitto, J.B. (eds.) (1992). *Steam and its Generation and Use*, 40e. Barberton, OH: Babcock and Wilcox.

Swales, G.L. and Ward, D.M. (1979). *Proc. Corrosion/79*, Paper No. 126. Houston, TX: NACE International.

Viswanathan, R. (2004). *Adv. Mater. Processes* 73.

Viswanathan, R. and Bakker, W.T. (2000). IJPGC 2000-15049, Proceedings of the 2000 International Joint Power Generation Conference, Miami Beach, FL, USA (23–26 July).

Viswanathan, R., Purget, R., and Rao, U. (2002). Proceedings of the 7th Liège Conference on Materials for Advanced Power Engineering, Energy Technology, 21, Part I–III, p. 1109.

Vossen, J.P.T., Gawenda, P., Rahts, K. et al. (1997). *Mater. High Temp.* 14: 387.

Wegst, C.W. (1995). *Stahlschlüssel*. Verlag Stahlschlüssel Wegst GmbH. ISBN: 3-922-599-11-7, 276.

Wilson, J.R. (1976). *Proceedings, Corrosion/76*, Paper No. 12. Houston, TX: NACE International.

Zahs, A., Spiegel, M., and Grabke, H.J. (1998). Proceedings of EUROCORR Conference.

Further Reading

Adams, T.N. (ed.) (1997). *Kraft Recovery Boilers*. TAPPI Press.

Betz, W. (ed.) (1986). *High Temperature Alloys for Gas Turbines and Other Applications, Part I*. D. Reidel Publishing Co.

Coutsouradis, D. (ed.) (1994). *Materials for Advanced Power Engineering*. Kluwer Academic Press.

French, D.N. (1993). *Metallurgical Failures in Fossil Fired Boilers*. London: Wiley.

Griffiths, T.R. and Phillips, N.J. (1992). *Mater. High Temp.* 10: 185.

Hellstrom, K., Hall, J., Malmberg, P. et al. (2014). *Energy Fuels* 28: 616.

Kawahara, Y. (2005). *Corros. Eng.* 54: 213.

Lai, G.Y. (1990). *High-Temperature Corrosion and Materials Applications*. Materials Park, OH: ASM International.

Lai, G.Y. (2007). *High Temperature Corrosion of Engineering Alloys*. Materials Park, OH: ASM International.

Laverde, D., Gómez-Acebo, T., and Castro, F. (2004). *Corros. Sci.* 46: 613.

McNallan, M.J., Thongteru, S., Liu, J.C. et al. (1993). *J. Phys. IV*, Coll. C9, Suppl. J. Phys. III, 3: 143.

Meadowcroft, D.B. and Manning, M.I. (eds.) (1983). *Corrosion Resistant Materials for Coal Conversion Systems*. London: Applied Science.

Reichel, H.H. (1988). *Mater. Corros.* 39: 54.
Rothman, M.F. (ed.) (1985). *High Temperature Corrosion in Energy System*. New York, NY: The Metallurgical Society of AIME.
Seiersten, M. and Kofstad, P. (1987). *High Temp. Technol.* 5: 115.
Schütze, M., Schorr, M., Renusch, D. et al. (2004). *Mater. Res.* 7: 111.
Stultz, S.C. and Kitto, J.B. (eds.) (1992). *Steam and its Generation and Use*, 40e. Barberton, OH: Babcock and Wilcox.
Syed, A.U., Simms, N.J., and Oakey, J.E. (2012). *Fuel* 101: 62.
Viswanathan, R. (2004). *Adv. Mater. Processes* 73.

Chapter 17

Testing and Evaluation

17.1 Introduction

One of the key parameters in high temperature oxidation is the parabolic rate constant. This is true as long as protective oxidation determines the material behavior. Consequently, measurement of the weight change of the specimen is the key experimental technique in high temperature oxidation. Generally, there are two possibilities. The first is to take a number of specimens of the same type, expose them to the respective atmosphere in a closed furnace in which defined atmospheres can be established, and take the specimens out after different oxidation states. Before and after the tests, the specimens are weighed on a high-resolution laboratory balance, and the weight change Δm provided by the surface area of the specimen, A, is plotted versus time. Therefore, before exposure, the surface area A of the specimens has to be determined accurately. If the results are plotted in a parabolic manner, that is, $\Delta m/A$ is squared while t remains linear, the rate constant can be determined directly from the slope, as discussed in Chapter 7.

A more elegant method is to use continuous thermogravimetry (Grabke and Meadowcroft 1995). In this case, a platinum or quartz string is attached to a laboratory balance that extends down into a furnace. At the lower end of the string, a coupon specimen is attached for which the surface area must be determined before the test. A movable furnace can also be installed that allows thermocyclic oxidation testing by periodically moving the furnace over and away from the specimen area. Ideally, the specimen should be in a quartz chamber or a chamber of another material that is highly corrosion resistant so that defined gas atmospheres can be used in the tests. The interior of the microbalance must be shielded against the aggressive gas atmospheres, usually by a counterflux of a nonreactive gas, such as argon. In a more sophisticated type of thermobalance, acoustic emission (AE) measurements can be made, for example, by acoustic emission thermography (AET) (see below; also Walter et al. 1993). This becomes possible if a waveguide wire is attached to the string hanging down from the balance, to which the specimen is attached. In particular, under thermocyclic conditions, AE measurements allow the determination of the critical conditions under which the oxide scales crack or spall (Schütze 1997). This type of scale damage is accompanied by mass loss due to spallation of the scale, and then this is directly reflected in the mass change measurements and can be correlated with AE results.

In some situations, internal oxidation or corrosion may occur that cannot be detected directly by thermogravimetric measurements. Therefore, it is necessary to perform metallographic investigations as well. In particular, for continuous thermogravimetric testing, at the end of each test, a metallographic cross section should be prepared in order to check whether the mass change effects measured in the tests are caused by surface scales alone or whether the metal cross section has been significantly affected. Furthermore, if the kinetics of internal corrosion are to be determined, it is necessary to perform discontinuous tests where specimens are taken out of the test environment after different testing times and then investigated by metallographic techniques (Baboian 1995; Birks et al. 2006; Glaser et al. 1994; Wouters et al. 1997).

Standard high temperature corrosion investigations also usually include an analysis of the corrosion products formed in the tests or under practical conditions because this allows conclusions as to which are the detrimental species in the environment and whether protective scales had formed. In most cases, this is done either in the scanning electron microscope (SEM) by using energy-dispersive X-ray analysis (EDX) or with metallographic cross sections in the electron probe microanalyzer (wavelength-dispersive X-ray analysis, WDX). Another tool may be glancing angle X-ray diffraction (GAXRD) technique, which allows analysis of the composition of thin layers.

Common experimental investigation techniques used to assess corrosion morphology, identify corrosion products, and evaluate mechanical properties are the following

High Temperature Corrosion: Fundamentals and Engineering, First Edition. César A. C. Sequeira.
© 2019 John Wiley & Sons, Inc. Published 2019 by John Wiley & Sons, Inc.

(Birks et al. 2006; Marcus and Mansfeld 2006; Rahmel 1982; Sequeira et al. 2008; Taniguchi et al. 2006):

(a) Corrosion morphology assessment
Optical microscopy
Scanning electron microscopy (SEM)
Electron probe microanalysis (EPMA)
Transmission electron microscopy (TEM)

(b) Corrosion products identification
X-ray diffraction (XRD)
Energy-dispersive X-ray analysis (EDX)
Secondary ion mass spectroscopy (SIMS)
X-ray photoelectron spectroscopy (XPS)
Auger electron spectroscopy (AES)
Laser Raman spectroscopy (LRS)

(c) Mechanical properties evaluation
Creep rupture
Postexposure ductility
Modulus of rupture (MOR).

In general, creep rupture, hardness, and MOR have been used equally to assess the mechanical properties of corroded test pieces. When the material is difficult to grip (as is a ceramic), its strength can be measured in bending. The MOR is the maximum surface stress in a bent beam at the instant of failure (International System [IS] units, megapascals; centimeter–gram–second units, 10^7 dyn cm^{-2}). One might expect this to be exactly the same as the strength measured in tension, but it is always larger (by a factor of about 1.3) because the volume subjected to the maximum stress is small and the probability of a large flaw lying in the highly stressed region is also small. (In tension all flaws see the maximum stress.) The MOR strictly applies only to brittle materials. For ductile materials, the MOR entry in the database is the ultimate strength.

The technical domains in which high temperature corrosion is of importance include thermal machines, chemical industry, incineration of domestic or industrial waste, electric heating devices, and nuclear engineering, and apart from purely environmental aspects, high temperature corrosion also constitutes a stage of some industrial processes of high financial or human cost (e.g. materials preparation with controlled properties, thermochemical surface treatment processes, etc.). Therefore, besides the oxidation problems discussed above, high temperature corrosion also involves other gaseous atmospheres (N_2, S_2, Cl_2, etc.), molten liquids (salts, metals, etc.), and more complex environments. Therefore, it is clear that to attain the expected performances of the systems and devices subjected to high temperature corrosion, as well as to characterize the corrosion scales and understand the corrosion mechanisms, it is necessary to use many experimental techniques. These include spectroscopic, electrochemical, and many other complex techniques. Spectroscopic techniques used for analysis of corrosion problems and characterization of thin and thick layers of corrosion scales are of considerable importance, but electrochemical techniques and other techniques using indirect measurements for the study of solid-to-solid, solid-to-liquid, and solid-to-gas properties are now becoming of great interest.

In the next section, brief considerations are included on the basic testing equipment and monitoring, at laboratory scale, as well as on optical microscopy and thermogravimetry. Then, a very brief summary of the main spectroscopic techniques in current use, their main limitations, and scope for development is provided. In fact, spectroscopic techniques used for chemical analysis of oxidation problems and characterization of thin layers of corrosion scales are more and more of considerable importance, thus deserving an entire section for their general discussion. In the following sections, numerous former and actual experimental techniques are considered, being possible to obtain more detailed methodology or results of specific techniques. In these sections, nondestructive inspection (NDI) techniques are also included.

The effects of temperature on mass transport and kinetics phenomena of corrosion nature along with its use in a number of technological industries of particular interest, such as nuclear, fossil-fueled, geothermal, high temperature fuel cells and high-energy batteries, and so on, require the knowledge of detailed mechanistic studies involving high temperature aqueous and solid-state electrochemistry. Thus, a number of electrochemical techniques and procedures are discussed in the last section of this chapter.

17.2 Testing Equipment and Monitoring

The reaction vessels for studying high temperature corrosion may be horizontal or vertical tubes, depending on the type of measurement required. Pyrex glass can be used up to 450 °C only and must be changed to vitreous silica (often improperly called "quartz") that can then be used up to 1050 °C. These glassy materials have the advantage of being transparent to light and of being joined and readily molded to shape by flame processing. For higher temperatures, ceramic materials such as mullite or alumina should be employed. Metallic reaction vessels are seldom used since they themselves may react with the oxidizing gas. For studies of corrosion by fluorine, F_2, or its compounds such as HF, SOF_2, or SO_2F_2, it should be noted that silica glasses are not stable, and, similarly, for halogen–carbon reactions where alumina is chlorinated, nickel-based alloys are used. It will also be necessary to use metallic vessels (termed autoclaves) when high pressure reactions are studied.

Tubular electric furnaces are of common use in air up to 1250 °C with metal wire heating elements (NiCr, FeCrAl,

NiCrAl), but, for higher temperatures, these elements have to be protected against oxidation. Heating elements made of SiC or $MoSi_2$ are self-protecting through the formation of a silica layer, and their use extends the temperature range of air furnaces to 1500 °C. Tungsten or molybdenum resistance furnaces can be used up to 2500 °C, provided that they are kept under vacuum to prevent oxide volatilization.

Reliable measurement of test temperature is of great importance because of the strong dependence of the reaction kinetics on temperature. Several types of thermocouples are available, depending on the temperature range being used:

- NiCr/NiAl (K type) up to 900–1000 °C.
- Pt-10%Rh/Pt (S type) for temperatures up to 1700 °C.
- W-Rh/W up to 2500 °C.

The higher the maximum temperature for these couples, the lower their sensitivity. Locating the thermocouple inside the reaction is obviously the best option for accurate temperature measurement, but the thermocouple in relation to the specimen within the furnace is also of major importance. A location inside the reactor tube would obviously be better. For particularly corrosive environments, it is sometimes useful to use stainless steel or Inconel sheeting, particularly for the K-type thermocouples. When the thermocouple tip has to be placed inside the reaction vessel, careful calibration measurements have to be performed to map the longitudinal and radial temperature gradients within the furnace. In all cases, effective draft proofing has to be placed at both ends of the furnace, between the reactor and furnace tubes, to avoid air convection currents that would disturb the temperature distribution within the vessel. The use of such insulation is particularly recommended for vertical furnaces.

Static or dynamic atmospheres may be used during oxidation testing. For the case of *static atmospheres*, the oxidant, usually a gas, is introduced into the reaction chamber after it has been evacuated, and the reaction vessel is then subsequently closed. Such atmospheres are characterized by the total pressure and the molar fraction (partial pressures, in the case of a gas) of each constituent. For the case of *dynamic atmospheres*, the oxidant continuously circulates in the open reaction chamber. The flow rate is then an additional experimental variable, and it is necessary to know this as part of the complete characterization of the oxidation test.

Static atmospheres should be used only when the reactive oxidizing species, assumed gaseous for illustration, are in overwhelmingly large concentrations so that the products of reaction do not have any significant effect on the original concentration. In all other cases, only dynamic atmospheres can ensure constant partial pressures of the reacting constituents and control over the buildup of reaction products. Gas flow rates in the range of 0.1–10 mm s^{-1} are commonly used, but simple mass balance calculations can ensure that the concentration of oxidant is in large excess compared with the amount lost during the reaction. This condition has to be fulfilled to avoid affecting the kinetics of reaction through a limitation on the supply of oxidant. Such a limitation may occur, for example, when very small amounts of highly reactive gases (HCl, SO_2, etc.) are diluted in an inert carrier gas. Experiments conducted at different flow rates can be usefully used to establish whether kinetic limitations apply for particular test conditions.

To monitor the extent of the corrosion reaction, a few common approaches are described below.

Geometrical monitoring uses the thickness of the growing oxide scale or of the recessing metal as a measure of the progress of the reaction. Discontinuous measurements are performed on one or several samples submitted to the same temperature and oxidizing environment. The measurement may be destructive (by using optical microscopy or SEM on cross sections), so that one sample is consumed for each data point, or nondestructive (by using ellipsometry; Rutherford backscattering, RBS; nuclear reaction analysis, NRA) so that the same sample may be used for several successive data point measurements. A continuous geometry-related measurement, seldom used, consists in following the electrical resistance increase of a recessing metallic wire during scaling.

Manometric monitoring can be used when the reaction being studied consumes the gaseous oxidant without any gas release. The decrease of the oxidant pressure in a closed reaction vessel is then used as a monitoring parameter. A highly sensitive pressure transducer must be used to allow experiments to be performed at near-constant pressure. An improved version of the method consists in using two vessels connected by a motorized vane. The first vessel contains the sample where the gas pressure is continuously measured and adjusted to a constant value by repeated small additions from the second vessel. In this latter vessel, the pressure decrease as a function of time is monitored and used as a measure of the progress of the reaction.

Gravimetric monitoring is the most commonly used method and consists in following the mass of the sample as a function of time. This can be done discontinuously by removing the specimen from the furnace, to allow weight measurements at room temperature, and then reinserting. Continuous measurements are possible using thermobalances (the approach is known as thermogravimetric monitoring) of which highly reliable samples are nowadays available, covering a large range of temperature and pressure conditions. It should be pointed out that the choice of the type of

gravimetric measurement, continuous or discontinuous, is not without consequence and may influence the kinetic results. Discontinuous monitoring using the same sample imposes thermal cycling, possibly leading to scale degradation and accelerated corrosion. This type of monitoring is, however, closer to many industrial service conditions where high temperature parts are generally submitted to thermal cycling. For more academic purposes, the continuous thermogravimetric measurements are preferred in order to better understand the mechanisms of isothermal corrosion.

Laboratory testing equipment and experimental monitoring of the corrosion extent other than oxidation processes are also briefly described in the context of the techniques analyzed below.

17.3 Optical Microscopy

Optical microscopy is a very common technique used for the corrosion morphology assessment, and it is outlined here for studying carbons and other lamellar structures.

Specimens are prepared by mounting the sample in a resin block and polishing the surface to optical flatness using alumina or diamond paste (if the specimen is massive enough, it can be polished without mounting). The polished surface is examined using reflected light microscopy usually with polarized light. To observe interference colors, due to the orientation of the graphitic lamellae at the surface, parallel polars are used with a half-wave retarder plate between the specimen and the analyzer. The general arrangement is shown in Figure 17.1, together with diagrams illustrating the generation of the interference colors.

The appearance of a surface is called its *optical texture*. Figures 17.2–17.4 illustrate the type of textures observed. The size and shape of the isochromatic areas can be estimated. Dimensions vary from the limit of resolution ~0.5 μm to hundreds of micrometers. The nomenclature used to describe the features has been developed over many years, and discussions are still underway to establish a more standard system. Table 17.1 gives definitions of the classes of optical anisotropy together with a definition of *optical texture index* (OTI), factor that is useful for characterizing a carbon material.

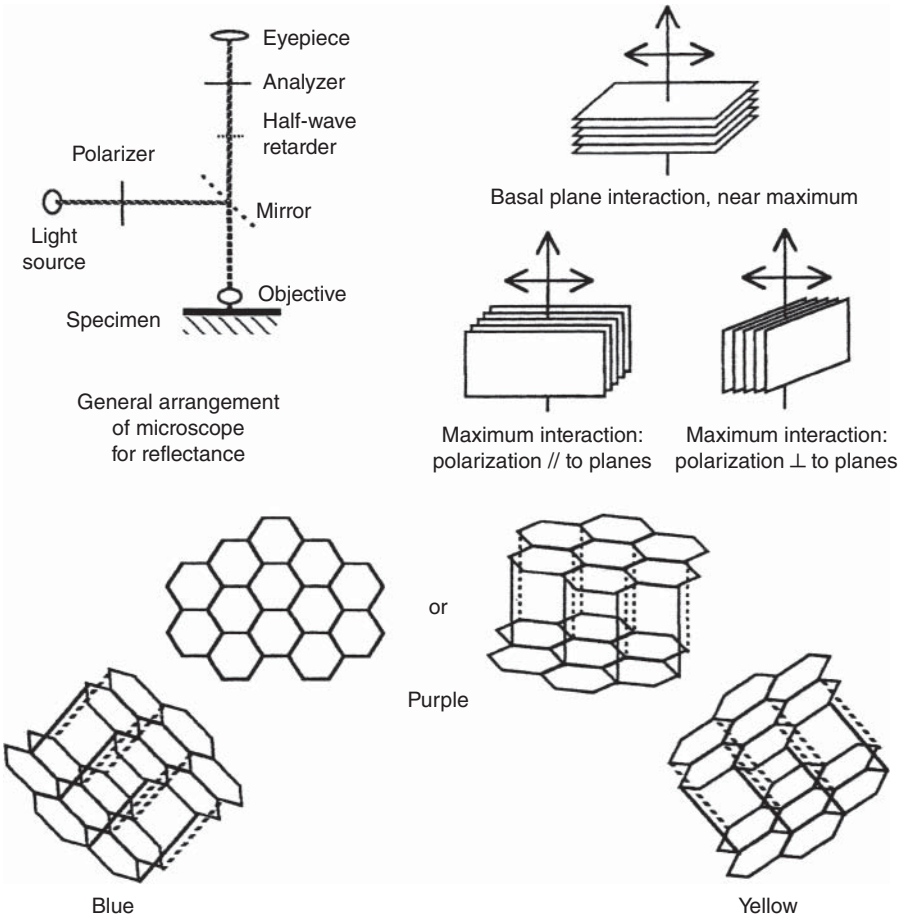


Figure 17.1 Polarized light optical microscopy and interference colors.

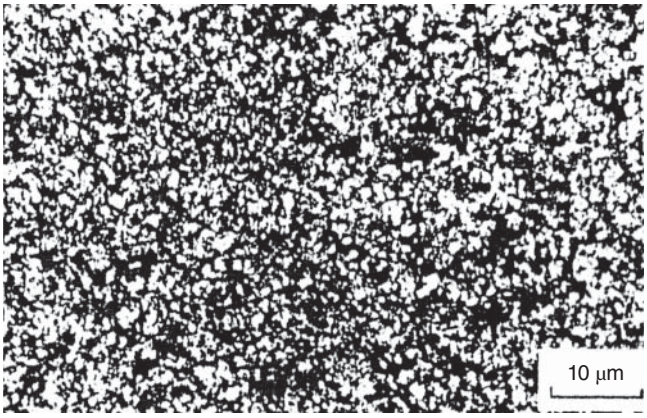


Figure 17.2 Optical micrograph of coke surface – fine-grained mosaic, OTI = 1.

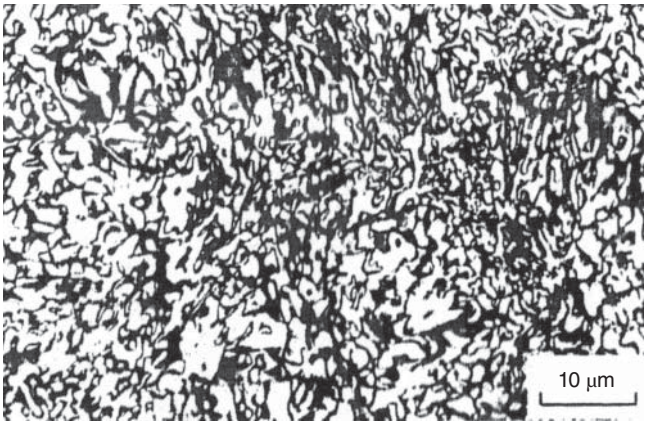


Figure 17.3 Optical micrograph of coke surface – medium and coarse mosaic, OTI = 3.



Figure 17.4 Optical micrograph of coke surface – coarse flow, OTI = 30.

Table 17.1 Description of optical anisotropy and OTI

Nomenclature used to describe optical texture		OTI factor
Isotropic (Is and Ip)	No optical activity	0
Fine mosaics (F)	<0.8 μm in diameter	1
Medium mosaics (M)	>0.8 to <2.0 μm in diameter	3
Coarse mosaics (C)	>2.0 to <10.0 μm in diameter	7
Granular flow (GF)	>2 μm in length >1 μm in width	7
Coarse flow (CF)	>10 μm in length >2 μm in width	20
Lamellar (L)	>20 μm in length >10 μm in width	30

By point counting the individual components of the microscope image and multiplying the fraction of points encountered for each component by the corresponding OTI factor and summing the values, the optical texture index for the sample can be obtained. This number gives a measure of the overall anisotropy of the carbon.

It must be stressed that this is only a comparative technique and that material characterized as isotropic may only be so at the level of resolution. This becomes obvious when a surface is examined with a higher-grade objective (not just higher power), allowing more anisotropy to be observed (distinguished).

Other uses of optical microscopy in the study of carbon materials are mainly concerned with coal petrography, a discipline based on the measurement of reflectance from the coal surface and dealing with coal materials in terms of macerals. These forms are identifiable as deriving from the original plant material via the coalification process. A related area is the study of char forms derived from the pyrolysis of coal.

17.4 Thermogravimetry

The most widely used method to follow the kinetics of high temperature oxidation and corrosion is to measure the mass change (amount of metal consumed, amount of gas consumed, amount of scale produced) with temperature: *thermogravimetry*. The simplest method of mass change monitoring is to use a continuous automatic recording balance. The apparatus suitable for this is shown diagrammatically in Figure 17.5, which is self-explanatory.

To increase the accuracy of these balances toward the microgram range, the physical interactions of the sample with the gas must be taken into account and combated. Three of these interactions are of importance.

17.4.1 Buoyancy

Thermogravimetric kinetic measurement will be perturbed, and errors introduced in all cases where buoyancy varies with time. To illustrate this, consider a solid of volume V immersed at temperature T in a perfect gas mixture of mean molar mass M at a pressure P. The effect of buoyancy can

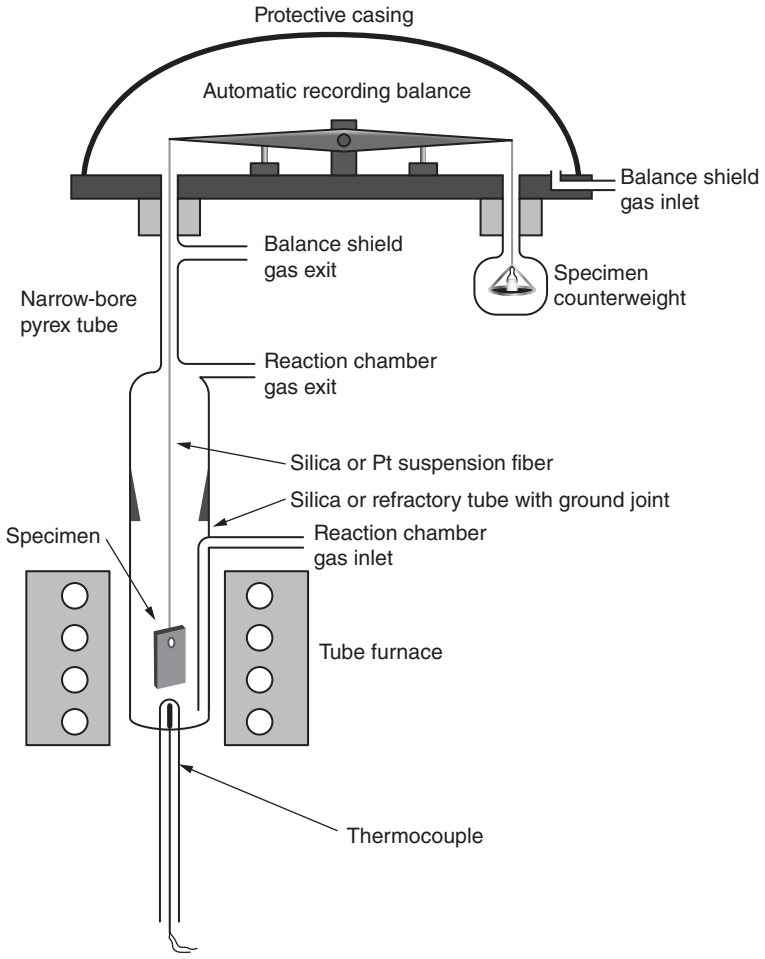


Figure 17.5 Typical experimental arrangement for measuring oxidation kinetics with an automatic recording balance (Birks et al. 2006).

then be described by

$$B = \alpha g V M \frac{P}{T} \tag{17.1}$$

where g is the acceleration due to gravity and α the ratio $T°/P°V°$ of the temperature, pressure, and molar volume of gases under normal conditions. This relation first shows that buoyancy depends on temperature so that temperature variations during the experiment lead to apparent mass changes, but these are easy to calculate. As example, consider a typical rectangular sample with dimensions $20 \times 10 \times 2\,\text{mm}^3$ placed in oxygen. Heating this sample from room temperature to 1000 °C will lead to an apparent increase in mass of approximately 0.5 mg. It can be ascertained that, to achieve maximum balance sensitivity under nominally isothermal measurements, care must be taken to ensure a high standard of temperature control of the furnace. For example, with temperature variations of ±3 °C near 300 °C, the apparent mass variations are of the order of ±2 µg; at higher temperatures, the error in the determination of mass is less, e.g. ±0.3 µg at 1000 °C, because of the lower gas density. Buoyancy force variations with the increase of sample volume during oxidation can also be calculated but are generally negligible compared with the accuracy of the thermobalances.

17.4.2 Convection Currents

Convection currents result from the effect of gravity on temperature-induced differences in the specific mass of gas at different locations within the reaction vessel. They become noticeable for pressures greater than 100–200 mbar and are manifested by convection loops that can perturb the thermogravimetric measurements.

In *open static reaction vessels*, the convection loops curl outside the reaction vessel, and the well-known chimney effect is observed (Figure 17.6a). Such a configuration has to be avoided, or one end of the reaction vessel has to be plugged.

In *closed static reaction vessels*, convection may occur due to radial temperature gradients, as shown schematically in Figure 17.6b where the sample is envisaged to have a temperature slightly lower than that of the vessel wall. The convection loops in this case lead to an apparent

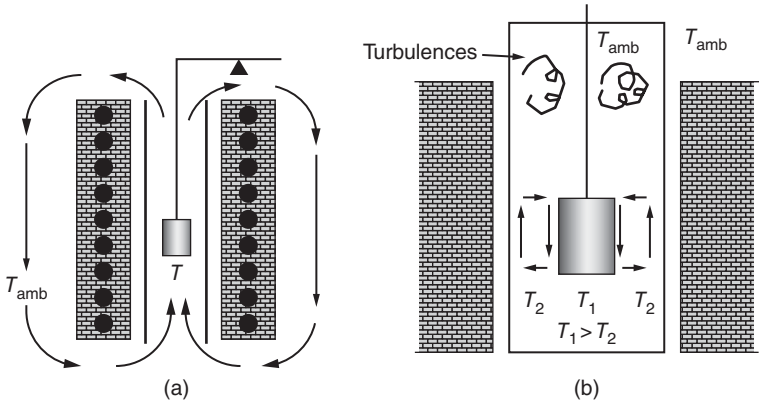


Figure 17.6 Convection currents in reaction vessels. (a) Vertical open vessel. (b) Closed static vessel.

mass increase. Near the top of the furnace, where strong radial and longitudinal gradients are present, convection phenomena are present. Such a region (20 cm above the furnace) is subject to turbulence that may be minimized by the use of thin suspension wires having no geometrical irregularities such as asperities or suspension hooks.

A semiquantitative assessment of the importance of these natural thermal gravity convection currents can be obtained through the use of the *Rayleigh number*, *Ra*. This dimensionless number is defined as

$$Ra = \frac{g\beta C_p \rho^2 b^3 \Delta T}{\eta K} \tag{17.2}$$

where g is the acceleration due to gravity, β the coefficient of thermal expansion of the gas (for a perfect gas: $\beta = 1/T$), C_p the thermal capacity of the gas at constant pressure, ρ the density of the gas, b the length of the non-isothermal zone, ΔT the temperature difference, η the dynamic viscosity of the gas, and K the thermal conductivity of the gas.

For low values of the Rayleigh number ($Ra < 40\,000$), natural thermal gravity convection may be neglected. For higher values, convection loops may perturb thermogravimetric measurements, sometimes creating very strong movements of the sample suspension system and leading to a drastic decrease in accuracy.

In dynamic reaction vessels, the imposed gas flow leads to forced convection whose effects are generally greater than those due to natural convection. The flow behavior within the vessel can then be described by the *Reynolds number* (*Re*). This dimensionless number is defined as

$$Re = \frac{\rho u L}{\eta} \tag{17.3}$$

where ρ is the density of the gas, u the linear velocity of the gas, L the characteristic length of the system, and η the dynamic viscosity of the gas, calculated using the following equation:

$$\eta = \frac{1}{3\sqrt{2\sigma}} \sqrt{\frac{8mkT}{\pi}} \tag{17.4}$$

where k is the Boltzmann's constant, m the mass of one gas molecule, T the absolute temperature of the reaction vessel, and σ the mean collisional cross section of a molecule ($\sigma = 4\pi r^2$, where r is the molecule radius).

This approach, though necessarily simple, provides insights into the factors that affect the accuracy of the experimental values obtained in thermogravimetric tests. It should be noted that the values given for the Rayleigh and Reynolds numbers have to be considered as an order-of-magnitude guide only. For example, a gas flow with a Reynolds number of 2000 may be turbulent in a tube of high internal roughness but perfectly laminar in a smooth silica tube.

17.4.3 Thermomolecular Fluxes

In contrast to convection forces, which are active at moderate and high gas pressures, thermomolecular fluxes appear at low pressures in the domain where the gas may be considered as a *Knudsen gas*. The term Knudsen gas describes a situation where molecules do not collide with each other but only with the vessel wall. Such behavior occurs for values greater than 1 of the dimensionless *Knudsen number* (*Kn*):

$$Kn = \frac{\lambda}{d} \tag{17.5}$$

where λ is the mean free path of molecules and d is a characteristic distance, e.g. the tube radius for a cylindrical reaction vessel.

In this Knudsen domain, gas pressure relates to temperature according to

$$\frac{P_2}{P_1} = \sqrt{\frac{T_2}{T_1}} \tag{17.6}$$

Consider a cylindrical sample immersed in a Knudsen gas and submitted to a temperature difference $T_2 - T_1$ applied across a horizontal plane whose trace is XY in Figure 17.7. This sample is then submitted to two resulting Knudsen forces:

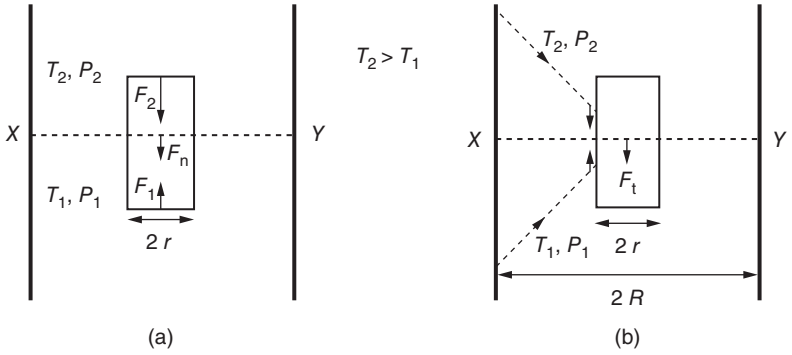


Figure 17.7 Normal and tangential forces acting on a vertical cylindrical sample submitted to a temperature gradient in a Knudsen gas.

- A resulting normal Knudsen force, F_n, acting on the horizontal circular section (Figure 17.7a).
- A resulting tangential Knudsen force, F_t, acting on the vertical surfaces of the cylindrical sample (Figure 17.7b).

The resulting force F_n arises from the difference in the pressure forces on the two circular bases of the cylinder (Figure 17.7a):

$$F_n = F_2 - F_1 - (P_2 - P_1)\pi r^2$$

$$F_n = \pi r^2 P_2 \left(1 - \sqrt{\frac{T_1}{T_2}}\right) \qquad (17.7)$$

The resulting tangential force is due to the difference in the momentum of the molecules hitting the vertical surface of the sample and arriving from the upper (hot) or the lower (cold) part of the reaction vessel (Figure 17.7b). Such a force was forecasted by Maxwell (1973). It can be expressed by

$$F_1 = \pi r(R - r) P_2 \left(1 - \sqrt{\frac{T_1}{T_2}}\right) \qquad (17.8)$$

In the intermediate domain, defined by a Knudsen number between 1 and 10^{-5}, normal and tangential forces are the result of a gas flux generated according to the exchange of momentum between molecules. The calculation of these forces is complex, but it can be shown that they increase with pressure and pass through a maximum before they decrease. This decrease results from the modification of gas properties and the appearance of a regime where the pressure in a closed isothermal vessel has a unique value.

Table 17.2 describes the different gas flow phenomena that may perturb thermogravimetric measurements and identifies the domains where they are active.

In order to limit all the perturbations described above, a symmetrical furnace setup is particularly efficient. In order to optimize performance, both furnaces are operated as nearly as possible at the same temperature and with the same temperature gradients.

Table 17.2 Gas flow regimes where perturbation of thermogravimetric measurements may occur

Knudsen number	Pressure domain (mbar; air, 298 K, $R = 5$ cm)	Type of gas flow	Observations
10^4–1	10^{-7}–10^{-3}	Thermomolecular	Knudsen forces
1–10^{-5}	10^{-3}–100	Intermediate	Knudsen forces
$\leq 10^{-5}$	≥ 100	Convection	Fluctuations around an equilibrium position

Setaram, for example, supplies accurate thermobalances of this type of symmetrical furnaces.

17.5 Spectroscopy

Chemical analysis by spectroscopy has made rapid advances in high temperature studies and almost always includes equipment for high-resolution microscopy. Several books and monographs are available, including most of the old and newly developed techniques (Kofstad 1988; Marcus and Mansfeld 2006). Glow discharge mass spectroscopy (GDMS) is fast, sensitive, accurate, simple, and reliable and can be used for surface analysis if the specimen can be attached to a vacuum cell (Bernéron and Charbonnier 1982).

The resolving power in-depth profiling is similar to AES and SIMS. A 1 kV glow discharge causes ion bombardment and surface erosion that is fed (optically) to a multichannel spectrometer for elemental analyses. Other long and complex methods of surface analysis, such as AES, SIMS, XPS, ISS (ion scattering spectroscopy), RBS, NRA, IIXA (ion-induced X-ray emission), and ESCA (electron spectroscopy for chemical analysis), are difficult for field use. Several authors have reviewed these methods. Tables 17.3–17.6 compare the techniques, and Figure 17.8

Table 17.3 Methods of material characterization by excitation and emission

Primary excitation	Detected emission	Methods of analysis: name and nomenclature
Photons, optical	Optical	Spectroscopy
		AA: atomic absorption
		IR: infrared
		UV: ultraviolet
		Visible
	Electrons	UPS: vacuum UV photoelectron spectroscopy
		Outer shell
Photons	Electrons	XPS: X-ray photoelectron spectroscopy
X-rays	X-rays	Inner shell; also called ESCA
		ESCA: electron spectroscopy for chemical analysis
		XFS: X-ray fluorescence spectrometry
		XRD: X-ray diffraction
Electrons	X-rays	EPMA: electron probe microanalysis
	Electrons	SEM: scanning electron microscopy
		TEM: transmission electron microscopy
		STEM: scanning transmission electron microscopy
		SAM: scanning AUGER microanalysis
		AES: Auger electron spectroscopy
Ions	Optical	SCANIIR: surface composition by analysis of neutral and ion impact radiation
	X-rays	IIXA: ion-induced X-ray analysis
	Ions (±)	ToFMS: time-of-flight mass spectrometry
		SIMS: secondary ion mass spectrometry
		IPM: ion probe microanalysis
		ISS: ion scattering spectrometry
		RBS: Rutherford backscattering spectrometry
Radiation	Optical	ES: emission spectroscopy
	Ions (±)	SSMS: spark source mass spectrography

Table 17.4 Summary of various characteristics of the analytical techniques

Characteristic	AES	XPS	ISS	SIMS	RBS	NRA	IXX
Sample alteration	High for alkali halogen organic insulators	Low	Low	Low	Very low	Very low	Very low
Elemental analysis	Good	Good	Good	Poor	Fair	Fair	Good
Sensitivity, variation, resolution	Good	Good	Fair	Good	Fair	Good	Good
Detection limits	0.1%	0.1%	0.1%	10^{-4}% or higher	10^{-3}% or higher	10^{-2}% or higher	10^{-2}% or higher
Chemical state	Yes	Yes	No	Yes	No	No	No
Quantification	With difficulty, required standards	With difficulty, required standards	With difficulty, required standards	With difficulty, required standards	Absolute, no standards	Absolute, no standards	Absolute, no standards
Lateral resolution	100 nm	2 mm	100 m	100 to 1 m	1 mm	1 mm	1 mm
Depth resolution	200 nm	To atomic layer	To atomic layer	To atomic layer	10 nm	10 nm	None
Depth analysis	Destructive, sputter	Destructive, sputter	Destructive, sputter	Destructive, sputter	Non-destructive	Non-destructive	Very difficult

Table 17.5 Outline of some important techniques to study metallic surfaces

Technique	Abbreviation	Information	Comments
Optical microscopy	OM	Surface topography and morphology	Inexpensive but modest resolving power and depth of field
Transmission electron microscopy	TEM	Surface topography and morphology	Very high resolution but requires replication; artifacts can be a serious problem
Scanning electron microscopy	SEM	Surface topography and morphology combined with X-ray spectroscopy gives "bulk" elemental analysis	Resolving power $\gg$ optical microscopy; preparation easier than TGEM and artifacts much less likely
X-ray photoelectron spectrometry	XPS (ESCA)	Chemical composition, depth profiling	Especially useful for studying adhesion of polymers to metals
Secondary ion mass spectroscopy	SIMS	Elemental analysis in "monolayer range," chemical composition, and depth profiling	Extremely high sensitivity for many elements
Auger electron spectroscopy	AES	Chemical composition, depth profiling, and lateral analysis	High spatial resolution that makes the technique especially suitable for composition–depth profiling
Contact angle measurement	—	Contamination by organic compounds	Inexpensive; rapid

Table 17.6 Types of samples and techniques nearly appropriate for their analysis

Required sample analysis	Appropriate technique
Depth profiling lower *Z* elements and thin films; trace or minor analysis of light elements; quantitative analysis	NRA
Depth profiling of higher *Z* elements and thin films; trace analysis of heavy elements in light matrix; quantitative analysis	RBS
Trace, minor, and major element analysis in thicker samples; quantitative analysis	IIX
Minor and major elements at surface or interface of small samples	AES
Trace elements at surface or interface of medium to small size samples; analysis of insulators; sputter profiling of light elements	SIMS
Chemical state analysis; analyses of organics and insulators	XPS
Analysis of outer atom layer; analysis of insulators	ISS

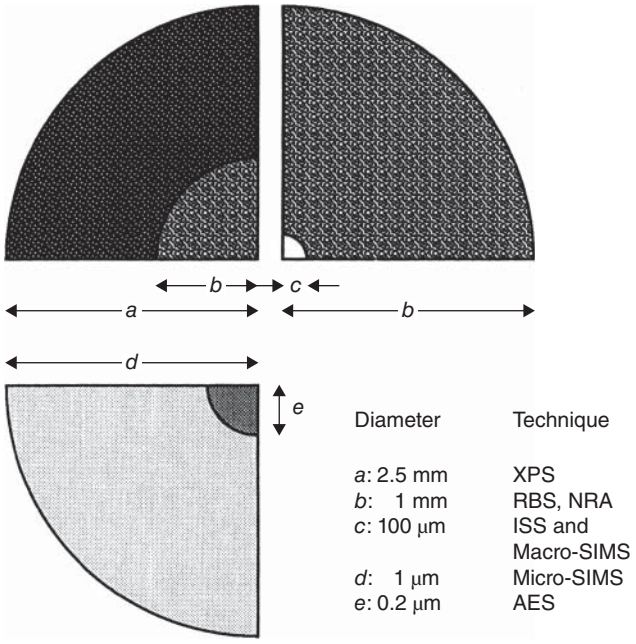


Figure 17.8 Schematic illustrating relative sizes of areas scanned by spectrometric analytical techniques.

shows the relative sizes of areas analyzed using these techniques.

Commonly used methods are optical and SEM for surface studies. TEM of interfaces has been explored. Selected area diffraction patterns (SADPs) show the orientation between different grains. In a ceramic coating, the interface between different phases can be coherent, semi-coherent, or incoherent. Coherent phases are usually strained and can be studied by TEM contrast analysis. Other aspects of analytical electron microscopy analysis are discussed (Hansmann and Mosle 1982; Thoma 1986). TEM resolution is better than 1 nm, and selected volumes of 3 nm diameter can be chemically analyzed. Methods of preparing thin TEM transparent foils are described (Doychak et al. 1989; Lang 1983).

Photoemission with synchrotron radiation can probe surfaces of an atomic scale (Ashworth et al. 1980; Pask and Evans 1980), but this method requires expensive equipment. Complex impedance measurements can separate

surface and bulk effects, but problems of interpretation still need to be resolved (Marcus and Mansfeld 2006). X-ray and gamma radiographs, as used in weld inspection, can be used to inspect coating for defects. The method has been discussed by Helmshaw (1982). Inclusions, cracks, porosity, and sometimes lack of fusion can be detected. Surface compositions of ion-implanted metals have been studied by RBS (Brewis 1982; Marcus and Mansfeld 2006). In this nondestructive way, a microanalysis of the near-surface region is obtained. Interpretation is relatively easy. Assessment of radiation damage in ion-implanted metals by electron channeling is described using SEM (Ashworth et al. 1980) for the characterization of surface films (Marcus and Mansfeld 2006).

AES and XPS analyze the top of the surface only, and erosion by ion bombardment or mechanical tapering is needed to analyze deeper regions. AES detects 0.1% of an impurity monolayer in a surface. Auger electrons are produced by bombarding the surface with low-energy (1–10 keV) electrons. In XPS the surface is exposed to a soft X-ray source, and characteristic photoelectrons are omitted. Both AES and XPS electrons can escape from only 1 nm depth from the surface, and so these are surface analytical methods (Brewis 1982; Marcus and Mansfeld 2006).

It is most important to avoid contamination during preparation for surface analysis; semiquantitative *in situ* analysis by AES has been reported (Bosseboeuf and Bouchier 1985). Nitrides and other compound refractory coatings are frequently analyzed by AES and RBS methods. Depth and crater edge profiling have been carried out for direct-current (DC) magnetron sputtered and activated reactive evaporation (ARE) samples of (Ti, Al)N, TiN, and TiC coatings (John et al. 1987; Kaufherr et al. 1987). Round-robin tests of characterization by including a range of analyses such as XPS, EPMA, XRS, AES, APMA, and XRD are not uncommon. Among these, XRD was felt to be unreliable (Perry et al. 1987).

Ion spectroscopy is a useful technique for surface analysis (Marcus and Mansfeld 2006). ISS uses low-energy backscattered ions (Czanderna 1975) and has a high sensitivity. SIMS has the possibility of sputter removal of layers, allowing depth profiling (Brewis 1982). It can act as a stand-alone system to solve surface analysis. Three-dimensional (3D) SIMS of surface-modified materials and examination of ion implantation is reported (Fleming et al. 1987). Lattice vacancy estimation by positron annihilation is another approach (Brunner and Perry 1987). TEM and SEM are valuable techniques, and replication methods using, for example, acetate replicas can nondestructively reveal surface features of specimens too thick for TEM (Brewis 1982; Grabke and Meadowcroft 1995). ARE coatings of V–Ti in C_2H_2 give wear-resistant (V, Ti)C coatings. The hardness is related to grain size, stoichiometry, free graphite, and cavity networks. SEM and XRD analysis could not be used to explain the large hardness variations obtained by varying temperature and gas pressure, but TEM revealed microstructural changes (Grabke and Meadowcroft 1995; Lang 1983; Marcus and Mansfeld 2006). Beta backscatter and X-ray fluorescence have low sensitivity ($0.5\,cm^2\ min^{-1}$ and $1\,cm^2\ h^{-1}$, respectively). Thickness and uniformity of silica coatings on steel have been determined by X-ray fluorescence measurements of Si concentrations along the surface (Bennett 1984; Lang 1983). Round-robin tests for microstructure and microchemical characterization of hard coatings have included XPS, UPS (UV photoelectron spectroscopy), AES, EELS (electron energy loss spectroscopy), EDX, WDX (wave-dispersive X-ray analysis), RBS, SIMS, TEM, STEM (scanning transmission electron microscope), and XTEM (X-ray transmission electron microscopy) (Bennett 1984; Bennett and Tuson 1989). Field emission STEM has been applied for profiling *Y* across a spinel–spinel grain boundary (Bennett 1984; Bose 2007; Grabke and Meadowcroft 1995; Sundgren et al. 1986).

In summary, when studying oxidation behavior at high temperatures, the foremost requirement is to monitor the extent and kinetics of attack. To obtain a complete mechanism understanding, such data have to be augmented by precise details of all the processes involved, starting with the chemical reaction sequence, leading to the formation of gaseous products and solid products at the reacting surface. The development and failure of protective surface scales crucially govern the resistance of most materials in aggressive environments at elevated temperatures. Knowledge is also essential on the changes throughout the exposures of the scale chemical composition, physical structure (including topography), stress state, and mechanical properties as well as on the scale failure sequence (e.g. by cracking and spallation).

All these processes involved in high temperature oxidation are dynamic. Therefore, to obtain unambiguous information, the main experimental approach in research should be based on *in situ* methods. These can be defined as being techniques that either measure or observe directly high temperature oxidation processes, as they happen in real time. Although numerous *in situ* methods have been developed to date, with several notable exceptions, the most important being controlled atmosphere thermogravimetry, the deployment of these techniques has been often limited. This may be attributed largely to experimental difficulty and also to the lack of suitable equipment. Current understanding of the chemical and physical characteristics, stress state, and mechanical properties of oxidation scales largely derives from postoxidation investigations. In fact, certain detailed aspects, for example, variations in mechanical properties and microstructure through scales,

can be revealed only by postoxidation studies. The two main experimental approaches, *in situ* oxidation and postoxidation, are not mutually exclusive, as they complement and augment each other. Nevertheless, at the current state of mechanistic knowledge of high temperature oxidation, further understanding of many critical facets (e.g. the breakdown of protective scales) will be revealed only by real-time experimentation. These requirements taken in conjunction with recent advances in both commercial and experimental equipment design/capabilities and in data storage/processing make it imperative that all investigators in this field be fully aware of the available *in situ* experimental test methods.

The purpose of this section is to provide a very brief summary of some major techniques in current use, their main limitations, and scope for development. Information on the detailed methodology of any technique or the complete results of any specific study using any such technique should be obtainable from the following sections and/or the references given to published papers.

17.6 Diffraction Techniques

Diffraction techniques are the most important to the analysis of crystalline solids – both phase and structural information. The techniques of greatest interest in this area include XRD, low-energy electron diffraction (LEED), reflection high-energy electron diffraction (RHEED), and neutron scattering. XRD is included even though it is not a surface-specific technique since it is by far the most common of the diffraction-based techniques used, i.e. this is the standard method for solving crystal structures for both single-crystal samples and powdered crystalline samples. Surface specificity is lost in XRD due to the geometry used and the fact that photons have long path lengths within solids for both elastic and inelastic collisions. The remainder are surface-specific techniques.

17.6.1 X-Ray Diffraction

The average bulk structure of many materials can be readily revealed using XRD. The technique provides a measure of the amount of ordered material present and can be used to give an indication of the size of the crystallites that make up the ordered structure.

The samples are usually prepared either as powders in capillaries or spread on a flat sample holder. The XRD pattern is recorded either on film or with a diffractometer. Figure 17.9 shows the arrangement of a powder diffractometer.

The resulting pattern is the amount of scattering over a range of scattering angles, θ, and can be analyzed in terms of diffraction peaks, their positions, and their widths. For the most accurate work, a standard (usually a crystalline salt) is added to the powder to provide internal calibration of the peak positions and widths, thereby allowing any instrumental factors to be taken into account.

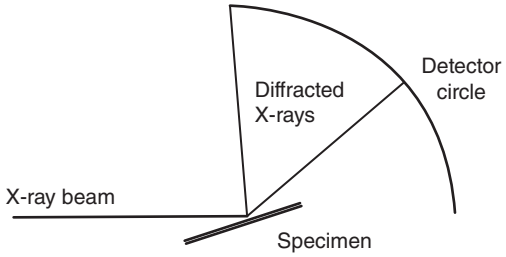


Figure 17.9 X-ray diffraction.

Although the main scattering derives from the ordered material present, some indication of the amount of disorder can be obtained by the background scatter. Similarly, the broadening of the diffraction peaks allows an estimation of the mean particle size to be made. Line broadening arises from both the strain or defects in the lattice and the finite crystal size. Assuming that the defects in the lattice reduce the extent of order, an effective crystallite size, t, can be estimated from the amount of broadening, β, using the *Scherrer equation*

$$t = \frac{\kappa \lambda}{\beta \cos \theta} \tag{17.9}$$

where λ is the wavelength, θ is the scattering angle, and the value of κ ($\sim$1) depends upon the shape of the crystallite, e.g. κ has the values of 0.9 for L_c and 1.84 for L_a.

β is the amount of broadening due to the sample, and the observed broadening, B, usually needs to be corrected for the instrumental broadening, b, using relationships such as

$$\beta^2 = B^2 - b^2 \tag{17.10}$$

The measuring of line broadening is illustrated in Figure 17.10.

The parameters usually quoted from XRD experiments are

$d_{(002)}$ interlayer spacing, L_c stack height, and L_a stack width.

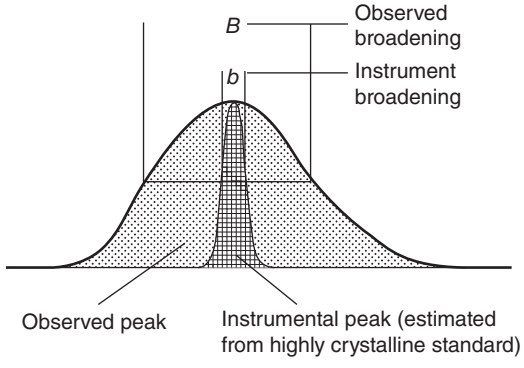


Figure 17.10 X-ray diffraction line broadening.

These give some indication of the degree of crystallization of the material. One specialized area of diffraction is that of fiber diffraction. Both normal and small-angle scattering patterns are used for this investigation. Materials with large surface area can also be successfully investigated by a combination of small (low) and normal (high) angle scattering. Small-angle scattering has also been used to give some indication of pore structure.

17.6.2 Low-Energy Electron Diffraction

Scattering of electrons from solid surfaces is one of the paradigms of quantum physics. The pioneering experiments of Davisson and Germer, in 1928, confirmed the Broglie's concept of the wave nature of particles (de Broglie 1925), a concept at the very heart of quantum mechanics (wave–particle dualism). Already in these early works, they recognized the potential of LEED as a tool for the determination of surface structures and applied it to gas adsorbate layers on Ni(111) (Davisson and Germer 1928a,b). This success was only possible due to two important properties of LEED: surface sensitivity and interference.

In fact, an alternation of the electron beam intensity with sample thickness was observed by Davisson and Germer (1928a,b). Electrons in an LEED experiment have a typical kinetic energy in the range of 20–500 eV.

Experiments with energies below this range are called very low-energy electron diffraction (VLEED), and those with higher energies medium-energy electron diffraction (MEED). At even higher energies, one uses grazing electron incidence and emission to obtain surface sensitivity, that is, RHEED. Due to the interaction of the incoming electron with the electrons in the sample, the former penetrates into the solid only a few angstroms. Typical penetration lengths taken from the "universal curve" (Figure 17.11) range from 5 to 10 Å (Rundgren 1999). Therefore, LEED spectra usually carry less information about the geometrical structure of the volume of the solid, i.e. the bulk, than of the solid's surface region.

Concerning interference, de Broglie showed that a particle with momentum p can be associated with a wave with wavelength $2\pi/p$ ($p = |p|$). For example, an electron in vacuum can be described by a plane wave:

$$\Psi(r, t) = \exp[i(k \cdot r - \omega t)] \qquad (17.11)$$

with wavenumber $k = 2\pi/\lambda$ and energy $E = \omega = k^2/2$. de Broglie's picture of electrons as waves and the interpretation of Davisson–Germer LEED experiments lead to the question: Are electrons waves? (Davisson 1928). Comparison was made to X-ray scattering in view of the determination of structural information, and Davisson came to the conclusion that if X-rays are waves, then electrons are, too.

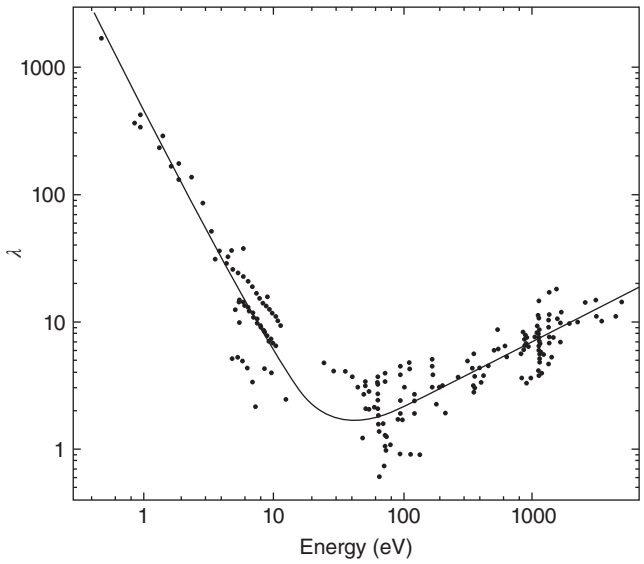


Figure 17.11 Compilation for elements of the inelastic mean free path λ_m (dots) in monolayers as a function of energy above the Fermi level. This "universal curve" is almost independent of the solid, for example, surface orientation of elemental composition. The solid line serves as a guide to the eye (Seah and Dench 1979).

However, he/she admitted that the picture of electrons as particles is better suited for the explanation of the Compton effect or the photoelectric effect.

The schematic setup of a LEED experiment is shown in Figure 17.12. A monoenergetic beam of electrons with kinetic energy E impinges on the sample. The reflected electron beams are detected and analyzed with respect to their direction and energy. Usually, one detects only elastically reflected electrons (for which the energy is conserved) and uses incidence normal to the surface. Therefore, a set of LEED spectra – or $I(E)$ curves – represents the current I of each reflected beam versus the initial energy E. Note

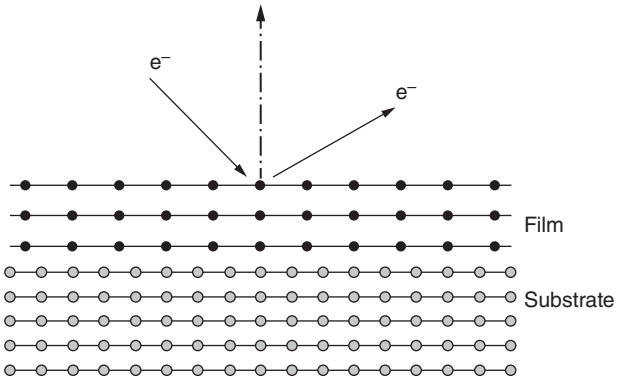


Figure 17.12 Scheme of the LEED setup. An incoming beam of electrons e^- is elastically scattered by the solid. The latter is considered as a compound of the substrate (gray circles) and a thin film (black circles). A reflected electron beam is detected. The dashed–dotted arrow represents the normal surface.

that the reflected intensities are roughly as large as 1/1000 of the incoming intensity.

In the wave picture of electrons, the LEED experiment can be regarded as follows. An incoming plane wave, the incident beam, is scattered at each site, and the outgoing plane waves, the outgoing beams, are measured. Both amplitude and phases of each outgoing wave are determined by the scattering properties and the position of each scatterer. For example, a change in the position of a scatterer will change the wave pattern in the solid and, therefore, will affect both amplitudes and phases of the outgoing waves. Because the LEED current of a beam is given by the wave amplitude, it carries information on both positions and scattering properties of the sites. This mechanism can be used, for instance, to obtain images of the geometrical structure in configuration space by LEED holography (Heinz et al. 2000).

Although LEED is sensitive to the outermost region of the sample, it is capable of detecting fingerprints of the electronic states of the film–substrate system. As mentioned previously, the LEED intensities depend on the electronic structure of the sample above the vacuum level and, therefore, contain information of the electronic structure of the entire film. In particular, quantized states that are confined to the film have a pronounced effect on the LEED spectra.

It took considerable time to develop theories that include multiple scattering of the LEED electron (Kambe 1967), which obviously is necessary for a proper description of LEED spectra. Textbooks that are introduced to the field and present computer codes for the calculation of $I(E)$ spectra were written by Pendry (1974) as well as van Hove et al. (1986). Van Hove and Tong also provide review articles (1979).

Additional information can be obtained if one uses a spin-polarized beam of incoming electrons, that is, spin-polarized low-energy electron diffraction (SPLEED), and uses a spin-sensitive detector, for example, a Mott detector or a SPLEED detector. Interestingly, the latter exploits the LEED mechanism itself for a spin resolution in the experiment. Pioneering works were carried out by Feder (1985) and by Kirschner and Feder (1979) on the experimental side.

17.6.3 Reflection High-Energy Electron Diffraction

The short history of RHEED study of oxides is relatively recent, and good general introductions to this matter date from Lagally (1985) and Lagally and Savage (1993); there one can find a clear explanation of the electron diffraction, reciprocal-space representation, reflection from imperfect surfaces, and so on.

RHEED patterns result from and contain detailed information on the crystalline properties of surfaces. In the field of oxide thin films, RHEED analysis is currently used mainly for qualitative information, simply to watch diffraction problems and to note their evolution in time. Even this can be quite useful and can reveal atomic scale information on how a sample is growing with reference to phenomenology developed by experience. As discussed below, it is possible to distinguish a flat two-dimensional (2D) surface from one having (usually unwanted) 3D nanoparticles. For the time being, we consider the former case.

At least in principle, the diagnostic value of RHEED monitoring could be substantially increased if it were supplemented by a quantitative analysis of the entire RHEED pattern. Ultimately, one could envision a numerical routine that solves the inverse problem in real time, that is, computes the real-space atomic arrangement on the surface that corresponds to a given RHEED image.

In Figure 17.13, a schematic of a typical calculation and of an experimental RHEED setup is shown. The electron beam (E) impinges onto the film surface (F) at a nearly grazing angle (θ) and is reflected (E') onto the screen (S).

The electron beam is coherent over several thousand angstroms and is nearly monoenergetic; in our case, the electron energy is typically $\approx$8.5–10.0 keV. The film surface is approximated as a perfect but finite rectangular $N \times M$ array of atoms with the lattice periods a and b, respectively.

Since typically $a \approx b \approx 4\,\text{Å} \gg \lambda_e \approx 0.15\,\text{Å}$, the electrons are strongly diffracted, and one expects to see multiple interference maxima on the screen. In this case, the refinement procedure provides an estimate of the size of in-plane crystallographic coherence, that is, an estimate of the numbers N and M.

To calculate the diffraction pattern, the scattering contributions from all of the atoms are summed. The resulting intensity distribution on the screen is given by

$$I(X,Y) \propto \left\{ \left[\sum_{i=j}^{N} \sum_{j=I}^{M} \cos(kR_{ij}) \right]^2 + \left[\sum_{i=I}^{N} \sum_{j=I}^{M} \sin(kR_{ij}) \right]^2 \right\} \tag{17.12}$$

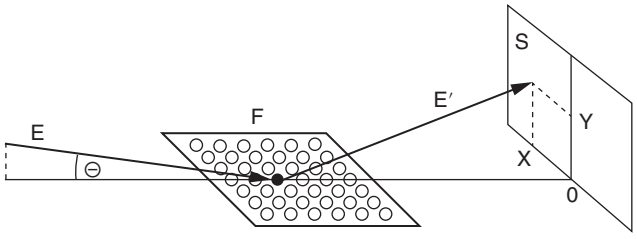


Figure 17.13 The model used in this chapter to calculate RHEED patterns. The electron beam (E) impinges onto the film (F) at a nearly grazing angle (0). The reflected beam (E′) forms a diffraction pattern on the screen S.

where

$$k = (\sqrt{2mE})/h \tag{17.13}$$

and

$$R_{ij} = \sqrt{(ia)^2 + Y_a^2 + (Z_a + ja)^2} + \sqrt{(X - ia)^2 + Y^2 + (Z - ja)^2} \tag{17.14}$$

where E and m are the electron energy and mass and $r = (ia)e_x + (ja)e_z$, R_a, $X_a e_x + Y_a e_y + Z_a e_z$ and $R = Xe_x + Ye_y + Ze_z$ are the positions of the (i, j)th atom in the plaquette, the electron source, and the screen pixel, respectively.

When the atoms are not all identical, their contributions are weighted by the respective form factors, S_{ij} (not shown in Eq. (17.13)).

As the first step to aid the reader's intuition, in Figure 17.13 we show the calculated RHEED patterns for three ideal but finite atomic lattices, 10×10, 10×100, and 10×1000 unit cells, respectively, with $a = b = 4$ Å. These three cases correspond to different degrees of crystallographic coherence in the direction that the electron beam is propagating. Here we have taken $Z_a = Z = 1\,000\,000$ Å, ensuring that we are in the far-field regime. We set $Y_a = 0$, which is equivalent to setting the azimuthal angle of the sample crystal to zero; the beam is almost parallel to the <100> film direction, except for the out-of-plane tilt by $\theta = 0.5°$. It can be seen from Figure 17.14 that as the long-range order along the beam direction is increased, the streaks get shorter and eventually evolve into a spot – the specular reflection image of the incoming electron beam. Note that a substantial domain of local flatness is required to obtain coherent scattering into a specularly reflected spot.

The presence of the specular spot is suggestive of essentially perfect crystalline order extending over thousands of unit cells. On the other hand, when they appear as streaks, this shows evidence for the presence of terracing and other surface irregularities. Hence, some amount of surface roughness or disorder typically transforms interference spots into streaks.

In Figure 17.15 we show the calculated RHEED pattern for the same 10×10 lattice model as in Figure 17.13a but with $Y_a = 200\,000$ Å; this corresponds to the azimuthal rotation of the sample by $\arctan(0.2) = 11.3°$. As the crystal is rotated around the (001) axis, the pattern apparently changes. Reversing the argument, one can infer the crystal orientation from the shape of the RHEED pattern. In practice, one simply rotates the substrate azimuthal orientation and brings it to a desired "low-index" orientation for analysis during growth.

In recent years, there has been a surge of interest in deposition of high-quality (i.e. single-crystal) films of complex oxides such as cuprate superconductors or perovskite

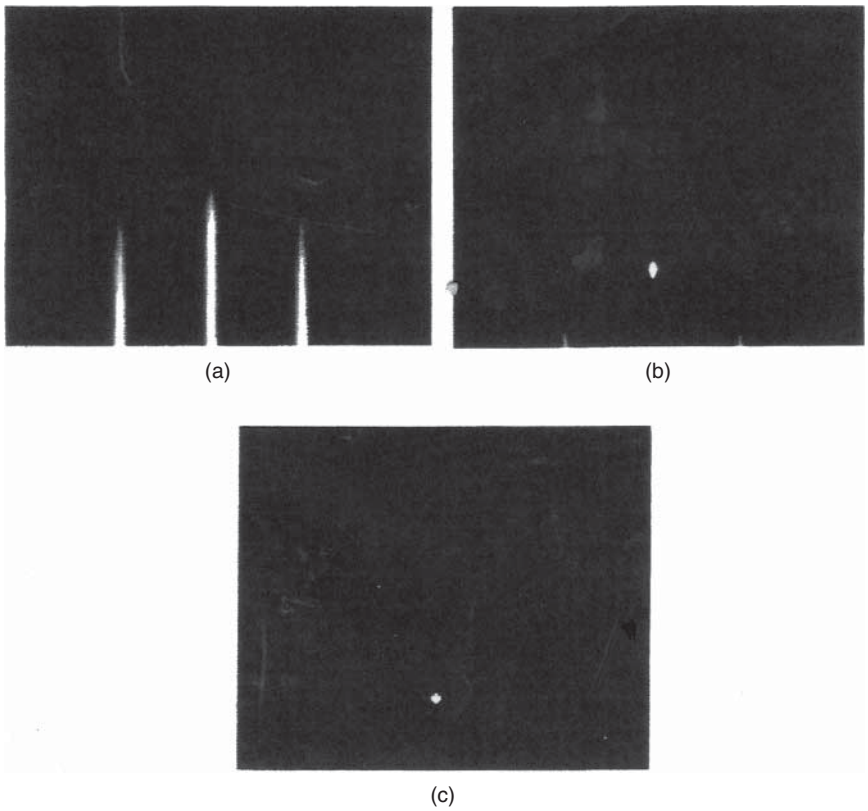


Figure 17.14 Calculated RHEED patterns for three finite atomic lattices: (a) 10×10, (b) 10×100, and (c) 10×1000 unit cells, respectively. The unit cell is a 4×4 Å^2. The incidence angle is $\Theta = 2.5°$, off the (100) direction.

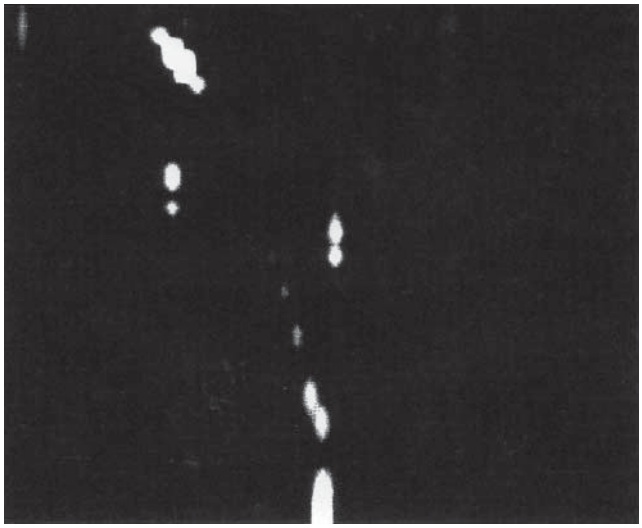


Figure 17.15 Calculated RHEED pattern for the same model as in Figure 17.13a but rotated azimuthally (around the vertical axis) by 11.3°.

ferroelectrics. The RHEED method is currently one of the important techniques for *in situ* real-time analysis of the growing surface of such films.

Here, we have reviewed some basic issues specific to RHEED monitoring of deposition of complex oxides.

The RHEED analysis can be made quantitative. This is being done by performing some numerical simulations and comparing the calculated RHEED patterns with the experimentally observed ones. In the future, it could be expected that real-time RHEED analysis can and will be further improved. For example, it could be expected that intelligent programs will be developed, including pattern recognition capability based on a built-in library of RHEED images, to aid the grower and ultimately even to control the growth.

17.6.4 Neutron Scattering

A neutron is an uncharged (electrically neutral) subatomic particle with mass $m = 1.675 \times 10^{-27}$ kg (1839 times that of the electron), spin 1/2, and magnetic moment -1.913 nuclear magnetrons. Neutrons are stable when bound in an atomic nucleus while having a mean lifetime of approximately 1000 seconds as a free particle. The neutron and the proton form nearly the entire mass of atomic nuclei, so they are both called nucleons. Neutrons are classified according to their wavelength and energy as "epithermal" for short wavelengths ($\lambda \sim 0.1$ Å) and "thermal" and "cold" for long wavelengths ($\lambda \sim 10$ Å). The desired range of λ is obtained by moderation of the neutrons during their production, either in reactions or spallation sources.

Neutrons interact with matter through strong, weak, electromagnetic, and gravitational interactions. However, it is their interactions via two of these forces – the short-range strong nuclear force and their magnitude moments – that make *neutron scattering* such a unique probe for condensed matter research. The most important advantages of neutrons over other forms of radiation in the study of structure and dynamics on a microscopic level are summarized below:

- Neutrons are uncharged, which allows them to penetrate the bulk of materials. They interact via the short-range strong nuclear force with the nuclei of the material under investigation.
- The neutron has a magnetic moment that couples to spatial variations of magnetization on the atomic scale. They are therefore ideally suited to the study of magnetic structures and the fluctuations and excitations of spin systems.

The energy and wavelength of neutrons may be matched, often simultaneously, to the energy and length scales appropriate for the structure and excitations in condensed matter. The wavelength, λ, is dependent on the neutron velocity following the de Broglie relation

$$\lambda = \frac{h}{mv} \tag{17.15}$$

where h is Planck's constant (6.636×10^{-34} J s) and v the particle velocity. The associated kinetic energy is

$$E = \frac{1}{2}mv^2 \; or \; E = \frac{h^2}{2(m\lambda)^2} \tag{17.16}$$

Because their energy and wavelength depend on their velocity, it is possible to select a specific neutron wavelength by the time-of-flight (TOF) technique. Neutrons do not significantly perturb the system under investigation, so the results of neutron scattering experiments can be clearly interpreted. Neutrons are nondestructive, even to delicate biological materials. The high-penetrating power of neutrons allows probing the bulk of materials and facilitates the use of complex sample environment equipment (e.g. for creating extremes of pressure, temperature, shear, and magnetic fields). Neutrons scatter from materials by interacting with the nucleus of an atom rather than the electron cloud. This means that the scattering power (cross section) of an atom is not strongly related with its atomic number, unlike X-rays and electrons where the scattering power increases in proportion to the atomic number. Therefore, with neutrons, light atoms such as hydrogen (deuterium) can be distinguished in the presence of heavier ones. Similarly, neighboring elements in the periodic table generally have substantially different scattering cross sections and so can be distinguished. The nuclear dependence of scattering also allows isotopes of the same element to have substantially different scattering lengths for neutrons. Hence, isotopic substitution can be used to label different parts of the molecules making up a material.

Neutron beams may be produced in two general ways: by nuclear fission in reactor-based neutron sources or by spallation in accelerator-based neutron sources. The two world's most intense neutron sources are the Institut Laue–Langevin (ILL) in Grenoble, France (ILL World Wide Web), and the ISIS facility at the Rutherford Appleton Laboratory in Didcot, UK (ISIS World Wide Web).

Neutrons have traditionally been produced by fission in nuclear reactors optimized for high neutron brightness. In this process, thermal neutrons are adsorbed by uranium-235 nuclei, which split into fission fragments and evaporate a very high-energy (megaelectron volts) constant neutron flux (hence the term "steady-state" or "continuous" source). After the high-energy (megaelectron volts) neutrons have been thermalized to megaelectron volt energies in the surrounding moderator, beams are emitted with a broad band of wavelengths. The energy distribution of the neutrons can be shifted to higher energy (shorter wavelength) by allowing them to come into thermal equilibrium with a "hot source" (at the ILL this is a self-heating graphite block at 2400 K) or to lower energies with a "cold source" such as liquid deuterium at 25 K (Finney and Steigenberger 1997). The resulting Maxwell distributions of energies have the characteristic temperatures of the moderators (Figure 17.16a). Wavelength section is generally achieved by Bragg scattering from a crystal monochromator or by velocity selection through a mechanical chopper. In this way, high-quality, high-flux neutron beams with a narrow wavelength distribution are made available for scattering experiments. One of the most powerful of the reactor neutron sources in the world is the 58 MW HFR (high-flux reactor) at the ILL.

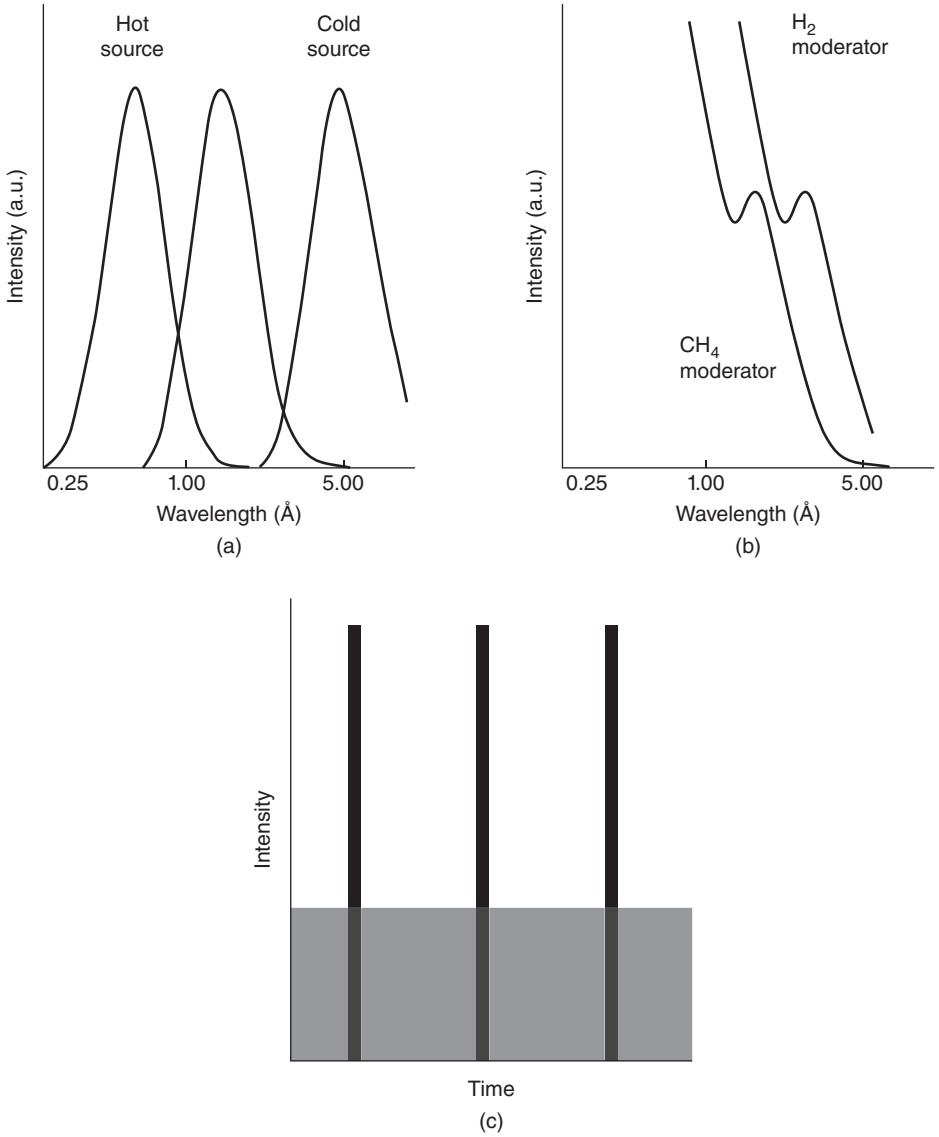


Figure 17.16 (a) Typical wavelength distributions for neutrons from a reactor, showing the spectra from a hot source (2400 K), a thermal source, and a cold source (25 K). The spectra are normalized so that the peaks of the Maxwell distributions are unity. (b) Typical wavelength spectra from a pulsed spallation source. The H_2 and CH_4 moderators are at 20 and 100 K, respectively. The spectra have a high-energy "slowing" component and a thermalized component with a Maxwell distribution. Again, the spectra are normalized at unity. (c) Neutron flux as a function of time at a steady-state source (gray) and a pulsed source (black). Steady-state sources, such as ILL, have high time-averaged fluxes, whereas pulsed sources, such as ISIS, are optimized for high brightness (not drawn to scale) (ISIS World Wide Web).

In accelerator sources, neutrons are released by bombarding a heavy metal target (e.g. U, Ta, W), with high-energy particles (e.g. H^+) from a high-power accelerator – a process known as spallation. The methods of particle acceleration tend to produce short intense bursts of high-energy protons and hence pulses of neutrons. Spallation releases much less heat per useful neutron than fission (typically 30 MeV per neutron, compared with 190 MeV in fission). The low heat dissipation means that pulsed sources can deliver high neutron brightness – exceeding that of the most advanced steady-state sources – with significantly less heat generation in the target. As said above, one of the most powerful spallation neutron sources in the world is the ISIS facility that is based around a 200 μA, 800 MeV, proton synchrotron operating at 50 Hz, and a tantalum (Ta) target that releases approximately 12 neutrons for every incident proton.

At ISIS, the production of particles energetic enough to result in efficient spallation involves three stages:

1. Production of H^- ions (proton with two electrons) from hydrogen gas and acceleration in a pre-injector column to reach an energy of 665 keV.
2. Acceleration of the H^- ions to 70 MeV in the linear accelerator (Linac) that consists of four accelerating tanks.
3. Final acceleration in the synchrotron – a circular accelerator 52 m in diameter that accelerates 2.8×10^{13} protons per pulse to 800 MeV. As they enter the synchrotron, the H^- ions pass through a very thin (0.3 μm) alumina foil so that both electrons from each H^- ion are removed to produce a proton beam. After traveling around the synchrotron (approximately 10 000 revolutions), with acceleration on each revolution from electromagnetic fields, the proton beam of 800 MeV is kicked out of the synchrotron toward the neutron production target. The entire acceleration process is repeated 50 times a second.

Collision between the proton beam and the target atom nuclei generates neutrons in large quantities and of very high energies. As in fission, they must be slowed by passage through moderating materials so that they have the right energy (wavelength) to be useful for scientific investigations. This is achieved by hydrogenous moderators around the target. These exploit the large inelastic scattering cross section of hydrogen to slow down the neutrons passing through by repeated collisions with the hydrogen nuclei. The moderator temperature determines the spectral distributions of neutrons produced, and this can be tailored for different types of experiments (Figure 17.16b). The moderators at ISIS are ambient temperature water (316 K, H_2O), liquid methane (100 K, CH_4), and liquid hydrogen (20 K, H_2).

The characteristics of the neutrons produced by a pulsed source are therefore significantly different from those produced at a reactor (Figure 17.16c). The time-averaged flux (in neutrons per second per unit area) of even the most powerful pulsed source is low in comparison with reactor sources. However, the judicious use of TOF techniques that exploit the high brightness in the pulse can compensate for this. Using TOF techniques on the white neutron beam gives a direct determination of the energy and wavelength of each neutron.

Scattering events arise from radiation–matter interactions and produce interference patterns that give information about spatial and/or temporal correlations within the sample. Different modes of scattering may be produced: elastic or inelastic but also coherent or incoherent. Coherent scattering from ordered nuclei produces patterns of constructive and destructive interference that contain structural information, while incoherent scattering results from random events and can provide dynamic information. In *small-angle neutron scattering* (SANS) (Bacon 1977), only coherent elastic scattering is considered, and incoherent scattering, which appears as a background, can be easily measured and subtracted from the total scattering. To further explain, coherent scattering is "in phase" and thus can contribute to small-angle scattering; incoherent scattering is isotropic and in a small-range experiment and thus contributes to the background signal and degrades signal to noise.

Neutrons interact with the atomic nucleus via strong nuclear forces operating at very short range ($\sim 10^{-15}$ m), i.e. much smaller than the incident neutron wavelength ($\sim 10^{-10}$ m). Therefore, each nucleus acts as a point scatterer to the incident neutron beam, which may be considered as a plane wave. The strength of interaction of free neutrons with the bound nucleus can be quantified by the scattering length, b, of the atom, which is isotope dependent. In practice, the mean coherent neutron scattering length density, ρ_{coh}, abbreviated as ρ, is a more appropriate parameter to quantify the scattering efficiency of different components in a system. As such, ρ represents the scattering length per unit volume of substance and is the sum over all atomic contributions in the molecular volume V_{m}:

$$\rho_{\text{coh}} = \frac{1}{V_{\text{m}}} \sum_{1} b_{i,\text{coh}} = \frac{DN_{\text{a}}}{\text{Mw}} \sum_{i} b_{i,\text{coh}} \qquad (17.17)$$

where $b_{i,\,\text{coh}}$ is the coherent scattering length of the ith atom in the molecule of mass density D and molecular weight Mw. N_{a} is Avogadro's constant. Some useful scattering lengths are given in Table 17.7, and scattering length density for selected molecules in Table 17.8 (King 1997). The difference in b values for hydrogen and deuterium is significant, and this is exploited in the contrast variation

Table 17.7 Selected values of coherent scattering length, b (King 1997)

Nucleus	$b/(10^{-12}\,\text{cm})$
^{1}H	−0.3741
^{2}H (D)	0.6671
^{12}C	0.6646
^{16}O	0.5803
^{19}F	0.5650
^{23}Na	0.3580
^{31}P	0.5131
^{32}S	0.2847
Cl	0.9577

Table 17.8 Coherent scattering length density of selected molecules, ρ, at 25 °C

Molecule		$\rho/(10^{10}\,\text{cm}^{-2})$
Water	H_2O	−0.560
	D_2O	6.356
Heptane	C_7H_{16}	−0.548
	C_7D_{16}	6.301
AOT	$(C_8H_{17}COO)CH_2CHSO_3$ (Na^+)	0.542
	$(C_8D_{17}COO)CH_2CHSO_3$ (Na^+)	5.180[a]

[a] Value calculated for the deuterated form of the surfactant ion only (i.e. without sodium counterions) and where the tails only are deuterated (King 1997).

technique to allow different regions of molecular assemblies to be examined; i.e. one can "see" proton-containing hydrocarbon-type material dissolved in heavy water, D_2O.

In neutron scattering experiments, the intensity I is measured as a function of a scattering angle, θ, which in the case of SANS is usually less than 10°.

For coherent elastic scattering, the incident wave vector of magnitude $2\pi/\lambda$, $|k_o| = |k_s| = 2\pi n/\lambda$, where n is the refractive index of the medium, which for neutron is ∼1, and K_s is the scattered wave vector, so the amplitude of the scattered vector, $|Q|$, can be obtained by geometry as

$$|\underline{Q}| = Q = 2|k_o| \sin\frac{\theta}{2} = \frac{4\pi}{\lambda}\sin\frac{\theta}{2} \tag{17.18}$$

The magnitude Q has dimensions of reciprocal length and units are commonly $Å^{-1}$; large structures scatter to low Q (and angle) and small structures at higher Q values.

Radiation detectors do not measure amplitudes as they are not sensitive to phase shift, but instead the intensity I_{sc} of the scattering (or power flux), which is the squared modulus of the amplitude

$$I_{sc}(\underline{Q}) = \langle|A(Q)|^2\rangle = \langle A(\underline{Q}) \cdot A^*(\underline{Q})\rangle \tag{17.19}$$

For an ensemble of n_p identical particles, Eq. (17.19) becomes (Dickinson 1995)

$$I_{sc}(Q) = n_p\langle\langle|A_{sc}(Q)^2|\rangle_o\rangle_s \tag{17.20}$$

where the ensemble averages are over all orientations, o, and shapes, s.

Therefore, there is a convenient relationship (Eq. (17.18)) between the two instrumental variables, θ and λ, and the reciprocal distance, Q, that is related with the positional correlations r between point scattering nuclei in the sample under investigation. These parameters are related with the scattering intensity $I(Q)$ (Eq. (17.20)) that is the measured parameter in an SANS experiment and contains information on intraparticle and interparticle structure.

17.7 Electron Microscopy

SEM and TEM are the two major types of electron microscopical examination of materials that present excellent opportunities for structural study and, equally, problems in specimen preparation and interpretation of the images produced. But two other techniques, high-resolution transmission electron microscopy (HRTEM) and low-energy electron microscopy (LEEM), deserve consideration today. In this section, these four techniques are briefly covered.

17.7.1 Scanning Electron Microscopy

SEM was a central part in a work for surface image and analysis. The SEM operates by scanning the surface with a beam of electrons, which are generated by an electron gun and focused with magnetic lenses down to a diameter of about 10 Å when hitting the specimen. The electrons interact with atoms at the surface, leading to emission of new electrons. These emitted electrons are collected and counted with a detector. SEM can be used in a mode detecting either secondary electrons (SEs) or backscattered electrons (BSE). SEs can escape only from a shallow region and offer the best image of surface topography. BSEs undergo a number of collisions before eventually scattering back out of the surface. They are generated from a larger region than SEs and provide information about specimen composition since heavier elements generate more BSEs and thus a brighter image.

The quality and resolution of SEM images are function of three major parameters: (i) instrument performance, (ii) selection of imaging parameters (e.g. operational control), and (iii) nature of the specimen. All three aspects operate concurrently, and neither of them should be or can be ignored or overemphasized.

One of the most surprising aspects of SEM is the apparent ease with which SEM images of 3D objects can

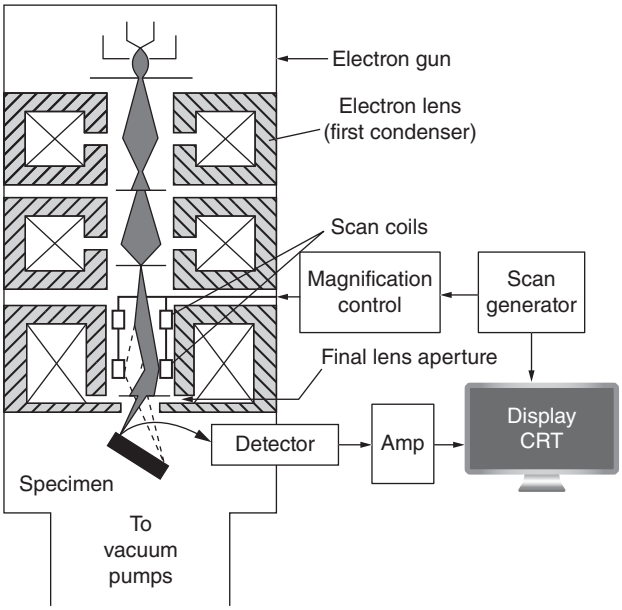


Figure 17.17 Main components of a typical SEM.

be interpreted by any observer with no prior knowledge of the instrument. This is somewhat surprising in view of the unusual way in which image is formed, which seems to differ greatly from normal human experience with images formed by light and viewed by the eye.

The main components of a typical SEM are electron column, scanning system, detector(s), display, vacuum system, and electronic controls (Figure 17.17).

The electron column of the SEM consists of an electron gun and two or more electromagnetic lenses operating in vacuum. The electron gun generates free electrons and accelerates these electrons to energies in the range of 1–40 keV in the SEM. The purpose of the electron lenses is to create a small, focused electron probe on the specimen. Most SEMs can generate an electron beam at the specimen surface with spot size less than 10 nm in diameter while still carrying sufficient current to form acceptable image. Typically, the electron beam is defined by probe diameter (d) in the range of 1 nm to 1 μm, probe current (i_b) – picoamperes to microamperes, and probe convergence (α) – 10^{-4}–10^{-2} rad.

In order to produce images, the electron beam is focused into a fine probe, which is scanned across the surface of the specimen with the help of scanning coils (Figure 17.17). Each point on the specimen that is struck by the accelerated electrons emits signal in the form of electromagnetic radiation. Selected portions of this radiation, usually SEs and/or BSEs, are collected by a detector, and the resulting signal is amplified and displayed on a TV screen or computer monitor. The resulting image is generally straightforward to interpret, at least for topographic imaging of objects at low magnifications.

The electron beam interacts with the specimen to a depth of approximately 1 μm. Complex interactions of the beam electrons with the atoms of the specimen produce a wide variety of radiation. The need of understanding of the process of image formation for reliable interpretation of images arises in special situations and mostly in the case of high-magnification imaging. In such case, knowledge of electron optics, beam–specimen interactions, detection, and visualization processes is necessary for successful use of the SEM power.

The purpose of the electron lenses is to produce a convergent electron beam with desired crossover diameter. The lenses are metal cylinders with cylindrical hole, which operate in vacuum. Inside the lenses, magnetic field is generated, which in turn is varied to focus or defocus the electron beam passing through the hole of the lens.

The general approach in SEM is to minimize the probe diameter and maximize the probe current. The minimum probe diameter depends on the spherical aberration of the SEM electron optics, the gun source size, the electron optical brightness, and the accelerating voltage.

The probe size, which directly affects resolution, can be decreased by increasing the brightness. The electron optical brightness β is a parameter that is function of the electron gun performance and design. For all types of electron guns, brightness increases linearly with accelerating voltage, so every electron source is 10 times as bright at 10 kV as it is at 1 kV. Decreasing the wavelength and the spherical aberration also decreases the probe size.

The *interaction volume* of the primary beam electrons and the sampling volume of the emitted secondary radiation are important both in the interpretation of SEM images and in the proper application of quantitative X-ray microanalysis. The image details and resolution in the SEM are determined not by the size of the electron probe by itself but rather by the size and characteristics of the interaction volume.

When the accelerated beam electrons strike a specimen, they penetrate inside it to depths of about 1 μm and interact both elastically and inelastically with the solid, forming a limiting interaction volume from which various types of radiation emerge, including BSE, SE, characteristic and bremsstrahlung X-rays, and cathodoluminescence in some materials.

The combined effect of elastic and inelastic scattering controls the penetration of the electron beam into the solid. The resulting region over which the incident electrons interact with the sample is known as interaction volume. The interaction volume has several important characteristics that determine the nature of imaging in the SEM.

The energy deposition rate varies rapidly throughout the interaction volume, being greatest near the beam impact point. The interaction volume has a distinct shape (Figure 17.18). For low-atomic-number target, it has

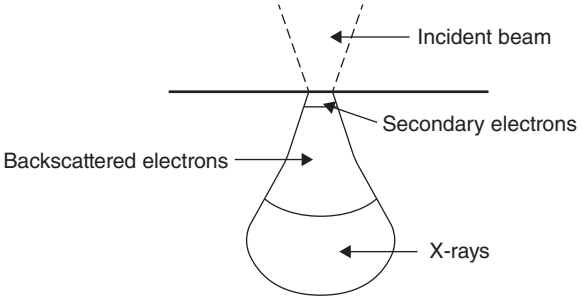


Figure 17.18 Excited volume and electron interaction within specimen.

distinct pear shape. For intermediate and high-atomic-number materials, the shape is in the form of hemisphere.

The interaction volume increases with increasing incident beam energy and decreases with increasing average atomic number of the specimen. For SEs, the sampling depth is from 10 to 100 nm, and diameter equals the diameter of the area emitting BSEs. BSE are emitted from much larger depths compared with SE.

Ultimately, the resolution in the SEM is controlled by the size of the interaction volume.

Since the SEM is operated under high vacuum, the specimen that can be studied must be compatible with high vacuum ($\sim 10^{-5}$ mbar). This means that liquids and materials containing water and other volatile components cannot be studied directly. Also, fine powder samples need to be fixed firmly to a specimen holder substrate so that they will not contaminate the SEM specimen chamber.

Nonconductive materials need to be attached to a conductive specimen holder and coated with a thin conductive film by sputtering or evaporation. Typical coating materials are Au, Pt, Pd, their alloys, and carbon.

There are special types of SEM instruments such as variable pressure scanning electron microscopy (VP-SEM) and environmental scanning electron microscopy (ESEM) that can operate at higher specimen chamber pressures, thus allowing for nonconductive materials (VP-SEM) or even wet specimens to be studied (ESEM). SEM can also be combined with a number of different techniques for chemical analysis, the most common being *energy-dispersive spectroscopy* (EDS). When the electron beam interacts with the surface, X-ray photons are generated. The energy of radiating photons corresponds to a transition energy that is characteristic for each element. Figure 17.17 illustrates the interaction volume from which electrons and X-rays are generated. With *wavelength-dispersive X-ray spectroscopy* (WDS), the radiated photons are diffracted by a crystal, and only X-rays with a specific wavelength will fall onto the detector. WDS analysis is more accurate but also more time consuming than EDS analysis and used in particular for analyses of light elements or separating overlaps in the EDS spectra.

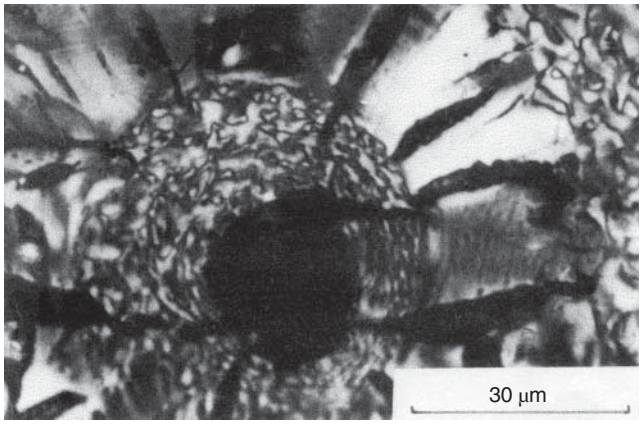


Figure 17.19 Optical micrograph of calcinated shot coke – before etching.

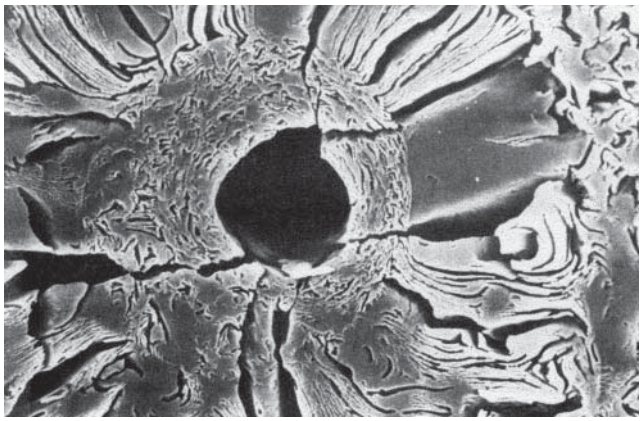


Figure 17.20 SEM micrograph of calcinated shot coke – after chromic acid etching.

Carbon surfaces that have been polished for optical microscopy show very few features in a SEM examination (no topography). However, etching the surface either chemically (with chromic acid) or by ion bombardment reveals a wealth of detail that can be related to the optical texture of the sample. A specialized application of this is the "same area" technique where a specific part of a polished surface that has been identified and characterized optically is reexamined by SEM following etching. Figures 17.19 and 17.20 show micrographs illustrating this technique.

SEM is an excellent method for monitoring the changes in topography following various treatments, such as gasification, heat treatment, etc. Figures 17.21 and 17.22 are micrographs of metallurgical (blast furnace) coke before and after reaction with carbon dioxide.

17.7.2 Transmission Electron Microscopy

TEM provides a means of obtaining high-resolution images of diverse materials. Figure 17.23 includes an outline of the

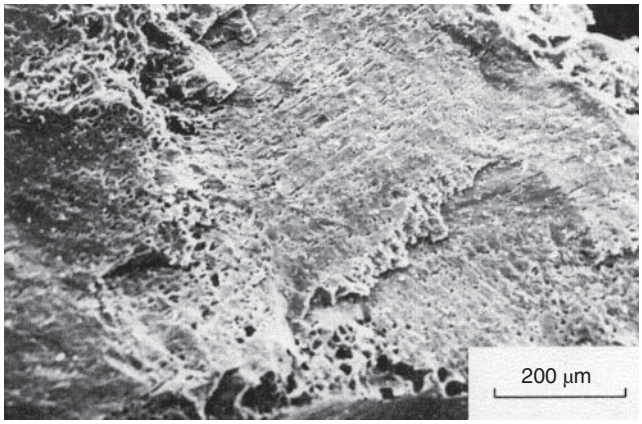


Figure 17.21 SEM micrograph of blast furnace coke – original surface.

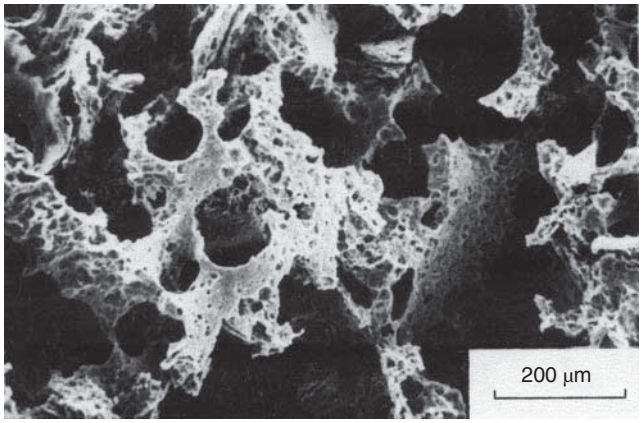


Figure 17.22 SEM micrograph of blast furnace coke – after 75% burn-off in CO_2.

general arrangement of a TEM. Electrons are generated in the same way as in SEM, using a tungsten filament, and focused by a condenser lens system. The electrons strike the thin-film specimen and may undergo any of several interactions with the specimen. One of these interactions, diffraction of the electrons by the periodic array of atomic planes in the specimen, ultimately produces the contrast that most commonly enables observation of structural details in crystalline material. The electrons that pass through the thin crystal without being diffracted are referred to as transmitted electrons.

Downstream of the specimen are several post-specimen lenses that include the lower half of the objective lens, a magnifying lens, an intermediate lens, and a projection lens. The series of post-specimen lenses is referred to as an image formation system. After passing through the image formation system, the electrons form an image either on a fluorescent screen or on a photographic film. The theoretical resolution in a TEM image approaches the wavelength of the incident electrons, although this is

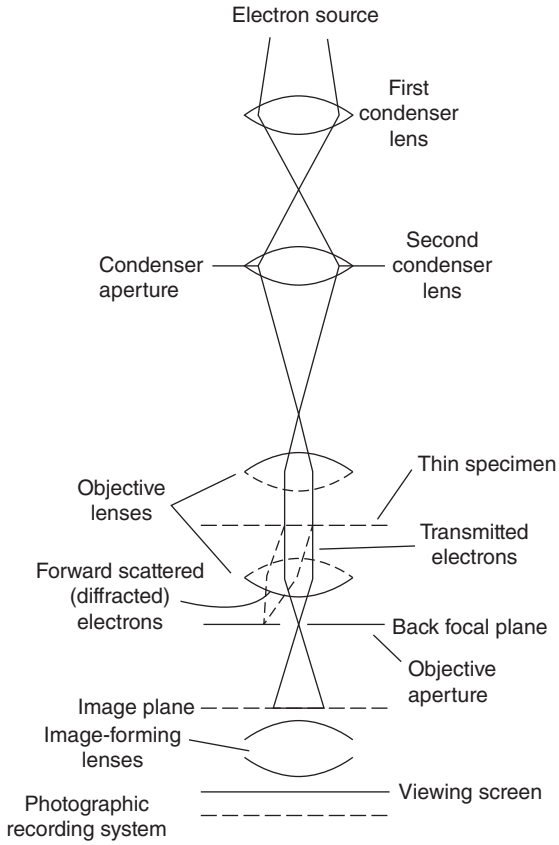


Figure 17.23 Schematic of a TEM.

generally not attained due to a spherical and chromatic aberration and aperture diffraction. Typical line-to-line resolution in TEM is around 1.5 Å.

The conventional TEM is thus capable of simple imaging of the specimen and generation of SADP. Images formed using transmitted electrons are known as bright-field (BF) images, while those due to specific (*hkl*) planes are known as dark-field (DF) images. An EDX system can be attached to a TEM to determine the elemental composition of various phases.

The techniques of TEM can be divided into three areas: *conventional transmission electron microscopy* (CTEM), *analytical transmission electron microscopy* (AEM), and HREM.

CTEM techniques include BF imaging, DF imaging, and selected area electron diffraction (SAD). These methods can be used to identify reaction products and to characterize the microstructure of the scale and the metal/scale interface. Defects, such as dislocations, voids, and microcracks, which play an important role on the growth and adhesion of the scale, can also be detected. With electron diffraction techniques, it is possible to determine the crystal structure and the relative orientation relationship between the metal and the scale.

The second area is AEM. The distribution of impurities and dopants as well as chemical profiles and compositional gradients can be determined with AEM techniques. AEM techniques include energy-dispersive X-ray spectroscopy (EDS) and EELS. A review and comparison between EDS and EELS was presented by Müllejans and Bruley (1993). The highest spatial resolution (0.4 nm) and smallest probe size (<1 nm) can be reached if these analytical methods are combined with a dedicated STEM, such as a VG HB501 STEM.

EELS can provide information about the chemical bonding at interfaces. For example, the oxidation states of metals can be investigated as has been demonstrated for Nb/α-Al_2O_3 interfaces (Bruley et al. 1994). It is possible by analyzing the energy-loss-near-edge structure (ELNES) of EELS spectra to determine the coordination and distance of atoms at interfaces. A line scan across the interface can provide information about the chemical width of the interfacial region.

The third area of TEM is HREM. Using HREM, the crystal lattice can be imaged, and the atomistic structure of materials can be investigated. The point-to-point resolution (Spence 1988) of conventional HREM instruments (400 kV) is about 1.7 Å (0.17 nm). However, a new generation of HREM instruments operates at 1250 kV with a point-to-point resolution of 1 Å (0.10 nm). With this resolution, the structure of many different interfaces and defects in materials can be investigated.

However, HREM can only be applied if special conditions are fulfilled. The thickness of the TEM sample has to be smaller than 10 nm. This means that very high quality of sample preparation is required. Lattice images of heterophase boundaries or grain boundaries are only possible if both crystals adjacent to the interface are oriented parallel to low-index Laue zones. The interface itself has to be parallel to the incoming electron beam, since small tilts away can change the lattice image and make interpretation difficult.

The interpretation of HREM micrographs is not possible on a naïve basis owing to phase shifts introduced by lens aberrations, defocus values, sample composition, and thickness. Therefore, computer calculations are necessary to simulate images of model structures of crystals and defects (e.g. interfaces) for comparison with experimental images (Spence 1988).

The preparation techniques of TEM are quite difficult. It is necessary to obtain a very thin section of the carbon, less than 100 nm, of a uniform thickness. Specimen breakage can often give good results, but this should be treated with caution as it can lead to random variations in thickness that cannot be fully interpreted in terms of the image produced. A more controlled method of producing suitable material is by cutting a thin section of a microtome and further thinning the center portion by ion bombardment. The uniform thickness is important because, in these investigations, it is the variation in the amount of material through which the electron beam passes that provides the image contrast, and fringe imaging can be an artifact of a tapered sample. When the conditions are correctly established, high-resolution TEM can provide direct imaging of the layer planes in carbon materials, reveal the complexity of the most regular structures, and show the ordering present down to the nanometer level.

In the following paragraphs (see Figure 17.24), a standard method for TEM cross-sectional preparation will be explained (Strecker et al. 1993). After characterization of the specimen surface with optical microscopy and SEM, two pieces of the metal carrying the corrosion scale are glued together as a sandwich (Figure 17.24a). The sandwich is glued within a brass tube, with an outer diameter of 3 mm (Figure 17.24b,c). Thin disks are cut from this tube and ground with SiC paper to a thickness of about 200 µm (Figure 17.24d). The disks are dimpled from both sides with a 3 µm diamond, resulting in a residual thickness of 10 µm.

The final step in thinning is ion milling. The samples are ion thinned with a low angle of incidence (4°) from both sides with a BalTec ion mill. This method produces cross-sectional samples with high efficiency (80%). The details of the preparation method will differ between different systems in order to obtain the optimal sample.

Although the effort for TEM sample preparations of the relevant systems is very high, TEM yields important information in the investigation of high temperature corrosion, as has been demonstrated with oxidation studies of Ni (Sawhill and Hobbs 1984), Fe and FeCrNi (Newcomb and Stobbs 1985), NiAl (Doychak and Rühle 1989), Ni_3Al (Bobeth et al. 1994; Schumann and Rühle 1994), and on thin oxide films, and the cross section of the scales for identification of various phases.

17.7.3 High-Resolution Transmission Electron Microscopy

HRTEM is the ultimate tool in imaging defects. In favorable cases, it shows directly a 2D projection of the crystal with defects and all. Of course, this only makes sense if 2D projection is down to some low-index direction, so atoms are exactly on top of each other. Accordingly, HRTEM is easy to grasp: consider a very thin slice of crystal that has been tilted so that low-index direction is exactly perpendicular to the electron beam. All lattice planes almost parallel to the electron, enough to the Braggs position, will diffract the primary beam. The diffraction pattern is the Fourier transform of the periodic potential for the electron in two dimensions. In the objective lens, all diffracted beams and the primary beam are their interference, which provides a back-transformation and leads to an enlarged picture of the periodic potential. This picture

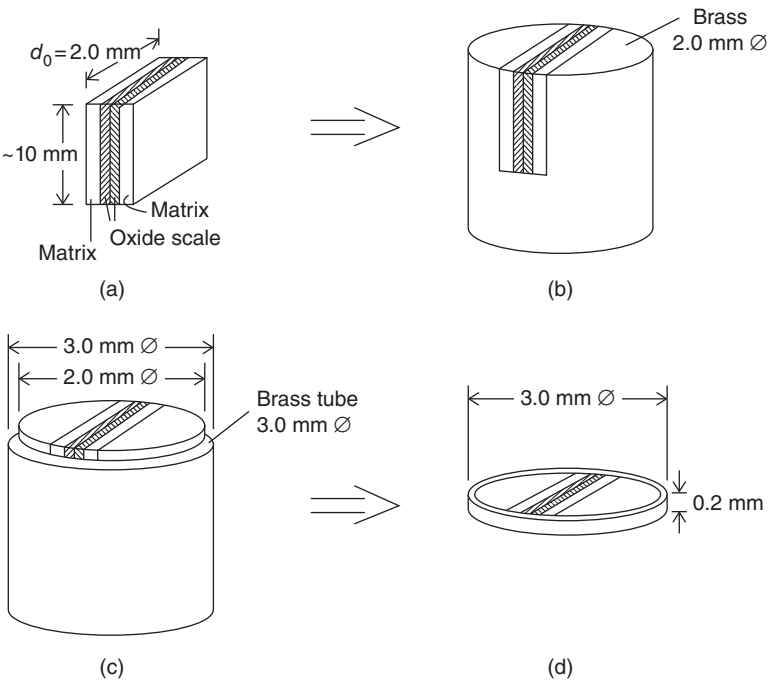


Figure 17.24 Schematic summary of the TEM cross-sectional preparation technique.

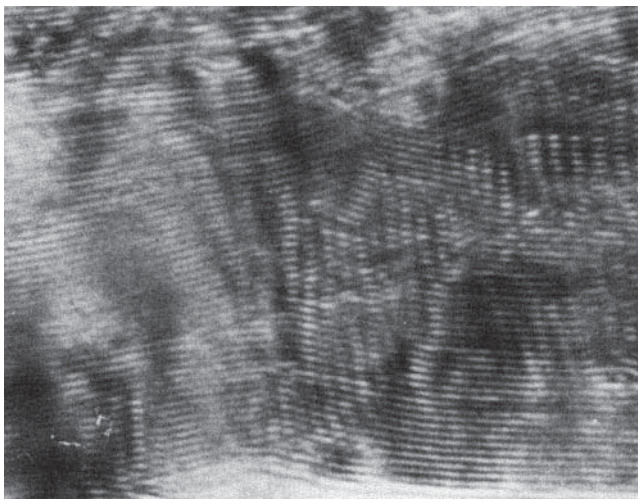


Figure 17.25 HRTEM micrograph of highly graphitic carbon – highly ordered.

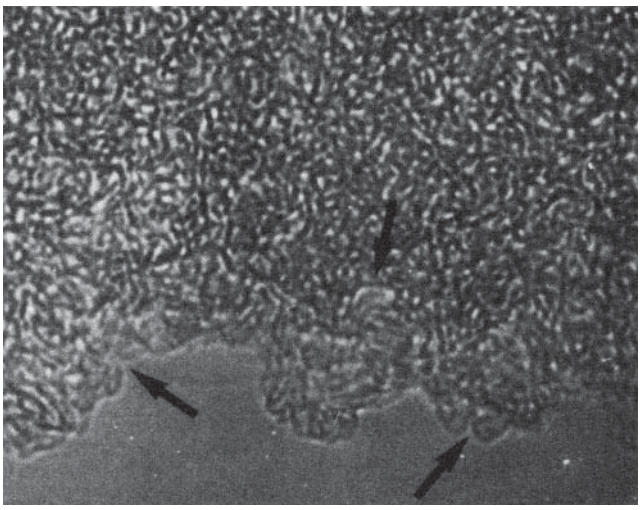


Figure 17.26 HRTEM micrograph of PVDC carbon (HTT 1473 K) – disordered.

is magnified by the following electron optical system and finally seen on the screen at magnifications of typically 10^6. The practice of HRTEM, however, is more difficult than the simple theory. Even so, significant work is now being conducted to analyze the cross sections of the scales to obtain information such as porosity voids and interface morphology between the metal substrate and oxide, as well as between the various oxide layers in a more complex sample. Figures 17.25 and 17.26 show two examples of the resolution layer planes in both highly ordered and less ordered materials obtained by HRTEM.

17.7.4 Low-Energy Electron Microscopy

LEEM is a branch of microscopy involving low-energy elastically BSEs for imaging of solid body surfaces.

LEEM was invented by Ernst Bauer in the early 1960s and has been widely used in surface research since the 1980s. In a microscope, primary low-energy (up to 100 eV) electrons are emitted onto a subject surface, and the electrons reflected from the surface are focused to create a magnified image of the surface. This type of microscope



Figure 17.27 Microscope image of slow electrons in the phase transition from 7×7 reconstruction to 1×1 reconstruction on the Si(111) surface. The 7×7 phase (bright sections) decorates atomic stages, while the surface of terraces is mostly covered with the 1×1 structure (dark sections). Image field size is 5 μm (Tromp 2000).

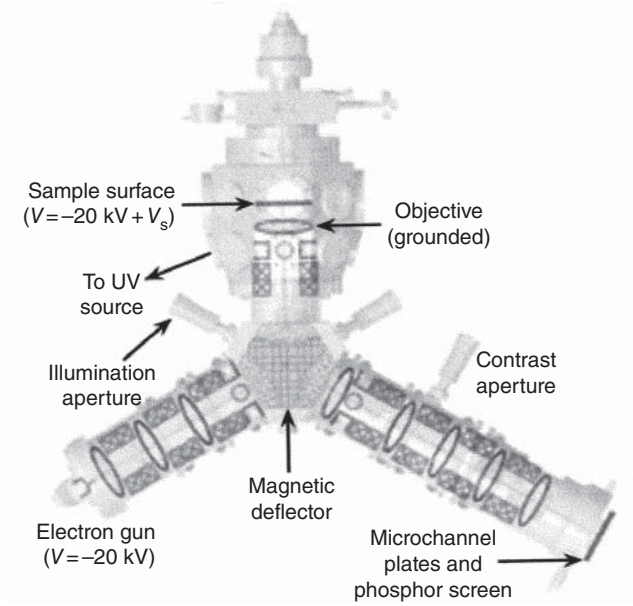


Figure 17.28 Typical LEEM experimental setup used for surface science studies.

has a spatial resolution of as much as several dozen nanometers. Image contrast depends on the variations of a surface's ability to reflect slow electrons due to differences in crystal orientation, surface reconstruction, or coverage. While microscopic images may be generated very quickly, LEEM is often used to examine dynamic processes occurring on different surfaces, including the growth of thin films, etching, adsorption, and phase transitions in real time. In illustration thereof, Figure 17.27 shows a microscopic image of the surface of Si(111) during phase transition from reconstruction 7×7 to reconstruction 1×1 occurring in an environment with temperature 860 °C (Tromp 2000).

A layout of the Elmitec LEEM system is shown in Figure 17.28. This instrument is capable of BF and DF imaging with 10 nm resolution, selected area low-energy electron diffraction (μLEED), and spectroscopic low-energy electron reflectivity (LEER) measurements. This is primarily used for characterizing epitaxial films of 2D materials, in which case the spatial and crystal orientation of the grains is determined (from imaging of the μLEED), along with the number of 2D layers in each grain (from LEER measurements).

The operation of this instrument is easy to grasp: electrons are produced in an electron gun containing a thermionic LaB_6 emitter, which is biased at typically −20 keV. Once the electron beam has left the emitter, it is accelerated to high energy by a grounded extractor into the illumination column, after which the beam is deflected toward the sample surface by a magnetic deflector. Passing through the grounded objective lens, the beam is rapidly decelerated to low energy due to the large potential difference between the objective and the sample, which is also close to −20 keV. A potential difference, V_s (start voltage or sample voltage), can be applied between the sample surface and the gun filament to alter the incident electron energy. Typically, incident energies of 0–50 eV are employed. The electrons are then reflected, or diffracted, from the sample surface. They pass through the magnetic deflector again and then are imaged (either as a diffraction pattern or as a real-space image) on the micro-channel plate. A contrast aperture is used to select particular diffraction spots for imaging. BF images are formed using the reflected (0, 0) spot, whereas DF images are formed using other, specifically selected, diffraction spots. Due to their low energies, the only electrons to leave the surface are those that originate from the top few atomic layers of the sample. Hence, LEEM is a very surface-sensitive technique.

LEEM has developed into one of the premier techniques for *in situ* studies of surface dynamical processes, such as epitaxial growth, phase transitions, chemisorption, and strain relaxation phenomena. Over the last few years, new LEEM instruments have been designed and constructed, aimed at improved resolution, improved diffraction capabilities, and greater ease of operation compared with present instruments (Bauer 1998).

17.8 Electron Spectroscopy and Ion Scattering

Electron spectroscopy is a group of analytical techniques to study the electronic structure and its dynamics in atoms and molecules. In general, an excitation source such as X-rays, electrons, or synchrotron radiation will eject an electron from an inner-shell orbital of an atom. Experimental applications include ion-resolution measurements on the intensity and angular distributions or emitted electrons as well as on the total and partial ion yields. Ejected electrons can only escape from a depth of approximately 3 nm or less, making electron spectroscopy most useful to study surfaces of solid materials. Depth profiling is accomplished by combining an electron spectroscopy with a sputtering source that removes the surface layers. Ion scattering techniques operate across a large energy range, from 1 keV to >10 MeV, each with different benefits and different aspects that can be investigated with each technique. Compared with other surface analytical techniques, the physics governing ion scattering is relatively simple. Being a real-space technique, the complexity of converting reciprocal-space data to real space is not required, and the overall equation governing collisions can be simply shown as a primary collision model. To obtain quantitative information about the species present at the surface of a material, it is necessary to understand the interaction potentials due to the effect of ion neutralization and scattering cross section. The main techniques considered are as follows.

17.8.1 Extended X-Ray Absorption Fine Structure

The origins of *extended X-ray absorption fine structure* (EXAFS) are attributed to Kossel and Kronig more than 85 years ago. The X-ray absorption of a material will in general display several sudden upward jumps (termed K, L edges) as the X-ray photon energy is increased, corresponding to specific electron excitations in the constituent elements of the material. Closer examination of the high-energy side of these edges (i.e. some hundreds of electron volts above the edge) reveals small oscillations in absorption, which are the fine structure referred to in EXAFS. These oscillations arise from small energy fluctuations associated with interference effects between an outgoing electron wave from the excited atom and that fraction that is scattered back by the surrounding atoms (Figure 17.29). Thus, they carry information about the local environment of an excited atom/ion. An appropriately weighted Fourier transform of these EXAFS spectra will produce a radial distribution plot, that is, a plot of the surrounding atomic density versus distance from the excited atoms.

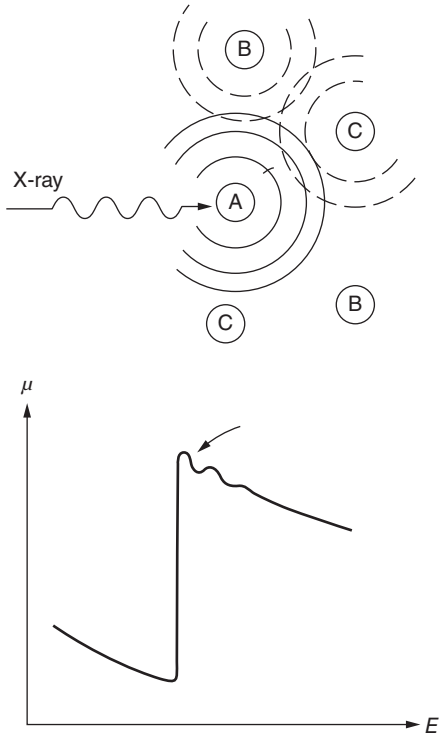


Figure 17.29 Basic principles of EXAFS. On excitation of atom A by an X-ray photon, the outgoing electron wave interferes with the fraction scattered back by the surrounding atoms B and C. The result is fine oscillations (arrowed) in the absorption versus energy curve above the edge.

The key feature of EXAFS is that each absorption edge is specific of a given atom type in the material, so that each EXAFS spectrum yields an individual atom type's view of its local environment. The technique does not require that the material be crystalline: indeed it can be amorphous or liquid. This contrasts sharply with conventional crystallography that seeks diffraction patterns from crystalline material, the diffraction patterns themselves being complex superpositions of scattering from all the constituent atomic/electron density. Considerable crystallographic skill is required to disentangle the diffraction contributions from each atom in order to produce a 3D structural map of the material. EXAFS can directly probe the structure of each atom type, though this structural information extends only to the nearer coordination shells around the given atom.

Not surprisingly, being such a direct and versatile technique, EXAFS has become an increasingly popular technique in all walks of materials science. In particular, catalytic processes can be studied where specific atomic interactions are implicated and also amorphous/glassy materials where crystallography can give only limited structural information. Although EXAFS spectra can in principle be collected using the weak bremsstrahlung (white) X-ray yield from laboratory

Table 17.9 Acronyms for various forms of EXAFS

Transmission EXAFS	The standard measurement mode is transmission
Fluorescent EXAFS (or FLEXAFS)	Complementary to transmission mode, where X-ray emission is detected particularly for dilute elements
XANES	Refers to the near-edge structure, usually the first 100 eV above the edge that, through multiple scattering, is also sensitive to local symmetry
SOXAFS	Soft (energy) EXAFS, e.g. 800 eV to 8 keV, particularly for K edges of light elements
SEXAFS	Surface EXAFS, usually by photoelectron detection
REFLEXAFS	SEXAFS performed by using the fluorescent mode with glancing incident X-rays totally externally reflected from the surface
QEXAFS	Quick EXAFS scans (~1 min)
ED-EXAFS	Energy-dispersive EXAFS: a geometry for extremely rapid EXAFS scans, dispersing the transmitted beam and measuring by fast position-sensitive detector

sources, the synchrotron, with its intense and continuous energy X-ray spectrum, is ideal for EXAFS. Practical collection times (minutes to hours) are therefore many orders of magnitude faster than laboratory measurements (days to weeks). The case for synchrotron EXAFS is now so strong in academic and industrial materials research programs that dedicated synchrotrons devote a sizeable fraction of their resources to EXAFS instrumentation.

EXAFS has evolved into many forms of measurement. A number of acronyms sprung up to describe the more popular versions of its use (Table 17.9).

The use of EXAFS for studies on catalysis has largely been mentioned. An exciting development in this pursuit is the marrying of EXAFS data with diffraction data. One example involves nickel-exchanged zeolite Y that is used for converting three acetylene molecules into one benzene molecule. By making *in situ* EXAFS and powder diffraction measurements in controlled environments, it has been possible to study the complex structural changes involved: during dehydration, some nickel cations move from the super cage into the smaller cages, while others remain attached to the walls of the super cage; further movement of the cations occurs during catalytic activity.

Glasses, unlike crystalline zeolites, do not display long-range order. Conventional X-ray/neutron scattering can give short-range structural information, but this is averaged over all atom types, and special techniques (anomalous absorption for X-rays, isotopic substitution for neutrons) are required to apportion scattering to individual atom types. EXAFS has proved to be a more discriminating probe of local structure in glasses.

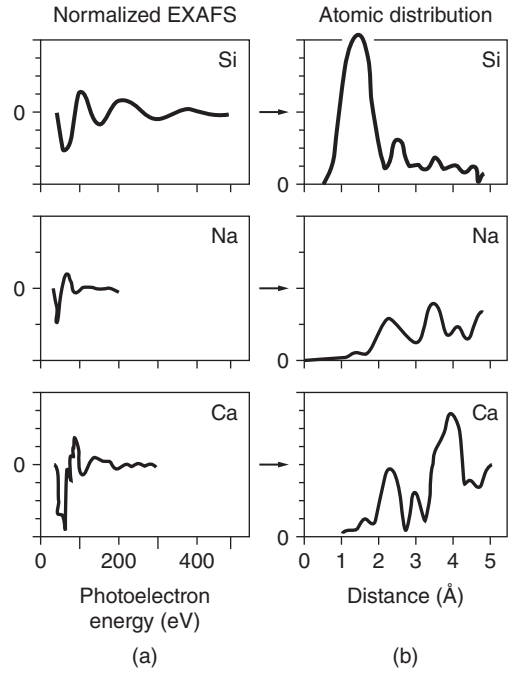


Figure 17.30 EXAFS spectra (a) and resulting atomic distributions (b) around Si, Na, and Ca, respectively, in soda lime–silica glass.

The differing environments of silicon, sodium, and calcium in soda lime–silica glass are readily obtained from the K-edge EXAFS spectra, Figure 17.30 (Greaves 1990): silicon is tetrahedrally coordinated with oxygen at 1.61 Å, sodium is sixfold coordinated with a short bond of 2.3 Å, while calcium is similarly octahedrally coordinated but with a longer oxygen distance of 2.5 Å. These EXAFS data are consistent with a modified random network model of the glass containing channels of mobile cations ionically bonded in non-bridging oxygens. This model is also consistent with the known bulk properties such as the reported emission of sodium on fracture, which appears to occur along these cation channels.

17.8.2 Photoemission

Photoemission is a low-energy technique exploited by surface science. It uses X-ray photons in the low 100 eV energy range (i.e. wavelengths ~100 Å). For example, photoemission spectra from an aluminum (111) surface, before and after exposure to oxygen gas at $\sim 2 \times 10^{-7}$ torr, record the very early stages of aluminum oxidation (McConville et al. 1987). The chemical shifts of the photoemission peaks can be interpreted in terms of various proposed models. One possibility is that at low coverage, the oxygen chemisorbs onto the aluminum surface in three different states. This is identified by three peak shifts corresponding to aluminum atoms bonded to one, two, or three chemisorbed oxygen atoms. At higher exposures, the oxygen may diffuse to form a complete oxide-like underlayer beneath the surface.

Although surface science is an expensive and time-consuming discipline, it addresses fundamental problems in materials science, involving the structure and composition of surfaces. These influence important technologies such as semiconductor growth, surface catalysis, and corrosion protection.

17.8.3 Auger and X-Ray Photoelectron Spectroscopy

These processes, described in detail elsewhere (Haugsrud 2003), are schematically illustrated in Figure 17.31. In both techniques, a surface atom is ionized by removal of an inner-shell electron. In XPS or ESCA, this is achieved by bombarding the surface with photons with energies between 1 and 2 keV. The resulting photoelectron has an energy given by

$$E = h_\gamma - E_K \tag{17.21}$$

The energy of the photoelectron is measured using a concentric hemispherical analyzer. Typically the energy can be measured to an accuracy of ±0.1 eV. Knowing the energy of the incident photon, the binding energy of the electron in the atom can be determined. In addition, changes in binding energy that occur when elements combine together can be detected, and the chemical state of the atom identified.

In AES, ionization is produced by bombarding the surface with electrons with energies from 2 to 15 keV. When an electron is ejected from an inner shell (K shell) of an atom, the resultant vacancy is soon filled by an electron from one of the outer shells (L). This releases energy, which may be transferred to another outer electron (L shell), which is ejected. The energy of the Auger electron is given by

$$E_{\text{Auger}} = E_K - E_{L_1} - E_{L_{2,3}} \tag{17.22}$$

The energy of the Auger electron is measured by either hemispherical or cylindrical analyzers. The former has better energy resolution and hence gives chemical state information, while the latter has a higher transmission function and is useful for kinetic studies.

XPS has the advantage that it can give reliable chemical state information but has limited spatial resolution, while AES has excellent spatial resolution (10 nm) but limited chemical state.

Concerning the oxide characterization, it is important to identify the initial stages and corresponding thin films that form initially. In this respect, both XPS and AES are useful.

Figure 17.32 shows the oxygen 1s peak during the initial stages of exposure of nickel to oxygen at room temperature and then the effect of heating on this oxide (Allen et al. 1979). Initially undissociated oxygen is detected (stage 1), which then dissociates forming a layer of dissociated and undissociated oxygen on the top of the nickel metal (stage 2). Oxygen then diffuses into the nickel (stage 3) that may be slow at room temperature, but as the temperature is increased, the speed of the reaction increases. By determining the temperature at which this diffusion occurs from the O 1s peak shift, the activation energy can be determined.

In binary and ternary alloys, the oxide that first forms is determined by the temperature and rate of arrival of the gas atoms. Figure 17.33 shows spectra from stainless steel exposed to low oxygen pressure at room temperature and 873 K. At room temperature, the initial oxide is an iron-rich spinel of the form Fe_3O_4, but, at high temperature and low gas pressure, the chromium-rich rhombohedral oxide Cr_2O_3 is able to form.

Elements present in the bulk in very small quantities can have a dramatic effect on the initial oxidation. Sulfur is present in austenitic steels at a level of approximately 200 ppm. At temperatures of 500 °C and above, the sulfur diffuses to the surface where it reacts with the impinging gas atoms to form SO_2 that is released into the environment (Wild 1977). Figure 17.34 shows the surface composition of a stainless steel, determined using AES, as a function of time exposed to 10^{-5} Pa oxygen at 873 K. Initially the surface has a high concentration of sulfur present, but this is gradually reduced by reaction with oxygen. It is only when the sulfur has been effectively removed from the bulk that the surface oxide can form. It then does this by forming the rhombohedral Cr_2O_3, but almost immediately manganese is incorporated into this oxide forming the spinel oxide $MnCr_2O_4$.

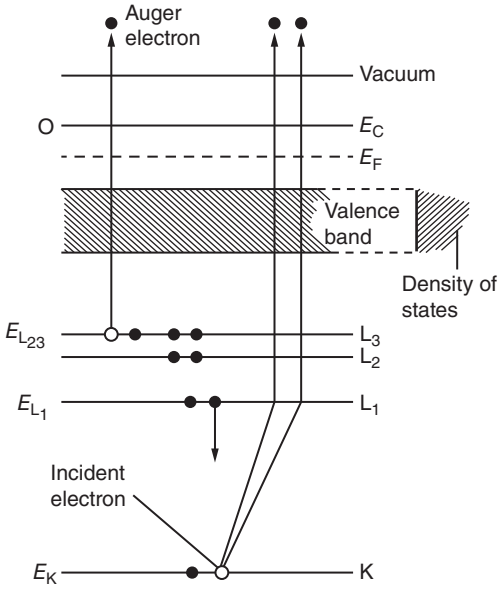


Figure 17.31 Schematic representation of the Auger process.

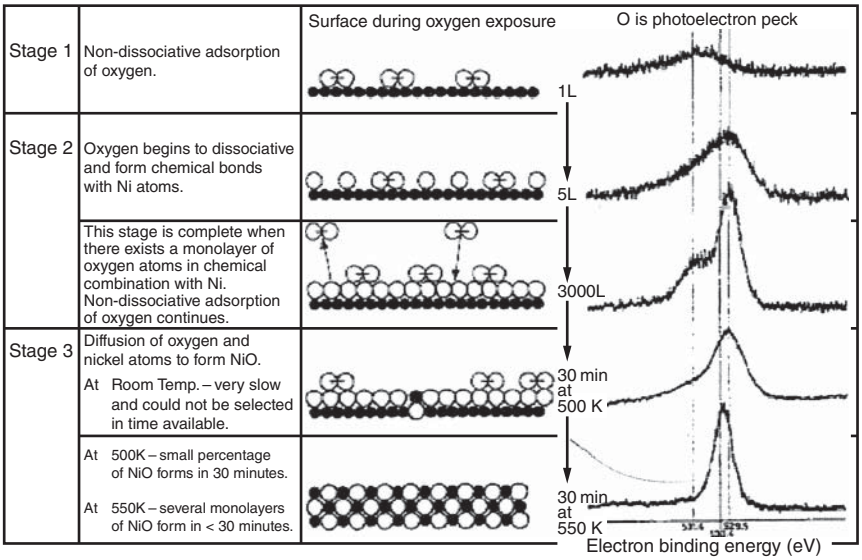


Figure 17.32 Changes in the oxygen O 1s peak during oxidation of nickel (Allen et al. 1979).

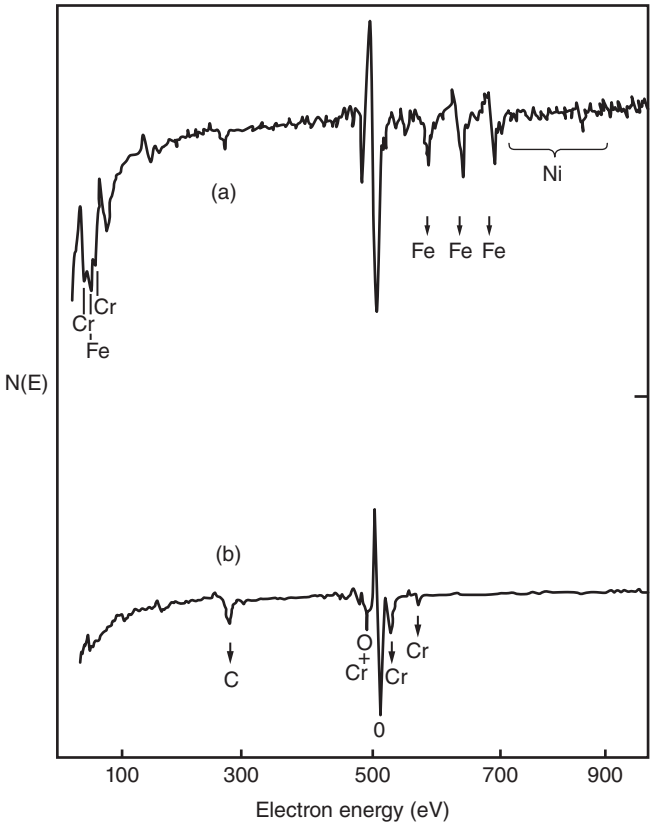


Figure 17.33 Auger spectra from stainless steel exposed to a low oxygen pressure. (a) Room temperature. (b) 873 K.

The surface layer to be analyzed by depth profiling using AES or XPS may be divided into different groups according to their thickness:

(a) Very thin layers of 1–5 nm thickness may be analyzed by angle resolution AES or XPS measurements.

(b) An ion sputtering may be used for layer thickness of 3–100 nm.

(c) For 100–2000 nm thick layers, depth profiling, lapping, or ball cratering may be applied.

(d) For layer thicknesses >2 mm, lapping or ball cratering is recommended.

Further information on the oxidation process during oxidation can also be obtained by AES and XPS. Complete characterization of oxides and other products can be

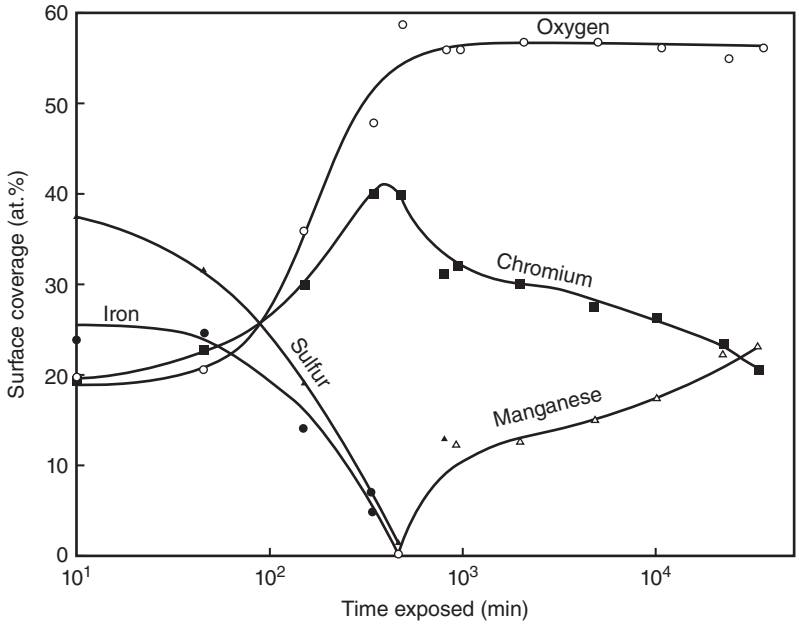


Figure 17.34 Surface composition of stainless steel during exposure to 10^{-5} Pa oxygen at 873 K (Wild 1977).

obtained by these surface analytical techniques combined with other specialized techniques (Birks et al. 2006; Khanna 2004; Levitin 2005; Schütze 1997; Tempest and Wild 1988).

17.8.4 Rutherford Backscattering

In RBS, the specimen to be analyzed is bombarded by a beam of α-particles with energy of approximately 0.9–3 MeV. The energy of the backscattered particles depends on the atomic number of the atom at which the particle is scattered and the distance of this atom from the specimen surface. Therefore, RBS is a nondestructive depth profiling method that is element and depth sensitive. Although a standard is needed to calibrate the experimental setup, RBS can be more or less considered as a nondestructive, absolute method (Quadakkers et al. 1992).

The quantitative depth information requires an iterative fitting procedure. In most laboratories, the program RUMP is being used. The information depth is c. 0.5–2 µm depending on the primary energy. The depth resolution is typically 10–30 nm and, in most cases, will therefore be determined by the irregularities of the oxide scale. A major requirement for the successful application of RBS is that the surfaces of the specimens have to be flat. An important limitation in using RBS is the overlapping of signals (Quadakkers et al. 1992). Figure 17.35 shows RBS spectra of an alumina scale on an yttria-containing FeCrAl alloy. The measured intensity at the high-energy edge of Fe unequivocally reveals the presence of a low concentration of this element at the alumina surface. The yield at slightly lower energies, however, might be caused by the presence of Fe in greater depth and/or Cr and/or Ti at the surface. Therefore, reliable in-depth information on the elements Fe, Cr, and Ti cannot be derived. The situation is different if a high Z element like Y is incorporated in the scale. Only then, quantitative in-depth concentration of this element, in this case up to around 0.3 µm, can be obtained. Because of the mentioned significant limitations, RBS cannot be considered as a suitable technique for standard depth profiling of corrosion scales. The method can sometimes be advantageous if heavy elements are to be analyzed in a light matrix. For analysis of light elements in a heavy matrix, NRA can, in some cases, be suitable.

17.8.5 Secondary Ion Mass Spectrometry

In SIMS, the specimen to be analyzed is bombarded by a beam of ions of energy 3–12 keV. The particles that are eroded from the surface by the bombardment leave the surface in the form of neutrals or ions (Rudenauer and Werner 1987). Analysis of the secondary ions by a mass spectrometer allows a chemical analysis of the specimen (corrosion scale) laterally and as a function of sputtering time, i.e. eroded depth (depth profiling by dynamic SIMS).

SIMS is a suitable method for the *depth profiling* of laterally uniform scales of 50 nm to 10 µm thickness. For thinner scales, AES/XPS might be more suitable, whereas for thicker scales conventional or tapered cross sections should be used. With modern ion sources, scales of up to several micrometers thickness can be analyzed within one hour. Compared with other surface analysis methods, SIMS is very suitable to measure trace elements because it can theoretically detect all elements and their isotopes, most of them down to concentrations in the ppb range; however the

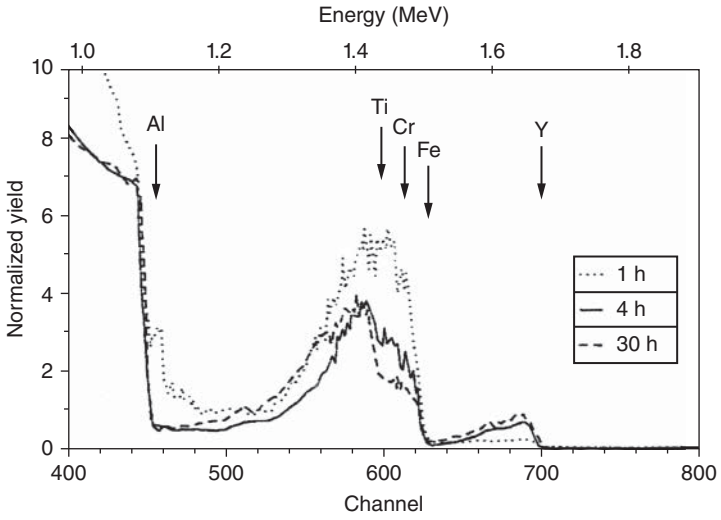


Figure 17.35 RBS spectra, α-particles, 2 MeV, showing Y, Fe(Cr, Ti), impurity in the outer part of an alumina scale on an FeCrAl-ODS alloy after various oxidation times at 1100 °C (Quadakkers et al. 1992).

sensitivity differs for the various elements, and, in practice, nitrogen, for example, appears to be difficult to measure.

The analysis of oxide scales can be hampered by the fact that the sputtering process induces charging of the specimen surface. Charging affects the primary ion beam and, more important, alters the part of the energy distribution contributing to the detected signal. For thin films this can be overcome by a gold coating (10–20 nm) of the specimen, but, in most cases, especially for thicker scales, charge neutralization by electron bombardment of the specimen is required.

Studies reported by Benninghoven et al. (1991) have shown that the matrix effect can strongly be reduced by using MCs^+-SIMS. In this technique, the oxidized specimen is bombarded by Cs^+ ions, whereas the positive molecule cluster ions of the elements (M) with Cs are being analyzed. Although the mechanisms of the molecule formation at the specimen surface are not yet completely understood, a number of recent studies seem to confirm the suitability of this technique for quantitative scale analysis, provided that the impact angle is larger than about 65° (depending on material and sputter yield). Figure 17.36 shows an example of the reduced matrix effect during analysis of an alumina scale formed on an FeCrAl alloy. It can be seen that a good approximation of the real concentration profiles is obtained by using *relative sensitivity factors* (RSFs) for the various elements (same RSFs for oxide and alloy) that lie in the same order of magnitude, in contrast to conventional SIMS, where the sensitivity factors for the various elements can differ by several orders of magnitude. Figure 17.36 illustrates that MCs^+-SIMS is capable of measuring concentrations as high as 60 at.% and as low as 0.01% simultaneously in one depth profile. If the RSFs are constant throughout the depth profiling, they provide the possibility to derive the relative sputter yields during the depth profile. Combined with an absolute measurement of the crater depth, a depth scale can then be derived. Further studies are necessary to prove the suitability of the MCs^+-SIMS technique.

If the oxide scale composition is not laterally homogeneous, depth profiles can only give limited information of the real element distribution in the scale because they give an average value over the analyzed area. In such cases, the good lateral resolution that is achieved by SIMS imaging can be used for scale characterization. The achievable lateral resolution depends on a number of experimental factors.

In imaging, even by using the MCs^+-SIMS technique, the matrix effect can make the mapping result difficult to interpret, because differences in sputter rates and/or ion yields of different phases in the oxide scale can indicate different concentrations of the various elements that, in reality, do not exist. Therefore, in multiphase scales, the intensities at every measured pixel of the image should be corrected to account for the differences in sputter rate and ion yield for obtaining the real element distribution. This obviously requires significant computer capacity; however, in using MCs^+-SIMS, promising results have been obtained.

The big advantage of the technique is its high sensitivity for most elements in many materials including insulating compounds. The profiling mode must be used with care due to the poorly defined relation between sputtering time and depth, particularly in nonhomogeneous materials such as oxidized metals.

An example of SIMS profiling is also given in Figure 17.37 for the case of the oxidation in oxygen of the binary nitride $Ti_xAl_{1-x}N$ obtained by chemical vapor deposition.

The figure shows that alumina, Al_2O_3, is located at the external part of the oxidized scale, whereas the internal part consists of a mixture of alumina and titania, $Al_2O_3 + TiO_2$.

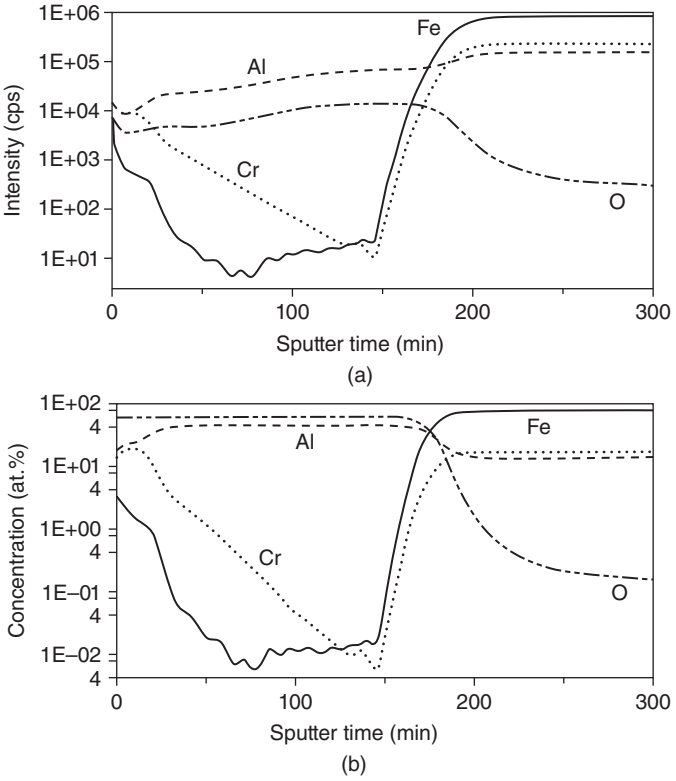


Figure 17.36 MCs^+ analysis of alumina scale on Fe–20Cr–5Al ODS alloy, composition in wt%, after 215 hours oxidation at 1100 °C SIMS parameter, 50 nA, 5.5 keV, scanning area 150 × 150 m, and charge compensation by electron gun. (a) Non-corrected intensities of main elements Fe, Cr, Al, O. (b) Intensities after isotope correction; multiplication with sensitivity factors, Al = 1, Cr = 0.85, Fe = 0.9, O = 6.5; and normalization to total corrected intensity.

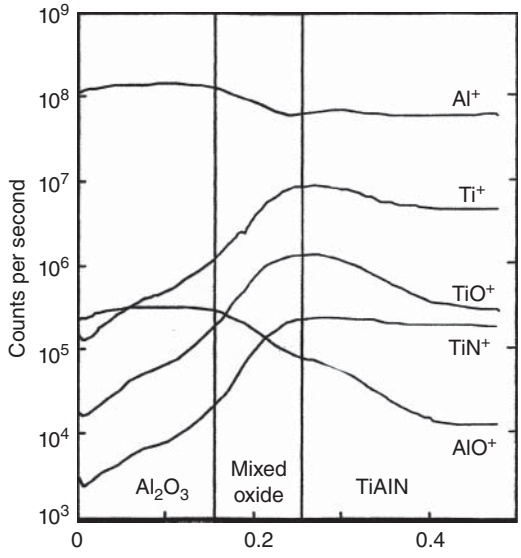


Figure 17.37 SIMS spectrum as a function of depth of the oxide scale formed by oxidation of TiAlN at 850 °C for 150 minutes using a 4 keV Xe^+ beam at 45° incidence.

17.8.6 Ion Scattering Spectroscopy

Using ion beams of much lower energies (0.2–2 keV), produced by low-cost and easy to use ion guns, may generate the same analytical information as RBS but limited to surface atoms. The physical phenomenon is not changed, and the expression of the kinematic factor describing the backscattering yield is always given by Eq. (17.23):

$$K = [(\cos\theta + \sqrt{\mu^2 - \sin^2\theta})/(1+\mu)]^2 \qquad (17.23)$$

where μ is the ratio m/M of the masses of the incident ion and of the target atom and θ is the angle at which the backscattering ions are collected. The technique is here called *ion scattering spectroscopy*, and this is mainly a surface analysis technique comparable with the electron spectroscopes described above. However, it is possible to obtain depth information by sputtering inward from the specimen surface. The lifetime t_m of the surface monolayer of the solid under ion sputtering is given by

$$t_m = \frac{C_s}{F_B S} \qquad (17.24)$$

where C_s is the surface concentration of the solid (atoms m^{-2}), F_B is the ion flux of the beam (ion m^{-2} s^{-1}), and S is the sputtering yield (number of sputtered atoms/number of incident ions). The first two of these parameters are easy to measure and control, but the third is more difficult to evaluate. The sputtering yield is dependent not only on the nature, energy, and the angle of incidence of the sputtering ions but also on the nature, crystalline orientation, and properties of the bombarded surface. For example, using Ar^+ ions of 1 keV to bombard pure polycrystalline aluminum at

60° incident angle gives a sputtering yield of about 2. Using a value of 1×10^{19} atoms m^{-2} for C_s, a monolayer removal time of one second ($t_m = 1$) needs a beam flux of 5×10^{18} ions m^{-2} s^{-1}, corresponding to an ion current of monocharged species of 0.8 A m^{-2}. Modern ion guns cover a large range of currents from 10^{-5} to 10 A m^{-2} so that an experimentally convenient choice of sputtering rate can usually be obtained.

17.8.7 Low-Energy Electron Loss Spectroscopy

Low-energy electron loss spectroscopy (LEELS) is a surface analysis technique that provides quantitative information about physicochemical properties of materials from their nano-size near-surface region. It is well known that physical phenomena such as *secondary electron emission* (SEE) can be used to investigate the near-surface area of a solid to obtain information on its crystal structure, elemental composition, and electronic configuration of its atoms (Luth 1993). Figure 17.38 shows the energy distribution of reflected SEE from a surface irradiated by an electron beam of primary energy E_0. Four ranges in $N(E)$ can be observed that are due to interactions between elastic and inelastic scattering together with SEE.

Region II is due mainly to electrons that have lost some of their energy by inelastic scattering; directly by the elastic peak, one finds electrons that have suffered discrete energy losses from the excitation of inter- and intraband electronic transitions, surface and bulk plasmons, hybrid modes of plasmons, and ionization losses (ionization spectroscopy). That range is usually 30–100 eV. Usually, the losses related to surface and bulk plasmon excitations are most intensive lines in the electron energy loss spectrum. The spectra of plasma oscillations are potential data carriers about composition and chemical state of elements on the surface of solid and in the adsorbed layers. The energy losses are called as characteristic losses because they do not depend on the primary electron energy E_0 and its value is individual for the chemical element and compound. Region II is called as *electron energy loss spectroscopy*. At energy $E_0 < 1000$ eV, it can be called as LEELS. On Figure 17.39 really LEELS spectra are shown with interpretation of losses for the Co–Cr–Mo alloy surface that was measured at the primary electron beam energy $E_0 = 350$ eV in dN/dE mode (Vasylyev et al. 2008).

LEELS, with its variants ionization spectroscopy and surface and bulk plasmon excitations (these are potential data carriers about composition and chemical state of elements on the surface and bulk of solid and in the adsorbed layers), is based on the measurement of the energy spectra of electrons, which have lost a particular portion of the energy ΔE_β for the excitation of electronic transitions that are typical for a given kind of atom β. The position of an intensity line (IL) in the spectrum with respect to the primary electron energy E_0 is determined by the binding energy of electrons in the ground state and by the distribution of the density of empty states, but it does not depend on the value of E_0, on the work function, or on the value of the surface charge.

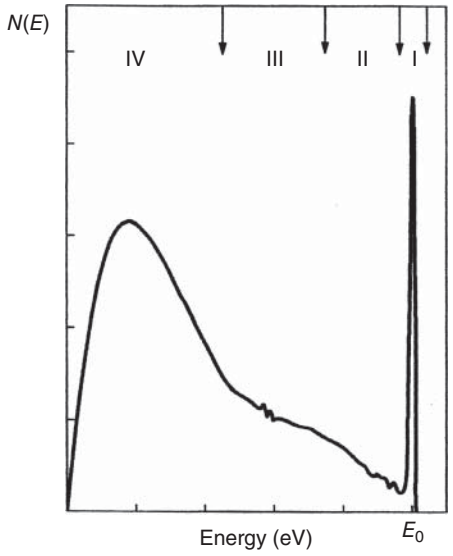


Figure 17.38 Total energy distribution of secondary electron emission from a surface that is irradiated by an electron beam of primary energy E_0.

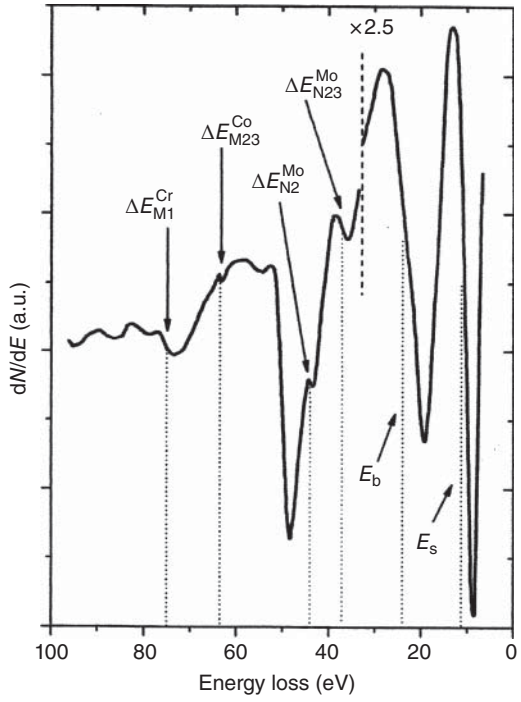


Figure 17.39 Example low EELS spectra obtained for the Co–Cr–Mo alloy surface at the primary energy $E_0 = 350$ eV with identification of energy losses (Vasylyev et al. 2008).

The calculation of the contribution to the intensity of an IL by the electrons having lost an amount of energy ΔE_β at the depth Z from the sample surface by the ionization of the core states of the atoms β is simple when a traditional experimental configuration is used (an incident beam of the primary electrons is directed perpendicularly to the sample surface ($\theta_0 = 0$), and the SE are registered at the angle θ with respect to the normal). In this case, calculations within the framework of a two-stage model allow us to obtain the following expression for the intensity of an IL (Vasylyev et al. 2006):

$$I_\beta = (Z, E_{0j}) = K\sigma_\beta \widetilde{r}_\beta n_\beta(Z) \exp(-Z/\Lambda_\beta) \qquad (17.25)$$

where K is an instrumental factor, σ_β is the ionization cross section of the core level, $n_\beta(Z)$ is the concentration of atoms at depth Z from surface, and $\widetilde{r}_\beta$ is the elastic scattering factor of electrons. Λ_β is the effective free path of electrons in a sample with respect to inelastic collisions, which is determined by the equation

$$\Lambda_\beta^{-1} = \lambda_0^{-1} + (\lambda_\beta \cos\theta)^{-1} \qquad (17.26)$$

For the Pt–Me (Me: Fe, Co, Ni, Cu) alloys (Seah and Dench 1979)

$$\lambda_0 = \frac{1194}{E_{0j}^2} + 0.429\, E_{0j}^{1/2}; \quad \lambda_\beta = \lambda(E_{0j} - \Delta E_\beta) \qquad (17.27)$$

An effective probing depth in IS amounts to $\sim 3\Lambda\beta$ because the SE created in the near-surface region of this thickness contribute with 95% to the total intensity of an IL. An increase in the effective probing depth upon increasing the energy E_0 also results in an increased contribution from the deeper layers of the concentration profile into the IL intensity. This enables us to carry out a layer-by-layer reconstruction of the concentration profiles of the elements using the energy dependencies of the IL.

In summary, LEELS with energy ionization losses allows investigation of the layer-by-layer concentration profile for the single-crystal alloys with monolayer resolution, element distribution on the depth for the polycrystalline alloys, and study of kinetics of surface processes at thermo-induced treatment or after ion irradiation of the surface.

Plasmon excitations are very sensitive to structural and chemical state of surface and bulk and can be used for the study of electronic states of free electrons in the near-surface region and influence of different kinetic processes on changing of electronic structure of materials.

Accordingly, LEELS with plasmon excitations can also define a surface–bulk interface with different physicochemical properties as compared with the bulk material. These results have good correlation with data of surface composition on depth that are obtained by ISS and AES.

17.9 Surface Microscopy

Surface microscopy includes atomic force microscopy (AFM), scanning tunneling microscopy, topographic confocal Raman imaging, low-energy electron microscopy, lateral force microscopy (LFM), surface force apparatus (SFA), and other advanced techniques. Here, we give some attention to scanning tunneling microscopy, AFM, SFA, and LFM.

17.9.1 Scanning Tunneling Microscopy

Classically, an object hitting an impenetrable barrier will not pass through. In contrast, objects with a very small mass, such as the electron, have wavelike characteristics that allow such an event, referred to as tunneling.

Electrons behave as beams of energy, and, in the presence of a potential $U(z)$, assuming 1-dimensional case, the energy levels $\Psi_n(z)$ of the electrons are given by solutions of Schrödinger's equation:

$$-\frac{h^2}{2m}\frac{\partial^2 \Psi_n(z)}{\partial z^2} + U(z)\Psi_n(z) = E\Psi_n(z) \qquad (17.28)$$

where h is the reduced Planck's constant, z is the position, and m is the mass of an electron.

Inside a barrier, $E < U(z)$ so the wave functions that satisfy this are decaying waves. Knowing the wave function allows one to calculate the probability density for that electron to be found at some location. In the case of tunneling, the tip and sample wave functions overlap such that when under a bias, there is some finite probability to find the electron in the barrier region and even on the other side of the barrier (Chen 1993).

When a small bias V is applied to the system, only electronic states very near the Fermi level, within eV (a product of electron charge and voltage, not to be confused here with electron volt unit), are excited. These excited electrons can tunnel across the barrier. In other words, tunneling occurs mainly with electrons of energies near the Fermi level. However, tunneling does not require that there be an empty level of the same energy as the electron for the electron to tunnel into on the other side of the barrier. It is because of this restriction that the tunneling current can be related to the density if available or filled states in the sample. The current due to an applied voltage V (assume tunneling occurs sample to tip) depends on two factors: (i) the number of electrons between E_f and eV in the sample and (ii) the number among them that have corresponding free states to tunnel into on the other side of the barrier at the tip. The higher the density of available states, the greater the tunneling current. When V is positive, electrons in the tip tunnel into empty states in the sample; for a negative bias, electrons tunnel out of occupied states in the sample into the tip (Chen 1993).

One can sum the probability over energies between E_f–eV and E_f to get the number of states available in this energy range per unit volume, thereby finding the local density of states (LDOS) near the Fermi level. Now, using Fermi's golden rule, which gives the rate for electron transfer across the barrier, it is possible to obtain the full tunneling current and consequently the Fermi distribution function that described the filling of electron levels at a given temperature.

A *scanning tunneling microscope* (STM) is an instrument for imaging surfaces at the atomic level, with a 0.1 nm lateral resolution and 0.01 nm (10 pm) depth resolution. It is based on the concepts of quantum tunneling reported above and can be used not only in ultrahigh vacuum (UHV) but also in air, water, and various other liquid or gas ambients and at temperatures ranging from near-zero kelvin to over 1000 °C.

The components of an STM include a scanning tip, a piezoelectric controlled height and an x, y scanner, coarse sample-to-tip control, vibration isolation system, and computer (Oura et al. 2003).

The resolution of an image is limited by the radius of curvature of the scanning tip of the STM. Additionally, image artifacts can occur if the tip has two tips at the end rather than a single atom; this leads to "double-tip imaging," a situation in which both tips contribute to the tunneling. Therefore, it has been essential to develop processes for consistently obtaining sharp, usable tips. Recently, carbon nanotubes have been used in this instance (Lapshin 2007).

The tip is often made of tungsten or platinum–iridium, though gold is also used. Tungsten tips are usually made by electrochemical etching, and platinum–iridium tips by mechanical shearing (Bai 1999). Maintaining the tip position with respect to the sample, scanning the sample, and acquiring the data are computer controlled. The computer may also be used for enhancing the image with the help of image processing, as well as performing quantitative measurements (Lapshin 2007).

17.9.2 Atomic Force Microscopy

AFM or *scanning force microscopy* (SFM) is a type of *scanning probe microscopy* (SPM) with demonstrated resolution in the order of fractions of a nanometer or more than 1000 times better than the optical diffraction limit. The technique allows force measurement manipulation and acquisition of topographical images.

In force measurement, AFMs can be used to measure the forces between the probe and the sample as a function of their mutual separation. This can be applied to perform force spectroscopy.

For imaging, the reaction of the probe to the forces that the sample imposes on it can be used to form an image of the 3D shape (topography) of a sample surface at a high resolution. This is achieved by raster scanning the position of the sample with respect to the tip and recording the height of the probe that corresponds to a constant probe–sample interaction. The surface topography is commonly displayed as a pseudocolor plot.

In manipulation, the forces between tip and sample can also be used to change the properties of the sample in a controlled way. Examples of this include atomic manipulation, scanning probe lithography, and local stimulation of cells.

An AFM typically consists of a small cantilever, a piezoelectric element, a tip or probe, a detector of deflection, and motion of the cantilever, the sample, an x, y, z drive, and the sample stage (Butt et al. 2005).

According to this configuration, the interaction between tip and sample, which can be an atomic scale phenomenon, is transduced into changes of the motion of cantilever that is a macroscale phenomenon. Several different aspects of the cantilever motion can be used to quantify the interaction between the tip and sample, most commonly the value of the deflection, the amplitude of an imposed oscillation of the cantilever, or the shift in resonance frequency of the cantilever (tip contact or static mode of motion, tip tapping or intermittent contact mode of motion and of the detection mechanism or noncontact mode of motion).

Various methods of detection can be used, e.g. interferometry, optical levers, the piezoresistive method, the piezoelectric method, and STM-based detectors (beam deflection measurement, capacitive detection, laser doppler vibrometry, etc.).

The AFM signals, such as sample height or cantilever deflection, are recorded on a computer during the x–y scan. They are plotted in a pseudocolor image, in which each pixel represents an x–y position on the sample and the color represents the recorded signal.

Noncontact mode AFM does not suffer from tip or sample degradation effects that are sometimes observed after taking numerous scans with contact AFM. This makes noncontact AFM preferable to contact AFM for measuring soft samples, e.g. biological samples and organic thin film. In the case of rigid samples, contact and noncontact images may look the same. However, if a few monolayers of adsorbed fluid are lying on the surface of a rigid sample, the images may look quite different. An AFM operating in contact mode will penetrate the liquid layer to image both the liquid and surface.

AFM has several advantages over the SEM. Unlike the electron microscope, which provides a 2D image of a sample, the AFM provides a 3D surface profile. In addition, samples viewed by AFM do not require any special treatments (such as metal/carbon coatings) that would irreversibly change or damage the sample and do not typically suffer from charging artifacts in the final

image. While an electron microscope needs an expensive vacuum environment for proper operation, most AFM modes can work perfectly well in ambient air or even in a liquid environment. This makes it possible to study biological macromolecules and even living organisms. In principle, AFM can provide higher resolution than SEM. It has been shown to give true atomic resolution in UHV and, more recently, in liquid environments. High-resolution AFM is comparable in resolution with scanning tunneling microscopy and TEM. AFM can also be combined with a variety of optical microscopy techniques such as fluorescent microscopy, further expanding its applicability. Combined AFM–optical instruments have been applied primarily in the biological sciences but have also found a niche in some materials applications, especially those involving photovoltaic research (Geisse, 2009).

Table 17.10 summarizes the functions of STM and AFM, thus clarifying the advantageous characteristics of these microscopy surface techniques. But it should be noticed that disadvantages also exist. For example, a disadvantage of AFM compared with SEM is the single scan image size; the scanning speed of an AFM is also by far slower than the scanning speed of a SEM. AFM images can also be affected by nonlinearity, hysteresis, and creep of the piezoelectric material and cross talk between the x, y, z axes that may require software enhancement and filtering (Lapshin, 1995, 2007).

Table 17.10 Summary of STM and AFM functions

	STM	AFM
Instrumentation	Tip, scanner, controller	Cantilever, scanner, optics controller
Conducting samples	Yes	Yes
Nonconducting samples	No	Yes
Resolution in vacuum	<0.1 Å	~Å
In dry air	<1 Å	~nm
In liquid	~nm	~10 nm
Operation in liquid	Tip coating	No coating needed
Modes of operation	Constant height	Constant height
	Constant current	Constant force Contact mode Tapping mode
Applications	Imaging	Imaging
	Tunneling spectroscopy	Force mapping
	Manipulation of atoms/molecules	Nanolithography

17.9.3 Surface Force Apparatus

The SFA (Israelachvili and Adams 1978) was the pioneer scientific instrument to measure nanoscale forces. It was originally designed to study colloidal interactions, including steric, electrostatic, van der Waals, and solvation forces, and, today, it can also be used to monitor the assembly of biomolecules in real time.

The SFA technique stems from right after World War II as David Tabor was studying frictional interactions between surfaces in the Cavendish laboratory. He/she had an industrial contract aimed at developing improved windscreen wipers, which led him to modelize the interactions between rubber and glass in water. Using hemispherical rubber samples pressed against a flat glass surface, his/her team could follow the interaction by interferometry. When the rubber/glass interaction experiments were performed in air, contact was immediately established, and the rubber hemisphere became flattened over some area even under zero (compression) force. Under negative (pulling) force, and up to the onset of separation, the contact area remained nonzero, suggesting that attractive forces were operating between these two solid surfaces. This observation led his/her team to develop the Johnson–Kendall–Roberts (JKR) theory (Johnson et al. 1971) for the adhesion between two solid bodies, which predicts that the pull-off force F to separate a deformable sphere of radius R from a plane is equal to

$$F = 3\pi R W_{\text{adh}}/2 \tag{17.29}$$

where W_{adh} is the adhesion free energy per unit area of the two surfaces.

At the same time, Samuel Tolansky was extensively studying the surface topography of crystals using *fringes of equal chromatic order* (FECO) (Tolanski 1949, 1955). FECO are obtained by passing a white light through a Fabry–Perot interferometer and are extremely sensitive to the surface topography down to the angstrom scale. They turned out to be also very useful for surface force measurements, since they could give the inter-surface distance and the deformation of two interacting surfaces with an unprecedented resolution.

In order to study surface forces with better-defined substrates, Tabor's team used mica that can be easily cleaved into atomically smooth thin sheets over several square centimeters. This allowed them to produce the first detailed measurements of van der Waals forces in the normal and retarded regimes (Tabor and Winterton 1969) (Figure 17.40). One of Tabor's students, named Jacob Israelachvili, adapted the original design of the SFA to operate in liquids and improved its mechanics. He/she also solved the complete set of equations of the FECO, therefore improving the accuracy of multiple-beam interferometry and making it more user friendly (Israelachvili 1973).

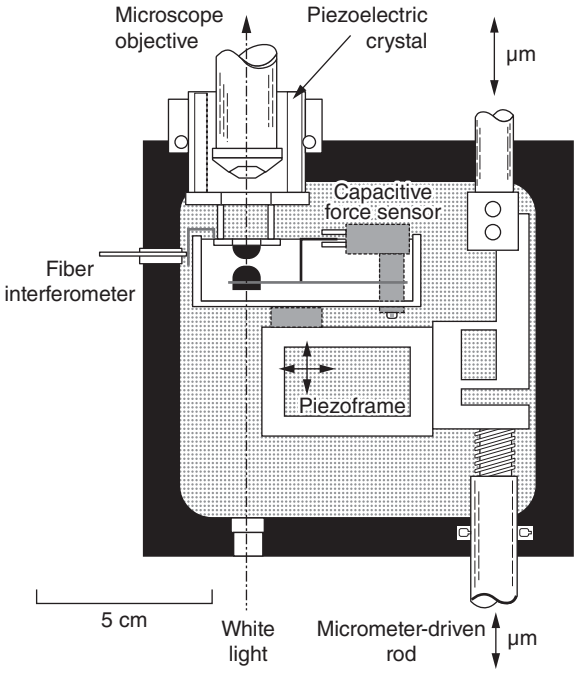


Figure 17.40 Schematic representation of the surface force apparatus. The distance between the surfaces is measured by an interferometric technique using white light and a spectrometer; by studying the FECO fringes, the separation of the mica plates can be monitored with sub-nanometer resolution. After calibrating the leaf spring constant, this distance can be translated to force providing a simultaneous measurement of force with 10^{-7} N resolution.

Notably, this allowed him to substantially improve the measurements of van der Waals forces. After this, Israelachvili and his/her coworkers studied various inter-surface and intermolecular forces, such as Derjaguin, Landau, Verwey, and Overbeek (DLVO) forces (repulsive electrostatic double-layer forces and attractive van der Waals forces), hydration forces, forces between lipid bilayers, and forces between receptors and their ligands (Israelachvili 1992).

In summary, the SFA is a powerful technique to study in real time and in a close-to-native environment the interactions between molecules. Its high resolution in distance and force allows the identification of any conformational changes and intermediate binding states that occur in the course of their assembly. In addition, as it measures the interaction produced by a large number of identical molecules, the SFA enables averaging out any effect coming from thermal fluctuations and thus makes it possible to obtain directly the energetics of assembly that single molecule techniques cannot currently do in a direct manner.

17.9.4 Lateral Force Microscopy

LFM provides surface-sensitive local information on nano-mechanical properties, such as friction coefficient, material stiffness (moduli), hardness, elastic–plastic yield points, and viscosity. On rating with nanoscale probing areas, it can largely avoid perturbation-induced material activation into metastable configurations, which makes LFM very sensitive to true (equilibrated) material properties. The technique gives useful information on contact mechanics, viscoelasticity, friction, force, and modulation, being necessary to have basic knowledge of subjects such as stress–strain relationships, classical understanding of friction, the Bowden–Tabor adhesion model of friction, models of single asperity contact, fully elastic models, Hertzian theory, contact stiffness, force modulation and material relaxation properties, transition and viscoelasticity, linear viscoelasticity, time–temperature equivalence of viscoelastic behaviors, and glass transition. Background on these subjects can be obtained in the open literature, namely, in books by Alkonis and MacKnight (1983), Hedvig (1977), Meyer et al. (1998), and Ward (1971).

LFM can be introduced in two embodiments: an SFM-based mechanical (sinusoidal) perturbation method referred to as *force modulation microscopy* (FMM) or *force modulation scanning force microscopy* (FMSFM) and *friction force microscopy* (FFM) to explore thermochemical properties in materials such as polymers around the glass transition and friction forces.

LFM measures lateral deflections (twisting) of the cantilever that arise from forces on the cantilever parallel to the plane of the sample surface. As depicted in Figure 17.41, lateral deflections of the cantilever usually arise from two sources: changes in surface friction and changes in slope. In the first case, the tip may experience greater friction as it traverses some areas, causing the cantilever to twist more strongly. In the second case, the cantilever may twist when

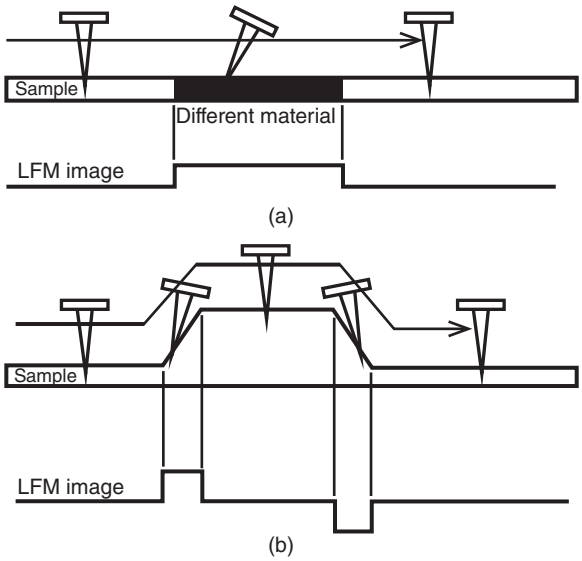


Figure 17.41 Lateral deflection of the cantilever from changes in surface friction (a) and from changes in slope (b).

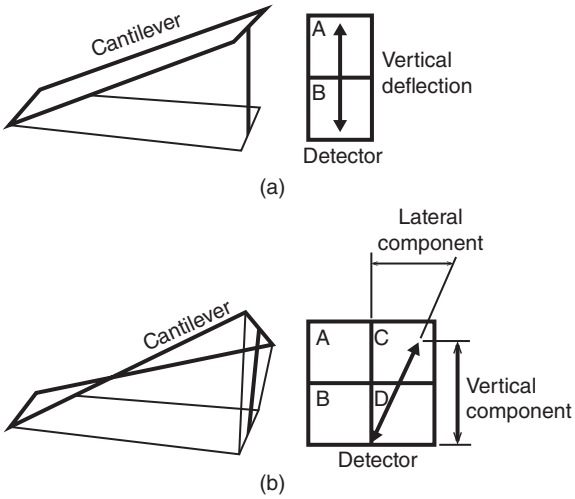


Figure 17.42 The PSPD for AFM (a) and LFM (b).

it encounters a steep slope. To separate one effect from the other, LFM and AFM images should be collected simultaneously.

LFM uses a *position-sensitive photodetector* (PSPD) to detect the deflection of the cantilever, just as for AFM. The difference is that for LFM, the PSPD also senses the cantilever's twist or lateral deflection. Figure 17.42 illustrates the difference between an AFM measurement of the vertical deflection of the cantilever and an LFM measurement of lateral deflection. AFM uses a "bi-cell" PSPD divided into two halves, A and B. LFM requires a "quad-cell" PSPD divided into four quadrants, A–D. By adding the signals from the A and B quadrants, and comparing the result with the sum from the C and D quadrants, the quad cell can also sense the lateral component of the cantilever's deflection. A properly engineered system can generate both AFM and LFM data simultaneously.

17.10 Optical Spectroscopy

Optical spectroscopy is the absorption and emission of light by matter. Probably two most exciting achievements of the optical spectroscopy are single molecule detection and ultrafast time resolution. The former shifts research work to a molecular scale and serves as the key tool in areas known as nano-chemistry and molecular devices. The latter extends the time scale to femtoseconds making possible direct studies of chemical reactions on the level of the chemical bond dynamics at the atomic scale. This research field is commonly called *femtochemistry* after Nobel Prize winner Ahmed H. Zewail.

The progress in the optical spectroscopy was possible because of great developments in laser physics, optics, electronics, and computers. Combining together newest lasers, advanced detectors, and high technology optical components, a researcher can assemble relatively easily a spectroscopy instrument with characteristics that were hardly achievable in the top-level laser research laboratories a few years ago. Naturally, the first step in this direction is to be informed on the tools available and to be able to evaluate the benefits and limitations imposed by different techniques. On the other hand, engineers and researchers, who are potentially interested in such spectroscopy applications, need to have a good basic background knowledge in optics and modern laser physics (Butcher and Cotter 1990; Rebane 1970; Yen and Selzer 1981). New optical spectroscopy instruments and methods cover steady-state absorption spectroscopy, steady-state emission spectroscopy, flash photolysis, time-correlated single photon counting, frequency domain emission spectroscopy, picosecond time resolution with streak camera, emission spectroscopy with optical gating methods, ultrafine spectrum resolution, optical polarization measurements, and others. These techniques do not exist for its own; they were developed for the purpose of investigation of certain objects, and the application of one or another method or combination of methods is justified by the object to be considered and the problem to be solved. In this section, some methods are analyzed and their benefits and limitations briefly evaluated.

17.10.1 Luminescence

Luminescence is the generic term for the emission of light that is not an effect of high temperature. So, luminescence can be determined as an appearance of cold body radiation. This radiation can either be part of a chemical reaction or a cause of subatomic motions or stress on a crystal. Another way to generate emission is *incandescence* where light is emitted by a substance as the result of heat (e.g. hot metal). *Chemiluminescence* is a light-emitting process based on a chemical reaction where the product has an excited intermediate. This intermediate emits light when falling into the ground state. Unlike fluorescence, electrons in chemiluminescent materials are excited by a chemical reaction and not by the absorption of photons. Chemiluminescence finds its technical application in light sticks, for example. A well-known chemiluminescent substance is luminol, which is used in criminalistics to find blood traces. Here, Fe^{2+} ions that are present in hemoglobin function as a catalyzer to bring luminol to its light-emitting configuration.

This leads us to the question: "What is fluorescence?" *Fluorescence* is a process where a substance emits light as an effect of the absorption of light of a shorter wavelength. The difference in wavelength is called *Stoke's shift*. In detail, fluorescence occurs if a substance absorbs light in the form of photons. This leads to a shift of electrons to a

higher-energy level. But this high-energy situation is very unstable, that is why electrons tend to return to their ground state. During this procedure, energy is released again in the form of photons that can be seen as a glow. In contrast to phosphorescence, electron energy shift is very fast, in fact in the range of nanoseconds. Any substance that is able to emit light of a distinct wavelength after excitation with another distinct wavelength is called *fluorochrome*. Most fluorescing substances occurring in the nature have a broad excitation and emission spectrum, but substances with clearly defined excitation and emission maxima are more useful for *fluorescence microscopy*.

Similar to fluorescence, *phosphorescence* is a light-emitting phenomenon where the phosphorescent material is excited with light. Even though it is closely related to fluorescence, it is much slower. In contrast to fluorescence, the reemission of photons is decelerated by the association of excited electron energy with a "forbidden" state. Their return to the ground state does not occur as fast as in the case of fluorescence because the energy is "trapped." Typical examples of phosphorescent materials are "glow-in-the-dark" toys that can be charged with an ordinary light bulb or daylight and then emit light for several minutes or even hours.

Knowing different characteristics such as excitation and emission maxima, brightness, quantum yields, etc. of a dye or protein or other luminescent material, the experimenter is able to choose a distinct candidate or observation condition to fulfill his/her requirements for a certain experimental setup. Furthermore, he/she is capable of interpreting results in a detailed way if he/she is aware of photophysical features of different luminescent materials (Moerner 1994). To exemplify the use of luminescence techniques to understand the origin of the luminescence centers and the luminescence mechanisms of solids, we will analyze briefly the emission properties of the blue-green emission exhibited by zinc oxide. This semiconductor has a high efficiency as a low-voltage phosphor and has been used in vacuum fluorescent displays (VFDs) and field emission displays (FEDs). Its mechanism of emission is not easily understood, and van Dijken et al. (2000), using quantum size effects, performed a study that improved the identification of the visible transition. Using nanocrystalline ZnO particles, they could vary the mean particle size and study the influence on the energetic position of the emission bands. Emission and absorption spectra, in the visible and UV bands, upon excitation and after different periods of particle growth, led to a linear relationship between the energetic positions for the maximum of the visible emission band and the maximum of the UV emission band. Assuming two possible mechanisms for the visible emission, (1) recombination of a shallowly trapped (delocalized) electron with a deeply trapped hole or (2) recombination of a shallowly trapped hole with a deeply trapped electron, it was considered the size dependence of the position of both emission bands, being shown that two possibilities for trap emission are recombination of delocalized electron with a deeply trapped hole (mechanism 1) and recombination of a delocalized hole with a deeply trapped electron (mechanism 2). Thus, the quantum size effect could be understood in terms of confinement of charge carriers, that is, from the size dependence, the visible emission band could be assigned to a transition of a photogenerated electron from the conduction band edge (or from a shallow level close to the conduction band edge) to a trap level positioned approximately 2 eV below the conduction band edge. This transition occurs in the bulk of the material and applies to ZnO in general.

17.10.2 Light Scattering

When light passes through matter, weak random scattered radiation appears. In the early sixteenth century, Leonardo da Vinci prophetically suggested scattering by particles of air as the explanation for the blueness of the sky. This idea was pursued by many scientists including Newton and Tyndall who tried with only limited success to identify the particles responsible for the scattering. Maxwell, studying the careful measurements of Rayleigh (1899a, b), finally proved that the molecules themselves turn the sky blue. After three centuries of thought, a correct and unambiguous explanation to all properties of scattering – frequency dependence, critical opalescence, index of refraction, etc. – became a reality.

In 1922, Brillouin predicted that if monochromatic radiation was allowed to scatter from an optical medium, side bands would appear (Brillouin 1922). He/she went on to theorize that the bands would result from a Doppler shift due to the generation of a sound wave produced by the light wave as it encountered molecules in its path. The frequency shift would be a function of the angle of observation and of the sound velocity in the medium. In 1923, Smekal considered, in the Bohr theory approximation, the scattering of light by a system having two quantized energy levels and predicted the effect to be discovered in 1928 by Raman (Smekal 1923). Working independently in Russia, Landsberg and Mandelstam (1928) discovered the same phenomenon in quartz: appearance of lines in the spectrum in addition to those from the source. (The Russians believed that their work actually antedated Raman's identifying the effect as "combinational scattering.") In 1930, Gross confirmed the theory of Brillouin, demonstrating that the Doppler-shifted frequencies appeared as predicted for both liquids and solids. By 1934, more than 500 papers related to the Raman effect had been published, and, in the early 1940s, this number had increased to a few thousand.

In the 1960s, light scattering was adrenalized with the invention of laser sources. Phenomena such as directional

effects in scattering processes and inelastic scattering from very small cross sections that had previously defied measurement could now be studied easily with laser sources. The great level of current enthusiasm in such investigations is evident from the impressive number of laboratories and scientists engaged in light scattering-related experiments.

Current work in the light scattering field is so extensive that, in this section, we shall only attempt to address Raman, Brillouin, and Rayleigh processes that provide valuable insights on the properties of the mobile sublattice in solid materials, particularly ionic materials and its relationship to disorder and the rigid host lattice.

When a beam of monochromatic light, say, from a laser of wavelength $\simeq$500 nm, strikes a sample, most of the incident beam is transmitted, as for X-rays discussed earlier. About one photon in 10^{14} is inelastically or quasi-elastically scattered and detected. The scattering arises from fluctuations in polarizability, caused by local changes in the relative permittivity (dielectric constant) of the medium. For liquids, one can probe density fluctuations and atomic collision processes (because the electron distribution is distorted in the colliding particles). In ordered solids, lattice vibrations, i.e. phonon modes, can be characterized. Ionic solids are more complicated because of the disordered nature of the mobile sublattice. The scattering processes incorporate some of the features of both liquids and solids, which complicates the interpretation. So, the dynamics of ordered solids is normally used as a basis.

In light scattering experiments on solids, the frequency, ω, and wave vector, k, of the incident and scattered beams are measured. This enables the frequency and momentum of the phonons that are created to be measured, so that a plot of ω as a function of k, the *phonon dispersion curve*, can be constructed. This is very informative for reasons that will now be considered.

Entities such as phonons, photons, and electrons that exhibit both wavelike and particle-like behavior can be visualized as packets of waves. The waves propagate with a certain velocity, the phase velocity, υ. The wave packet also moves with a velocity called the group velocity, υ_g. If the two velocities are the same, then ω is proportional to k. As the frequency rises, the two velocities become different, a process described as dispersion. The velocities are approximately given by the expressions

$$\upsilon = \omega/k; \quad \upsilon_g = \mathrm{d}\omega/\mathrm{d}k \tag{17.30}$$

The energy and thus the information content propagate at υ_g, which can therefore be thought of as the velocity of the entity, in this case the phonon.

The phonon dispersion curve shows a periodic behavior of period a. It becomes flat at $k = \pm\pi/2a$, so that $\mathrm{d}\omega/\mathrm{d}k$, and hence υ_g, is zero. This marks the end of a region of k space called the first *Brillouin zone*. A marginally larger k value takes the curve into the second zone. The group velocity is still zero, but there is a quantum jump in frequency and consequently an abrupt increase to a new phase velocity. As k is further increased, the curve exhibits a roughly sigmoidal shape, rising to a maximum at the center of the second zone where $k = \pm\pi/a$; a curve that is its mirror image rises to this same maximum from a horizontal minimum at the opposite edge of the second zone at $k = \pm 3\pi/2a$. Because of the inherent properties of the periodicity, it is permissible to translate the latter curve so that it runs from the first zone boundary, $k = \pm\pi/2a$, to the zone center, $k = 0$.

This allows the phonon dispersion curve to be displaced as two branches, a lower acoustic branch and an upper optical branch. Each branch contains several lattice vibrational modes. The acoustic modes can be either transverse, the vibration direction being normal to the wave vector, or longitudinal, the vibration being in a direction parallel to the wave vector.

In the long-wavelength (low k) limit near the zone center, the optical branch contains lattice vibrations arising from motions within the unit cell that take place in such a way that the center of mass remains stationary and the acoustic branch contains the vibrations pertaining to the movement of the unit cell as a whole. Near the zone center, optical frequencies are much larger than acoustic frequencies, but their values become closer as the zone boundary is approached.

The boundaries lie at about $10^8\,\mathrm{cm}^{-1}$, which corresponds to interatomic spacings. Neutrons have wave vectors of this order, and so the whole of the first Brillouin zone can, in principle, be probed by neutron scattering experiments. The wave vectors of the visible photons used in light scattering experiments are much smaller than this, so that in general only the zone center can be explored.

Originally, *Raman scattering* was used to describe optical branch excitations, and *Brillouin scattering* to describe acoustic mode studies. Because the type of instrument used varies with frequency regime, it is now found more convenient to refer to studies above $1\,\mathrm{cm}^{-1}$ (or 30 GHz or 0.125 MeV), carried out with grating spectrometers, as Raman scattering. This enables the term Brillouin scattering to be used for the lower-frequency range; a Fabry–Perot interferometer is normally employed (see Figure 17.43). For quasi-elastic scattering, in which the energy transfer to the sample is very small (i.e. less than $10\,\mathrm{mJ\,mol}^{-1}$ or 30 MHz or 10^{-3} cm^{-1}), a photon heating method is used, and the process is called *Rayleigh scattering*.

Theoretical studies of solid materials are often concerned with calculating phonon dispersion curves, but experimentally it can be more useful to obtain a plot of intensity I against frequency, which in the long-wavelength limit is the lattice vibrational spectrum. I is a complicated function of K, ω, and time; it can be related to the

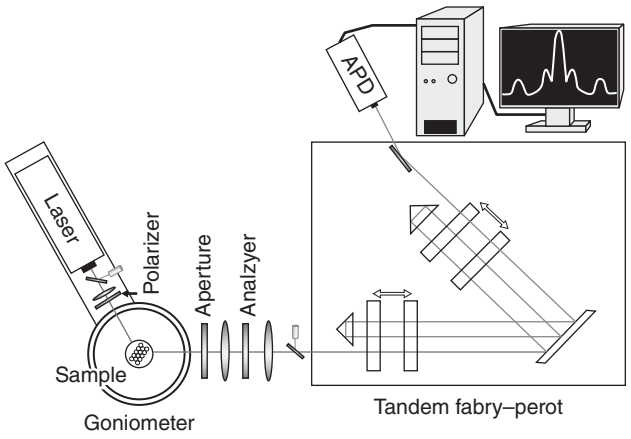


Figure 17.43 BLS setup with six-pass tandem Fabry–Perot interferometer. Electronic stabilization over days to weeks is achieved by permanent compensation using a diverted part of the unscattered light as a reference beam. The goniometer allows to record dispersion relations with continuous q range. For the eigenmode spectra, the scattering angle is not relevant (Still 2008).

polarizability, which is a function of dipole moment and field. The polarizability tensor (or matrix) expressing this dual dependence can alternatively be written in terms of two other variables, position, vector, and time, in which form it can be related to the van Hove correlation function $\langle r_{1^-}(O)r_2(t)\rangle$. Consequently, light scattering concerns the positions of atoms relative to their neighbors rather than to the individual movement of individual particles and therefore resembles coherent rather than incoherent neutron scattering.

In solids, a harmonic approximation can be used, which makes it possible to express the scattered intensity as the sum of a series of terms, I_1, I_2, etc. I_1 is the first-order scattering in which one phonon is involved, I_2 is the second-order scattering involving two phonons, and so on. Although, as stated above, first-order scattering involves only phonons near the Brillouin zone center, this need not to be the case for second-order scattering. The conservation of momentum requires that the sum of the momenta of the two phonons created is equal to the difference in momentum between the incident and scattered beam. If the two phonons have almost equal magnitudes but opposite directions, the second-order scattering condition is still fulfilled, and they can be anywhere within the Brillouin zone. Thus the region near the zone boundary, corresponding to atomic scale behavior, can be explored. The second-order intensity is weak, and the peaks are relatively broad. As in molecular spectra, the first- and second-order scattering processes are subject to symmetry restrictions. For liquids, the harmonic approximation is not appropriate. The incident beam still couples with dielectric fluctuations, but these are now caused by density fluctuations and by atomic collisions (which distort the electron distribution in the colliding particles), rather than by lattice vibrations.

For ionic solids, the nature of the response in a light scattering experiment depends on the depth of the potential energy wells in the mobile ion sublattice. Using a defect-type material in which the wells are relatively deep, as an example, the residence time at a site, about 3 ps, is several times larger than the TOF between sites, so that a jump diffusion model is appropriate. The ions have time to execute many vibrations about the site, and the frequencies of these are comparable with lattice vibrational modes so that they are accessible to light scattering experiments. Unfortunately, they are very anharmonic, and, in addition, the high proportion of defects destroys much of the translational symmetry. These two factors make it difficult to apply a treatment in terms of well-defined phonons with definite momentum k and frequency ω.

Despite these reservations certain relevant parameters can be determined (Balkanski 1978). If the vibrations of the mobile ions are fairly well decoupled from the rest of the lattice, then a vibrational frequency, which can be taken as the attempt frequency in a hopping model, can be measured (Mahan and Roth 1976). The temperature dependence of the frequency and line width of this vibration can give site occupancy factors and other information (Allen and Remeika 1974). Hopping between sites of different polarizabilities produces fluctuations detectable by light scattering (Balkanski et al. 1976).

For the class of ionic solids containing materials such as α-Ag I, the wells are very shallow, and mobile ion diffusion is virtually continuous. Hence a jump diffusion model is not really applicable, and a phonon treatment is even less appropriate.

Diffusional motion produces broad Rayleigh wings, which are high-frequency tails to the quasi-elastic scattering line. For certain purposes, it is useful to emphasize the peaks in the high-frequency region of 10–200 cm^{-1} at the expense of the Rayleigh wings by measuring reduced Raman intensity I_{red} (Vashishta et al. 1979). This is related to the Raman intensity I by

$$I_{\mathrm{red}} = \omega I/(1+n) \simeq \omega^2 I \qquad (17.31)$$

where n is the Bose–Einstein factor, $1/[\exp(\hbar\omega/kT) - 1]$, i.e. the number of quanta associated with a particular vibrational mode (Dekker 1975). In Brillouin scattering, the frequency of the acoustic modes together with knowledge of the wave vector will provide the velocity of sound in the material from which the elastic constants of the material can be determined.

In summary, light scattering techniques are particularly well suited for probing low-lying acoustic phonons and the Rayleigh scattering (Z-branch behavior) and other optical events near the zone center, whereas the behavior of other regions of k space is not easy to examine. Neutron

scattering is complementary because it gives results pertaining to phonons throughout the Brillouin zone but is at its weakest near the zone center. Many investigations have been considered in detail in recent publications.

17.10.3 Ellipsometry

Ellipsometry is a branch of reflection spectroscopy at oblique incidence using polarized light, which yields information about the optical constants of materials, the thickness of overlying layers, and the presence of disturbed and roughened layers. When applied to film-covered surfaces, the ellipsometric signal is generated by interference of components of the probing light beam that are multiply reflected at phase boundaries between the substrate and the film (or films). The technique works best when the films are less than, or up to, a few multiples of the wavelength of the light. Because the detection optics collects and sums contributions from these reflected rays, ellipsometry can also be used to investigate discontinuous and island film structure (Figure 17.44).

Each ellipsometric datum point yields two numbers delta and psi (Δ and ψ) that together define the complex reflection ratio ρ of the reflection coefficients in the directions parallel to (r_p) and perpendicular to (r_s) the plane of incidence. This relationship is

$$\rho = r_p/r_s = \tan\psi \cdot \exp i\Delta \qquad (17.32)$$

Each reflection coefficient, and their ratio, is a complex number containing both information on the amplitude of the p and s components of the electric vector of the light wave and their absolute phase changes.

The individual reflection coefficients at each boundary are determined by (i) the complex *refractive indices* (RIs) of the two materials on each side of the boundary and (ii) the angle of incidence. The relationships linking these quantities are called the *Fresnel equations*. When more than one boundary is involved (i.e. there are films on the surface), the function relating the input to the output polarization state is much more complicated and involves the Fresnel equations for each boundary and the thicknesses of all the films. In this case the equations are known as the *Drude equations*. The complex refractive indices N of the substrate and films are evidently important quantities. They are defined by

$$N = n + ik \qquad (17.33)$$

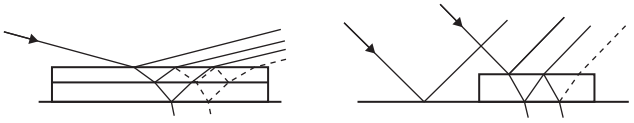


Figure 17.44 Surface with film(s) or island films showing interference effects to which the ellipsometric signal owes its complex dependence on film thickness and optical constants.

where n is the real part, and k, the extinction coefficient, is a measure of the light-absorbing power of the material. It is simply related to the more familiar constant α, which can be measured by transmission in a spectrophotometer:

$$\alpha = 4\pi k/\lambda \qquad (17.34)$$

where λ is the vacuum wavelength of the light. For transparent materials, therefore, $k = 0$ and the refractive index is a simple number. For these materials, n can be measured by various instruments such as the Abbé refractometer. For absorbing materials, ellipsometry provides a simple method (in theory!) to measure n.

In practice, measuring n by ellipsometry usually requires a good deal of care. The sample must be prepared in a flat and smooth form and free of all surface contamination. This is a consequence of one of the prime features of the technique, the great sensitivity of the ellipsometric quantities Δ and ψ to surface films.

For a bare surface, the relationship between each Δ and ψ datum pair and n and k is simple in the sense that there is a one-to-one mapping between the two data domains. This is portrayed in the form of the nomogram in Figure 17.45, which also shows the positions of a few specific materials.

The original ellipsometric experiments were carried out using the so-called nulling ellipsometer (Figure 17.46a). The incident state is defined by a linear polarizer P and a *quarter wave plate* (QWP). This combination can generate light of any polarization state as P is rotated relative to QWP. The analyzer A is a linear polarizer. These three optical components are mounted in accurately divided circles so that their azimuths (i.e. the angle between their optic axes and the plane of incidence) can be measured. By iteratively adjusting polarizer and analyzer, keeping the QWP at an azimuth of 45°, a condition can be found where there is no light passing to the detector – the null condition. Δ and ψ are then given directly from the azimuths of P and A.

In the alternative photometric ellipsometer (Figure 17.46b), polarization analysis is carried out by rotating one

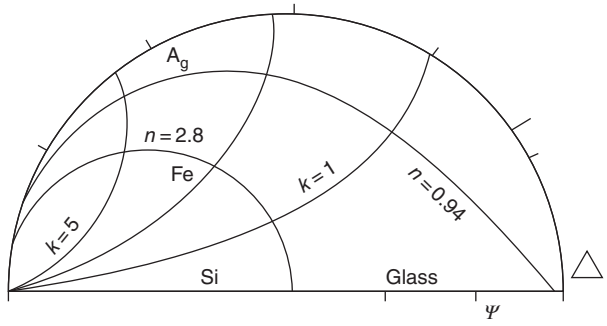


Figure 17.45 Polar nomogram showing one-to-one mapping between ψ, Δ, and n, k pairs for a bare surface. Transparent materials are located on the basal diameter; "perfect" metals lie on the periphery.

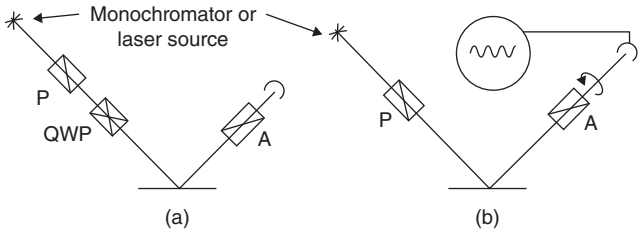


Figure 17.46 Basic optical arrangements for (a) nulling ellipsometer and (b) a photometric ellipsometer.

of the elements continuously and solving for Δ and ψ by Fourier analysis of the time-dependent detector output.

Very many designs for automated ellipsometers have been published. Choosing a suitable design usually involves trading off accuracy or resolution against speed of operation. Most commercially available ellipsometers employ rotating polarizer or analyzer designs.

Ellipsometric data can be interpreted on two levels – qualitative and quantitative. For qualitative purposes, particularly in dynamic systems, the display of the data in the ψ–Δ plane gives traces (the ψ–Δ signatures) that are highly characteristic of changes in the condition of the surface. Inspection of these traces, which ideally should be done in real time as the process is carried out, can very often answer such questions as: Is there a film on the surface? Is it growing or thinning? How thick is it? Is the surface smooth, and is it becoming roughened?

Quantitative analysis always starts with as detailed a model of the system as is available. If this is simple, such as a transparent layer on a smooth substrate, the Drude equations can often be solved uniquely. If there are more films, analysis involves multiparameter fitting by an iterative refinement process. These points are best illustrated by examples reported in the literature (Azzam and Bashara 1977; Compton 1989; Gottesfeld 1989; Losurdo and Ingerl 2013; Tompkins and McGahan 1999; Tompkins and Irene 2005).

17.10.4 Optical Spectroscopy in the Infrared, Visible, and Ultraviolet

These techniques deal with the interaction of ultraviolet, visible, and infrared (IR) radiation with matter. They use optical materials to disperse and focus the radiation, being identified as optical spectroscopies.

17.10.4.1 Electromagnetic Radiation Light

It is a form of energy whose behavior is described by the properties of both waves and particles; consider that light as a wave is better to explain refraction, and consider that light as a particle is better to explain absorption and emission. An electromagnetic wave is characterized by several fundamental properties, including its velocity, amplitude, frequency, phase angle, polarization, and direction of propagation. For ultraviolet and visible electromagnetic radiation, the wavelength is usually expressed in nanometers ($1\ \text{nm} = 10^{-9}$ m), and for IR radiation it is given in microns ($1\ \mu\text{m} = 10^{-6}$ m). The relationship between wavelength, λ, and frequency, υ, or wavenumber, $\overline{\upsilon}$, is

$$\lambda = c/\upsilon \quad \overline{\upsilon} = 1/\lambda \tag{17.35}$$

where c is the velocity of light ($\sim 3 \times 10^8\ \text{m s}^{-1}$) and $\overline{\nu}s$ are frequently used to characterize IR radiation with the units given in cm^{-1}. The interaction between matter and electromagnetic radiation is easiest to understand if we assume that radiation consists of a beam of energetic particles called photons. When a *photon* is absorbed by a sample, it is "destroyed," and its energy (in joules), acquired by the sample, being related to its frequency, wavelength, and wavenumber by the following equalities:

$$E = h\nu = hc/\lambda = hc\,\overline{\nu} \tag{17.36}$$

where h is the Planck's constant ($=6.626 \times 10^{-34}\ \text{J s}^{-1}$). For convenience, we divide electromagnetic radiation into different regions – the electromagnetic spectrum – based on the type of atomic molecular transition (Y-rays, nuclear; X-rays, core-level electrons; ultraviolet (UV), valence electrons; visible (Vis), valence electrons; infrared (IR), molecular vibrations; microwave, molecular rotations, and electron spin; radio waves, nuclear spin) that give rise to the absorption or emission of photons. A spectroscopic measurement is possible only if the photon's interaction with the sample leads to a change in one or more of its characteristic properties. Table 17.11 provides a list of representative techniques in which there is a transfer of energy between the photon and the sample.

When a photon of energy hν strikes the atom or molecule, absorption may occur if the difference in energy, ΔE, between the ground state and the excited state is equal to the photon's energy. An atom or molecule in an excited state may emit a photon and return to the ground state. The photon's energy, $h\nu$, equals the difference in energy, ΔE, between the two states (see Figure 17.47). When a sample absorbs electromagnetic radiation, the number of photons passing through it decreases. The measurement of this decrease in photons, called *absorbance*, is a useful analytical signal.

The energy of IR radiation produces a change in a molecule's or a polyatomic ion's vibrational energy, but is not sufficient to effect a change in its electronic energy. As shown in the energy level diagram in Figure 17.48, vibrational energy levels are quantized; that is, a molecule may have only certain, discrete vibrational energies. The energy for an allowed vibrational mode, E_v, is

$$E_\text{v} = \nu + \frac{1}{2}h\nu_0 \tag{17.37}$$

Table 17.11 Examples of spectroscopic techniques involving an exchange of energy between a photon and the sample

Type of energy transfer	Region of electromagnetic spectrum	Spectroscopic technique
Absorption	γ-ray	Mossbauer spectroscopy
	X-ray	X-ray absorption spectroscopy
	UV/Vis	UV/Vis spectroscopy
		Atomic absorption spectroscopy
	IR	Infrared spectroscopy
		Raman spectroscopy
	Microwave	Microwave spectroscopy
	Radio wave	Electron spin resonance spectroscopy
		Nuclear magnetic resonance spectroscopy
Emission (thermal excitation)	UV/Vis	Atomic emission spectroscopy
Photoluminescence	X-ray	X-ray fluorescence
	UV/Vis	Fluorescence spectroscopy
		Phosphorescence spectroscopy
		Atomic fluorescence spectroscopy
Chemiluminescence	UV/Vis	Chemiluminescence spectroscopy

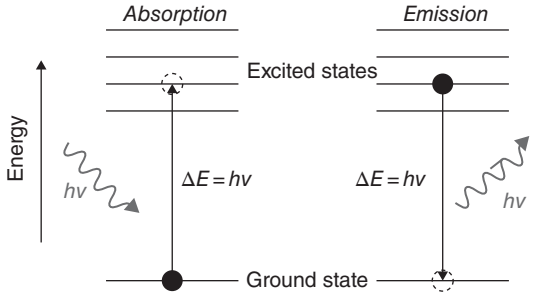


Figure 17.47 Simplified energy diagram showing the absorption and emission of a photon by an atom or a molecule.

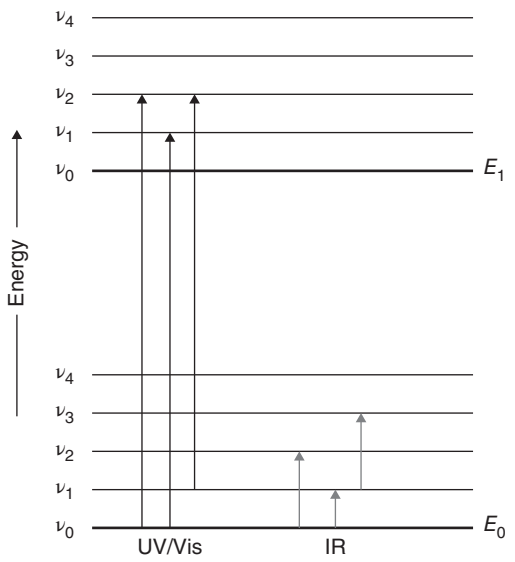


Figure 17.48 Diagram showing two electronic energy levels (E_0 and E_1), each with five vibrational energy levels (ν_0–ν_4). Absorption of ultraviolet and visible radiation leads to a change in the analyte's electronic energy levels and, possibly, a change in vibrational energy as well. A change in vibrational energy without a change in electronic energy levels occurs with the absorption of infrared radiation.

where ν is the vibrational quantum number, which has values of 0, 1, 2, …, and ν_0 is the bond's fundamental vibrational frequency. The value ν_0, which is determined by the bond's strength and by the mass at each end of the bond, is a characteristic property of a bond.

At room temperature, most molecules are in their ground vibrational state ($\nu = 0$). A transition from the ground vibrational state to the first vibrational excited state ($\nu = 1$) requires absorption of a photon with an energy $h\nu_0$. Transitions in which $\Delta\nu$ is ±1 give rise to the fundamental absorption lines. Weaker absorption lines, called overtones, result from transitions in which $\Delta\nu$ is ±2 or ±3. The number of possible normal vibrational modes from a linear molecule is $3N-5$, and for a nonlinear molecule is $3N-6$, where N is the number of atoms in the molecule. Not surprisingly, IR spectra often show a considerable number of absorption bands. Even a relatively simple molecule, such as ethanol (C_2H_6O), for example, has $3 \times 9 - 6$ or 21 possible normal modes of vibration, although not all of these vibrational modes give rise to an absorption.

Four types of transitions between quantized energy levels account for most molecular UV/Vis spectra. Table 17.12 lists the approximate wavelength ranges

Table 17.12 Electronic transitions involving n, σ, and π molecular orbitals

Transition	Wavelength range (nm)	Examples
$\sigma \rightarrow \sigma^*$	<200	C—C, C—H
$n \rightarrow \sigma^*$	160–260	H_2O, CH_3OH, CH_3Cl
$\pi \rightarrow \pi^*$	200–500	C=C, C=O, C=N, C≡C
$n \rightarrow \pi^*$	250–600	C=O, C=N, N=N, N=O

for these transitions, as well as a partial list of bonds, functional groups, or molecules responsible for these transitions. Of these transitions, the most important are $n \rightarrow \pi^*$ and $\pi \rightarrow \pi^*$ because they involve important functional groups that are characteristic of many analytes and because the wavelengths are easily accessible. The bonds and functional groups that give rise to the absorption of ultraviolet and visible radiation are called *chromophores*.

The interpretation of UV/Vis and IR spectra receives adequate coverage elsewhere in the chemistry curriculum, notably in organic chemistry, and is not considered further in this text (Sharma 2005).

With the availability of computerized data acquisition and storage, it is possible to build digital libraries of standard reference spectra. The identity of an unknown compound can often be determined by comparing its spectrum against a library of reference spectra, a process known as *spectral searching*. Comparisons are made using an algorithm that calculates the cumulative difference between the sample's spectrum and a reference spectrum. For example, one simple algorithm uses the following equation:

$$D = \sum_{i=1}^{n} |(A_{\text{sample}})_i - (A_{\text{reference}})_i| \qquad (17.38)$$

where D is the cumulative difference, A_{sample} is the sample's absorbance at wavelength or wavenumber i, $A_{\text{reference}}$ is the absorbance of the reference compound at the same wavelength or wavenumber, and n is the number of digitized points in the spectra. The cumulative difference is calculated for each reference spectrum. The reference compound with the smallest value of D provides the closest match to the unknown compound. The accuracy of spectral searching is limited by the number and type of compounds included in the library and by the effect of the sample's matrix on the spectrum.

17.10.5 Fourier Transform Infrared Spectroscopy

The goal of any absorption spectroscopy is to measure how well a sample absorbs light at each wavelength. *Fourier transform infrared* (FTIR) *spectroscopy* is a way to do this, but instead of shining a monochromatic light beam at a sample as in UV/Vis spectroscopy, a beam containing many frequencies of light at once is shined, and it is measured how much of that beam is absorbed by the sample. Subsequently, the beam is modified to contain a different combination of frequencies, giving a second data point. This process is repeated many times. The broadband light shines into a *Michelson interferometer* – a certain configuration of mirrors, one of which is moved by a motor. As this mirror moves, each wavelength of light in the beam is periodically blocked, transmitted, blocked, transmitted, by the interferometer, due to wave interference. Different wavelengths are modulated at different rates so that at each moment the beam coming out of the interferometer has a different spectrum. Afterward, a computer turns all of these raw data (light absorption for each mirror position called an *interferogram*) and works backward to infer what is the absorption at each wavelength. The processing required turns out to be a common algorithm called the *Fourier transform* (a mathematical process), hence the name Fourier transform spectroscopy.

In a Michelson interferometer adapted for FTIR, light from the polychromatic IR source, approximately a blackbody radiator, is collimated and directed to a beam splitter. Ideally 50% of the light is refracted toward the fixed mirror, and 50% is transmitted toward the moving mirror. Light is reflected from the two mirrors back to the beam splitter, and some fraction of the original light passes into the sample compartment. There, the light is focused on the sample. On leaving the sample compartment, the light is refocused on to the detector. The difference in optical path length between the two arms and the interferometer is known as the retardation or *optical path difference* (OPD). An interferogram is obtained by varying the retardation and recording the signal from the detector for various values of the retardation. The form of the interferogram when no sample is present depends on factors such as the variation of source intensity and splitter efficiency with wavelength. This results in a maximum at zero retardation, when there is constructive interference at all wavelengths, followed by a series of "wiggles." The position of zero retardation is determined accurately by finding the point of maximum intensity in the interferogram. When a sample is present, the background interferogram is modulated by the presence of absorption bands in the sample.

The interferogram is converted to a spectrum by Fourier transformation. This requires it to be stored in digital form as a series of values at equal intervals of the path difference between the two beams. To measure the path difference, a laser beam is sent through the interferometer, generating sinusoidal signal where the separation between successive maxima is equal to the wavelength.

The result of Fourier transformation is a spectrum of the signal at a series of discrete wavelengths. The range of

wavelengths that can be used in the calculation is limited by the separation of the data points in the interferogram. The shortest wavelength that can be recognized is twice the separation between these data points. For example, with one point per wavelength of a helium–neon reference laser at 0.633 μm (15 800 cm^{-1}), the shortest wavelength would be 1.266 μm (7900 cm^{-1}). Because of aliasing any energy at shorter wavelengths would be interpreted as coming from longer wavelengths and so has to be minimized optically or electronically. The spectral resolution, i.e. the separation between wavelengths that can be distinguished, is determined by the maximum OPD. The wavelengths used in calculating the Fourier transform are such that an exact number of wavelengths fit into the length of the interferogram from zero to the maximum OPD as this makes their contributions orthogonal. This results in a spectrum with points separated by equal frequency intervals.

Important advantages of a Fourier transform (FT) spectrometer compared with a scanning (dispersive) spectrometer are (Griffiths and Holmes 2002):

1. *The multiplex or Fellgett's advantage*: This arises from the fact that information from all wavelengths is collected simultaneously. It results in a higher signal-to-noise ratio for a given scan time for observations limited by a fixed detector noise contribution (typically in the thermal IR spectral region where a photodetector is limited by generation–recombination noise).
2. *The throughput or Jacquinot's advantage*: Although no slits are needed, FTIR spectrometers do require an aperture to restrict the convergence of the collimated beam in the interferometer. This is because convergent rays are modulated at different frequencies as the path difference is varied. Such an aperture is called a Jacquinot stop. For a given resolution and wavelength, this circular aperture allows more light through than a slit, resulting in a higher signal-to-noise ratio.
3. *The wavelength accuracy or Connes' advantage*: The wavelength scale is calibrated by a laser beam of known wavelength that passes through the interferometer. This is much more stable and accurate than in dispersive instruments where the scale depends on the mechanical movement of diffraction gratings. In practice, the accuracy is limited by the divergence of the beam in the interferometer that depends on the resolution.

FTIR spectrometers are mostly used for measurements in the mid- and near-IR regions. For the mid-IR region, 2–25 μm (5000–400 cm^{-1}), the most common source is a silicon carbide element heated to about 1200 K. The output is similar to a blackbody. Shorter wavelengths of the near IR, 1–25 μm (10 000–4000 cm^{-1}), require a higher temperature source, typically a tungsten–halogen lamp. The long-wavelength output of these is limited to about 5 μm (2000 cm^{-1}) by the absorption of the quartz envelope. For the far IR, especially at wavelengths beyond 50 μm (200 cm^{-1}), a mercury discharge lamp gives higher output than a thermal source.

Mid-IR spectrometers commonly use pyroelectric detectors that respond to changes in temperature as the intensity of IR radiation falling on them varies. The sensitive elements in these detectors are either deuterated triglycine sulfate (DTGS) or lithium tantalate ($LiTaO_3$). An ideal beam splitter transmits and reflects 50% of the incident radiation. However, as any material has a limited range of optical transmittance, several beam splitters may be used interchangeably to cover a wide spectral range.

17.10.5.1 Attenuated Total Reflectance

Attenuated total reflectance (ATR) is an accessory of the FTIR spectrometer to measure surface properties of solid or thin-film samples rather than their bulk properties. Generally, ATR has a penetration depth of about 1–2 μm depending on the sample conditions.

FTIR can be used in all applications where a dispersive spectrometer was used in the past. In addition, the improved sensitivity and speed have opened up new areas of application. Spectra can be measured in situations where very little energy reaches the detector and scan rates exceed 50 spectra a second. FTIR is used in geology, chemistry, materials, corrosion, biology, and research fields. Moreover, it has been used in microscopy and imaging for analyzing tissue sections and examining the homogeneity of pharmaceutical tablets, also as a detector in chromatography because its speed allows spectra to be obtained from compounds as they are separated by a gas chromatograph, and as a qualitative identifier of the gas species evolved as a material is heated, this identification being complemented by quantitative information provided by measuring the corresponding weight loss – thermogravimetric analysis–infrared spectrometry (TG-IR).

17.10.6 Nonlinear Optical Spectroscopy

One of the modern optical techniques that has attracted much attention in recent times is surface optical *second harmonic generation* (SHG) and *sum-frequency generation* (SFG). This is because the technique has very high surface specificity and wide applicability.

Being an optical technique, it can be used to probe all types of interfaces as long as they can be assessed by light. The unusually high surface specificity together with the submonolayer sensitivity allows spectroscopic study

of an interface even if the associated bulk absorbs in the same spectral region. Because the SFG output is highly directional, spatial filtering can be employed in addition to spectral filtering to suppress the unwanted luminescence and scattering background noise. The technique can therefore be used for *in situ* remote sensing study of a surface even in a very hostile environment. Finally, the spatial and spectral resolutions of the technique are only limited by spatial and spectral mode quality of the exciting lasers. The time resolution is limited by the laser pulse width that can be in the picosecond or femtosecond range.

These advantages have rendered SFG (SHG) an extremely powerful and versatile tool for surface and interface studies. Applications that have already been successfully demonstrated appear in almost all areas of surface science, ranging from physics to chemistry, biology, and materials science. Many of them are highly unique, providing good opportunities to explore new areas of research in various disciplines. In the case of SFG, these include, for example, studies of buried interfaces, etching, interfaces of pure liquids, corrosion, electrochemical processes, surface dynamics, catalytic reactions in real atmosphere, surface monolayer microscopy, ultrafast surface dynamics, and so on (Cremer et al. 1996; Du et al. 1994; Ponath and Stegeman 1991; Qi et al. 1995).

The study of solid–solid interfaces can be considered a good example to illustrate the power and versatility of the optical spectroscopy technique in the field of corrosion and electrochemistry. So, in this subsection, we shall discuss only this example.

When two dissimilar materials are brought in contact with each other, a new class of physical problems is clearly a challenging scientific task. The interface of this system, as compared with the bulk, has intrinsically different physical properties that strongly depend on the interfacial atomic arrangement and the electronic structure of the two materials joined at the junction. The development of a microscopic understanding of these exciting physical problems is clearly a challenging scientific task.

Different physical phenomena are responsible for the new properties of the system. For example, a new interfacial bond can have electronic states that are different from the neighboring bulk materials; a new charge distribution, resulting from interdiffusion or defects, generates a different band profile, which can lead to new electronic states. All of these phenomena influence the macroscopic physical properties of the entire system and in particular the thin overlayer.

Thin films are fundamentally important in their own right. Charge transport, low-dimensional excitations, defect states, and deformation potentials in thin films are all the subject of much research. The increased attention in this area results in part from the existence of many interesting physical phenomena that only exist in materials with low dimensionality. In general, the bulk physical properties of a thin overlayer are dependent on the interface, particularly as the overlayer thickness becomes comparable with the diffusion length of the free carriers. Solid–solid interfaces and thin films are also of technological importance. The successful growth, fabrication, and characterization of electronic devices is a direct consequence of an accurate fundamental knowledge of buried interfaces.

Solid–solid interfaces are buried under a thick overlayer that is greater than the escape and penetration depth of an electron in a solid. This makes buried interfaces inaccessible to the electronic diagnostic techniques currently being used widely in surface science. Linear optical scattering is a powerful probe to investigate the bulk of a material; however, it gives very little interface specificity. On the other hand, second-order nonlinear optical probes are intrinsically sensitive to interfaces and have proven to be a powerful tool in surface diagnostics. For example, the results of surface studies using second-order nonlinear optics, namely, SFG and SHG, corroborate the results obtained using electronic techniques.

Therefore, nonlinear optical methods are well suited for studying buried interfaces, both because they are able to penetrate bulk material and because they have demonstrated interface sensitivity. Demonstration of surface sensitivity of SHG and SFG was the subject of research for many years. While the surface sensitivity of SHG and SFG has been used extensively, few SHG studies have been performed on buried solid interfaces particularly using its spectroscopic aspect (Heinz et al. 1989).

The first nonlinear optical spectroscopy experiments on solid–solid interfaces were carried out by Heinz et al. on CaF_2/Si(111) (1989). SFG and SHG measurements as a function of the fundamental photon energy were used to determine an interfacial bandgap (Figure 17.49). The interesting result of this work is due to the new interfacial bond combination. It was found that the Ca (4s) and Si (3p) orbitals hybridize to produce bonding and antibonding bands at the interface with an energy separation well within the bandgap of the CaF_2. Heinz et al. detected a transition between the bonding and antibonding orbitals of the interface states. In contrast to CaF_2/Si(111) interfaces, other band profiles and electronic states were found by other workers, and to understand many applications of the nonlinear optical spectroscopy (sensitivity to buried interfaces, interfacial defects, lattice relaxation, substrate surface reconstruction, band bending, nonlinear susceptibility of thin overlayers, interfacial trap lifetime, relative interfacial trap density, and critical thickness, as well as interfacial charge), it is convenient to make a general discussion of second-order nonlinear optics as given below.

The response of a material to strong optical fields of lasers can be nonlinear. This nonlinearity is characterized through the susceptibility that gives rise to a nonlinear

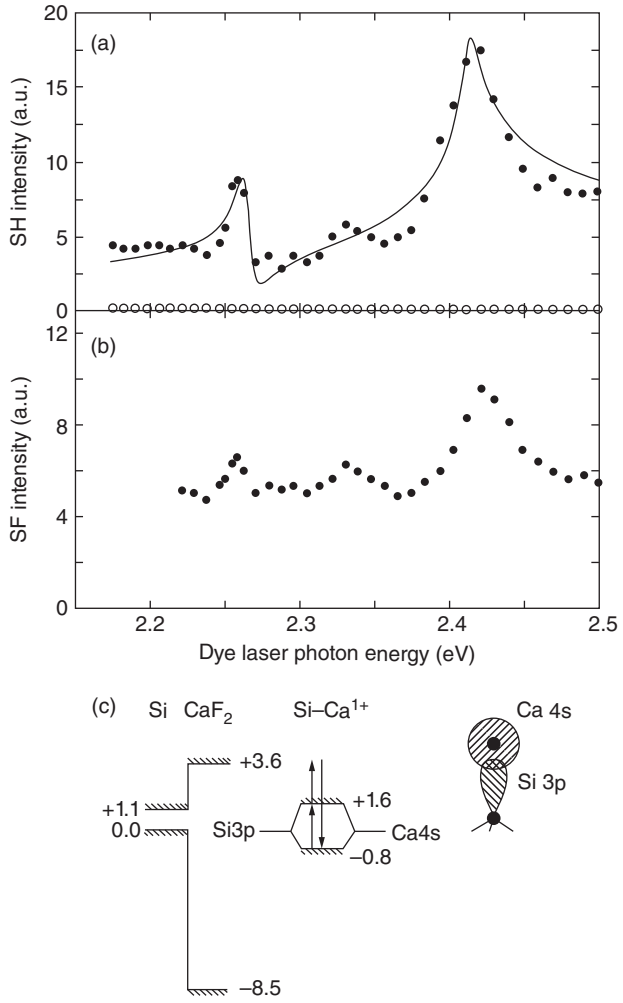


Figure 17.49 (a) Resonant second-harmonic and (b) resonant sum-frequency generation of CaF_2/Si(111). The filled symbols represent signal from the interface, and the open symbols stand for signal from the oxide Si(111) surface. (c) The interfacial band profile of CaF_2/Si(111). The schematic representation of hybridized Si(3p) dangling bond and Ca^+(4s) orbitals is also displayed (Heinz et al. 1989).

polarization source, P^{NLS}. The nonlinear source polarization radiates an electromagnetic wave with angular frequency that is different from the frequency of the incident laser beam. The propagation of the radiated electric field, E, must obey the nonlinear wave equation (Shen 1984)

$$\nabla \times \nabla \times E^{(\omega_3)} + \frac{\epsilon}{c^2}\frac{\partial^2}{\partial t^2}E^{(\omega_3)} = -\frac{4\pi}{c^2}\frac{\partial^2}{\partial t^2}P^{(\omega_3)} \qquad (17.39)$$

where ω_3 is the angular frequency of the nonlinear polarization and ϵ is the frequency-dependent linear dielectric constant of the medium. We are only interested in the second-order nonlinear response of the system, where we can write

$$\omega_3 = \omega_1 + \omega_2 \qquad (17.40)$$

Here, ω_1 and ω_2 are the angular frequencies of the incident laser beams. Generation of an electric field at ω_3 is called sum-frequency generation when $\omega_1 \neq \omega_2$ and second-harmonic generation when $\omega_1 = \omega_2 \equiv \omega$. The nonlinear polarization is related to the incident beam as follows:

$$P_i^{(\omega_3)} = \chi_{ijk}^{(\omega_3)} : E_j^{(\omega_1)} E_k^{(\omega_2)} + \Gamma_{ijkl}^{(\omega_3)} : E_j^{(\omega_1)} \nabla_k E_l^{(\omega_2)} \quad (17.41)$$

The first part is the second-order term in the expansion of P as a function of local electric field. This is the dipole contribution. The second term arises from the nonlocal response of the system, which is the expansion of P as a function of the derivative of the electric field. This term carries the electric quadrupole and magnetic dipole contributions. The higher-order term of P can be written as

$$P_i^{(2\omega)} = (\delta - \beta - 2\gamma)(E \cdot \nabla) E_i + \beta E_i (E \cdot \nabla) + \gamma \nabla_i (E \cdot E) + \zeta E_i \nabla_i E_i \qquad (17.42)$$

Here, δ, β, γ, and ζ are phenomenological constants. It should be noted that the first three terms are isotropic in character and the last term is anisotropic with respect to the orientation of the crystal. Under the dipole approximation, the nonlinear polarization, P^{NLS}, for SHG can be written as

$$P_i^{(2\omega)} = \chi_{ijk}^{(2\omega)} : E_j^{(\omega)} E_k^{(\omega)} \qquad (17.43)$$

The *second-order susceptibility*, $\chi^{(2\omega)}$, is the response of the system at 2ω and couples the incident photons to the medium. The underlying physics of the second-order nonlinear optics can be explained via this susceptibility (Adler 1964; Keller 1986; Yariv 1988). A general and useful derivation for the $\chi^{(2)}$ uses one body density matrix. The resulting expression for $\chi_{ijk}^{(2)}$ is

$$\chi_{ijk}^{(2)} = -N\frac{e^3}{h^2}\sum_{g,n,n'} \frac{\langle g|r_i|n'\rangle\langle n'|r_j|n\rangle\langle n|r_k|g\rangle}{(2\omega - \omega_{ng} + i\Gamma_{ng})(\omega - \omega_{n'g} + i\Gamma_{n'g})} \qquad (17.44)$$

where N is the number density of electrons and r_i is the space operator in the ith direction. The states $|g\rangle$, $|n\rangle$, and $|n'\rangle$ are eigenstates of the unperturbed system, and Γ is a damping factor. The expression $\chi_{ijk}^{(2)}$ carries eight terms describing the different time ordering of the photons. The multiplication of three matrix elements in each term presents the coupling of the photons with matter in three separate steps. The summation indicates that the process must go over all possible excited states. One of the possible matrix processes is shown in Figure 17.49.

The odd number of matrix elements in the numerator of each term also shows the sensitivity of $\chi^{(2)}$ to the symmetry of the system. For example, if a system is invariant under inversion symmetry, the product of $(r_i)_{gn'}(r_j)_{n'n}(r_k)_{ng}$, independent of the subscripts i, j, k, is always zero. The nonzero

value of $\chi^{(2)}$ appears in the presence of a broken symmetry. This property of $\chi^{(2)}$ makes second-order nonlinear optics a powerful tool for studying the interfaces where symmetry in the normal direction to the junction is broken.

The resonant nature of $\chi^{(2)}$, as expressed in the denominator of each term, is another important aspect of the second-order susceptibility. Whenever the energy of the input beam (fundamental) or output beam (upconverted photon) matches a transition, $\chi^{(2)}$ becomes a large pure imaginary number. This results in a peak in the SH or SF spectra. Of course, to estimate the peak intensity, we must also consider the joint density of states of the system.

With the use of symmetry, the number of nonzero elements of $\chi^{(2)}$ can be appreciably reduced, and with the knowledge of the relationships between the nonzero elements of the $\chi^{(2)}$ tensor, we can predict the dependence of the second-order polarization, $P^{(2\omega)}$, on second-order susceptibility, $\chi^{(2)}$, an azimuthal angle ϕ, which is the angle between plane of incidence and a fixed axis of the crystal.

The higher-order bulk contribution is nonlocal and can be written as

$$P_i = \Gamma_{ijkl}\, E_j\, \nabla_k\, E_l \tag{17.45}$$

The fourth rank tensor, Γ_{ijkl}, can be studied using the symmetry of the system. For example, for cubic materials such as GaAs and ZnSe (with 43 m symmetry), the only nonzero elements are

$$\begin{aligned}
&\Gamma_{xxxx} = \Gamma_{yyyy} = \Gamma_{zzzz}\\
&\Gamma_{yzyz} = \Gamma_{zxzx} = \Gamma_{xzxz} = \Gamma_{yxyx} = \Gamma_{xyxy}\\
&\Gamma_{yyzz} = \Gamma_{zzyy} = \Gamma_{zzxx} = \Gamma_{xxzz} = \Gamma_{xxyy} = \Gamma_{yyxx}\\
&\Gamma_{yzzy} = \Gamma_{zyyz} = \Gamma_{zxxz} = \Gamma_{xzzx} = \Gamma_{xyyx} = \Gamma_{yxxy}
\end{aligned} \tag{17.46}$$

With S-in/S-out polarization configuration, the second-order polarization along the y-axis is

$$P_y = \Gamma^{(\mathrm{L})}_{yyiy}\, E_y\, \mathrm{k}_i\, E_y \tag{17.47}$$

The subscript i can only be equal to x and z. The fourth rank tensor element $\Gamma^{(\mathrm{L})}_{yyiy}$ represents its value in the lab frame and can be transformed to the crystal frame by a rotation operator. Using Eqs. (17.46) and (17.47), we can rewrite the expression as

$$P_y = -\frac{1}{4}\sin(4\phi)(\Gamma^{(\mathrm{C})}_{xyyx} + \Gamma^{(\mathrm{C})}_{yxyx} - \Gamma^{(\mathrm{C})}_{xxxx} + \Gamma^{(\mathrm{C})}_{xxyy})E_y^2 k_x \tag{17.48}$$

with

$$\zeta = \Gamma_{xxxx} = \Gamma_{xyyx} = \Gamma_{yxyx} = \Gamma_{xxyy} \tag{17.49}$$

the polarization can be rewritten in the form

$$P_y = \zeta\, \frac{\sin(4\phi)}{4} E_y^2 k_x \tag{17.50}$$

Clearly in this polarization configuration, one can study the isotropic contribution of higher-order nonlinearity (i.e. ζ).

With conventional parameters (Bloembergen et al. 1968)

$$\Gamma^{(\mathrm{C})}_{xxxx} = \gamma + \zeta \tag{17.51}$$

$$\Gamma^{(\mathrm{C})}_{xxyy} = \beta \tag{17.52}$$

$$\Gamma^{(\mathrm{C})}_{xyyx} = \gamma + \beta + 2\zeta \tag{17.53}$$

$$\Gamma^{(\mathrm{C})}_{xyxy} = 2\gamma \tag{17.54}$$

we can rewrite the polarization as

$$P_y = \Gamma_{zyiy} E_y^2 k_i = \Gamma^{(\mathrm{L})}_{zyxy} E_y^2 + \Gamma^{(\mathrm{L})}_{zyzy} E_y^2 k_z = \Gamma^{(\mathrm{C})}_{xxzz} E_y^2 k_z = \frac{\gamma}{2} E_y^2 k_z \tag{17.55}$$

This relationship suggests that in the S-in/P-out polarization configuration, one can study the tensor element γ at $\phi = 0$. However, at this orientation, the surface or interface also contributes to the radiation. Thus, one can only study the linear combination of γ and the surface tensor elements.

Now that we have established how the second-order nonlinear source polarization depends on the susceptibilities, we can study the field generated by this polarization. The complete form of the nonlinear field is quite complex. This is mostly due to the boundary conditions and the coupling to the linear fields. Even the description of the SH field in a simple semi-infinite slab is not straightforward, and therefore we do not extend these complex studies here.

The general considerations presented above demonstrate that nonlinear optics explains nonlinear response of properties such as frequency, polarization, phase, or path of incident light. These nonlinear interactions give rise to a host of optical phenomena. Among the frequency-mixing processes, the Bloembergen report (1998) called our interest to SHG and SFG, as discussed here:

SHG or frequency doubling, generation of light with a doubled frequency (half of the wavelength) in which two photons are destroyed, creating a single photon at two times the frequency.

SFG, generation of light with a frequency that is the sum of two other frequencies.

17.11 Nondestructive Inspection Techniques

A number of nondestructive methods are used, and their classification has been based on the sound, light, and electrical devices employed. Ultrasonic, AE, thermal and holographic interferometry, radiography, Eddy current, thermoelectric measurements, dye penetration, automatic thermal impedance scanning (ATIS), and others are largely discussed in the open literature. Here, some of the NDI techniques are described (Sharpe 1980; Thonsen et al. 1987).

17.11.1 Fluorescent Penetrant Inspection

Fluorescent penetrant inspection (FPI) technique consists in wetting a clean and dry surface to be inspected by a liquid "penetrant" consisting of a dye in a carrier fluid. The dye has the property of fluorescing in the visible spectrum of light at wavelengths between 4000 and 7000 Å when illuminated by ultraviolet light also known as black light (3200–4000 Å). Because of surface tension forces, the dye penetrates into cracks. A developer (colored powder that draws penetrants in contact by capillary action) spread over the surface absorbing the penetrant from around the cracks provides contrast for visual indication of cracks. Finally, the treated hardware is illuminated by ultraviolet light in a dark chamber and observed at a magnification of 3–5×. This technique is appropriate for detecting surface-connected pores and cracks in a large class of materials, including coatings (Conner and Connor 1994).

17.11.2 Eddy Current

When an alternating electrical current flows through a coil known as the "probe," an alternating magnetic field is established along the coil axis. If the coil is brought into the proximity of an electrically conducting material surface such that the magnetic field intersects the surface, *Eddy currents* are generated in the material in the form of circular loops. These currents induce a secondary field, which tends to oppose the primary magnetic field of the coil. Defects in the material (tube wall, for example) are changing the secondary field and consequently the impedance of the coil. The change of the coil impedance can be measured in input/output phase and amplitude. The Eddy current response from a material is affected by several parameters that include the electrical conductivity of the material as well as its magnetic permeability, the frequency of the inducing alternating current, the proximity of the probe to the surface, and lift-off. For example, the strength of the Eddy currents decreases with distance from the coil, i.e. Eddy current density decreases exponentially with depth, and this phenomenon, known as the skin effect, is shown in Figure 17.50.

In this figure, μ is the *permeability* that can be a problem in Eddy current testing because the relative permeability of a given ferromagnetic material can vary during testing, causing permeability noise signals that can override the Eddy current sights being sought. σ is the electrical conductivity of the material (Stoll 1974).

17.11.3 Frequency Scanning Eddy Current Technique

The frequency scanning Eddy current technique (FSECT) is a variant of the Eddy current technique in which the Eddy current probe operates within a range of frequency, typically between 100 kHz and 10 MHz. Impedance is measured as a function of the frequency (Rinaldi et al. 2006). An example of where FSECT is used is in heat exchanger tube inspections. Heat exchanger assemblies are often a collection of tubing that have support brackets on the outside. When attempting to inspect the full wall thickness of the tubing, the signal from the mounting bracket is often troublesome. By collecting a signal at the frequency necessary to inspect the full wall thickness of the tube and subtracting a second signal collected at a lower frequency (which will be more sensitive to the bracket but less sensitive to features in the tubing), the effects of the bracket can be reduced (Antonelli et al. 1997). The interest in pulsed Eddy current instruments is largely due to their ability to, in essence, perform multi-frequency measurements very quickly and easily.

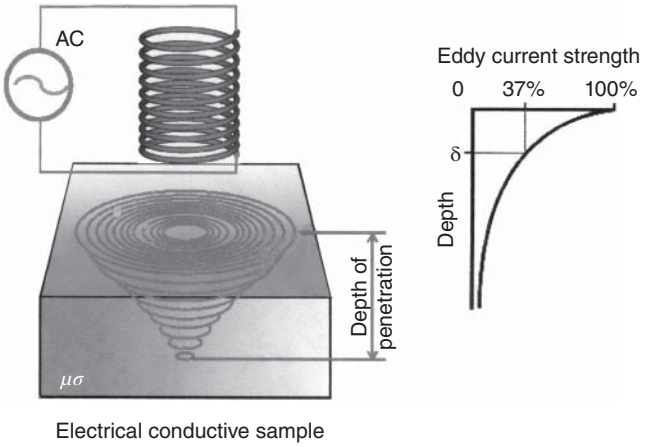


Figure 17.50 Eddy current field depth of penetration and density.

17.11.4 Ultrasonic Inspection

Ultrasonic testing (UT) uses a modulated carrier wave, the modulation feature, allowing effectively about 900 times the acoustic energy of an unmodulated wave. The carrier wave frequency is set to suit the transducer used. Ultrasonic tomography can test the homogeneity of a coating. In this method, the coating is tested ultrasonically from several directions, and sound attenuation is measured. Equations are developed to distinguish porous areas. UT is suitable for volume production, but interpretation of faults is difficult (Kauppinen 1997). Lithium sulfate crystals cease to be piezoelectric above 130 °C, but lead metaniobate works up to 400 °C, and oxygen-purged lithium niobate works up to 900 °C. Coupling pastes are available for use up to 550 °C. It is easier to avoid direct contact and to generate the sound using an AC induction coil with an additional constant magnetic field. However, the transducer coil needs to be 0.5–1 mm from the hot surface and thus requires protection (Drury 2004).

17.11.5 Infrared Imaging

IR energy coming from a material (for example, a TBC-coated sample) is focused by the optics onto an IR camera. The detector in the camera sends information to sensor electronics for image processing. The electronics translate the data coming from the detector into an image that can be viewed in the viewfinder or on a standard video monitor or screen. *Infrared imaging* (IRI) is the art of transforming an IR image into a radiometric one, which allows temperature values to be read from the image. So, every pixel in the radiometric image is, in fact, a temperature measurement. In order to do this, complex algorithms are incorporated into the IR camera. This makes the IRI a perfect technique for industrial applications (Ferber et al. 2000).

17.11.6 Pulse-Echo Thermal Wave Infrared Imaging

This is a variant of IRI. The basic premise of the *pulse-echo thermal wave infrared imaging* is that defects generated in a TBC locally change the thermal conductivity. A flash lamp delivers a pulse of heat to the surface of a TBC-coated sample. The areas with underlying defects appear hotter because of slower desorption of heat by conduction. The temperature also decays slowly. Analysis of the distribution of temperature and decay times, obtained by an IR camera–computer system, provides information on the details of damage accumulation (Newark and Chen 2005; Thompson and Chimenti 1999).

17.11.7 Phase of Thermal Emission Spectroscopy

This technique does not require any special sample preparation and requires access only to the top surface of a material, particularly a coating as TBCs, allowing nondestructive measurements to be made on coatings in almost any condition with arbitrary substrate shape and dimension. The method can simultaneously provide thermal conductivity and volumetric heat capacity of the coating as well as the thermal contact resistance of the interface. At the core of the *phase of thermal emission spectroscopy* lies a periodically modulated laser beam, such as from a CO_2 laser (wavelength 10.6 μm), which heats up the TBC. The frequency determines the depth of thermal penetration over a large range. The heated ceramic coating emits thermal radiation, which is intercepted by a detector that then measures the difference in phase between the incident heating signal and the emitted signal. A mathematical model relates the phase difference to thermal properties of the TBC system and contact thermal resistance at delaminations (Bennett and Yu 2005).

17.11.8 Acoustic Emission

Materials and coatings, when subjected to tensile or compressed loadings, release stress waves or AEs, which can be detected by piezoelectric sensors. For example, initiation and growth of vertical cracks in a TBC and delamination at the ceramic–bond coat interface during thermal cycling under an IR lamp can be correlated with significant AE activity (Voyer et al. 1998).

In the *photoacoustic technique*, a sample is placed inside a specially designed cell (resonant or nonresonant acoustically) containing a suitable gas and a sensitive microphone. The sample is then illuminated with chopped radiation. Light absorbed by the sample is converted, in part, into heat by non-radiative de-excitation processes within the sample. The resulting periodic heat flow from the sample to the surrounding gas creates pressure fluctuations in the cell, which are detected by the microphone as a signal that is phase coherent at the chopping frequency. The signal is subsequently analyzed by a lock-in amplifier and displayed on the *x*–*y* recorder, either as a function of the wavelength of the incident radiation or as a function of the scanning position. The resulting photoacoustic signal is directly related to the amount of light absorbed by the sample. This is especially the case for highly opaque and low fluorescence systems. Furthermore, since only the absorbed light is converted to sound, scattered light presents no difficulties. A quantitative treatment shows that, in addition, both the magnitude and the phase of the photoacoustic signal depend on the thermal properties of the sample and those of the gas in the cell, as well as on the chopping frequency. This technique has become a powerful NDI method (Ball 2006; Steinmann and Hintermann 1985).

17.11.9 Mid-Infrared Reflectance

IR spectroscopy is the study of the interaction of radiation with molecular vibrations that can be used for a wide range of sample types either in bulk or in microscopic amounts over a wide range of temperatures and physical states. Combining IR spectroscopy with reflection theories, the absorption properties of a sample can be extracted from the reflected light. Reflectance techniques may be used for samples that are difficult to analyze by the conventional transmittance method. Upon interaction of electromagnetic radiation with a sample surface, depending on the characteristics of the surface area and its environment, the light may undergo three types of reflection: internal reflection, specular reflection, and diffuse reflection (Figure 17.51).

Internal reflection spectroscopy (IRS), often termed as ATR spectroscopy, became a popular spectroscopic technique in the early 1960s. An internal reflection occurs when a beam of radiation enters from a more dense

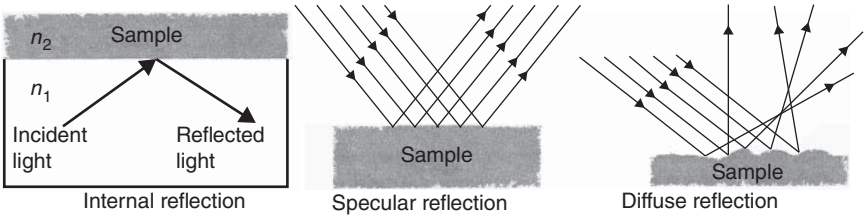


Figure 17.51 Illustration of different reflection types.

medium (with a higher refractive index, n_1) into a less dense medium (with a lower refractive index, n_2); the fraction of the incident beam reflected increases as the angle of incidence rises. When the angle of incidence, θ, is greater than the critical angle, θ_c, (which is a function of refractive index of two media), all incident radiations are completely reflected at the interface, resulting in total internal reflection. Total internal reflection of light at the interface between two media of different refractive indices creates an evanescent wave that penetrates into the medium of lower refractive index. An ATR spectrum can be obtained by measuring the interaction of the evanescent wave with the sample, and this phenomenon can be used for NDI of a variety of materials including soft solid materials, liquids, powders, gels, pastes, surface layers, polymer films, etc.

Specular reflectance techniques basically involve a mirrorlike reflection from the sample surface that occurs when the reflection angle equals the angle of incident radiation. It is used for samples that are reflective (smooth surface) or attached to a reflective back. Thus, specular techniques provide a reflectance measurement for reflective materials as a reflection–absorption (transreflectance) measurement for the surface films deposited on, or pressed against, reflective surfaces. The most common applications of this technique are the evaluation of surfaces such as coatings, thin films, and contaminated metal surfaces.

In diffuse reflection spectroscopy (DRS), the electromagnetic radiation reflected by roughened surfaces is collected and analyzed. Light incident onto a solid sample may be partly reflected regularly (specular reflection) by the sample surface, partly scattered diffusely, and partly penetrates into the sample. The latter part may be absorbed within the particles or be diffracted at grain boundaries, giving rise to diffusely scattered light in all directions. In *mid-infrared reflectance* (MIR), the DRS is associated with reflected lights produced by diffuse scattering (Figure 17.52) in the mid-IR region, leading to absorption spectra of thin films, opaque materials, roughened surfaces, coatings, etc. The best reflectance measurements are usually conducted in a FTIR spectrometer with an attachment (Ulbrich sphere) to integrate reflected waves over the hemisphere (Figure 17.53) (DeMasi-Marcin et al. 1990; Eldridge et al. 2003).

In the description above of MIR, the terms reflection and reflectance are used several times, which may be confusing. Thus, the reader should note that reflection is the act of reflecting, or the state of being reflected, or yet the property of a propagated wave being thrown back from a surface. Reflectance is the physics definition for the ratio of the flux reflected to that incident on a surface.

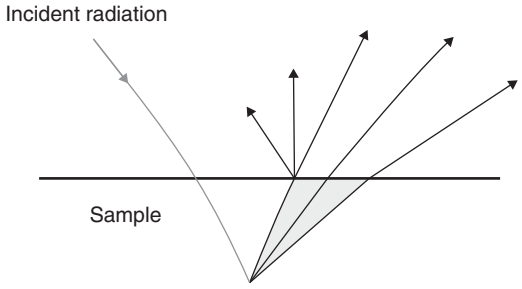


Figure 17.52 Representation of diffuse reflectance.

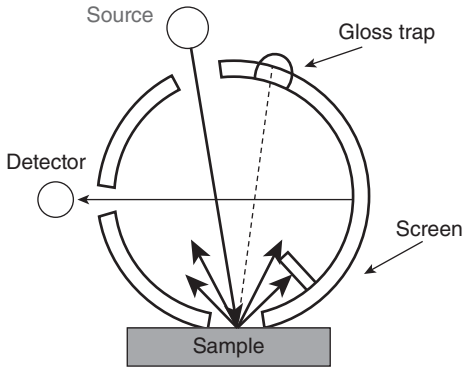


Figure 17.53 Integrating Ulbrich sphere.

17.11.10 Photoluminescence Piezospectroscopy

Typical alloys and metallic bond coats on which TBCs and other coatings are applied always contain Cr either as part of the composition or as an impurity. The Cr atoms are incorporated within the aluminum oxide structure of the aluminum thermally grown oxide (TGO) in the form of Cr^{3+} ions. But Cr^{3+} ions are also contained in much more materials. For example, Cr^{3+} ions are naturally occurring impurities within the crystal structure of α-alumina. On irradiation with a laser beam of appropriate frequency, the outer electron in orbit around the Cr ion core absorbs

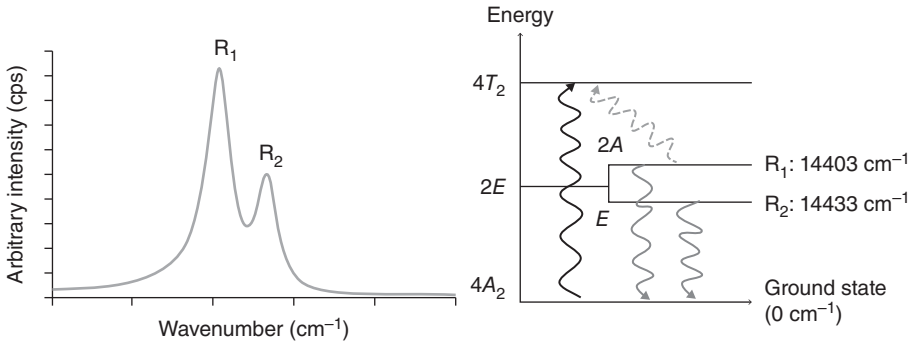


Figure 17.54 Spectral emission of α-alumina.

the incident laser radiation, which raises the electron to a higher-energy level. The electron subsequently falls to a lower-energy level, releasing energy known as fluorescent radiation or *luminescence*. Since the product is stimulated by radiation in the visible spectrum, it is called photo-stimulated luminescence, and it can be spectrographically analyzed. The emitted photons from the characteristic R-lines have two distinct peaks known as R_1 and R_2, located at 14 403 and 14 433 cm^{-1} frequencies for a stress-free aluminum oxide such as α-alumina (Figure 17.54) (Tolpygo and Clarke 2000). Additional lines corresponding to other aluminum oxide impurities such as θ-alumina may also be present. This is the basic principle of photoluminescence (PL).

The *piezospectroscopic* (PS) *effect*, as shown in Figure 17.55, relates the frequency shifts of the *R*-lines to residual stress in the samples like ruby and polycrystalline alumina. The stress sensing capabilities of α-alumina are possible due to these frequency shifts that are caused by deformation of the crystal field surrounding the Cr^{3+} ions (Gell et al. 2004; Molis and Clarke 1990).

While the calibration of the PS effect or PS coefficient (see Figure 17.55) has been determined for many materials in tension and compression, the PS behavior of alumina nanocomposites and other Cr^{3+} materials has only recently been determined in compression (Geller 2002; Raghavan et al. 2008).

Photoluminescence piezospectroscopy (PLPS) combines PL and PS to be used as an NDI technique. During the early years of single-crystal ruby (also known as Cr^{3+}-doped sapphire crystal) luminescence studies, one major success was the observation that a frequency shift of the characteristic R_1 and R_2 peaks occurred when uniaxial stress was applied. Forman et al. (1972) first applied the use of spectral shifts of ruby *R*-lines to measure the hydrostatic stress in diamond anvil cells and developed the following equation to relate the frequency shifts of the *R*-lines to residual stress:

$$\Delta\upsilon = \pi_{ii}\sigma_{\text{av}} \tag{17.56}$$

where $\Delta\upsilon$ is the frequency shift, π_{ii} is the PS tensor or FS coefficient, and σ_{av} is the residual stress. PL combined with PS analysis has been used to assess damage and estimate life remaining in actual use.

17.11.11 Interferometric Techniques

In *interferometric techniques* two monochromatic beams of light originating from the same source are used to create an interference pattern that contains information about the object under inspection. Analysis of the interference patterns provides data on various features of the object, including defects.

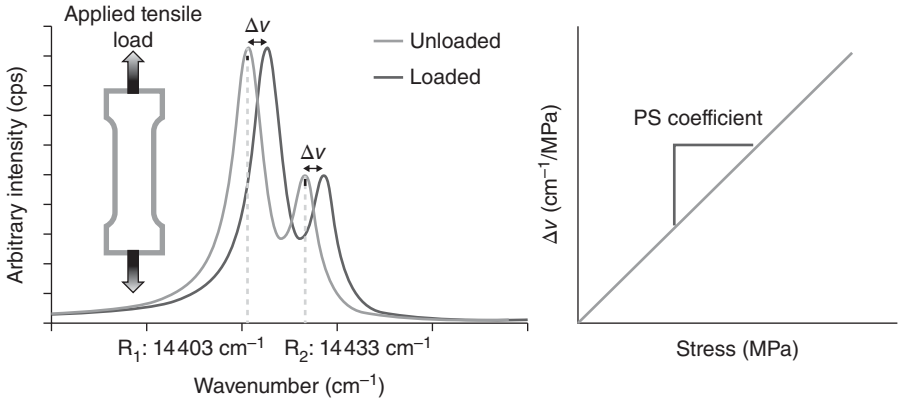


Figure 17.55 Piezospectroscopic effect.

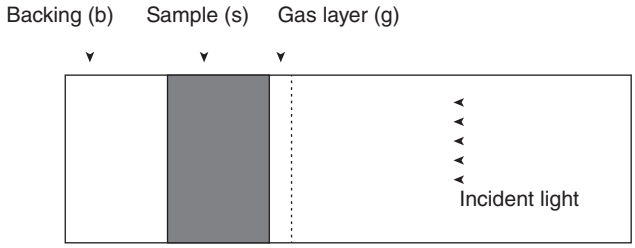


Figure 17.56 Layered structure used in the work of Rosencwaig and Gersho.

17.11.12 Thermal Wave Interferometry

The use of *thermal wave interferometry* (TWI) to characterize the thickness and thermal properties of thin films is well established and follows the pioneering work of Rosencwaig and Gersho (1976) several decades ago. Thermal wave interference occurs in layered structures in response to a modulated heat source and describes a condition where the properties of the interface influence the phase and amplitude of the temperature oscillations at the surface. Initially, these oscillations were resolved by means of the photoacoustic method that involves the measurement of pressure variations and to thermal expansion and contraction of the boundary layer of gas (Figure 17.56). However, with the widespread availability of low-cost IR detectors, photothermal radiometry is now preferred over the photoacoustic method for applications involving the measurement of thin-film properties on plasma-sprayed wear coatings, TBCs, etc. (Almond et al. 1987; Rajic 2000; Rajic et al. 2008).

17.11.13 Holography

This is the science and practice of making holograms, i.e. photographic recordings of a light field, rather than of an image formed by a lens, and it is used to display a fully 3D image of the holographed subject, which is seen without the aid of special glasses or other intermediate optics. It consists of two steps. The first step is to create a hologram by optically separating a laser beam into a reference beam (which is projected on a high-resolution holographic film after expanding and filtering the beam to cover the film uniformly) and a second beam (also expanded and filtered) that is reflected off the object. This beam, which carries information about the topography of the object, meets the reference beam at the holographic film, creating an interference pattern that is captured on the film as the hologram. The second step is to illuminate the finished hologram by a beam akin to the original reference beam. This reconstructed image may be compared with the actual object to identify changes in shapes, dimensions, textures, etc. Holograms can now also be entirely computer generated and show objects as scenes that never existed.

17.11.14 Shearography

Shearography or electronic speckle pattern interferometry (ESPI) is a measuring and testing method similar to holographic interferometry. When a surface area is illuminated with a highly coherent laser light, a stochastic interference pattern is created. This interference pattern is called a speckle and is projected on a rigid camera's charge-coupled device (CCD) chip. Analogous with ESPI, to obtain results from the speckle, we need to compare it with a known reference light. Then, using the test object itself as the known reference, it shears the image, so a double image is created. The superposition of the two images represents the surface of the test object at this unloaded state. By applying a small load, the material will deform. A nonuniform material quality will generate a nonuniform movement of the surface of the test object. A new shearing image is recorded at the loaded state and is compared with the sheared image before load. If a flaw is present, it will be seen. Shearography is used in the production and development in aerospace, wind rotor blades, automotive, and materials research areas. Flaws that are easily detected by shearography and ESPI are disbonds, delaminations, wrinkles, porosities, foreign impurities, and impact damages (Silva Gomes et al. 2000).

17.11.15 Electron Backscatter Diffraction

Electron backscatter diffraction (EBSD) is used to identify the orientation features of the coating and the effects of the substrate alloys. This can help us to understand the growth mechanism of the coatings, e.g. of the low activity vapor aluminide coating made at different temperatures and times. In EBSD, the accelerated electrons in the primary beam of a SEM can be diffracted by atomic layers in crystalline materials. Electron backscatter patterns are generated, which are projections of the geometry of the lattice planes in the crystal, and they can give direct information about the crystalline structure and crystallographic orientations of the grains from which they originate. In crystal orientation mapping, the electron beam is scanned over the sample on a grid of points, and at each point a diffraction pattern obtained, and the crystal orientation measured according to a color allocated reference. When applying EBSD, the polished sample is placed in the SEM and inclined approximately by 70° relative to normal incidence of the electron beam. The EBSD scheme and one example of orientation map are shown in Figure 17.57. The CCD camera is equipped with a phosphor screen integrated with a digital frame grabber. Then the CCD camera is used to collect the Kikuchi lines through the phosphor screen. The pattern of Kikuchi lines on the phosphor screen is electronically digitized and processed to recognize the individual Kikuchi lines. These data are

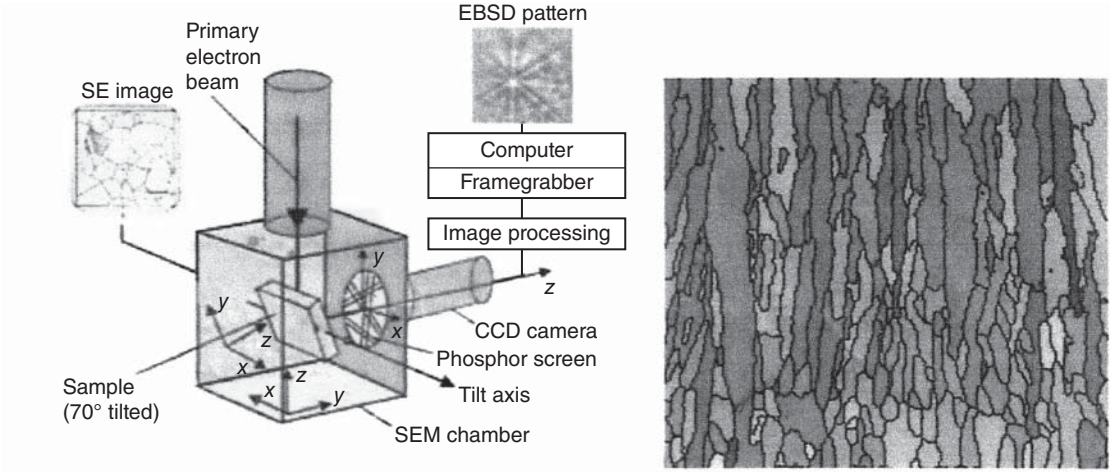


Figure 17.57 (a) EBSD scheme. (b) One example of orientation map of the grains, different colors corresponding to different orientations.

transmitted to a computer to identify the phase, to index the pattern, and to determine the orientation of the crystal from the pattern that was generated. EBSD analysis needs strict preparation of the specimen surface. In general, the specimens are prepared firstly by the same procedure of SEM, after which they are polished in silica for 30 minutes to obtain a much finer surface roughness.

17.11.16 Glow Discharge Optical Emission Spectrometry

Glow discharge optical emission spectrometry (GDOES), which is an optical emission spectrometry technique using glow discharge plasma, gives the quantitative depth distribution of elements in a thin surface on a metallic material. The only requirement is the use of primary vacuum calibration of the GDOES instrument with samples of known chemical analyses and a matrix composition similar to that of the samples to be analyzed. Glow discharge has been used to study atomic structures for many years. Recently, it has also been applied in the quantitative depth profiling of metallic and nonmetallic coating area (Baschi et al. 2007; Coustumer et al. 2003; Suzuki and Katita 2005). For example, the GDOES technique is being very useful to analyze the chemical composition profiles on advanced coating layers on metallic alloy substrates at different temperatures and hold times coating. The depth profiles are obtained by measuring emission intensities for constituent elements as a function of sputtering time. The quantitative relationship between the composition and depth is also estimated according to a normalization procedure. The element content is normalized by the ratio of the local amounts of the specific element to its average content in the substrate. The *x*-axis depth is roughly obtained assuming a constant material removal rate.

The layers to be analyzed should be flat, well adherent to the substrate, and vacuum resistant (nonporous, without cracks). Which discharge mode (U = const., i = const., P = const.) should be chosen for depth profiling of oxide/corrosion scales seems difficult to answer. Whereas some investigators prefer the i = const. mode, since it provides a positive ignition behavior of the discharge, other operators use the U = const. mode because of a more reliable quantification of the depth profiles. The choice of the optimal discharge parameter settings for a good depth resolution in combination with satisfying detection limits is somewhat problematic as depth resolution and detection sensitivity are opposite effects. Optimal discharge conditions for an 8 mm GD lamp at the U = const. mode and a discharge voltage setting of 600–700 V. If possible, both modes should be applied in the analysis to have a comparison of the analytical results.

The standard experimental parameter set that should be registered for each GDOES analysis independent of the actual sample is voltage, current, pressure, total light, and the emission lights ArI, ArII, OI, OII, NI, NII, CI, and CII.

17.12 Traditional Electrochemical Methods

Different corrosion phenomena may have a serious impact on metals and alloys, ionic solids, and other materials employed in high temperature environments. To be able to mitigate the risk of detrimental corrosion phenomena of many of these materials, a mechanistic understanding of the contributing processes is required, as discussed in this book. The present chapter is discussing the development and application of different techniques in order to obtain information about processes affecting the oxidation and

corrosion behavior of typical materials in operating high temperature plants.

In this and the next two sections, some conventional, non-conventional, and combined electrochemical procedures are described. Conventional or traditional techniques are based on the measurement of current and potential and, in the case of liquid electrodes, of the surface tension.

17.12.1 Potentiometry

Potentiometry has been used extensively in ionic liquids and solids for the determination of electromotive force (emf) series in the different ionic systems, for measuring Gibbs and excess free energies, and for the study of the stability of various species.

The simplest application of potentiometry is the determination of the standard electrode potentials, $E^{0\prime}s$, of electroactive species and, hence, of their relative thermodynamic stability in a given medium. The equilibrium potential of a redox reaction $O + ne^- = R$ is given by the Nernst equation

$$E = E^0 + \frac{RT}{nF} \ln \frac{a_O}{a_R} \tag{17.57}$$

where E can be measured with respect to a reference electrode (RE) in a cell such as

$$\text{Reference electrode}//a_O, a_R/\text{M (inert electrode)}$$

The cell potential is given by

$$E_{cell} = E^{0\prime}_{O/R} + \frac{RT}{nF} \ln \frac{C_O}{C_R} \tag{17.58}$$

considering $E_{ref} = 0$ and the junction potential negligible. From Eq. (17.58), the number of electrons may be evaluated from the slopes of the plots of E_{cell} versus $\ln C_O/C_R$; the formal electrode potential $E^{0\prime}$ can be calculated from the same plot by extrapolating $C_O/C_R = 1$.

Potentiometric methods have been employed extensively for the study of the self-dissociation of solvents such as molten alkali metal chloroaluminates by using concentration cells of the type

$$Al/AlCl_3\text{–}NaCl_{satd}//AlCl_3\text{–}NaCl/Al \tag{17.59}$$

where the cell voltage depends on the free chloride concentration. This is determined by the ratio $AlCl_3$/NaCl through equilibria involving species such as $AlCl_4^-$, $Al_2Cl_7^-$, $Al_3Cl_{10}^-$, and Al_2Cl_6. By fitting the experimental cell voltage with models involving different species, information about the existence of these species and the equilibrium constants for equilibrium reactions in which they participate have been derived. The chemistry and electrochemistry of chalcogens, such as tellurium, selenium, and sulfur, in chloroaluminate melts have been investigated in a similar way as well as the formation of chloride complexes for certain transition metal ions. The existence of different low oxidation states and the constants of the relevant equilibrium reactions have been derived from the experimentally measured cell voltages (Mamantov 1978).

17.12.2 Chronoamperometry

Chronoamperometry or large amplitude potential step experiment is one of the most facile electroanalytical techniques. A chronoamperometric experiment involves stepping the working electrode potential from a value where no electrode reaction takes place to a potential where electrolysis occurs. This step may be either positive or negative of the initial potential in order to cause an oxidation or reduction reaction, respectively, to take place. If the potential step is sufficiently large so that the desired electrode reaction is driven at the mass transfer limited rate, then the current–time transient that results from the experiment will exhibit a decay that is proportional to $t^{-1/2}$, where t is the time. For a planar electrode this decay is expressed quantitatively by the Cottrell equation for the reversible electrode reaction $O - ne^- = R$ as

$$i = nFAC^*_O \sqrt{\frac{D_O}{\pi t}} \tag{17.60}$$

where A is the electrode area (cm^2), C^*_O is the bulk concentration of the oxidized species initially present in the solution ($mol\,cm^{-3}$), and D_O is the diffusion coefficient of the oxidized species ($cm^2\ s^{-1}$).

If the step potential is close to the $E^{0\prime}$ value for the O/R couple, the current can be expressed as

$$i = \frac{nFAC^*_{Ox}}{1 + \xi\theta} \sqrt{\frac{D_{Ox}}{\pi t}} \tag{17.61}$$

where ξ is given by

$$\xi = \sqrt{D_{Ox}/D_{Red}} \tag{17.62}$$

and θ is the ratio of concentrations at the electrode surface as determined by the Nernst equation

$$\theta = \frac{C_{Ox}(0,t)}{C_{Red}(0,t)} = \exp\left[\frac{nF}{RT}(E - E^{0\prime})\right] \tag{17.63}$$

Under Cottrel conditions, $\theta = 0$ and Eq. (17.61) reverts to Eq. (17.60). Once again, we must emphasize that these equations apply only to reversible (Nernstian) electrochemical reactions.

It is also possible to perform double-step chronoamperometry in which the potential of the working electrode is switched to a second fixed value after a certain length of

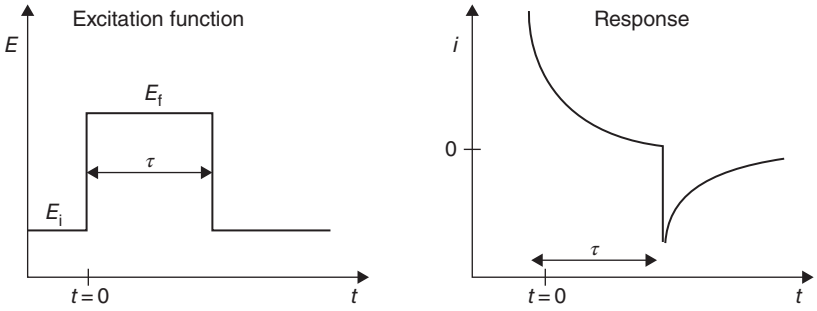


Figure 17.58 Potential excitation function and current response for double-step chronoamperometry.

time τ. Often, the potential is returned to the initial value, which enables the experimenter to check for chemical reactions affecting the species electrogenerated in the first potential step. A typical excitation function and current response are given in Figure 17.58.

Chronoamperometry is not very commonly used in practice, but books and papers on applications of chronoamperometry to high temperature corrosion studies appear with some frequency (Antunes et al. 2013; Bosh et al. 2007; Iacoviello et al. 2017).

17.12.3 Chronopotentiometry

In *chronopotentiometry* a controlled current is applied between a working electrode, operating under semi-infinite linear diffusion conditions, and an *auxiliary electrode* while monitoring the potential of the working electrode versus an RE. For a simple electrode process $O + ne^- = R$ with only O initially present in solution, the potential of the working electrode depends on the concentration ratio [O]/[R] at the electrode surface as determined by the Nernst equation. At some point after initiation of the current, the concentration of O becomes too small to sustain the imposed current, and the working electrode potential changes rather abruptly to some other value corresponding to another process that will support the imposed current.

The time elapsed from the beginning of the electrolysis to the sudden potential change is called the transition time τ; the potential–time curve is called a chronopotentiogram. A typical chronopotentiogram resulting from the cathodic reduction of S_4^{2-} to S_2^{2-} in the LiCl–KCl eutectic at 423 °C at a gold electrode is shown in Figure 17.59.

The Sand equation

$$\tau^{1/2} = \frac{\pi^{1/2} n F A D_O^{1/2} C_O^*}{2i} \tag{17.64}$$

relates the transition time to the constant current and the concentration of the electroactive species for a simple diffusion-controlled process.

Chronopotentiometry has been widely used in molten salt electrochemistry for the determination of diffusion coefficients, the study of metal deposition, and the study of coupled chemical reactions and adsorption.

A technique called electromigrational depletion chronopotentiometry occurs in systems such as BeF_2–MF or $AlCl_3$–MCl where the transference numbers of Be^{2+} and Al^{3+} are almost zero (with respect to the fluoride or chloride ions), and hence the only current carrying species is the alkali metal ion. This technique has been

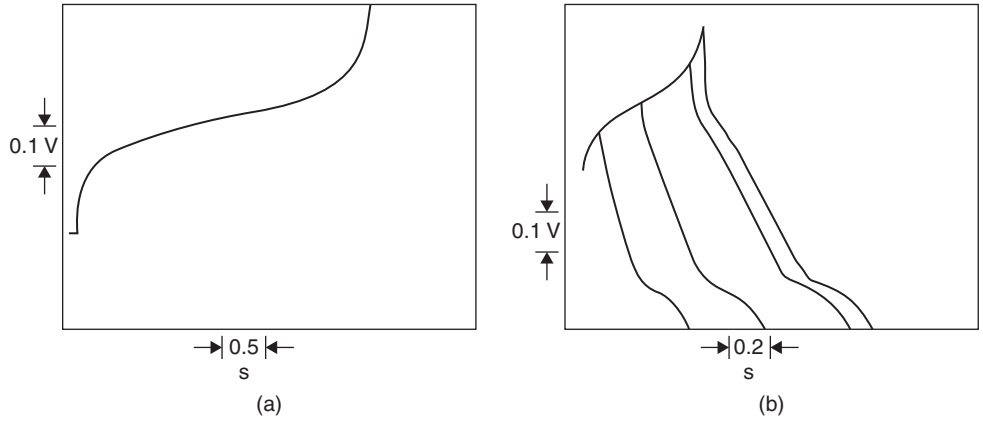


Figure 17.59 Cathodic chronopotentiometry of K_2S_6 in LiCl–KCl eutectic; 423 °C; Au electrode. (a) $[K_2S_6] = 20 \times 10^{-2}$ M, $i = 20.2$ mA cm^{-2}. (b) Current-reversed chronopotentiometry, $[K_2S_6] = 6.0 \times 10^{-3}$ M, $i = 15.9$ mA cm^{-2} (Weaver and Inman 1975).

applied in several cases to study concentration profiles in high temperature systems such as batteries and fuel cells (Vallet et al. 1980). Chronopotentiometry has also been largely applied to high temperature corrosion studies in ionic liquids and solids, heavy metals, and other materials systems (Acton 2012; Johannesen and Andersen 1989; Roberge 2006).

17.12.4 Chronocoulometry

Electrolysis under potentiostatic control is a useful technique for electrosynthesis, electroanalysis, selective electrodeposition of metals, coulometric generation of reagents, and the determination of the number of electrons transferred in a redox reaction. This technique more often called *chronocoulometry* is almost always performed under Cottrell conditions. Integration of the current given in Eq. (17.60) as a function of time yields

$$Q = 2nFAC^*_{Ox}\sqrt{\frac{D_{Ox}\cdot t}{\pi}} \qquad (17.65)$$

where all the symbols have their usual meaning. Therefore, the charge passed from the diffusion-controlled reduction of solution species Ox increases with the square root of time. What gives chronocoulometry its key advantage against chronoamperometry? While the latter is based on raw data that can be directly measured in simple experiments, the former requires current integration (a very simple operation with computer-controlled instrumentation). The key difference, however, is that chronoamperometric currents decay quickly as a function of time, while chronocoulometry features a signal that increases continuously with time.

Equation (17.65) predicts that Q versus $t^{1/2}$ plots will be linear with a zero intercept. In practice, the intercept is usually small but different from zero because some charge (Q_{dl}) is passed at the very early stages of the experiment to charge the electrode–solution interface. Furthermore, chronocoulometry is a technique suitable for the study of species absorbed at the electrode surface. If we assume that we have a surface excess Γ_{Ox} of reducible electroactive species absorbed at the electrode surface, one would anticipate that this material will be reduced instantaneously at the beginning of the experiment (diffusion plays no role in the reduction of adsorbed species). Therefore, we can write a more complete equation describing all the charge contributions that will be encountered in such an experiment:

$$Q = Q_{dl} + nFA\,\Gamma_{Ox} + 2nFAC^*_{Ox}\sqrt{\frac{D_{Ox}\cdot t}{\pi}} \qquad (17.66)$$

The two first terms are independent of time, and their accumulated value sets the intercept of the Q versus $t^{1/2}$ plot (see Figure 17.60). Anson and coworkers were the first ones to propose the use of chronocoulometric plots to study species absorbed on the electrode surface (Anson 1966).

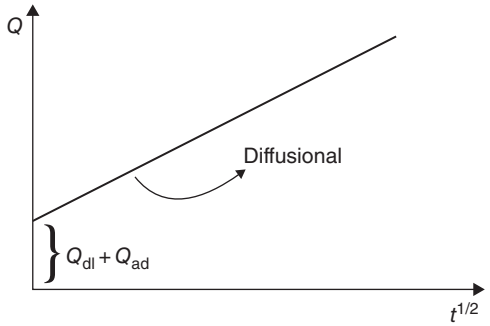


Figure 17.60 Charge components in a chronocoulometric (Q versus $t^{1/2}$) plot.

Chronocoulometry is one of the best methods available for the determination of diffusion coefficients and has been applied to many studies of high temperature corrosion (Scheffler and Hussey 1984; Weissberger and Rossiter 1971).

17.12.5 Cyclic Voltammetry

In *cyclic voltammetry* the potential of a stationary electrode, initially set at a value where no electrode reaction occurs, is swept linearly at a certain rate into the potential region where an electroactive species is reduced or oxidized. When the potential reaches values where charge transfer occurs, the current gradually increases, reaches a maximum, and then decreases. At this point, the direction of the potential sweep may be reversed, causing the reoxidation (if the initial scan was a reduction process) of the product formed during the forward scan.

For a simple diffusion-controlled process (i.e. a process where the rate of the electron transfer is so rapid that the ratio O/R at the electrode surface is given by the Nernst equation) of the type $O + ne^- = R$ where both O and R are soluble, the peak current is given by the Randles–Sevčik equation (Bard and Faulkner 2001)

$$i_p = 0.4463\frac{n^{3/2}F^{3/2}}{R^{1/2}T^{1/2}}AD_O^{1/2}C_O^*\nu^{1/2} \qquad (17.67)$$

where ν ($V\,s^{-1}$) is the scan rate and the other symbols have their usual meanings. From Eq. (17.67) it turns out that, under the stated conditions, the ratio $i_p/\nu^{1/2}$ (current function) is constant for different scan rates. Other relevant parameters of a cyclic voltammogram are the peak potentials E_{pc} and E_{pa}; the half-peak potentials, $E_{p/2}$; and the current ratio i_{pa}/i_{pc}. The variation of these parameters with the potential scan rate is determined by the overall electrode mechanism, and diagnostic criteria, deduced from theoretical calculations, may be used to establish

the electrochemistry involved in the electron transfer. The reversibility of the redox couples may be deduced by observing the differences between the half-peak potential and the peak potential or between the peak potentials of the forward and reverse portions of the cyclic voltammograms. For a reversible couple, these parameters are invariant with the scan rate and are equal to

$$E_p - E_{p/2} = \frac{2.2RT}{nF} \text{ and } \Delta E_p = E_{pa} - E_{pc} = \frac{2.3RT}{nF} \quad (17.68)$$

The current function and the current ratio are also independent of the scan rate.

The behavior of quasi-reversible and irreversible systems may be described by the shifts of E_p with ν and by the variation of ΔE_p with the same parameter. Heterogeneous rate constants may be determined using the appropriate equations. Total irreversibility is characterized by the absence of a peak upon reversal.

Preceding, following, or catalytic homogeneous chemical reactions, coupled with the charge transfer and adsorption of the product or of the reactants, modify the shapes of the cyclic voltammograms in ways that are characteristic for each electrode mechanism. Follow-up chemical reactions may, for instance, be detected by examining the variation of the current ratio with the scan rate. This function decreases from unity with decreasing scan rate, while the peak potential shifts cathodically (for a reduction) with increasing scan rate.

A fairly complete account of possible electrode mechanisms and of the respective diagnostic criteria may be found in Bard and Faulkner (2001).

Many workers have performed extensive studies on the electrochemistry of materials in molten salts, ionic liquids, ionic solids, and so on (Gellings and Bouwmeester 1997; Mamantov and Marassi 1987). See also Section 17.13.

17.12.6 Linear Sweep Voltammetry

The simplest potential sweep method is linear sweep voltammetry (LSV). In this technique, the potential of the working electrode is varied linearly with time between two values, the initial and final potentials. Let us assume that we start the experiment with a solution containing a reducible compound Ox as the only electroactive species. The voltammetric scan is started at a potential at which no electrochemical reactions may take place, that is, $E > E_{1/2}$. Normally, the potential will be linearly scanned in the negative direction, and faradaic currents will be detected near, around, and beyond the half-wave value, that is, in the potential region where the conversion Ox → Red is favored. If the solution is kept quiescent (so that diffusion is the only mass transport mechanism possible) and the Ox/Red couple is electrochemically reversible, the electrochemical conversion gives rise to a characteristic cathodic wave

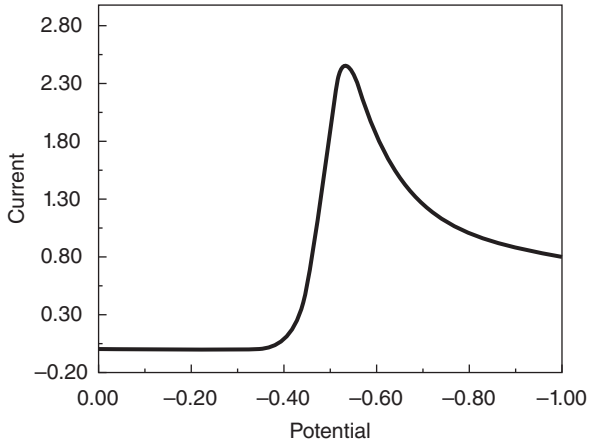


Figure 17.61 A typical linear sweep voltammogram. $E_{1/2} = -0.500$ V.

(Figure 17.61) with a maximum current value given by the Randles–Sevčik equation

$$i_p = (2.69 \times 10^5)\, n^{3/2} A C_{Ox} (D_{Ox} \nu)^{1/2} \quad \text{at } 25^\circ\text{C} \quad (17.69)$$

where the peak current i_p is given in μA, A is the projected electrode area (in cm^2), D_{Ox} is the diffusion coefficient of the electroactive species expressed in $cm^2\ s^{-1}$, C_{Ox} is its concentration (mM), and ν is the scan rate in $V\ s^{-1}$. It is important to use the specified units as the equation contains a numeric factor that results from the evaluation of several constants.

The Randles–Sevčik equation is one of the most important equations in voltammetry. Of course, it applies only when the current is diffusion controlled and hemispherical diffusion is unimportant (we are assuming that a planar electrode of conventional size is used). Note that the current depends on the square root of the scan rate. The implicit time dependence ($t^{-1/2}$) is identical to that expressed by the Cottrell equation for a potential step experiment.

It is important to point out that the potential of the voltammetric peak does not equal the half-wave potential of the corresponding redox couple. For reversible electrochemical couples, the cathodic peak occurs 20–30 mV more negative than the $E_{1/2}$ value, and its position is independent of the scan rate. The position of the peak represents the onset of diffusion control on the current. That is, beyond the peak potential, the current does not depend on the potential anymore and is fully controlled by the rate of diffusion, which decreases gradually as the thickness of the diffusion layer increases. Therefore, it is necessary to go past the half-wave potential to reach the necessary Cottrell-like conditions. For slower (irreversible) electrochemical couples, a peak may or may not be reached. If the voltammogram exhibits a peak, the corresponding peak potential will shift cathodically as the scan rate increases.

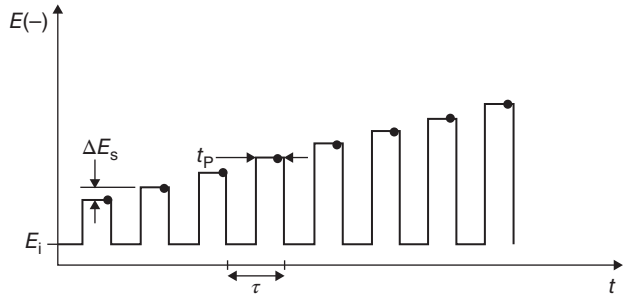


Figure 17.62 Potential excitation function for NPV experiments. The dots indicate current measuring points.

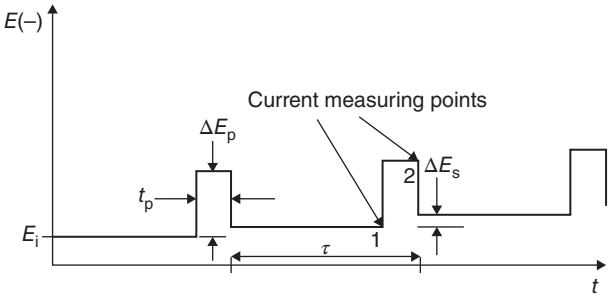


Figure 17.63 A typical excitation function for DPV. See text for symbol definitions.

LSV is greatly applied in high temperature corrosion studies (Acton 2012, 2013; Bosh et al. 2007).

17.12.7 Normal and Differential Pulse Voltammetry

The potential excitation used in *normal pulse voltammetry* (NPV) is illustrated in Figure 17.62. It essentially consists of a series of short duration pulses of gradually increasing magnitude. After each pulse, the potential returns to the initial value, a feature that is unique to this technique and gives rise to special applications.

Using pulse widths (t_p) in the millisecond regime, the current measured at the end of each pulse is essentially faradaic in nature. The scan rate can be readily calculated by dividing the potential step size (ΔE_s) by the period of the waveform (τ). The single feature that makes NPV a useful technique for chemists is the periodic return of the potential to the initial value. This is particularly useful in cases in which the electrogenerated species is insoluble in the electrolytic solution, as the cyclic return to the initial potential periodically regenerates the initial conditions, cleaning the electrode surface from insoluble deposits and leading to current–potential curves that are relatively unaffected by the precipitation of the electrogenerated species.

The potential excitation function used in *differential pulse voltammetry* (DPV) is illustrated in Figure 17.63. The waveform is composed of a series of potential pulses. After each pulse, the potential returns to a value that is slightly more negative (in a cathodic scan or more positive in an anodic scan) than the value preceding the pulse; ΔE_s is the net potential charge that takes place after a full waveform cycle. Two current samples are taken during every cycle of the excitation function (points 1 and 2). The quantity of interest is $\delta i = i_2 - i_1$. The differential pulse voltammogram is simply a plot of δi against the potential value at the beginning of the corresponding waveform cycle, and this voltammogram shows a peaked output.

The shape of the DPV response can be quantitatively treated. The events during each waveform cycle correspond to those in a double potential step experiment. At the beginning of the cycle, the base potential E is enforced until the application of the pulse. After the pulse, a new fixed potential $E + \Delta E_p$ (ΔE_p is the pulse amplitude) is applied during the pulse width t_p. It can be shown that

$$\delta i = \frac{nFAD_{Ox}^{1/2} C_{Ox}^{*}}{\pi^{1/2}\,(t_2 - t_1)^{1/2}} \left[\frac{P(1-\sigma^2)}{(\sigma + P)\,(1 + P\sigma)}\right] \tag{17.70}$$

where $(t_2 - t_1)$ is the time difference between the two current readings and the parameters P and σ are defined as follows:

$$P = \left(\frac{D_{Ox}}{D_{Red}}\right)^{1/2} \exp\left[\frac{nF}{RT}\left(E + \frac{\Delta E_p}{2} - E^{0\prime}\right)\right] \tag{17.71}$$

$$\sigma = \exp\left(\frac{nF \cdot \Delta E_p}{2RT}\right) \tag{17.72}$$

The bracketed factor of Eq. (17.71) describes the potential dependence of the differential current δi. At $E \gg E^{0\prime}$, P is very small and δi approaches zero. It can be readily shown that the maximum differential current value is reached when $P = 1$. Therefore, using Eq. (17.71) we can demonstrate that

$$E_{max} = E^{0\prime} + \frac{RT}{nF} \ln\left(\frac{D_{Ox}}{D_{Red}}\right)^{1/2} - \frac{\Delta E_p}{2} \tag{17.73}$$

which combined with equation

$$E_{1/2} = E^{0\prime} - \left(\frac{RT}{2nF}\right) \ln\left(\frac{D_{Ox}}{D_{Red}}\right) \tag{17.74}$$

yields

$$E_{max} = E_{1/2} - \frac{\Delta E_p}{2} \tag{17.75}$$

Note that ΔE_p values are negative in cathodic scans and positive in anodic scans. Typical ΔE_p values range from 10 to 100 mV. The maximum or peak current is given by the expression

$$(\delta i)_{max} = \frac{nFA \cdot D_{Ox}^{1/2} \cdot C_{Ox}^{*}}{\pi^{1/2}\,(t_2 - t_1)^{1/2}} \left(\frac{1-\sigma}{1+\sigma}\right) \tag{17.76}$$

Since σ depends on the value of ΔE_p (see Eq. (17.72)), the magnitude of the pulse amplitude is crucial for determination of the peak current. It can be readily shown that the ratio $(1-\sigma)/(1+\sigma)$ decreases with $|\Delta E_p|$. However, it would be detrimental to increase $|\Delta E_p|$ too much as this would tend to broaden the peak, thus jeopardizing the resolution of peaks arising at close potential values. The best compromise is reached by using $|\Delta E_p|$ values in the range of 25–50 mV. Small $|\Delta E_p|$ values are used to resolve close peaks (Christensen and Hamnet 1994; Gosser 1993).

17.12.8 Square Wave Voltammetry

The excitation signal in *square wave voltammetry* (SWV) consists of a symmetrical square wave pulse of amplitude E_{sw} superimposed on a staircase waveform of step height ΔE_s, where the forward pulse of the square wave coincides with the staircase step. The net current is obtained by taking the difference between the forward and reverse currents $(i_1 - i_2)$ and is centered on the redox potential. The peak height is directly proportional to the concentration of the electroactive species, and direct detection limits as low as 10^{-8} M are possible. Generally the current–potential response of a reversible redox couple Ox/Red to a cathodic scan patterned after the potential excitation function, such as that given in Figure 17.64, is given by the following expression:

$$i = \frac{nFAD_{Ox}^{1/2} \cdot C_{Ox}^{*}}{\sqrt{\pi t_p}} \cdot \psi(\Delta E_p, \Delta E_s) \qquad (17.77)$$

where t_p stands for the waveform's pulse width (one-half of the waveform's period in this case) and $\psi(\Delta E_p, \Delta E_s)$ is the dimensionless current function that depends on the waveform's potential parameters, as defined in Figure 17.64. This dimensionless current function is useful because for a given excitation waveform, all reversible redox couples will exhibit the same normalized current response. Unfortunately, the response is hard to calculate, requiring the use of numerical techniques.

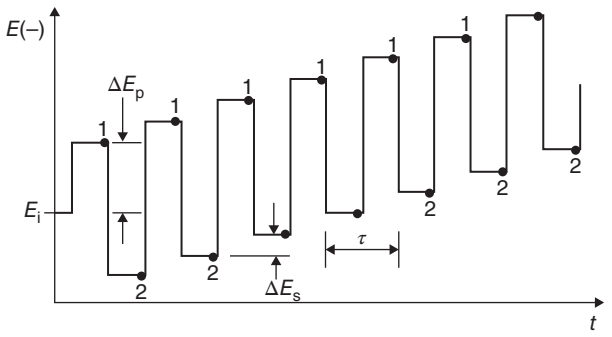


Figure 17.64 A typical excitation function for square wave voltammetry.

SWV has several advantages. Among these are its excellent sensitivity and the rejection of background currents. Another is the speed (for example, its ability to scan the voltage range over one drop during polarography with the DME). This speed, coupled with computer control and signal averaging, allows for experiments to be performed repetitively and increases the signal-to-noise ratio. Applications of SWV include the study of electrode kinetics with regard to preceding, following, or catalytic homogeneous chemical reactions, determination of some species at trace levels, and its use with electrochemical detection in HPLC (Kissinger and Heineman 1984; Osteryoung and Osteryoung 1985; Rudolph et al. 1994).

17.12.9 Rotating Disk and Rotating Ring-Disk Voltammetry

The motion of a *rotating disk electrode* (RDE) drags a layer or fluid near the disk surface along with it as it rotates. At the same time, this liquid layer is subjected to centrifugal forces that cause it to move radially away from the rotational axis of the electrode describing an S-shaped path as it does so. As a consequence of fluid motion parallel to the disk surface, new liquid is drawn to the disk along a path that is parallel to the rotational axis of the electrode.

According to the simple Nernst diffusion layer concept, a thin layer of stagnant solution is present at the electrode surface, within which the concentration of the electroactive species that is undergoing oxidation or reduction varies linearly from its value in the bulk solution to a new value at the electrode surface. The current i is then given approximately by the expression

$$i = \frac{nFAD(C^* - C^x)}{\delta} \qquad (17.78)$$

where A is the electrode area; C^* and C^x are the concentrations of the electroactive species in the bulk solution and at the electrode surface, respectively; δ is the thickness of the diffusion layer; and the other parameters have been previously defined. For an RDE in a solution with a kinematic viscosity ν, Levich (1962) showed that the diffusion layer thickness is dependent on the inverse square root of the angular velocity ω of the rotating electrode:

$$\delta = 1.6\, D^{1/3} \nu^{1/6} \omega^{-1/2} \qquad (17.79)$$

The limiting current i_l that is observed at a rotating electrode when the potential is sufficiently negative (in the case of a reduction) or positive (in the case of an oxidation) to yield $C_O^x = 0$ is given by Eq. (17.80) written here for a reduction process:

$$i_l = 0.62\, nFAD_O^{2/3} C_O^* \nu^{-1/6} \omega^{1/2} \qquad (17.80)$$

By standard convention, Eqs. (17.78) and (17.80) are preceded by a minus sign for an oxidation process and are

positive for a reduction reaction. The current–potential relationship for a Nernstian electrode reaction at an RDE is given by the following expression when both the oxidized and reduced forms of the redox couple are present in solution:

$$E = E_{1/2} + \frac{RT}{nF} \ln \frac{i_l^c - i}{i - i_l^a} \tag{17.81}$$

where $E_{1/2}$ is the half-wave potential of the redox couple and i_l^c and i_l^a are the cathodic and anodic limiting currents, respectively. $E_{1/2}$ is related to the formal potential of the redox couple, $E^{0\prime}$, by the expression

$$E_{1/2} = E^{0\prime} + \frac{RT}{nF} \ln \left(\frac{D_R}{D_O} \right)^{2/3} \tag{17.82}$$

where D_R and D_O are the diffusion coefficients of the reduced and oxidized species, respectively. The general shape of a Nernstian RDE wave is identical to that for a current-sampled conventional voltammogram.

In the *rotating ring-disk electrode* (RRDE) technique, a thin ring surrounds the disk and is electrically isolated from it by a thin insulating annulus. The potentials of the ring and disk are controlled separately by means of a bipotentiostat, which is a device for controlling the potentials of two working electrodes versus a single RE simultaneously. An electroactive species can be made to undergo reduction (oxidation) at the disk electrode and then oxidation (reduction) at the ring electrode as it is swept from the disk to the ring by fluid flow across the face of the rotating electrode. The efficiency with which the species originating at the disk is "collected" at the ring is expressed through the equation

$$N = -\frac{i_{ring}}{i_{disk}} \tag{17.83}$$

where N is the collection efficiency and i_{ring} and i_{disk} are the currents observed at the ring and disk electrodes, respectively. The quantity N depends on the electrode geometry, and theoretical equations are available that allow its calculation (Albery and Hitchman 1971). The applicability of the RRDE technique is comparable with the nonconvective reversal techniques like cyclic voltammetry, double potential step chronoamperometry, and reverse-current chronopotentiometry, which are often used to investigate the fate of a product resulting from an initial electron transfer reaction. Variation of the parameter N from its value in the case of a simple, stable product can be used for diagnostic purposes and to obtain quantitative information about the kinetics of coupled chemical reactions. The added advantage of the RRDE technique is that measurements may be made under steady-state conditions. Some potential applications of the RDE/RRDE have been summarized (Czichos et al. 2011; Delahay and Tobias 1966; Gerischer and Tobias 1984; Newman 1962; Papavinasam 2014).

17.12.10 Charge and Capacitance Measurements

The formation of adsorbed reactants or intermediates is common in electrochemical processes. The coverage, θ, of an adsorbed species is, therefore, an important parameter in the understanding of reaction mechanisms.

The quantitative measurement of adsorbate coverage electrochemically can be carried out in two ways:

(a) The amount of charge required wholly to oxidize or reduce the layer may be measured and the surface coverage calculated from Faraday's law or from comparison with a reference adsorbate on the same surface (*charge of electrode film*).

(b) The capacitance of the double layer can be measured and compared with that found for the "bare" surface under identical conditions (*capacitance of electrode film*).

If the amount of charge passed for complete conversion of a surface film is Q_B and the number of electrons per adsorbed molecule required is n, then it is clear that

$$Q_B = nF\Gamma \tag{17.84}$$

where Γ is the surface coverage in moles. If the maximum surface coverage for the species is Γ_{max}, corresponding to a charge Q_B^{max}, then the coverage, θ, is given by

$$\theta = \frac{Q_B}{Q_B^{max}} \tag{17.85}$$

Note that this is an operational definition and Q_B^{max} may not correspond to complete coverage of the surface. To relate θ as measured in Eq. (17.85) with the true surface area, at least on platinum, it is common to measure the charge passed in oxidation of the hydride region of the cyclic voltammogram. This charge, denoted Q_H, takes the value $210\,\mu C\,cm^{-2}$ for smooth polycrystalline platinum and is largely independent of the sweep rate. Furthermore, if a partial electrode film is already present, the hydride layer will only form on the unoccupied part of the surface, and if the hydride oxidation charge is now Q_H^F, then

$$\theta = \frac{Q_H - Q_H^F}{Q_H} \tag{17.86}$$

This type of measurement is shown in Figure 17.65, which shows the cyclic voltammogram for platinum in sulfuric acid in the absence (dotted line) and presence (continuous line) of methanol. The region shown shaded with slanting lines can be used to estimate Q_B and hence to calculate θ from Eq. (17.86), and the region shaded with horizontal lines can be used to calculate θ from Eq. (17.85) and to estimate the value of n.

Experimental details are reasonably straightforward. At the beginning of the experiment, the surface must be

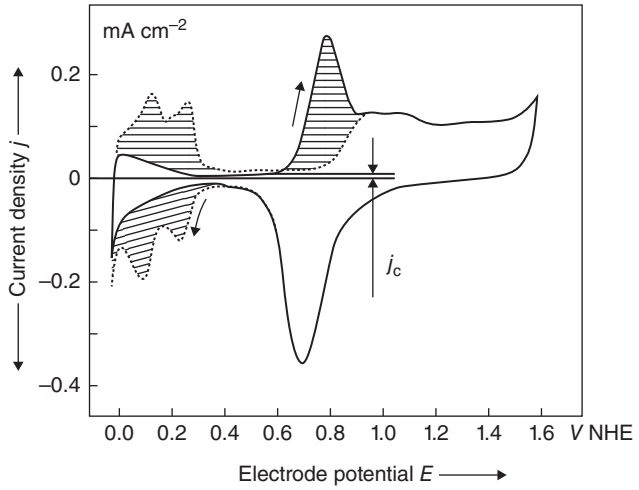


Figure 17.65 Cyclic voltammogram ($\upsilon = 100\,\text{mV s}^{-1}$) for the determination of electrode coverage. Dotted line: measurement in the base electrolyte of 0.5 M H_2SO_4. Continuous line: measurement following adsorption of methanol at 0.5 V versus NHE from a 0.25 M solution of methanol in 0.5 M H_2SO_4.

fully cleaned and prepared in a reproducible manner, and the electrode must then be maintained under potential control at all times during the deposition of the film. The determination of the value of Q_B can, in principle, be carried out in the same solution from which the film is adsorbed, but this carries the obvious danger of charge transfer to the solution itself. To avoid this, while at the same time retaining the potential control, necessitates a cell design capable of replacing the adsorbate solution with one corresponding only to the background electrolyte. This presents no problems if the adsorption process is slow and irreversible, but the rate at which the electrolyte can be exchanged in simple cells is limited, and if very short adsorption times are to be measured, more attention has to be paid to cell design.

If C_0 is the capacitance of the electrolyte double layer in the absence of film formation and C the capacitance measured after an adsorbed film has formed, then in general $C < C_0$, since the presence of an adsorbed layer will increase the thickness of the double layer. Assuming that the decrease, $C - C_0$, is proportional to the coverage of absorbed species and that C_{min} is the measured capacitance for the case of maximum coverage, then

$$\theta = \frac{C_0 - C}{C_0 - C_{min}} \tag{17.87}$$

Experimentally, again the method is straightforward: the electrode surface must, as before, be cleaned and prepared in a reproducible state, and the capacitance measured by AC method as described above. A powerful variant is to use AC cyclic voltammetry, in which the capacitance of the surface is measured continuously by the techniques described above as the electrode is scanned; this allows the possibility of following film formation in real time during a potential sweep. This is frequently termed tensammetry and was a method used to identify the presence of adsorbed surfactants in polarographic experiments (Lipkowski and Ross 1992).

17.13 Nontraditional Electrochemical Methods

Apart from the classical methods described above, there are a few more techniques, purely electrochemical, that have been used in the area of high temperature corrosion, particularly in the last three decades, and that deserve attention. They are electrochemical impedance spectroscopy (EIS), electrochemical noise (ECN), and solid-state voltammetry.

17.13.1 AC Impedance Plots

AC impedance plots are well-established techniques, especially for the study of liquid systems, but here we will be focused on ionic solids that are important materials in high temperature corrosion systems.

Conductivity measurements are normally carried out under AC conditions because polarization effects are minimized. Many electrochemical parameters including conductivity are a function of the applied frequency. This is because the alternating current is out of phase with the applied AC voltage, and this perturbs the various processes within the cell (such as surface, interfacial, and bulk ionic transport, double-layer formation at the electrode–electrolyte interfaces, and charge-transfer reactions at working electrodes) in different ways.

One type of frequency dependence occurs when electromagnetic vibrations, particularly those in the microwave and far-IR region, are transmitted through an ionic solid. What is discussed here, however, is the dependence of the *impedance*, Z, on the angular frequency, ω, of the small-amplitude-applied AC electric field. Z is a complex quantity involving not only resistance, R, but also capacitance, C, and inductance, L, and the Z–ω relationship is usually represented in the complex plane in the form of an impedance plot, admittance plot, permittivity plot, or modulus plot. In principle, the various forms of impedance spectra provide detailed and separate information about many of the processes within the electrochemical cell. This is done by comparing the experimental plots with those that would have been generated by model systems called *equivalent circuits*. These consist of resistances, capacitances, and/or inductances in appropriate series and/or parallel combinations. The weakness of the method is that the choice of equivalent circuit is not unique. For example, resistances and capacitances can be combined on the basis

either of a Maxwell model or of a Voigt model (which involve quite different series and parallel combinations) to provide the same overall impedance. The appropriate choice can only be made on the basis of assumptions about the relative configurations of, and importance of, the various parts of the cell process that cause the impedance. The different plots emphasize different regions of the frequency spectrum, and therefore the choice of the most appropriate plot depends on which part of the cell process is dominant.

EIS is a very well-established technique, and an outline of its basic principles will be given here since the fundamentals of the method as applied to solid-state systems have been comprehensively reviewed from 1976 Mahan and Roth (1976) until recently.

The AC voltage and current across a cell have the form

$$V = V_{\max} \sin(\omega t) \tag{17.88}$$

$$I = I_{\max} \sin(\omega t - \phi) \tag{17.89}$$

where ϕ is the phase angle. If ϕ is negative, so that the current leads the voltage, the impedance is composed of a frequency-independent resistance term, R, and a capacitance term, $-j/\omega C$ or $-1/j\omega C$, where $j = (-1)^{1/2}$. If ϕ is positive, then the V leads I, and Z is composed of R and an inductance term, $+j\omega L$. In the complex plane representation, real quantities, i.e. those not involving j, are plotted on the x-axis, and imaginary quantities are plotted on the y-axis. The conventional Argand diagram used by electrical engineers displays positive imaginary quantities, i.e. inductances, in its upper part and negative imaginary quantities, i.e. capacitances, in its lower part. Because not so many inductive processes take place in electrode processes, electrochemists normally invert the y-axis so that the data, which are of a predominantly R/C nature, fall mainly in the upper quadrant of the diagram. This convention will be used in the description here.

The R, C, and L components can be combined in series or in parallel. A circuit consisting of a resistance, R_s, in series with a capacitance, C_s, will have an impedance:

$$Z = R_s - j/\omega C_s \tag{17.90}$$

The impedance plot in this case is a vertical straight line intersecting the x-axis at R_s; the y-coordinate decreases as ω increases. The magnitude of $Z(\omega)$ is the length of a line from the origin to the point on the plot corresponding to the value of ω; this line is inclined at ϕ to the x-axis. For a parallel network involving resistance, R_p, and capacitance, C_p, then

$$\frac{1}{Z} = \frac{1}{R_p} + j\omega C_p = Y \tag{17.91}$$

where Y is the admittance. The impedance plot is now a semicircle of radius $R_p/2$, which meets the x-axis both at R_p (for which $\omega = 0$) and the origin ($\omega = \infty$). Z is again given by the length of the line from the origin to the plot.

Additional complications arise in the equivalent circuit used to model a real cell incorporating a working electrode. Elements must be present that account for the impedances due to the various electrode processes discussed in Chapter 6, namely, the double-layer capacitance, C_{dl}, the charge transfer, and the diffusion steps. The charge-transfer contribution can be characterized by a *transfer resistance*, R_t, since the current that flows as a result of the applied voltage is in phase with the potential. R_t is usually proportional to the rate of the electrode reaction. The concentration-dependent diffusion term is a function of frequency, however, because the bulky ions move too slowly to respond in phase with the applied potential at high frequencies.

A suitable ansatz (or simplified expression) for the interfacial impedance at a working electrode is

$$Z = [j\omega C_{dl} + 1/(R_t + W)]^{-1} \tag{17.92}$$

where W, the *Warburg impedance*, is given by

$$W = \lambda\omega^{-1/2} - j\lambda\omega^{-1/2} \tag{17.93}$$

the Warburg coefficient, λ, being a function of the concentrations and the diffusion coefficients of the oxidizing and reducing species.

Ionic solid systems often involve grain boundaries between polycrystals and interparticle boundaries within compacted powders, and elements have to be incorporated in the equivalent circuit to account for these. Inductive effects can also arise, particularly at high frequencies. These can be caused by the measuring lead impedance and also by rough electrode–electrolyte interfaces. They give rise to appropriate semicircles, vertical lines, and Warburg lines that lie in the lower quadrant of the conventional electrochemical complex diagram. The high- and low-frequency ends are inverted with respect to the capacitance contributions.

The selection of the correct combination of elements to produce an equivalent circuit that corresponds to an experimental plot that may well take the form of a faintly wavy, roughly vertical line requires not only ingenuity but also faith. In practice, to select the most likely out of several equivalent circuits, assumptions are made about which processes are physically likely to be working in series and which are in parallel. Also, the separation of bulk and interfacial effects is aided by the fact that they depend in different ways on sample length and area (McGeehin and Hooper 1977).

Highly convoluted combinations of lines and semicircles in the impedance plot can sometimes be more easily interpreted from an alternative complex plane representation. An admittance plot has conductivity rather than resistance as the real axis and is suited to predominantly parallel

networks. It is also effectively possible to interchange the real and imaginary axes by considering the permittivity (or its reciprocal, the modulus) in place of the impedance (or its reciprocal, the admittance). The permittivity, ε, is defined as

$$\varepsilon = C_p l / A\varepsilon_0 \tag{17.94}$$

where l and A are the cell length and area and ε_0 is the permittivity of free space ($= 8.854 \times 10^{-11}$ F cm^{-1}). In a permittivity plot, the real axis is C_p and the imaginary axis is $Y/j\omega$; in a modulus plot, the real axis is $1/C_s$, and the imaginary contribution is $j\omega Z$. The merits of these alternative representations have been reviewed elsewhere.

The normal range of the frequency, $f(=\omega/2\pi)$, is 100 Hz to 100 kHz, but the regime down to 1 mHz can provide valuable information about the charge-transfer process and assist in separating bulk and interfacial behavior. High-frequency studies can also be carried out.

Experimentally, bridge techniques were much used, but because the determination of a complete plot could take many hours, during which time the cell behavior could change, it is now common to use automated systems.

Many recent impedance studies of solid-state systems have been carried out to elucidate electrokinetic behavior, to explain cell failure, and to provide reliable conductivity values. 2D nucleation has been investigated, and the behavior of powered and sintered systems studied. Temperature-dependent Warburg coefficients had to be used to explain the behavior of solid–solid interfaces. Some examples of impedance studies on a selection of high temperature materials are given in recent papers and books (Bosch 2005; Lasia 2014; Liu et al. 2006; Orazen and Tribollet 2008).

17.13.2 Electrochemical Noise

The foundations of ECN technology for corrosion studies lie in the original work undertaken by Iverson (1968). Initial work studied the fluctuations of electrochemical potential (Hladky and Dawson 1982). Subsequently, the combination of electrochemical potential and current noise arising from the coupling current between two nominal identical electrodes was investigated in detail (Gabrielli et al. 1986). In 1986, Eden et al. introduced the concept of ECN resistance and described statistical methods for analysis of ECN (Eden et al. 1995). In the 1990s, important advances in ECN analysis techniques were made. Mansfeld et al. (1996) introduced the concept of spectral noise resistance (impedance) and studied the spectral noise resistance in the frequency domain. Bertocci and Huet (1997) further used power spectral density to study the spectral noise resistance on a firmer theoretical basis. The spectral noise resistance at the zero-frequency limit and the polarization resistance were found to be well correlated (Bertocci et al. 1997).

Systems used for measuring ECN signals have several key components that depend on the type of noise measurements being undertaken. A typical arrangement is shown in Figure 17.66.

It is common practice to use a three-electrode cell (sensor). The noise signals being measured require some form of signal conditioning, and this is included in the interface. For the purpose of logging data from a series of sensors, a multiplexer is often incorporated. This may be configured in two particular ways, either before or after the signal conditioning units; the latter is shown in the diagram. The data acquisition unit and the computer controller may be either an integrated subsystem or separate devices.

ECN can be performed with a single working electrode (WE), under potentiostatic or galvanostatic control, or with two WEs connected through a zero resistance ammeter (ZRA). Figure 17.66a,b shows how to measure the ECN and EPN (electrical potential noise) generated by a single WE. Under potentiostatic control, the current $(I_o + \Delta I)$ is measured across the resistor R (Figure 17.66a) or using a current-to-voltage converter connected to the WE. For

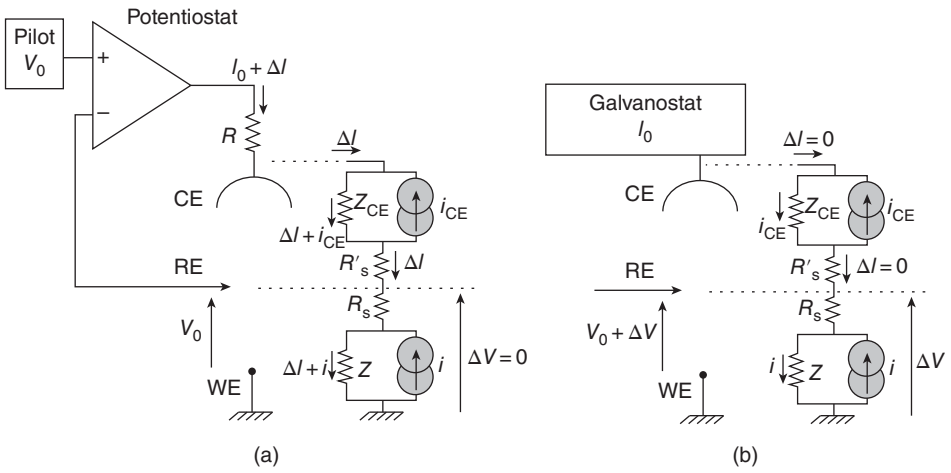


Figure 17.66 Electrical scheme and equivalent circuit of the measurement methods of ECN and EPN of a single WE. (a) Potentiostatic method. (b) Galvanostatic method.

EPN measurements (Figure 17.66b), ΔV is measured between the RE and the WE. In the case of measurement at the corrosion potential ($I_o = 0$), the galvanostat is not needed. Both figures also exhibit the equivalent circuit between the counter electrode (CE) and the WE, in which the fluctuations due to anodic and cathodic processes occurring on the CE and WE are modeled by current noise sources i and i_{CE} in parallel to the respective impedances Z and Z_{CE} (which include double-layer capacitances), in a manner similar to the thermal noise modeling explained above. The RE is here considered to be noiseless, and the thermal noise of the solution resistance R_s is neglected. Ohm's law between the RE and WE gives for Figure 17.66b:

$$\Delta V(f) = Z(f)\, i(f) \tag{17.95}$$

In this equation, all terms are complex and frequency dependent; $\Delta V(f)$ and $i(f)$ are the FTs of the real and time-dependent quantities $\Delta V(t)$ and $i(t)$. In the same way, ΔV in Figure 17.66a, which is equal to 0 since the electrode potential is controlled, is

$$\Delta V(f) = R_s \Delta I(f) + Z(f)[\Delta I(f) + i(f)] = 0 \tag{17.96}$$

which gives

$$\Delta I(f) = -\frac{Z(f)\, i(f)}{R_s + Z(f)} = -i(f) \tag{17.97}$$

when the solution resistance is negligible, or, in the time domain

$$\Delta I(t) = -i(t) \tag{17.98}$$

Equations (17.95) and (17.97) show that both EPN ΔV and ECN ΔI do not depend on the current fluctuations i_{CE} generated by anodic or cathodic processes on the CE and, second, that they obey equation for the Fourier transform $\Delta I(f)$ and $\Delta V(f)$ of $\Delta I(t)$ and $\Delta V(t)$:

$$\Delta V(f) = -Z(f)\Delta I(f) \tag{17.99}$$

where $Z(f)$ is the impedance of the WE at frequency f, which can also be rewritten as

$$\Delta V_g(f) = -Z(f)\, \Delta I_p(f) \tag{17.100}$$

where the indices g and p emphasize that ΔV_g and ΔI_p are not measured in the same experiment (as in cell configurations with two WEs), but in two different experiments, under galvanostatic and potentiostatic control, respectively. The derivation also shows that the current noise flowing in the WE is $\Delta I + i = 0$ under potential control and i under current control. The current noise generated by corrosion processes on the WE crosses the solution toward the CE in the former case, while it flows back toward cathodic areas on the WE in the latter.

Many sources of ECN have been identified in corrosion systems, with some of them appearing in all systems, while others are specific to the system under investigation:

1. *Fluctuations of the concentration of the reacting species at the metal–electrolyte interface*. These fluctuations may be first induced by elementary fluctuations in the flux of molecules or ions. The PSD of the resulting ECN can be deduced from the reaction mechanism, involving chemical and electrochemical reactions, by considering that the flux fluctuations can be modeled by white Poisson noise (Gabrielli et al. 1993).
2. *Fluctuations in surface morphology*. Metals are generally polycrystalline materials, consisting of grains of different forms, sizes, and orientations. Various chemical elements are concentrated on the grain boundaries. In addition, cracks, inclusions, voids, etc. are present inside metals. These microstructural features cause metals to be susceptible to random variations in physical properties and, consequently, in their corrosion behavior.
3. *Fluctuations in electrode activity*. Breakdown and repair of passive films are widely known processes for generating current transients of large amplitude, due to the nucleation, growth, and death of metastable pits. Two types of current transients have been reported in the literature (Gabrielli et al. 1990). The first one, defined by a slow rise followed by a sudden decay, seems to be characteristic of pitting corrosion or iron and iron-based alloys. This shape has been interpreted as a sudden decrease in the corrosion rate in the pit due to a rapid change between different steady states of these metals. The second transient type, defined by a sudden rise followed by a slow decay, seems to be characteristic of pitting corrosion of aluminum and to nonchemical initiation of the localized corrosion, such as abrasion, scratching, and laser illumination. This transient is related with a sudden failure of the protective layer, due to a drastic change in the anodic reaction resistance on a small area of the electrode, followed by a repassivation process.
4. *Fluctuations in electrode active surface*. Various phenomena may lead to changes in the electrode active surface. For example, during stress corrosion cracking (SCC), the propagation of a crack provokes the formation of bare metal at the crack tip. Generation on the bare surface in sudden bursts results in current or potential transients whose shape and sign depend on the anodic and cathodic reactions occurring on the bare surface in the crack tip solution. In contrast, hydrogen bubbles growing on an electrode in acidic medium screen the electrode surface, yielding locally nonuniform current distribution around the attached

bubbles, which can be considered in first approximation as a decrease in active surface area. The growth and detachment of bubbles give rise to fluctuations in the size of the active surface, which lead to fluctuations in the ohmic component (changes in solution resistance) and in the kinetic component (changes in the charge-transfer and polarization resistances) of the ECN signal.

5. *Fluctuations in electrolyte velocity*. For corrosion processes controlled by mass transport, fluctuations in electrolyte velocity yield fluctuations in the concentration of reacting species at the surface and therefore give rise to ECN. In a model system, such as the oxidation of potassium ferri–ferrocyanide at the diffusion limiting plateau on a platinum electrode, natural convection in a quiescent electrolyte has been shown to generate current fluctuations of very low amplitude, which could be reduced to an extremely low level by adding a gel layer on the electrode, thus "freezing" the electrolyte. On the contrary, ECN of much larger amplitude was measured when stirring the electrolyte or when using an RDE so as to work in laminar or turbulent flows. This effect is likely to occur in pipelines in which turbulence is enhanced by the presence of oil/gas/brine mixtures. This effect has also, for example, been observed during corrosion of carbon steel in HCl at pH 3, where ECN was drastically increased by electrolyte movement generated by stirring or by a submerged jet.
6. *Fluctuations due to external perturbations*. Localized corrosion in abrasion/erosion systems is provoked by continuous impingement of solid particles or gas bubbles that locally break down the passive film or remove the corrosion product film. Under potentiostatic control this gives rise to current transients very similar to those observed in pitting corrosion of aluminum triggered by chloride ions with sudden rise and slow decay. Mechanical damage produced by scratching or laser illumination also induces localized corrosion and, consequently, high levels of ECN.

Recent developments in ECN and applications in studies of high temperature corrosion are described by Gabrielli and Williams (2014), Gao et al. (1990), Mabbutt et al. (2013), Mansfeld et al. (2000), and others.

17.13.3 Solid-State Voltammetry

In the field of aqueous corrosion, electrochemical techniques are well-known avenues to investigate key characteristics of a corrosion system under study. Thermodynamic information can be obtained on the equilibrium potentials of electrode reactions as well as kinetic information such as diffusion coefficients for species participating in these reactions. High temperature electrochemical techniques using appropriate solid-state electrochemical cells, sensors, pumps, etc. offer opportunities to electrochemically study high temperature oxidation, defect structures, electrical conductivities, and diffusivities of high temperature materials. For these developments, the principles of the parabolic oxidation law and solid electrolyte cells have been derived from the same origin developed by Carl Wagner, being proved that the solid electrochemical techniques are, in fact, essential and useful for fundamental studies of high temperature oxidation (Saito 2000; Weast 1986).

Historically, electrochemistry in the absence of a bulk liquid phase has focused on the problems of energy storage and production. Only on the last three decades, it has become possible to apply conventional electrochemical methods with solid-state electrolytes for the characterization of materials, measurement of electron transfer rates, determination of analytic species using amperometric sensing, etc. The characterization of high temperature materials by *solid-state voltammetry* primarily has focused on superionic solids, ionically conducting compounds, and diverse mixed ionic–electronic materials (Dimitrov et al. 1993; Kawamura et al. 1995; Maruyama et al. 1987).

With transient electrochemical measurements in solid-state systems, the ultimate goal is to have the situation where regardless of the details of the charge propagation mechanism, the overall mass transport is diffusional and related to apparent (effective) diffusion, D_{app} (D_{eff}). Clearly, it is important to distinguish between the semi-infinite diffusion and thin-layer-like cases. The diagnostic criterion applicable to a thin-layer system is that, for a given experimental time, t, the diffusion layer thickness, $(2D_{app}f)^{1/2}$, is smaller than the material thickness, d. At the semi-infinite linear diffusion limit, $(2D_{app}f)^{1/2} \ll d$, the voltammetric peak shows the classical diffusive tail, and the peak current, i_p, depends linearly on the square root of scan rate, $\upsilon^{1/2}$, according to the Randles–Sevčik dependence (see Eqs. (17.67) and (17.69)). At the thin-layer limit, $(2D_{app}t)^{1/2} \gg d$; now the shape of the voltammetric peaks is more Gaussian type, and i_p depends linearly on υ.

It is assumed above that the redox reactions are electrochemically reversible and there is no significant migration and ohmic limitations. However, such problems could appear, particularly at shorter film scales, and they will complicate the interpretation of voltammetric experiments in solid-state systems. Hence, it is crucial to perform diagnostic experiments, which include the plotting of dependencies of i_p on $\upsilon^{1/2}$ or υ, before any quantitative conclusions are made. For example, a nonzero intercept in the linear $i_p - \upsilon^{1/2}$ dependence for a metal hexacyanoferrate pressed powder (Kulesza and Galus 1992) was indicative of some, presumably ohmic, limitations in the

predominantly diffusional charge propagation model that is characteristic of the system. Nevertheless, conventional voltammetric measurements can provide basic, qualitative, or semiquantitative information about the thermodynamics and dynamics of redox reactions in the investigated material.

The development of ultramicroelectrode (UME) techniques (Heinze 1993) has led to an improvement in the quality of solid-state voltammetric data as well as to new diagnostic and analytical possibilities.

One of the most useful properties of UMEs is, in addition to their compact size and utility in characterization of small samples, that they are much less susceptible to distortion caused by uncompensated resistance because the small currents make ohmic drops negligible. Further, UMEs have redefined the capabilities of cyclic voltammetry at fast scan rates as a result of their much smaller uncompensated resistance and low background (capacitance) currents (Sequeira and Santos 2010).

An important feature of the UME-based solid-state voltammetric measurements of certain bulk, mixed-valence, ionically conducting materials is that, by analogy to conventional solution experiments, the mass transport depends on the time domain or, more precisely, on the value of the dimensionless time parameter $\tau = 4D_{app}t/r^2$ where r is the electrode radius. In the fast scan rate (short-time) experiments, where $\tau \ll 1$, the diffusion field is small compared with the electrode radius; here, the charge propagation mechanism follows the pattern predicted for linear (planar) diffusion perpendicular to the electrode surface. The result is a typical peak-shaped voltammogram with a diffusional tail. For reversible processes in materials characterized by fast (interfacial and bulk) charge transport, the peak current follows the Randles–Sevčik relationship, in which i_p is proportional to $v^{1/2}$ (with effectively a zero intercept).

The latter dependence is an important diagnostic criterion for the applicability of the planar diffusion model with no kinetic limitations. On the other hand, large values of τ, which correspond to the slow scan rate (long-time) experiment, cause the hemispherical diffusion layer to greatly exceed the size of the electrode; here, spherical (radial) diffusion becomes predominant. In the limit, this situation produces a sigmoidal steady-state voltammogram. Currents generated at UMEs are dependent on their geometry; for a disk-shaped microelectrode, the limiting plateau current is as follows:

$$i_{lim} = 4nFrD_{app}C_o \tag{17.101}$$

An important case is that of material with properties that are amenable to interrogation in either experimental time domain (linear of spherical diffusion) at an UME. By performing cyclic voltammetric or potential step experiments at each limit, data are generated that allow calculation of the concentration of mixed-valence redox centers, C_o, and the apparent (effective) diffusion coefficient, D_{app} (D_{eff}), for charge propagation in the material. It is noteworthy that this approach is designed for bulk materials; that is, for a given experiment time, t, the thickness of the material must exceed the diffusion layer thickness $(2D_{app}t)^{1/2}$. In addition, it is expected that the systems are characterized by fast dynamics of charge propagation. For materials that have a rather low D_{app} (e.g. below 10^{-10} cm^2 s^{-1}), impractically slow scan rates or extraordinary small UMEs are required for radial diffusion ($\tau \gg 1$).

A more focused study of initial oxidation of engineering alloys by high temperature cyclic voltammetry has been described by Öijerholm et al. 10 years ago (2007). By using an oxygen ion-conducting electrolyte, i.e. yttria-stabilized zirconia (YSZ) and an RE whose potential is fixed by the ambient gas, measurements could be performed at temperatures between 500 and 800 °C. The CV measurements were carried out in a four-electrode cell, as shown in Figure 17.67. The CE consists of a sputtered Pt layer on one of the large faces of a rectangular piece of single crystalline YSZ. On the opposite side of

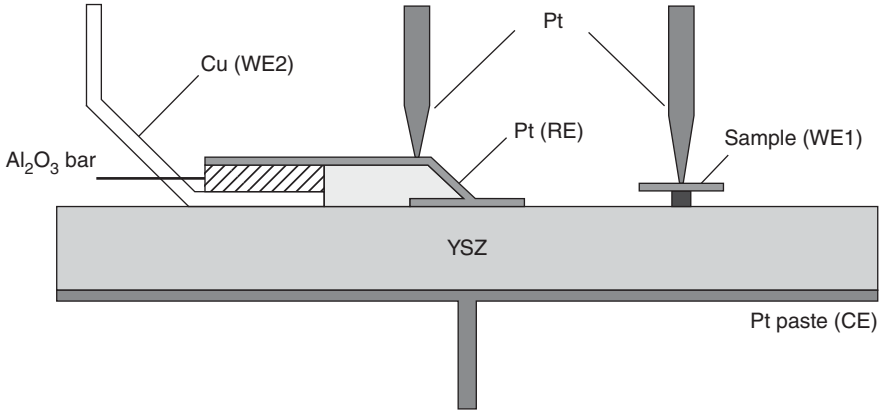


Figure 17.67 Schematic cross-sectional image of the experimental setup (Öijerholm et al. 2007).

the YSZ crystal, one quasi-RE and two working electrodes (WE1, WE2) are contacted by means of a spring force. The RE consists of a small Pt plate, whose potential is determined by the oxygen activity in the ambient gas. WE1 is the sample to be investigated, and WE2 is a Cu wire used for calibration purposes. To keep a low oxygen partial pressure, the electrochemical cell was flushed with high purity nitrogen gas.

Because the oxygen partial pressure may drift in the electrochemical cell during a measurement, it was necessary to calibrate the RE directly after each measurement on the sample. That was done by an independent CV measurement on the Cu electrode (WE2) immediately after the CV curve of the Cu_2O/Cu system obtained from that measurement gives the potential of the RE relative to the potential of the Cu_2O/Cu electrode, $E_{\text{vs.RE}}^{Cu_2O/Cu}$. The standard potential of the Cu_2O/Cu electrode with respect to the reversible oxygen electrode (ROE) at 1 atm O_2 (or unitary fugacity of oxygen), $E_{\text{vs.ROE}}^{Cu_2O/Cu}$, could be calculated from thermodynamic data. A correction of the potential scale of the measurements on the samples can then be made according to Eq. (17.102):

$$E_{\text{vs.ROE}}^{\text{sample}} = E_{\text{vs.RE}}^{\text{sample}} - E_{\text{vs.RE}}^{Cu_2O/Cu} + E_{\text{vs.ROE}}^{Cu_2O/Cu} \tag{17.102}$$

Because the total reaction in the system YSZ/electrode/oxygen is given by

$$2V_{O_{YSZ}}^{\bullet\bullet} + O_2 + 4e^- = 2O_{O_{YSZ}}^{X} \tag{17.103}$$

The oxygen activity in the surrounding of the sample (WE1) electrode ($a_{O_2}^{\text{Sample}}$) is related to $E_{\text{vs.ROE}}^{\text{sample}}$ by the Nernst equation

$$\frac{a_{O_2}^{\text{Sample}}}{a_{O_2}^{\text{ROE}}} = \exp\left(\frac{E_{\text{vs.ROE}}^{\text{sample}} 4F}{RT}\right) \tag{17.104}$$

in which the activity of the ROE ($a_{O_2}^{\text{ROE}}$) is equal to 1.

A change in the sample potential is therefore directly related to the oxygen activity experienced by the sample. A scan from low to high potentials at a given temperature consequently reveals at which oxygen activity the sample oxidizes by the appearance of current peaks.

By choosing samples of Ni, Co, and Fe alloys with electrode contact area of 0.007 cm^2, CVs were obtained for 100 $mV\,s^{-1}$ scan rates at 500, 600, and 800 °C. Figure 17.68 shows the voltammograms recorded for a 26.5Cr iron alloy; these shapes are similar to the CV for iron published by van Manen et al. (1992). The peaks correspond to the redox reactions FeO/Fe, Fe_3O_4/FeO, and Fe_2O_3/Fe_3O_4, respectively, by comparing the standard potential calculated from literature data (Weast 1986) (arrows in the diagrams) with the measured standard potential as described by Fafilek et al. (1996). It was assumed that the large current due to oxygen reduction (pumping) at low potentials covered the peaks for Cr_2O_3 and $FeCr_2O_4$. The high current observed at high potentials was considered to include contributions from both oxygen evolution (pumping) and oxidation reaction leading from chromium (III) oxide to chromium (VI) oxide.

The voltammogram curves are clear, oxidation of Fe into different valence oxides being observed by the multiple peaks. Goncharov (2004), Kofstad (1988), and Tsuji and Hirokawa (1996) also describe the formation of iron oxides on the surface of Fe–Cr alloys in the investigated temperature range of 500–800 °C.

Further high temperature corrosion studies by solid-state voltammetry are provided by Chang et al. (2015), Fafilek (1998), and Gellings and Bouwmeester (1997).

17.14 Combined Electrochemical Methods

The traditional and nontraditional purely electrochemical measurements can be very precise, but they give no direct information on the microscopic structure of the electrochemical interface. In this section, we treat several methods that can provide such information. None of them are endemic to electrochemistry; they are mostly skillful adaptations of techniques developed in other branches of physics and chemistry.

17.14.1 Scanning Electrochemical Microscopy

Scanning electrochemical microscopy (SECM) is a surface analytical technique that can determine local information on a microscopic scale. It has been developed for a wide range of application in the area of chemical activity imaging, due to its ability to probe interfacial electron and ion transfer processes occurring nonuniformly at interfaces (Zhu et al. 2007, 2008). It works by measuring a current on an UME immersed in a solution containing an electroactive species (commonly termed as redox mediator) and located in close proximity to a reactive substrate surface. A typical SECM setup is shown in Figure 17.69. It uses a piezoelectric-based positioner and controller to precisely position the UME (tip) in any of three axes at a known scan speed (typically 1–20 $\mu m\,s^{-1}$). A bipotentiostat is employed to simultaneously control the potential of both the tip and the substrate against the RE and to monitor the faradaic current flow. Hardware on the PC supplies control signals to the piezo positioner and collects data from the tip and substrate. The UME is usually either a conductive disk of noble metal (such as Pt or Au) or a carbon fiber, with

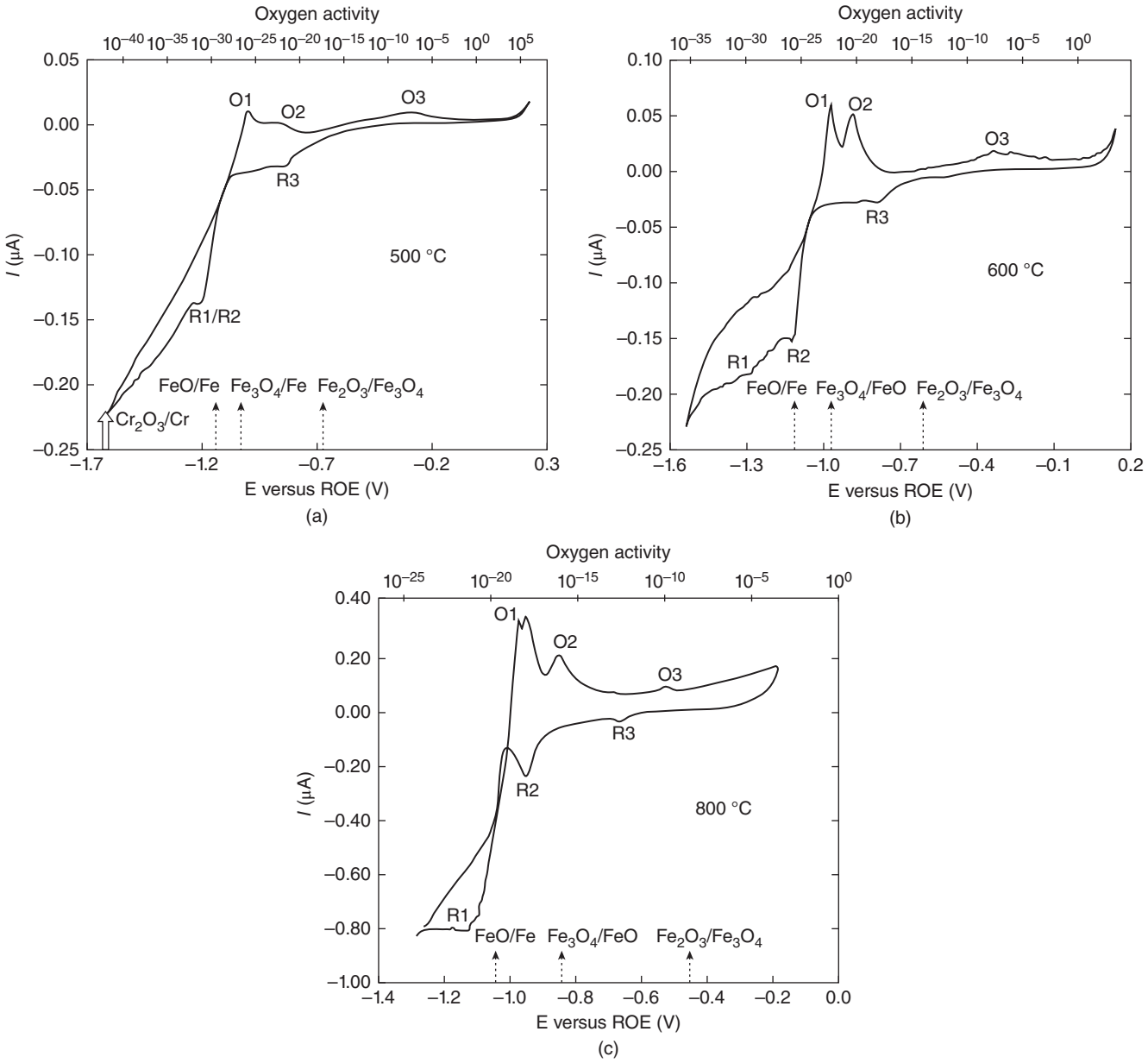


Figure 17.68 (a–c) Voltammograms recorded at 500, 600, and 800 °C for the ferritic stainless steel (Sandvik 4C54). The scan rate was 100 mV s^{-1} in all cases. The oxidation peaks are indicated with "O" and reduction peaks with "R." The calculated standard potentials for the redox reactions of iron are indicated with arrows. As an example, the calculated standard potential for the redox reactions of Cr is also shown in (a) (Öijerholm et al. 2007).

a diameter ranging from 2 to 25 μm, set in an insulating sheath of glass.

Substrates can be a variety of solid surfaces (such as metals) that perturb the electrochemical response of the tip, and this perturbation provides information about the nature and properties of the substrate and how they vary with position on the substrate surface. In practice, the UME is set at a sufficiently large potential where the tip current is controlled by the diffusion of the electroactive species. For a disk-shaped UME, the diffusion-limited current ($j_{T,\infty}$) can be calculated from the relationship (Bard and Mirkin 2001)

$$j_{T,\infty} = 4nFD_{C_0}a \tag{17.105}$$

where c_0 is the concentration of species in the electrolyte and a is the tip radius.

The most frequent mode of operation of SECM is the feedback mode, where only the tip current is monitored. When the tip approaches closely to a flat substrate,

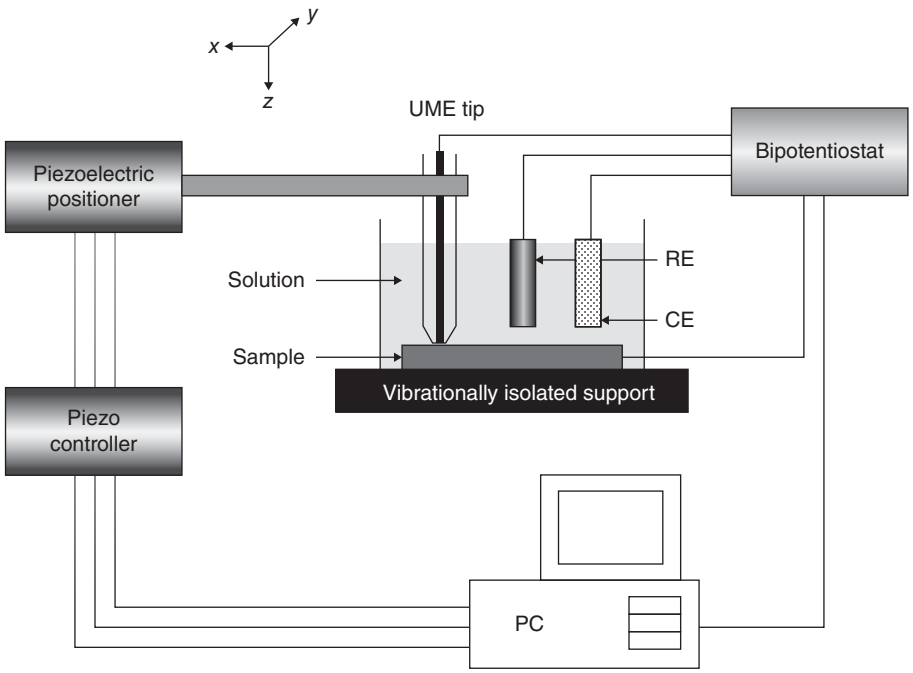


Figure 17.69 Typical SECM setup.

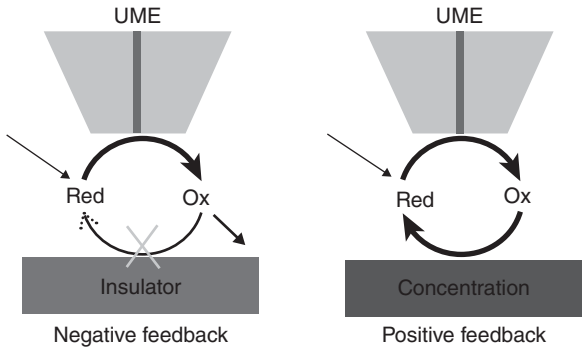


Figure 17.70 Illustration of feedback modes in SECM.

diffusion of the species from the bulk solution to the tip is blocked, and the tip current becomes inherently related to the electrochemical activity of the substrate. When the tip is approaching an insulating substrate, the tip current should noticeably decrease (negative feedback) since the concentration of electrochemically active species is limited. However, for a conductive substrate, the tip current should increase due to a regeneration current at the tip (positive feedback). Figure 17.70 illustrates the feedback modes in SECM.

For a substrate with different reactive sites, SECM measurements can be performed by scanning the UME tip laterally across the substrate surface to acquire SECM images. The surface is scanned with the UME tip at an initially fixed separation (i.e. in the constant height mode). However, due to surface topography, the tip to substrate separation varies as the scan is performed. Consequently, the tip current contains information on both the surface reactivity and the topography. However, probe approach curves (PACs) can be recorded at specific surface sites to separate the influences of topography and localized reactivity. A PAC is produced by recording the normalized current versus normalized distance as the tip approaches a surface site.

In many measurements, SECM is used in the constant height mode to examine the surface reactivity of a passive alloy. The UME is a 5 µm diameter disk-shaped Pt electrode insulated in a glass sheath with an RG value of 6, for example (the ratio of the radius of the insulating sheath to the radius of the conductive disk). Ferrocenemethanol ($0.9\,\text{mmol}\,\text{dm}^{-3}$), for example, can be used as the redox mediator in a classic $0.1\,\text{mol}\,\text{dm}^{-3}$ NaCl solution.

17.14.2 Infrared Spectroelectrochemistry

In *infrared spectroelectrochemistry* (IRSEC), absorption of IR radiation is a first-order process, and, in principle, a surface or an interface can generate a sufficiently strong signal to yield good IR spectra. However, most solvents, in particular water, absorb strongly in the IR. There is no special surface enhancement effect, and the signal from the interface must be separated from that of the bulk of the solution.

To minimize the absorption from the solution, optical thin-layer cells have been designed. The working electrode has the shape of a disk and is mounted closely behind an IR transparent window. For experiments in aqueous solutions, the intervening layer is about 0.2–2 µm thick. Since the solution layer in front of the working electrode is thin, its resistance is high; this increases the time required for

double-layer charging – time constants of the order of a few milliseconds or longer are common – and may create problems with a nonuniform potential distribution.

Two different techniques have been devised to separate the interfacial and the bulk signal. In the first one, IR spectra are recorded at two different electrode potentials and subsequently subtracted. In this way, the signal from the bulk is eliminated because it is independent of potential. The recorded spectra are usually presented in the form

$$\frac{\Delta R}{R}(\nu) = \frac{R_2(\nu) - R_1(\nu)}{R_1(\nu)} \tag{17.106}$$

where $R_1(\nu)$ and $R_2(\nu)$ are the reflectances at a frequency ν and at electrode potentials ϕ_1 and ϕ_2 that must be sufficiently far apart to yield significantly different spectra. The other technique uses the different surface sensitivity for s- and p-polarized light – the former has its polarization vector perpendicular, and the latter parallel to the plane of incidence. Due to the different boundary conditions, s-polarized light has a node at the metal surface, and p-polarized light an antinode. Therefore, only p-polarized light produces spectra that are sensitive to the interfacial structure. In *infrared reflection–absorption spectroscopy* (IRRAS), the polarization of the incident beam is modulated between s- and p-polarization. On subtraction, the bulk signal cancels, and an IR spectrum of the interface at a given potential is obtained. In contrast to *electrochemically modulated infrared spectroscopy* (EMIRS), this method gives direct as opposed to difference spectra, but it is somewhat less sensitive.

IRSEC can be used on all kinds of electrodes and for all substances that are IR active. It is particularly useful for the identification of reaction intermediates and has been used extensively for the elucidation of the mechanisms of technologically important reactions (Clark and Hester 1985; Gale 1988).

17.14.3 Electrochemical Surface Forces Apparatus

Electrochemical surface potentials and interfacial charge distributions influence technologically important processes such as electrochemical and electrocatalytic synthesis and, conversely, corrosive degradation, dissolution of inorganic surfaces, and the passivation of metals and alloys. Both anodic oxide growth and metal dissolution pose a critical hurdle that limits lifetime and performance of catalytic nanoparticles and nuclear waste storage containers.

Consequently, measurement and control of interfacial charge distributions and chemical reactions at electrode interfaces play a critical role in advancing toward higher performance materials, devices, and tribological systems. One unique path to controlling and manipulating both interaction forces and interfacial electrochemical reactions at material interfaces is through controlling and measuring the electrochemical surface potentials and electrochemical currents at confined interfaces.

Electrochemical surface forces apparatus (ECSFA) attachments that enable the measurement and control of both interaction forces and friction between similar and dissimilar opposing surfaces *in situ* in an electrolyte (as well as in weakly conducting and dielectric media) have been described by Valtiner et al. (2012). These newly ECSFA designs consist of a three-electrode setup, using a Pt CE, both atomically smooth and rough metal working electrodes, and a specifically designed Ag/AgCl (in 3 N KCl) micro-RE that provides stable and accurate reference potentials. Additionally, one of the surfaces can be mounted on a 3D sensor–actuator attachment, which enables independent and simultaneous force measurements and displacements of a surface in three orthogonal directions, allowing one to measure and correlate friction forces and applied electrode potentials. For this particular setup, the three-electrode setup is implemented in a miniature bath, allowing ECSFA measurements in small liquid volumes of about 1–2 ml (which is convenient when using expensive liquids and solutions). As opposing surfaces, both (i) atomically smooth back-silvered mica and (ii) atomically smooth back-silvered mica modified with a molecularly smooth self-assembly monolayer of (3-aminopropyl)-triethylsylane (APTES) deposited by means of vapor deposition are used. Figure 17.71 shows a schematic of the electrochemical attachment that was designed for the SFA 2000 (Israelachvili et al. 2010). White light multiple-beam interferometry allows the measurement of the separation distance between the two surfaces (with 0.1 nm resolution) and the surface geometry (with micrometer resolution) using the so-called FECO.

Valtiner et al. (2012) show that the ECSFA provides a powerful tool to study interfacial interaction forces and distances, while simultaneously interfacial chemistries, compositions, and ion distributions can be controllably modulated using electrode potential control or current control.

In summary, and focusing on corrosion and materials interfaces, the ECSFA provides a very useful tool not only for the study of oxide films grown on noble metals but also for studying cathodic metal deposition, dissolution of passive films, and various oxidation–reduction reactions of rheological and/or organic thin films adsorbed on electrochemically active interfaces.

17.14.4 Electrochemical Electron Spin Resonance

A free electron possesses a magnetic dipole moment whose component along the direction of an external applied magnetic induction B is

$$\mu = g\mu_B m_S \tag{17.107}$$

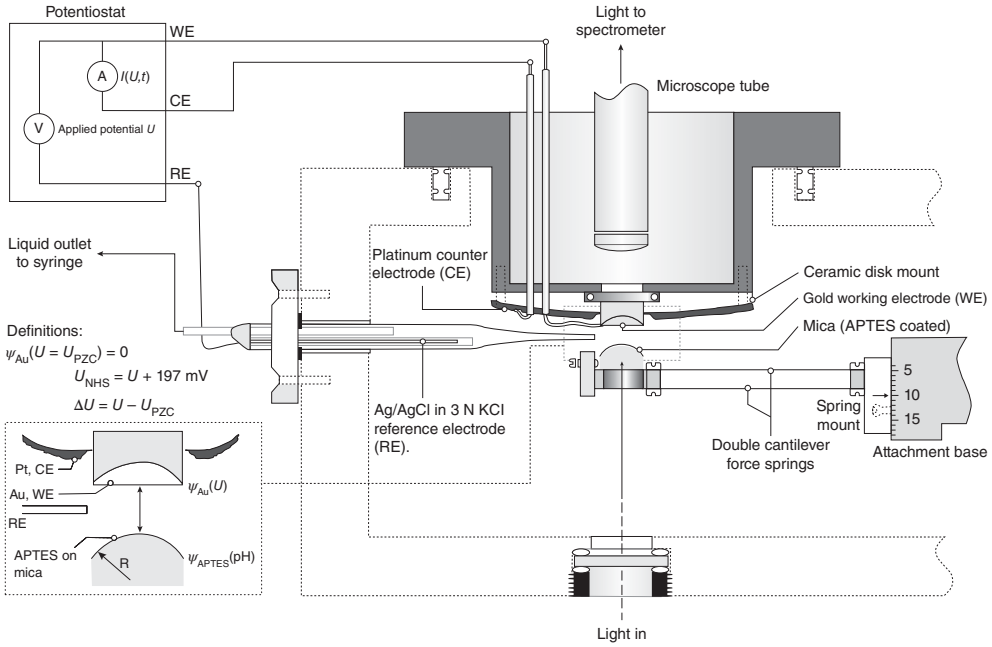


Figure 17.71 Schematic of the electrochemical three-electrode setup used in the ECSFA. In this setup, an external electrode potential is applied to the gold electrode and measures forces and distances using the procedure outlined in the text. Using $\Delta U = U - U_{PZC}$, the applied electrode potential, U, is referenced to the so-called potential of zero charge U_{PZC} for which $U = U_{PZC}$. At U_{PZC}, the effective gold surface potential ψAu(U_{PZC}), as measured by means of force–distance data, is zero. U_{PZC} depends on the surface orientation and roughness (Valtiner et al. 2012).

where m_S is the spin quantum number component along B, g is a number close to 2 for a free electron, and μ_B is the Bohr magneton of magnitude $\frac{e_0 h}{4\pi m_e} = 9.274 \times 10^{-24}\,\mathrm{J\,T^{-1}}$. The energy of this dipole in an external magnetic induction, B, is

$$E = -\mu B = +g\mu_B m_S B \tag{17.108}$$

Therefore, the difference in energy between the electron in the spin quantum number states 1/2 and −1/2 is

$$\Delta E = h\nu = g\mu_B B \tag{17.109}$$

and we can see that the degeneracy of the spin is raised by the magnetic induction. Transitions between the two levels can be induced by radiation of frequency ν in the above formula; for a field strength of 0.4 T, this corresponds to electromagnetic radiation of frequency ∼10 GHz, which lies in the microwave region. The basic electron spin resonance (ESR) experiment thus involves placing the sample in a microwave resonator (the source) between the poles of a magnet and adjusting the magnetic flux until absorption of microwaves by the sample takes place.

In the field of chemistry, free spins are usually encountered in the form of unpaired electrons in organic radicals or transition metal complexes. In such compounds, the simple expression (17.108) will break down both through interelectronic coupling (which affects the value of g) and coupling to the nonzero spins of the surrounding nuclei, which will give rise to a complex and highly characteristic splitting of the ESR signal into absorption peaks appearing at different values of the magnetic field. Both the magnitude and multiplicity of the splitting contain information on the molecular structure of the radical, often allowing unambiguous identification of the species involved, particularly if isotopic enrichment ^{13}C is permitted.

In the classical ESR experiment, radicals are introduced into the ESR cell that is placed in the microwave resonator. It should be realized that polar solvents and normal glassware also absorb microwaves, and the spectroscopic measurements are therefore carried out in small-volume flat cells made from quartz. With this equipment, it is possible to detect radical concentrations as low as 10^{-9} M.

The first ESR cells consisted of a quartz capillary, in which, for example, the front surface of a mercury thread formed the working electrode. Subsequently, Koopman and Gerischer (1966) described a three-electrode cell, in which a piece of platinum foil placed in the middle of a flat cell served as a working electrode, while RE and CE were placed above and below the resonance cavity as shown in Figure 17.72.

Assuming that the technique is sensitive only to the number of spins and not to their spatial distribution, we can show the detection limit to the limiting number of spins by forming the product of C_{lim} and V, the volume of the cell. Typically, V is about 10^{-5} dm^3, so, equating the rate of formation of the radicals (i/nF) to the rate of their disappearance (kVC_{lim}, where the lifetime $\tau = \ln 2/k$), we find that for $C_{lim} \approx 10^{-5}$ M and $i \approx 10$ mA, the limiting lifetime will be of the order of milliseconds.

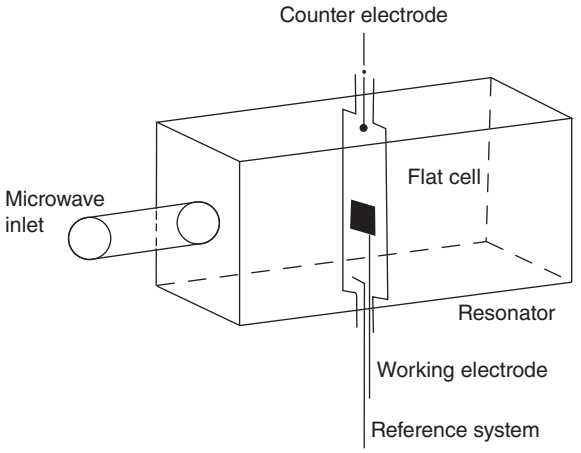


Figure 17.72 Electrochemical ESR cell (Koopman and Gerischer 1966).

Electrochemical electron spin resonance (EESR) is not limited to the detection of radical products that form at a specific potential: the time-dependent evolution of a radical product following a potential step can be studied, or the radical signal can be determined during potential cycling. It is also possible to follow the decay of the radical after the current is interrupted, allowing the measurement of the radical decay rate constant K. Measurements have also been extended to electrode films, particularly interesting results being obtained from the study of conducting polymers.

17.14.5 Electrochemical Mass Spectroscopy

In the technique of mass spectroscopy, atoms, molecules, or molecular fragments are identified by the ratios of their masses to the charge Z created on the mass spectrometer. This ratio is usually denoted by the symbol m/e, which has the value 1 for singly charged ^1H (more accurately, 1.007 825) and ∼7.8 for $^{12}C_6\ ^1H_6{}^+$. In the classical mass spectrometer, the substance to be identified is evaporated under reduced pressure, and the vapor is passed through an electron beam with an energy of ∼10 eV, which suffices to ionize some of the molecules in the vapor to ions. These ions are focused by an electric field in the ionization chamber and accelerated into the analyzer, where they are separated by a magnetic flux. The flux induces the ions to follow a circular path of radius r; if the accelerating electric field has voltage U, the radius of this circular path is

$$r = \frac{(2mU/e_0)^{1/2}}{B} \tag{17.110}$$

And if the analyzer geometry only allows ions of radius r_{crit} to pass, then

$$\frac{m}{e_0} = \frac{B^2 i_{crit}^2}{2U} \tag{17.111}$$

Thus, by varying U or B, ions of differing m/e_0 will arrive at the detector, which is usually a secondary electron multiplier for optimal sensitivity.

Classical electron beam ionization has the property that the particles, once ionized, usually fragment into many fractions. This is particularly true for organic molecules in the medium mass range, where complex spectra result in which the mass peak due to unfragmented molecular ion (the molecular peak) may be missing completely. This especially complicates the analysis of mixtures. Other ionization processes can reduce or even eliminate this disadvantage: field desorption, for example, in which adsorbed molecules are ionized under careful control from a surface by a strong inhomogeneous ($\sim 10^6$ V cm^{-1}) electric field and appear predominantly as the molecular ions, allows the relatively easy assignment of the spectra of mixtures. Other possibilities for ionization include photoionization and ionization through chemical reaction, through collisions with fast atoms, or simply through contact of the material with a hot metal band.

An important characteristic in mass spectroscopy is the mass resolution, $m/\Delta m$. A resolution of 1000 means that ions of mass 1000 can just be separated from those of mass 1001, and a resolution of this magnitude is normally sufficient to identify ions of medium mass in simple cases.

In *electrochemical mass spectroscopy* (ECMS), the critical factor is the sensitivity of the complete experiment: if the charge passed at the electrode is Q, the current yield for the detected species is a and the number of electrons per molecule produced is n, then the current signal at the mass spectrometer detector, Q_{MS}, has the value

$$Q_{MS} = K \cdot \frac{aQ}{n} \tag{17.112}$$

where the transfer factor, K, contains the losses associated with desorption and mass transfer in the electrochemical cell, material transfer to the spectrometer, and losses in the spectrometer itself. K can be measured, and values of 10^{-8} are attainable. Since Q_{MS} values of 10^{-14} are measurable, this implies that values of $\sim 10^{-6}$ C for Q will lead to a detectable signal that, for an electrode of 1 cm^2, corresponds to $\sim 1\%$ of a monolayer.

The direct coupling of the electrode processes to the mass spectrometer can be achieved by using a porous working electrode both as a wall of the electrochemical cell and as the inlet system to the spectrometer. In this way, volatile material from the electrode surface can be transferred rapidly to the ion source of the spectrometer, and the corresponding mass signal can be measured and correlated with the time axis corresponding to the variation of potential of the electrode, giving online information on volatile products or intermediates of the electrode reaction.

Clearly, the joining of the cell to the spectrometer is all important and is illustrated in Figure 17.73. Central is a steel frit (to allow the electrode to withstand the pressure difference of c. 1 bar) upon which is placed a hydrophobic microporous PTFE membrane. On this, in turn, is placed a porous metal or carbon layer that acts as the working electrode, and the current collector is a length of platinum wire pressed onto this layer. The electrode is cleaned by multiple cycling in background electrolyte before admission of the

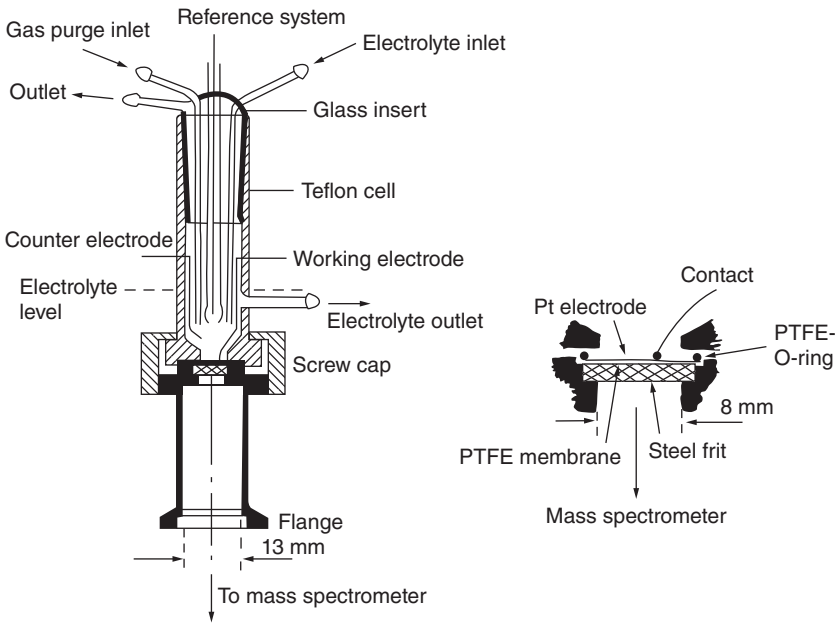


Figure 17.73 Electrochemical cell with porous working electrode acting as the window of a mass spectrometer (Bard 1991).

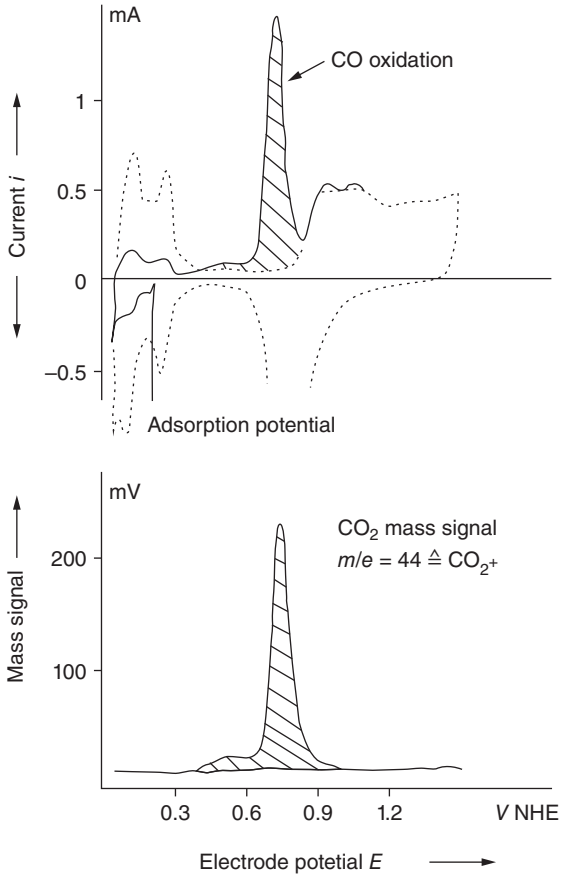


Figure 17.74 Proof of CO_2 as the main product of oxidation of adsorbed CO during linear sweep voltammetry with a scan speed of 12.5 mV s^{-1} (Wolter and Heitbaum 1984).

adsorbate solution, and the online capability of the experiment allows this cleaning process to be closely monitored. It is also possible to replace the porous electrode layer by a compact or rotating electrode placed in close proximity to the PTFE.

The type of experiment possible is shown in Figure 17.74, which reproduces the oxidation of CO adsorbed from CO-saturated sulfuric acid solution. The online mass spectrometry clearly shows that the main product is indeed CO_2 and the uncomplicated electrochemistry allows the transfer factor K defined above to be measured with confidence.

17.14.6 Electrochemical STM

STM was originally designed for operation in UHV. It was soon realized afterward that it should also work in solution. A major difference is the decrease of the tunneling barrier height in solution. Experimental values of ~1.5 eV have been reported, which is much smaller than the values of ~4 eV for UHV operation. It follows that for the same bias voltage and set point current (or tunneling gap resistance

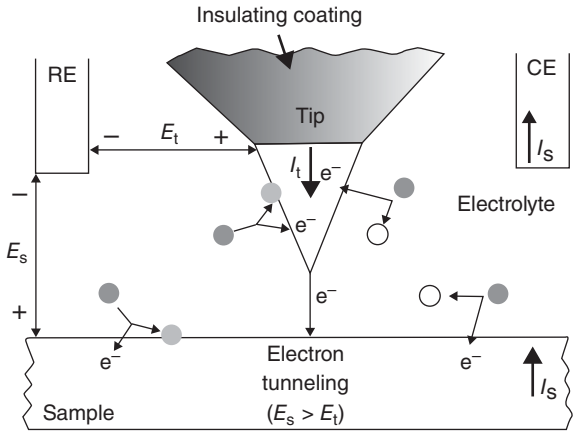


Figure 17.75 Schematic configuration of the electrochemical STM. RE and CE are the currentless reference electrode and counter electrode, respectively. E_s and E_t are the potentials of the sample and tip, respectively. I_s and I_t are the sample current and tip current, respectively. I_t is the sum of the faradaic current resulting from the electrochemical reaction at the tip surface and tunneling current between tip and sample.

$R_t = V/I$), the microscope will operate at larger tip–surface distance in solution than in UHV. Assuming a bias of 0.1 V and a tunneling current of 2 nA ($R_t = 5 \times 10^7\ \Omega$), a tunneling distance of 0.89 nm is calculated using a barrier height of 4 eV. It increases to 1.45 nm with a barrier height of 1.5 eV, in excellent agreement with values measured in solution.

Figure 17.75 illustrates schematically the configuration of an *electrochemical scanning tunneling microscope* (ECSTM). The tip is immersed in the electrolyte and acts as an electrode with electrochemical reacting taking place at the tip–electrode interface and generating a faradaic current. The faradaic current at the tip is superimposed to the tunneling current and affects the STM operation since the feedback circuit cannot discriminate between the two currents. It is therefore necessary to minimize the faradaic current at the tip relative to the tunnel current.

The most effective minimization of the faradaic current at the tip is obtained by reduction of the tip surface in contact with the electrolyte. This is done by covering most of the immersed portion of the tip by an insulating coating that can be made of glass, epoxy varnish, silicone polymer, Apiezon wax, nail polish, or electrophoretic paint. Well-prepared coatings will leave only ~10 µm or less uncoated at the very end of the tip. Further minimization of the faradaic current at the tip is achieved by polarizing the tip in the double-layer charging region (PtIr) or at the corrosion potential (W). This combined minimization allows to decrease the faradaic current to values of 50 pA or less, extremely small relative to the usual set point tunneling current of 0.5–10 nA used in ECSTM, thus ensuring absence of interference with the functioning of the STM.

ECSTM investigations can provide invaluable information, in particular molecular-scale information, on the structural modifications related to corrosion processes such as active dissolution, adsorption, passivation, and initial stages of localized corrosion of metallic materials (Wiesendanger and Guntherodt 1995).

17.14.7 Electrochemical AFM

The implementation of AFM to electrochemical measurement is easier than that of STM. This results from the fact that the material used for the integrated cantilever tip assembly that is commercially available is inert in most aqueous solutions. In addition, even in the case where electrochemical reaction would occur at the solution/tip interface, this has no direct effect, in contrast with STM, on the measurement of the signal that is used to probe the surface. In AFM, the cantilever tip assembly does not constitute a fourth electrode, and a conventional potentiostat can be used to control the sample potential.

The same general design as for ECSTM cells can be used. The limitations of *electrochemical atomic force microscopy* (ECAFM) regarding the correlation between the local information and integrated macroscopic information, the possible tip-shielding effects on the corrosion behavior, the kinetic of the mass transport, and the small volume of the electrochemical cell are the same as those described above for ECSTM.

Immersing the cantilever tip assembly and surface in solution has several consequences. It avoids the formation of a capillary bridge between tip and surface, which allows a better control of the adhesive force in contact mode (see above). In resonant contact mode, the fluid medium tends to damp the normal resonance frequency of the cantilever, which complicates this mode of operation. The noncontact mode becomes impractical because the van der Waals forces are even smaller, which can be a substantial limitation (e.g. for biological applications).

ECAFM is now a widely used technique for corrosion studies. It is often preferred to ECSTM despite the generally lower level of spatial resolution that can be achieved, because the obtained topographic information is independent of the conductivity of the corrosion products. Moreover, the setting up of the experiment is easier than that of ECSTM (Schmutz and Frankel 1999; Williams et al. 1998).

17.14.8 Electroreflectance Spectroscopy

Aqueous solutions are transparent to electromagnetic radiation in the visible and ultraviolet region of the spectrum up to photon energies of about 6 eV. Therefore, light with a wavelength in this region is a useful probe for the electronic properties of the electrochemical interface. In *electroreflectance spectroscopy* the reflectivity of the electrode is measured at two different potentials, and the difference recorded. It is common practice to plot $\Delta R/R$, the change in the reflectivity normalized by the reflectivity at the reference potential, versus the photon energy of the incident beam. The resulting spectra are difference spectra, just as in EMIRS.

The reflectivity of bulk materials can be expressed through their complex dielectric functions $\hat{\epsilon}(\omega)$ (i.e. the dielectric constant as a function of frequency), the imaginary part of which signifies absorption. In the early days of electroreflectance spectroscopy, the spectra were often interpreted in terms of the dielectric functions of the participating media. However, dielectric functions are macroscopic concepts, ill suited to the description of surfaces, interfaces, or thin layers. It is therefore preferable to interpret the data in terms of the electronic transitions involved wherever possible.

Electroreflectance spectroscopy has been successfully applied to numerous systems such as oxide films and adsorbed dyes. It is most useful when the observed features can be related to specific electronic transitions.

17.14.9 Second Harmonic Generation

Since the advent of strong and comparatively cheap laser light sources, nonlinear optical effects can be investigated with relative ease. For the study of surfaces and interfaces, SHG has found widespread application. The principle of this method is quite simple; a laser beam of frequency ω and of well-defined polarization is incident on the interface, and the signal at a frequency 2ω is recorded. Within the electric dipole approximation, SHG is forbidden in bulk phases with a center of symmetry and hence in practically all phases of interest to electrochemists. So all the signal at 2ω comes from the interface, where the symmetry is broken; hence SHG is an inherently surface-sensitive technique, and the problem of separating the surface signal from that of the bulk does not arise. On the other hand, SHG is usually performed with a fixed wavelength of the incident beam; in this case it does not give spectra like IR and Raman spectroscopy. The interpretation of the observed signal is not always straightforward and has to rely on theory to a greater extent.

At present, the whole field is developing rapidly; a few applications of SHG that will certainly become important in the future are:

1. On single-crystal surfaces, the SHG signal depends on the polar angle of incidence. This can be used to investigate the structure and symmetry of the surface.
2. SHG can be extended to a true spectroscopy by varying the frequency of the incident laser beam. Electronic structures such as surface states and surface plasmon resonances show up in the frequency dependence of the signal (Friedrichs et al. 1991).

17.14.10 Scanning Tunneling Microscope

The STM was discovered in 1982 by Binning and Rohrer and is based on the existence of a so-called tunneling current, i_t, between two metals placed very close together, but not in electric contact, in a vacuum. If a potential, V_b, is maintained between the two metals, and the distance apart, d, is of atomic dimensions, the tunneling current is given by

$$i_t \sim CV_b e^{-2kd} \tag{17.113}$$

where C is proportional to the product of the density of states at the Fermi level of the two metals and k is a function of the electronic work functions of the two metals, the form of the function corresponding to the height of the potential barrier through which the electron must tunnel. The tunneling process is essentially quantum mechanical in origin and arises because the wave functions of the electrons in the two metals show a small finite spatial extension into the region between them. The tunneling current is extremely sensitive to d, decreasing to about a factor of ~3 for every additional angstrom separation. The situation is illustrated in Figure 17.76.

The central idea of the microscope is to exploit this sensitivity to the metal separation by forming a fine metallic tip and rastering this tip over the electrode surface. The control of the tip is through a set of piezoelectric elements (which are formed from crystals whose dimensions alter slightly as a function of the presence of an electric field), allowing the tip to be moved both laterally and vertically. As the tip is moved laterally over the surface and encounters areas of different heights, the tunneling current alters; in the most common instrumental arrangement, this alteration is incorporated into a feedback circuit such that the vertical position of the tip is also altered so as to restore the tunneling current to its preset value. The vertical movements of the tip then constitute a depth profile that can be combined with the lateral rastering to generate a 3D map of the surface of extremely high resolution: vertical displacements of less than 0.1 Å are detectable as are lateral displacements of less than 1 Å.

In practice, the manufacture of the tips is the most demanding technical problem; in fact, it is very difficult to generate tip radii of much below micron size, and the efficacy of the technique relies on the presence of single adventitious atoms, or groups of atoms, on the tip through which the tunneling current dominates. Remarkably, the technique has found application in electrolyte solutions, in spite of the expected screening of the tip–electrode potential, and such processes as metal deposition and dissolution and the formation and dissolution of oxide layers have now been extensively studied. Technical difficulties that have been encountered on the transition to electrolytes have primarily been associated with the electrochemical activity of the tip, giving rise to measured currents that contain contributions from both tunneling and faradaic components. The latter can be minimized, however, by coating all but the very end of the tip with electrochemically inactive varnish.

Atomic resolution is not always the goal of scanning tunneling microscopy. For investigating the deposition and dissolution of metals, for corrosion, or for porous electrodes, an intermediate resolution in the nanometer or even micrometer range is often sufficient. With a fast scan rate, morphological changes on this scale can even be followed in real time. However, the presence of the tip can disturb the observed process significantly, either by the strong local field or by inhibiting the transport of particles, which may make the interpretation difficult.

17.14.11 Electrochemical Surface-Enhanced Raman Spectroscopy

Vibrational spectroscopies such as Raman and IR are useful methods for the identification of chemical species. Raman scattering is a second-order process, and the intensities are comparatively low. A quick estimate shows that normal Raman signals generated by species at a surface or an interface are too low to be observable. Furthermore, in the electrochemical situation Raman signals from the interface may be obscured by signals from the bulk of the electrolyte, a problem that also occurs in electrochemical IR spectroscopy (see above).

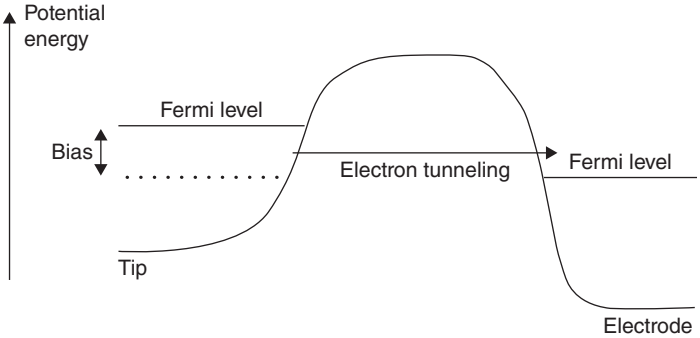


Figure 17.76 Potential barrier for electron tunneling.

Fortunately, in favorable cases enhancement mechanisms operate, which increase the signal from the interface by a factor of 10^3–10^6, so that spectra of good quality can be observed – hence the name *surface-enhanced Raman spectroscopy* (SERS). However, these mechanisms seem to operate only on metals with broad free-electron-like bands, in particular on the sp metals copper, silver, and gold. Furthermore, the electrodes must be roughened on a microscopic scale. These conditions severely limit the applicability of Raman spectroscopy to electrochemical interfaces. Nevertheless, SERS is a fascinating phenomenon, and though not universally applicable, it can yield valuable information on many interesting systems, and its usefulness is expected to increase as instrumentation and preparation techniques improve.

The necessary roughening of the electrodes is usually produced by oxidation–reduction cycles. For this purpose, the electrode surface is first oxidized, so the metal cations or poorly soluble salts such as AgCl are produced. When the electrode potential is stepped back into the reduction region, the cations are deposited producing a slightly roughened surface. This procedure is repeated several times to produce the desired surface conditions. Detection sensitivity and resolution are two important criteria when comparing advanced techniques in terms of their capability to provide high-quality information from interfaces, as provided in Table 17.13.

Two enhancement mechanisms are thought to operate on such surfaces. The first one is known as *electromagnetic enhancement* and depends on the presence of so-called large-scale roughness, that is, metal clusters with dimensions of 50–100 Å. Such clusters enhance both the incident and the outgoing radiation through a resonance effect. The magnitude of the enhancement depends on the size and shape of the metal cluster and on the complex dielectric constant $\in_M$ of the metal. Only free-electron-like metals have suitable values of the imaginary part of $\in_M$ to produce the desired effect.

The other mechanism involves *atomic size roughness* (i.e. single adatoms or small adatom clusters) and is caused by electronic transitions between the metal and the adsorbate. One of the possible mechanisms, *photoassisted metal to adsorbate charge transfer*, is illustrated in Figure 17.77. It depends on the presence of a vacant broadened adsorbate orbital above the Fermi level of the metal. In this process, the incident photon of frequency ω_0 excites an electron in the metal, which subsequently undergoes a virtual transition to the adsorbate orbital, where it excites a molecular

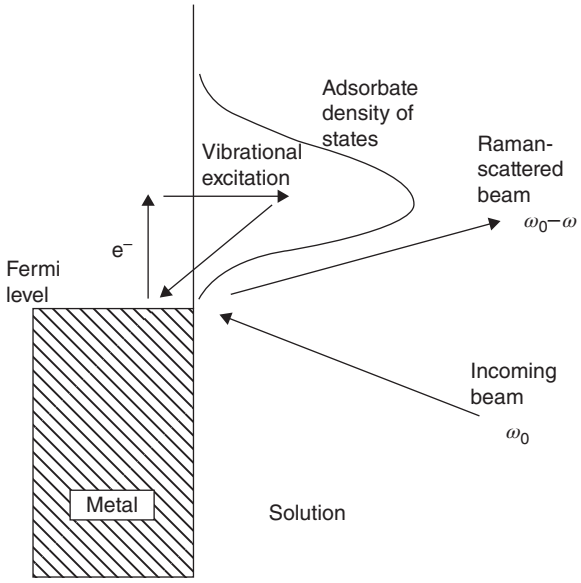


Figure 17.77 Enhancement through electron exchange between metal and adsorbate.

Table 17.13 A comparison of the sensitivity, energy, time, and spatial resolution of electrochemical methods, Raman spectroscopy, and scanning tunneling microscopy (STM) in practical electrochemistry study (Tian and Zhang 2014)

	Electrochemistry	EC-Raman spectroscopy	ECSTM
Sensitivity	Submonolayer	Submonolayer[a]	Submonolayer
Energy resolution	10^{-2} V	10^{-4} eV ($\sim$1 cm^{-1})[b]	STS is not available[c]
Spatial resolution	0.1–1 μm[d]	1 μm	1 Å
Time resolution (s)	10^{-7}–10^{-6}	10^{-8}[e]–10^{-3}[f]	0.04[g]

[a] With surface-enhanced Raman spectroscopy.

[b] With excitation in the visible.

[c] Scanning tunneling spectroscopy; although inelastic electron tunneling spectroscopy provides a higher resolution at about 0.05 eV at very low temperatures (several kelvin), it is not practical for electrochemistry.

[d] With scanning electrochemical microscopy.

[e] With pulsed laser.

[f] With continuous-wave laser.

[g] 0.04 s per STM image.

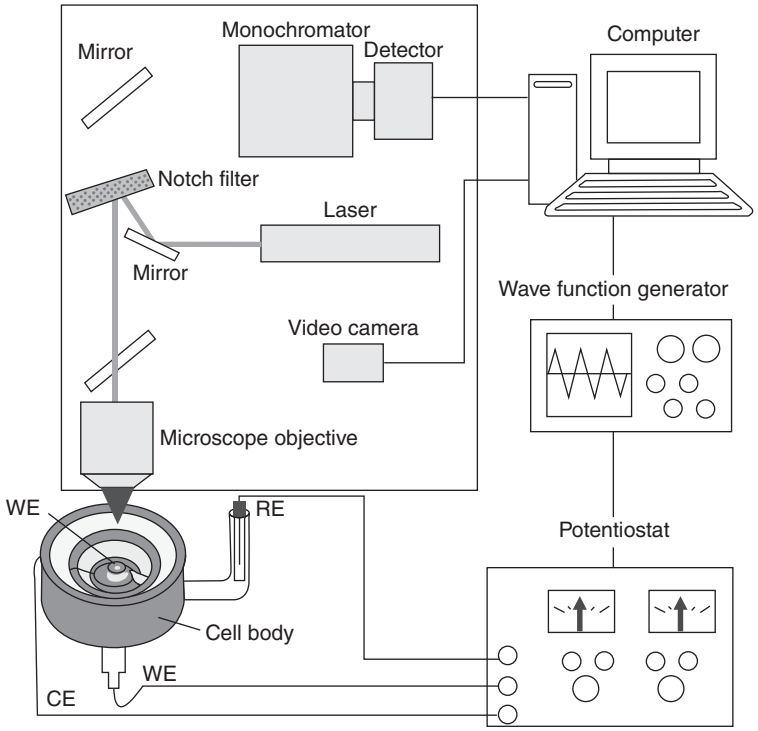


Figure 17.78 Diagram showing the experimental setup for EC-SERS, which includes a Raman spectrometer (in the block), potentiostat, computer, wave function generator, and an EC-SERS cell. WE, working electrode; CE, counter electrode; RE, reference electrode (Wu et al. 2008).

vibration of frequency ω. When the electron returns to the Fermi level of the metal, a photon of frequency $(\omega_0 - \omega)$ is emitted. The presence of the metal adatoms enhances the metal–adsorbate interaction and hence increases the cross section for the electronic transitions. Furthermore, this interaction may shift the relative positions of the adatom orbital and the Fermi level of the metal into a favorable region.

Figure 17.78 shows the experimental setup for *in situ electrochemical surface-enhanced Raman spectroscopy* (EC-SERS). This includes a laser to excite the SERS of samples, a Raman spectrometer to disperse and detect the Raman signal, a computer to control the Raman instrument for data acquisition and manipulation, a *potentiostat* or *galvanostat* to control the potential of the working electrode, and an EC-SERS cell to accommodate the electrode–electrolyte interface to be studied. It may be necessary to place a plasma line filter in the incident path for some lasers to obtain a truly monochromatic incident light. The detector of the Raman system can be single-channel photomultiplier tube (PMT), an avalanche photodiode (APD), or a multichannel CCD; currently, the latter has become the dominant configuration. In the case of time-resolved studies, it may be necessary to include a function generator to generate various types of potential–current controls over the electrode and also to trigger the detector accordingly to acquire the time-resolved SERS signal.

During recent years, SERS spectra have been used to acquire basic information on new corrosion inhibitors, namely, for Cu, Fe corrosion, passivity of Fe alloys, etc. So, three decades after the pioneering studies of EC-SERS, this spectroscopy is becoming a standard technique in studies of corrosion, adsorption, electrodeposition, and so on (Musiani et al. 2014).

17.14.12 Electrochemical Quartz Crystal Microbalance

Faraday discovered his/her famous second law by comparing mass changes of an electrode with the amount of charge passed. For this purpose, he/she had to take his/her electrodes out of solution, dry them, and weigh them *ex situ*. A modern, highly sensitive *in situ* method of determining mass changes is the quartz crystal microbalance. This is based on the inverse piezoelectric effect, in which the application of an electric field deforms a crystal. An alternating field of a suitable frequency can strike resonance and produce a standing wave, whose frequency depends on the vibrating mass.

The quartz balance uses a thin quartz crystal, a few hundred micrometers thick, with thin, vapor-deposited gold films on the two sides. Such a crystal has a fundamental mode for shear waves with a frequency in the 1–15 MHz region, which can be excited by application of a corresponding alternating voltage on the two electrodes. The resonance frequency is very sensitive to small mass changes of the system. One of the two electrodes is brought in contact with an electrolyte solution and is used as a working electrode either in its bare form or covered with

a thin film of some other material. Any change Δm in the mass of the electrode gives rise to a change Δf in the resonance frequency of the crystal. Unless the mass change is very large or the film on the electrode very thick, this relation is linear:

$$\Delta f = -C_{\mathrm{m}} \Delta m \tag{17.114}$$

with $C_{\mathrm{m}***}$ of the order of $50\,\mathrm{Hz\,cm^{-2}\,\mu g^{-1}}$. Frequency changes of the order of 1 Hz can easily be detected, and a quick estimate shows that mass changes due to the deposition of less than a monolayer of a heavy adsorbate such as Pb or Ag can be detected.

While the mass is not a specific quantity for a chemical species, the quartz microbalance is a useful device in cases where the chemical identity of the participating species is known or where they are only a few candidates, which can be distinguished by their molecular masses (Ward 1995).

17.14.13 Electrochemical Strain Microscopy

Electrochemical strain microscopy (ESM), conceptually illustrated in Figure 17.79, is a novel SPM technique capable of probing electrochemical reactivity and ionic flows in solids on the sub-10-nm level, 3–4 orders of magnitude below the effective resolution of conventional electrochemical methods.

ESM is based on detecting the strain response of a material to an applied electric field through a blocking or electrochemically active SPM tip (a tip that is functionalized directly or placed in an ion-containing medium). A biased SPM tip concentrates an electric field in a nanometer-scale volume of material, inducing interfacial electrochemical processes at the tip–surface junction and ionic currents through the solid. The intrinsic link between concentration of ionic species and oxidation states of the host cation and the molar volume of the material results in electrochemical strain and surface displacement. This is the case for many ionic and mixed ionic–electronic conductors such as ceria, cobaltites, nickelates, magnetites, etc.

There are a number of different operational regimes for ESM, schematically described in Figure 17.80. Figure 17.80a shows a blocking tip electrode, where the electron transfer between tip and surface and the nonuniform electrostatic field result in mobile ion redistribution within the solid but no electrochemical process at the interface. Figure 17.80b shows ESM electronic conductivities; the AC electric field is concentrated in the tip–surface junction. Figure 17.80c shows the situation in ambient conditions, where the formation of a liquid droplet at the tip–surface junction provides a Li-ion reservoir, rendering electrodes partially reversible. A similar effect can occur for blocking electrodes at high biases (Li extraction and tip plating) or for Li-electrolyte-coated electrodes. Finally,

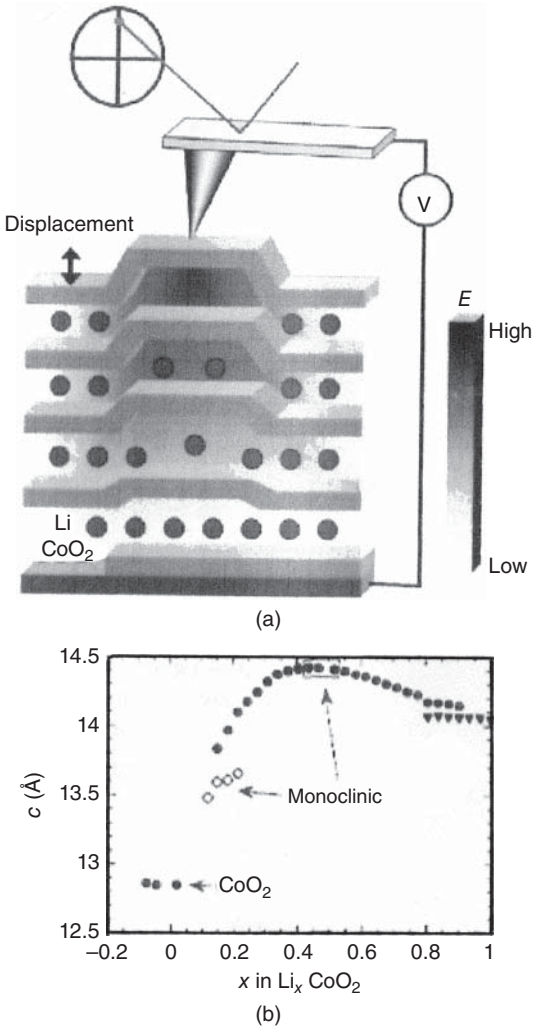


Figure 17.79 Principle of electrochemical strain microscopy. (a) During ESM, a periodic bias is applied to the SPM tip in contact with the sample surface. The applied bias induces ionic motion in the sample, and the resulting surface deformation is detected by the SPM probe and electronics, generating an image that maps the ionic motion at the nanoscale. (b) The dependence of the c-lattice parameter (perpendicular to layers) on lithiation in prototypical Li_xCoCO_2 cathode material. In the operation region of Li-ion batteries (from $x = 1$ to $x = 0.5$), the lattice parameter changes linearly with x by 40 pm. Combined with the ~1 pm sensitivity limit of the Cypher AFM, this suggests that a lithiation state change of just 10% can be measured through 1 unit cell of material.

Figure 17.80d shows ESM being performed on the surface of the top electrode device, where both the ionic currents are limited by the cathode and anode. In the cases shown in (a) and (b), the electric field created by the probe is localized, in (d) the field is uniform, and in (c) the field localization is controlled by solution conductivity and modulation frequency. In all cases, the tip detects local strain induced by the local or nonlocal electric field.

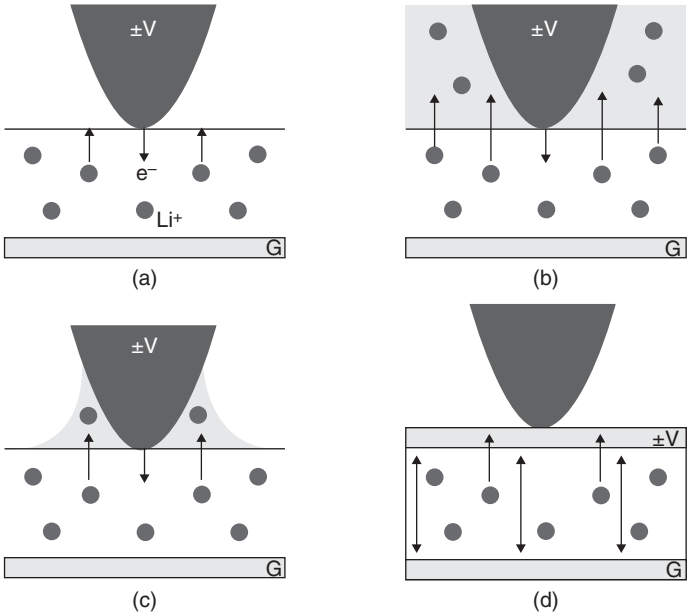


Figure 17.80 Operational regimes for electrochemical strain microscopy. (a) A blocking tip electrode (low humidity or vacuum). (b) Li-containing electrolyte. (c) Ambient conditions with a liquid droplet at the tip–surface. (d) On the surface of the top electrode device.

The remarkable aspect of the strain detection in ESM, as opposed to current-based techniques, is that the signal originates only from stress induced by ion motion, whereas electric currents contain (and are often dominated by) contributions from electronic conduction (direct current) and double-layer and instrumental capacitances. The fact that ionic diffusion is intrinsically slow, and hence the ionic currents are intrinsically small, imposes very significant and stringent limitations to current detection. While this is also relevant to strain detection, the simple analysis of the detection limits suggests that electrochemical strains can be measured in volumes 10^6–10^8 times smaller than faradaic currents.

In summary, ESM is a technique capable of probing electrochemical reactivity and ionic flows in solids on the sub-10-nm level. The method uses the intrinsic link between electrochemical processes and strains, as opposed to faradaic current detection in classical electrochemical methods. This different and unique detection principle allows electrochemical measurements in nanometer-scale volumes that can be extended to a broad spectrum of time and voltage spectroscopies. It is anticipated that ESM will be a key analytical capability for investigating and improving performance of materials and devices (Morozovska et al. 2010).

References

Acton, Q.A. (ed.) (2012). *Heavy Metals – Advances in Research and Application: 2012 Edition*. Atlanta, GA: Scholarly Editions.

Acton, Q.A. (ed.) (2013). *Sulfur Compounds – Advances in Research and Application: 2013 Edition*. Atlanta, GA: Scholarly Editions.

Adler, E. (1964). *Phys. Rev.* 134: A 728.

Albery, W.J. and Hitchman, M.L. (1971). *Ring-Disc Electrodes*. Oxford: Clarendon Press.

Alkonis, J.J. and Macknight, W.J. (1983). *Introduction to Polymer Viscoelasticity*, 2e. London: Wiley.

Allen, S.J. and Remeika, J.P. (1974). *Phys. Rev. Lett.* 33: 1478.

Allen, E.C., Tucker, P.M., and Wild, R.K. (1979). *Oxid. Met.* 13: 223.

Almond, D.P., Patel, P.M., and Reiter, H. (1987). *Mater. Eval.* 45: 471.

Anson, F.C. (1966). *Anal. Chem.* 38: 54.

Antonelli, G., Ruzzier, M., and Necci, F. (1997). ASME 97-GT-1, 1.

Antunes, R.A., de Oliveira, M.C.L., and Pillis, M.F. (2013). *Int. J. Electrochem. Sci.* 8: 1487.

Ashworth, V., Grant, W.A., and Procter, R.P.M. (eds.) (1980). *Ion Implantation in Metals*. London: Pergamon.

Azzam, R.M.A. and Bashara, N.M. (1977). *Ellipsometry and Polarized Light*. Amsterdam, Holland: North Holland.

Baboian, H. (ed.) (1995). *High-Temperature Gases (Corrosion Tests and Standards: Applications and Integration)*. Washington, DC: ASTM.

Bacon, G.E. (1977). *Neutron Scattering in Chemistry*. London: Butterworths.

Bai, C. (1999). *Scanning Tunneling Microscopy and its Applications*, 2e. Shanghai: Springer.

Balkanski, M., Leite, R.C.C., and Porto, S.P.J. (eds.) (1976). *Proceedings of the 3rd International Conference on Light Scattering in Solids*. Paris, France: Flamarion Press.

Balkanski, M. (ed.) (1978). *Proceedings of the International Conference on Lattice Dynamics*. Paris, France: Flamarion Press.

Ball, D.W. (2006). *Spectroscopy* 21: 1.

Bard, A.J. (ed.) (1991). *Electroanalytical Chemistry*, vol. 17. New York: Marcel Dekker.

Bard, A.J. and Faulkner, L.R. (2001). *Electrochemical Methods*. New York: Wiley.

Bard, A.J. and Mirkin, M.V. (2001). *Scanning Electrochemical Microscopy*. New York: Marcel Dekker.

Baschi, S.D., Dutta, M., Bandyopadhyay, N., and Rajesh, N. (2007). *Surf. Coat. Technol.* 201: 4547.

Bauer, E. (1998). *Surf. Rev. Lett.* 5: 1275.

Bennett, M.J. (1984). *J. Vac. Sci. Technol.* B12: 800.

Bennett, M.J. and Tuson, A.T. (1989). *Mater. Sci. Eng.* 92: 190.

Bennett, T.D. and Yu, F. (2005). *J. Appl. Phys.* 97: 013520-1.

Benninghoven, A., Janssen, K., Tumpner, J., and Werner, H. (eds.) (1991). *Proceedings SIMS VIII* (15–20 September 1991), 91. Chichester: Wiley.
Bernéron, R. and Charbonnier, J.C. (1982). Proceedings of the 7th ICVM Conference, Tokyo, Japan, p. 592.
Bertocci, U., Gabrielli, C., Huet, F., and Keddham, M. (1997). *J. Electrochem. Soc.* 144: 31.
Bertocci, U. and Huet, F. (1997). *J. Electrochem. Soc.* 144: 2786.
Birks, N., Meier, G.H., and Pettit, F.S. (2006). *Introduction to the High Temperature Oxidation of Metals*, 2e. Cambridge: Cambridge University Press.
Bloembergen, N., Chang, R.K., Jha, S.S., and Lee, C.H. (1968). *Phys. Rev.* 174: 813.
Bloembergen, N. (ed.) (1998). *Non Linear Optics*, 4e. Singapore: World Scientific.
Bobeth, M., Pompe, W., Rockstroh, M., and Schuman, E. (1994). *Acta Metall. Mater.* 42: 579.
Bosch, R.-W. (2005). *Corros. Sci.* 47: 125.
Bose, S. (2007). *High Temperature Coatings*. Amsterdam, Holland: Elsevier.
Bosh, R.W., Feron, D., and Celis, J.P. (eds.) (2007). *Electrochemistry in Light Water Reactors: Reference Electrodes, Measurement, Corrosion and Tribocorrosion Issues, EFC 49*. Boca Raton, FL: CRC Press.
Bosseboeuf, A. and Bouchier, D. (1985). *Surf. Sci.* 162: 695.
Brewis, D.M. (ed.) (1982). *Surface Analysis and Pretreatment of Plastics and Metals*. London: Applied Science.
Brillouin, L. (1922). *Ann. Phys. (Paris)* 17: 88.
Bruley, J., Brydson, R., Müllejans, H. et al. (1994). *J. Mater. Res.* 9: 2574.
Brunner, J. and Perry, A.J. (1987). *Thin Solid Films* 153: 103.
Butcher, P.N. and Cotter, D. (1990). *The Elements of Nonlinear Optics*. Cambridge: Cambridge University Press.
Butt, H., Capella, B., and Kappl, M. (2005). *Surf. Sci. Rep.* 59: 1.
Chang, C.H., Hsia, B., Alper, J.P. et al. (2015). *ACS Appl. Mater. Interfaces* 7: 26658.
Chen, C.J. (1993). *Introduction to Scanning Tunneling Microscopy*. Oxford: Oxford University Press.
Christensen, P.A. and Hamnet, A. (1994). *Techniques and Mechanisms in Electrochemistry*. New York: Chapman and Hall.
Clark, R.J.H. and Hester, R.E. (eds.) (1985). *Advances in Infrared and Raman Spectroscopy*, vol. 12. London: Wiley Heyden.
Compton, R.G. (ed.) (1989). *Comprehensive Chemical Kinetics*. Amsterdam, Holland: Elsevier.
Conner, J.A. and Connor, W.B. (1994). *JOM* 46: 35.
Coustumer, P.L., Heino, M.M., Chapon, P. et al. (2003). *Surf. Interface Anal.* 35: 623.
Cremer, P.S., Su, X., Shen, Y.R., and Somorjai, G.A. (1996). *J. Am. Chem. Soc.* 118: 2942.
Czanderna, A.W. (ed.) (1975). *Methods of Surface Analysis*. London: Elsevier.
Czichos, H., Saito, T., and Smith, L. (eds.) (2011). *Springer Handbook of Metrology and Testing*. Berlin: Springer-Verlag.
Davisson, C. and Germer, L.H. (1928a). *Phys. Rev.* 31: 155.
Davisson, C. and Germer, L.H. (1928b). *Phys. Rev.* 31: 307.
Davisson, C.J. (1928). *J. Franklin Inst.* 205: 597.
de Broglie, L. (1925). *Compte Rendu* 180: 498.
Dekker, A.J. (1975). *Solid-State Physics*. London: MacMillan.
Delahay, P. and Tobias, C.W. (eds.) (1966). *Advances in Electrochemistry and Electrochemical Engineering*, vol. 4. New York: Wiley.
DeMasi-Marcin, J.T., Sheffler, K.D., and Bose, S. (1990). *J. Eng. Gas Turbines Power Trans. ASME* 112: 521.
Dickinson, E. (ed.) (1995). *New Physico-Chemical Techniques for the Characterization of Complex Food Systems*, 268–294. Glasgow: Blackie.
Dimitrov, S., Ranganathan, S., Weyl, A., and Janke, D. (1993). *Steel Res.* 64: 63.
Doychak, J., Smialek, J.L., and Mitchell, T.E. (1989). *Metall. Trans. A* 20A: 499.
Doychak, J. and Rühle, M. (1989). *Oxid. Met.* 31: 431.
Drury, J.C. (2004). *Ultrasonic Flaw Detection for Technicians*, 3e. UK: Silverwing Ltd.
Du, Q., Freysz, E., and Shen, Y.R. (1994). *Science* 264: 826.
Eden, D.A., Carr, A.N., and Dawson, J.L. (1995). US Patent 5,425,867.
Eldridge, J.I., Spuckler, C.M., Nesbitt, J.A., and Street, K.W. (2003). *Ceram. Eng. Sci. Proc.* 24: 511.
Fafilek, G., Leeb, K., and Breiter, M.W. (1996). *Solid State Ionics* 86, 1415–88.
Fafilek, G. (1998). *Solid State Ionics* 623: 113–115.
Feder, R. (ed.) (1985). *Polarized Electrons in Surface Physics*, Advanced Series in Surface Science. Singapore: World Scientific.
Ferber, M.K., Wereszczek, A.A., Lance, M. et al. (2000). *J. Mater. Sci.* 35: 2643.
Finney, J. and Steigenberger, U. (1997). *Phys. World* 10: 12, 27.
Fleming, R.H., Meeker, G.P., and Blattner, R.J. (1987). *Thin Solid Films* 153: 197.
Forman, R.A., Piermarini, G.J., Barnett, J.D., and Block, S. (1972). *Science* 176: 284.
Friedrichs, A., Shannon, C., and Pettinger, B. (1991). *Surf. Sci.* 251: 587.
Gabrielli, C., Huet, F., Keddham, M. et al. (1986). *Mater. Sci. Forum* 8: 491.
Gabrielli, C., Huet, F., Keddham, M., and Oltra, R. (1990). *Corrosion* 46: 266.
Gabrielli, C., Huet, F., and Keddham, M. (1993). *J. Chem. Phys.* 99: 7232.
Gabrielli, C. and Williams, D.E. (2014). *Developments in Electrochemistry: Science Inspired by Martin Fleischmann*, 1e (ed. D. Pletcher, Z.-Q. Tian and D.E. Williams). Chichester: Wiley.
Gale, R.J. (ed.) (1988). *Spectroelectrochemistry, Theory and Practice*. New York: Plenum Press.
Gao, G., Stott, F.H., Dawson, J.L., and Farrell, D.M. (1990). *Oxid. Met.* 33: 79.
Geisse, N.A. (2009). *Mater. Today* 12: 40.
Gell, M., Sridharan, S., Wen, M., and Jordan, E. (2004). *Int. J. Appl. Ceram. Technol.* 1: 316.
Geller, E. (ed.) (2002). *Dictionary of Material Science*. New York: McGraw-Hill.
Gellings, P.J. and Bouwmeester, H.J.M. (eds.) (1997). *The CRC Handbook of Solid State Electrochemistry*. Boca Raton, FL: CRC Press.
Gerischer, H. and Tobias, C.W. (1984). *Advances in Electrochemistry and Electrochemical Engineering*, vol. 13. New York: Wiley.
Glaser, B., Rahts, K., Schorr, M., and Schütze, M. (1994). *Sonderband des Praktischen Metallographie*, Bd. vol. 25, 75. Germany: Dechema Forschung Institute.
Silva Gomes, J.F., Monteiro, J.M., and Vaz, M.A.P. (2000). *Mech. Mater.* 32: 837.
Goncharov, O.Y. (2004). *Inorg. Mater.* 40: 1295.
Gosser, D.K. (1993). *Cyclic Voltammetry: Simulation and Analysis of Reaction Mechanisms*. New York: VCH Publishers.
Gottesfeld, S. (1989). *Electroanal. Chem.* 15: 143.
Grabke, H.J. and Meadowcroft, D.B. (eds.) (1995). *Guidelines for Methods of Testing and Research in High Temperature Corrosion*. London: The Institute of Materials, EFC Publication No. 14.
Greaves, E.N. (1990). *Glass Sci. Technol.* 48: 1.
Griffiths, P.R. and Holmes, C. (2002). *Handbook of Vibrational Spectroscopy*, vol. I. Chichester: Wiley.
Hansmann, H. and Mosle, J. (1982). *Adhesion* 26: 18.
Haugsrud, R. (2003). *Corros. Sci* 45: 1289.
Hedvig, P. (1977). *Dielectric Spectroscopy of Polymers*. New York: Wiley.
Heinz, T.F., Himpsel, F.J., Palange, E., and Burstein, E. (1989). *Phys. Rev. Lett.* 63: 644.
Heinz, K., Starke, U., and Bernhardt, J. (2000). *Prog. Surf. Sci.* 64: 163.
Heinze, J. (1993). *Angew. Chem. Int. Ed. Engl.* 32: 1068.

Helmshaw, R. (1982). *Industrial Radiology*. London: Applied Science.
Hladky, K. and Dawson, J.L. (1982). *Corros. Sci.* 22: 231.
Iacoviello, F., Di Cocco, V., and D'Agostino, L. (2017). *Procedia Struct. Integrity* 3: 276.
ILL World Wide Web http://www.ill.fr (accessed 11 July 2018).
ISIS World Wide Web http://www.isis.rl.ac.uk.
Israelachvili, J.N. (1973). *J. Colloid Interface Sci.* 44: 259.
Israelachvili, J.N. and Adams, G.E. (1978). *J. Chem. Soc., Faraday Trans. I* 74: 975.
Israelachvili, J.N. (1992). *Intermolecular and Surface Forces*. London: Academic Press.
Israelachvili, J., Min, Y., Akbulut, M. et al. (2010). *Rep. Prog. Phys.* 73: 036601.
Iverson, W.P. (1968). *J. Electrochem. Soc.* 115: 617.
John, H.A., Hofman, S., and Munz, W.-D. (1987). *Thin Solid Films* 153: 45.
Johnson, K.L., Kendall, K., and Roberts, A.D. (1971). *Proc. R. Soc. London, Ser. A, Math. Phys. Sci.* 324: 301.
Johannesen, O. and Andersen, A.G. (eds.) (1989). *Selected Topics in High Temperature Chemistry, Defect Chemistry of Solids*. Amsterdam: Elsevier.
Kambe, K. (1967). *Z. Naturforsch., A: Phys. Sci.* 22: 1280.
Kaufherr, N., Fenske, G.R., Busch, D.E. et al. (1987). *Thin Solid Films* 153: 45.
Kauppinen, P. (1997). *The Evaluation of Integrity and Elasticity of Thermally Sprayed Ceramic Coatings by Ultrasonics*, 130. Espoo, Finland: Technical Research Center of Finland, VTT Publication 325.
Kawamura, K., Saiki, A., Maruyama, T., and Nagata, K. (1995). *J. Electrochem. Soc.* 142: 3073.
Keller, O. (1986). *Phys. Rev. B* 33: 990.
Khanna, A.S. (2004). *Introduction to High Temperature Oxidation and Corrosion*. Materials Park, OH: ASM International.
King, S.M. (1997). Small-Angle Neutron Scattering, a report on ISIS Web page.
Kirschner, J. and Feder, R. (1979). *Phys. Rev. Lett.* 42: 1008.
Kissinger, P.T. and Heineman, W.R. (1984). *Laboratory Techniques in Electroanalytical Chemistry*. New York: Marcel Dekker.
Kofstad, P. (1988). *High Temperature Corrosion*. London: Elsevier Applied Science Publishers.
Koopman, R. and Gerischer, H. (1966). *Ber. Bunsen Ges. Phys. Chem.* 70: 118.
Kulesza, P.J. and Galus, Z. (1992). *J. Electroanal. Chem.* 323: 261.
Lagally, M.C. (1985). *Methods Exp. Phys.* 22: 237.
Lagally, M.C. and Savage, D.B. (1993). *MRS Bull.* 18: 24.
Landsberg, G. and Mandelstam, L. (1928). *Naturwissenschaften* 16: 57.
Lang, E. (ed.) (1983). *Coatings for High Temperature Applications*. New York: Applied Science.
Lapshin, R.V. (1995). *Rev. Sci. Instrum.* 66: 4718.
Lapshin, R.V. (2007). *Meas. Sci. Technol.* 18: 907.
Lasia, A. (2014). *Electrochemical Impedance Spectroscopy and its Applications*. New York: Springer Science & Business Media.
Levich, V.G. (1962). *Physicochemical Hydrodynamics*. Englewood Cliffs, NJ: Prentice Hall.
Levitin, V. (2005). *High Temperature Strain of Metals and Alloys: Physical Fundamentals*, 1e. Weinheim: Wiley.
Lipkowski, J. and Ross, P.N. (eds.) (1992). *Adsorption of Molecules at Electrode Surfaces*. New York: VCH.
Liu, L., Li, Y., Zeng, C., and Wang, F. (2006). *Electrochim. Acta* 51: 4736.
Losurdo, M. and Ingerl, K. (eds.) (2013). *Ellipsometry at the Nanoscale*. Heidelberg: Springer-Verlag.
Lüth, H. (1993). *Springer Series in Surface Science*, vol. 15, 1. Berlin, Heidelberg: Springer-Verlag.
Mabbutt, S., Simms, N., and Oakey, J. (2013). *Corros. Eng. Sci. Technol.* 44: 286.
Mahan, G.D. and Roth, W.L. (eds.) (1976). *Superionic Conductors*. New York: Plenum Press.
Mamantov, G. (ed.) (1978). *Characterization of Solutes in Non-Aqueous Solvents*. New York: Plenum.
Mamantov, G. and Marassi, R. (eds.) (1987). *Molten Salt Chemistry*. Dordrecht, Holland: D. Reidel.
Mansfeld, F., Chen, C., Lee, C., and Xiao, H. (1996). *Corros. Sci.* 38: 497.
Mansfeld, F., Huet, F., and Mattos, O.R. (ed.) (2000). New Trends in EIS and ENA, Proceedings ECS, vol. 2000–24, Pennington, NJ.
Marcus, P. and Mansfeld, F. (eds.) (2006). *Analytical Methods in Corrosion Science and Engineering*. Boca Raton, FL: CRC Press, Taylor & Francis Group.
Maruyama, T., Sasaki, S., and Saito, Y. (1987). *Solid State Ionics* 23: 107.
Maxwell, J.C. (1973). *A Treatise on Electricity and Magnetism, vols. I, II*. Oxford: Clarendon Press.
McConville, C.F., Seymour, D.L., Woodruff, D.P., and Bao, S. (1987). *Surf. Sci.* 188: 1.
Mcgeehin, P. and Hooper, A. (1977). *J. Mater. Sci.* 12: 1.
Meyer, E., Overney, R.M., Dransfeld, K., and Gyalog, T. (1998). *Nanoscience*, 1e. Singapore: World Science Publisher.
Moerner, W.M. (1994). *J. Lumin.* 60-62: 997.
Molis, S.E. and Clarke, D.R. (1990). *J. Electron. Struct. Ceram.* 73: 3189.
Morozovska, A., Eliseev, E., Balke, N., and Kalinin, S.V. (2010). *J. Appl. Phys.* 108: 053712.
Müllejans, H. and Bruley, J. (1993). *J. Phys IV* 3: 2083.
Newark, G. and Chen, X. (2005). *Surf. Coat. Technol.* 190: 7.
Newcomb, S.B. and Stobbs, W.M. (1985). *J. Microsc.* 140: 209.
Newman, J.S. (1962). *Electrochemical Systems*. Englewood Cliffs, NJ: Prentice Hall.
Öijerholm, J., Fafilek, G., and Pan, J. (2007). *Electrochem. Solid-State Lett.* 10: C47.
Orazen, M.E. and Tribollet, B. (2008). *Electrochemical Impedance Spectroscopy*, 1e. Hoboken, NJ: Wiley.
Osteryoung, J. and Osteryoung, R.A. (1985). *Anal. Chem.* 57: 101A.
Oura, K., Katayama, M., Zotov, A.V. et al. (2003). *Surface Science, An Introduction*. Berlin: Springer-Verlag.
Papavinasam, S. (2014). *Corrosion Control in the Oil and Gas Industry*. London: Elsevier.
Pask, J. and Evans, A. (eds.) (1980). *Surfaces and Interfaces in Ceramic Metal Systems*. New York: Plenum.
Pendry, J.B. (1974). *Low Energy Electron Diffraction*. London: Academic Press.
Perry, A.J., Strandberg, C., Sproul, W.D. et al. (1987). *Thin Solid Films* 153: 169.
Ponath, H.E. and Stegeman, G.I. (eds.) (1991). *Nonlinear Surface Electromagnetic Phenomena*, 1e, vol. 29. Amsterdam: North Holland.
Qi, J., Angerer, W., Yeganeh, M.S. et al. (1995). *Phys. Rev. Lett.* 75: 3174.
Quadakkers, W.J., Schmidt, K., Grubmeier, M., and Walura, E. (1992). *Mater. High Temp.* 10: 85; Nucl. Inst. Method., B66, 1 (1992).
Raghavan, S., Imbrie, P., and Crossley, W. (2008). *Appl. Spectrosc.* 62: 759.
Rahmel, A. (ed.) (1982). *Aufbau von Oxidschichten auf Hochtemperaturwerkstoffen und ihre technische Bedeutung*. Oberusel, Germany: Deutsche Gesellschaft für Metallkunde.
Rajic, N. (2000). *J. Nondestr. Eval.* 191: 141.
Rajic, N., Weinberg, S., and Rowlands, D. (2008). *Development of A Low Cost Thermoelastic Stress Analysis System*. Australia: Defence Science and Technology Organisation, DSTO-TR-2164.
Rayleigh, L. (1899a). *Philos. Mag.* 47: 375.
Rayleigh, L. (1899b). *Colloid Papers* IV: 397.
Rebane, K.K. (1970). *Impurity Spectra of Solids*. New York: Plenum.
Rinaldi, C., Bicego, V., and Colombo, P.P. (2006). *J. Eng. Gas Turbines Power Trans. ASME* 128: 73.
Roberge, P.R. (ed.) (2006). *Corrosion Basics – An Introduction*, 2e. Houston, TX: NACE International.

Rosencwaig, A. and Gersho, A. (1976). *J. Appl. Phys.* 47: 64.
Rudenauer, F.G. and Werner, H.W. (1987). *Secondary Ion Mass Spectrometry*. New York: Wiley.
Rundgren, J. (1999). *Phys. Rev.* B59: 5106.
Rudolph, M., Reddy, D.P., and Feldeberg, S.W. (1994). *Anal. Chem.* 66: 589A.
Saito, Y. (2000). *Mater. High Temp.* 17: 471.
Sawhill, H.T. and Hobbs, L.W. (1984). 9th International Conference on Metallic Corrosion, Vol. 1, p. 21.
Scheffler, T.B. and Hussey, C.L. (1984). *Inorg. Chem.* 23: 1926.
Schmutz, F. and Frankel, G.S. (1999). *J. Electrochem. Soc.* 146: 4461.
Schumann, E. and Rühle, M. (1994). *Acta Metall. Mater.* 42: 1481.
Schütze, M. (1997). *Protective Oxide Scales and their Breakdown*. Chichester: Wiley.
Seah, M.P. and Dench, W.A. (1979). *Surf. Interface Anal.* 1: 2.
Sequeira, C.A.C., Chen, Y., Santos, D.M.F., and Song, X. (2008). *Corros. Prot. Mater.* 27: 114.
Sequeira, C.A.C. and Santos, D.M.F. (2010). *Z. Phys. Chem.* 224: 1297.
Smekal, A. (1923). *Naturwissenschaften* 11: 873.
Sharma, B.K. (2005). *Instrumental Methods of Chemical Analysis*, 24e. Meerut: Goel Publishing House.
Sharpe, R.S. (1980). *Research Techniques in NDT*, vol. 6. London: Academic Press.
Shen, Y.R. (1984). *The Principles of Nonlinear Spectroscopy*. New York: Wiley.
Spence, J.C.H. (1988). *Experimental High-Resolution Microscopy*, 2e. Oxford: Oxford University Press.
Steinmann, P.A. and Hintermann, H.E. (1985). *J. Vac. Sci. Technol.* A3: 2459.
Still, T. (2008). *J. Phys. Condens. Matter* 20: 404203.
Stoll, R.L. (1974). *The Analysis of Eddy Currents*. Oxford: Oxford University Press.
Strecker, A., Salzberger, U., and Mayer, J. (1993). *Pract. Metall.* 30: 482.
Sundgren, J.E., Rockett, A., Greene, J.E., and Helmersson, U. (1986). *J. Vac. Sci. Technol.* A4: 2770.
Suzuki, S. and Katita, K. (2005). *J. Surf. Anal.* 12: 174.
Tabor, D. and Winterton, R.H. (1969). *Proc. R. Soc. London, Ser. A, Math. Phys. Sci.* 312: 435.
Taniguchi, S., Maruyama, T., Yoshiba, M. et al. (eds.) (2006). *High Temperature Oxidation and Corrosion 2005, Materials Science Forum*, vol. 522–523. Zürich: Trans. Tech. Publications Ltd.
Tempest, P.A. and Wild, R.K. (1988). *Oxid. Met.* 30: 209.
Thoma, M.J. (1986). *Vac. Sci. Technol.* A4: 2633.
Thonsen, C., Maris, H.J., and Tanc, J. (1987). *Thin Solid Films* 154: 217.
Tian, Z.-Q. and Zhang, X.-M. (2014). *Developments in Electrochemistry: Science Inspired by Martin Fleischmann*, 1e (ed. D. Pletcher, Z.-Q. Tian and D.E. Williams). Chichester: Wiley.
Thompson, D.O. and Chimenti, D.E. (eds.) (1999). *Review of Progress in Quantitative Non-Destructive Evaluation*, vol. 18A. New York: Springer Science and Business Media, LLC.
Tolanski, S. (1949). *Multiple-Beam Interferometry of Surfaces and Films*. Clarendon: Oxford University Press.
Tolanski, S. (1955). *An Introduction to Interferometry*. London: Longmans Green & Co.
Tolpygo, V.K. and Clarke, D.R. (2000). *Mater. High Temp.* 17: 59.
Tompkins, H.G. and McGahan, W.A. (1999). *Spectroscopic Ellipsometry and Reflectometry*. New York: Wiley.
Tompkins, H.G. and Irene, E.A. (eds.) (2005). *Handbook of Ellipsometry*. New York and Heidelberg: Springer-Verlag.
Tromp, R.M. (2000). *IBM J. Res. Dev.* 44: 503.
Tsuji, K. and Hirokawa, K. (1996). *Appl. Surf. Sci.* 103: 451.
Vallet, C.E., Heatherly, D.E., and Braunstein, J. (1980). *J. Electrochem. Soc.* 127: 1.
Valtiner, M., Banquy, X., Kristiansen, K. et al. (2012). *Langmuir* 28: 13080.
van Dijken, A., Meulenkamp, E.A., Vanmaekelbergh, D., and Meijerink, A. (2000). *J. Lumin.* 90: 123.
Van Hove, M.A. and Tong, S.I. (1979). *Surface Crystallography by LEED*. Heidelberg: Springer-Verlag.
van Hove, M.A., Weinberg, W.H., and Chan, C.M. (1986). *Low Energy Electron Diffraction*. Berlin: Springer-Verlag.
van Manen, P.A., Weewer, R., and de Wit, J.H.W. (1992). *J. Electrochem. Soc.* 134: 728.
Vashishta, P., Mundy, J.N., and Shenoy, G.K. (eds.) (1979). *Fast Ion Transport in Solids*. Amsterdam, Holland and New York: North Holland.
Vasylyev, M.A., Tinkov, V.A., Blaschuk, A.G. et al. (2006). *Appl. Surf. Sci.* 253: 1081.
Vasylyev, M.A., Tinkov, V.A., and Gurin, P.A. (2008). *Appl. Surf. Sci.* 254: 4671.
Voyer, J., Gitzhofer, F., and Boulos, M.I. (1998). *J. Therm. Spray Technol.* 7: 181.
Walter, M., Schütze, M., and Rahmel, A. (1993). *Oxid. Met.* 39: 389.
Ward, I.M. (1971). *Mechanical Properties of Solid Polymers*. London: Wiley.
Ward, M.D. (1995). *Physical Electrochemistry, Principles, Methods and Applications* (ed. I. Rubinstein). New York: Marcel Dekker, Inc.
Weast, R.C. (ed.) (1986). *Handbook of Chemistry and Physics*. Boca Raton, FL: CRC Press.
Weaver, M.J. and Inman, D. (1975). *Electrochim. Acta* 20: 429.
Weissberger, A. and Rossiter, B.W. (eds.) (1971). *Physical Methods of Chemistry*. New York: Wiley Interscience.
Wiesendanger, R. and Guntherodt, H.G. (eds.) (1995). *Scanning Tunneling Microscopy II: Further Applications and Related Scanning Techniques*. Berlin: Springer-Verlag.
Wild, R.K. (1977). *Corros. Sci.* 17: 87.
Williams, D.E., Mohinddin, T.F., and Zhu, Y.Y. (1998). *J. Electrochem. Soc.* 145: 2664.
Wolter, O. and Heitbaum, J. (1984). *Ber. Bunsen Ges. Phys. Chem.* 88: 2.
Wouters, Y., Galerie, A., and Petit, J.P. (1997). *Solid State Ionics* 104: 89.
Wu, D.Y., Li, J.F., Ren, B., and Tian, Z.-Q. (2008). *Chem. Soc. Rev.* 37: 1025.
Yariv, A. (1988). *Quantum Electronics*, 3e. New York: Wiley.
Yen, W.M. and Selzer, P.M. (eds.) (1981). *Laser Spectroscopy of Solids, Springer Topics in Applied Physics*, vol. 49. Berlin: Springer.
Zhu, R., Nowierski, C., Ding, Z. et al. (2007). *Chem. Mater.* 19: 2533.
Zhu, R., Qin, Z., Noel, J.J. et al. (2008). *Anal. Chem.* 80: 1437.

Further Reading

Abramczyk, H. (2005). *Introduction to Laser Spectroscopy*. Amsterdam, Holland: Elsevier.
Abruña, H.D. (ed.) (1991). *Electrochemical Interfaces*. New York: VCH.
Bauer, E. (2014). *Surface Microscopy with Low Energy Electrons*. New York: Springer Science and Business Media.
Bennett, M.J. and Lorimer, G.W. (eds.) (1991). *Microscopy of Oxidation*. London: The Institute of Metals.
Benzaid, A., Huet, F., Jerôme, M. et al. (2002). *Electrochim. Acta* 47: 4325.
Bond, A.M. (2002). *Broadening Electrochemical Horizons Principles and Illustration of Voltammetric and Related Techniques*. New York: Oxford University Press Inc.
Boyd, R.W. (1992). *Nonlinear Optics*. San Diego, CA: Academic Press.
Brault, J.W. (1996). *Appl. Opt.* 35: 2891.
Bromage, J. (2004). *J. Lightwave Technol.* 22: 79.
Campagna, M. and Rosei, R. (eds.) (1990). *Photoemission and Absorption Spectroscopy of Solids and Interfaces with Synchrotron Radiation*. Amsterdam, Holland: North-Holland.

Fleming, G.R. (1986). *Chemical Applications of Ultrafast Spectroscopy*. New York: Oxford University Press.
Goldberg, I.B. and Bard, A.J. (1971). *J. Phys. Chem.* 75: 3281.
Graham, M.J. (1995). *Corros. Sci.* 37: 1377.
Graham, M.J. (2000). *Mater. High Temp.* 27: 1.
Graham, M.J. and Hussey, R.J. (1995). *Oxid. Met.* 44: 339.
Griffiths, P. and de Hasseth, J.A. (2007). *Fourier Transform Infrared Spectrometry*, 2e. Chichester: Wiley.
Gross, E. (1930). *Nature* 126: 201, 400, 603.
Gu, Z. and Ubachs, W. (2014). *J. Chem. Phys.* 161: 104320.
Guidelli, R. (ed.) (1992). *Electrified Interfaces in Physics, Chemistry and Biology*, NATO ASI Series C. Dordrecht: Kluwer Academic Publishers.
Hamaguchi, C. (2010). *Basic Semiconductor Physics*, 2e. Heidelberg: Springer-Verlag.
Harrison, P. (2000). *Quantum Wells, Wires and Dots*. Chichester: Wiley.
Hertig, H., Mrosan, E., and Ziesche, P. (1987). *Multiple Scattering Theory of Point Defects in Metals: Electronic Properties*, Teubner-Texte zur Physik, vol. 11. Leipzig: Teubner.
Ibach, H. (1991). *Electron Energy Loss Spectroscopy*. Heidelberg: Springer-Verlag.
Ichimiya, A. and Cohen, P.I. (2004). *Reflection High Energy Electron Diffraction*. Cambridge: Cambridge University Press.
Israelachvili, J.N. (2011). *Intermolecular and Surface Forces*, 3e. Waltham, MA: Academic Press.
Jedlinski, J. (1992). *Solid-State Phenom*, vol. 335, 21–22.
Kevan, S.V. (ed.) (1992). *Angle-Resolved Photoemission: Theory and Current Applications*. Amsterdam, Holland: Elsevier.
Khanna, A.S. (2002). *Introduction to High Temperature Oxidation and Corrosion*. Materials Park, OH: ASM International.
Kubaschewski, O. and Hopkins, B.E. (1967). *Oxidation of Metals and Alloys*, 2e. London: Butterworths.
Legat, A. (2000). *Corrosion* 56: 1086.
Levenson, M.D. and Kano, S.S. (1988). *Introduction to Nonlinear Laser Spectroscopy*. Boston, MA: Academic Press.
Lindner, P. and Zemb, T. (eds.) (1991). *Neutron, X-ray and Light Scattering*. Amsterdam, Holland: Elsevier Science Publishers.
Mahoney, C.M. (ed.) (2003). *Cluster Secondary Ion Mass Spectrometry Principles and Applications*. New York: Wiley.
Marriott, J.B. (ed.) (1988). *High-Temperature Alloys – Their Exploitable Potential*. Amsterdam, Holland: Elsevier.
Mirabella, F.M. Jr. (ed.) (1993). *Internal Reflection Spectroscopy – Theory and Applications*. New York: Marcel Dekker, Inc.
Morris, M.D. (ed.) (1993). *Microscopic and Spectroscopic Imaging of the Chemical State*. New York: Marcel Dekker.
Musiani, M., Liu, J.-Y., and Tian, Z.-Q. (2014). *Developments in Electrochemistry: Science Inspired by Martin Fleischman*, 1e (ed. D. Pletcher, Z.-Q. Tian and D.E. Williams). Chichester: Wiley.
Naiva, H.S. (ed.) (2001). *Handbook of Advanced Electronic and Photonic Materials and Devices*. London: Academic Press.
O'Connor, D.J., Saxton, B.A., and Smart, R.S.C. (eds.) (1992). *Surface Analysis Methods in Material Science*. London: Springer.
Pankove, J.I. (1971). *Optical Process in Semiconductors*. New York: Dover Publications.
Parson, W.W. (2007). *Modern Optical Spectroscopy*. Berlin: Springer-Verlag.
Persson, B.N. (1998). *Sliding Friction: Physical Principles and Applications*. Berlin: Springer-Verlag.
Psaras, P.A. and Langford, H.D. (eds.) (1987). *Advancing Materials Research*. Washington, DC: National Academy Press.
Raman, C.V. (1928). *Indian J. Phys.* 2: 387.
Raman, C.V. and Krishnan, K.S. (1928). *Nature* 121: 501.
Revie, R.W. (ed.) (2011). *Uhlig's Corrosion Handbook*, 3e. Hoboken, NJ: Wiley.
Schwartz, L. and Cohen, J.B. (1987). *Diffraction from Materials*. Berlin: Springer-Verlag.
Shionoya, S. and Yen, W.M. (eds.) (1999). *Phosphor Handbook*. Boca Raton, FL: CRC Press.
Silverman, D.C. (2011). *Uhlig's Corrosion Handbook*, 3e (ed. R. Winston Revie), 1129. Hoboken, NJ: Wiley.
Smith, B.C. (2011). *Fundamentals of Fourier Transform Infrared Spectroscopy*. Boca Raton, FL: CRC Press.
Solé, J.G., Bausá, L.E., and Jaque, D. (2005). *An Introduction to the Optical Spectroscopy of Inorganic Solids*. Chichester: Wiley.
Theophile, T. (ed.) (2012). *Infrared Spectroscopy – Materials, Science, Engineering and Technology*. Rijeka, Croatia: InTech Europe.
Vickerman, J.C. and Gilmore, I.S. (eds.) (2009). *Surface Analysis – The Principal Techniques*, 2e. London: Wiley.
Watts, J.F. and Wolstenholme, J. (eds.) (2003). *An Introduction to Surface Analysis by XPS and AES*. London: Wiley.
Weinberger, P. (1990). *Electron Scattering Theory of Ordered and Disordered Matter*. Oxford: Clarendon.
Williams, D.C. and Carter, C.B. (2009). *Transmission Electron Microscopy*. USA: Springer-Verlag.

Chapter 18

Protective Coatings

18.1 Introduction

The last 20 years have seen a fast and steady increase of research into HTC. A quick survey with Scopus using the keywords "high temperature corrosion," "high temperature oxidation," and "high temperature coatings" showed that in 1995, 1335 papers were published and 13 620 patents applied for; in 2005, the figures increased to 4350 and 46 585, while in 2010 they increased to 7890 and 85 060, respectively. This is a direct result of the many investigations into high performance structural materials for aerospace, energy and automobile applications, and also long-life corrosion-resistant bulk and coating materials for engineering components working in complex environments, such as oxidizing, sulfidizing, carburizing, or chloridizing environments, with or without additional mechanical action of solid particles on the material surface.

Metals and alloys must be effectively protected against these corrosive environments through the formation of protective oxide layers with the characteristics of slow growth, high resistance to cracking and spallation, and strong reheating ability. The prevention of high temperature corrosive attacks on materials plays a critical role in aspects such as reliability, quality, safety, and profitability of any industrial sector associated with high temperature processes (e.g. coal, oil, and fluidized-bed systems, gas turbine and diesel engine systems, nuclear power systems, other power and energy generation and tribology sectors, and electronic and semiconductor components). There are many measures to protect the materials against their degradation at elevated temperatures, and some of them are described in the listed references. In particular, the excellent book *Introduction to the High Temperature Oxidation of Metals*, by Birks et al. (2006), describes a procedure concerned with the use of gaseous atmospheres to control surface reactions during reheating for working or heat treatment. Its main application is in this area of heat treatment simply to prevent surface damage, and the interested reader should study it for a deeper understanding of the subject. But the great stringent requirement of high temperature strength and corrosion resistance is a composite system in which mechanical strength is achieved by alloy development and corrosion resistance by surface coating or surface modification.

Corrosion and oxidation *protective coatings* work by forming a thin oxide barrier on the surface as shown in Figure 18.1. This barrier separates the base metal and coating from the reactive gases. This barrier is extremely thin, on the order of 100 microinches or 2 μm. Without this barrier, the reaction gases would oxidize and corrode both the base metal and the coating itself. This oxide barrier is typically alumina, Al_2O_3, although chromia, Cr_2O_3, will also provide protection (chromium assists in the formation of the alumina oxide barrier). More recently, silicon is also being used as a beneficial oxide scale former.

The role of the coating is to form this oxide barrier. Ideally, this barrier is perfectly adherent to the substrate, has no imperfections, and grows very slowly after first forming. Since one cannot achieve ideal oxide barriers, the coating must be able to reform the oxide barrier should some of it become damaged due to cracking, spallation, etc. The role of the coating is to act as a reservoir of the oxide-forming elements, which are primarily aluminum and chromium. Thus, these coatings contain as much aluminum and chromium as possible. This chapter briefly deals with various coating systems and processes for their application, which are available for protection. Categories of coatings, methods of their production, brief considerations on their degradation, and present and future applications are also described.

18.2 Coating Systems

18.2.1 General

The need for coating systems in the domain of high temperature arose by the 1960s when improved performance criteria could not be met adequately in spite of new materials with superior physical, mechanical, and metallurgical

High Temperature Corrosion: Fundamentals and Engineering, First Edition. César A. C. Sequeira.
© 2019 John Wiley & Sons, Inc. Published 2019 by John Wiley & Sons, Inc.

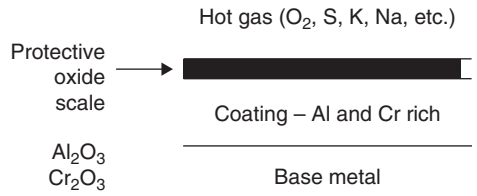


Figure 18.1 Scheme of a high temperature coating protecting the base metal by forming a protective oxide.

properties. Operating efficiency and production economy had to be considered and an improvement sought.

In this section, a brief overview of the main categories of coating systems is provided.

18.2.2 Diffusion Coatings

Nowadays the coatings for high temperature applications include mainly diffusion coatings, overlay coatings, and thermal barrier coatings (TBCs). The protective character of *diffusion coatings* attributes to the protective nature of the Al_2O_3, Cr_2O_3, and SiO_2 scale formed, respectively, on the aluminides, chrominides, or silicides at elevated temperatures. Diffusion coatings have first been developed and still are the most used coating. Aluminide diffusion coatings are proved to be the cost-effective solution for high temperature oxidation, which are used widely for protecting turbine blades and vanes. The properties of the aluminide coating depend on the process methodologies used to deposit the coating, the substrate composition, and the subsequent treatment. The coating deposition rate and morphology depend on the process temperature and time. Processing temperature influences the rate of diffusion, at which alloy elements may diffuse and the metallurgy of the surface compound may form; thus, it is a critical parameter in the processing and manufacturing of diffusion coatings. The coating time at temperature defines the thickness of the coating formed during the diffusion step. The thickness of the coating is also a main factor of protecting property of the coatings. Two basic mechanisms typify the diffusion coatings, depending on whether the main diffusing species is aluminum diffusing from the coating to substrate of the base metal of the substrate alloy diffusing outward to the coating layer. These coatings are usually produced by pack cementation, out-of-pack cementation, and chemical vapor deposition (CVD), which involve the diffusion of a predominant element such as aluminum to form "diffusion coating" layers. It should be noted that coatings are typically fine grained with more grain boundaries compared with substrate materials. Diffusion rates in coatings are therefore expected to be faster than in substrate of similar composition. The three main diffusion coating mechanisms will be analyzed in the next section. Here, the diffusion coating mechanisms will be briefly considered, taking the diffusion aluminide coatings as an example.

Aluminizing is achieved by two different processes that are based on the activity of aluminum in the gas phase and the aluminizing temperature. The low activity high temperature (LAHT) process is a "one-step" method with outward diffusion of Ni to form β-NiAl coating. On the other hand, the high activity low temperature (HALT) process concerns the inward diffusion of aluminum, typically giving rise to a δ-Ni_2Al_3 coating, which requires subsequent heat treatment to convert it to β-NiAl. This is because δ-Ni_2Al_3 is a brittle phase that has lower mechanical property than β-NiAl. As might be expected, the mechanisms by which the coatings grow are also different. For the LAHT process, the aluminum activity is insufficient for it to be the predominant diffusing species, and accordingly, coatings form by diffusion of Ni from the alloy substrate into the region of the coating. For the HALT process, the aluminum activity in the gas phase and at the surface of the coating is high enough to facilitate the inward of Al into the alloy substrate. The growth mode is an important factor when considering coating integrity, since coatings formed by outward Ni diffusion can trap diluent particles (alumina) brought by aluminizing packs. While in the coating β-NiAl phase layer of LTHA, much unwanted phases can precipitate dispersively, which decrease the mechanical property of the coating. Which coating process is selected depends upon a number of features, e.g. heat treatment specifications for the substrate alloy, applications, nature of packs available, integrity issues, etc.

In LAHT aluminizing (low aluminum content in the pack [1.2–1.5 wt% of Al], 900–1150 °C), the aluminum is deposited on the surface, but at reduced rate, and nickel simultaneously diffuses outward to the surface. Then a β-NiAl surface layer forms. The interdiffusion coefficient in the β-NiAl phase of the Al–Ni system varies strongly with composition. At 1050 °C, the minimum value of interdiffusion coefficient is not at the stoichiometric composition, but displaced to the low-Al side by 1–2 at.% (that is 48–49 at.% of Al). Ni diffuses predominantly in low-Al β-NiAl.

The rapid nickel diffusion to the surface, coupled with the low aluminum activity at the surface, effectively holds the surface aluminum content close to 50 at.%. Hence, LAHT coatings are near stoichiometric at the surface and Ni rich within the substrate β-NiAl phase. This structure ensures outward of Ni transport and the outward growth of the coating microstructure. Another important result is that slowly diffusing elements Ta, W, Re, and Mo from substrate are unable to diffuse to form significant concentration levels in the outwardly growing β-NiAl. The outer zinc zone of this coating therefore appears much "cleaner" and is free from such precipitates as observed in

the HALT coatings. The limited solubility of Cr, as well as Ta, Mo, and W, in the β-NiAl phase produces precipitates of topologically close-packed (TCP) phases, forming an *interdiffusion zone* (IDZ) under the "clean" β-NiAl phase layer. Thus, the IDZ includes the complicated TCPs and β-NiAl phases. This coating composition and structure are less dependent on the alloy composition. The further diffusion processes between such aluminide coatings and Ni-based alloys are determined by the aluminum activity in the β-NiAl phase. As long as this is lower than the equilibrium activity among β, IDZ, and $\gamma + \gamma'$ matrix, Ni will diffuse out of the base alloy into the β phase. The coating grows further outward.

The kinetics of the formation of aluminide coating on pure Ni by LAHT has also been studied, and this mechanism is illustrated in Figure 18.2.

In respect to the HALT theory interpreted above, if the activity of Al is low, Ni preferentially diffuses out through the coating and combines with Al to form NiAl. The coating grows outward. In this case, Ni diffuses faster than inward diffusion of Al. Pack particles are entrapped in the coating. These particles are assumed to be dragged out by the diffusion of Ni.

As previously mentioned, HALT coatings are processed at lower temperature (700–950 °C) as the first step, with a higher aluminum content (1.7–2.7 wt% of Al). The substrate material (γ-Ni + γ'-Ni_3Al) reacts with the depositing aluminum, forming a surface layer of δ-Ni_2Al_3 over the layer of β-NiAl. The diffusivity of Al through δ-Ni_2Al_3 is very high, and substantial amounts of Al can be forced deeper and deeper into the material. In δ-Ni_2Al_3 phase layer, the diffusivity of Ni is near zero, while Al diffuses rapidly; thus the formation of surface layer of δ-Ni_2Al_3 results from the inward diffusion of aluminum. Substrate alloying elements such as W, Mo, Ta, and Re are selectively diffusing at the coating/substrate interface. Once the solubilities of alloying elements of W, Mo, Ta, Re, and Cr are saturated, many precipitates rich in these elements will occur for their limited solubility to β-NiAl phase and distribute in the entire coating structure. After a second step of heat treatment at higher temperature (950–1100 °C), Ni is able to diffuse outward to transform the brittle δ-Ni_2Al_3 phases into Al-rich β-NiAl. This step is also usually combined with the heat treatment required to recover substrate properties.

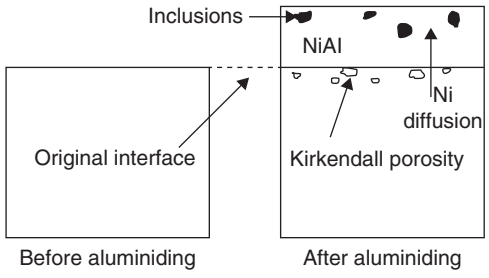


Figure 18.2 Diffusion aluminide formation on pure Ni.

Now we have preliminary concepts of LAHT and HALT, and then we can primarily establish whether the coating belongs to one process or the other. However, in the actual manufacturing there are all kinds of operations by adding different amounts of Al and at different temperatures. Therefore, the resulting coating could be significantly different and have very complex structures.

Coating–superalloy interdiffusion is principally responsible for the phase transformations, oxidation behavior, and degradation of the mechanical properties of the coating. Moreover, the diffusion behavior in the multicomponent coating layers is very complicated due to the interactions among the components. Thus, diffusion is an important factor to be considered when designing β-NiAl coatings.

18.2.3 Overlay Coatings

Diffusion-type coatings, used successfully on early gas turbines, were tied to the substrate composition, microstructure, and design. Later, some changes were introduced: (i) in superalloy composition, such as reduction in Cr and increase in other refractory metals; (ii) in microstructure, by castings with more segregation; and (iii) in design, by air cooling and with thin walls (which introduced higher thermal stresses). These changes required coatings that were much more independent of the substrate. *Overlay coatings* met this necessity.

Overlay coatings also overcome the process restrictions encountered in diffusion coatings, especially the variants, viz. Cr/Al, Ta + Cr, or the Pt aluminides, all of which give better stability and oxide hot corrosion resistance than Al alone. MCrAlY compositions (M = Ni, Co, Fe alone or in combination; Y represents oxygen-reactive elements such as Zr, Hf, Si, and Y) are the principals in the series of overlay coatings developed by the *electron beam evaporated physical vapor deposition* (EBPVD) technique for multiple load use. More than 4 million aerofoils have been successfully processed by EBPVD.

MCrAlY overlay used in gas turbines are usually Ni and/or Co with high Cr, 5–18% Al, and Y addition around less than 1% for stability during cyclic oxidation. They are multiphase alloys with ductile matrix, e.g. gamma Co–Cr, containing a high fraction of brittle phase, e.g. beta CoAl. The Cr provides oxidation hot corrosion resistance, but too much Cr affects substrate phase stability. The success of most overlay coatings is the presence (and perhaps location) of oxygen active elements such as Y and Hf, which promote alumina layer adherence during thermal cycling, giving increased coating protectivity at lower Al levels. Y mostly appears along grain boundaries if a MCrAlY is cast

but is homogeneous if plasma sprayed. Thus MCrAlY with 12% Al are more protective than the more brittle diffusion aluminides with 30% Al.

Overlay claddings deposited by hot isostatic pressing (HIP), electron beam evaporation, or sputtering methods are diffusion bonded at the substrate/coating interface, but the intention here is not to convert the whole coating thickness to NiAl or CoAl. There is thus more freedom in coating composition, whose properties can be maximized to the type required. Composition based on NiCr, CoCr, NiCrAl, CoCrAl, NiCrAlY, CoCrAlY, FeCrAlY, and NiCrSi have been successful in gas turbine engines. They are generally alumina formers with only 10% Al unlike the 30% in nickel aluminide coatings. Cr increases the Al activity, which allows this feature. Higher Al levels cause brittleness and a higher DBTT, and the Al levels are generally held below 12% (5–10% preferred). The coatings are also more ductile than NiAl and CoAl and can be rolled and bonded by HIP. In general, NiCrAlY give best results against high temperature oxidation, while CoCrAlY are best for hot corrosion.

18.2.4 Thermal Barrier Coatings

TBCs are ceramic coatings applied over metal substrates to insulate them from high temperatures. They consist of zirconium oxide, ZrO_2, stabilized by about 8 wt% yttria, Y_2O_3, or magnesia, MgO. They are applied over a bond coat that is usually an MCrAlY overlay coating but can be a diffusion coating. The ceramic layer is typically 5–15 mils thick, and the overlay bond coat is usually 3–8 mils thick.

The bond coat improves the adhesion of the ceramic top coat by reducing the oxide buildup underneath the ceramic. (The ceramic is porous to oxygen and will spall off when the oxide formed on the bond coat is sufficiently thick.) The bond coat is applied in the same manner as for overlay coatings.

The ceramic layer is normally plasma sprayed in an air environment. This layer can also be made by electron beam physical vapor deposition (EBPVD), which is used on aircraft engines. The ceramic layer made by EBPVD is columnar grained and is more resistant to spalling than the plasma-sprayed TBC.

Another type of ceramic layer that has been developed is called a segmented TBC. It has cracks through the thickness of the ceramic, which are perpendicular to the substrate surface. These cracks provide increased resistance to spallation, similar to EBPVD ceramic layers. The segmented TBC is made by a proprietary plasma spray process, and very thick ceramic layers can be made.

The TBC protects the metal by acting as an insulator between the metal and the hot gases. The thermal conductivity of the ceramic is 1–2 orders of magnitude lower than the metal. Although thin, the TBC can significantly reduce the metal temperature provided that the metal component is air cooled. (The air cooling provides a heat sink.) Furthermore, the ceramic has a higher reflectivity than the metal. This means that more of the radiative heat is reflected away, which is important for combustion hardware.

During startup and shutdown, the TBC improves the thermal fatigue life by reducing the magnitude of the temperature transients the metal is exposed to. A 10 mil thick TBC on airfoils in experimental aircraft engines has achieved more than 300 °C reduction of metal temperature. During steady-state operation, the TBC lowers the temperature of the underlying metal, thereby improving its durability. It also reduces the severity of hot spots.

The principal failure mechanism of TBCs is the spallation of the ceramic layer. Spallation is caused by the synergistic interaction of bond coat oxidation and thermal cycling. The oxidation occurs at the interface between the bond coat and the ceramic. As more oxide forms at this interface, the ceramic layer is more likely to spall.

18.3 Coating Processes

18.3.1 General

There are three major processes by which the diffusion coatings can be formed: CVD, pack cementation, and out-of-pack cementation, which involve the diffusion element such as aluminum (chromium or silicon). Overlay coatings can be applied by CVD, physical vapor deposition (PVD), high velocity oxygen/flame (HVOF), or plasma spray. Plasma spray is one of the most widely used processes today. TBCs are usually deposited by PVD, EBPVD, and plasma spraying techniques. All these processes and a few more advanced techniques for producing high temperature coatings are described in this section.

18.3.2 Chemical Vapor Deposition

CVD is a process wherein a stable solid reaction product nucleates and grows on a substrate in an environment where a vapor-phase chemical dissociation or chemical reaction occurs. It uses a variety of energy sources, viz. heat, plasma, ultraviolet light, etc., to enable the reaction and operates over a wide range of pressures and temperatures. CVD is a long-established, economically viable industrial process in the field of extraction and pyrometallurgy. Some of the well-known processes are:

The Mond process:

$$Ni(CO)_4 \xrightarrow{150^\circ C} Ni + 4CO \qquad (18.1)$$

The Van Arkel process:

$$TiI_4 \xrightarrow{1200^\circ C} Ti + 2I_2 \qquad (18.2)$$

The Kroll process:

$$TiCl_4 + 2\,Mg \xrightarrow{900^\circ C} Ti + 2MgCl_2 \qquad (18.3)$$

The method has also been used to form freestanding, simple, and complex shaped articles from metals that are not very amenable to fabrication, e.g. W:

$$WF_6 + 3H_2 \rightarrow W + 6HF \qquad (18.4)$$

The technology of CVD took on new dimensions with a fresh view taken at the deposition aspects of the process. This transition of emphasis from extraction to deposition of the CVD phenomenon has made CVD an important sector of coating technology for producing new materials and coatings with improved resistance to wear, erosion and corrosion, good thermal shock resistance, and neutron absorption characteristics. Components from micro- to macro-sizes are now coated by CVD. In the deposition area of CVD, the lamp and electronics industry uses many of the earlier processes to obtain longer service life and better performance for a number of products. The CVD industry took a bigger leap when demands arose for new high temperature materials with greater high temperature corrosion resistance and strength in all the sectors using gas turbines and other propulsion hardware, in the military science, engineering, and aviation fields. In parallel, CVD technology has had rapid application in the semiconductor industry, the many branches of fuel and energy – nuclear, fluidized bed, oil, solar and chemical industries and the tool industry. Solid-state devices; electrode materials; thermionic devices; erosion-, corrosion-, and wear-resistant components; fission barriers; and many more applications can be listed in CVD technology.

It would be confusing and misleading to list a number of processes as CVD methods in as much as different high temperature coatings cannot be merely termed as diffusion coatings. The minor or major parameters that influence the actual achievement of the coating itself are those that facilitate categorization. Otherwise, conventional CVD, plasma-assisted CVD (PACVD), laser-assisted CVD (LACVD), pack, vacuum pack, pack-slip, vacuum pack-slip, CCRS, or RS may all be just CVD. Similarly, diffusion coatings can be obtained by first hot dipping, spraying, cladding, fused salt electrodeposition, electrophoresis, plasma, or all PVD, and all the above "CVD" methods. What gives the distinction to any process?

The obvious factor that emerges is that a basic CVD process has a number of limitations, e.g. the types of reactions possible and available, and the minimum substrate temperature that has to be maintained. This results in restricting any eventual substrate/deposit configuration and control. Improved techniques stretch the reactant–product spectrum and can also (i) lower the temperature; (ii) reduce the hazards and mismatch in the morphological aspects, viz. nucleation and growth; (iii) alter the physical–mechanical properties favorably; and (iv) provide better bonding.

CVD technology offers the following favorable aspects to semiconductor industry:

(i) A wide range of silicon epitaxy thicknesses and resistivity.
(ii) A low cost, highly productive method of depositing polysilicon, Si_3N_4, and high temperature SiO_2.
(iii) A proven technology for passivating silicon devices with low temperature deposition of silicon oxide and silicon nitride.

A wide range of metallic and inorganic coatings can be produced by CVD. In many instances CVD coatings exhibit unique properties, which are difficult to produce by other methods.

A CVD process was seen as a thermochemical process in which the substrate is regarded as a collector of the deposit, and the substrate/deposit interaction is both undesirable and unnecessary for deposit growth. However, for a CVD deposit, the post-deposition state is a mandatory parameter to meet the service requirements; substrate/deposit interaction to some degree is expected. Further, heat treatment, and therefore diffusion, is often a step following the primary CVD process (or even during deposition, since the substrate is heated). Thus, substrate/deposit interaction always occurs and is also one of the ways deposit consolidation can be achieved.

A CVD reactor is the apparatus-equipment configuration that carries out the CVD process. CVD reactors are categorized on the basis of the temperature and pressure under which they operate. A CVD reactor can have a cold wall or a hot wall depending on the experimental optimization parameters. When the reactor wall surrounding the heated substrate is comparatively cool relative to the temperature of the substrate, it is a cold-wall reactor. The substrate is heated directly, and product deposition occurs mostly on the heated component. In a hot-wall reactor, the deposition product can nucleate both on the reactor wall and the heated substrate, though to different degrees, if a temperature difference prevails across the wall substrate area and zone. The substrate may be independently heated or not, but the reactor itself is heated in order to facilitate the process.

The CVD reactor assembly consists of three components: (i) the reactant supply system, (ii) the deposition systems, and (iii) the reactant–product retrieval, recycle, and disposal system. The entire reactant supply (using solid and/or gaseous reactants) has to be carefully balanced before introduction into the reactor system, predicted to reach the required partial pressures at the temperatures of reaction and deposition. The primary features

to consider concerning the substrate preparation are the substrate/deposit adherence and growth. CVD reactions can be exothermic but mostly are endothermic. This could result in substrate cooling. On a production scale, large volumes of gases are handled, which can induce convective coating. Both these situations have to be compensated. Substrate heating optimization involves achievement of the correct temperature profile and coating exposure time. The substrate/reactor parameters in a deposition system should be designed to achieve a laminar flow. The input can be parallel, perpendicular, or angular to the substrate depending on the substrate holder design. The movement (rotation, lateral, etc.) of the substrate within this region also compensates to some extent any nonuniformity in the deposition.

CVD occurs through a chemical reaction; therefore, the thermodynamics of the system that can drive the chemical reaction, the basic chemical kinetics to provide information on the reaction rate, and mass and heat transfer profiles that are influenced by the reactor and substrate size and design, require consideration.

Mass transport of a CVD system links diffusion control, chemical kinetics, and fluid-flow dynamics. Diffusion growth can be ascertained from chemical kinetics by rate constant of growth $= \underline{A} \exp(-E/kT)$, where E is the activation energy, k is the Boltzmann's constant, and T is the temperature. With increase in substrate temperature, the growth rate changes at a transition temperature from a predominant kinetics to a diffusion control, the latter being mostly under mass transport influence (Figure 18.3).

Many models of CVD reactors and their kinetics have appeared in the recent literature, but space restrictions impose our departure to the next coating process.

18.3.3 Pack Cementation

Pack cementation is an extended CVD method in which the substrate to be coated is introduced in a retort and surrounded by a powder mixture, which is composed of the source alloy(s), an activator, and an inert filler. The retort is then heated to the desired coating temperature usually under inert or reducing environment. In these conditions, the source element reacts with the activator, forming a gaseous transporting species. This diffuses through the pack to the substrate surface where it decomposes, allowing the metallic element to be deposited to penetrate into the substrate by solid-state diffusion.

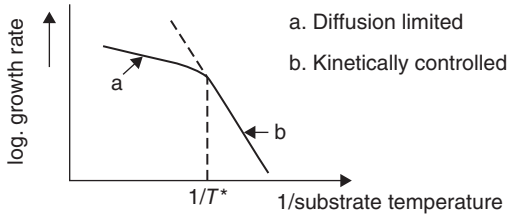


Figure 18.3 Growth rate curve of a CVD process – schematic.

As for all diffusion coatings, the microstructure is highly dependent on the substrate, which is coated. For this reason, process conditions have to be optimized for each material.

The first "cementation process" was presented by Allison and Hawkins in 1914, who deposited Al on iron and on steel. But it is only since the 1960s that this process stimulated interest because of the development of coatings for the protection of gas turbine blades, especially those made of Ni-based superalloys. The process has then been extended to Co and Fe-based alloys. Concerning the elements deposited, these are mainly Al followed by Cr and Si. Nevertheless, codeposition of two or three elements became possible with the theoretical understanding of the process. The extensive works on Cr–Al codeposition published by Rapp on steels (1989, 1994, 1997) and by Young et al. on nickel-based alloys (da Costa et al. 1994a,b, 1996; Gleeson et al. 1993) are the major examples, but development of Cr–Si (Rapp 1996), Al–Si (Wynns and Bayer 1999), Ti–Al (Weber 2004), and Ti–Si–Al (Rosado and Schütze 2003) coatings can also be mentioned. Eventually, more recent investigations seem to focus on the addition of reactive elements such as Y, Ce, or Hf by codiffusion.

The principles of the pack cementation technique changed remarkably little since 1914, but the composition and the quality of the substrate–deposit systems have been optimized in reply to the requirements of a large range of service applications.

From an industrial point of view, the pack cementation technique has been used very extensively for nearly 60 years for coating gas turbine blades (Mévrel et al. 1986). Nowadays it is estimated that on first-stage gas turbine blades, more than 80% of all coated airfoils are coated by pack cementation (Goward 1998).

The coating of larger pieces has been the subject of some research investigations and even leads to the development of a few patents, showing that coating even inside a tube is possible by this technique (Baldi 1980; Wynns and Bayer 1998). During the 1990s the US company Alon developed several industrial processes involving the pack cementation technique. The purpose was to protect ethylene cracker furnace components from carburization and coke formation (Kurlekar and Bayer 2001). With Alon's facilities, 15 m long furnace tubes can be coated with Al, Cr, and/or Si on an industrial scale, producing 100 000 linear meters of tubes per year (Alon). After one year service in an ethane cracking furnace, the coating reduced the coke formation by a factor of 2, and post-exposure analysis revealed that the coating microstructure was essentially unchanged (Ganser et al. 1999).

Table 18.1 Different pack mixes and processing parameters for various pack cementation coatings

Coating type	Source composition	Processing parameters
Pack aluminizing, inward diffusion in Ni_2Al_3 in nickel alloys	5–20% Al (Al–10Si), 0.5–3% NH_4Cl, balance Al_2O_3 powder	1–4 h at 650–680 °C in air, argon, H_2; heat treat 4–6 h at 1095 °C in argon
Pack aluminizing, inward diffusion in NiAl in nickel alloys	44% Al, 56% Cr, NH_4Cl, balance Al_2O_3 powder	5–10 h at 1040 °C in vacuum (argon, H_2)
Pack aluminizing, outward diffusion in NiAl in nickel alloys	2–3% Al, 20% Cr, 0.25% NH_4HF_2, balance Al_2O_3 powder	25% at 680 °C in argon, 2–5 h
Pack aluminizing of cobalt alloys	8% Al, 22% Cr, 1% NH_4F, balance Al_2O_3 powder	4–20 h at 980–1150 °C in argon
Gas-phase aluminizing, outward diffusion in NiAl in nickel alloys	10% Co_2Al_5, 2.5% NaCl, 2.5% $AlCl_3$, balance Al_2O_3 powder	3 h at 1095 °C in argon
Gas-phase aluminizing, outward diffusion in NiAl in nickel alloys	30% Al–70% Cr alloy granules, NH_4F	4 h at 1150 °C in argon
Pack or gas-phase chromizing of nickel alloys	15% Cr, 4% Ni, 1% Al, 10.25% NH_4Cl, balance Al_2O_3 powder	3 h at 1040 °C in argon

Typically the powder pack mixture consists of three components:

- A metallic source: A fine powder of the element(s) to be deposited on the surface of the substrate (Al, Cr, Si, Ti, or combinations of these elements).
- A halide salt activator as, for example, NaCl, NH_4Cl, $AlCl_3$, NaF, NH_4F.
- An inert filler powder (e.g. Al_2O_3) preventing the powder mixture from sintering at high temperature.

Table 18.1 lists different packs that can coat various elements with the corresponding temperatures and heat treatment durations.

Figure 18.4 illustrates the major chemical reactions involved in the general pack cementation process. In order to allow a better understanding of the following paragraph, the reactions are written for the particular example of aluminizing of iron activated by NH_4Cl.

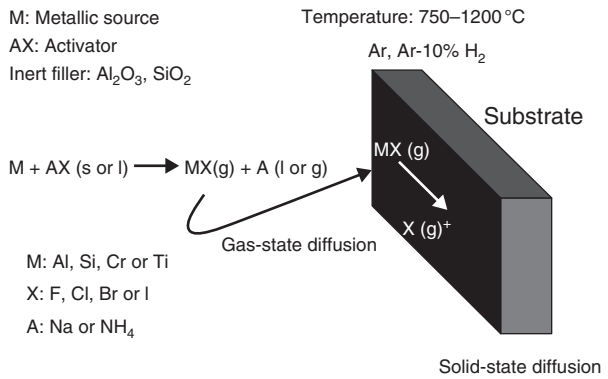


Figure 18.4 The main chemical reactions involved in the pack cementation process.

The whole process relies on the formation of gaseous halides according to the general reaction:

$$x\mathrm{Al} + y\mathrm{NH_4Cl} \rightarrow \mathrm{Al}_x\mathrm{Cl}_y + y\mathrm{NH_3} + \frac{y}{2}\mathrm{H_2} \qquad (18.5)$$

$AlCl_3$, $AlCl_2$, AlCl, Al_2Cl_6, and Al_2Cl_4 are the chlorides involved in a chloride-activated aluminizing process.

The partial pressures of each of the gaseous halides formed are established by their thermodynamic stability, which varies with the process conditions: composition of the pack, type of activator, temperature, pressure, and type of inert or reducing environment.

In the case of aluminum deposition, $AlCl_3$ is the major halide formed at low temperature, whereas at higher temperature the activity of AlCl becomes higher.

Once they are formed, the halide molecules diffuse through the gas phase to the substrate (e.g. iron) surface, where they adsorb and decompose owing to the general reactions:

Disproportionation:

$$(x+1)\,\mathrm{AlCl}_x \rightarrow x\mathrm{AlCl}_{x+1} + \mathrm{Al} \qquad (18.6)$$

Displacement/exchange:

$$\mathrm{Fe} + \mathrm{AlCl}_x \rightarrow \mathrm{FeCl}_x + \mathrm{Al} \qquad (18.7)$$

Direct reduction:

$$\frac{x}{2}\mathrm{H_2} + \mathrm{AlCl}_x \rightarrow x\mathrm{HCl} + \mathrm{Al} \qquad (18.8)$$

Dissociation:

$$\mathrm{AlCl}_x \rightarrow \frac{x}{2}\mathrm{Cl_2} + \mathrm{Al} \qquad (18.9)$$

By using alkaline or earth alkaline halide activators as, for instance, NaCl, KCl, or $CaCl_2$, the precipitation of the activator salt has also to be considered (Ravi et al. 1989):

Precipitation:

$$AlCl + Na \rightarrow NaCl + Al \qquad (18.10)$$

The aluminum formed at the surface of the substrate of Reactions (18.6)–(18.10) can then diffuse into the solid substrate, forming the desired coating.

The predominance of the Reactions (18.6)–(18.10) depends, first of all, on the stability of the gaseous halides involved. The deposition particularly occurs by disproportionation Reaction (18.6) when, first, the vapor pressure of the substrate halide is low and when, secondly, the coating element has higher and lower halides of comparable vapor pressures in order to set atomic aluminum-free. When the vapor pressure of the substrate halide becomes comparable to the gaseous species of the coating element, the contribution of the exchange Reaction (18.7) becomes important. The latter reaction even gets undesirable if the vapor pressure of the substrate halide becomes higher than the source supplier halide, as it would lead to a significant metal loss and to porous coatings. In a NaCl-activated pack, this phenomenon can occur during chromizing or siliconizing of iron, whereas Reaction (18.7) stays minimal during aluminizing (Kung and Rapp 1989).

The reader may, at this point, easily catch the compromise that has to be found. Because halide molecules must diffuse through the gas phase from the pack to the substrate, the coating composition depends on the gaseous halide activity and their stability or their ability to decompose at the substrate surface. Hence, the formation and the decomposition of the gaseous halide have to be optimized at the same time in the pack and at the substrate surface, respectively.

Furthermore, it is a prerequisite that the thermodynamic activity of the incorporated element is always lower at the surface than in the pack (Gupta and Seigle 1980). This activity gradient drives the gas-phase diffusion of the halide molecules from the pack to the substrate surface. As a consequence, a desired coating composition cannot be obtained by simply using a master alloy of the same composition (Rapp 1989).

Moreover, the concept of "major depositing species" has been defined. This corresponds to the gaseous species that is responsible for the major part of the deposition. In the case of a Cr–Al codeposition process by a chloride-activated pack, Rapp (1989) and da Costa et al. (1994a,b) showed that although the vapor pressure of $AlCl_3$ is several orders of magnitude higher than that of Cr halides and other Al halides, the codeposition is possible by optimizing the process conditions so as to get comparable vapor pressures of AlCl and $CrCl_2$. Indeed, $AlCl_3$ is too stable and does not decompose enough at the substrate surface. The Al transport occurs via AlCl. This is thus considered as the major transporting species for Al, whereas $CrCl_2$ is the major transporting species for the deposition of Cr (Rapp 1989).

The formation of the coating can be described in the light of diffusion couples (Wachtell 1974). The coating actually corresponds to the IDZ between the substrate element(s) and the deposited element(s). The driving force for the solid-state diffusion is the activity gradient between the pack/coating and the coating/substrate interface.

The aluminizing of iron can thus be treated as a binary diffusion couple, involving pure Al and pure Fe. As a consequence, the phases formed in the coating should follow the FeAl binary phase diagram (Figure 18.5).

As can be seen from this diagram, the aluminizing of iron can form several intermetallic phases, $FeAl_3$, Fe_2Al_5, $FeAl_2$, FeAl, or Fe_3Al as well as solid solution of Al in Fe. The effective formation of these phases is however controlled by the powder composition, the temperature, and the duration of the process. These parameters especially control the diffusion fluxes, which determine the final coating structure.

Goward and Boone (1971) distinguished the low and the high activity pack structures (Figure 18.6), as already discussed in Section 18.2.2. Their investigations considered the aluminizing of a nickel-based superalloy. Two powder pack mixtures differing in the nature of the Al source (pure Al or Ni_2Al_3) were investigated at about 800 and 1100 °C, respectively. The observations lead the authors to consider that the high activity pack (with the powder containing pure Al) structure is characterized by a high aluminum content at the surface with the coating phase Ni_2Al_3. The underlying phases down to the coating–substrate interface followed the Ni–Al phase diagram with decreasing Al content. For the low activity pack (with the powder containing Ni_2Al_3), the coating is single-phased β-NiAl, which is directly in contact with the substrate.

The difference was attributed to the diffusion fluxes:

- In the high activity pack conditions, the coating formation was attributed to exclusive inward Al diffusion, the diffusion of Ni being minimal at low temperature.
- In low activity packs, the coating formation was interpreted as single Ni outward diffusion. This last mechanism also requires higher temperatures to allow diffusion of Ni.

One example of nickel aluminide diffusion coating produced by LAHT pack cementation process is illustrated in Figure 18.7. The coating consisted of a well-defined to "clean" layer with NiAl as its major phase and a large diffusion zone underneath.

An example of SEM-BSE (backscatter electron) image of LTHA coating on Ni-based superalloy CMSX4 (this is a typical second generation Ni-based single-crystal superalloy characterized by the replacement of most of the Ti with Ta, by relatively high Co and low Mo content) is

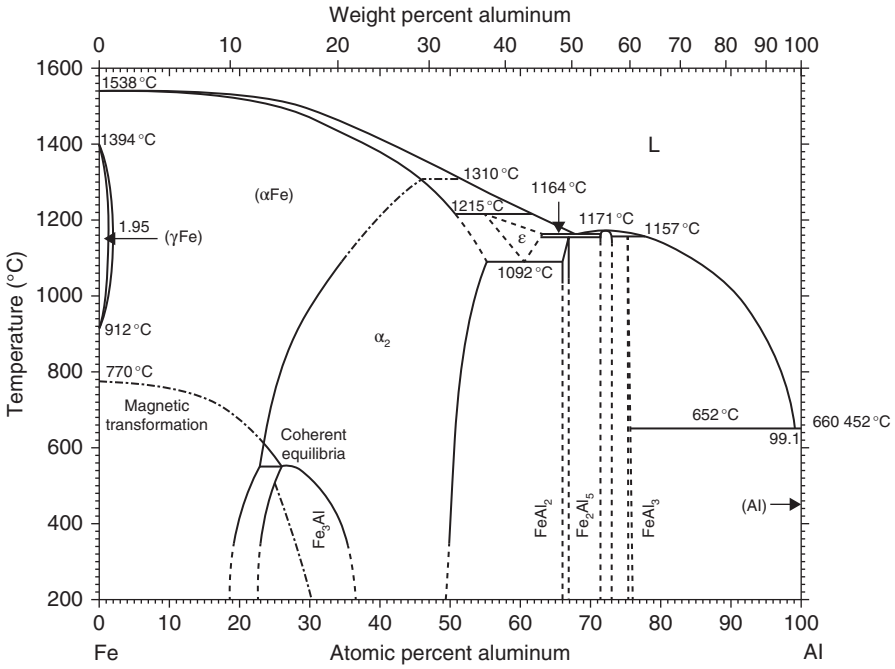


Figure 18.5 FeAl phase diagram. Source: Massalski (1986).

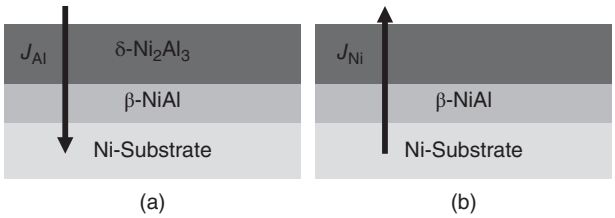


Figure 18.6 Simplified scheme of the two archetypes of pack cementation aluminizing structures on Ni drawn on the basis of Goward and Boone's work (1971). J_{Al} and J_{Ni} designate the fluxes of Al and Ni, respectively. (a) High activity pack structure inward diffusion of coating element(s) at low temperature. (b) Low activity pack structure outward diffusion of substrate element(s) at high temperature.

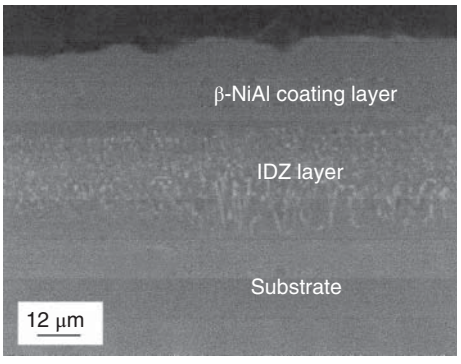


Figure 18.7 A nickel aluminide diffusion coating produced using LAHT pack cementation process.

shown in Figure 18.8. This coating was deposited using an aluminizing pack containing 2 wt% Al at 900 °C and was heat-treated for 2 hours at 1120 °C and then for 24 hours at 845 °C. The β-NiAl phase layer is uniform in thickness,

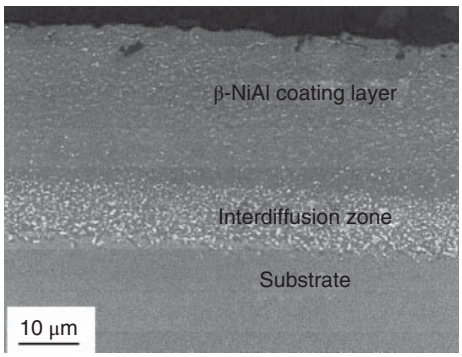


Figure 18.8 A nickel aluminide diffusion coating produced using LTHA pack cementation process on CMSX4. Source: Das et al. (1998).

and many precipitates (white small particles) distributed dispersively in the entire β-NiAl phase layer. Squillace et al. (1999) has also analyzed clearly the coating structure after the first step of LTHA. Three layers are visible: the inner layer has a striated appearance, the outer layer is equiaxed with many inclusions, and the middle layer is featureless. The coating layer has deposited very high amount of Al. In the book entitled *High Temperature Coatings* by Bose (2007), it was presumed that higher inward diffusion of Al with lower outward Ni diffusion has avoided the formation of Kirkendall porosity and also eliminated the embedded pack particles.

Although mixed types of mechanisms can occur as a result of varying pack activities, substrate compositions, and temperature, during practical application of the coating process, it is still of great use nowadays to relate the observed structures to two archetypes (Figure 18.6).

The aluminizing of iron shows the same kind of behavior. At 900 °C, a three-layer structure with Fe_2Al_5, $FeAl_2$, and FeAl is formed in high activity packs, and a single-phased FeAl coating in low activity packs (Levin et al. 1998).

With the help of thermodynamic calculations performed with a computer software, the activities of the gaseous halides can be determined considering all pack reactions together. Such considerations allow the optimization of the pack concentration and process conditions needed to form the desired coating phase. More precisely, the activities of the gaseous halide depend on the reactants involved in the halide formation and thus on the type of metallic source mixed to the pack powder. Therefore, the direct dependence of the coating structure with the master alloy determines whether the coating deposition occurs in a high or low activity process.

The activator is also a determining reactant involved in Reaction (18.5) too, from which it can be said that an unstable activator results in high halide partial pressures. Moreover, concerning the choice of cation for the activator, some researchers recommend the use of ammonium salts, because of their decomposition at high temperature. Indeed, the NH_3 produced in Reaction (18.5) is not stable above 350 °C decomposing by the following reaction:

$$2NH_3 \rightarrow N_2 + 3H_2 \qquad (18.11)$$

which shows a double advantage:

- The formation of hydrogen enhances the deposition of coating element(s) through the reduction Reaction (18.8).
- The precipitation Reaction (18.10) does not occur, leaving the chlorides behind for reacting with the master alloy.

Concerning the thermodynamic aspects of pack cementation, it is also necessary to note that as a consequence of the temperature dependence of the Reactions (18.5)–(18.11), the process temperature directly influences the formation of gaseous halides and their decomposition, as well as the values of the gaseous and solid-state diffusivities that also influence the kinetics of the cementation process.

Like all CVD processes, pack cementation involves gas–solid reactions. For many cementation coatings, the coating process can be considered as six steps in series (Cockeram and Rapp 1995). Usually at the beginning of the process, the flux of master alloy element delivered by halide molecules on the surface is slower than the limiting flux of this element dictated by the solid-state diffusion. Consequently, the beginning of the process follows the gas diffusion kinetics, and the growth of the depleted zone is rate limiting. At the end of the transition regime (regime after which equilibrium in the pack is achieved), the aluminum flux delivered by the gas phase equals the maximum uptake into the solid phase. At that moment, the kinetics limitation of the process changes from gas diffusion to solid-state diffusion.

18.3.4 Out-of-Pack Cementation

The *out-of-pack or over-pack process* operates in a manner similar to pack cementation except that the components to be coated are suspended either above the pack or below the pack (vapor generator) retort.

The transport of aluminum species from the vapor phase to the substrate occurs by gas-phase diffusion and by solid-phase diffusion of aluminum into the substrate to form the aluminide phases. The former increases the surface concentration of aluminum in the coating, while the latter decreases it. The surface composition of the coating tends to reach a steady-state value in a short time after the commencement of the process. In the vapor-phase aluminizing, the rate of transport of aluminum to the substrate is much faster than the solid-phase diffusion of aluminum into the substrate. Thus the composition of aluminide coating is decided by the kinetics of the solid-phase diffusion. The coating process is divided into a number of steps. They are:

(a) Formation of the aluminum subchlorides by the reaction of the aluminum metal or alloy and the aluminum chloride vapor.
(b) Transport of the subchlorides to the substrate by gas-phase diffusion.
(c) Reaction leading to the deposition of aluminum at the substrate surface.
(d) Diffusion of aluminum into substrate with the formation of the coating consisting of different intermetallic phases.
(e) Diffusion of the reaction products from the substrate back to the reactor.

Steps (a) and (c) are very fast at the operating temperature; therefore, the thickness of the coating process is controlled by step (b) the vapor transport and (d) the solid-phase diffusion. Step (e) decides the purity of the coating.

The schematic diagram of the out-of-pack process is given in Figure 18.9. The coating vapors are transported to the components by an inert carrier gas. Plumbing is designed that the vapors can access to both external and internal surfaces of the components. The retort is inserted into a furnace and held at the desired temperature for the selected duration.

This approach results in a much cleaner and uniform coating for very complicated geometry components, with no entrapped pack particles.

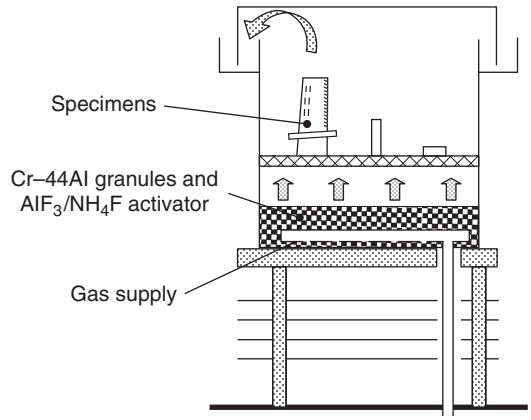


Figure 18.9 Schematic of the out-of-pack vapor-phase aluminizing process. Source: Nicholls et al. (2010).

In industry, for example, components are aluminized using a proprietary SIFCO vapor-phase aluminizing process. A picture of the facility is shown in Figure 18.10a. At the beginning of the vapor-phase coating process, the components, activators, and fillers are loaded into a coating box, and then the coating box is covered with a retort. During the vapor-phase process, the coating box is heated to an elevated temperature of about 1080 °C, held for three to four hours, and then cooled down to room temperature. The temperature profile during the aluminizing process is shown in Figure 18.10b.

18.3.5 Physical Vapor Deposition

PVD is a coating process in which the atoms of the coating material are evaporated and then deposited onto the surface of the part (Boone 1986). The process must be carried out in a vacuum chamber. Coating materials can be pure metals, metallic alloys, or ceramics. Most materials can be coated by the PVD process.

Electron beams are usually used to vaporize the coating material, in which case the process is called "electron beam physical vapor deposition," or EBPVD. A schematic of the EBPVD process is shown in Figure 18.11. The electron beams are focused by magnets on the ingot of the coating material, causing it to melt. Due to the vacuum environment, a vapor cloud of the coating material forms over the molten ingot pool. This vapor rises and deposits on the part to be coated. The evaporated atoms move in a straight line from the molten ingot to the part. Complete coating coverage is obtained by rotating and tilting the part in the vapor cloud.

Diffusion normally occurs during the PVD process at the substrate–coating interface. This diffusion forms a metallurgical bond of the coating with the substrate. However, post-deposition diffusion treatments are commonly performed to improve the bond and the coating. Glass bead peening is also frequently used to close areas of unbonded columnar grain structure to produce a fully dense structure.

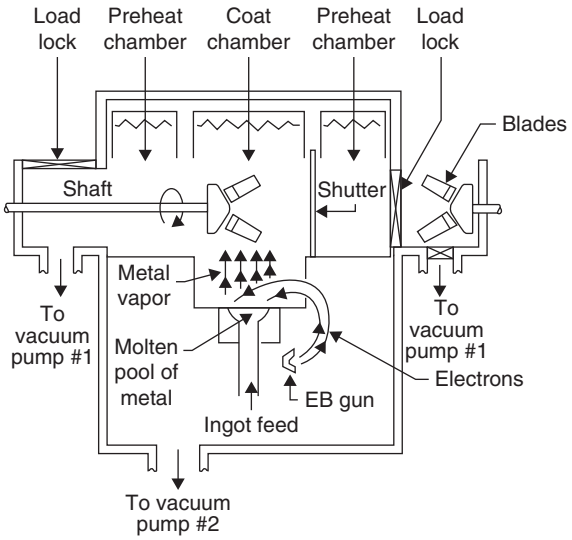
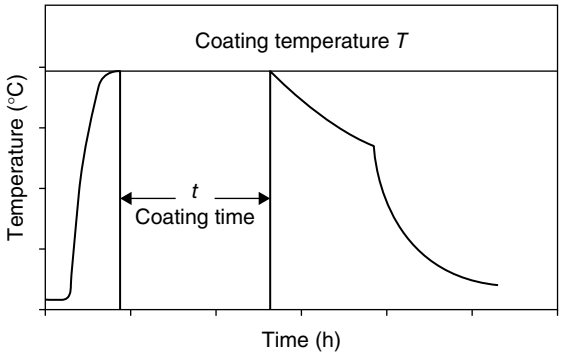


Figure 18.11 Schematic of an electron beam physical vapor deposition (EBPVD) process.



(a)



(b)

Figure 18.10 (a) SIFCO vapor-phase coating process facility. (b) Vapor-phase coating thermal cycle process.

The PVD process is a line-of-sight process, so internal and recessed surfaces cannot be coated. A good vacuum is required to prevent oxidation of the reactive vapor cloud and the substrate surface, since oxide layers can result in a nonadherent coating.

Because of the large part size of industrial gas turbine components and limited chamber size of PVD coaters, the cost of PVD coatings for industrial gas turbine parts can be quite high. These costs may decrease as larger PVD coaters become commercial.

18.3.6 Plasma Spraying

Plasma spraying is a process in which a powder of the coating material is heated and accelerated toward the part being coated by a plasma gas stream. Since it is a line-of-sight coating process, it is necessary to rotate and tilt the part and plasma gun during coating. Internal passages, such as cooling holes, cannot be coated by plasma spray. There are several books and reviews on plasma spraying, and some of them are listed in Futher Reading.

The plasma is generated from a high current arc with inert gases and powder particles, which is then accelerated toward the part, as shown in Figure 18.12. The particles strike the substrate surface at a high velocity. (Prior to spraying, the substrate surface is roughened by an abrasive process, such as grit blasting.) The particles cool very quickly on the roughened surface. The coating is attached to the substrate by the mechanical interlocking of the coating and the surface irregularities. In addition, chemical bonds can form, and post spraying heat treatments can be used for further interdiffusion of the coating and substrate.

Particles continue to be deposited at a high rate, such as a million particles per second. Each particle forms into the irregularities of the previous particles and the coating is built up. These solidified particles are called splats and cool very quickly. Voids form in the coating due to gas that is trapped by the plasma spray, and oxides are deposited due to particles that are oxidized. Sometimes particles are not heated enough and become embedded in the coating as spherical particles.

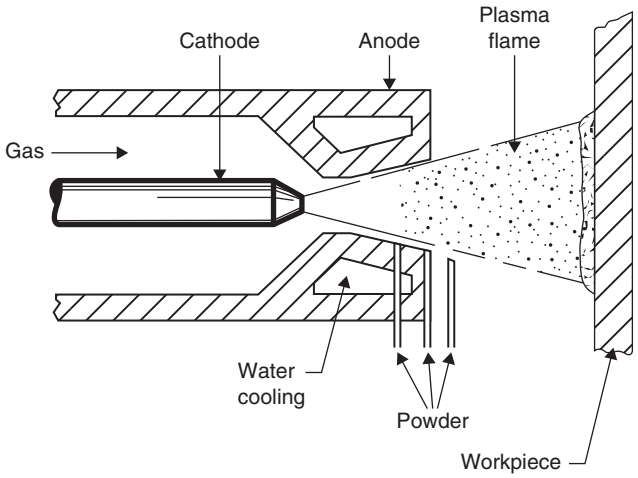


Figure 18.12 Schematic of a plasma gun. Source: Gill and Tucker (1986).

A post-coating heat treatment is often carried out to ensure coating–substrate bonding through interdiffusion and to homogenize the structure of the coating. This is normally performed at 980–1090 °C in a vacuum or inert atmosphere for periods of 1–10 hours.

Plasma spraying can be performed in air at atmospheric pressure (air plasma spraying), in air with an inert shielding gas such as argon (shielded plasma spraying), or in a vacuum chamber. The vacuum processes are called vacuum plasma spraying (VPS) or low pressure plasma spraying (LPPS). A schematic of the air plasma spray and LPPS processes is shown in Figure 18.13. The LPPS process decreases contamination of the powder and base metal from oxidation and, therefore, substantially improves coating quality. The process also produces high density coatings with virtually no unmelted particles, and it allows the substrate to be heated without oxidizing. Shielded plasma spray can produce excellent coatings but requires special procedures and equipment to be used (Taylor et al. 1985).

When the plasma spraying is carried out in air or in an inert gas, the particles cool and slow down as they leave the plasma jet and collide with the gas molecules. If air is used, oxidation of the particles occurs. Inert gas greatly reduces, but does not completely eliminate, this oxidation.

18.3.7 High Velocity Oxygen/Fuel

Another method of spraying coatings, called *high velocity oxygen/fuel (HVOF)*, has been developed. In this method, the powder is both heated and propelled by a high velocity flame onto the substrate. The high velocity allows denser coatings to be made than can be achieved by conventional plasma spray processes. Plasma spray produces a hotter flame than HVOF but has a lower particle velocity. The higher particle velocity of HVOF produces a denser coating, which improves the properties of the coating. HVOF is in commercial use for wear-resistant coatings, which are made from ceramic powders. It is in developmental use for high temperature coatings.

The HVOF coating also has much less oxidation of the particles than air plasma spray. Thus, HVOF coatings can be produced that are far superior to air plasma-sprayed coatings, despite the HVOF process being carried out in an air environment.

HVOF is being considered as an alternative to low pressure plasma spraying (PPS or VPS) (Kong et al. 2003) because of its lower cost. While LPPS coatings are still of

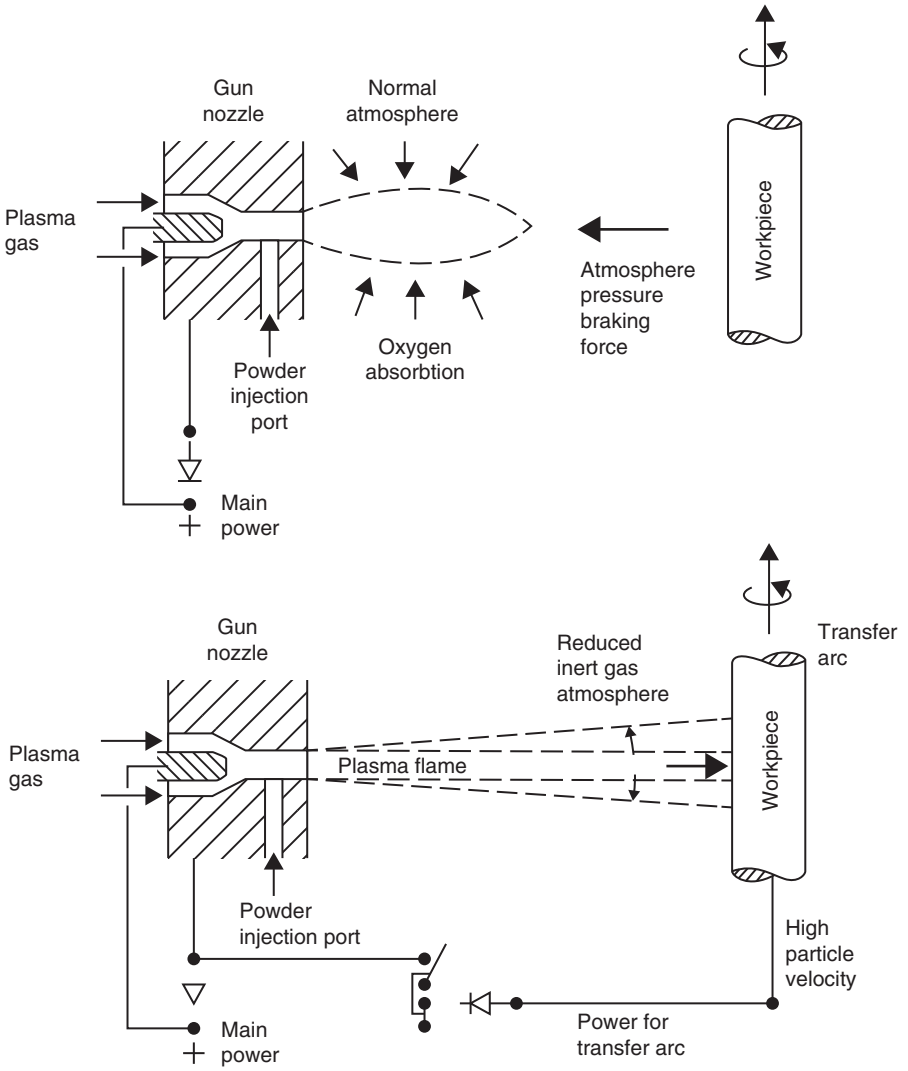


Figure 18.13 Schematic of air plasma spray and LPPS process. Source: Nicoll (1984).

higher quality than HVOF coatings, the quality of HVOF coatings may be sufficient for many applications.

18.3.8 Other Coating Processes

The most common methods of forming protective coatings are described in the previous subsections. But nowadays there are many more advanced processes with several advantages and applications that require, at least, a brief discussion. In general, these coating processes provide excellent properties such as strong bonding and low porosity and are smooth and homogeneous. Examples are as follows.

18.3.8.1 Sputtering Process

This is a momentum transfer process in which a fast particle ejects an atom from a (usually) cathodic surface. The sputtering yield is the number ejected per incident particle (ion). Only about 1% of the bombardment energy gives sputtered (ejected) atoms, and about 75% causes target (cathode) heating. Yield increases with mass and energy of the incident particle until it dissipates too deep, and it also increases (by about a factor of 2) with off-normal angles of incidence up to 70° and then decreases.

Yield increase is disproportionately fast with dose due to surface damage, progressively reducing bonding; it decreases with gas pressure due to backward scattering. Agglomeration of low yield materials can lead to surface cone deposits. The substrate is placed near the cathode so that the sputtered atoms will coat it. Low deposition rates and a great difficulty in synthesizing intermediate compound film is an inherent consequence of the reactive *sputtering* process mechanism. Among sputter deposition methods, the most widely investigated are plasma diode, triode, magnetron, RF, sputter ion plating (SIP), ion beam, and plasma-assisted PVD (PAPVD) processes. Magnetron

sputtering is widely investigated since the application of refractory and high temperature wear-resistant materials deposition found increasing industrial use. The RF sputtering technique is similar to the planar diode sputtering technique, except that the DC is replaced by an RF power supply. Reactive sputtering occurs when one or more of the coating species is gaseous, e.g. sputtering of Al in O_2 to form Al_2O_3, Ti to form TiO_2, Nb in N_2 to form NbN, etc. Ion beam sputtering is a technique in which a sputtering target is held obliquely in an ion beam from an independent ion source. The substrate is placed suitably to receive the coating, resulting in unique coating properties.

SIP is carried out in a vacuum chamber at 300 °C lined with coating source plates at −1 kV (which causes ion bombardment and consequent sputtering of material from them). The components for coating are held (in the volume enclosed by the source plates) at about −100 V to ion polish their surface to promote a dense coating without significant re-sputtering. SIP is a very simple technique. A clean atmosphere (10–100 mTorr) is obtained using only a mechanical pump and a getter. The specimens can be cleaned by ion bombardment before the SIP begins. No manipulation of the specimens is needed. SIP has good throwing power due to the distribution of sputtered source material around the components and to the scattering effect of the low pressure gas (about 1 Pa). The nascent deposits of the substrates are ion-polished by low-energy ions attracted to the surface by a small negative voltage (−100 V). Coating rates are not high (typically 10 μm h^{-1}), but adequate thicknesses (125 μm) can be deposited overnight onto a batch of turbine blades.

References listed in this chapter include useful sources of information on these sputtering techniques.

18.3.8.2 Ion Plating

A comprehensive review and bibliography (1963–1980) on *ion plating* is given by Mattox (1994), who invented the technique in 1964. The system is similar to the inert gas discharge used in sputtering, but the substrate is the cathode. Better adhesion results. High defect concentrations are put in the surface, and physical mixing of the coating and substrate surface occurs. A higher "throwing power" than vacuum evaporation methods is due to gas scattering, entrainment, and redeposition on the charged substrate. Ion plating is the most used method for steel tools coating. Irregular shapes are coated with little variation in adhesion, thickness, composition, and structure.

Ion plating with Al to protect U from oxidation has been successful in contrast to vacuum deposition that has been very unsuccessful due to the thin oxide that forms on U immediately after cleaning. In Ar glow discharge Al ion plating (Figure 18.14), the specimen surface is sputter cleaned by positive ion bombardment and is then held contamination-free until and during the ion plating process. The high energy of ion collision with the surface heats it and promotes chemical reaction and interfacial diffusion (Bland 1968). Before ion plating U, the specimen was first deoxidized in 50% HNO_3 and electropolished in phosphoric acid. It was then suspended from a water cooled cold finger in a $<5 \times 10^{-6}$ Torr vacuum chamber, above a W filament of the same area as the specimen. Al evaporation clips were put on the W. The filament was grounded, and the specimen held at 0.5 KV potential (drawing typically 0.5 mA cm^{-2}). Ar was leaked into about 10 μm Hg pressure and the high voltage applied, to clean the substrate with Ar^+ ions. About 10 minutes later, the filament was slowly heated to deposit the Al. Then the filament, Ar, and high voltage were turned off in sequence. An axial magnetic field can be used to increase the electron path length and thus the ionization (Mattox 1994; Bland 1968; Thornton 1983, 1986).

Ion plating is good for wear- and erosion-resistant coatings, due to its good adhesion characteristics, e.g. HfN for low friction and TiC for deformation and bonding resistance. For an incompatible coating and substrate, ion plating can be used as a "strike" for electroplating. The very good adhesion of ion-plated coatings (much better than vacuum evaporated coatings) is attributed to the high energy of deposition. Two other advantages of ion plating are the good coverage of complicated shapes and the good structures and structure-dependent properties, at low substrate temperatures.

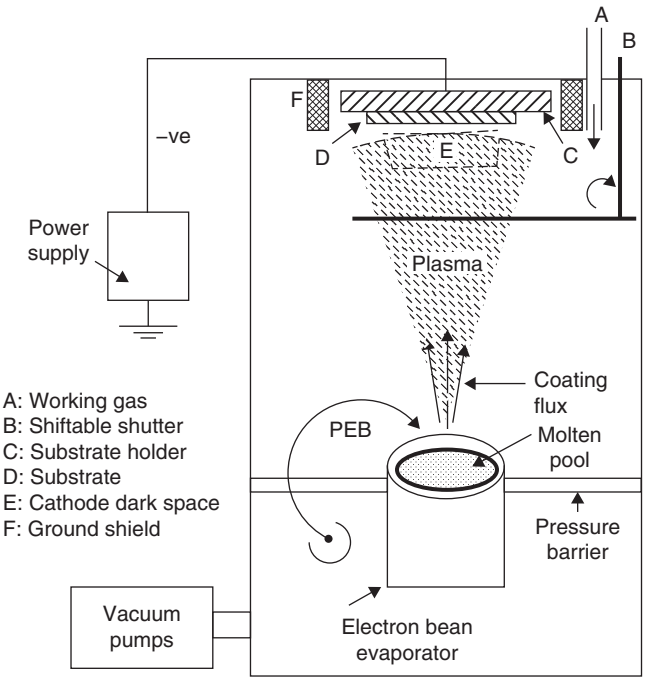


Figure 18.14 Ion-plating apparatus: schematic diagram. Source: Hocking et al. (1989).

18.3.8.3 Slurry Coating

This coating method, known as the *slurry* or slurry-fusion technique, can be used on its own for coating purposes without coupling it to a subsequent vacuum-pack step, or it can be used for local repair or augmenting purposes. The slurry-fusion technique is different from the slip-pack method in that the initial metal mix is of an even finer mesh, and the process is always carried out at a temperature above the melting point of the slurry–composite–elemental metals or alloy. It can be performed at ambient pressures, but it is more common under vacuum or in low pressure inert gas atmosphere.

The uniformity of the bisque on the substrate and a thorough initial blending of the slurry are the first two essential features. Also, the substrate must be non-oxidized, blasted, and acid pickled. Failure in these will lead to non-adherence, nonuniform composition and variable thickness in the heat-treated deposits. The advantage is that it avoids long heat-up and cool-down times.

Slurries of Ni, Cr, B, and Si (Fe,C) powders can be melted onto steel in vacuum or inert atmosphere, giving wear-resistant coatings. Fluxing forms boron silicates (oxides reduction) and good adhesion results. Hardness and wear properties are reported (Knotek et al. 1987).

Apart from metals and alloys, ceramic coatings have also been applied in many situations. Although they have proved very successful experimentally, three primary causes have been given for their failure: (i) the use of overage slurries, which have not been adequately reworked to eliminate agglomeration of the suspended frit, (ii) improper curing or baking of the applied slurry due to lax temperature control, and (iii) the presence of impurities, such as Al compounds during the baking (fusing cycle), which will alter the flow characteristics of the bisque. The above three causes are also more or less valid for all metallic slip mixtures.

18.3.8.4 Hot-Dip Coating

Hot dipping is one of the oldest coating methods, which can be used to a limited extent for high temperature applications where the substrate can tolerate quite a wide variation in coating thickness and uniformity. The principle of hot-dip coating is relatively simple. The substance to be coated is dipped into the hot molten metal. At first, the liquid reacts with the metal, forming an intermetallic compound. This is followed by some diffusion. Usually hot-dip coatings are not kept in liquid for a long time. Thus, extensive diffusion as in the case of pack and slurry coatings is not expected in this case. Hot-dipped aluminized steel strip usually has 14–50 μm of Al on its surface. The process is usually carried out on a continuous feeding arrangement. Substrate pre-cleaning is carried out by hot reducing gas ($N_2 + H_2$ at 800 °C) as a last stage following the conventional steel cleaning steps. The Al melt bath is usually ceramic lined. Thermal cycling makes the steel less ductile but stronger. Brittle $FeAl_3$ forms and should be <10 μm thick if ductility is required.

18.3.8.5 Flame Spraying

TBCs are most often produced by spraying techniques. *Flame spraying* of ceramics for rocket nozzle coatings, MHD generating channels, jet engine combustions chambers, gas turbines, etc. is widely used. A wire or powder feed of the coating material is fed through an oxy-fuel gas, e.g. C_2H_2 or C_3H_8 flame. The wire is fed at a controlled rate that allows its tip to melt and to be blown off by the fast-flowing compressed air. Wire flame spraying is viewed to be more economical than a powder feed. However, powder feed operation has been developed to more sophisticated levels in recent years and should prove its advantage over solid material feed. Coating thicknesses range from about 50 μm upward. Uses include corrosion protection at ambient and high temperatures, rebuilding worn parts, and providing wear, abrasion, and erosion resistance. Flame-sprayed coatings contain many round particles (i.e. not lamellar) that are not molten on impact. Porosity of flame-sprayed coatings can be reduced by vacuum impregnation, but only about 0.1 mm is permeable by the resin. In this technique, inert gas can be used instead of compressed air, for shielding from oxidation, and the substrate can be independently heated to obtain better adherence.

18.3.8.6 Arc Spraying

Two feedable wires are made electrodes for a DC electric arc, and molten droplets are blown onto the substrate by a compressed air jet. Although similar to flame spraying, the molten droplets temperatures are higher in *arc spraying*. High-speed deposition of thick coatings is readily obtained for large components. Local interface welding is found for Al arc sprayed on steel and in other cases. Arc spraying does not give as fine a spray as flame spraying. Nozzle design can be altered to optimize the spraying. Spraying wires must be accurately spooled and wear of wire guides causes problems. Appropriate attachments can be used to allow coating down the bores of long cylinders with diameters of 12 cm or more. The adhesion of arc-sprayed coatings is stronger than flame-sprayed coatings, although the particle velocities are 100 and 180 m s^{-1}, respectively.

18.3.8.7 Clad Surfacing

Cladding is a broad term used that includes methods such as explosive impact and magnetic impact bonding, or HIP or

cladding (HIC), or mechanical bonding such as extrusion. This would introduce an overlapping between cladding and diffusion bonding when the above methods have to be categorized.

Cladding methods can be classified on the basis of the speed with which substrate to coating material bonding can be achieved. In general, the substrate is referred to as the backing plate, and the coating material is called the flyer plate. Ferrous materials form the most handled clad components, with Ni-based alloys coming second. Other cladding alloys like Co alloys on steel are less used, mainly in view of cost and availability. More detailed information may be obtained from the references listed at the end of this chapter.

Among the cladding methods listed, rolling and extrusion processes are perhaps the most widely applied. Explosive bonding was accidentally discovered in 1957; HIP and electromagnetic impact bonding (EMIB) are comparatively new; diffusion bonding process spans the early twentieth century ferrous technology to date on Ni-based and other high temperature alloys for special applications. Both rolling and extrusion methods are practiced for ferrous alloys with a wide variety of compositions and applications for a number of Ni-based alloy/ferrous alloy combinations; Al alloys and others have also been developed to meet increasing requirements for corrosion and oxidation resistance for ambient and high temperature applications in a variety of sulfur- and chloride-containing environments and for high temperature uses ranging over energy, aviation, and nuclear industries. Type 310 steel coextruded with 50Cr–50Ni alloy has been reported to have very good service under hot corrosion conditions in boiler and other systems. Both rolled and extruded composite materials are only demand limited, with the normal metallurgical limitations. Cladding materials are usually strip form, but powders can be employed quite effectively.

Some of the special features in rolling and/or extrusion are:

(i) A thin primary layer of electrodeposit usually ensures a better bond between the substrate creep resisting steel and the overlay clad material.

(ii) Cladding can be given with the substrate as a sandwich.

(iii) With a parting agent, usually Cr_2O_3, several composite pairs or trios can be packed together in a single thin container or "can" of steel and then rolled together. The can is sometimes evacuated or backfilled with N_2.

(iv) The exposed edges of the clad/substrate configuration are sealed by welding to prevent relaxation stresses from wrenching apart the rolled or extruded product.

18.3.8.8 Laser Surface Alloying

The application of laser in coating technology has developed rapidly since 1980 although the first attempt at *laser surface alloying* (LSA) was reported in 1964 (Cunningham 1964). Laser cladding by powder fusion progressed from research to development during 1974–1978 (Powell and Steen 1981). Now lasers are used as one of the main means of application of coatings, as a manipulated auxiliary in other deposition processes such as CVD and PVD techniques, as well as in a number of surface-modifying methods such as cladding, welding, and spraying. The practical utility of lasers has stretched far beyond the area of coating technology itself.

The laser is a singular source of heat produced by means of highly energetic, coherent, monochromatic beam of photons that can be manipulated to operate in focused or defocused states. It is capable of attaining very rapid rates of heating and is clean, intense, and localized. It can be produced either in a continuous form or pulsed. A laser beam incident on a substrate can heat, melt, vaporize, or produce plasma depending on the manipulation of the controlling parameters. The principal sections of a laser are given in Table 18.2.

The overall portability and efficiency of the equipment and its repair and maintenance costs have to be considered in its eventual selection for use. The wider application of lasers used in LSA coatings became possible when multi-kilowatt CO_2 lasers came into production in 1970. Now CW CO_2 lasers are available from a few watts to many kilowatts power; CW Nd YAG lasers of 400 W and above are also being produced and used for laser surface processing.

LSA uses a laser beam as the heat source that is excellent due to the directionality, high intensity, and high spatial resolution of the laser beam. It heats a specific area very fast followed by faster cooling, resulting in a novel microstructure. The desired material can either be added simultaneously along with laser irradiation, or

Table 18.2 Principal sections of a laser

Section	Factors in design
Amplification of light	Optical quality; types of windows; means of heat removal; repair and efficiency; cost
Excitation	Power supply; I stage amplifying state auxiliary supply for cooling, pumps, etc.; weight, performance, efficiency; cost
Optical feedback system	Reflector components: mirrors, lenses, coating modulators; windows; mechanical and optical stability

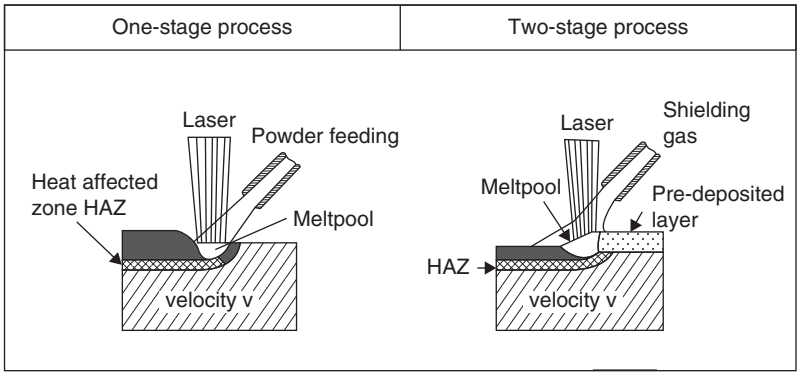


Figure 18.15 One- and two-stage processes of laser surface alloying. Source: Khanna (2002).

laser irradiation is carried out on the surface where the material has already been placed by some of the coatings already discussed. The schematic of the direct powder feed method, as well as the two step coating method, is shown in Figure 18.15.

The very rapid heating and cooling cycle allows a great extension of alloying possibilities, as conventional limits, such as solubility limits, seem to be overcome. Typical structures are extremely fine dendritic that contain the added elements or compounds in the interdendritic regions. The metallurgical stability of such structures is quite good and has been demonstrated by several applications.

18.3.8.9 Hybrid LPC Plasma Coating

LPC plasma spraying is used for the production of high-quality, non-oxidizing, refractory alloy coatings. The main aim of such coatings is to simultaneously heat treat the plasma coating by laser heat and thus get a pore-free dense coating. It is basically a direct feed method, in which instead of powder feeding, a jet of plasma adds the desired material, simultaneously processed by laser. The apparatus consists of a big stainless steel tank with vacuum arrangements, a port for the plasma torch, and laser beam. In addition, a very sophisticated sample handling system is needed that can be moved in the *X–Y* direction or rotated at various angles.

Another application of LPC plasma spraying is to form intermetallic coatings that are difficult to form by plasma spraying alone. A hard Mo, Ti, Ni coating on SS41 was formed with very good hardness.

18.3.8.10 Ion Beam-Assisted Deposition

The versatility of the ion implantation process for the protection of metals has been further extended over recent years by combining a vacuum coating process with ion implantation. This can usually be carried out by straightforward adaptation of the implantation equipment. By the continuous or sequential processes of deposition and ion bombardment, it is possible to build up the coating to a thickness of a micrometer or even more. Furthermore, it is possible to choose an ion species that may react with this coating to convert it, partially or completely to a desired compound. At the same time, the interface between the coating and the substrate, always a plane of weakness, can be improved by ion beam mixing. Energetic ions, caused to pass through such an interface, can induce collisional mixing together with radiation-enhanced forms of diffusive interpenetration to create a graded interface with excellent adhesion.

Among the field of ion-assisted coatings (IAC), the term *ion beam-assisted deposition (IBAD)* is reserved for the situation in which deposition and ion bombardment are carried out simultaneously. The extra energy imparted to the deposited atoms causes atomic displacements at the surface and the bulk as well as enhanced migration of atoms along the surface. These resulting atomic motions are responsible for improved film properties, including better adhesion and cohesion of the film, modified residual stress, and higher density, when compared with a simple PVD-deposited coating. Refractory coatings such as (Si_3N_4) can be synthesized at very low temperatures when reactive ion beams or an evaporant is used.

Ion implantation and laser processing of surfaces can improve the cracking tolerance of structural alloys. Alumina remains crystalline if ion is implanted with Cr, Ti, or Zr and its hardness increases. It becomes less sensitive to fracture when scratched (McHargue and Yust 1984). Figure 18.16 shows the abrupt transition from tensile to compressive stress in evaporated Cr films on Xe ion implantation.

IBAD is a coating process highly versatile for metals, ceramics, semiconductors, and dielectrics. At present, it is also largely applied to the fields of lithography and etching.

18.3.8.11 Plasma Powder Welding

Plasma powder welding (PPW) is a powder welding system using the plasma arc. The welding material powder form is

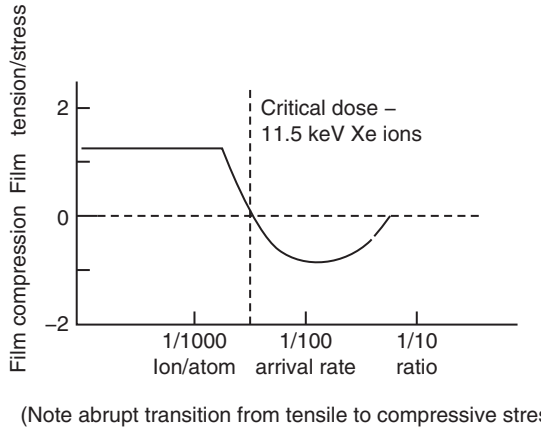


Figure 18.16 Stress generation in Cr films in Xe atmosphere.

introduced into a transferred plasma arc generated between the work (+ electrode) and a tungsten electrode (− electrode) and is deposited as a metal layer on the surface of the work. A schematic of the setup is shown in Figure 18.17.

The technique has now been set up for mass production for surface modification, coatings and claddings for corrosion protection, wear resistance, and high temperature corrosion resistance. It is also possible to carry out the coatings inside the pipes. PPW is receiving a lot of attention nowadays because of its applicability to a wide range of materials and the possibility of obtaining high-strength surface layers.

18.3.8.12 Electroplating

The *electroplating* of metals from aqueous solutions and fused salts has its roots in the work of Faraday, who enunciated the fundamental laws bearing his name, laws that relate the quantity and electrical charge passed between the electrodes in solution and the quantity and valence of material deposited. Long before more modern methods of depositing coatings were developed, many of the principles relevant to electroplating, such as the thermodynamics of electrode potentials and the kinetics of diffusion and the movement of ions under an applied field in solution, as well as their discharge at the electrode surface, had been worked out.

A very good method for improving the properties of electroplated coating is the pulsed reversed current (RC) technique (Kollia et al. 1991).The cathodic current is periodically interrupted by an anodic pulse that briefly redissolves some of the just deposited coating. This introduces two more parameters into the plating process: the pulse frequency ν and the duty cycle $T/(T + T')$,where T is the (cathodic) deposition time and T' is the (anodic) dissolution time. Obviously, $T > T'$. Optimizing RC conditions can lead to improvements in coating smoothness, and texture, somewhat comparable to the use of organic brighteners.

Another technique that is receiving increased attention is the electrodeposition of layered alloy coatings, usually called cyclic multilayered (or *compositionally modulated*) *alloy* (CMA) coatings that goes back to early work by Brenner (1963).

As pointed out by Lashmore and Dariel (1988), electrodeposition presents, in principle, several advantages over vapor-phase methods for the production of layered alloys. Among them is the strong tendency for the coating to grow epitaxially and thus form materials with a texture determined by the substrate; the process is inexpensive and can easily be scaled up for plating large parts; and it is carried out at room temperature, avoiding coating–substrate diffusion.

These alloys have been of interest for their mechanical, electrical, and magnetic properties (Focke and Lashmore 1992). It has been shown (Dini 1993) that CMAs exhibit increased fracture strength, as much as three times that of

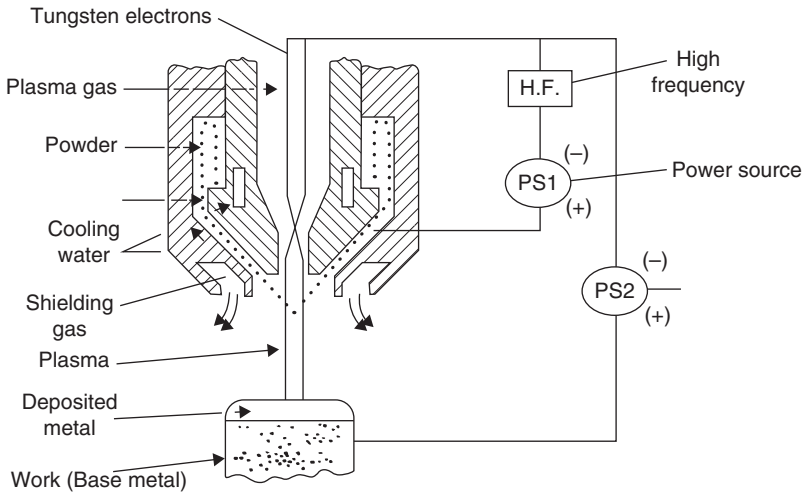


Figure 18.17 Schematic diagram of a PPW process device. Source: Khanna (2002).

constituent metals, and enhanced wear performance in both dry sliding and in lubricating conditions.

Much remains to be learned about CMAs – which alloys can be plated, optimization of the plating parameters, and relation of the coating characteristics, such as layer spacing, to the properties of interest, but it is already clear that work in this field is worth pursuing.

Taken in context with the other coating methods considered in this chapter, electrodeposition of only four metals seem to be of relevance to high temperature: Ni, Co, Cr, and Pt. Electroplating of Ni, Co, and Cr is very well established industrially, and the limited use of Pt coating is merely cost oriented; Pt can also be coated from fused salts and more effectively. Many types of acid and alkali electrolytes are known for Ni and Co plating, namely, sulfate, chloride, sulfate–chloride, fluoroborate, sulfamate, cyanide, pyrophosphate, etc. The metals can be deposited at good current efficiencies but have to be guarded against residual stresses. Plating conditions and post-deposition heat treatments are usually employed to control stress.

Metalliding is the term coined for surface-modifying and surface-hardening processes by electrodepositing refractory metals or metalloids on cheaper or softer substrates from fused salt electrolytes. Electrodeposition at fused salt temperatures (400–900 °C) also results in "cementation" and "diffusion bonding" as refractory metals and metalloids are discharged as particulates and not as coherent deposits. Substrates that are soft (Cu) are easily oxidizable. Fe-, Ni-, Co-, Mo-, W-, Nb-, Ti-, Cr-, etc. can be diffusion coated with Be, B, Al, Si, Ti, V, Cr, Mn, Y, Zr, and rare earths in fused fluoride or chloride electrolytes. Improved component characteristics are noteworthy. Fused salt electroplating is attracting more interest in the fields of surface hardening and corrosion protection (Matiasovsky et al. 1987).

The advantages of aqueous electroplating are as follows:

(i) Bulk substrate handling.
(ii) Large sizes acceptance in plating tanks.
(iii) Requiring very little surface finish on finished product.
(iv) Easy control of deposit thickness and grain size (throwing power drawbacks can be compensated).
(v) Well-bonded coatings.
(vi) Speed and economy.

The advantages of metalliding are as follows.

Small-scale, small-size, specialized, or strategically important components can be considered for technological development for coating by molten salt electrolysis if the cost justification can be made, in view of the fact that a one-step diffusion coating can be achieved with greater ease. Metalliding deposits and heat-treats the substrate simultaneously to produce sound diffusion-bonded refractory products.

Among metals and alloys that can be electrodeposited from aqueous and molten electrolytes, only the Pt-group metals are relevant for high temperature coatings because of their high melting points and corrosion resistance. Platinum, especially, has been used as a diffusion barrier layer in aluminiding Ni-based alloys and also with MCrAlY coatings.

Both aqueous and fused salt electrolytes have been used. Molten chlorides and cyanides have been used as base electrolytes to which the metal compound is an optional addition. Operating temperature ranges over 400–600 °C. Deposits from cyanide melts appear to be bright and uniform. Moreover, the electrolyte is H-free and Pt, Ir, and Ru are commonly plated this way.

Stainless steel and Mo are plated with Ir to protect from air oxidation at 600 °C, but at 1000 °C the attack is worse than unplated steel. Mo was protected at 600 and 1000 °C. Ir coatings are used to protect graphite; 100 μm thick Ir is good to 1000 °C in air; 120 μm of Rh protects Mo and W to 1300°. Ir coat protects C, Ta, Nb, W, and Mo from high temperature oxidation. A rate of deposition of 20 μm h^{-1} and 270 μm thickness is easily obtained. Coatings thicker than 20 μm are pore-free, coherent, dense, and columnar, harder than wrought Ir. Pull-off tests using epoxy (for Pt on Mo) always break the epoxy. Ti plated with 25 μm of Pt and boiled one day in 50% HCl showed no Ti in the acid. Pt on Nb is also excellent. Electroformed Pt crucibles are also very good. Fused salt-plated Pt is very ductile. The difference between aqueous and molten salt electrodeposition is that diffusion bonding (surface alloying) occurs in the latter case.

Pt from aqueous electrolyte (dinitro-sulfate platinous acid) is highly stressed unlike the fused salt deposit, but rhodium can be plated satisfactorily up to 40 μm thick from sulfate solutions. Palladium can be plated better than rhodium. Ru up to 14 μm thickness has been deposited on graphite at 5.4 mA cm^{-2} with Ru concentration held at 0.26 wt%.

Substrates particularly considered for Pt-group metal coating are the refractory group alloys of Mo, W, Ta, Nb, and V that tend to form volatile oxides at high temperatures weakening their usefulness as corrosion-resistant materials. (Platinum itself forms a volatile oxide.) The refractory metal alloy substrates are etched in fused salt electrolytes (anodic or cathodic as the case may be) in order to achieve satisfactory bonding of thick coatings of the Pt-group metals.

One of the main factors that controls the choice of plating platinum, iridium, or other related metals will be the cost. The offsetting factor will be that the scrap metal cost

will be high and coating renewal should not be as expensive as an initial application. Once again, cost justification will allow these metals to be used in areas where diffusion barrier layers and corrosion-resistant coatings are required and the components are small and strategically important.

18.4 Coating Degradation

Coating degradation is a serious problem at high temperatures in corrosive atmospheres, and much effort has gone into reducing it. The degradation modes of coatings are essentially the same as those for cyclic oxidation of metals and alloys, hot corrosion, sulfidation, carburization, erosion–corrosion, etc., described in the previous chapters. However, additional factors arise with coatings; since they are relatively thin, they contain a finite reservoir of scale-forming elements (Al, Cr, Si), and interdiffusion with the substrate can both deplete the scale-forming element and introduce other elements into the coating. Additional mechanical effects also arise, which can lead to deformation of the coating. Mechanical effects are also critical to the durability of TBCs. Physical and mechanical properties of coatings (microstructure- and temperature-related properties, namely, thermal expansion, thermal cycling, thermal conductivity, and interdiffusion; physico-mechanical properties such as adhesion, stresses, strength, ductility, creep, and hardness; and mechanical properties such as wear and erosion) are very interrelated and are strongly influenced by each other and in turn also affect the chemical properties of the coatings. In summary, the mechanism by which a multicomponent substrate/coating/reactant configuration leads to coating degradation and termination of component service life is very, very complex. It is beyond the scope of this chapter to address the complex high temperature systems, and here we will only discuss chemical degradation of a few key individual coating systems, namely, aluminides, silicides, and TBCs.

18.4.1 Aluminides

The overall durability of any coating can be assessed as its specific resistance to degradation to corrosion, rupture, and thermal fatigue. Degradation of *aluminide coatings* is largely dependent on the coherence of the Al_2O_3 layer, which is largely influenced by the available Al activity from the substrate, and the transition metal it is alloyed with in the diffusion band.

Diffusion processes from the substrate always happen in conjunction with those occurring in the coating itself. At an early stage, Al in the aluminide coating is expected to diffuse into the substrate. But as degradation proceeds, the diffusion direction reverses with Ni from the substrate entering the coating that is being consumed. This situation is ideal for Kirkendall void formation (Sequeira and Amaral 2014) and causes physical dislodgement of coating if the void coalesces at the substrate/coating interface. Although Al_2O_3 is generally considered as an n-type oxide, it is argued that it is so only at low p_{O_2}. Thus, at 600 °C, crystalline alpha Al_2O_3 grows beneath an amorphous film of gamma Al_2O_3 by inward diffusion of O_2. At 1300–1750 °C, Al_2O_3 is n-type up to $p_{O_2} = 10^{-5}$ and becomes p-type at higher oxygen pressures.

Nickel aluminide is still the best aluminide system in the gas turbine field although aluminiding was first used to benefit steels. At the commencement of oxidation, the non-protective gamma alumina forms and spalls easily. A more dense and adherent alpha alumina then forms, and as long as this remains undamaged, it confers protective kinetics on the substrate. However, a damage and repair cycle soon causes Al depletion, which affects the diffusion mode and composition of the NiAl below the scale. Below the critical Al concentration, the single-phase NiAl now rendered Ni rich tends to precipitate the gamma primer Ni_3Al phase that causes NiO to react with Al_2O_3 to form spinels and also NiO on its own develops porosity during growth, thus increasing mass transport. Appearance of the gamma prime phase thus marks the onset of the rapid oxidation stage. In a mixed gamma and gamma prime, the gamma phase is more readily oxidizable and forms a voluminous, porous multiphased non-protective scale.

Chromium is the principal metal linked with aluminiding, and most high temperature alloys rely on the oxides of Cr and Al for a consolidated resistance to degradation. The degradation in a chrome-aluminide layer is influenced closely by the major element diffusion and degradation mode and the temperature effect on them. In general, nickel-based alloys form Cr-rich intermediate layers during aluminizing unlike Fe-based alloys. Fe–25Cr was found to be the most resistant to sulfide-forming and sulfur-containing environments at temperatures less than 800 °C where Ni- and Co-based alloys fail, the latter especially in Na_2SO_4 deposition conditions. Oxidation with thermal cycling and isothermal oxidation in exposure to fused Na_2SO_4 showed that the beneficial effect of Cr was to arrest spallation, and change in the coating microstructure was considered instrumental in restricting pitting of the chrome-aluminide diffusion coating. It is postulated that the Cr-enriched zone acts as a barrier to refractory metal diffusion, e.g. Mo, W, V, from the substrate and their subsequent oxidation. An internal sulfidation zone where the spinel $(Cr,Al)_3S_4$ can exist with a broad range of Cr/Al ratio has also been characterized.

A mathematical model has been developed to explore carbon diffusion through aluminided layers to form Cr_7C_3 (Marijnissen and Klostermann 1980).

The extension of aluminided coating life for degradation is rarely achieved by Al alone. At its simplest, it is a dual metal system like Ni–Al, Co–Al, Cr–Al, or Pt–Al, and its most complex a minimum of four and a maximum of six elements are formulated, usually of the general form MCrAl–X1 or MCrAlY–X2. These formulae are the most investigated: M = Ni, Co, Fe; X1 and X2 = Ce, Hf, Pt group, Si, Ta, Ti, Y, Zr, etc.; unusual additives such as Mn, Zn, and Cu have also been investigated. Investigations on gas turbine coating systems have mostly concerned NiCrAlX1–X2 and CoCrAlX1–X2 compositions, while the coal gas conversion systems have concentrated on FeCrAlX1–X2 systems.

Yttrium is the only additive that has been very widely investigated in all the three systems, viz. FeCrAl, NiCrAl, and CoCrAl, in both laboratory and rig evaluation tests. Other additives have been tested in addition or as an alternative. Degradation of M–Cr–Al–X systems is mostly the degradation of the M–Cr–Al scale. The mechanisms for the remarkable beneficial effect yttrium has on scale retention especially under thermal cycling conditions have been reviewed (Lacombe 1987; Stringer 1987).

The directions investigations need to take would be to see how metal–oxide bonds are established, how stress generation modes change, how scale plasticity gets affected at the metal/scale interface both for the substrate metal and the growing scale, how vacancy and void formations are affected, how preferential growth in directions toward and inward into the substrate occur, and how do cracks propagate (Stringer 1987).

Additives such as Y (and Ce, Hf, Zr, etc.) are referred to as active additions. The observed effects as summarized from various investigations are (Lacombe 1987):

(i) Y influences the scale plasticity due to the alteration in scale microstructure.

(ii) Oxide pegs are grown, which anchor scale to substrate.

(iii) Mechanical property differences are graded between the scale and the substrate.

(iv) Scale growth mechanisms are influenced by influencing the diffusion parameters, thus reflecting on the transport and growth of the barrier layer.

(v) Pore formations are eliminated by vacancy coalescence effects.

(vi) Chemical links between the scale and substrate are improved.

The beneficial effect by Y is not realized unless its levels are kept low as an additive. Y is shown to produce a series of oxides, viz. $Y_3Al_5O_{12}$, $YAlO_3$, $Y_4Al_2O_9$ apart from two spinels – $Ni(Cr_{0.7}Al_{0.3})_2O_4$, $Ni(Cr_{0.45}Al_{0.55})_2O_4$, and oxides of Y, Al, and Ni when its concentration is varied over 0–5.5 wt% in triode sputtered NICrAlY coatings on NiCrAl substrates, when oxidized in one hour cycles in air at 1100 °C. Convoluted surface oxides, with fractures, voids entrapped in the mid-layers, and internal yttrium oxides, were also identified.

Y and Hf decrease the corrosion rate of NiCrAl-, NiCrAlTi-, and NiCrAlZr- alloys, but this beneficial effect does not extend in full over the hot corrosion environment in the range of 600–800 °C because of liquid product or liquid product deposit formations. The medium is particularly damaging to CoCrAlY coatings. Earlier theories postulated appear to be on lines similar to those discussed above (Bolshakov and Fedorov 1956). $Co_{22}Cr_{11}Al_{0.3}Y$ deposited on IN-738 superalloy by EBPVD and implanted Y and Hf on $Co_{22}Cr_{11}Al$ were both found to degrade badly at 700 °C under hot corrosion conditions.

Using CoCrAlY or NiCrAlY as the main coating system, many permutations and combinations have been studied: Hf has been a prime additive element (Hocking and Vasantasree 1986), Zr and Si follow close, and several others have been tested, e.g. W, Mo, Mn, Ce, Zn, and Cu. Overlay and underlay coating systems are well known. The degradation in all these involves interlayer – adhesion – compatibility to thermal cycling and stress and of corrosion interdiffusion effects during hot corrosion, high temperature oxidation/carburization, nitridation, etc.

18.4.2 Silicides

Silicon is the third element chosen in hot corrosion systems for its ability to form a barrier layer to resist degradation, the protectivity relying on the formation on SiO_2. It offers the best melt fluxing resistance in hot corrosion environments at high p_{SO_3}. The pattern of growth and retention of SiO_2 alone or as an oxide associate is influenced by the manner in which Si is introduced into the system, as an element additive to form an alloy by slurry or CVD methods or by deposition or controlled oxidation to form SiO_2 or deposition as ceramics such as SiO_xN_y or Si_3N_4 on SiAlON. Although normally very stable, the degradation of SiO_2 can occur through cracking, peeling, spallation, or vaporization loss as SiO (Pettit and Goward 1983).

Si deposited on titanium substrates via silane (SiH_4) formed Ti_5Si_3, which was found to decrease the oxidation rate over the temperature range of 700–1020 °C in O_2. Scale formation was found to be a mixed oxide ($TiO_2 + SiO_2$) layer at temperatures below 875 °C, while above 900 °C, an outer TiO_2 and an inner, inward growing TiO_2SiO_2 developed.

Silicon-containing protective scales can be formed by Ni–5Si, Ni–11.5Si, a chromia–silica scale on Ni–40Cr–5Si and Ni–40Cr–11.5Si, and an alumina–silica scale on CoCrAlY–5Si and CoCrAlY–5S and CoCrAlY–12.5Si. Co-silicides melt above 1200 °C and no liquid silicates form below 1380 °C. But a solid-state reaction between

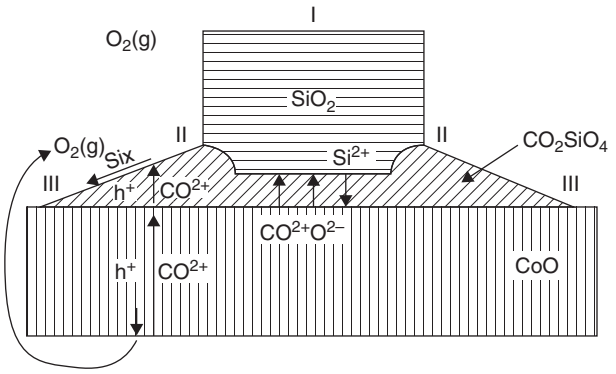


Figure 18.18 The morphology of the reaction $2Co + SiO_2 = Co_2SiO_4$ in air. SiX is a silicon containing adsorbed particle of unknown composition that diffuses rapidly along the surface. Source: From Schmalzried (1974).

CoO and SiO_2 is said to occur by an unusual surface diffusion process (Figure 18.18) (Schmalzried 1974). None of the refractory Cr silicides melt below 1300 °C, but a Ni–50Cr with a protective Cr_2O_3 scale is pitted extensively when pressed in contact with a Si/SiC composite for 120 hours at 1150 °C in air. A NiCr silicide underlayer in the molten state at 1150 °C is envisaged (Ni-5 wt% Si solid solution and silicides Ni_3Si and Ni_5Si_2).

Very good resistance to vanadic attack has been reported for silicon-coated Ni–20Cr alloys at 900 °C with a reduction of as much as 80% in the corrosion rate. No breakaway effects were observed for more than 600 hours at 900 °C in $80V_2O_5$–$20Na_2SO_4$ melts. The increased protection appears to be due to the development and retention of a Cr-rich barrier layer beneath a Si-rich surface with the slag showing little reaction with Si. Although Si coated by pack, vapor deposition, plasma spraying, or ion-plating methods was uniformly effective, ion-plated coatings were found to be the most reliable with good adhesion, uniform composition, and even thickness. The combined effect of molten sodium sulfate and vanadate is catastrophic in most cases as shown in studies on binary and ternary Ni–Cr(10–30 wt%)–X alloys (X = Al, Si, V) and IN-738 (Sidky and Hocking 1987).

18.4.3 Thermal Barrier Coatings

Failure of TBCs could be initiated by poor bonding to the substrate matrix or the coating parameters such as porosity, microstructure–microcrack distribution, thickness, phase distribution and cohesive strength, or the relative thermal expansion mismatch and residual stress of the substrate–coating system. Ceramic sintering and bond coat inelasticity could also contribute to TBC degradation. Bond coat pre-oxidation causes degradation by adhesion failure. The actual failure generally occurs within the ceramic layer near the bond coat and is believed to be due to slow crack growth and microcrack linkup with the ceramic.

Ceramic coatings degrade by spallation due to transient thermal stresses aggravated by salts that induce hot corrosion. For non-oxide-based ceramics such as silicon carbide and nitride, resistance depends strictly on the nature of secondary phases at grain boundaries due to the densification of additives, e.g. MgO, Y_2O_3, Al_2O_3, etc. Reaction-bonded Si_3N_4 and self-bonded SiC coatings were severely attacked in vanadic sulfate melts at 820–1100 °C when exposed to a residual oil-fired environment in burner rigs. Tested in both crucible and burner rigs with melt compositions based on Na_2SO_4 with additions of NaCl, $NaCl + V_2O_5$, and $NaCl + Li_2O$ (950 °C, 200 hours), reaction-bonded Si_3N_4 was found to be highly dependent on the overall environmental conditions for its corrosion. Excellent resistance was observed in oxidizing and acidic media but very poor resistance in reducing and mildly alkaline environments. Several crystalline phases also occur on the ceramic surface during the corrosion reactions. Sintered SiC also suffered a similar attack in sulfate melts at 900 °C, less in oxidizing conditions but more in basic melts or slags especially with carbonaceous material. However SiC was inert in pure N_2, H_2, or H_2–H_2S mixtures at 900 °C.

A good bonding interlayer between the ceramic coating and the substrate superalloys is vital for TBC survival. Titanium carbide and nitride are well-bonded to superalloys if the Ni_3Ti intermetallic phase is controlled. An excess produces a rough deposit and thus poor bonding. A marginal carburization is also a requirement for good bonding.

Without an interlayer, ceramic substrate interactions are inevitable. MgO, Al_2O_3, SiO_2 (as fused quartz), SiC, and Si_3N_4 were all found to react with a Ni-based superalloy substrate, with the most severe being SiC over 700–1150 °C, with conditions at the interface held at minimized p_{O_2}. Si and C diffused inward, forming silicides and carbides with the degree of reaction on the ceramic side being similar to that of the substrate below 900 °C and less above 900 °C.

High temperature systems are expanding and cheaper fuels are being used. More studies appear to be needed on hybrid substrate systems and in fused salt media with nitrates, carbonates, and phosphates in conjunction with sulfates and chlorides of Ca, K, Mg, and Na; additive effects also need further clarification. Degradation studies of multilayer coatings are complex and need further investigations. Poor reproducibility in processing TBC systems is felt to be reflected in their degradation assessments (Begley and Wadley 2012). Metastable phase systems and their degradation are an open field.

18.5 Summary and Future Trends

Three basic types of coatings are used in high temperature systems: diffusion coatings, overlay coatings, and TBCs. They are more resistant to high temperature attack than the base material because they contain large amounts of elements such as Al and Cr, which form oxide scales that act as a physical barrier that reduces the rate of high temperature attack to very low values. When these scales are lost due to spallation, erosion, or other physical, mechanical, or chemical damage, a new scale forms from the scale-forming elements in the coating. When these elements have been consumed below a minimum level for protection, then the coating ceases to protect the base material, and the coated component must be refurbished. The protective elements in coatings are essentially Al, Cr, and Si because they form the protective oxide scale. Ni and Co are the main elements forming the matrix of the coatings. Other elements used in coatings, but in smaller quantities, are Pt, Rh, Pd, Y, Hf, and Ta. These elements improve both the oxidation and hot corrosion resistance of the coating. Yttrium and hafnium improve the adherence of the oxide scale to the substrate by reducing the amount of the oxide that spalls off during a thermal cycle. Remember that Si improves the hot corrosion resistance, and Pt, Rh, and Pd also reduce oxide spalling. The non-scale-forming elements are sometimes called active elements because of their affinity for oxygen. It has been shown that these elements form sulfides with sulfur in the coating. If unreacted, this sulfur migrates to the oxide-coating interface, weakening this interface and increasing the amount of oxide spalling.

There are essentially two basic forms of high temperature corrosion: oxidation and hot corrosion. Oxidation results in the formation of an external oxide scale that may or may not be protective. A protective scale grows slowly (due to a slow rate of diffusion through the scale) and is adherent to the metal substrate. For non-protective scales, an internally oxidized region occurs beneath the metal surface. High temperature oxidation accelerates with high temperatures. High temperature or type I hot corrosion occurs at 850–930 °C when sulfur is present along with potassium or sodium, being caused by alkali metal salts that melt and destroy the oxide scale; once the oxide scale is breached, sulfidation and oxidation of the metal occur. Low temperature or type II hot corrosion occurs at 600–750 °C, being caused by the mixture of alkali sulfates and alloy metal sulfates, and requires a significant partial pressure of SO_3. This corrosion results in pitting of the metal surface, a porous layered scale, little base metal depletion, and few internal sulfides.

High temperature coatings are sacrificial in nature. They are designed to be consumed during the operation of the engine and then replaced during the refurbishment of the component. The important aspect to note about coating degradation is that it is controlled by the chemistry of the coating, and not by the thickness of the coating. The prediction of coating degradation, as well as base material attack, is not well developed. Chan et al. (1998) were the first developers of methods for predicting coating degradation by high temperature oxidation, which is more amenable to prediction than hot corrosion.

Most coatings undergo a ductile-to-brittle transition with temperature. Below a certain temperature, the coatings show very little ductility, but, above this temperature, their ductility increases rapidly with increasing temperature. Components must be designed and operated such that the tensile strain in the coating does not exceed the strain to cause cracking in the coating. The cracking is most likely during the shutdown of the engine, when the surface of the component goes into tension. The most severe situation occurs during an emergency shutdown (or trip).

Recoating is widely carried out to restore the surface protection to the base material when the coating has either been breached or its protective ability exhausted. For the process of recoating, it is necessary to obtain a fresh surface for the new coating to be applied. When the thickness of the base material becomes too thin, especially adjacent to interior cooling surfaces, the component can no longer be repaired or recoated.

Further developments in coating technology for diffusion and overlay coatings will be driven by economics and reliability. Economic developments are directed to less expensive coatings; that is, efforts will be focused upon application methods that have less processing steps, including secondary operations. Reliability developments are directed to the inspectability of coatings, both when made and in the field, and the life protection of the coatings. With the development of advanced gas turbine engines and then of high temperature areas and systems that require coating applications, the near-term focus on TBCs will be on developing TBC materials with improved durability and performance. Considering this, some perspectives of TBCs can be summarized as follows:

1. For current yttria-stabilized zirconia YSZ-based TBCs, a strong and retentive bonding between the thermally grown oxide (TGO) and the bond coat is the key to determine the duration of TBCs, which can be greatly improved by controlling compositions and processing of the bond coat.
2. Great efforts have been invested in searching for new ceramic materials with better performance than the current YSZ. For example, recent work in this area consists of studying the properties of rare earth base zirconate materials (La, Gd, Sm, Yb, etc.), which are promising candidate materials (due to

their high melting point, low thermal conductivity, high temperature phase stability, and good sintering resistance) and evaluating the effect of zirconate compositions (for three, four, and five component systems) on the phase stability, thermal conductivity, and thermal/chemical stability with alumina. Such investigation is considered to keep in accordance with the new ceramic materials and the new generation single-crystal advanced materials, namely, novel superalloys.

3. Innovative methods, along with new scientific techniques, should be developed for the assessment of TBC performance and the prediction of TBC lifetime more efficiently and accurately.

In conclusion, coatings are a vital area in all phases of advanced technology. The development and evaluation of protective coatings are expensive, and considering the present economic crisis, there is now an urgent need to conserve resources and optimize test programs and for a greater coordinated dissemination of information. Universities, research institutes, and industry are urged to take a more active interest on this area.

18.6 Questions

18.1 What is the necessity of coatings for high temperature operating components?

18.2 Which is the best classification for various types of coatings?

18.3 What are columnar coatings, and under what conditions are such coatings formed?

18.4 Why are CVD coatings called diffusion coatings? Explain with a specific example.

18.5 What are the main limitations of CVD coatings?

18.6 Under what conditions does one get low activity coatings and high activity coatings? Which of the two is better, and why?

18.7 Differentiate between the properties of flame spray and HVOF coatings.

18.8 Do atmospheric plasma coatings have sufficient porosity and bond strength? If not, how is it rectified?

18.9 What are the advantages of the transferred arc process over atmospheric plasma spray?

18.10 How is the IBAD method different from other ion beam-based techniques?

References

Allison, G. and Hawkins, M.W. (1914). *GEC Rev.* 17: 947.

Baldi, A.L. (1980). Modified diffusion coating of the interior of a steam boiler tube. US Patent 4,208,453.

Begley, M.R. and Wadley, H.N.G. (2012). *Acta Mater.* 60: 2497.

Birks, N., Meier, G.H., and Pettit, F.S. (2006). *Introduction to the High Temperature Oxidation of Metals*. London: Cambridge University Press.

Bland, R.D. (1968). *Electrochem. Technol.* 6: 272.

Bolshakov, K.A. and Fedorov, P.I. (1956). *Zh. Obgch. Khim.* 26: 348.

Boone, D.H. (1986). *Mater. Sci. Technol.* 2: 220.

Bose, S. (2007). *High Temperature Coatings*. Oxford: Elsevier.

Brenner, A. (1963). *Electroplating of Alloys*, vol. 1 and 2. New York, NY: Academic Press.

Chan, K.S., Cheruvu, N.S., and Leverant, G.R. (1998). ASME Paper No. 98-GT-478.

Cockeram, B.V. and Rapp, R.A. (1995). *Metall. Mater. Trans. A* 26A: 777.

da Costa, W., Gleeson, B., and Young, D.J. (1994a). *J. Electrochem. Soc.* 141: 1464.

da Costa, W., Gleeson, B., and Young, D.J. (1994b). *J. Electrochem. Soc.* 141: 2690.

da Costa, W., Gleeson, B., and Young, D.J. (1996). *Surf. Coat. Technol.* 88: 165.

Cunningham, F.E. (1964). The use of lasers for the production of surface alloys. M.Sc. thesis. Cambridge, MA: MIT.

Das, D.K., Singh, V., and Joshi, S.V. (1998). *Metall. Mater. Trans. A* 29: 2173–2188.

Dini, J.W. (1993). *Electrodeposition: The Materials Science of Coatings and Substrates*. Park Ridge, NJ: Noyes.

Focke, T. and Lashmore, D.S. (1992). *Scr. Metall.* 27: 651.

Ganser, B., Wynns, K.A., and Kurlekar, A. (1999). *Mater. Corros.* 50: 700.

Gill, B.J. and Tucker, R.C. Jr. (1986). *Mater. Sci. Technol.* 2: 207.

Gleeson, B., Cheung, W.H., da Costa, W., and Young, D.J. (1993). Proceedings of the 8th Asian-Pacific Corrosion Control Conference, Bangkok, Thailand, p. 43.

Goward, G.W. (1998). *Surf. Coat. Technol.* 73: 108–109.

Goward, G.W. and Boone, D.H. (1971). *Oxid. Met.* 3: 475.

Gupta, B.K. and Seigle, L.L. (1980). *Thin Solid Films* 73: 365.

Hocking, M.G. and Vasantasree, V. (1986). *Mater. Sci. Technol.* 2: 318.

Hocking, M.G., Vasantasree, V., and Sidky, P.S. (1989). *Metallic and Ceramic Coatings Production, High Temperature Properties and Applications*. Harlow, Essex: Longman Scientific and Technical.

Khanna, A.S. (2002). *Introduction to High Temperature Oxidation and Corrosion*. Materials Park, OH: ASM International.

Knotek, O., Leyendecker, T., and Jungblut, F. (1987). *Thin Solid Films* 153: 83.

Kollia, C., Loizos, Z., and Spyrellis, N. (1991). *Surf. Coat. Technol.* 45: 155.

Kong, J., Zhou, C., Gong, S., and Xu, H. (2003). *Surf. Coat. Technol.* 165: 281.

Kung, S.C. and Rapp, R.A. (1989). *Oxid. Met.* 32: 89.

Kurlekar, A. and Bayer, G.T. (2001). *Hydrocarbon Process.* 80: 80.

Lacombe, P. (1987). *Mater. Sci. Eng.* 96: 1.

Lashmore, D.S. and Dariel, M.P. (1988). *J. Electrochem. Soc.* 135: 1218.

Levin, L., Ginzburg, A., Klinger, L. et al. (1998). *Surf. Coat. Technol.* 106: 209.

Marijnissen, G.H. and Klostermann, J.A. (1980). *Behaviour of High Temperature Alloys in Aggressive Environments* (ed. E. Lang), 720. London: Applied Science Publishers Ltd.

Massalski, T.B. (1986). *Binary Alloy Phase Diagrams*. Materials Park, OH: ASM.

Matiasovsky, K., Fellner, P., Chrenkova, M. et al. (1987). *Chem. Pap.* 41: 527.

Mattox, D.M. (1994). Surface preparation for film and coating deposition processes. In: *Deposition Technologies for Films and Coatings*, Chapter 3, 2e (ed. R.F. Bunshah), 108–131. New Jersey: Noyes.

McHargue, C.J. and Yust, C.S. (1984). *J. Am. Ceram. Soc.* 67: 117.

Mévrel, R., Duret, C., and Pêchoir, R. (1986). *Mater. Sci. Technol.* 2: 201.

Nicholls, J.R., Long, K.A., and Simms, N.J. (2010). *Scheris' Corr.* 4: 2532.

Nicoll, A.R. (1984). Protective coatings and their processing. In: High Temperature Materials and Coatings Course, Finland, p. 2.

Pettit, F.S. and Goward, G.W. (1983). *Coatings for High Temperature Applications* (ed. E. Lang), 1 and 341 . New York: Applied Science.
Powell, J. and Steen, W.M. (1981). *Conference Proceedings of Metallurgical Society of AIME* (ed. K. Mukherjee and J. Mazumder), 217–222. Warrendale, PA: AIME.
Rapp, R.A. (1989). Proceedings of Corrosion, 89, Paper 532, New Orleans, LA, USA.
Rapp, R.A. (1996). Method of depositing chromium and silicon on a metal to form a diffusion coating. US Patent 5,589,220.
Rapp, R.A., Wang, G., and Pangestuti, E. (1994). Codeposition of chromium and silicon diffusion coatings in Fe-base alloys using pack cementation. US Patent 5,364,659.
Rapp, R.A., Wang, G., and Weissert, T. (1997). *High Temperature Coatings* (ed. M. Khobaib and R.C. Krutenat), 131. Warrendale, PA: TMS.
Ravi, V.A., Choquet, P.A., and Rapp, R.A. (1989). *Oxidation of High Temperature Intermetallics* (ed. T. Grobstein and J. Doychak), 127. The Minerals, Metals and Materials Society.
Rosado, C. and Schütze, M. (2003). *Mater. Corros.* 54: 381.
Schmalzried, H. (1974). *Solid State Reactions*, 165. Weinheim: Wiley-VCH.
Sequeira, C.A.C. and Amaral, L. (2014). *Trans. Nonferrous Met. Soc. China* 24: 1.
Sidky, P.S. and Hocking, M.G. (1987). *Corros. Sci.* 27: 183.
Squillace, A., Bonetti, R., Archer, N.J., and Yeatman, J.A. (1999). *Surf. Coat. Technol.* 118: 120–121.
Stringer, J. (1987). *Mater. Sci. Eng.* 87: 1.
Taylor, T.A., Overs, M.P., Gill, B.J., and Tucker, R.C. Jr. (1985). *J. Vac. Sci. Technol., A* 3: 2526.
Thornton, J.A. (1983). *Thin Solid Films* 107: 3.
Thornton, J.A. (1986). *J. Vac. Sci. Technol., A* 4: 3059.
Wachtell, R.L. (1974). *Science and Technology of Surface Coating* (ed. B.N. Chapman and J.C. Anderson), 105. London: Academic Press.
Weber, T. (2004). Korrosions chutzschichten fur Apparatewerkstoffe unter sulfidierenden Bedingungen bei hohen temperaturen. Ph.D. thesis. RWTH Aachen, Germany.
Wynns, K.A. and Bayer, G.T. (1998). Aluminium-silicon diffusion coating. UK Patent WO9820182.
Wynns, K.A. and Bayer, G.T. (1999). Two step pack cementation for stabilizing Al-Si diffusion coating. US Patent 5,873,951.

Further Reading

Belmonte, M. (2006). *Adv. Eng. Mater.* 8: 693.
Bushan, B. (1999). *Diamond Relat. Mater.* 8: 1985.
Cha, S.C., Gudenau, H.W., and Bayer, G.T. (2002). *Mater. Corros.* 53: 195.
Fahr, A., Roge, B., and Thornton, J. (2006). *J. Therm. Spray Technol.* 15: 46.
Franchi, D. and Rostagno, M. (2005). *Metall. Ital.* 97: 21.
Gao, W. and Li, Z. (eds.) (2008). *Developments in High-Temperature Corrosion and Protection of Materials*. Cambridge: Woodhead Publ. Ltd.
Gerdeman, D.A. and Hetch, N.H. (1972). *Arc Plasma Technology in Materials Sciences*. New York: Springer-Verlag.
Goswami, B., Sahay, S.K., and Ray, A.K. (2004). *High Temp. Mater. Processes* 23: 211.
Hampikian, J.M. and Dahotre, N.B. (eds.) (1999). *Elevated Temperature Coatings*. Warrendale, PA: TMS.
He, J. and Schoenung, J.M. (2002). *Mater. Sci. Eng., A* 336: 274.
Herman, H. (1988). *Plasma-Sprayed Coatings*. New York: Scientific American.
Jackson, M.R., Bewlay, B.P., Rowe, R.G. et al. (1996). *JOM* 48: 39.
Kawahara, Y. (2005). *Corros. Eng.* 54: 213.
Lang, E. (ed.) (1983). *Coatings for High Temperature Applications*. London: Applied Science Publishers.
Lang, E. (ed.) (1989). *The Role of Active Elements in the Oxidation Behaviour of High Temperature Metals and Alloys*. Amsterdam: Elsevier.
Lau, M.L., Strock, E., Fabel, A. et al. (1998). *Nanostruct. Mater.* 10: 723.
Malyshev, V.V. (2004). *Prot. Met.* 40: 525.
Mévrel, R. (1989). *Mater. Sci. Eng., A* 120: 13.
Miller, R.A. (1987). *Surf. Coat. Technol.* 30: 1.
Newkirk, J.B. (ed.) (1980). *High Temperature Materials*. Tel-Aviv: Freund Publ. House.
Padture, N.P., Gell, M., and Jordan, E.H. (2002). *Science* 296: 280.
Pawlowksi, L. (1995). *The Science and Engineering of Thermal Spray Coatings*. New York: Wiley.
Peters, M., Leyens, C., Schulz, U., and Kaysser, W.A. (2001). *Adv. Eng. Mater.* 3: 193.
Picas, J.A., Forn, A., Igartua, A., and Mendoza, G. (2003). *Surf. Coat. Technol.* 174: 1095.
Rohr, V., Schütze, M., Fortuna, E. et al. (2005). *Mater. Corros.* 52: 12.
Sathiyanarayanan, S., Rajagopal, G., Palaniswamy, N., and Raghavan, M. (2005). *Corros. Rev.* 23: 355.
Sequeira, C.A.C. (2013). *Corrosion and Materials in the Oil and Gas Industries* (ed. R. Javaherdashti, C. Newaoha and H. Jan), 243. Boca Raton, FL: CRC Press.
Shah, S.I. and Glocker, D. (eds.) (1996). *Handbook of Thin Film Process Technology*. Bristol: IOP Publishing Ltd.
Stern, K.H. (1996). *Metallurgical and Ceramic Protective Coatings*. London: Chapman and Hall.
Stover, D., Pracht, G., Lehman, H. et al. (2004). *J. Therm. Spray Technol.* 13: 76.
Tellkamp, V.L., Lau, M.L., Fabel, A., and Lavernia, J. (1997). *Nanostruct. Mater.* 9: 489.
Verma, A.R.B. and van Ooij, W.J. (1997). *Surf. Coat. Technol.* 89: 132.
Warner, B.M. and Punola, D.C. (1997). *Surf. Coat. Technol.* 94–95: 1.

Chapter 19

Examples of Engineering Importance

19.1 Introduction

It is a widely accepted fact that 25% of steel produced each year is damaged by corrosion but that only a small part of this is caused by high temperature corrosion (HTC). However, HTC generally occurs in state-of-the-art technologies for which the consequences of failures have a particularly high financial, environmental, and human cost.

The technical domains in which HTC is of importance can be categorized into five headings, as reported in the literature and described in this book:

- Thermal machines (internal combustion or gas turbines), used for surface, marine, and air transportation or for energy conversion (steam or gas turbines), including their inlet and outlet devices (for example, catalytic converters).
- Chemical industry, i.e. organic chemistry (steam cracking, catalytic dehydrogenation, chlorination, etc.), inorganic chemistry (soda/chlorine, sulfur, isotopic separation, etc.), or metallurgical industry (roasting, van Arkel process, thermal and thermomechanical treatments, etc.).
- Incineration of domestic or industrial waste.
- Electric heating devices (electrical resistances, furnace walls, etc.).
- Nuclear engineering (fuel cladding, guiding and lifting systems, liquid metal circuits, etc.).

Besides these purely environmental aspects, high temperature oxidation constitutes a stage of some industrial processes, for example, to obtain materials with controlled properties. Thermal oxidation of silicon wafers to obtain a scale of silica (SiO_2) with a thickness less than about 100 nm (grid dielectric) is the basic manufacturing process of integrated metal–oxide semiconductor (MOS) transistors. The last stage stripping of stainless steel (SS) requires an oxidation step to obtain an appropriate surface state for cold wire drawing. This operation is generally carried out in a gas oven under complex atmospheres. Similarly, the formation of a bonding layer on steel support structures for catalytic convertors to limit pollution involves an oxidation process. It should also be pointed out that all thermochemical surface treatment processes (nitriding, carburizing, siliciding, boriding), using either chemical vapor deposition techniques of pack cementation, are analyzed and characterized using the tools and concepts of HTC.

Table 19.1 gives several examples of industrial devices working at high temperatures with their maximum temperature of utilization and expected useful life.

This table clearly shows that the expected performances of these devices can be attained only if HTC phenomena are taken into account from the outset, i.e. at the design state. The improvement of energy conversion efficiencies, which is one of the key economic factors in the present technological development, is accentuating this necessity. But in the near future, many more important engineering systems requiring increased operating efficiencies will be confronted with HTC issues; therefore a general background on some of existing systems, which are subject to a number of corrosion problems, requires consideration. For example, nuclear power systems require a fail-safe feature and cannot afford a major failure with catastrophic consequences. A high degree of predictability and reliability of component performance is vital, and the temperature range is wide, from 100 °C to more than 700 °C. They use many low-alloy carbon steels and ferritic and austenitic steels in their nuclear reactors. The selection of these materials for component fabrication depends on the temperature, environment, and service conditions. It is enough to understand that HTC plays here a key role.

Among the various industries in which HTC is a widespread problem, the energy arena involving (i) the study of processing and properties of high temperature materials, by means of ceramic science, chemistry, electrochemistry, chemical engineering, electrical engineering, mechanical engineering, metallurgy, and physics, and (ii) the experimental observations for predicting behavior, from scientific principles to engineering design and from

High Temperature Corrosion: Fundamentals and Engineering, First Edition. César A. C. Sequeira.
© 2019 John Wiley & Sons, Inc. Published 2019 by John Wiley & Sons, Inc.

Table 19.1 Typical useful life of various industrial devices

Useful life	Applications	T_{max} (°C)
Several minutes	Rocket engines	2400
	Heat shields of spaceships	1650
10–20 h	Superficial coatings of space shuttles	1750
100–200 h	Ingot molds in steelworks	1350–1500
1 000 h	Filaments of incandescent lamps	2500
2 000–3 000 h	Petrol engines	600–800
10 000–20 000 h	Diesel engines	800–900
	Resistance heaters in industrial furnaces	1300–1600 1050–1100
	Jet engines of passenger aircraft	
400 000 h	Nuclear fuel cladding in PWRs	300–350
1 000 000 h	Industrial gas turbines	1000
3 000 000 h	Steam turbines	650

atomic scale models to performance while in use, constitutes our choice as summarized below for two types of energy technologies: advanced energy conversion sources and nuclear power plants (NPPs).

Among energy conversion sources being developed for using commonly available fossil and hydrocarbon-based fuels, fuel cells have attracted most attention from utilities, automotive manufacturers, and military hardware designers. Desirable characteristics are silent operation, ecological soundness, significantly high electrical conversion efficiency (up to 70% chemical to electrical), modularity of construction (from a few watts to megawatts), and multifuel capability (coal-derived syngas, gaseous, and liquid hydrocarbons). Fuel cells also offer the ability to hybridize with gas turbines, as well as the potential to develop near-zero emissions power plants and to capture greenhouse gas from the exhaust, ultimately leading to a hydrogen economy and infrastructure. At present, widespread use of fuel cells is limited by performance and longer operational life.

In the next three sections, three types of high temperature fuel cells are addressed: molten carbonate fuel cells (MCFCs), solid oxide fuel cells, and direct carbon fuel cells (DCFCs). Corrosion processes operating in these cell systems, which lead to electrical performance degradation, are presented and discussed, and corrosion mitigation schemes are highlighted. The understanding of corrosion processes in these fuel cells is also expected to help in developing robust materials and a knowledge base for technologies such as high temperature steam electrolysis for highly efficient hydrogen production, energy storage, and gas separation membranes.

NPPs typically use fissile $^{235}UO_2$ as fuel. Fission results in the release of thermal energy that is used to heat pressurized water. The pressurized water flows through heat exchanger tubes, heating secondary water to produce steam, which drives a turbine using the Rankine cycle. Under normal operating conditions, aqueous corrosion of reactor components is the degradation mode of concern. Aqueous corrosion is outside the scope of this book. However, under loss of coolant accident (LOCA) conditions, temperatures rapidly increase and HTC reactions control the reactor failure and radioactive product release. Three high temperature reaction mechanisms during LOCA are of particular note. First, the zirconium alloy (Zircaloy) fuel cladding reacts with steam. Due to exothermic nature of Reaction (19.1),

$$Zr + 2H_2O\,(g) = ZrO_2 + 2H_2\,(g) \qquad (19.1)$$

oxidation proceeds at a runaway rate at temperatures above about 1200 °C, generating large amounts of hydrogen. The high levels of hydrogen can result in explosions, which damage the reactor containment systems. Second, volatile fission products are released from the fuel matrix, react with the steam/hydrogen gas mixture flowing through the reactor core, and can be released into the environment through the damaged containment. Finally, the high temperature fuel reacts with reactor vessel and structural materials, forming a molten mixture. Subsequent injection of water can result in dissolution of the reacted fuel mixture, which can be released to the environment with subsequent cooling water leaks.

Of these three issues, the oxidation of zirconium alloys is most well understood. Current research focuses on developing alternative fuel cladding materials to replace zirconium alloys with more slowly oxidizing materials. Further evaluation of these candidate fuel cladding materials, including their response to radiation exposure, is needed.

A second area of concern during LOCA is the release of fission products during vaporization reactions. Short-lived fission products including ^{131}I and ^{137}Cs are of interest due to their radioactive danger. Vapor species such as Cs(OH) and CsI are expected to form in amounts greater than the metal vapor partial pressures, increasing transport rates out of the hot core.

This issue demonstrates the need for accurate thermochemical measurements and calculations, which usually use estimated thermochemical data.

Finally, consideration of reactions occurring during reactor core melting is of importance. Melted fuel will react with concrete stainless steel reactor vessel components and zirconium alloy fuel cladding, as well as other structural components of the reactor. The resulting phase assemblage is expected to be very complex, with long-term environmental hazards due to potential radioactive material release

if complete isolation of contaminated water is not maintained. Therefore, development of more oxidation-resistant fuel cladding and improved thermochemical data for gas, liquid, and solid phases formed during LOCA events are needed.

The nuclear energy technology is a complex world. Many more subsystems and components are subject to HTC problems, as it will be shortly addressed in Section 19.5.

19.2 Molten Carbonate Fuel Cells

19.2.1 Introduction

Today's growing energy needs in many countries must be satisfied both cost-effectively and reliably while still conserving our environment and resources for future generations. A technology that supports these requirements is the fuel cell. It will have a major role in the evolution of serving society's energy needs (Reiser and Schroll 1981).

There are a number of different fuel cell types. They are characterized by the electrolyte used and the operating temperature. Low temperature fuel cells are *alkaline fuel cells* (AFC), the proton exchange membrane fuel cell (PEMFC), and the phosphoric acid fuel cell (PAFC). These cells operate at 80, 100, and 220 °C, respectively. At this low temperature, the strain on materials is only moderate; however expensive noble metal catalysts are required to facilitate the electrode reactions. High temperature fuel cells such as the MCFC and the solid oxide electrolyte fuel cell (SOFC) operate at 650 °C and 900–1000 °C, respectively. At these temperatures, HTC can become a serious problem, and the choice of the proper materials has great influence on the lifetime and performance of the fuel cells.

In principle, fuel cells function like batteries. The difference is the continuous supply of fuel, in most cases hydrogen or hydrocarbons like methane. The fuel is electrochemically oxidized at the anode, while oxygen is electrochemically reduced at the cathode. When hydrocarbons such as natural gas are used as fuel, a reforming step has to precede the fuel cell reactions. The reforming converts the methane into hydrogen and CO_2 by Reactions (19.2) and (19.3):

$$CH_4 + H_2O = CO + 3H_2 \tag{19.2}$$

$$CO + H_2O = CO_2 + H_2 \tag{19.3}$$

Reaction (19.2) is strongly endothermic while Reaction (19.3) is slightly exothermic. In total, the reforming requires energy and therefore lowers the net efficiency of the system. To facilitate the reactions, a reforming catalyst is usually employed.

The hydrogen is consumed by the electrochemical fuel cell reaction, which liberates two electrons for each hydrogen molecule. The electrons flow via an electrical load to the cathode where they are involved in the reduction of oxygen. Equations (19.4)–(19.8) describe in a simplified manner the reactions taking place for the different fuel cell types at the anode and the cathode (Table 19.2).

In the fuel cells, the chemical energy of the reactants is directly converted to electrical power and heat.

The electrical efficiency of fuel cell systems ranges from about 40% to 65%. By stacking a number of cells on top of each other, the voltages of the individual cells are added up to technically relevant stack voltages. Nowadays, an individual cell supplies about 800 mV at a load of 160 mA cm^{-2}. It is an important goal to improve this number in the future by reducing losses in the cells caused by polarization and ohmic resistivities. Fuel cell stacks produce DC power, which is converted to AC power by means of an inverter before it is supplied to the grid.

Reducing our carbon footprint is widely acknowledged as one of modern society's top priorities, as well as building a sustainable economy based on knowledge and innovation for enduring opportunities of development. MCFCs offer rich potential in these terms as a forward-looking and highly flexible way to reduce CO_2 emissions, providing more efficient and cleaner, greener energy, making use of both fossil and renewable sources.

MCFCs are a key technology for stationary applications, especially in the size of hundreds to thousands of kilowatts, which is a very interesting power range in view of the increasing decentralization of energy supply and the increased need for high-quality power independent of the grid. After several years of research programs and

Table 19.2 Electrode reactions for fuel cells

Fuel cell type	Anode reactions	Cathode reactions	
AFC	$H_2 + 2OH^- = 2H_2O + 2e^-$	$1/2O_2 + H_2O + 2e^- = 2OH^-$	(19.4)
PEM	$H_2 + 2R-O^- = 2R-OH + 2e^-$	$1/2O_2 + 2R-OH + 2e^- = 2R-O^- + H_2O$	(19.5)
PAFC	$H_2 + HPO_4^{2-} = H_3PO_4 + 2e^-$	$1/2O_2 + H_3PO_4 + 2e^- = HPO_4^{2-} + H_2O$	(19.6)
MCFC	$H_2 + CO_3^{2-} = CO_2 + H_2O + 2e^-$	$1/2O_2 + CO_2 + 2e^- = CO_3^{2-}$	(19.7)
SOFC	$H_2 + O^{2-} = H_2O + 2e^-$	$1/2O_2 + 2e^- = O^{2-}$	(19.8)

Table 19.3 Contact list for MCFC deployment

Company	Contact name	Email address
Fuel Cell Energy (USA)	Ramki Venkataraman	rvenkataraman@fce.com
POSCO Energy (South Korea)	Tae-Won Lee	twlee@poscoenergy.com
Fuel Cell Energy Solutions (Germany)	Andreas Frömmel	afroemmel@fces.de
Franco Cell (France)	Marc Lemarignier	ml@francocell.eu
ENEA (Italy)	Stephen McPhail	stephen.mcphail@enea.it
University of Perugia (Italy)	Gabriele Discepoli	laboratorio.fuelcell@unipg.it
University of Genoa (Italy)	Barbara Bosio	barbara.bosio@unige.it
Fraunhofer-IKTS (Germany)	Mykola Vinnichenko	mykola.vinnichenko@ikts.fraunhoffer.de
	Roland Weidl	roland.weidl@ikts.fraunhofer.de
KTH (Sweden)	Carina Lagergren	carinal@kth.se
Chimie ParisTech (France)	Michel Cassir	michel.cassir@chimie-paristech.fr
Warsaw Univ. Technology (Poland)	Jarek Milewski	milewski@itc.pw.edu.pl
University of Connecticut (USA)	Prabhakar Singh	singh@engr.uconn.edu
KIST (South Korea)	Jong-Hee Han	jhan@kist.re.kr

extensive demonstration, MCFC-based systems are now appearing in commercial ventures of multiple megawatts, providing clean energy to commercial and small/midsize industrial customers all over the world. Especially in this phase of early deployment, and with a view to stay at the forefront of smart solutions for the evolving energy paradigm, to improve the technology, increase reliability, and reduce manufacturing costs, a lot of effort is still required from research and development to safeguard the relevancy and make real the enormous potential of MCFC solutions in the near and long-term future.

The investment cost for MCFC systems is decreasing steadily and is below US$ 4000 kW^{-1} today, and further cost reduction would be achieved if the production volume increased. MCFC is the most mature high temperature fuel cell technology available nowadays, with several plants already producing energy, as reported above. The installed power is already about 24 MW (around 85 units), with 6 MW being installed in Europe and 18 MW in North America and Asia. Two main companies are responsible for the field trials: Fuel Cell Energy (FCE) in the United States and CFC Solutions in Germany. CFC Solutions recently presented results after 25 000 hours (about three years) of operation for one of their main field trials. The shutdown of the power plant was planned and was not due to any failure. Furthermore, FCE has proved high reliability in their systems and has produced to date more than 20 GWh electrical energy in total. Typical customers are food and beverage industries, hotels, hospitals, prisons, wastewater treatment plants, and manufacturing industries, where key values such as reliability, efficiency, and green technology are important and where the fuel for the power plant is sometimes their own waste.

However, companies such as Ansaldo Fuel Cells in Italy are also not behind, and research centers in South Korea and Japan are developing the technology in close collaboration with industry. Table 19.3 gives a contact list for MCFC deployment.

In the present section the basic principles of MCFCs and the status of the fuel cell development will be considered briefly, followed by a more emphasized analysis on its limitations by corrosion problems and cost issues.

19.2.2 The Operating Principles of an MCFC

The first MCFC was demonstrated by Broers in 1958, and the first MCFC at high pressure was built by Reiser and Schroll in 1980. At present, the MCFC is the most efficient fuel cell, and this will be discussed hereinafter. The MCFC, operating at a temperature between 600 and 650 °C, is generally considered a second-generation fuel cell. It can be used with coal gas and even more so with natural gas as a fuel (Glasstone and Sesonske 1994).

The electrodes are porous, favorable for gas diffusion in the reaction zone, i.e. at the contact between gaseous reactants, liquid electrolyte, and electrode.

Molten carbonates are an extremely corrosive medium for the majority of metals and alloys at temperatures around 600 °C. Therefore, the choice of materials at a reasonable cost, to be used as stable cathodes under an oxidizing atmosphere such as air or oxygen–CO_2 mixtures, is limited. Only semiconducting oxides are materials with such properties. In the MCFC, the currently used material for the cathode is lithiated nickel oxide. Initially, the cathode is metallic nickel, but during the first period of time of cell operation, a lithiation and oxidation of the nickel occurs spontaneously in the presence of lithium carbonate under an oxidizing atmosphere at high temperature. The original structure of the material is completely changed

due to these phenomena. The cathode mass acquires many very small pores, which increase the contact surface area between the electrolyte and the gaseous reactant. The thickness of the NiO cathode ranges from 0.4 to 0.8 mm, and it has an electronic conductivity of approximately $5\,\Omega^{-1}\,cm^{-1}$.

The MCFC anode operates under reducing atmosphere, at a potential typically 700–1000 mV more negative than that of the cathode. Many metals are stable in molten carbonates under these conditions, and several transition metals have electrocatalytic activity for hydrogen oxidation. Nickel, cobalt, copper, and alloys in the form of powder or composites with oxides are usually used as anode materials. Ceramic materials are included into the anode composition to stabilize the anode structure (pore growth, shrinkage, loss of surface area) at the time of sintering. An alloy powder of Ni + 2–10 wt% Cr can be used. The initial formation of Cr_2O_3, followed by surface formation of $LiCrO_2$, can stabilize the anode structure.

The electrode has a particular structure. A mixture of $LiAlO_2$ and alkali carbonates (typically >50 vol%) is hot-pressed (about 5000 psi) at temperatures slightly below the melting point of the carbonate salts. In this way, a porous matrix support material of ceramic particles ($LiAlO_2$) is formed that contains a capillary network filled with molten electrolyte. The ceramic material in the electrolyte structure represents a mechanical resistance, which does not participate in the electrical or electrochemical processes. The prepared electrolyte has a thickness of 1–2 mm, and it is very difficult to produce it in large shapes.

The preferred electrolyte is a binary lithium–potassium carbonate consisting of 62 mol% Li_2CO_3 and 38 mol% K_2CO_3, with a liquidus temperature of 490 °C.

Figure 19.1 shows an outline of an MCFC cell that uses a gaseous mixture of $H_2 + CO$. The principal electrode reactions are

$$\text{Coal gasification} \quad C + H_2O \xrightarrow{O_2} CO + H_2 \qquad (19.9)$$

$$\text{Anode} \quad H_2 + CO_3^{2-} \rightarrow CO_2 + H_2O + 2e^- \qquad (19.10)$$

$$CO + CO_3^{2-} \rightarrow 2CO_2 + 2e^- \qquad (19.11)$$

$$\text{Overall anode} \quad H_2 + CO + 2CO_3^{2-} \rightarrow 3CO_2 + H_2O + 4e^- \qquad (19.12)$$

$$\text{Cathode} \quad 4e^- + 2CO_2 + O_2 \rightarrow 2CO_3^{2-} \qquad (19.13)$$

$$\text{Overall fuel cell} \quad CO + H_2 + O_2 \xrightarrow{4F} CO_2 + H_2O \qquad (19.14)$$

$$\text{Overall power plant} \quad C + O_2 \xrightarrow{4F} CO_2 \qquad (19.15)$$

A gaseous mixture of H_2 and CO can be obtained by coal gasification or reforming of natural gas. That mixture reacts at the anode with molten CO_3^{2-} ions to produce CO_2 and H_2O vapors, releasing electrons to the external circuit. Also, in the anode compartment, in the presence of metallic cell parts, at 650 °C, CO present in the fuel gas reacts with H_2O vapor, yielding hydrogen, as shown in Eq. (19.3).

At the anode, hydrogen is oxidized more easily than CO, so Reaction (19.10) is more important than Reaction (19.11). For this reason, the main electroactive species is hydrogen.

Carbon dioxide produced at the anode is recycled to the cathode where it reacts with electrons and atmospheric oxygen to regenerate the carbonate ion consumed at the anode. Two mechanisms have been proposed for the anode reaction. The first is

$$2H_2 + 4M = 4MH \quad (M = Ni) \qquad (19.16)$$

$$2MH + 2CO_3^{2-} \rightarrow 2OH^- + 2CO_2 + 2M + 2e^- \quad \text{(r.d.s.)} \qquad (19.17)$$

$$2MH + 2OH^- = 2H_2O + 2M + 2e^- \qquad (19.18)$$

The second is Reaction (19.16) with Reaction (19.17) followed by

$$2OH^- + CO_2 = H_2O + CO_3^{2-} \qquad (19.19)$$

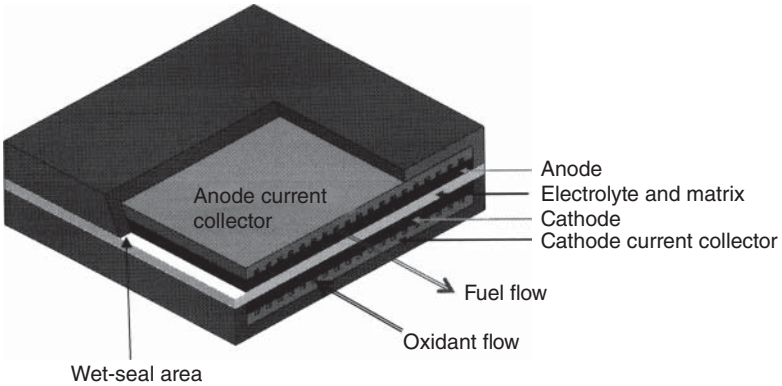


Figure 19.1 Schematic view of an individual MCFC.

where Reaction (19.17) is the rate-determining step (r.d.s.).

The cathodic mechanism is complex, and it depends on the melt composition, especially the acidity of the electrolyte, namely, the cation composition. In less acidic electrolytes (see Reaction 19.21), the peroxide mechanism prevails:

$$O_2 + 2CO_3^{2-} = 2O_2^{2-} + 2CO_2 \tag{19.20}$$

$$2O_2^{2-} + 4e^- \rightarrow 4O^{2-} \quad \text{(r.d.s.)} \tag{19.21}$$

$$4O^{2-} + 4CO_2 = 4CO_3^{2-} \tag{19.22}$$

where O_2^{2-} is the peroxide ion and O^{2-} is the oxide ion.

In acidic melts, however, the superoxide mechanism is dominant (Reaction 19.24):

$$3O_2 + 2CO_3^{2-} = 4O_2^- + 2CO_2 \tag{19.23}$$

$$2O_2^- + 2e^- \rightarrow 2O_2^{2-} \tag{19.24}$$

$$2O_2^{2-} + 4e^- \rightarrow 4O^{2-} \tag{19.25}$$

$$4O^{2-} + 4CO_2 = 4CO_3^{2-} \tag{19.26}$$

The relative basicity of the commonly used alkali carbonates is

$$\text{(basic)} \qquad Li_2CO_3 > Na_2CO_3 > K_2CO_3 \qquad \text{(acidic)}$$

The cathode reaction mechanism is not so well understood, and more studies are necessary to elucidate it as a function of the electrode material and electrolyte composition.

The reversible cell potential for an MCFC depends on the gas composition at the anode (partial pressures of H_2, H_2O, and CO_2) and at the cathode (partial pressures of O_2 and CO_2):

$$E_{\text{rev}} = E^0 + \frac{RT}{2F} \ln \left\{ \left[\frac{p_{H_2} P_{O_2}^{1/2}}{P_{H_2O}} \right] \cdot \left[\frac{P_{CO_{2,c}}}{P_{CO_{2,a}}} \right] \right\} \tag{19.27}$$

where the subscripts a and c refer to the anode and cathode gases, respectively. When the CO_2 partial pressures in the cathode and the anode gases are identical, the cell potential depends only on the partial pressures of H_2, O_2, and H_2O. The values of E^0 (the standard cell potential) for hydrogen oxidation and for several other reactions at 650 °C are given in Table 19.4.

From Eq. (19.27) it follows that a pressure increase from P_1 to P_2 causes an increase in the reversible cell voltage:

$$\Delta E = \frac{RT}{4F} \ln \left(\frac{P_2}{P_1} \right) = 46 \log \left(\frac{P_2}{P_1} \right) \tag{19.28}$$

Therefore, a 10-fold increase in cell pressure corresponds to an increase of 46 mV in the reversible cell potential at 650 °C. Both the cell voltage and the gas solubility in the electrolyte increase with the gas pressure.

A serious difficulty is the solubility of the nickel oxide cathode in the electrolyte. The solubility of NiO depends on the CO_2 partial pressure, according to the equilibrium

$$NiO + CO_2 = Ni^{2+} + CO_3^{2-} \tag{19.29}$$

The equilibrium constant of this reaction is about 5.7×10^{-6} at 600 °C. The NiO solubility is low in basic electrolytes or at high oxide ion concentrations (O^{2-}). Under the conditions of an operating fuel cell, the dissolution reaction that takes place is

$$NiO \rightarrow Ni^{2+} + O^{2-} \tag{19.30}$$

Therefore, in the presence of an excess of O^{2-} ions, the solubility of NiO is suppressed. The solubility of NiO is lowered by a factor of 3 in the Li_2CO_3–Na_2CO_3 mixture compared with the Li_2CO_3–K_2CO_3 mixture. The Ni^{2+} ions formed at the cathode migrate toward the anode under the influence of the electrical field and the concentration gradient. At the anode, the Ni^{2+} ions are reduced and deposited, and for this reason short circuiting of the cell can result after some time. Alternative cathode materials are $LiCoO_2$, $LiFeO_2$, and $LiMnO_3$ (see Section 19.2.4). Recently, many corrosion studies of the materials used in MCFC were made (see Sections 19.2.3–19.2.7). These works led to an increase of cell life up to 50 000 hours.

The internal reforming MCFC has a particular construction. In the anode chamber there is a catalyst for the reforming reaction of natural gas. In this case, the following reactions occur at the anode:

$$CH_4 + H_2O \rightarrow 3H_2 + CO \tag{19.31}$$

$$3H_2 + 2CO_3^{2-} \rightarrow 3H_2O + 3CO_2 + 6e^- \tag{19.32}$$

$$CO + CO_3^{2-} \rightarrow 2CO_2 + 2e^- \tag{19.33}$$

Table 19.4 Thermodynamic characteristics and voltages of fuel cell reactions at 650 °C

Reaction	ΔG^0 (kJ mol^{-1})	E^0 (V)
$H_2 + 1/2O_2 = H_2O$	−196.92	1.020
$CO + 1/2O_2 = CO_2$	−202.51	1.049
$CH_4 + 2O_2 = CO_2 + 2H_2O$	−800.89	1.038
$CH_4 + H_2O = CO + 3H_2$	−7.62	0.010
$CH_4 + CO_2 = 2CO + 2H_2$	−2.04	0.003
$CO + H_2O = CO_2 + H_2$	−5.58	0.029
$2CO = C + CO_2$	−14.62	0.076

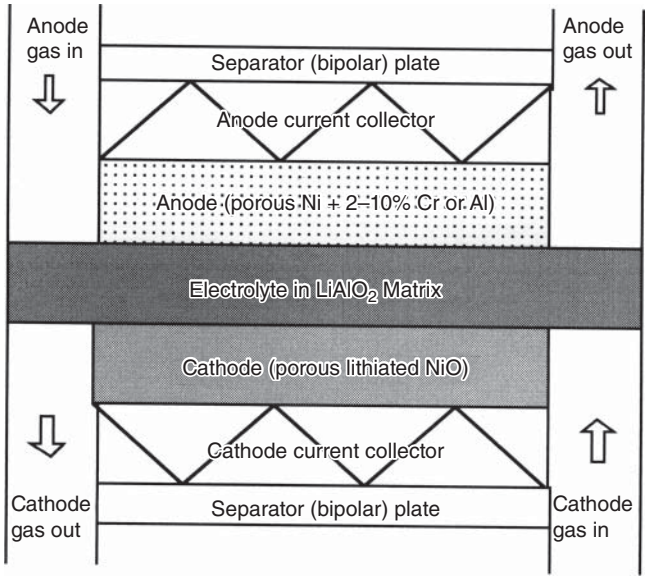


Figure 19.2 The principle of a molten carbonate fuel cell stack.

$$\text{Overall reaction} \quad CH_4 + 4CO_3^{2-} \rightarrow 2H_2O + 5CO_2 + 8e^- \tag{19.34}$$

The main product from the reforming reaction, which is H_2, is consumed in the anode reaction.

Figure 19.2 attempts to show the principle of an MCFC stack. The separator plates (also called bipolar plates) and current collectors function as the single-cell housing components and provide cell-to-cell electronic contact. $H_2 + CO$ enter at the anode side by flowing through the anode corrugated current collector. The oxidizing gas, consisting of O_2, CO_2, and H_2O, flows through a corrugated current collector at the cathode side.

In general, the single operating cell voltage is of the order of 800 mV for current densities of the order of 160 mA cm^{-2}. To produce larger currents and useful voltages, it is necessary to increase the electrode active area and to stack individual cells in series. It is in this context that the bipolar plates, which are in contact with the anode and cathode current collectors, play a key role, connecting the single or individual cells in series. Therefore, cells with thicknesses of about 5 mm and areas larger than 1 m^2 can be superposed, composing stacks of many MW. Recent studies of research and development deal with issues of the component materials and their corrosivity in the molten salt environment, as discussed in the following subsections.

19.2.3 MCFC Anode Materials

The MCFC anode is a porous structure like the cathode, which allows diffusion of gases and collects current from triple-phase boundary (TPB) interfaces at reaction sites. General materials required for MCFC anode have good electrical conductivity and structural stability and suitable catalytic properties for the type of fuel used. Since the reaction kinetics (oxidation of fuel) is faster at the anode side of MCFC at the operating temperature, the base metal catalysis (Ni) is sufficient for hydrogen fuel. Therefore less surface area is acceptable in the case of the anode as compared with the cathode. Since the early stages of development of MCFC, the pure Ni-based anodes have demonstrated reasonable electrochemical performance with polarization losses of less than 30 mV at 160 mA cm^{-2}.

One of the issues with the pure Ni anode is performance degradation and shrinkage due to creep and sintering. Furthermore, the manufacturing processes and typical operating conditions of MCFC lead to compressive stress at high temperatures on MCFC components including the anode. These conditions are clearly favorable for the creep-type failures of metallic components in MCFC.

The creep exponents of pure Ni anode are close to the Nabarro–Herring-type creep (diffusion of vacancies within crystal lattice) or Coble-type creep (diffusion of vacancies via grain boundaries). Apart from the creep, the decrease in the surface area and shrinkage due to sintering (via neck formation–mass transport) cause the degradation in performance of anodes during the initial few days of MCFC operation. To overcome these problems, alloying of Ni anode with various metals such as Cr, Al, and Cu is a common approach taken by the developers. Arresting the creep by addition of intermetallics is a well-proven technique used in high temperature metals engineering. Wee et al. (2005) studied the effect of addition of intermetallic powders (Ni_3Al) on the sintering and creep resistance of the NiO anodes. They found that the addition of 5 wt% Ni_3Al phase along with 3 wt% Al decreases the shrinkage and also prevents the porosity collapse.

As in the case of cathodes, an improvement in the electrochemical performance of the anode is desired. As MCFC operation relies on the ionic exchange between the melt and solid electrodes, the wetting of the electrodes (the wetting angle) especially on the anode side is an important parameter determining the MCFC performance. The wetting angle for standard MCFC anodic gas composition is around 50° with $(Li/Na)_2CO_3$ and 31° $(Li/K)_2CO_3$. Hence, efforts are being made to improve the wetting of the anode using the coatings or additives. Apart from the material composition and morphology, the electrolyte melt distribution and amount in the anode pores are important characteristics that determine the performance of the anode. For Ni–Cr anode 5–25% electrolyte fill demonstrates the maximum performance with Li/Na carbonate melt as an electrolyte (Yoshikawa et al. 2006). However, some researchers have investigated the use of anodes as an electrolyte reservoir to compensate for the electrolyte loss from the matrix during long-term operation of MCFC.

Youn et al. (2006) reported the use of Ni-10 wt% Cr anode as an electrolyte reservoir. The anode was coated with boehmite (γ-AlO(OH)) solution via a dip coating process, which was then converted into Li-aluminate particles *in situ* during the cell operation. The surface modifications allowed an increase in the electrolyte filling of anode to 50–60 vol%. The coating resulted in good electrolyte wettability as compared to bare Ni surface, which partially compensates for the decrease in conductivity by providing additional sites for the reaction. The polarization characteristics of a coated cell with additional electrolyte were found to be slightly inferior to a standard cell (25 vol% electrolyte), but the results suggest that the surface modification could be used to modify the anode surface to make it function as an electrolyte reservoir.

As MCFC systems are considered mainly for stationary power generation, significant efforts have been made over the past few decades to develop MCFC systems fueled with "real-world fuels" such as natural gas, digester gas, and allied hydrocarbon fuels. These fuels can be reformed to H_2 and CO inside the MCFC unit or externally using a separate reformer.

Since heat from the electrochemical oxidation of fuels and steam form can be used for reforming inside the anode chamber, the MCFCs with direct *in situ* reforming (DIR) are more efficient than those with external reforming. In a high temperature fuel cell such as SOFC operating at temperatures from 800 to 900 °C, the reforming can be achieved using the Ni–YSZ anode itself as a catalyst. In the case of MCFC, DIR is achieved by placing the reforming catalysts into the fuel channels as the catalytic activity of the conventional MCFC anode is not sufficient for reforming because of the lower surface area and lower operating temperature of MCFC.

The placing of the catalyst in fuel channels can be accommodated by modification of cell hardware. Typically, supported metal-type catalysts are used for internal reforming. Commercial suppliers of MCFC systems (such as FCE and Mitsubishi) and research organizations (CNR-TAE Institute) developing MCFCs have tested DIR MCFCs with catalysts such as NiO/MgO, Ni/alumina, and Ru/ZrO_2.

Apart from internal reforming catalysts, the anode itself needs to be tolerant of impurities such as sulfur and carbon. To make the anodes more tolerant toward the impurities, the anode materials have been modified by coating with additives or catalysts. Fang et al. (1998) reported the surface alloying of NiO anode with niobium using a molten fluoride process. The surface alloying demonstrated significantly lower corrosion rate (0.02 nm yr^{-1} compared with 0.17 mm yr^{-1} for bare NiO) in a carbonate bath and improved electrocatalytic activity toward CO oxidation. The lower solubility is attributed to the formation of a composite phase NiO, Nb_2O_3, and the improvement in the wetting angle and increased surface area after the surface treatment.

Other approaches to mitigate the problem of deactivation of DIR catalysts are indirect internal reforming (IIR) and the use of a separator plate. In IIR, the reforming catalyst unit is kept in thermal contact with the MCFC unit with exit ports of the IIR unit connected to entry port of the anode (Baker 1989). In this arrangement, the catalyst is not exposed to the anodic atmosphere, and thus it increases the life of the catalyst. Furthermore, the IIR arrangement also offers a better thermal gradient in the stack as compared with DIR. However, the efficiency of IIR unit is lower than DIR as hot steam formed at the anode is not used in IIR. To combine the advantages of both IIR and DIR systems, the commercial developers FCE, Inc. and MELCO used a hybrid approach (Vielstich et al. 2007). The partially reformed fuel from IIR catalyst is further reformed at the anode with DIR. The hybrid design improves the thermal distribution inside the cell and thus improves the overall performance and stability.

19.2.4 MCFC Cathode Materials

The cathode is most often made of lithiated NiO, usually oxidized and lithiated *in situ*. The dissolution of the cathode material has been one of the main issues for MCFC research although posttest characterization of the recently performed long-term field trials has shown that the problem may be smaller than the models have predicted. The nickel oxide dissolves according to the mechanism described above, in which nickel oxide and carbon dioxide form nickel ions and carbonate ions, as shown in Eq. (19.34).

The dissolved nickel ions are then transported from the electrolyte in the pore of the cathode into the matrix. Near the cathode, the nickel ions react with hydrogen, dissolve in the melt, and precipitate as metallic nickel, forming chains that eventually short-circuit the cell (Yoshikawa et al. 2001). Since the time to short circuit the cell depends on the equilibrium concentration of nickel dissolved in the melt, research has aimed at a reduced solubility of the cathode. This can be done in three ways: changing to another cathode material, stabilizing the present nickel oxide, or changing the melt composition.

Alternatives to nickel oxide as cathode material should have equal or higher electrocatalytic activity, good conductivity, even lower dissolution, mechanical stability, and low cost combined with an inexpensive manufacturing process. Over the years, several alternative materials have been investigated for use as cathode in MCFC (Bergman et al. 2001; Selman et al. 1990; Uchida et al. 1999; Young 1960). $LiCoO_2$ and $LiFeO_2$ have been tested more extensively. $LiCoO_2$ has a lower solubility than nickel oxide at carbon dioxide pressures below 2 atm and a comparable performance, but the higher cost, brittleness,

and the higher contact resistance limit the use of $LiCoO_2$. On the other hand, $LiFeO_2$, which has low dissolution and is less expensive, has a too low electrocatalytic activity and conductivity to be used as cathode material. One solution to the problem has been binary or ternary mixtures of the oxides $LiCoO_2$, $LiFeO_2$, and NiO (Wijayasinghe et al. 2006). Coatings onto the nickel oxide, most often containing cobalt or iron, have however been the most common approach to stabilizing the nickel oxide with promising results (Escudero et al. 2005), regarding both the solubility of nickel and the performance. To further increase the stability or conductivity, a number of oxides, added to all the three types of cathode materials (pure oxides, mixtures, and coatings), have been investigated (Huang et al. 2004).

The cathode dissolution is also lowered by increasing the basicity of the melt where the basicity is defined as the ability to donate oxide ions. Ota et al. (1992) showed that the degree of basicity for the three carbonates was (in decreasing order) $Li_2CO_3 > Na_2CO_3 > K_2CO_3$ by varying the melt composition in the region where the acidic dissolution mechanism is valid. Therefore, lithium–sodium carbonate as well as electrolytes with high contents of lithium carbonate is considered to have lower nickel solubility than the traditional lithium–potassium carbonate. However, increased lithium contents result in lower solubility and diffusivity of the gases in the melt, and the gas solubility and reaction rate of sodium containing melts are more temperature dependent. Therefore, a change in the electrolyte composition may cause lower or uneven performance, and the cell design and the operating conditions will determine the melt composition used.

Instead of changing to another alkali carbonate, the basicity of the melt could be increased by adding oxides of alkaline earth metals or lanthanum.

Although lanthanum seems to have the best effect to decrease the solubility of NiO, Matsuzawa et al. (2005) and Mitsushima et al. (2002) showed that a combination of adding MgO to the melt and having a MgO containing cathode results in a synergy effect, leading to even lower nickel dissolution. It is not clear, however, if the effect of the additives will remain during long-term operation since the segregation of the electrolyte can cause the additives to migrate to the anode side, thus decreasing the additive concentration at the cathode side of the cell (Carlin 1996).

It should be noted though that recent evaluation of long-term field trials on single cells (25000–40 000 hours) shows a lower effect of the nickel oxide dissolution than the models have predicted. This brings research in the field of nickel dissolution up to date, where the models and predictions have to be reviewed and improved to better predict the results before more experimental work is performed.

19.2.5 MCFC Bipolar Current Collectors

Needless to say, protection of the *bipolar plate* from corrosion is essential for the entire stability and performance of the cell. From a design point of view, the bipolar plate is frequently composed of three distinct metallic components: the *separator plate*, the *current collector*, and the *center plate*. Schematically, separators are corrugated plates that must fulfill the following main functional requirements: (i) separate fuel and oxidant gas streams; (ii) create flow channels for the gases to pass the electrodes; (iii) provide electrical contact between adjacent cells (in combination with the current collectors and the center plates); and (iv) provide a tight gas flange by extending the electrolyte tile to the plate edges where it is sandwiched between two plates (wet seals) (Figure 19.3). The purpose of the current collectors and center plates is mostly to reduce the contact and corrosion areas of the separator plate with the electrolyte.

Separator plates, current collectors, and center plates must simultaneously satisfy various chemical, electrical, and mechanical requirements, and therefore they are usually made of the same materials. For the sake of simplicity, we will refer to them as a whole with the term bipolar plate.

The most critical requirement is undoubtedly the corrosion resistance as the bipolar plate must tolerate a wide range of aggressive chemical conditions intermediate between the highly oxidizing cathode environment and the highly reducing character of the anode in the presence of a liquid salt. Strictly speaking, the bipolar plate experiences different corrosion conditions along its length.

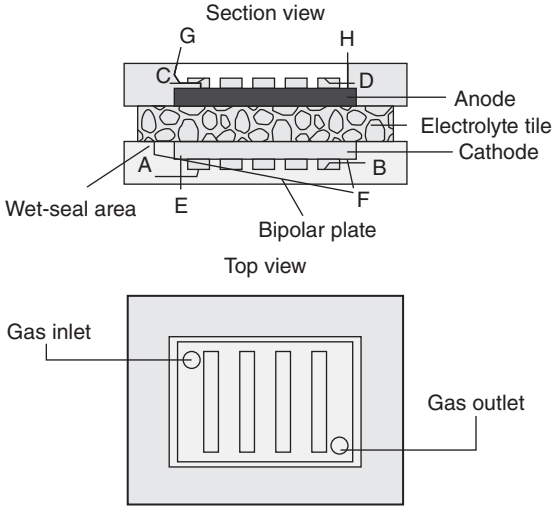


Figure 19.3 Side view and top view sections of a molten carbonate single cell showing the different corrosion areas of the bipolar plate: see text for explanation of letters A–H.

In Figure 19.3, the letters A–H identify such corrosion cell as:

(A) Regions in contact with thin layers of molten carbonate in highly oxidizing gas environment.

(B) Regions in contact with thin layers of molten carbonate in a less oxidizing gas environment.

(C) Regions in contact with thin layers of molten carbonate in a reducing gas environment.

(D) Regions in contact with thin layers of molten carbonate in a less reducing gas environment.

(E) Regions in contact with deep layers of aerated molten carbonate.

(F) Regions in contact with deep layers of scarcely aerated molten carbonate.

(G) Regions in contact with deep layers of molten carbonate in a mixed reducing/carburizing gas environment.

(H) Regions in contact with deep layers of molten carbonate in a poorly reducing gas environment.

In a rather, although widely used, oversimplified approach, these different corrosion areas can be conveniently grouped in (i) cathode region (points A, B, E, F), (ii) anode region (C, D, G, H), and (iii) anode (H) and cathode (F) wet-seal regions.

Design modifications have been found useful to mitigate the corrosion problems by reducing the wetting areas with electrolyte. For instance, Shimada (1996) describes a "soft" plate that is flexible enough to adsorb the deformation of the active components by means of flat springs contained inside the wet seal that ensure the necessary component pressures. In this way, a pressed current collector with a gas flow channel function could be used instead of a corrugated separator to reduce wetting and, in turn, corrosion areas. A similar pressed plate structure directed to reduce the number of components and the contact areas has been tested with promising results in terms of corrosion and electrolyte loss (Selman et al. 1997).

Another important requirement is that the bipolar plate material should be a metallic conductor. Additionally, the corrosion products must also be sufficiently conductive ($\sigma > 10^4\,\mathrm{S\,cm^{-1}}$) and insoluble in the carbonate melt. Finally, several mechanical requirements are associated with fluid flow, high temperature mechanical resistance, proper contact of the components, weldability, and easy formability.

Table 19.5 lists about 60 different high temperature alloys that have been so far evaluated by various developers (Yuh et al. 1995).

The austenitic stainless steels 316L and 310S are the current choices for their appropriate cathode-side corrosion resistance and a relatively low cost. Regarding the role of alloying elements in the corrosion resistance of commercial steels, chromium is the element that confers the best corrosion resistance under both cathode and anode conditions, whereas nickel is less important or has a slight negative effect in oxidizing environments. Aluminum results in high corrosion resistance but also in corrosion layers with high electrical resistance.

To improve their anode-side corrosion resistance, Ni-cladded or Cr-plated stainless steels can be used there (nickel is thermodynamically stable in the reducing anode gas conditions). Both electroless and electrolytic plating methods have been evaluated, but they are rarely used due to their higher costs and to a lesser corrosion resistance. With the Ni-clad structure very dense, a 50–100 μm thick layer is adequate to provide the best protection to corrosion, thermal cycles, and interdiffusion. High nickel-based alloys show appropriate anode-side corrosion, although they are scarcely used because of their cost and an insufficient resistance in the cathode compartment.

It is easily understood that the formation of a corrosion scale with a poor electrical conductivity could result in a voltage loss so that the ohmic drop at the bipolar plate/electrode interface would tend to increase as the corrosion proceeds. The increase of ohmic drop on the cathode side due to scale growth is estimated to contribute to the cell decay rate for less than 0.8 mV/1000 hours (≈1%/1000 hours), if AISI 316L is used (Fujita and Urushibata 1996). However, this number may not be acceptable for a 40 000 hour operation in future MCFC systems, where a cell decay rate of 0.25%/1000 hours has been recently targeted. The following table evidences that the bipolar plate corrosion is one of the most important

Table 19.5 Candidate alloys evaluated for the MCFC bipolar plate (Yuh et al. 1995)

Fe-based alloys
304, 304L, 310, 310S, 314, 316, 316L, 330, 347, 405, 430, 446, 17-APH, 18SR, A118-2, Al26-1S, Al29-4, Al439, Glass seal 27, Ferralium 255, RA 253 mA, Nitronic 50, 20Cb3, Crutemp-25, Sanicro-33, IN800, IN840, A-286
Ni, Co-based alloys
IN600, IN601, IN671, IN706, IN718, IN825, IN925, RA333, Ni200, Ni201, Ni270, Haynes 230, Haynes 625, Haynes 188, Haynes 556, Nichrome, Monel 400, Hastelloy C-276
Al-containing alloys
MA856, FeCrAl + Hf, Haynes 214, Fecralloy, IJR406, 85H, Kanthal AF, Kanthal A-1, Ni_3Al, FeAl

Table 19.6 Items to study to attain a 40 000 h stack life (Tatsumi et al. 1996)

	Items	Counter measures
1	Decay due to polarization	Optimization of pore structures Control of fill ratio Decrease in electrolyte loss Pressed bipolar plate (smaller contact areas) Li/Na-type electrolyte Lower solubility of the cathode
2	Decay due to ohmic loss	Soft seal-type separator Improved bipolar plate materials Pressed bipolar plate High-quality Al coating
3	Decay due to ionic resistance	Optimization of electrolyte pore structures Restriction of $LiAlO_2$ phase transformations Decrease in electrolyte loss
4	Decay due to Ni dissolution	Li/Na-type electrolyte Improved cathode (NiO + Mg, Fe)

items to be solved for reducing the cell decay (Tatsumi et al. 1996) (Table 19.6).

Based on posttest analysis of failed MCFCs, the influence of corrosion is not limited to ohmic losses, but many results have indicated that corrosion degrades also the functionality of the cell components (both metallic and active ones). A good presentation of this problem has been discussed by Singh (1983) to which the reader is invited to refer for a more detailed analysis. Here a brief excerpt of his work is presented. The main corrosion factors contributing to the cell performance decay can be grouped in the following categories: (a) dimensional and (b) mechanical change of the plate, (c) loss of electrolyte and gas leakage, and (d) chemical contamination of electrodes and electrolyte.

(a) *Dimensional changes*: A dimensional stability of the bipolar plate may be undetermined if the anodic side of the plate is not being protected by nickel cladding. Uncoated stainless steel in fact experiences excessive scale growth on the anode side, resulting in an intolerable increase of plate thickness. These dimensional changes tend to generate compressive stresses in the cell components causing formation of cracks and breakdown of the most brittle cell components such as tile and electrodes. Excessive scaling also results in the scale crack with anomalies in the gas path geometry. The cell decay rate may be enhanced because of fluctuations in the gas composition and localized use of the fuel.

(b) *Mechanical changes*: Mechanical and load-bearing properties of the bipolar plate components have been sometimes observed to be strongly affected by scaling and carburization processes. Excessive scaling on stainless steels reduces in fact the effective thickness of the metallic component, whereas carburization, i.e. precipitation of chromium-rich carbides inside the metal matrix and at grain boundaries, may lead to hardening of the component. Both the effects are deleterious because the reduction of mechanical resistance could cause the breaking of the remaining metallic components.

(c) *Electrolyte and gas leakage*: The electrolyte loss is caused by reactions between the oxide scale grown on the bipolar plate and the molten carbonate, resulting in a consumption of the alkali metal electrolyte components and formation of reaction products such as $LiCrO_2$, K_2CrO_4, Li_2CrO_4, $LiFeO_2$, and others. The increasing and never recovered loss of carbonate melt during cell operation causes an increase of the polarization at electrodes and an increase of the internal resistance at the electrolyte. Likewise, excessive electrochemical corrosion in the wet-seal area may lead to poor scaling with both gas leakage and electrolyte loss effects.

(d) *Chemical contamination*: Formation of both soluble and insoluble oxide layers normally occurs during the corrosion reactions between the metallic components and the carbonate melt. Thus, at the anode compartment, corrosion of stainless steels proceeds with the initial formation of soluble iron oxide, which later precipitates at the melt–gas interface (fluxing dissolution). At the cathode side, under very oxidizing conditions, soluble chromates become the more stable corrosion products. The dissolution of these oxide contaminants into the electrolyte changes the melt chemistry in terms of oxide ion activity (acid/basic properties). Also the NiO cathode electrode can be contaminated by incorporation of aliovalent iron(III) or chromium(III) ions. This changes the defective structure of the cathode, which could result in changes of its electronic conductivity.

19.2.6 MCFC Wet Seal

The cell-perimeter seal area simultaneously experiences reducing and oxidizing environments (Donado et al. 1984). MCFC seal is provided by a molten electrolyte-filled matrix (wet seal).

The concept of the *wet-seal* flange is nowadays largely applied in the MCFC bipolar plate fabrication as a method of minimizing corrosion and sustaining large differential pressures across the stack. Successive improvements have been performed in the seal design from the pioneeristic work of Davtyan in the 1940s (1946). In the "wet-seal

technique," the bipolar plate is pressed against the flat surface of the electrolyte tile (i.e. the solid porous support filled with the carbonate mixture). At the MCFC working temperature, the molten electrolyte wets the metallic surface and forms the gas wet seal. Although the width dimension of the wet-seal area is relatively small (usually 5–10 mm, i.e. about only five times the tile thickness), it has long been realized that corrosion of the wet-seal area metal is particularly critical and may lead to a poor sealing with consequent gas leakage and rapid decay of the cell performance. An excessive corrosion may also lead to a critical electrolyte loss from the tile causing catastrophic failure (Donado et al. 1984). The use of the wet-seal technique results in the onset of galvanic couples whose corrosion currents are often limited by the mass transfer rates of O_2 and CO_2. Fe and Ni-based alloys have been found to offer limited resistance to this kind of attack since their corrosion products are usually too conductive to block the current paths. Thus, for instance, AISI 316L was so severely corroded as anode wet-seal material during short-term tests (2000 hours) cannot be absolutely used without protection (Lovering 1982). Corrosion in the cathode wet seal was found to be about 2 orders of magnitude lower than at the anode side (Lovering 1982); therefore AISI 316L could be used without significant problems in the cathode wet seals in short-term MCFC operation (a few thousand hours).

Methods of minimizing the galvanic corrosion of wet seals are very limited. A review on this subject has been published by Pigeaud et al. (1981). Based on the consideration that an insulating material is desirable to break the corrosion cells, the possibility of using more than one type of material for the bipolar plate was early examined. Aluminum-containing alloys, such as Kanthal A-1, reduce the corrosion rate in the anode gas environment by at least 2 orders of magnitude to less than 0.002 cm in 1000 hours with respect to the AISI 316L (Lovering 1982). This is ascribed to the formation of an insulating $LiAlO_2$ thin surface layer. However, this approach was not pursued for the high costs of fabrication of metallic bipolar plates. Aluminum foil gaskets were also investigated but with unsatisfactory results because the Al melting point (c. 660 °C) is so close to the MCFC operating temperature that even small temperature fluctuations in the cells can melt the gasket (Yuh et al. 1987). Currently, the only followed approach is to protect the stainless steel by deposition of aluminum diffusion coatings in the wet-seal area. Aluminized stainless steels are in fact known to provide HTC resistance in both oxidizing and reducing environments by forming a dielectric alumina thin film. In the presence of carbonate, alumina converts to $LiAlO_2$, which is also effective in inhibiting the corrosion cells with a minimal consumption of electrolyte, thus providing the required long-term stability to the wet seal.

Various aluminizing processes have been so far evaluated for their effectiveness, including painting, thermal spraying, vacuum deposition, and pack cementation (Yuh et al. 1987, 1995). At the present time, the ion vapor deposition (IVD) method followed by a diffusion heat treatment is generally considered to offer the most protective and adherent aluminized coating in the MCFC wet-seal environment. A detailed description of the principles of IVD coating method is given in the *Metals Handbook* (1982). Diffusion bonding is obtained at 900–1000 °C for one to three hours in a reducing atmosphere. The resultant IVD coating is dense and uniform, mainly consisting of an intermetallic MAl–M_3Al structure (M = iron, nickel plus 5–10 wt% Cr). Concentration of Al in the diffusion layer ranges from the 50 wt% of the outer layer to the 30 wt% of the inner layer, values that are much higher than those obtainable by other methods (Yuh et al. 1987). This confers to the IVD coatings the sufficient long-term stability and durability required for a 40 000 hour cell operation.

19.2.7 MCFC Electrolyte and Matrix

MCFCs use mixtures of alkali carbonates as electrolyte. Structure and properties of alkali carbonate melts are under study since the beginning of the 1960s (Bloom 1992). During cell operation, the carbonate ions take part in the anode and cathode reactions according to Eq. (19.12). At the cathode, they are created and at the anode they are consumed in equal amounts. Hence, ionic conduction in the MCFC is achieved by transporting carbonate ions from the cathode to the anode. Eutectic or close to eutectic binary (Li/K; Li/Na; Na/K) as well as ternary (Li/Na/K) mixtures of carbonates are suitable for MCFC application. Varying compositions of the ternary system have been investigated at many research institutes. It was found that, regarding cell performance, the blend Li/Na/K (56.8 : 31.2 : 12) gave the best results. Similar results were obtained by the Energy Research Corporation (ERC) (Yuh and Pigeaud 1989).

The performance and lifetime of MCFCs depend to a great extent on the proper choice of the electrolyte. Critical factors for the selection are, for instance, ionic conduction, gas solubility, wetting characteristics in contact with metallic and ceramic surfaces, vapor pressure, viscosity, surface tension, and corrosion stability of materials in contact with the electrolyte. In the past decades, most of the work has been done using mixtures of lithium carbonate and potassium carbonate. The mixture has a eutectic melting point of 761 K (488 °C) at a mole ratio of 62 : 38 (Li/K).

Recently, the Li/Na carbonate electrolyte is getting increasing attention. Earlier reports that this electrolyte leads to increased corrosion have not been confirmed. There are some properties that make the Li/Na carbonate attractive:

- Higher ionic conductivity reduces the cell resistance.

- Lower vapor pressure gives longer operation time due to less electrolyte loss.
- Lower NiO solubility leads to better cathode stability and prolonged lifetime.
- Reduced electrolyte creepage gives less corrosion and improved cell stability.

It can be seen that the Li/Na blend provides many superior characteristics compared with the currently used Li/K blend. However, there are also shortcomings. One is the reduced solubility of gases in the Li/Na melt. This gives rise to higher polarization resistance and lower cell performance.

A direct comparison of the Li/Na and Li/K electrolyte is given by Yuh and Pigeaud (1989). Table 19.7 shows the result. Data for Li/K and gas solubility have been added from other sources.

The table illustrates that five superior ($\Uparrow$), three approximately equal ($\Longleftrightarrow$), and one inferior ($\Downarrow$) quality ratings can be assigned to the Li/Na blend as compared with the standard Li/K blend. It is noteworthy that the solubility of the cathode material NiO is 2.5 times smaller in the Li/Na electrolyte.

The high surface tension/large contact angle may lead to problems because it retards the filling of the porous components. In an experimental study, ERC observed this effect with laboratory cells. It could be overcome however by small changes in the assembly and start-up procedure. Laboratory cells with Li/Na electrolyte were operated up to 5000 hours. After the test, the cell components did not show stronger corrosion as compared with standard electrolyte cells. Little Ni precipitation in the matrix was found, and the particle growth was comparable with Li/K carbonate.

The reduced oxygen solubility of the Li/Na blend gives rise to some concern. Low gas activity in the melt generates high polarization resistance, which lowers the cell performance. The Institute of Gas Technology (IGT) in Des Plaines, IL, seems to have overcome this problem because they reported some time ago that fuel cells using Li/Na carbonate electrolyte routinely exhibit higher performances and lower decay rates than equivalent cells using Li/K carbonate electrolyte when operated at an isothermal temperature of 650 °C. However, Li/Na cells show lower performance than the Li/K cells at temperatures below 600 °C. The loss in performance was determined to be due to increased cathode polarization.

The electrolyte in an MCFC is contained in a ceramic *electrolyte matrix* structure. Early developers used MgO, which turned out to be not stable enough. Today, lithium aluminate ($LiAlO_2$) is used, which has a very low solubility in the carbonate melt.

The matrix was formerly manufactured by a sintering process, which resulted in a so-called electrolyte tile. These structures were very stiff and therefore easily cracked with subsequent gas crossover in the cells. With the advent of the tape casting technology, a more appropriate manufacturing method could be used, which also allowed the manufacturing of larger area components. The matrix obtained by this process is a flat tape with very uniform thickness. The fine $LiAlO_2$ powder is contained in an organic binder, which gives the tape high flexibility. The matrix is incorporated in the cells in this state. During the start-up of the cells, the organic binder is burned out, and the remaining fine pores are filled with the electrolyte.

However, there are stability aspects with $LiAlO_2$ as well, namely, the growth that can take place in number and size of large crystallites at the expense of very fine particles, leading to losses of the surface area. Furthermore, a phase transformation of the $LiAlO_2$ crystal structure has been observed that leads to increases in bulk volume. Such changes in particle size and shape due to sintering, and the structural expansion of the ceramic matrix as a result of phase transformation, can have an impact on the overall

Table 19.7 Comparison of Li/Na and Li/K electrolytes for MCFC (Yuh and Pigeaud 1989)

Endurance-related properties	Rating	Characteristic value at 650 °C		
		Li/Na	Li/K	Unit
NiO cathode loss	$\Uparrow$	1.3	4	$\mu g\,h^{-1}\,cm^{-2}$
Corrosion (310 S)	$\Longleftrightarrow$	29	50	$\mu m\,yr^{-1/2}$
$LiAlO_2$ stability	$\Longleftrightarrow$	99+	99+	%
Electrolyte creepage	$\Uparrow$			
Vaporization loss	$\Uparrow$	0.12	n.d.	$\mu g\,h^{-1}\,cm^{-2}$
Performance-related properties				
Conductivity	$\Uparrow$	2.4	1.65	$1\,(\Omega\,cm)^{-1}$
Porous cathode impedance	$\Uparrow$	−0.23	n.d.	$\Omega\,cm^2$
Surface tension/contact angle	$\Downarrow$	77	n.d.	Degrees on Ni in fuel gas
Melting point	$\Longleftrightarrow$	505	488	°C
O_2 solubility	$\Downarrow$	1.6	4.2	$10^{-7}\,mol\,cm^{-3}\,atm^{-1}$

n.d., No data.

porosity and pore size distribution. This affects both the matrix capillarity and its bulk strength with consequent problems for the distribution of electrolyte between matrix and electrodes.

In the past two decades, there was renewed interest in $LiAlO_2$ phase stability because long-term carbonate fuel cell testing (up to 34 000 hours) has indicated particle growth, pore coarsening, and γ-to-α phase transformations accompanied by a change in the density during the MCFC operation (Heiming and Krauss 1996; Hyun et al. 2001; Kim et al. 2004; Li et al. 2001; Söllner 1997; Terada et al. 1998; Tomimatsu et al. 1997).

19.2.8 MCFC Hardware Materials

The stack module and balance-of-plant (BOP) hardware materials undergo temperatures between 200 and 900 °C and can experience various thermal and gas atmosphere transients during operation. The materials are generally less exposed to molten electrolyte and experience less hot corrosion. Nevertheless, excessive oxide spallation may cause undesirable debris formation and fouling. Another important consideration is cost. BOP materials contribute a significant portion of the total power plant material cost. For lower temperature service (<600 °C), lower-cost standard ferritic stainless steels (FSS) may be acceptable. Standard high Cr austenitic stainless steels may be usable for up to 750 °C. Although alumina-forming alloys may be usable at temperatures even beyond 800 °C, their high cost may prohibit usage in significant quantities. Therefore, high-cost materials can only be used sparingly. FCE (Fuel Cell Energy, Inc., Danbury, CT 06813, USA) has accumulated extensive material experience through long-term, multiyear DFC (FCE's direct fuel cell power plant) power plant field operations. FCE has also conducted extensive long-term material tests in simulated environments; oxidation, debris formation, and mechanical properties (yield strength, ductility, and creep) have been measured for numerous heat-resistant alloys. Higher Cr (>22 wt% Cr) stainless steels demonstrated no corrosion issue, as shown by the gas manifold in field use for more than five years. The medium Cr (∼18 wt% Cr) stainless steels, although having a faster corrosion rate, have shown to be adequate for 20-year service for thick-walled piping/equipment application. However, faster corrosion could occur for thin-walled material such as expandable bellow at certain locations experiencing electrolyte vapor attack.

Al-coated FSS are potential alloys to reduce cost compared with austenitic alloys. For example, medium Cr austenitic stainless steel used for the module vessel lining has shown significant oxide debris spallation, but at a higher cost. FCE has identified a low-cost Al-coated FSS that has demonstrated excellent corrosion and spallation resistance.

Stress corrosion cracking (SCC) that could lead to sudden high gas leakage was also occasionally observed. A sensitized structure is developed during service. The stainless steels inherently become brittle due to high temperature phase transformation as discussed above, and it is well known that temperature, environment, and stress are key factors contributing to SCC (Sedricks 1996). Therefore, thermomechanical stresses could be minimized to avoid such brittle failure. Moisture condensation should also be eliminated to prevent the SCC failure.

19.2.9 MCFC Future Directions

Hot corrosion attack and galvanic corrosion are the major corrosion problems historically afflicting the bipolar plate materials. Although these problems have been solved, at least partially, by appropriate selection of materials and protection techniques, the result is that the capital cost of the current solutions is too high. To reduce material costs it is required to improve cell performance (lower cell decay rates) and possibly operate at higher current densities (∼300 mA cm^{-2} against ∼150 mA cm^{-2}).

The cost of bipolar materials constitutes a relevant part of the total stack cost so that economical Fe-based alloys are desirable. However, Fe-based alloys cheaper than AISI 316L or 310S stainless steels could be used only if sufficiently cost-effective protection techniques can be individuated. Alternatively, the development of highly corrosion-resistant alloys specifically designed for MCFC may result in the final application of uncoated but more expensive materials (for instance, Inconel alloys). In these last years, we have noticed a renewed interest in corrosion studies of metals and model alloys to better understand the effects of alloying elements added to the Fe-based alloys as this appears essential to individuate innovative metallic materials and protective surface treatments (Spiegel et al. 1997).

In this context, it has been carried out a systematic investigation on binary Fe and Ni-based alloys to evaluate the effect of Al and Ti additions on both electrochemical corrosion behavior and scale conductivity of these alloys. It was found that the addition of 4 wt% Al to a Fe–21Cr alloy decreases drastically the corrosion current, whereas analogous addition of Al or Ti to a Fe–20Ni alloy does not show any effect. The addition of a 4 wt% Ti to the ternary Fe–21Cr–4Al increases the electrical conductivity of the corrosion protective layer without minimizing the corrosion resistance. By a similar approach, a 30Cr–45Ni–1Al–0.03Y–Fe alloy has been developed by Ohe et al. (1996). The alloy shows a much better corrosion resistance than AISI 310S in 300 hour salt coating test under both anode and cathode gas conditions, suggesting that this alloy could be applied without nickel cladding and aluminum diffusion coatings. The alloys proposed by these

two works could represent interesting alternative to the use of stainless steels, provided that their cost-effectiveness would be demonstrated.

A different strategy for material cost savings is to investigate innovative coatings for the wet seals. In particular, aluminization methods, which do not require the expensive post-deposition diffusion heat treatment, would be highly desirable. Recently, some investigators have used thermal spraying of Al-containing powders (FeCrAlY, NiAl, Ni_3Al, FeAl) with poor results due to the porous structure of the coatings produced, which are not corrosion protective enough (Yuh et al. 1995). As the corrosion resistance of the Al diffusion coating relies on the *in situ* formation of an intermetallic iron–aluminum structure, the behavior of a bulk intermetallic alloy FeAl has been extensively studied by Frangini et al. (1996) and Frangini (2000). It has been found that the corrosion resistance of the FeAl aluminide is comparable with that of IVD aluminized 310S steel in both cathode and fuel gas. The use of this alloy for protecting the wet seal deserves further research to individuate a suitable technique to deposit FeAl layers with the desired structure and corrosion properties. Other researchers have focused their attention on suitable ceramic coating materials to protect Fe-based alloys under anode gas showing that TiN, TiC, and Ce-based ceramics are promising anode-side coatings (Keijzer 1997).

It is clearly apparent from this overview that the fundamental mechanisms of hot corrosion and scale fluxing of stainless steels, especially in the anode reducing gas, remain to be better defined. The influence of the different corrosion tests on the final results has been mentioned; much work remains yet to find suitable standardized methods for the purpose of materials screening and long-term performance predictions. In addition, the corrosion effects on the various cell performance decay modes deserve further attention, especially in the long-term stack operation (>30 000 hours).

In summary, it is vital to find advanced solutions for cost reduction of metallic materials and coating technologies that could, in turn, further increase the stack performance and extend useful lifetime. Although MCFC is approaching to a mature technology, the search of innovative materials for the new generation of MCFC plants still offers great opportunities for studies to both scientists and developers.

19.3 Solid Oxide Fuel Cells

19.3.1 Introduction

The *solid oxide fuel cell* (SOFC) technology has attracted significant attention due to the fuel flexibility and environmental advantages of this highly efficient electrochemical device. However, typical SOFC operating temperatures near 1000 °C introduce a series of drawbacks related to electrode sintering and chemical reactivity between cell components. Aiming at solving these problems, researchers around the world have attempted to reduce the SOFC operating temperature to 500–750 °C or lower. It would result in the use of inexpensive interconnect materials, minimization of reactions between cell components, and, as a result, longer operational lifetime. Furthermore, decreasing the operation temperature increases the system reliability and the possibility of using SOFCs for a wide variety of applications such as in residential and automotive devices. On the other hand, reduced operating temperatures contribute to increasing ohmic losses and electrode polarization losses, decreasing the overall electrochemical performance of SOFC components. Thus, to attain acceptable performance, reducing the resistance of the electrolyte component and polarization losses of electrodes are two key points. Losses attributed to the electrolyte can be minimized by decreasing its thickness or by using high-conductivity materials such as doped ceria and apatite-like ceramics. Regarding electrode losses, the higher activation energy and lower reaction kinetics of the cathode compared with those of the anode limit the overall cell performance. Therefore, the development of new functional SOFC materials with improved electrical/electrochemical properties, combined with controlled microstructures, becomes a critical issue for the development of solid oxide fuel cells. These topics as well as the operating principles of an SOFC, the requirements of interconnect materials, namely, the corrosion resistance, and the oxidation resistance, scale properties, and microstructures of chromium containing alloy/cathode interfaces will be discussed along the following subsections.

19.3.2 The Operating Principles of an SOFC

The heart of the high temperature SOFC is an yttria-stabilized zirconia (YSZ) $Zr(Y)O_2$ film, which acts as a solid electrolyte, allowing high conductivity for O^{2-} ions at about 1000 °C. The addition of yttrium stabilizes the cubic fluorite structure of ZrO_2, which otherwise has a monoclinic → tetrahedral → cubic phase transition with increasing temperature. Yttrium doping up to 98 mol% also increases the ionic conductivity by introducing oxygen vacancies.

The perovskite $(La,Sr)(Mg,Ga)O_3$ (LSMG) and related compositions have higher ionic conductivities than YSZ and are potentially more compatible with a wider range of cathode materials (Ishihara et al. 1994). The main drawbacks of LSMG are the high reactivity with the commonly used Ni–YSZ anode and the uncertain cost of Ga sources (Feng et al. 1996; Singhal 2013). Doped

ceria-based oxides such as $Ce_{1-x}Gd_xO_2$ are considered the most promising electrolyte materials for intermediate temperature (<600 °C) SOFC due to their ionic conductivity at low temperatures (Steele 2000). At higher operating temperatures, these materials suffer from high electrical conductivities under reducing conditions (Mogensen et al. 2000). These electrolyte materials, whose main purpose is to transport oxide ions from the cathode to the anode, should possess high ionic conductivity, low electronic conductivity, good chemical stability in the oxygen partial pressure gradient between the anode and the cathode, and good sinterability to enable a fully dense structure to be fabricated. The electrolytes are dry solids. This property eliminates many engineering problems of water management, which tend to complicate the design and operation of other types of fuel cells, considering that the critical temperature of water is 374.15 °C, so it cannot exist in the liquid phase above this temperature. Waste heat is produced at high temperature and can be used for different purposes, making the overall efficiency of electricity and heat production very high. In fact, the waste heat produced in this type of fuel cell can even be used to produce electricity in a conventional heat engine. In this mode of cogeneration, fuel can be converted to electricity at an overall efficiency exceeding 60%.

The SOFC anode material should have catalytic activity toward electrochemical oxidation of the fuel, a high electrical conductivity, and high stability in the reducing environment. In addition, if the electrode is to be used in a fuel cell running of hydrocarbon fuels, the anode should display catalytic activity toward the water shift and reforming reactions and a tolerance to sulfur as well. Nickel is a relatively cheap metal that has a very high catalytic activity toward the oxidation of H_2 (Setoguchi et al. 1992). However, nickel cannot be used on its own due to a high coefficient of thermal expansion (CTE) and problems with Ni grain growth, leading to microstructural coarsening (Singhal 2013). The solution has been to make a porous ceramic-metal composite (cermet) of Ni and YSZ. The role of the YSZ, in addition to lowering the CTE and hindering Ni coarsening, is to extend the TPB area at which the anode reaction can take place, as illustrated in Figure 19.4, for the boundary where the fuel gas, Ni, and YSZ phases meet (Mogensen and Skaarup 2000).

Carbon deposition covers the active sites of the anodes, resulting in the loss of cell performance. In high carbon activity environments, iron, nickel, cobalt, and alloys based on these metals could corrode by a process known as metal dusting (see Section 9.4). Metal dusting involves the disintegration of bulk metals and alloys into metal particles at high temperatures (300–850 °C) in environments that are supersaturated with carbon. The Ni corrosion process strongly depends on the temperature and the gas composition, and, in general, the Ni corrosion rate increases with temperature.

The presence of sulfur (primarily in the form H_2S) in the fuel gas can also affect the performance of Ni–YSZ cermet anodes. The electrode polarization resistance ($\Omega\ cm^2$) increases by a factor of 2 by adding only 5 ppm of H_2S at 950 °C in 97% H_2/3% H_2O system. The poisoning effect of sulfur-containing fuel gas on electrode performance depends on the total sulfur content and the temperature (Singh and Minh 2004). Several alternative anode materials have been suggested, for example, Cu–CeO_2 composites (Brett et al. 2005) and $La_xSr_{1-x}TiO_3$ (Marina et al. 2002). Nevertheless, Ni–YSZ remains the most commonly used anode material today.

The cathode material in an SOFC should have high catalytic activity toward oxygen dissociation and reduction and high electrical conductivity and be chemically stable in the oxidizing environment. Most economically viable candidate materials belong to the perovskite family, with lanthanum strontium manganite (LSM) being the most popular choice to date. By doping $LaMnO_3$ with Sr, a CTE closely matching YSZ and an appreciable electrical conductivity can be achieved (Yang 2008). The electrocatalytic activity of LSM is modest but may be significantly improved by infiltration or impregnation with catalytic nanoparticles (Jiang 2006). Because LSM is nearly a pure electronic conductor, it is often mixed with YSZ in order to increase the TPB area at which the oxygen reduction reaction can take place (Ji et al. 2005). Cathode materials with mixed ionic and electronic conductivity would be preferable since the electrochemically active region would then be extended from the cathode–electrolyte interface to the whole cathode surface. A promising material in this respect is (La,Sr)(Co, Fe)O_3 (LSCF). A challenge with LSCF is that it reacts with YSZ to form insulating $SrZrO_3$ (Simmer et al. 2006); however, this can be prevented by using doped ceria as the electrolyte material or as a buffer layer between the cathode and YSZ electrolyte (Choi et al. 2012).

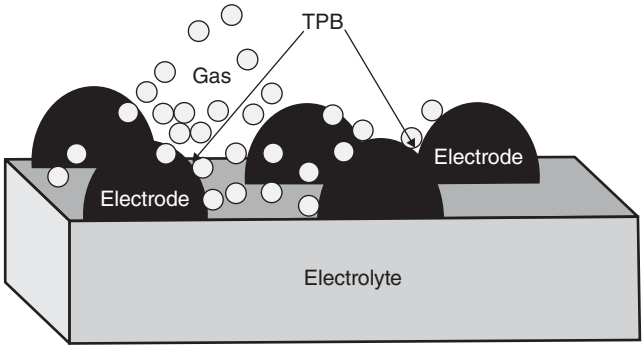


Figure 19.4 Triple-phase boundary (TPB) model.

A major challenge for all the conventional cathode materials is sensitivity toward chromium poisoning (Park et al. 2014). Volatile Cr(VI) species released from the metallic interconnect have been found to deposit both specifically on the electrochemically active TPB sites (Konysheva et al. 2006) and randomly along the cathode–electrolyte interface (Jiang et al. 2005). Although the exact deposition and poisoning mechanisms are under debate, it is clear that the cell voltage degrades faster than usual in the presence of volatile Cr species (Jiang and Chen 2014). There is however a large difference in how sensitive the different cathode materials are toward Cr poisoning, and new cathode materials with reportedly higher Cr tolerance are under development (Park et al. 2014).

The cathode process (the air electrode) in an SOFC normally involves the reduction of molecular oxygen to oxygen anions ($2O^{2-}$) using electrons external to the cell:

$$O_2 + 4e^- \rightarrow 2O^{2-} \tag{19.35}$$

In order to accomplish this reaction, the cathode should be able to dissociate O_2 and be electronically conductive. The oxygen anions formed are transported through the ionically conducting (but electronically insulating) solid electrolyte to the anode where they react electrochemically with the fuel gas (CH_4, H_2, CO, etc.):

$$H_2 + O^{2-} \rightarrow H_2O + 2e^- \tag{19.36}$$

if H_2 is used as fuel, to generate an electrical voltage. The latter reaction can be written following the Kröger–Vink notation as

$$H_2 + O^{2-}_{YSZ} \rightarrow H_2O + 2e^- + O_{\ddot{O},YSZ} \tag{19.37}$$

where O^{2-}_{YSZ} is an oxygen ion in the YSZ electrolyte lattice site and $O_{\ddot{O},YSZ}$ is an oxygen vacancy in YSZ. It should be noted that the majority of H_2 is generated by reforming hydrocarbons. The overall process is

$$2H_2 + O_2 \rightarrow 2H_2O \tag{19.38}$$

Figure 19.5 is a schematic diagram showing how SOFCs work.

The primary advantages of fuel cells are that they provide continuous power (as long as fuel and oxidizer are supplied), have a low weight with a high output power, and have an efficiency of about 70%. These advantages make them very useful for manned missions. The main disadvantages of fuel cells are their expense and the possibility that a loss of cooling can result in an explosion. Consequently, elaborate control systems are required to keep them operating.

In any event, as long as hydrogen and oxygen are continuously fed to the fuel cell, the flow of electric current will be sustained. To meet the requirements of the application, interconnect material is used to connect single cells together in series or parallel to achieve high output voltage, current, and power performance. Thus, it is possible to form a fuel cell stack of any desired voltage or current. The number of fuel cells in the stack determines the total voltage, and the surface area of each cell determines the total current. Multiplying the voltage (V) by the current density ($A\,cm^{-2}$) will yield the total electrical power density ($W\,cm^{-2}$) generated.

The active components of the SOFC (anode, electrolyte, and cathode) can be arranged in a variety of geometric configurations. The two most common designs are the tubular and planar configurations. Tubular cells can be fabricated by extruding the first layer and subsequently depositing the others by, e.g. electrochemical vapor deposition or atmospheric plasma spraying. This design has the advantage of not requiring high temperature seals to isolate the air and fuel, and tubular cells typically display excellent long-term stability (Singhal 2013). However, the power density is limited to about $0.2\,W\,cm^{-2}$, and the manufacturing costs are high. On the other hand, the planar design requires less complicated processing and can achieve higher power densities. In early designs, planar cells were mechanically supported by a relatively thick (150 μm) YSZ electrolyte and needed to operate at high temperatures (>900 °C) to achieve sufficiently high ionic transport through the electrolyte (Singhal 2013). Advances in ceramic processing lead to the development of anode-supported cells and a reduction of the electrolyte thickness to 10–20 μm. This resulted in lower ohmic losses across the electrolyte and consequently allowed

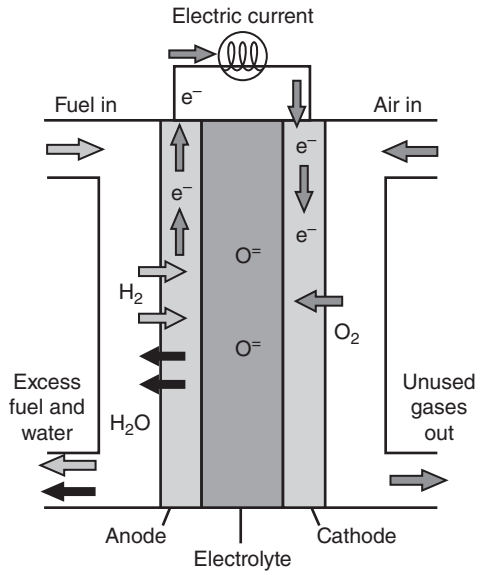


Figure 19.5 Illustration of solid oxide fuel cell components and basic operating principle.

the operating temperature with the LSM/YSZ/Ni–YSZ combination of materials to be reduced to around 800 °C (Zhu and Deevi 2003a,b). The latest development in SOFC design is aiming toward even lower operating temperatures (~600 °C) with metal-supported cells (Tucker 2010). Metal-supported cells are expected to decrease the price and increase the robustness of SOFC considerably; however, so far their performance and stability is far inferior to the anode-supported design.

The interconnect is the means by which electronic connection is achieved between two neighboring fuel cells. It physically separates the fuel cell, in the anode cavity, and at the same type helps to maintain the structural integrity of the SOFC stack. The interconnect material is conventionally made of ceramic materials, such as lanthanum chromite ($LaCrO_3$) doped with either CaO or SrO, or $La_xSr_{(1-x)}CrO_3$ (LSC), a typical high temperature ceramic interconnect material.

The recent development of sintering procedures below 1000 °C, which should allow the use of metal substrates, represents a significant advance that will enable the development of more rugged SOFC systems. The importance of the interconnect materials relies on their electrical conductivity, and more than 70% of the electrical losses in an SOFC system are due to the interconnect design. The high cost of raw materials and manufacturing, difficulties in obtaining high density lanthanum chromite parts, the tendency of chromite to be reduced at the fuel gas/interconnect interface, and the recent trend in developing lower temperature operation (700–850 °C) using new electrolytes with improved conductivity make it feasible for $LaCrO_3$ to be replaced by metals or alloys as the interconnect materials. A very used metal interconnect is an alloy that is largely chromium with 5 wt% iron and 1 wt% yttria to give dispersion strengthening.

This alloy has almost the same CTE as YSZ and has the benefit of improved strength and toughness compared with lanthanum chromite. However, it requires coating to prevent chromium migration and is also an expensive option at the present time.

If it is assumed that the electrolyte component should not contribute more than 0.15 Ω cm^2 to the total cell area-specific resistance (ASR), then for a thick-film thickness (ξ) of 15 μm, the associated specific ionic conductivity (σ) of the electrolyte should exceed 10^{-2} S cm^{-1} ($\sigma = \xi/\text{ASR} = 0.0015\,\text{cm}/0.15\,\Omega\,\text{cm}^2$).

The advantages of metallic interconnects over ceramic interconnects include lower material and manufacturing costs, the possibility of easier and more complex shaping, better electrical and thermal conductivity, and no deformation or failure due to different gas atmospheres across the interconnection. Interconnects can be manufactured by machining, pressing, or, in the case of powder metallurgical alloys, near-net-shape sintering. The gas distribution is usually achieved by parallel channels with the ridges that separate the channels serving as electrical contact with the electrodes.

It is generally accepted that the oxidation of SS and nickel-based alloy materials is one of the most serious disadvantages for their application in SOFCs. At low temperatures, pitting corrosion of SS is the main limitation for industrial applications.

FSS are today by far the most popular choice as the interconnect material, particularly for planar cells (Fergus 2005; Yang 2008).

In 2003, a review of several FSS commercially available at the time was made by Quadakkers et al. (2003), who concluded that the specific combination of properties required of an SOFC interconnect necessitated the development of new, more specialized alloys. After systematic investigations of several steels (Piron-Abellan et al. 2002), Crofer 22 APU was introduced in the market. The composition of Crofer 22 APU and other alloys developed for the application as SOFC interconnect materials are given in Table 19.8.

Some common features of these alloys are (i) high content of Cr to ensure a sufficiently large "Cr reservoir" for long-term stability, (ii) addition of Mn to promote the formation of an outer $MnCr_2O_4$ scale and therefore reduce Cr volatility (Holcomb and Alman 2006), and (iii) addition of rare earth elements (e.g. La or Zr) for improved scale adherence and oxidation resistance (Alman and Jablonski 2007). Some of the alloys also have small additions of Ti that form fine internal TiO_2 precipitates during oxidation, which are believed to aid in strengthening the near-surface region of the alloy (Quadakkers et al. 2003). Two different strategies

Table 19.8 Composition (in wt%) of some ferritic stainless steels developed for the application as SOFC interconnects as specified by manufacturers

Alloy	Fe	Cr	Mn	Si	Al	La	C	Other
Crofer 22 APU	bal.	20–24	0.3–0.8	<0.5	<0.5	0.04	<0.03	<0.2 Ti
ZMG232L	bal.	21–23	1.0	<0.1	<0.5	0.03–0.1	<0.1	0.1–0.4 Zr
Sanergy HT	bal.	22	<0.5	<0.3			<0.05	1.0 Mo; 0.75 Nb
Crofer 22 H	bal.	20–24	0.8	0.1–0.6	<0.1	0.04–0.2	<0.03	0.2–1.0 Nb; 1.0–3.0 W; <0.2 Ti

have been adopted by the manufacturers to prevent the formation of a continuous, electrically insulating SiO_2 layer. Crofer 22 APU and ZMG232 are fabricated by a vacuum induction melting process by which the Si content in the steel can be reduced down to a minimum. The costs of vacuum induction melting are however high. For this reason, Crofer 22 H and Sanergy HT instead rely on additions of Nb and Mo or W to bind up the Si in the alloy by formation of Laves phases. The formation of such Laves phases has the additional benefit of improving the creep and hot tensile strength of the alloy (Froitzheim et al. 2008).

19.3.3 Interconnect-Related Corrosion Issues

Metallic materials used as interconnects for SOFCs face several issues, the three major being degradation due to corrosion, evaporation of chromium, and influence in electrical resistance due to the growing chromia scale. These aspects are considered here.

19.3.3.1 Corrosion/oxidation

The corrosion resistance of FSS relies on the selective oxidation of Cr to form an outer Cr_2O_3 scale. Before reviewing the literature on oxidation of FSS, the oxidation of pure Cr will be briefly considered.

When pure Cr is oxidized in near atmospheric oxygen partial pressure above 700 °C, a Cr_2O_3 scale usually grows in accordance with parabolic oxidation kinetics. However, depending on sample preparation and surface finish, the parabolic rate constant reported in the literature varies by more than 4 orders of magnitude (Lillerud and Kofstad 1980).

The lattice diffusion coefficients of both Cr and O are, however, very small (Sabioni et al. 1992), and it has been increasingly acknowledged that fast diffusion paths such as grain boundaries, pores, and microcracks likely dominate the growth rate of Cr_2O_3 on pure Cr (Sabioni et al. 1992).

The formation of a single-phase chromia scale on FSS requires a chromium content of 16–20%, depending on the exposure conditions, surface treatment, and the presence of other alloying elements and impurities. FSS intended for application as SOFC interconnect materials are in most cases reported to obey parabolic oxidation kinetics with k_p in the range of 10^{-14} to 10^{-13} $g^2\ cm^4\ s^{-1}$ when oxidized in air at 800 °C. The chromia scale is believed to grow mainly by outward diffusion of chromium. Minor alloying elements may have a significant influence on the oxidation rate. Huczkowski et al. (2006) reported that Si and Al in the alloy are internally oxidized and that the volume increase accompanying this internal oxidation leads to metal protrusion into the oxide scale, which increases the oxidation rate. The addition of small quantities of rare earth reactive elements (RE) such as Y, La, and Nd is, on the other hand, reported to have a beneficial effect on the oxidation resistance of Cr_2O_3-forming alloys, both in terms of reducing the growth rate of Cr_2O_3 and improving the scale adhesion (Alman and Jablonski 2007). The exact mechanism behind the so-called RE effect has not been established, although several suggestions have been put forth (Pint 1996).

The oxidation rate of some FSS has been reported to increase with decreasing specimen thickness (Asensio-Jimenez et al. 2013). The effect is mostly pronounced >850 °C but could also be of practical significance at 800 °C during long-term operation. Huczkowski et al. (2004) suggested that the higher oxidation rate of thinner components is due to faster depletion of minor alloying elements and microcracking of the scale occurring during thermal cycling. It was later proposed that although these factors may contribute, the effect is primarily a result of compressive growth stresses leading to plastic deformation of the thin specimens. Accordingly, the oxidation rate of Laves phase that strengthened Crofer 22 H shows a markedly reduced dependence of thickness compared with Crofer 22 APU.

When Cr evaporation contributes significantly to the mass change during oxidation, the oxidation kinetics of FSS can shift from parabolic to paralinear (Sachitanand et al. 2016). At 800 °C the typical Cr evaporation rate reported for FSS is in the range of $2–8 \times 10^{-10}\ kg\ m^{-2}$ (Stanislowski et al. 2007). A correlation has been found between the Cr evaporation rate and Mn content in the alloys: alloys with higher contents of Mn usually have lower evaporation rates due to the formation of an outer $MnCr_2O_4$ spinel layer (Holcomb and Alman 2006). The activation energy for Cr evaporation is lower than the typical activation energy for oxidation of FSS, meaning that the relative importance of Cr evaporation becomes greater at lower operating temperatures (Falk-Windisch et al. 2015).

The thermodynamic driving force for oxidation in the anode atmosphere is generally lower than in air due to the lower oxygen partial pressure. However, the minimum p_{O_2} to oxidize Cr to Cr_2O_3 at 800 °C is only 10^{-20} atm; thus most FSS are observed to form an outer Cr_2O_3 scale also in the anodic atmosphere (Liu 2008). The reports on whether the oxidation rates in anodic atmospheres are lower (Palcut et al. 2010), higher (Linder et al. 2013), or the same (Alnegren et al. 2016) as in air are conflicting. Niewolak et al. (2014) suggested that the disagreement in literature could be related to different Mn contents in the steels. They reported a lower long-term oxidation rate in simulated anode atmosphere than in air when the Mn content was sufficient to form a continuous Cr–Mn spinel layer on the surface. The potentially greatest threat for the stability of metallic interconnects on the anode side is

the observed diffusion of Ni from the anode into the FSS, leading to austenite formation.

In addition to having different mechanical and diffusion properties, the austenite phase has a higher CTE than ferrite, which can be detrimental for long-term mechanical stability during thermal cycling.

Most oxidation characterizations of metallic interconnects are performed either in air or reducing atmospheres, separately investigating the behavior in the cathode and anode environments, respectively. A number of investigations have shown that dual atmospheric conditions, i.e. simultaneous exposure to the two atmospheres on each side of the alloy, can significantly affect the oxidation behavior on the air side (Zhao and Fergus 2012). The oxide scale formed under dual atmosphere conditions is reported to contain more Fe than the scale formed when oxidized in air only, and Fe-rich nodules and hematite are typically observed in the top layers of the scale. The so-called dual atmosphere effect is believed to be caused by hydrogen diffusion through the steel, although there is no agreement about the exact mechanisms for how permeated hydrogen affects air-side oxidation behavior.

There is also some disagreement in literature about the severity of this effect. For the same alloy in which Yang et al. (2003) found a considerable difference in the oxidation behavior in dual atmosphere compared with single atmosphere, Rufner et al. (2008) reported only moderate effects, while Kurokawa et al. (2004) observed no effect at all. Differences in alloy specimen thickness in the three experiments have been suggested as a possible explanation for the discrepancy (Gannon and Amendola 2012). Local formation of Fe-rich oxides on the air side has also been observed on a metallic interconnect after two years' operation in a full SOFC stack at 700 °C; however the observation in this case was attributed to inhomogeneities in the alloy rather than the dual atmospheric conditions.

Besides designing alloys to form protective oxide scales that prevent the metal from breakaway corrosion, so-called RE can be added to the alloy. RE belonging to the rare earth elements such as cerium, lanthanum, yttrium, or zirconium are known to improve the corrosion resistance of alumina- and chromia-forming alloys significantly when added in small quantities. It is proposed that additions of atoms with a high mass and high oxygen affinity are more beneficial for the protection of an alloy (Whittle and Stringer 1980). Up to now there is no clear consensus on the mechanism of the RE effect. Proposed by Whittle and Stringer in 1980, there are different suggestions on why RE enhance corrosion resistance. There have been discussions for decades about the so-called effect of RE. Several mechanisms have been proposed to explain the beneficial effect of RE. The most discussed effects are a change in the oxide growth mechanism, improvement in the chemical bonding between substrate and oxide, or a change of the oxygen vacancy diffusion (the so-called vacancy sink model).

19.3.3.2 Chromium Evaporation

The scale growth of some metals and alloys may be affected by volatilization of the scaling elements. This is particularly important during the oxidation of Cr and Cr-containing alloys. In dry oxygen or air, the dominant volatilization reaction is (Young 2008)

$$\frac{1}{2}Cr_2O_3(s) + \frac{3}{4}O_2(g) = CrO_3(g) \tag{19.39}$$

In the presence of water vapor, the dominant reaction becomes

$$\frac{1}{2}Cr_2O_3(s) + H_2O + \frac{3}{4}O_2(g) = CrO_2(OH)_2(g) \tag{19.40}$$

Very low amounts of water vapor are required in air below 1000 °C before $CrO_2(OH)_2$ (g) becomes by far the most dominant species, and Reaction (19.40) is the most relevant under conditions experienced by the SOFC interconnect.

The scale thickness with time will be determined by a combination of the parabolic rate constant for scale growth, k_p, and the linear rate constant for reactive evaporation of Cr, k_s (Tedmon 1966):

$$\frac{dx}{dt} = \frac{k_p}{2x} - k_s \tag{19.41}$$

During initial stages of exposure, the increase in the scale thickness will be faster than the vaporization process, and close to parabolic oxidation behavior will be observed. However, as the growth rate drops with increasing scale thickness, vaporization will become increasingly important. After a certain period of time, the two processes will become balanced by each other, resulting in a constant oxide scale thickness. This so-called limiting oxide scale thickness, x_l, is given by (Tedmon 1966)

$$x_l = \frac{k_p}{2k_s} \tag{19.42}$$

The rate of Cr volatilization has been found to increase with increasing gas flow rate, oxygen partial pressure, and water vapor content in the gas (Key et al. 2014).

19.3.3.3 Electrical Conduction of Oxide Scales

Given that one of the main purposes of the interconnect material is to provide electrical contact between the anode and cathode of adjacent cells, the electrical conductivity of the interconnect is of great importance. This is usually

characterized in terms of contact or ASR, which can be expressed as (Skilbred and Haugsrud 2012):

$$\mathrm{ASR} = \tau_s l_s + 2\tau_o l_o \tag{19.43}$$

where τ_s and l_s are the resistivity and thickness of the steel substrate, respectively, and τ_o and l_o are the resistivity and thickness of the oxide layer on each side of the substrate, respectively. The generally accepted ASR limit for the interconnect during its service lifetime is 100 mΩ cm^2 (Zhu and Deevi 2003a,b). The electrical resistivity of steel is several orders of magnitude smaller than the resistivity of the oxide scale, such that the first term in Eq. (19.43) may be omitted. Since the ASR of a metallic interconnect will be primarily determined by the thickness and resistivity of the oxide scale, it should ideally show the same time dependence as the growth rate of the oxide scale. In practice, however, this is rarely the case for reasons explained as follows.

The oxide scale formed on most interconnect alloys consists of Cr_2O_3 and possibly $(Mn,Cr)_3O_4$. The electrical conductivity of $(Mn,Cr)_3O_4$ is generally slightly higher than that of Cr_2O_3. The electrical conductivity of Cr_2O_3 can be divided into two temperature regimes:

1. At high temperatures (>1000 °C), pure Cr_2O_3 displays n-type intrinsic conductivity, independent of the oxygen partial pressure (Holt and Kofstad 1994a).
2. At lower temperatures (<1000 °C), pure Cr_2O_3 is a p-type extrinsic conductor showing some dependence on the oxygen partial pressure. The electrical conductivity at 800 °C is typically reported to be in the range of $1–8 \times 10^{-2}$ S cm^{-1} (Holt and Kofstad 1994b); however the value can vary even more with the presence of unintentional impurities or intentional dopants. For example, doping Cr_2O_3 with Y_2O_3 or La_2O_3 has been found to increase the electrical conductivity. One reason for the complex ASR behavior is thus a change in the impurity level and defect chemistry of the thermally grown chromia scale. Another factor, as pointed out by Linder et al. (2014), is that the typical morphology of a thermally grown chromia scale favors a nonhomogeneous current distribution, in which large parts of the current flow across thinner regions of the scale. There have also been some reports that the current applied during ASR measurements influences the growth rate of the chromia scale (Kodjamanova et al. 2013).

An illustration of the general four-point experimental setup for measuring ASR is shown in Figure 19.6. The contact material can be either a noble metal such as gold, silver, or platinum or a ceramic oxide like LSM ($La_{1-x}Sr_xMnO_3$) or LSC ($La_{1-x}Sr_xCoO_3$). The measured ASR will depend on the choice of contact material, with noble metals typically resulting in lower values and different development over time than the ceramic oxides (Wu et al. 2013). The oxides used for contacting are similar to the cathode materials used in SOFC and should therefore give a better estimation of the contact resistance in a real fuel cell stack. The disadvantage with these materials is however their tendency to sinter and react with the oxide scale on the interconnect. This results in an initially decreasing ASR that may mask the resistance increase due to growth of the chromia scale (Megel et al. 2011). On the other hand, noble metals should, in theory, not react with the alloy or oxide scale and therefore provide a theoretical estimation of solely the interconnect's contribution to ASR. In practice, it has been shown that prolonged contact with Pt can lead to accelerated oxidation. In summary, noble metals could be a suitable choice for short-term measurements and for comparison of different alloys and coatings, while ceramic oxides can provide valuable information on how the contact resistance will develop in an actual SOFC stack during long-term operation. Due to the different ASR values obtained with different contacting materials, it is challenging to compare the ASR reported by different sources directly against each other.

19.3.4 Protective Coatings for Metallic Interconnects

The challenges of high Cr evaporation and oxidation rates make it unrealistic to use bare FSS as the interconnect material in SOFC, despite the advancements made in developing new alloys specifically targeted toward this application (Stanislowski et al. 2007). For example, stack tests at the Research Center Juelich with one of the most promising new alloys, Crofer 22 APU, as the interconnect showed voltage degradation of 21%/1000 hours, which was mainly attributed to Cr poisoning of the LSM cathode.

Today, it is generally acknowledged that the metallic interconnect will need to be coated in order to survive the expected service lifetime of 40 000 hours.

The requirements for a suitable interconnect coating material are much the same as for the interconnect itself

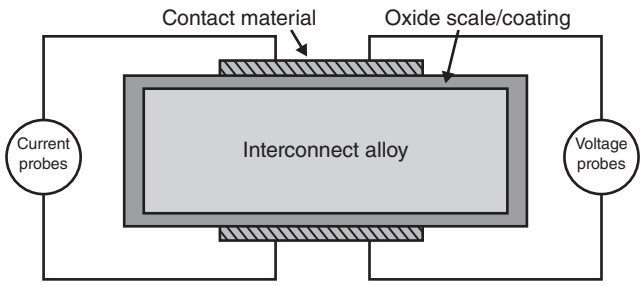


Figure 19.6 Illustration of the general four-point setup for measuring area-specific resistance of interconnect materials.

in terms of thermal expansion, electrical conductivity, cost, and ease of manufacturing. In addition, since the purpose of the coating is to improve oxidation resistance and reduce Cr evaporation from the FSS, the coating material should possess low chromium and oxide ion diffusion coefficients. The majority of suggested coating materials can be divided into three categories and will be briefly reviewed as follows.

As already mentioned, the addition of RE such as La, Ce, and Y to FSS may improve scale adhesion and oxidation resistance. RE are usually added as an alloying element to the steel; however, they have also been explored as surface coatings with several reports of reduced oxidation rates and ASR (Alman and Jablonski 2007). Nevertheless, the long-term benefits appear to be limited: Fontana et al. (2012) measured the ASR of La_2O_3 and Y_2O_3 coated Crofer 22 APU and found that after 23 000 hours of oxidation at 800 °C, both coatings had exceeded the 100 mΩ cm^2 maximum set as a limit for the interconnect. An even greater shortcoming of RE coatings is that they have negligible effect on the Cr evaporation rate (Sattari et al. 2015).

Lanthanum-based perovskite oxides are used as cathodes in SOFC and were early on identified as possible protective coatings for metallic interconnects. The most widely investigated compositions are accordingly similar to common cathode materials, for example, $La_{1-x}Sr_xMnO_3$ (LSM) (Kurokawa et al. 2007), $La_{1-x}Sr_xCoO_3$ (LSC), and $La_{1-x}Sr_xFeO_3$ (LSF) (Yang et al. 2006). These perovskites offer the benefits of having high electrical conductivities, suitable CTEs, and good compatibility with other SOFC components. Several studies have demonstrated that perovskite coatings can reduce the Cr evaporation rate of stainless steel by several orders of magnitude (Kurokawa et al. 2007) and decrease the FSS oxidation rate. There are, however, also examples of studies reporting none or only modest benefits on Cr retention (Schlupp et al. 2014) and corrosion resistance (Yang et al. 2006). The discrepancies can be explained by differences in powder properties and deposition methods in the mentioned references, leading to differences in coating density. Difficulty with processing the perovskite coatings, particularly with obtaining dense structures at sufficiently low temperatures, is considered one of their major drawbacks.

$(Mn,Co)_3O_4$ spinel oxide was first proposed as a possible coating material by Larring and Norby (2000). Most of the work has been done on $MnCo_2O_4$, and $Mn_{1.5}Co_{1.5}O_4$, although Cu–Mn, Cu–Fe, and pure Co spinels have also received some attention.

Note that several of these coating materials are deposited as a metallic layer, e.g. as a Co metal. During exposure to air at elevated temperatures, these metals are quickly oxidized to spinel-type oxides. The listed coatings may thus be regarded as a form of spinel oxide coatings.

Contrary to perovskites, spinel coatings may be sintered to sufficient density at temperatures that do not damage the alloy substrate significantly; thus they may be deposited by relatively cheap powder-based methods such as spray coating (Chen et al. 2010), screen printing, and electrophoretic deposition (EPD) (Mirzaei et al. 2016). Densification of the coatings is usually carried out by a two-step procedure involving heat treatment first in reducing atmospheres and then in oxidizing atmospheres. During the first step, $MnCo_2O_4$ is reduced according to

$$MnCo_2O_4 \rightarrow MnO + 2Co + \frac{3}{2}O_2 \qquad (19.44)$$

When the coating is subsequently heat-treated in air, the spinel phase is reformed, and densification is believed to be promoted by a reaction-sintering-type mechanism (Gambino et al. 2015).

$(Mn,Co)_3O_4$ coatings have been demonstrated to be very effective in limiting Cr evaporation from FSS (Trebbels et al. 2009). Several studies have shown that $(Mn,Co)_3O_4$ coatings also have a positive effect on the oxidation resistance and ASR (Stevenson et al. 2013).

However, there has been some concern about the long-term stability of these coatings. The lifetime of $Mn_{1.5}Co_{1.5}O_4$ coated Crofer 22 APU was investigated by Liu et al. (2009) and Akanda et al. (2014) based on mechanical modeling and experimental measurements of the interfacial shear stress versus strength and the interfacial fracture energy, respectively. The lifetime was estimated based on the time before spallation with 4.2 μm determined to be critical Cr_2O_3 scale thickness in both studies. Liu et al. (2009) predicted a lifetime of 15 500 hours at 800 °C, while Akanda et al. (2014) predicted a lifetime of 34 700 hours at 750 °C.

The most commonly suggested alloys for an SOFC interconnect application are designed to form a chromium manganese spinel as the outer oxide layer. The conductivity of this chromium manganese spinel is generally higher than that of pure chromia. The electrical conductivity of chromium manganese spinel increases with higher manganese content, while the activation energy decreases with increasing manganese content (Lu et al. 2005). Thus, additional coatings for decreasing the evaporation of chromium are inevitable. The most promising coatings for lowering chromium evaporation are cobalt spinel coatings, but others such as copper spinels have also been considered. Since all barrier coatings are oxidized before, or in the very first moments of exposure, it is necessary that they are good conductors. Petric and Ling (2007) have done extensive study on the conductivity of different spinels. Table 19.9 lists conductivities and the CTE at 800 °C (except where noted) of different transition metal spinels. They concluded in their study that spinels formed of cobalt manganese, copper manganese, and copper iron are, from the conductivity and thermal expansion point of view, most promising for an interconnect coating.

Table 19.9 Specific conductivities σ (given in $S\,cm^{-1}$) and thermal expansion coefficients α (given in $ppm\,K^{-1}$) of different spinels at 800 °C, except where noted (Petric and Ling 2007)

	Mg	Mn	Co	Ni	Cu	Zn
Al	$MgAl_2O_4$ $\sigma = 10^{-6}$ $\alpha = 9.0$	$MnAl_2O_4$ $\sigma = 10^{-3}$ $\alpha = 7.9$	$CoAl_2O_4$ $\sigma = 10^{-5}$ $\alpha = 8.7$	$NiAl_2O_4$ $\sigma = 10^{-4}$ $\alpha = 8.1$	$CuAl_2O_4$ $\sigma = 0.05$ $\alpha = -$	$ZnAl_2O_4$ $\sigma = 10^{-6}$ $\alpha = 8.7$
Cr	$MgCr_2O_4$ $\sigma = 0.02$ $\alpha = 7.2$	$Mn_{1.2}Cr_{1.8}O_4$ $\sigma = 0.02$ $\alpha = 6.8$	$CoCr_2O_4$ $\sigma = 7.4$ $\alpha = 7.5$	$NiCr_2O_4$ $\sigma = 0.73$ $\alpha = 7.3$	$CuCr_2O_4$ $\sigma = 0.40$ $\alpha = -$	$ZnCr_2O_4$ $\sigma = 0.01$ $\alpha = 7.1$
Mn	$MgMn_2O_4$ $\sigma = 0.97$ $\alpha = 8.7$	Mn_3O_4 $\sigma = 0.10$ $\alpha = 8.8$	$CoMn_2O_4$ $\sigma = 6.4$ $\alpha = 7.0$	$NiMn_2O_4$ $\sigma = 1.4$ $\alpha = 8.5$	$Cu_{1.3}Mn_{1.7}O_4$ $\sigma = 225$ (750 °C) $\alpha = 12.2$	$ZnMn_2O_4$
Fe	$MgFe_2O_4$ $\sigma = 0.08$ $\alpha = 12.3$	$MnFe_2O_4$ $\sigma = 8.0$ $\alpha = 12.5$	$CoFe_2O_4$ $\sigma = 0.93$ $\alpha = 12.1$	$NiFe_2O_4$ $\sigma = 0.26$ $\alpha = 10.8$	$CuFe_2O_4$ $\sigma = 9.1$ $\alpha = 11.2$	$ZnFe_2O_4$ $\sigma = 0.07$ $\alpha = 7.0$
Co		$MnCo_2O_4$ $\sigma = 60$ $\alpha = 9.7$	Co_3O_4 $\sigma = 6.7$ $\alpha = 9.3$			

19.4 Direct Carbon Fuel Cells

19.4.1 Basic Overview

Most fuel cells invariably use gaseous or liquid fuels. A fuel cell technology that has attracted attention only recently, the DCFC uses solid fuel (carbon) and converts the chemical energy in the carbon to electricity through its direct participation in the fuel cell reactions and electrochemical oxidation. The fuel use can be almost 100% compared with about 85% for most other fuel cells. The electrical efficiency is expected to be above 70% – almost twice those of current generation coal-fired plants leading to 50% reduction in greenhouse gas emissions. The amount of CO_2 for storage/sequestration is also halved. Moreover, the exit gas is almost pure carbon dioxide stream, requiring no or minimal gas separation and processing for sequestration. Therefore, the energy and cost penalties to capture the CO_2 will be significantly less than for other technologies. However, the technology is at an early stage of development requiring many complex challenges to be overcome, related to materials and corrosion, fuel delivery mechanism, and system development, before it can be commercialized. This section gives an overview of this technology focusing on its main corrosion issues (Jiang et al. 2017).

DCFCs convert the chemical energy into electricity without the need for gasification. It is the direct oxidation of fine (submicron) carbon particles in an electrochemical cell at high temperatures (600–900 °C) with the overall fuel cell reaction being

$$O_2\,(air) + 4e^- = 2O^{2-} \tag{19.45}$$

$$C + 2O^{2-} = CO_2 + 4e^- \tag{19.46}$$

It is important to note that reactions at fuel cell electrodes can only occur at interfaces or lines of contact where the reactant, electronic conductor, and ionically conductive phase all meet. These interfaces are known as *triple-phase boundaries* (Vohs and Gorte 2009).

The reactions in DCFC produce almost pure carbon dioxide, provided that high purity carbon is used as the fuel, which can be contained in a concentrated stream and easily captured for downstream use or disposal, avoiding the need for costly gas separation technologies.

Figure 19.7 shows the thermodynamic efficiency as a function of temperature for different fuel types. With increasing temperature the free energy available for many fuel oxidation reactions decreases due to the entropy term. For example, for hydrogen and carbon monoxide, it is 83% and 91% at 25 °C and 69% and 61%, respectively, at 980 °C. However, for carbon oxidation reaction, the

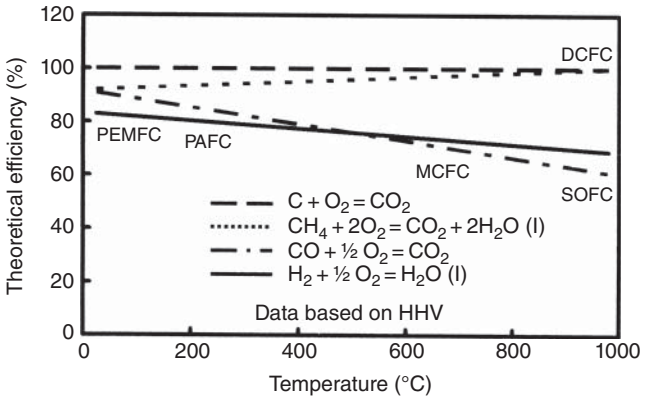


Figure 19.7 The maximum or theoretical efficiency for different fuels as a function of the operating temperature of the fuel cell.

Table 19.10 Different types of direct carbon fuel cells

Fuel/anode	Electrolyte	Cathode	T (°C)
Solid graphite rod as fuel and anode $C + 4OH^- = 2H_2O + CO_2 + 4e^-$	Molten hydroxides $OH^- \leftarrow$	Air as oxidant $O_2 + 2H_2O + 4e^- = 4OH^-$	~600
Carbon particles as fuel in molten carbonate and anode $C + 2CO_3^{2-} = 3CO_2 + 4e^-$	Molten carbonates $CO_3^{2-} \leftarrow$	Air as oxidant $O_2 + 2CO_2 + 4e^- = 2CO_3^{2-}$	~800
Carbon particles in a fluidized bed $C + 2O^{2-} = CO_2 + 4e^-$	Oxygen ion conducting ceramic electrolyte $O^{2-} \leftarrow$	Air as oxidant $O_2 + 4e^- = 2O^{2-}$	800–950
Fuel in contact with molten tin $Sn + 2O^{2-} = SnO_2 + 4e^-$			
Carbon particles as fuel in molten carbonate and anode $C + 2O^{2-} = CO_2 + 4e^-$			

entropy term (ΔS) is near zero, and the thermodynamic efficiency is independent of temperature and remains close to 100%.

In the case of DCFC, the fuel and products are distinct separate phases (solid and gas), making their separation and recycling of unspent fuel easier. Thus, the fuel use can be almost 100%. For most other types of fuel cells for which the fuel cell reaction products are gases mixed with incombustible fuel, the fuel use is typically 80–85%.

Allowing for 20–25% voltage efficiency losses, the stack efficiency for DCFC is predicted to be about 75–80% with system electrical efficiencies in the 65–70% range taking into consideration system-related losses. With heat recovery, the overall system efficiency is expected to be well above 80–85%. However, the fuel processing requirements for DCFC are somewhat unclear at this stage, and there will be some losses associated with coal purification and processing that may reduce the overall efficiency. The system electrical efficiency alone is almost twice those of current generation coal-fired plants and significantly higher than other fuel cell types. Thus, compared with conventional coal-fired power plants, there is a potential for about 50% reduction in greenhouse gas emissions and significantly less quantity of CO_2 that would need to be sequestered.

A variety of fuels including coal (both brown and black), coke, tar, biomass, and organic waste can be used as the raw fuel. To avoid downstream processing of exit effluent and to avoid degradation of fuel cell components, some processing of fuel is required to remove impurities and to turn the fuel into submicron-size carbon particles for easy combustion at the electrode–electrolyte interface. The quality of carbon and its structure appear to influence the electrode kinetics for its direct oxidation and thus have an effect on the fuel cell performance and power densities.

The basic DCFC technologies under development are summarized in Table 19.10.

These types of DCFCs with their issues, particularly corrosion degradation, are described below.

19.4.2 DCFC with Molten Carbonate as Electrolyte

The majority of the DCFC technologies being developed at present are based on MCFC or SOFC. In a direct carbon MCFC, the carbon oxidation reaction at the anode side proceeds by reaction of the solid fuel with carbonate anions.

Carbonates are good oxidizing agents but electronic insulators so that the performance of these cells is usually limited by electron transfer to the external circuit:

$$C + 2CO_3^{2-} \rightarrow 3CO_2 + 4e^- \qquad (19.47)$$

In the case of direct carbon SOFCs, the overall anode reaction is that of the carbon being oxidized by oxygen anions from the solid oxide electrolyte. However, direct contact between the solid fuel and the solid electrolyte is inefficient.

Various anode designs have been employed in order to make contact between the fuel and the oxygen ions from the solid electrolyte. Typically, this occurs through intermediate steps, making the anode reaction mechanisms more involved, as will be discussed below:

$$C + 2O^{2-} \rightarrow CO_2 + 4e^- \qquad (19.48)$$

The Nernst potential of carbon oxidation corresponding to the global cell reaction

$$C + O_2 = CO_2 \qquad (19.49)$$

is ∼1 V. An ideal DCFC would be able to operate at this voltage no matter how much current is being drawn and operate at 100% voltage efficiency. In practical use, all fuel cells have kinetic and resistive losses and have to operate at a voltage at which is a trade-off between fuel cell efficiency and cost. For example, if the voltage efficiency were to be increased by decreasing the current density, the active area would need to be increased by decreasing the current density and the active area would need to be increased to obtain the necessary power that, in turn, would increase capital costs.

With fuel cell electrolytes and their respective air-contacting cathodes being well studied and considered as standard, the main challenge in making a practical DCFC involves the design of an anode system that efficiently contacts the carbon fuel with the oxidizing species from the electrolyte. This will help minimize cell performance losses and make the high level of efficiencies, theoretically achievable by DCFCs, possible.

There are various approaches being developed for this purpose, namely, the direct carbon MCFC. This type of DCFC is based on a conventional MCFC with the CO_3^{2-} ions migrating from the cathode toward the anode. At MCFC operating temperatures, carbon can be oxidized to CO_2 via the cathode and anode reactions shown above (Eqs. (19.8), (19.47), and (19.48)).

Since molten carbonates are good oxidizers but poor electronic conductors, the main factor limiting the performance in direct carbon MCFCs is the slow anode kinetics associated with the limited TPB caused by the lack of contact of the fuel with an electronic conductor. The corrosion issues described in Sections 19.2 and 19.3 for MCFCs and SOFCs are also observed in the DCFCs, apart from further problems posed by the TPB issues.

The operating schematic of a typical direct carbon MCFC is shown in Figure 19.8 and is similar to that used by Cherepy et al. (2005). In this system, the anode consists of a porous Ni scaffold containing the molten carbonate mixture. The fuel consists of a conductive form of carbon present at a high enough concentration in a slurry with the molten carbonate as the carrier. This configuration helps the electrochemical reaction to occur out of direct electrical contact with the metallic current collector, since the conductivity of the carbon also facilitates current collection.

Since the carbon fuel is directly oxidized by the carbonate anions, the open-circuit potential for these DCFCs is ∼1 V, the same as that of the carbon oxidation reaction (Eq. (19.48)). The best possible performance levels in these DCFCs have been observed only when conductive carbons are used as fuels. However, not all forms of carbon are conductive, and one of the main drawbacks of DCFCs based on MCFCs is their reduced fuel flexibility.

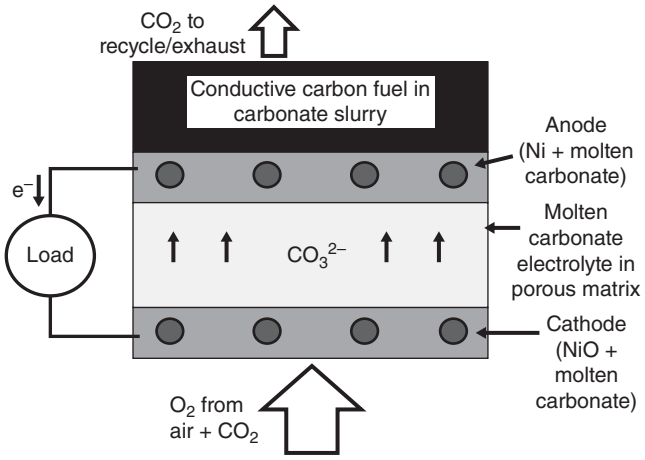


Figure 19.8 Operating schematic of a direct carbon MCFC.

Moreover, it has been found that the reactivity of the carbon used, i.e. low crystallinity, presence of surface reactive sites, small particle size, and high surface area, is also related to the performance of these DCFCs (Cherepy et al. 2005; Cooper 2004). Conductive carbons are not the most reactive forms of carbon, and their poor reactivity will always contribute to the anode polarization losses. Therefore, the ideal fuel required by these DCFCs is a form of carbon fuel with sufficient electronic conductivity and chemical reactivity to minimize performance losses due to the anode reaction (Cherepy et al. 2005).

Apart from the issues associated with sluggish anode kinetics and high costs associated with producing carbon in a suitable form, DCFCs based on molten carbonates (usually of lithium, potassium, and sodium at 750–800 °C) also have problems due to ash buildup in the electrolyte and poor durability due to the highly corrosive nature of the molten carbonate mixture causing damage to other cell components (Selman 2006).

Other major technical issues related to this type of fuel cell are high cathode polarization losses, corrosion of metal clad bipolar plates, and upscaling. Furthermore, the fuel-related issues include lack of a suitable fuel delivery system for a long-term and continuous operation, poor understanding of relationship between carbon structure and its chemical and electrochemical activity, and electrolyte tolerance to high percentages of contaminants such as sulfur, ash, etc. Therefore, these DCFCs require a lot more development in order to be made practical.

19.4.3 DCFC with Oxygen Ion Conductor as Electrolyte

Using conventional SOFC cathode and electrolyte materials, there are currently three major types of anode technologies being developed to enable the use of solid carbonaceous fuels in SOFCs.

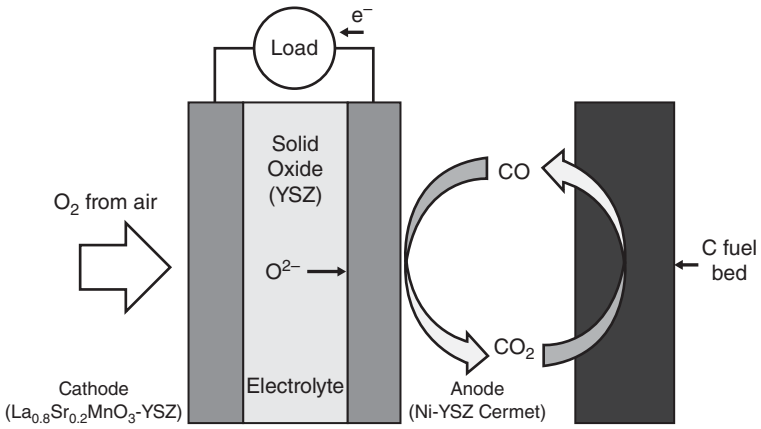


Figure 19.9 Operating schematic of a gasification-driven direct carbon SOFC.

19.4.3.1 Gasification-Driven Direct Carbon SOFCs

These DCFCs are similar to the conventional gas-fueled SOFCs. The cell components used in gasification-driven direct carbon SOFCs are the same as in conventional SOFCs, and the composite anode consists of the porous ceramic scaffold containing an electronically conductive and catalytic material as shown in Figure 19.9. The conventional Ni–YSZ cermet is the common anode used in gasification-driven direct carbon SOFCs.

In these fuel cells being developed by Gur and Huggins (1992), oxygen anions from the electrolyte react with CO in the porous anode to form CO_2 and release electrons. A fraction of the CO_2 is then recycled and passed through a bed of carbon particles to form CO by the reverse Boudouard reaction. The CO produced from the Boudouard gasifier is then cycled to the anode for oxidation:

$$CO + O^{2-} \rightarrow CO_2 + 2e^- \tag{19.50}$$

$$CO_2 + C \rightarrow 2CO \tag{19.51}$$

The main issue with this $CO_2 \leftrightarrow CO$ shuttling mechanism is that the reverse Boudouard reaction is an endothermic reaction and is kinetically very slow. This reaction needs very high temperatures to occur, and a considerable amount of heat is required to maintain the temperature of the gasifier (Gur et al. 2010). Therefore, low fuel consumption along with high heat demands drastically brings down the efficiencies of these fuel cells.

Mostly, the developmental work on this technology has so far been concentrated on button cells of ceramic electrolyte disk with nickel-based anode and lanthanum strontium manganate (LSM)-based cathode (Hasegawa and Ihara 2008; Lee et al. 2008). The major technical issues apart from those associated with SOFC are the solid fuel delivery to anode–electrolyte interface and lack of understanding of carbon oxidation reaction mechanisms at the interface.

19.4.3.2 Direct Carbon SOFCs with Molten Carbonate Anodes

This technology is "hybrid" of the key elements of both direct carbon MCFC and direct carbon SOFC designs. Essentially, both electrolytes from the MCFC and SOFC are used within one cell with the fuel dispersed within the molten carbonate electrolyte. The physical cell resembles a typical SOFC cell with the molten carbonate residing in the anode chamber as shown in Figure 19.10 (Jiang 2008).

This technology uses circulating molten carbonates containing carbon fuel as the anode and oxygen ion-conducting ceramic as the electrolyte (Balachov et al. 2005). In one configuration, the cell employs a cathode-supported tubular cell geometry. Air is supplied via a concentric tube to the cathode consisting of a metal current collector and LSM as the catalyst layer. The circulating molten carbonates mixed with carbon fuel particles are supplied to the anode, which also has a metal

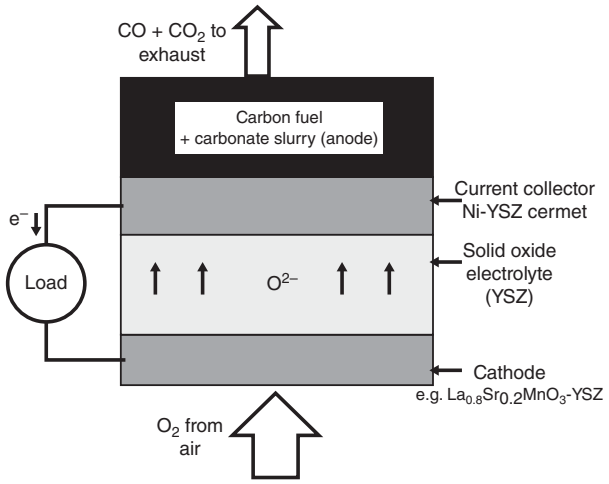


Figure 19.10 Operating schematic of a direct carbon SOFC with a molten carbonate anode.

mesh/coil current collector. Various types of fuel such as biomass, coal, tar, etc. have been tested on these cells.

These DCFCs are also called *hybrid direct carbon fuel cells* (HDCFCs) and were conceived at SRI International (Heydorn and Crouch-Baker 2006). This "hybrid" concept helps alleviate some issues associated with the stand-alone versions of the direct carbon MCFC and SOFC. In the hybrid fuel cell, the cathode is separated from the molten carbonate by the SOFC electrolyte, thus reducing the possibility of cathode corrosion as observed in direct carbon MCFCs (Jiang and Irvine 2011; Nabae et al. 2008). It also negates the need to recycle CO_2 because the SOFC cathode can operate directly on air. However, the primary motivation for incorporating the molten carbonate in the SOFC anode chamber is for it to serve as an ionically conductive anode for the SOFC electrolyte. This will allow the oxygen to directly contact the carbon fuel and facilitate the oxidation. In HDCFCs, oxygen anions from the SOFC electrolyte contact the carbon particles via the molten carbonate anode to produce a mixture of CO and CO_2 in a manner similar to a direct carbon MCFC (Jiang and Irvine 2011).

Nevertheless, molten carbonates lack electronic conductivity, and the performance of these cells still remains limited due to a lack of TPB as in the case of the direct carbon MCFC. Performances can be somewhat improved by introducing an electronically conductive, high surface area metallic mesh for current collection with a reactive form of carbon fuel (Nabae et al. 2009) or by using a conductive form of carbon fuel in the molten carbonate anode (Lipilin et al. 2006). Optimal performance can only be achieved if the conductive fuel is always present in the anode at a high enough concentration and if it has a morphology that allows an intimate physical contact with the current collector. Therefore, the incorporation of an electronic conductor will always be a performance-limiting factor for these fuel cells, requiring an optimal preparation of the fuel–carbonate mixture (Jain et al. 2009) and adversely affecting their fuel flexibility. Also, etching of the electrolyte (Jiang et al. 2012) and corrosion of the current collectors on the anode side can be a problem for the cell durability. Further issues of these cells are the corrosion of the nickel anode and other cell components and the stability of the YSZ electrolyte in molten carbonate environments – for example, formation of lithium zirconate in the presence of Li/K carbonate eutectic mixture at 700 °C (Pointon et al. 2006).

19.4.3.3 Direct Carbon SOFCs with Molten Metal Anodes

The use of a molten metal as an anode for SOFCs was pioneered by Tao et al. at CellTech Power (2007a,b). A very clear advantage of this technology is that the entire anode will be electronically conductive. Moreover, metals are known to react with oxygen to form oxides and have certain amounts of oxygen solubility; therefore, metals could serve as oxygen transport media as well. The appropriate choice of metal could be very promising in that the entire anode would be active for fuel oxidation, given the high electronic conductivity of all metals and the possibility for good oxygen transport in some of them.

In choosing a molten metal for operation at 1273 K, Tao et al. considered the following metals based on their melting temperatures: Al, Ga, Ge, In, Sn, Sb, Ti, Pb, Bi, Po, Ag, Hg, and Cd. This group then considered the possibility that the metals could be reduced under typical anode conditions by examining the free energy, ΔG, of reduction for the respective metal oxides. For example, Al and Ga were eliminated from consideration because they form very stable oxides that cannot be reduced by carbon. Ge and In were less desirable because their open-circuit voltage (OCV) was too close to that of carbon, making them poor fuel oxidation catalysts. Cd, Sb, Pb, Po, Ti, Bi, and Hg were ruled out because their volatility was too high at 1273 K. This left Sn and Ag as the two remaining anode choices. Based on the work carried out by CellTech Power, as discussed afterward, it is still unclear why Ag has a positive ΔG for oxidation at 1273 K and will not form an oxide. The reason for choosing Sn is probably its higher OCV. This will allow oxygen transport to occur in the form of tin dioxide (SnO_2) at a higher potential when the metal is saturated with dissolved oxygen at high currents (Tao et al. 2009).

Most of the work carried out by CellTech Power using their molten Sn anode SOFC concept has been focused only on operation with H_2 and JP-8 (jet fuel) as the fuels at 1273 K (McPhee et al. 2011; Tao et al. 2007a,b). In these experiments, a thin layer (300–500 μm) of molten Sn was held in contact with an SOFC electrolyte using a porous ceramic separator as shown in Figure 19.11. Surface

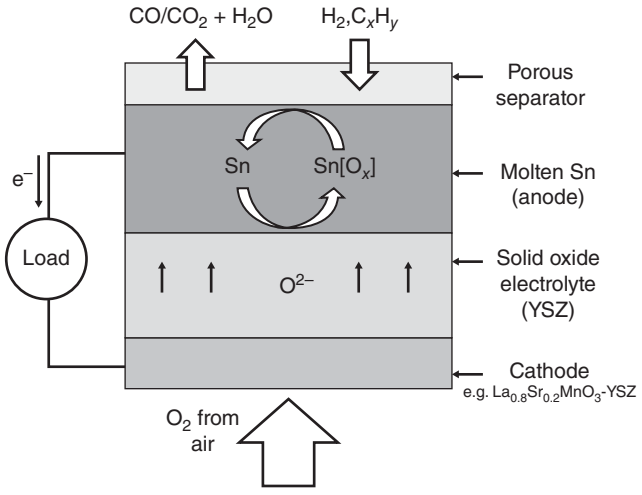


Figure 19.11 Operating schematic of CellTech Power's molten Sn anode SOFC.

tension prevents molten Sn from entering the porous ceramic, so that gaseous fuel (H_2 or gaseous pyrolysis products of JP-8) and gaseous oxidation products (H_2O and CO) can make contact with the Sn surface. The OCV of the cell based on the Sn oxidation and oxygen (from air) as the oxidant at the cathode would be 0.78 V, which is lower than the oxidation potentials for H_2 and other hydrocarbons at 1273 K (Tao et al. 2007a). Therefore, the SnO_2 formed can be readily reduced by H_2 and other carbonaceous fuels:

$$Sn + 2O^{2-} \rightarrow SnO_2 + 4e^- \tag{19.52}$$

$$SnO_2 + 2H_2 \rightarrow Sn\,(l) + 2H_2O \tag{19.53}$$

Reaction (19.53) is exothermic. Such a cell with molten tin as the anode in contact with carbon fuel produces electricity by direct oxidation of carbon at about 1000 °C. The operation of this system was suggested to rely on the diffusivity of the dissolved oxygen from the electrolyte in molten tin and the diffusivity of the gaseous fuel into the molten tin for the fuel oxidation to occur (Abernathy et al. 2011; Tao et al. 2007a):

$$Sn + xO^{2-} \rightarrow Sn[O^{2-}]_x \tag{19.54}$$

$$Sn[O^{2-}]_x + xH_2 \rightarrow Sn\,(l) + xH_2O + 2xe^- \tag{19.55}$$

In these fuel cells, H_2 fuel from the feed stream diffuses through the porous separator into the molten tin where it is oxidized by the dissolved oxygen (Eq. (19.55)). The liquid JP-8 fuel was directly injected into the hot zone of the anode chamber and underwent pyrolysis. The pyrolysis products, consisting of a mixture of various gaseous hydrocarbon components, then diffuse through the porous separator and contact the molten tin to get oxidized by the dissolved oxygen. However, the effect of formation of pyrolysis soot, which clogs the porous separator and causes cell failure, was not clearly discussed. The performance levels observed with H_2 as the fuel were significantly higher than those observed with JP-8. This is because a small molecule such as H_2 would have much higher diffusivity in the molten tin compared with the much larger hydrocarbon molecules formed in the case of JP-8. Therefore, for JP-8 the anode polarization losses would be much higher, resulting in lower power levels.

At high temperatures such as 1273 K, the diffusivities of the fuel and oxygen in tin still might not have high enough values, even for H_2, and their contributions to the ohmic and anode polarization losses can be significant. Given that the electrolyte and cathode losses for an SOFC at 1273 K are nearly zero, the poor performances observed in these experiments prove that almost all of the losses are due to sluggish oxygen transport in the molten Sn anode (Koslowske et al. 2009). Note that the polarization losses are usually obtained by potential–current density curves and impedance spectra.

From the work carried out by CellTech Power, it was clear that molten Sn did not provide an efficient anode mechanism for fuel oxidation. However, the factors limiting the performance of these electrodes and the properties of SnO_2 to serve as the oxygen-carrying medium to the fuel still needed to be studied. Moreover, the operating temperature used in this study was too high and could compromise cell component stability in conventional SOFCs, leading to excessive anodic polarization losses. (Tao et al. 2007a). With the advancement in cell fabrication techniques, new catalytic materials for the cathode, and the use of thin electrolytes, the typical operating temperature for an SOFC can be as low as 973 K (Vohs and Gorte 2009). Studying the practicality of Sn as an anode at these lower temperatures would actually determine if it could be a realistic solution.

Due to the inherent benefits of having a molten metal anode-based direct carbon SOFC, a further investigation of the oxygen transport properties of molten Sn and other molten metal anode candidates was warranted in order to understand their suitability for oxidizing solid carbon and improving the DCFC performance.

19.4.4 DCFC with Molten Salt as Electrolyte

This type of fuel cells uses molten hydroxide (NaOH or KOH) as the electrolyte contained in a metallic container, which also acts as a cathode (Zecevic et al. 2003). Fuel is fed to the cell in the form of a rod made from graphite or coal-derived carbon dipped into the electrolyte. This fuel rod also acts as an anode of the cell. Air is purged into the molten salt at the bottom of the container to supply oxygen at the cathode. Typical operating temperatures are in the range of 500–650 °C. The electrochemical reactions that occur in the cell are as follows:

$$C + 4OH^- \rightarrow 2H_2O\,(g) + CO_2 + 4e^- \tag{19.56}$$

$$O_2 + 2H_2O + 4e^- \rightarrow 4OH^- \tag{19.57}$$

Although the use of molten hydroxide offers a number of advantages such as high ionic conductivity and higher electrochemical activity of carbon that result in lower operating temperatures, it is affected due to the formation of carbonates in the melt. The carbonates are formed by the product CO_2 and/or carbon reacting with hydroxide ions in the melt.

William Jacques was the first person to build a direct carbon fuel of this type in 1896. The major technical issues for the commercialization of this type of cells are the high corrosion rates of metals used in the cell and technology upscaling.

There is a further class of carbon-based fuel cells in which carbon is first oxidized either inside the cell as a part of the system design or externally to CO according to reaction (19.51).

The CO thus formed then reacts at the electrode–electrolyte interface with O^{2-} to form CO_2.

A dual reaction mechanism is also possible. The carbon particles that make direct contact with the electrolyte react with O^{2-} and are converted to CO_2 as in DCFC, and the carbon particles that do not make direct contact with the electrolyte are oxidized first to CO and then in an electrochemical reaction to CO_2.

19.4.5 Conclusions

The DCFC technology is at an early stage of development with considerable effort required to take it to the pre-commercialization stage. Most groups are testing single cells or small stacks. The power densities are low, typically in the 100–120 mW cm^{-2} range, compared with 300–600 mW cm^{-2} for many other fuel cell types and strongly dependent on the fuel delivery system and the anode catalyst or current collector used. Table 19.11 summarizes the technology status.

Some major technical challenging issues for DCFC are:

- Mode of solid fuel delivery to anode (solid or in molten salt or metal) to maximize interaction at the electrode and electrolyte interface.
- Fuel processing and fuel quality requirements, for example, the effect of contaminants in coal, carbon structure, and surface area on the DCFC performance.
- Understanding the electrochemical reaction kinetics and mechanism for carbon oxidation (direct and indirect) at the anode–electrolyte interface.
- Stacking of single-cell or multicell construction to build reasonable size modules for technology comfort.
- Reducing corrosion of cell components, especially where molten salts are used either as the electrolyte or fuel carrier by suitable choice and development of materials and protective coatings.
- Scale-up from laboratory tests (few watts) to prototypes in the several hundred watts to kilowatts range using continuous fuel feed rather than the batch mode.
- Increasing lifetime that is currently too short (even for reasonable demonstration of the technology), reducing degradation rates, and understanding fuel cell and component degradation mechanisms.
- Demonstration of the technology with acceptable power densities at predicted efficiency.

Two important factors have been identified as affecting the performance of molten metal anodes for SOFCs: the thermodynamic oxidation potential of the metal and the tendency for the oxide to form a film at the electrolyte interface. For example, the formation of an insulating layer of high-melting solid SnO_2 on the surface of the electrolyte blocks the transfer of O^{2-} ions to the anode. So, it is very clear that a metal that forms an insulating solid oxide cannot be used as an anode. For operation of the cells in the battery mode, where the metal is oxidized, the oxidation potential determines the OCV that can be achieved. Oxide films at the YSZ interface can effectively block charge transfer at the electrolyte interface if the oxide is a poor ionic conductor. However, both of these limitations have possible solutions, although further work is required to pursue these solutions.

In the other types of DCFCs, degradation problems are also being observed, requiring extensive exploration. At this stage, the overall investment in DCFC technology is relatively small in comparison with other major fuel cell technologies. Most of the research in universities is directed at individual components of the fuel cell system using small button cells: fuel quality and processing, anode

Table 19.11 Technology status of various types of DCFCs

DCFC technology	Status
Molten hydroxide	Average power densities of 40 mW cm^{-2} for over 540 h of operation with peak power density of 180 mW cm^{-2}. The maximum efficiency achieved is 60%
Molten carbonate	Power densities to 100–120 mW cm^{-2} and 80% efficiency with fuels such as fossil chars, petroleum coke, carbon blacks
Solid oxide Solid carbon fuel	The peak power density achieved is reported to be 140 mW cm^{-2} at 900 °C with synthetic carbon agitated with CO_2
Solid oxide Carbon mixed with molten metal	The peak power density achieved so far is about 160 mW cm^{-2}, respectively, from hydrogen and liquid fuel JP-8. The company has built and tested cells, small stacks, and systems for short periods of time
Solid oxide Carbon mixed with molten carbonate	The peak power density achieved is 120 mW cm^{-2} using acetylene black as the fuel. SRI International has tested a 6 W six-cell (six cathode/electrolyte tubes in a single salt bath) demonstration stack using different fuels

materials and electrochemistry, fuel delivery system, optimization of the cathode and electrolyte, cell design, and understanding the reaction mechanisms.

Some research organizations (SARA, Contained Energy, and SRI International) are investigating complete systems and building stacks. The power densities obtained from single cells are typically below $150\,\mathrm{mW\,cm^{-2}}$. For comparison, power densities of 150–200 and $400–500\,\mathrm{mW\,cm^{-2}}$, respectively, have been reported for molten carbonate and solid oxide fuel cell stacks. A substantial effort is required to demonstrate DCFC technology in the kilowatt range with reasonable lifetime (several thousand hours) with acceptable corrosion rates.

19.5 Nuclear Power Plants

19.5.1 Nuclear Renaissance

By the end of the last century, nuclear energy has gained a widespread renewal of interest as an important contributor to energy security, supply, and sustainability. A number of new designs of NPPs have emerged recently, in attempts to achieve advances in the following areas: sustainability, competitive economics, safety and reliability, proliferation resistance, and physical protection. Actually, in the framework of the Generation IV International Forum (GIF), a task force has announced in 2002 the selection of six reactor technologies, which would represent the future shape of nuclear fission energy: these reactors operate at higher temperatures than today's reactors, allowing new and attractive applications, such as the thermochemical production of hydrogen. In addition to these six concepts for deployment between 2010 and 2030, the GIF has recognized a number of International Near-Term Deployment advanced NPPs available before 2015. Moreover, several international research projects are ongoing, which concern subcritical accelerator-driven systems for radioactive waste incineration, in conjunction with partitioning and transmutation technologies. In worldwide context, it is urgent to create a low carbon economy (Andrews and Jelley 2007; Marshall 1983; Petti et al. 2009).

All these new projects deal with very complex systems, which comprise the nuclear reactor, its energy conversion systems, and the necessary facilities for the entire fuel cycle. In this context, innovative techniques, which are nowadays available from multiphysics modeling (MPM) and object-oriented modeling (OOM), together with the advanced strategy of model predictive control (MPC), could be usefully employed for the simulation and control of such new complex systems. These innovative techniques allow different degrees of detail (from a zero-dimensional lumped description to a three-dimensional (3D) distributed parameter geometry) and different modeling scales (from single components (steam generators, control rods, pumps, valves, fuel rods, etc.)) or subsystems (such as the nuclear steam supply system (NSSS) and the turbine, generator, and feedwater system (TGFS)) to the overall NPP and possibly till the entire fuel cycle.

In short, MPM allows more flexibility to evaluate the interaction effects in comparison with conventional tools of analysis; nevertheless, it could become computationally unpractical for very complex 3D domains. By means of the MPM approach, a detailed description of the single component/subsystem of an NPP is viable, but neither the simulation of transients at the overall system level nor the analysis of the control-relevant dynamics during the NPP normal operation is manageable: to these last two purposes, OOM techniques may answer successfully.

Actually, recent advances in OOM of complex dynamical systems allow a declarative, highly modular, and acausal approach that brings new interesting possibilities in the development of system simulators: this means that it is possible to build the overall model for an NPP by connecting the models of its single components or subsystems through rigorously defined interfaces or connectors (also referred to as physical ports). Among the new paradigms of the OOM approach, a fundamental role is played by the following: the definition of physical ports as the standard interfaces to connect a certain component model in order to reproduce the structure of the overall system; the definition of models in a non-causal form that allows reuse, abstraction, and unconditional connection; and the mutual independence of the model interfaces (the physical ports) and its internal description, which means that the user can adopt the conventional modeling or the innovative maximum power point (MPP) techniques to simulate the behavior of the single component/subsystem. In particular, the internal description of the component/subsystem has to be written independently of its boundary conditions, which are not necessarily declared a priori as inputs or outputs; this OOM paradigm marks a fundamental difference with conventional block-diagram-oriented (causal) simulation languages, in which each model must have definite input and output signals.

In short, the principal aims of OOM are thus to obtain an NPP model, which is accurate enough to reproduce the control-relevant dynamics during normal operation, validated against the more accurate, safety-oriented models; to integrate the NPP model with the control system and with other relevant subsystems at its boundaries; and to provide a whole range of degrees of detail, so that the correct balance between accuracy and simulation speed can always be struck, depending on the specific simulation needs.

NPPs are highly complex, nonlinear, time-varying, and constrained systems, whose control represents one of the most relevant issues to be solved during the design process. The control strategy usually adopted in the current

NPPs is based on a classical feedforward and feedback (typically with a proportional–integral configuration) scheme. Techniques for the optimal control of nuclear reactors have been extensively studied in the past two decades, but it is still difficult to design optimal controllers for nuclear systems because of variations in nuclear system parameters and modeling uncertainties.

Among the most promising control techniques, MPC methodology has so far received attention as a powerful tool for the control of industrial process systems, and it has been recently applied for the first time to an NPP with very good results. MPC is an effective means to deal with large multivariable constrained control problems. Its main idea is to choose the control action by repeatedly solving online an optimal control problem: this aims at minimizing a performance criterion over a future horizon, possibly subject to constraints on the manipulated inputs and outputs, where the future behavior is computed according to a model of the plant.

Currently, there are some 450 operational nuclear reactors worldwide. They are predominantly pressurized water reactors (PWRs) (60% of total) and boiling water reactors (BWRs) (21%). The rest are advanced gas-cooled reactors (AGRs), deuterium-moderated reactors, Canadian deuterium uranium reactors (CANDU) and D_2O-PWRs, light water graphite-moderated reactors, RBMKs, and fast breeder reactors (FBRs).

In the long term (2040), a new range of sophisticated generation IV design is expected to become available including the modular "pebble-bed" reactor being developed in South Africa. These plants are intended to be "fail-safe" in design. Beyond 40 years, there is the dream of nuclear fusion as a major source of energy. The experimental International Thermonuclear Experimental Reactor (ITER) fusion reactor to be built in Cadarache, France, represents the next step in that direction.

For the improvement of these reactors and the development of the new generation of civil nuclear reactors, the adoption of MPC methods could be very interesting and useful, especially when several constraints on the physical variables of the various plant/component subsystems have to be fulfilled; moreover, MPC could be advantageous to guarantee a rapid and smooth power maneuvering, in view of the economical and safe operation of NPPs as well as of the importance of load-following strategy.

In short, the MPC approach has many advantages over the conventional control strategy, above all because it is possible to handle constraints in a systematic manner during the design and implementation of control; nevertheless, difficulties may arise for guaranteeing closed-loop stability, for handling model uncertainty, and for reducing online computations.

With hundreds of new reactors planned worldwide, university training is being required on a significant scale, and development and expansion of introduction and higher-level courses on nuclear engineering as well as teaching texts on nuclear science and engineering are being prepared. Areas of particular interest include:

- Nuclear chemistry.
- Nuclear and particle physics.
- Reactor physics and transport theory.
- Nuclear fuels and materials.
- Fuel cycle and isotopes.
- Nuclear safety and security.
- Nuclear medicine and biology.
- Nuclear radiation detection and protection.
- Radiation shielding/radiation applications.
- Thermal hydraulics/neutronics.
- Fusion engineering.
- Accelerators, spectrometers, and detectors.
- Nuclear magnetic resonance spectroscopy.
- Pulse power techniques and applications.

Nuclear fuels and materials is a topic of particular interest in the context of HTC because it involves the need for novel and sophisticated materials, with high mechanical strength and corrosion resistance, as well as higher specific properties for nuclear applications. Clearly the innovative techniques described above, for the simulation and control of NPPs, would be excellent contributors for this resurgent industry and to wider global development in this field. In this direction there are now good websites that provide current information about the field (European Nuclear Society 2017; International Nuclear Safety Center 2017). These sites are highly focused on the choice of materials. They center on a pair of databases for materials of fission and fusion-based nuclear engineering – fuels, materials for fuel cladding, moderators and control rods, first-wall materials, materials for pressure vessels, and heat exchangers, providing data for their properties. Where relevant, the records contain data for both nuclear and engineering properties. The databases are accessed through the CES EduPack software, allowing its full data retrieval and selection functionality to be exploited. Further information on these matters is available at www.matuk.co.uk/energy.htm.

In this section, the main reactor systems are introduced, identifying their principal materials. Then, their properties for nuclear systems and their proposed uses will be considered. A last subsection will deal with degradation and corrosion of the materials, namely:

- Research on corrosion and erosion, crack nucleation and growth mechanisms, environmentally assisted cracking, creep–fatigue interactions, and thermal cycling.

- Research on irradiation damage effects on materials, especially at the high energies and high doses expected in future fusion reactors.
- Further studies of long-term degradation of waste storage materials and of the design and construction of waste storage facilities.

19.5.2 Nuclear Reactor Types

Six reactor systems and their most important materials are introduced in this subsection. The direct cycle BWR system generates steam that is fed to the same sort of steam turbine used in coal or gas-fired power systems. The nuclear core assembly consists of an array of Zircaloy 2 tubes encasing enriched UO_2 ceramic fuel pellets. Some of the fuel rods contain gadolinium oxide (Gd_2O_3), which acts as a burnable "poison" absorbing neutrons when the fuel is fresh but burning up as the fuel decays, buffering the neutron flux. The power is controlled by control rods inserted from the bottom of the core and by adjusting the rate of the water flow. The control rods are made of boron carbide (B_4C) clad in stainless steel 304 or 304L. Water is circulated through the reactor core where it boils, producing saturated steam (water line of 304 SS) (Gen IV Nuclear Energy Systems 2007).

Light water acts as both a coolant and a moderator, slowing down high-energy neutrons. The steam is dried and passed to the turbine generator through an stainless steel steam line (304, 316 SS, or Cr steel). On exiting the turbine (of Cr–Mo steel), the steam is condensed (Al–Cu–Ni or titanium condenser materials), demineralized, and returned as water to the reactor. The pressure vessel is of SA508 or SA533I, 308L SS cladding.

The BWR operates at constant steam pressure (7 MPa), like conventional steam boilers and with a steam temperature of about 560 K.

The core of a PWR is not unlike that of a BWR. It has some 200 tube assemblies containing ceramic pellets consisting of either enriched uranium dioxide (UO_2) or a mixture of both uranium and plutonium oxides known as mixed oxide fuel (MOX). These are encased in Zircaloy 4 cladding. Either B_4C-Al_2O_3 pellets or borosilicate glass rods are used as burnable poisons. Water, pumped through the core at a pressure sufficient to prevent boiling, acts as both a coolant and a moderator, slowing down high-energy neutrons. The water, at about 600 K, passes to an intermediate heat exchanger (IHX). The power is controlled by the insertion of control rods from the top of the core and by dissolving boric acid into the reactor water. As the reactivity of the fuel decreases, the concentration of dissolved boron ions is reduced by passing the water through an ion exchanger. Control rods made of boron carbide (B_4C) or an Ag–In–Cd alloy are clad in Inconel 627 or stainless steel (304) tubes.

The primary pressurized water loop of a PWR carries heat from the reactor core to a steam generator. The loop is under a working pressure of about 15 MPa – sufficient to allow the water in it to be heated to near 600 K without boiling. The heat is transferred to a secondary loop generating steam at 560 K and about 7 MPa, which generates heat that drives the turbine.

The pressure vessel is of SA508 or SA533 clad with 308L SS or Inconel 617; the water line is of 304 SS; the steam line is of 304, 316 SS, or Cr steel; the turbine is of Cr–Mo steel; the condenser is of Al–Cu–Ni or titanium; and the steam generator is of SA533 or Inconel 600.

The *liquid metal cooled fast breeder reactor* (LMFBR) is a liquid sodium-cooled reactor that makes use of a fast neutron spectrum and a closed fuel cycle. The liquid sodium coolant transfers heat from the reactor core and is pumped through the primary loop at about 800 K. The sodium in this loop becomes radioactive, requiring an intermediate sodium-filled heat exchange loop to prevent possible leakage of radioactive material outside the containment structure (concrete). The sodium in this secondary sodium loop, made of type 324 and 316 stainless steel, alloy 800, or Cr–Mo steels, passes to a steam generator where it heats water to generate steam at 750 K. The turbine and generator are essentially the same as those of a BWR or PWR.

A variety of fuel materials have been proposed. These include mixed uranium and plutonium oxides (~25% PuO_2), metal alloys such as U–Pu–Zr, and mixed uranium or thorium carbides and nitrides. The usual choice is a fuel assembly made up of mixed uranium dioxide (UO_2) and plutonium dioxide (PuO_2) fuel rods clad in type 316 stainless steel. This is surrounded by the "breeding blanket" containing depleted UO_2 pellets. The control rods, such as those of a BWR, are boron carbide (B_4C) clad in type 316 stainless steel and enter from the top of the core.

An LMFBR can have either pool or loop designs. A pool design has the IHX and primary sodium pumps immersed in the reactor vessel, while a loop design has these elements external to it. One of the selected generation IV systems, the sodium-cooled fast reactor (SFR), uses a similar design to LMFBR described above. The next-generation lead-cooled fast reactor (LFR) uses liquid lead as a coolant and uses a somewhat different reactor design.

The AGR is graphite moderated and cooled with carbon dioxide (CO_2). The core consists of high-strength graphite bricks mounted on a steel grid. Fuel rods of enriched UO_2 clad in stainless steel (20Ni–25Cr) are placed in graphite sleeves and inserted into vertical channels in the bricks. Gas circulators blow CO_2 up through the core and down into steam generators. Holes in the graphite allow access to the gas. The outlet temperature of the CO_2

is about 943 K at a pressure of 4 MPa. The graphite in the core is kept at temperatures below 723 K to avoid thermal damage.

The reactor core, gas circulators, and steam generators are encased in a pressure vessel made of prestressed concrete lined with a mild steel to make it gas tight. Mild steel is used in areas of the pressure vessel that are exposed to temperatures between less than 623 K. In regions at temperatures between 623 and 793 K, annealed 9Cr–1Mo steel is used, while austenitic steel (316 H) is used for regions hotter than this. Power is primarily controlled through the insertion of control rods made of boron steel, with backup by insertion of nitrogen into the cooling gas or by releasing fine boron-rich balls into the gas stream.

The *very high temperature reactor* (VHTR) is a proposed fourth-generation design, moderated with graphite and cooled with helium gas. The development of new materials able to tolerate the higher operating temperatures presents a major engineering challenge.

The outlet temperature of the coolant is about 1123–1223 K at a pressure of 7 MPa. Internal reactor temperatures may reach up to 1470 K. Candidate materials for regions at temperatures between about 1030 and 1270 K are alloys 617, X, XR, 230, 602CA, or variants of alloy 800H. For regions with temperatures higher than this, the leading material candidates are composites with a carbon fiber reinforced carbon matrix (Cf/C) or carbon fiber reinforced silicon carbide (SiCf/SiC). The most promising pressure vessel material is modified 9Cr–1Mo steel. Some designs maintain the vessel at lower temperatures, in which case current pressure vessel materials could be used such as SA508 steels.

The helium coolant is heated in the reactor vessel and flows to the IHX. Heat is transferred to a secondary loop with either helium, nitrogen and helium, molten salt, or pressurized water. The materials of the IHX depend on the operating temperatures and the nature of the secondary coolant; Alloy 617 is a primary candidate. The heated fluids can either be used to drive a turbine or to produce hydrogen.

All VHTR designs make use of tri-structural isotropic (TRISO)-coated fuel particles. The particles are 750–830 μm in diameter and consist of a kernel of fuel material coated with two layers of pyrolitic carbon with a layer of silicon carbide in between. These particles can be used in either prismatic or pebble-bed reactors. In a prismatic reactor, the kernel consists of enriched uranium oxycarbide (UCO), and the particles are packed into cylindrical compacts, which are placed into graphite fuel elements. However, a pebble-bed reactor uses particles with an enriched uranium dioxide (UO_2) kernel, and these are formed into 60 mm diameter spheres (the "pebbles"). The fuel pebbles are fed into the core mixed with nonfuel graphite pebbles that act as reflectors to even the heat generation.

The ITER is an experimental fusion reactor designed to produce 500 MW of power from an input of 50 MW (Barabash et al. 2007; Ioki et al. 1998). It is a step toward the use of the fusion energy for electricity production and other commercial applications.

In all proposed fusion reactors, energy is released from the fusion of deuterium and tritium nuclei. This requires a temperature of about 100 MK at which the gases form a plasma. No materials operate at such temperatures, so the ITER uses magnetic confinement to contain the plasma, allowing fusion without contact between the plasma and the containing walls. The ITER uses a tokamak design. The plasma is contained in a torus shape using strong magnetic fields produced by circumferential superconducting coils and a large central solenoid. The coils are made of a superconducting niobium–tin alloy (Nb_3Sn) or niobium–titanium (NbTi) alloy cooled to 4 K with supercritical helium.

The plasma is enclosed in a sealed torus vacuum vessel made up of two steel walls with water coolant circulating between them. The main structural materials are 316L(N)-IG, 304, and 660 stainless steels. The interior of the vacuum vessel is covered with the blanket that shields the vessel and magnets from heat and neutron radiation. This consists of shield modules attached to the vacuum vessel inner wall. Each module has a 316L(N)-IG stainless steel shield block carrying a first wall panel of beryllium facing the plasma. These are joined to a heat sink made of a copper alloy (CuCrZr) with 316L(N)-IG stainless steel tubes with a coolant flowing through them. It is the energy transferred to this coolant that would be used in electricity production in future plants.

At the bottom of the vacuum vessel is the diverter, which removes heat, helium, and plasma impurities. Materials of the diverter facing the plasma must withstand temperatures of up to 3300 K. The current choice of materials is a carbon fiber composite (CFC SEP NB31) and tungsten (99.94 wt% W). The entire structure, including the magnets, is enclosed in an stainless steel vacuum cryostat.

It can be easily understood from the information above that the nuclear reactors are systems of great engineering complexity whose structural materials require improved performances that impose a significant effort to be established. In Section 19.5.3 further details on these matters are available.

19.5.3 Materials for Nuclear Reactors

Apart from the structural materials reported above, many more materials are being used and developed for fuels, control-rod materials and special reactor-grade steels,

and graphites, as exemplified below (Frost 1995; Roberts 1981):

- Graphite (isotropic, HTR grade IG-110).
- Graphite (semi-isotropic AGR Gilsoncarbon).
- Uranium dioxide (UO_2).
- Uranium carbide (UC).
- Mixed oxide $(U,Pu)O_2$ (MOX) 20% PuO_2.
- Uranium nitride.
- Zirconium–1.5% tin alloy, reactor grade, "Zircaloy 4."
- 9Cr–1Mo steel.
- Modified 9Cr–1Mo–V steel (Grade 91).
- SA-508 Gr. 3, Cl 1 and Cl 2.
- SA-533 Gr B.

The nuclear industry presents unique challenges for these and other reactor materials, ranging from microstructural processes to long-term component integrity. Irradiation on the materials causes important effects on microstructures, dimensional stability, mechanical properties, and increments in the number of corrosion and degradation issues in nuclear power and high-level nuclear waste storage. Some of these effects are introduced as follows:

- Changes in mechanical properties and dimensional stability in neutron-irradiated materials are related to microstructural changes such as the formation of voids, loops, and precipitates.
- Neutron irradiation can also affect the stability of austenite in stainless steel. Irradiation promotes the growth of ferrite, with the effect increasing with greater levels of cold work.
- Irradiation can also alter grain boundary composition. In general, irradiation can cause an inverse Kirkendall segregation in which slow-diffusing elements (e.g. nickel) enrich grain boundaries and faster-moving solutes (e.g. chromium) are depleted from near grain boundary regions (Ford et al. 1999).
- Irradiation-induced void formation can produce density changes, potentially resulting in dimensional changes in reactor components. Swelling has been observed in metals (Figure 19.12) as well as in ceramics. Mitigation requires modifications to material design (e.g. alloying,) or selection (Leggett and Waters 1999). Creep and associated stress relaxation can cause unwanted dimensional changes but can also relieve stresses due to swelling in contained systems (Garner et al. 1999).
- Neutron irradiation can result in increased strength and a corresponding decreased toughness as shown in Figures 19.13 and 19.14. These trends are associated with the development of dislocation loops, precipitates, and voids. Irradiation-induced grain boundary compositional changes can also lead to brittle intergranular fracture (Allen et al. 2005).

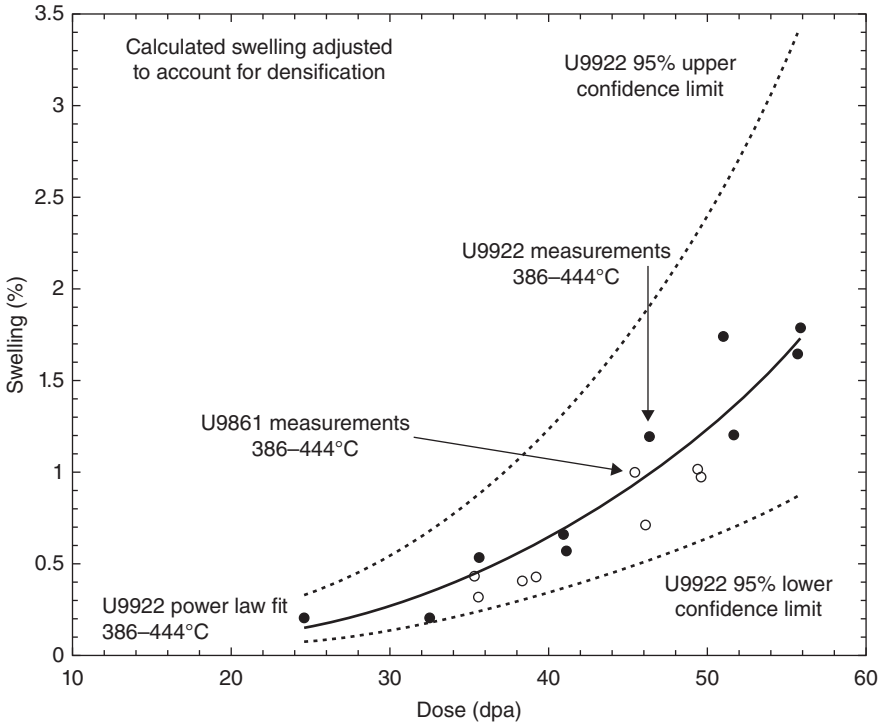


Figure 19.12 Swelling as a function of temperature for two EBR-II 316 stainless subassemblies (Ford et al. 1999).

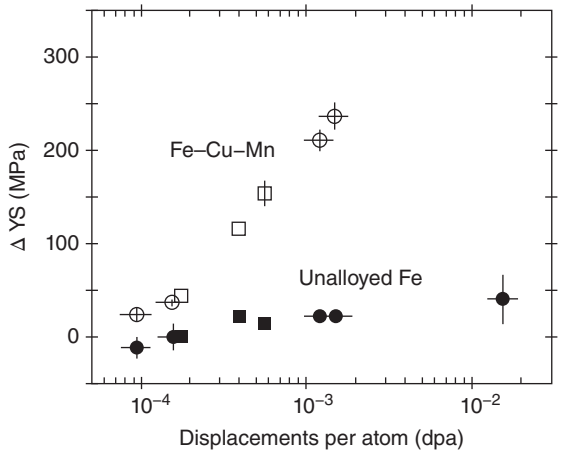


Figure 19.13 Effect of irradiation on yield strength of iron and steel (dpa is the average number of displacements per atom due to irradiation) (Ford et al. 1999).

Helium generated due to nuclear transformation reactions can diffuse to grain boundaries. Bubbles can subsequently form, especially in structures under a tensile load. This can result in helium embrittlement and a reduction in creep resistance (Yamamoto et al. 2004).

The damage regions typical of radiated materials are outlined in Figure 19.15. The prevalent damage mechanisms under service conditions must be considered to prevent failure.

- Corrosion-related phenomena remain important for materials developments. Figure 19.16 presents a Pourbaix diagram for a nickel-based alloy, showing internal oxidation products observed in SCC studies.

  Irradiation-assisted stress corrosion cracking (IASCC) is likely related to both the irradiation hardening and grain boundary composition changes mentioned above. Additionally, radiation can also affect the water chemistry, potentially resulting in a more aggressive environment (Gold and Simonen 1993).

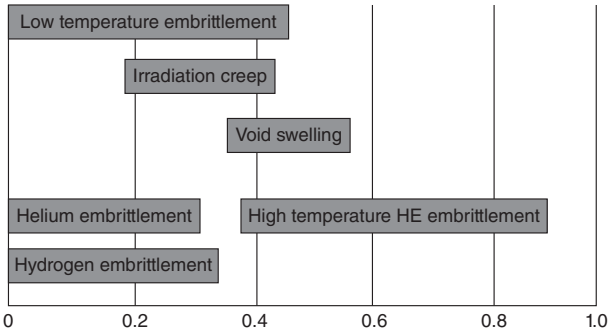


Figure 19.15 Damage mechanisms for metals as a function of temperature (Allen et al. 2002).

Further corrosion issues in nuclear power systems are discussed in Section 19.3.4.

- Long-term nuclear waste repositories will require containment system stability for greater than 10 000 years (Desai 2005). As such, corrosion studies for candidate materials such as Alloy 22 in Figure 19.17 are critical. General corrosion, hydrogen-induced cracking, and SCC data is being extrapolated over the 10 000-year specified timeframe based upon estimated environmental conditions (e.g. ionic species accumulation, microbial activity, radiation-induced degradation, thermal conditions, etc.).

Thermal conductivity, Young's modulus, ultimate tensile strength, and yield strength of the materials applied in the nuclear systems are some of the properties that need much consideration particularly when dealing with the principal structural materials and the considerable change in their properties under neutron irradiation. A key material is the

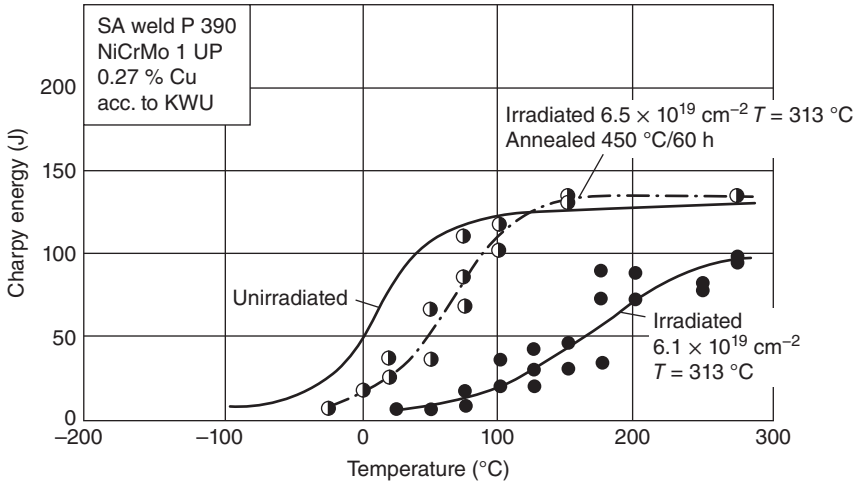


Figure 19.14 Irradiation causes a decrease in toughness of welded joint, making failure likely at higher temperatures (Theus and Weeks 1988).

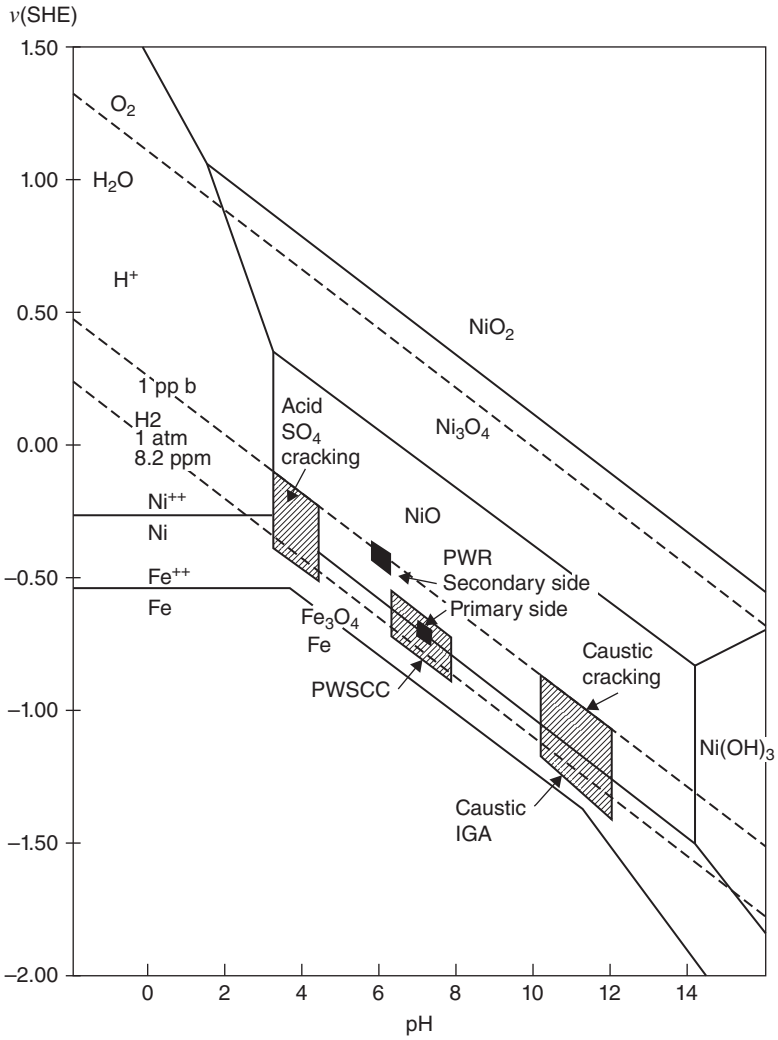


Figure 19.16 Pourbaix diagram for nickel-based alloy 600 in an aqueous solution (300 °C) (Ford et al. 1999).

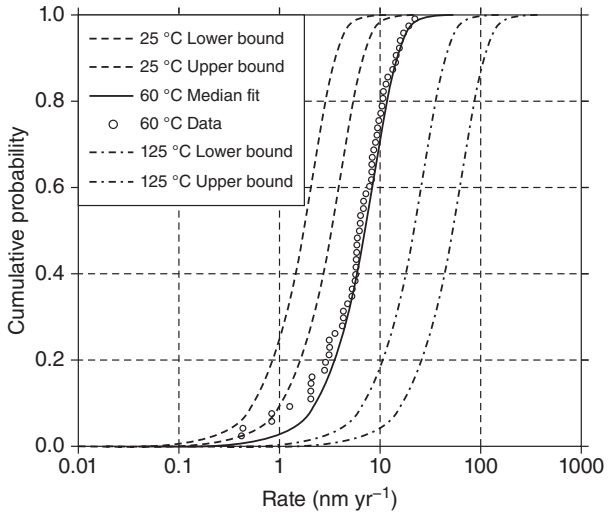


Figure 19.17 General corrosion rate for Alloy 22 waste package outer barrier (Allen et al. 2005).

nuclear sector in Zircaloy 2. By searching this name in the Nuclear Power Systems database (e.g. see CES EduPack's Level 3), it is possible to record the results shown in Table 19.12. Nuclear properties for zirconium (the base of Zircaloy) are contained in the extended elements database, which includes the *binding energy per nucleon*, *thermal neutron absorption cross section*, *thermal neutron scattering cross section*, *fission cross section*, and, for fuels, the *half-life*. These properties are defined in more detail in the Glossary of Selected Terms used in HTC.

About 85% of zirconium metal, 5000–6000 t yr^{-1}, is used in the nuclear industry. Commercial-quality zirconium still contains 1–3% hafnium. This contaminant is unimportant except in nuclear applications. For nuclear reactor materials, the zirconium metal should have a very low hafnium content of less than 0.01 wt%. Most Zr metal is produced by the reduction of the zirconium ($ZrCl_4$) chloride with magnesium metal in the Kroll process.

Table 19.12 The record for the cladding material Zircaloy 2 (reactor grade)

Designation			
ASTM Standard B350-80: zirconium–tin Alloy, UNS R60802			
Trade names			
Zircaloy 2; Sandvik Zircaloy 2, Sandvik Steel Co. (USA); Zircaloy-2, Sandvik/Coromant (USA); Zircaloy 2, Westinghouse Electric Corp. (USA)			
Composition (summary)			
Zr/1.2–1.7Sn/0.07–0.2Fe/0.05–0.15Cr/0.03–0.08Ni/+ various lesser impurities			
Composition details			
Base	Zr (zirconium)		
Cr (chromium)	0.05	—	0.15%
Fe (iron)	0.07	—	0.2%
Ni (nickel)	0.03	—	0.08%
Sn (tin)	1.2	—	1.7%
Zr (zirconium)	97.9	—	98.7%
Density	6450	—	6650 kg m^{-3}
Price	*24.7	—	27.2 USD kg
Mechanical properties			
Young's modulus	*90	—	105 GPa
Shear modulus	*30	—	40 GPa
Bulk modulus	*100	—	150 GPa
Poisson's ratio	*0.35	—	0.38
Yield strength (elastic limit)	240	—	490 MPa
Tensile strength	410	—	520 MPa
Compressive strength	*240	—	490 MPa
Flexure strength (modulus of rupture)	*240	—	490 MPa
Elongation	14	—	32%
Hardness – Vickers	200	—	240 HV
Fatigue strength at 10^7 cycles	*160	—	260 MPa
Fracture toughness	*115	—	150 MPa $m^{-1/2}$
Mechanical loss coefficient (tan δ)	*3e−4	—	9e−4
Thermal properties			
Melting point	2100	—	2130 K
Maximum service temperature	*643	—	783 K
Thermal conductivity	11	—	14 W m K^{-1}
Specific heat capacity	274	—	286 j kg K^{-1}
Thermal expansion coefficient	5.5	—	5.9 μstrain/°C
Typical uses			
Fuel rod cladding in boiling water reactors (BWRs)			
Warning			
May become radioactively contaminated during use. Small pieces of zirconium, e.g. machine chips and turnings, can be a fire hazard. Nonradioactive zirconium is toxic, but only if ingested in large quantities			
Other notes			
The mechanical properties of Zr alloys vary strongly with oxygen impurity levels. Zirconium ore naturally contains a few per cent hafnium, which has very similar properties to Zr. For nuclear applications, this has to be removed, as Hf absorbs neutrons			

For zirconium production, the van Arkel–de Boer process (1925) and the Kroll process (1955) are the two main processes applied in the industry. The van Arkel–de Boer process is also known as the iodide process or the crystal bar process, developed by the Dutch chemists van Arkel and de Boer in 1925. It is the first industrial process for the commercial production of pure ductile metallic zirconium and is still in use for the production of small quantities of ultrapure titanium and zirconium. The van Arkel–de Boer process involves the use of elemental iodine and crude metal, in the form of a sponge or alloy scrap, to form a volatile metal iodide at a low temperature. At a high temperature, the metal iodide will thermally decompose into pure metal and gaseous iodine.

The Kroll process is a process used to produce titanium metal, developed in 1945 by the metallurgist Kroll from Luxembourg. For the production of zirconium, the process uses magnesium to reduce zirconium chlorides. It is currently the dominant method for the production of zirconium. The operating temperature for this reaction to produce sponge zirconium is about 950 °C. The sponge is subjected to shredding, acid leaching, water washing, and drying and then compressed into an electrode. The electrode is finally melted in a vacuum arc furnace to remove volatile impurities, and a homogeneous product is obtained. The Kroll process is a multistep batch process.

Other industrial methods as reviewed by Haygarth and Graham (1999) include the reduction of tetrafluorides with calcium and electrolysis in fluoride-containing salts, with comparable product purity to that from the Kroll process. The major drawback is the off-gas containing chlorofluorocarbons (CFCs), which is environmentally harmful.

Zirconium and hafnium occur together in the nature, and their separation has been a challenging issue. For use in the nuclear industry, zirconium should be free of hafnium. Since the discovery of hafnium through the crystal bar process, a number of separation methods have been developed, with rough classification into hydro- or pyrometallurgical routes. Hydrometallurgical methods include crystallization, solvent extraction, and ion exchange (Donia et al. 2011; Taghizadeh et al. 2011).

The pyrometallurgical methods were developed based on the differences between zirconium and hafnium in oxidation and reduction characteristics, volatility, electrochemical properties, and molten metal–molten salt equilibrium. The extractive distillation process using carbochlorination of zircon is in operation by CEZUZ in France (Niselson et al. 2009).

Megy (1978) first reported a process that has the vapors of zirconium and hafnium tetrachlorides passing over zirconium metal to form solid zirconium trichloride and unreacted hafnium tetrachloride vapor. The separation factor for this option ranges from 8 to 12 per stage. Megy and Freund (1979) have also tried to separate zirconium and hafnium using a molten salt phase and a molten zinc bath. The best system they have tested was a salt containing 18.5 wt% NaCl, 22.5 wt% KCl, and 60 wt% Na_2ZrF_6 at a temperature of approximately 775 °C. A separation factor of more than 300 was obtained.

A new and more compact process for the production of pure zirconium with a sufficiently low content of hafnium has been developed by Xiao and van Sandwijk (2010). The separation process aims at improving Megy's process, in particular by providing a purification process with a higher thermodynamic separation potential at a lower temperature. Various compact process routes for the production of pure zirconium have been proposed. Zirconium–hafnium separation is the key of the process, and it can be implemented into a total production process in various ways, either in the pre-processing of the starting materials and/or in the post-processing of the intermediate products. Figure 19.18 shows the implementation of Zr–Hf separation in an integrated molten salt electrolysis route starting from crude zirconium production.

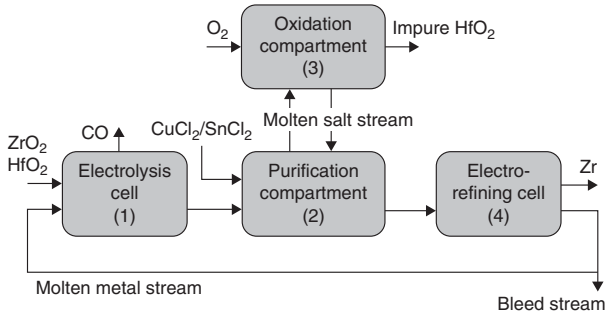


Figure 19.18 A new process for producing reactor-grade zirconium.

The process starts with a hafnium-containing ZrO_2 ore (Xiao and van Sandwijk 2010). The liquid metal cathode consists of copper and tin, and a $CaCl_2$-based salt can be used as an electrolyte. CaO can be added into the electrolyte at the start of the process, and graphite is used as the anode. During electrolysis, the following half-reactions occur at the electrodes:

$$CaO \rightarrow Ca^{2+} + O^{2-} \tag{19.58}$$

$$Ca^{2+} + 2e^- \rightarrow Ca \tag{19.59}$$

$$O^{2-} + C \rightarrow CO\,(g) + 2e^- \tag{19.60}$$

CaO has a high solubility in the electrolyte, and when a sufficient potential difference is applied, Ca^{2+} ions are reduced at the cathode to calcium metal. Calcium metal then dissolves in both molten metal and salt, where it reacts with zirconium oxide to form zirconium metal, as shown in Eq. (19.61):

$$ZrO_2 + 2Ca \rightarrow 2CaO + Zr \tag{19.61}$$

Hafnium oxide reacts in a similar manner. Contaminations in the mineral feed (more noble than zirconium) may also coprecipitate on the cathode and end up in the molten metal. But except for hafnium, they are all more noble than zirconium and will not cause problems in the electrorefining step. The generated calcium oxide will dissolve back into the salt electrolyte.

Initially a chloride-based electrolyte system was investigated: (i) a mixture of equimolar NaCl–KCl and (ii) a mixture of equimolar NaCl–$CaCl_2$, with 3.5–5.0 mol% of fluoride additions (AlF_3, Na_3AlF_6, KF, and NaF). However, the solubility of ZrO_2 turned out to be very low in the chloride-based salt. In order to obtain a sufficient solubility

of ZrO_2 in the electrolyte, fluoride-based electrolytes will be further investigated.

The purification step of hafnium removal from zirconium is carried out under an inert atmosphere (preferably argon) by using a $CuCl_2$-bearing molten salt with the following reaction:

$$Hf_{[metal]} + 2CuCl_{2[salt]} \rightarrow 2Cu_{[metal]} + HfCl_{4[salt]} \quad (19.62)$$

With this reaction, hafnium in the molten metal is preferably transferred to the molten salt phase, and, consequently, $CuCl_2$ is reduced to metallic copper, dissolving into the Zr-containing Cu-based low-melting alloy. The kinetics of the interfacial reactions between molten metal and molten salt is usually very fast. The equilibrium composition for both phases can be established in laboratory experiments. Thermodynamic prediction of the reaction system gives very encouraging results for this separation process.

In the electrorefining step, the liquid metal (alloy) anode consists of zirconium and low-melting more noble metals such as copper and tin, with a very low content of hafnium. The cathode is a pure zirconium sheet or block. The molten salt electrolyte is a mixture of alkali and alkali earth chlorides, typically also containing some zirconium chloride. Upon applying a potential difference between the two electrodes, the following half-reactions take place:

$$Zr \rightarrow Zr^{2+} + 2e^- \quad (19.63)$$

$$Zr^{2+} + 2e^- \rightarrow Zr \quad (19.64)$$

For metals at elevated temperatures, especially liquid metals, the exchange current density as defined by the Butler–Volmer equation is extremely large. Therefore, it is believed that no or very little Zr^{3+} or Zr^{4+} ion forms at the anode. When the potential difference is not too high, the other metals in the alloy are not oxidized, because they are more noble than zirconium. Similarly, reduction of the alkali or alkali earth chlorides in the salt does not occur either, because they are less noble than zirconium.

Processes described above for the production of reactor-grade zirconium involve many corrosion phenomena, and this aspect coupled with the importance of the zirconium in the nuclear industry explains the detailed considerations included in this book.

Further materials used in each nuclear reactor system are tabulated in Tables A.25–A.27.

19.5.4 Corrosion in Nuclear Applications

Today, the risk of catastrophic failure of a power-producing system is low. This can be attributed to the strict adherence to the standards that are imposed on component designers and manufacturers as well as on plant operators. The setting of these standards clearly involves thorough knowledge of the properties of the materials of construction and an understanding of their behavior in the local environment. That environment may itself be adjusted for overall optimum performance by specifying the optimum chemistry control strategies. The prime example of such chemistry control is the specification of an alkalinity level in the feedwater systems of steam-raising plants, including nuclear secondary coolants, which is necessary to minimize corrosion of piping and components and to keep systems clean of dissolved and particulate corrosion products and impurities. In a nuclear reactor core, materials must be able to withstand not only the operational conditions (pressure, temperature, and water chemistry) but must show minimal degradation from the effects of radiation (high gamma and neutron flux). Radiation effects on materials may include loss of ductility, shape change from radiation-enhanced creep and growth, and enhanced corrosion resulting from hydrogen ingress (deuterium ingress for the case of heavy water systems) (Sequeira and Santos 2011).

While the current performance record of power plants is generally good, technology is not standing still. The push for bigger returns on capital investment and the accompanying trends toward higher plant efficiencies and longer component lifetimes lead to even more severe operating conditions in power systems. Inevitably, the demands on materials of construction escalate. The predominant materials of construction in steam-raising equipment and nuclear systems are the metals and alloys. Their interaction with the operating environment very much dictates the chemistry control to be practiced by plant operators.

As described above, a nuclear reactor is a complex system of different connected materials that must behave optimally in unison to ensure the safe and efficient operation of the plant. Even under the strictest chemistry control practices and careful plant operation, the corrosion and subsequent degradation of the plant components are the inevitable consequences of thermodynamics; the metals that make up the pipes, valves, fittings, and vessels all tend to revert back to their thermodynamically stable state – usually an oxide, hematite (Fe_2O_3), for example, the basis of rust on iron and steel. In some cases, the degradation of system components is exacerbated by vibration, fatigue, or fretting or by the interaction with high velocity coolant, creating *flow-accelerated corrosion* (FAC); in all cases, component lifetimes are shortened. Thus, knowledge of the basic forms of corrosion is a prerequisite to understanding the materials selection chemistry requirements of nuclear reactor systems.

These basic forms of corrosion involve general corrosion in gas-cooled systems and water-cooled systems, FAC, galvanic corrosion, SCC and intergranular attack, crevice corrosion and pitting, fretting wear and flow-induced

vibration, delayed hydride cracking and hydride blistering, and microbiologically induced corrosion. FAC, sometimes called flow-assisted corrosion, was formerly referred to as erosion–corrosion, but the last term is now usually confined to attack in a corrosion medium aggravated by mechanical forces such as those arising from abrasion by solid particles. Most of these corrosion phenomena are aqueous forms of corrosion typical of the nuclear reactor components under normal operating conditions, which are outside the scope of this book.

However, under LOCA conditions, temperatures rapidly increase, and HTC reactions control the reactor failure and radioactive product release. These mechanisms recently achieved notice in light of the failures at the Fukushima Daiichi power plant after the magnitude 9.0 earthquake and resulting tsunami (Pool 2011). Three high temperature reaction mechanisms during LOCA are of particular note. First, the zirconium alloy (Zircaloy) fuel cladding reacts with steam. Due to the exothermic nature of Reaction (19.65),

$$Zr + 2H_2O\,(g) = ZrO_2 + 2H_2\,(g) \tag{19.65}$$

oxidation proceeds at a runaway rate at temperatures above about 1200 °C, generating large amounts of hydrogen (Tanabe 2012). The high levels of hydrogen can result in explosions, which damage the reactor containment systems. Second, volatile fission products are released from the fuel matrix, react with the steam/hydrogen gas mixture flowing through the reactor core, and can be released into the environment through the damaged containment (Cubicciotti and Sehgal 1984). Finally, the high temperature fuel reacts with the reactor vessel and structural materials forming a molten mixture. Subsequent injection of water can result in dissolution of the reacted fuel mixture, which can be released to the environment with subsequent cooling water leaks (Burns et al. 2012a,b).

Of these three issues, the oxidation of zirconium alloys is the most well understood (Cheng et al. 2012; Tanabe 2012). Current research focuses on developing alternative fuel cladding materials to replace zirconium alloys with more slowly oxidizing materials.

Thus, Si-, Al-, and Cr-containing materials are all candidates for fuel cladding with better oxidation performance in LOCA. Cheng et al. (2012) examined the oxidation rates of alternative cladding materials and concluded that SiC, high Cr (>20 wt%) alloys, or Al-forming alloys all show significantly improved oxidation resistance at high temperature LOCA conditions.

A second area of concern during LOCA is the release of fission products during vaporization reactions. Short-lived fission products including ^{131}I and ^{137}Cs are of interest due to their radioactive danger. Vapor species such as Cs(OH) and CsI are expected to form in amounts greater than the metal vapor partial pressures, increasing transport rates out of the hot core. Cubicciotti (1985) has calculated the equilibrium partial pressures of these and many other fission vapor products as a function of temperature, H_2O/H_2 ratio, and pressure under LOCA-relevant conditions. Equilibrium calculations are expected to be relevant due to the high temperatures of interest. In addition, Cubicciotti also calculated vapor transport rates based on his equilibrium thermodynamic calculations. Many of the calculations use estimated thermochemical data, demonstrating the need for more accurate thermochemical measurements and calculations.

Finally, consideration of reactions occurring during reactor core melting is of importance. Melted fuel will react with concrete stainless steel reactor vessel components of the reactor (Burns et al. 2012a,b; Cubicciotti 1985). The resulting phase assemblage is expected to be very complex with long-term environmental hazards due to potential radioactive material release if complete isolation of contaminated water is not maintained.

Development of more oxidation-resistant fuel cladding and improved thermochemical data for gas, liquid, and solid phases formed during LOCA events are needed.

Since we are going nuclear again, requiring materials and structures with enhanced performances, namely, ability to operate at much higher temperatures, many worldwide organizations are being active with the resulting corrosion issues whose nature is particularly aggressive.

That is the case of the European Federation of Corrosion whose Working Party on Nuclear Corrosion was reorganized in 1986 with the objective of concentrating on nine topics of relevance to the nuclear power industry. These technical topics were extended to 11 in 1991, and then the novel structure of the Working Party became based on the following topics:

- Pressurized water reactors (PWR)
- Boiling water reactors (BWR)
- High temperature reactors (HTR)
- Liquid metal fast breeder reactors (LMFBR)
- Fuel cladding
- Fusion reactors
- Advanced gas-cooled reactors (AGR)
- Decontamination
- Reprocessing
- Waste disposal
- Irradiation-assisted stress corrosion cracking (IASCC).

The first meeting of the Working Party took place in 1987 at Frankfurt, Germany, and the second took place in 1991 at Handeck, Switzerland (EFC 1989, 1992). Along the last 25 years, FCT, other corrosion societies, and many other

organizations, namely, the International Atomic Energy Agency (IAEA), NACE, NASA, DECHEMA, CEGB-UK, Berkeley Nuclear Laboratories, Belgian Nuclear Research Centre, TMS, etc., are developing a great effort to try to understand, monitor, control, and inhibit corrosion problems in the nuclear industry. The interested reader should go to the open literature and find out books, reports, proceedings, lecture courses, and many other recent publications on the major corrosion problems encountered in the nuclear field. We will finalize this subsection with brief considerations on the corrosion of zirconium alloys and on fluoride molten salts (Taboada 1964).

Zirconium is the eleventh most abundant element in the Earth's crust, making it more prevalent than the common transition metals copper, lead, nickel, and zinc. It occurs naturally as the minerals zircon (zirconium silicate ($ZrSiO_4$)) and zirconia (zirconium oxide (ZrO_2)) and always in conjunction with 0.5–2.5% hafnium (Hf), a metal that has very similar chemical and physical properties, making it difficult to separate the two elements. Zirconium or, more specifically, the alloys fabricated from it are the most important of the nuclear reactor materials. They are resistant to corrosion in many process environments, nuclear heat transport systems in particular, and they have excellent nuclear properties, making them the predominant materials for construction of in-core components (fuel sheathing, pressure tubes, and calandria tubes). Zirconium itself has a neutron absorption cross section of 0.18 b, making it nearly transparent to the thermal neutrons in a water-cooled and water-moderated reactor. Zirconium alloys used in nuclear reactors must be highly processed to keep the hafnium concentration below 100 ppm since its neutron absorption cross section is 102 b, nearly 600 times that of zirconium (see Section 19.5.3). Higher concentrations of hafnium would increase the parasitic absorption of neutrons in the reactor core and reduce the fuel burn-up. Pure zirconium has an HCP structure that transforms to BCC at 862 °C before melting at 1850 °C. It is a reactive metal that combines easily with oxygen, hydrogen, nitrogen, carbon, and silicon and in air retains its metallic luster because of a very thin but protective zirconia oxide (ZrO_2) layer. A protective but thicker zirconia layer is retained during exposure to high temperature water, making zirconium alloys ideal for service in water reactor cores. The pure metal is alloyed with small amounts of elements such as tin, chromium, iron, nickel, and niobium to improve mechanical strength and corrosion resistance and to reduce hydrogen pickup. In the CANDUs, the alloy Zircaloy 2 is used for the calandria tubes and was the initial choice as the pressure tube material. Zircaloy 2 contains 1.2–1.7 wt% Sn, 0.07–0.2 wt% Fe, 0.05–0.15 wt% Cr, and 0.03–0.08 wt% Ni. It is also the material used for BWR fuel cladding. For fuel sheathing in CANDUs and fuel cladding in PWRs, Zircaloy 4 was developed and used because it was observed to have a lower overall corrosion rate and a reduced tendency to pick up hydrogen. It has a similar composition to that of Zircaloy 2 except for the nickel content, which is reduced to a maximum of 0.007 wt%, and the iron content, which is increased to 0.18–0.24 wt%.

The corrosion of zirconium alloys has been postulated as occurring in three stages, which have been characterized as follows (Hillner et al. 2000):

- Pre-transition, when a thin, black, tightly adherent oxide thickens according to sub-parabolic (often assumed cubic) kinetics.
- Transitory, apparently corresponding to successive "cubic" periods of decreasing duration, when the thickening film cracks and becomes porous and new oxide grows at the M–O.
- Post-transition, when kinetics become rapid and linear and white or gray oxide is formed.

The transition occurs at film thicknesses of 2–5 μm.

Much of the early research leading to our understanding of the corrosion and hydriding of zirconium and its alloys was conducted by Cox (1976). The basic electrochemical reaction is the formation of a compact oxide film based on zirconia (ZrO_2) via Reaction (19.65).

The pre-transition film is adherent and compact zirconia of tetragonal crystal structure that grows via the solid-state diffusion through the oxide of ions/vacancies and electrons/holes. Electron diffusion is rate determining and drives the cathodic reaction by reducing water to form hydrogen. The hydrogen generated enters the metal in atomic form and at high enough concentrations precipitates within the lattice as flakes of hydride of nominal composition between ZrH and ZrH_2, making the material brittle. The post-transition oxide has monoclinic crystal structure and is much less protective than the pre-transition oxide, hence the accelerated corrosion. Since these processes occur with no oxide dissolution or release of cations to the coolant, the weight gain of laboratory specimens is an accurate gage of corrosion (Allen et al. 2012).

The oxide thicknesses on Zircaloy 4 cladding on high-burn-up PWR fuel may reach 100 μm or more but on the advanced alloys are generally less than half that amount. Concentrations of LiOH of more than ~4 ppm may exacerbate the corrosion rate. BWR exposures of Zircaloy 2 clad fuel induce nodular corrosion, whereby white spots of thick oxide appear on the underlying black oxide and grow with increasing exposure. The severity of nodular corrosion depends upon the metallurgy of the alloy and the aggressiveness of the environment but rarely causes problems (although spalled oxide has occasionally caused abrasion damage in BWR control-rod drive mechanisms). So-called shadow corrosion, where galvanic

effects thicken ZrO_2 films in proximity to components made of non-zirconium alloys such as stainless steel control-blade handles, is an additional mechanism in the low-conductivity and low-hydrogen environment of the BWR. BWR fuel is also subject to increased corrosion when the surface temperature is increased by the deposition of copper-containing crud that impairs the nucleation of steam bubbles. Such crud-induced localized corrosion (CILC) has led to fuel failures. These mechanisms of corrosion of zirconium alloys are reviewed in detail in the report of Adamson et al. (2007).

Because of its relatively low burn-up, CANDU fuel sheathing develops a very thin protective oxide, and failures from coolant-induced general corrosion are almost inexistent. The Zr–2.5%Nb pressure tubes in CANDUs and other PWRs also experience low corrosion rates, and their general corrosion over the 20–30-year lifetime in reactor is acceptable. The oxidation, however, forces hydrogen (actually, deuterium from the heavy water coolant) into the metal lattice, and this is much aggravated by deuterium that migrates into the pressure tube ends across the rolled joint between it and the stainless steel end fittings, which also experience general corrosion. Hydriding (deuteriding) can then be a problem if concentrations exceed the terminal solid solubility (TSS), leading to precipitation of hydride "platelets," brittleness, and possible cracking if excessive stresses are experienced (Simpson and Ells 1974).

The Zr–Nb alloy of CANDU pressure tubes is subjected to several other forms of degradation (growth and creep), and these will be life limiting for the components in one form or another and are the primary reason for which a midlife refurbishment (after approximately 30 years of operation) is required on CANDU reactors.

Differential elongation could cause feeder pipes at reactor ends to contact and chafe each other, which must be avoided. Because of the material condition of the Zr-2 calandria tubes, they do not elongate to the extent of applying significant loads on the end shields.

The pressure tubes also sag with increased exposure time due to the elongation described above and from diametral creep. The diametral creep meant that fuel channels in the middle of the core, where the combination of neutron flux, pressure, and temperature is highest, would suffer from significant portions of the coolant flow bypassing the fuel bundles, reducing the heat transfer efficiency and leading to reductions in the margins to dry-out. The remedy was then to derate – reduce the reactor power. Pressure tube/calandria tube sag also meant that the pressure tubes in some reactors approached the calandria tubes closely and occasionally may have contacted one of the horizontal reactivity mechanism control tubes spanning the calandria. The pressure tube and its matching calandria tube are separated by wire-wound toroidal spacers or garter springs that accommodate relative movement between the two. The pressure tube will sag more between the spacers than will the calandria tube due to higher temperature and pressure operation and the weight of the fuel bundles. Should the spacers move out of position from vibration during operation, there is a risk that the hot pressure tube touches the cool calandria tube, inducing a thermal gradient or "cold spot" on the wall of the pressure tube. This will cause any hydrogen/deuterium in the vicinity to diffuse down the temperature gradient and form a hydride or hydrogen blister at the surface. Above a certain size, the blister will crack to accommodate the volume change and may initiate a delayed hydride crack that could penetrate the tube wall. These degradation processes worsen with time of operation, and therefore pressure tube rehabilitation programs need to be undertaken.

A mechanistic understanding of the corrosion situation in reactor requires a clear distinction between "corrosion under irradiation" and "irradiation-induced corrosion." The former was perceived to describe a situation wherein corrosion rates under irradiation differ from those predicted from laboratory data based only on the temperature dependence of these data, any local changes in water chemistry, and a thermal hydraulic calculation of the oxide–metal interface temperature. The latter describes a change in corrosion rate arising from a direct effect of some component of the radiation field on a rate-controlling step in the corrosion process, wherever this step may be. In such a case, the effect could not be simulated without the use of irradiation.

Most work that assesses the in-reactor behavior of zirconium alloys finds a small factorial difference that cannot be predicted purely from laboratory data and thermal hydraulics. There is, however, no agreement as to whether this difference results from a direct effect of irradiation or whether some other factor (e.g. Li^+ concentration in PWRs or Cu deposition in BWRs) can explain the observed differences.

In order to provide an improved understanding of the phenomena, a close interaction is needed between those workers involved in studies in reactor of those factors influencing the corrosion behavior of both current and potential future cladding alloys and those workers performing experiments to study the micromechanistic process.

High temperature molten salts based on chloride or fluoride compounds have several applications in the nuclear field. In the front-end nuclear fuel cycle, molten salts are used for the purification and production of zirconium alloy, which is used as fuel cladding. Then, a pyrochemical treatment in $NaCl–AlCl_3$ molten salt at 350 °C enables the separation of zirconium and hafnium, which is a neutronic poison. In the nuclear fuel fabrication process, conversion of uranium oxide ore requires large quantities of fluorine that is obtained by the electrolysis of 2HF–KF molten salt at 95 °C. Several pyrochemical processes based on chloride or fluoride molten salts have also been conceived

in the back-end nuclear fuel cycle to separate actinides from lanthanides during nuclear waste recycling. Because fluoride mixtures are thermodynamically stable at high temperature, with very high boiling points, these liquids have been considered as heat transfer or cooling fluids, as coolants for thermal energy, and in nuclear fission and fusion systems. Several criteria have to be considered when choosing a structural material: mechanical strength at high temperature, irradiation resistance (in the case of materials under neutron flux), and chemical corrosion resistance (which depends on the material composition and microstructure and on the physical chemistry of the molten salt). As it will be shown, the liquid fluoride salt coolant must be thermodynamically relative to the chosen materials in order to avoid corrosion when using molten fluorides in nuclear systems (Cabet 2001).

Several fluoride molten salts have been investigated for nuclear applications: $LiF{\cdot}BeF_2$ (66–33 mol%) (FLiBe) at Oak Ridge National Laboratory (USA), $LiF–ThF_4–UF_4$ (77–20–3 mol%) at CNRS (France), LiF–NaF–KF (46.5–11.5–42 mol%) (FLiNaK) in AHTRs, etc.

In a fluoride melt, the main oxidizing impurities are said to be H_2O (in general this is present in the solid constituents to be fused) and HF (formed in the melt by several reactions):

$$MF_x + x/2H_2O\,(g) = MO_{x/2} + xHF\,(g) \qquad (19.66)$$

$$MF_x + zH_2O\,(g) = MO_zF_{(x-2z)} + 2zHF\,(g) \qquad (19.67)$$

Generally, the salt mixture is fused at a temperature lower than the hydrolysis temperature of the pure salt. Therefore, the solvation process increases the metallic fluoride stability and strongly reduces its hydrolysis process (less than 10 ppm for FLiNaK).

H_2O (g) is easily eliminated under an argon flux at temperatures above 300 °C. Moreover, traces of water are not stable in the fluoride salt after melting, as the water reacts with the fluoride ions to produce HF (g) and oxides.

Although oxide ions have no direct influence on the structural material corrosion, because O^{2-} is not oxidizing toward metals, the elimination of oxides is nevertheless required to prevent the precipitation of metallic oxides (especially UO_2). O^{2-} ions react with an excess of HF according to the reaction

$$O^{2-} + 2HF\,(g) \rightarrow H_2O\,(g) + 2F^- \qquad (19.68)$$

It was suggested that this purification could be performed by bubbling pure gaseous HF or HF/H_2 mixtures into the salt. Due to its high solubility in the fluoride salts, HF (g) is strongly retained in the salt and is responsible for structural material corrosion as observed in corrosion tests. Therefore, the use of pure HF (g) is not recommended for salt purification because it will result in the severe corrosion of the structural material.

A purification procedure of molten salt with no introduction of pure HF (g) is strongly recommended to prevent corrosion reactions. The fluoride mixture could be dried under high vacuum prior to melting. It was observed that after a vacuum treatment (10^{-5} Torr) at 400–425 °C, the cathodic and anodic residual currents (due to O^{2-} oxidation of HF/H_2O reduction) were smaller than those measured by other authors in the same melt pretreated with HF and H_2 (Santarini 1981). The elimination and purification of salts for removing oxides and sulfurs can also be performed by gas mixture bubbling. In this case, the HF/H_2O gas composition has to be carefully chosen to prevent an excess of HF and an increase of salt redox potential.

In the case of MSR, the molten salt chemical composition varies with fission reaction and therefore with the operating time. In particular, it was assessed that the redox potential of the fuel salt will increase while in service. The fissile element in the moltent salt fast reactor (MSFR) system is ^{233}U, which is present with two oxidation states in the salt, (IV) and (III), as UF_4 and UF_3, respectively. Then, the redox potential of the fuel salt depends on the $x(UF_4)/x(UF_3)$ mole fraction according to the Nernst relation.

When the fission reactions occur, the fission products are essentially LnF_3 lanthanides (with oxidation state (III)) and gaseous products or noble metals (M) (with oxidation state 0). The result of the fission reactions on the salt chemistry can be schematized by

$$UF_3 + n \rightarrow LnF_3 + M \qquad (19.69)$$

$$UF_4 + n \rightarrow LnF_3 + M + \frac{1}{2}F_2\,(g) \qquad (19.70)$$

When the fission reaction (Eq. (19.70)) occurs, gaseous fluorine is produced. As fluorine is the most oxidizing species, the salt redox potential increases according to

$$UF_3 + \frac{1}{2}F_2\,(g) \rightarrow UF_4 \qquad (19.71)$$

Consumption of UF_3 by Eqs. (19.69) and (19.71) leads to an increase of the redox potential. The fluorine production, and consequently the fuel potential, strongly enhances the corrosion of the structural materials during the reactor's operating time. As it will be shown below, addition of a reducing agent is required to curb the increase of the salt potential and thus to limit corrosion.

Some fission products such as S, Se, and Te are also harmful to the metallic structures due to their oxidizing properties, specifically due to their negative oxidation states ((−I) and (−II)). In particular, corrosion tests have shown that a low concentration of metallic tellurium is strongly corrosive and causes intergranular attacks on

Ni alloys, resulting in severe embrittlement. Analysis of stability phase diagrams calculated for tellurium in fluoride salts, combined with experimental results, showed that the deleterious effect of Te can be canceled by applying a cathodic polarization to the material. In this case, tellurium, electrochemically reduced to Te(−II), reacts with ZrF_4 (salt constituent) to form $ZrTe_2$.

The oxidation state of the fission products (Te, for example) depends on the redox potential at the time of its formation. For high values of the salt potential, Te should be in metallic form and could react with the structural material according to

$$x\mathrm{Te} + y\mathrm{Ni} \rightarrow \mathrm{Ni}_y\mathrm{Te}_x \tag{19.72}$$

$$\mathrm{Cr}_x + \mathrm{Te}_y \rightarrow \mathrm{Cr}_x\mathrm{Te}_y \tag{19.73}$$

The tellurium is thought to be responsible for the formation of brittle tellurium compounds at the alloy grain boundaries. For low salt potentials, tellurium is produced in a Te(−II) state and combines with metallic salt cations (as oxide ions behave).

A main cause of sustained corrosion in MSR is the existence of thermal gradients within the molten fuel salt, which may be responsible for mass transfer (Santarini 1981). This was experimentally demonstrated by Koger using thermal-convection loops; it was observed that adding an oxidizing agent to a molten salt increases the overall corrosion rate (Koger 1972).

The oxidation of Cr (the most reactive metal in structural materials) depends on the salt potential and therefore on the mole fraction $x(UF_4)/x(UF_3)$. This can be written according to the equilibrium equation

$$2\mathrm{UF}_4 + \mathrm{Cr} \rightarrow 2\mathrm{UF}_3 + \mathrm{CrF}_2 \tag{19.74}$$

whose constant K_N has been experimentally determined as a function of the temperature (Baes 1969; Grimes 1964):

$$\mathrm{Ln}\,(K_N) = (-183910.87 + 57.63\mathrm{T})/(\mathrm{RT}) \tag{19.75}$$

The change in the equilibrium mole fraction of dissolved CrF_2 as a function of temperature is the driving force for the mass transfer experimentally observed from hot areas to cold areas in thermal-convection loops. Dissolution of chromium occurs in hot parts. And the formed CrF_2 may be reduced in colder sections. The dissolution of chromium should be negligible for the lower salt potential values (U ratio equals 10).

It was observed that the redox potential, diffusion coefficients, salt composition hydraulic conditions, and operating time all influence the mass transfer process.

Values of K_N derived from Grimes' experimental results for nickel, chromium, and iron at different temperatures indicate that nickel is chemically stable in most fluoride salt and is not affected by oxidation. The constants for iron range between those of chromium and nickel. Therefore, iron could be affected by oxidation under uncontrolled redox conditions. This supports a well-known experimental observation: Ni-based alloys are more appropriate from a chemical point of view for use in MSR systems than stainless steels. Most of the experimental results (Olander 2002; Pourbaix 1990) and observations can be understood by a thermodynamical approach based on data from pure compounds. Thermodynamical diagrams that give the stability domains of elements under their different forms as a function of potential and oxoacidity (related to the oxide concentration in the salt) have been calculated in fluoride molten salts for the main elements of the structural alloys, Ni, Fe, Cr, Mo, and W. The calculation procedure using the thermodynamical data of pure compounds has been described previously (Rouquette-Sanchez and Picard 2004). In this paper, the approach is described for pure metals. In the case of alloys, the calculations have to be corrected using the activities of each constituent element of the alloy (the activity can be assumed to be equal to the mole fraction for very dilute solutions or in cases where the activity coefficients are unknown). The fluoroacidity of the molten salt, which is given by the amount of free fluoride ions in the salt, has a large influence on the speciation of oxides and metallic fluorides. The fluoroacidity depends on the fluoride salt composition. For instance, in the case of FLiNaK, the fluoride activity is assumed to be equal to 1 because the salt is totally dissociated and the salt is (fluoro)basic. In the case of $LiF–BeF_2$, BeF_2 is a (fluoro)acid salt, which forms complexes with fluorides. Therefore, the amount of free fluoride ions depends on the $LiF–BeF_2$ ratio. In the case of $Li–BeF_2$ (66–34 mol%), the activity of free fluoride ions is very low, the metal speciation is low, and the activity coefficient of the metals is close to unity (Baes 1974). Therefore, the speciation of the metallic fluoride depends on the molten salt fluoroacidity, the redox potential MF_x/M depends on the speciation, and thus the chemical behavior of the metals depends on the salt composition.

Combining the phase diagrams for the metals and the potential range of the salt indicates that nickel and tungsten cannot be oxidized under usual salt application conditions, iron and molybdenum can be oxidized under the highest oxidizing conditions and under most potentials, and chromium is not stable but oxidizes to CrF_2 or CrF_3. As can be observed in the calculated diagrams, the potential can be controlled in two ways. The first way is using a reductant to manage a soluble/soluble redox system as is proposed in the case of molten salt reactor: the use of a metallic Be is recommended for molten salt reactor experiment (MSRE) and molten salt breeder reactor (MSBR) concepts and also in fusion concepts to reduce impurities or fission products produced during the neutronic reactions. In the case of MSFR

concept, metallic Th is recommended (Delpech 2009). The second way is the gas mixture: as it is shown on the diagrams, a given gas composition fixes the redox potential and the oxoacidity of the salt. To control the salt potential in the AHTR systems, a gas mixture could be envisaged (see also Chapter 3).

Salt chemistry also has to comply with given specifications (especially in terms of solubility for fissile elements and fission products), but control of the oxidation potential of the salt seems to be achievable. It is a challenge to measure the melt potential within molten fluoride salts and hence to be able to anticipate an increase of the redox potential. Reference electrodes have been proposed, generally based on the reference redox system, NiF_2/Ni (Winand and Chaudron 1967). Russian researchers have developed and innovated system using a dynamic reference electrode (Afonichkin et al. 2009).

A unique method to protect the structural material was investigated in the 1980s. The device or facility walls were cooled down for the formation of a frozen salt layer on the wall surface. The dissolution reactions are then strongly decreased. Corrosion tests performed in FLiBe have shown that the method results in a corrosion rate of lower than 0.5 μm yr^{-1} (EDF and PUK 1975).

The corrosion is often investigated by specimen immersion for various times in various conditions and analyzed afterward. Electrochemical experiments using techniques such as corrosion potential monitoring, cyclic potentiodynamic polarization, and electrochemical impedance spectroscopy (EIS) helped to show that the corrosion rate in molten chloride/fluoride systems had fast kinetics and was limited by mass transfer.

Innovative electrochemical techniques are under development at LECIME, CNRS-ENSCP, Paris, and at CEA, DEN, DPC, SCCME, GIF-sur-Yvette, both in France, and at VTT, Espoo, in Finland, apart from many other places. A push that is necessary to refer is the work in high temperature electrochemistry and electrochemical engineering that is being applied at Savannah River National Laboratory (SRNL) (Garcia-Diaz et al. 2016) to mitigate corrosion in nuclear systems, develop novel methods of nuclear fuel processing, and recover tritium in fusion energy technologies. It is hoped that this and other areas of expertise would find solutions to the energy challenges that we will face globally in the future.

References

Abernathy, H., Gemmen, R., Gerdes, K. et al. (2011). *J. Power Sources* 196: 4564.

Adamson, R., Garzarolli, F., Cox, B. et al. (2007). Corrosion Mechanism in Zirconium Alloys. ZIRAT 12 Special Topic Report. ANT International.

Afonichkin, V.K., Bovet, A.L., Ignatiev, V.V. et al. (2009). *J. Fluoride Chem.* 130: 83.

Akanda, S.R., Walter, M.E., Kidner, N.J., and Seabaugh, M.N. (2014). *Thin Solid Films* 565: 237.

Allen, T., Bruemmer, S., Kassner, H. et al. (eds.) (2002). Higher Temperature Reactor Materials Workshop, ANL-02/12 June.

Allen, T.R., King, P.J., and Nelson, L. (eds.) (2005). *Proceedings of the 12th International Conference on Environmental Degradation of Materials in Nuclear Power Systems – Water Reactors*. Warrendale, PA: TMS.

Allen, T.R., Konings, R.J.M., and Motta, A.T. (2012). *Compr. Nucl. Mater.* 5: 49.

Alman, D.E. and Jablonski, P.D. (2007). *Int. J. Hydrogen Energy* 32: 3743.

Alnegren, P., Sattari, M., Froitzheim, J., and Svensson, J.E. (2016). *Corros. Sci.* 110: 200.

Andrews, J. and Jelley, N. (2007). *Energy Science*. Oxford: Oxford University Press.

Asensio-Jimenez, C., Niewolak, L., Attendorf, H. et al. (2013). *Oxid. Met.* 79: 15.

Baes, C.F. (1969). Proceedings of Nuclear Fuel, USAEC-CONF 690801.

Baes, C.F. (1974). *J. Nucl. Mater.* 51: 149.

Baker, B. (1989). US Patent 4,877,693.

Balachov, I.I., Dubois, L.H., Hornbostel, M.D., and Lipilin, A.S. (2005). The Carbon Fuel Cell Seminar, Palm Springs, CA.

Barabash, V., Peacock, A., Fabritsiev, S. et al. (2007). *J. Nucl. Mater.* 367–370: 21.

Bergman, B., Lagergren, C., Lindbergh, G. et al. (2001). *J. Electrochem. Soc.* 148: A38.

Bloom, H. (1992). *Discuss. Faraday Soc.* 32: 7.

Brett, D.J.L., Atkinson, A., Cumming, D. et al. (2005). *Chem. Eng. Sci.* 60: 5649.

Broers, G.H.J. (1958). High temperature galvanic fuel cell. PhD thesis. Holland: University of Amsterdam.

Burns, P.C., Ewing, R.C., and Navrotsky, A. (2012a). *Science* 335: 1284.

Burns, P.C., Ewing, R.C., and Navrotsky, A. (2012b). *Science* 335: 1184.

Cabet, C. (2001). Rapport Technique CEA, RT-SCCME 558.

Carlin, R.T. (ed.) (1996). *Molten Salts X*, PV96-7. Pennington, NJ: The Electrochemical Soc., Inc.

Chen, L., Sun, E.Y., Yamanis, J., and Magdefrau, N. (2010). *J. Electrochem. Soc.* 157: B931.

Cheng, T., Keiser, J.R., Brady, M.P. et al. (2012). *J. Nucl. Mater.* 427: 396.

Cherepy, N.J., Krüger, R., Fiet, K.J. et al. (2005). *J. Electrochem. Soc.* 152: A80.

Choi, J.J., Park, D.S., Seong, B.G., and Bae, H.Y. (2012). *Int. J. Hydrogen Energy* 37: 9809.

Cooper, J.F. (2004). *2nd International Conference on Fuel Cell Science, Engineering and Technology*. Rochester, NY: ASME.

Cox, B. (1976). *Advances in Corrosion Science and Technology*, vol. 5 (ed. M.G. Fontana and R.W. Staehle), 173. New York: Plenum Press.

Cubicciotti, D. (1985). *Pure Appl. Chem.* 57: 1.

Cubicciotti, D. and Sehgal, B.R. (1984). *Nucl. Technol.* 65: 266.

Davtyan, O.K. (1946). *Bull. Acad. Sci. USSR Cl. Sci. Tech.* 107: 215.

Delpech, S. (2009). MSFR: material issues and the effect of chemistry control. Proceedings of GIF Symposium, Paris, France, p. 201.

Desai, V. (2005). *JOM* 57: 18.

Donado, R.A., Marianowski, L.G., and Maru, H.C. (1984). *J. Electrochem. Soc.* 131: 2541.

Donia, A.M., Atia, A.A., Daher, A.M., and Elshehy, E.A. (2011). *J. Dispersion Sci. Technol.* 32: 193.

EDF and PUK (1975). Brevét Français 2,314,558.

EFC (1989). *Corrosion in the Nuclear Industry*. London: The Institute of Metals, EFC Publication No. 1.

EFC (1992). *Corrosion Problems Related to Nuclear Waste Disposal*. London: The Institute of Metals, EFC Publication No. 7.

Escudero, M.J., Rodrigo, T., Mendoza, L. et al. (2005). *J. Power Sources* 140: 81.

European Nuclear Society (2017). www.euronuclear.org (accessed 14 July 2018).
Falk-Windisch, H., Svensson, J.E., and Froitzheim, J. (2015). *J. Power Sources* 287: 25.
Fang, B., Liu, X., Wang, X., and Duan, S. (1998). *J. Electroanal. Chem.* 441: 1.
Feng, M., Goodenough, J.B., Huang, K., and Milliken, C. (1996). *J. Power Sources* 63: 47.
Fergus, J.W. (2005). *Mater. Sci. Eng., A* 397: 271.
Fontana, S., Chevalier, S., and Caboche, G. (2012). *Oxid. Met.* 78: 307.
Ford, F.P., Bruemmer, S.M., and Was, G.S. (eds.) (1999). *Proceedings of the 9th International Conference on Environmental Degradation of Materials in Nuclear Power Systems – Water Reactors*. Warrendale, PA: TMS.
Frangini, S. (2000). *Oxid. Met.* 53: 139.
Frangini, S., Di Bartolomeo, A., Giorgi, L., and Masci, A. (1996). *Denki Kagaku* 64: 508.
Froitzheim, J., Meier, G.H., Niewolak, L. et al. (2008). *J. Power Sources* 178: 163.
Frost, B.R.T. (1995). *Nuclear Materials*, Materials Science and Technology, VCH Series, vol. 10A and 10B (ed. R.W. Cahn, P. Haasen and E.J. Kramer). Weinheim: VCH.
Fujita, Y. and Urushibata, H. (1996). *The Second International Fuel Cell Conference*, 215. Japan: Kobe.
Gambino, L.V., Magdefrau, N.J., and Aindow, M. (2015). *Mater. High Temp.* 32: 142.
Gannon, P. and Amendola, R. (2012). *JOM* 64: 1470.
Garcia-Diaz, B.L., Olson, L., Martinez-Rodriguez, M. et al. (2016). *J. S. C. Acad. Sci.* 14: 11.
Garner, F.A., Toloczko, M.B., and Sencer, B.H. (1999). *J. Nucl. Mater.* 276: 123.
Gen IV Nuclear Energy Systems (2007). Generation IV Nuclear Energy Systems Ten-Year Program Plan-Fiscal Year 2007. Appendices 1.0 and 5.0.
Glasstone, S. and Sesonske, A. (1994). *Nuclear Reactor Engineering*, 4e. New York: Chapman and Hall.
Gold, R.E. and Simonen, E.P. (eds.) (1993). *Proceedings of the 6th International Conference on Environmental Degradation of Materials in Nuclear Power Systems – Water Reactors*. Warrendale, PA: TMS.
Grimes, W.R. (1964). Chemical Basis for Molten-Salt Reactors. ORNL Report, ORNL-3708, 238.
Gur, T.M. and Huggins, R.A. (1992). *J. Electrochem. Soc.* 139: 295.
Gur, T.M., Homel, M., and Virkar, A.V. (2010). *J. Power Sources* 195: 1085.
Hasegawa, S. and Ihara, M. (2008). *J. Electrochem. Soc.* 155: B58.
Haygarth, J.C. and Graham, R.A. (1999). TMS Annual Meeting, San Diego, California, USA (18 February–15 March).
Heiming, A. and Kraus, P. (1996). *gwf-Gas/Erdgas* 137: 189.
Heydorn, B. and Crouch-Baker, S. (2006). *Fuel Cell Review*. New York: IOP.
Hillner, E., Franklin, D.G., and Smee, J.D. (2000). *J. Nucl. Mater.* 278: 334.
Holcomb, G.R. and Alman, D.E. (2006). *Scr. Mater.* 54: 1821.
Holt, A. and Kofstad, P. (1994a). *Solid State Ionics* 69: 127.
Holt, A. and Kofstad, P. (1994b). *Solid State Ionics* 69: 137.
Huang, B., Chen, G., Li, F. et al. (2004). *Electrochim. Acta* 49: 5055.
Huczkowski, P., Shemet, V., Piron-Abellan, J. et al. (2004). *Mater. Corros.* 55: 825.
Huczkowski, P., Christiansen, N., Shemet, V. et al. (2006). *Fuel Cells* 6: 93.
Hyun, S.H., Cho, S.C., Cho, J.Y., and Ko, D.H. (2001). *J. Mater. Sci.* 36: 441.
International Nuclear Safety Center (2017). http://www.forum.istc.int. (accessed 23 March 2017).
Ioki, I., Barabash, B., Cardella, A. et al. (1998). *J. Nucl. Mater.* 258–263: 74.
Ishihara, T., Matsuda, H., and Takita, Y. (1994). *J. Am. Chem. Soc.* 116: 3801.
Jacques, W.W. (1896). *Electr. Rev.* 970: 826.
Jain, S.L., Lakeman, J.B., Pointon, K.D. et al. (2009). *Energy Environ. Sci.* 2: 687.
Ji, Y., Kilner, J.A., and Carolan, M.F. (2005). *Solid State Ionics* 176: 937.
Jiang, S.P. (2006). *Mater. Sci. Eng., A* 418: 199.
Jiang, S.P. (2008). *J. Mater. Sci.* 43: 6799.
Jiang, S.P. and Chen, X. (2014). *Int. J. Hydrogen Energy* 39: 505.
Jiang, C.R. and Irvine, J.T.S. (2011). *J. Power Sources* 196: 7318.
Jiang, S.P., Zhang, S., and Zhen, Y.D. (2005). *J. Mater. Res.* 20: 747.
Jiang, C.R., Ma, J.J., Bonaccorso, A.D., and Irvine, J.T.S. (2012). *Energy Environ. Sci.* 5: 6973.
Jiang, C.R., Ma, J., Corre, G. et al. (2017). *Chem. Soc. Rev.* 46: 2889.
Keijzer, M. (1997). *Corros. Sci.* 39: 483.
Key, C., Eziashi, J., Froitzheim, J. et al. (2014). *J. Electrochem. Soc.* 161: C373.
Kim, S., Hyun, S.H., Lim, T.H., and Hong, S.A. (2004). *J. Power Sources* 137: 24.
Kodjamanova, P., Fu, Q., and Gautier, L. (2013). *Oxid. Met.* 79: 53.
Koger, J.W. (1972). Corrosion and Mass Transfer Characteristics of $NaBF_4$–NaF (92.8 mol %) in Hastelloy N. ORNL Report, ORNL/TM-3866, 21.
Konysheva, E., Penkalla, H., Wessel, E. et al. (2006). *J. Electrochem. Soc.* 153: A765.
Koslowske, M.T., McPhee, W.A., Bateman, L.S. et al. (2009). *Ceramic Engineering and Science Proceedings*, vol. 30, 27. American Ceramic Society.
Kroll, W.J. (1955). *J. Franklin Inst.* 260: 169.
Kurokawa, H., Kawamura, K., and Maruyama, T. (2004). *Solid State Ionics* 168: 13.
Kurokawa, H., Jacobson, C.P., DeJonghe, L.C., and Visco, S.J. (2007). *Solid State Ionics* 178: 287.
Larring, Y. and Norby, T. (2000). *J. Electrochem. Soc.* 147: 3251.
Lee, A.C., Li, S., Mitchell, R.E., and Gür, T.M. (2008). *Electrochem. Solid-State Lett.* 11: B20.
Leggett, R.D. and Waters, L.C. (1999). *J. Nucl. Mater.* 276: 123.
Li, I., Kim, W., Moom, Y. et al. (2001). *J. Power Sources* 101: 90.
Lillerud, K.P. and Kofstad, P. (1980). *J. Electrochem. Soc.* 127: 2397.
Linder, M., Hocker, T., Holzer, L. et al. (2013). *J. Power Sources* 243: 508.
Linder, M., Hocker, T., Holzer, L. et al. (2014). *J. Power Sources* 272: 595.
Lipilin, A.S., Balachov, I.I., Dubois, L.H. (2006). et al. US Patent 2006/0019132.
Liu, Y. (2008). *J. Power Sources* 179: 286.
Liu, W.N., Sun, X., Stephens, E., and Khaleel, M.A. (2009). *J. Power Sources* 189: 1044.
Lovering, D.G. (ed.) (1982). *Molten Salt Technology*. New York: Plenum Press.
Lu, J.G., Zhu, J.H., Payzant, E.A., and Paranthaman, M.P. (2005). *J. Am. Ceram. Soc.* 88: 1050.
Marina, O.A., Canfield, N.L., and Stevenson, J.W. (2002). *Solid State Ionics* 149: 21.
Marshall, W. (1983). *Nuclear Power Technology*. Oxford: Clarendon Press.
Matsuzawa, K., Mizusaki, T., Mitsushima, S. et al. (2005). *J. Power Sources* 140: 258.
McPhee, W.A.G., Bateman, L., Koslowske, M. et al. (2011). *J. Fuel Cell Sci. Technol.* 8 (4): 041007.
Megel, S., Girdauskaite, E., Sauchuk, V. et al. (2011). *J. Power Sources* 196: 7136.
Megy, J.A. (1978). US Patent 4,072.506.

Megy, J.A. and Freund, H. (1979). *Metall. Trans. B* B10: 413.
Metals Handbook (1982). *Surface Cleaning, Finishing and Coatings*, 9e, vol. 5, 346. Metals Park, OH: American Society for Metals.
Mirzaei, M., Simchi, A., Faghihi-Sani, M.A., and Yazdanyar, A. (2016). *Ceram. Int.* 42: 6648.
Mitsushima, S., Matsuzawa, K., Kamiya, N., and Ota, K. (2002). *Electrochem. Acta* 47: 3823.
Mogensen, M. and Skaarup, S. (2000). *Solid State Ionics* 132: 261.
Mogensen, M., Sammes, N.M., and Tompsett, G.R. (2000). *Solid State Ionics* 129: 63.
Nabae, Y., Pointon, K.D., and Irvine, J.T.S. (2008). *Energy Environ. Sci.* 1: 148.
Nabae, Y., Pointon, K.D., and Irvine, J.T.S. (2009). *J. Electrochem. Soc.* 156: B716.
Niewolak, L., Young, D.J., Hattenford, H. et al. (2014). *Oxid. Met.* 82: 123.
Niselson, L.A., Egorov, E.A., Chuvilina, E.L. et al. (2009). *J. Chem. Eng. Data* 54: 726.
Ohe, K., Shimada, T., Ariga, N., and Masamura, K. (1996). *The Second International Fuel Cell Conference*, 185. Japan: Kobe.
Olander, D. (2002). *J. Nucl. Mater.* 300: 270.
Ota, K., Mitsushima, S., Kato, S. et al. (1992). *J. Electrochem. Soc.* 139: 667.
Palcut, M., Mikkelsen, L., Neufeld, K. et al. (2010). *Corros. Sci.* 52: 3309.
Park, E., Taniguchi, S., Daio, J.T. et al. (2014). *Solid State Ionics* 262: 421.
Petric, A. and Ling, H. (2007). *J. Am. Ceram. Soc.* 90: 1515.
Petti, D., Crawford, D., and Chauvin, N. (2009). *Fuels for Advanced Nuclear Energy Systems*, vol. 34. MRS Bulletin.
Pigeaud, A., Skok, A.J., Patel, P.S., and Maru, H.C. (1981). *Thin Solid Films* 83: 449.
Pint, B.A. (1996). *Oxid. Met.* 45: 1.
Piron-Abellan, J., Tietz, F., Gil, A. et al. (2002). Proceedings of the 5th European Solid Oxide Fuel Cell Forum, Luzerne, Switzerland.
Pointon, K., Lakeman, B., Irvine, J.T.S. et al. (2006). *J. Power Sources* 162: 750.
Pool, R. (2011). *Eng. Technol.* 6: 32.
Pourbaix, M. (1990). *Corros. Sci.* 30: 963.
Quadakkers, W.J., Piron-Abellan, J., Shemet, V., and Singheiser, L. (2003). *Mater. High Temp.* 20: 115.
Reiser, C.A. and Schroll, C.R. (1981). Abstracts, National Fuel Cell Seminar, Norfolk, VA.
Roberts, J.T.A. (1981). *Structural Materials in Nuclear Power Systems*. New York: Plenum Press.
Rouquette-Sanchez, S. and Picard, G.S. (2004). *J. Electroanal. Chem.* 572: 173.
Rufner, J., Gannon, P., White, P. et al. (2008). *Int. J. Hydrogen Energy* 33: 1392.
Sabioni, A.C.S., Huntz, A.M., Philibert, J. et al. (1992). *J. Mater. Sci.* 27: 4782.
Sachitanand, R., Sattari, M., Svensson, J.E., and Froitzheim, J. (2016). *Fuel Cells* 16: 32.
Santarini, E. (1981). *J. Nucl. Mater.* 99: 269.
Sattari, M., Sachitanand, R., Froitzheim, J. et al. (2015). *Mater. High Temp.* 32: 118.
Schlupp, M.V.F., Kim, J.W., Brevet, A. et al. (2014). *J. Power Sources* 270: 587.
Sedricks, A.J. (1996). *Corrosion of Stainless Steels*. Hoboken, NJ: Wiley Interscience.
Selman, J.R. (2006). *J. Power Sources* 160: 852.
Selman, J.R., Shores, D.A., Maru, H.C., and Uchida, I. (eds.) (1990). *Molten Carbonate Fuel Cell Technology*, PV90-16. Pennington, NJ: The Electrochemical Society Inc.
Selman, J.R., Uchida, I., Wendt, H. et al. (eds.) (1997). *Carbonate Fuel Cell Technology IV*, PV97-4. Pennington, NJ: The Electrochemical Society Inc.
Sequeira, C.A.C. and Santos, D.M.F. (2011). *Nucl. Eng. Des.* 241: 4903.
Setoguchi, T., Okamoto, K., Eguchi, K., and Arai, H. (1992). *J. Electrochem Soc.* 139: 2875.
Shimada, T. (1996). *Denki Kagaku* 64: 533.
Simmer, S.P., Anderson, M.D., Engelhard, M.H., and Stevenson, J.W. (2006). *Electrochem. Solid-State Lett.* 9: A478.
Simpson, C.J. and Ells, C.E. (1974). *J. Nucl. Mater.* 52: 289.
Singh, P. (1983). *Corrosion in Batteries and Fuel Cells and Corrosion in Solar Energy Systems*, PV-83/1 (ed. C.J. Johnson and L. Polman), 124. Pennington, NJ: The Electrochemical Society Inc.
Singh, P. and Minh, N.Q. (2004). *Int. J. Appl. Ceram. Technol.* 1: 5.
Singhal, S.C. (2013). *Solide Oxide Fuel Cells: Facts and Figures, Green Energy and Technology* (ed. J.T.S. Irvine and P. Connor), 1. London: Springer.
Skilbred, A.W.B. and Haugsrud, R. (2012). *J. Power Sources* 206: 70.
Söllner, O. (1997). PhD thesis. University Konstanz, Germany.
Spiegel, M., Biedenkoff, P., and Grabke, H.J. (1997). *Corros. Sci.* 39: 1193.
Stanislowski, P., Wessel, E., Hilpert, K. et al. (2007). *J. Electrochem. Soc.* 154: A295.
Steele, B.C.H. (2000). *Solid State Ionics* 129: 95.
Stevenson, J.W., Yang, Z.G., Xia, G.G. et al. (2013). *J. Power Sources* 231: 256.
Taboada, A. (1964). Metallurgical Developments for MSRE. ORNL Report, ORNL-3708, p. 331.
Taghizadeh, M., Ghanadi, M., and Zolfonoun, E. (2011). *J. Nucl. Mater.* 412: 334.
Tanabe, F. (2012). *J. Nucl. Sci. Technol.* 49: 18.
Tao, T., Bateman, L., Bentley, Z., and Slaney, M. (2007a). *ECS Trans.* 5: 463.
Tao, T., Bateman, L., Bentley, Z., and Slaney, M. (2007b). *ECS Trans.* 7: 1389.
Tao, T., White, R., and Klotz, S. (2009). DIIC Document, 11.
Tatsumi, M., Nagashima, I., Shimada, T., and Miki, A. (1996). *The Second International Fuel Cell Conference*, 203. Japan: Kobe.
Tedmon, C.S. (1966). *J. Electrochem. Soc.* 113: 766.
Terada, S., Higaki, K., Nagashima, I., and Ito, Y. (1998). *J. Power Sources* 75: 223.
Theus, G.J. and Weeks, J.R. (eds.) (1988). Proceedings of the 3rd International Conference on Environmental Degradation of Materials in Nuclear Power Systems – Water Reactors TMS, Warrendale, PA, USA.
Tomimatsu, N., Ohzu, H., Akasaka, Y., and Nakagawa, K. (1997). *J. Electrochem. Soc.* 144: 4182.
Trebbels, R., Markus, T., and Singheiser, L. (2009). *J. Fuel Cell Sci. Technol.* 7: 011013.
Tucker, M.C. (2010). *J. Power Sources* 195: 4570.
Uchida, I., Hemmes, K., Lindbergh, G. et al. (eds.) (1999). *Carbonate Fuel Cell Technology*, PV99-20. Pennington, NJ: The Electrochemical Society Inc.
Van Arkel, A.E. and de Boer, J.H. (1925). *Z. Anorg. Allg. Chem.* 148: 345.
Vielstich, W., Larum, A., and Gasteiger, H.R. (eds.) (2007). *Handbook of Fuel Cells – Fundamentals, Technology and Applications*. Hoboken, NJ: Wiley.
Vohs, J.M. and Gorte, R.J. (2009). *Adv. Mater.* 21: 943.
Wee, J., Song, D., Jun, C. et al. (2005). *J. Alloys Compd.* 390: 155.
Whittle, D.P. and Stringer, J. (1980). *Philos. Trans. R. Soc. London, Ser. A* 295 (1413): 309.
Wijayasinghe, A., Bergman, B., and Lagergren, C. (2006). *Solid State Ionics* 177: 165.
Winand, R. and Chaudron, G. (1967). *Comptes Rendus* 264C: 649.
Wu, W., Wang, G.L., Guan, W.B. et al. (2013). *Fuel Cells* 13: 743.
Xiao, Y. and van Sandwijk, A. (2010). European Patent EP20098160442.

Yamamoto, N., Chuto, T., Murase, Y., and Nakagawa, J. (2004). *J. Nucl. Mater.* 329–333: 993.
Yang, Z. (2008). *Int. Mater. Res.* 53: 39.
Yang, Z., Walker, M.S., Singh, P., and Stevenson, J.W. (2003). *Electrochem. Solid-State Lett.* 6: B35.
Yang, Z., Xia, G.G., Maupin, G.D., and Stevenson, J.W. (2006). *Surf. Coat. Technol.* 201: 4476.
Yoshikawa, M., Mugikura, Y., Watanabe, T. et al. (2001). *J. Electrochem. Soc.* 148: A1230.
Yoshikawa, M., Boden, A., Sparr, M., and Lindbergh, G. (2006). *J. Power Sources* 158: 94.
Youn, J.Y., Yoon, S.P., Han, J. et al. (2006). *J. Power Sources* 157: 121.
Young, G.J. (ed.) (1960). *Fuel Cells*. New York: Reinhold Publishing Corporation.
Young, D.J. (2008). *High Temperature Oxidation and Corrosion of Metals*, vol. 1. Elsevier.
Yuh, C.Y. and Pigeaud, A. (1989). DOE Report, DE AC21-86MC3264, Final Report.
Yuh, C., Singh, P., Paetsch, L. and Maru, H.C. (1987). Corrosion 87, Paper 276, San Francisco, CA.
Yuh, C., Johnsen, R., Farooque, M., and Maru, H. (1995). *J. Power Sources* 56: 1.
Zecevic, S., Patton, E.M., and Parhani, P. (2003). *Direct Carbon Fuel Cell Workshop*. Pittsburgh, PA: NETL.
Zhao, Y. and Fergus, J.W. (2012). *J. Electrochem. Soc.* 159: C109.
Zhu, W.Z. and Deevi, S.C. (2003a). *Mater. Sci. Eng., A* 348: 227.
Zhu, W.Z. and Deevi, S.C. (2003b). *Mater. Res. Bull.* 38: 957.

Further Reading

Béguin, F. and Frackowiac, E. (eds.) (2009). *Carbons for Electrochemical Energy Storage and Conversion Systems*. Boca Raton, FL: CRC Press.
Bellanger, G. (2004). *Corrosion Induced by Low-Energy Radionuclides*. Amsterdam, Holland: Elsevier.
Benes, O., Bellmann, M., and Conings, R.J.M. (2010). *J. Nucl. Mater.* 405: 186.
Bessada, C., Rakhmatullin, A., Rollet, A.L., and Zanghi, D. (2007). *J. Nucl. Mater.* 360: 43.
Bosch, R.-W., Féron, D., and Celis, J.-P. (eds.) (2007). *Electrochemistry in Light Water Reactors*. Cambridge: Woodhead Publishing Ltd., EFC Publication No. 49.
Cao, D., Sun, Y., and Wang, G. (2007). *J. Power Sources* 167: 250.
Cesário, M. and Macedo, D.A. (eds.) (2017). *Functional Materials for Solid Oxide Fuel Cells: Processing, Microstructure and Performance*, vol. 1. Bentham Books, Bentham Science Publishers.
Choppin, G.R. and Khankhasayev, M.K. (eds.) (1999). *Chemical Separation Technologies and Related Methods of Nuclear Waste Management*. Dordrecht, Holland: Kluwer Academic Publishers.
Conocar, O., Donyere, N., and Lacquement, J. (2005). *J. Nucl. Mater.* 344: 136.
Dahotre, N.B. and Hampikian, J. (eds.) (1999). *Elevated Temperature Coatings: Science and Technology*, vol. III. Warrendale, PA: TMS Publications.
Durante, G., Vegni, S., Capobianco, P., and Golgovici, F. (2005). *J. Power Sources* 152: 204.
Falk-Windisch, H., Claquesin, J., Sattari, M., and Svensson, J.E. (2017). *J. Power Sources* 343: 1.
Féron, D. (ed.) (2012). *Nuclear Corrosion Science and Engineering*. London: Woodhead Publishing.
Féron, D. and Macdonald, D. (2003). *Prediction of Long Term Corrosion Behaviour in Nuclear Waste Systems*, EFC36. Maney Publishing.
Fomin, G.S. (2003). *Encyclopedia of International Corrosion Standards*. London: Maney Publishing.
Fujii, T., Nagai, T., Uehara, A., and Yamana, H. (2007). *J. Alloys Compd.* 441: L10.
Garche, J. (ed.) (2009). *Encyclopedia of Electrochemical Power Sources*. Amsterdam, Holland: Elsevier.
Gaune-Escard, M. and Haarberg, G.M. (eds.) (2014). *Molten Salts Chemistry and Technology*, 1e. Chichester: Wiley.
Giddey, S., Badwal, S.P.S., Kulkarni, A., and Munnings, C. (2012). *Prog. Energy Combust. Sci.* 38: 390.
Grabke, H.J. and Meadowcroft, D.B. (eds.) (1995). *Guidelines for Methods of Testing and Research in High Temperature Corrosion*, EFC14 . CRC Press.
Harston, J. (2007). *Corrosion in Refineries*, EFC42. London: Woodhead Publishing.
Hemmes, K., Houwing, M., and Woudstra, N. (2010). *ASME J. Fuel Cell Sci. Technol.* 7: 051008-1.
Huang, K. and Goodenough, J.B. (2009). *Solid Oxide Fuel Cell Technology. Principles, Performance and Operations*. London: Woodhead Publishing.
Huggins, R.A. and Batteries, A. (2009). *Materials Science Aspects*. Springer Science and Business Media.
Kofstad, P. and Bredesen, R. (1992). *Solid State Ionics* 52: 69.
Kuznetsov, S.A., Hayashi, H., Minato, K., and Gaune-Escard, M. (2006). *Electrochim. Acta* 51: 2463.
Lima, A.S., Nascimento, A.M., Abreu, M.F.G., and de Lima-Neto, P. (2005). *J. Mater. Sci.* 40: 139.
Lindstrom, R., Maurice, V., Klein, L., and Marcus, P. (2007). *The Use of Electrochemical Scanning Tunnel Microscopy (EC-STM) in Corrosion Analysis*, EFC44. Elsevier.
May, I., Alvares, R., and Bryan, N.D. (eds.) (2006). *Recent Advances in Actinide Science*. London: Royal Society of Chemistry.
Murakami, T. and Koyama, T. (2011). *J. Electrochem. Soc.* 158: 1.
Nishimura, T., Koyama, T., Iizuka, M., and Tanaka, K. (1998). *Prog. Nucl. Energy* 32: 381.
Oltra, R. (ed.) (2007). *Local Probe Techniques for Corrosion Research*, EFC45. Woodhead Publishing.
Otto, N.C., Warner, B.T., Smaga, J.A., and Battles, J.E. (1983). US Patent 4,401,714.
Peterson, D. (1988). *J. Phase Equilib.* 9: 490.
Raja, S. (ed.) (2011). *Stress Corrosion Cracking, Theory and Practice*. London: Woodhead Publishing.
Schlögl, K., Mayhofer, K.J.J., Hanzlik, M., and Arenz, M. (2011). *J. Electroanal. Chem.* 662: 355.
Schütze, M. and Malessa, M. (eds.) (2007). *Standardisation of Thermal Cycling Exposure Testing*, EFC53. London: Woodhead Publishing.
Schütze, M. and Quadakkers, W. (eds.) (2007). *Novel Approaches to the Improvement of High Temperature Corrosion Resistance*, EFC47. London: Woodhead Publishing.
Schütze, M. and Quadakkers, W. (eds.) (2008). *Novel Approaches to the Improvement of High Temperature Corrosion Resistance*, EFC97. London: Woodhead Publishing.
Schütze, M., Quadakkers, W., and Nicholls, J. (eds.) (2001). *Lifetime Modelling of High Temperature Corrosion Processes*, EFC34. Maney Publishing.
Shreir, L.L., Jaman, R.A., and Burstein, G.T. (eds.) (1994). *Corrosion*, 3e, vol. 1, Metal/Environmental Effects, vol. 2, Corrosion Control. London: Butterworth-Heinemann.
Singhal, S.C. and Mizusaki, J. (eds.) (2005). *Solide Oxide Fuel Cells IX, PV 2005–07*, The Electrochemical Society Proceedings Series. Pennington, NJ: The Electrochemical Society.
Sorrell, C.C., Nowotny, J., and Sugihara, S. (eds.) (2005). *Materials for Energy Conversion Devices*. Woodhead Publishing.
Straka, M., Korenko, M., and Lisý, F. (2010). *J. Radioanal. Nucl. Chem.* 284: 245.
Stringer, J. (2004). *Mater. Res.* 7: 1.

Sundamacher, K., Kienle, A., and Pesch, H.J. (2007). *Molten Carbonate Fuel Cells. Modeling, Analysis, Simulation and Control* (ed. J.F. Berndt and G. Huppmann). Weinheim: Wiley-VCH.

Tipping, P.G. (ed.) (2010). *Understanding and Mitigating Ageing in Nuclear Power Plants*. London: Woodhead Publishing.

Volkovich, V.A., Griffiths, T.R., and Tied, R.C. (2003). *Phys. Chem. Chem. Phys.* 5: 3053.

Walters, L.C., Porter, D.L., and Crawford, D.C. (2002). *Prog. Nucl. Energy* 40: 513.

Xu, H. (ed.) (2011). *Thermal Barrier Coatings*. London: Woodhead Publishing.

Yu, B., Zhang, W.Q., Chen, J. et al. (2008). *Sci. China, Ser. B Chem.* 51: 289.

Zhang, J.-S. (2010). *High Temperature Deformation and Fracture of Materials*. London: Woodhead Publishing.

Zhou, X., Tae-Sik, O., Vohs, J.M., and Gorte, R.J. (2015). *J. Electrochem. Soc.* 162: F567.

Chapter 20

Case Studies

We hope that the interest in including a chapter on case studies connected with high temperature corrosion in relevant industrial situations and related with theoretical, experimental, or other studies will contribute for the proper analysis and solution of problems with some complexity or difficulty. The case studies presented here have been adapted from recent literature on practical and fundamental problems that have been analyzed and subsequently solved using relatively innovative approaches. The references listed in Further Reading were the main sources for this examination.

20.1 Making Stainless Steels

Mild steel is an excellent structural material, but at low temperature it rusts, and at high it oxidizes rapidly. For many applications, there is a great demand of corrosion-resistant steel. In response to this demand, a range of stainless irons and steels has been developed. When mild steel is exposed to hot air, it oxidizes quickly to form FeO (or higher oxides). But if one of the elements near the top of Table 20.1 with a large energy of oxidation is dissolved in the steel, then this element oxidizes preferentially (because it is much more stable than FeO), forming a layer of its oxide on the surface. And if this oxide is a protective one, such as Cr_2O_3, Al_2O_3, SiO_2, or BeO, it stifles further growth and protects the steel.

A considerable quantity of this foreign element is needed to give adequate protection. The best is chromium, 18% of which gives a very protective oxide film: it cuts down the rate of attack at 900 °C, for instance, by more than 100 times.

Other elements, when dissolved in steel, also cut down the rate of oxidation. Al_2O_3 and SiO_2 both form in preference to FeO (Table 20.1) and form protective films (Table 20.2). Note that 0.7 T_M was chosen in Table 20.2 because this is a typical figure for the operating temperature of a turbine blade or similar component. Thus, 5% Al dissolved in steel decreases the oxidation rate by 30 times, and 5% Si by 20 times. The same principle can be used to impart corrosion resistance to other metals. We shall discuss nickel and cobalt in the next case study – they can be alloyed in this way – and so can copper; although it will not dissolve enough chromium to give a good Cr_2O_3 film, it will dissolve enough aluminum, giving a range of stainless steel called "aluminum bronzes." Even silver can be prevented from tarnishing (reaction with sulfur) by alloying it with aluminum or silicon, giving protective Al_2O_3 or SiO_2 surface films. And archeologists believe that the Delhi pillar – an ornamental pillar of cast iron that has stood, uncorroded, for some hundreds of years in a particularly humid spot – survived because the iron has some 6% silicon in its composition.

Ceramics themselves are sometimes protected in this way. Silicon carbide, SiC, and silicon nitride, Si_3N_4, both have large negative energies of oxidation (meaning that they oxidize easily). But when they do, the silicon in them turns to SiO_2 that quickly forms a protective skin and prevents further attack.

This protection by alloying has one great advantage over protection by a surface coating (such as chromium plating or gold plating): it repairs itself when damaged. If the protective film is scored or abraded, fresh metal is exposed, and the chromium (or aluminum or silicon) it contains immediately oxidizes, healing the break in the film.

20.2 Corrosion Protection of Turbine Blades

The development of turbine blade materials to meet the challenge of increasing engine temperatures must satisfy the requirements listed in Table 20.3.

These requirements severely limit our choice of very resistant materials. For example, ceramics, with their high softening temperatures and low densities, are ruled out for aeroengines because they are far too brittle (they are under evaluation for use in land-based turbines, where the risks and consequences of sudden failure are less severe).

High Temperature Corrosion: Fundamentals and Engineering, First Edition. César A. C. Sequeira.
© 2019 John Wiley & Sons, Inc. Published 2019 by John Wiley & Sons, Inc.

Table 20.1 Energy of oxides formation at 273 K

Material	Oxide	Energy (kJ mol^{-1} of oxygen (O_2))
Beryllium	BeO	−1182
Magnesium	MgO	−1162
Aluminum	Al_2O_3	−1045
Zirconium	ZrO_2	−1028
Uranium	U_3O_8	≈−1000
Titanium	TiO	−848
Silicon	SiO_2	−836
Tantalum	Ta_2O_5	−764
Niobium	Nb_2O_5	−757
Chromium	Cr_2O_3	−701
Zinc	ZnO	−636
Silicon nitride, Si_3N_4	$3SiO_2 + 2N_2$	≈−629
Silicon carbide, SiC	$SiO_2 + CO_2$	≈−580
Molybdenum	MoO_2	−534
Tungsten	WO_3	−510
Iron	Fe_3O_4	−508
Tin	SnO	−500
Nickel	NiO	−439
Cobalt	CoO	−422
Woods, most polymers, CFRP		≈−400
Diamond, graphite	CO_2	−389
Tungsten carbide cermet (mainly WC)	$WO_3 + CO_2$	−349
Lead	Pb_3O_4	−309
Copper	CuO	−254
GFRP		≈−200
Platinum	PtO_2	≈−160
Silver	Ag_2O	−5
PTFE		≈zero
Gold	Au_2O_3	+80
Alkali halides		≈+400–≈+1400
Magnesia, MgO Silica, SiO_2 Alumina, Al_2O_3 Beryllia, BeO	Higher oxides	Large and positive

Table 20.2 Time, in hours, for material to be oxidized to a depth of 0.1 mm at 0.7 T_M in air

Material	Time	Melting point (K)
Au	$>10^{20}$	1336
Ag	Very long	1234
Al	Very long	933
Si_3N_4	Very long	2173
SiC	Very long	3110
Sn	Very long	505
Si	2×10^6	1683
Be	10^6	1557
Pt	1.8×10^5	2042
Mg	$>10^5$	923
Zn	$>10^4$	692
Cr	1600	2148
Na	>1000	371
K	>1000	337
Ni	600	1726
Cu	25	1356
Fe	24	1809
Co	7	1765
Ti	<6	1943
WC cermet	<5	1700
Ba	≪0.5	983
Zr	0.2	2125
Ta	Very short	3250
Nb	Very short	2740
U	Very short	1405
Mo	Very short	2880
W	Very short	3680

Data subject to considerable variability due to varying degrees of material purity, prior to surface treatment and presence of atmospheric impurities such as sulfur. T_M is the absolute melting point temperature (K).

Table 20.3 Alloy requirements

(a) Resistance to creep
(b) Resistance to high temperature oxidation
(c) Toughness
(d) Thermal fatigue resistance
(e) Thermal stability
(f) Low density

Cermets offer no great advantage because their metallic matrices soften at a too much low temperature. The materials that best fill present needs are the nickel-based superalloys.

The alloy used for turbine blades in the high pressure stage of an aircraft turbofan engine is a classic example of a material designed to be resistant to dislocation (power-law) creep at high stresses and temperatures. At takeoff, the blade is subjected to stresses approaching 250 MN m^{-2}, and the design specification requires that this stress be supported for 30 hours at 850 °C without more than 0.1% irreversible creep strain. In order to meet these stringent requirements, an alloy based on nickel has evolved with the rather mind-boggling specification given in Table 20.4. The point of all these complicated additions of foreign atoms to the nickel is straightforward. It is (i) to have as many atoms in solid solution as possible (the cobalt, the tungsten, and the chromium); (ii) to form stable, hard precipitates of compounds like Ni_3Al, Ni_3Ti, MoC, and TaC to obstruct the dislocations; and (iii) to form a protective surface oxide film of Cr_2O_3 to protect the blade itself from attack by oxygen. These superalloys resist creep so well that they can be used at 850 °C, and they are so hard that cannot be machined easily by normal methods and

Table 20.4 Composition of typical creep-resistance blade

Metals	wt%
Ni	59
Co	10
W	10
Cr	9
Al	5.5
Ta	2.5
Ti	1.5
Hf	1.5
Fe	0.25
Mo	0.25
C	0.15
Si	0.1
Mn	0.1
Cu	0.05
Zr	0.05
B	0.015
S	< 0.008
Pb	< 0.0005

must be precision-cast (for example, by investment casting that produces a fine-grained material that may undergo a fair amount of diffusion creep and that may fail rather soon by cavity formation) to their final shape. Due to this, the blades are expensive, the total cost of a rotor of 102 blades being €200 000. To stave off failure, the alloys are directionally solidified (DS) to give long grains with grain boundaries parallel to the applied stress. DS alloys are standard in high performance engines and are now also in use in civil aircrafts. The improved creep properties of the DS alloy will allow the engine to run at a flame temperature approximately 50 °C higher than before, for a doubling in production cost. Figure 20.1 shows how this evolutionary process has resulted in a continual improvement of creep properties of nickel alloys over time and shows how the amounts of the major foreign elements have been juggled to obtain these improvements – keeping a watchful eye on the remaining necessary properties. The figure also shows how improvements in alloy manufacture – in this case the use of directional solidification – have helped to increase the operating temperature. Nevertheless, it is clear from the graph that improvements in nickel alloys are now nearing the point of diminishing returns.

Internal cooling of the blade enabled the inlet temperature of the turbine to be increased immediately by 100 °C with no change in alloy composition. Later, film cooling constituted a continuous improvement in turbine blades (Figure 20.2). But by further ducting cold air through the blades will begin to reduce the thermal efficiency, and thus a unique characteristic of some alloys, called eutectics, was explored. These eutectics form spontaneously on aligned

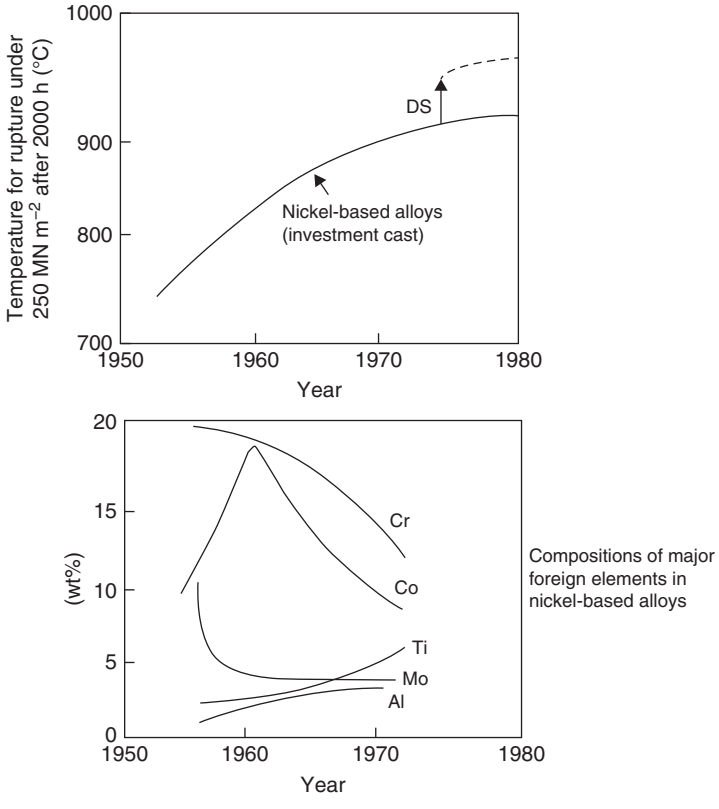


Figure 20.1 Superalloy developments by a sort of creepy Darwinism.

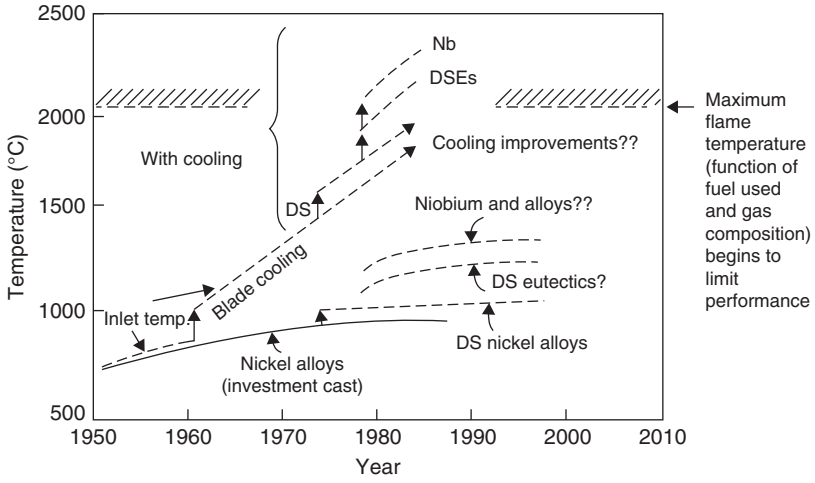


Figure 20.2 Temperature evolution and future materials trends in turbine blades.

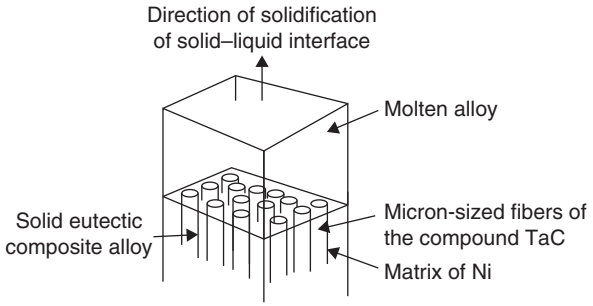


Figure 20.3 Directionally solidified eutectics for turbine blades.

Table 20.5 High temperature composites

Matrix	Reinforcing phase	Reinforcing phase geometry
Ni	TaC	Fibers
Co	TaC	Fibers
Ni_3Al	Ni_3Nb	Plates
Co	Cr_7C_3	Fibers
Nb	Nb_2C	Fibers

reinforced structure, which is usually a compound with high melting temperature, whose fibers improve the creep properties of the resulting composite alloy.

Figure 20.3 shows how eutectics are made, and Table 20.5 lists some typical high temperature composites under study for turbine blade applications.

As shown in Figure 20.2, if directionally solidified eutectics (DSEs) prove successful, they will allow the metal temperature to be increased by ≈100 °C above conventional DS nickel alloys and the inlet temperature by ≈200 °C (because of a temperature scaling effect caused by the blade cooling). Further improvements in alloy design are underway in which existing nickel alloys and DSEs are being blended to give a fiber-reinforced structure with precipitates in the matrix.

The ceramics best suited for structural use at high temperatures (≥1000 °C) are listed in Table 20.6 and compared with nickel-based superalloys. The comparison shows that all the ceramics have attractively low densities, high moduli, and high melting points (and thus excellent creep strength at 1000 °C); and many are completely resistant to oxidation – they are oxides already. But several have poor thermal conductivity (leading to high thermal stresses), and all have very low toughness.

To overcome their major problems, ceramic matrix components are under development: they combine strong, exceptionally perfect, fibers (such as silicon carbide or alumina, grown by special techniques) in a matrix of ceramics (silicon carbide or alumina again), made by conventional means to give a material that you might think of as "high temperature wood."

Any major materials development program, such as that on the DSEs, can only be undertaken if a successful outcome would be cost effective. The cost of the materials themselves must also be considered. For example, the use of greater quantities of exotic materials, such as hafnium, will drive the cost of blades up. But if new alloys offer improved life or inlet temperature, there is a strong incentive to pursue them.

As we saw above, the alloys used for turbine blades contain large amounts of chromium, dissolved in solid solution in the nickel matrix. Now, if we look at Table 20.1, we see that the formation of Cr_2O_3 releases much more energy (701 kJ mol^{-1} of O_2) than NiO (439 kJ mol^{-1} of O_2). This means that Cr_2O_3 will form in preference to NiO on the surface of the alloy. Obviously, the more Cr in the alloy, the greater the preference for Cr_2O_3. At the 20% level, enough Cr_2O_3 forms on the surface of the turbine blade to make the material act a bit as if it were chromium. Suppose for one moment that our material is chromium.

Table 20.6 Ceramics for high temperature structures

Material	Density ($mg\,m^{-3}$)	Melting or decomposition (D), temperature (K)	Modulus ($GN\,m^{-2}$)	Expansion coefficient $\times 10^{+6}$ (K^{-1})	Thermal conductivity at 1000 K ($Wm^{-1}\,K^{-1}$)	Fracture toughness K_c ($MN\,m^{-3/2}$)
Alumina, Al_2O_3	4.0	2320	360	6.9	7	≈5
Glass-ceramics (pyroceramics)	2.7	>1700	≈120	≈3	≈3	≈3
Hot-pressed silicon nitride, Si_3N_4	3.1	2173 (D)	310	3.1	16	≈5
Hot-pressed silicon carbide, SiC	3.2	3000 (D)	≈420	4.3	60	≈3.5
Nickel alloys (Nimonics)	8.0	1600	200	12.5	12	≈100

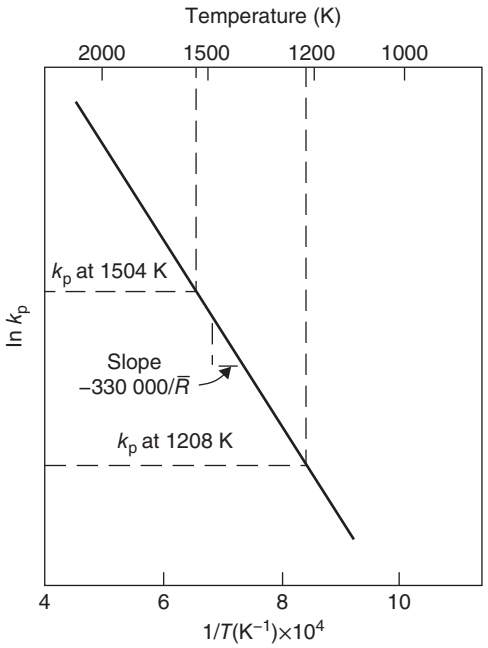


Figure 20.4 K_p variation with temperature.

Table 20.2 shows that Cr would lose 0.1 mm in 1600 hours at 0.7 T_M. Of course, we have forgotten one thing, 0.7 T_M for Cr is 1504 K (1231 °C), whereas, as already mentioned, for Ni it is 1208 K (935 °C). We should, therefore, consider how Cr_2O_3 would act as a barrier to oxidation at 1208 K rather than at 1504 K (Figure 20.4). The oxidation of Cr follows parabolic kinetics with an activation energy of $330\,kJ\,mol^{-1}$. Then the ratio of the times required to remove 0.1 mm (from equation $K_p = A_p \exp(-Q_p/\bar{R}T)$, where A_p and Q_p are constants) is

$$\frac{t_2}{t_1} = \frac{\exp -(Q/\bar{R}T_1)}{\exp -(Q/\bar{R}T_2)} = 0.65 \times 10^3 \qquad (20.1)$$

Thus, the time at 1208 K is $t_2 = 0.65 \times 1.6 \times 10^6$ hours = 1.04×10^6 hours. Note that in Eq. (20.1), t_1 and t_2 are the oxidation times with $t_2 > t_1$.

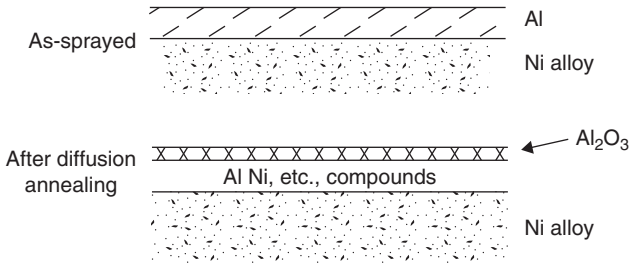


Figure 20.5 Protection of turbine blades by sprayed-on aluminum.

Now, as we have said, there is only at most 20% Cr in the alloy, and the alloy behaves only partly as if it were protected by Cr_2O_3. In fact, experimentally, we find that 20% Cr increases the time for a given metal loss by only about 10 times, i.e. the time taken to lose 0.1 mm at blade working temperature becomes 600×10 hours = 6000 hours rather than 10^6 hours.

Why this large difference? Well, whenever you consider an alloy rather than a pure material, the oxide layer – whatever its nature (NiO, Cr_2O_3, etc.) – has foreign elements contained in it, too. Some of these will greatly increase either the diffusion coefficients in, or electrical conductivity of, the layer and make the rate of oxidation through the layer much more than it would be in the absence of foreign elements contamination.

This 0.1 mm loss in 6000 hours from a 20% Cr alloy at 950 °C, though better than pure nickel, is still not good enough. The obvious way out of this problem is to coat the blades with a protective layer (Figure 20.5). This is usually carried out by spraying molten droplets of aluminum onto the blade surface to form a layer, some microns thick. The blade is then heated in a furnace to allow the Al to diffuse into the surface of the Ni. During this process, some of the Al forms compounds such as AlNi with the nickel – which are themselves good barriers to oxidation of the Ni – while the rest of the Al becomes oxidized up to give Al_2O_3.

Because oxides are usually quite brittle at the temperatures encountered on a turbine blade surface, they can crack, especially when the temperature of the blade changes and differential thermal contraction and expansion

stresses are set up between alloy and oxide. These can act as ideal nucleation centers for thermal fatigue cracks, and because oxide layers in nickel alloys are well stuck to the underlying alloy (they would be useless if they were not), the crack can spread into the alloy itself.

The properties of the oxide film are thus very important in affecting the fatigue properties of the whole component. The pure refractory metals Nb, Ta, Mo, and W have high melting temperatures (2740, 3250, 2880, and 3680 K, respectively) and should therefore have very good creep properties. But they oxidize very rapidly indeed (see Table 20.2) and are utterly useless without coatings. The problem with coated refractory metals is that if a break occurs in the coating (e.g. by thermal fatigue, erosion by dust particles, etc.), catastrophic oxidation of the underlying metal will take place, leading to rapid failure. The "unsafeness" of this situation is a major problem that has to be solved before we can use these on-other-counts potentially excellent materials.

The ceramics SiC and Si_3N_4 do not share this problem. They oxidize readily (Table 20.1); but, in doing so, a surface film of SiO_2 forms that gives adequate protection up to 1300 °C. And because the film forms by oxidation of the material itself, it is self-healing.

20.3 Oxidation of Silicides for VLSI Applications

Electronic materials are those used in electrical industries, electronics and microelectronics, and the substances for the building up of integrated circuits (ICs), circuit boards, packaging materials, communication cables, optical fibers, displays, and various controlling and monitoring devices. Discovery, development, and application of new materials are the robust power for the development of human society.

Processing of electronic materials mainly includes crystal growth, epitaxy, lithography, deposition, annealing, doping (diffusion or ion implantation), etching (dry or wet), and metallization. In *ICs*, the fundamental electronic switching device is the (complementary) *metal oxide semiconductor field effect transistor* (MOSFET), which has at least three terminals – the gate, source, and drain. The gate electrode is separated electronically from the source and drain by a thin dielectric film, which is commonly SiO_2. Formation of this film could be accomplished by using sputtering, evaporation, chemical vapor deposition, or atomic layer deposition. Thermal oxidation is also used to grow the gate dielectric films due to its ease in processing control, but it results in many problems in association with material degradation at high temperature; these problems lead to the formation of oxides, carbides, sulfides, nitrides, etc., but when these oxidation processes are well controlled, they have been finding many applications in the modern electronics industry for surface cleaning, film growth, preparation of new materials, and building up of novel structures for devices. To date, Si is still the backbone of the modern semiconductor industry due to its (i) availability in a wide variety of sizes and shapes, (ii) mature material preparation and property control, (iii) native oxide films on its surface, and (iv) compatibility to planar IC technology.

Silicides of transition metals are used in two distinct ways in *very large scale integrated* (*VLSI*) *circuits*: (i) in the contact pads of individual devices on a chip and (ii) in the interconnection lines. For the latter applications, two particular properties of the silicides make them desirable: their metallic electrical conductivity and the possibility to produce a protective coating of SiO_2 under heat treatment in an oxidizing ambient. Of those two attributes, the second one is particularly attractive because it offers inherent advantages in multilevel metallization schemes. To use this feature of silicides successfully, an understanding of the oxidation process is needed. It is convenient to subdivide the subject into two parts, depending on whether the silicide rests on a substrate of excess silicon or whether the substrate is inert, that is, the substrate is in a fully oxidized state, such as SiO_2. Other reasons for the use of silicides in VLSI applications are their very low resistance; good process compatibility with Si, e.g. ability to withstand high temperatures; oxidizing ambients; various chemical cleans used during processing; little or no electronization; easy to dry etch; and good contacts to other materials. But these benefits rise many problems in integrating silicides in an IC, and under this point of view, the actual preferred silicides are WSi_2, $TiSi_2$, NiSi, and $CoSi_2$. Table 20.7 indicates preferred silicides for VLSI application. The main techniques used for the formation of these silicides are (i) metal deposition on Si and formation by thermal heating, laser irradiation, or ion beam mixing (these are sensitive to interface cleanliness and heavy doping, selective silicidation on Si possible, and widely used for silicides of Pt, Pd, Co, and Ti), (ii) co-evaporation (E-gun) of metal and Si (poor process control, poor step coverage, and good tool for research but not used in manufacturing), and (iii) sputtering from a composite target (possibility of high level of contaminants like C, O, Na, and Ar; poor step coverage; used for $MoSi_2$ and WSi_2).

20.3.1 Oxidation of Silicides on Silicon

Typically, silicides are not used alone as interconnections, but with an underlayer of polycrystalline Si. Upon thermal treatment in an oxidizing ambient, most silicides form a SiO_2 overcoat while the silicide layer below is morphologically preserved. The rate of growth of the SiO_2 layer is different for the different silicides, and these rates also

Table 20.7 Overall properties of preferred silicides for VLSI applications

Silicide	Thin-film resistivity (μΩ cm)	Sintering temperature (°C)	Stable on Si up to (°C)	Reaction with Al at (°C)	nm of Si consumed per nm of metal	nm of resulting silicide per nm of metal	Barrier height to n-Si (eV)
PtSi	28–35	250–400	~750	250	1.12	1.97	0.84
$TiSi_2$ (C54)	13–16	700–900	~900	450	2.27	2.51	0.58
$TiSi_2$ (C49)	60–70	500–700			2.27	2.51	
Co_2Si	~70	300–500			0.91	1.47	
CoSi	100–150	400–600			1.82	2.02	
$CoSi_2$	14–20	600–800	~950	400	3.64	3.52	0.65
NiSi	14–20	400–600	~650		1.83	2.34	
$NiSi_2$	40–50	600–800			3.65	3.63	0.66
WSi_2	30–70	1000	~1000	500	2.53	2.58	0.67
$MoSi_2$	40–100	800–1000	~1000	500	2.56	2.59	0.64
$TaSi_2$	35–55	800–1000	~1000	500	2.21	2.41	0.59

differ from that of pure Si. They can be represented by the linear–parabolic growth law

$$x^2 + Ax = B\,(t + \tau) \tag{20.2}$$

where x is the oxide thickness, t the oxidation time, B the parabolic rate constant, B/A the linear rate constant, and τ a fitting parameter that takes into account the initial transient oxide growth. Table 20.8 lists the growth kinetics of silicides. There are some discrepancies between different studies of the same silicides, but the overall differences between various silicides cannot be explained by details of the silicide preparation method. What then is the origin of these differences? An analysis of the results leads to the following observations:

(i) The parabolic rate constant is the same for constant oxidizing conditions, regardless of the substrate (single crystalline Si, polycrystalline Si) or the silicide. The rate constant is equal to that observed for pure Si under similar oxidizing conditions (wet or dry). Variations in the partial pressure of water vapor can explain the remaining differences for wet oxidation. The conclusion is that the diffusion process through the oxide is the same for all combinations of Si substrates and silicides. This also implies that the physical properties of the oxide are similar. The dissimilarities in the oxidation rates listed in Table 20.8 thus originate in the linear terms of the growth law.

(ii) The linear term in the growth law can be related with three processes: the mass transport by diffusion across the silicide of fixed thickness and the reactions of the two interfaces of the silicide layer, i.e. the formation of SiO_2 at the silicide/SiO_2 interface, and the transfer of Si from the Si substrate into the silicide layer at the Si/silicide interface. This latter process is similar in nature to the reaction that takes place during the formation of a silicide by thermal annealing of a metallic film with a Si substrate. In those reactions, at low temperatures at which they can be analyzed in detail (~300–600 °C), the transport across the growing silicide layer is the rate-limiting step in all cases where the growth law has been firmly established (with the exception of $CrSi_2$, where the growth is clearly linear in time). This says that the transfer of Si from the substrate to the silicide is not the rate-limiting step. At the low temperatures at which these facts are established (for the formation of a silicide by thermal annealing), the rate of the Si consumption is of the same order as that observed during the oxidation process listed in Table 20.8. But at those rates, the reaction at the Si/silicide interface is not rate limiting already at low temperatures; thus, it must be negligible also at the high temperature during oxidation. The cause for the dissimilar linear rate constants in the oxidation process is thus connected with differences in the oxidation process of the various silicides at the silicide/SiO_2 interface, with differences in the transport across the silicide or with both.

(iii) The observed differences in the oxide thickness caused by dissimilarities in the linear (initial) part of the oxidation can be correlated with the process of atomic transport through the silicide layer. Table 20.9 compares the dominant moving species for silicide formation by thermal reaction with a metal film and for oxidation. They are the same, with the exception of the special cases of Cr and Pd. On the assumption that only one species dominates the transport, there are two distinct limiting cases that can be distinguished, according to whether Si or metal moves.

When the metal moves, it must be supplied from the dissociation of the silicide at the silicide/SiO_2

Table 20.8 Kinetics of SiO_2 growth by thermal annealing of silicide films on various substrates in oxidizing ambient

Silicide film	Substrate	Kinetics (x = thickness, t = time)	Condition	Rate constants at temperature (°C)		
				B/A (cm s^{-1})	B (cm^2 s^{-2})	
Si	Si <100>	$x^2 + Ax = B\,(t + \tau)$	Wet	3.5×10^{-8}	8.0×10^{-13}	1000
		$x^2 + Ax = B\,(t + \tau)$	Dry	2.0×10^{-9}	3.3×10^{-14}	1000
$TiSi_2$	Si <Si amorphous>	$x^2 + Ax = B\,(t + \tau)$	Wet	5.6×10^{-8}	6.4×10^{-13}	1000
$TiSi_2$	Si <poly>	$x^2 + Ax = B\,(t + \tau)$	Wet	6.6×10^{-8}	6.4×10^{-13}	1000
$CoSi_2$	Si <111>	$x^2 = Bt$	Wet		5.1×10^{-13}	1000
	<100>	$x^2 = Bt$	Dry		3.1×10^{-14}	1000
$NiSi_2$	Si <111>	$x^2 = Bt$	Wet		2.2×10^{-13}	900
	Si <100> Si <poly> SiO_2	$x^2 = Bt$	Dry		1.1×10^{-14}	900
$MoSi_2$	SiO_2	$x^2 + Ax = B\,(t + \tau)$	Dry	2.8×10^{-9}	1.9×10^{-14}	1000
$MoSi_2$	Si <100>	$x^2 + Ax = Bt$	Wet	1.2×10^{-7}	1.0×10^{-12}	1000
RhSi	Si <100>	$x^2 + Ax = Bt$	Wet	1.1×10^{-7}	1.0×10^{-12}	1000
Rh_3Si_4	Si <111>	$x^2 + Ax = Bt$	Wet	1.0×10^{-7}	1.0×10^{-12}	1000
$TaSi_2$	Si <poly>	$x^2 = Bt$	Wet		1.4×10^{-13}	1000
	Si <poly> Si <100> <111>	$x^2 = Bt$	Dry		2.8×10^{-14}	1000
$TaSi_2$	Si <111>	$x^2 + Ax = Bt$	Wet	8.2×10^{-8}	1.0×10^{-12}	1000
WSi_2	Si <poly>	$x^{1.82} = B^*t$	Wet		$B^* = 4.4 \times 10^{-12}$[a]	1000
	SiO_2	$x^{1.82} = B^*t$	Wet		$B^* = 6.9 \times 10^{-12}$[a]	1000
WSi_2	Si <(poly)>	$x^2 + Ax = Bt$	Wet	1.3×10^{-7}	6.8×10^{-13}	1000
$IrSi_{1.75}$	Si <111>	$x^2 + Ax = Bt$	Wet	5.8×10^{-8}	8.5×10^{-13}	1000

[a]Units of B^* are in centimeters and seconds with appropriate powers.

Source: Adapted from Bartur and Nicolet (1984).

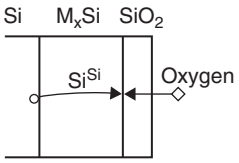
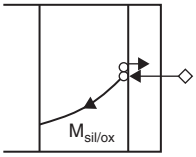
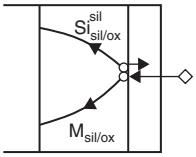
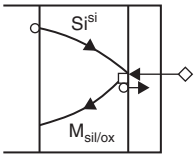
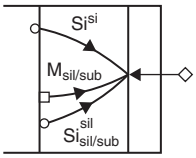
Table 20.9 Dominant diffusion species during silicide formation and oxidation

Silicide	Dominant diffusion species during the following processes	
	Silicide formation	Silicide oxidation
$TiSi_2$	Si	Si
$CoSi_2$	—	Co
$NiSi_2$	Ni	Ni
Pd_2Si	Si, Si and Pd	Si
PdSi	Pd and Si	Pd
PtSi	Pt	Pt
$CrSi_2$	Si	Cr

Source: Adapted from Bartur (1983).

interface as a result of the oxidation process. At the elevated temperatures of oxidation, the metal transport process is quite fast, as it is known from silicide formation reactions with metal films, whose rates are similar at lower temperatures. If the dissociation process at the silicide/SiO_2 interface is very effective, the oxidation process will be controlled only by the oxygen arrival at the interface, and the linear term in the growth equation should be negligible. Experiments indeed confirm this scenario for $CoSi_2$ and PdSi. When the dissociation process is so effective that it produces an excess of weakly bonded metal and Si at the interface, the possibility of an additional transport of Si down to the substrate, in parallel to the transport of metal, also arises. In this case, both atomic species participate in the mass transport. This situation has been identified for $CrSi_2$, $NiSi_2$, and PdSi. Note that the cases of $CoSi_2$ and PtSi differ from these three cases only quantitatively in that the Si transport may be too small to be measured for $CoSi_2$ and PdSi. Qualitatively, these five silicides are all similar. One would expect that these conditions of ready dissociation and rapid mass transport through the silicides favor the highest possible oxidizing rates. Indeed, the silicides that dissociate during oxidation ($CoSi_2$, $NiSi_2$, PdSi, PtSi) have the highest oxidation rates. Note that the lowest eutectic temperature in the Pt–Si system is 830 °C; oxidation studies performed at 750 °C yield a combined linear and quadratic growth law. From the point of view of low temperature

Table 20.10 The different possible movements for mass transport during silicide oxidation

Moving species during oxidation	Schematic description		Experimental results
Si →		Si supply	$TiSi_2$ Pd_2Si
M ←		Dissociation	$CoSi_2$ PdSi
M ← Si ←		"Excess" dissociation	$CrSi_2$ $NiSi_2$ PtSi
M ← Si →		Dissociation and Si supply	
M → S →		Si supply causes metal release and diffusion	
M → Si ← M → Si ←	These processes do not preserve the silicide		

Source: Adapted from Bartur (1983).

processing, the near-noble metal silicides are thus preferred candidates for IC interconnections. These results are summarized in Table 20.10. It is seen that there are two additional transport cases that are conceivable when both species move and the silicide layer is preserved during oxidation. These cases have not been seen experimentally.

The second limiting case is represented by $TiSi_2$. Silicon is the main diffusion species there. The transport of Si across $TiSi_2$ is one of a few cases where the diffusion mechanisms have been identified for the silicide formation by reaction with a Ti film using radioactive tracers. The Si diffuses from the substrate by a process that involves the atoms in the silicide lattice (e.g. by Si vacancies). In this case, dissociation of the silicide needs to occur. In the initial phase of the oxidation, where the supply of oxygen is high because the oxide layer is thin, the reaction at the silicide/SiO_2 interface reduces the overall rate of oxidation, and the linear rate constant B/A begins to be important as well. As a result, the growth is slowed down initially as compared with the previous limiting case.

There are uncertainties in the reported values of the linear rate constant for different silicides, because the measurements are difficult to be done accurately. It is nonetheless clear that for both wet and dry oxidation, the linear rate constant is higher for silicides than it is for silicon. The observation can be linked to the metallic properties of the silicides.

An electron transfer process in one or several of the steps of the oxidation reaction at the interface can readily alter and accelerate the reaction. That electron transfer process is more probable when the surface is metallic than when semiconducting. Support for this idea is provided by the wet oxidation of Ir_3Si_5. This silicide is known to be a semiconductor. Its linear rate constant is indeed larger than that of silicon but smaller than that of the metallic silicides. The actual processes that determine the value of the linear rate constant for oxidation of different silicides on silicon remain to be established. This subject is one of the main open issues of silicide oxidation that awaits clarification.

(iv) Thermodynamically, the formation of pure SiO_2 is the expected outcome for all but a few silicides. The available thermal data are uncertain and incomplete. From estimates of the standard heats of reaction, only $ZrSi_2$ and $HfSi_2$ are not expected to form SiO_2, but metal oxide instead, and $TiSi_2$, $NbSi_2$, and $TaSi_2$ are marginal cases. $HfSi_2$ and $NbSi_2$ have indeed been reported to disintegrate and to form a mixture of metal and Si oxides. $TiSi_2$ forms SiO_2 also but seems to do so only above 900 °C. Recent ternary phase diagrams for Ti, Ta, Mo, and W also predict that with excess Si, SiO_2 is in equilibrium with the disilicides of these metals. The general conclusion is that the thermodynamical argument correctly predicts the general oxidation behavior and identifies the marginal cases. The appearance of SiO_2 is thus not the result of kinetic limitations at the silicide/SiO_2 interface, but indicates instead that the reaction is there controlled by constraints of thermal equilibrium.

These considerations suggest that silicides in which the metal is the dominant moving species offer an advantage over the others when low temperature oxidation is desired, but other considerations, such as the diffusion of metal atoms from the silicide into the Si substrate or the electrical resistivity of the silicides, are important in practical applications as well.

20.3.2 Oxidation of Silicides on SiO_2

When the substrate cannot be oxidized, as in the case of SiO_2, the metal to silicon ratio increases as the oxidation proceeds. In those cases that have been most studied ($NiSi_2$ and $CoSi_2$), the system evolves slowly enough that thermal equilibrium prevails. The ternary phase diagram then will predict if and when the metal will begin to oxidize, even when this does not occur in the presence of excess silicon. When a tieline connects a particular silicide to a metal oxide, the pure metal and SiO cannot coexist at thermal equilibrium. In such a case, a metal oxide begins to form when sufficient silicon has been extracted from the silicide layer into the SiO_2 to increase the metal to silicon ratio to that of the particular silicide. Titanium and tantalum are examples of this type. When $TiSi_2$ is transformed beyond Ti_5Si_3, titanium oxides begin to form. On the other hand, if a tieline connects the metal to SiO_2, it becomes possible to reduce the silicide film to an elemental metal. It has been proposed that metallic interconnection lines could be formed in this manner, in a way that would be quite compatible with existing polycide technology. Two difficulties need to be overcome to carry out such a scheme with $NiSi_2$ or $CoSi_2$. Firstly, silicon must be extracted from the metal to levels below 1 at.% (less than 10% of the solid solubility limit); otherwise the electrical resistivity of the metal approaches or even exceeds that of the original silicide. Secondly, the metal film tends to break up into islands, which can interrupt the electrical continuity of a line. It remains to be established if these difficulties are general to all metals that can coexist in equilibrium with SiO_2.

Several reviews discussing silicides, their properties, and their application to VLSI technology contain sections on oxidation of silicides (see Further Reading).

20.4 Naphthenic Acid Corrosion in Petrochemical Plants

New technologies and processes that are being applied in the petrochemical industry are requiring higher operating temperatures and pressures of the process units. Therefore, catastrophic consequences such as firing and/or explosion might be caused by the failures initiated by severe corrosion and oxidation attacks of the materials. The major high temperature corrosion attacks in the petrochemical industry include high temperature oxidation, high temperature sulfidation, high temperature naphthenic acid corrosion, and high temperature carburization. Extensive studies and tests on these problems at a laboratory scale have been reported, but the acquired knowledge is not sufficient to guide field corrosion protection practice. Thus the rational selection of materials for the construction of processing units based on the analyses of the nature of the materials and their actual operating conditions is the key to controlling high temperature corrosion.

Oxidation, sulfidation, and carburization are three types of phenomena that are treated in Chapters 7–9 of this book. Here, we will only consider two case studies of naphthenic acid corrosion.

Naphthenic acid in crude oils is a rather complex mixture, with a saturated ring structure and a molecular weight ranging from 180 to 700. Its content is usually expressed by the total acid number (TAN; as milligrams of KOH required to neutralize the acid in 1 g of oil).

During the refining processes, naphthenic acid is heated, distilled, vaporized, and condensed. Then it can dissolve into the distillate oil, resulting in corrosion problems. Particularly at temperatures higher than 240 °C, serious corrosion reactions take place:

$$2RCOOH + Fe \rightarrow Fe(COO)_2 + H_2 \quad (20.3)$$

$$FeS + 2RCOOH \rightarrow Fe(COO)_2 + H_2S \quad (20.4)$$

Iron naphthenate, the product of naphthenic acid corrosion, is oleo-soluble; therefore, the corroded metal surfaces are normally clean and free of scales. In the regions with high temperature and high flow velocity, naphthenic acid corrosion will result in the formation of shape-edged streamline grooves along the flow direction. In the areas with low flow velocity, shape-edged pits will be formed. Since $Fe(COO)_2$ can dissolve into oils and then be removed easily by the flowing media, it is difficult to form protective scales on the metal surface. Even FeS formed on the surfaces can react with naphthenic acid: fresh metallic surfaces will be exposed to the corrosive media, and corrosion can proceed continuously.

TANs of the crude oil and the distillate oil are the key factor to evaluate high temperature naphthenic acid corrosion. It is generally accepted that when the TAN is higher than 0.5 mg KOH g^{-1}, high temperature naphthenic acid corrosion will occur. Since naphthenic acid exists together with other oils that have similar boiling points, only the actual acid number of the distillate oils can determine the corrosivity and the corrosion rate. Under atmospheric distillation conditions, the highest acid number of the distillate oil will be shown in the temperature range of 371–426 °C and at 260 °C in vacuum distillation towers.

Two case studies in high temperature naphthenic acid corrosion that deserve description are those with high TAN and low sulfur and those with high TAN and high sulfur.

20.4.1 High TAN/Low Sulfur Environment

In the atmospheric and vacuum units of a refinery, in which heavy crude oils with sulfur lower than 0.5% and TAN of about 3.0 mg KOH g^{-1} were processed, severe corrosion was observed. Localized corrosion, consisting of a lot of pits, was formed on the inner wall of the tower wall on the third floor, manufactured by using carbon steel and 316L stainless steel. Collapse of the packing materials (316L SS) of the fourth floor led to a high hole, and the oil collection tank on the third floor was also corroded. Failure analysis showed that (i) the TAN of the vacuum distillate oil might be quite high resulting in an increase of the concentration of the corrosive medium and then an increase of naphthenic acid corrosion rate, (ii) FeS scales cannot be formed on the metal surfaces since the sulfur content is low, (iii) the vacuum distillation system is in the state of negative pressure operation, and (iv) the electric desalting and alkali injecting process might not work very well, being unable to decrease the concentration of the corrosive medium in the oil to a low level to decrease the corrosion rate. To control the corrosion, it was suggested to change the packing materials of the third/fourth floors and the oil collection tank, and the desalting/injection processes should be improved to decrease the content of the corrosive media in the oils to inhibit the corrosion process.

20.4.2 High TAN/High Sulfur Environment

The average TAN of another refinery was 1.0 mg KOH g^{-1}, the sulfur content was 0.8%, and the density was 0.9 g cm^{-3}. The packing/component materials were 304 SS. Collapse of the packing materials on the second floor due to corrosion was observed, as well as holes on the bottom of the oil collection plates. Most packing material on the fourth floor was corroded. Failure analysis showed that since 304L has a relatively low resistance to these corrosion processes, severe attack occurred. In addition, higher loads in the vacuum distillation system and very high velocity of the processing media contributed to the severe corrosion. It was suggested that all the packing materials should be upgraded to 316L SS; moreover, the oil collection tank should be changed, and the load and velocity of flow should also be decreased.

As illustrated by these two case studies, corrosion by naphthenic acids is a complicated process, and the research studies published in the open literature are not enough to explain the corrosive behaviors. Although it was found that the presence of naphthenic acids would lead to the formation of a protective iron oxide or magnetite layer, more questions relating to this issue arise and need further investigation:

1. The formation mechanism of iron oxide layer should be investigated in detail. Although it has been indicated that decomposition of iron naphthenates might result in magnetite, preliminary experimental results suggested that the steel had to be corroded before a protective layer could be formed.
2. Factors determining the protectiveness of iron oxide layer should be examined. Sulfur compounds, naphthenic acid structures, metallurgy, and temperature were expected to be important factors.
3. The layer protectiveness should be explored using a wider range of parameters. Although the iron oxide layer was protective in the challenge with TAN up to 3.5 at 343 °C, it was conceivable that the layer would fail if TAN and temperature were high enough.

Moreover, the layer protectiveness against sulfidation should be investigated.

4. The actual corrosion models should be improved. The overestimation relating to challenge corrosion rates should be addressed.

Apart from this kind of recommendations for future work on this issue, techniques to control high temperature naphthenic acid corrosion must be developed and rapidly implemented. For example, during operation the corrosion rate of the equipment should be monitored regularly to ensure that the processing units can run safely; high velocity of flow and occurrence of turbulence should be avoided in engineering design and practical operation; the TAN of crude oils can be decreased through suitable mixing processes, i.e. addition of crude oils with a low TAN into crude oils with a high TAN may obtain a mixed crude oil with a low TAN, which partly solves the naphthenic corrosion.

Surface modification is also one of the effective ways to improve the resistance of carbon steels against high temperature naphthenic acid corrosion. Therefore, some components in the vacuum distillation towers can be built by using carbon steels with suitable aluminizing treatments.

Currently, Mo-containing 316 SS and 317 SS (>2.5% Mo) are the best materials against high temperature naphthenic acid corrosion. However, in the regions with high-speed flowing media or strong impacts, even 316 SS will suffer severe attack.

20.5 Oxidation of Ceramic Matrix Composites

The class of monolithic and composite ceramic materials termed engineering, technical, or advanced ceramics exhibits an attractive range of properties relative to metallic counterparts commonly used in a number of high temperature applications. In particular, retention of mechanical properties to temperatures in excess of 1200 °C presents the opportunity to plant designers to increase operating temperatures, improve process efficiencies, and reduce the levels of emitted pollutants. Lower densities of ceramic materials than competing metallic counterparts permit the achievement of higher specific strength and thus increased pay loads and reduced energy consumption. Advanced ceramics are thus attractive candidate structural materials for use in energy production and conversion and in engines. Continued progress to actual adoption in commercial installations has been hindered mainly by poor mechanical reliability and uncompetitive production costs. Advances in manufacturing technology are yielding improvements in mechanical performance and gradually reducing the cost of production. While the financial systems for determining cost are well developed and understood, the judgment of component reliability is dependent on the availability of a solid base of valid materials test data.

Independently of these issues, it is a fact that structural ceramics are finding more and more applications in high temperature systems, as shown in Table 20.11, and therefore oxidation and corrosion at high temperatures becomes an important field of study. Ceramics can be classified according to the type of protective oxide they form. These include silica formers (SiC, Si_3N_4), alumina-forming non-oxides (AlN, Al_4C_3), and boria-forming ceramics (BN). Next, transition metal carbides and nitrides that form the corresponding transition metal oxides, as well as the ceramics that form the mixed oxide scales, are also deserving attention. Finally, the oxidation of ceramic matrix composites (CMCs), which involves several parallel processes, is an important current area of research. These CMCs are the most promising ceramics today for high temperature structural applications. They include whiskers, particulates, and continuous fillers in a ceramic matrix to impart improved fracture toughness. Most of the current research on CMCs is focused on SiC inert fiber coatings in matrices of oxides, Si_3N_4, or SiC. The most adequate coatings are graphite carbon and boron nitride. Thus, the entire composite has a slowly oxidizing phase (fibers and matrix) and an easily oxidizable phase (fiber coating). Generally, at high temperatures, SiO_2 rapidly forms on the outside of the matrix, and attack of the fiber coating is minimized. Even a matrix crack may quickly seal. However, at intermediate (500–1000 °C) temperatures, silica forms very slowly, and oxidative attack of the fiber coating becomes a critical issue. The most thorough treatment of this problem is from Filipuzzini (1994) for carbon-coated SiC fibers in a SiC matrix. The initial treatment consisted of a matrix with unidirectional fibers with one end exposed. The process consisted on a two-step oxidation of carbon and concurrent oxidation of the fiber and surrounding matrix. As carbon oxidizes, an annular region around the fiber is left. Filipuzzini first measured oxidation properties of each of the constituent parts of the composite as well as the composite as a whole. Standard thermo-gravimetric analysis (TGA) methods and resistivity measurements gave an indication of the amount of carbon consumed. These data were used in an overall description of the composite oxidation. By introducing analytical models with appropriate boundary conditions, it was possible to generate TGA oxidation curves, indicating that thinner carbon coatings give better performance. This analysis has been extended to other situations. For example, the examination of the oxidation of SiC matrices with carbon fibers indicated that the low temperature oxidation is kinetically controlled by reaction of oxygen with the fibers and high temperature oxidation is diffusion controlled by diffusion of oxygen to

Table 20.11 Current uses of ceramics

Application	Ceramics	Approximate use temperatures (°C)	Environment
Turbine engine components, combustor liners, blades, and vanes	SiC, Si_3N_4, composites	900–1400	Combustion gases, deposits: Na, Mg, Ca sulfates, sodium vanadates
Piston engine components, pistons, valves	SiC, Si_3N_4, composites	900–1400	Combustion gases
Industrial furnaces, heat exchangers	SiC, composites	900–1400	Combustion gases, various deposits
Coal combustion, particle filters	SiC, composites	700–1000	Combustion gases, slag deposits
Chemical process vessels, coal gasifiers, waste incinerators	SiC, Si_3N_4, composites	900–1400	Various gases: air, H_2S, HCl
Re-entry shields	SiC, composites	1000–1800	Reduced pressure: N_2, O_2, CO_2, N, O
High temperature semiconductors	SiC	Use: 600 Processing: 1200	Air
Electronic substrates	AlN	Use: 600 Processing: 1200	Air
Fiber coatings for composites, crucibles, insulators	BN	900–1400	Fiber coatings: reduced pressure combustion gases, crucibles, vacuum, inert gases
Rocket engine throats	HfC, ZrC	1500–2000	H_2/O_2 combustion products
Liquid metal containers, processing and heat transfer	Transition metal carbides	600–1400	Vacuum or inert gas and liquid metals

the fibers. Finite difference models of this process were developed.

The other commonly used fiber coating is hexagonal BN. There are several important phenomena in the oxidation of a silicon-based composite with BN fiber coatings. As the silicon-based material and the BN oxidize, both B_2O_3 and the SiO_2 form. These react to form low-melting borosilicate melts. Related to this, boron enhances the oxidation of silica-forming materials. Also, water vapor readily reacts with B_2O_3 oxidation product and forms volatile $H_xB_yO_z$ (g) species, which leads to effective volatilization of BN. However, unlike carbon volatilization, distinct interfaces are not formed with the BN. Rather there is a "plug" of borosilicate formed and a gradual transition from oxide to nitride. Jacobson, in 1999, described a model that explains the formation of this borosilicate plug, based on gas-phase diffusion of the $H_xB_yO_z$ (g) species outward and boron-enhanced oxidation of the SiC. Exposures of the SiC fiber to BN fiber coatings in a SiC matrix were conducted at 700 and 800 °C in 1 and 10% H_2O/O_2 atmospheres with one end of the test sample ground off to expose the fiber ends and coatings. Then recession distances were measured, but exact distances were difficult to determine as interfaces were not always sharp. Therefore, an adjustable parameter of boron-influenced SiC oxidation rates had to be introduced. Using substantially enhanced oxidation rates, reasonable agreement between the model and experimentally measured recession distances was obtained. Nowadays, the oxidation of CMCs continues to be a major issue because these ceramics are finding novel applications and are being exposed to more complex corrosive environments.

20.6 Shell Corrosion of Rotary Cement Kilns

The subject of reinforcement corrosion is widely described in the open literature, but descriptions of corrosion that occurred in dry-process, rotary, cement-clinker kilns and other structures producing cement seldom appear in literature. Here we describe observed corrosion of kiln shells reported by Potgieter, in 2004, which occurred at two rotary cement kilns, in South Africa.

A rotary cement kiln can be seen as a complex chemical reactor with various temperature zones and differing container wall constituents in the different temperature zones. Further on, the number of preheaters, raw material composition, and operating conditions can all influence the corrosion occurring in a rotary cement kiln. The chemical composition of the raw material used and type of refractory used are the main variables contributing to corrosion. Chlorine, sulfur, and alkalis are usually present in the kiln, leading to the production of low-melting eutectics

that, in combination with the oxidizing atmosphere that exists in the kiln, are aggravating factors that can further salt infiltration into the refractory and ultimately hasten corrosion that occurs on the kiln shell.

In practice, the observed corrosion processes are similar to those occurring in steam boiler walls that are covered with deposits; thus the kiln acts as a wall deposit. The iron from the steel shell, in contact with the oxidizing atmosphere, originates several iron oxides (Fe_3O_4 in particular) with hematite (Fe_2O_3) at the scale–brick interface. Sulfur from the fuel can react in the oxidizing atmosphere of the kiln to produce SO_2 and SO_3 acid gases. In the oxygen-restricted environment between the refractory lining and the kiln shell, it is conceivable that SO_2 or SO_3 can act as the oxygen donors and react with the iron giving further magnetite (Fe_3O_4) and iron sulfides (troilite, FeS; pyrite, FeS_2).

The corrosion scales examined in this case study were removed from two shells of two kilns during maintenance when the dolomite bricks in the transition zones were replaced. The scales were brittle and porous with a layered brownish appearance and a few salt crystals. Kiln 1 was a long (140 m) dry-process rotary furnace with only one preheater at the feed end; kiln 2 was a short (85 m) kiln furnace with five preheaters fixed at the feed end of the kiln. In both kilns, corrosion occurred in the transition zone at about 30 m from the coated clinkering zone. Chemical analyses of the corrosion products of the kiln shell showed high concentrations of both chloride and potassium, suggesting a chloride type of attack; the corrosion products from kiln 2 shell showed high sulfate and calcium concentrations, suggesting a sulfur-dominant type of corrosion attack. The positive identification of $CaSO_4$ observed by X-ray diffraction (XRD) could be explained by an excess of sulfur oxides present in kiln 2 atmospheres and their penetration through the refractory lining; it was essentially sulfidation corrosion. The other corrosion products showed elevated KCl concentration. Whereas chlorine gas can react with the kiln 1 shell, the alkalis can only penetrate the refractory brick lining as part of a salt melt that in rotary cement kilns is conceivable to occur at about 350–400 °C. Therefore, the situation is typical of hot corrosion processes. The severe problem is made worst by the practice, at this plant, of recirculating kiln and dust from the electrostatic precipitators, a dust that is rich in alkalis originating from raw materials of high alkali content. Potgieter and his collaborators recommended (i) to use a denser brick (e.g. magnesia–zirconia and magnesia-enriched dolomite), (ii) to avoid the recycling kiln dust to the raw meal, and (iii) to consider a chloride or alkali bypass.

20.7 Corrosion of Steels in a Linear α Olefin Plant

Linear α olefins (LAOs) are a range of industrially important α olefins, which are commonly manufactured by oligomerization of ethylene and by Fischer–Tropsch synthesis followed by purification. HCl formation during α-SABLIN (LAOs) commercial plant operation is the main reason for the production of organic chloride as well as of alkylated toluene by Friedel–Crafts alkylation reaction. The HCl and organic chloride affect the product quality originating gross corrosion at the separation section downstream. Consequently, the LAO plant is subjected to many inspection shutdown, which, in turn, affect the sustainability of the plant operation.

Steel materials, namely, carbon steel (CSA516-70) and ferritic (SS410) and austenitic (SSS304L) stainless steels, are currently used in the construction of the α-SABLIN commercial plant, and, therefore, Amin et al., at Saudi Arabia and Egypt (2014), published a case study on this issue, comparing the high temperature corrosion behavior of these three alloys in an autoclave at 270 °C and 29 bar to select the proper alloys to be used as a construction material for the most vital parts of the SABLIN's plant. Alloy samples and plant solution were prepared by traditional means and then subjected to immersion tests of different duration (3–30 days). Corrosion rates were calculated by thermogravimetry, and the corrosion products were analyzed by OM, SEM, and XRD. It was observed that at any given immersion time, the corrosion rate of the three tested samples decreased following the order CSA516 ≫ SS410 ≫ SS904L. It was also revealed that the average corrosion rates of CSA516 and SS410 follow the kinetics of zero-order reaction, up to 14 days of immersion, deviation from zero-order kinetics being quite clear at larger immersion (30 days of immersion). For SS304L, the kinetics of zero-order reaction was observed over the entire immersion time, as the alloy's surface is almost free from corrosion products, even after 30 days of immersion in the corrosion test solution. XRD patterns of the corrosion products of alloys CSA516, SS410, and SS304L displayed the presence of goethite (α-FeOOH), $FeCl_2$, Fe_3O_4, and γ-Fe_2O_3 in the case of CSA516; goethite (α-FeOOH), $FeCl_2$, Fe_3O_4, γ-Fe_2O_3, Fe, and Fe_2O_3/$(Fe,Cr)_3$ in the case of SS410; and goethite (α-FeOOH), Fe_3O_4, Fe, Fe_2O_3/$(Fe,Cr)_3O_4$, and (Fe, Ni) in the case of SS304L. $FeCl_2$ was not detected by the XRD of SS304L, meaning that the corroded surface is free of it, that is, its corrosion resistance is higher. The optical etched image of CSA516 showed the presence of ferrite and pearlite multiphase structure. The presence of ferrite grains and pearlite grains (which are also mechanical mixtures of lamellar ferrite and lamellar iron carbide or cementite) creates galvanic cells, thus enhancing the corrosion process. The chromium

in SS410 (>12%) and SS304L (>18%) combines with oxygen in the atmosphere to form a thin, invisible layer of chrome-containing oxide passive film, as confirmed from the formation of $(Fe,Cr)_3O_4$ phase. The high carbon content of alloy SS410 (C = 0.15%), as compared with that of SS304L (C = 0.03%), gives a real chance for this alloy to form Fe and Cr carbides in its microstructure. These carbides also decrease the corrosion resistance of alloy SS410 as compared with SS304L. Furthermore, the low Cr and Ni contents of alloy SS410, in addition to its high carbon content, as compared with SS304L, are the most likely reasons why SS410 recorded corrosion rates higher than those of SS304L. SEM images showed that the corrosion products accumulate on the surfaces of the carbon steel and the ferritic stainless steel, the austenitic stainless steel being free from corrosion products. But shallow pits were observed on its surface, probably due to the presence of the aggressive chloride ions. In summary, it was found that SS304L recorded the highest corrosion resistance among the tested samples, taking into account its high Cr and Ni contents and the high stability of $(Fe,Cr)_3O_4$. The high C content and low Cr and Ni contents are the reasons why SS410 recorded corrosion rates higher than those of SS304L. The presence of ferrite grains in contact with pearlite grains in the microstructure of CSA516 creates galvanic cells that explain its low corrosion resistance. The roughness of the surfaces of the three tested samples, examined by OM/SEM, justified the previous findings.

References

Amin, M.A., Mohsen, Q., Mostafa, N.Y. et al. (2014). *Int. J. Electrochem. Sci.* 9: 2631.

Bartur, M. (1983). *Thin Solid Films* 107: 55.

Bartur, M. and Nicolet, M.A. (1984). *J. Electrochem. Soc.* 131: 371.

Filipuzzini, L., Camus, G., Naslain, R., and Thebault, J. (1994). *J. Am. Ceram. Soc.* 77: 459.

Jacobson, N.S., Morschen, G.N., Bryant, D.R., and Tressler, R.E. (1999). *J. Am. Ceram. Soc.* 82: 1473.

Potgieter, J.H., Godoi, R.H.M., and van Grieken, R. (2004). *J. South Afr. Inst. Min. Metall.* 14: 603.

Further Reading

Amin, M.A., Khaled, K.F., Mohsen, Q., and Arida, H.A. (2010). *Corros. Sci.* 52: 1684.

Borisenko, V.E. (ed.) (2000). *Semiconducting Silicides*. Berlin: Springer-Verlag.

Burt, V. (ed.) (2015). *Corrosion in the Petrochemical Industry*, 2e. Materials Park, OH: ASM International.

Cardwell, D.A. and Ginley, P.S. (eds.) (2003). *Handbook of Superconducting Materials*. Bristol: Institute of Physics Publishing.

Charles, J.A., Crane, F.A.A., and Furness, J.A.G. (1997). *Selection and Use of Engineering Materials*, 3e. London: Butterworth-Heinemann.

Chirkin, A.D., Lavrenko, V.O., and Talash, V.M. (2009). *Powder Metall. Met. Ceram.* 48: 330.

D'Heurle, F. (1995). *J. Phys. III* 5: 1707.

Einspruck, N.G., Cohen, S.S., and Gildenblatt, G.S. (eds.) (1987). *VLSI Metallizaton*. London: Pergamon Press.

El Kamel, M., Galtayries, A., Vermont, P. et al. (2010). *Surf. Interface Anal.* 42: 605.

Embury, J.D. (ed.) (1990). *Proceedings of the International Symposium on High Temperature Oxidation and Sulphidation Processes*. Toronto: Pergamon Press.

Fordham, R.J. (ed.) (1990). *High Temperature Corrosion of Technical Ceramics*. London: Elsevier.

Gandhi, S. (1994). *VLSI Fabrication Principles*. New York: Wiley.

Guo, J., Yang, S., Shang, C. et al. (2008). *Corros. Sci.* 51: 242.

Hull, D. and Clyne, T.W. (1996). *An Introduction to Composite Materials*, 2e. Cambridge: Cambridge University Press.

Jacobson, N.S. (1993). *J. Am. Ceram. Soc.* 76: 3.

Jones, E.S. and Østergard, M.J.L. (1999). *ZKG. Int.* 52: 68.

Kittel, C. (1996). *Introduction to Solid State Physics*, 7e. London: Wiley.

Kofstad, P. (1988). *High Temperature Corrosion*. London: Elsevier.

Kurokawa, K. and Yamauchi, A. (2007). *Solid State Phenom.* 127 (227).

Landsberg, P.T. (ed.) (1992). *Basic Properties of Semiconductors*, Handbook of Semiconductors, vol. 1. Amsterdam: Elsevier.

Lappin, G. (1989). *Alpha Olefins Applications Handbook*. Boca Raton, FL: CRC Press.

Madou, M. (1997). *Fundamentals of Microfabrication*. Boca Raton, FL: CRC Press.

McEvily, A.J. (2002). *Metal Failures*. London: Wiley.

Murarka, S.P. (1983). *Silicides for VLSI Applications*. New York: Academic Press.

Murarka, S.P. (1995). *Intermetallics* 3: 173.

Nagase, M., Horiguchi, S., Shiraishi, K. et al. (2003). *J. Electroanal. Chem.* 559: 19.

Narushima, T., Goto, T., Hirai, T., and Iguchi, Y. (1997). *Mater. Trans., JIM* 38: 821.

Nickel, K.G. (ed.) (1994). *Corrosion of Advanced Ceramics*. Dordrecht: Kluwer Academic Publishers.

Oh, B.H., Jang, Y.S., and Shin, Y.S. (2003). *Mag. Concr. Res.* 55: 117.

Potgieter, J.H. (1997). *S. Afr. J. Chem.* 50: 111.

Probst, M.B. (1986). *Ceramic Components for Engines*. London: Elsevier.

Qian, K., Robbins, W.K., Hughey, C.A. et al. (2001). *Energy Fuels* 15: 1505.

Qu, D.R., Zheng, Y.G., Jing, H.M. et al. (2006). *Corros. Sci.* 48: 1960.

Rapp, R.A. (1983). *High Temperature Corrosion*. Houston, TX: NACE.

Redl, F.X., Black, C.T., Papaefthymiou, G.C. et al. (2004). *J. Am. Chem. Soc.* 126: 14583.

Saxena, J.P. (2003). *Refractory Engineering and Kiln Maintenance in Cement Plants*. New Delhi: Tech Books International.

Schroder, D. (1990). *Semiconductor Material and Device Characterization*. London: Wiley.

Seeger, K. (2002). *Semiconductor Physics: An Introduction*. Berlin: Springer.

Shewmon, P.G. (1989). *Diffusion in Solids*, 2e. Warrendale, PA: TMS AIME.

Stott, F.H., Wood, G.C., and Stringer, J. (1995). *Oxid. Met.* 44: 113.

Strausser, Y.E. (ed.) (1993). *Characterization in Silicon Processing*. Boston, MA: Butterworth-Heinemann.

Sze, S.M. (1994). *Semiconductor Sensors*. New York: Wiley.

Turnbull, A., Slavcheva, E., and Shone, B. (1998). *Corrosion* 54: 922.

Uchina, E., Fergus, J., Schiller, D. et al. (eds.) (2009). *ECS Transactions*, vol. 16, Issue 44. Pennington, NJ: The Electrochemical Society.

Yépez, O. (2007). *Fuel* 86: 1162.

Yi, B.L. (2003). *Fuel Cells*. Beijing: Chemical Industrial Press.

Young, W.C. and Budynas, R.G. (2001). *Roark's Formulas for Stress and Strain*, 7e. New York: MacGraw-Hill.

Appendix A

Table A.1 Selected elements

Elements	Symbol	Atomic number	Atomic mass (amu)	Melting point (°C)	Density (solid) (mg m^{-3} [=g cm^{-3}])	Crystal structure (20 °C)	Approximate atomic radius (nm)[a]	Valence (most common)	Approximate ionic radius (nm)[b]
Hydrogen	H	1	1.0078	−259.14	—	—	0.046	1+	Very small
Helium	He	2	4.003	−272.2	—	—	0.176	Inert	—
Lithium	Li	3	6.94	180	0.534	bcc	0.1519	1+	0.068
Beryllium	Be	4	9.01	1289	1.85	hcp	0.114	2+	0.035
Boron	B	5	10.81	2103	2.34	—	0.046	3+	~0.025
Carbon	C	6	12.011	>3500	2.25	hex	0.077	—	—
Nitrogen	N	7	14.007	−210	—	—	0.071	3−	—
Oxygen	0	8	15.999	−218.4	—	—	0.060	2−	0.140
Fluorine	F	9	19.00	−220	—	—	0.06	1−	0.133
Neon	Ne	10	20.18	−248.7	—	fcc	0.160	Inert	—
Sodium	Na	11	22.99	97.8	0.97	bcc	0.1857	1+	0.097
Magnesium	Mg	12	24.31	649	1.74	hcp	0.161	2+	0.066
Aluminum	Al	13	26.98	660.4	2.70	fcc	0.14135	3+	0.051
Silicon	Si	14	28.09	1414	2.33	[c]	0.1176	4+	0.042
Phosphorus	P	15	30.97	44	1.8	—	0.11	5+	~0.035
Sulfur	S	16	32.06	112.8	2.07	—	0.106	2−	0.184
Chlorine	Cl	17	35.45	−101	—	—	0.101	1−	0.181
Argon	Ar	18	39.95	−189.2	—	fcc	0.192	Inert	—
Potassium	K	19	39.10	63	0.86	bcc	0.2312	1+	0.133
Calcium	Ca	20	40.08	840	1.54	fcc	0.1969	2+	0.099
Titanium	Ti	22	47.90	1668	4.51	hcp	0.146	4+	0.068
Chromium	Cr	24	52.00	1875	7.20	bcc	0.1249	3+	0.063
Manganese	Mn	25	54.94	1246	7.2	—	0.112	2+	0.080
Iron	Fe	26	55.85	1538	7.88	bcc	0.1241	2+	0.074
						fcc	0.1269	3+	0.064
Cobalt	Co	27	58.93	1494	8.9	hcp	0.125	2+	0.072
Nickel	Ni	28	58.71	1455	8.90	fcc	0.1246	2+	0.069
Copper	Cu	29	63.54	1084.5	8.92	fcc	0.1276	1+	0.096
Zinc	Zn	30	65.37	419.6	7.14	hcp	0.139	2+	0.074
Germanium	Ge	32	72.59	937	5.35	[c]	0.1224	4+	—
Arsenic	As	33	74.92	~809	5.73	—	0.125	3+	—
Krypton	Kr	36	83.80	−157	—	fcc	0.201	Inert	—
Silver	Ag	47	107.87	961.9	10.5	fcc	0.1444	1+	0.126
Tin	Sn	50	118.69	232	7.3	bct	0.1509	4+	0.071
Antimony	Sb	51	121.75	630.7	6.7	—	0.1452	5+	—
Iodine	I	53	126.9	114	4.93	ortho	0.135	1−	0.220
Xenon	Xe	54	131.3	−112	2.7	fcc	0.221	Inert	—
Cesium	Cs	55	132.9	28.4	1.9	bcc	0.267	1+	0.167

(*continued*)

High Temperature Corrosion: Fundamentals and Engineering, First Edition. César A. C. Sequeira.
© 2019 John Wiley & Sons, Inc. Published 2019 by John Wiley & Sons, Inc.

Table A.1 (*continued*)

Elements	Symbol	Atomic number	Atomic mass (amu)	Melting point (°C)	Density (solid) (mg m^{-3} [=g cm^{-3}])	Crystal structure (20 °C)	Approximate atomic radius (nm)[a]	Valence (most common)	Approximate ionic radius (nm)[b]
Tungsten	W	74	183.9	3410	19.4	bcc	0.1367	4+	0.070
Gold	Au	79	197.0	1064.4	19.32	fcc	0.1441	1+	0.137
Mercury	Hg	80	200.6	−38.86	—	—	0.155	2+	0.110
Lead	Pb	82	207.2	327.5	11.34	fcc	0.1750	2+	0.120
Uranium	U	92	238.0	1133	19	—	0.138	4+	0.097

[a]One-half of closest approach of two atoms in the elemental solid. For noncubic structures, the average interatomic distance is given; for example, in hcp, the atom is slightly ellipsoidal.

[b]Radii for CN = 6; otherwise 0.97 $R_{CN=8} \approx R_{CN=6} \approx 1.1\, R_{CN=4}$. Patterned after Ahrens.

[c]Diamond cubic.

Table A.2 Ionization potentials of the elements (1 kcal = 4.1833 kJ = 4.3359×10^{-2} eV)

Atomic number	Element	Ionization potential (kcal g^{-1} atom)						
		First	Second	Third	Fourth	Fifth	Sixth	Seventh
1	H	313.6						
2	He	566.8	1254.5					
3	Li	124.3	1743.8	2822.5				
4	Be	214.9	419.9	3548.9	5020			
5	B	191.3	580.0	874.4	5798	7845		
6	C	259.6	562.2	1103.6	1487	9039	11 294	
7	N	335.3	682.8	1093.7	1786	2256	12 727	15 376
8	0	313.8	810.6	1266.8	1785	2626	3185	17 044
9	F	401.7	806.6	1444.7	2012	2633	3623	4628
10	Ne	497.2	947.1	1475.8	2241	2915	3641	
11	Na	118.4	1090.5	1652.2	2280	3196	3999	4806
12	Mg	176.3	346.6	1847.6	2521	3256	4310	5195
13	Al	138.0	434.0	655.8	2583	3547	4391	5578
14	Si	187.9	376.8	771.6	1041	3844	4730	4767
15	P	243.3	453.1	695.5	1184	1499	5082	6072
16	S	238.9	539.6	807.1	1091	1672	2030	6480
17	Cl	300.0	548.8	920.0	1234	1563	2230	2636
18	Ar	363.4	636.9	943.1	1379	1730	2105	2859
19	K	100.0	733.5	1060.6	1404		2299	2721
20	Ca	140.9	273.7	1180.9	1545	1946		2952
21	Sc	151.3	295.2	570.7	1704	2121	2562	3180
22	Ti	157.5	312.9	648.9	997	2301	2767	3247
23	V	155.4	337.8	684.9	1107	1504	2972	3482
24	Cr	156.0	380.2	715	1162	1685	2090	3710
25	Mn	171.4	360.6	738	1200	1750	2260	2740
26	Fe	182.2	373.1	757.0	1315	1800	2350	2950
27	Co	181.3	393.2	772.1	1220	1925	2445	3040
28	Ni	176.0	418.5	810.6	1290	1800	2540	3140
29	Cu	178.1	467.9	680.3	1358	1890	2445	3230
30	Zn	216.6	414.2	922.3	1430	1980	2580	3280
31	Ga	138.4	473.0	705.6	1471			
32	Ge	181.7	367.3	785.7	1049	2145		
33	As	226.2	465.8	645.7	1151	1441		
34	Se	224.8	495.8	781.7	985	1678	1877	
35	Br	273.0	498.1	592.6	1153			
36	Kr	322.8	566.4	848.6	1568			

(*continued*)

Table A.2 (*continued*)

Atomic number	Element	Ionization potential (kcal g^{-1} atom)						
		First	Second	Third	Fourth	Fifth	Sixth	Seventh
37	Rb	96.3	634.2	1084	1845			
38	Sr	131.2	254.4					
39	Y	147.1	282.0	470.4				
40	Zr	157.6	297.9	553.4	779	1910	2280	2720
41	Nb	158.7	320.2	558.1	882	1140	2380	2880
42	Mo	164.4	352.1	622	933	1290	1660	2880
43	Tc	166.7	342.9	668	991	1360	1750	2165
44	Ru	169.8	382.6	659	1070	1450	1870	2310
45	Rh	172.1	367.1	714	1050	1545	1960	2420
46	Pd	192.1	447.8	770	1125	1520	2070	2530
47	Ag	174.7	495.3	827.9	1198	1610	2050	2670
48	Cd	207.3	389.7	876.3				
49	In	133.4	434.2	643.4	1333			
50	Sn	169.1	337.4	703.3	909	1859		
51	Sb	199.2	438.1	569.6	1015	1280		
52	Te	207.7	495.8	703.3	869	1384	1660	
53	I	240.7	438.1					
54	Xe	279.7	489.1	737.9	1061	1753		
55	Cs	89.3	578.8	807	1176	1337		
56	Ba	120.1	230.6					
57	La	129.4	263.6	470.4				
58	Ce	159	341.3					
59	Pr	133						
60	Nd	145.3						
61	Pm	—						
62	Sm	129	258					
63	Eu	130.8	259					
64	Gd	142.0	276					
65	Tb	155						
66	Dy	157						
67	Ho	—						
68	Er	140						
69	Tm	141						
70	Yb	143	279					
71	Lu	142	339					
72	Hf	127	343	485	715			
73	Ta	178	—	515	763	1040		
74	W	184	323	555	815	1105	1405	
75	Re	182	302	600	868	1175	1475	1820
76	Os	200	346	576	920	1240	1570	1910
77	Ir	210	370	622	900	1310	1660	2030
78	Pt	208	428.0	656	946	1270	1730	2120
79	Au	212.6	472.7	692	1002	1340	1680	2210
80	Hg	240.5	432.4	791	1660	1890		
81	Tl	140.8	470.9	685	1165			
82	Pb	171.0	346.0	736	971	1600		
83	Bi	168.0	445.0	586	1040	1284		
84	Po	194						
85	At	212						
86	Rn	247.9						
87	Fr	91.8						
88	Ra	121.7	233.8					
89	Ac	158		678				
90	Th	160						
91	Pa	—						
92	U	92						

Table A.3 The periodic table of elements

Light metals												Nonmetals					Inert gases
IA																	VIIIA
H	IIA				Heavy metals						IIIA	IVA	VA	VIA	VIIA	He	
1																2	
Li	Be	←Brittle metals→					←Ductile metals→				Low melting	B	C	N	O	F	Ne
3	4											5	6	7	8	9	10
Na	Mg	IIIB	IVB	VB	VIB	VIIB	VIIIB			IB	IIB	Al	Si	P	S	Cl	Ar
11	12											13	14	15	16	17	18
K	Ca	Sc	Ti	V	Cr	Mn	Fe	Co	Ni	Cu	Zn	Ga	Ge	As	Se	Br	Kr
19	20	21	22	23	24	25	26	27	28	29	30	31	32	33	34	35	36
Rb	Sr	Y	Zr	Nb	Mo	Tc	Ru	Rh	Pd	Ag	Cd	In	Sn	Sb	Tc	I	Xe
37	38	39	40	41	42	43	44	45	46	47	48	49	50	51	52	53	54
Cs	Ba		Hf	Ta	W	Re	Os	Ir	Pt	Au	Hg	Tl	Pb	Bi	Po	At	Rn
55	56	57–71	72	73	74	75	76	77	78	79	80	81	82	83	84	85	86
Fr	Ra	Ac	Th	Pa	U	Np	Pu	Am	Cm	Bk	Cf	Es	Fm	Md	No	Lr	
87	88	89	90	91	92	93	94	95	96	97	98	99	100	101	102	103	
		La	Ce	Pr	Nd	Pm	Sm	Eu	Gd	Tb	Dy	Ho	Er	Tm	Yb	Lu	
		57	58	59	60	61	62	63	64	65	66	67	68	69	70	71	

Table A.4 Specific gravity and density of some materials

Material	Specific gravity ($g\,cm^{-3}$)	Density ($lb\,in.^{-3}$)	Density ($lb\,ft^{-3}$)
Air (STP)	0.001293	0.0000466579	0.080625
Aluminum	2.70	0.097	168.5
Antimony	6.618	0.2390	413.0
Boron	2.535	0.0916	158.2
Brass (approx.)	8.50	0.3067	530.02
Bronze (approx.)	8.75	0.3157	545.6
Cadmium	8.648	0.3123	539.6
Calcium	1.54	0.0556	96.1
Chromium	7.1	0.2562	442.7
Cobalt	8.71	0.3145	543.5
Columbium (niobium)	8.4	0.3031	523.8
Copper	8.89	0.3210	554.7
Cork	0.24	0.00866	14.9
Gasoline	0.67	2.4177	41.7
Glass (approx.)	2.5	0.0902	155.9
Gold	19.3	0.6969	1204.3
Iridium	22.42	0.8096	1399.0
Iron, cast (approx.)	7.50	0.2562	442.7
Lead	11.34	0.4096	707.7
Magnesium	1.741	0.0628	108.6
Manganese	7.3	0.2636	455.5
Mercury	13.55	0.4892	845.3
Molybdenum	10.2	0.3683	636.5
Nickel	8.8	0.3178	549.2
Platinum	21.37	0.7717	1333.5
Silver	10.5	0.3789	654.7
Steel (approx.)	7.85	0.2833	489.4
Tantalum	16.6	0.5998	1035.8
Tin	7.29	0.2633	454.9
Titanium	4.5	0.1621	280.1
Tungsten	19.0	0.6856	1184.7
Uranium	18.7	0.6753	1166.9
Vanadium	5.69	0.2052	354.8
Water	1.0	0.036	62.355
Wood (approx.)	0.8018	2.89	50.0
Zinc	7.1	0.2562	442.7

Table A.5 Temperature conversion table: Celsius to Fahrenheit

°C	°F	°C	°F	°C	°F	°C	°F	°C	°F	°C	°F	°C	°F
0	32	30	86	60	140	90	194	290	554	600	1112	900	1652
1	33.8	31	87.8	61	141.8	91	195.8	300	572	610	1130	910	1670
2	35.6	32	89.6	62	143.6	92	197.6	310	590	620	1148	920	1688
3	37.4	33	91.4	63	145.4	93	199.4	320	608	630	1166	930	1706
4	39.2	34	93.2	64	147.2	94	201.2	330	626	640	1184	940	1724
5	41	35	95	65	149	95	203	340	644	650	1202	950	1742
6	42.8	36	96.8	66	150.8	96	204.8	350	662	660	1220	960	1760
7	44.6	37	98.6	67	152.6	97	206.6	360	680	670	1238	970	1778
8	46.4	38	100.4	68	154.4	98	208.4	370	698	680	1256	980	1796
9	48.2	39	102.2	69	156.2	99	210.2	380	716	690	1274	990	1814
10	50	40	104	70	158	100	212	390	734	700	1292	1000	1832
11	51.8	41	105.8	71	159.8	110	230	400	752	710	1310	1010	1850

(*continued*)

Table A.5 (*continued*)

°C	°F	°C	°F	°C	°F	°C	°F	°C	°F	°C	°F	°C	°F
12	53.6	42	107.6	72	161.6	120	248	410	770	720	1328	1020	1868
13	55.4	43	109.4	73	163.4	130	266	420	788	730	1346	1030	1886
14	57.2	44	111.2	74	165.2	140	284	430	806	740	1364	1040	1904
15	59	45	113	75	167	150	302	440	824	750	1382	1050	1922
16	60.8	46	114.8	76	168.8	160	320	450	842	760	1400	1060	1940
17	62.6	47	116.6	77	170.6	170	338	460	860	770	1418	1070	1958
18	64.4	48	118.4	78	172.4	180	256	470	878	780	1436	1080	1976
19	66.2	49	120.2	79	174.2	190	374	480	896	790	1454	1090	1994
20	68	50	122	80	176	200	392	490	914	800	1472	1100	2012
21	69.8	51	123.8	81	177.8	210	410	500	932	810	1490	1110	2030
22	71.6	52	125.6	82	179.6	212	413.6	510	950	820	1508	1120	2048
23	73.4	53	127.4	83	181.4	220	428	520	968	830	1526	1130	2066
24	75.2	54	129.2	84	183.2	230	446	530	986	840	1544	1140	2084
25	77	55	131	85	185	240	464	540	1004	850	1562	1150	2102
26	78.8	56	132.8	86	186.8	250	482	550	1022	860	1580	1160	2120
27	80.6	57	134.6	87	188.6	260	500	560	1040	870	1598	1170	2138
28	82.4	58	136.4	88	190.4	270	518	570	1058	880	1616	1180	2156
29	84.2	59	138.2	89	192.2	280	536	580	1076	890	1634	1190	2174
1200	2192	1400	2552	1600	2912	1800	3272	2000	3632	2200	3992	2400	4352
1210	2210	1410	2570	1610	2930	1810	3290	2010	3650	2210	4010	2410	4370
1220	2228	1420	2588	1620	2948	1820	3308	2020	3668	2220	4028	2420	4388
1230	2246	1430	2606	1630	2966	1830	3326	2030	3686	2230	4046	2430	4406
1240	2264	1440	2624	1640	2984	1840	3344	2040	3704	2240	4064	2440	4424
1250	2282	1450	2642	1650	3002	1850	3362	2050	3722	2250	4082	2450	4442
1260	2300	1460	2660	1660	3020	1860	3380	2060	3740	2260	4100	2460	4460
1270	2318	1470	2678	1670	3038	1870	3398	2070	3758	2270	4118	2470	4478
1280	2236	1480	2696	1680	3056	1880	3416	2080	3776	2280	4136	2480	4496
1290	2354	1490	2714	1690	3074	1890	3434	2090	3794	2290	4154	2490	4514
1300	2372	1500	2732	1700	3092	1900	3452	2100	3812	2300	4172	2500	4532
1310	2390	1510	2750	1710	3110	1910	3470	2110	3830	2310	4190	2510	4550
1320	2408	1520	2768	1720	3128	1920	3488	2120	3848	2320	4208	2520	4568
1330	2426	1530	2786	1730	3146	1930	3506	2130	3866	2330	4226	2530	4586
1340	2444	1540	2804	1740	3164	1940	3524	2140	3884	2340	4244	2540	4604
1350	2462	1550	2822	1750	3182	1950	3542	2150	3902	2350	4262	2550	4622
1360	2480	1560	2840	1760	3200	1960	3560	2160	3920	2360	4280	2560	4640
1370	2498	1570	2858	1770	3218	1970	3578	2170	3938	2370	4298	2570	4658
1380	2516	1580	2876	1780	3236	1980	3596	2180	3956	2380	4316	2580	4676
1390	2534	1590	2894	1790	3254	1990	3614	2190	3974	2390	4334	2590	4694

Table A.6 Conversion lists

Prefixes		
Prefix	Symbol	Factor
exa	E	10^{18}
peta	P	10^{15}
tera	T	10^{12}
giga	G	10^{9}
mega	M	10^{6}
kilo	k	10^{3}
milli	m	10^{-3}
micro	μ	10^{-6}
nano	n	10^{-9}
pico	p	10^{-12}
femto	f	10^{-15}
atto	a	10^{-18}

(*continued*)

Table A.6 (*continued*)

Abbreviations		
atm = atmosphere	gal = gallon	MPa = megapascal
A = ampere	hp = horsepower	N = Newton
Å = angstrom	h = hour	nm = nanometer
Btu = British energy	in. = inch	Pa = Pascal
C = coulomb	J = joule	psi = pounds/square inch
°C = degree Celsius	K = Kelvin	s = second
cal = calorie	kg = kilogram	T = temperature
cm = centimeter	L = liter	W = watt or weight
eV = electron volt	min = minute	μ = micron
°F = degrees Fahrenheit	mm = millimeter	μm = micrometer
g = gram	mol = mole	Ω = ohm = V A^{-1}

Greek alphabet								
Alpha	α	A	Iota	ι	I	Rho	ρ	P
Beta	β	B	Kappa	κ	K	Sigma	σ	Σ
Gamma	γ	Γ	Lambda	λ	Λ	Tau	τ	Υ
Delta	δ	Δ	Mu	μ	M	Upsilon	υ	Y
Epsilon	ε	E	Nu	ν	N	Phi	φ	Φ
Zeta	ζ	Z	Xi	ξ	Ξ	Chi	χ	X
Eta	η	H	Omicron	ο	O	Psi	ψ	Ψ
Theta	θ	Θ	Pi	π	Π	Omega	ω	Ω

Area	
$1\ m^2 = 10^4\ cm^2$	$1\ cm^2 = 10^{-4}\ m$
$1\ m^2 = 10.76\ ft^2$	$1\ ft^2 = 0.0929\ m^2$
$1\ cm^2 = 0.155\ in.^2$	$1\ in.^2 = 0.4516\ nm^2$
$1\ cm^2 = 102\ mm^2$	$1\ mm^2 = 10^{-2}\ cm^2$

Corrosion rate	
$1\ mm\ yr^{-1} = 39.37$ mils yr^{-1} (mpy)	$1\ mil\ yr^{-1} = 2.54 \times 10^{-2}\ mm\ yr^{-1}$
$1\ \mu m\ yr^{-1} = 3.937 \times 10^{-2}$ mils yr^{-1}	$1\ \mu m\ yr^{-1} = 25.40$ mils yr^{-1}

Current rate	
$1\ A\ m^{-2} = 9.29 \times 10^{-2}\ A\ ft^{-2}$	$1\ A\ ft^2 = 10.764\ A\ m^{-2}$
$1\ A\ cm^{-2} = 6.452\ A\ in.^{-2}$	$1\ A\ in.^{-2} = 0.155\ A\ cm^{-2}$
$1\ A\ mm^{-2} = 6.452 \times 10^2\ A\ in.^{-2}$	$1\ A\ in.^{-2} = 1.55 \times 10^{-3}\ A\ mm^{-2}$
$1\ \mu A\ cm^{-2} = 6.452\ \mu A\ in.^{-2}$	$1\ \mu A\ in.^{-2} = 0.155\ \mu A\ cm^{-2}$

Density	
$1\ kg\ m^{-3} = 10^{-3}\ g\ cm^{-3}$	$1\ g\ cm^{-3} = 10^3\ kg\ m^{-3}$
$1\ kg\ m^{-3} = 0.0624\ lb_m\ ft^{-3}$	$1\ ft^3 = 16.02\ kg\ m^{-3}$
$1\ g\ cm^{-3} = 62.40\ lb_m\ ft^{-3}$	$1\ lb_m\ ft^{-3} = 0.016\ g\ cm^{-3}$
$1\ g\ cm^{-3} = 0.0361\ lb_m\ in.^{-3}$	$1\ lb_m\ in.^{-3} = 27.70\ g\ cm^{-3}$

Electricity and magnetism	
$d\phi/d\chi = V\ cm^{-1}$	V = volts
1 mho = 1 s	1 s = 1 mho
$1\ s = ohm^{-1} = \Omega^{-1}$	$1\ \Omega = 1\ s^{-1}$
$1\ \Omega\ cm = 1.00 \times 10^{-2}\ \Omega\ cm$	$1\ \Omega\ m = 100\ \Omega\ cm$
$1\ \Omega\ cm = 1\ \Omega\ cm$	$1\ \Omega = V\ A^{-1}$
1 maxwell = 10^{-2} μweber	1 μweber = 100 maxwell

(*continued*)

Table A.6 (*continued*)

Energy	
$1\,J = 2.778 \times 10^{-7}$ kW h	$1\,kW\,h = 3.60 \times 10^{6}$ J
$1\,J = 0.239$ cal	1 cal = 4.184 J
$1\,J = 9.48 \times 10^{-4}$ Btu	$1\,Btu = 1.05 \times 10^{3}$ J
$1\,J = 0.7376$ ft lb_f	1 ft lb_f = 1.3558 J

Flow rate	
$1\,l\,min^{-1} = 2.1189\,ft^3\,h^{-1}$	$1\,ft^3\,h^{-1} = 0.4719\,l\,min^{-1}$
$1\,l\,min^{-1} = 3.53 \times 10^{-2}\,ft^3\,min^{-1}$	$1\,ft^3\,min^{-1} = 28.31$
$1\,l\,min^{-1} = 15.85\,gal\,h^{-1}$	$1\,gal\,h^{-1} = 6.31 \times 10^{-2}\,l\,min^{-1}$
$1\,l\,min^{-1} = 0.2642\,gal\,min^{-1}$	$1\,gal\,min^{-1} = 3.7854\,l\,min^{-1}$
$1\,m^3\,s^{-1} = 2.1189 \times 10^{3}\,ft^3\,min^{-1}$	$1\,ft^3\,min^{-1} = 4.7195 \times 10^{-4}\,m^3\,s^{-1}$
$1\,m^3\,s^{-1} = 35.315\,ft^3\,s^{-1}$	$1\,ft^3\,s^{-1} = 2.8317 \times 10^{-2}\,m^3\,s^{-1}$
$1\,m^3\,s^{-1} = 3.66 \times 10^{6}$ in.^{3} min^{-1}	1 in.^{3} $min^{-1} = 2.73 \times 10^{-7}\,m^3\,s^{-1}$

Force	
$1\,N = 10^{5}$ dynes	1 dyne $= 10^{-5}$ N
$1\,N = 0.2248\,lb_f$	$1\,lb_f = 4.48$ N
$1\,N = 2.248 \times 10^{-4}$ kips	$1\,kip = 4.448 \times 10^{3}$ N
$1\,N = 0.1019\,Kg_f$	$1\,Kg_f = 9.81$ N

Length		
1 m = 10 A	1 A = 10^{-10} m	1 mil = 25.40 μm
$1\,m = 10^{9}$ nm	1 nm = 10^{-9} m	1 yd = 0.9144 m
$1\,m = 10^{6}$ μ	1 μ = 10^{-6} m	1 mile = 1.61 km
$1\,m = 10^{3}$ mm	1 mm = 10^{-3} m	
$1\,m = 10^{2}$ cm	1 cm = 10 mm	
1 m = 39.36 in.	1 in. = 25.4 mm	
1 m = 3.28 ft	1 ft = 12 in.	

Mass	
$1\,kg = 10^{3}$ g	1 g = 10^{-3} kg
$1\,kg = 2.205\,lb_m$	$1\,lb_m = 0.4536$ kg
$1\,g = 2.205 \times 10^{-3}\,lb_m$	$1\,lb_m = 45.36$ g
1kg = 10^{-3} metric ton	1 metric ton = 10^{3} kg
$1\,kg = 1.1023 \times 10^{-3}$ short ton	1 short ton = $2 \times 10^{3}\,lb_m$
$1\,kg = 9.8421 \times 10^{-4}$ long ton	1 long ton = 1.016×10^{3} kg
1 metric ton = 1.1023 short ton	$1\,lb_m = 5 \times 10^{-4}$ short ton
1 metric ton = 0.98421 long ton	1 long ton = 1.106 metric ton
$1\,kg = 6.85 \times 10^{-2}$ slug	1 slug = 14.59 kg

Physical constants

Quantity	Symbol	SI units
Planck constant	h	6.626×10^{-34} J s
Boltzmann constant	k_B	$1.381 \times 10^{-23}\,J\,K^{-1}$
Avogadro constant	N_A	$6.023 \times 10^{23}\,mol^{-1}$
Electron mass	m_c	9.109×10^{-31} kg
Proton mass	M_P	1.672×10^{-27} kg
Charge of electron or proton	e	1.602×10^{-19} C
Faraday constant	F	$9.649 \times 10^{4}\,C\,mol^{-1}$
Gas constant	R	8.314 J (mol K)
Molar volume at STP	V_m	$2.241 \times 10^{-2}\,m^3\,mol^{-1}$
Permittivity of vacuum or dielectric constant	ε_o	$8.854 \times 10^{-12}\,F\,m^{-1}$
Permeability of vacuum inductance	μ_o	$4\pi \times 10^{-7}\,H\,m^{-1}$
Stefan–Boltzmann constant	σ	$5.670 \times 10^{-8}\,W\,(m^2\,K^4)^{-1}$
Speed of light in vacuum	c	$2.998 \times 10^{8}\,m\,s^{-1}$
Gravitational acceleration	g	$9.807\,m\,s^{-2}$

(*continued*)

Table A.6 (*continued*)

Power	
$1\,W = 1\,J\,s^{-1}$	$1\,Btu\,s^{-1} = 1\,ft\,lb_f\,s^{-1}$
$1\,kW = 0.9478\,Btu\,s^{-1}$	$1\,Btu\,s^{-1} = 1.0551\,kW$
$1\,kW = 56.869\,Btu\,min^{-1}$	$1\,Btu\,min^{-1} = 1.758 \times 10^{-2}\,kW$
$1\,kW = 3.4121 \times 10^{3}\,Btu\,h^{-1}$	$1\,Btu\,h^{-1} = 2.9307 \times 10^{-4}\,kW$
$1\,kW = 1.3405 \times 10^{-3}\,hp$	$1\,hp = 746\,kW$

Pressure (fluid)	
$1\,Pa = 1\,N\,m^{-2}$	$1\,atm = 760\,mmHg, °C$
$1\,Pa = 9.87 \times 10^{-6}\,atm$	$1\,atm = 1.0133 \times 10^{5}\,Pa$
$1\,MPa = 9.87 \times 10^{-3}\,atm$	$1\,atm = 101.33\,MPa$
$1\,Pa = 1.00 \times 10^{-5}\,bar$	$1\,bar = 1.00 \times 10^{5}\,Pa$
$1\,Pa = 1.45 \times 10^{-4}\,psi$	$1\,psi = 6.895 \times 10^{5}\,Pa$
$1\,MPa = 0.145\,ksi$	$1\,ksi = 6.895\,MPa$
$1\,Pa = 7.501 \times 10^{-3}\,torr\,(mmHg, °C)$	$1\,torr = 1.333 \times 10^{2}\,Pa$
$1\,Pa = 2.953 \times 10^{-4}\,in\,Hg, 32\,°F$	$1\,in\,Hg\ 32\,°F = 3.386 \times 10^{3}\,Pa$
$1\,Pa = 2.0886 \times 10^{-2}\,lb_g\,ft^{-2}$	$1\,atm = 14.7\,psi$

Temperature	
$T\,(K) = T(°C) + 273.15$	$T(R) = T(°F) + 459.67$
$\Delta T(K) = \Delta T\,(°C)$	$T(R) = (9/5)T(K) + 459.67$
	$T(°F) = (9/5)T(°C) + 32$
	$T(°C) = (5/9)\,[T(°F) - 32]$

Velocity	
$1\,m\,s^{-1} = 1.1811 \times 10^{4}\,ft.\,h^{-1}$	$1\,ft.\,h^{-1} = 8.4667 \times 10^{-5}\,m\,s^{-1}$
$1\,m\,s^{-1} = 1.9685 \times 10^{2}\,ft\,min^{-1}$	$1\,ft.\,min^{-1} = 5.08 \times 10^{-3}\,m\,s^{-1}$
$1\,m\,s^{-1} = 3.281\,ft\,s^{-1}$	$1\,ft.\,s^{-1} = 0.305\,m\,s^{-1}$
$1\,m\,s^{-1} = 39.37\,in.\,s^{-1}$	$1\,in.\,s^{-1} = 2.54 \times 10^{-3}\,in.\,s^{-1}$

Volume	
$1\,m^3 = 10^6\,cm^3$	$1\,cm^3 = 10^{-6}\,cm^3$
$1\,cm^3 = 10^3\,mm^3$	$1\,mm^3 = 10^{-3}\,cm^3$
$1\,m^3 = 35.32\,ft^3$	$1\,ft^3 = 0.0283\,m^3$
$1\,cm^3 = 0.061\,in.^3$	$1\,in.^3 = 16.39\,in.^3$
$1\,l = 10^3\,cm^3\,(cc)$	$1\,cm^3 = 10^{-3}$
1 US gal = 3.785 l	$1\,l = 0.264\,gal$

Table A.7 Hardness conversion table (approximate value)

C 150 kg	A 60 kg	15-N 15 kg	B 100 kg	15-T 15 kg	Diamond pyramid hardness 10 kg	Knoop hardness 500 g and over	Brinell hardness 3000 kg	G 150 Kg	Tensile strength (approx.)
									1000 lb. per square inch inexact and only for steel
70	86.5	94.0	—	—	1076	972	—	—	
69	86.0	93.5	—-	—	1004	946	—	—	
68	85.5	—	—	—	942	920	—	—	
67	85.0	93.0	—	—	894	895	—	—	
66	84.5	92.5	—	—	854	870	—	—	
65	84.0	92.0	—	—	820	846	—	—	

(*continued*)

Table A.7 (*continued*)

C 150 kg	A 60 kg	15-N 15 kg	B 100 kg	15-T 15 kg	Diamond pyramid hardness 10 kg	Knoop hardness 500 g and over	Brinell hardness 3000 kg	G 150 Kg	Tensile strength (approx.)
64	83.5	—	—	—	789	822	—	—	
63	83.0	91.5	—	—	763	799	—	—	
62	82.5	91.0	—	—	739	754	—	—	
61	81.5	90.5	—	—	716	754	—	—	
60	81.0	90.0	—	—	695	732	614	—	
59	80.5	89.5	—	—	675	710	600	—	
58	80.0	—	—	—	655	690	587	—	
57	79.5	89.0	—	—	636	670	573	—	
56	79.0	88.5	—	—	617	650	560	—	—
55	78.5	88.0	—	—	598	630	547	—	301
54	78.0	87.5	—	—	580	612	534	—	291
53	77.5	87.0	—	—	562	594	522	—	282
52	77.0	86.5	—	—	545	576	509	—	273
51	76.5	86.0	—	—	528	558	496	—	264
50	76.0	85.5	—	—	513	542	484	—	255
49	75.5	85.0	—	—	498	526	472	—	246
48	74.5	84.5	—	—	485	510	460	—	237
47	74.0	84.0	—	—	471	495	448	—	229
46	73.5	83.5	—	—	458	480	437	—	221
45	73.0	83.0	—	—	446	466	426	—	214
44	72.5	82.5	—	—	435	452	415	—	207
43	72.0	82.0	—	—	424	438	404	—	200
42	71.5	81.5	—	—	413	426	393	—	194
41	71.0	81.0	—	—	403	414	382	—	188
40	70.5	80.5	—	—	393	402	372	—	182
39	70.0	80.0	—	—	383	391	362	—	177
38	69.5	79.5	—	—	373	380	352	—	171
37	69.0	79.0	—	—	363	370	342	—	166
36	68.5	78.5	—	—	353	360	332	—	162
35	68.0	78.0	—	—	343	351	322	—	157
34	67.5	77.0	—	—	334	342	313	—	153
33	67.0	76.5	—	—	325	334	305	—	148
32	66.5	76.0	—	—	317	326	297	—	144
31	66.0	75.5	—	—	309	318	290	—	140
30	65.5	75.0	—	—	301	311	283	92.0	136
29	65.0	74.5	—	—	293	304	276	91.0	132
28	64.5	74.0	—	—	285	297	270	90.0	129
27	64.0	73.5	—	—	278	290	265	89.0	126
26	63.5	72.5	—	—	271	284	260	88.0	123
25	63.0	72.0	—	—	264	278	255	87.0	120
24	62.5	71.5	—	—	257	272	250	86.0	117
23	62.0	71.0	—	—	251	266	245	84.5	115
22	61.5	70.5	—	—	246	261	240	83.5	112
21	61.5	70.0	100	93.0	241	251	240	82.5	116
20	61.0	69.5	99	92.5	236	246	234	81.0	112
—	60.0	—	98	—	—	241	228	79.0	109
—	59.5	—	97	92.0	—	236	222	77.5	106
—	59.0	—	96	—	—	—	216	76.0	103
—	58.0	—	95	91.5	—	—	210	74.0	101
—	57.5	—	94	—	—	—	205	72.5	98
—	57.0	—	93	91.0	—	—	200	71.0	96

(*continued*)

Table A.7 (*continued*)

C 150 kg	A 60 kg	15-N 15 kg	B 100 kg	15-T 15 kg	Diamond pyramid hardness 10 kg	Knoop hardness 500 g and over	Brinell hardness 3000 kg	G 150 Kg	Tensile strength (approx.)
—	56.5	—	92	90.5	—	211	195	69.0	93
—	56.0	—	91	—	—	206	190	67.5	91
—	55.5	—	90	90.0	—	201	185	66.0	89
—	55.0	—	89	89.5	—	196	180	64.0	87
—	54.0	—	88	—	—	192	176	62.5	85
—	53.5	—	87	89.0	—	188	172	61.0	83
—	53.0	—	86	88.5	—	184	169	59.0	81
—	52.5	—	85	—	—	180	165	57.5	80
—	52.0	—	84	88.0	—	176	162	56.0	78
—	51.0	—	83	87.5	—	173	159	54.0	77
—	50.5	—	82	—	—	170	156	52.5	75
—	50.0	—	81	87.0	—	167	153	51.0	74
—	49.5	—	80	86.5	—	164	150	49.0	72
—	49.0	—	79	—	—	161	147	47.5	—
—	48.5	—	78	86.0	—	158	144	46.0	—
—	48.0	—	77	85.5	—	155	141	44.0	—
—	47.0	—	76	—	—	152	139	42.5	—
—	46.5	—	75	85.0	—	150	137	41.0	—
—	46.0	—	74	—	—	147	135	39.0	—

The values in this table correspond to the values shown in the corresponding joint SAE–ASM–ASTM Committee on Hardness Conversions as printed in ASTM E 48, Table 3.

Table A.8 Selected melting points, °F (°C)

YSZ	NiCoCrAlY	NiAl	Ni-based superalloy	Alumina
~2690 (4874)	~1260 (2300)	~1638 (2980)[a]	1260–1343 (2300–2450)	2030 (3686)

[a]Interface melting at ~1296 °C (2365 °F).

Table A.9 Selected coefficients of thermal expansion ($°C \times 10^{-6}$)

Temperature (°C)	NiCoCrAlY	NiAl	Pt aluminide	Ni-based superalloy	Alumina	APS 7YSZ	EB-PVD 7YSZ (perp. to column)
25	13.3	14	13.6	12.2	8		
300	14.1	14.2	14.4	12.9	8.3	9.82	8.2
500	15	14.6	14.9	13.5	8.6	9.64	8.6
700	16.1	14.6	15.6	14.1	8.8	9.88	10.7
900	18	14.9	16.6	15.1	9.2	10.19	12.2

Table A.10 Properties of TBCs

	Dense YSZ	APS 7YSZ	EB-PVD 7YSZ	NiCoCrAlY	NiAl	(Ni,Pt)Al
Density ($g\,cm^{-3}$)	6.1	5	5.1	~7–7.5 (APS is ~6.5)	~5.9	~4 ($PtAl_2$ is 6.25)
Thermal conductivity ($W\,(m\,K)^{-1}$ at 1000 °C)	2.5	0.6–1.1	1.5–2	20–35	~75	
Specific heat ($J\,g^{-1}°C$)		0.582–0.603		0.628–0.712	0.64	
Emittance at 0.8–0.9 μm		0.25	0.325–0.35			
Debye temperature (°C)	106					
Knoop hardness		~4		~2–3		

Table A.11 Chemical tests and reactions for some common metals

Reagents	Carbon steel	SS types 302 and 204	SS types 316 and 317	SS types 304, 321, and 347	SS types 303, 414, and 430F	Aluminum	Magnesium	Nickel	Monel	Inconel
Nital-10% nitric acid in methanol	Blackens surface	No reaction					Cleans surface or turns gray	Slow reaction turns blue green	Slow reaction turns blue green[a]	No reaction
Hydrochloric acid	Reacts to clean surface	No reaction		Attacks releasing gas	Attacks, leaving black smudge; rotten egg odor	Blackens surface	Blackens surface	Cleans surface	Cleans surface	No reaction
Copper sulfate solution	Leaves copper color	No reaction					Reacts, leaving heavy black smudge	No reaction		
Sodium hydroxide	No reaction					Reacts, leaving gray smudge	No reaction			
Sulfuric acid	Cleans surface	Leaves dark surface with green crystals		Slow attack, leaving tan surface	No reaction		Strongly reacts, foams, and leaves clean surface	No reaction		
Zinc chloride in water	No reaction						Reacts and turns black	No reaction		
Ferrous chlorides	No reaction						Reacts and turns black	No reaction		

SS, Stainless steels

[a]Monel may be distinguished from nickel that looks alike by the following test. Place a few drops of nital on the surface of the specimen. It will turn blue green if it is either monel or nickel. Then place a small piece of soft iron (a nail will do) in the solution on the sample. If there is no reaction, the metal is nickel, but if the iron turns copper colored, copper ions have been transferred from the copper in the metal, and it can be assumed that it is monel, which contains copper, zinc, and tin and will react with so many acids to turn them black, and that chemical tests would be of no value for them. Silver will turn black in sulfuric acid.

Table A.12 Selected Young's modulus

	APS 7YSZ	EB-PVD 7YSZ	NiCoCrAlY	Pt aluminides	Superalloys	Alumina	Plain aluminide
E (GPa)						380–400	
Temperature, °C (°F)							
24 (75)	2.5	35–40	170		200–220	400	100 (<100)
							190 (<110)
538 (1000)	2.5						290 (<111)
871 (1600)	2.3						
982 (1800)	2					350	
1093 (2000)	1.8					340	
1204 (2200)	1.75					330	
Poisson's ratio, *V*				0.3	0.3	0.25	

Table A.13 Properties of selected engineering materials (20 °C)

Material	Density, mg m^3 (=g cm^3)	Thermal conductivity (W mm^{-2})/(°C mm^{-1})[a]	Linear expansion °C^{-1}[b]	Electrical resistivity, ρ ohm m[c]	Average modulus of elasticity, $\overline{E}$ MPa	psi
Metals						
Aluminum (99.9+)	2.7	0.22	22.5×10^{-6}	29×10^{-9}	70 000	10×10^6
Aluminum alloys	2.7 (+)	0.16	22×10^{-6}	$\sim45\times10^{-9}$	70 000	10×10^6
Brass (70 Cu–30 Zn)	8.5	0.12	22×10^{-6}	62×10^{-9}	110 000	16×10^6
Bronze (95 Cu–5 Sn)	8.8	0.08	18×10^{-6}	$\sim100\times10^{-9}$	110 000	16×10^6
Cast iron (gray)	7.15	—	10×10^{-6}	—	140 000 (±)	20×10^6 ±
Cast iron (white)	7.7	—	9×10^{-6}	660×10^{-9}	205 000	30×10^6
Copper (99.9+)	8.9	0.40	17×10–6	17×10^{-9}	110 000	16×10^6
Iron (99.9+)	7.88	0.072	11.7×10^{-6}	98×10^{-9}	205 000	30×10^6
Lead (99+)	11.34	0.033	29×10^{-6}	206×10^{-9}	14 000	2×10^6
Magnesium (99+)	1.74	0.16	25×10^{-6}	45×10^{-9}	45 000	6.5×10^6
Monel (70 Ni–30 Cu)	8.8	0.025	15×10^{-6}	482×10^{-9}	180 000	26×10^6
Silver (sterling)	10.4	0.41	18×10^{-6}	18×10^{-9}	75 000	11×10^6
Steel (1020)	7.86	0.050	11.7×10^{-6}	169×10^{-9}	205 000	30×10^6
Steel (1040)	7.85	0.048	11.3×10^{-6}	171×10^{-9}	205 000	30×10^6
Steel (1080)	7.84	0.046	10.8×10^{-6}	180×10^{-9}	205 000	30×10^6
Steel (18 Cr–8 Ni stainless)	7.93	0.015	16×10^{-6}	700×10^{-9}	205 000	30 x10^6
Ceramics						
Al_2O_3	3.8	0.029	9×10^{-6}	$>10^{12}$	350 000	50×10^6
Brick						
Building	2.3 (±)	0.0006	9×10^{-6}	—	—	—
Fireclay	2.1	0.0008	4.5×10^{-6}	1.4×10^6	—	—
Graphite	1.5	—	5×10^{-6}	—	—	—
Paving	2.5	—	4×10^{-6}	—	—	—
Silica	1.75	0.0008	—	1.2×10^6	—	—
Concrete	2.4 (±)	0.0010	13 × 10–6	—	14 000	2×10^6
Glass						
Flat	2.5	0.00075	9×10^{-6}	10^{12}	70 000	10×10^6
Borosilicate (fibers)	2.4	0.0010	2.7×10^{-6}	$>10^{15}$	70 000	10×10^6
Silica	2.2	0.0012	0.5×10^{-6}	10^{18}	70 000	10×10^6
Vycor	2.2	0.0012	0.6×10^{-6}	—	—	—
Wool	0.05	0.00025	—	—	—	—
Graphite (bulk)	1.9	—	5×10^{-6}	10^{-5}	7000	1×10^6
MgO	3.6	—	9×10^{-6}	10^3 (1100 °C)	205 000	30×10^6

(*continued*)

Table A.13 (*continued*)

Material	Density, mg m^3 (=g cm^3)	Thermal conductivity (W mm^{-2})/(°C mm^{-1})[a]	Linear expansion °C^{-1}[b]	Electrical resistivity, ρ ohm m[c]	Average modulus of elasticity, $\overline{E}$ MPa	psi
Quartz (SiO_2)	2.65	0.012	—	10^{12}	310 000	45×10^6
SiC	3.17	0.012	4.5×10^{-6}	0.025 (1100 °C)	—	—
TiC	4.5	0.030	7×10^{-8}	50×10^{-8}	350 000	50×10^6
Polymers						
Melamine-formaldehyde	1.5	0.00030	27×10^{-6}	10^{11}	9000	1.3×10^6
Phenol-formaldehyde	1.3	0.00016	72×10^{-6}	10^{10}	3500	0.5×10^6
Urea-formaldehyde	1.5	0.00030	27×10^{-6}	10^{10}	10 300	1.5×10^6
Rubber (synthetic)	1.5	0.00012	—	—	4–75	600–11 000
Rubber (vulcanized)	1.2	0.00012	81×10^{-6}	10^{12}	3500	0.5×10^6
Low density polyethylene	0.92	0.00034	180×10^{-6}	10^{13}–10^{16}	100–350	14 000–50 000
High density polyethylene	0.96	0.00052	120×10^{-6}	10^{12}–10^{16}	350–1250	50 000–180 000
Polystyrene	1.05	0.00008	63×10^{-6}	10^{16}	2800	0.4×10^6
Polyvinylidene chloride	1.7	0.00012	190×10^{-6}	10^{11}	350	0.05×10^6
Polytetrafluoroethylene	2.2	0.00020	100×10^{-6}	10^{14}	350–700	50 000–100 000
Polymethyl methacrylate	1.2	0.00020	90×10^{-6}	10^{14}	3500	0.5×10^6
Nylon	1.15	0.00025	100×10^{-6}	10^{12}	2800	0.4×10^6

Data in this table were taken from numerous sources.

[a] Alternatively (W mm^{-2})/(K mm^{-1}). Multiply by 1.92 to get Btu/(ft^2 s)/(°F in^{-1}).

[b] Or (K^{-1}); divide by 1.8 to get °F^{-1}.

[c] Multiply ohm m by 39 to get ohm in.

Table A.14 Compositions of selected superalloys for high temperature environments

Alloy	Approximate nominal composition (wt%)												
	Al	B	C	Co	Cr	Hf	Mo	Ni	Ta	Ti	W	Zr	Others
Nickel-based polycrystalline													
Waspaloy	1.2	0.005	0.07	13.5	19.5		4.2	Bal		3		0.09	Fe 15.8
Hastelloy X	2		0.15	1.5	22		9	Bal			0.6		Fe 15. 8
IN-718	0.05		0.04		19		3	Bal		0.9			Fe 18, Nb 5, Cu 0.25
IN-792	3.2	0.02	0.2	9	13		2	Bal		4.2	4	0.1	Nb 2
IN-100	5.5	0.015	0.17	15	9.5		3	Bal		4.8		0.06	V 1
B-1900 + Hf	6	0.015	0.11	10	8	1.2	6	Bal	4.3	1		0.08	
René 80	3	0.015	0.17	9.5	14		4	Bal		5	4	0.03	
René 80 + Hf	3	0.015	0.08	9.5	14		4	Bal		4.8	4	0.02	Hf 0.75
IN-738	3.4	0.01	0.17	8.5	16		1.7	Bal	1.7	3.4	2.6	0.1	Nb 0.9
MAR-M247	5.5	0.016	0.15	10	8.4	1.4	0.6	Bal	3	1	10	0.06	
DS MAR-M247[a]	5.5	0.015	0.15	10	8.4	1.4	0.6	Bal	3	1	10	0.06	
MAR-M200	5	0.015	0.15	10	9			Bal		2	12	0.05	Nb 1
DS MAR-M200 + Hf	5	0.015	0.13	10	9	2		Bal		2	12	0.05	Nb 1
Nickel-based single crystal													
PWA 1480	5			5	10			Bal	12	1.5	4		
PWA 1483	3.7			9	12.8		1.9	Bal	4	4.2	3.8		
PWA 1484	5.7			10	5	0.1	1.9	Bal	8.7		5.9		Re 3
René N	3.7			7.5	9.3		1.5	Bal	4	4.2	6		
René N4	4.2	0.004		7.5	9.75	0.15	1.5	Bal	4.8	3.5	6		Nb 0.5
René N5	6.2			7.5	7	0.15	1.5	Bal	6.5		5		Re 3, Y 0.01
René N6	5.75			12.5	4.2	0.15	1.4		7.2		6		Re 5.4, Y 0.01
CMSX-2	5.6			4.6	8		0.6	Bal	6	1	8	0.06	
CMSX-4	5.6			9	6.5		0.6		6.5	1	6		
Cobalt based													
MAR-M509			0.6	Bal	23.5			10	3.5	0.2	7	0.5	
FSX-414		0.01	0.25	Bal	29			10			7.5		Fe 1

[a] DS, directionally solidified.

Table A.15 Composition of various stainless steels

Type UNS	Designation	C	Mn	Si	Cr	Ni	P	S	Others
Austenite type									
201	S20100	0.15	5.5–7.5	1.0	16–18	5–5.5	0.06	0.03	0.25N
205	S20500	0.12	14–15.5	1.0	16.5–18	1–1.75	0.06	0.03	0.32–0.4N
301	S30100	0.15	2.0	1.0	16–18	6–8	0.045	0.03	
302	S30200	0.15	2.0	1.0	17–19	8–10	0.045	0.03	0.6Mo
303	S30300	0.15	2.0	1.0	17–19	8–10	0.2	0.06	
304	S30400	0.08	2.0	1.0	17–19	8–10.5	0.045	0.03	
304 L	S30403	0.03	2.0	1.0	17–19	8–10.5	0.045	0.03	
310	S31000	0.25	2.0	1.5	24–26	8–12	0.045	0.03	
310S	S31008	0.08	2.0	1.5	24–26	19–22	0.045	0.03	
314	S31400	0.25	2.0	1.5–3	23–26	19–22	0.045	0.03	
316	S31600	0.08	2.0	1.0	16–18	10–14	0.2	0.10	2–3Mo
316L	S31603	0.03	2.0	1.0	16–18	10–14	0.045	0.03	2–3Mo
317	S31700	0.08	2.0	1.0	18–20	11–15	0.045	0.03	3–4Mo
321	S32100	0.08	2.0	1.0	17–19	9–12	0.045	0.03	0.4–0.7Ti
348	S34800	0.08	2.0	1.0	17–19	9–13	0.045	0.03	0.2Co, 0.10Ta 0.8–1.0Nb
Ferrite type									
405	S40500	0.08	1.0	1.0	11.5–14.5	—	0.04	0.03	0.1–0.3Al
409	S40900	0.08	1.0	1.0	10.5–11.75	0.5	0.045	0.045	0.1–0.3Al
429	S42900	0.08	1.0	1.0	14–16	—	0.04	0.03	
430	S43000	0.12	1.0	1.0	16–18	—	0.04	0.03	
434	S43400	0.12	1.0	1.0	16–18	—	0.04	0.03	0.75–1.25Mo
442	S44200	0.2	1.5	1.0	23–27	—	0.04	0.03	
446	S44600	0.2	1.5	1.0	23–27	—	0.04	0.03	0.25N
Martensite type									
403	S40300	0.15	1.0	1.0	11.5–13	—	0.04	0.03	
410	S41000	0.15	1.0	1.0	11.5–13.5	—	0.04	0.03	
414	S41400	0.15	1.0	1.0	11.5–13.5	1.25–2.5	0.04	0.03	
416	S41600	0.15	1.0	1.0	12–14	—	0.06	0.15 min	0.6Mo
420	S42000	0.15	1.0	1.0	12–14	—	0.04	0.03	
422	S42200	0.2–0.25	1.0	0.75	11.5–13.5	0.5–1.0	0.04	0.03	0.75–1.25Mo 0.75–1.25W 0.15–0.3V
431	S43100	0.2		1.0	15–17	1.25–2.5		0.04	0.03
440A	S44002	0.6–0.75		1.0	1.0	16–18	—	0.04	0.03–0.07Mo
440B	S44003	0.75–0.95		1.0	1.0	16–18	—	0.04	0.03–0.07Mo
440C	S44004	0.95–1.2		1.0	1.0	16–18	—	0.04	0.03–0.07Mo
Duplex (ferritic–austenitic) type									
329	S32900	0.20	1.0	0.75	23–28	2.5–5	0.04	0.03	1.2Mo
44LN	S31200	0.03	2.0	1.0	24–26	5.5–6.5	0.045	0.03	1.2–2Mo
DP-3	S31260	0.03	1.0	0.75	24–26	5.5–7.5	0.03	0.03	2.5–3.5Mo
Uranus 50	S32404	0.04	2.0	1.0	20.5–22.5	5.5–8.5	0.03	0.01	2–3Mo 1–2Cu 0.2N
Ferralium									
225	S32550	0.04	1.5	1.0	24–27	4.5–6.5	0.04	0.03	2–4Mo 1.5–2.5Cu 0.1–0.25N

Table A.16 Composition of various chromia-forming superalloys

Type	UNS number	C	Cr	Ni	Co	Fe	Mo	W	Others
Incoloy 800	N08800	0.05	21	32.5	—	Bal	—	—	0.3Al, 0.3Ti
Incoloy 800H	N08810	0.08	21	32.5	—	Bal	—	—	0.4Al, 0.4Ti
Incoloy 802	N08802	0.4	21	32.5	—	Bal	—	—	
Incoloy 903	NI9903	—	—	38	15	Bal	—	—	1.4Ti, 0.9Al, 3Cb
Incoloy DS	—	0.06	17	35	—	Bal	—	—	2.3Si
Inconel 600	N06600	0.08	15.5	Bal	—	8.0	—	—	
Inconel 601	N06601	0.10	23.0	Bal	—	14.4	—	—	1.4Al
Inconel 625	N06625	0.1	21.5	Bal	—	2.5	9.0	—	3.6Cb
Inconel 706	N09706	0.03	16.0	Bal	—	37	—	—	1.8Ti, 0.2Al, 2.9Cb
Inconel 718	N07718	0.04	18	Bal	—	18.5	3.0	—	5.1Cb
Hastelloy X	N06002	0.1	22	Bal	1.5	18.5	9.0	0.6	
Nimonic 70	—	—	20	Bal	—	25	—	—	1Al, 1.25Ti, 1.5Cb
Nimonic 75	—	0.10	19.5	Bal	—	0.25	—	—	0.15Al, 0.4Ti
Nimonic 81	—	0.03	30	Bal	—	—	—	—	0.9Al, 1.4Ti
Nimonic 90	N07090	0.07	19.5	Bal	16.5	—	—	—	1.5Al, 2.5Ti
Nimonic 115	—	0.15	15	Bal	15	—	4.0	—	5Al, 4Ti
Waspaloy	N07001	0.08	19	Bal	14	—	4.3	—	1.5Al, 3Ti, 0.05Zr, 0.006B
Udimet 500	—	0.08	18	Bal	18.5	—	4.0	—	2.9Al, 2.9Ti, 0.05Zr, 0.006B
Udimet 520	—	0.05	19	Bal	12	—	6.0	1.0	2Al, 3Ti, 0.005B
Udimet 700	—	0.03	15	Bal	18.5	—	5.2	—	5.3Al, 3.5Ti, 0.03B
René 77	—	0.07	15	Bal	15	—	4.2	—	4.3Al, 3.3Ti, 0.04Zr, 0.015B
René 80	—	0.17	14	Bal	9.5	—	4.0	4.0	3Al, 5Ti, 0.03Zr, 0.015B
IN-738	—	0.17	16	Bal	8.5	—	1.7	2.6	3.4Al, 3.4Ti, 1.7Ta, 0.1Zr, 0.9Cb, 0.01B
IN-792	—	0.12	12.4	Bal	9.0	—	1.9	3.8	3.1Al, 4.5Ti, 1.7Ta, 0.1Zr, 0.02B

Table A.17 Composition of alumina-forming superalloys

Type	C	Al	Cr	Ni	Co	Fe	Mo	W	Others
IN-713C	0.12	6	12.5	Bal	—	—	4.2	—	0.8Ti, 2Cb, 0.012B, 0.10ZR
IN-713LC	0.05	6	12.0	Bal	—	—	4.5	—	0.6Ti, 2Cb, 0.1Zr, 0.01B
B-1900	0.1	6	8.0	Bal	10.0	—	6.0	—	1.0Ti, 4.0Ta, 0.1Zr, 0.015B
IN-100	0.18	6	10.0	Bal	15.0	—	3.0	—	1.0Ti, 4.0Ta, 0.1Zr, 0.015B
IN-162	0.12	6.5	10.0	Bal	—	—	4.0	2.0	1.0Ti, 1.0Cb, 2.0Ta, 0.1Zr, 0.02B
IN-731	0.18	5.5	9.5	Bal	10.0	—	2.5	—	4.6Ti, 0.06Zr, 0.015B, 1.0 V
M-21	0.13	6	5.7	Bal	—	—	2.0	11.0	0.12Zr, 1.5Cb, 0.02B
M-22	0.13	6.3	5.7	Bal	—	—	2.0	11.0	3Ta, 0.6Zr
MAR-M200	0.15	5	9.0	Bal	10.0	1.0	—	12.5	2Ti, 0.05Zr, 0.015B, 1.0Cb
MAR-M246	0.15	5.5	9.0	Bal	10.0	—	2.5	10.0	1.5Ti, 1.5Ta, 0.05Zr, 0.015B
René 100	0.16	5.5	9.5	Bal	15.0	—	3.0	—	4.2Ti, 0.006Zr, 0.015B
TAZ-8A	0.12	6	6.0	Bal	—	—	4.0	4.0	8Ta, 1Zr, 2.5Cb, 0.004B
TAZ-8B (DS)	0.12	6	6.0	Bal	5.0	—	4.0	4.0	8Ta, 1Zr, 1.5Cb, 0.004B

Table A.18 Composition of a few common alloys

Type	Cr	Ni	Fe	Ti	Al	Co	Mo	Others
MA 956	20.0	—	Bal	0.5	4.5	—	—	$0.5Y_2O_3$
MA 754	20.0	Bal	1.0	0.5	0.3	—	—	$0.6Y_2O_3$
MA 6000	15.0	Bal	0.75	2.88	4.38	16.0	2.0	2Ta, 4 W, $1.13Y_2O_3$
TD-Ni		Bal	—	—	—	—	—	$2ThO_2$
TMO-2	6.0	Bal	—	0.8	4.2	9.7	2.0	12.4 W, 4.7Ta, 0.01B, 0.05Zr, 0.05C, $1.1Y_2O_3$

Table A.19 Properties of selected nonferrous metals and alloys

Material	Density ($g\,cm^{-3}$)	Elastic modulus ($psi \times 10^6$ [$MPa \times 10^3$])	Electrical conductivity ($[ohm\,m]^{-1} \times 10^6$)	Thermal conductivity ($W\,m^{-1}\,K$)	Coefficient of thermal expansion ($[°C]^{-1} \times 10^6$)	Melting temperature or range (°C)
Aluminum (>99.5)	2.71	10 (69)	36	231	23.6	646–657
Aluminum alloy 2014 (4.4Cu–0.8 Si–0.8Mn–0.5 Mg)	2.80	10.5 (72)	29	192	22.5	507–638
Copper (99.95)	8.94	17 (117)	59	386	9.8	1085
Brass (70Cu–30Zn)	8.53	16 (110)	16	120	20.0	915–955
Bronze (92Cu–8Sn)	8.80	16 (110)	7.5	62	18.2	880–1020
Magnesium (>99)	1.74	6.5 (44.8)	22	160	25.2	650
Nickel (>99)	8.90	30 (207)	15	90	13.3	1453
Silver (>99)	10.49	11 (75.9)	63	428	19.0	962
Titanium (>99)	4.51	15.5 (107)	2.4	17	9.0	1670
Tungsten (>99)	19.25	59 (407)	19	178	4.5	3410

Table A.20 Properties of selected ferrous metals and alloys

Material	Density ($g\,cm^{-3}$)	Elastic modulus ($psi \times 10^6$ [$MPa \times 10^3$])	Electrical conductivity ($[ohm\,m]^{-1} \times 10^6$)	Thermal conductivity ($W\,(m\,K)^{-1}$)	Coefficient of thermal expansion ($[°C]^{-1} \times 10^6$)	Melting temperature or range (°C)
Iron	7.87	30 (207)	10	80	11.8	1538
Gray cast iron	7.15	Variable	~1	46	10.8	1538
Nodular cast iron	7.12	24 (165.5)	~1.5	33	11.8	1538
Malleable cast iron	7.20–7.45	25 (172)	0.25–0.35	51	11.9	1538
Low carbon steel (1020)	7.86	30 (207)	5.9	52	11.7	1495–1520
Medium carbon steel (1080)	7.85	30 (207)	5.8	52	11.3	1495–1505
High carbon steel (1080)	7.84	30 (207)	5.6	48	11.0	1385–1475
Stainless steels						
Ferritic, Type 446	7.50	29 (200)	1.5	21	10.4	1425–1510
Austenitic, Type 316	8.0	28 (193)	1.4	16	16.0	1370–1400
Martensitic, Type 410	7.80	29 (200)	1.8	25	9.9	1480–1530

Table A.21 Properties of selected ceramic materials

Material	Density ($g\,cm^{-3}$)	Elastic modulus ($psi \times 10^6$ [$MPa \times 10^3$])	Electrical conductivity ($[ohm\,m]^{-1} \times 10^6$)	Thermal conductivity ($W\,(m\,K)^{-1}$)	Coefficient of thermal expansion ($[°C]^{-1} \times 10^6$)	Melting temperature or range (°C)
Aluminum oxide (Al_2O_3)	3.97	53 (366)	10^{10}–10^{12}	30	8.8	2050
Magnesium oxide (MgO)	3.58	30 (207)	$\sim 10^8$	38	13.5	2800
Silicon carbide (SiC)	3.22	68 (469)	0.1–1	42	4.7	~2700
Fused silica (SiO_2)	2.20	11 (76)	–	1.4	0.5	—
Soda–lime glass	2.5	10 (69)	$\sim 10^{11}$	1.0	9.0	—
Pyrex glass	2.2	10 (69)	$\sim 10^{14}$	1.2	3.0	—

Table A.22 Typical tensile properties of selected superalloys

Temperature		Tensile strength		Yield strength		Elongation
°C	°F	MPa	ksi	MPa	ksi	%
Cobalt-based alloys						
Haynes 25 (L-605), sheet						
21	70	1010	146	260	67	64
540	1000	800	116	250	36	59
650	1200	710	103	240	35	35
760	1400	455	66	260	38	12
870	1600	325	47	240	35	30
Haynes 188, sheet						
21	70	960	139	485	70	56
540	1000	740	107	305	44	70
650	1200	710	103	305	44	61
760	1400	635	92	290	42	43
870	1600	420	61	260	38	73
S-816, bar						
21	70	965	140	385	56	30
540	1000	840	122	310	45	27
650	1200	765	111	305	44	25
760	1400	650	94	285	41	21
870	1600	360	52	240	35	16
Nickel-based alloys						
Astroloy, bar						
21	70	1410	205	1050	152	16
540	1000	1240	180	965	140	16
650	1200	1310	190	965	140	18
760	1400	1160	168	910	132	21
870	1600	770	112	690	100	25
D-979, bar						
21	70	1410	204	1010	146	15
540	1000	1300	188	925	134	15
650	1200	1100	160	860	129	21
760	1400	7	104	655	95	17
870	1600	345	50	305	44	18
Hastelloy X, sheet						
21	70	785	114	360	52	43
540	1000	650	94	290	42	45
650	1200	570	83	275	40	37
760	1400	435	63	260	38	37
870	1600	255	37	180	26	50

(*continued*)

Table A.22 (*continued*)

Temperature		Tensile strength		Yield strength		Elongation
°C	°F	MPa	ksi	MPa	ksi	%
IN-102, bar						
21	70	960	139	505	73	47
540	1000	825	120	400	58	48
650	1200	710	103	400	58	64
760	1400	440	64	385	56	110
870	1600	215	31	200	29	110
Nimonic 75, bar						
21	70	750	109	—	—	41
540	1000	635	92	—	—	41
650	1200	538	78	—	—	42
760	1400	290	42	—	—	70
870	1600	145	21	—	—	68
Nimonic 80A, bar						
21	70	1240	179	620	90	24
540	1000	1100	160	530	77	24
650	1200	1000	145	550	80	18
760	1400	760	110	505	73	20
870	1600	400	58	260	38	34
Inconel 601, sheet						
21	70	740	107	340	49	45
540	1000	725	105	150	2	38
650	1200	525	76	180	26	45
760	1400	290	42	200	29	73
870	1600	160	23	140	20	92
Inconel 625, bar						
21	70	855	124	490	71	50
540	1000	745	108	405	59	50
650	1200	710	103	420	61	35
760	1400	505	73	420	61	42
870	1600	285	41	475	40	125
Inconel 706, bar						
21	70	1300	188	980	142	19
540	1000	1120	163	895	130	19
650	1200	1010	147	825	120	21
760	1400	690	100	675	98	32
Inconel 718, bar						
21	70	1430	208	1190	172	21
540	1000	1280	185	1060	154	18
650	1200	1230	178	1020	148	19
760	1400	950	138	740	102	25
870	1600	340	49	330	48	88
Inconel 718, sheet						
21	70	1280	185	1050	153	22
540	1000	1140	166	945	137	26
650	1200	1030	150	870	126	15
760	1400	675	98	625	91	8
Inconel X-750, bar						
21	70	1120	162	635	92	24
540	1000	965	140	580	84	22
650	1200	825	120	565	82	9
760	1400	485	70	455	66	9
870	1600	235	34	165	24	47

(*continued*)

Table A.22 (*continued*)

Temperature		Tensile strength		Yield strength		Elongation
°C	°F	MPa	ksi	MPa	ksi	%
M-252, bar						
21	70	1240	180	840	122	16
540	1000	1230	178	765	111	15
650	1200	1160	168	745	108	11
760	1400	945	137	715	104	10
870	1600	510	74	485	70	18
Nimonic 90, bar						
21	70	1240	180	805	117	23
540	1000	1100	160	725	105	23
650	1200	1030	150	685	99	20
760	1400	825	120	540	78	10
870	1600	430	62	260	38	16
Nimonic 105, bar						
21	70	1140	166	815	118	12
540	1000	1100	160	775	112	18
650	1200	1080	156	800	116	24
760	1400	965	140	655	95	22
870	1600	605	88	365	53	25
Nimonic 115, bar						
21	70	1240	180	860	125	25
540	1000	1090	158	795	115	26
650	1200	1120	163	815	118	25
760	1400	1080	157	800	116	22
870	1600	825	120	550	80	18
Pyromet 860, bar						
21	70	1300	188	835	121	22
540	1000	1250	182	840	122	15
650	1200	1110	161	850	123	17
760	1400	910	132	835	121	18
René 41, bar						
21	70	1420	206	1060	154	14
540	1000	1400	203	1010	147	14
650	1200	1340	194	1000	145	14
760	1400	1100	160	940	136	11
870	1600	620	90	550	80	19
René 95, bar						
21	70	1620	235	1310	190	15
540	1000	1540	224	1250	182	12
650	1200	1460	212	1220	177	14
760	1400	1170	170	1100	160	15
Inconel 600, bar						
21	70	620	90	250	36	47
540	1000	580	84	195	28	47
650	1200	450	65	180	26	39
760	1400	185	27	115	17	46
870	1600	105	15	62	9	80
Udimet 500, bar						
21	70	1310	190	840	122	32
540	1000	1240	180	795	115	28
650	1200	1210	176	760	110	28
760	1400	1040	151	730	106	39
870	1600	640	93	495	72	20

(*continued*)

Table A.22 (*continued*)

Temperature		Tensile strength		Yield strength		Elongation
°C	°F	MPa	ksi	MPa	ksi	%
Udimet 520, bar						
21	70	1310	190	860	125	21
540	1000	1240	180	825	120	20
650	1200	1170	170	795	115	17
760	1400	725	105	725	105	15
870	1600	515	75	515	75	20
Udimet 700, bar						
21	70	1410	204	965	140	17
540	1000	1280	185	895	130	16
650	1200	1240	180	855	124	16
760	1400	1030	150	825	120	20
870	1600	690	100	635	92	27
Udimet 710, bar						
21	70	1190	172	910	132	7
540	1000	1150	167	850	123	10
650	1200	1290	187	860	125	15
760	1400	1020	148	815	118	25
870	1600	705	102	635	92	29
Unitemp AF2-1DA, bar						
21	70	1290	187	1050	152	10
540	1000	1340	194	1080	157	13
650	1200	1360	197	1080	157	13
760	1400	1150	167	1010	146	8
870	1600	830	120	715	104	8
Waspaloy, bar						
21	70	1280	185	795	115	25
540	1000	1170	170	725	105	23
650	1200	1120	162	690	100	34
760	1400	1400	115	675	98	28
870	1600	525	76	515	75	35

Table A.23 Approximate values of DBTT of aluminides and MCrAlYs

Coating	Estimated DBTT, °C (°F)
NiAl	868–1060 (1594–1940)
(Ni,Pt)Al	>Plain aluminide
CoAl	878–1070 (1612–1958)
Co18Cr9Al1Y	150–200 (302–392)
Co18Cr11Al1Y	250–300 (482–572)
Co20Cr12.5Al1Y	600–650 (1112–1202)
Co29Cr6Al1Y	700–800 (1292–1472)
Co27Cr12AlY	800–900 (1472–1652)
Ni20Cr9-11AlY	25–200 (77–392)
Ni38Cr11AlY	600–650 (1112–1202)
$PtAl_2$	870–1070 (1598–1958)
Commercial platinum aluminide (temperature at which fractures at 3% strain)	~930 (1706)

Table A.24 Registered trademarks and trademarks

Registered trademarks	Company
AL, ALLEGHENY, ALMAR, AM, AL-6XN, AL 29-4, AL 29-4C	Allegheny Ludlum Steel Corporation
ALLCOR	Teledyne Industries, Inc.
APKL	Inco Family of Companies
ARMCO	American Rolling Mill Company
ASTROLOY	Reichhold Chemicals, Inc.
CARPENTER	Carpenter Technology Corporation
CHLORIMET	Duriron Company
CHROMEL	Hoskins Manufacturing Company
CMSX	Cannon-Muskegon Corporation
COLMONOY	Wall Colmonoy Corporation
COR-TEN	USX Corporation
CROLOY	Babcock & Wilcox Company
CRONIFER	VDM Technologies Corporation
CRUCIBLE	Crucible Steel Company
CUSTOM 450, CUSTOM 455	Carpenter Technology Corporation
DISCALOY	Westinghouse Electric Corporation
E-BRITE	Allegheny Ludlum Steel Corporation
ELGILOY	Elgiloy Company
ESSHETE	British Steel Corporation
FECRALLOY	UK Atomic Energy
FERRALIUM	Bonar Langley Alloys, Ltd.
GATORIZED	United Technology Corporation
HASTELLOY, HAYNES	Haynes International, Inc.
HNM	Colt Industries, Inc.
HWT	Allegheny Ludlum Steel Corporation
ILLIUM	Stainless Foundry & Engineering Company
INCOLOY, INCONEL, INCO-WELD, INCO	Inco Family of Companies
JESSOP	Jessop Steel
KANTHAL	The Kanthal Corporation
MA, MONEL	Inco Family of Companies
MANAURITE	Acieries du Manoir Pompey
MANGANAL	Stulz-Sickles Steel Company
MARATHON	Marathon Corporation
MERL	United Technology Corporation
MF-1	Allegheny Ludlum Industries
MULTIMET	Haynes International, Inc.
MULTIPHASE	SPS Technologies, Inc.
MO-RE	Duraloy Blaw-Knox, Inc.
MONIT	Granges Nyby AB
MP, MP35N	SPS Technologies, Inc.
NICHROME	Driver-Harris Company
NICROTUNG	Westinghouse Electric Corporation
NICROFER, NICORROS, NIMOFER	VDM Technologies Corporation
NITRONIC	Armco Steel Corporation
NI-SPAN-C, NIMONIC	Inco Family of Companies
PYROMET	Carpenter Technology Corporation
RENÉ	General Electric Company
RENÉ 41	Teledyne Industries, Inc.
REP	Whittaker Corporation
SANICRO, SANDVIK	Sandvik Aktiebolag
SEA-CURE	Crucible Materials Corporation
SM	Sumitomo Metal Industries, Ltd.
STELLITE	Stoody Deloro Stellite, Inc.
SUPERTHERM, THERMALLOY, THERMAX	Abex Corporation
TENELON	USX Corporation
UDIMET	Special Metals, Inc.

(*continued*)

Table A.24 (*continued*)

Registered trademarks	Company
UDDEHOLM	Uddeholms Aktiebolag
UNILOY, UNITEMP	Universal Cyclops Steel Corporation
URANUS	Creusot-Loire Steel Company
WASPALOY	United Technology Corporation
RA330, RA330HC, RA333, RA85H	Rolled Alloys
253MA, 254SMO, 44LN	Avesta Jernverks Aktiebolag
800HT	Inco Family of Companies
20Cb-3, 7-Mo PLUS, 20Mo-4, 20Mo-6, 625 PLUS	Carpenter Technology Corporation
22H	Duraloy Blaw-Knox, Inc.
PH15-7Mo, PH13-8Mo, 17-4PH, 15-5PH	Armco Steel Corporation
JS700	Jessop Steel Company
ALFA-II, ALFA-IV, OR-1, MF-2, A-286	Allegheny Ludlum Steel Corporation
12SR, 18SR, 17-7PH, PH13-8Mo	Armco Steel Corporation
MAR-M	Martin Marietta Corporation
214, 230, 556, HR-160, HR-120	Haynes International, Inc.
C-22, G-30, ULTIMET	Haynes International, Inc.
FECRALOY "A"	UK Atomic Energy

Table A.25 Materials for nuclear power systems, listed by subsystem.

Materials in fission reactors					
Fuel and cladding	Coolant/ moderator	Control	Pressure vessel	Piping/ internals	IHX/steam generator
PWR (Andrews and Jelley 2007; Glasstone and Sesonske 1994; Roberts 1981)					
Enriched UO_2/MOX Zircaloy 4	Light water	Ag-In-Cd B_4C 304 SS Inconel 627 Boric acid Borosilicate glass Al_2O_3	SA508 Gr. 3 Class 1.2 SA533 Gr. B 308SS, Inconel 617 (clad)	304 SS 316 SS ASTM 516 Gr. 70 308L	SA533 Gr. B Inconel 600 Incoloy 800 SA515 Gr. 60
BWR (Andrews and Jelley 2007; Glasstone and Sesonske 1994; Roberts 1981)					
Enriched UO_2 Gd_2O_3 Zircaloy 2	Light water	B_4C 304 SS	SA508 Gr. 3 Class 1.2 SA533 Gr. B 308 L SS (clad)	304 SS 316, 316 L 304 L 347 Inconel SA106 Gr. B SA333 Gr. 6	SA533 Gr. B Inconel 600 Incoloy 800 SA515 Gr. 60
AGR (Frost 1995; Marshall 1983)					
Enriched UO_2 25Cr–20Ni SS Graphite	CO_2 Graphite	Boron steel Cd Nitrogen Boronated glass	Prestressed concrete Mild steel	Mild steel Annealed 9Cr–1Mo steel 18Cr–12Ni SS	Mild steel Annealed 9Cr–1Mo steel 18Cr–12Ni SS
LMFBR (Andrews and Jelley 2007; Roberts 1981, Generation IV Nuclear Energy Systems, Appendix 5.0 2007)					
MOX U–Pu–Zr MC MN 316 SS Depleted UO_2	Liquid sodium	B_4C 316 SS Eu_2O_3 EuB_6	304 SS 316 SS 316 FR	304 SS 316 SS 316 FR Alloy 718	$2^{1/}$4Cr–1Mo steel (SA336) 9Cr–1Mo steels (modified) Incoloy 800 304 SS 316 SS
VHTR (Petti et al. 2009, Generation IV Nuclear Energy Systems, Appendix 1.0, 2007)					
UCO UO_2 Pyrolytic carbon Silicon carbide	Helium Graphite Nitrogen Molten salt	Cf/C, SiCf/SiC (clad)	Modified 9Cr–1MoV steel P91 SA508 Gr. 3 Class 1.2 SA533 Gr. B	Alloys 617 X, XR, 230, 602CA, 800H Carbon fiber Reinforced carbon Cf/C SiCf/SiC	Alloy 617 Alloy 230

(*continued*)

Table A.25 (*continued*)

Materials in fusion reactors	
ITER (Barabash et al. 2007; Ioki et al. 1998; Tokamak.aspx)	
Material	Forms
Thermal shield	
Stainless steel AISI 304L	Plates, tubes
Ti–6Al–4V	Plates
Steel grade 660	Fasteners
Inconel 718	Bolts
Al_2O_3 coatings	Plasma-sprayed insulation
Glass epoxy G10	Insulation
Ag coating	Coating, 5 μm (emissivity)
Vacuum vessel and ports	
Stainless steel 316L(N)-IG	Plates, forgings, pipes
Stainless steel AISI 304	Plates
Steel 660	Fasteners, forgings
Ferritic stainless steel 430	Plates
Borated steels 304B7 and 304B4	Plates
Inconel 718	Bolts
Stainless steel 316L (B8M)	Bolts
Austenitic steel XM-19 (B8R)	Bolts
Pure Cr	Clad
VV support	
Stainless steel AISI 304	Plates, rods
Steel 660	Fasteners
Inconel 718	Bolts
NiAl bronze	Rods
PTFE	Plates
First wall	
Beryllium (S-65C or equivalent)	Armor tiles
CuCrZr	Plates/cast/powder heat sink
Stainless steel 316L(N)-IG	Plates, pipes
Blanket and support	
316 L(N)-IG	Plates, forgings, pipe cast, powder HIP
Ti–6Al–4V	Flexible support
CuCrZr	Sheets
Inconel 718	Bolts
NiAl bronze	Plates
Al_2O_3 coatings	Plasma-sprayed insulation
CuNiBe or DS Cu	Collar
Diverter	
Cf/C (NB31 or equivalent)	Armor tiles
Tungsten	Armor tiles
CuCrZr	Tubes, plates
Stainless steel 316L(N)-IG	Plates, forgings, tubes
Steel 660	Plates, bolts
Austenitic steel XM-19	Plates, forgings
Inconel 718	Plates
NiAl bronze	Plates, rods

Table A.26 Materials in PWRs

Alumina, pressed and sintered	Stainless steel, austenitic, AISI 304, wrought, annealed
Boron carbide (hot pressed)	Stainless steel, austenitic, AISI 308, wrought, annealed
Borosilicate – 2405	Stainless steel, austenitic, AISI 308L, wrought, annealed
Carbon steel, AISI, 1020, normalized	Stainless steel, austenitic, AISI 316, wrought, annealed
Mixed oxide (U,Pu)O_2 (MOX) 20% PuO_2	Stainless steel, austenitic, AISI 347, wrought
Nickel–Cr–Co–Mo alloy, Inconel 617, wrought	Stainless steel, ferritic, AISI 403, wrought, annealed
Nickel–Fe–Cr alloy, Incoloy 800, annealed	Thoria, ThO_2
Nickel–chromium alloy, Inconel 600, wrought, annealed	Titanium alpha–beta Th–-6Al–4V
SA-508 Gr. 3 Cl 1 and 2	Uranium dioxide, UO_2
SA-533 Gr. B	Zirconium–tin alloy, Zircaloy 4, 1.5% Sn (reactor grade)

Table A.27 Materials proposed for use in fusion reactors

Beryllium grade 0-50, hot isostatically pressed	Beryllium grade 1-250, hot isostatically pressed
Beryllium grade S-200FH, hot isostatically pressed	Carbon fiber reinforced carbon matrix composite (Vf:40%)
Carbon fiber reinforced carbon matrix composite (Vf:50%)	Epoxy SMC (glass fiber)
Epoxy/E-glass fiber, woven fabric composite, qI laminate	Nickel iron aluminum bronze, (wrought) (UNS C63020)
Hi conductivity Cu–Cr–Zr (wp) (UNS C18100)	Nickel–chromium alloy, Inconel 718, wrought
Nickel iron aluminum bronze, (wrought) (UNS63020)	OFHC copper, 1/2 hard, (wrought) (UNS C10200)
Nickel–chromium alloy, Inconel 718	Silver, commercial purity, fine, cold worked, hard
PTFE (unfilled)	Stainless steel, austenitic, AISI 304, wrought, annealed
Stainless steel, austenitic, 316L(N)-IG	Stainless steel, austenitic, AISI 316, wrought, annealed
Stainless steel, austenitic, AISI 304L, wrought	Nitronic 50, XM-19, wrought, (nitrogen strengthened)
Stainless steel, austenitic, AISI 316L, wrought	Stainless steel, ferritic, AISI 430, wrought, annealed
Stainless steel, ferritic, AISI 430F, wrought, annealed	Stainless steel, ferritic, AISI 430FR, wrought, annealed
Titanium, alpha–beta alloy, Ti-6Al-4V, annealed, generic	Tungsten, commercial purity, R07004, annealed

References

Andrews, J. and Jelley, N. (2007). *Energy Science*. Oxford, UK: Oxford University Press.

Barabash, V., Peacock, A., Fabritsiev, S. et al. (2007). *J. Nucl. Mater.* 367–370: 21.

Ioki, I., Barabash, B., Cardella, A. et al. (1998). *J. Nucl. Mater.* 258–263: 74.

Petti, D., Crawford, D., and Chauvin, N. (2009). *Fuels for Advanced Nuclear Energy Systems*, vol. 34. MRS Bulletin.

Gen IV Nuclear Energy Systems (2007). Generation IV Nuclear Energy Systems Ten-Year Program Plan-Fiscal Year 2007. Appendices 1.0 and 5.0.

Roberts, J.T.A. (1981). *Structural Materials in Nuclear Power Systems*. New York, UK: Plenum Press.

Frost, B.R.T. (1995). *Nuclear Materials*, Materials Science and Technology, VCH Series, vol. 10A and 10B (ed. R.W. Cahn, P. Haasen and E.J. Kramer). Weinheim, Germany: Wiley-VCH.

Marshall, W. (1983). *Nuclear Power Technology*. Oxford: Clarendon Press.

Glasstone, S. and Sesonske, A. (1994). *Nuclear Reactor Engineering*, 4e. New York, NY: Chapman and Hall.

List of Acronyms

AA	Atomic absorption
AE	Acoustic emission
AEI	Absorbed electron images
AEM	Auger electron microscopy
AES	Auger electron spectroscopy
AET	Acoustic emission thermography
AFC	Alkaline fuel cells
AFM	Atomic force microscopy
AGR	Advanced gas-cooled reactor
AISI	American Iron and Steel Institute
APD	Avalanche photodiode
API	American Petroleum Institute
ASC	Advanced steam cycle
ASTM	American Society for Testing and Materials
ASR	Area specific resistance
ATIS	Automatic thermal impedance scanning
ATR	Attenuated total reflection
BCC	Body centered cubic
BCT	Body centered tetragonal
BOP	Balance-of-plant
BWR	Boiling water reactor
CANDU	Canadian deuterium uranium reactor
CCD	Charge-coupled device
CCRS	Controlled composition reaction sintering
CE	Counter electrode
CEV	Carbon equivalent for structural steel
CILC	Crud-induced localized corrosion
CMA	Cyclic multilayered alloy
CSP	Concentrated solar power
CTE	Coefficient of thermal expansion
CTEM	Conventional transmission electron microscopy
CVD	Chemical vapor deposition
CVN	Charpy V-notch
D_2O-PWR	Deuterium-moderated reactor
DBTT	Ductile-to-brittle transition temperature
DCFC	Direct carbon fuel cell
DDL	Diffuse double layer

High Temperature Corrosion: Fundamentals and Engineering, First Edition. César A. C. Sequeira.
© 2019 John Wiley & Sons, Inc. Published 2019 by John Wiley & Sons, Inc.

DIR	Direct *in situ* reforming
DLVO	Repulsive electrostatic double-layer forces and attractive van der Waals forces
DRS	Diffuse reflection spectroscopy
DOE	(US) Department of Energy
DPV	Differential pulse voltammetry
DS	Directional solidification
EBPVD	Electron beam evaporated physical vapor deposition
EBSD	Electron backscatter diffraction
ECAFM	Electrochemical atomic force microscopy
ECMS	Electrochemical mass spectroscopy
ECN	Electrochemical noise
EC-SERS	Electrochemical surface-enhanced Raman spectroscopy
ECSFA	Electrochemical surface forces apparatus
ECSTM	Electrochemical scanning tunneling microscope
EDX	Energy-dispersive X-ray analysis
EELS	Electron energy loss spectroscopy
EESR	Electrochemical electron spin resonance
EIS	Electrochemical impedance spectroscopy
ELNES	Energy-loss-near-edge-structure
E-PBR	Extended Pilling–Bedworth ratio
EMIB	Electromagnetic impact bonding
EMIRS	Electrochemically modulated infrared spectroscopy
EN	Euronorm
EPD	Electrophoretic deposition
EPMA	Electron probe microanalysis
EPN	Electrode potential noise
ES	Emission spectroscopy
ESCA	Electron spectroscopy for chemical analysis
ESEM	Environmental scanning electron microscopy
ESM	Electrochemical strain microscopy
ESPI	Electronic speckle pattern interferometry
EXAFS	Extended X-ray absorption fine structure
FAC	Flow-accelerated corrosion
FBR	Fast breeder reactor
FCC	Face centered cubic
FED	Field emission display
FECO	Fringes of equal chromatic order
FFM	Friction force microscopy
FLD	Forming limiting diagram
FMM	Force modulation microscopy
FMSFM	Force modulation scanning force microscopy
FPI	Fluorescent penetrant inspection
FSECT	Frequency scanning Eddy current technique
FSS	Ferritic stainless steel
FTIR	Fourier transform infrared spectroscopy
GAXRD	X-ray diffraction by the grazing angle
GDMS	Glow discharge spectroscopy
GDOES	Glow discharge optical emission spectrometry
GIF	Generation IV International Forum
GTL	Gas-to-liquid (hydrocarbon processing technologies)
HA	Hydrogen attack
HALT	High activity low temperature
HAZ	Heat affected zone
HCP	Hexagonal close packed

HDCFC	Hybrid direct carbon fuel cells
HIC	Hydrogen-induced cracking
HIC	Hot isostatic cladding
HIP	Hot isostatic processing
HREM	High resolution electron microscopy
HRTEM	High resolution transmission electron microscopy
HTC	High temperature corrosion
HTF	Heat transfer fluid
HTHC	Type I hot corrosion
HTNR	High temperature NO_x reduction
HVOF	High velocity oxygen/fuel
IAC	Ion assisted coating
IAEA	International Atomic Energy Agency
IASCC	Irradiated assisted stress corrosion cracking
IBAD	Ion beam assisted deposition
ID	Inside diameter
IDZ	Interdiffusion zone
IFNR	In furnace NO_x reduction
IHX	Intermediate heat exchanger
IIR	Internal indirect reforming
IIXA	Ion induced X-ray analysis
IPM	Ion probe microanalysis
IR	Infrared spectroscopy
IRI	Infrared imaging
IRRAS	Infrared reflection absorption spectroscopy
IRS	Internal reflection spectroscopy
IRSEC	Infrared spectroelectrochemistry
ISS	Ion scattering spectroscopy
ITER	International thermonuclear experimental reactor
ITSOFC	Intermediate temperature solid oxide fuel cell
IVD	Ion-vapor deposition
LACVD	Laser assisted chemical vapor deposition
LAHT	Low activity high temperature
LDR	Limiting drawing ratio
LEED	Low-energy electron diffraction
LEEM	Low-energy electron microscopy
LEELS	Low-energy electron loss spectroscopy
LEER	Low-energy electron reflectivity
LFA	Lateral force microscopy
LFM	Lateral force microscopy
LFR	Lead-cooled fast reactor
LMFBR	Liquid metal cooled fast breeder reactor
LPPS	Low pressure plasma spraying
LRS	Laser Raman spectroscopy
LSA	Laser surface alloying
LSV	Linear sweep voltammetry
LTHC	Type II hot corrosion
MAP	Mechanical alloy processing
MCFC	Molten carbonate fuel cell
μLEED	Selected-area low-energy reflectivity
MD	Metal dusting
MEED	Medium-energy electron diffraction
MIR	Mid-infrared reflectance
MOR	Modulus of rupture

MOX	Mixed oxide fuel
MPC	Model predictive control
MPM	Multi-physics modeling
MSBR	Molten salt breeder reactor
MSFR	Molten salt fast reactor
MSRE	Molten salt reactor experiment
NACE	National Association of Corrosion Engineers
NDE	Non-destructive examination
NDI	Non-destructive inspection
NPP	Nuclear power plants
NPV	Normal pulse voltammetry
NRA	Nuclear reaction analysis
NSCR	Non-selective catalytic reduction
NSSS	Nuclear steam supply system
OCV	Open circuit voltage
ODS	Oxide dispersion strengthening
OFA	Over fire air ports
OOM	Object-oriented modeling
OPD	Optical path difference
OTI	Optical texture index
PAC	Probe approach curve
PACVD	Plasma assisted chemical vapor deposition
PAFC	Phosphoric acid fuel cell
PAPVD	Plasma assisted physical vapor deposition
PBR	Pilling–Bedworth ratio
PEMFC	Proton exchange membrane fuel cell
PL	Photoluminescence
PLPS	Photoluminescence piezospectroscopy
PM	Powder metallurgy
PMT	Photomultiplier tube
PPW	Plasma powder welding
PS	Piezospectroscopy
PSPD	Position-sensitive photodetector
PWR	Pressurized water reactor
QWP	Quarter wave plate
RBMK	Light water graphite moderated reactor
RDE	Rotating disk electrode
RE	Reactive elements
RRDE	Rotating ring-disk electrode
RBS	Rutherford backscattering spectrometry
RS	Reactive sputtering/Raman spectroscopy
RF	Radio frequency
RHEED	Reflection high-energy electron diffraction
SAM	Scanning auger microanalysis
SANS	Small-angle neutron scattering
SCANIIR	Surface composition by analysis of neutral and ion impact radiation
SCC	Stress corrosion cracking
SCR	Selective catalytic reduction
SECM	Scanning electrochemical microscopy
SEE	Secondary electron emission
SEM	Scanning electron microscopy
SERS	Surface-enhanced Raman spectroscopy
SFA	Surface force apparatus
SFG	Sum-frequency generation

SFM	Scanning force microscopy
SFR	Sodium-cooled fast reactor
SHG	Second harmonic generation
SIMS	Secondary ion mass spectrometry
SIP	Sputter ion plating
SOFC	Solid oxide fuel cell
SOHIC	Stress-oriented hydrogen-induced cracking
SPLEED	Spin-polarized low-energy electron diffraction
SPM	Scanning probe microscopy
SRI	Spall resistance index
SSC	Sulfide stress cracking
SSMS	Spark source mass spectrography
STEM	Scanning transmission electron microscopy
STM	Scanning tunneling microscope
SWV	Square wave voltammetry
TBC	Thermal barrier coating
TCP	Topologically-close packed
TEM	Transmission electron microscopy
TES	Thermal energy storage
TGFS	Turbine, generator and feedwater system
TG-IR	Thermogravimetric analysis–infrared spectrometry
TGO	Thermally grown oxide
TIPS	Transformation induced plasticity steels
TOF	Time-of-flight
ToFMS	Time-of-flight mass spectrometry
TOFD	Time of flight diffraction
TPB	Triple-phase boundary
TSS	Terminal solid solubility
TTT	Time temperature transformation
TWI	Thermal wave interferometry
UCO	Uranium oxycarbide
UHV	Ultra-high vacuum
UME	Ultramicroelectrode
UNS	Unified numbering system
UPS	UV photoelectron spectroscopy
UT	Ultrasonic testing
UTS	Upper tensile stress
UV	Ultraviolet
VFD	Vacuum fluorescent display
VHTR	Very high temperature reactor
VLEED	Very low-energy electron diffraction
VOD/AOD	Vacuum ladle treatment
VPS	Vacuum plasma spraying
VP-SEM	Variable pressure scanning electron microscopy
WDX	Wavelength dispersive X-ray fluorescence spectrometer
WE	Working electrode
XFS	X-ray fluorescence spectroscopy
XPS	X-ray photoelectron spectroscopy
XRD	X-ray diffraction
XTEM	X-ray transmission electron microscopy
YSZ	Yttria stabilized zirconia
ZRA	Zero-resistance ammeter

Glossary of Selected Terms Used in High Temperature Corrosion

Abrasive	Material such as sand, crushed chilled cast iron, crushed steel grit, aluminum oxide, silicon carbide, flint, garnet, or crushed slag used for cleaning or surface roughening.
Absolute pressure	Pressure above zero pressure; the sums of the gage and atmospheric pressures.
Acoustic emission	AE is commonly defined as transient elastic waves within a material, caused by the rapid release of localized stress energy. Hence, an event source is the phenomenon which releases elastic energy into the material, which then propagates as an elastic wave. Acoustic emissions can be well detected within the 1 kHz and 1 MHz range. AE can be used not only to locate but also to characterize the source mechanisms, i.e. crack growth, friction, delamination, matrix cracking, etc.
Activation	The changing of a passive surface of a metal to a chemically active state. Contrast with passivation.
Active	The negative direction of electrode potential. Also used to describe corrosion and its associated potential range when an electrode potential is more negative than an adjacent depressed corrosion-rate (passive) range.
Active oxidation	This mechanism, comprising inward penetration of chlorine into the scale, formation of chlorides at the oxide/metal interface, evaporation of the chlorides and conversion of the evaporating chlorides into oxides, which occurs at more or less distance from the surface (depending on p_{O_2}), leads to loose, fragile, multilayered oxides which are unprotective (therefore: active oxidation). Fe and Cr are rapidly transferred into such a scale, Ni and Mo are relatively resistant. In many cases, the grain boundaries of the materials are strongly attacked and this is due to a susceptibility of chromium carbides to chloridation. In contrast, the carbides Mo_2C, TiC, and NbC are less attacked than the matrix. Alloys on the basis Fe–Cr–Si proved to be rather resistant, and the alloying elements Ni and Mo clearly retard the attack in an oxidizing and chloridizing environment.
Active–passive material	A metal or alloy that corrodes to an extent and then passivates due to an oxide film formation on its surface.
Active–passive transition	Transition from an active to a passive condition on a metal surface – influenced by potential and environment.

High Temperature Corrosion: Fundamentals and Engineering, First Edition. César A. C. Sequeira.
© 2019 John Wiley & Sons, Inc. Published 2019 by John Wiley & Sons, Inc.

Activity	A measure of the chemical potential of a substance, where chemical potential is not equal to concentration that allows mathematical relations equivalent to those for ideal systems to be used to correlate changes in an experimentally measured quantity with changes in chemical potential.
Age hardening	Hardening by aging, usually after rapid cooling or cold working.
Aliovalent solute	Impurity solute in ionic crystals whose valence differs from that of a host ion. Aliovalent solutes disturb the electrical neutrality and must be associated with other effects (either lattice defects or electrons) compensating their charge.
Allotropy	The possibility of the existence of two or more different crystal structures for a substance (generally an elemental solid).
Alloy	A metallic substance that is composed of two or more elements.
Alloy design	By using physical metallurgy, solid-state processing, solidification processing and engineering, physical simulation, multiscale materials modeling, computational design, X-ray characterization of materials and other advanced procedures, it is possible to innovate, develop, design, and expand the scope for discovery and implementation of novel alloys for advanced industrial systems.
Alloy steel	A ferrous (or iron-based) alloy that contains appreciable concentrations of alloying elements (other than C and residual amounts of Mn, Si, S, and P). These alloying elements are usually added to improve mechanical and corrosion resistance properties.
Aluminides	An aluminide is a compound that has aluminum with more electropositive elements. Since aluminum is near the non-metals on the periodic table, it can bond with metals differently from other metals. The properties of an aluminide would be intermediate between a metal alloy and an ionic compound.
Aluminizing	Forming of an aluminum or aluminum alloy coating on a metal by hot dipping, hot spraying, or diffusion.
Angstrom	A unit of length equal to one ten-billionth of a meter.
Anion	A negatively charged ion such as SO_4^{-2}.
Anodic dissolution	A corrosion process caused by an anodic overpotential, which depends on the exchange current density.
Annealing	A generic term denoting a treatment consisting of heating to and holding at a suitable temperature, followed by cooling at a suitable rate, used primarily to soften metallic materials, but also to simultaneously produce desired changes in other properties or in microstructure.
Anode	The electrode of an electrolytic cell at which oxidation is the principal reaction. (Electrons flow away from the anode in the external circuit. It is usually the electrode where corrosion occurs and metal ions enter solution.)
Anode corrosion efficiency	The ratio of the actual corrosion (weight loss) of an anode to the theoretical corrosion (weight loss) calculated by Faraday's law from the quantity of electricity that has passed.
Arc spraying	It is a form of thermal spraying where two consumable metal wires are fed independently into the spray gun. These wires are then charged and an arc is generated between them. The heat from this arc melts the incoming wire, which is then entrained in an air jet from the gun. This entrained molten feedstock is then deposited onto a substrate. This process is commonly used for metallic, heavy coatings.
Ash	The incombustible inorganic matter in fuel.
Austenite	A solid solution of one or more elements in face-centered cubic iron. Unless otherwise designated (such as nickel austenite), the solute is generally assumed to be carbon.
Austenitic	The name given to the face-centered cubic (FCC) crystal structure of ferrous metals. Ordinary iron and steel has this structure at elevated temperatures; certain stainless steels (300 series) also have this structure at room temperature.

Austenitizing	Forming austenite by heating a ferrous alloy into the transformation range (partial austenitizing) or above the transformation range (complete austenitizing). When used without qualification, the term implies complete austenitizing.
Auxiliary electrode	An electrode commonly used in polarization studies to pass current to or from a test electrode, usually made of noncorroding material.
Bainite steel	An austenitic transformation product found in some steels (and cast irons), designated by bainite steels. Bainite forms at temperatures between those at which pearlite and martensite transformations occur. The microstructure consists of α-ferrite and a fine dispersion of cementite.
Bainite	An austenitic transformation product found in some steels (and cast irons), designated by bainite steels. Bainite forms at temperatures between those at which pearlite and martensite transformations occur. The microstructure consists of α-ferrite and a fine dispersion of cementite.
Binding energy per nucleon	The binding energy B is the energy required to break apart a nucleus into its constituent nucleons. The difference between the mass of the isolated nucleons and the mass of a bound nucleus is the mass defect Δm. The total binding energy of the nucleus B is given by $$B = \Delta m\, c^2$$ where c is the speed of light in a vacuum. The binding energy per nucleon is B/A where A is the number of nucleons in the nucleus. The usual unit is keV, and $1\,\text{keV} = 1.6 \times 10^{-16}\ J = 3.38 \times 10^{-17}$ cal. It varies between isotopes so that some are more stable than others. The value listed in the database is that for the most abundant isotope unless otherwise stated.
Biofouling	A process referring to the adsorption of organics, micro-, and macroorganisms on a surface of a material in sequence.
Black plague	This is an accelerated form of corrosion that appears in superalloys, like Nimonic 105 and others, associated with sulfidation phenomena.
Body-centered cubic	A common crystal structure found in some elemental metals. Within the cubic unit cell, atoms are located at corner and cell center positions.
Boiler	A closed vessel in which water is heated, steam is generated, steam is superheated, or any combination thereof is done, under pressure or vacuum by the application of heat from combustible fuels, electricity, or nuclear energy.
Boiler efficiency	A term often substituted for *combustion efficiency* or *thermal efficiency*. True boiler efficiency is the measure of fuel-to-steam efficiency.
Boundary layer	The wall region in turbulent flow where the flow changes from fully turbulent to viscous, composed of the logarithmic region, the buffer region and the viscous region.
Brittle fracture	Separation of a solid accompanied by little or no macroscopic plastic deformation. Typically, brittle fracture occurs by rapid crack propagation with less expenditure of energy than for ductile fracture.
Cast iron	Generically, a ferrous alloy, the carbon content of which is greater than the maximum solubility in austenite at the eutectic temperature. Most commercial cast irons contain between 3.0 and 4.5 wt% C, and between 1 and 3 wt% Si.
Cathode	The electrode of an electrolytic cell at which reduction is the principal reaction. Electrons flow toward the cathode in the external circuit.
Cation	A positively charged ion such as Cu^{2+}.
Cavitation	Repeated nucleation, growth, and violent collapse of cavities or bubbles containing vapor and/or gas within a liquid. Cavitation originates from a local decrease to hydrostatic pressure in the liquid produced by motion of the liquid (flow cavitation) or by pressure fluctuations within the liquid induced by vibration of a solid boundary (vibratory cavitation).
Cavitation erosion	Progressive loss of material from a solid surface following cavitation when the cavities or bubbles collapse on or near the surface.

Cavitation erosion–corrosion	The conjoint action of cavitation erosion and corrosion.
Cavitation number	σ is a measure of the intensity of cavitation: $$\sigma = (p - p_v)/0.5\ \rho u^2$$ where p is the static pressure (absolute), p_v is the vapor pressure, ρ is the density, and u is the free stream velocity. When $\sigma = 0$, the pressure is reduced to the vapor pressure and cavitation will occur. Note: $\text{NPSH}_\text{A} = (\sigma + 1)\ u^2/2g$.
Cementite	A compound of iron and carbon, known chemically as iron carbide and having the approximate chemical formula Fe_3C. It is characterized by an orthorhombic crystal structure.
Cermet	A physical mixture of ceramics and metals; examples are alumina plus nickel and zirconia plus nickel.
Chemical vapor deposition	A coating process, similar to gas carburizing and carbonitriding, in which a reactant atmosphere gas is fed into a processing chamber where it decomposes at the surface of the workpiece, liberating one material for either absorption by or accumulation on the workpiece. A second material is liberated in gas form and is removed from the processing chamber, along with excess atmosphere gas.
Chlorine-cycle	This process describes corrosion in oxidizing–chlorinating environments. For example, if volatile metal chlorides exist in the high temperature environment in contact with a metal, the oxidation manifested by the metal can be accelerated because the chlorides diffuse toward the oxygen-rich outer part of the metal scale creating loose metal oxide process layers (which do not protect the metal) and forming chloride which is released and again penetrates the oxide scale, thus creating a cycle.
Chromizing	A surface treatment at elevated temperature, generally carried out in pack, vapor, or salt bath, in which an alloy is formed by the inward diffusion of chromium into the base metal.
Clad metal	A composite metal containing two or more layers that have been bonded together. The bonding may have been accomplished by co-rolling, coextrusion, welding, diffusion bonding, casting, heavy chemical deposition, or heavy electroplating.
Cladding	It is the act or process of bonding one metal to another, usually to protect the inner metal from corrosion.
Cleavage fracture	A fracture, usually of polycrystalline metal, in which most of the grains have failed by cleavage, resulting in bright reflecting facets. It is associated with low-energy brittle fracture.
Coating degradation	All coatings suffer degradation over time, regardless of the exposure to which they are subjected. The irregularities that arise can be very varied, for example, blistering, chalking, flaking, or rusting of the painted or coated substrate. The assessment of the type and size of these defects must be made in the most universal way possible, so that anybody involved can communicate effectively with all other interested parties. Accordingly, the International Organization for Standardization (ISO) and the ISO standards are strongly recommended.
Coating strength	(i) A measure of the cohesive bond within a coating, as opposed to the coating-to-substrate bond (adhesive strength). (ii) The tensile strength of a coating, usually expressed in kPa.
Coating stress	The stresses in coating resulting from rapid cooling of molten material or semi-molten particles as they come into contact with the substrate. Coating stresses are a combination of body and textural stresses.
Cold working	Deforming metal plastically under conditions of temperature and strain rate that induce strain hardening. Usually, but not necessarily, conducted at room temperature. Contrast with *hot working*.
Combustion	The rapid chemical combination of oxygen with the combustible elements of a fuel, resulting in the release of heat.

Combustion efficiency — The effectiveness of the burner in completely burning the fuel. A well-designed burner will operate with as little as 10–20% excess air, while converting all combustibles in the fuel to useful energy.

Compressive stress — A stress that causes an elastic body to deform (shorten) in the direction of the applied load. Contrast with tensile stress.

Concentration polarization — That portion of the polarization of a cell produced by concentration changes resulting from passage of current through the electrolyte.

Contact resistance — Partial interruption of electrical continuity between two surfaces caused by poorly conductive surface films or by excessive surface roughness.

Copper-bearing steel — A low-carbon "mild" steel but containing ~0.20–0.25% copper – not a "weathering" steel – and with corrosion rate relatively insensitive to minor variations in composition.

Corrosion — The degradation of a material by its environment.

Corrosion fatigue — The process in which a metal fractures prematurely under conditions of simultaneous corrosion and repeated cyclic loading at lower stress levels or fewer cycles than would be required in the absence of the corrosive environment.

Corrosion fatigue strength — The maximum repeated stress that can he endured by a metal without failure under definite conditions of corrosion and fatigue and for a specific number of stress cycles and a specified period of time.

Corrosion potential — The potential of a corroding surface in an electrolyte relative to that of a reference electrode measured under open-circuit conditions.

Corrosion product — Substance formed as a result of corrosion.

Corrosion rate — The amount of corrosion occurring per unit time (for example, mass change per unit area per unit time, penetration per unit time).

Corrosion resistance — The ability of a metal to withstand corrosion in a given corrosion system.

Corrosivity — The tendency of an environment to cause corrosion in a given corrosion system.

Covalent bond — A primary interatomic bond that is formed by the sharing of electrons between neighboring atoms.

Creep — Time-dependent strain occurring under stress. The creep strain occurring at a diminishing rate is called *primary creep*; that occurring at a minimum and almost constant rate, *secondary creep*; and that occurring at an accelerating rate, *tertiary creep*.

Crevice corrosion — Corrosion that takes place inside a crevice.

Critical stress for crack propagation — This is the subcritical value of the stress intensity under conditions where fracture mechanics predicts that failure should not occur, but that is in fact sufficient for cracks to develop and propagate in the presence of a corrodent. The rate at which crack begins propagating is, most of the time, the rate at which the corrosive ions can diffuse to the crack tip.

Cross-section — The cross-section for a process is the measure of a probability of the process occurring. For a neutron induced process, it is the effective area presented by a target nuclei to a beam of neutrons, and thus has the dimensions of area. For a thin sheet of nuclei with number density n and an incident neutron beam of flux Φ, the rate of the process occurring per unit volume R is given by

$$R = \Phi n \sigma$$

where σ is the cross-section (also called the microscopic cross-section). The usual unit is barns and $1\,\text{b} = 10^{-24}\,\text{cm}^2 = 10^{-28}\,\text{m}^2$.

- *Absorption cross-section*, σ_a. The microscopic cross-section for the absorption of a neutron by an atom. This is the sum of the fission and capture cross-sections.
- *Scattering cross-section*, σ_s. The microscopic cross-section for the scattering of a neutron by an atom.
- *Fission cross-section*, σ_f. The microscopic cross-section for the absorption of a neutron by an atom and the subsequent splitting of the target atom.

Different isotopes have different values of σ. Unless otherwise stated the value is given for a natural mixture of isotopes. The value σ is strongly dependent on neutron energy; the values in the database are for thermal neutrons of energy 0.025 eV.

Deacon process This is a process used during the manufacture of alkalis (the initial end product was sodium carbonate) by the Leblanc process. Hydrogen chloride gas was converted to chlorine gas, which was then used to manufacture a commercially valuable bleaching powder and, at the same time, the emission of waste hydrochloric acid was curtailed. To some extent this technically sophisticated process superseded the earlier manganese dioxide process. Invented by Henry Deacon in 1874, the process was based on the oxidation of hydrogen chloride ($HCl \rightarrow Cl_2$). The reaction takes place at about 400–450 °C in the presence of a variety of catalysts including copper chloride ($CuCl_2$).

Dealloying Selective removal of an element from an alloy by corrosion.

Dendrite A crystal that has a treelike branching pattern, being most evident in cast metals, slowly cooled through the solidification range.

Descaling Removing the thick layer of oxides formed on some metals at elevated temperatures.

Dew point The temperature at which moisture will condense from humid vapors into a liquid state.

Diffuse double layer An electrochemical envelope surrounding a particle in aqueous solution of an inner tightly packed layer of adsorbed ions and an outer layer of loosely adsorbed ions.

Diffusion coating Any process whereby a base metal or alloy is either (i) coated with another metal or alloy and heated to a sufficient temperature in a suitable environment or (ii) exposed to a gaseous or liquid medium containing the other metal or alloy, thus causing diffusion of the coating or of the other metal or alloy into the base metal, with resultant changes in the composition and properties of its surface.

Dislocation A linear imperfection in a crystalline array of atoms. Two basic types are recognized: (i) an edge dislocation corresponds to the row of mismatched atoms along the edge formed by an extra, partial plane of atoms within the body of a crystal and (ii) a screw dislocation corresponds to the axis of a spiral structure in a crystal, characterized by a distortion that joins normally parallel planes together to form a continuous helical ramp.

Dimensionless groups

Reynolds number: $Re = u_b l\rho/\mu$, is the ratio of inertial forces to viscous forces. Its size determines the nature of the flow. In single phase pipe flow $Re < 2000$ the flow is laminar. At $Re > 4000$ the flow is turbulent.

Schmidt number: $Sc = \mu/\rho D$, is the ratio of momentum diffusivity (kinematic viscosity, μ/D) to mass diffusivity.

Sherwood number: $Sh = kl/D$, is the ratio of convective mass transport to diffusive transport

where l is a characteristic dimension (e.g. pipe diameter) (m), μ is the viscosity (Pa s), u_b is the bulk flow velocity ($m\,s^{-1}$), D is the diffusion coefficient ($m^2\,s^{-1}$), k is the mass transfer coefficient ($m\,s^{-1}$), and ρ is the density ($kg\,m^{-3}$).

Dispersion hardening A means of strengthening materials wherein very small particles (usually less than 0.1 μm) of a hard yet inert phase are uniformly dispersed within a load-bearing matrix phase.

Dual phase steels Low carbon steels containing two phases, a fine dispersion of 10–20 vol% martensite in a matrix of ferrite.

Ductile fracture Fracture characterized by tearing of metal accompanied by appreciable gross plastic deformation and expenditure of considerable energy. Contrast with *brittle fracture*.

Ductile-to-brittle transition temperature The DBTT is the temperature at which the slope of the strain-temperature curve changes significantly.

Ductility A measure of a material's ability to undergo appreciable plastic deformation before fracture; it may be expressed as percent elongation (% EL) or percent reduction in area (% RA) from a tensile test.

Ductility – transition temperature	It is the temperature that divides a lower temperature regime where the fracture is said to be non-ductile from a higher temperature range where considerable plastic deformation accompanies failure.
Eddy current	Eddy currents are closed loops of induced current circulating in planes perpendicular to the magnetic flux. They normally travel parallel to the coil's winding and the flow is limited to the area of the inducing magnetic flux. Eddy currents concentrate near to the surface adjacent to an excitation coil and their strength decreases with distance from the coil. Non-insulating materials and coatings can be sensed as inductance changes by a search coil, but considerable skill is needed and there are edge limitations.
Elastic modulus	The modulus of elasticity or Young's modulus is a mechanical property of linear elastic solid materials that defines the relationship between stress (force per unit area) and strain (proportional deformation) of a material.
Electrochemical impedance spectroscopy (EIS)	The frequency-dependent complex-valued proportionality factor E/I, between the applied potential (or current) and the response current (or potential) in an electrochemical cell. This factor becomes the impedance when the perturbation and response are related linearly (the factor value is independent of the perturbation magnitude) and the response is caused only by the perturbation. The value may be related to the corrosion rate when the measurement is made at the corrosion potential.
Electrochemical potential (electrochemical tension)	The partial derivative of the total electro-chemical free energy of the system with respect to the number of moles of the constituent in a solution when all other factors are constant. (It is analogous to the chemical potential of the constituent, except that it includes the electrical as well as chemical contributions to the free energy).
Electrode potential	The potential of an electrode in an electrolyte as measured against a reference electrode. (The electrode potential does not include any resistance losses in potential in either the solution or external circuit. It represents the reversible work to move a unit charge from the electrode surface through the solution to the reference electrode.)
Electrolyte	A nonmetallic substance that carries an electric current, or a substance which, when dissolved in water, separate into ions which can carry an electric current.
Electrolytic cell	An assembly, consisting of a vessel, electrodes, and an electrolyte, in which electrolysis can be carried out.
Electrolytic cleaning	A process of removing soil, scale, or corrosion products from a metal surface by subjecting it as an electrode to an electric current in an electrolytic bath.
Electromotive force series (emf series)	A list of elements arranged according to their standard electrode potentials, with "noble" metals such as gold being positive and "active" metals such as zinc being negative.
Electron backscatter diffraction	In EBSD the accelerated electrons in the primary beam of a SEM are diffracted by atomic layers in crystalline materials. Electron backscatter patterns are generated giving direct information about the crystalline structure and crystallographic orientations of the grains from which they originate.
Electron beam evaporated physical vapor deposition	In this process, a vapor cloud is created in a highly evacuated chamber by melting ingots or granules of the coating material. The melting is achieved by the use of focused electron beams. The vapor species consist of atoms, molecules, ions, and clusters of atoms. The component to be coated is rotated in the vapor, which deposits to form the coating. In this process the deposition is proportional to the vapor pressure of the coating constituent. Moreover, the microstructure of the deposited coating generally exhibits a texture with intercolumnar grain boundaries perpendicular to the substrate surface.
Electroplating	This is a process that uses electric current to reduce dissolved metal cations so that they form a coherent metal coating on an electrode. The term is also used for electrical oxidation of anions onto a solid substrate.
Embrittlement	The severe loss of ductility or toughness or both, of a material, usually a metal or alloy.
Environmental cracking	Brittle fracture of a normally ductile material in a corrosive environment. Environmental cracking is a general term that includes corrosion fatigue, hydrogen embrittlement, and stress cracking.

Equilibrium (reversible) potential	The potential of an electrode in an electrolytic solution when the forward rate of a given reaction is exactly equal to the reverse rate. (The equilibrium potential can only be defined with respect to a specific electrochemical reaction.)
Equilibrium reaction	A chemical reaction which proceeds primarily in one direction until the concentrations of reactants and products reach an equilibrium.
Erosion	The progressive loss of material from a solid surface as a result of mechanical interaction between that surface and a fluid, a multicomponent fluid, or solid particles carried with the fluid.
Erosion-corrosion	A conjoint action involving erosion and corrosion in a flowing single or multiphase corrosive fluid leading to the accelerated loss of material. Encompasses a wide range of processes including solid particle impingement erosion–corrosion, liquid droplet impingement erosion–corrosion, cavitation erosion-corrosion, and single-phase erosion of protective films leading to accelerated-corrosion. The relative contributions of erosion and corrosion to the total material loss vary with the type of erosion-corrosion. With metals, the mechanical or "chemical" erosion of protective films leading to accelerated-corrosion is a major factor. Erosion predominates with cavitation and liquid impingement erosion-corrosion.
Eutectic structure	A two-phase microstructure resulting from the solidification of a liquid having the eutectic composition; the phases exist as lamellae that alternate with one another.
Exchange current density	The rate of charge transfer per unit area when an electrode reaches dynamic equilibrium (at its reversible potential) in a solution; that is, the rate of anodic charge transfer (oxidation) balances the rate of cathodic charge transfer (reduction).
Face-centered cubic	A crystal structure found in some of the common elemental metals. Within the cubic unit cell, atoms are located at all corner and face-centered positions.
Faraday	A quantity of electric charge equal to $96\,500\,\mathrm{C} = 26.81\,\mathrm{Ah}$ required to oxidize or reduce one equivalent weight.
Fatigue life	The total number of cycles or time to failure; that is, to induce fatigue damage and to initiate a dominant fatigue flaw that propagates the failure.
Fatigue limit	The applied stress amplitude below which a material is expected to have an infinite fatigue life, or can sustain a specified number of cycles without failure, usually 10^7 or 10^8 cycles; also called the endurance limit.
Fatigue strength	The maximum stress that can be sustained for a specified number of cycles without failure, with the stress being completely reversed within each cycle unless otherwise staled.
Ferrite	A solid solution of one or more elements in body-centered cubic iron. Unless otherwise designated (for instance, as chromium ferrite), the solute is generally assumed to be carbon. On some equilibrium diagrams, there are two ferrite regions separated by an austenite area. The lower area is alpha ferrite; the upper, delta ferrite. If there is no designation, alpha ferrite is assumed.
Fiber-reinforced polymeric composite	An engineering material consisting of several distinctive phases interacting to achieve maximum strength and mechanical properties.
Flame spraying	It can be defined as the deposition of minute particles of a material to form a coating on a substrate by passing the particles through a continuous flame generating device such as an oxyacetylene torch.
Fluorescent penetrant inspection	This technique is a type of dye penetrant inspection in which a fluorescent dye is applied to the surface of a non-porous material in order to detect defects that may compromise the integrity or quality of the part in question. It is used in many industries due to its low cost and simplicity.
Fouling	This is the deposition of more loosely bonded deposits on the heat-absorbing surfaces in the convection pass, such as superheater and reheater, that are not exposed to radiant heat. Soot blowers using steam are generally adequate for removing the ash deposits on the fouled tube surfaces in the boiler.

Flow-accelerated corrosion (FAC)	A term sometimes used to describe the accelerated corrosion caused by flow-enhanced dissolution and thinning of protective films in carbon steel pipes protected by magnetite carrying deaerated hot water or mixtures of water and steam. The FAC is more usually referred to as an erosion-corrosion process.
Flow-dependent corrosion	Corrosion processes for which the corrosion rate varies with the velocity of flow of a single or multiphase fluid. In erosion-corrosion processes the material loss increases with flow rate. In pitting corrosion of stainless alloys and corrosion processes involving transport of passivators and inhibitors to the solid surface, the effect of increased flow rate is beneficial.
Flow-induced corrosion	Corrosion resulting from increased fluid turbulence intensity and mass transfer as a result of the flow of a fluid over a surface. A breakaway velocity is often involved for a given system.
Fracture mechanics	A quantitative analysis for evaluating structural behavior in terms of applied stress, crack length, and specimen or machine component geometry.
Fracture toughness	A generic term for measures of resistance to extension of a crack. The term is sometimes restricted to results of fracture mechanics tests, which are directly applicable in fracture control. However, it commonly includes results from simple tests of notched or precracked specimens that are not based on fracture mechanics analysis. Results from test of the latter type are often useful for fracture control, based on either service experience or empirical correlations with fracture mechanics tests. See also *stress-intensity factor*.
Free corrosion potential	Corrosion potential in the absence of net electrical current flowing to or from the metal surface.
Free energy	A thermodynamic quantity that is a function of internal energy and entropy of a system.
Frequency scanning Eddy current technique	This technique involves collecting data at several different frequencies and then comparing the data or mixing the data in some way. The impedance of an eddy current probe may be affected by many factors, namely the variations in operating frequency. In the simple case where interest is confined to detecting defects or other abrupt changes in geometry, a simple probe can be used to eliminate unwanted factors, providing they vary in a gradual manner. For example, variations in electrical conductivity and tube thinning affect both coils of a differential probe simultaneously. However, if unwanted parameters that occur abruptly are affecting the measurements, they can sometimes be negated by mixing signals collected at different frequencies.
Fuel	A substance containing combustible material used for generating heat.
Galvanic corrosion	When two dissimilar conducting materials in electrical contact with each other are exposed to an electrolyte, a current, called the galvanic current, flows from one to the other. Galvanic corrosion is that part of the corrosion that occurs at the anodic member of such a couple. The extent of galvanic corrosion is directly related to the galvanic current by Faraday's law.
Galvanostat	An electronic apparatus that controls the current between a sample under study (the working electrode) and a counter (or auxiliary) electrode.
Gibbs free energy	Thermodynamic function; also called free energy, free enthalpy, or Gibbs function.
Glow discharge optical emission spectrometry	GDOES is an optical emission technique using glow discharge plasma to give the quantitative depth distribution of elements in a thin surface on a metallic material.
Grain	An individual crystal in a polycrystalline metal or alloy; it may or may not contain twinned regions and subgrains; a portion of a solid metal (usually a fraction of an inch in size), in which the atoms are arranged in an orderly pattern.
Grain boundary	A narrow zone in a metal corresponding to the transition from one crystallographic orientation to another, thus separating one grain from another; with the atoms in each grain arranged in an orderly pattern; the irregular junction of two adjacent grains.
Grain-boundary corrosion	Same as *intergranular corrosion*.
Graphitization	A metallurgical term describing the formation of graphite in iron or steel, usually from decomposition of iron carbide at elevated temperatures. Not recommended as a term to describe *graphitic corrosion*.

Green rot
: A form of high-temperature corrosion of chromium-bearing alloys in which green chromium oxide (Cr_2O_3) forms, but certain other alloy constituents remain metallic; some simultaneous carburization is sometimes observed.

Gray cast iron
: A cast iron alloyed with silicon in which the graphite exists in the form of flakes. A fractured surface appears gray.

Growth (particle)
: During a phase transformation and subsequent to nucleation, the increase in size of a particle of a new phase.

Grueneisen constant
: This describes the effect that changing the volume of a crystal lattice has on its vibrational properties and, as a consequence, the effect that changing temperature has on the size or dynamics of the lattice. The term is usually reserved to describe the single thermodynamic property, γ, which is a weighted average of the many separate parameters γ_i entering the original Grueneisen's formulation in terms of the phonon nonlinearities. Because of the equivalences between many properties and derivatives within thermodynamics (e.g. see Maxwell relations), there are many formulations of the Grueneisen constant which are equally valid, leading to numerous distinct, yet correct, interpretations of its meaning. Some of the formulations for the Grueneisen constant include:

$$\gamma = V\left(\frac{\mathrm{d}P}{\mathrm{d}E}\right)_V = \frac{\alpha K_T}{C_V \rho} = \frac{\alpha K_S}{C_P \rho} = \frac{\alpha \nu_s^2}{C_P}$$

where V is volume, C_P and C_V are the principal (i.e. per-mass) heat capacities at constant pressure and volume, E is the energy, α is the volume coefficient of thermal expansion, K_S and K_T are the adiabatic and isothermal bulk moduli, ν_s is the speed of sound in the medium, and ρ is density. The Grueneisen constant is dimensionless.

Half life
: The time after which the number of a given radioactive nuclides in a sample halve by radioactive decay. If there are N_o radioactive nuclides at a time $t = 0$, the number of radioactive nuclides N at a time t is given by

$$N = N_o \exp - \lambda t$$

where λ is the decay rate. The half life $t_{1/2}$ is the time at which $N = N_o/2$, giving

$$t_{1/2} = \frac{(\ln 2)}{\lambda}$$

The usual unit is hours.

Hall coefficient
: The determination of the Hall coefficient (K) involves passing a direct current through the unknown semiconductor material, and at the same time a magnetic field is applied normal to the direction of current flow. A transverse voltage develops (the so-called Hall voltage), the sign of which depends on the nature of the material under investigation. The e.m.f. generated (V, volts) is proportional to the applied current (I, amp) and the magnetic field strength (H, gauss), and inversely proportional to the material thickness (t, cm) in the direction of the magnetic field. The proportional constant is termed the Hall coefficient, i.e. $V = R\,(IH/t) \times 10^{-8}$.

Halogenation
: The metal-halogen reaction, or halogenation reaction, differs from other reactions, such as oxidation, in that most reaction products are characteristic of high vapor pressures and, in some cases, low melting points. The volatile halides (reaction products) formed on the metal surface can no longer provide protection against further corrosion. This is in contrast with most oxides, which generally exhibit very low vapor pressures and high melting points. Furthermore, many halides exhibit low melting points. Once the reaction products become molten, the alloy loses all protection against further corrosion, leading to rapid attack. Among the halogenation processes, chlorination (attack by chlorine) and fluorination (attack by fluorine) are largely used in gas turbines, coal-fired boilers, oil-fired boilers, waste-to-energy boilers, black liquor recovery boilers, and so forth.

Hexagonal close-packed	A crystal structure found for some metals. The HCP unit cell is of hexagonal geometry and is generated by the stacking or close-packed planes of atoms.
High temperature	Temperatures high enough that water, when present in the corrosive environment, will be present as the vapor rather than the liquid.
High strength low alloy steels	Relatively strong, low carbon steels, with less than about 10 wt% total of alloying elements.
High velocity oxygen/fuel	This is a technology evolving from the D-Gun Process. In one of the gun designs, the HVOF nozzle system consists of an internal combustion chamber attached to a two-dimensional converging–diverging Laval nozzle. A combustible mixture of fuel and oxygen under high pressure is ignited in the combustion chamber to create a continuous flame. The combustion products exit the nozzle at supersonic velocity with associated "shock diamonds." Coating materials in the form of powder are injected into the flame axially or radially. The expanding jet of gas carries the heated powder particles, which on impact with the substrate plastically deform, cool and solidify.
HITEC	This is a molten oxidizing eutectic mixture of water soluble, inorganic salts of potassium nitrate (53 wt%), sodium nitrite (40 wt%) and sodium nitrate (53 wt%), pale yellow; below its melting point (142 °C), it is a white granular solid. It is a heat transfer medium for heating, and cooling between 149 and 538 °C that is used in process operations such as reactor temperature maintenance, high-temperature distillation, reactant preheating, rubber curing, and rotational molding. Because of the high heat transfer coefficient, high heat capacity, thermal stability, low degree of corrosivity, and low cost of HITEC, it has been used in solar technology, namely CSPs, and other technologies of TES for the phase change material stage, the inertized asbestos-containing waste, and reducing levelized electricity cost.
Holography	Holography denotes the techniques and tools of capturing and "replaying" the three-dimensional light information that reflects from illuminated objects. In the making of a hologram, one laser beam is split into two – the reference beam and the object beam – and both meet on the holographic film where an interface pattern is recorded. Projecting laser light, or ordinary white light (depending on the type of hologram), back through the film "structures" the light is just the way it originally reflected from the object. The eye sees the original subject in three dimensions even though the material object is no longer present.
Hot corrosion	This is generally regarded as attack in the joint presence of sulfur and oxygen. Typically, attack is considered to be triggered by molten alkali metal salts that melt above 700 °C. Sodium sulfate, with a melting point of 884 °C, derived from sodium chloride and sulfur from the fuel, is considered to be closely involved in the mechanism of hot corrosion. This mechanism is considered to have four stages: Oxidation (incubation); mild sulfidation; oxide failure; and catastrophic attack (internal sulfides via a porous voluminous complex oxide/deposit layer). Hot corrosion is an irreversible autocatalytic process.
Hot dip coating	It is a process wherein a base metal is caused to pass beneath the surface of a coating bath of a molten coating metal and is thereafter subjected to jet finishing, the base metal having been appropriately pretreated so as to be at the proper coating temperature and so as to have its surface oxide-free when passing through the bath of molten coating metal.
Hot working	Deforming metal plastically at such a temperature and strain rate that recrystallization takes place simultaneously with the deformation, thus avoiding any strain hardening.
Hybrid LPC plasma coating	It is a direct feed method, in which instead of powder feeding, a jet of plasma adds the desired material, simultaneously processed by laser. It is used for the production of high quality, non-oxidizing, refractory alloy coatings.
Hydrogen bond	A strong secondary interatomic bond that exists between a bound hydrogen atom (its unscreened proton) and the electrons of the adjacent atoms.

Hydrogen embrittlement	It is diffusible hydrogen that is harmful to the toughness of metals such as iron. There is no doubt that hydrogen embrittles iron, both austenitic and ferritic, and it does so at incredibly low average concentration. It has been known since 1875 that it is diffusible hydrogen that is harmfull. The conventional wisdom is that diffusion is necessary so that the hydrogen can concentrate at stress concentrations such as the tips of sharp cracks and therefore has greater consequences than indicated by a low average concentration. It follows, therefore, that the harmful influence of diffusible hydrogen can be mitigated by preventing its entry into steel or by rendering it immobile once it penetrates the material.
Hydrogen-induced cracking (HIC)	A type of cracking usually caused by hydrogen atoms that diffuse into steel and recombine at traps (such as elongated inclusions) causing microscopic blisters to form, which subsequently link and propagate; also known as stepwise cracking.
Hydrophobicity	A condition in which water is repelled.
Imperfection	A deviation from perfection; normally applied to crystalline materials wherein there is a deviation from atomic/molecular order and/or continuity.
Impingement erosion (gas bubble)	A term sometimes applied to the erosive role (removal of protective film) of impinging gas bubbles in the erosion-corrosion of heat exchanger tube inlets.
Impingement erosion (liquid droplet)	The progressive loss of material from a solid surface due to continued exposure to repeated discrete impacts by liquid droplets which generate impulsive and destructive contact pressures on the solid target.
Impingement erosion (solid particle)	Erosion by impinging solid particles suspended in a flowing fluid.
Impingement erosion–corrosion	A conjoint action of impingement erosion and corrosion.
Infrared imaging	In this technique, the intensity of radiation in the infrared part of the electromagnetic spectrum is recorded and converted to a visible image. It is very attractive for heat-insulating materials, e.g. TBCs.
Inhibitor	A chemical that reduces the rate of corrosion when added to the environment in small concentrations.
Inhibitor efficiency	The percentage reduction in corrosion rate caused by an inhibitor.
Interdiffusion zone	The IDZ is the internal zone or zone near the alloy interface that during the low activity high temperature aluminizing process loses Ni. It consists primarily of NiAl matrix with elongated precipitates of Cr-rich σ phases and refractory elements, which have low solubility in the β NiAl phases.
Interferometric techniques	These are techniques in which the principle of optical interference plays the key role. When a monochromatic beam makes a journey to and from a material and meets other beam coming directly from the same source, an interference pattern forms, whose analysis can be used for NDI of coatings and other materials.
Intergranular corrosion	Preferential corrosion at or adjacent to the grain boundaries of a metal or alloy.
Intergranular cracking	Cracking or fracturing that occurs between the grains or crystals in a polycrystalline aggregate. Also called intercrystalline cracking.
Intergranular fracture	Brittle fracture of a metal in which the fracture is between the grains, or crystals, that form the metal. Also called intercrystalline fracture. Contrast with transgranular fracture.
Internal oxidation	The formation of isolated particles of corrosion products beneath the metal surface. (This occurs as the result of preferential oxidation of certain alloy constituents by inward diffusion of oxygen, nitrogen, sulfur, etc.)
Interstitial solid solution	A solid solution wherein relatively small solute atoms occupy interstitial positions between the solvent or host atoms.
Ion beam assisted deposition	IBAD is a materials engineering technique which combines ion implantation with simultaneous sputtering or another PVD technique. This technique is especially useful to create a gradual transition between the substrate material and the deposited film, with less built-in strain than is possible by other techniques.

Ion plating	This is a PVD process that uses concurrent or periodic bombardment of the substrate and depositing film by atomic-sized energetic particles. Ion plating is used to deposit hard coatings of compound materials on tools, adherent metal coatings, optical coatings with high densities, and conformal coatings on complex surfaces.
Ionic bond	A coulombic interatomic bond that exists between two adjacent and oppositely charged ions.
Kellogg's method	This is a form of constructing vapor species diagrams, or Kellogg diagrams, or stability or predominance-area diagrams, which present the vapor pressure of compounds as a function of convenient variables such as partial pressure of gaseous compounds. More specifically, they are isothermal diagrams that show the ranges of gas compositions over which a condensed phase can exist either by itself or in equilibrium with another condensed phase.
Kirkendall effect	This is the motion of the boundary layer between two metals that occurs as a consequence of the difference in diffusion rates of the metal atoms. The effect can be observed, for example, by placing insoluble markers at the interface between a pure metal and an alloy containing that metal, and heating to a temperature where atomic diffusion is possible; the boundary will move relative to the markers.
Laser surface alloying	This is a coating strategy achieved by incorporating additional alloying elements in the surface melt region produced by the laser. The objective of LSA is to alloy completely added elements into the near surface while avoiding alloying element loss by vaporization or dissolution in the substrate.
Law of Levers	Mathematical expression whereby the relative phase amounts in a two-phase alloy at equilibrium may be computed.
Low-alloy steel	Iron-carbon alloys with less than 2% carbon, and a total alloying content of up to 12%.
Lux-flood model	This acid–base model was a revival of oxygen theory of acids and bases, proposed by Lux in 1939, further improved by Flood circa 1947 and is still used in modern geochemistry and electrochemistry of molten salts. This definition describes an acid as an oxide ion (O^{2-}) acceptor and a base as an oxide donor. For example, MgO (base) + CO_2 (acid) = $MgCO_3$, $CaO + SiO_2 = CaSiO_3$, and NO_3^- (base) + $S_2O_7^{2-}$ (acid) = $NO_2^+ + 2SO_4^{2-}$.
Martensite	A metastable iron phase supersaturated in carbon that is the product of a diffusionless (athermal) transformation from austenite.
Metal dusting	Accelerated deterioration of metals in carbonaceous gases at elevated temperatures to form a dustlike corrosion product.
Metal recession	This provides some measure of the corrosion intensity based on the metal loss calculated during the corrosion process. Accurate quantitative measurements of metal recessions for many high temperature materials are a matter of particular interest in phenomena such as metal dusting, carburization, nitridation, and others.
Metallic bond	A primary interatomic bond involving the nondirectional sharing of nonlocalized valence electrons ("sea of electrons") that are mutually shared by all the atoms in the metallic solid.
Metalliding	This is the term coined for surface modifying and surface hardening processes by electrodepositing refractory metals or metalloids on cheaper or softer substrates from fused salt electrolytes, at temperatures of 400–900 °C.
Metastable	Non-equilibrium state that may persist for a long time.
Microstructure	The structural features of an alloy (e.g. grain and phase structure) that are subject to observation under a microscope.
Mid-infrared reflectance	In this technique, IR spectroscopy is combined with reflection theories and then the absorption properties of a rough sample can be extracted from the reflected light. The reflectance has three components; reflection from the external surface, scattering within the sample (e.g. coating of TBC based on YSZ), and reflection from the interface between the sample (e.g. ceramic coating) and substrate (e.g. metallic bond coat). With continued operation (e.g. thermal cycling), cracks may develop linking up within the sample near the interface, which introduces air gaps with large changes in index of refraction from 2 to 1, resulting in increased reflectance whose measurements by FTIR spectroscopy can be used for NDI of defects.

Miller indices	A set of three integers (four for hexagonal) that designate crystallographic planes, as determined from reciprocals of fractional axial intercepts.
Molten carbonate fuel cell	In this cell, $Li_2CO_3/K_2CO_3/Na_2CO_3$ salts are the electrolyte. Heated to 650 °C, the salt melts and conducts CO_3^{2-} from the cathode to the anode, where hydrogen reacts with the ions to produce water, carbon dioxide, and electrons. These travel through an external circuit, providing electrical power along the way, and return to the cathode. There, oxygen from air and carbon dioxide recycled from the anode react with the electrons to form CO_3^{2-} that replenish the electrolyte and transfer current through the fuel cell. MCFCs work well with catalysts made of nickel, which is much less expensive than platinum.
Nernst equation	An equation that expresses the exact electromotive force of a cell in terms of the activities of the products and reactants of the cell.
Nucleation	The initial stage in a phase transformation. It is evidenced by the formation of small particles (nuclei) of the new phase, which are capable of growing.
Out-of-pack cementation	In this process, the pack mix is held in trays. The masked components to be coated are positioned above the pack in a retort with the option of flowing inert gas. Plumbing is so designed that the vapors, generated in the pack from the volatile halides, have access to both external and internal surfaces of the component to be coated. The retort is inserted into a furnace and held at the desired temperature for the selected duration. The process, which effectively involves chemical vapor deposition (CVD), typically yields low activity (outward-growing) coating.
Overlay coating	Overlay coatings have been developed with minimal direct contribution of the substrate alloy, offering wide flexibility for the incorporation of minor elements. They have a typical composition represented by MCrAlX, where M stands for Ni, Co, and occasionally Fe, and X represents oxygen-reactive elements such as Zr, Hf, Si, and Y.
Overpotential	The change in potential of an electrode from its equilibrium steady state value when current is applied.
Oxidation	Loss of electrons by a constituent of a chemical reaction. Also refers to the corrosion of a metal that is exposed to an oxidizing gas at elevated temperatures.
Oxidized surface (on steel)	Surface having a thin, tightly adhering, oxidized skin (from straw to blue in color), extending in from the edge of a coil or sheet.
Oxidizing agent	A compound that causes oxidation, thereby itself being reduced
Oxidizing atmosphere	An atmosphere which tends to promote the oxidation of immersed materials.
Pack cementation	This is a method in which a CVD process takes place with the substrate surrounded by a mass of the depositing medium. “Cementation” is a misnomer. The substrate is “packed” in a “cement” consisting of a mixture of the master alloy (the source alloy), a salt as activator and an inert filler. Normally, a pack is placed in a heated “retort” under an inert or reducing hydrogen atmosphere.
Passive	The state of a metal surface characterized by low corrosion rates in a potential region that is strongly oxidizing for the metal.
Passive–active cell	A corrosion cell in which the anode is a metal in the active state and the cathode is the same metal in the passive state.
Passivity	A condition in which a piece of metal, because of an impervious covering of oxide or other compound, has a potential that is much more positive than that of the metal in the active state.
Pearlite	A two-phase microstructure found in some steels and cast irons; it results from the transformation of austenite of eutectoid composition and consists of alternating layers (or lamellae) of α-ferrite and cementite.
Peltier coefficient	See thermoelectric power.
Permeability	Also called magnetic permeability, is a constant of proportionality that exists between magnetic induction and magnetic field intensity. This constant is equal to approximately 1.257×10^{-6} henry per meter ($H\,m^{-1}$) in free space (a vacuum). Materials that cause the lines of flux to move farther apart, resulting in a decrease in

	magnetic flux density compared with a vacuum, are called diamagnetic. Materials that concentrate magnetic flux by a factor of more than 1 but less than or equal to 10 are called paramagnetic; materials that concentrate the flux by a factor of more than 10 are called ferromagnetic. In engineering applications, permeability is often expressed in relative rather than in absolute terms.
Pesting	Some materials suffer from rapid oxidation in oxygen-containing environments, which results in complete disintegration of the material into gray-green powdery products and is known as pesting. The oxidation attack often has its origin into inhomogeneities, so that structural defects, like pores or microcracks, are required for pesting.
pH	The negative logarithm (to the base 10) of hydrogen ion activity, or $pH = -\log_{10} a_{H^+}$.
Phase diagram	A graphical representation of the relationship between environmental constraints (e.g. temperature and sometimes pressure), composition, and regions of phase stability, ordinarily under conditions of equilibrium.
Phase of thermal emission spectroscopy	In this technique, a laser beam is used to locally heat the specimen, and the mid-infrared thermal emission is observed. Two different materials and different thicknesses of each material can be examined. The phase difference to thermal properties and contact thermal resistance can be related by a mathematical model.
Photoacoustic technique	Here, the sample is illuminated by a laser beam, and then a well-defined effective volume is heated because of absorption of the electromagnetic radiation. The area illuminated depends on the focusing of the laser light. A characteristic optical penetration depth exists, which depends on the wavelength of the incident light. In addition, the chopping frequency dictates an effective thermal diffusion length for the heat to couple to the gas environment. It is a combination of these two effects which limits the depth of the material evaluated. The presence of flaws inhomogeneities in the illuminated region will change the effective volume, and if the flaw is a different material (foreign inclusion) than the host, the absorption coefficient will also differ. If a crack or void is present, the effective volume will differ. The combination of these effects will give rise to a change in the magnitude and phase of the acoustic signal. The technique can be applied to study the microstructures of solid surfaces.
Photoluminescence piezospectroscopy	This is a combination of photoluminescence with the piezospectroscopic effect. Certain materials, when irradiated with a laser beam of appropriate frequency, release energy known as fluorescent radiation or luminescence. The spectral photon emission can be analyzed and compared with a similar spectral emission for the same material under stress. Stress in the material results in shifting of the characteristic R-lines relative to stress-free material. Spectrographic analysis of the shift in frequency versus the residual stress can be used as an NDI technique.
Physical vapor deposition	A coating process in which the cleaned and masked component to be coated is heated and rotated on a spindle above the streaming vapor generated by melting and evaporating a coating material source bar with a focused electron beam in an evacuated chamber.
Pitting	Localized corrosion of a metal surface at points or small areas.
Plasma powder welding	PPW is a technique in which a powder welding system uses the plasma arc. The welding material in powder form is introduced into a transferred plasma arc generated between the work and a tungsten electrode and is deposited as a metal layer on the surface of the work.
Plasma spraying	Here, thermal energy used to melt the coating material is derived from sustained plasma coated by electrical discharge. The process consists of three steps. First, coating material of the right composition is produced in the appropriate form, generally powders, but also in wire or rod form. Second, the coating material is melted using the thermal energy. Third, the molten material is propelled to the substrate to form the coating deposit.
Plastic deformation	The permanent (inelastic) distortion of metals under applied stresses that strain the material beyond its elastic limit.

Point defect	A crystalline defect associated with one or, at most, several atomic sites.
Polarization	Change of potential caused by current flow.
Potentiostat	An electronic device that controls the potential of an electrode (usually called the working electrode) with respect to a reference electrode by automatically applying the required current between the counter (or auxiliary) electrode and the working electrode.
Precipitation hardening	Hardening caused by the precipitation of a constituent from a super-saturated solid solution. See also age hardening.
Protective coatings	These are a class of materials with the potential to withstand relatively high temperatures (>250 °C), while providing protection against corrosion and oxidation of the substrate. The primary requirement of a protective coating is to have qualities superior to that of the substrate in order to shield the component from an aggressive environment. The system is invariably hybrid, whether it has been achieved by means of a surface modification of the component substrate itself or one or more other materials have been applied as a coating to the component surface. In either case, surface treatment is involved, and the combination of coated surface, with its treatment, and substrate is called a coating system.
Pulse-echo thermal wave infrared imaging	This is a variant of the IRI that makes quantitative determinations of the depths of delaminations and other defects in composite materials, by following the time dependence of the temperature in a region above the defect, as compared to that over an undamaged region of the sample.
Radiation damage	A general term for the alteration of properties of a material arising from exposure to ionizing radiation (penetrating radiation), such as X-rays, gamma rays. Neutrons, heavy-particle radiation, or fission fragments in nuclear fuel material.
Recrystallization	(i) Formation of a new, strain-free grain structure from that existing in cold worked metal, usually accomplished by heating. (ii) The change from one crystal structure to another, as occurs on heating or cooling through a critical temperature.
Refractory metal	A metal having an extremely high melting point, for example, tungsten, molybdenum, tantalum, niobium, chromium, vanadium, and rhenium. In the broad sense, this term refers to metals having melting points above the range for iron, cobalt, and nickel.
Scale	An accumulation of corrosion products on a surface.
Seeback coefficient	See thermoelectric power.
Sensitization	Precipitation of chromium carbides at grain boundaries in stainless steels, due to heating in certain temperature ranges, and resulting in susceptibility to intergranular attack by some environments.
Shearography	This is a technique based on holographic interferometric principles. However, it uses two lasers to create interference patterns that appear as speckles. The process has been evaluated in inspecting delamination in TBCs, non-contact properties, strain and vibration analyses, etc.
Short-circuit diffusion	Phenomena such as alloying, sintering, and oxidation, for example, which demand consideration of interface- or dislocation-enhanced diffusion just to name a couple of them, have high technological importance, attracting continuously attention to short-circuit diffusion paths in metals and alloys. The interface structure, its kinetics, stability and possible structure transformations are strongly affected by solute segregation, both of the alloying components and residual impurities. Typically one- and two-dimensional defects are considered as short-circuits in materials, such as dislocation lines, dislocation walls, grain boundaries (i.e. interfaces between differently oriented grains), and phase boundaries (i.e. interfaces between different phases which could even be equally oriented). Furthermore, such defects are triple lines or triple junctions, i.e. lines along which three differently oriented grains meet in a polycrystalline material, and free surfaces where possible short-circuit paths are sketched. The short-circuit defects, such as dislocations and grain boundaries, could have a strong impact on the process of interdiffusion, especially since the diffusion rates of atoms are typically enhanced along these defects.

Silicides	A silicide is a compound that has silicon with (usually) more electropositive elements. Silicon is more electropositive than carbon. Silicides are structurally closed to borides than to carbides. Similar to borides and carbides, the composition of silicides cannot be easily specified as covalent molecules. The chemical bonds in silicides range from metal-like structures to covalent or ionic.
Single crystal	A crystalline solid for which the periodic and repeated atomic pattern extends throughout its entirety without interruption.
Slagging	This is the deposition of molten, partially fused deposits on the furnace walls and the upper furnace radiant superheaters exposed to radiant heat, in the boiler.
Slurry	A suspension of solid particles in a flowing liquid.
Slurry coating	It is a low-cost approach for the production of environmental barrier coatings that can withstand high temperature, high pressure, high gas velocity, and the presence of water vapor. Here, components are dipped into a slurry (ceramic particles suspended in a solvent medium), and subsequently dried and heat treated at elevated temperatures to promote densification.
Solid solution	A homogeneous crystalline phase that contains two or more chemical species. Both substitutional and interstitial solid solutions are possible.
Solid-state reactions	These are reactions related with the preparation, structure, crystalline, electronic, and magnetic properties, as well as applications of solid materials, namely polymers, ceramics, binary and ternary oxide materials, nanomaterials, etc.
Sputtering	A coating process in which thermally emitted electrons collide with inert gas atoms, which accelerate toward and hit a negatively charged electrode that is a target of the coating material. The impacting ions dislodge atoms of the target material, which are in turn projected to and deposited on the substrate to form the coating.
Stainless steel	A steel alloy that is highly resistant to corrosion in a variety of environments. The predominant alloying element is chromium, which must be present in a concentration of at least 11 wt%; other alloy additions, to include nickel and molybdenum, are also possible.
Strengthening	Important mechanical characteristic of a metal, usually understood by the relation between dislocation motion and mechanical behavior of metals. Because macroscopic plastic deformation corresponds to the motion of large numbers of dislocations, the ability of a metal to plastically deform depends on the ability of dislocations to move. Since hardness and strength (both yield and tensile) are related to the ease with which plastic deformation can be made to occur, by reducing the mobility of dislocations, the mechanical strength may be enhanced, that is, greater mechanical forces will be required to initiate plastic deformation. In contrast, the more unconstrained the dislocation motion, the greater is the facility with which a metal may deform and the softer and weaker it becomes. Virtually, all strengthening techniques rely on this simple principle: restricting or hindering dislocation motion renders a material harder and stronger.
Stress	The intensity of the internally distributed forces or components of forces that resist a change in the volume or shape of a material that is or has been subjected to external forces. Stress is expressed in force per unit area and is calculated on the basis of the original dimensions of the cross-section of the specimen.
Stress concentration factor (K_t)	A multiplying factor for applied stress that allows for the presence of a structural discontinuity such as a notch or hole; K_t equals the ratio of the greatest stress in the region of the discontinuity to the nominal stress for the entire section.
Stress-corrosion cracking	A cracking process that requires the simultaneous action of a corrodent and sustained tensile stress. (This excludes corrosion-reduced sections which fail by fast fracture. It also excludes intercrystalline or transcrystalline corrosion, which can cause an alloy to disintegrate without either applied or residual stress.)

Stress-intensity factor	A scaling factor, usually denoted by the symbol *K*, used in linear-elastic fracture mechanics to describe the intensification of applied stress at the tip of a crack of known size and shape. At the onset of rapid crack propagation in any structure containing a crack, the factor is called the critical stress-intensity factor, or the fracture toughness.
Stress-oriented hydrogen-induced cracking (SOHIC)	A form of hydrogen-induced cracking in which the arrays of hydrogen blisters are oriented perpendicular to the orientation of the stress.
Structure	The arrangement of the internal components of matter: electron structure (at a subatomic level), crystal structure (at an atomic level), and microstructure (at a microscopic level).
Substitutional solid solution	A solid solution wherein the solute atoms replace or substitute for the host atoms.
Sulfidation	The reaction of a metal or alloy with a sulfur-containing species to produce a sulfur compound that forms on or beneath the surface on the metal or alloy.
Sulfide stress cracking (SSC)	A form of hydrogen embrittlement that occurs in high-strength steels and in localized hard zones in weldments of susceptible materials, caused by the combined action of tensile stress and corrosion in the presence of water and hydrogen sulfide.
Supercooling	Cooling to below a phase transition temperature without the occurrence of the transformation.
Tafel slope	The slope of the straight-line portion of a polarization curve, usually occurring at more than 50 mV from the open-circuit potential, when the curve is presented in a semilogarithmic plot in terms of volts per logarithmic cycle of current density (commonly referred to as volts per decade).
Tempered steels	The microstructural product resulting from a tempering heat treatment of a steel alloy. The microstructure consists of extremely small and uniformly dispersed cementite particles embeded within a continuous α-ferrite matrix. Toughness and ductility are significantly enhanced by tempering.
Tensile strength	It is a measurement of the force required to pull something such as rope, wire, or a structural beam, to the point where it breaks. The tensile strength of a material is the maximum amount of tensile stress that it can take before failure, for example breaking.
Thermal barrier coating	This is generally a combination of multiple layers of coatings, with each layer having a specific function and requirement. Essentially these coatings consist of a ceramic coating, typically ZrO_2, known as zirconia (125–1000 μm), a thermally grown oxide (TGO), predominantly A_2O_3 (0.5 to about 10 μm), and a metallic bond coat (50–125 μm) on the substrate alloy.
Thermal conductivity	For steady state heat flow, the proportionality constant between the heat flow and the temperature gradient. Also, a parameter characterizing the ability of a material to conduct heat.
Coefficient of thermal expansion	The fractional change in length divided by the change in temperature.
Thermal fatigue	The restraint to the dimensional expansion and/or concentration that would normally occur in a structural member with variations in temperature. It is normally indicated at elevated temperatures by fluctuating thermal stresses; mechanical stresses from an external source need not to be present.
Thermal shock	The fracture of a brittle material as a result of stresses that are introduced by a rapid temperature change.
Thermal stress	A residual stress introduced within a body resulting from a change in temperature.

Thermal wave interferometry	This technique furnishes a measurement of the relative phase between a modulated heat flux applied to a thin film by a diode laser and the oscillatory temperature response of the film. The relative phase is then converted to a thickness estimate by means of an inverse solution of the heat diffusion equation. Estimates of the sample thickness profile furnished by the facility (that can resolve variations in sample thickness of less than 1.5 μm) can be compared to and corroborated by independent measurements obtained using an eddy current probe and a surface profilometer. Other thin film properties can also be measured.
Thermoelectric power	The principles involved in thermoelectric power measurements (as defined either by Seebeck or Peltier effects) are as follows. If a temperature difference T existing between the ends of a semiconductor specimen produces and e.m.f. of QT mV, then Q is defined as the thermoelectric power (mV/deg.). Considered in the alternative manner, if a current is impressed through the opposite faces of a semiconductor via metallic contacts, heat is absorbed at one metallic/semiconductor junction, and liberated at the other (the so-called Peltier effect). The Peltier coefficient is defined as the number of joules of heat absorbed or liberated reversibly per coulomb of charge passing through the junction. In practice, thermoelectric measurements are often made by arranging for the material to be contained within a standard temperature gradient (measured by thermocouples) and noting the sign of the e.m.f. generated, the so-called Seebeck voltage, defined as $Q = \pi/\Delta T$. The sign of π is indicative of the nature of the semiconductor material.
Time temperature transformation diagram	A plot of temperature versus the logarithm of time for a steel alloy of definite composition. Used to determine when transformations begin and end for an isothermal (constant temperature) heat treatment of a previously austenitized alloy.
Toughness	The ability of a metal to absorb energy and deform plastically before fracturing.
Transference numbers	This is a dimensionless parameter which informs about the contribution of the particular charged species present in the electrolyte (ions and electrons!) to the overall charge transport across an electrochemical cell.
Transformation Induced Plasticity (TRIP) Steels	These are steels that retain austenite embedded in a primary matrix of ferrite. In addition to a minimum of five volume percent of retained austenite, hard phases such as martensite and bainite are present in varying amounts. They tipically require the use of an isothermal hold at an intermediate temperature which produces bainite.
Turkdogan's method	The Turkdogan model, which assumes an enhancement of the concentration gradient of metal vapor in the gas caused by homogeneous condensation, may be summarized by stating "the rate of vaporization of any substance already enhanced by natural or forced convection can be further enhanced when a temperature gradient exists by the process of condensation of the vapor at distances close to the surface of the vaporizing object."
Ultrasonic testing	In this technique, an ultrasonic probe is introduced into the hardware by a piezoelectric transducer, which may also act as a detector probe, converting mechanical strains into electrical signal and vice-versa. The ultrasonic frequency (0.1–25 MHz) is such as to generate elastic waves in the solid material, and these waves propagate through the sample, striking defects and undergoing reflection known as echoes. The probe detects all waves and displays them on an oscilloscope as a spectrum of echoes arriving at different times. Analysis of the spectrum provides indication of shape, size, and location of the defects.
Vacancy	A normally occupied lattice site from which an atom or ion is missing.
Van der Waals bond	A secondary interatomic bond between adjacent molecular dipoles, which may be permanent or induced.
White cast iron	A low silicon and very brittle cast iron in which the carbon is in combined form as cementite. A fractured surface appears white.
Wrought alloy	A metal alloy that is relatively ductile and amenable to hot working or cold working during fabrication.
Yield strength	The stress at which a material exhibits a specified deviation from proportionality of stress and strain. An offset of 0.2% is used for many metals.

Author Index

Aaranson, H.I., 100, 106
Abernathy, H., 529
Abramov, A.V., 305, 306
Acton, Q.A., 448, 450
Adam, N.K., 172
Adams, G.E., 426
Adamson, R., 543
Adler, E., 438
Afonichkin, V.K., 546
Agarwall, D.C., 17, 351
Ahmad, T.H., 26, 37
Aindow, M., 523
Akanda, S.R., 523
Akasaka, Y., 515
Akbulut, M., 462
Akeiz, C.S., 167
Akhtar, A., 294
Akinc, M., 334
Albery, W.J., 452
Alcock, C.B., 3, 101, 112, 121, 197, 276, 351
Alfantazi, A.M., 321
Ali, S.L., 225
Alkonis, J.J., 427
Allen, E.C., 418, 419
Allen, S.J., 431
Allen, T., 536
Allen, T.R., 535, 537, 542
Allison, G., 482
Alman, D.E., 519, 520, 523
Almeraya, C.F., 354
Almond, D.P., 444
Alnegren, P., 520
Alper, J.P., 459
Alvorado, G., 284
Amaral, L., 155, 298, 496
Amaya, M., 314
Amendola, R., 521
Amin, M.A., 564
Ancy-Moret, M.F., 100
Andersen, A.G., 448
Anderson, A.B., 221
Anderson, M.D., 517
Andersson, J.-O., 103
Ando, S., 252
Andrew, K.F., 198
Andrews, J., 531, 588
Andrews, P., 25
Andrieu, E., 370
Angerer, W., 437
Anghel, C., 290
Anson, F.C., 448
Antonelli, G., 440
Antunes, R.A., 447
Appen, A.A., 144
Arai, H., 517
Archer, N.J., 485
Argent, E.J., 297
Ariga, N., 515
Armilt, J., 207, 351, 371
Arora, N., 253
Arper, A.M., 100
Arvia, A.J., 173, 178, 318
Asensio-Jimenez, C., 520
Ashby, M.F., 53
Ashworth, V., 400, 401
Asteman, H., 198, 280, 281, 292
Atia, A.A., 539
Atkinson, A.A., 3, 157, 206, 292, 517
Atmani, H., 304
Attendorf, H., 520
Au, S.F., 311
Audubert, M.R., 175
Aydin, I., 264
Azaroff, L.V., 130, 143
Azzam, R.M.A., 433

Baboian, H., 391
Backentoss, G., 165, 166
Bacon, G.E., 64, 408
Bae, H.Y., 517
Baerlecken, E., 26
Baes, C.F., 545
Bai, C., 425
Baker, B., 509
Baker, B.A., 258
Bakker, W.T., 363, 369
Balachov, I.I., 527, 528
Baldi, A.L., 482
Baldwin, M.J., 271
Bale, C.W., 120
Balkanski, M., 431
Balke, N., 472
Ball, D.W., 441
Bandyopadhyay, N., 445
Banquy, X., 462, 463
Bao, S., 417
Barabash, B., 534, 589
Barabash, V., 534, 589
Barbero, E., 335
Barbot, J.F., 167
Bard, A.J., 175, 448, 460, 465
Barin, I., 299
Barnes, J.J., 252, 266, 267
Barnett, J.D., 443
Barralis, J., 100, 247
Barret, P., 208, 351
Bartur, M., 351, 558, 559
Baschi, S.D., 445
Bashara, N.M., 433
Basu, S.K., 113, 114

High Temperature Corrosion: Fundamentals and Engineering, First Edition. César A. C. Sequeira.

© 2019 John Wiley & Sons, Inc. Published 2019 by John Wiley & Sons, Inc.

Bateman, L.S., 528, 529
Baturova, L.P., 309
Baudo, G., 120, 121, 178, 316
Bauer, E., 414, 415
Baxter, L.L., 280
Bayer, G.T., 482
Bayer, R.G., 252
Becker, P., 254
Bedworth, R.E., 2, 196, 206, 233
Begley, M.R., 498
Belcher, P.R., 340
Bell, T., 273
Bellamy, B.A., 226
Bellegia, M., 167
Belton, G.R., 100
Beltran, A.M., 342, 352
Bénard, J., 3, 215
Bennett, M.J., 214, 351, 401
Bennett, T.D., 441
Benninghoven, A., 421
Bentley, Z., 528, 529
Béranger, G., 206, 228
Berglund, R., 226
Bergman, B., 509, 510
Bergman, P.A., 342, 343
Berkani, M., 299
Bernamati, G., 335
Bernard, C., 102, 199, 247
Berneron, R., 398
Bernhardt, J., 404
Berry, W.E., 333
Berthier, Y., 256, 257
Bertocci, U., 179, 455
Besson, J., 212
Betteridge, W., 18, 258, 342
Bevis, M.J., 333
Bicego, V., 440
Biedenkoff, P., 515
Biggeri, V., 166
Birchenall, C.E., 236
Bird, R.J., 340
Birks, N., 3, 108, 110–112, 197, 198, 203, 204, 211, 213, 215, 228, 293, 342–344, 351, 391, 392, 396, 420, 477
Black, H.L., 237, 239
Blackburn, M.J., 304
Blanchard, C., 167
Bland, R.D., 490
Blander, M., 173, 297
Blankenship, F.F., 173
Blaschuk, A.G., 424
Blattner, R.J., 228, 401
Block, F.E., 110
Block, S., 443
Bloembergen, N., 439
Bloom, H., 513
Bobeth, M., 413
Bockris, J.O.'.M., 175, 300
Bodalo, A., 304
Boden, A., 508
Boehme, D.R., 308
Bogren, E.C., 193, 194
Boldyrev, V.V., 35
Bolshakov, K.A., 497
Bolt, N., 379
Bolton, M.J., 237
Boltzmann, L., 153
Bombara, G., 178, 316
Bonaccorso, A.D., 528
Bonetti, R., 485
Bongartz, K., 227
Bonix, J., 334, 335
Bonnet, F., 256, 257
Boone, D.H., 484, 485, 487
Borchi, E., 166
Borgstedt, H.U., 326, 336, 352
Bornstein, N.S., 3, 25, 228, 300, 317, 342, 343, 351
Bosch, R.-W., 455
Bose, S., 401, 442, 485
Bose, S.K., 252, 280
Bosh, R.W., 447
Bösker, G., 158
Bosseboeuf, A., 401
Bosselet, F., 334
Bouchier, D., 401
Boulos, M.I., 441
Boussetta, H., 150
Bouwmeester, H.J.M., 162, 449, 459
Bovet, A.L., 546
Bracht, H., 149, 158
Bradshaw, R.W., 299, 308
Brady, M.P., 541
Brandon, D., 55
Brassart, F.A., 198
Brasunas, A.d.S., 228
Bratland, D., 303
Braunstein, J., 448
Breiter, M.W., 459
Brendryen, S., 251, 258
Brenner, A., 494
Brennor, S.S., 228
Bressers, J., 224
Brett, D.J.L., 517
Brevet, A., 523
Brewis, D.M., 401
Brickner, K.G., 265
Briggs, N., 258
Bright, M.A., 335
Brillouin, L., 429–432
Bringas, J.E., 4
Broers, G.H.J., 505
Brooks, J.A., 10
Brouwer, G., 187
Brown, C.T., 300, 317
Browning, G.V., 171
Bruemmer, S., 536
Bruemmer, S.M., 535–537
Brühl, S., 273
Bruley, J., 413
Brunauer, S., 209
Brunner, J., 401
Bruzzi, M., 166
Bryant, D.R., 563
Brydson, R., 413
Bube, R.H., 144
Buerger, M.J., 50
Bühler, H.E., 264
Bukan, N.G., 172
Bullock, E., 237
Burgel, R., 265
Burns, P.C., 541
Burrows, B.W., 176, 296, 316
Burson, J.H., 255
Burstein, E., 437, 438
Burton, J.J., 158
Buscail, H., 290
Busch, D.E., 401
Busen, K.M., 166
Butcher, P.N., 428
Butler, J.A.V., 172, 175
Butt, H., 425
Bychkov, A.V., 303
Bystram, M.C.T., 14, 15

Cabet, C., 253, 544
Caboche, G., 523
Cabrera, N., 2, 196
Cahn, J.W., 247
Cahn, R.W., 147
Caillet, M., 228
Caley, W.F., 353
Calvert, J.M., 220
Camp, E., 255
Camus, G., 562
Canfield, N.L., 517
Canterford, J.H., 276
Cao, Y., 265, 271, 272
Capella, B., 425
Caplan, D., 198, 210, 212, 221
Cardella, A., 534, 589
Carlin, R.T., 510
Carling, R.W., 308
Carolan, M.F., 517
Carr, A.N., 455
Carreau, J.-L., 309
Carter, W.E., 167
Casino, R.G., 318
Casteels, F., 330
Castelletti, L.C., 272, 273
Cathcart, J.V., 207
Catlow, C.R., 245
Cayard, M.S., 245
Celis, J.P., 447

Chalmers, B., 338
Chamberlain, J., 44
Chamelot, P., 303
Chan, C.M., 404
Chan, K.S., 499
Chang, C.H., 459
Chang, R.K., 439
Chang, S.L., 213
Chang, S.Y., 265
Chaolin, Z., 303
Chapon, P., 445
Charbonnier, J.C., 398
Charnock, J.M., 303
Chase, M.W., 100, 110
Chatillon, C., 102, 199, 247
Chattopadhyay, B., 220, 279
Chaudron, G., 546
Chaula, B.R., 167
Chauvin, N., 531, 588
Chen, C., 455
Chen, C.J., 242
Chen, G., 510
Chen, L., 523
Chen, X., 441, 518
Chen, Y., 378, 392
Cheng, T., 541
Cherepy, N.J., 526
Cheruvu, N.S., 499
Cheung, W.H., 482
Chevalier, S., 523
Chia, H.C., 253
Chiba, R., 287
Chik, M.P., 158
Chimenti, D.E., 441
Chipman, J., 73
Chitraub, M., 149
Cho, J.Y., 515
Cho, S.C., 515
Cho, W.D., 280
Choi, J.J., 517
Chopra, O.K., 337
Choquet, P.A., 483
Chrenkova, M., 495
Christ, H.J., 247, 265
Christensen, P.A., 451
Christiansen, N., 520
Christl, W., 207
Chun, C.M., 255, 257
Chung, J.H., 271
Chuto, T., 536
Chuvilina, E.L., 539
Ciuffreda, A.R., 287
Clark, R.J.H., 462
Clarke, D.R., 294, 443
Clelland, J., 352
Coakham, J.W., 77, 78
Coats, A.W., 378
Cockeram, B.V., 486
Coen-Porisini, F., 36
Cohen, M., 198, 210, 212
Cohen, P., 287
Cole, D.M.I., 255
Colom, F., 304
Colombo, P.P., 440
Colson, H., 213
Colson, J.C., 206, 228
Colton, R., 276
Coltters, R.G., 247
Compton, R.G., 171, 433
Condé, J.F.G., 342, 343, 351, 352
Conner, J.A., 440
Connor, W.B., 440
Conway, B.E., 173, 175
Coons, W.C., 260
Cooper, A.A.R., 221
Cooper, J.F., 526
Corengia, P., 273
Corish, J., 252
Corre, G., 524
Cortes, M., 309
Cotter, D., 428
Couper, A.S., 238, 239
Coustumer, P.L., 445
Coutsouradis, D., 235, 237, 351
Covington, A.K., 332
Cox, B., 542, 543
Cox, D., 26
Coyle, R.T., 305, 309, 310
Crabos, F., 370
Crank, J., 155
Crawford, D., 531, 588
Cremer, P.S., 437
Cristofori, D., 167
Crossley, W., 443
Crouch-Baker, S., 528
Cubicciotti, D., 214, 541
Cui, C., 305
Cumming, D., 517
Cunningham, F.E., 492
Curnutt, J.L., 100, 110
Cutler, A.J.B., 178, 319, 345, 351
Czanderna, A.W., 401
Czichos, H., 452

da Costa, H.F., 270
da Costa, W., 482, 484
da Silva, L.C.C., 155
Dabasi, F., 206, 228
D'Agostino, L., 447
Daher, A.M., 539
Daio, J.T., 518
Dalgaard, S.B., 26
Damaskin, B.B., 178
Danek, G.J. Jr., 318, 321, 345
Danner, G., 300–302
Dao-xin, L., 272
Dariel, M.P., 494
Darken, L.S., 100, 153–155
Das, A.K., 285
Das, D.K., 485
Datta, P.K., 239
Davin, A., 235, 237, 351
Davis, H.J., 178
Davis, J.R., 13, 355
Davisson, C., 403
Davisson, C.J., 403
Davtyan, O.K., 512
Dawson, J.L., 455, 457
de Boer, J.H., 538
de Broglie, L., 403
de Bruyn, H.J., 251, 258
de Groot, S.R., 173
de la Calle, J.M., 357
de Oliveira, M.C.L., 447
de Van, J.H., 310
de Wit, J.H.W., 220, 309, 310, 459
Deadmore, D.L., 227
Deal, B.E., 210
Deb, D., 354
Decrescente, M.A., 3, 300, 317, 342, 343, 351
Deevi, S.C., 519, 522
DeJonghe, L.C., 523
Dekker, A.J., 431
Delahay, P., 452
Delamore, C.W., 333
Delimarski, Y.K., 317
Delong, H.C., 299
Delpech, S., 546
DeMasi-Marcin, J.T., 442
Dench, W.A., 403, 424
Derricott, R.T., 252
Desai, P.D., 25
Desai, V., 536
DeVan, J.H., 303
Devanathan, M.A.V., 172
Dewey, M.A.P., 342, 345
Di Bartolomeo, A., 516
Di Cocco, V., 447
Dickinson, E., 409
Dieckmann, R., 158
Diehl, J., 147
Dieter, G.E., 79
Digges, T.G., 338
Dimitrov, S., 457
Ding, Z., 459
Dini, J.W., 494
Ditzenberger, J.A., 166
Doering, H., 318, 321
Domagala, R.F., 265
Donachie, M.J. Jr., 18, 19, 24
Donachie, S.J., 19
Donado, R.A., 512, 513
Dong, H., 272

Donia, A.M., 539
Donner, A., 26
Dooley, R.B., 287
Douglass, D.L., 265, 279, 293, 351
Dovey, D.M., 251
Doychak, J., 400, 413
Dransfeld, K., 427
Dravnieks, A., 235
Dresher, W.H., 342, 343
Drury, J.C., 440
Dryepondt, S., 370
Du, Q., 437
Duan, S., 509
Dubois, L.H., 527, 528
Dufour, P., 290
Duke, F.R., 173
Dunbobbin, B.R., 308
Dupnok, A., 165
Duret, C., 351, 482
Durham, R.N., 254
Durkin, J., 45
Dutta, M., 445
Dybkov, V.I., 327, 328, 333
Dzhafarov, T.D., 167

Ebara, R., 307
Ebbinghaus, B., 281
Eberle, C.S., 305
Eberle, F., 260
Ecer, G.M., 221
Edeleanu, C., 177, 298
Eden, D.A., 455
Edwin, E.H., 251, 258
Egorov, E.A., 539
Eguchi, K., 517
Ehlers, J., 291
El-Dashan, M.E., 345
Eldridge, J.I., 442
Eliseev, E., 472
Ellingham, H.J.T., 100, 101, 180, 197
Elliott, P., 351, 354
Ells, C.E., 543
Elshehy, E.A., 539
Eltester, B., 369
Embury, J.D., 212
Emmett, P.H., 209
Emsley, A.M., 305
Ende, V., 101, 106
Engelhard, M.H., 517
Engell, H.J., 164
Engstrom, A., 120
Ennis, P.J., 291, 370
Epstein, L.F., 331
Erdey-Gruz, T., 175, 176
Eriksson, G., 103
Escudero, M.J., 510
Esnouf, C., 334
Evans, A., 400
Evans, E.L., 276, 298
Evans, H.E., 208, 227, 356
Evans, U.R., 199, 299
Evans, W., 77, 78
Ewing, R.C., 541
Eyring, H., 209
Eziashi, J., 521
Ezis, A., 163, 164

Fabritsiev, S., 534, 589
Fafilek, G., 458–460
Faghihi-Sani, M.A., 523
Faik, A., 321
Fairbanks, J.W., 351
Falk-Windisch, H., 520
Fan, Z., 333
Fang, B., 509
Fang, H.L., 270
Farhi, R., 204
Farina, C.A., 379
Farooque, M., 511, 516
Farrel, R.M., 342, 345
Farrell, D.M., 457
Faulkner, L.F., 175
Faulkner, L.R., 448
Fazio, C., 335
Fedelich, B., 224
Feder, R., 404
Federsel, K., 308
Fedorov, P.I., 497
Fehlner, F.P., 32
Feitknecht, W., 32
Feldeberg, S.W., 451
Fellner, P., 495
Felton, E.J., 221
Feng, M., 516
Feng, Q., 224
Feng, X.K., 304
Fenske, G.R., 401
Ferber, M.K., 441
Fergus, J., 253
Fergus, J.W., 519, 521
Fernandez, A.G., 309
Feron, D., 447
Fewell, M.P., 271
Fichera, M., 379
Fielder, W.L., 353
Fiet, K.J., 526
Filipuzzini, L., 562
Finney, J., 407
Firsova, E.G., 307, 309
Fischer, W.A., 26
Fisher, J.C., 159
Fleischer, R.L., 25, 220
Fleming, R.H., 228, 401
Flengas, S.N., 173
Flood, H., 120, 173, 177, 316
Fluck, D.E., 304
Focke, T., 494
Foger, K., 250
Foley, R.T., 237
Folkesson, N., 281, 282
Fontana, M.G., 280
Fontana, S., 523
Ford, F.P., 535–537
Ford, M., 17
Förland, T., 120, 173, 177, 316
Forman, R.A., 443
Foroulis, Z.A., 100, 216, 238, 314
Forseth, S., 247
Fort, W.C. III, 239
Fouletier, J., 197
Fox, D.S., 25
Francis, J.M., 253
Franck, F.C., 158
Frangini, S., 309, 310, 516
Frankel, G.S., 467
Franklin, D.G., 542
Frees, G., 336
Freund, H., 539
Freund, H.J., 253
Freysz, E., 437
Friedrichs, A., 467
Friend, W.Z., 16
Fritscher, K., 290
Frohberg, M.G., 267
Froitzheim, J., 520, 521, 523
Fromm, E., 197, 206, 215
Frost, B.R.T., 329, 535, 588
Frumkin, A.N., 172
Fryburg, G.C., 351, 353
Fu, Q., 522
Fuchs, G.E., 224
Fuentealba, E., 309
Fujikawa, H., 370
Fujita, Y., 511
Fukusumi, M., 353
Fuller, C.S., 164, 166
Funkenbusch, A.W., 228

Gabrielli, C., 455–457
Galasiu, I., 297, 300
Galasiu, R., 297, 300
Gale, R.J., 462
Galerie, A., 197, 391
Galus, Z., 457
Gambino, L.V., 523
Ganesan, P., 226, 240
Gannon, P., 521
Ganser, B., 482
Gao, G., 457
Garcia-Diaz, B.L., 171, 546
Garfinkel, H.M., 173
Garnaud, G., 213
Garner, F.A., 535
Garzarolli, F., 543

Gaskell, D.R., 100, 101, 197
Gasteiger, H.R., 509
Gatos, H.C., 165
Gaune-Escard, M., 299
Gaur, H.C., 175
Gautier, L., 522
Gawenda, P., 370
Geary, A.L., 179
Gehrling, R., 290
Geisse, N.A., 426
Gell, M., 443
Geller, E., 443
Gellings, P.J., 162, 449, 459
Gemmen, R., 529
Gerdes, K., 529
Gerischer, H., 175, 452, 464
Germanaz, P., 304
Germer, L.H., 403
Gerritsen, H.J., 144
Gersho, A., 444
Gesmundo, F., 3, 25, 152, 210, 215, 216, 220, 293
Ghabone, L., 309
Ghanadi, M., 539
Ghosh, H., 268, 269
Gibbs, J.W., 105
Gibson, J.G., 298
Gibson, J.M., 208
Giggins, C.S., 100, 115–118, 264, 281, 351
Gil, A., 519
Gil, L., 273
Gilbert, G.N.J., 6, 7
Gill, B.J., 488
Gill, D.D., 308
Ginzburg, A., 486
Giorgi, L., 516
Giovanelli, D., 171
Girdauskaite, E., 522
Giselbrecht, W., 370
Gitanjaly, M., 356
Gitman, L.J., 38
Gitzhofer, F., 441
Gladi, J., 150
Glaser, B., 391
Glasstone, S., 136, 209, 505, 588
Gleeson, B., 3, 227, 482, 484
Gleiter, H., 160
Glushko, V.P., 298
Glushkova, V.B., 144
Godoi, R.H.M., 563, 564
Goebel, J.A., 3, 171, 264, 343, 344, 351
Gogia, A.K., 24
Gold, R.E., 536
Gommans, R., 247
Goncharov, O.Y., 459
Gong, S., 488
Gontijo, L.C., 272, 273
Gonzalez, A., 45
Gonzalez, G., 334
Gonzalez, R.J.G., 354
Goodenough, J.B., 516
Gorbokov, A.V., 167
Gordon, C., 173
Gorman, J.W., 238, 239
Gorte, R.J., 524, 529
Gosser, D.K., 451
Goto, K.S., 194, 351
Goto, T., 25
Gottesfeld, S., 433
Goward, G.W., 3, 264, 343, 344, 351, 482, 484, 485, 497
Grabke, H.J., 3, 215, 245, 247, 250–258, 261, 264, 265, 267, 280, 281, 351, 356, 367, 369, 370, 380, 391, 401, 515
Graham, M.J., 206, 210–212, 224
Graham, R.A., 539
Grahame, D.C., 173
Grant, C.J., 319
Grant, N.J., 228
Grant, W.A., 400, 401
Grantham, L.F., 310
Grauer, R., 32
Graves, A.D., 172, 178
Gray, J.A., 115, 116
Gray, P.S., 343
Gray, R.D., 18
Greaves, E.N., 417
Green, M.A., 166
Greene, J.E., 401
Greene, N.D., 177
Gregory, J.N., 309
Griffiths, P.R., 436
Griffiths, T.R., 369
Grimes, W.R., 545
Grodner, A., 225
Grosboll, M.P., 257
Gross, L., 255
Groult, H., 303
Grove, A.S., 210
Grubmeier, M., 420, 421
Grunberg, S., 225
Grünling, H.W., 370
Grzesik, Z., 152, 242
Guan, H.R., 293
Guan, W.B., 522
Guggenheim, E.A., 136, 173
Guillot, S., 321
Gulbransen, E.A., 100, 110, 198
Gummel, H.R., 167
Gunn, M.W., 166
Gunnarsson, G., 309
Guntherodt, H.G., 467
Gupta, B.K., 3, 484
Gür, T.M., 527
Gurin, P.A., 423
Gurrappa, I., 24, 227, 356
Gurry, R.W., 100, 154
Gust, W., 159
Guttmann, V., 265, 356
Gutzeit, J., 238, 239
Gyalog, T., 427

Haarmann, K., 371
Haasen, P., 147
Hack, K., 103
Hagel, K.C., 35
Hagel, W.C., 16, 18, 19, 223, 224, 342
Hall, D.J., 251
Halstead, W.D., 345
Hamel, C., 303
Hamnet, A., 451
Hampton, A.F., 239
Han, G., 280
Han, J., 509
Han, S., 265
Hancock, H.A., 351, 353
Hancock, P., 237, 340, 352
Hannay, N.B., 34, 35, 143, 144, 168, 241
Hansmann, H., 400
Hara, M., 311, 354
Harada, Y., 379
Hardt, R.W., 237
Harper, M.A., 227
Harris, N.L., 326
Harrison, J.M., 252
Hartley, G.S., 154, 155
Haruyama, S., 179, 310
Hasegawa, S., 527
Hashimoto, A., 292
Hashimoto, S., 311
Hasselman, D.P.H., 23
Hastings, I., 26
Hatfield, W.H., 15
Hattenford, H., 520
Hauffe, K., 199, 234, 236, 237
Haugsrud, R., 418, 522
Hawkins, M.W., 482
Haworth, C.W., 58, 59, 82
Haycock, E.W., 235
Haycock, G.W., 213
Haygarth, J.C., 539
Hayman, C., 342, 345
He, Y., 178
Heatherly, D.E., 448
Hed, A.Z., 222, 351
Hedge, S., 294
Hedvig, P., 427
Heffelfinger, M.T., 308
Heiming, A., 515
Heine, D., 305
Heineman, W.R., 451
Heino, M.M., 445
Heinz, K., 404
Heinz, T.F., 437, 438

Heinze, J., 458
Heinze, S., 290
Heitbaum, J., 466
Heitmüller, R.J., 363
Heitz, E., 212, 312
Helmersson, U., 401
Helmshaw, R., 401
Hemmes, K., 309, 311, 509
Hemmings, P.L., 115, 116
Hendry, A., 385
Henkhaus, R., 212, 312
Henry, S., 291
Herda, W.R., 17
Hertzman, S., 248, 253, 256
Heslop, J., 342
Hester, R.E., 462
Heubner, U., 16, 251, 254
Heubner, V., 251, 254
Heydorn, B., 528
Heyne, L., 188
Hicks, B., 227
Hidalgo, V.H., 357
Higaki, K., 515
Hill, M.P., 305
Hill, V.L., 237, 239
Hillert, M., 247, 249, 255–257
Hillner, E., 542
Hills, G.J., 172, 176, 296, 316
Hilpert, K., 520, 522
Hilton, D.A., 227
Himpsel, F.J., 437, 438
Hindam, H., 221
Hintermann, H.E., 441
Hirai, T., 25
Hirokawa, K., 459
Hirth, J.P., 164, 212
Hitchman, M.L., 452
Hladky, K., 455
Ho, M.X., 309
Hobbs, L.W., 220, 413
Hochman, R.F., 245, 255–257, 261
Hocker, T., 520, 522
Hocking, M.G., 3, 121, 126, 173, 178, 239, 297, 300–302, 317, 318, 345, 350, 351, 357, 490, 497, 498
Hodge, N., 309
Hodgkiess, T., 220, 222
Hoff, H., 304
Hoffman, E.E., 309
Hoffman, J.J., 265, 266
Hofman, S., 401
Hoglund, L., 120
Hogmark, S., 333
Holcomb, G.R., 519, 520
Hollingshead, R.S., 353
Holm, R.A., 227
Holmes, C., 436
Holmes, D.R., 207, 371
Holmes, P.J., 143
Holt, A., 522
Holzer, L., 520, 522
Homel, M., 527
Hong, S.A., 515
Honma, A., 354
Hooper, A., 454
Hooper, G.W., 197
Hopkins, B.E., 3, 200
Hopkins, H.H., 234
Hopkinson, B., 45
Horing, J., 251, 252
Hornbostel, M.D., 527
Hörnlund, E., 290, 293
Horton, C.A.P., 299
Hossain, M.K., 251
Hou, P.Y., 228
Howard, R.A., 45
Howe, J.M., 159
Howell, M., 310
Howes, H.A.H., 239
Hsia, B., 459
Hsu, H.S., 310
Hu, Z.Q., 293
Huang, B., 510
Huang, K., 516
Huang, L., 293
Huczkowski, P., 520
Huenert, D., 253
Huet, F., 455–457
Huggins, R.A., 149, 527
Hughes, A.E., 157
Huglen, R., 303
Hugo, M., 254
Hultgren, A., 255–257
Hultquist, G., 290, 291, 293
Hulvat, J., 158
Hume-Rothery, W., 58, 59, 82
Humphreys, A., 239
Humphries, M.J., 237, 287
Huntz, A.M., 520
Hussey, C.L., 448
Hussey, R.J., 206
Hwang, S., 325
Hyde, K.R., 226
Hyun, S.H., 515

Iacoviello, F., 447
Ignatiev, V.V., 546
Iguchi, Y., 25
Ihara, M., 527
Ikeshima, T., 371
Ilschner, B., 370
Ilschner-Gench, C., 278
Imbrie, P., 443
Indacochea, J.E., 305, 306
Inden, G., 255
Ingerl, K., 433
Ingraham, R.R., 112, 118–120
Ingram, M.D., 173
Inman, D., 172, 178, 447
Ioki, I., 534, 589
Iredale, J.V., 309
Irene, E.A., 433
Irvin, J.C., 165, 166
Irvin, J.E., 325
Irvine, J.T.S., 528
Ishihara, T., 516
Ishii, K., 287
Ishikawa, T., 307
Ishwar, V.R., 354
Islam, S., 221
Israelachvili, J., 462
Israelachvili, J.N., 426, 427
Ito, Y., 515
Itoh, M., 388
Iverson, W.P., 455
Ives, D.J.G., 301
Iyer, S.R., 354

Jablonski, P.D., 519, 520, 523
Jack, D.H., 265
Jack, K.H., 265, 267
Jacob, K.T., 100, 351
Jacobson, C.P., 523
Jacobson, N.S., 25, 281, 319, 563
Jacques, W.W., 529
Jaffee, R.I., 342
Jain, S.L., 528
Jakobi, D., 247, 254
Janke, D., 457
Janssen, K., 421
Jansson, B., 103
Jansson, S.A., 100, 110, 216
Janz, G.J., 173, 299, 301
Jeffes, J.H.E., 100–102, 104, 121
Jelley, N., 531, 588
Jenkins, I., 251
Jesper, H., 336
Jha, S.S., 439
Ji, Y., 517
Jiang, C.R., 524, 528
Jiang, S.P., 517, 518, 527
Jiménez, L., 273
Johannesen, O., 448
Johannesson, B., 309
Johansson, L.-G., 198, 228, 281, 292
John, H.A., 401
John, R.C., 224, 239
Johnsen, R., 511, 516
Johnson, J.R.T., 292
Johnson, K.L., 426
Jones, D.P.H., 53
Jones, J.J., 251
Jonsson, B., 226

Jordan, E., 443
Joshi, S.V., 485
Jun, C., 508
Jungblut, F., 491

Kacjrzak, L., 75
Kado, S., 225
Kalinin, S.V., 472
Kambe, K., 404
Kamiya, N., 311, 510
Kanal, L.N., 45
Kanary, L.E., 353
Kane, R.D., 245
Kane, R.H., 254
Kaplan, W.D., 55
Kappl, M., 425
Kassner, H., 536
Kassner, T.F., 245
Katayama, M., 425
Kather, A., 363
Katita, K., 445
Kato, M., 314
Kato, S., 510
Kattak, C., 338
Kaufherr, N., 401
Kaufman, L., 338
Kauppinen, P., 440
Kaur, I., 159
Kawahara, Y., 280
Kawakami, M., 351
Kawamura, K., 457, 521
Kawamura, T., 379
Kayalova, S.S., 144
Kaysser, W.A., 24
Kazantsev, G.N., 178
Keblinski, P., 159, 160
Keddham, M., 455, 456
Keijzer, M., 309, 311, 516
Keiser, J.R., 303, 541
Keller, O., 438
Kelley, K.K., 298
Kellogg, H.H., 113, 114, 276
Kendall, K., 426
Keppert, M., 303
Kerridge, D.H., 303, 326
Key, C., 521
Keys, L.H., 26, 37
Khaleel, M.A., 523
Khandros, I.Y., 252
Khanna, A.S., 3, 197, 420, 493, 494
Khatak, H.S., 370
Khoi, N.N., 212
Kidner, N.J., 523
Kildisheva, E.V., 378
Kilner, J.A., 517
Kim, B., 310
Kim, J.W., 523
Kim, K.Y., 325
Kim, M.C., 325
Kim, S., 515
Kim, T.H., 271
Kim, W., 515
Kimura, H., 252
King, K., 369
King, P.J., 535, 537
King, S.M., 408, 409
Kingery, W.D., 294
Kinnibrugh, R.R., 178
Kirchheiner, R., 254
Kirkendall, E.O., 153, 154
Kirschner, J., 404
Kissinger, P.T., 451
Kittell, C., 141
Kitto, J.B., 287, 364, 365
Kittrel, W.C., 257
Klěecka, A., 309
Klinger, L., 486
Kloewer, J., 17
Klostermann, J.A., 496
Klotz, S., 528
Klower, J., 228, 251, 254
Knacke, O., 115, 117
Kneeshaw, J.A., 239
Knotek, O., 491
Ko, D.H., 515
Kodjamanova, P., 522
Kofstad, P., 3, 36, 197–201, 203, 211, 216, 220–222, 239, 241, 243, 247, 258, 259, 281, 290, 293, 351, 364, 367, 398, 459, 520, 522
Koger, J.W., 299, 303, 305, 545
Kohl, F.J., 351, 353
Kohler, L.K., 354
Kojima, T., 311, 312
Kolasa, B., 208
Kollia, C., 494
Kong, J., 488
Kong, J.H., 272, 273
Königsberger, E., 103
Konings, R.J.M., 542
Konysheva, E., 518
Koopman, R., 464
Kosko, B., 45
Koslowske, M., 528
Koslowske, M.T., 529
Kostyrko, O.S., 305, 306, 313
Kozma, L., 159
Krajak, R., 258
Kranzmann, A., 253
Kraus, P., 515
Krikke, R.H., 251, 252
Kristiansen, K., 462, 463
Kröger, F.A., 131, 134, 137, 201, 202, 205, 221, 242, 280, 294
Kroll, W.J., 40, 481, 537–539
Krüger, R., 526
Kruizenga, A.M., 308, 313
Krupp, U., 265
Krutenat, R.C., 228
Kubaschewski, O., 3, 11, 101, 121, 197, 200, 234, 276, 298, 351
Kudo, T., 245
Kuiry, S.C., 280
Kulesza, P.J., 457
Kumar, V., 253
Kung, S.C., 484
Kunst, R.N., 173
Kurlekar, A., 482
Kurokawa, H., 521, 523
Kvernes, I., 290

Labid, M., 150
Lacombe, P., 497
Ladenberger, M., 308
Laford, M., 308
Lagally, M.C., 404
Lagergren, C., 509, 510
Lai, G., 16, 280, 351
Lai, G.Y., 3, 16, 197, 226, 227, 237, 245, 254, 261, 264–267, 280, 304, 305, 309, 310, 335, 351, 354, 362
Laidler, K.J., 209
Laitinen, H.A., 175, 179
Lakeman, B., 528
Lakeman, J.B., 528
Lamorte, M.F., 166
Lance, M., 441
Landsberg, G., 429
Lang, E., 3, 400, 401
Langmuir, I., 209
Langova, S., 309
Lantelme, F., 303
Lapshin, R.V., 425, 426
LaQue, F.L., 178
Larpin, J.P., 290
Larring, Y., 523
Larum, A., 509
Lashmore, D.S., 494
Lasia, A., 455
Laurent, V., 334
Lavernia, E.J., 314
Lavine, M.C., 165
Lawrence, D.F., 352
Lawrence, E.J., 303
Lawrence, N.S., 171
Laxton, J.W., 345
LeBlanc, O.H. Jr., 351
Lee, A.C., 527
Lee, C., 455
Lee, C.H., 439
Lee, K.-Y., 313
Lee, W.H., 354
Lee, Y.Y., 281
Leeb, K., 459

Lees, D.G., 220
Lees, D.J., 385
Lefebvre, H.M., 307
Leggett, J.T., 25
Leggett, R.D., 535
Leikis, D.I., 172
Leistikow, S., 370
Leite, R.C.C., 431
Lemmer, J.F., 45
Leonard, R.B., 177
Leonardi, R., 379
Lepeticorps, Y., 334
Lethinen, B., 265
Leverant, G.R., 499
Levi, T.P., 258
Levich, V.G., 451
Levin, L., 486
Levitin, V., 420
Lewis, D., 297
Leyendecker, T., 491
Leyens, C., 24, 290
Li, C.X., 273
Li, F., 510
Li, I., 515
Li, J.F., 470
Li, J.G., 228
Li, M.H., 357
Li, N., 336
Li, S., 527
Li, Y., 253, 455
Liang, W., 273
Lichter, B.D., 237
Lidiard, A.B., 140
Liebhafsky, H.A., 171
Lillerud, K.P., 220, 520
Lim, T.H., 515
Limbäck, M., 290
Lin, C.-Y., 248
Lin, R.Y., 354
Lindbergh, G., 309, 508, 509
Linder, M., 520, 522
Ling, H., 523, 524
Lions, J., 119
Lipilin, A.S., 527, 528
Lipkowski, J., 453
Littlewood, R., 12, 127, 173, 297
Litz, J., 265
Liu, C.H., 317
Liu, H., 303
Liu, L., 253, 455
Liu, W.N., 523
Liu, X., 335, 509
Liu, Y., 520
Logan, H.L., 375
Loizos, Z., 494
Long, K.A., 487
Lorenz, K., 26
Loriers, J., 213
Losurdo, M., 433
Lovering, D.G., 296, 297, 513
Lowell, C.E., 227
Lu, J.G., 523
Lu, L.Y., 310
Lukezich, S.J., 266
Lundberg, M., 256
Luth, H., 423
Luthra, K.L., 351
Lux, H., 120, 173, 177, 316
Lyons, V., 166

Ma, J., 524
Ma, J.J., 528
Mabbutt, S., 457
MacEwen, S.R., 26
Machado, R., 272, 273
MacKenzie, J.D., 300
Macknight, W.J., 427
MacKowiak, J., 100
Mackrodt,W.C., 245
Maeda, K., 287
Maeder, G., 100, 247
Magdefrau, N., 523
Magdefrau, N.J., 523
Mahan, G.D., 431, 454
Maier, J., 182
Makarov, D.V., 307
Makkus, R.C., 309
Maloney, M.J., 280
Mamantov, G., 171, 296, 299, 446, 449
Manca, P., 144
Mandelstam, L., 429
Manning, J.R., 153, 168
Manning, M.I., 206, 207, 364, 371
Mansfeld, F., 36, 37, 179, 392, 398, 401, 455, 457
Manukhina, T.I., 313
Mar, R.W., 308
Marassi, R., 449
Marchbanks, M.F., 325
Marchiano, S.L., 173
Marcus, P., 36, 37, 256, 257, 392, 398, 401
Margolin, H., 293
Marianowski, L.G., 512, 513
Marijnissen, G.H., 496
Marina, O.A., 517
Maris, H.J., 439
Maris-Sida, M.C., 228, 290, 293, 294
Markov, B.F., 317
Markus, H., 327
Markus, T., 523
Maroni, V.A., 255
Marquis, F.D.S., 312, 378
Marriott, J.B., 252, 255
Marshall, W., 531, 588
Martin, M., 162, 163
Martinez, H.P., 258
Martinez, L., 314
Martinez, V.A., 354
Martinez-Rodriguez, M., 171, 546
Martini, C., 335
Maru, H., 511, 516
Maru, H.C., 509, 512, 513
Maruyama, T., 197, 392, 457, 521
Masamura, K., 515
Masci, A., 309, 516
Massalski, T.B., 75, 485
Masset, P.J., 305
Masuyama, F., 369
Matano, C., 153
Matheson, J.E., 45
Matiasovsky, K., 495
Matsuda, H., 516
Matsunaga, M., 299
Matsuzawa, K., 510
Mattos, O.R., 457
Mattox, D.M., 490
Matyas, A.G., 163, 164
Maupin, G.D., 523
Maxwell, J.C., 398
Mayer, J., 413
Mayer, K.H., 370
McCarthy, K.J., 352
McCaughey, J.M., 327
McConville, C.F., 417
McDowell, D.W. Jr., 268
McGahan, W.A., 433
McGarrow, H.E., 225
Mcgeehin, P., 454
McGurn, J.F., 226
McHargue, C.J., 493
McNallen, M.J., 280, 281
McPhee, W.A., 529
McPhee, W.A.G., 528
Meadowcroft, D.B., 215, 351, 356, 364, 391, 401
Meeker, G.P., 228, 401
Megel, S., 522
Megy, J.A., 539
Mehandru, S.P., 221
Mehl, R.F., 155
Mehrer, H., 149, 158
Meier, G., 197
Meier, G.H., 3, 25, 100, 108, 110–112, 197, 198, 203, 211, 215, 221, 228, 290, 293, 342–344, 351, 391, 392, 396, 420, 477, 520
Meijering, J.K., 228
Meijerink, A., 429
Melendres, C.A., 304
Meller, R., 254
Mendoza, L., 510
Menendez, A.C., 357
Menzies, I.A., 239
Merli, P.G., 167

Merrick, R.D., 238, 287
Merz, M., 255, 356
Metselaar, R., 168, 334
Meulenkamp, E.A., 429
Meussner, R.A., 236
Mévrel, R., 351, 482
Meyer, E., 427
Meyer-Rau, S., 326
Michalik, M., 291
Mihalisin, J.R., 267
Miki, A., 512
Mikkelsen, L., 520
Milliken, C., 516
Min, Y., 462
Minchington, I., 258
Minh, N.Q., 300, 517
Mirkin, M.V., 460
Mirzaei, M., 523
Mishin, Y., 159, 160
Mishra, B., 305
Misra, A.K., 304, 351
Mistry, P., 239
Mitchell, R.E., 527
Mitchell, T.E., 400
Mitsushima, S., 510
Miyagawa, O., 352
Mizusaki, T., 510
Moccari, A., 225
Moen, R.A., 325
Moerner, W.M., 429
Mogensen, M., 517
Mohinddin, T.F., 467
Mohsen, Q., 564
Moina, C., 273
Molis, S.E., 443
Mollah, A.H., 221
Möller, W., 265
Monceau, D., 201, 370
Monteiro, J.M., 444
Monteiro, M., 284, 290, 292
Monty, C.J.A., 150
Moom, Y., 515
Moon, D.P., 157, 206
Moran, J.J., 267
Morozovska, A., 472
Morral, F.R., 18
Morrill, W., 237
Morschen, G.N., 563
Mortimer, D., 369
Mosca, V., 340
Moseley, P.T., 226
Mosle, J., 400
Mostafa, N.Y., 564
Motohira, N., 311
Mott, N.F., 2, 32, 196
Motta, A.T., 542
Motzfeldt, K., 120, 177, 316
Mougin, J., 291
Mrowec, S., 3, 126, 151, 152, 201, 205, 208, 212, 237, 241–243, 351
Mu, D., 178
Mugikura, Y., 509
Mullejans, H., 413
Müller-Lorenz, E.M., 255, 258, 261, 369
Mumford, J.D., 254, 255, 257
Mundy, J.N., 431
Munford, J.D., 255
Munir, Z.A., 214
Munroe, P.R., 250, 255, 258
Munz, W.-D., 401
Murase, Y., 536
Murch, G.E., 148, 158
Murtagh, M.J., 158

Nabae, Y., 528
Nagashima, I., 512, 515
Nagata, K., 457
Nakagawa, J., 536
Nakagawa, K., 515
Nakagawa, T., 354
Nakajima, H., 155, 307
Nakayayama, Y., 252
Nandy, T.K., 224
Naray-Szabo, I., 130
Narushima, T., 25
Naslain, R., 562
Natesan, K., 3, 239, 245, 255, 351
Naumann, F.K., 258
Naumenko, D., 227
Naumov, V.S., 303
Navrotsky, A., 541
Necci, F., 440
Nelson, G.A., 285
Nelson, H.G., 100
Nelson, L., 535, 537
Nenno, S., 353
Nesbitt, J.A., 442
Neufeld, K., 520
Newark, G., 441
Newcomb, S.B., 214, 413
Newkirk, J.B., 353
Newman, J.S., 452
Newton, R., 228
Newton, R.F., 173
Ni, C.S., 310
Nichkov, I.F., 178
Nicholls, J.R., 487
Nichols, J.R., 3, 25, 351, 355
Nickel, H., 370
Nicolas, F., 304
Nicolet, M.A., 558
Nicoll, A.R., 351, 489
Nieken, H.P., 281
Niewolak, L., 520
Nihoul, J., 255
Nii, H., 271
Niselson, L.A., 539
Nishikata, A., 120, 179, 309, 310, 355
Nishimoto, A., 271
Nishiyama, Y., 245, 247
Nishizawa, T., 247
Niu, Y., 152, 215, 216
Noel, J.J., 259
Nohara, K., 13
Norby, T., 291, 523
Norell, M., 198, 265, 271, 272, 281, 292
Norton, J.F., 228, 237, 239, 252
Nourbakhsh, S., 293
Nowick, A.S., 148, 158
Nowierski, C., 459
Numata, H., 120, 179, 309, 319, 351

Oakey, J., 457
O'Brien, M.H., 334
Odgers, M., 228, 291, 292
Oh, J.M., 280
Ohashi, N., 13
Ohe, K., 515
Ohno, I., 179
Ohzu, H., 515
Oijerholm, J., 458, 460
Okamoto, I., 333
Okamoto, K., 517
Okamoto, P.R., 75
Okanda, Y., 353
Okumura, H., 354
Olander, D., 545
Oldenkamp, R.D., 310
Oliveira, M., 290
Olson, D.L., 305
Olson, L., 171, 546
Olsson, R.G., 257
Oltra, R., 456
Onal, K., 228, 290
Onishi, K., 287
Ono, Y., 13
Onsager, L., 182
Opila, E., 253
Opila, E.J., 3, 292
Orazen, M.E., 455
Oren, D., 167
Oryshich, I.V., 305, 306, 313
Osteryoung, J., 451
Osteryoung, R.A., 451
Ostvold, T., 303
Ostwald, C., 370
Ota, K., 510
Ota, K.I., 311
Otero, E., 178
Othman, N., 253
Othman, N.K., 253
Otsuka, N., 245, 247, 370
Oura, K., 425
Overney, R.M., 427

Overs, M.P., 488
Ozekin, A., 254
Ozerov, R.P., 378
Ozeryanaya, I.N., 299, 313

Paetsch, L., 513
Page, T.F., 333
Palange, E., 437, 438
Palcut, M., 520
Palladino, A.E., 294
Palombarini, G., 335
Pan, C., 309
Pan, J., 458, 460
Panas, I., 292
Pangestuti, E., 482
Papavinasam, S., 452
Paranthaman, M.P., 523
Parascandola, S., 265
Pardo, A., 178
Parhani, P., 529
Park, D.S., 517
Park, E., 518
Park, J.K., 271
Parker, J.C., 378, 379
Parker, J.D., 363
Parsons, R., 173
Parthasarathy, T.A., 285, 287
Pask, J., 400
Patel, P.M., 444
Patel, P.S., 513
Patterson, J.W., 193, 194
Patton, E.M., 529
Paul, L.D., 354
Payzant, E.A., 523
Peacock, A., 534, 589
Pearson, J., 101, 106
Pearson, W.B., 251
Pêchoir, R., 482
Pelton, A.D., 100, 117
Pendry, J.B., 404
Peng, D.Q., 271
Penkalla, H., 518
Peraldi, R., 371
Perez, F.J., 178, 309
Perkins, R.A., 25, 115, 116, 239, 260, 264
Perry, A.J., 401
Peters, M., 24
Petersen, E.M., 252
Petit, J.P., 391
Petkovic, R.A., 254
Petot-Ervas, G., 204
Petric, A., 523, 524
Pettersson, C., 280, 282
Pettersson, J., 280, 282
Pettersson, R., 248, 253, 256
Petti, D., 531, 588
Pettinger, B., 467
Pettit, F.S., 3, 100, 102, 108, 110–112, 115–118, 171, 197, 198, 200, 203, 210, 211, 213, 215, 221, 228, 264, 281, 290, 293, 342–344, 351, 391, 392, 396, 420, 477, 497
Philibert, J., 201, 205, 520
Phillipot, S.R., 160
Phillips, C., 255
Phillips, N.D., 378
Piatti, R.C.V., 178
Picard, G.S., 307, 545
Pieraggi, B., 201
Piermarini, G.J., 443
Pigeaud, A., 513, 514
Pijolat, M., 253
Pillai, S.R., 370
Pilling, N.B., 2, 196, 206, 233
Pillis, M.F., 447
Pingfang, S., 120
Pint, B.A., 3, 220, 228, 371, 520
Pippel, E., 255–259
Piron-Abellan, J., 513, 519, 520
Plomp, L., 309, 310
Podesta, J.J., 318
Podesta, J.P., 178
Pohlman, S.L., 305
Pointon, K., 528
Pointon, K.D., 528
Pöjjing, J., 158
Pollock, T.M., 224
Polovov, I.B., 303
Polyakov, A.Y., 167
Polyakov, E.G., 303
Pompe, W., 413
Ponath, H.E., 437
Pons, J., 254
Pool, R., 541
Pope, M.C., 204
Porcayo-Calderon, J., 314
Porto, S.P.J., 431
Potgieter, J.H., 563, 564
Pourbaix, M., 545
Pourbaix, M.J.N., 177, 298
Pourbaix, M.S.N., 112, 113, 127
Powell, J., 492
Pozzi, G., 167
Prakash, S., 351, 354, 356
Prange, F.A., 255
Prazak, M., 177, 178
Prescott, G.R., 237
Prescott, R., 206, 211, 224
Priest, J.M., 271
Prigogine, I., 173
Procter, R.P.M., 400, 401
Prophet, H., 100, 110
Przybylski, K., 151, 212, 237
Purget, R., 370, 371
Pye, D., 264

Qi, J., 437
Qin, Z., 259
Qiu, C., 334
Quadakkers, J., 370
Quadakkers, W.J., 3, 227, 228, 291, 370, 420, 421, 513
Quataert, D., 36
Quets, J.M., 342, 343
Quigg, H.T., 342

Radd, F.J., 260
Radhakrishnan, V., 354
Raghavan, S., 443
Rahmel, A., 3, 120, 121, 173, 207, 212, 225, 236, 237, 245, 252, 264, 265, 290–293, 296, 312, 314, 351, 353, 355, 367, 391, 392
Rahts, K., 370, 391
Rai, J.S., 268, 269
Rajesh, N., 445
Rajic, N., 44, 444
Rakhmatullin, A., 303, 321
Ramanarayanan, T.A., 254, 255, 257, 351
Ramasubramanian, N., 36
Rameau, J.J., 304
Randles, J.E.B., 175
Ranford, R.E., 173
Ranganathan, S., 457
Rao, D.B., 100
Rao, U., 370, 371
Rao, Y.K., 112, 119
Rapp, R., 325
Rapp, R.A., 3, 25, 100, 163, 164, 178, 193, 194, 212, 213, 237, 278, 279, 291, 349–351, 482–484, 486
Raška, P., 309
Raspopin, S.P., 178
Rathenau, G.W., 228
Ratz, G.A., 265
Ratzer-Scheibe, H.J., 178
Rau, H., 241
Ravi, V.A., 483
Rayleigh, L., 429
Raynaud, G.M., 291
Reavis, J.G., 303
Rebane, K.K., 428
Reddy, D.P., 451
Reddy, K.P.R., 221
Redey, L., 300
Reed, R.C., 223, 294
Reed, T.B., 276
Rees, A.G., 131
Reese, E., 280, 281, 380
Reinders, F., 267
Reiser, C.A., 504, 505
Reiter, H., 444
Remeika, J.P., 431
Ren, B., 470

Renusch, D., 290, 292, 370
Revie, R.W., 18
Rey, M., 300–302
Reynolds, W.C., 103
Rhee, W.H., 293
Richardson, F.D., 100–102, 104, 105, 121
Rinaldi, C., 440
Rizzo, F., 284, 290, 292
Roberge, P.R., 448
Robert, F., 166
Robert, M.W., 253
Roberts, A.D., 426
Roberts, J.T.A., 535, 588
Robertson, J., 371
Rocabois, P., 102, 199, 247
Rockett, A., 401
Rockstroh, M., 413
Rodrigo, T., 510
Roe, D.K., 179
Roger, F., 309
Rollet, A.L., 303
Ropital, F., 256, 257
Rorbo, K., 267
Rosa, C.J., 35
Rosado, C., 482
Rosborough, D.F., 378, 379
Rose, A., 144
Rosencwaig, A., 444
Ross, P.N., 453
Rossiter, B.W., 448
Rostoker, W., 327
Roth, H.A., 343
Roth, W.L., 431, 454
Rothman, M.F., 239, 280, 304, 351, 372
Rouillard, F., 253
Rouquette, S., 304
Rouquette-Sanchez, S., 545
Rowlands, D., 444
Roy, S.K., 280
Rudenauer, F.G., 420
Rudolph, M., 451
Rufner, J., 521
Ruhle, M., 413
Rundgren, J., 403
Ruppel, W., 144
Ruth, L.A., 363
Ruther, W.E., 225
Ruzzier, M., 440

Sabioni, A.C.S., 520
Sabol, G., 26
Sachitanand, R., 520, 523
Sachs, K., 228, 291, 292
Sadique, S.E., 221
Saenz, E., 178
Sahin, O., 293
Saiki, A., 457
Saito, T., 452
Saito, Y., 457
Salanne, M., 303
Salzberger, U., 413
Samandi, M., 273
Sammes, N.M., 517
Sandstrom, R., 265
Sankar, P., 370
Sannikov, V.I., 313
Santarini, E., 544, 545
Santos, D.M.F., 204, 392, 458, 540
Sarou-Kanian, V., 303
Sarrazin, P., 197, 212
Sasaki, S., 457
Sasaki, T., 307, 314
Sass, S.L., 158
Sastri, V.S., 226
Sato, Y., 354
Sattari, M., 520, 523
Sauchuk, V., 522
Saunders, S.R.J., 284, 290, 292, 351, 355, 356
Savage, D.B., 404
Sawhill, H.T., 413
Sawyer, J.W., 228
Schaefer, A.O., 239
Schaeffler, A.L., 14
Scharfstein, L.R., 238
Scheffler, T.B., 448
Schenck, H., 267
Scherrer, H., 149
Scherrer, S., 149
Schick, H., 101
Schilling, W., 147
Schillmoller, C.M., 254
Schirmer, R.M., 342
Schlupp, M.V.F., 523
Schmalzried, H., 100, 117, 118, 162, 498
Schmidt, F., 338
Schmidt, K., 420, 421
Schmidt, M., 24
Schmutz, F., 467
Schnaas, A., 250, 254
Schneider, A., 255, 261
Schneider, R., 255–259
Schorr, M., 265, 290, 292, 353, 370, 391
Schöttky, W., 130, 131
Schroeder, M., 163
Schroll, C.R., 504, 505
Schulte, M., 207
Schulz, W., 253
Schumacher, D., 147
Schumann, E., 413
Schumann, P.A. Jr., 165
Schuster, H., 370
Schütze, M., 3, 36, 207, 225, 227, 265, 290, 292, 370, 391, 420, 482
Schwenk, W., 212, 312
Schwitzgebel, G., 182
Seabaugh, M.N., 523
Seah, M.P., 403, 424
Sedricks, A.J., 515
Sedriks, A.J., 272
Seeger, A., 147, 158
Segerdahl, K., 228
Sehgal, B.R., 541
Seigle, L.L., 484
Seitz, F., 131, 155, 201, 202
Selman, J.R., 509, 511, 526
Selzer, P.M., 428
Sencer, B.H., 535
Seon, F., 120
Seong, B., 325
Seong, B.G., 517
Sequeira, C.A.C., 121, 126, 155, 173, 178, 186–188, 204, 228, 296, 298–302, 312, 315, 317, 318, 320, 321, 345, 351, 354, 378, 392, 458, 496, 540
Sesonske, A., 505, 588
Setoguchi, T., 517
Setterlund, R.B., 237
Seybolt, A.U., 342, 343
Seymour, D.L., 417
Shamatani, Y., 179
Shannon, C., 467
Sharma, B.K., 435
Sharpe, R.S., 439
Shatynski, S.R., 100
Shaw, P.H., 310
Shedden, B.A., 273
Sheffler, K.D., 442
Shemet, V., 513, 520
Shen, Y.R., 437, 438
Shenoy, G.K., 431
Sherby, O.D., 225
Shewmon, P.G., 168
Shida, Y., 370
Shifler, D.A., 354
Shih, C.Y., 280, 281
Shimada, T., 511, 512, 515
Shinata, Y., 311, 351
Shirn, G.A., 166
Shivpuri, R., 325
Shoemaker, L., 371
Shores, D.A., 351, 509
Shouzen, D., 307
Siddiqi, A.A., 269
Sidky, P.S., 239, 297, 300, 350, 351, 357, 490, 498
Siegel, N.P., 308
Sigler, D.R., 221
Silva Gomes, J.F., 444
Simchi, A., 523
Simco, F., 303
Simmer, S.P., 517
Simms, N., 457
Simms, N.J., 228, 487

Simonen, E.P., 536
Simons, A.L., 171
Simpson, C.J., 543
Sims, C.T., 16, 18, 19, 223, 224, 342
Singer, J., 366
Singh, P., 512, 513, 517, 521
Singh, S., 253, 356
Singh, V., 485
Singhal, S.C., 516–518
Singheiser, L., 513, 523
Skaarup, S., 517
Skarda, J., 258
Skelton, R.P., 299
Skilbred, A.W.B., 522
Skinner, E.N., 267
Skok, A.J., 513
Slaney, M., 528, 529
Slusser, J.W., 308
Smaardijk, E.J., 291
Smalley, R.E., 257
Smallman, R.E., 58, 59, 82, 85
Smart, D.W., 157, 206
Smee, J.D., 542
Smeggil, J.G., 221, 228, 351
Smekal, A., 429
Smeltzer, W.W., 212, 314, 352
Smialek, J.L., 3, 221, 319, 400
Smigelskas, A.D., 153, 154
Smirnov, N.B., 167
Smit, K., 251, 252
Smith, C.A., 252
Smith, D.I., 273
Smith, D.L., 337
Smith, F.N., 226
Smith, G., 371
Smith, G.D., 226, 240, 258
Smith, G.P., 309
Smith, L., 452
Smith, P.J., 252
Smith, R.W., 333
Smith, S., 119
Smith, T., 35
Smyrl, W.H., 304
Söllner, O., 515
Somorjai, G.A., 437
Song, D., 508
Song, X., 392
Sorell, G., 237, 287
Sörensen, M.R., 160
Sorlie, M., 303
Sorokin, Y.I., 308
Spafford, B.F., 379
Sparr, M., 508
Spauschus, H.O., 237
Spence, J.C.H., 413
Spiegel, M., 280, 367, 380, 515
Spies, F., 258
Sproul, W.D., 401
Sproule, G.I., 221
Spuckler, C.M., 442
Spyrellis, N., 494
Squillace, A., 485
Sridharan, S., 443
Srinivasan, S.R., 252
Srolovitz, D.J., 254
Staehle, R.W., 280
Stanislowski, P., 520, 522
Starke, U., 404
Starr, F., 115, 116
Staubli, M., 370
Stearns, C.A., 352, 353
Steele, B.C.H., 517
Steen, W.M., 492
Stegeman, G.I., 437
Steigenberger, U., 407
Steinkusch, W., 245, 252, 254
Steinmann, P.A., 441
Steinmetz, P., 197
Stephens, E., 523
Stern, M., 3, 179, 352
Stevens, C.G., 345
Stevenson, J.W., 517, 521, 523
Sticher, J., 117, 118
Stieltjes, F.H., 137
Still, T., 431
Stiphout, P.C.M., 220
Stobbs, W.M., 413
Stoklosa, A., 208
Stoll, R.L., 440
Stoloff, N.S., 16, 19, 223
Stölwijk, N.A., 149, 158
Stolwijk, N.S., 158
Stott, F.H., 119, 220, 280, 281, 352, 457
Strafford, K.N., 3, 239, 352
Strandberg, C., 401
Stratchan, J.F., 326
Strauss, R., 256, 258
Strauss, S., 255, 258, 261, 264, 267
Strecker, A., 413
Street, K.W., 442
Streiff, R., 228
Stringer, J., 3, 119, 214, 228, 237, 342, 345, 351, 352, 497, 521
Stringer, J.A., 356
Strochi, P.M., 340
Stultz, S.C., 287, 364, 365
Su, X., 437
Subramanian, P.R., 75
Sullivan, C.P., 18
Sulonen, M.S., 248
Sun, E.Y., 523
Sun, X., 523
Sun, X.F., 293, 357
Sundgren, J.E., 401
Sundheim, B.R., 297
Sundman, B., 103
Sundqvist, M., 333
Sung, J.H., 272, 273
Surek, T., 338
Suzuki, A., 159, 160
Suzuki, S., 445
Svensson, J.-E., 198, 228, 281, 292, 520
Swales, G.L., 379
Swalin, R.A., 101
Swaminathan, V.P., 266
Swartz, J.C., 338
Szakálos, P., 248, 253, 256, 259
Sze, S.M., 167

Taboada, A., 542
Tabor, D., 426
Taghizadeh, M., 539
Tait, R.A., 239
Takeishi, Y., 310
Takemoto, T., 333
Takita, Y., 516
Tamba, A., 120, 121, 178, 316
Tanabe, F., 541
Tanc, J., 439
Taniguchi, S., 197, 392, 518
Tanimoto, K., 312
Tannenbaum, E., 166
Tao, T., 528, 529
Tappin, G., 226
Tasaka, A., 304
Tassa, O., 25
Tassen, C.S., 226
Tatsumi, M., 512
Taxil, P., 303
Taylor, A.F., 352
Taylor, J.W., 328
Taylor, R.I., 157, 206
Taylor, T.A., 488
Techorrewski, R., 45
Tedmon, C. Jr., 278
Tedmon, C.S., 198, 213, 521
Telle, R., 326
Teller, E., 209
Tempest, P.A., 420
Tenini, J.W., 269
Terada, S., 515
Thebault, J., 562
Theus, G.J., 536
Thiele, M., 370
Thoma, M.J., 228, 400
Thomas, C.W., 258
Thomas, T.M., 305, 309, 310
Thompson, A.W., 10
Thompson, D.O., 441
Thomson, R.M., 142
Thonsen, C., 439
Thonstad, J., 297, 300
Thorley, A.W., 330, 336

Thornton, J.A., 490
Thuillier, J.A., 254
Tian, Z.-Q., 469, 470
Tietz, F., 519
Tighe, N.J., 163, 164
Tilak, B.V.K.S.R.A., 172
Tinkov, V.A., 423, 424
Tipping, P.G., 325
Tischer, R.P., 179
Titcomb, J.B., 308
Tiwari, S.N., 354
Tjokro, K., 265
Tobias, C.W., 452
Tobolski, J., 290–292, 367
Toda, K., 311
Toh, C.H., 250, 255, 258
Tökei, Z., 370
Tolanski, S., 426
Toloczko, M.B., 535
Tolpygo, V.K., 443
Tomeczek, J., 321
Tomimatsu, N., 515
Tompkins, H.G., 433
Tompkins, R.P.T., 299
Tompsett, G.R., 517
Tong, A.H., 165
Tong, S.I., 404
Toplygo, V., 294
Tortorelli, P.F., 337
Traud, W., 171, 176
Trebbels, R., 523
Trémillon, B., 120
Tremillon, B.L., 307
Treska, M., 220
Tressler, R.E., 563
Trethewey, K.R., 44
Tribollet, B., 455
Tromp, R.M., 415
Tsai, W.-T., 248
Tseitlin, K.L., 308
Tsui, E.S.-M., 166
Tsuji, K., 459
Tsukuda, Y., 304
Tsuru, T., 120, 309, 355
Tuck, C.W., 228, 291, 292
Tucker, M.C., 519
Tucker, P.M., 418, 419
Tucker, R.C. Jr., 488
Tumpner, J., 421
Tunca, N., 333
Turkdogan, E.T., 257, 276
Turnbell, D., 131
Turnbull, A., 287
Turnbull, D., 158, 201, 202
Tuson, A.T., 401
Tveten, B., 291, 293
Tyzack, C., 330, 336
Uchida, I., 509, 511
Uhlig, H.H., 18
Ukshe, E.A., 172
Urushibata, H., 511
Vaillant, J.C., 371
Valdes, A., 45
Vallet, C.E., 448
Valtiner, M., 462, 463
van Arkel, A.E., 538
van Bueren, H.G., 56
van de Voorde, M., 237
van der Bruck, U., 254
van der Pauw, L.L., 166
van Dijken, A., 429
van Gool, W., 134, 143
van Grieken, R., 563, 564
van Hove, M.A., 404
van Manen, P.A., 459
van Sandwijk, A., 539
Vandenberghe, B., 371
Vandervelden, F., 177
Vanmaekelbergh, D., 429
Varela, F.J.B., 357
Vasantasree, V., 239, 297, 300, 350–352, 357, 490, 497
Vashishta, P., 431
Vasylyev, M.A., 423, 424
Vaz, M.A.P., 444
Verink, E.D., 42
Verma, K.M., 268, 269
Verma, S.K., 239, 240
Vetter, K.J., 175
Viala, J.C., 334, 335
Viani, F., 25, 152, 210, 220, 293
Vicentini, B., 340
Vickers, A.J., 166
Vielstich, W., 509
Vijh, A.K., 144
Villa, H., 101, 107
Vincent, C., 335
Vincent, H., 335
Vink, A.J., 131
Vink, H.J., 201, 202
Vink, J.H., 131, 137
Virkar, A.V., 527
Virr, M.J., 378, 379
Visco, S.J., 523
Viswanathan, R., 342, 363, 369–371
Vogel, D., 264, 267
Vohs, J.M., 524, 529
Volkovich, V.A., 303
Volmer, M., 175, 176
von Baumbach, H.H., 203
von Bogdandy, L., 164
Vossen, J.P.T., 309, 310, 370
Voter, A.F., 160
Voyer, J., 441
Vuci, Z., 150
Wachtell, R.L., 484
Wada, H., 314
Waddams, J.A., 343
Wadley, H.N.G., 498
Wagenhein, N.T., 352
Wagner, C., 130, 163, 171, 176, 182, 192, 199, 203, 210, 211, 235, 237, 241, 277–279, 352
Wagner, C.L., 378
Wagner, C.Z., 203
Wagner, J.B., 3, 200, 210, 241
Walec, T., 126
Walker, M.S., 521
Walter, M., 225, 391
Walter, M.E., 523
Walura, E., 420, 421
Wang, F., 455
Wang, G., 482
Wang, G.L., 522
Wang, K., 305
Wang, W., 299, 312
Wang, X., 509
Wang, Y., 303
Ward, A.G., 328
Ward, D.M., 379
Ward, I.M., 427
Ward, J., 255
Ward, M.D., 471
Wareham, B.A., 352
Wartlick, B.D., 167
Was, G.S., 535–537
Watanabe, T., 509
Waters, L.C., 535
Watzenburger, O., 281
Weast, R.C., 276, 457, 459
Weaver, M.J., 447
Weber, T., 126, 482
Webster, S.J., 227
Wee, J., 508
Wee, J.H., 313
Weeks, J.R., 338, 536
Weertman, J., 87
Weertman, J.R., 87
Weewer, R., 459
Wegst, C.W., 371
Wehefritz, V., 241
Weinberg, S., 444
Weinberg, W.H., 404
Weinem, D., 24
Weinruch, S., 227
Weiss, J., 265
Weissberger, A., 448
Weissert, T., 482
Welker, M., 265
Wells, A.F., 130
Welsch, G., 25

Wen, M., 443
Wen, T.T., 253
Wendt, H., 511
Wenwer, F., 158
Werber, T., 237
Wereszczek, A.A., 441
Werner, H., 421
Werner, H.W., 420
Wert, C.A., 142
Wessel, E., 518, 520, 522
Westbrook, J.H., 25, 220
Westman, C., 265
Weyl, A., 457
Wheatfall, W.L., 318, 321
White, D.E., 6
White, D.P., 345
White, J.L., 300
White, P., 521
White, R., 528
White, S.H., 303
White, W., 175
Whittenberger, J.D., 227, 304
Whittle, D.P., 3, 220, 221, 521
Whitton, J.L., 36
Wicks, C.E., 110
Wiesendanger, R., 467
Wight, J.C., 343
Wijayasinghe, A., 510
Wild, R.K., 418–420
Wildgoose, G.G., 171
Williams, D.E., 457, 467
Willis, P.A., 257
Wilson, J.R., 379
Wilson, R.W., 340
Winand, R., 546
Winterton, R.H., 426
Wojcik, C.C., 25
Wolf, D., 160
Wolf, I., 245, 251
Wolfe, L.H., 254
Wolski, K., 253
Wolter, O., 466
Woltersdorf, J., 255–259
Wood, G.C., 3, 220, 222, 279, 293, 352
Woodruff, D.P., 417
Woolf, A.A., 332
Worrel, W.R., 100
Wortley, L., 352
Wortmann, J., 308
Wouters, Y., 291, 370, 391
Wright, I.G., 197, 220, 225, 254, 352
Wu, C.X., 355
Wu, D.Y., 470
Wu, W., 299, 312, 522
Wu, W.T., 353
Wuchina, E., 253
Wulpi, D.J., 94
Wylie, R.D., 260
Wynns, K.A., 482

Xia, G.G., 523
Xiao, H., 455
Xiao, Y., 539
Xu, H., 488
Xu, J., 335
Xu, X., 310

Yamada, S., 304
Yamada, T., 307
Yamakov, V., 159
Yamamoto, N., 536
Yamanis, J., 523
Yamazaki, M., 225
Yamazaki, T., 225
Yan, M., 333
Yanagida, M., 312
Yang, J.C., 208
Yang, Y., 305
Yang, Z., 517, 519, 521, 523
Yang, Z.G., 523
Yariv, A., 438
Yates, D.H., 240
Yaxin, X., 303
Yazawa, A., 102, 247
Yazdanyar, A., 523
Ybarra, G., 273
Yeadon, M., 208
Yeatman, J.A., 485
Yeganeh, M.S., 437
Yen, W.M., 428
Yeomans, J.A., 333
Yoo, D.K., 272, 273
Yoon, S.P., 509
Yoshiba, M., 197, 314, 352, 392
Yoshikawa, M., 508, 509
Yoshitake, H., 310
Youn, J.Y., 509
Young, D., 253, 281, 521
Young, D.J., 237, 250, 253–255, 258, 265, 281, 291, 482, 484, 520, 521
Young, E.W.A., 220
Young, G.J., 509
Yu, F., 441
Yu, M., 265, 325
Yuh, C., 511, 513, 516
Yuh, C.Y., 513, 514
Yun-tao, X., 272
Yurek, E.J., 163, 164
Yurek, G.J., 164, 212
Yurkinsky, V.P., 307, 309
Yust, C.S., 493

Zahrani, E.M., 321
Zahs, A., 280, 367
Zastawnik, M., 237
Zaza, F., 309
Zecevic, S., 529
Zeng, C., 303, 312, 455
Zeng, C.L., 299
Zeng, Z., 255
Zetmeisl, M.J., 352
Zeuthen, A.W., 224, 228
Zhang, J., 253, 255
Zhang, S., 518
Zhang, X.-M., 469
Zhang, Y.S., 178, 349, 350
Zhang, Z.Y., 357
Zhao, C., 253
Zhao, Y., 521
Zhen, Y.D., 518
Zhou, C., 488
Zhou, W., 310
Zhu, J.H., 523
Zhu, R., 178, 259, 459
Zhu, W.Z., 519, 522
Zhu, Y.Y., 467
Zhu, Z., 310
Zinke, M., 258
Zolfonoun, E., 539
Zotov, A.V., 425
Zurek, J., 291

Subject Index

absorbance, 433, 435
AC impedance plots, 453–455
acoustic emission (AE), 356, 391, 441, 596
active oxidation, 281, 596
addition reactions, 34, 343
adsorption isobar, 209
advanced ceramics, 25, 41, 562
advanced gas-cooled reactor (AGR), 26, 532, 533, 535, 541, 588
AES. *See* auger electron spectroscopy (AES)
age-hardening alloys, 71–72, 94
AGR. *See* advanced gas-cooled reactor (AGR)
air, 20, 64, 102, 196, 240, 253, 264, 277, 284, 298, 340, 366, 392, 479, 502, 551, 570
aliovalent solutes, 280, 597
alkaline fuel cells (AFC), 504
allotropy, 18, 64, 72, 597
alloys, 1, 51, 101, 146, 171, 196, 233, 245, 264, 276, 284, 298, 325, 340, 363, 392, 477, 502, 551
alloy-design, 1, 282, 554, 597
alloy steels, 4, 5, 7–9, 15, 32, 33, 51, 63, 66, 78–79, 89, 102, 197, 207, 238, 256, 257, 267, 284, 285, 305, 332, 379, 386, 387, 597, 606, 608
alumino-silicate refractories, 22, 325, 334
ammonia converter, 267, 268
analytical transmission electron microscopy, 412
annealing, 28, 30, 71, 76, 90, 153–156, 225, 227, 277, 297, 304, 555–558, 597
anti-frenkel defect, 134, 140
ashes, 27, 30, 38–40, 363, 383
atomic force microscopy (AFM), 424–426, 428, 467, 471
atomic-size roughness, 469
attenuated total reflectance, 436
auger electron spectroscopy (AES), 271, 272, 307, 308, 392, 398–401, 418–420, 424
austenite, 6, 7, 9–11, 16, 73, 74, 76–79, 223, 247, 248, 259, 260, 271–273, 521, 535, 580, 597, 598, 603, 608, 609, 614
austenitic stainless steels, 5, 9, 11, 13–15, 26, 61, 225, 226, 253, 267, 271–273, 280, 285, 308, 310, 329, 330, 335–337, 379, 380, 387, 511, 515, 565
automatic thermal impedance scanning (ATIS), 439

bainite steel, 79, 598
band edges, 184, 185, 429
bandgap, 143, 144, 184, 185, 437
bandgap energy, 184, 185
basic slags, 21
binding energy per nucleon, 537, 598
bipolar plate, 508, 510–513, 515, 526
black plague, 3, 340, 598
body-centered cubic structures, 53
boiling water reactors (BWRs), 532, 533, 538, 541–543, 588
boudouard reaction, 245, 527
breakaway oxidation, 33, 225, 227, 228, 253
Brillouin scattering, 430, 431
Brillouin zone, 430–432
brittle fracture, 83, 91–94, 96, 598, 599, 601, 602, 607
bronzes, 61, 62, 71, 72, 314, 378, 551, 570, 578, 582, 589, 590
BWRs. *See* boiling water reactors (BWRs)
bystram diagram, 14, 15

capacitance of electrode film, 452
capital budgeting techniques, 38, 41
carbon, 2, 51, 110, 146, 171, 197, 233, 245, 267, 279, 284, 305, 325, 350, 364, 392, 496, 502, 561
carburization, 3, 17, 27, 28, 30, 31, 34, 39, 40, 100, 171, 224, 245–261, 264, 265, 321, 330, 340, 364, 386, 482, 496–498, 512, 560, 605, 608
cash flow, 41, 42
casting, 1, 4, 9, 11, 16, 18, 20, 58, 63, 64, 67, 251, 325, 332, 335, 356, 479, 514, 553, 599
cast iron, 5–7, 60, 62, 63, 72, 77, 78, 335, 338, 551, 578, 582, 596, 598, 605, 609, 614
cast metals, 56, 62, 63, 89, 90, 254, 601
cementite, 72–79, 245, 255–257, 260, 261, 267, 564, 598, 599, 609, 613, 614
center plate, 510
ceramics, 1, 4, 5, 20, 25, 26, 29, 31, 38, 41, 96, 110, 119, 147, 171, 183, 198, 264, 276, 297, 303, 311, 312, 319, 325, 326, 332–335, 338, 340, 358, 392, 400, 441, 480, 487, 488, 491, 493, 497–500, 502, 506, 513, 514, 516–519, 522, 525, 527–529, 533, 535, 551, 554–556, 562–563, 578, 583, 599, 608, 612, 613
char, 30, 395, 530
charge of electrode film, 452
chaudron diagram, 246
chemical diffusion, 149–152, 160–162, 164, 179, 182
chemical potential, 34, 100, 103, 105, 108, 109, 136, 137, 143, 149, 152, 160, 162, 163, 172, 180, 190–194, 204, 235, 236, 332, 597, 602
chemical potential of the electrons, 143

High Temperature Corrosion: Fundamentals and Engineering, First Edition. César A. C. Sequeira.
© 2019 John Wiley & Sons, Inc. Published 2019 by John Wiley & Sons, Inc.

chemical vapor deposition (CVD), 421, 478, 480–482, 486, 492, 497, 502, 518, 556, 599, 609
chemiluminescence, 428, 434
chemisorption, 31, 34, 209, 415
china clay, 21
chlorine-cycle, 281, 599
chrome-magnesite, 21
chromite, 21, 519
chromophores, 435
chronoamperometry, 300, 446–448, 452
chronocoulometry, 448
chronopotentiometry, 300, 311, 321, 447–448, 452
closed static reaction vessels, 396
coal-ash corrosion, 371–373, 387, 388
coal gasification, 30, 40, 115, 117, 119, 197, 237, 239, 256, 260, 314, 506
coal liquefaction, 30
cobalt-based alloys, 18–19, 101, 226, 237, 264, 266, 304, 309, 333, 335, 341, 351, 352, 583
combustion products, 27–30, 41, 171, 225, 253, 367, 563, 606
complementary electronic defects, 132
composites, 23, 25, 41, 63, 64, 89, 163, 171, 227, 297, 333, 340, 358, 388, 477, 491, 492, 498, 506, 509, 517, 527, 534, 554, 556, 562–563, 590, 599, 603, 611
compositionally modulated alloy, 494
conduction band, 135, 139, 142, 143, 184, 185, 203, 429
conventional transmission electron microscopy, 412
coring, 70–71
corrosion
  economics, 41–44
  management, 41, 44–46
  products, 1, 3, 27, 28, 31, 101, 102, 110, 119, 126, 171, 179, 186, 197, 201, 207, 212, 233, 234, 238, 239, 251, 257–260, 278, 280, 281, 297–299, 303, 304, 307, 310–312, 321, 336, 346, 347, 349, 350, 362, 372, 376, 377, 391, 392, 457, 467, 511–513, 540, 564, 565, 600, 602, 607, 608, 611
couper-gorman curves, 238, 239
covalent bond, 4, 53, 75, 600
creep, 1, 2, 4, 9, 17, 20, 25, 31, 35, 37, 54, 55, 62, 88–89, 130, 146, 158–160, 214, 223–226, 240, 251, 252, 255, 265, 266, 287–289, 291, 292, 325, 342, 352, 357, 358, 363, 364, 369–371, 381, 383–385, 388, 392, 426, 492, 496, 508, 514, 515, 520, 532, 535, 536, 540, 543, 552–554, 556, 600
critical crack length, 91, 92
crystal growth, 55, 59–60, 556
current collector, 310, 465, 508, 510–512, 526–528, 530
CVD. *See* chemical vapor deposition (CVD)
cyclic voltammetry, 448–449, 452, 453, 458

darken equation, 156
deacon reaction, 281
decarburization, 7, 27, 28, 245–247, 267, 268, 285, 287, 293, 321, 327
deformation, 7, 9, 10, 13, 18, 37, 54–56, 63, 76, 79–92, 96, 157, 163, 164, 207, 226, 265, 266, 279, 285, 292, 365, 370, 426, 437, 443, 471, 490, 496, 511, 519, 520, 598, 601, 602, 606, 610, 612
dendrites, 60, 61, 70, 71, 183, 329, 601
depth profiing, 272, 398, 400, 401, 416, 419–421, 445, 468
differential pulse voltammetry (DPV), 450–451
diffusion coefficient, 35, 36, 146, 149–153, 155–161, 163–165, 168, 179, 182, 188, 204, 205, 210–213, 219, 220, 235, 241, 249, 276, 278, 282, 315, 328, 375, 446–449, 452, 454, 457, 458, 520, 523, 545, 555, 601
diffusivity dispersion, 158
dimensional stability, 6, 21, 512, 535
direct carbon fuel cell, 310, 503, 524–531
dislocations, 4, 18–20, 25, 34, 54–56, 59, 63, 65, 71, 75, 76, 82, 84–90, 92–95, 130, 132, 157, 158, 202, 205, 212, 261, 285, 291, 292, 370, 412, 535, 552, 601, 611, 612
dispersion hardening, 5, 55, 75, 601
dissociative mechanism, 148, 149, 158
doping, 35, 148, 161, 184, 185, 187, 217, 221–222, 236, 240–243, 280, 282, 516, 517, 522, 556
drawing, 13, 14, 63, 101, 108–110, 114, 281, 383, 490, 502
drude equations, 432, 433
dual-phase steels, 79, 601
ductile fracture, 93–95, 598, 601
ductile-to-brittle transition, 15, 95, 96, 499, 601
dynamic atmospheres, 393

earing index, 13, 14
EBSD. *See* electron backscatter diffraction (EBSD)
ECMS. *See* electrochemical mass spectroscopy (ECMS)
ECN. *See* electrochemical noise (ECN)
ECSFA. *See* electrochemical surface forces apparatus (ECSFA)
EDS. *See* energy dispersive spectroscopy (EDS)
EELS. *See* electron energy loss spectroscopy (EELS)
effective charge of the defect, 131
effective diffusion coefficient, 205, 212, 458
effective diffusivity, 158
effective parabolic constant, 212
Einstein diffusion coefficient, 150
Einstein-Smoluchowski relation, 150
EIS. *See* electrochemical impedance spectroscopy (EIS)
elastic deformation, 80–82
electrochemical AFM, 467
electrochemical analysis, 119–128
electrochemical electron spin resonance (EESR), 462–464
electrochemical impedance spectroscopy (EIS), 320, 453, 454, 546, 602
electrochemically modulated infrared spectroscopy (EMIRS), 462, 467
electrochemical mass spectroscopy (ECMS), 464–466
electrochemical noise (ECN), 178, 320, 453, 455–457
electrochemical potential, 143, 188–191, 204, 211, 287, 455, 602
electrochemical STM, 466–467
electrochemical strain microscopy (ESM), 471–472
electrochemical surface-enhanced raman spectroscopy, 468–470
electrochemical surface forces apparatus (ECSFA), 462, 463
electrolyte matrix, 514
electromagnetic enhancement, 469
electron backscatter diffraction (EBSD), 444–445, 602
electron energy loss spectroscopy (EELS), 401, 413, 423
electronic imperfections, 130
electron spectroscopy for chemical analysis (ESCA), 307, 353, 398–400, 418
electroreflectance spectroscopy, 467
Ellingham diagrams, 101–103, 118, 180, 197
ellipsometry, 393, 432–433
EMIRS. *See* electrochemically modulated infrared spectroscopy (EMIRS)
energy bonds, 183
energy dispersive spectroscopy (EDS), 411, 413
energy gap, 142, 144
energy levels, 141–143, 183–186, 424, 429, 433, 434, 443
environment damage, 38, 41, 44–46

equilibrium diagrams, 10, 66–73, 75, 76, 78, 113, 121, 173, 216, 603
equivalent circuits, 453–456
ESCA. *See* electron spectroscopy for chemical analysis (ESCA)
ESM. *See* electrochemical strain microscopy (ESM)
eutectic composition, 67, 68, 89, 603
exchange reactions, 34, 484
extended Pilling-Bedworth ratios (EPBR), 250, 251
extended x-ray absorption fine structure, 416–417
external hydrogen embrittlement, 284

face-centered cubic structures, 52
fatigue, 2, 18, 20, 91–97, 313, 325, 357, 358, 480, 496, 532, 538, 540, 552, 556, 600, 603, 613
fatigue failures, 93, 94
FECO. *See* fringes of equal chromatic order (FECO)
femtochemistry, 428
fermi level, 142, 143, 149, 185, 186, 403, 424, 425, 468–470
ferrite, 6–11, 15, 17, 73–79, 86, 273, 280, 369, 521, 535, 564, 565, 580, 598, 601, 603, 609, 613, 614
ferritic stainless steels (FSS), 4, 9, 10, 13–15, 225, 267, 271, 273, 460, 515, 519–523, 565, 589
fibers, 22, 25, 39, 41, 63, 64, 92, 95, 403, 459, 534, 554, 556, 562, 563, 578, 588, 590, 603
films, 2, 77, 110, 132, 157, 173, 196, 252, 277, 284, 297, 326, 341, 367, 400, 489, 513, 551
fireclays, 21, 23, 578
first Fick's law, 149, 180
Fischer-Tropsch gas-to-liquid, 256
Fisher model, 159
fission cross-section, 537, 600
fluorescence, 399, 401, 428, 429, 434, 441
fluorescence microscopy, 429
fluorescent penetrant inspection (FPI), 440, 603
fluorochrome, 429
force modulation microscopy (FMM), 427
force modulation SFM, 427
forming, 1, 2, 7, 13, 14, 18, 25, 28, 31–35, 37, 73, 74, 87, 112, 119, 196, 211, 219, 220, 227, 229, 235, 253, 254, 257, 266, 278, 282, 290, 292, 293, 312, 325, 334–336, 342, 353, 364, 368–370, 378, 380, 410, 418, 464, 468, 477–479, 482, 484, 489, 491, 496, 498, 499, 503, 509, 513, 515, 520, 521, 541, 551, 562, 563, 581, 597–599
fourier transform, 413, 416, 435–436, 456
fourier transform infrared spectroscopy (FTIR), 435–436, 442, 608
FPI. *See* fluorescent penetrant inspection (FPI)
fracture, 9, 14, 18, 22, 30, 31, 53–55, 63, 64, 80, 81, 83, 87–89, 91–97, 163, 207, 214, 253, 255, 258, 259, 279, 301, 304, 417, 493, 494, 497, 523, 535, 538, 555, 562, 586, 598–602, 604, 605, 607, 612–614
Frank-Turnbull mechanism, 149
free energy-concentration diagrams, 103–110
Frenkel disorder, 132, 134, 202
Fresnel equations, 432
friction force microscopy (FFM), 427
fringes of equal chromatic order (FECO), 426, 427, 462
FSS. *See* ferritic stainless steels (FSS)
FTIR. *See* fourier transform infrared spectroscopy (FTIR)
fuel cans, 26

galvanic cells, 78, 181, 186, 188, 564, 565
gaseous hydrogen embrittlement, 285
gas turbines, 1, 5, 16, 19, 20, 24, 30, 31, 40, 119, 171, 178, 197, 223, 227, 228, 233, 240, 280, 290, 296, 297, 318, 319, 321, 340–342, 344, 345, 349–374, 477, 479–482, 488, 491, 496, 497, 499, 502, 503, 605
GDOES. *See* glow discharge optical emission spectrometry (GDOES)
geometrical monitoring, 393
glasses, 29, 297, 392, 417, 444
glow discharge optical emission spectrometry (GDOES), 445, 604
grain boundaries, 2, 15, 16, 19, 20, 26, 29, 32, 55, 56, 59, 60, 75, 79, 83–86, 88–90, 92, 93, 130, 146, 158–160, 181, 196, 202, 205, 206, 212, 220–224, 228, 236, 247, 249, 251, 257, 259–261, 287, 290, 293, 294, 298, 304, 305, 326, 327, 329, 330, 336, 346, 352, 354, 370, 375, 401, 413, 442, 454, 456, 478, 479, 498, 508, 512, 520, 535, 536, 545, 553, 596, 602, 604, 607, 611
grain growth, 15, 20, 57, 59, 77, 89–91, 159, 160, 205, 212, 277, 517
grain structure, 20, 57, 58, 60–62, 76, 90, 370, 487, 611
graphitization, 6, 7, 77–78, 255–257, 260, 604
gravimetric monitoring, 393
gray cast iron, 63, 78, 582, 605
green rot, 3, 30, 251, 253, 258, 259, 340, 605
Griffith Microcrack theory, 91

half life, 167, 537, 605
hall coefficient, 166, 241, 605
halogenation, 100, 171, 265, 276–282, 605
halogens, 28, 34, 100, 171, 265, 276–282, 307, 392, 399, 436, 605
hardness, 8, 62, 76, 77, 80–82, 87, 88, 90, 214, 264, 273, 285, 333, 334, 392, 401, 427, 491, 493, 496, 538, 574–576, 612
hart equation, 205
Haycock-Loriers model, 213
Haynes, 18, 26, 27, 306, 313, 341, 354, 511, 583, 587, 588
HDCFC. *See* hybrid direct carbon fuel cells (HDCFC)
heat treatment, 1, 5, 7, 13, 20, 24, 29, 40, 56, 62, 63, 76–77, 79, 88, 215, 224, 245, 285, 287, 297, 305, 325, 351, 352, 369, 411, 477–479, 481, 483, 488, 495, 513, 516, 523, 556, 613, 614
Hedvall effect, 35
hexagonal close packed structures, 50
high resolution transmission electron microscopy (HRTEM), 159, 409, 413–414
high strength low alloy steel (HSLA), 79, 606
high temperature, 1, 48, 100, 130, 146, 171, 196, 236, 246, 264, 276, 284, 296, 329, 340, 361, 391, 477, 502, 551
high temperature alloys, 1, 2, 16–18, 87, 101, 196, 207, 224, 239, 240, 266, 330, 341, 352, 492, 496, 511
high temperature NOx reduction (HTNR), 386
hole, 33, 36, 48, 50, 51, 53, 54, 56, 58, 62, 66, 73, 94, 95, 130, 131, 133, 135, 139, 142, 143, 163, 179, 184–187, 189–191, 193, 194, 220–222, 234, 242, 243, 255, 267, 277, 279, 280, 410, 429, 488, 533, 542, 561, 612
Hooke's law, 54, 80
hot corrosion, 3, 19, 29, 31, 40, 115, 119, 223, 224, 253, 282, 296, 316, 340–358, 371, 374, 479, 480, 492, 496–499, 515, 516, 564, 606
hot working, 90, 227, 599, 606, 614
HRTEM. *See* high resolution transmission electron microscopy (HRTEM)
HSLA. *See* high strength low alloy steel (HSLA)
hybrid direct carbon fuel cells (HDCFC), 310, 528

hybrid solutes, 148, 158
hydrogen
  attack, 3, 39, 238, 267, 284, 288, 289
  4bond, 4, 606
  damage, 284, 285, 288, 289
  embrittlement, 284, 285, 602, 607, 613

impedance, 37, 178, 319, 320, 400, 439, 440, 453–456, 514, 529, 546, 602, 604
imperfections, 48–56, 65, 79, 84, 86, 92, 94, 130, 143, 160, 202, 204, 205, 234, 368, 477, 601, 607
impurity diffusion, 146, 151, 158, 159
impurity diffusion coefficients, 151
incandescence, 428
infrared imaging, 286, 441, 607, 611
infrared reflection absorption spectroscopy (IRRAS), 462
infrared spectroelectrochemistry (IRSEC), 461–462
in furnace NOx reduction (IFNR), 386
insulating refractories, 22
interaction volume, 410, 411
intercalation, 34
interdiffusion coefficient, 151–154, 156, 478
interferogram, 435, 436
interferometric techniques, 427, 443, 607
intergranular fracture, 93, 535, 607
intergranular penetration, 28, 329, 338, 352, 353
intermetallics, 15, 18–20, 25, 29, 31, 37, 60, 71, 223, 239, 312, 325, 326, 329, 331–333, 335, 358, 484, 486, 491, 493, 498, 508, 513, 516
internal disorder, 134, 140
internal hydrogen embrittlement, 284
internal oxidation, 7, 27, 101, 214, 218, 219, 228, 259, 293, 294, 298, 312, 322, 391, 520, 536, 607
international thermonuclear experimental reactor, 532, 593
interstitials, 24, 25, 48, 51, 53–55, 66, 73, 75, 76, 79, 86–88, 130–135, 137–139, 146–149, 158, 160, 161, 181, 202–204, 209, 220–222, 237, 241, 277, 279, 280, 292, 293, 607, 612
interstitial solid solution, 55, 66, 76, 86, 88, 146, 607, 612
intrinsic diffusion coefficients, 153, 155
intrinsic ionization, 135, 138–140, 142, 143
intrinsic semiconductors, 185, 220
inverse spinels, 33
ionic bond, 608
iron, 2, 48, 101, 157, 173, 196, 237, 245, 264, 278, 287, 297, 325, 354, 361, 418, 482, 551
iron-carbon equilibrium system, 72–76
IRSEC. *See* infrared spectroelectrochemistry (IRSEC)
isoconcentration diffusion, 149
isocorrosion diagrams, 372, 373

kaolinite, 21, 366
Kellogg's Method, 276, 608
Kick-out mechanism, 148, 149, 158
Kirkendall effect, 146, 153–155, 298, 608
Kirkendall velocity, 153
Knudsen gas, 397, 398
Knudsen number, 397, 398

Langmuir equation, 209
lateral force microscopy (LFM), 424, 427–428
laves phases, 18, 19, 25, 520
law of levers, 67, 75, 608
LDR. *See* limiting drawing ratio (LDR)
LEED. *See* low-energy electron diffraction (LEED)
LEELS. *See* low-energy electron loss spectroscopy (LEELS)
LEEM. *See* low-energy electron microscopy (LEEM)
limiting drawing ratio (LDR), 13, 14
line imperfections, 54–55, 84
liquid metal cooled fast breeder reactor (LMFBR), 533, 541, 588
longini mechanism, 149
low-alloys steels, 4, 5, 7–9, 32, 79, 89, 102, 207, 256, 257, 284, 285, 305, 379, 386, 387, 606, 608
low-energy electron diffraction (LEED), 31, 402–404, 415
low-energy electron loss spectroscopy (LEELS), 423–424
low-energy electron microscopy (LEEM), 409, 414–415, 424
luminescence, 428–429, 437, 443, 610

Magneli phases, 34
magnesite, 21, 32, 33, 307, 371, 383
manometric monitoring, 393
martensite, 10, 12–15, 76–79, 273, 369, 580, 598, 601, 608, 614
martensitic stainless steels, 14, 273
Matano plane, 153–155
M_d Values, 13
mechanical strength, 21, 23, 300, 477, 532, 542, 544, 612
metal dusting, 3, 17, 40, 245–261, 517, 608
metallic bond, 4, 53–54, 442, 608, 613
metalliding, 495, 608
metallurgical structures, 48–98, 226, 351
metal recession, 206, 221, 277–279, 608
metastable solid solutions, 69
Michelson interferometer, 435
microalloyed castings, 251
microstructure, 4, 5, 7, 9–11, 15, 18, 19, 63, 71, 74, 75, 79, 81, 90, 97, 163, 214, 221, 223, 227, 273, 276, 289, 290, 293, 401, 412, 478, 479, 482, 492, 496–498, 516, 535, 544, 565, 597, 598, 602, 603, 608–610, 613
mid-infrared reflectance (MIR), 441–442, 608
Miller indices, 49, 51, 609
MIR. *See* mid-infrared reflectance (MIR)
modified McConomy curves, 238
mohs scale, 82
molten-carbonate fuel cell (MCFC), 256, 309–312, 503–516, 525–528, 609
molten metals, 3, 19, 29, 56–58, 64, 296, 321, 322, 325–339, 491, 528–530, 539, 540
molten salts, 3, 28–29, 34, 39, 40, 59, 126, 171–173, 178, 179, 281, 296–322, 342, 351–357, 364, 367, 368, 371, 379, 380, 389, 447, 449, 495, 508, 529–530, 534, 539, 540, 542–545, 588, 608
mullite, 21, 300–303, 392

Nelson curve, 285–287
Nernst-Einstein equation, 205
network solids, 183
neutral refractories, 21
neutron scattering, 402, 406–409, 417, 430, 431, 537
nickel-based alloys, 16–17, 28, 29, 72, 239, 255, 258, 259, 261, 265, 267, 280, 303, 304, 308–310, 318, 319, 333, 335–338, 341, 343, 344, 351, 352, 363, 379, 392, 482, 496, 511, 519, 536, 537, 553, 583
nickel-iron alloys, 16
nitridation, 17, 28, 39, 100, 171, 264–273, 497, 608
nitriding, 17, 215, 264, 265, 267, 268, 271–273, 307, 502, 599
nitrogen, 9, 10, 17, 24, 27–29, 35, 79, 146, 197, 215, 223, 236, 238, 253, 264–269, 271–273, 291, 303, 305, 307, 329, 330, 332, 334, 336, 337, 365, 385, 387, 421, 459, 534, 542, 566, 588, 590, 607
normal pulse voltammetry (NPV), 41, 42, 450
notch toughness, 95
NPV. *See* normal pulse voltammetry (NPV)
n-type, 32, 35, 36, 133, 164, 166, 181, 184, 185, 202, 203, 209, 210, 212, 220, 222, 235, 237, 240, 241, 327, 338, 409, 479, 496, 522

n-type conductors, 133
nuclear reactor materials, 25–26, 537, 542
nuclear reactors, 25–26, 28, 31, 223, 296, 325, 407, 502, 531–542

oil-ash corrosion, 373, 374, 378, 379, 388
OPD. *See* optical path difference (OPD)
open metals, 158
open static reaction vessels, 396
optical microscopy, 56, 84, 392–395, 400, 411, 413, 426
optical path difference (OPD), 435, 436
optical texture, 394, 395, 411
optical texture index (OTI), 394, 395
ostwald ripening, 219
OTI. *See* optical texture index (OTI)
over fire air ports (OFA), 385
oxidation rate constant, 212
oxide cracking, 37
oxide-dispersion strengthened, 226
oxides of carbon, 27–28
oxidizing Potential–Basicity diagram, 120–128
oxygen, 2, 59, 101, 130, 146, 171, 196, 239, 247, 264, 276, 287, 297, 329, 340, 362, 396, 479, 504, 552
oxygen deficient, 132–135, 137–139, 222

PAFC. *See* phosphoric acid fuel cell (PAFC)
paralinear oxidation, 213
passivation, 112, 126, 127, 173, 177, 276, 297, 299, 304, 307, 308, 318–320, 345, 346, 354, 462, 467, 481, 596
pearlite, 6, 63, 72–75, 78, 247, 564, 565, 598, 609
pesting, 3, 610
phase diagram, 7, 10, 11, 21, 77–79, 106, 107, 115, 237, 256, 276, 327, 329, 331, 335, 337, 345, 349, 350, 484, 485, 545, 560, 610
phase of thermal emission spectroscopy, 441, 610
phase stability diagrams, 100, 112–115, 117–119, 257, 310
phonon dispersion curve, 430
phosphorescence, 429, 434
phosphoric acid fuel cell (PAFC), 504
photoacoustic technique, 441, 610
photoassisted metal to adsorbate charge transfer, 469
photo-emission, 400, 417–418
Photo-excitation, 184
photoluminescence piezospectroscopy (PLPS), 442–443, 610
photon, 185, 399, 402, 411, 416–418, 428–430, 433, 434, 437–439, 443, 467, 469, 470, 492, 610
physisorption, 209
piezospectroscopic effect, 443, 610
Pilling-Bedworth ratio, 206, 207, 250
plane defects, 130
plane imperfections, 55
plastic deformation, 37, 63, 80–82, 84–88, 92, 96, 157, 163, 164, 207, 279, 285, 292, 520, 598, 601, 602, 610, 612
PLPS. *See* photoluminescence piezospectroscopy (PLPS)
pO^{2-}, 120, 121, 124–128, 173, 175–178, 297–300
point defect, 25, 34, 35, 130–133, 135–141, 143, 146, 152, 158, 160, 161, 202–205, 208, 209, 221, 236, 242, 290, 291, 611
point imperfections, 54
Poisson's ratio, 207, 538, 578
polaron hopping, 205
polycrystalline metals, 80, 81, 83, 86, 599, 604
position-sensitive photodetector (PSPD), 428
potential–pO^{2-}diagrams, 124
potentiometry, 311, 446
precipitation hardening, 62, 63, 71, 79, 87–89, 611
pressurized water reactor (PWR), 532, 541, 542, 588
principle of electroneutrality, 131, 137
proton exchange membrane fuel cell (PEMFC), 504
p-type, 32, 35, 36, 133, 161, 165, 166, 181, 183–185, 203, 209, 210, 212, 220, 222, 237, 240, 241, 293, 496, 508, 522
p-type conductors, 133, 161
pulse-echo thermal wave infrared imaging, 441, 611
PWR. *See* pressurized water reactor (PWR)

quarter wave plate, 432

radiation damage, 25, 26, 401, 611
raman scattering, 430, 468
Rayleigh number, 397
Rayleigh scattering, 430, 431
recovery, 25, 40, 42, 86, 89–91, 179, 341, 361, 479, 512, 525, 546, 605
recrystallisation, 37, 71, 79–91, 159, 301, 304, 606, 611
reflection high-energy electron diffraction (RHEED), 402–406
refractive indices, 432, 442
refractories, 1, 5, 20–23, 27, 29, 305, 325, 334
refractory containers, 21, 334
refractory metals, 4, 5, 23–24, 89, 223, 224, 236, 296, 297, 303, 305, 330, 336, 350, 351, 479, 495, 496, 556, 608, 611
relative sensitivity factors (RSFs), 421
Reynolds number, 326, 331, 397, 601
RHEED. *See* reflection high-energy electron diffraction (RHEED)
rotating disk electrode (RDE), 451, 452, 457
rotating ring-disk electrode (RRDE), 452
Rutherford backscattering, 393, 399, 420

safety, 16, 38, 41, 44–46, 215, 284, 477, 531, 532
SANS. *See* small angle neutron scattering (SANS)
scales, 2, 82, 101, 146, 171, 196, 233, 247, 264, 276, 287, 299, 341, 361, 391, 477, 502, 556
scale-forming regime, 32–33
scanning electrochemical microscopy (SECM), 300, 459–461, 469
scanning force microscopy (SFM), 425, 427
scanning probe microscopy (SPM), 425, 471
scanning tunneling microscope (STM), 425, 426, 466–469
scattering length, 406, 408, 409
scattering length density, 408, 409
SCC. *See* stress-corrosion cracking (SCC)
Scherrer equation, 402
Schöttky disorder, 132, 202
SCR. *See* selective catalytic reduction (SCR)
SECM. *See* scanning electrochemical microscopy (SECM)
secondary electron emission (SEE), 423
secondary ion mass spectrometry (SIMS), 307, 392, 398–401, 420–422
second Fick's law, 149
second harmonic generation, 436, 438, 467
second order susceptibility, 438, 439
seebeck or peltier coefficient, 241
selective catalytic reduction (SCR), 269–271, 273
selective oxidation, 101, 197, 219, 224, 256, 260, 279, 284, 290, 291, 370, 520
self-diffusion, 147–151, 157, 159, 160, 163, 204, 205, 211, 213, 220, 241, 278, 282, 377
self-diffusion coefficient, 150, 151, 157, 204, 205, 211, 213, 220, 241, 278, 282
Selmatel, 45
semiconductors, 6, 41, 142–144, 158, 164, 167, 181, 183–186, 189, 202, 203, 209, 210, 220, 222, 237, 240, 241, 293, 418, 429, 477, 481, 493, 502, 556, 560, 563, 605, 614
semiconductor electrodes, 183, 186
separator plate, 311, 508–510
SERS. *See* surface-enhanced raman spectroscopy (SERS)

SFA. *See* surface force apparatus (SFA)
SFG. *See* sum-frequency generation (SFG)
SFM. *See* scanning force microscopy (SFM)
shear modulus, 81, 84, 538
shearography, 444, 611
short-circuit diffusion, 36, 130, 205, 206, 212, 277, 611
sillimanite, 21, 303
SIMS. *See* secondary ion mass spectrometry (SIMS)
single crystal, 20, 32, 34, 57, 80, 82–86, 89, 91, 93, 157, 162, 223, 224, 294, 297, 356, 375, 402, 405, 424, 443, 458, 467, 484, 500, 557, 579, 612
slip mechanisms, 18, 82–84
small angle neutron scattering (SANS), 408, 409
SOFC. *See* solid-oxide fuel cell (SOFC)
solidification, 9, 10, 20, 54–62, 67, 69, 71, 89, 90, 223, 224, 340, 553, 597, 601, 603
solid-oxide fuel cell (SOFC), 162, 256, 503, 504, 509, 516–529, 531
solid solutions, 16–20, 24, 55, 62, 64–67, 69, 71, 73, 74, 76, 78, 79, 86–89, 94, 97, 106, 107, 109, 110, 137, 146, 155, 216–218, 223–226, 239, 242, 273, 332, 336, 351, 369, 370, 484, 498, 552, 554, 597, 603, 607, 611–613
solid solution strengthening, 18, 24, 79, 87, 88, 224–226, 239, 369
solid-state reactions, 34, 35, 130, 160, 247, 259, 314, 378, 497, 612
solid-state voltammetry, 453, 457–459
spalling, 17, 21, 22, 33, 110, 206–208, 228, 265, 284, 292, 293, 308, 356, 357, 480, 499
spalling resistance, 17, 21
spectral searching, 435
spinels, 9, 32, 33, 35, 207, 218, 220, 222, 251, 253, 258–260, 272, 282, 290, 293, 294, 305, 342, 401, 418, 496, 497, 520, 523, 524
SPM. *See* scanning probe microscopy (SPM)
square wave voltammetry (SWV), 300, 451
stainless steel, 4, 58, 116, 225, 248, 264, 280, 285, 298, 325, 378, 393, 493, 502, 551
static atmospheres, 393
steam, 1, 6, 15, 16, 26, 27, 30, 39, 119, 223, 245, 252, 254, 256, 284, 287, 290, 291, 336, 341, 361–364, 367, 369–371, 380–388, 502, 503, 509, 531, 533, 534, 540, 541, 543, 564, 588, 598, 603, 604
steel, 4, 51, 102, 157, 197, 238, 245, 264, 280, 284, 298, 325, 340, 361, 393, 482, 502, 551
stellite, 18, 26, 27, 341
STM. *See* scanning tunneling microscope (STM)
stoke's shift, 428
strain, 9, 13, 19, 21, 23, 64, 75, 79–82, 85–90, 95–97, 140, 157, 163, 206, 207, 222, 248, 273, 304, 384, 402, 415, 427, 471–472, 499, 504, 552, 586, 599–602, 606, 607, 610, 611, 614
strain ratio, 13
stratified scales, 213–214
strengthening, 5, 16–20, 24, 35, 62, 75, 79, 87–88, 90, 223–227, 239, 352, 369, 519, 601, 612
strengthening mechanisms, 5, 19, 35, 79, 88
stress, 7, 54, 158, 198, 234, 250, 276, 285, 304, 325, 340, 363, 392, 479, 508, 552
stress-corrosion cracking (SCC), 15, 61, 62, 304, 308, 380, 386, 456, 515, 536, 540, 541, 612
structural defects, 130, 610
structure of alloys, 60, 64–66
substitutional solid solution, 65, 79, 87, 613
sulfidic corrosion, 238
sulfur-containing gases, 28, 340, 367
sum-frequency generation (SFG), 436–439
superalloys, 4, 5, 16, 19–20, 24, 25, 79, 89, 222–224, 226, 227, 254, 284, 290, 293, 294, 318, 321, 340–343, 350, 352–354, 356–358, 479, 482, 484, 497, 498, 500, 552–554, 576, 578, 579, 581, 583, 598
supercooling, 57, 59, 613
surface-enhanced raman spectroscopy (SERS), 468–470
surface force apparatus (SFA), 424, 426–427, 462
Swift cup test, 13, 14
SWV. *See* square wave voltammetry (SWV)
system Fe/Na_2SO_4 at 900°C, 127

tarnishing, 34, 551
TEM. *See* transmission electron microscopy (TEM)
tensile strength, 8, 75, 364, 520, 536, 538, 574–576, 583–586, 599, 613
thermal conductivity, 6, 12, 15, 21–23, 25, 26, 325, 326, 363, 364, 371, 397, 441, 480, 496, 500, 519, 536, 538, 554, 555, 576, 578, 579, 582, 583, 613
thermal excitation, 184, 185, 434
thermal expansion coefficient, 524, 538
thermal neutron absorption cross-section, 537
thermal neutron scattering cross-section, 537
thermal shock, 7, 21–23, 300, 301, 326, 349, 366, 481, 613
thermal stress, 23, 206, 207, 386, 479, 498, 554, 613
thermal wave interferometry (TWI), 444, 614
thermochemical analysis, 100–119
thermoelectric power, 130, 241, 609, 611, 614
thermogravimetric monitoring, 393
thermogravimetry, 199, 261, 353, 355, 387, 391–398, 401, 436, 464
thin-film regime, 31–32
threshold response, 185
time temperature transformation diagrams, 614
time value of money, 41, 44
titanium alloys, 24, 61, 62, 96, 332
topologically closed packed phases, 223
topotactic reaction, 34
toughness, 2, 5, 7, 9, 15, 91, 95–97, 251, 254, 325, 369, 519, 535, 536, 538, 552, 554, 555, 562, 602, 604, 607, 613, 614
TPB. *See* triple-phase boundary (TPB)
tramp elements, 223
transference number, 191, 192, 194, 277, 278, 447, 614
transfer resistance, 319, 454
transformation induced plasticity steels (TIPS), 79
transmission electron microscopy (TEM), 159, 282, 392, 399–401, 409, 411–414, 426
Tribaloy alloys, 18
triple-phase boundary (TPB), 508, 517, 518, 526, 528
Turkdogan's method, 276, 614
TWI. *See* thermal wave interferometry (TWI)

ultrasonic testing, 440, 614
upper tensile stress (UTS), 81

vacancies, 25, 54, 130, 146, 181, 202, 234, 277, 291, 298, 370, 401, 497, 508, 559
vacancy sink model, 521
vacuum "aging" of the scale, 277
valence band, 135, 142, 143, 184, 185
van der Waals adsorption, 209
van der Waals bond, 4, 614
vapor species diagrams, 100, 110–112, 198, 608
very high temperature reactor (VHTR), 534, 588
Vitallium, 18

Wagner-Hauffe rules, 221, 222
Warburg impedance, 454
Wavelength-Dispersive X-Ray Spectroscopy (WDS), 411
websites for HTC, 45
wet-seal, 510–513, 516
white cast iron, 63, 78, 614
work hardening, 18, 62, 82, 87, 88
wrought alloys, 18, 63, 223, 226, 239, 254, 261, 614

XPS. *See* X-ray photoelectron spectroscopy (XPS)
X-ray photoelectron spectroscopy (XPS), 271, 272, 392, 398–401, 418–420

yield stress, 80–82, 84, 86, 87, 93, 94
young's modulus, 4, 80, 81, 91, 207, 536, 538, 578, 602

WILEY END USER LICENSE AGREEMENT

Go to www.wiley.com/go/eula to access Wiley’s ebook EULA.